

Prashant M. Pawar · Babruvahan P. Ronge ·
Ranjitsinha R. Gidde · Meenakshi M. Pawar ·
Nitin D. Misal · Anupama S. Budhewar ·
Vrunal V. More · P. Venkata Reddy *Editors*

Techno-Societal 2022

Proceedings of the 4th International
Conference on Advanced Technologies
for Societal Applications—Volume 2

Techno-Societal 2022

Prashant M. Pawar · Babruvahan P. Ronge ·
Ranjitsinha R. Gidde · Meenakshi M. Pawar ·
Nitin D. Misal · Anupama S. Budhewar ·
Vrunal V. More · P. Venkata Reddy
Editors

Techno-Societal 2022

Proceedings of the 4th International
Conference on Advanced Technologies for
Societal Applications—Volume 2

 Springer

Editors

Prashant M. Pawar
SVERI's College of Engineering
Pandharpur
Pandharpur, Maharashtra, India

Babruvahan P. Ronge
SVERI's College of Engineering
Pandharpur
Pandharpur, Maharashtra, India

Ranjitsinha R. Gidde
SVERI's College of Engineering
Pandharpur
Pandharpur, Maharashtra, India

Meenakshi M. Pawar
SVERI's College of Engineering
Pandharpur
Pandharpur, Maharashtra, India

Nitin D. Misal
SVERI's College of Engineering
(Polytechnic), Pandharpur
Pandharpur, Maharashtra, India

Anupama S. Budhewar
SVERI's College of Engineering
Pandharpur
Gopalpur, Maharashtra, India

Vrunal V. More
SVERI's College of Pharmacy
Pandharpur
Pandharpur, Maharashtra, India

P. Venkata Reddy
Amity University
Dubai, United Arab Emirates

ISBN 978-3-031-34647-7 ISBN 978-3-031-34648-4 (eBook)
<https://doi.org/10.1007/978-3-031-34648-4>

© The Editor(s) (if applicable) and The Author(s), under exclusive license to Springer Nature Switzerland AG 2024

This work is subject to copyright. All rights are solely and exclusively licensed by the Publisher, whether the whole or part of the material is concerned, specifically the rights of translation, reprinting, reuse of illustrations, recitation, broadcasting, reproduction on microfilms or in any other physical way, and transmission or information storage and retrieval, electronic adaptation, computer software, or by similar or dissimilar methodology now known or hereafter developed.

The use of general descriptive names, registered names, trademarks, service marks, etc. in this publication does not imply, even in the absence of a specific statement, that such names are exempt from the relevant protective laws and regulations and therefore free for general use.

The publisher, the authors, and the editors are safe to assume that the advice and information in this book are believed to be true and accurate at the date of publication. Neither the publisher nor the authors or the editors give a warranty, expressed or implied, with respect to the material contained herein or for any errors or omissions that may have been made. The publisher remains neutral with regard to jurisdictional claims in published maps and institutional affiliations.

This Springer imprint is published by the registered company Springer Nature Switzerland AG
The registered company address is: Gewerbestrasse 11, 6330 Cham, Switzerland

Paper in this product is recyclable.

Preface

The technologies developed without consideration of social needs will not have a major impact on society. The useful societal technologies can only be developed through the interactions of an inspired and intellectual community having the background of science and engineering. The main goal of these interactions should be to develop techno-societal products, processes and technologies. During these interactions, one may propose the technology for a particular domain or a region, which can be extended to other similar domains as well as regions. On the other hand, some of the theoretical researchers may have essential knowledge and theories, and through these interactions, applications of those technologies can be evolved. The applications developed through such interactions will not only create an impact by solving the societal problems but will also help in making these products sustainable. Some groups working closely for solving societal problems may be in need of technologies which can be identified through such multidisciplinary interactions. SVERI's College of Engineering has initiated these interactions under the series of International Conferences organized in alternate years with the title 'Techno-Societal'. Great response to the proceedings of our First International Conference 'Techno-Societal: 2016' was observed when articles of these proceedings were accessed more than 114,000 times. In the subsequent Second International Conference 'Techno-Societal: 2018', the combined number of accesses for volume 1 and volume 2 was more than 139,000. In the Third International Conference 'Techno-Societal: 2020', the accesses have crossed 87000 till date for both the volumes. The editorial team has decided to publish the proceedings of the Fourth International Conference 'Techno-Societal: 2022' in two volumes.

This book is a compendium of selected and best papers presented on December 9 and 10, 2022, during the international conference 'Techno-Societal: 2022' organized by SVERI's College of Engineering, Pandharpur, India. In this fourth International Conference on Advanced Technologies for Societal Applications, more than 375 full papers of original works and 18 keynote addresses were presented from various areas of technology. The conference has offered various sessions under its name. Selected 208 papers are being published in the two volumes. The Volume 2 is classified into following six topical areas:

1. Advanced Technologies for Water, Energy, Transportation, Housing and Sanitation.
2. Advances in Pharmacy, Nutraceuticals and Traditional Medicines.
3. Chemical and Physical Processes.
4. Deployable Environment or Health Care Technologies.
5. Mechatronics, Micro-Nano Related for Bio and Societal Applications.
6. Advanced Assessment Employees and Employment Sectors.

Pandharpur, India

Prashant M. Pawar

Pandharpur, India

Babruvahan P. Ronge

Pandharpur, India

Ranjitsinha R. Gidde

Pandharpur, India

Meenakshi M. Pawar

Pandharpur, India

Nitin D. Misal

Pandharpur, India

Anupama S. Budhewar

Pandharpur, India

Vrunal V. More

Dubai, United Arab Emirates

P. Venkata Reddy

Contents

Advanced Assessment of Various Employment Sectors	
A Consumers Approaches Towards Online Shopping in India: Challenges and Perspectives	3
Savita Pramod Vaidya	
Determinants of Dividend Policy: Evidence from Indian Pharma Sector	13
Himanshu Jain, Vijay Anant Athavale, and Akhilesh Kumar Mishra	
Biophilic Architecture: Meeting the Wellbeing Standards of Employees	23
Pratima Kiran Mandadi, Manjari Khanna Kapoor, Ramesh Raghavendran, and Aanchal Sharma	
An Analysis of Emerging Trends of Corporate Governance in India	35
Pramod Damodar Vaidya	
An Assessment of the Influences of Information Technology on Higher Education Curriculum in India	45
Santosh Gopal Kulkarni	
Advanced Technologies for Water, Energy, Transportation, Housing and Sanitation	
Ultrasonic Assisted Electrochemical Machine: A Review	57
Aniket B. Pawar, Pradeep V. Jadhav, D. B. Jadhav, and D. S. Bilgi	
Computational Studies on Selection of EV	65
Nitish Vernekar, Atulchandra Tripathi, Tushar Patel, Umesh Hosmani, Prashant Revankar, and Krishnaraja Kodancha	

Analysis of Spatio-temporal Characteristics of Rainfall Using Precipitation Concentration Index (PCI) and Heatmap for Solapur District of Maharashtra, India	73
Wasim Ayub Bagwan	
Forecasting of PM₁₀ Concentrations in Indian Medium-Sized City Using New Combined Grey Model	87
Sagar Shinde and Vilas Karjinni	
Transmission Line Fault Detection and Classification: ANN Approach	97
Vaibhav A. Ghodeswar and Mirza A. Beg	
Review on Smart Digital Technologies in Construction Sector	107
Pandurang Bhise, Yash Annapurne, Kuldip Lalge, Samarth Patil, and Rohan Sawant	
Testing Strength of Grassed Paver Block Made by Waste Material and Coir Fibre	119
Anil Shirgire, Hemchandra Pawar, Satyawan Jagdale, Ravikant Sathe, Vijaykumar Javanjal, and Swati Ambadkar	
Performance Evaluation of Kota's Black Soil Using Perma-Zyme	125
Jitendra Kumar Sharma and Sakshi Khandelwal	
RULA and REBA's Evaluation of the Work Posture of the Power-Loom Industry: A Case Study	137
S. G. Kolgiri, M. D. Jagtap, and S. L. Sathe	
Experimental Investigation on Injection System of Diesel Engine for Material Compatibility with Waste Cooked Oil Biodiesel	147
Rajesh Gurani, Malikasab Bagawan, and Prashant Tadalagi	
Traffic Sign Recognition System Using YOLO: Societal System for Safe Driving	157
Kuldeep Vayadande, Rohit Patil, Ayush Patni, Pavankumar Bhadane, Siddhant Pawar, Rahul Ponnuru, and Varad Ingale	
A Review on Performance of Annular Raft Foundation	167
Ajay Pratap Singh Rathor and Jitendra Kumar Sharma	
A Novel Intelligence System for Accident Prevention, Detection, and Reporting System for Smart City	175
Poornima Mallur, Shree Umarani, Shree Umarani, and Salma S. Shahapur	
Waste Water Treatment by Using Constructed Wetlands	183
Anil Shirgire, Hemchandra Pawar, Satyawan Jagdale, and Ravikant Sathe	

Seismic Analysis of Water Tank with Different Configuration to Find Optimal Solution 195
 Sandip Nirmal, Prashant M. Pawar, and Ravikiran P. Jadhav

Low Cost Housing Structure Using Bamboo as Reinforcement 203
 Aishwarya S. Ingawale, Prashant M. Pawar, Sonali P. Patil, and Ravikiran P. Jadhav

Techniques to Share and Store Large Data in Used System to Reduce Network Traffic and Cost 211
 Punam S. Kamble and Namdev M. Sawant

Ultra-Fast Charging Challenges in Grid Connected Charging Station: A Review 221
 Nilam S. Patil and Rajin M. Linus

Sustainable Integrated Renewable Energy System for a Cluster of Remote Villages in Indian Context 231
 Naveen Rayaral and Prashanth P. Revankar

Overview of Autonomous Vehicle and Its Challenges 243
 Chinmay Amrutkar, Anushka Satav, Puskaraj D. Sonawwanay, and Ashish H. Pawar

Identification and Protection of Landslide Prone Areas in Karul Ghat Region 253
 Rohan Sawant

Indian Scenario of Electric Vehicles—A Review 261
 Niket B. Adhia, Shikhar R. Takke, and Puskaraj D. Sonawwanay

Enhancement of Power Quality Approach Using Unified Power Quality Conditioner 271
 Buddhapriy B. Gopnarayan and Vijay A. Sawant

Design and Analysis of GFRP and Chicken Mesh Confined Brick Masonry Columns 281
 Mrunal M. Pawar, Mukund M. Pawar, and Sonali P. Patil

Effect of Fly Ash and Ground Granulated Blast Furnace Slag on Fracture Parameters of Sustainable Concrete 295
 Sudhanshu S. Pathak and Gaurang R. Vesmawala

Trip Generation and Trip End Modal Split Modelling for East Zone of Surat City 305
 Omkar Bidkar, Ravikiran Jadhav, Prashant Bhaganagare, Ravikant S. Sathe, and Mangesh Survase

Improving Conversion Efficiency of Solar Panel by Cooling System 315
 Suryaji S. Kale, S. S. Gawade, and B. R. Birajdar

Influence of Accessibility Factors on Travel Mode Choice in an Emerging Metropolitan City, Surat	327
Yogesh Survase, Omkar Bidkar, Nitin More, Girish Falmari, Satyawan Jagdale, and Ravikant Sathe	
Categorizing and Ranking Comfort Design Requirements of Transportation Buses in India	333
A. B. Rathod and R. T. Vyavahare	
Use of Poly Contrast Interference Photography (PIP) for Energy Field Analysis of Concrete Pavement	343
Dipak M. Kolekar, Sunil S. Pimplikar, Rohit R. Salgude, Rohan R. Yadav, and Ashlesha S. Deshmukh	
Energy Generation System Through Solar and Fast-Moving Vehicles	361
Basavraj R. Birajdar and Suryaji S. Kale	
Machinability of Carbon Fiber Reinforced Silicon Carbide Composite Material—A Review	373
Sunilkumar Harsur, Ramdas Biradar, Pallavi Jadhav, Shital Waware, Kamalkishor Maniyar, and Pushparaj Warke	
Electric Vehicle Industry—Challenges and Opportunities	383
Asmita Saravade, Megha Burungal, Laxmi Brungi, Kiran Lakkam, and Amitkumar Shinde	
3D Printing in Construction Industry: A State of Art	389
Pruthviraj Zadbuke, Yogesh Patil, Nishad Sheje, Sahil Nachane, and Rohan Sawant	
Optimization of Car Tie Rod with the Help of Finite Element Analysis	399
Pramod Navale and Sameer Katekar	
Calculative Study for Fuel Cell Based Vehicle Propulsion	409
Siddharth Gandhi and Abhijeet Chavan	
Design Interventions Towards Optimization of Drive Features in Electric Bicycle in Adherence to ISO 4210	419
Theodore Mohandas Tatpati, Jeevith Arambooru, Krishnaraja Kodancha, and P. P. Revankar	
Solar Thermal Energy Storage Technology: Current Trends	429
Pravin Prabhu and Sanjay Sawant	
A Review on Material Compatibility on the Fuel Flow System of a Diesel Engine with Waste Cooked Oil Biodiesel	439
Rajesh Gurani, B. J. Patil, Malikasab Bagawan, and Prashant Tadalagi	

Boosting Performance with the Integration of Stochastic Energy Storage into Hybrid Electric Vehicles	449
Dipti Tamboli, Mohan Thakre, and Pranali Thakre	
Implications of Multiple Energy Source Integration for Electric Mobility	461
Dipti Tamboli, Mohan Thakre, and Pranali Thakre	
Advances in Pharmacy, Nutraceuticals and Traditional Medicines	
Design, In Vitro Evaluation of Sustained Release Matrix Tablet of Enalapril Maleate Employing Natural Polymer-Olibanum Gum and Its Resin Component	475
Pravin B. Awate, Mahesh K. Gupta, Dipak P. Kardile, Vishwas C. Bhagat, and Rajkumar V. Shete	
Optimization of Thermo-reversible Nasal Gel of Carbamazepine for Better Control in Chronic Epilepsy	487
Utkarsha S. Shivsharan, Avinsah H. Hosmani, and Yogesh S. Thorat	
Antimicrobial Activities of Organic Solvent Extracts of <i>Citrus aurentifolia</i>, <i>Eucalyptus globulus</i> and <i>Jasmine grandiflorum</i> Against Certain Microorganisms	495
Vaibhav Gaikwad, Anil Landge, Dharba Sastry, and Rushikesh Shelke	
Evaluation of Phytochemical, Antioxidant of <i>Fumaria parviflora</i> (Lam.) Methanolic Extract of Whole Plant by HPTLC Analysis	503
Madhu Singh, Shamshad Ather, Himanshu Gupta, Kapil Singh Thakur, and Mansee Thakur	
Treating Fungal Infections by Herbal Transdermal Patches	513
Sonam Toraskar, Vijay Chakote, Shweta Bahire, and Pooja Patil	
Current Advances in Tablet in Tablet as Drug Delivery System: A Review	519
Satish Vasant Mandave and Narendra Kumar Pandey	
Design and Optimization of Novel Floating Agent <i>Saccharomyces boulardii</i> Probiotic Formulation Based Floating Tablet of Valsartan	529
Chittam Suvarna and Bhosale Ashok	
Isolation and Characterization of Bioactive Compound from <i>Euphorbia pulcherrima</i> (Wild) Leaves	541
Prashali Shinde and Gurdeep Singh	
High Performance CeO₂ Nanoparticles for Real-Time NO₂ Detection	549
R. N. Dhanawade, N. S. Pawar, G. M. Hingangavkar, Y. M. Jadhav, T. M. Nimbalkar, M. A. Chougule, R. N. Mulik, and V. B. Patil	

Achieving Germ-Free Rejuvenation of Skin by Medicated Beauty Soap with Richness of Essential Oils	557
Pooja Patil, Mithun Maniyar, Pradnya Mane, Bhagyashree Yadav, and Pratiksha Mali	
In Silico Prediction and Screening of Potential Immunomodulators Using Autodock Vina	567
Snehal Kashid, Ashish Suttee, and Prasad Kadam	
Phytochemical Studies and Anticariogenic Activity of Some Folklore Plants for Dental Care	579
M. I. Mujawar, E. N. Gaviraj, and S. P. Ghunaki	
Evaluation of Ondansetron Hydrochloride Interactions with Mannitol	587
Mangala J. Khandekar, Swarup R. Lahoti, Ravindra G. Kulkarni, and Aasiya N. Choudhary	
Phytochemical Screening, Isolation, Characterizations of Stem Extract of <i>Parkinsonia Aculeate</i> Linn	597
Snehal Patil, Sunil More, Sneha Ghule, and Shweta Bahire	
Chemical and Physical Processes	
Tailored Synthesis of CuO/2D-BiVO₄ for Enhanced CO₂ Photoreduction to Methanol	607
Prasad Kulkarni, Aniruddha Chatterjee, Ganesh Kotiye, and Shravanti Joshi	
Synthesis and Evaluation of Some Fused Ring System of Thiazole for Their Antimicrobial Activity	615
Ramdas Naiknaware, Ravi Ajudia, Hemant Bansode, and Sweta Bahire	
Experimental and CFD Analysis of Heat Transfer Enhancement in Channel	627
Vaibhav H. Bansode and Munna Verma	
Heat Transfer Augmentation in Forced Convection with Regularly Spaced Inserts—A Review	637
Suryaji S. Kale and S. S. Gawade	
Thermoluminescence Studies in Europium Doped KSr₂Br₅ and CsBa₂I₅ Halide Phosphors	651
Chhagan D. Mungmode, Dhananjay H. Gahane, Chetan V. Chanmal, and Sanjiv V. Moharil	
Deployable Environment or Health Care Technologies	
Analysis and Design of Pyrolysis System for Islampur City	659
Shridhar Kumbhar and Priyanka Bamane	

Intermittent Water System—A Review of Literature	669
Nitin P. Sonaje and Mukund M. Pawar	
Extraction of Cellulase from Soil Microorganisms by Using Banana Peels as Substrate	677
Samir Pachpute, Chetan Pawar, and Sanjana T. Philip	
In Vitro Leaf Injection Method for Detecting the Pathogenicity of Pomegranate Bacterial Blight Pathogen	689
Mrudula M. Bendigeri, Girish R. Pathade, and Yasmin C. Attar	
Disha: The Facility Locator for the Disabled	695
Kuldeep Vayadande, A. Dhiwar, D. Khadke, R. Golawar, S. Khairnar, S. Wakchoure, S. Bhoite, and D. Prasad	
Face Mask Detection and Recognition Using CNN Deep Learning Models	707
Aniket Muley, Tukaram Navghare, and Vinayak Jadhav	
Ergonomics-Based Postural Assessment of Rural Water Fetcher	717
Sonalı Patil, Sanjay More, K. K. Sangale, Rakesh Birajdar, and Muntasim Bhajjan	
Design and Implementation of Plastic and Microplastic Collection System	725
Abhishek N. Bhagat, Kashmira V. Dixit, and Amarnath D. Landge	
Ward Assignment Prediction in Multi-speciality Hospital Using DDPGO Technique	733
Gajanan Krishna Bhoi, G. A. Patil, and U. L. Kulkarni	
Evaluation of Some Medicinal Plants as an Antimicrobial Agent for Drinking Water Treatment	743
Sachin G. Chonde and Sonal G. Chonde	
Identification and Analysis of Musculoskeletal Disorder Among Indian Truck Driver	753
A. B. Rathod and R. T. Vyavahare	
A Comprehensive Review of COVID-19 Detection and Prediction Using of ML/DL Method	761
Md. Sadab, Deepak Kumar, and Ved Parkash	
Construction of Spreadability Testing Apparatus	771
Vrunal V. More, Prajakta K. Khule, Mithun G. Maniyar, Anil V. Landge, and Pradip A. Jadhav	
Elucidation: Reduction of Environment and Health Issues Due to Non-exhaust Pollution	777
S. P. Jadhav and S. H. Sawant	

Mechatronics, Micro-nano Related for Bio and Societal Applications

Influence of Uneven Patch Zeta Potential on Electroosmotic Mixing Characteristics in a Heterogeneously Charged Micromixer	787
Sumit Kumar Mehta, Anindya Nath, and Sukumar Pati	
Heat Transfer Enhancement in Micro-fin Tube Using Coil Wire Insertions of Different Lengths	797
Roheshkumar S. Lavate, K. B. Sutar, Avishi Saini, Ankita Shakshi, and Parth Sethi	
Numerical Study of a Miniature Concentration Gradient Generators (CGGs) of Various Shapes	807
Sachin Gavali, Prashant M. Pawar, and Digvijay D. Ronge	
Computational Analysis of Fluid Flow in Split and Recombine Micro-channel with Circular Obstacles	817
Sanjay A. Pawar and Vimal Kumar Chouksey	
Comparison of Experimental and Analytical Results of Impact of Various Geometrical Configurations on Pressure Drop Through Micro-channel	827
Sachin M. Kale, Digambar T. Kashid, Avinash K. Parkhe, Sandip S. Wangikar, Chetan C. Jadhav, and Sunil S. Gaikwad	
Manganese Oxide Nanofibers for High Performance Supercapacitors	839
S. S. Gavande, A. C. Molane, A. S. Salunkhe, Y. M. Jadhav, T. M. Nimbalkar, R. N. Mulik, and V. B. Patil	
A Critical Review of Recent Research on the Application of Nanofluids in Heat Exchanger	847
Shital Waware, Sunilkumar Harsur, Ramdas Biradar, Pallavi Jadhav, Kamalkishor Maniyar, and Pushparaj Warke	
CFD Analysis of Hydrodynamic Journal Bearing with Rectangular Top Inlet	855
Smeet Ashar, Abhijeet Chavan, and Pradnya Patil	
Brain Tumour Segmentation Using cGAN with Residual (ResNet) Technique	867
Meenakshi M. Pawar, Suvarna D. Pujari, Swati P. Pawar, and Anchit Narwadkar	
Effect of Patch Length on Electroosmotic Mixing Characteristics Inside a Heterogeneously Charged Micromixer	877
Anindya Nath, Sumit Kumar Mehta, and Sukumar Pati	

Breast Cancer Detection Using Deep Neural Network (DNN) on Histopathological Data 887
Suvarna D. Pujari, Meenakshi M. Pawar, Swati P. Pawar, and Mohua Biswas

Image Processing for Protein Detection in the Egg Using a Microfluidics System 897
Sachin M. Khomane, Pradeep V. Jadhav, Saurabh S. Kale, Revansiddha S. Gaur, Suryakant B. Nilgar, Siddheshwar K. Mali, and Prasanna S. Thalpati

Minimization of Droplet Size Using Baffle in T-Junction 907
Manash Protim Boruah

Development of a CFD Based Artificial Neural Network Metamodel for the Design of Micromixer 917
Digvijay Ronge and Prashant Pawar

Modeling and Simulation of Check/Flap Valve Used in Micropump Applications 929
Ranjitsinha R. Gidde, Amarjit P. Kene, and Prashant M. Pawar

Characterization of Polydimethylsiloxane for Viscoelastic Properties of Using DMA 935
Ranjitsinha R. Gidde, Amarjit P. Kene, and Prashant M. Pawar

Advanced Assessment of Various Employment Sectors

A Consumers Approaches Towards Online Shopping in India: Challenges and Perspectives



Savita Pramod Vaidya

Abstract Online shopping is a type of shopping where people can easily buy things and services online. We can get a sense of how much everything costs when purchased online through online shopping. Customers can buy a variety of goods and services through it, and sellers can keep track of their business and transactions online. It saves time and is convenient for shopping. It could be said that traditional shopping methods have evolved to make shopping simpler, more enjoyable, and more adaptable. The best way to shop for a wide range of items at once and from any location is online. As a result, we can consider online shopping to be one of the most enjoyable and convenient ways to shop. It saves money and time by reducing the crowd at the market. At the time, online shopping turned out to be a necessity. Because in today's highly competitive world, people are too busy working in their offices to shop. Their lives will be made easier and faster by this technology. The primary objective of this research is to investigate consumer attitudes toward Indian online shopping as well as the obstacles and perspectives of this expanding industry.

Keywords Online shopping · E-shopping · Challenges · Perspectives and consumer buying behavior · E-commerce · Indian economy

1 Introduction

The concept of online shopping, online shopping is a type of electronic commerce that allows consumers (buyers) and businesses (sellers) to interact more easily through the use of technology (for example, online that can be used on desktop computers, laptops, smartphones, etc.). In other words, it serves as a platform where both buyers and sellers meet to fulfill their respective purpose by providing them with a virtual marketplace. The consumer finds a product that interests him, needs or desires by visiting the website or retailer's websites or by searching for the desired product on a search engine such as Google that will be provided for him with the wide catalogue

S. P. Vaidya (✉)

K.P. Mangalvedhekar Institute of Management, Sholapur, India

e-mail: pdv1122@gmail.com

© The Author(s), under exclusive license to Springer Nature Switzerland AG 2024

P. M. Pawar et al. (eds.), *Techno-Societal 2022*,

https://doi.org/10.1007/978-3-031-34648-4_1

of websites or retailers selling the desired product. Consumers are free to choose the alternative that best suits their interests, need or desire. The same can be done through desktop, laptop, mobile phones, etc. However, in many cases, the option to pay cash on delivery is offered through the retailer which means that the consumer can order the product or book the service online and can pay at the time the product is delivered or the service is used. In terms of delivering the ordered product, retailers offer options including shipping, shopping and in-store pickup as well.

2 Objectives of the Study

1. Research the online shopping scenario.
2. To investigate the top online shopping facilitators in India.
3. Research the current state of online shopping in India.
4. To investigate Indian consumers' attitudes toward online shopping.
5. To comprehend the difficulties of online shopping in India.

3 Study Hypothesis

Online shopping is an important part of the e-commerce industry and the fastest growing sector of the economy.

4 Research Methodology

In this paper, researcher has adopted descriptive study methods and secondary data. The data and information which is used in the paper is drawn from reliable and creditable resources such as related books by various authors, related research papers, various journals and articles on the online shopping and its perspectives and challenges related data which are available on online and offline mode.

5 Review of Literature

Choubey and Solanki [5], a lesson examining shopping intentions for different age groups, as well as income groups. To ascertain results for the above-mentioned purpose; A total of 120 responses were obtained from the city of Indore. It was revealed that the lower age group is the most familiar with the online shopping trend. In comparison, consumers under the age of 45 found themselves more confident in using the Internet and shopping online. On the other hand, income has been found to

be an unimportant determinant of online shopping. While online shopping was more accessible to higher-income consumers, it was not an intrinsic criterion for online shopping.

Aahamad and Zafar [1], this study emphasized various factors that influence the purchasing decision of customers. These factors range from website design, customer support, data security, and platform reliability [34]. Moreover, they find that different type of online shoppers has a difference in their perception.

Chakravarthy [4], this study explores the effects of demographic profile on customer perception, attitude, and behaviour while shopping online and discusses variance in customer perception due to demographics.

Prasad and Raghu [8], in their empirical study, recorded the main determinants and motivational factors for purchasing groceries from the Internet. They have conducted semi-structured formal interviews with buyers of food products from online e-stores in Karnataka, Bangalore. They have identified seven determinants, i.e., convenience, security, trust, help desk, flexibility, customization, and price promotions that significantly influence the behavior of customers in buying food online.

Tandon [13], the purpose of this paper is to learn about the factors that influence online shopping in India. It adds new predictors of online shopping to the Unified Theory of Acceptance and Use of Technology Model 2 (UTAUT2). Furthermore, the effect of these variables on customer satisfaction is tested experimentally.

Undalea and Patilb [14], this paper attempts to investigate the moderating effect of online shopping experience on intent to use e-governance portals. We surveyed 365 villagers across Maharashtra: one of India's leading states. The result confirmed that the online shopping experience modifies the relationship between: "perceived security and privacy" and "attitude"; "perceived security and privacy" and "intent to use"; "perceived interest" and "position"; and 'attitude' and 'intent to use'.

Almugari et al. [2], this study found that customer satisfaction with online shopping in India is significantly and positively influenced by product information, website design, security, privacy, and perceived usefulness. Additionally, a correlation between perceived interaction and customer satisfaction with online shopping was not found to be statistically significant. This study's findings will help online retailers better understand the roles that website design, product information, security and privacy, perceived interaction, and perceived benefits play in improving online shopping and customer satisfaction in emerging markets like India.

6 An Online Shopping Scenario

The following paragraphs shed light on the state of online shopping in India, including its history, the various online shopping players in the Indian market, and the current situation. (a) The history of online shopping: The study showed that the introduction of the method of online shopping has its origins in 1979 when Michael Aldrich invented online shopping in the United Kingdom. Moreover, the first player for business-to-business online shopping was Thomson Holidays, UK, followed by the

introduction of online shopping by the telecom sector in France to facilitate online ordering in 1982 and the site was named Minitel. Moreover, in 1984, the first business-to-consumer online shopping platform called “Tesco” was introduced with Mrs. Snowball, the first online home shopper. Following that, online shopping began to gain traction in various parts of the world, and the mention of various facilities, such as sales of wine, flowers, and chocolates, which are the leading retail categories, has fueled the growth of online shopping. Since then, the significant growth in online shopping has resulted in the inclusion of almost all products and services in the online shopping catalogue. The following paragraphs provide an overview of online facilitators and the various services they offer in India [3, 6, 7, 9].

7 India’s Best Providers of Online Shopping Assistance

The following is a list of India’s top ten online shopping portals:

Flipkart.com

Flipkart.com is the most well-known Indian online retailer, offering original goods to customers. Clothing, music, electronics, books, health products, children’s toys and accessories, perfumes, toys, movies, home appliances, shoes, and stationery are just a few of the many items they stock.

Myntra.com

Myntra.com is an all-in-one destination for fashion and lifestyle products-related online shopping. Recently, the company was included on a list of popular online shopping sites in the country. Myntra.com has sold exclusive options of accessories, footwear, cosmetics, and apparel from more than 500 well-known Indian and international brands ever since it entered the online business world. Adidas, Puma, Nike, United Colors of Benetton, and others are notable examples.

Snapdeal.com

Under the direction of Rohit Bansal and Kunal Bahl, Snapdeal.com launched its online business platform in 2010. In India’s list of online shopping sites, they currently hold favorable positions. Lifestyle, clothing, accessories, electronics, toys, restaurants, chocolates, personal care, books, and more are just a few of their many offerings for women and men alike.

Amazon

One of the most well-known names in the world of online shopping for electronics, books, and other goods is Amazon. The Amazon India website and services are being redesigned to accommodate India’s rapidly expanding online shopping population. In order for you to enjoy a safe and secure online shopping experience, easy returns, convenient electronic payments and cash on delivery, 24 × 7 backed Amazon customer service, and comprehensive and globally recognized purchase protection,

they are committed to ensuring that your purchases on Amazon.in are 100% protected from the A-to-Z Guarantee of Amazon.

E-Bay

The largest online shopping mall in the world is E-Bay. E-Bay is a marketplace that people and businesses use to buy and sell almost anything online. Everything can be found on E-Bay. T-shirts, shoes, candles, furniture, jewelry, watches, crafts, laptops, perfume, computers, microwave ovens, toys, baby products, weighing scales, and a lot more are among the items on this list.

Naaptol

One of India's fastest-growing e-commerce websites is Naaptol.com. Manu Agarwal led the establishment of the business in 2008. They managed to create a buzz in the market a year later, when they emerged as an online marketing platform. Naaptol had a lot of products in its store, like cameras, tablets, home appliances, mobile phones, and so on. In 2009 and 2010, they sold more than Rs. 10 crore. One of the best e-commerce websites in India, Naaptol offers faster delivery of all purchased goods.

Yebhi.com

Yebhi.com is an online shopping platform that has been in operation since 2010 and is experiencing rapid expansion. It's a high-end lifestyle shopping website that helps brands sell shoes on top Indian online shopping sites. Other product categories, including fashion apparel, accessories, jewelry, mobile phones, and bags, have seen the most success in sales for them. Yebhi.com has its own warehouse operations that aid in full order fulfillment and expedited shipping.

Paytm.com

In the beginning, Paytm was a mobile recharge and bill payment website. Now, Paytm sells everything from home appliances to clothes for men, women, and kids to laptops and cell phones to home decor at low costs. Paytm has achieved rapid growth in a short amount of time, allowing it to rank among the top ten Indian shopping websites.

8 The State of Online Shopping in India Right Now

In general, online shopping is benefiting from an increase in sales and customers. India's e-commerce industry grew to \$12.6 billion in 2013 from \$3.8 billion in 2009; 17 billion in 2014 and 23 billion in 2015, the e-retail industry was worth \$2.3 billion, and 70% of businesses in 2014 were related to travel (Press Trust of India, 2014). According to a study conducted by the Internet and Mobile Association of India, the travel industry accounted for 61% of the online shopping market by the end of 2016 [11]. According to Nair (2017), online retail sales of \$681 billion US were reported in 2016, placing it third in e-commerce sales behind China and the United States. Additionally, according to the Forrester Research reports cited by Rohini and Kajapriya,

the e-commerce market in India has grown to \$35 billion by 2016 from \$15 billion in 2014. In addition, according to Nair's (2017) report from Forrester Research, the Indian Internet market is anticipated to reach \$64 billion by 2021, growing at a compound annual growth rate of 31.2% over 5 years. In addition, the retail industry is anticipated to spend \$500 million to \$1 billion more on logistics between 2017 and 2020, according to the Associated Chambers of Commerce and Industry (Assocham), in response to the growing use of online shopping by consumers.

9 Indian Consumer Attitudes Toward Online Shopping

Customers enjoy numerous advantages when they shop online. People's reliance on online shopping is growing by the day. During the pandemic, online shopping proved to be a lifesaver. Here are some of the primary benefits of shopping online [10, 12]:

1. Convenience

The greatest benefit is convenience. Where else can you shop in comfort while still wearing your pajamas in the middle of the night? You can complete your purchase in a matter of minutes and there are no long lines or money changers to locate. We can shop around the clock at online stores, which also reward us with a "pollution-free" shopping experience. You won't find a better place to buy informational products like e-books, which you can get right away once you finish paying. Online purchases of downloadable goods eliminate the need for any physical goods at all, benefiting the environment as well!

2. Competitive Prices and the Best

Online transactions can be done at lower costs and at lower prices because the products come directly from the seller or manufacturer to you without the involvement of brokers. In addition, it is simpler to find a better deal by comparing prices. Coupons and discounts are also offered by many online businesses.

Because online retailers are only required to collect sales tax if they have a physical location in your state, not only are the prices lower, but you may also be able to save money on taxes. You've saved a lot of money by opening a savings account for parking and fuel!

3. More Options and Variety

Amazing options are available online. You can get almost any brand or item you're interested in. You don't need to fly to get the most recent international trends. Instead of being restricted by your geographical location, you can shop at retailers in other parts of the state, the nation, or even the world. A significantly larger selection of colors and sizes than you'll find in stores. In addition, there is more stock, so you will always be able to find the size and color you want. Some online stores even ship orders for items that are out of stock when they arrive.

4. **Facilitate Easier Gift Sending**

It's simple to send gifts to friends and family no matter where they are. You take care of all shipping and packaging. They will typically wrap it for you as a present! Now, distance need not be a reason not to send a gift on holidays like birthdays, weddings, anniversaries, Valentine's Day, Mother's Day, and Father's Day, among others.

5. **Greater Control**

When we choose traditional shopping, we frequently overspend and purchase things that aren't exactly what we wanted (but we can't find better alternatives in the store). You can get precisely what you want and need because you don't have to let the store's catalog order what you buy online.

6. **Simple to Compare Prices**

Online shopping has made it much simpler to compare and search for products and their prices. For hardware, for instance, you can find links to the best prices as well as consumer reviews and product comparisons for all available options. The majority of retailers and products can be searched for experience, ratings, and direct reviews.

7. **No Throngs**

If you're anything like me, you despise crowds at your store. It can be a huge hassle, especially on weekends, holidays, and during festivals. Additionally, there are times when feeling rushed or rushed occurs when we are squeezed in with shoppers. You won't have to fight for a parking spot. When you shop online, you can avoid all of these problems.

8. **No Obligation**

When we shop abroad, we frequently buy things we don't really need because shopkeepers try to persuade us or use their sales skills to get us to buy them.

10 **Obstacles of Indian Online Shopping**

There are downsides to shopping online: the ten most problematic items when shopping online are listed below.

1. **Gas and Packaging Have a Negative Impact on the Environment**

Having your purchases delivered to your door in multiple layers of plastic packaging and cartons is good for you but bad for the environment. Even if you try to recycle cardboard, shopping online generates unnecessary waste.

2. **Shipping Delays and Problems**

There are bad days for even the biggest and best online retailers and shipping companies, so unless you pick up your purchases from a store, you can never be sure they will arrive on time. More often than you can imagine, items are delivered to the wrong address, deflected, damaged, or lost.

3. Fraud Hazard

There is a greater chance of fraud if you shop online: scams involving counterfeit goods, fake websites, identity theft, phishing, hacking, and credit card fraud are common.

4. Too Much Time Spent Online

It's possible that all of your screen time will overwhelm you, especially if your job requires you to look at a computer all day. When you shop online, it can quickly become a marathon of scrolling and clicking through rabbit holes, and before you know it, you've been online for the majority of the day. Although the internet is a wonderful destination, you probably do not want to live there.

5. Reduced Interaction with Others

You will never need to leave your home if you complete all of your work online. This might be cool for a while, but there will probably come a time when you just want to go outside, talk to real people, get involved in your community, and just be a part of the crowd. You might also want to get some fresh air and change the scenery. Sometimes, real-life interaction is superior to what a computer screen can offer.

6. Concerns About the Specific Results You are Obtaining

Online shopping necessitates a leap of faith unless you are extremely familiar with the brand or product. It doesn't always work out for your benefit. Sizes are frequently off. Just by looking at a picture, you can't tell what the texture, fabric, fit, cut, quality, weight, or durability are. Holding something that looks great can make you feel uneasy, awkward, or cheap.

7. Complex Method of Return

While some sellers make the process simple, others make it harder for you to return their products or get your money back. You may not always be able to receive a reimbursement for any shipping costs. If you buy in person, you can avoid the hassle of labeling, packing, shipping, tracking, and filling out all the necessary forms. If you manually choose your items, you won't have to return them as frequently either.

8. Websites that Are Hard to Use, False, or Complicated

You can't unsubscribe from some websites' mailing lists if you sign up for them. Your email is full of ads because some people sell your email address to other people. You might not be able to buy, return, or contact customer service because the websites don't always give a good or accurate description of the products.

9. Lack of Sales Support

While you are on your own online, there is typically someone available to assist you in the store. This is very bad for you if you are unsure or if you are in any doubt. Because there was no one to talk to, you might have to make impulsive purchases and mistakes that you will later regret.

10. Support from Local Retailers is Lacking

All of the local stores would cease to operate if everyone started shopping online. We will have to relocate more and more to shop in a real store when all of the city's stores close. E-commerce's negative, and sometimes devastating, effects on jobs and local economies have already been felt by a lot of people and places.

11 Conclusion

The number of people who shop online today is fairly high. Many people now buy things online due to the growing popularity of online shopping. However, many people still prefer to buy things in person. People have the option of shopping in person or online, depending on what works best for them. Indians' current business dealings could be transformed by the revolutionary tool of online shopping. Business services will be made easier all over the world as a result of its benefits being incorporated into the Indian economy. Due to consumer perceptions of online shopping, actual information should be investigated for security, protection, and trust in India.

References

1. Aahamad, M. L., & Zafar, S. M. (2017). Consumer perception towards online shopping. *Asian Research Journal of Business Management*, 4(3), 1–14. <https://doi.org/10.24214/arjbm/4/3/113129>
2. Almugari, F., Khaled, A. S., Alsyani, M. K., Al-Homaidi, E. A., & Qaid, M. M. (2022). Factors influencing consumer satisfaction toward online shopping: A special reference to India context. *International Journal of Procurement Management*, 15(2), 236–256.
3. Bhandari, N., & Kaushal, P. (2013). Online consumer behavior: An exploratory study. *Global Journal of Commerce & Management Perspective*, 2(4), 98–107.
4. Chakravarthy, B. S. (2017). An empirical analysis on customer perception towards digital marketing. *International Journal of Commerce, Business and Management (IJCBM)*, 5(4), 118–123.
5. Choubey, V., & Solanki, S. S. (2014). Influence of age and income on online shopping adoption. *Shodh: Pioneer Journal of IT & Management*, 10(1), 149–153.
6. Khare, A., & Rakesh, S. (2011). Antecedents of online shopping behavior in India: An examination. *Journal of Internet Commerce*, 10(4), 227–244.
7. Nagra, G., & Gopal, R. (2013). A study of factors affecting on online shopping behavior of consumers. *International Journal of Scientific and Research Publications*, 3(6), 1–4.
8. Prasad, C. J., & Raghu, Y. (2018). Determinant attributes of online grocery shopping in India—An empirical analysis. *IOSR Journal of Business and Management*, 20(2), 18–31. <https://doi.org/10.9790/487X-2002051831>
9. Richa, D. (2012). Impact of demographic factors of consumers on online shopping behavior: A study of consumers in India. *International Journal of Engineering and Management Sciences*, 3(1), 43–52.
10. Rohm, A. J., & Swaminathan, V. (2004). A typology of online shoppers based on shopping motivations. *Journal of Business Research*, 57(7), 748–757. [https://doi.org/10.1016/S0148-2963\(02\)00351-X](https://doi.org/10.1016/S0148-2963(02)00351-X)

11. Sharma, S., Gupta, B., & Sharma, V. (2014). A study on gender differences in online shopping behaviour. *Pioneer Journal of IT & Management*, 10(1), 352–355.
12. Shrivastava, A., & Lanjewar, D. U. (2011). Behavioural business intelligence framework based on online buying behaviour in Indian context: A knowledge management approach. *International Journal of Computer Technology and Applications*, 02(06), 3066–3078.
13. Tandon, U. (2021). Predictors of online shopping in India: An empirical investigation. *Journal of Marketing Analytics*, 9(1), 65–79.
14. Undalea, S., & Patilb, H. (2022). Moderating effect of online shopping experience on adoption of e-Governance in rural India. *Asia Pacific Journal of Information Systems*, 32(1), 32–50.

Determinants of Dividend Policy: Evidence from Indian Pharma Sector



Himanshu Jain, Vijay Anant Athavale, and Akhilesh Kumar Mishra

Abstract In the present research paper, the financial statements of 15 Indian pharma firms have been analyzed to gauge the impact of the firm's characteristics on the dividend policy of the given firms. The researcher has identified some of the important firm's characteristics like Earnings Per Share, Dividend Per Share, Current Ratio, Quick Ratio, and Firm Size which affect the dividend policy of a firm. The factors influencing dividend policy have been studied using correlation matrices, Housman test and panel data analysis. The outcomes of the correlation matrix exhibited that there is insignificant correlation between DPR and CR, QR, and firm size. According to the results of the pooled ordinary least square model, DPR is unaffected by EPS, DPS, CR, QR, and firm size. According to the outcomes of the random effect model, the firm size, EPS, DPS, CR, and QR had insignificant on DPR.

Keywords Sustainable Development Goals · Societal development · Dividend policy · Dividend payout ratio · Firm size

1 Introduction

The 17 Sustainable Development Goals, which are meant to be accomplished by 2030, were adopted by the UN General Assembly in 2015. The 8th goal is about "decent work and economic growth" [1]. Economic growth leads to societal development. The government of a democratic country like India, home to more than 1.40 billion people, always follows a mandate for economic growth and the sustainable development of society. The economic development of such a big population depends upon the optimum exploration and utilization of resources. In a democratic

H. Jain (✉) · A. K. Mishra
Panipat Institute of Engineering and Technology, Panipat, Haryana, India
e-mail: himanshujain259@gmail.com

V. A. Athavale
Walchand Institute of Technology, Sholapur, Maharashtra, India

country like India, the Government of the country keeps working for societal development and provides resources for the society to develop. But in a country like India Government cannot do it alone, it requires support from the private sector as well. A well-developed private sector's contribution is required for societal development. And a well-developed private sector requires abundant resources to sustain and grow, especially finance resources and finance is available if it is paid off well and on time. So financial management of these corporates is very critical.

There are three pillars of financial management/corporate finance, i.e., investment decision, financing decisions and dividend decision, which leads a business to success or failure. In this paper, the researcher has considered studying the dividend decision, which is still a controversial issue but one of the important aspects of corporate finance. It has great implications for the various stakeholders of any business firm, e.g., investors, lenders, and managers. Dividends are simply a benefit to shareholders as compensation for the risk taken by investing in the firm. It is also known as the distribution of earnings among shareholders in proportion to their ownership interests. As per signaling theory dividend is used as an indicator of the company's performance. Bhattacharyya [2] also endorsed that firms issue dividends to give a signal of good quality to their investors. The company's increased dividend payments will be seen by the shareholders as a sign that management has high expectations for future cash flows [3]. On the other hand, the decrease in dividend payments is seen as a management's expectation of future low cash flows.

Since the ground-breaking works of Gordon [4], and Lintner [5, 6], about the dividend decision, the debate over its application has been ongoing. Black [3] penned that "the harder we look at the dividend picture, the more it seems like a puzzle, with pieces that just do not fit together". Many dividend theories have been developed to justify how the dividend decision has been taken and whether it affects the value of the firm or not. But still there are many unanswered questions like why do companies pay dividends? Why shareholders are so much concerned about the dividend? Which are the factors affecting the dividend decision? Do dividend decisions affect a firm's value?

After much research, the answer is not similar that what the factors that determine the dividend policy are. The result of the studies varied from country to country and from different periods. There were no fixed factors defined that can be used as a perfect model. According to Black [3] factors like transaction costs, taxes, investors' expectations and capital structure are the main factors that affect the dividend policy of a firm. After Black's work, a number of additional factors have been added to explain the dividend policy, such as the level of regulation in the industry, free cash flow available to the company, the firm's life cycle stage, the ownership structure availability of investment opportunity and the agency costs. Various research papers serve as inspirations for the current study, which examines several corporate characteristics such as Earnings Per Share, Dividend Per Share, Current Ratio, Quick Ratio, and Firm Size, to assess whether these variables have any impact on the firm's dividend policy or not.

2 Literature Review

2.1 Prior Researches on Determinants of Dividends

In their study, Aviation et al. [7] examined the dividend policies of emerging economies and compared them with those of US companies. According to the study's findings, ROE and market to book value have a favorable influence on US companies' dividend decisions. A debt ratio and tangibility have a detrimental impact on a company's decision to pay dividends. Variables reacted similarly in both markets, however, businesses in emerging markets were more responsive than those in the US market. According to the pooled cross research, companies in developing markets pay more dividends than companies in the US market.

Decisions on dividends are influenced by a firm's liquidity condition. Companies that have more cash in hand are expected to pay more dividends than companies with inadequate cash. Therefore, liquidity has a positive correlation with a company's likelihood of paying cash dividends. Signaling theory provides strong support for this related relationship [8].

According to Myers [9], this tendency can be caused by the expense of issuing fresh equity. According to this theory, profitability and leverage have a negative relationship. Companies that are more profitable produce enough revenue to retain more of their earnings. According to the pecking order idea, companies that are more profitable and use retained earnings as a source of capital would pay smaller dividends.

Soondur et al. [10] examine the factor influencing the dividend policy of 30 companies listed on Mauritius Stock Exchange. The duration of the study period was 2009–2013. It was found with the help of fixed and random effect models that retained earnings, net income and the dividend policy had a significant inverse relationship. On the other hand, Earnings Per Share and Dividend policy had a strong positive correlation.

2.2 Prior Researches on Dividends of Indian Firms

Using factor analysis on the given factors, Gupta and Banga [11] discovered that the dividend policy was based on factors such as growth, profitability, liquidity, leverage, and profitability. When regression analysis was done on the identified components, it was discovered that liquidity and leverage were important factors in influencing dividend policy in Indian firms.

Devaki [12] looked at the dividend payout ratio of Indian corporate hotels' shareholding patterns. The panel data have been analyzed to determine the impact of shareholding patterns on dividend policy. The results exhibited that the dividend distribution was positively impacted by earnings, revenue, the age of the company, the debt-to-equity ratio, size, and institutional holdings.

In their study, Thirumagal and Vasantha [13] identified the factors that influence dividend payout in a sample of five industries—infrastructure and construction, energy, information technology, and pharmaceuticals—and discovered that leverage, prior dividends, company size, firm risk, and profitability were the key factors.

In her research, Sangeetha [14] found that while risk has a negative and significant influence, characteristics including liquidity, profitability, inflation, and size of the business have a considerable negative effect on dividend policy on the NSE firms evaluated for the study. The lagged dividend, yield curve, and taxation do not significantly affect the dividend policy, according to the study of investment opportunities.

3 Methodology

3.1 Sample

The financial statement of 15 firms from the Indian Pharma sector was studied. For the analysis data for 10 years, FY 2012–2013 to 2021–2022 was taken. The name of the companies is Sun Pharmaceutical Industries Ltd., Cipla Ltd., Dr. Reddy's Laboratories Ltd., Divi's Laboratories Ltd., Apollo Hospitals Enterprise Ltd., Piramal Enterprises Ltd., Torrent Pharmaceuticals Ltd. Biocon Ltd., Alkem Laboratories Ltd., Aurobindo Pharma Ltd., Abbott India Ltd., Zydus Lifesciences Ltd., Lupin Ltd., Laurus Labs Ltd., Glaxosmithkline Pharmaceuticals Ltd. The data pertaining to the above-mentioned firms was collected from the CMIE ProwessIQ database.

3.2 Tools and Techniques

Different accounting ratios have been used for the study purpose. Statistical tools like descriptive statistics, correlation matrix, Hausman test, random effect model, and OLS method of regression were used for the analysis purpose. Following is the construction of the regression model:

$$\text{DPR} = \beta_0 + \beta_1 (\text{EPS}) + \beta_2 (\text{DPS}) + \beta_3 (\text{CR}) + \beta_4 (\text{QR}) + \beta_5 (\text{FM}) + \mu_{it}$$

Table 1 shows the basic definitions of significant variables used in the present study.

Table 1 Definition of significant variables for the study

Variable name	Symbol	Definition	Formula
Dividend payout ratio	DPR	Ratio of total dividend paid to the shareholder in relation to the total net income	$DPS/EPS*100$
Earnings Per Share	EPS	Firm's total earnings divided by the total number of outstanding equity shares	Total earnings/ No. of outstanding shares
Dividend Per Share	DPS	All dividends paid to each shareholder during a certain time period	Total dividend/ No. of outstanding shares
Current ratio	CR	This indicator assesses a company's capability to meet company's short-term liabilities	Current assets/ Current liabilities
Quick ratio	QR	Measures a company's short-term liquidity situation and its capacity to satisfy short-term obligations quickly convertible into cash	Quick assets/ Current liabilities
Firm size	FS	Size of the total assets of the firm	Total assets (Natural logarithm)

4 Data Analysis and Interpretation

The results of the descriptive statistic of selected variables are presented in Table 2. The earnings per share have shown high fluctuation as ranging between -43.40 to 7,942 with an average of Rs. 100.23. The standard deviation of EPS was the highest showing greater risk. The average dividend per share was Rs. 19.06 with a maximum value of Rs. 275 and a minimum value of Rs. 0.00. The dividend payout ratio, current ratio and quick ratio are not stable showing high fluctuations during the study period. The firm size of the firm indicates that there are fewer fluctuations with an average of 3.94.

Table 2 Descriptive statistics

	Minimum	Maximum	Mean	Std. deviation	Variance
Dividend payout ratio	-10	25.10	0.37	1.92	3.67
Earnings Per Share (Rs.)	-43.40	7,942	100.23	647.05	418,674.69
Dividend Per Share (Rs.)	0.00	275	19.06	37.74	1,500.55
Current ratio	0.21	7.11	2.26	1.33	1.78
Quick ratio	0.19	5.11	1.62	0.98	0.96
Firm size	2.85	4.59	3.94	0.38	0.14

Correlation among the selected variables has been calculated and examined. The results of the same have been discussed as follows. It is seen from Table 3 that EPS has a significant correlation with DPR while CR and QR have a partial correlation with DPR at 1% level of significance. DPR has positively correlated with CR, QR, and Firm size but the correlation has not been significant. CR has a highly significant correlation with QR. EPS has a significant and positive correlation with QR at 5% of the significance level. QR has a highly significant and positive correlation with CR (1% of significance) and correlates with EPS too (5% level of significance).

Table 4 depicts the results of pooled ordinary least square model used for the study. EPS, DPS, CR, QR and Size were the independent variables and DPR was the dependent variable. EPS and CR have a negative and insignificant relationship with the dependent variable, DPR. Inversely, DPS, QR and firm size have a positive and insignificant relation with DPR. All five independent variables have an insignificant effect on DPR. R-square value is 0.0193 which means that all independent variables have caused a 1.93% variance in the Dividend payout ratio.

Hausman Test: The researcher has run the Hausman test to appropriateness between Random effect model and fixed effect model. Hypotheses are as under.

H₀: Random effect model is appropriate.

H_a: Fixed effect model is appropriate.

Table 5 depicts the results of Hausman test. The *P*-value of Chi-square is higher than the Probable value is 0.05 which means that the alternative hypothesis is rejected and the null hypothesis is accepted. Hence it is concluded that the Random effect model is appropriate and fit.

A random effect is also known as the variance components model. It is used for random variables. It is assumed that the data under consideration are taken from a hierarchy of several populations, each of whose variations are linked to the population.

Table 6 indicates the random effect model of independent variables EPS, DPS, CR, QR and the dependent variable is DPR. The above model indicates that explanatory variables like DPS, QR and Size have positively affected to DPR. But effect has been

Table 3 Correlation matrix

	DPR	EPS	DPS	CR	QR	FS
DPR	1.000					
EPS	0.698***	1.000				
DPS	-0.134	0.164	1.000			
CR	0.312***	0.152	-0.253**	1.000		
QR	0.364***	0.235**	-0.206*	0.982***	1.000	
FS	-0.279**	-0.385***	0.109	-0.089	-0.084	1.000

***Significance at 1%

**Significance at 5%

*Significance at 10%

Table 4 Regression analysis

Dependent variable	DPR			
Method	Panel least squares			
Sample	2013–2022			
Periods included	10			
Variable	Coefficient	Std. error	t-Statistic	Prob
C	0.28320289	1.817134855	0.155851333	0.876368475
EPS	-0.00008596	0.000246134	-0.349281486	0.727388237
DPS	0.004788048	0.004404169	1.087162578	0.278781350
CR	-0.475803528	0.494355259	-0.962472876	0.337425556
QR	0.595976317	0.677436544	0.879752239	0.380459333
Size	0.030277689	0.440147354	0.068789891	0.945252294
R-squared	0.019349237			
Adjusted R-squared	-0.014701136			
S.E. of regression	1.930485221			
F-statistic	0.568253307			
Significance F	0.724214763			

Table 5 Hausman test

Test cross-section random effects			
Test summary	Chi-sq. statistic	Chi-sq. <i>df</i>	Prob
Cross-section random	1.90	5	0.8628

found statistically insignificant. Explanatory variables like EPS and CR have positive but insignificant affected on DPR. R-square is 0.0985 and the adjusted R-square is (-0.0055). R-square indicates that explanatory variables combine caused variations of 00.56% in the dependent variable (DPR).

Table 6 Random effect model

Dependent variable: DPR			
Method: Panel EGLS (Cross-section random effects)			
Sample: 2013–2022			
Periods included: 10			
Variable	Coefficient	Std. error	Prob
C	-5.222296	7.030941	0.458
EPS	-0.0264271	0.0102385	0.010
DPS	0.377372	0.0135132	0.005
CR	-3.93505	2.906912	0.176
QR	4.024914	3.758493	0.284
Size	0.9718804	0.7157638	0.175
R-squared	0.0985		
Adjusted R-squared	-0.005576		
S.E. of regression	14.54983		
F-statistic	0.951207		
Prob(F-statistic)	0.459272		

5 Conclusion

The research study shows that selected companies have unstable dividend payment policy. The correlation matrix depicts that EPS has maximum effect on DPR among the selected variables. CR has strong correlation with QR and other variables have insignificant correlation among them. FS have a inverse but insignificant correlation with DPR. Panel data analysis has been used and the result indicates that EPS, DPS and size of the firm are insignificant to DPR and CR has inversely correlated with DPR. The outcome of the random effect model demonstrates that DPS, QR, and size have all had a favourable impact on DPR.

This research covered the 15 biggest Indian pharma firms that represent the significant size of the Indian pharma sector. These companies need to take care of all stakeholders for the sustainable growth of society, as well as their own. Investors as critical stakeholders need to be motivated to keep invested in the company by paying them well and on time as per their expectations and market trend. So, in this regard, this study may be helpful to understand the nitty gritty of the dividend decision of a corporate which may affect the sustainable growth of any industry. Sustainable growth of Industry will help achieve the 8th goal of the United Nations General Assembly, i.e., “decent work and economic growth”.

References

1. United Nations General Assembly. (2015). *Transforming our world: The 2030 agenda for sustainable development*. Draft resolution referred to the United Nations summit for the adoption of the post2015 development agenda by the General Assembly at its sixty-ninth session. UN Doc. A/70/L.1 of 18 September 2015.
2. Bhattacharya, S. (1979). Imperfect information, dividend policy, and “the bird in the hand” fallacy. *The Bell Journal of Economics*, 10, 259–270.
3. Black, F. (1976). The dividend puzzle. *The Journal of Portfolio Management*, 2(2), 5–8.
4. Gordon, M. J. (1959) Dividends, earnings, and stock prices. *The Review of Economics and Statistics*, 41(2), 99–105.
5. Lintner, J. (1956). Distribution of incomes of corporations among dividends, retained earnings, and taxes. *The American Economic Review*, 46(2), 97–113.
6. Lintner, J. (1962). Dividends, earnings, leverage, stock prices and the supply of capital to corporations. *The Review of Economics and Statistics*, 44(3), 243–269.
7. Aivazian, V., Booth, L., & Cleary, S. (2003). Do emerging market firms follow different dividend policies from US firms? *Journal of Financial research*, 26(3), 371–387.
8. Ho, H. (2003). Dividend policies in Australia and Japan. *International Advances in Economic Research*, 9(2), 91–100.
9. Myers, S. C., & Majluf, N. S. (1984). Corporate financing and investment decisions when firms have information that investors do not have. *Journal of Financial Economics*, 13(2), 187–221.
10. Soondur, S. A. K., Maunick, D., & Sewak, S. (2016) Determinants of the dividend policy of companies listed on the stock exchange of Mauritius. In *Proceedings of the Fifth Asia-Pacific Conference on Global Business, Economics, Finance and Social Sciences (AP16) Mauritius Conference* (pp. 21–23).
11. Gupta, A., & Banga, C. (2010). The determinants of corporate dividend policy. *Decision*, 37(2), 0304–0941.
12. Devaki, S. (2012). Shareholding patterns and dividend payout: An empirical analysis in Indian corporate hotels. *International Journal of Multidisciplinary Research*, 2(1), 49–63.
13. Thirumagal, P. G., & Vasantha, S. (2017). Dividend payout determinants: Evidence from Indian industries. *International Journal of Pure and Applied Mathematics*, 117(21), 811–829.
14. Brahmaiah, B., Srinivasan, P., & Sangeetha, R. (2018). Determinants of corporate dividend policy in India: A dynamic panel data analysis. *Academy of Accounting and Financial Studies Journal*, 22(2), 1–13.

Biophilic Architecture: Meeting the Wellbeing Standards of Employees



Pratima Kiran Mandadi, Manjari Khanna Kapoor, Ramesh Raghavendran, and Aanchal Sharma

Abstract Biophilic design is an architectural concept, actively is in assuring the mental and physical wellness of their users. The focus here is to identify significance of biophilic designing over interior architecture and its impact on wellness and health of the employee. Further explore the benefits of biophilic elements in the workplace where the employees work based on IEQ and interior design parameters. This study relies on a descriptive research method and structured questionnaires were used to collect primary data. The paper underlines two case studies of IT companies located in Hitech city, Hyderabad. The sample size is 215 employees of the companies. The finding shows that biophilic designing works as an integrated component of interior designing to intensify workplace productivity and assure employees health by applying nature designing solutions. The outcome depicted that IEQ and Interior design parameters with office layout and its impact on employee well-being and productivity.

Keywords Biophilic architecture · Impact of greenery in work space · Benefits of biophilic architecture in the workplace · Impact of biophilic design on the employee's wellness

P. K. Mandadi (✉) · M. K. Kapoor
G.D. Goenka University, Sohna Road, New Delhi, India
e-mail: pratima@gdgu.org

R. Raghavendran
JNAFA University, Hyderabad, Telangana, India

A. Sharma
DIT University, Dehradun, India

1 Introduction

1.1 *Biophilic Architecture*

Biophilic design can be looked at as a bridging between the conventional designing and modern designing domain, as it attempts to reunite the indoor and outdoor world through sensitive use of natural ingredients like shape, material, color, and sound. This type of design is claimed to contribute to sustainability, overcoming the lack of contact with the environment and appropriately handling natural resources [1].

From an interior design perspective, intervention in biophilic design has enormous opportunities like utilizing natural design features for aesthetic purposes by the means of greenery, potted plants, fish tanks or others. Designers can also incorporate living wall concepts that enhance the connectedness between nature and humans. Further, features like biomorphic shapes, natural color palette, wood flooring or ceiling, organic patterns in carpeting also intensify the biophilic architecture [1, 2]. Working environments which incorporate natural ingredients have higher levels of creativity, innovation skills, motivation, and wellbeing among the employees. A study [3] reveals that levels of well-being can be intensified by 15% if workers are surrounded with greenery and sunlight in their workplace.

1.2 *Interior design and Impact of greenery in workspace*

In simple words, biophilic design is the amalgamation of nature into a building environment that can work as a cost-effective mechanism to improve IEQ (Indoor Environmental Quality) factors [2]. Implanting greenery in workspace has several advantages such as:

- Improve humidity level.
- Moderating air quality and temperature.
- Assuring restoration impact such as attention restoration.
- Enhance cognitive functioning and emotional satisfaction.
- Greenery always provides visual comfort and acts as stress relief and intensifies positive emotions.
- It also encourages concentration and productivity in the workspace.
- Reduce absenteeism and mental fatigue.

One of the research [4] findings indicates that interior designing is incorporated with work productivity and work culture. Another work [5] emphasizes on how interior design enhances employee engagement and wellbeing of the employee based on workplace features like IEQ factors. The findings demonstrate that IAQ and IEQ are the most crucial ingredient in the interior designing world, directly related with occupancies well-being and their work productivity.

1.3 Background

The term biophilia was introduced by the eminent social psychologist Erich Fromm in the decade 1960's, to define the "love of life" that embraces living organisms and sustainable life [1]. Until 1990, its concentration revolved around life or living organisms but after that these scholarly or academicians shifted toward determining the correlation between humans and nature. With the beginning of the twenty-first century, the concept of biophilia was developed within architectural phenomenon and attained enormous attention amongst interior design. Because it encompasses the emotional aspects of human wants and correlates it with the environment beneath the manufacturing architecture.

As people spend around 90% of their time indoors, exploring workplace design that is based on sustainability, wellness, and performance oriented is the major concentration of this research. The paper underlines case studies (two companies A and B) that are IT companies located in Hitech city Hyderabad, intended to provide a layout of an emerging innovative design framework for the workplace.

2 Literature Reviews

2.1 Interior Design and Biophilic Architecture

Indoor interiors play a significant role in enhancing workplace productivity, employee's well-being [4, 5], and its incorporation with nature strategy obtained little attention in comparison to other designing strategies such as ergonomic, thermal comfort, lighting position and others. The paper [6] emphasizes on biophilic designing as an integrated component of interior designing to intensify workplace productivity and assure employees health by applying nature designing solutions. The study threw light on international instances that successfully adopted biophilic design architectures in their workplaces and along with number of tools (interior design, building design and output space design) that reconnect employees with nature and benefits that can be illustrated from their cognitive, psychological, and physiological wellness outcomes. Office workers specifically in Jakarta are suffering from stress and related mental illness as 61% of the employees are experiencing depression and stress. The major reason for stress in the working environment was dense urban areas. Reshaping or reframing connectivity between nature and humans has become significant from a conservation perspective. Thus, the study [7] emphasizes biophilic design to produce co-working stress-free space and ensure mental and physical well-being of the employees. The study [8] has tried to explore the relationship between the interior of a space and the employee by focusing on 6 parameters: office layout, furniture, light, greenery, control, and noise.

The main purpose of the research [9] is to identify the insights of European coworkers and the significance of biophilic attributes in working space. The concept

of biophilic design has a positive impact on interior ambience. The research focuses on holistic sensory experience and its implication on distinct levels of spatial experimentation that directly and indirectly impact on well-being and productivity of the employees. The finding reveals that the presence of biophilic aspects shows their predominance to blend with the general ambience and become an integral part of the workspace.

2.2 Some Successful Case Studies of Biophilic Architecture

The study [10] reports that the workplace which incorporates nature resembling color is found to have a more positive impact on employee well-being in comparison to the dull or grey shades which are negatively associated with wellness and can intensify the stress level of occupants. Case study [3] of Amazon building “Spheres” provides one of the most amazing examples of biophilic design where 40,000 species of plant are implanted collected from 30 distinct countries with a wide variety of living walls that provide vegetated surface. The motive behind recharge space is to foster connectivity among employees with nature in modernized tech architecture. The design also embraces a glass dome letting it offer ample natural light. Another case study [3] of second home coworking, Lisbon, Portugal shows incredible biophilic designing feature as the workplace flourish to with apple naturalite and surrounded with thousands of plants in usual terracotta pots have several benefits such as (a) provide innovative and peculiar décor, (b) privacy for a screen, (c) air purification. Amorphous furniture provides a “wabi-sabi” feeling where an amalgamation of traditional and contemporary is illustrated having vintage table lamps and lamp shades among others.

2.3 Research Question

What are the benefits of biophilic architecture in the workplace? And investigating the impact of biophilic design on the workplace specifically over the wellness amongst the employees?

2.4 Importance of the Study

The significance of biophilic design is based on its multi-sensory and cohesive strategy. One of the utility of biophilic designing in the workspace, is offering better opportunities for interior designing by amalgamation of natural and environmental ingredients that transform the interior pattern by natural light, ambience, and spiritual connection with human and nature.

2.5 Research Objectives

The research paper would seek to fulfil the following listed objectives:

- To investigate the existence and benefits of biophilic elements in the workplace where the employees work. (Workstations, common areas, foster spaces and informal spaces etc.)
- To analyze the factors of workplace interior design where biophilic elements are affecting the employee's performance.
- To assess whether workplace biophilic design is one of the factors that is affecting employees' well-being in offices

3 Research Methodology

3.1 Case Studies

The focus of the study is on two case studies A and B, which are located in Hitech City, Hyderabad. Both the IT workplace is designed based on the relevant parameters like heating and cooling to maintain the indoor temperatures, humidity control and illumination level with natural daylight and appropriately utilizing the greenery in their workspace.

3.2 Research Approach

The study uses qualitative methodology that is based on a descriptive approach to conduct the smooth analysis. The descriptive research approach is intended to examine and gather the raw data that can be converted into knowledge and informative data about the interior design of the office and extrapolate the following/drawn inferences. The statistical techniques were used to analyze the employees' response towards the workplace biophilic interior design and its impact on employee wellbeing.

3.3 Participants Selection

Around 215 employees as participants who were willing to share electronically were considered belonging to a distinct age group and working experience comprising male and female both. The question was prepared based on the parameters of Building Use Studies (BUS), along with those existing studies which are similar to the theme of this research. The questioner incorporated a five-point Likert scale.

4 Analysis of Study

The descriptive approach, based on the sampling survey method, was successfully applied in the research to gauge how the participants felt about the study's theme. The analysis section carefully examines the survey's raw data and transforms it into prominent data that is crucial for determining the research question, formulating the research question, and achieving the study's goal. Further, discuss the research question and prove them based on evidence (Table 1).

Biophilic design and its benefit over employee health:

To explore the benefit of Biophilic feature in interior design, the study prominently explores three parameters like

- Happy and Motivated
- Reduce Stress and Anxiety level
- Creative and Productive

The first component is Happy and Motivated

As natural elements like daylight fresh air greenery increase a neurotransmitter in the human body called serotonin which is also a kind of happy hormone. This new transmitter increases happiness. Also, illustrated from Fig. 1 which demonstrates the perception of the employees and reveals that 74% of the participants believe that they feel happy and mood was improved when they access the biophilic design of their workplace.

The natural elements also improve cognitive functioning and enhance concentration and dedication. It also promotes a sense of vitality and purpose among the employees. The figure shows 65% of the participants feel that they are motivated and inspired when they are performing work related activities in biophilic surroundings in the workplace.

Table 1 The demographic description of the responses who participate in the research

Demographic variable	Categories	No. of responses	Percentage (%)
Gender	Male	113	53
	Female	102	47
Age group	23–30 years	67	31
	30–45 years	111	52
	Above 45 years	37	17
Professional experience	1–5 years	60	28
	6–10 years	86	40
	11–15 years	35	16
	16–20 years	25	12
	21–25 years	9	04



Fig. 1 Happy and motivation

Reduce stress and anxiety level

As Fig. 2 shows that around 72% of the employees agreed that they reduce fatigue while 69% believe that they reduce their stress while working around natural elements. Another group of employees around 83% noted that when they are working in daylight, near a window, or near greenery they find that they lower their perceived stress.

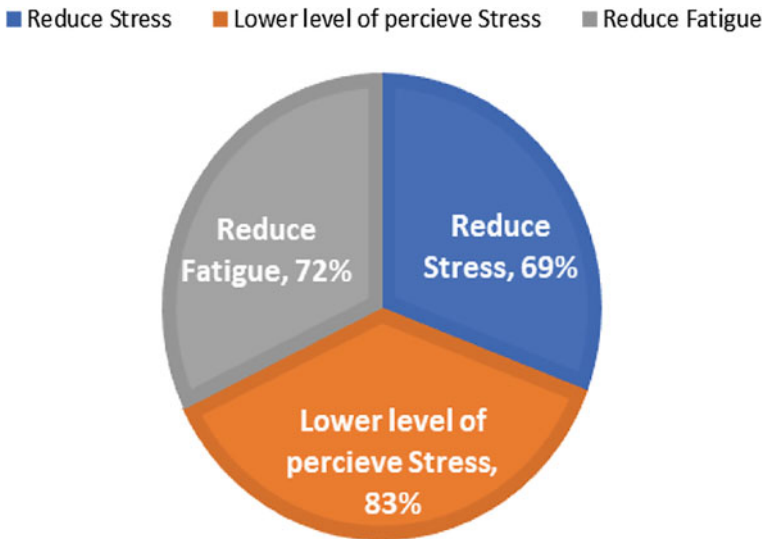


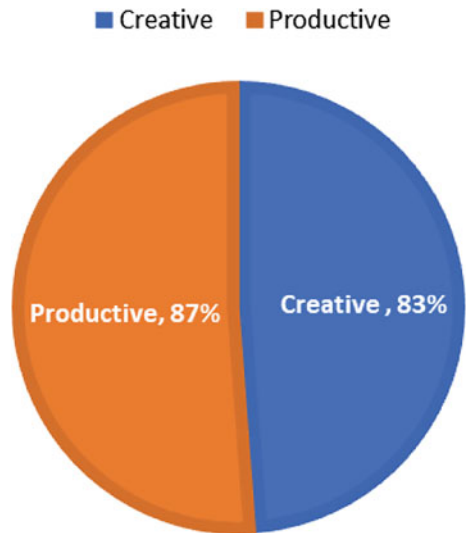
Fig. 2 Reduce stress and anxiety

Figure 3 shows that 87% of the employees feel that their productivity increases while they are surrounded with biophilic components. Further, 83% of the employees believe that their mind becomes more active and generates more ideas when they are associated with greenery and natural elements.

The finding shows (Fig. 4) that employees were well satisfied with their ventilation system as 85% of the participants agreed with the ventilation comfort in the workplace, around 75% of the participants were satisfied with the thermal comfortability. Around 49% of the participants had light access in their desk and 69% of the participants were having sufficient artificial light. 71% of employees do not find any challenges associated with acoustic. 94% of the participants showed satisfaction toward the overall interior ambience of their workplace.

The components that showed biophilic design were the space factor and the natural analogue feature. 96% of the participants show that they are surrounded by facilities like natural light, fresh air and others. Further around 75% of the employees were satisfied with the natural analogue they found in their workplace in the form of biophilic design features like e-wall, flooring, carpet, modular furniture and others. The finding shows (Fig. 5) that the biophilic features under interior design factors from the viewpoint of employees like blending natural ingredients with modern tech. The finding shows that, the factors that embrace nature in the space like plants, natural light, fresh air and windows. Around 96% of the participants were great that their workplace interior design embedded all these features in an effective manner. Another component like indirect correlation with nature embedded features like wall coloring, flooring and ceiling palette, and furniture shows natural analogue components of biophilic design. The data reveals that 75% of the participants agreed that workplace interior design reflects natural analogue features appropriate [11].

Fig. 3 Creativity and productive



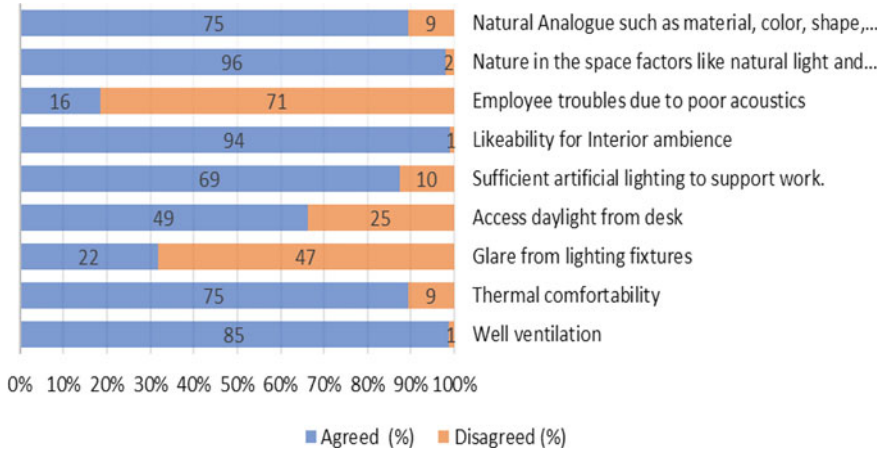


Fig. 4 IEQ factors

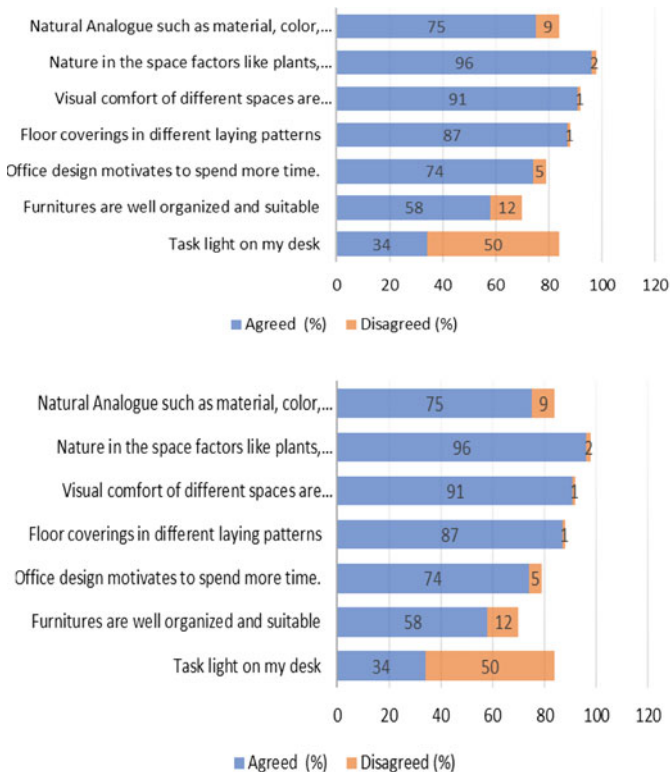


Fig. 5 a, b Interior design factors

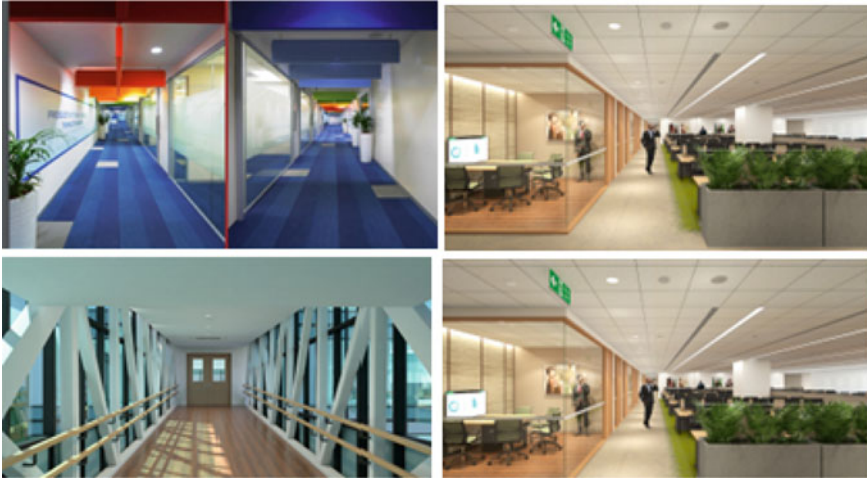


Fig. 6 Passage area, open office, cafeteria, connecting bridge

5 Results

Impressive biophilic features like large windows for natural light, potted plants in terracotta pots and vibrant colors of the room. It has been designed to encourage the interaction between the occupants and other stakeholders. Appropriate acoustical fittings to set tone and the color and tone of the office. Potted plants are located at specific distances in the passage offering an amazing biophilic touch in the modern design. Chairs and tables complimenting interior walls and offering a beautiful view outside. One of the best blends of modern interior design and biophilic architecture with open-large windows, plants and impelling decor. Bright colored chairs in rows giving a spacious look and feel. Stress on the point of amalgamation of amorphous furniture enhancing the ambience along with the ceiling pattern. Open ceilings with ducting, hanging plants, daylight and large windows enhanced its interior look. Provide a peaceful ambience for occupants to have healthy meals (Fig. 6).

6 Conclusion

In the workplace, there are a number of reasons that lead to enhanced stress and mental illness among the workforce. On the other hand, a positive impact on wellness is related to reducing the level of stress and anxiety. Biophilia architecture not only improves employee's creativity by 15% but also reduces the financial cost of the place as it enhances the well-being of the whole workplace and community. Because it works on the principle of not only improving technical innovation to enhance luxury but also create absolute benefit over employees psychological and physiological

well-being. In Interior Design color plays an influencing role over physiological and psychological well-being of humans.

References

1. Zhong, W., Schröder, T., & Bekkering, J. (2022). Biophilic design in architecture and its contributions to health, well-being, and sustainability: A critical review. *Frontiers of Architectural Research*, 11(1), 114–141.
2. Hähn, N., Essah, E., & Blanusa, T. (2021). Biophilic design and office planting: a case study of effects on perceived health, well-being and performance metrics in the workplace. *Intelligent Buildings International*, 13(4), 241–260.
3. Biofilico. (2019). *Benefits of Biophilic Design in Offices and Coworking Spaces*. London
4. Mandadi, P., Sharma, A., & Raghavendran, R. (2022) A critical analysis model on design of office interiors in Hyderabad. *Journal of Advanced Management Science*, 10(2), 51–57.
5. Kiran Mandadi, P., & Zutshi, N. S. (2021). Correlation of workplace culture with implication of wellbeing in corporate interiors—A case of Hyderabad (India). *Turkish Online Journal of Qualitative Inquiry*, 12(6).
6. Mahmoud El-Bannany, R., Hassan, K., & Mohamed Assem, K. (2022). Practices of biophilic patterns in workplace design. *Engineering Research Journal-Faculty of Engineering (Shoubra)*, 52(1), 15–31.
7. Suharjanto, G., Taufik, C., Mariana, Y., & Suryawinata, B. A. (2020). The implementation of biophilic design in co-working space design as a concept of healthy sustainable architecture. *IOP Conference Series: Earth and Environmental Science*, 426(1), 012090.
8. Colenberg, S., Jylhä, T., & Arkesteijn, M. (2021). The relationship between interior office space and employee health and well-being—A literature review. *Building Research & Information*, 49(3), 352–366.
9. Mohora, I. (2019). Importance of biophilic attributes in European coworking spaces. In *Proceedings of INTCESS*, pp. 979–988.
10. Cooper, C., & Browning, B. Human space: The global impact of biophilic design in the workplace. In *Human Spaces Report*.
11. Nieuwenhuis, M., Knight, C., Postmes, T., & Haslam, S. A. (2014). The relative benefits of green versus lean office space: Three field experiments. *Journal of Experimental Psychology: Applied*, 20(3), 199.

An Analysis of Emerging Trends of Corporate Governance in India



Pramod Damodar Vaidya

Abstract Corporate governance is receiving a lot of attention these days because of its links to the health of the economy in particular and its contributions to people's living standards in general. Corporate governance is simply concerned with corporate decision-making and other managerial activities carried out by those in charge of corporations and organizations. Corporate governance is defined as the combination of law, regulations, and appropriate voluntary private sector practices that enable companies to impress financial and human capital while also respecting the interests of other stakeholders and society at large.

Keywords Corporate governance concept · Corporate governance objectives · Corporate governance importance · Emerging trends in corporate governance in India

1 Introduction

Corporate governance, these days, has received wide attention because of its relationships with the health of the economy in particular and its contributions to people's living standards in general. Corporate governance is simply related to corporate decision-making and other managerial activities undertaken by the people who lead the affairs of corporations and organizations. It describes the different aspects of the role and functions of the different bodies that govern institutional entities. This alignment necessitates a commitment to the company's ongoing interactions with key stakeholders. Corporate governance is a term that refers to managing a company's affairs in a way that ensures fairness to customers, investors, vendors, the government, and society at large. Accountability and fiduciary duty are important topics in corporate governance because they require the implementation of guidelines and mechanisms to ensure good behavior and protect shareholders. Another major focus

P. D. Vaidya (✉)
K.P. Mangalvedhekar Institute of Management, Sholapur, India
e-mail: solapur0000@gmail.com

is efficiency, through which the corporate governance system should aim to improve economic results [1–3, 5, 6].

2 Objectives of the Study

1. To comprehend the concept of corporate governance.
2. Research the significance of corporate governance.
3. Research corporate governance objectives.
4. To investigate corporate governance in India.
5. Examine emerging corporate governance trends and issues in India.

3 Hypothesis of Study

Corporate governance is a recent phenomenon that is playing important roles in the conduct of a company's affairs and advocating for the implementation of guidelines and mechanisms to ensure good behavior and protect shareholders.

4 Research Methodology

In this paper, “researcher has adopted descriptive study methods and secondary data. The data and information which is used in the paper is drawn from reliable and creditable resources such as related books by various authors, related research papers, various journals and articles on the corporate governance and its emerging trends and issues in context to India which are available on online and offline” mode.

5 Review of Literature

Gollakota and Gupta [8], the purpose of this paper is to discuss the implications for corporate governance in India and to trace the development and persistence of various forms of business ownership in conjunction with the values and institutions that shaped those forms. A research paper that combines multiple frameworks and examines broad historical trends. There are many types of ownership: professional, family, government, and foreign (multinational corporations). Different forms of business ownership emerged as a result of shifting values and institutional and legal frameworks during each period. However, the end result has been the amalgamation of various co-ownership models, and there is evidence that values have evolved to be more balanced [9].

government utilities, government utilities, and public utilities. Corporate Governance is concerned with services guaranteed by financing suppliers in order to obtain offers on return on investment. Corporate governance refers to the combination of laws, regulations, and practices that are essential for good governance and managers who are able to independently approve corporate strategy and major business plans and decisions, as well as appoint, head, and certify management and replace management as needed.

This definition was given in 1996, the IMI Governance Working Group said Governance is the process by which elements in society and power influence and influence the Kumar Mangalam Birla Commission Report Committee acknowledged that “the primary objective of corporate governance is to enhance the value of participation in the long term, while protecting interests of other stakeholders at the same time”. In its references to stakeholders as major contributors to the country’s development and prosperity, the SEBI (Narayanamurthy) Commission on Corporate Governance in 2003 was more specific [12].

7 Corporate Governance Needs in India

Indian firms are now ranked among the best in the developing world. 14 Several Indian companies are reorganizing to become multinationals by investing abroad and establishing branches or subsidiaries. Customers, employees, investors, the government, and society are all stakeholders in the company. In this modified scenario, the Indian company must be completely honest and transparent with its stakeholders in all of its transactions. This has become so prevalent in today’s business world, where companies need access to global capital pools, must invite and retain the best human capital from around the world, must partner with merchants in large associations, and must also live in harmony with the environment.

Corporate governance is no longer merely a voluntary virtue in India; it is now mandated by law and other regulatory frameworks. The Indian Companies Act 1956 has been amended, and other measures have been introduced, based on numerous studies/committee reports conducted at both the international and national levels, in order to integrate the topic of corporate governance for the Indian corporate sector. Few realize that corporate governance would not have gained widespread acceptance if there had been no “economic payoff.”

8 Objectives of Corporate Governance

The Securities and Exchange Board of India (SEBI) defines corporate governance as management’s acceptance of shareholders’ inalienable rights as the true owners of the company, as well as their role as trustees on their behalf. According to SEBI’s

definition, Corporate Governance is an ethics and a moral duty derived from the Gandhian Principle of Guardianship and Guidelines of the Indian Constitution.

9 Importance of Corporate Governance

Corporate governance is ingrained in a nation's economic DNA for numerous reasons. Similar to how a civilized nation-state's government is obligated to provide safe drinking water, clean air, effective communication, etc. It can also be said that it is its duty to create an orderly and open business environment that will earn the trust and confidence of investors from both domestic and foreign countries. According to research, investor information and monitoring costs can be excessively taxing, so foreign investors are turning away from poorly managed businesses in nations with relatively weak shareholder protections and related legal institutions. In a similar vein, domestic investors may prefer to invest abroad in nations where corporate governance standards and legal protection frameworks are considered to be more appropriate, unless domestic equity returns are higher, than in nations where laws that permit citizens to invest abroad are either weak or poorly enforced. Enticing enough to adequately cover the dangers posed by poor governance. Corporations have risen to prominence in the last century and a half due to their adaptability and efficiency, as we will see later. In many cases, their assets and revenues exceed the GDP of many nations. Companies are ultimately managed by individuals. Being human nature as it is, aided frequently by greed, sound advice, and examples that appear to be successful; those in charge of the business's operations have a real chance of taking away the wealth and assets that contribute to it. Despite governments' general aversion to and reluctance to proactively intervene in such matters, it is in the country's economic and national interest to stop such dishonest practices.

10 Emerging Trends and Corporate Governance Issues in India

This concept of law saw the emergence of its offshoots after the early years of sponsoring the concept of corporate governance. Initially, coordination around the role of the "board of directors" was only for a long time; however, the corporate governance system has now expanded its scope to study the role of management, secondary market, institutional investors, other stakeholders, particularly employees, whistle-blowing policy, and the most recent addition is corporate citizenship and corporate social responsibility. While the focus was on the role that directors could play in monitoring fraud and corporate abuse, thinkers proposed director "independence" as a solution to the problem of poor governance.

As a result, finding independent directors without specialized knowledge was made difficult in the appropriate control condition; independent persons with specialized knowledge of financial accounts were asked to be preferred over others due to the limited number of available positions. This necessitated the formation of the Audit Committee, which was comprised of members of the Board of Directors, to investigate the company's audit system in accordance with standard accounting practices. A true audit can only be performed by someone who is financially literate. Moreover, the concept of various other committees around the world like Remuneration Committee, Nomination Committee etc. has evolved to make the work of Directors (particularly Independent Directors) as a watchdog in the interest of stakeholders.

10.1 System of Corporate Governance in India

The Indian corporate governance system is said to be a hybrid of the market-based systems that predominate in the United States and the United Kingdom, as well as the banking systems that predominate in Germany and Japan. There have been many interesting nuances in the historical development of Indian corporate laws. Along with numerous foreign-owned and foreign-owned businesses. There were numerous Indian management agencies that were regulated. In fact, each large trading group, such as Tatas, Birlas, and Dalminas, had a number of management agencies, some of which were listed.

Despite dissatisfaction with its performance, the agency management system continued to play a critical role in enhancing family ownership and control in the corporate sector until its abolition in 1969. Prior to independence, India inherited one of the world's most pitiful economies, but the manufacturing sector accounted for one-tenth of the national product. As a result, India emerged far stronger than most other colonies in terms of corporate laws and the financial system. The Companies Act of 1956 governs the operation of joint stock companies and protects the rights of shareholders. Prior to the start of liberalization, the Indian organized sector was under the control of public institutions, and its performance, like that of the private sector, had always been poor. Also, not up to par [14].

10.2 Pre-Independence Period up to the 1970

The managing agency system, which emerged as the foundation upon which the Indian economy developed, is responsible for the birth of Corporate India. Although it is not possible to pinpoint the exact beginning of the managing agency system, it is generally accepted that it developed as soon as the East India Company was wound up and ceased trading in 1833. A miniature version of the limited liability existed in the handling organization system. Company and was constructed in such a way that,

in exchange for a small ownership stake or agency fees, the agents would take care of company promotion, finances, and administration.

The Act was useful in preventing and resolving such issues due to errors made by managing agents that led to severe crises in corporate governance. The Act's Sections 146–424 deal with management and administration. Chapter III of the Act, Sections 325–355 specifically address the regulations pertaining to managing agents. The appointment or reappointment of managing agents was outlawed by the Act on April 3, 1970.

10.3 The Period from 1970 to 1990s

Although the Companies Act 1956 abolished the agency management system on 3 April 1970, a new type of ownership structure emerged in the Indian business landscape much earlier. While the government retained the majority of strategic industries, the private sector. It saw the rise of a new class of property owners. The country's private sector was taken over by new wealthy management agents and capitalist families.

The emergence of this class signaled the beginning of a new type of relationship between politics and business. Another change in industry ownership can be seen as capital markets develop. The general public began investing in the industry through stock exchanges, resulting in the formation of a new class of ownership in the form of retail shareholders. However, these shareholders were unable to seize control of the corporation. Instead, they had to hand over control to management and be content with the annual earnings. However, these shareholders were unable to seize control of the corporation. Instead, they had to hand over control to management and be content with the annual results.

10.4 Changes Since Liberalization: The Period from 1990's Onwards

The Indian government began to accept a significant overhaul of the country's corporate governance system toward the end of the 1990s. Through Article 49 of the Agreement on Stock Exchange Listing, SEBI announced extraordinary corporate governance reforms in 2000 after raising awareness from prominent industry groups and large corporations. With the country's reforms, corporate governance came under international pressure. The extent to which corporate governance issues are being addressed in accordance with Part VI of the Companies Act 196 has been discovered to be lacking. Bad management practices in the industry were encouraged by lax government regulations, secret dealings, the interdependence of business and politics, and an ineffective judicial system. By announcing stringent measures in

the event of noncompliance with the laws, general economic reforms altered the formalization of the mechanism.

Managers' distribution of managerial resources is becoming increasingly short-sighted in order to avoid becoming entangled in market-based punishment mechanisms like hostile buyouts, forced takeovers, and poor performance evaluations. Because of this myopia, clever strategies have been used to avoid being perceived as performing poorly. As a result, these professionals' decisions to boost the company's wealth had significant effects on society as a whole. While the company's primary stakeholders are its shareholders, the management appears to have an impact on a wide range of other stakeholders, including workers, customers, society, the government, suppliers, and future generations.

The differences between a family or promoter and a professional manager have always meant that the former took the brunt of the annoyance of the latter. The company's promoter and prominent industrialist, Nusli Wadia, fired the charismatic CEO of Britannia Industries in June 2003, recalling the Alagh family's dominance on corporate boards in this nation. Due to the decline in Indian corporate governance, businesses seeking outside capital have had to primarily rely on government sources. Established in 1992, the Securities and Exchange Board of India (SEBI) is India's stock market regulator. Indian companies began looking for equity capital to fund the expansion of market spaces created by outsourcing growth and liberalization by the middle of the 1990s. Corporate governance reform has been among the outcomes of the need for capital. Only at prices that are set by the government can public share offers be made. As a result, the notion of a managerial revolution in Indian industry is merely a fantasy. Although professionals take over the company's management, owners of promoters or master groups retain most control, as previously mentioned. Corporate controllers, also known as promoters and major groups, have historically held sway over the company's direction, despite the fact that professional managers have a significant impact on businesses' financial performance. The majority of social responsibility initiatives came from observers. Companies have emerged as pioneers in the adoption of corporate governance practices wherever the controlling group has shown some interest in increasing the wealth and value of the other holding group. In the 1980s, the social welfare-minded Tata Iron and Steel leadership set the stage for other dominant groups with similar values to contribute to societal development. India witnessed a remarkable reform in corporate governance following the beginning of financial liberalization in 1991. India had functioning stock markets, a thriving industrial sector, a properly established banking sector, and fairly well-developed British-derived corporate governance when it gained independence in 1947.

11 Conclusion

Corporate governance contributes to the development of a corporate culture based on awareness, transparency, and openness. It is a collection of voluntary laws, rules, regulations, procedures, and practices designed to help businesses maximize

long-term shareholder value. Increases customer satisfaction as well as shareholder value and wealth. With increased government awareness, the focus shifts from the economic to the social sphere, creating an environment of greater transparency and accountability for the company's well-being and survival. Effective corporate governance is recognized as a critical tool for risk management and social and economic development, which is enabled by ensuring economic efficiency, growth, and stakeholder trust.

References

1. Becht, M., Bolton, P., & Röell, A. (2003). Corporate governance and control. In *Handbook of the Economics of Finance* (Vol. 1, pp. 1–109). Elsevier.
2. Claessens, S. (2006). Corporate governance and development. *The World Bank Research Observer*, 21(1), 91–122.
3. Das, A. (2019). *Corporate governance in India*. Routledge. Taylor & Francis Group.
4. Das, S. C. (2021). *Corporate governance in India: An evaluation*. PHI Learning Pvt. Ltd.
5. Dharmapala, D., & Khanna, V. (2013). Corporate governance, enforcement and firm value: Evidence from India. *Journal of Law Economics and Organization*, 29(5), 1056–1084.
6. Ghosh, S. (2006). Do board characteristics affect corporate governance? Firm level evidence for India. *Applied Economics Letters*, 13(7), 435–443.
7. Goel, P. (2018). Implications of corporate governance on financial performance: An analytical review of governance and social reporting reforms in India. *Asian Journal of Sustainability and Social Responsibility*, 3(1), 1–21.
8. Gollakota, K., & Gupta, V. (2006). History, ownership forms and corporate governance in India. *Journal of Management History*, 12(2), 185–198.
9. Kumar, N., & Singh, J. P. (2012). Outside directors, corporate governance and firm performance: Empirical evidence from India. *Asian Journal of Finance and Accounting*, 4(2), 39–55.
10. Manawaduge, A. S. (2012). *Corporate governance practices and their impacts on corporate performance in an emerging market: The case of Sri Lanka* (Ph.D. Thesis). School of Accounting and Finance, University of Wollongong, Australia. <https://ro.uow.edu.au/theses/3676/>
11. Mishra, A. K., Jain, S., & Manogna, R. L. (2021). Does a corporate governance characteristic influence firm performance in India? Empirical evidence using dynamic panel data analysis. *International Journal of Disclosure and Governance*, 18(1), 71–82.
12. Pandya, B. H. (2013). Impact of corporate governance practices on the firm's performance: An Indian perspective. *International Journal of Current Business and Economics*, 2(9), 43–51.
13. Som, L. S. (2006). Corporate governance codes in India. *Economic and Political Weekly*, 30, 4153–4160.
14. Varma, J. R. (1997). Corporate governance in India: Disciplining the dominant shareholder. *IIMB Management Review*, 9(4), 5–18.
15. Yermack, D. (2017). Corporate governance and blockchains. *Review of Finance*, 21(1), 7–31.

An Assessment of the Influences of Information Technology on Higher Education Curriculum in India



Santosh Gopal Kulkarni

Abstract Since independence, there has been a significant increase in the number of colleges and universities at the university level, which is reflected in the current state of the higher education sector. In order to provide a high-quality education to all students, higher education systems have developed significantly over the past five decades. The work that universities and other higher education institutions do has changed as a result of the general use of information and communication technology. Education's significance and information and communication technology's (ICT) sufficiency as a social need are growing in the conscious world of today. In order to improve public mobility and level the playing field for value and social justice, social acceptance of information and communication tools is crucial. Because of the rapid development of ICT, this aspect has gained more traction.

Keywords Education · Higher education · e-Learning · Online learning · Information technology (IT) · Information and communication technology (ICT)

1 Introduction

Higher education lays the groundwork for enhancing one's quality of life and finding solutions to issues that are required to support economic prosperity and preserve democracy in the nation. From "national education" to "global education," "one-time education for a few" to "lifelong learning for all," and "from teacher-centered to learner-centered education" have all been replaced in higher education. In order to offer courses entirely online or as a complement to traditional courses, many higher education institutions have adopted e-learning (blended learning). This makes it possible for students of all ages and abilities to continue their education at any time and from any location. In India, programs of study that can lead to a degree or diploma are referred to as tertiary education. Similar to the majority of other nations, higher education in India includes both university and non-university components.

S. G. Kulkarni (✉)

K.P. Mangalvedhekar Institute of Management, Sholapur, India

e-mail: skmimcollegework@gmail.com

© The Author(s), under exclusive license to Springer Nature Switzerland AG 2024

P. M. Pawar et al. (eds.), *Techno-Societal 2022*,

https://doi.org/10.1007/978-3-031-34648-4_5

Private universities, prestigious universities, and institutions of national significance typically confer degrees, whereas other non-university institutions frequently confer diplomas or certificates. In terms of increased accessibility, higher education in India is undergoing a significant transformation at the moment. Knowledge is being developed and put into use in the higher education setting as a result of rapid technological change and novel means of obtaining and exchanging information. Colleges and universities must find ways to improve the quality of online learning in order to maximize learning, including effectively integrating technology with course content and instruction, in light of all these changes [1–3].

2 Study Objectives

1. Understand the higher education scenario in India.
2. To examine the Government of India's IT-based learning initiatives.
3. To study technology trends in higher education in India.
4. To analyse application of various IT based learning and assessment methods.
5. To study challenges of utilizing IT in higher education.

3 Hypothesis of Study

Information and technology (IT) applications are playing an important role in the field of higher education in India.

4 Research Methodology

In this paper, “researcher has adopted descriptive study methods and secondary data. The data and information which is used in the paper is drawn from reliable and creditable resources such as related books by various authors, related research papers, various journals and articles on the Higher Education, Application of IT in field of Higher Education in India which are available on online and offline” mode.

5 Review of Literature

Pushpanadham et al. [12], the authors of this article concentrate on the concept of knowledge management and how it can be accomplished through e-learning with the assistance of research studies conducted in the region. The article also discusses the innovations that have occurred in India's higher education system, particularly

the incorporation of ICT into teaching, learning, and knowledge management. The article discusses emerging issues, online learning challenges, and potential strategies for making the best use of these resources.

Marriott et al. [8], this paper reports on the findings of a study that looked at undergraduate students' changing use of ICTs and their attitudes toward Internet use while studying accounting at two UK universities. Although the quantitative study shows a significant increase in students' voluntary use of the Internet and email, the qualitative study shows that students are hesitant to consider online teaching. The paper concluded that because this was a study for undergraduates attending university, they preferred a particular type of educational experience.

Jain and Agrawal [5], this paper examines the current state of the ICT industry as well as the ICT education and training (E&T) system, taking into account the issues raised above. It also provides future forecasts, an overview of ICT related practices in ICT, and identifies deficiencies in the aforementioned system and practices.

Tamil Nadu has five colleges. Dewan [4], the purpose of this paper is to assess the current state of technology in these institutes. This will serve as a foundation for the advancement of information and communication technologies (ICT) in higher education. The study also aims to make suggestions and recommendations for improving higher education quality in India. According to the survey, the current state of technology in higher education institutes is insufficient for using technology effectively in education. As a result, the benefits of traditional classroom instruction and ICT tools should be combined into a single system.

Sarkar [13], the purpose of this paper is to shed light on the significance of information and communication technology (ICT) in twenty-first-century higher education. The paper argued, in particular, that although ICT has only had a minor impact on educational practice so far, this will change dramatically over time and make ICT a potent force for change in many educational practices. The study makes it abundantly clear that various Indian states are rapidly expanding their use of ICT in education. When ICT is used in education, one of the most common issues is that decisions are made based on technological capabilities rather than educational requirements.

6 Higher Education Scenario in India

The current situation since independence, there has been a tremendous increase in the number of Universities/University level Institutions and Colleges. At the moment, the following are the main types of University/University-level Institutions: Central Universities, State Universities, Private Universities, Deemed-to-be Universities, Institution of National Importance, and Institution under State Legislature Act.

- In India, higher education institutions fall into three broad categories: colleges, universities, and other independent institutions
- On the AISHE website, 754 universities, 39,071 colleges, and 11,923 stand-alone institutions are listed.

- There are 118 Dual Mode Universities, the majority of which are situated in Tamil Nadu, and they also provide distance education.
- The total number of students enrolled in higher education between 2015 and 2016 is estimated to be 34.6 million, with 16.2 million female and 18.6 million male students. 46.2% of all students are women.
- About 11.05% of all higher education enrolment is made up of distance learning, and 46.3% of those students are female.
- Enrolment in higher education according to level: a mere 0.4% of Ph.D. students enrolled in undergraduate courses, 11.3% in graduate courses, and 79.3% in undergrad courses.
- The distribution of undergraduate enrolment in streams: Courses in the arts, humanities, and social sciences attract the most students. With 16.04% enrolment, science is the second major field; Technology and engineering, with 15.57% enrolment [1–3].

7 India's Government's IT-Based Learning Initiatives

Online learning modules with a lot of content have started to supplement teacher-led learning in many organizations. Initiatives from the government are also not far behind. The National Mission for Education through Information and Communication Technology (NMEICT) was designed as a centrally sponsored plan to use ICT's potential in education for the benefit of all students in higher education institutions at any time and in any setting. During the eleventh 5-year plan period, it was anticipated that this would be a significant intervention in increasing the gross enrolment ratio in higher education by 5 percentage points. Access, equality, and quality are the three fundamental principles of education policy.

The National Program for Technology-Enhanced Learning, or NPTEL for short, is a joint effort by the Indian Institute of Science (IISc) and seven Indian Institutes of Technology (IIT Bombay, Delhi, Guwahati, Kanpur, Kharagpur, Madras, and Roorkee) to develop science and engineering course materials. The Ministry of Human Rights and Development of the Indian Government provides funding for the project known as the National Program for Technology Enhanced Learning (NPTEL). The NPTEL project focused on the following areas: (1) higher education; (2) vocational education; (3) distance education; and (4) open, ongoing, and continuous learning.

- A large number of students who are unable to enrol in academic institutions will be able to access high-quality content from them through NPTEL.
- Government Funded Institutions, Supported Institutions, Government Agencies, Government Institutions, Government Institutions, Private Institutions, Companies, and Individuals have free and it has been demonstrated that Tamil Nadu accounted for up to 40% of all NPTEL applicants between 2016 and 2017.
- Online study platforms are still dominated by Tamil Nadu. Along with university students, teachers, doctors, and IT staff choose the courses in large numbers.

This, according to NPTEL sources, is because the state is accepting and has a strong network with colleges. This kind of contributing numbers are also significantly influenced by the faculty shortage in numerous engineering colleges in the interior of Tamil Nadu. The Comprehensive Education Portal, or “SAK-SHAT”, is a helpline that makes extensive use of e-learning concepts and ICT-based methodology to meet the requirements of the entire learning community, including students enrolled in a variety of educational establishments and lifelong learners. Source: The Ministry of Human Rights and Development’s 2014–2015 Annual Report [6, 7].

8 Technology Trends in Higher Education in India: IT/ICT Content Delivery

With the increased penetration of computers and the Internet, institutions have begun to provide content using ICT/ICT in higher education.

8.1 Consortium of Digital Libraries

In addition, UGC has established its own Consortium of Digital Libraries to provide access to peer-reviewed journals and bibliographic databases.

8.2 Mobility

Students and faculty can perform a variety of tasks thanks to the certification of BlackBerry, iPhone, and other smartphone devices with Internet access. Administration, sharing class notes, downloading lectures, instant messaging, and other tasks are all possible wherever cell phone service is available.

8.3 Gamification

The use of game theory and game mechanics in non-game contexts to engage users and motivate them to perform better is known as gamification in online learning.

8.4 Technologies that Are Worn

The terms “wearable technology,” “wearable devices,” and “wearable devices” all refer to electronic technologies or computers embedded in clothing and accessories that are comfortable to wear on the body.

8.5 Social Education

The rise of Web 2.0 and social networks like blogs and wikis, as well as new online video repository and delivery sites like YouTube, iTunes U, and Big Think, are all influencing a new trend in higher education.

9 Application of Different IT-Based Learning and Assessment Methods

9.1 Blended Learning

Blended learning is a formal or informal educational programme that combines online digital media with traditional classroom methods. It necessitates both the physical presence of the teacher and the student, as well as some student control over time, place, path, or speed. While students continue to attend classes on campus, face-to-face classroom practices are blended with computer-mediated content and delivery.

9.2 Online Training

The terms “e-learning” and “online learning” are frequently used interchangeably by authors. An approach to education known as online education is one that makes use of the Internet, a network, or individual electronic devices to communicate and work together in an educational setting. The way information is shared and exchanged improves as a result of the internet. To increase online participation, many universities are focusing on teleconferencing and video conferencing. Students enrolling in e-learning to drive market expansion are motivated by self-learning, distance learning, and robust government initiatives.

9.3 Online Libraries

Digital libraries are both an access point to other online resources and a repository for locally produced academic outputs. The creation of digitized repositories for books, papers, dissertations, journals, and other institution-specific paperwork is becoming more actively pursued by many educational establishments. The explosion of information, issues with storage, the difficulty of searching traditional libraries, and environmental factors (save trees!!) are some of the common factors that influence the shift to digital and the requirements of the upcoming generation.

9.4 Online Books

A simple definition of an e-book is a digital copy of a paperback book. Academics are beginning to see e-books as a form of the future. E-books' popularity is rising simultaneously with the general use of tablet computers. According to Sharon Kerr, the head of accessibility services at Macquarie University, e-books improve students' learning experiences due to the inclusion of multimedia.

9.5 Assignments for Videos

Digital videos have not yet been widely adopted by educational institutions, according to a review of previous research. However, there is a lot of evidence to suggest that digital video assignments increase student engagement with the learning process. Online assignments offer direct assistance with the assignment as well as any and all assistance necessary to guide students through the task completion process.

9.6 Data Sources for Research

Online database libraries are collections of accurate and up-to-date information from books, journals, and other sources that can be searched. For academic purposes, many search engines and databases offer bibliographic information on where to find relevant books and journals.

9.7 Methods of Informal Learning

Wikis, blogs, and YouTube are widely regarded as educational and professional networking tools on social media.

9.8 Content of the Lecture Capture

Audio and video will be included in lecture recordings, which are recordings of classroom lectures and presentations. In order to record lectures in the classroom, you need a room with special equipment that can automatically record events. Tools and software for recording lectures are available on the market.

9.9 Online Tests

Grades are determined and the learning experience is enhanced by using online tests and quizzes. The quick response has given this momentum, which inspires students and increases their participation in learning. Computer-based test centers offer online access to numerous certification exams. Students' positions are helped by the availability of placement practice exams online [9–11].

10 Difficulties of Involving Data Innovation in Advanced Education

There are a great deal of difficulties individuals faces in web-based training in India. A portion of these difficulties to be defeated are:

1. **Deficient Advanced Foundation:** Albeit the Public authority of India is showing a drive to foster computerized framework, substantially more should be finished toward this path. Rapid web and stable power supply is the most serious issue. India positions 89th all around the world as far as web speed and steadiness. As indicated by a World Financial Discussion report, just 15% of families approach the Web, and versatile broadband is as yet accessible for not very many individuals, simply 5.5 memberships per 100 individuals. In addition, broadband access is right now something like 600 paths, to a great extent in and around the main 50–100 Indian urban communities, leaving rustic regions with unfortunate network. 5G organization innovation is a prerequisite of today which will speed up information download.

2. **Restricted Social Communication:** As online schooling can be gotten to at home or in whatever other helpful area, there is exceptionally restricted direct connection with the educator and others doing the course. As indicated by Dhirendra Kumar (2010), particularly those independent courses, there is less conversation among partners. Most conversations occur through email, discussion board, or conversation gatherings. There is no air nearby to work on friendly collaboration. So you can't foster any friendly bonds that assistance in vocation development.
3. **Sketchy Believability of Degrees:** Albeit the business is beginning to perceive online degrees, there are still a ton of deceitful and unaccredited degrees being offered on the web. Increasingly more trick administrators are giving phony declarations that contain no qualifications. These tricks lose the validity of online certificates, yet in addition the likely boss' confidence in web-based programs [14].
4. **Inspiration:** A few understudies should be paid to get to class. On account of online self-programs, the understudy might hesitate. The dropout rate from online schooling is exceptionally high. Self-inspiration and discipline are expected to follow through with jobs and burden them on time. Assuming you experience issues working freely, remaining coordinated and fulfilling time constraints, you might battle with a web-based program.
5. **Coarse Language:** India is a multilingual nation, and most of the populace comes from provincial regions. The substance presented by the vast majority of the web-based courses is in English. Subsequently, those understudies who can't communicate in English experience the ill effects of the accessibility of language content. Consequently, it is the obligation of PC experts, instructors, executives, language content makers and content distributors to sit together and give a feasible system and standard answer for students who just know Indian dialects [15].

11 Conclusion

This exploration chiefly centers around the job of data and correspondence innovation in advanced education for the twenty-first hundred years. The utilization of data and correspondence innovation overall has changed crafted by colleges and establishments of advanced education. In the realm of the ongoing cognizant circumstance, the significance of schooling and the sufficiency of ICT as a social need is extending. Social acknowledgment of data and specialized instruments is essential to improve portability among the overall population and increment the battleground for worth and civil rights. This paper talked about the advancement of data and correspondence innovation in India. ICT has assumed an exceptionally dynamic part for understudies, educators, research and managerial staff in advanced education. This exploration additionally centers around data and correspondence innovation as a problem solver in the public arena and advanced education. This paper talked about the difficulties and advantages of ICT in advanced education. In light of the

multitude of above conversations, ICT is the best and feasible stage for advanced education. ICT assumes a fundamental part as a strong influencer among numerous instructive practices, for example, taking a web-based test, paying expenses on the web, and getting to online books and magazines. In this way, ICT in advanced education further develops the showing growing experience, and gives web based learning offices to thousands to thousands of students who can't exploit the advantages of advanced education because of many tests, like time, cost, geographical area, and so forth. It gives the means to a lot of this action to understand the potential it holds.

References

1. Arora, E., & Nagpal, C. (2020). ICT: A boon for higher education in 21st century. *South Asian Journal of Marketing & Management Research*, 10(8), 46–52.
2. Bhatt, R. M. (2008, September). ICT for Success of Education from an Indian Perspective. In *IFIP International Conference on the History of Computing* (pp. 147–155). Springer, New York, NY.
3. Dave, D. (2019). An analytical study of the role of ICT in Higher Education. *Journal of Global Economy*, 15(1 (Special)), 56–61.
4. Dewan, A. (2010, July). Scope of technology in higher education in India: A study. In *2010 International Conference on Technology for Education* (pp. 234–235). IEEE.
5. Jain, R., & Agrawal, R. (2007). ICT education and training services: Current scenario and future prospects in India. *Vision*, 11(2), 41–55.
6. Kamal, B. N., & Banu, A. T. (2010). ICT in higher education—A study. *Canadian Journal on Data, Information and Knowledge Engineering*, 1(1), 1–12.
7. Mahenge, M. P., & Sanga, C. (2016). ICT for e-learning in three higher education institutions in Tanzania. *Knowledge Management & E-Learning: An International Journal*, 8(1), 200–212.
8. Marriott, N., Marriott, P., & Selwyn, N. (2004). Accounting undergraduates' changing use of ICT and their views on using the Internet in higher education—A research note. *Accounting Education*, 13(sup1), 117–130.
9. Menon, S., & Suresh, M. (2022). Enablers of technology agility in higher education. *The International Journal of Information and Learning Technology*. 39(2), 166–196.
10. Mir, S. A. (2019). ICT integrated higher education: Prospects and challenges. *International Journal of Research in Economics and Social Sciences (IJRESS)*, 8(2), 1–4.
11. Pegu, U. K. (2014). Information and communication technology in higher education in India: Challenges and opportunities. *International Journal of Information and Computation Technology*, 4(5), 513–518.
12. Pushpanadham, K., Khirwadkar, A., & Joshi, S. M. (2002). Knowledge management through e-learning: An emerging trend in the Indian higher education system. *International Journal on E-Learning*, 1(3), 47–54.
13. Sarkar, S. (2012). The role of information and communication technology (ICT) in higher education for the 21st century. *Science*, 1(1), 30–41.
14. Singh, M., Adebayo, S. O., Saini, M., & Singh, J. (2021). Indian government E-learning initiatives in response to COVID-19 crisis: A case study on online learning in Indian higher education system. *Education and Information Technologies*, 26(6), 7569–7607.
15. Toro, U., & Joshi, M. (2012). ICT in higher education: Review of literature from the period 2004–2011. *International Journal of Innovation, Management and Technology*, 3(1), 20–23.

Advanced Technologies for Water, Energy, Transportation, Housing and Sanitation

Ultrasonic Assisted Electrochemical Machine: A Review



Aniket B. Pawar, Pradeep V. Jadhav, D. B. Jadhav, and D. S. Bilgi

Abstract One of the most important steps in micro-machining is electrochemical machining. Yet, increasing the process's machining efficiency is still a difficult undertaking in the micro-domain. Additionally, it concentrates on the ultrasonic vibration electrochemical machine and procedure assisted by a magnetic field. More substantial depth micro-feature machining is still challenging. The benefit of using a magnetic field and ultrasonic vibrations to overcome this difficulty has been noted by numerous researchers. The magnetic field and ultrasonic vibrations were typically used in isolation in investigations. The process can be considerably enhanced by the interaction of a magnetic field with ultrasonic vibrations. The improvement of the magnetic field in the ultrasonic pulse ECM along with the material removal rate (MRR), surface integrity, hole taper, energy consumption, and hostile environment were used to examine the machining performance.

Keywords Magnetic field · Ultrasonic vibrations · Pulse ECM · MRR · Overcut

1 Introduction

Electrochemical machining (ECM) involves the electrochemical response for metallic materials. In stable electrochemical machining, the protecting side-effects and the created heat are eliminated from the between terminal region by the quick electrolyte stream flying through the openings penetrated in the device cathode since the apparatus size is large enough [1]. In any case, the apparatus terminal is tiny for the electrolyte opening for miniature electrochemical machining, and the electrolyte stream is presently not accessible. As an endeavor, the expulsion of side effects by a customary bouncing development of the instrument cathode was proposed, and the

A. B. Pawar (✉) · P. V. Jadhav · D. B. Jadhav · D. S. Bilgi
Department of Mechanical Engineering, B. V. U., College of Engineering, Pune,
Maharashtra 411 043, India
e-mail: apawar770@gmail.com

A. B. Pawar
Rajarambapu Institute of Technology, Uran Islampur, Maharashtra 414415, India

© The Author(s), under exclusive license to Springer Nature Switzerland AG 2024
P. M. Pawar et al. (eds.), *Techno-Societal 2022*,
https://doi.org/10.1007/978-3-031-34648-4_6

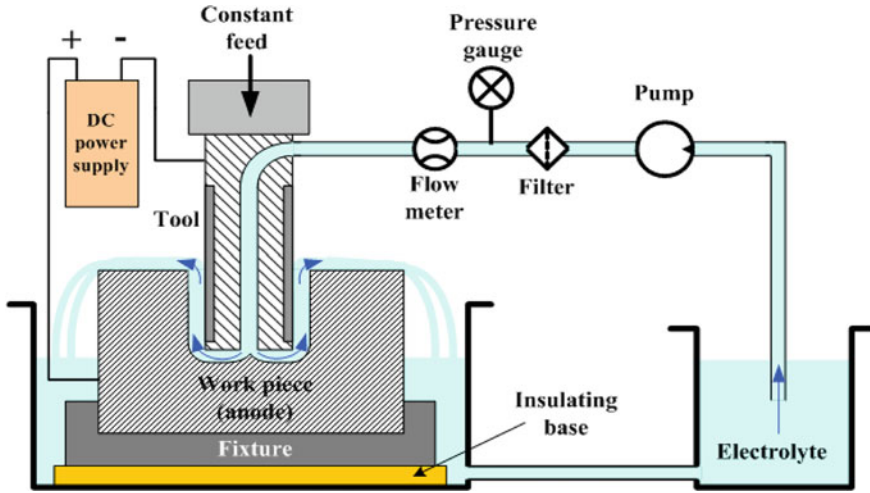


Fig. 1 Schematic diagram of ECM [4]

viability was tentatively confirmed [2]. It is observed that the machining exactness was further developed by the apparatus hopping movement. Be that as it may, the entire machining time expanded since the machining was interfered with during the leap.

Consequently, to eliminate the results, get high machining speed, and recreate exactness, the creators recommended eliminating side effects between the terminal regions by applying ultrasonic vibration to the instrument [3]. Unique about the device cathode hop, ECM machining by applying ultrasonic vibration enjoys quicker machining speed due to the side-effects between terminals during machining. It is because the results are eliminated from the between terminals during machining process. In any case, the impact of the electrolyte focus on the machining qualities and machining of the WC compound, a run-of-the-mill challenging-to-cut material, were not examined (Fig. 1).

2 Need for UV-Assisted ECM

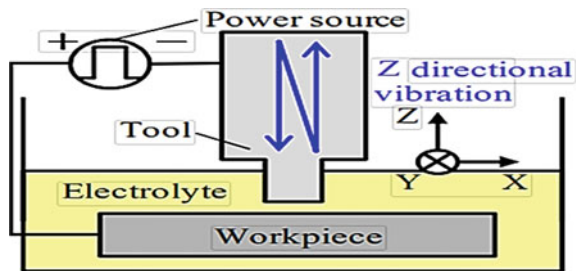
One of the biggest problems with ECM and micro ECM is their low throughput/MRR. This test is significantly simpler to evade when visually impaired highlights are carved in miniscule proportions. The overall MRR increases as the ultrasonic vibration assisted ECM combines the impact of ultrasonic cleaning at the tiny flash hole of a few microns with the traditional release actuated material expulsion. Two factors are the main causes of this. Miniature planes are created as a result of the ultrasonic vibration's activation of cavitation, which rises into the electrolyte at the flash hole and successfully removes debris from the machined zone.

Moreover, the release frequency rises, raising the MRR, as new electrolytes are injected into the flash hole and waste is swiftly and consistently evacuated. The machining flimsiness caused by the tiny flash hole (in the range of microns), which results in a lengthy machining process, a lower MRR, and surface defects, is another test for ECM and micro ECM. Expulsion of debris from the tiny flash hole turns into a test when using a bite-the-dust sinking small ECM to machine large apertures or intricate 3D microstructures. What if it is not quickly and effectively eliminated? In that instance, the rubbish spreads flotsam and jetsam fragments, causing bubbles between the work piece and the electrode and halting the machining operations. Also, because to the trash’s better centralization in the tiny flash hole, arcing (nonstop beginning) occurs on the waste, producing flotsam and jetsam particles to stick to the machined surface and resulting in surface and sub-surface defects. These two main issues in ECM and small ECM were resolved with the use of ultrasonic vibration, which improved ECM’s capacity for complicated 3D microstructures and deep opening micromachining. In addition, the UV-aided ECM can be helpful in the machining of large 3D designs using wire ECM, high viewpoint proportion, and bite-the-dust sinking ECM.

3 Principle of UV-Assisted ECM

A hybrid approach called ultrasonic vibration (UV) assisted ECM combines ultrasonic vibration of the work piece and electrode with a traditional ECM or micro-ECM procedure. To increase the efficacy of the process’ flushing, ultrasonic vibration (at a frequency of 20 kHz or higher) is used in this procedure. The application of ultrasonic vibration to the tool electrode work piece can depend on the applications and difficulties encountered throughout the ECM/micro-ECM process. Figure 2 displays the process mechanics for each of the situations.

Fig. 2 Principle of UV-assisted ECM [5]



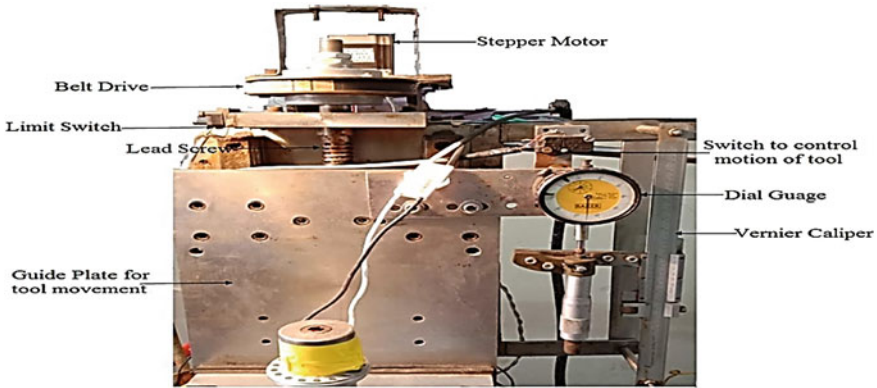


Fig. 3 Photograph of components of Tool Feed arrangement [6]

4 Ultrasonic Vibration Applied to the Tool Electrode

Tool feed mechanism used for USAPECM. The primary function of the tool feed mechanism was to provide vertical feed to the tool assembly against the stationary work piece. The tool feed mechanism unit's subcomponents were the Stepper motor, belt, pulley, lead screw, Vernier caliper, limit switches and carbon brush connectors [6] (Fig. 3).

Rotary motion of stepper motor (2 kg/cm torque) was converted into precise linear motion of tool using the pulley, belt and stainless-steel lead screw. This existing setup tool can be advanced with minimum and maximum 0.8 and 2.2 mm/min feed rates. The maximum vertical movement to the tool electrode is restricted to 120 mm. A short circuit between the tool electrode and work piece was observed when the MRR was less than the tool feed rate [6]. The Servo control mechanism senses the gap current in IEG. If it is greater than the set value, it will stop the further downward movement of the tool electrode and avoids the failure of the tool, power supply unit and ultrasonic unit.

5 Ultrasonic Vibration Applied to the Workpiece

The piezoelectric transducer receives information from the beat generator, which generates the ultrasonic vibration as a sinusoidal wave with a desired recurrence (PZT). As shown in Fig. 4, the work piece receives the ultrasonic vibration transmitted by the PZT actuators through a junction plate. A web based input control system is used to monitor the flash hole and maintain the dependability of the machining [7]. The forward and backward movement of the work piece during vibration results in progressions into the flash hole and dielectric fluid tension over time, maintaining a sinusoidal relationship between the flash hole and strain contrast over time [8].

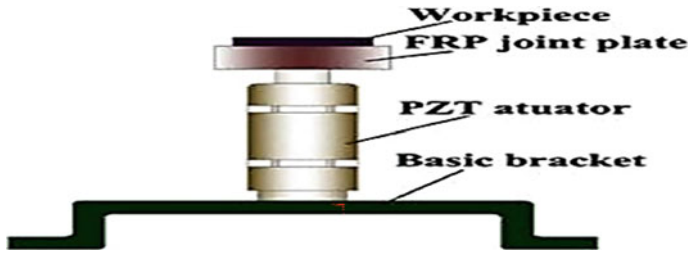


Fig. 4 Vibration applied to work piece [9]

Using ultrasonic vibration, both the original ECM and the smaller ECM were able to resolve those two major problems resolve those.

6 Result and Discussion

6.1 Effect of UVA on Material Removal Rate (MRR)

MRR associated with ECM assisted by ultrasonic vibration is invariably higher than that with unaltered ECM. MRR pattern for a beat on the season of 5 s, both with and without UVA-ECM. As can be observed from the increase in release current, the MRR increases overall, and with UVA-ECM, the increase is slightly greater than that of conventional ECM. Similar to this, a higher voltage boosts the MRR since the release energy is higher [10]. In addition to tiny air pockets and a catapulting stream, longitudinal vibration from the device terminal results in a compressive and rarefaction wave lead.

This wave front starts an intense, accelerated mass exchange across the flash hole that resembles a syphon and causes the selective expulsion of flotsam and jetsam. Electrolytes are supported by the ultrasonic device’s vibration, which divides the dielectric particles into more subdued ones using a half-pattern of hardware that lowers. Due to the impact of rarefaction, the last half of the hardware up development pattern contributes to the creation of air pockets. Also, due to the energy exchange and the power of the charged particle’s ultrasonic vibration in the flash whole, acoustic-electric flow is produced. The start delay is also shortened by acoustic wave-activated collisional ionization. Cavitation oddities are also produced by pressure and rarefaction due to ultrasonic vibration. Due to the application of UVA, the several characteristics discussed above ultimately encourage increased MRR. By synchronizing UVA recurrence to the ECM recurrence and further developing trash departure, Kremar et al. [11] reported a 400% expansion of MRR.

6.2 *Effect of UVA on Surface Roughness and Metallurgical Characteristics*

Due to UVA and the abrasiveness of the generated surface, the ECM process with UV assistance generates the MRR. In this instance, the surface unpleasantness of WC increases significantly over that of conventional ECM. As heartbeat duration and current increase, so does the roughness of the generated surface. The reduction in start latency and increased average heartbeat energy may be the cause of this augmentation. Moreover, when the release of the UVA-ECM nears its conclusion, a larger drop in plasma strain causes large soft particles to shoot out of the liquid pool, creating more deep voids [12]. When the voltage increases, the distance between the device and the work piece increases, resulting in improved waste flushing. The final result is increased cavitation, which increases the roughness of the surface on both the device and work piece surfaces [13, 14].

7 Conclusion

In order to further improve the cycle soundness and execution, ultrasonic-assisted ECM is a hybrid technique that combines the actual characteristics of ultrasonic vibration with the ECM and micro ECM interaction. The ultrasonic vibration was seen as applied in both the work piece and gadget terminal, considering the applications and plans to be machined. This survey paper gives an outline of the standard ECM and ultrasonic vibration helped ECM, as well as incorporates an exhaustive survey of different parts of ultrasonic vibration helped ECM, including significant difficulties and rules to determine the difficulties later on in research. It tends to be closed from the writing that ultrasonic vibration help expands the MRR, surface harshness and apparatus wear proportion because of the decreased arcing, latent heartbeats, cavitation impact and stable release. The MRR can be improved by expanding vibration sufficiency, voltage and current. Increments in release voltage, current, beat term and ultrasonic vibration sufficiency cause expanded surface harshness. In contrast, higher recurrence vibration brings about a lower surface unpleasantness because of the age of numerous release channels. At last, it very well may be inferred that ultrasonic vibration-helped ECM is a successful interaction to machine intricate multiscale structures and hard-to-cut materials on a range of materials and different metals. This further develops the cycle capacity of the conventional ECM and miniature ECM process [15, 16].

References

1. Wilson, J. F. (1971). *Practice and theory of electrochemical machining*. John Wiley & Sons, pp. 79–83.
2. Terada, A., & Natsu, W. (2010). Improvement of ECM characteristics by removing by-products from gap area with tool motion control. In *Proceedings of JSPE 2010 Autumn Meeting*, pp. 227–228 (in Japanese)
3. Natsu, W., Nakayama, H., & Yu, Z. (2012). Improvement of ECM characteristics by applying ultrasonic vibration. *International Journal of Precision Engineering and Manufacturing*, 13(7), 1131–1136.
4. Sharma, K., & Om, J. (2020). A review paper on electro chemical machining. *IJARIE*, 6(1), 2395–4396.
5. Kurogi, S., Natsu, W., & Yu, Z. (2012). Investigation of machining characteristics of ultrasonic vibration assisted ECM. *Applied Mechanics and Materials*, 217–219, 2555–2559.
6. Jadhav, D. B., & Jadhav, P. V. (2021). Effect of process parameters on performance measures of hybrid electrochemical machining (p. 73).
7. Garn, R., Schubert, A., & Zeidler, H. (2011). Analysis of the effect of vibrations on the micro-EDM process at the workpiece surface. *Precision Engineering*, 35, 364–368.
8. Jahan, M., Wong, Y., & Rahman, M. (2012). Evaluation of the effectiveness of low frequency workpiece vibration in deep-hole micro-EDM drilling of tungsten carbide. *Journal of Manufacturing Processes*, 14, 343–359.
9. Tong, H., Li, Y., & Wang, Y. (2008). Experimental research on vibration assisted EDM of micro-structures with non- circular cross-section. *Journal of Materials Processing Technology*, 208, 289–298.
10. Zhixin, J., Jianhua, Z., & Xing, A. (1995). Ultrasonic vibration pulse electro-discharge machining of holes in engineering ceramics. *Journal of Materials Processing Technology*, 53, 811–816.
11. Kremer, D., Lhiaubet, C., Moisan, A. (1991). A study of the effect of synchronizing ultrasonic vibrations with pulses in EDM. *CIRP Annals*, 40, 211–214.
12. Abdullah, A., & Shabgard, M. R. (2008). Effect of ultrasonic vibration of tool on electrical discharge machining of cemented tungsten carbide (WC-Co). *International Journal of Advanced Manufacturing Technology*, 38, 1137–1147.
13. Zhang, J., Lee, T., Lau, W., & Ai, X. (1997). Spark erosion with ultrasonic frequency. *Journal of Materials Processing Technology*, 68, 83–88.
14. Koczypiec, S. (2006). *Research on ultrasonically assisted electrochemical machining with universal electrode tool* (Ph.D. thesis). Cracow University of Technology (in Polish).
15. Yang, I., Park, M., & Chu, C. N. (2009). Micro ECM with ultrasonic vibration using semi cylindrical tool. *International Journal of Precision Engineering and Manufacturing*, 10(2), 5–10.
16. Perusich, S. A., & Alkire, R. C. (2017). Ultrasonically induced cavitation studies of electrochemical passivity and transport mechanism. II. Experimental. *Journal of the Electrochemical Society*, 138(3), 708–7136, 8–13.

Computational Studies on Selection of EV



Nitish Vernekar, Atulchandra Tripathi, Tushar Patel, Umesh Hosmani, Prashant Revankar, and Krishnaraja Kodancha

Abstract In recent years, the vehicle sector has grown enormously. More companies are starting to invest in the development of new electric vehicle-related technologies as EV technology advances. The range of an electric vehicle (EV) is the most crucial component in customer's decision matrix to choose EVs. The list of EV is topped by a brand with a range of 776 and 110 km constitute the lower end of range. The EV market today is more complicated owing to advanced features catching up to make potential buyer perplexed about which EV to purchase. This work presents a comprehensive approach to access EVs comparing their range. The simulation study carried out in the MATLAB Simulink/Simscape environment giving scope to vary motor power and battery capacity. The results can assist the user to compare alternatives and select the ideal EV by analyzing data from simulations for NEDC and WLTP drive cycles.

Keywords Drive cycle · EVs · Computational studies

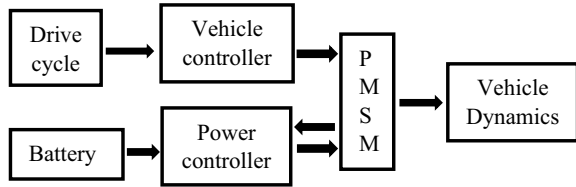
1 Introduction

Model simulation is a computer-based modeling technique that can quickly address real-world problems to evolve effective solution. The analysis of EV involves multi-variable optimization and use of simulation can be very effective. In EV simulation, blocks from libraries are used to build the model, which comprises the lithium-ion battery, a Permanent Magnet Synchronous Motor (PMSM), the motor controller, the battery, motor cooling system and vehicle dynamics. The longitudinal driver, which

N. Vernekar
Design Engineering, KLE TU, Hubli, Karnataka, India

A. Tripathi · T. Patel
LTTS, Vadodara, Gujarat, India

U. Hosmani · P. Revankar (✉) · K. Kodancha
KLE Technological University, Hubli, Karnataka, India
e-mail: pp_revankar@kletech.ac.in

Fig. 1 Block diagram of EV

is part of the motor controller, identifies inaccuracy by taking reference velocity from motor and correcting it to the proper value to match the driving cycle [1]. The motor controller also contains torque demand management in order to supply accurate torque to the vehicle according to the driving cycle, which includes torque for downhill inclination [2]. The most widely utilized drive cycles for range estimation are WLTP and NEDC [3].

Figure 1 shows block diagram for the EV constituted of PMS motor, which has an efficiency ranging from 92 to 97%, employed in the simulation with the cooling function using convection [4]. The battery cooling is of utmost importance in function of EV that includes air cooling, also known as natural convection. The vehicle dynamics block formulates vehicle resistance caused by drag, gravity and rolling forces [2]. EVs are compared with respect to these three drive cycles because, two vehicles have varying battery capacities and motor power. The charging of batteries requires continuous supply of electricity obtained through grid. To alter the grid voltage, batteries are configured in rows and columns. The model employs regenerative braking since the motor functions as a generator during braking and deceleration via a DC–DC converter.

2 Literature Study

In recent years, there has been a significant change in research toward electric vehicles. Simple model of an electric vehicle can be created using an H-bridge, a Pulse Width Modulation (PWM) controller, and a simple DC motor that can execute the drive cycle in MATLAB [5]. Induction motors can be utilized instead, and regenerative braking can be included to recover kinetic energy and return it to the battery [6]. Joshua et al. [1] performed a similar type of investigation by comparing two performance automobiles by varying battery capacity and motor power. The loads in EVs due to battery and humans can change the vehicle stability as per tests for popular brand of car using an electric vehicle with an induction motor [7]. A model with a permanent magnet motor was used to analyze power flow in regeneration and driving [8]. A 3-DOF (Degrees of Freedom) car body can be directly imported from the MATLAB library, and the magic tyre model can be used to investigate vehicle dynamics [9]. Various drive cycles, like as NEDC and Federal Test Procedure (FTP), are accessible on MATLAB software for range estimate while taking into account actual environmental factors of wind, temperature, rolling resistance and drag [2]. The

efficiency of motors may also be evaluated using simulation model by employing several types of motors such as Brush Less Direct Current (BLDC), PMSM and similar designs to determine best to meet the needs. A study was conducted on a two-motor, two-speed arrangement that boosted motor efficiency and running range over a one-speed setup for the Plug-in Hybrid Vehicle (PHEV). The modifications were made to differential [10]. Forces such as aerodynamic drag, grading resistance and rolling resistance all play an important role in car dynamics that must be calculated and to be accounted in the model. C segment vehicle is considered for the simulation, for which the drag co-efficient ranges from 0.2 to 0.3, on account of roads made of concrete, a rolling co-efficient of 0.01–0.03 can be used [2]. The torque is important parameter as it is part of the power train. Currently all-wheel drive vehicles are popular owing to their higher stability compared to two-wheel drive vehicles. They use complex controllers and torque vectoring systems. Studies have reported other controllers, such as sliding mode utilized for AWD (all-wheel drive) electric vehicles. AWD EVs produce more energy during regeneration and are more efficient than a single motor two-wheel drive. Furthermore, features such as ABS (Anti-lock Brake System) and traction control systems operate better with four-motor drive than the differential [11]. In EVs, regeneration means preserving kinetic energy during braking and deceleration as motor functions as a generator in cut-off mode, which is doable in a simple model with the help of H-bridge [12]. The complicated models adopt DC–DC converters for this purpose. Energy Efficient Torque Allocation (EETA) technology is utilized to improve traction efficiency while also performing regeneration activities [13].

3 Methodology

MATLAB is widely used simulation tool for system model analysis by R&D industries to investigate complex real-world problem through mathematical route. The model in this work was created using MATLAB Simulink and Simscape. A PMSM was utilized with thermal port and received torque inputs from torque demand management, which additionally included torque due to tilt. A longitudinal driver (block) was employed to remedy fault and deliver acceleration and deceleration orders to torque demand management. The drive cycles provided the reference velocity to the driver. A basic gear was employed to change the torque to the wheels, and it was further attached to the wheel and axel (block) for rotational and translation conserve. The drag, grad, and rolling inputs were sent to the wheel and axel. The battery was built to provide requisite voltage, with each cell containing 3.6 V and being connected in series and parallel. To keep the PMSM within operating range of 100 °C, natural convection was employed for the motor and the battery and liquid cooling was used for the PMSM.

4 Modelling of Electric Vehicle

To model an EV, certain key components include motor, power train, battery, controller, cooling unit, vehicle dynamics and driver inputs. The model is created in MATLAB Simulink and Simscape a quick overview of these components as well as the specifications utilized for model simulation.

4.1 PMSM

The simulation was carried out using a permanent magnet synchronous motor as the efficiency of these are in the range of 92–97% as compared to Induction Motor (IM), the efficiency of the PMSM also depends on the operating temperatures. The two vehicles investigated have distinct power and torque configurations as indicated in Table 2.

4.2 Battery

Lithium-ion batteries are widely used in EVs due to their high energy to weight ratio with each cell having a potential of 3.6 V and connected in series and parallel combination to obtain required voltage and current. The battery capacities of the two models examined are shown in Table 2 that highlight variation.

4.3 Vehicle Controller

The vehicle controller employs a torque demand management, which works on the longitudinal driver acceleration and deceleration inputs and also sums the torque to inclination and limits the torque within the range of electric car. Equation (1) gives the torque due to inclination were, α is the inclination angle.

$$T = MgR \sin(\alpha) \quad (1)$$

4.4 Vehicle Dynamics

Vehicle dynamics defines the transient variation in the drive cycle due to various conditions encountered in a motion cycle, hence it must be included for simulation

in order to be realistic. The wheel and axel (block) is utilized to provide rotational and translation motion conserves. The forces related to aerodynamic drag, grading resistance and rolling resistance are all included in dynamics [2]. The tractive forces are given by the Eqs. (2, 3 and 4).

$$F_d = 0.5 \times C_d \times \rho \times A_f \times (V - V_w)^2 \quad (2)$$

$$F_r = Mg \cos(\alpha) \quad (3)$$

$$F_g = Mg \sin(\alpha) \quad (4)$$

The SUV constants for the aero drag coefficient are taken to be 0.25 (C_d), and the surface that is taken into consideration for the rolling coefficient is fresh concrete road with a value of 0.015 (f_r).

4.5 Cooling System

A cooling system is linked with motor and battery in electric vehicles. The model employs liquid cooling, using water as a coolant with a density of 1,000 kg/m³ and a specific heat of 4.187 J/kg K, as well as natural convection integrated with the motor with a co-efficient of 25 W/m²K. To keep both motor and battery functioning within their operational ranges, the battery is cooled naturally by convection with a co-efficient of 10 W/m²K.

4.6 Driver Inputs

Initially, only throttle and brake inputs were utilized to validate the system; later, the driving cycles were employed. A longitudinal driver performs function of an error detector in the system by feeding the acceleration and deceleration to the torque demand management using motor feedback and vehicle velocity. The simulation employed two drive cycles, WLTP and NEDC as they are used widely for the purpose of emissions, fuel efficiency and range for electric vehicle. To estimate range, drive cycles were repeated. The parameters of the drive cycles are highlighted in Table 1.

5 Results of Simulation

The Brand A and Brand B were taken into consideration for simulation and the specifications of these EVs are revealed in Table 2.

Table 1 Drive cycles

Parameters	WLTP	NEDC
Time (sec)	1,535	1,600
Distance (km)	100/395	129/280
Average speed (km/h)	327	230
Top speed (km/h)	120	125

Table 2 Vehicle simulation parameters

Parameters	Brand-A	Brand-B
Weight (kg)	1,535	1,600
Power (kW)/torque (Nm)	100/395	129/280
System voltage (V)	327	230
Battery capacity (Ah)	120	125
Wheel radius (m)	0.216	

After construction, the model was put through only the throttle and the brake commands to check the correctness of the system later many drive cycles were tested to ensure appropriate operation. The simulation for drive cycles were compared for variation of speed with time. The WLTP replaces the NEDC drive cycle and includes special provisions for testing of various categories of hybrid electric and electric vehicles. The WLTP dynamo test is accepted globally for convectional, Hybrid and electric. The WLTP drive cycle comes with two phases: low and medium which gives us a drive conditions similar to city.

Figure 2 provides the fluctuation of distance with time for Brand A, WLTP drive cycle. The Brand A’s battery capacity is lower than that of the Brand B, yet there is no much difference in the ranges of the EV as the Brand A gives a range of 420 km.

Figure 3 gives the variation of distance with time for Brand A, WLTP drive cycle with a range of 425 km for the battery capacity of 125 Ah.

Figure 4 depicts variation of distance with time for the Brand A, NEDC drive cycle. The NEDC was used in earlier times and is currently replaced by WLTP drive

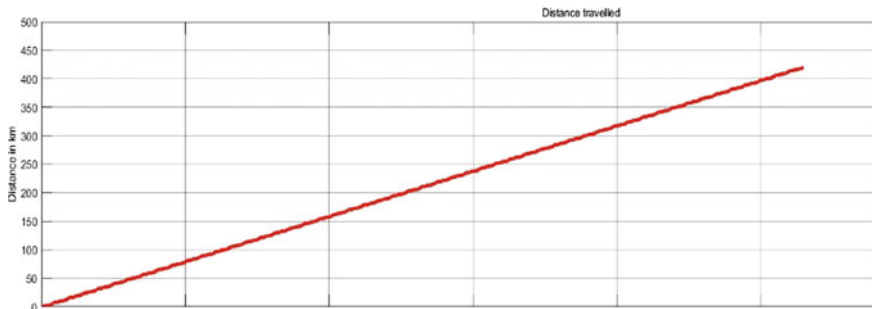


Fig. 2 Variation of distance with time for WLTP drive cycle (420 km)—Brand A

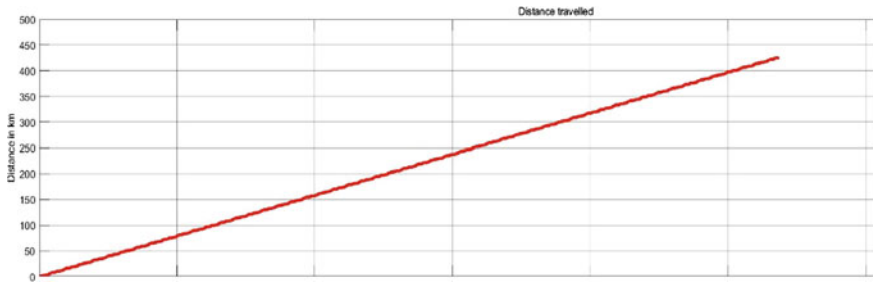


Fig. 3 Variation of distance with time for WLTP drive cycle (425 km)—Brand B

cycle. For NEDC the Brand A was providing a range of 531 km as the motor power and grid voltage used is lower than that of the other. The Brand B offered a range of around 375 km for the same cycle, which is substantially less than Brand A as shown in Fig. 5.

As expected, results were different for both the brands as they change in the motor torque, power, battery capacity, weight and grid voltages.

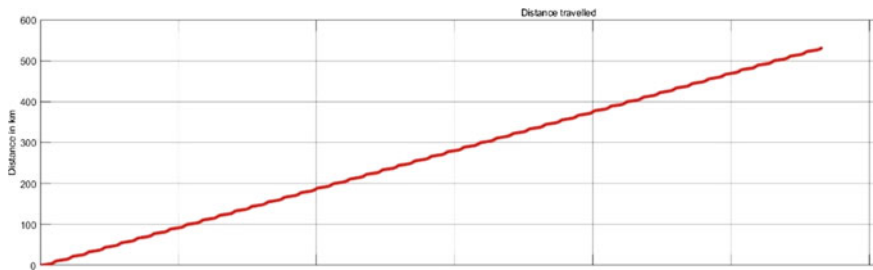


Fig. 4 Variation of distance with time for NEDC drive cycle (531 km)—Brand A

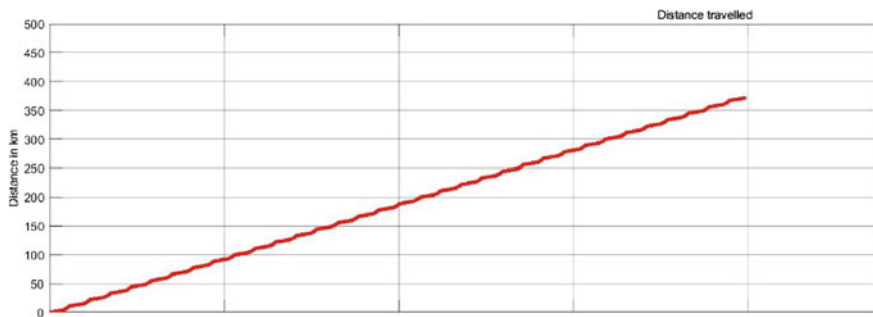


Fig. 5 Variation of distance with time for NEDC drive cycle (372 km)—Brand B

6 Conclusions

Owing to rising cost of fossil fuels and associated greenhouse gas release causing environmental harm, there is a need for vehicle that travels more distance per charge. Despite EVs having high initial they are eco-friendly and have lower operation cost. The salient observations from the simulation are as follows,

The WLTP driving cycle is longer and closer to actual driving conditions than the NEDC and the Brand B outperforms Brand A by a margin of 1.2%.

The NEDC drive cycle is not practical due to its deviation from actual driving. Here Brand A is leading with 29% more range than Brand B and the reason could be the grid voltages of both the EVs as, the Brand A uses a higher bus voltage than that of Brand B and can be advantageous considering regenerative braking.

References

1. Slough, J., Belcher, M., Tsui, T., & Bhattacharya, S. (2021). Modelling and simulation of electric vehicles using Simulink and Simscape. In *IEEE 94th vehicular technology conference*.
2. Kiyakli, A. O., & Solmaz, H. (2018). Modelling of an electric vehicle with matlab/simulink. *International Journal of Automotive Science and Technology*, 2(4), 9–15.
3. Lokhande, N., Deore, A., Dinani, J., & Sayed, N. (2021). Range estimation of electric vehicle using matlab. In *6th International conference for convergence in technology*.
4. Kumar, K. B. (2020). Simulation of electric vehicle drive with MATLAB/simulink. *International Journal of Advances in Engineering and Management*, 2(1), 22–27.
5. Sharmila, B., Srinivasan, K., Devasena, D., Suresh, M., Panchal, H., Ashokkumar, R., Meenakumari, R., Kumar, K., & Shah, R. R. (2021). Modelling and performance analysis of electric vehicle. *International Journal of Ambient Energy*, 43(1), 5034–5040.
6. Mali, A., Shukla, A., Husain, A., Hole, K., & Edake, V. (2021). Design and analysis of powertrain for electric vehicle. *International Research Journal of Engineering and Technology*, 8(8), 1223–1242.
7. Chauhan, S. (2015). Motor torque calculations for electric vehicle. *International Journal of Scientific and Technology*, 4(8).
8. Husain, I., & Islam, M. S. (1999). *Design, modelling and simulation of an electric vehicle system*. SAE technical paper series, 1999-01-1149.
9. Sinha, R., & Bangia, S. (2021). Performance analysis of electric vehicle based on various working scenarios. *International Transaction Journal of Engineering, Management and Applied Sciences and Technology*, 12(1), 1–15.
10. Mohd, T. A. T., Hassan, M. K., & Aziz, W. A. (2015). Mathematical modeling and simulation of an electric vehicle. *Journal of Mechanical Engineering and Sciences*, 8, 1312–1321.
11. Hadboul, R. M., & Ali, A. M. (2021, June). Modeling, Simulation and Analysis of Electric Vehicle Driven by Induction Motor. In *IOP Conference Series: Materials Science and Engineering* (vol. 1105, no. 1, p. 012022). IOP Publishing.
12. Chen, J., Yu, J., Zhang, K., & Ma, Y. (2018). Control of regenerative braking systems for four-wheel-independently-actuated electric vehicles. *Mechatronics*, 50, 394–401.
13. Pappalardo, C. M., Lombardi, N., Dašić, P. V., & Guida, D. (2019, July). Design and development of a virtual model of an electric vehicle of category L7. In *IOP Conference Series: Materials Science and Engineering* (vol. 568, no. 1, p. 012114). IOP Publishing.

Analysis of Spatio-temporal Characteristics of Rainfall Using Precipitation Concentration Index (PCI) and Heatmap for Solapur District of Maharashtra, India



Wasim Ayub Bagwan 

Abstract The current study is concerned with the spatio-temporal variability of the annual precipitation concentration in the Solapur district of Maharashtra. Rainfall from the year 1971 to 2013 has been considered for the current analysis. Along with the Precipitation Concentration Index (PCI), in this study heatmap and spatial interpolation approach were used to show the rainfall distribution in the Solapur district. The PCI has the potentiality in managing the water resources and risk related to natural hazards like drought as it indicates the fluctuations in the concentration. The fluctuations in the spatio-temporal pattern of rainfall have a great impact on the frequency of droughts. In this paper, monthly PCI in Solapur district has been carried out from 1971 to 2013. In addition to PCI, heatmap and spatial interpolation approach were used to show the spatial distribution of rainfall and PCI in the study region. Inverse Distance Weighted (IDW), a spatial interpolation technique was applied in a geoinformatics platform to show the rainfall surface. The PCI has the potentiality in managing the water resources and risk related to natural hazards like drought as it indicates the fluctuations in the concentration. Another, synoptic visualization technique named heatmap has been employed at individual weather station level to display the rainfall pattern.

Keywords Drought analysis · Drought prone region · Heatmap · Precipitation Concentration Index (PCI) · Rainfall distribution · Solapur district

W. A. Bagwan (✉)

School of Rural Development, Tata Institute of Social Sciences, Tuljapur 413601, Maharashtra, India

e-mail: wasim.bagwan16@gmail.com

1 Introduction

Rainfall is one of the crucial climatic patterns shaping the regional environment. It is one of the drivers of natural hazards like drought, floods, etc. and these activities could have profound impacts on the natural and human environment [1]. One of the key characteristics of Indian rainfall and its monsoonal is in its nature. The Indian climate varies substantially due to unstable monsoon and other weather conditions. India receives 80% of its rainfall from June to September. It's because of its uneven nature some regions experience extreme floods whereas some go under severe drought conditions. Due to this, the intensity and duration of rainfall play a major role in rainfall variability across the country [2]. The variability of the amount of precipitation received within an environment has an influence on many natural processes like groundwater availability, changes in fluvial regime, soil loss, and likelihood [3]. South-west monsoon (June–September) is the main rainy season in India which contributes 70–79% of the average annual rainfall [4]. Drought is the severe and recurrent characteristic of the climate which is the impact of rainfall over time [5]. It is also a multifaceted and least understood of all-natural hazards, which affects more people as compared to other natural hazards Basically, drought is categorized into four classes; hydrological drought, meteorological drought, socio-economic drought, and vegetative drought. Meteorological drought is generally described by rainfall and humidity and its duration [6]. The Precipitation Concentration Index (PCI) has applicability in the valuation of the amount of seasonal rainfall concentration and delivers information for the comparison of dissimilar climates in terms of rainfall regimes for different periods [7]. The investigation aimed to display the spatial rainfall pattern over the Solapur district and to study the annual average standards of PCI for each weather station from the year 1971 to 2013.

2 Study Area

Solapur District is located in the Maharashtra state of India (Fig. 1). It is located at $74^{\circ}36'27.473\text{E}$ – $76^{\circ}25'43.854\text{E}$ (Longitude) to $17^{\circ}6'5.793\text{N}$ – $18^{\circ}33'18.585\text{N}$ (Latitude). The district covers $14,844.6\text{ km}^2$ which is 4.82% of Maharashtra state. The district has 338.8 km^2 of urban area whereas $14,505.8\text{ km}^2$ is a rural area. The district is divided into 11 blocks. It is the fourth largest district of Maharashtra state of land area and seventh largest in terms of population. According to the terrain conditions, the district is divided into three natural zones as Eastern zone, Central or transitional zone, and Western zone. All the eleven blocks of the district are susceptible to drought conditions. The entire district comes under the rains shadow zone [8]. According to Koppen-Geiger classification, the Solapur district comes under two climate zone viz. 3: Aw Tropical, savannah, and 5: BWk Arid, desert, cold zone [9].

Weather stations in Solapur district



Fig. 1 Location of weather stations in Solapur district of Maharashtra state, India

3 Material and Methodology

3.1 Data

For the current analysis, monthly rainfall data of 10 weather stations from the period 1971 to 2013 were used to calculate the PCI and to display the rainfall pattern. Figure 1, shows the locations of the weather stations. The rainfall data were provided by the India Meteorological Department (IMD), Pune. To locate the weather stations Google Earth Pro software has been used and the KML file was created which then imported into SAGA GIS software and converted into a shape file.

3.2 Precipitation Concentration Index (PCI)

To define the temporal rainfall pattern, Oliver [10] proposed the Precipitation Concentration Index (PCI). This index is used to quantify the periodic variation in the rainfall [11]. PCI is measured in terms of % [12].

$$PCI = \frac{\sum_{i=1}^{12} P_i^2}{(\sum_{i=1}^{12} P_i)^2} \times 100 \tag{1}$$

where P_i indicates monthly rainfall of the i th month which can be calculated for each weather station and each year during the period under study. For the proper and precision output of the results of PCI based on the large volume of rainfall data ‘precintcon’, an R package was employed in the R Studio software interface.

3.2.1 Computation of Rainfall Variability

The coefficient of variation (CV) was calculated to analyze the rainfall variability.

$$CV = \frac{\sigma}{\bar{x}} \quad (2)$$

$$CV(\%) = \frac{\sigma}{\bar{x}} \times 100 \quad (3)$$

where σ is the standard deviation and \bar{x} is the average of the rainfall of rainfall from 1971 to 2013 respectively. CV (%) is the coefficient of variation in percentage.

3.3 Implementation of the Heatmap, PCI Charts, and IDW Interpolation

Heatmaps are 2-D representing of data where values of a certain parameter are shown as colors. Heatmaps are having immense importance to paper, reports, and presentation purposes as it summarizes the large quantity of data that would be much more difficult to understand it presented numerically. To showcase the heatmap of the rainfall pattern at each weather station in the Solapur district, a superheat R package [13] was used in the R Studio software. The plotting of the PCI charts based on the PCI values at each station ‘precintcon’ package [14] has been used in the R studio platform. Further, we used Inverse Distance Weighted (IDW) stated as, the influence of a magnitude that is taken from any location in space drops inversely with distance [15]. It further elaborates that, a site situated near to weather station, from which readings have been taken, will have a value equal to the value measured in the weather station and the opposite is true for the place located further away from such weather stations. The weighting factor is provided by taking the inverse of the distance or by taking the inverse of its square or log [15]. For the IDW interpolation System for Automated and Geoscientific Analyses (SAGA) GIS; an open-source software was used [16].

4 Results and Discussion

4.1 Distribution of Rainfall Pattern and PCI

According to this investigation of rainfall distribution during the temporal resolution from 1971 to 2013, the average rainfall value was observed in the study area was 635.36 mm/year with a standard deviation of 29.18. Figure 2 shows the spatial distribution of rainfall in the study area. The distribution of rainfall ranges between 577.94 mm/year and 722.95 mm/year. The western part of the study region receives less rainfall as compared to the eastern part. The average rainfall value in India was found to be 1,190 mm/year [17], hence the present study area receives less rainfall as compared to the average rainfall value of India.

The average PCI across the entire district for the 4 decades for each of the 10 weather stations was calculated. The IDW interpolation method was used to display the spatial dispersal of PCI. It displayed a spatial increasing trend from east to west. The PCI values range between 21.5 and 27.6% and come under the category of strong irregularity as suggested by [11]. Precipitation Concentration Index (PCI) for the Solapur district based on monthly rainfall data is displayed in Fig. 3. The PCI value for the study area has shown a minimum of 22.4% and a maximum of 27.2%, respectively with mean PCI 24.78% and standard deviation 1.23. The PCI shows a trend in decreasing range from east to westward of the Solapur district. Its distribution was not uniform across the study area. By analyzing the PCI range with Table 1, we have found that in the entire district the seasonal concentration was in ‘strong irregularity’.

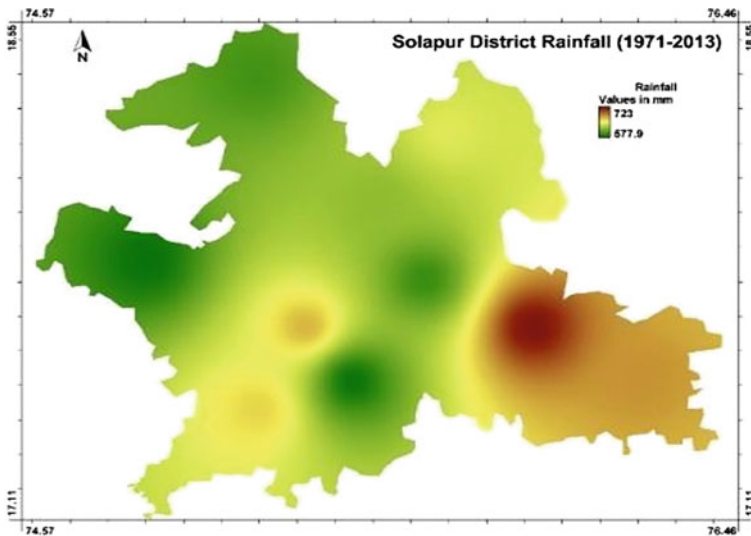


Fig. 2 Rainfall pattern from 1971 to 2013

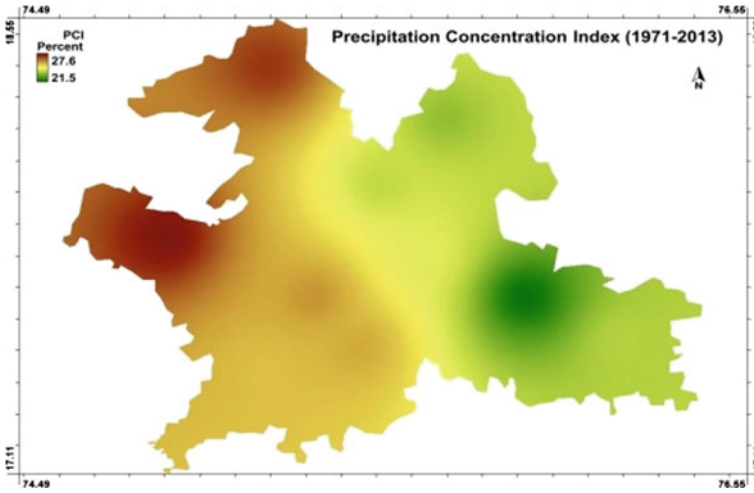


Fig. 3 Pattern of PCI from 1971 to 2013

Table 1 Classification of Precipitation Concentration Index [11]

S. no.	PCI range	PCI seasonal concentration
1	<10	Uniform
2	11–15	Moderate seasonal
3	16–20	Irregular distribution
4	>20	Strong irregularity

4.2 Analysis of PCI Chart

The distribution of average annual Precipitation Concentration Index (PCI) values for the temporal resolution from 1971 to 2013, for each of 10 weather stations separately, is listed in Table 2.

1. Akkalkot weather station, which is located in the southeast part of the district, and has an average rainfall value of 682.05 mm/year with a standard deviation of 232.45. Figure 4a depicts the PCI chart of Akkalkot weather station. The PCI value of this weather station was found to be 23.69. The range of PCI of Akkalkot weather station was found between 13.49 and 32.54% in 1997 and 2003, respectively.
2. Barshi weather station located in the northeast of the Solapur district, the average rainfall at this location was found to be 643.38 mm/year with std. dev. of 196.11 mm. The average PCI value was 23.32% and ranges from 16.12 to 32.29% in 1977 and 1984, respectively. Figure 4b shows the PCI chart of Barshi weather station.

Table 2 List of weather stations with PCI and rainfall with descriptive statistics [18]

Period	Data unavailable year	Weather stations	Average PCI	Average rainfall in mm	Std. dev	CV (%)
1971–2013	2007	Akkalkot	23.69	682.05	232.45	34.08
1971–2013	2007	Barshi	23.32	643.38	196.11	30.48
1971–2013	2007	Karmala	26.94	597.3	225.20	37.70
1971–2013	1978, 1983, 2007	Madha	23.86	619.71	226.62	36.57
1971–2013	2007	Malshiras	27.56	577.94	305.31	52.83
1971–2013	2007	Mangalwedha	25.55	579.78	208.32	35.93
1971–2013	2007	Mohol	24.28	594.72	205.89	34.62
1971–2013	2007	Pandharpur	25.81	670.68	256.78	38.29
1971–2013	2007	Sangola	25.29	662.47	263.26	39.74
1971–2013	–	Solapur Observatory	21.51	722.96	214.05	29.61

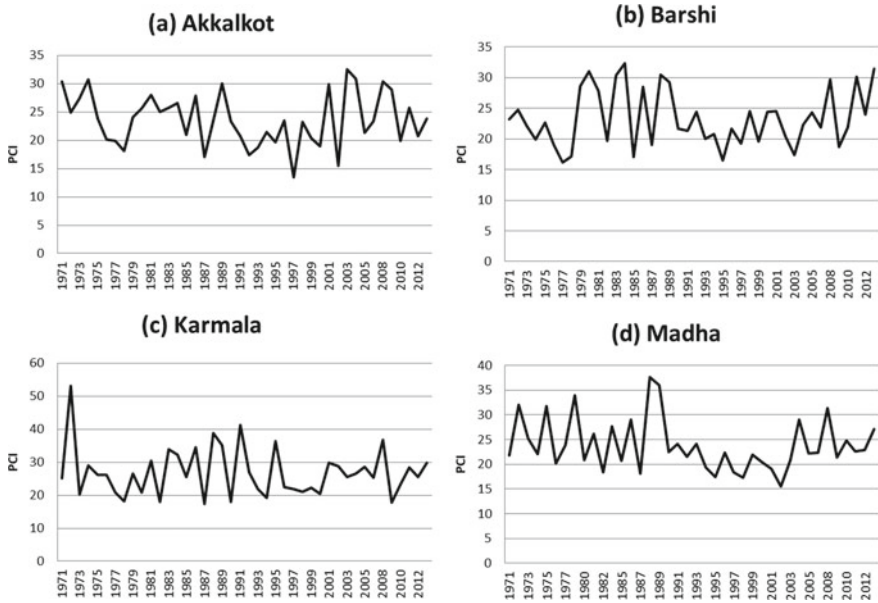


Fig. 4 PCI chart of **a** Akkalkot, **b** Barshi, **c** Karmala and **d** Madha

- From Fig. 4c, Karmala weather station is located in North West of the study region. Karmala received 597.30 mm/year of rainfall with std. dev. of 225.20. The average PCI value was found to be 26.94% and range between 17.47 and 53.12%. The extreme value of PCI was found at this station in the year 1972; which was the worst drought in the history of India.
- Madha weather station is located near the center of the district. Madha received 619.71 mm/year with std. dev. of 226.62 and the average PCI was found to be 23.86%. The PCI ranges from 15.53 to 37.69%. During 1988 and 1989 there occurred strong irregularity in the amount of rainfall. The PCI chart was displayed in Fig. 4d.
- Malshiras weather station is located on the west side of the Solapur district. It received 577.94 mm/year of rainfall with std. dev. of 305.31. The average PCI value was found to be 27.56% and ranges between 15.85 and 49.41%. In the years 1999 and 2008 it was faced high fluctuation in the rainfall and hence high PCI value was found. Figure 5a shows the PCI chart of Malshiras weather station.
- Mangalwedha weather station is located in the southern part of the area under investigation. From 1971 to 2013 it has received average rainfall of 579.78 mm/year with std. dev. of 208.32. The average PCI value was found to be 25.55%. The range of PCI was found between 14.85 and 37.76%. Figure 5b indicates the PCI chart of Mangalwedha. In the years 1986 and 1988, this region faced strong irregularity in the amount of rainfall.

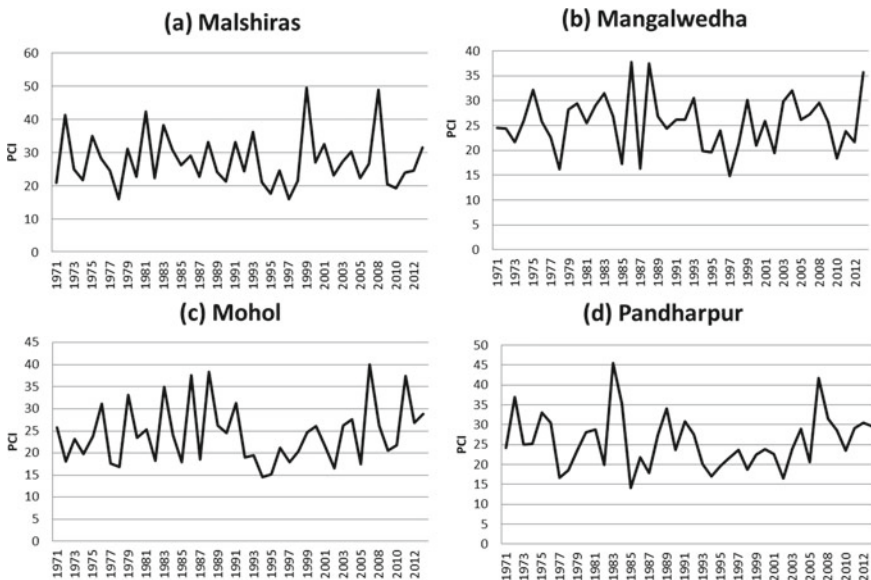


Fig. 5 PCI chart of a Malshiras, b Manalwedha, c Mohol and d Pandharpur

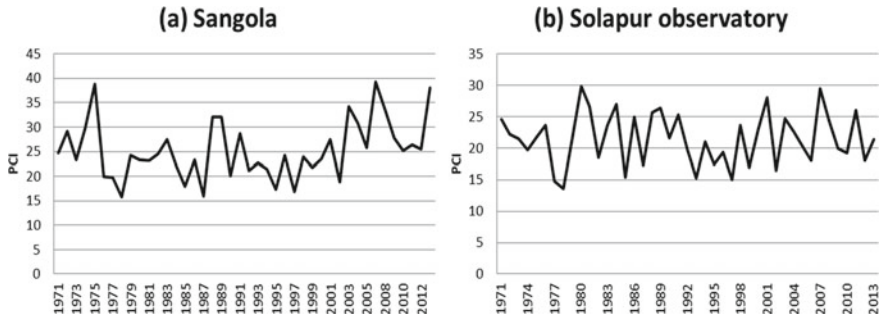


Fig. 6 PCI chart of **a** Sangola, **b** Solapur observatory

7. Mohol weather station is located close to the center of the district. It received an average rainfall of 594.72 mm/year with std. dev. of 205.89. The average PCI value at Mohol was 24.28%. The minimum PCI was 14.63% and the maximum was 40.01%. Figure 5c displays the PCI chart of Mohol. In the years 1994 and 1995 rainfall was in moderate concentration and in the year 2006 it faced very severe irregularity.
8. Pandharpur weather station is located proximate the midpoint of the district. From 1971 to 2013 it has received average rainfall of 670.68 mm/year with std. dev. of 256.78. The average PCI value was found to be 25.81. The minimum PCI was 14.11% and the maximum was 45.49%. In the year 1983 severe irregularity was observed. And, in the year 1985 moderate seasonality was observed. Figure 5d portrays the PCI chart of the Pandharpur.
9. Sangola is located southwest of the Solapur district. During the considered temporal scale, it has received average rainfall of 662.47 mm/year with std. dev. of 263.26. The average PCI value observed at this location was 25.29%. The minimum value of PCI was 15.86% and the maximum was 39.33%. In the years 1975 and 2006 strong irregularity was observed. Figure 6a depicts the PCI chart of Sangola weather station.
10. Solapur observatory is located in Solapur city. Where it has received an average annual rainfall of 722.96 mm/year with std. dev. of 214.05. The average PCI observed value was 21.51%. The minimum value of PCI was 13.6% and the maximum was 29.78%. In the year 1979, it has found severe irregularity and the lowest value was observed in the year 1978. Figure 6b depicts the PCI chart of Solapur weather station.

4.3 Description of Heatmaps at Respective Weather Stations

Heatmap is showing the value of particular variables in the form of color gradients in the form of row and columns. In the case of the heatmap of rainfall, as used herein in this study, the row represents the year and columns represent the month. According to Fig. 7a, which indicated the heatmap rainfall pattern of Akkalkot weather station, the main period of rainfall starts from June to October. Along with this, in the month of April and May pre-monsoon rainfall also has occurred. Figure 7b shows the condition of rainfall at Barshi weather station. The rainfall was concentrated in the month from May to November. Figure 7c shows the heatmap of the Karmala weather station. From the month of June to November there was major rainfall duration. From 1971 to 1990 pre-monsoon rainfall frequency was high at this weather station. Figure 7d shows the rainfall condition at the Madha weather station. The main period of rainfall was found to be June to November. Madha receives a high amount of rainfall in the month of September. Mohol weather station receives pre-monsoon rainfall in the month of April and May. The rainfall condition at Malshiras is displayed in Fig. 7e using a heatmap. Normal monsoon takes place from June to October. Also, it received pre-monsoon rainfall in the month of May. But, in June 1999 there occurred a huge amount of rainfall which was more than the average amount of rainfall in a year. The rainfall pattern at Mangalwedha is shown in Fig. 7f, which gives an overview of the condition of the rainfall pattern. The monsoon was mainly concentrated in the months from June to October. Generally, a high amount of rainfall occurs in the month of September and October at Mangalwedha. It also receives pre-monsoon in the month of May and post-monsoon in the month of November. And, by analyzing the recorded rainfall at Mohol station, heatmap as shown in Fig. 7g, the location has a history to get more rainfall in the month of September. Generally, monsoon lasts here by the month of November. Pandharpur weather station received rainfall mainly from June to November. Also, it received pre-monsoon in the month of May. This weather station receives a good amount of rainfall in the month of September and October. Figure 7h displays the heatmap of the Pandharpur weather station. At Sangola weather station, June to October was the main monsoon period. But, in the month of May pre-monsoon rainfall frequency was quite high before the year 2005. By analyzing the heatmap portrayed in Fig. 7i representing the condition of rainfall at Sangola, in the month of September and October, this location received a good amount of rainfall. Solapur weather station receives rainfall mainly during the monsoon season, i.e., June–November, but it has also recorded to receive a good amount of pre-monsoon rainfall in the month of April and May. Figure 7j represents the heatmap condition at Solapur weather station.

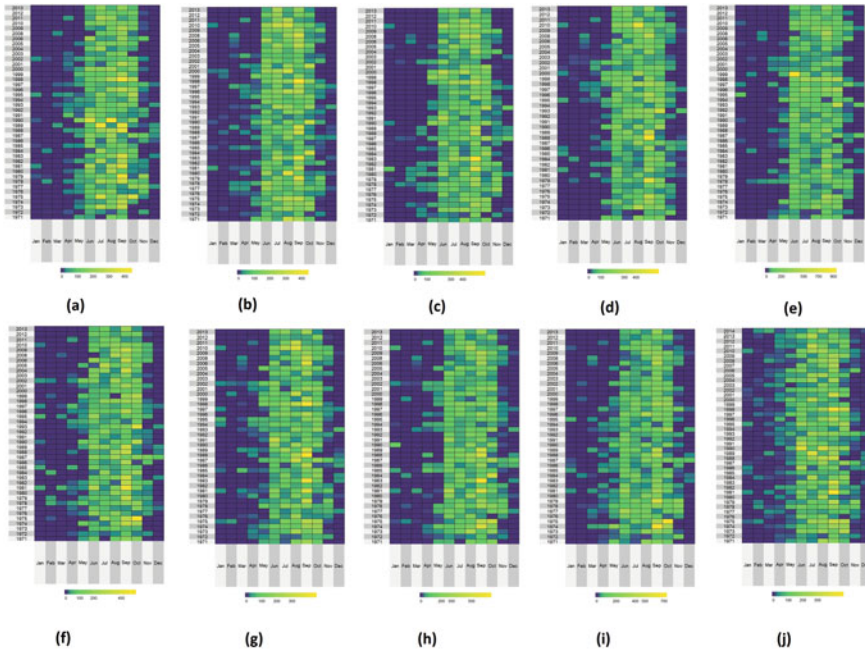


Fig. 7 Heatmap showing rainfall pattern of weather stations in Solapur District at each block level weather station

5 Conclusion

The PCI is an indicator of the variability of rainfall within an environment and hence helps in showing the water availability. From the analysis of the weather station by looking at the PCI line trend we can have closer look at drought conditions. The PCI has the potentiality in managing the water resources and risk related to natural hazards like drought as it indicates the fluctuations in the concentration. Heatmap is a very useful technique in finding the high values of rainfall at a glance. And the technique has also answered questions like in which year and less or high rainfall has taken place? Whereas, heatmap helps in the analysis of rainfall and gives a synoptic view at each weather station, and can help in understanding the climate scenarios. Additionally, the shift in the rainfall can be easily detected using this technique. The PCI and heatmaps is very useful and applicable tool to recognize the precipitation behavior and can be applied to understand other droughts related analysis.

Code

Arrange the data according to this

```
Year MonthPrecipitation
1971 1 0
1971 2 0
1971 3 0
1971 4 0
1971 5 56
1971 6 41.3
1971 7 0
1971 8 141.5
1971 9 101
1971 10 0
```

Select file like this

```
> library (precintcon)
> ak<-read.data(choose.files())// choose .CSV file of above arranged data
> view(ak)
> pci(ak)
> pplot.pci(ak)
```

For heatmpap

Data arrangement in .CSV file

```
YearJanFebMarAprMay Jun JulAug Sep OctNov Dec
1971 0 0 0 0 56 41.3 0 141.5 101 0 0 0
1972 0 0.6 0 5 0 62 28 5 71 0 49 0
```

R Studio code

```
>library(superheat)
>Any1<- read.csv("C:/Users/DES/Desktop/Heatmaps/Mangalwedha2.csv",header= TRUE, sep = ",")
> View(Any1)
> row.names(Any1)<-Any1$Year
> Mang<-subset(Any1,select = -c(Year))
> superheat(as.matrix(Any1))
```

Acknowledgements I would also like to thank India Meteorological Department (IMD), Pune for providing precipitation data at given weather stations. Also, grateful to datawrapper.de for platform to map Fig. 1.

Availability of code Coding is included in the manuscript.

Conflict of interest None.

References

1. Shi, P., Wu, M., Qu, S., Jiang, P., Qiao, X., Chen, X., & Zhang, Z. (2015). Spatial distribution and temporal trends in precipitation concentration indices for the Southwest China. *Water Resources Management*. <https://doi.org/10.1007/s11269-015-1038-3>

2. Nandargi, S., & Aman, K. (2018). Precipitation concentration changes over India during 1951 to 2015. *Scientific Research and Essays*, 13(3), 14–26. <https://doi.org/10.5897/SRE2017.6540>
3. Adegun, O., & Balogun, I. (2015). Analysis of rainfall distribution in Owerri and Enugu, Nigeria using precipitation concentration index. *Ethiopian Journal of Environmental Studies and Management*, 8(4), 408. <https://doi.org/10.4314/ejesm.v8i4.6>
4. Kumar, K. N., Rajeevan, M., Pai, D. S., Srivastava, A. K., & Preethi, B. (2013). On the observed variability of monsoon droughts over India. *Weather and Climate Extremes*. <https://doi.org/10.1016/j.wace.2013.07.006>
5. Modaresi Rad, A., Khalili, D., Kamgar-Haghighi, A. A., Zand-Parsa, S., & Banimahd, S. A. (2016). Assessment of seasonal characteristics of streamflow droughts under semiarid conditions. *Natural Hazards*, 82(3), 1541–1564. <https://doi.org/10.1007/s11069-016-2256-6>
6. Bandyopadhyay, N., & Saha, A. K. (2016). A comparative analysis of four drought indices using geospatial data in Gujarat, India. *Arabian Journal of Geosciences*, 9, 11. <https://doi.org/10.1007/s12517-016-2378-x>
7. Zhang, K., Yao, Y., Qian, X., & Wang, J. (2019). Various characteristics of precipitation concentration index and its cause analysis in China between 1960 and 2016. *International Journal of Climatology*, 39(12), 4648–4658. <https://doi.org/10.1002/joc.6092>
8. Solapur.gov.in. (2020). *An official website of Solapur district by the Govt. of India*. <https://solapur.gov.in/en/geography>
9. Beck, H. E., Zimmermann, N. E., McVicar, T. R., Vergopolan, N., Berg, A., & Wood, E. F. (2018). Present and future Köppen-Geiger climate classification maps at 1-km resolution. *Scientific Data*, 5(1), 180214. <https://doi.org/10.1038/sdata.2018.214>
10. Oliver, J. E. (1980). Monthly precipitation distribution: A comparative index. *Professional Geographer*. <https://doi.org/10.1111/j.0033-0124.1980.00300.x>
11. Michiels, P., Gabriels, D., & Hartmann, R. (1992). Using the seasonal and temporal Precipitation concentration index for characterizing the monthly rainfall distribution in Spain. *CATENA*. [https://doi.org/10.1016/0341-8162\(92\)90016-5](https://doi.org/10.1016/0341-8162(92)90016-5)
12. Mayowa, O. O., Pour, S. H., Shahid, S., Mohsenipour, M., Harun, S. B., Heryansyah, A., & Ismail, T. (2015). Trends in rainfall and rainfall-related extremes in the east coast of peninsular Malaysia. *Journal of Earth System Science*. <https://doi.org/10.1007/s12040-015-0639-9>
13. Barter, R. L., & Yu, B. (2018). Superheat: An R package for creating beautiful and extendable heatmaps for visualizing complex data. *Journal of Computational and Graphical Statistics*, 27(4), 910–922. <https://doi.org/10.1080/10618600.2018.1473780>
14. Pova, L., & Nery, J. (2016). Precipitation intensity, concentration and anomaly analysis. Version 2.3.0. <https://cran.rproject.org/web/packages/precintcon/precintcon.pdf>
15. Carrega, P. (2010). *Geographical information and climatology*. Wiley.
16. Conrad, O., Bechtel, B., Bock, M., Dietrich, H., Fischer, E., Gerlitz, L., & Böhner, J. (2015). System for Automated Geoscientific Analyses (SAGA) v. 2.1.4. *Geoscientific Model Development*, 8(7), 1991–2007. <https://doi.org/10.5194/gmd-8-1991-2015>.
17. Kaur, S., & Purohit, M. K. (2015). *Rainfall statistics of India*. ESSO/IMD/HS R. F. REPORT/04(2016)/22.
18. wikipedia. (2022). https://en.wikipedia.org/wiki/Solapur_district

Forecasting of PM₁₀ Concentrations in Indian Medium-Sized City Using New Combined Grey Model



Sagar Shinde and Vilas Karjinni

Abstract Indian medium-sized city, Kolhapur, has witnessed consistent growth in ambient PM₁₀ concentrations over the last few years, and an accurate forecast is essential. However, for any forecast model, its prediction accuracy and capacity are prerequisites. Accordingly, a combined grey model was developed by combining the grey model [GM (1,1)] and the simple exponential smoothing (SES) model. The new model grey simple exponential smoothing model, abbreviated as GSESM, is newly utilized for PM₁₀ concentrations. To demonstrate the applicability of the proposed GSESM, the GM (1,1) and SES models are also introduced. The PM₁₀ concentrations data from 2008 to 2019 and 2020 were used for in-sample and out-of-sample calculations, respectively. With the relatively lowest mean average percentage error (MAPE = 2.89%) value in the out-of-sample case and reasonable development coefficient ($-a = 0.0068$) value, the GSESM proves it is not only highly accurate but also it can be used for mid-long term forecasts. Finally, the GSESM was utilized to forecast PM₁₀ concentrations (2021–2025).

Keywords Medium-sized city · PM₁₀ concentrations · Combined grey model · Forecasting

1 Introduction

Air pollution has become a significant global health, environmental, economic, and social problem. For instance, in 2016, the World Health Organization (WHO) estimated that 92% of the world's population lives where air quality levels exceed WHO limits [1]. Various major air pollutants responsible for severe air pollution include nitrogen dioxide (NO_x = NO + NO₂), sulfur dioxide (SO₂), carbon monoxide (CO),

S. Shinde (✉)

Shivaji University, Kolhapur and SETI, Panhala, Kolhapur, Maharashtra, India
e-mail: sagar.shinde@seti.edu.in

V. Karjinni

Kolhapur Institute of Technology's College of Engineering (Autonomous), Kolhapur, Maharashtra, India

particulate matter [PM; particles with aerodynamic diameters (in μm) under 10 (PM_{10}) and 2.5 ($\text{PM}_{2.5}$)], ground-level ozone (O_3), and lead (Pb). Further, the United States Environmental Protection Agency (U.S. EPA) has specified these six common air pollutants as part of the 1971 Clean Air Act [2]. The main reason for selecting these pollutants is that they are harmful to human health, widespread, and come from multiple sources [3]. Of these pollutants, air pollution related to PM has emerged as an increasing cause of concern worldwide, especially in developing nations such as India. For example, in 2014, WHO reported that PM-related air pollution was the fifth leading cause of death in India and responsible for nearly 620,000 premature deaths in 2012 [4]. This is true because PM is a complex mix of microscopic particles and liquid droplets made up of acids, organic chemicals, metals, and soil or dust particles. Some of the various health effects that are associated with PM are; cardiovascular, respiratory, and cerebrovascular; detailed information can be found in Anderson et al. [5]. PM_{10} can be either a primary or a secondary pollutant. In the former case, its origins may be natural emissions such as sand storms, forest fires, volcano eruptions, and sea sprays, and anthropogenic emissions mostly by combustion from industrial, agricultural, urban sources, and traffic [6]. The Central Pollution Control Board (CPCB) in 2010 reported that motor vehicles, especially diesel-driven vehicles, are the significant sources of PM [7]. Some authors from India have studied the trends of PM in Indian cities. For example, Gupta and Kumar [8] have studied PM trends in four Indian metropolitan cities (Delhi, Mumbai, Kolkata, and Chennai) and found that the PM concentrations were higher than the prescribed standards of CPCB, India, as well as WHO guidelines. CPCB has identified 17 nonattainment cities in Maharashtra (namely, Akola, Amravati, Aurangabad, Badlapur, Chandrapur, Jalgaon, Jalna, Kolhapur, Latur, Mumbai, Nagpur, Nasik, Navi Mumbai, Pune, Sangli, Solapur, and Ulhasnagar) based on the observation of exceedance concerning the National Ambient Air Quality Standards (NAAQS) 2009 consecutively from 2011 to 2015 [9]. A health risk (HR) study conducted by Maji et al. [10] reported that between 2004 and 2013, PM_{10} was responsible for total mortality (TM), cardiovascular mortality (CM), and respiratory mortality (RM) in Kolhapur city. Together these studies have shown that the study of PM is necessary. In the intensive literature, however, the studies have focused on metropolitan cities and limitedly focused on medium-sized cities. Hence, there is a need to focus on such kinds of cities. Kolhapur is one of the oldest and culturally significant cities of Maharashtra, India, lying along the bank of the river Panchganga. It is famous for the Mahalaxmi temple and other natural and man-made tourist attractions. Kolhapur city, spread across an area of 66.82 km^2 , is located 574 m above mean sea level and situated between $16^\circ 46'$ and $16^\circ 39'$ North and $74^\circ 11'$ and $74^\circ 17'$ East longitude. The climate of Kolhapur is tropical and experiences three seasons, summer with hot weather (March–May), monsoon (June–October), and winter with cold weather (November–February). The annual mean maximum and minimum temperature is around 31 $^\circ\text{C}$ and 19 $^\circ\text{C}$, respectively. The average rainfall is about 1,100 mm, received from both the southwest and northeast monsoon winds. As per the 2011 Census report, the population of Kolhapur city crossed over five lakhs [11]. After reviewing extensive literature, Luthra [12] devised a definition for an Indian medium-sized city based

on the population (i.e., population between 500,000 and 1,000,000). According to this definition, Kolhapur emerged as a medium-sized city in 2011, and Kolhapur city was selected as a study area in this study. Although the city has no significant industries [13], the number of motor vehicles is increasing rapidly; for example, nearly 26,000 new vehicles are added annually in Kolhapur city, which is the primary source of high PM₁₀ levels [14]. Several studies are available in the literature due to the importance of forecasting PM concentrations. The applied models are either less data-demanding (fewer datasets required) or data-driven (more datasets required), or combined models (a combination of two or more models). It is well known that the grey model (GM), simple exponential smoothing (SES), and regression analysis are less data-demanding models, while the Box–Jenkins, Autoregressive Integrated Moving Average (ARIMA), and Artificial Neural Network (ANN) are data-driven models. Various studies are as follows:

Fan et al. [15] used the grey and metabolic grey models to forecast PM₁₀ concentrations in Harbin City, China. They found that the air quality will enhance in the future, conforming to Grade 2 of China's Ambient Air Quality Standard using the metabolic one. Yadav and Nath [16] applied the exponential smoothing and autoregressive (AR) models to forecast the 1-month value of PM₁₀ for Allahabad city, India. The study results showed that the exponential smoothing model outperformed the AR models with the lowest MAPE than the AR models.

Hosamane et al. [17] used the ARIMA model to forecast the PM₁₀ concentrations of the SG Halli area of Bengaluru. They concluded that the ARIMA model well predicted the PM₁₀ concentrations, and the results could help city planners. Chelani et al. [18] applied the ANN model to predict the ambient PM₁₀ concentration. They used the root mean square of error (RMSE) and explored ANN models' predictability to forecast PM₁₀ concentration.

Díaz-Robles et al. [19] combined the ARIMA and ANN to improve forecast accuracy and developed a novel hybrid model to forecast the PM₁₀ in Temuco, Chile. They concluded that the hybrid model could capture 100% and 80% of alert and pre-emergency episodes, respectively. Wongsathan and Seedadanb [20] combined ANN and ARIMA models and developed a hybrid model to forecast the Chiangmai city moat's PM₁₀ concentrations. They found that the new model outperformed both models.

The presented literature here sheds light on the applicability of both the SES and GM models in forecasting the PM₁₀ and the usefulness of the combined model. Motivated by the above, this study proposes a combined model based on the grey and the SES models to get both models' benefits. The new model is the grey simple exponential smoothing model (GSESM). Compared with the individual grey and exponential smoothing models, the proposed GSESM combines two models into a single model, thereby can improve prediction accuracy. To the best of the authors' knowledge, in the literature, there is no report about the use of the proposed GSESM to forecast the PM₁₀ or else in any other field. Therefore, this paper applies the proposed GSESM to predict PM₁₀. The main goal of this study is to assess the reliability and validity of the GSESM to forecast the PM₁₀ in Kolhapur city.

2 Methodology

The SES and GM (1,1) are the most frequently used models in the forecasting field. The procedures of these models and the new proposed model (GSESM) are presented below, followed by the performance measures.

2.1 SES Model

The SES is the simplest case in exponential smoothing techniques. The equation for SES model is (Karmaker [21]):

$$F_{t+1} = \alpha y_t + (1 - \alpha)F_t \tag{1}$$

F_{t+1} is the forecast value at the time $t + 1$, y_t is the actual time series value,

F_t is the forecast value of the variable Y at the time t ,

α is the smoothing constant; the value of α ranges from 0 to 1 ($0 \leq \alpha \leq 1$).

Here the value of α is selected as 0.5 and inserted into Eq. (1), then Eq. (1) becomes:

$$F_{t+1} = 0.5y_t + (1 - 0.5) * F_t \tag{2}$$

2.2 GM (1,1)

The grey system theory (GST) was first introduced in the 1980s by Deng, and since then, it has become more prevalent in several forecasting fields. Among different models in the GST, probably the GM(1,1) is more popular. The term GM(1,1) stands for the grey model with a first-order and one-variable grey model. The steps of GM(1,1) are shown below (Wang et al. [22]):

Set the original data sequence is:

$$X^{(0)} = \{x^{(0)}(1), x^{(0)}(2), \dots, x^{(0)}(n)\} \tag{3}$$

The AGO is derived as:

$$X^{(1)} = \{x^{(1)}(1), x^{(1)}(2), \dots, x^{(1)}(n)\} \tag{4}$$

The basic form of the GM (1,1) is:

$$x^{(0)}(k) + az^{(1)}(k) = b; \quad k = 2, 3, \dots, n \tag{5}$$

where $x^{(0)}(k)$ is the grey derivative, a is the development coefficient, $z^{(1)}(k)$ is the mean value of adjacent data, b is the driving coefficient and n is the sample size of the data. a is the development coefficient; a is an important parameter, and there are specific ranges of this parameter that ascertains the length of prediction, for instance, when $-a \leq 0.3$, then the model could be used for medium- and long-term prediction

$z^{(1)}$ can be obtained by applying the mean operator on the $X^{(1)}$ series of data. $z^{(1)}$ is defined as follows:

$$z^{(1)}(k) = \frac{1}{2}[x^{(1)}(k) + x^{(1)}(k - 1)], \quad k = 2, 3, \dots, n \tag{6}$$

The parameters a and b can be obtained by applying the least square method.

The time response function of GM(1,1) is as follows:

$$\hat{x}^{(1)}(k + 1) = \left(x^{(0)}(1) - \frac{b}{a}\right)e^{-ak} + \frac{b}{a}, \quad k = 1, 2, \dots, n \tag{7}$$

Finally, the simulation and forecasting values of GM (1,1) can be evaluated as follows:

$$\hat{x}^{(0)}(k + 1) = \hat{x}^{(1)}(k + 1) - \hat{x}^{(1)}(k) = (1 - e^a)\left(x^{(0)}(1) - \frac{b}{a}\right)e^{-ak}, \quad k = 1, 2, \dots, n \tag{8}$$

where $\hat{x}^{(0)}(k + 1)$ is the predicted value of $x^{(0)}(k + 1)$ at time $(k + 1)$, $\hat{x}^{(1)}(k + 1)$ is the predicted value of $x^{(1)}(k + 1)$ at time $(k + 1)$, $\hat{x}^{(1)}(k)$ is the smoothened data and $x^{(0)}(1)$ is the first data point of raw series.

2.3 GSESM

In this model, the SES model is combined with GM (1,1). The procedure of the GSESM is given as follows:

Firstly, by retaining the first value of raw data, the remaining raw datasets were replaced by using the second forecast value of the SES model up to the n values.

Then Eq. (3) of GM (1,1) becomes:

$$x^{(0)} = (x^{(0)}(1), F_t(2), F_t(3), \dots, F_t(n)) \tag{9}$$

Secondly, the new AGO was obtained as:

$$x^{(1)} = (x^{(1)}(1), x^{(2)}(2), x^{(3)}(3), \dots, x^{(1)}(n)) \quad (10)$$

where $x^{(1)}(1) = x^{(0)}(1)$ and F_t are the forecast values obtained as per Eq. (2) of the SES model.

The original data set can be improved using Eq. (10); the remaining steps are in line with the original GM (1,1) model calculation steps. It is hypothesized that the new GSESM would provide higher forecast accuracy than both the SES and GM (1,1) models.

2.4 Performance Measure

Various performance measures are available in the literature to evaluate the forecasting capability of the prediction models; mean absolute percentage error (MAPE) is the most widely used criterion among them. In this paper, the MAPE was used to evaluate the model performance. The MAPE can be calculated as follows [22]:

$$MAPE = \frac{1}{n} \sum_k^n \left| \frac{Actual - Predicted}{Actual} \right| \times 100\% \quad (11)$$

where $k = 2, 3, \dots, n$ for all models. According to Lewis, lower values of MAPE indicate a higher forecasting ability of the model (when MAPE < 10 highly accurate prediction) [23]. Researchers have employed Microsoft Excel or MATLAB software to develop the GM (1,1) model; herein, Microsoft Excel will be used for all mathematical works.

3 Data

The ambient air quality monitoring network provides spatial and temporal variations of ambient air concentrations of various pollutants that further help assess the level of pollution concerning the ambient air quality standards. The Maharashtra Pollution Control Board (MPCB) has allotted the monitoring work of Kolhapur city to the Department of Environmental Science, Shivaji University, Kolhapur, and the monitoring is conducted under the National Air Quality Monitoring Programme (NAMP). There are three Ambient Air Quality Monitoring Stations (AAQMS) located at different locations [Shivaji University Campus (SUC)—residential; Ruikar Trust (RT)—rural and other areas; Mahadwar Road (MR)—residential] in the city that has successfully been operated since 2005–2006. At all stations, the monitoring frequency is 2 days in a week. These stations collectively represent the air quality of the entire city. Three locations with station name, station code, type, and geographical locations (latitude and longitude both in degrees) are well presented in the Energy and Resources Institute (TERI) [24]. The average annual concentrations of PM₁₀

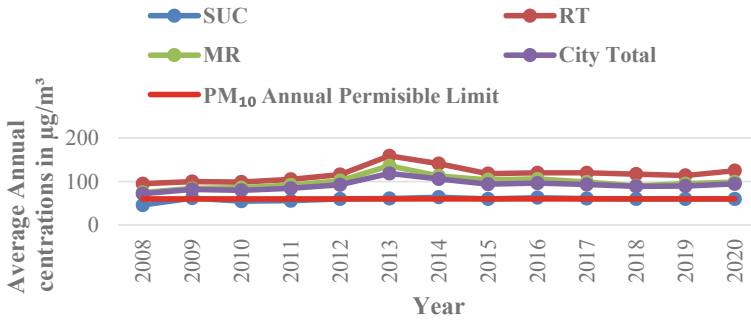


Fig. 1 Average annual concentrations of PM₁₀ from 2008 to 2020

from 2008 to 2020 at three stations taken from TERI [24] and estimated for the entire city are presented in Fig. 1.

Except for three years for SUC (2008, 2010, and 2011), at all stations and in the entire city, the PM₁₀ concentrations exceeded the annual PM₁₀ standard of 60 µg/m³ (Fig. 1). Figure 1 clearly illustrates that the PM₁₀ concentrations in Kolhapur city show an increasing trend, and this growth is likely to be further accelerated.

4 Results and Discussion

This paper applies three different models, namely, the SES, GM (1,1), and GSESM. The main aim of this study was to assess the reliability and validity of the newly developed GSESM model to forecast the PM₁₀ concentrations in Kolhapur city. The PM₁₀ concentrations data presented in Fig. 1 were used to develop all models and evaluated their accuracy using the MAPE criterion. For all mathematical works, Microsoft Excel software was used. The overall procedure is given as follows: firstly, the respective models were developed by using Eqs. (1)–(10). Using Eqs. (2) and (8), the forecast values were obtained for the SES and GM (1,1), respectively. The proposed GSESM was developed by replacing Eq. (3) of the traditional GM (1,1) with Eq. (10) and obtained forecast values. Except for Eq. (3), the remaining steps were in line with the original GM (1,1) model calculation steps. Secondly, using Eq. (11), the MAPE of each model was calculated. The forecast values and MAPE of each model are summarized in Table. 1.

In general, Table 1 reveal that all models perform well in forecasting the PM₁₀ concentrations. However, there were slight differences among these models in terms of accuracy. The in-sample MAPE (2009–2019) for SES model, GM (1,1), and GSESM were 8.52%, 7.78%, and 7.86%, respectively; similarly, the out-of-sample MAPE values (2020) for these models were 3.90%, 3.13%, and 2.89%, respectively (Table 1). According to the MAPE range given in Vivas et al. [23], all models were highly accurate (MAPE < 10%) in both sample cases. Surprisingly, the prediction

Table 1 Forecast values and MAPE of each model

Year/MAPE	Models		
Year	SES	GM (1,1)	GSESM
2008	72.00	72.00	72.00
2009	72.00	89.75	90.41
2010	77.00	90.44	91.02
2011	78.50	91.13	91.64
2012	81.42	91.83	92.26
2013	87.04	92.54	92.89
2014	102.85	93.25	93.52
2015	104.43	93.96	94.16
2016	99.21	94.69	94.80
2017	97.77	95.41	95.44
2018	95.55	96.15	96.09
2019	92.28	96.88	96.75
MAPE (%) (2009–2019)	8.52	7.78	7.86
2020	90.97	97.63	97.41
MAPE (%) (2020)	3.90	3.13	2.89

accuracy of the GSESM was slightly better than that of the SES and GM (1,1), and GSESM outperformed both competing models, thus proving the hypothesis. Additionally, the development coefficient (a) plays an essential role and is used to reckon the forecasting capacity of GM (1,1); when $a \leq 0.3$, the model can be employed in mid-long-term forecasting [22]. The development coefficient (a) of the GM (1,1) and GSESM were obtained as 0.0076 and 0.0068, respectively. Hence, both models were best for mid-long-term forecasts. Thus, the GSESM not only proved its reliability and validity in forecasting the PM_{10} concentrations in Kolhapur city but also demonstrated its use for the mid-long-term forecasts. Hence, the GSESM could be the best option to forecast the PM_{10} concentrations in Kolhapur city. Finally, the GSESM was employed to forecast Kolhapur city’s PM_{10} concentrations from 2021 to 2025, and the forecast results are presented in Table 2.

The forecast results show that by 2025, the PM_{10} concentrations in Kolhapur city will be as high as 99.43 (Table 2). The results can help in scientific planning and decision making on the developmental needs in Kolhapur city. The main contribution of this study is that it not only tries to add a new combined grey model but also demonstrates its suitability. The research results demonstrated that the main advantages of the proposed GSESM are that it requires limited datasets, Microsoft Excel

Table 2 GSESM forecast values, 2021–2025

Year	2021	2022	2023	2024	2025
Forecast value	97.17	97.73	98.29	98.86	99.43

is sufficient for its development, and it can successfully forecast the PM₁₀ concentrations. The main novelty of this work is the development of the proposed GSESM, which has never been reported in the literature.

5 Conclusions

Based on the basic concepts of the GM (1,1) and SES model, this paper proposes a new combined grey model as the GSESM to accurately forecast the PM₁₀ concentrations in Kolhapur city. The GSESM was developed by changing the AGO values of the original GM (1,1) by the forecast values obtained by the SES model. The forecasting accuracy and capacity of the GSESM was compared with both the SES and GM (1,1) models. All models were developed using PM₁₀ concentrations data from 2008 to 2019, while the data of 2020 was kept aside to check each model's out-of-sample performance. Results showed that all models were highly accurate based on the MAPE in both sample cases. Surprisingly, the GSESM provided the lowest MAPE, followed by GM (1,1) and SES models. The GSESM can tremendously reduce the errors, hence significantly improving prediction accuracy. Similarly, with a reasonable value of development coefficient (α), the GSESM could be used in the mid-long-term forecasts. Thus, in this case, the GSESM proved its reliability and efficiency in forecasting the PM₁₀ concentrations. Finally, the GSESM was utilized to forecast the PM₁₀ concentrations from 2021 to 2025. Projections indicate that the PM₁₀ concentrations will increase over the stipulated period. Accordingly, the government should take proper actions. Moreover, the proposed GSESM could have more comprehensive applications in forecasting other pollutants.

References

1. Gupta, S. K., & Elumalai, S. P. (2019). Dependence of urban air pollutants on morning/evening peak hours and seasons. *Archives of Environmental Contamination and Toxicology*, 76, 572–590.
2. Suh, H. H., Bahadori, T., Vallarino, J., & Spengler, J. D. (2000). Criteria air pollutants and toxic air pollutants. *Environmental Health Perspectives*, 108, 625–633.
3. Castner, J., Gittere, S., & Seo, J. Y. (2015). Criteria air pollutants and emergency nursing. *Journal of Emergency Nursing*, 41, 186–192.
4. Gulia, S., Mittal, A., & Khare, M. (2018). Quantitative evaluation of source interventions for urban air quality improvement—A case study of Delhi city. *Atmospheric Pollution Research*, 9, 577–583.
5. Anderson, J. O., Thundiyil, J. G., & Stolbach, A. (2012). Clearing the air: A review of the effects of particulate matter air pollution on human health. *Journal of Medical Toxicology*, 8, 166–175.
6. Clarke, K., Kwon, H. O., & Choi, S. D. (2014). Fast and reliable source identification of criteria air pollutants in an industrial city. *Atmospheric Environment*, 95, 239–248.
7. Shinde, S., & Karjinni, V. (2019). Impact of traffic growth on air quality: A case study of Delhi, India. *Proceedings of the Institution of Civil Engineers Civil Engineering*, 172, 39–44.

8. Gupta, I., & Kumar, R. (2006). Trends of particulate matter in four cities in India. *Atmospheric Environment*, 40, 2552–2566.
9. Kaushik, G., Patil, S., & Chel, A. (2018). Air quality status and management in tier II and III Indian Cities: A case study of Aurangabad City, Maharashtra. In: Hussain, C. M. (eds.) *Handbook Environmental Materials Management* (pp. 1–22). Springer, Cham
10. Maji, K. J., Dikshit, A. K., & Deshpande, A. (2016). Human health risk assessment due to air pollution in 10 urban cities in Maharashtra, India. *Cogent Environmental Science*, 2, 1–16.
11. The Energy and Resources Institute (TERI). (2016). *Environmental Status Report of Kolhapur City 2015–16*. Final Report.
12. Luthra, A. (2006). Para transit system in medium sized cities problem or Panacea. *ITPI Journal*, 3, 55–61.
13. Sathe, Y., Ayare, A., & Srinikethan, G. (2011). Application of US EPA PMF model to source apportionment of trace elements in Atmospheric Aerosols at Kolhapur, Maharashtra (India). *Journal of Environmental Research and Development*, 5, 597–607.
14. The Times of India (TOI). *With more vehicles in Kolhapur, air pollution levels rise*. <https://timesofindia.indiatimes.com/city/kolhapur/with-more-vehicles-in-kolhapur-air-pollution-levels-rise/articleshow/36081234.cms>
15. Fan, Q., Li, Y., & Ren, N. (2009). Application of grey prediction model to forecast the main air contaminant PM₁₀ in Harbin City. In *3rd International Conference on Bioinformatics and Biomedical Engineering, ICBBE* (pp. 1–4). IEEE, Beijing
16. Yadav, V., & Nath, S. (2017). Forecasting of PM₁₀ using autoregressive models and exponential smoothing technique. *Asian Journal of Water, Environment and Pollution*, 14, 109–113.
17. Hosamane, S. N., Prashanth, K. S., & Virupakshi, A. S. (2020). Assessment and prediction of PM₁₀ concentration using ARIMA. In *First International Conference on Advances in Physical Sciences and Materials* (pp. 1–9). J. Phys. Conf. Ser. 1706, IOP Publishing Ltd.
18. Chelani, A. B., Gajghate, D. G., & Hasan, M. Z. (2002). Prediction of ambient PM₁₀ and toxic metals using artificial neural networks. *Journal of the Air and Waste Management Association*, 52, 805–810.
19. Díaz-Robles, L. A., Ortega, J. C., Fu, J. S., Reed, G. D., Chow, J. C., Watson, J. G., & Moncada-Herrera, J. A. (2008). A hybrid ARIMA and artificial neural networks model to forecast particulate matter in urban areas: The case of Temuco, Chile. *Atmospheric Environment*, 42, 8331–8340.
20. Wongsathan, R., & Seedaran, I. (2016). A hybrid ARIMA and neural networks model for PM-10 pollution estimation: The case of Chiang Mai city Moat Area. In *International Electrical Engineering Congress, iEECON2016, Procedia Computer Science* (vol. 86, pp. 273–276). Chiang Mai
21. Karmaker, C. L. (2017). Determination of optimum smoothing constant of single exponential smoothing method: A case study. *Int. J. Res. Ind. Eng.*, 6, 184–192.
22. Wang, Y. W., Shen, Z. Z., & Jiang, Y. (2018). Comparison of ARIMA and GM(1,1) models for prediction of hepatitis B in China. *PLoS ONE*, 13, 1–11.
23. Vivas, E., Allende-Cid, H., & Salas, R. (2020). A systematic review of statistical and machine learning methods for electrical power forecasting with reported MAPE score. *Entropy*, 22, 1–24.
24. The Energy and Resources Institute (TERI). (2020). *Air quality status of Maharashtra 2019–20*. Prepared for Maharashtra Pollution Control Board (MPCB)

Transmission Line Fault Detection and Classification: ANN Approach



Vaibhav A. Ghodeswar and Mirza A. Beg

Abstract Various tools are identified for transmission line fault identification and classification. The proposed algorithm is very helpful for advancement in relay such that the relay can be trained and will be able to detect and classify transmission line faults immediately. The transmission line faults have been simulated at different locations such as at 300, 600, and 900 km in MATLAB Simulink. The proposed method decomposes the signal into five detail-level using wavelets. The energy of five detail level components of various fault situations has been calculated. The premeditated energy is given as input to the artificial neural classifier. Classification accuracy up to 95.6% is obtained.

Keywords Wavelet · Daubechies · Energy · Artificial neural network · MATLAB

1 Introduction

Transmission lines are spread over a vast geographical area in open fields. The transmission line is frequently subjected to faults, disrupting power transmission. The faults need to be detected immediately and the faulty section to be isolated from the healthy section by the combined action of a protective relay and circuit breaker. In this modern power system, the transmission line plays an important role.

A lot of work has been carried out by researchers on power transmission line fault identification and classification [1]. There are advanced feature extraction methods available for example S-transform, Hilbert transform, Parks transform, etc., and classification methods are also available such as artificial neural networks (ANN), support vector machines (SVM), numerical methods, genetic algorithms (GA), fuzzy-based expert systems, decision trees (DT), etc., having their advantages and disadvantages. ANN is one of the advanced techniques for power transmission line fault classification due to its working capability in offline mode [2]. The feature extraction using wavelet has been proposed in this presented work, artificial neural network for fault

V. A. Ghodeswar (✉) · M. A. Beg

Mauli Group of Institutions College of Engineering and Technology, Shegaon, MS 444203, India
e-mail: ghodeswarvaibhav@gmail.com

recognition on three-phase transmission lines is allocated in [3]. Progressive techniques for fault detection and classification in electrical power transmission systems are offered in [4]. Accurately classify the fault depending upon the type of fault depending upon low impedance and high impedance fault by changing the signal decomposition level explains in [5].

2 Proposed Work

To analyze transmission line fault and further validate the proposed scheme (Fig. 1), a model of 300 km as shown in Fig. 2, has been considered. The system and line parameters are given in Table 1. The system has been developed in MATLAB Simulink.

The proposed system is implemented using Bergeron's traveling wave transient program. (EMTP). Figure 1 shows two generator systems connected by a long-distance power transmission line the following system has developed faults that have been created at different locations such as at 300, 600, and 900 km. The developed system is shown.

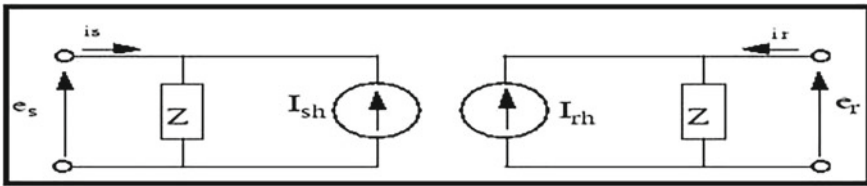


Fig. 1 Representation of transmission line model

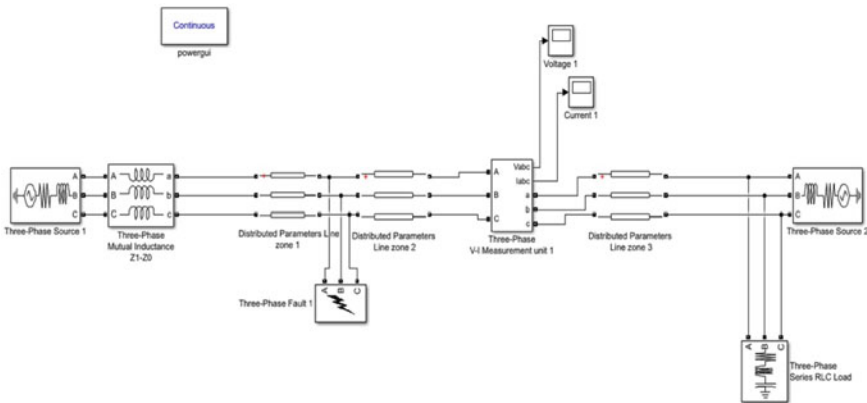


Fig. 2 Transmission line faults at 300 km

Table 1 Energy calculation for phase AB (300 km)

Energy	LL 300 km	LG 300 km	LLL 300 km
	AB	AG	ABC
EIA I1	1.43E+02	26.8143	82.50086
EIA I2	1.57E+03	72.42728	2.47E+02
EIA I3	1.02E+04	2.43E+02	1.84E+03
EIA I4	5.54E+04	2.43E+02	1.84E+03
EIA I5	2.81E+05	3.95E+04	1.66E+05
EIB I1	1.38E+02	17.18799	3.11E+02
EIB I2	1.56E+03	55.15325	2.80E+03
EIB I3	1.00E+04	1.79E+02	2.60E+04
EIB I4	5.55E+04	1.05E+03	1.82E+05
EIB I5	2.80E+05	1.59E+04	5.72E+05
EIC I1	19.61151	17.5908	3.77E+02
EIC I2	44.80941	50.35456	3.10E+03
EIC I3	1.38E+02	1.51E+02	2.96E+04
EIC I4	5.23E+02	1.22E+03	2.04E+05
EIC I5	7.60E+03	1.65E+04	6.70E+05

The various fault created are LL, LG, LLL in MATLAB Simulink, and voltage and current signals were captured. Similarly, faults are created at 600 and 900 km. The raw signals of voltage and current are recorded (Figs. 3, 4 and 5).

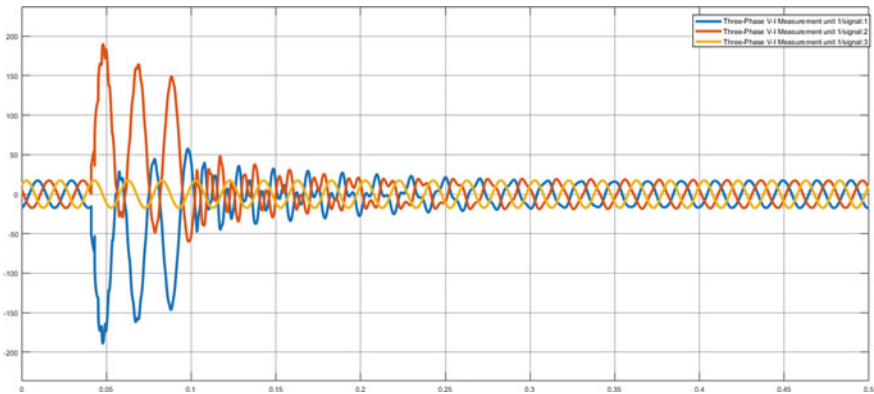


Fig. 3 Current waveform 300 km LL fault (Phase AB)

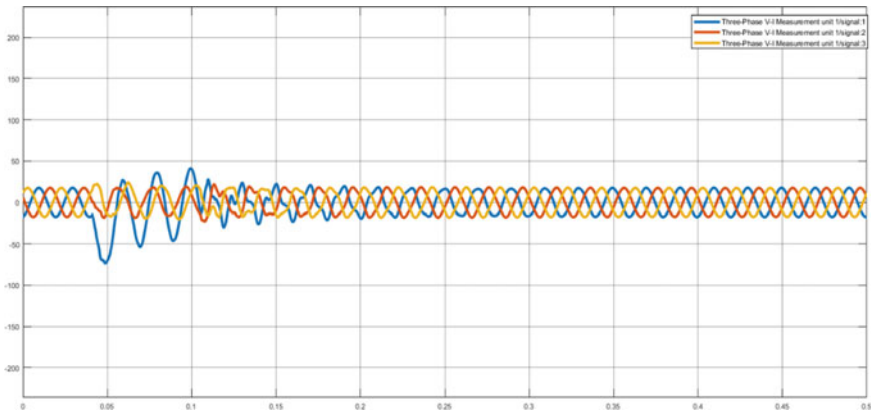


Fig. 4 Current waveform 300 km LG fault (Phase AG)

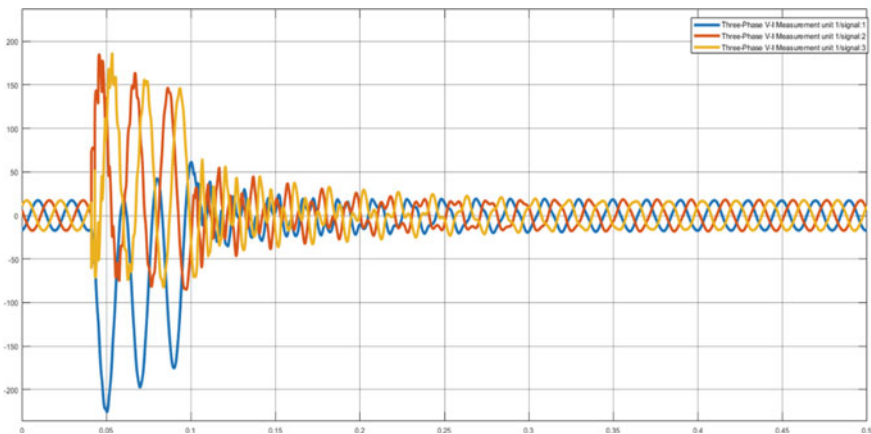


Fig. 5 Current waveform 300 km LLL fault (Phase ABC)

Similarly, various waveforms for faults between BC, CA, BG, CG, and ABC at 600 and 900 km are recorded.

3 Result and Discussion

Wavelet decomposition at five details has been taken out and its output energy determined for power transmission line fault identification and discrimination (Figs. 6, 7 and 8) [6].

Similarly, currents for faults between BC, CA, BG, CG, and ABC at 600 km and 900 km are recorded. The calculation has been done for phase B and phase C; these

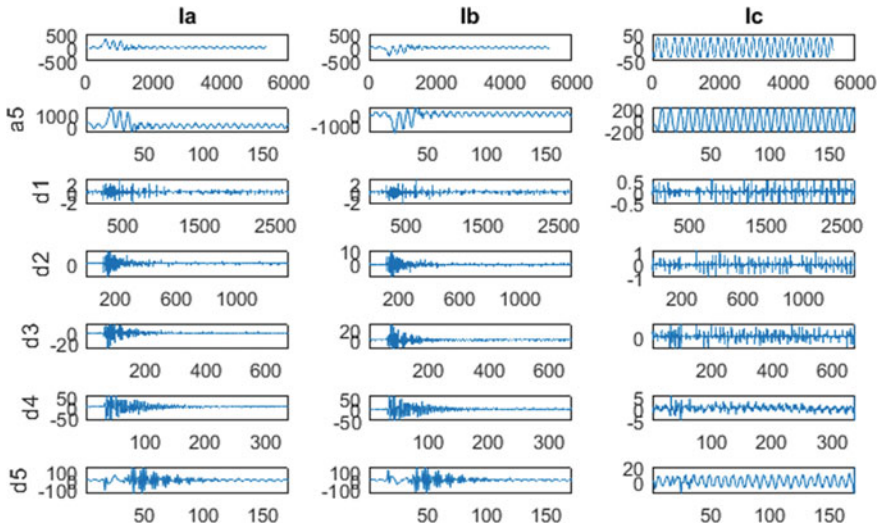


Fig. 6 DWT results for line to line, i.e., (A-B) fault 300 km

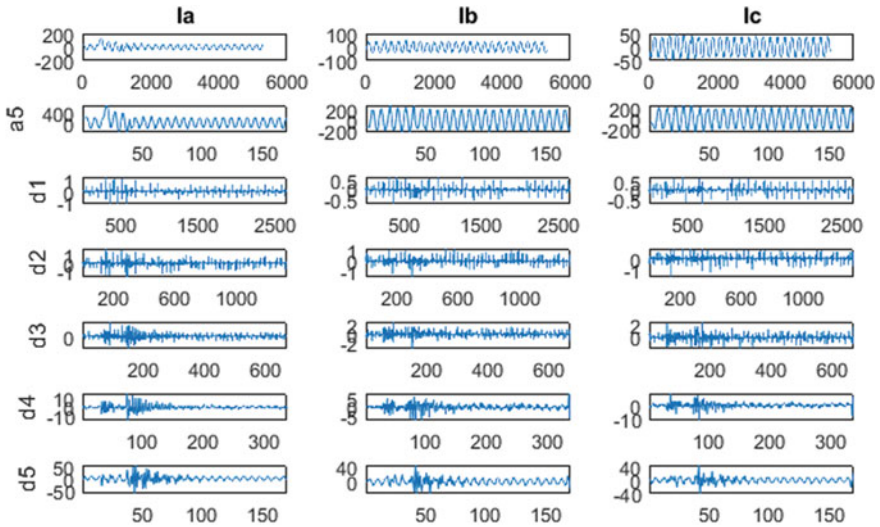


Fig. 7 DWT results for line to line, i.e., (A-G) fault 300 km

calculated energy samples are given as input to the neural network. the energy of the signal decomposed is calculated using the formula: $E = \sum_{-\infty}^{\infty} |x(n)|^2$, where $x(n)$ is the energy of the discrete signal. The energy of the coefficient of DWT is calculated and shown for phase AB in tabulated form (Tables 2 and 3).

Similar calculations for another phase have been done.

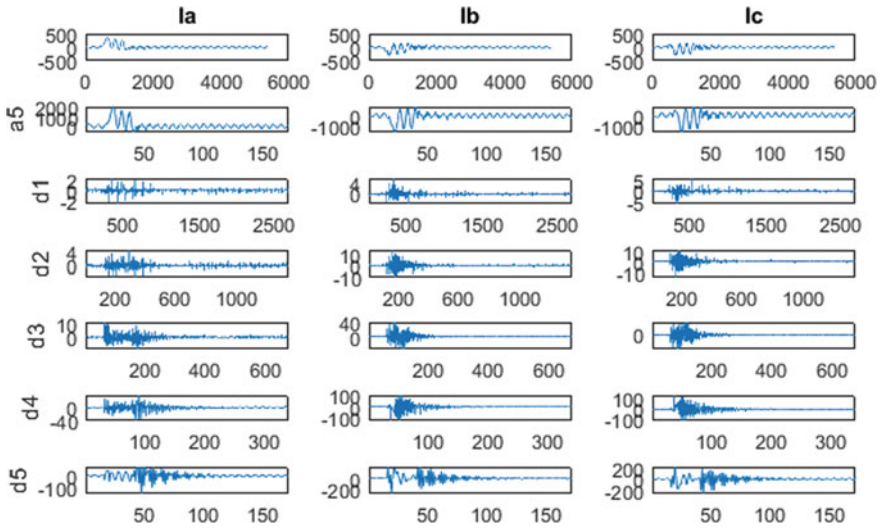


Fig. 8 DWT results for line to line, i.e., (ABC) fault 300 km

Table 2 Energy calculation for phase AB (600 km)

Energy	LL 600 km	LG 600 km	LLL 600 km
	AB	AG	ABC
EIA I1	5.25E+02	7.876409	33.03301
EIA I2	1.00E+03	20.17433	1.20E+02
EIA I3	7.01E+03	8.52E+01	8.42E+02
EIA I4	2.65E+04	8.06E+02	5.42E+03
EIA I5	6.23E+04	7.60E+03	2.80E+04
EIB I1	5.24E+02	2.469541	1.81E+03
EIB I2	9.99E+02	8.785918	3.42E+03
EIB I3	6.95E+03	3.52E+01	2.19E+04
EIB I4	2.61E+04	3.10E+02	6.74E+04
EIB I5	6.26E+04	2.99E+03	1.73E+05
EIC I1	1.79357	2.327347	2.00E+03
EIC I2	4.409334	8.315164	3.82E+03
EIC I3	1.51E+01	3.85E+01	2.37E+04
EIC I4	5.29E+01	3.17E+02	7.22E+04
EIC I5	7.37E+02	3.18E+03	2.16E+05

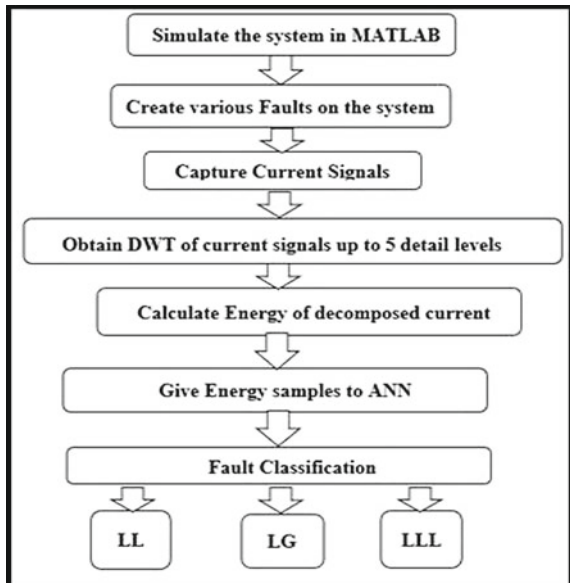
Table 3 Energy calculation for phase AB (900 km)

Energy	LL 900 km	LG 900 km	LLL 900 km
	AB	AG	ABC
EIA I1	3.23E+02	75.0248	97.61064
EIA I2	9.76E+02	4.76E+02	4.64E+02
EIA I3	6.75E+03	1.91E+03	4.25E+03
EIA I4	2.75E+04	1.16E+04	1.94E+04
EIA I5	9.31E+04	3.86E+04	6.87E+04
EIB I1	3.21E+02	21.91959	6.94E+02
EIB I2	9.74E+02	1.23E+02	4.24E+03
EIB I3	6.76E+03	4.56E+02	1.28E+04
EIB I4	2.81E+04	2.62E+03	6.95E+04
EIB I5	9.25E+04	1.10E+04	1.13E+05
EIC I1	3.309535	1.10E+04	6.97E+02
EIC I2	9.88E+00	1.18E+02	4.42E+03
EIC I3	26.03357	4.41E+02	1.30E+04
EIC I4	9.75E+01	2.67E+03	9.13E+04
EIC I5	1.51E+03	1.15E+04	1.56E+05

3.1 Implementation of the Proposed Scheme

Figure 9 describes the process of implementation of the proposed technique.

Fig. 9 Flow chart



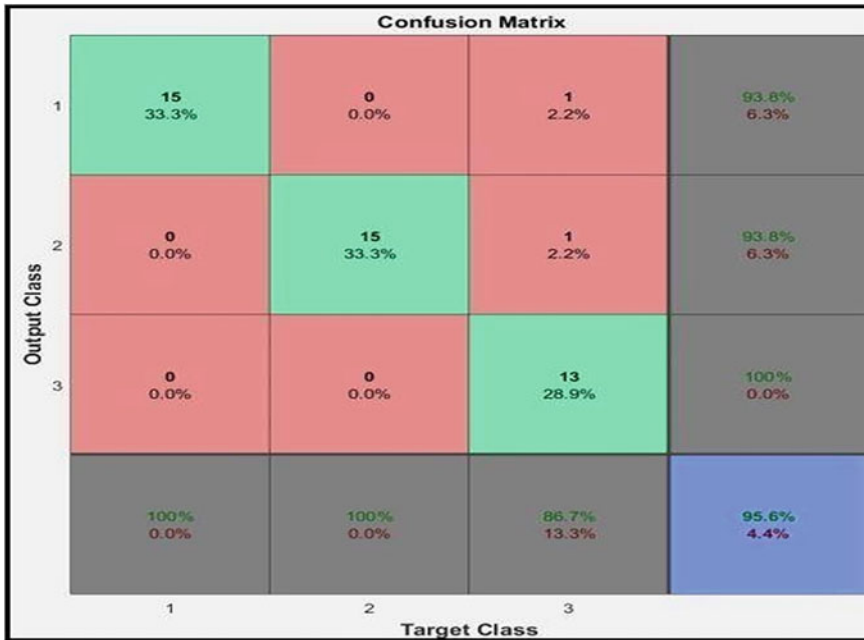


Fig. 10 Fault classification matrix

In this research work, Artificial Neural [7] Network is used and trained with supervised learning. The neural network uses 3 input layers, 3 hidden layers, and 3 output layers during fault classification. The energy of the current signal in the feature extracted is fed to the neural network in MATLAB and several iterations are varied data sheets and decided by the trial-and-error method. In the ANN transfer function ‘tansig’, the learning rule, ‘learned’, momentum 0.7, and maximum epochs 1,500 iterations are used to train that network. The training percentage is 70% and testing is 30%. For this the number of iterations is varied and the performance of the network is evaluated. The matrix shown below clearly indicates that the proposed algorithm in this presented work can classify the power transmission line fault with 95.6% (Fig. 10).

4 Conclusion

The research paper clearly explains the importance of wavelet and ANN combination for the identification and discrimination of the various symmetrical and unsymmetrical faults of the power transmission line. In the future the training data reduction will be the prime target as the training data reduced the output of classification will come rapidly and a more sensitive relay and protection system can be developed.

References

1. Kesharwani, S., & Singh, D. K. (2014). Simulation of fault detection for protection of transmission line using neural network. *International Journal of Science, Engineering and Technology Research (IJSETR)*, 3(5), 1367–1371.
2. Padhy, S. K., Panigrahi, B. K., Ray, P. K., Satpathy, A. K., Nanda, R. P., & Nayak, A. (2018). Classification of Faults in a Transmission Line using Artificial Neural Network. In *2018 International Conference on Information Technology (ICIT)* (pp. 239–243).
3. Upadhyay, S., Kapoor, S. R., & Choudhary, R. (2018). Fault classification and detection in transmission lines using ANN. In *IEEE International Conference (ICIRCA)*.
4. Tîrnovan, R. A., & Cristea, M. (2019). Advanced techniques for fault detection and classification in electrical power transmission systems: An overview. In *2019 8th International Conference on Modern Power Systems (MPS)* (pp. 1–10).
5. Wilamowski, B. M., & Yu, H. (2010). Improved computation for Levenberg–Marquardt training. *IEEE Transactions on Neural Networks*, 21(6), 930–937.
6. Fan, R., Yin, T., Huang, R., Lian, J., & Wang, S. (2019, October). Transmission line fault location using deep learning techniques. In *2019 North American Power Symposium (NAPS)* (pp. 1–5). IEEE.
7. Shaik, A. G., & Pulipaka, R. R. V. (2015). A new wavelet-based fault detection, classification and location in transmission lines. *International Journal of Electrical Power & Energy Systems*, 64, 35–40.
8. Mahmud, M. N., Ibrahim, M. N., Osman, M. K., & Hussain, Z. (2015). Selection of suitable features for fault classification in transmission line. In *2015 IEEE International Conference on Control System, Computing and Engineering (ICCSC)* (pp. 591–596). IEEE.
9. EiPhyoThwe, M. M. (2016). Fault detection and classification for transmission line protection system using artificial neural network. *Journal of Electrical and Electronic Engineering*, 4(5), 89–96. <https://doi.org/10.11648/j.jeee.20160405.11>
10. Yadav, A., & Dash, Y. (2014). An overview of transmission line protection by artificial neural network: fault detection, fault classification, fault location, and fault direction discrimination. *Advances in Artificial Neural Systems*, 2014, 1–20.
11. Mishra, D. P., & Ray, P. (2018). Fault detection, location and classification of a transmission line. *Neural Computing and Applications*, 30, 1377–1424.
12. Padhy, S. K., Panigrahi, B. K., Ray, P. K., Satpathy, A. K., Nanda, R. P., & Nayak, A. (2018). Classification of Faults in a Transmission Line using Artificial Neural Network. In *2018 International Conference on Information Technology (ICIT)*, Bhubaneswar, India (pp. 239–243).
13. Yu, R., Wang, Y., Zou, Z., & Wang, L. (2020). Convolutional neural networks with refined loss functions for the real-time crash risk analysis. *Transportation Research Part C: Emerging Technologies*, 119, 102740.
14. de Bruin, T., Verbert, K., & Babuska, R. (2017). Railway track circuit fault diagnosis using recurrent neural networks. *IEEE Transactions on Neural Network Learning Systems*, 28(3), 523–533.
15. Adhikari, S., Sinha, N., & Dorendrajit, T. (2016). Fuzzy logic based on-line fault detection and classification in the transmission line. *Springer Plus*, 5(1), 1002.

Review on Smart Digital Technologies in Construction Sector



Pandurang Bhise, Yash Annapurne, Kuldip Lalge, Samarth Patil, and Rohan Sawant

Abstract Despite the fact that it contributes to the provision of the necessary building and supporting civil infrastructure, the construction industry has not been able to achieve its full potential due to productivity issues, poor planning, and poor coordination. These difficulties may be alleviated by utilizing a digitalized solution for the coordination and planning of construction activities. As a result, the purpose of the study was to investigate the digital technologies that construction professionals have access to during construction planning. Utilizing digital technologies for construction planning has been shown to save time, improve quality, and cut down on errors, according to construction professionals. According to the study, there was a statistically significant difference in the benefits, such as increased flexibility and real-time access to information and a decrease in construction errors. It suggested that professionals in the construction industry invest more in cutting-edge digital solutions to meet the industry's challenges.

Keywords Construction industry · Digital technology · Microsoft project planning

1 Introduction

The construction industry has particular characteristics that necessitate close coordination. The large quantities of construction data and the large number of stakeholders in a construction project necessitate careful management [1, 2] pointed out that the nature of the system used to create or store construction information makes it frequently difficult to retrieve, out-of-date, and incomplete. Reference [3] stated that this can be attributed to the construction industry's manual or traditional tools. Though, the utilization of data and correspondence advancements (ICTs) have shown the potential in tending to the intricacy of development exercises and increment efficiency [4, 5]. In order to provide their services to the construction industry, various professionals employ various software. When drawing and designing their structures,

P. Bhise · Y. Annapurne · K. Lalge · S. Patil · R. Sawant (✉)
Department of Civil Engineering, Dr. D.Y. Patil Institute of Technology, Pimpri, Pune, India
e-mail: rohan.sawant@dypvp.edu.in

the architects, for instance, use CAD software like Revit, Sketch Up, and Draft Sight [5–8], while Engineers use STAAD Pro, S-Frame, QGIS/ArcGIS, SAP 2000, Orion, RAPT, ETABS, Solid Works, and Builders use Microsoft Project and Primavera [9], Quantity Surveyors use Microsoft Excel, Master Bill, Scud, CATO Pro, and so on for their measurement in conjunction with CAD software [10].

Digital technologies and their applications in construction planning are the primary focus of this study. The study by [9] found that a significant amount of resource mismanagement on construction sites is caused by a lack of planning. On construction sites, problems like materials not being available when they are needed, over- or under-ordering of building materials, improper inventory procedures, material delivery delays, and so on can be seen [11, 12]. The project delivery performance would unavoidably suffer as a result of poor planning.

1.1 Smart Construction

The goals of smart construction are to increase profitability, decrease life costs, increase sustainability, and expand client benefits. The Internet of Things (IoT) sensors and devices that are available for energy management, transportation, a smart waste management system, and smart lighting are utilized in the construction of smart cities. This not only changes the construction industry, but it also increases the benefits of a home for tenants.

2 Smart Digital Technology Used in Construction Industry

2.1 The Internet of Things (IoT)

The Internet of Things (IoT) is fundamentally altering the operations of the industry and is already a crucial component of building science. Sensors and intelligent units that can communicate with one another and be managed from a single platform make up the Internet of Things. This has significant ramifications because it implies that a new method of working that is extra intelligent, more effective, and safer is now very likely.

What implications does this have for building?

Smart equipment can be used to carry out routine tasks and can also be intelligent enough to keep itself running smoothly. For example, if a cement mixer runs out of cement, it can use a sensor to make itself more ready, increasing productivity and efficiency. A development's carbon footprint may be drastically decreased thru using smart generation.

2.2 Building Information Modeling

We give a visual image of the physical and operational properties of building facilities through smart AEC businesses (architect, engineering, and construction) using BIM (building information modeling). This allows them to better successfully plan, design, build, and maintain buildings and infrastructure.

2.3 Big Data

The term “massive information” refers to extraordinarily huge information units that may be used to make higher enterprise choices. This statistics is being accumulated from offerings and searches at the Internet, cell phones, virtual photographs, social media, and several different virtual communicate equipment like Skype, email, and textual content messages.

Big data is being used in construction:

The top-rated phasing of production sports may be decided through reading huge information from the weather, visitors, and network and enterprise activity. It is viable to system the sensor information from machines which are used on web sites to reveal while they’re lively and idle. Bridge flexing ranges and visitors strain information may be recorded to discover out-of-bounds events. This information may again be fed again into constructing records modeling (BIM) structures to time table vital renovation tasks.

2.4 Primavera

It is primarily project management software that allows participants in the project to share ideas. In construction projects, the information about resource allocation and scheduling is simple to use. It is primarily utilized for project planning, monitoring, control, and reporting. In the construction industry, project managers use it.

2.5 Global Positioning System (GPS)

The Global Positioning System is applied in several construction-associated activities. It includes purchaser collectors, floor manipulate stations, and satellites. It has been broadly utilized in geodesy, photogrammetry, marine surveying, and mapping. It’s far able to supplying three-D arrangements, consisting of points, lines, and planes.

a. **Surveying**

Construction companies are using GPS devices instead of traditional surveying equipment. Using the GPS devices, they can get accurate and complete data about an area.

b. **Handheld and Vehicle Units**

Vehicles equipped with GPS can assist drivers in locating a work site from which they must deliver materials. GPS sensors can be attached to vehicles for large projects to ensure that they meet project requirements.

2.6 Artificial Intelligence and Machine Learning

Machine learning (ML) is a subfield of synthetic intelligence wherein statistical strategies are used to provide a laptop the capacity to research from facts. Imagine a global wherein laptop structures may want to mechanically calculate and layout residence plans, application robots, and different machines. This innovation is as of now on hand and being applied today.

Artificial intelligence (AI) can energy equipment to carry out repetitive responsibilities like pouring concrete, laying bricks, and welding. Sites may be monitored for protection risks the usage of geo-place to discover chance regions and notify people or with the aid of photographs and popularity generation to decide whether or not an employee is carrying the precise PPE.

2.7 Radio Frequency Identification

Radio frequency identification uses radio signals to identify a specific target. Without coming into mechanical or optical contact with the identification system, it can read and write the same data. RFID is made up of tags, readers, and antennas.

2.8 Robotics and Drones

The production web website online itself is a massive impediment due to the fact robots requires managed surroundings and non-variable, repetitive tasks. Using drones to bring materials to the job site can cut down on the number of vehicles needed. Robots can be used to speed up and improve the quality of masonry and bricklaying work. Autonomous or remotely controlled vehicles are being used to demolish structural components.

2.9 Wireless Zig Bee Module

A brand-new technique for two-manner Wi-Fi networks is Zig Bee. Low complexity, low power, low transition speed, low information rate, Wi-Fi sensor, and coffee expenses are the number one desires of Zig Bee. The self-restoration and self-configuring Zig Bee Wi-Fi mesh era may be without problems carried out and aid as much as 65,000 nodes, relying at the topologies. It affords a simple, powerful fee and battery lifestyles for any applications. The transmission variety is among 10 and one hundred meters.

2.10 5G and Wi-Fi 6

The fifth era of remote innovation known as 5G commitments quicker speeds, further developed traffic the board, and less blockage. In comparison to its predecessors, the most recent Wi-Fi technology standard is making progress. Without sacrificing speed or performance, users will be able to communicate effectively, share large-scale drawings, and run applications that use a lot of resources.

2.11 Cement Based Piezo-Electric Sensors

Continuous tracking and assessment of the system of harm by using acoustic emission AE indicators is one purpose that structural fitness tracking era for concrete systems is of such tremendous significance in brand new world. A present day, AE-particular cement-primarily based totally piezoelectric composite sensor become brought with present day performance. During construction, those sensors had been inserted into the muse of strengthened concrete frames and used to reveal the structure's harm.

2.12 3D Printing

3D printing is quickly becoming an essential construction technology offering for the construction industry when you consider how it will change material sourcing. This technology goes beyond the designer's table by layer-by-layer building a three-dimensional object from a computer-aided design model.

Today, the construction industry is reaping the benefits of 3D printing technology.

With 3D printing, prefabrication can be done either off-site or on-site. It is currently conceivable to print significant construction materials and have them prepared to utilize right away, in contrast to customary structure strategies. Because it speeds up the delivery of materials, construction companies gain a lot from this.

2.13 Virtual Reality (VR) Technologies/Augmented Reality (AR)

The construction enterprise will gain significantly from digital fact and augmented fact technology. Augmented fact (AR) provides virtual factors to a stay view, while digital fact (VR) implies an entire immersion level in. When mixed with BIM technology, the opportunities of VR/AR technology are endless.

Benefits and applications of AR/VR technology in the construction industry today.

You can get a close-up look at how the layout might flow through virtual tours and walk-through construction models. The value of augmented and virtual reality technology for safety and training enhancements cannot be overstated. With the help of hazard simulations, risk assessments, which were once a difficult and delicate process, became routine.

2.14 Mobile and Cloud Technologies

The construction industry has changed and evolved significantly thanks to mobile and cloud technologies. These technologies make it possible to share data in real time between construction sites and all parties involved. Tools for project management or review, for instance, which are essential for engineers and architects are now always accessible.

2.15 Block Chain Technology

The construction sector has seen a rise in the significance of block chain technology in recent months. The creation of a digital currency or crypto currency (such as Bitcoin or Ethereum) in 2008 gave rise to this technology.

What is Block chain?

The term “block chain” refers to a distributed ledger of digital data that is controlled or verified by a network of computers through peer-to-peer peer verification. Each node in the chain is in charge of ensuring the safety of its data by digitally signing each piece of data. This makes it possible to exchange data quickly and securely without the involvement of any third parties.

Use cases for block chain technology in construction technology Smart contracts Block chain technology has the potential to establish a process that is error-free for creating, managing, and monitoring contracts. In order to carry out the terms of a contract, the Block chain network makes use of a type of digital protocol known as a smart contract. Implementing smart contracts using block chain technology not only eliminates intermediary parties and their services but also increases efficiency.

Work flow improvements

Transparency in the construction process is made possible by block chain technology, which also has an impact on project workflow optimization. Additionally, it contributes to timely decision-making, reduces risk, and keeps disagreements to a minimum by encouraging more collaborative work.

2.16 Self-healing Concrete

Self-healing concrete will be used on homes, roads, and buildings in 2021. Imagine applying cutting-edge technology to problems like building cracks and structural deterioration. Despite the fact that the technology is still in its infancy, it may provide excellent relief from such problems. By 2030, many anticipate that the construction industry will use approximately 5 billion metric tons of concrete annually, with concrete being the most widely produced and used material. Need To Switch To Digital Construction in 2022: Machine learning, robotics, 3D priming, and building information modeling are just some of the digital technologies that are ready to take you into the next normal in the years to come. The need to switch to digital construction is driving businesses to take action as the ambiguity and complexity of construction projects grows on a daily basis. In fact, the pandemic has served as a push toward digitalization in the construction industry, which has been long overdue. Construction technology is proving to be a catalyst for change in a time when the need for real-time collaboration is of the utmost importance. Contractors and subcontractors should use construction technology for a lot of good reasons. Although the construction sector is poised to see the integration of a number of digital technologies, it has historically been slow to adopt technology. Firms' improved innovation capabilities, increased profitability, and improved productivity are among the advantages of digitalization.

3 Reasons to Switch to Digital Construction

1. Reduce Uncertainty in Order to Meet Project Objectives
2. Customer Orientation and Marketing
3. Enhance Communication and Real-Time Collaboration
4. Enhance Communication and Real-Time Collaboration
5. Manually Task Automat for Increased Efficiency
6. Simplify Business and Operations
7. Adoption of Construction-Specific Cloud Technologies.

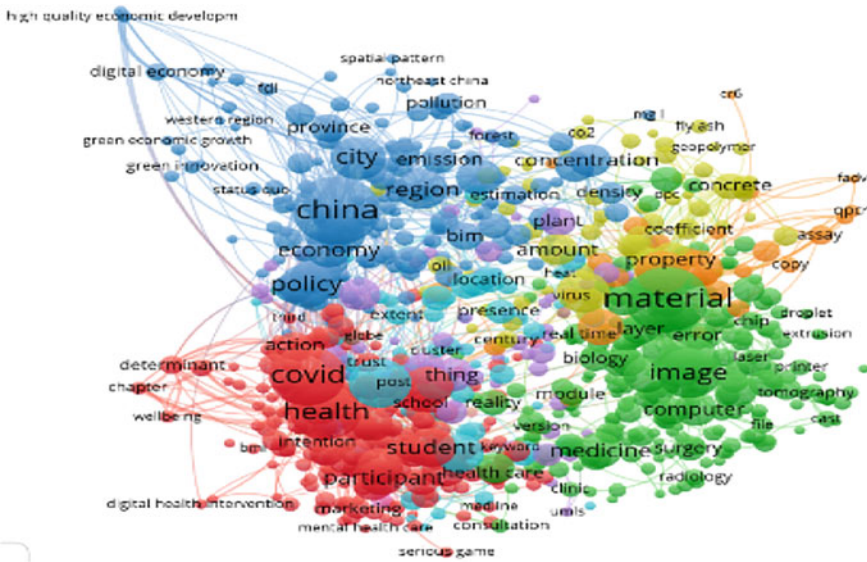


Fig. 1 The network visualization of literacy topic area

4 Result and Discussion

The Visualization of the Topic Area “Scientific Literacy” Using VOSviewer

4.1 Analysis of Author Keyword Co-occurrence

Topic mapping is essential for bibliometric research. All of the issue categories associated with the terms “scientific literacy” as a whole are depicted in Fig. 1. Six distinct mapping visualizations can be generated by VOSviewer during the bibliometric analysis. The strength of a pair of topic areas or keywords was represented by the thickness of the connecting line.

4.2 In Terms of Country, Co-authorship is as Follows

Figure 2 depicts nations that place an emphasis on scientific literacy research. According to the data, the most scientific literacy research studies have been conducted in India and the United States, followed by Canada, Australia, and Turkey. Meanwhile, scientific literacy research in Indonesia is still in its infancy, as the VOSviewer mapping results demonstrate.

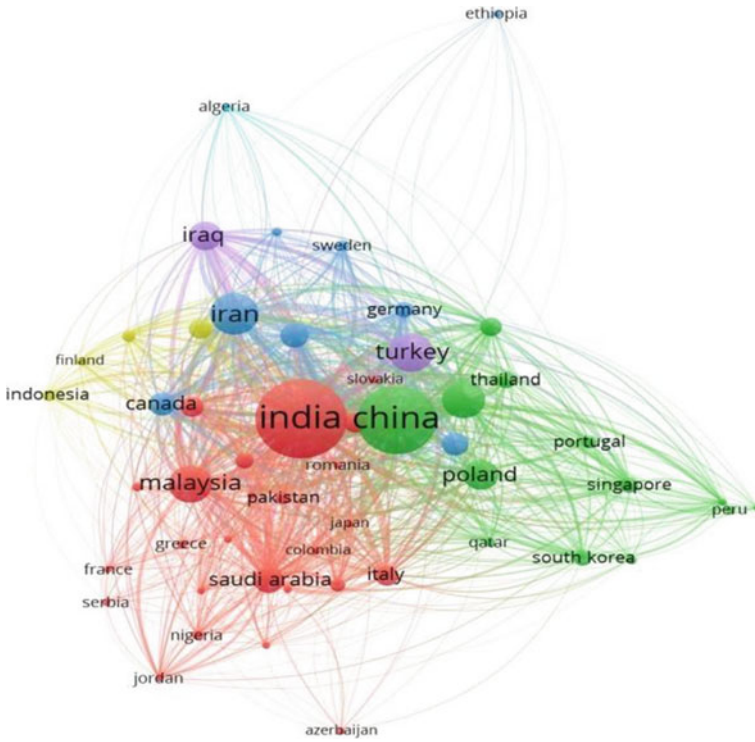


Fig. 2 The visualization of countries related to scientific literacy research

4.3 Co-authorship in Terms of Authors

The barrier is set at four for the author’s minimum number of documents. The word, its authors, organizations, and nations are taken into account by this analytical parameter. It is important to note that the Scopus and web of science databases found that 328 of the 1549 authors met their requirements (Fig. 3).

4.4 Co-authorship in Terms of Organizations

The most citations and the highest link strength are held by Stony Brook University (SBU), New York, United States. Figure 4 shows analysis between organizations. The unit of organizations’ co-authorship is determined by disregarding at least two publications’ citations.

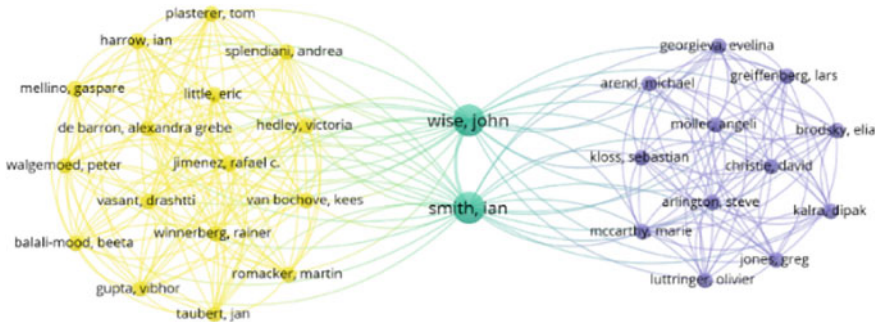


Fig. 3 Network analysis of co-authorship in terms of authors

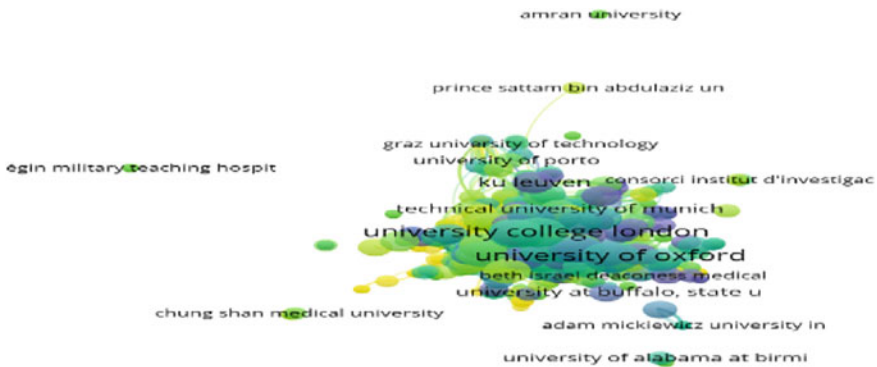


Fig. 4 Network analysis of co-authorship in terms of organizations

5 Conclusion

The study’s goal was to learn about the digital tools available to construction professionals when planning a construction project. It turned out that Microsoft and waste management management systems are the two digital technologies that construction workers use the most. We believe that construction professionals use similar digital technologies in their planning activities based on the study’s findings. When using digital technologies for construction planning, construction professionals see the advantages of improved quality, improved record keeping, and time savings. Additionally, the study revealed a statistically significant difference in benefits.

References

1. Abba, T., Afolabi, A. O., Ajibola, P., & Olanrewaju, P (2020) Digital technologies and construction planning, Published under licence by IOP Publishing Ltd. In *IOP Conference Series: Materials Science and Engineering, International Conference on Engineering for Sustainable World (ICESW 2020)* 10th–14th August 2020 (Vol 1107). Ota, Nigeria.
2. Oladapo, A. A. (2007). An investigation into the use of ICT in the Nigerian construction industry. *Journal of Information Technology in Construction*, 12, 261–277.
3. Mohamed, S., & Stewart, R. A. (2003). An empirical investigation of users' perceptions of web-based communication on a construction project. *Automation in Construction*, 12, 43–53.
4. Betts, M. (1999). *Strategic management of information technology in construction*. Blackwell Publishers.
5. Liston, K. M., Fischer, M. A., & Kunz, J. C. (2000). Designing and evaluating visualization techniques for construction planning. In *Proceedings of the 8th International Conference on Computing in Civil and Building Engineering ICCCBE-VIII* (pp. 1293–3000). Stanford University Stanford, CA.
6. Samuelson, O. (2002). IT-Barometer 2000: The use of IT in the Nordic construction industry. *Journal of Information Technology in Construction*, 7, 1–26.
7. Rivard, H. (2000). A survey on the impact of information technology on the Canadian architecture engineering and construction industry. *Journal of Information Technology in Construction*, 5, 37–56.
8. Arif, A. A., & Karam, A. H. (2001). Architectural practices and their use of IT in the Western Cape Province South Africa. *Journal of Information Technology in Construction*, 6, 17–34.
9. Ojelabi, R. A., Oyeyipo, O. O., Afolabi, A. O., & Amusan, L. M. (2018). Presence of client social relationship management with in the Nigeria construction industry. *Buildings*, 8(4), 60–75.
10. Ibem, E. O., Aduwo, E. B., Ayo-Vaughan, A., & Tunji-Olayeni, P. F. (2018). A survey of digital technologies used in the procurement of building projects: empirical evidence from Nigeria. *Asian Journal of Scientific Research*, 11(4), 456–465.
11. Kasim, N. B., Anumba, C. J., & Dainty, A. R. J. (2005). Improving materials management practices on fast-track construction projects. In *21st Annual ARCOM Conference SOAS* (Vol. 2, pp. 793–802). University of London.
12. Davtalab, O., Kazemian, A., & Khoshnevis, B. (2018) Perspectives on a BIM-integrated software platform for robotic construction through contour crafting. *Automation Construction* 89, 13–23. [CrossRef].

Testing Strength of Grassed Paver Block Made by Waste Material and Coir Fibre



Anil Shirgire, Hemchandra Pawar, Satyawar Jagdale, Ravikant Sathe, Vijaykumar Javanjal, and Swati Ambadkar

Abstract At construction sites in metro city, the activity such as demolition of building, construction of big tower and renovation of building are throwing concrete waste in huge amount. This produced waste is either diverted for land filling in nearby areas or used for dumping. The different type of paver block uses this concrete waste for bulk production. In this study, the representation of the concept of sustainable use of concrete waste which was used in manufacturing of interlocking grassed paver blocks with coir fibre and compressive strength of concrete was determined.

Keywords Concrete waste · Grassed paver block · Compressive strength and coir fibre

1 Introduction

The grassed Paver Block is used to provide pavement in parking areas as well in gardens. Traditional types of construction practices are not suitable for many operating and environment problem because it produces waste. This Waste was used in interlocked grassed paver block [1–3]. Grassed Paver Block is durable as compare to bitumen and also aesthetically excellent. In India this technology is came from 25 years. It was used places like footway paths, areas of parking. It is now largely used in many purposes. Hot bitumen mix has many limitations. Instead of bitumen paving blocks are better to use. The present study was done for following reasons: (1) To study the grassed paver block feasibility. (2) To proportionate concrete waste

A. Shirgire (✉) · V. Javanjal
Dr D Y Patil Institute of Technology, Pimpri, Pune, India
e-mail: anil.shirgire@gmail.com

H. Pawar · S. Jagdale · R. Sathe
SVERI's College of Engineering, Pandharpur, India

S. Ambadkar
G H Raisoni University Amravati, Amravati, India



Fig. 1 Grassed paver block

received from demolition activity in making of grassed paver blocks [4, 5]. (3) To carry out various strength tests at testing lab on grassed paver block.

2 Materials

The Locally available Cement, sand, fine aggregate and coarse aggregate was used as per design mix. Also the concrete waste was selected from the 5 sites after visiting these sites in Pune. Suitable selections of sites were done which fulfilled requirement of materials [4–7]. Sites near Pimpri, Kale wadi and Wakad were selected which comprised old structures of 45 years old. It was demolished for construction of new building. After then the material was transported for crushing purpose (Fig. 1).

3 Tests on Materials

3.1 Test on Cement

The results of the conducted experiments are presented in the Table 1.

3.2 Compressive Strength Test

See Fig. 2; Tables 2, 3, 4, 5 and 6.

From Figs. 3 and 4 the average compressive strength of paving block with the percentage of 0.3% coir fibre gives best possible end result as comparing to 0.1 and 0.5% coir fibre percentage respectively.

Table1 Test on cement

S. No.	Test performed on cement	Results
1	Fineness in m ² /kg	236
2	Standard consistency test of cement	28%
3	Initial setting time in minutes	31 min
4	Final setting time in minutes	607 min
5	Compressive Strength, N/mm ² in Days	
	04-days	38
	07-days	47.0
	28-days	58.0
6	Soundness test in mm	8 mm
7	Specific gravity of cement	3.15

Fig. 2 Compression test set up**Table 2** Test on normal aggregate and recycled aggregate

S. No.	Test performed on normal aggregate	Test results obtained of normal aggregate	Test results obtained of recycled aggregate
1	Specific gravity	2.5	2.35
2	Water absorption (%)	1.4	6.9
3	Crushing value (%)	33	13.25
4	Impact value (%)	18.79	14.3
5	Bulk density	20 mm size-1515 kg/m ³ 10 mm size-1500 kg/m ³	20 mm size-1320 kg/m ³ 10 mm size-1260 kg/m ³
6	Flakiness index (%)	21	13.3
7	Elongation index (%)	23	16

Table 3 Results of compression test after 14 days (100% fully replacement)

S. No.	Sample	Coir fibre percentage	Weight of sample (Kg)	Compressive strength (N/mm ²)	Average strength (N/mm ²)
1	1	0.1	3.9	15.0	15.22
	2		3.4	15.4	
	3		3.1	16.3	
	4		3.3	16.5	
2	1	0.3	3.2	21.3	20.10
	2		3.8	20.5	
	3		3.3	19.4	
	4		3.4	19.5	
3	1	0.5	3.4	19.2	18.54
	2		3.3	18.7	
	3		3.3	18.9	
	4		3.9	18.0	

Table 4 Results of compression test after 14 days (40% partially replacement)

S. No.	Sample	Coir fibre percentage	Weight of sample (Kg)	Compressive strength (N/mm ²)	Average strength (N/mm ²)
1	1	0.1	3.9	23.8	23.10
	2		3.4	23.4	
	3		3.1	23.9	
	4		3.3	23.3	
2	1	0.3	3.2	26.4	26.40
	2		3.8	25.8	
	3		3.3	26.0	
	4		3.4	26.4	
3	1	0.5	3.4	24.3	24.50
	2		3.3	24.7	
	3		3.3	25.1	
	4		3.9	25.3	

Table 5 Results of compression test after 28 days (100% partially replacement)

S. No.	Coir fibre percentage	Sample No.	Weight of sample (Kg)	Compressive strength (N/mm ²)	Average strength (N/mm ²)
1	0.1	1	3.9	24.2	24.41
		2	3.4	24.6	
		3	3.1	25.4	
		4	3.3	25.0	
2	0.3	1	3.2	26.2	26.52
		2	3.8	26.0	
		3	3.3	26.3	
		4	3.4	27.3	
3	0.5	1	3.4	23.7	23.12
		2	3.3	22.8	
		3	3.3	23.9	
		4	3.9	23.7	

Table 6 Results of compression test after 28 days (40% partially replacement)

S. No.	Coir fibre percentage	Sample No.	Weight of sample (Kg)	Compressive strength (N/mm ²)	Average strength (N/mm ²)
1	0.1	1	3.9	32.0	30
		2	3.4	31.1	
		3	3.1	29.9	
		4	3.3	31.1	
2	0.3	1	3.2	32.4	31
		2	3.8	32.0	
		3	3.3	32.4	
		4	3.4	33.2	
3	0.5	1	3.4	27.9	28
		2	3.3	27.9	
		3	3.3	29.3	
		4	3.9	28.9	

Fig. 3 Average Compressive strength of paving blocks at 14 days

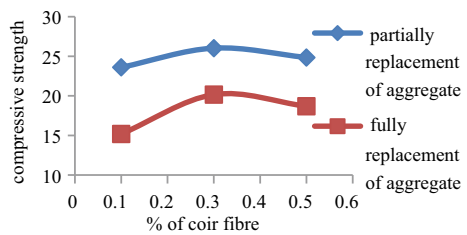
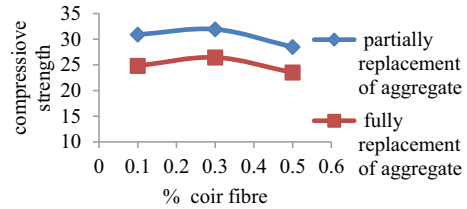


Fig. 4 Average Compressive strength of paving blocks at 28 days



4 Conclusion

The grass paving blocks average compressive strength with the 0.3% coir fibre gives expected adequate result as compared to 0.1% and 0.5% coir fibre respectively. The Average Compressive strength of paving block of 0.3% coir fibre of partially replaced demolished aggregate [8] at 14 and 28 days are 28 and 20% higher than fully replaced demolished aggregate respectively. The Average Compressive strength of paving block at 28 days is 22 and 31% higher than average compressive strength of paving block at 14 days of partially and fully replaced aggregate respectively. Water absorption of recycled aggregate is slightly more than regular aggregate [8]. The grasses paver block was found appropriate from these findings for use in parking areas, hence it is recommended to use grassed paver block as it provides required strength.

References

1. Kulkarni, V. P., Gaikwad, S. K. B. (2020). Comparative study on coconut shell aggregate with conventional concrete. *Journal of Engineering and Innovative Technology (IJEIT)*, 2, 12–19.
2. Navya, G. (2021). Experimental investigation on properties of concrete paver block with inclusion of natural fibre. *International Journal of Engineering Research and Applications*, 4(8)(Version 6), 34–38. www.ijera.com ISSN: 2248-9622.
3. Umoh, A. A., & Kamang, E. E. J. (2005). The compressive strength of medium grade concrete made with waste sandcrete blocks aggregate. *International Journal of Environmental Issues*, 3(1), 177–186.
4. IS 10262-2009, Specification for concrete mix design.
5. IS 1199-1959 (1959). *India standard method of sampling and analysis*. New Delhi: India standard Institute.
6. IS 12269-1999, Specification for 53 grade OPC.
7. IS 15658-2006, Specification for concrete paver block.
8. IS 2385-1963 Part 3, Method of test of aggregate for concrete specific gravity.

Performance Evaluation of Kota's Black Soil Using Perma-Zyme



Jitendra Kumar Sharma and Sakshi Khandelwal

Abstract Kota's Black Soil (KBS) is an expansive soil, and it shrinks and swells in response to changes in moisture. Present research is focused on the use of Perma-zyme to stabilize Kota's Black Soil. This research shows a series of testing on Kota's Black Soil as well as tests on Perma-zyme stabilized KBS with varied Dosages ranging from 1 to 2 m³ in intervals of 0.25 m³ soil per 200 mL of Perma-zyme. On addition of Perma-zyme the soil shows notable improvements in its engineering and index properties such as; Plasticity, Density, and Uniaxial Strength (in compression). It is observed that the plasticity is decreased by 25% in comparison to virgin soil and significant raise in the uniaxial strength of the soil is perceived in terms of UCS. Optimum dosage yielded maximum UCS of 2.71 and 3.19 kPa for 0–7 days' water retention period, respectively.

Keywords Kota's black soil (KBS) · Perma-zyme · Swelling · Soil stabilization · Unconfined compressive strength

1 Introduction

Soil stabilization is a practice by which the mechanical properties of soil are enhanced with addition of stabilizer. It is useful as it improves shear strength of soil, control swelling and shrinking behavior of soil. There are many types of natural and synthetic stabilizers [1, 2] available which are cast-off for soil stabilization. Lime, Fly-ash, bitumen, wheat-husk, cement-kiln-ash, brick-dust, wet and dry marble-dust, powdered and paste Kota's-stone-dust, saw-dust, etc. are used as natural stabilizers while polymer and their emulsions, enzymes, acid etc. are used as a non-traditional stabilizer. Recently, the bio-stabilization comes into play which includes application of enzyme on soil. Bergmann and Roger [3] performed an experimental study on the bio-enzyme and from the study it was concluded that the introduction of bio-enzyme significantly improves the properties of the soil, which is further dominated in the

J. K. Sharma (✉) · S. Khandelwal
Department of Civil Engineering, Rajasthan Technical University, Kota, Rajasthan, India
e-mail: jksharma@rtu.ac.in

case of clayey soil. The hydro electrical double layer plays an important role for the interaction between soil and the enzyme. Shukla et al. [4] carried out an experimental investigation program on five types of soils with enzyme. It is observed that as the clay fraction in soil raises, the capability of the bio-enzyme is raises. Based on the results of the study a flexible pavement was designed which shows that the thickness of the altered clayey soil pavement is reduced by 30%. Venkatasubramanian and Dhinakaran [5] performed tests on three types of soils with Terra-zyme and studied with various dosage of Terra-zyme. A raise of 157–673% in CBR is perceived after 4 weeks of water retention and a raise of 152–200% in UCS of the altered soil. Agarwal, and Kaur [6] performed a study on black soil with various dosage of Terra-zyme from 0 to 0.80 mL/kg of soil and cured for 1 and 7 days. It is concluded that the uniaxial strength (in compression) was improved by approx. 200%. Saini and Vaishnav [7] mixed local soil with Perma-zyme in various dosages from 1.5 to 3 m³/200 mL of Perma-zyme at an interval of 0.5 m³. The 3rd dosage of enzyme is the most suitable as the plastic (Liquid and Plastic) properties were decreased and the CBR in soaked condition was raised for water retention period of 14 days. Senand Singh [8] investigated the effect of Terra-zyme on black soil using Terra-zyme in various dosage from 1.5 to 3 m³ of soil per 200 mL with water retention period of 0, 14, 21, and 28 days. According to study, marginal changes in maximum dry density from 1.48 to 1.63 gm/cc and optimum moisture content from 23.00 to 20.40% was perceived while CBR and UCS were raised by 387% and 154% respectively as compared to the native soil. Panchal et al. [9] performed an experimental study on stabilization of soil using terra-zyme and found that the CBR of soil was increased significantly. Rajoria and Kaur [10] presented a literature study on the application of bio-enzyme as stabilizer for soils and concluded that the bio-enzymes are eco-friendly and sustainable. Kanniyappan et al. [11] performed an investigation on black cotton soil stabilized with bio-enzyme and noticed that the CBR of stabilized earth is increased such that the pavement thickness was reduced to 40%. Similar study was performed by Shrinivas et al. [12] using bio-enzyme for stabilization of subgrade in Gujrat, India. The results of the study were quite promising as the swelling is reduced and CBR was increased. Sodhi and Ocean [13] used Alkazyme for the stabilization of soil and noticed that the UCS of the stabilized earth was improved significantly. Srinivas et al. [14] presented a study on the effect of bio-enzyme for the swelling characteristics of soil and concluded that the free swell index was significantly reduced. Sirinivas et al. [14] performed a comparative experimental study on the stabilization of expansive soil with lime and bagasse ash, and bio-enzyme and found that bio-enzyme was much better than lime for controlling the shrinkage. Shil et al. [15] performed stabilization of sub-grade soil using bio-enzyme and confirmed the feasibility of the bio-enzyme as a stabilizer. In the literature, various bio-enzymes (i.e. Terra-zyme, Alka-zyme, Fujibeton etc.) were used for the stabilization of different type of soils. In this present work, an experimental study is conducted for enhancing the chemo-mechanical properties of the Kota's Black Soil (Highly Expansive) by adding Perma-zyme (Vegetable Enzyme). Various laboratory tests were accompanied for characterization of soil and to study the effect of enzyme on mechanical properties (Density, Swelling Pressure,

Strength, and CBR) of soil. Based on the research work an optimal dosage of enzyme is determined for treatment of the soil.

2 Material Introduction

2.1 Kota's Black Soil

Central India mostly and a part of South India (19% of Total land of the country) is occupied with Black Soil [16]. It is residual deposits formed from decomposition of basalt. Kota's Black Soil has high swell ability and plasticity. It essentially consists of the clay mineral montmorillonite (2:1 mineral), which is the most hydrophilic mineral of clay, thus these soils have high shrink and high swelling properties. The unconfined compressive strength of these type of soils is very low during wet season. It has low bearing capacity in presence of moisture because of high compressibility.

2.2 Perma-Zyme

Perma-zyme fluid stabilizer is especially verbalized to upgrade the engineering behavior of soil by accelerating physical–chemical equilibrium in soil, altering inner ingredients into more moisture and force resilient form to enhance the chattels of cohesive (clayey) soils. Perma-zyme is a bio enzyme concentrate made from the fermentation of plant-based organic matter. The accelerating enzymes in Perma-zyme are usual protein molecules that boost up physical–chemical reactions. These catalysts fast-track changes in the road materials to convert it into new lattice structure. Perma-zyme permanently binds the soil particles together to create a concrete like surface (Fig. 1).

Fig. 1 Perma-zyme liquid



3 Methodology

This research study was carried out in three phases as shown in Fig. 2. In the primary phase the soil characterization was finished by leading various tests on virgin Kota's Black Soil and in the subsequent stage, Perma-zyme was added to the soil in four dosages, 1, 2, 3, and 4 given in below section and in third stage series of tests were conducted after water retention of 0, and 7 days with various dosages of Perma-zyme.

3.1 Preparation of Enzyme Solution

The enzyme dosage varies from 200 to 200 mL/1 m³ of the Kota's Black Soil, and it relies on soil characteristics. In the experimental study the Perma-zyme dosages used for Kota's Black Soil was 200 mL for volume 2–1 m³ of soil. The maximum dry density of virgin soil is 1.60 gm/cc (Table 1).

3.2 Details of Laboratory Test

In this study, different tests were conducted for characterization of the Kota's Black Soil and the evaluation of the chemo-mechanical properties of the stabilized Kota's

Fig. 2 Experimental program

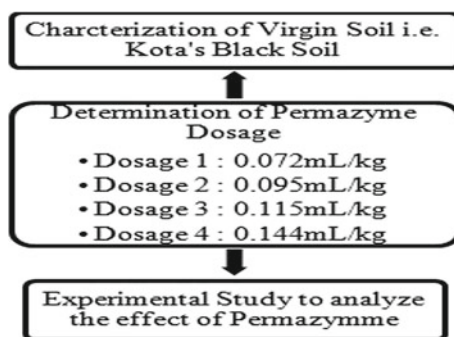


Table 1 Dosage of Perma-zyme

Dosage	Dosage of Perma-zyme per m ³ of soil	mL/kg of soil
Dosage1	200 mL/2 m ³	0.067
Dosage2	200 mL/1.5 m ³	0.089
Dosage3	200 mL/1.25 m ³	0.107
Dosage4	200 mL/1 m ³	0.144

Table 2 List of laboratory tests

S. No.	Laboratory test	Indian standard	Property determined
1	Sieve analysis	IS:2720 (Part IV)	Grain size distribution characterization of Soil
2	Consistency limit test	IS:2720 (Part V)	Liquid limit, plastic limit
3	Differential free swell	IS:2720 (Part XL)	Differential free swelling
4	Light compaction	IS:2720 (Part VII)	Maximum dry density optimum moisture content
5	Unconfined compression	IS:2720 (Part X)	Undrained cohesion
6	California bearing ratio	IS:2720 (Part XVI)	CBR
7	Odometer	IS:2720 (Part XLI)	Swelling pressure

Black Soil with different dosage of Perma-zyme. The procedure used for the characterization and mechanical properties determination was adopted from the Indian Standard codes, which are shown in Table 2.

4 Results and Discussion

4.1 Grain Size Distribution

The results of the sieve analysis test are shown in Fig. 3. Figure 3 is a semi logarithmic plot which consists of sieve size (in mm, on x-axis in log scale), and percentage finer (on y-axis). From the Fig. 3, it is concluded that the Kota's Black Soil is fine grained soil. For further characterization of the Kota's Black Soil, consistency limit tests are performed, which are discussed in the Sect. 4.2.

4.2 Consistency Limit Test

The Atterberg's limit of soil is shrinkage limit, plastic limit, and liquid limit. The liquid limit was determined from the Cone Penetrometer test as discussed in [IS:2720 (Part V)]. The liquid limit of Kota's Black Soil is 55.22%. As per Indian Soil Classification System the soil is classified as Highly Compressible soil. For further classification of the soil type, plastic limit test was performed and plasticity index was calculated using the Eq. 1.

$$\text{Plasticity Index (IP)} = \text{Liquid Limit} - \text{Plastic Limit} \quad (1)$$

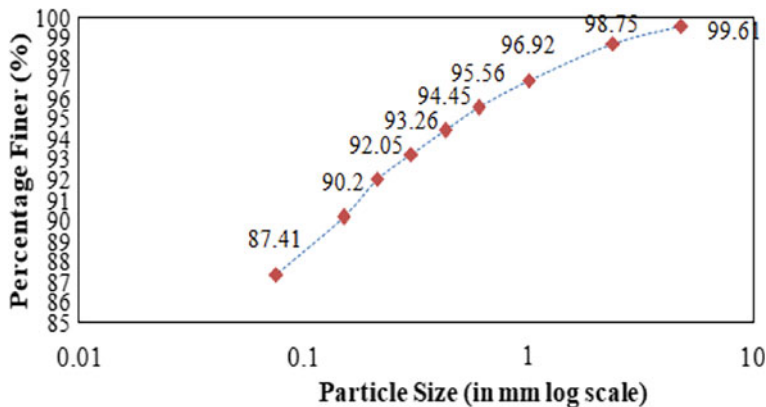


Fig. 3 Grain size distribution curve

As per Indian Soil Classification System, the soil is classified. If the IP calculated lies above the A – Line, the soil is classified as Clay, otherwise Silt. Where, Liquid Limit is in Percentage

$$A - \text{Line (IP)} = 0.73 \times (\text{Liquid Limit} - 20) \tag{2}$$

From Fig. 4, it is cleared that the Kota’s Black Soil is clayey and is highly compressible, so the soil is classified as CH as per Indian Soil Classification System. The effect of Perma-zyme on the consistency limits of Kota’s Black Soil was further studied and presented in Fig. 4 and Table 3. It is cleared that the due to introduction of the Perma-zyme the compressibility of the soil is reduced.

It is observed that Liquid limit is decreased from 55.22 to 41.80% and 55.22% to 35.78% after 0, and 7 days respectively at 3rd dosage (1.25 m³/200 mL). Plastic limit test was performed on expansive soil with various dosages. It is perceived that the plastic limit is decreased with addition of Perma-zyme after water retention of 0, and 7 days from 27.157 to 22.252%, and 27.157% to 21.84% respectively. The greatest decrement is noted for 3rd dosage (1.25 m³/200 mL).

Figure 5 shows the bar graph for the plasticity index for various dosages of Perma-zyme with soil, which is the change between liquid (W_L) and plastic (W_P) limit. A reduction in Plasticity Index (I.P.) is perceived with the addition of Perma-zyme. The maximum drop in plasticity index is perceived for the 3rd dosage of the Perma-zyme which consists of 1.25 m³/200 mL. The minimum plasticity index is 19.55% and 13.94% for 0 and 7 days water retention period respectively.

Fig. 4 A line (soil classification)

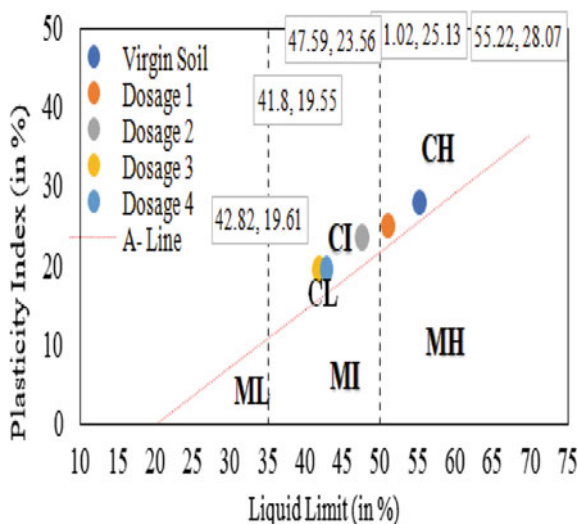


Table 3 Consistency limit of Kota's Black soil altered with Perma-zyme

Retention period	0 days		7 days	
	Liquid limit (W _L)	Plastic limit (W _P)	Liquid limit (W _L)	Plastic limit (W _P)
Virgin soil	55.22	27.15	—	—
Dosage1	51.02	25.89	48.42	25.71
Dosage2	47.59	24.03	44.13	24.04
Dosage3	41.80	22.25	35.78	21.84
Dosage4	42.82	23.21	37.64	22.21

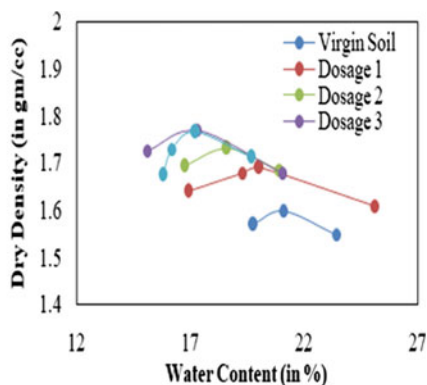
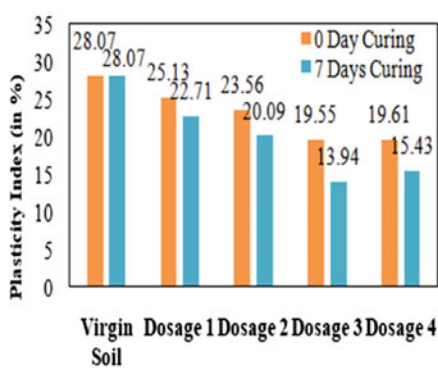


Fig. 5 Bar chart of plasticity index with various dosages of Perma-zyme with 0 and 7 days water retention period

4.3 Density Compaction Test

Figure 6 is the representation of the compaction test done in the laboratory on the various sample. From the Fig. 6, it is clear that the due to addition of Perma-zyme the dry density is increasing whereas the optimum moisture is reducing. The maximum dry density was perceived for the 1.25 m³/200 mL dosage of the Perma-zyme (3rd Dosage). In Table 4, it is perceived that the maximum dry density of Kota’s Black Soil is 1.60 gm/cc, which is raised up to 1.77 gm/cc because of the addition of the Perma-zyme (3rd Dosage). The percentage raise in dry density is 10%, which may be because of the induced chemical reaction due to addition of Perma-zyme.

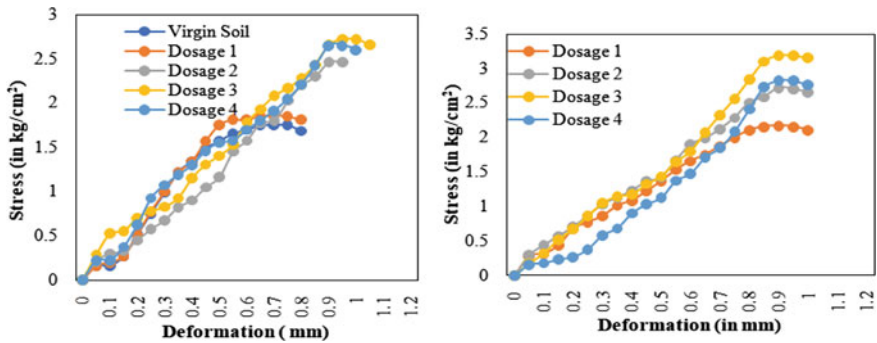


Fig. 6 Results of unified compression test for black soil with varying percentage of Pera-zyme (water retention period = 0 and 7 Days)

Table 4 Results of density compaction test

Specimen	Maximum dry density (gm/cc)	Percentage variation in maximum dry density (%)	Optimum moisture content	Percentage variation in optimum moisture content
Virgin soil	1.60	–	21.10	–
Dosage1	1.69	+ 5.62	20.05	–4.97
Dosage2	1.73	+ 8.12	18.60	–11.85
Dosage3	1.77	+ 10.62	16.30	–22.74
Dosage4	1.76	+ 10.00	17.24	–18.29

Table 5 Results from unified compression test

Water retention period	UCS (kg/cm ²)	Percentage variation	UCS (kg/cm ²)	Percentage variation
	0 days		7 days	
Virgin soil	1.74	–	1.74	–
Dosage1	1.86	6.89	2.17	24.71
Dosage2	2.46	41.37	2.72	57.47
Dosage3	2.71	55.74	3.19	83.33
Dosage4	2.65	52.29	2.82	62.06

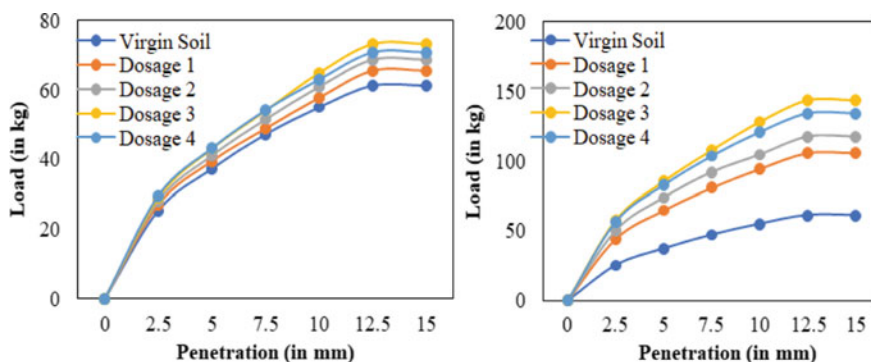


Fig. 7 CBR test results with mix specimen (0 day curing)

4.4 Unified Compression Test

Table 5 shows the results of UCS test carried out in laboratory on virgin and altered soil with and without water retention period of 7 days. It is perceived that the Water retention raises the strength of the altered soil.

The optimum strength was obtained for the 3rd dosage of the Perma-zyme (200 mL/1.25 m³ of soil), which is 2.71 and 3.19 kg/cm² for 0 and 7 days water retention period. The increment in the UCS of soil is about 55.74 and 83.33% for 0 and 7 days water retention respectively with respect to virgin soil (1.74 kg/cm²). Figures 7 and 8 show the stress–strain (Load v/s deformation) graph obtained from the laboratory test performed on the altered and native soil.

4.5 California Bearing Ratio (CBR) Test

California Bearing Ratio Test is performed to determine the CBR value of soil. Kota’s Black Soil was cured with 4 different dosage of enzyme (Perma-zyme) at

Fig. 8 Percentage variation of CBR value

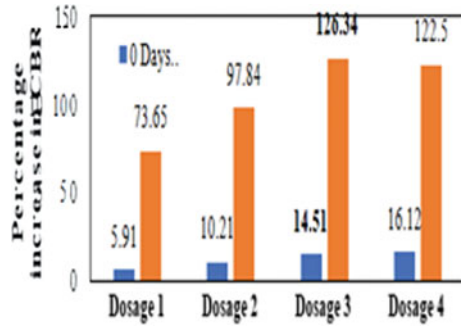


Table 6 Variation of CBR test results obtained for BCS with different dosage of Perma-zyme and curing

Test specimen	Curing period	CBR in %	% increase
Virgin soil	–	1.86	–
Dosage 1	0	1.97	5.91
	7	3.23	73.65
Dosage 2	0	2.05	10.21
	7	3.68	97.84
Dosage 3	0	2.13	14.51
	7	4.21	126.34
Dosage 4	0	2.16	16.12
	7	4.14	122.5

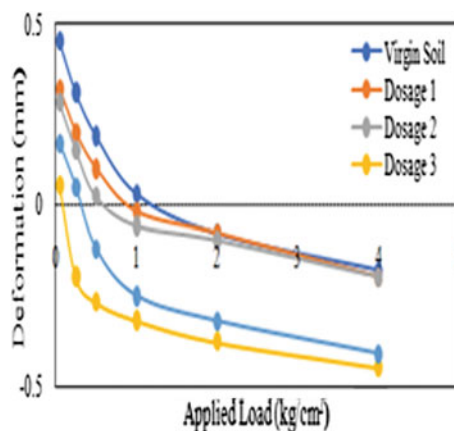
optimum moisture content and maximum dry density. CBR samples were prepared with various dosages by standard method and kept in plastic bags for testing on different days such as 0 and 7 days.

From Table 6, it is noticed that the CBR value of Kota’s Black Soil is 1.86% in soaked condition. When Perma-zyme is mixed with Kota’s Black Soil CBR value of soil is enhanced up to 2.16 at dosage 200 mL/1 m³. After curing of 7 days CBR value increase to 126.34%. The graphical representation of load and penetration with varying curing period is given in Fig.7 and the percentage increments of CBR value with different dosage and curing period is shown in Fig. 8.

5 Conclusions

In this study Kota’s Black Soil was altered by using Perma-zyme to improve geotechnical properties of Kota’s Black Soil. The underlined conclusions are established on the basis of this study: The plasticity (I_p) index of Kota’s Black Soil is 28.06% which decreases to 19.55 and 13.93% at 3rd dosage for water retention period of 0, 7 days respectively. The maximum dry density and optimum moisture content of Kota’s

Fig. 9 Variation of swelling pressure



Black Soil is perceived 1.60 gm/cc and 21.10% respectively. The dry density is raised from 1.60 to 1.77 gm/cc and the corresponding moisture content is decreased from 21.10 to 17.24% at 3rd dosage. The Uniaxial Strength (in compression) of Kota's Black Soil is 1.59 kg/cm², which was raised to 55.74 and 83.33% at 3rd dosage for water retention period of 0 and 7 days respectively. The CBR value of Kota's Black Soil is 1.86%. The extreme percentage increment of CBR value with curing period of 0, 7 days are 14.51%, 126.24% respectively at 3rd dosage (1.25 m³/200 mL) (Fig. 9).

References

1. Gidigasu, S. S. R., & Gawu, S. K. Y. (2013). The mode of formation, nature and geotechnical characteristics of black cotton soils-a review. *Science Resource Essays*, 1, 377–390.
2. Etim, R. K., Eberemu, A. O., & Osinubi, K. J. (2017). Stabilization of black cotton soil with lime and iron ore tailings admixture. *Transportation Geotechnics*, 10, 85–95.
3. Bergmann, R. (2000). *Soil stabilizers on universally accessible trails*. USDA Forest Service.
4. Mukherjee, I., Das, S. K., Kumar, A., & Shukla, L. (2020). Sludge amendment affects the persistence, carbon mineralization and enzyme activity of atrazine and bifenthrin. *Bulletin of Environmental Contamination and Toxicology*, 105(2), 291–298.
5. Venkatasubramanian, C., & Dhinakaran, G. (2011). Effect of bio-enzymatic soil stabilization on unconfined compressive strength and California bearing ratio. *JEAS-Journal of Engineering and Applied Sciences*, 6(5), 295–298.
6. Agarwal, P., & Kaur, S. (2014). Effect of bio-enzyme stabilization on unconfined compressive strength of expansive soil. *International Journal of Research in Engineering and Technology*, 3(5), 30–33.
7. Saini, V., & Vaishnava, P. (2015). Soil stabilization by using terrazyme. *International Journal of Advances in Engineering and Technology*, 8(4), 566.
8. Sen, J., & Singh, J. P. (2015). Stabilization of black cotton soil using bio-enzyme for a highway material. *International Journal of Innovative Research in Science, Engineering and Technology*, 4(12), 12453–12459.

9. Panchal, S., Khan, M. M., & Sharma, A. (2017). Stabilization of soil using bio-enzyme. *International Journal of Civil Engineering and Technology*, 8(1), 234–237.
10. Rajoria, V., & Kaur, S. (2014). A review on stabilization of soil using bio-enzyme. *International Journal of Research in Engineering and Technology*, 3(1), 75–78.
11. Kanniyappan, S. P., Kumar, R. D., Faizuneesa, A., & Saranya, S. Experimental investigation on black cotton soil using bio-enzyme as a soil stabilizer in road construction. *International Journal of Civil Engineering and Technology (IJCIET)*.
12. Chitragar, S. F., Shivayogimath, C. B., & Mulangi, R. H. (2019). Study on strength and volume change behavior of expansive soil using non-traditional (bio-enzyme) and traditional (lime and bagasse ash) stabilizers. In *Geotechnics for Transportation Infrastructure* (pp. 587–594). Springer.
13. Sodhi, P. S., & Ocean, Y. K. (2018). Stabilization of soil using acidic bio-enzyme (Terrazyme). *International Journal of Innovation Resource Science Engineering Technology*, 7(8).
14. Chitragar, S. F., Shivayogimath, C. B., & Mulangi, R. H. (2021). Laboratory investigation of black cotton soil modified with bioenzyme and aggregates for pavement subgrade. In *Recent Trends in Civil Engineering* (pp. 341–351). Springer.
15. Shil, T., Pradhan, R., Nanda, S., & Mohapatra, B. G. (2021). Strengthening of soil subgrade using bio-enzyme. In *Recent developments in sustainable infrastructure* (pp. 13–25). Springer.
16. Gosavi, M., Patil, K. A., Mittal, S., & Saran, S. (2004). Improvement of properties of black cotton soil subgrade through synthetic reinforcement. *Journal of the Institution of Engineers (India): Civil Engineering Division*.

RULA and REBA's Evaluation of the Work Posture of the Power-Loom Industry: A Case Study



S. G. Kolgiri, M. D. Jagtap, and S. L. Sathe

Abstract Musculoskeletal disorders are a major complaint for employees in India. Most power-loom industries currently involve manual labor, making the issues of work-related musculoskeletal disorders and injuries at diverse body sites of vital concern. In the current study, video was recorded in order to measure work processes, workload assessment, and work stress. The Rapid Upper Limb Assessment (RULA) technique was used to measure risk factors associated with complaints of the upper extremities. While the Rapid Entire Body Assessment was used to measure the body problems (REBA). This ergonomic study provides insight into the power loom industry's workforce's posture analysis. The 15 power-loom industry employees at MIDC Solapur were the subjects of the study (Maharashtra, India). Images were then extracted for examination from a video clip that documented the workers' various activities. Thus, it was determined that the power loom industry lacks ergonomics awareness and understanding. The personnel are working beyond the safe limit, according to RULA and REBA's assessment of the situation using postural analysis. The majority of employees have hunched-over postures. Therefore, there is a moderate to high risk of musculoskeletal problems among the workforce, so to prevent WMSDs or their symptoms, some interventions are used, including training, ergonomic changes, rest alleviation, and exercises.

Keywords Musculoskeletal disorders (MSDs) · RULA · REBA · SSIs · Ergonomics

S. G. Kolgiri (✉)

P. G. Moze College of Engineering, Pune, India

e-mail: somnathswami024@gmail.com

M. D. Jagtap

S. B. Patil College of Engineering, Indapur, India

S. L. Sathe

Vishwabharati Academy's College of Engineering, Ahmednagar, India

1 Introduction

The textile industry is important to the development of nations like India since it employs the vast majority of industrial workers. In India, the most prevalent work-related issue is musculoskeletal disorders, which affect the majority of employees. The majority of labor is still done standing up and by hand in this industries, so difficulties with job-related musculoskeletal disorders and accidents to various body parts remain a major worry [1, 2]. When work-related upper limb issues are identified, the survey method known as RULA (Rapid Upper Limb Assessment) was developed for use in ergonomics assessments of workplaces [3]. The REBA is a postural analysis tool that takes into account the potential dangers to the musculoskeletal system in a variety of occupations and evaluates the working postures present in the service sectors of the health care and other [4, 5]. Work-related musculoskeletal diseases, chronic venous insufficiency, premature delivery and spontaneous abortion, carotid atherosclerosis, and other health impacts have all been linked to prolonged standing at work. However, by using engineering and administrative controls, those injuries can be reduced [6]. It has been noted that workers in the industries where work is done lack ergonomics understanding. The presence of musculoskeletal issues in the welding process, where workers are knelt, indicates the necessity to alter body postures [7]. Although the implementation of ergonomic principles would help to improve machine efficiency and productivity, it would primarily benefit human operators by making them feel safe and comfortable [8]. Workers struggle to do the required task in challenging circumstances. Workers who operate in these demanding settings frequently develop a variety of musculoskeletal problems. These problems develop in the body of the worker as a result of repeated lifting, variable lifting heights, environmental factors, etc. [9]. The importance of ergonomics in workplace design, its influence on industrial workstation design, its interdisciplinary nature, and its implications for how industrial engineering functions [10]. The study initiate that there were a number of gaps in the tools, equipment, and work environment that had an impact on the workers' health and safety [11]. Designing methods and processes with an eye toward ergonomics can assist reduce or eliminate workplace risks while also raising productivity and quality standards for the organization [12]. Musculoskeletal disorders are caused by awkward posture, lifting, violent movement, and manual work done quickly. The main goal of the current study is to assess how people who are participating in different casting operations' work posture [13]. Although using ergonomic principles would increase machine productivity and efficiency, it would largely benefit human operators by making them feel secure and at ease. [14]. It was determined that the small-scale forging sector lacks ergonomics planning and techniques. A sizable chunk of the workforce is slouching while they work. The study suggested that there is an urgent need to implement ergonomics intervention with sufficient worker awareness [15]. According to the study's findings, an ergonomic workstation design can greatly enhance the operators' physiological performance [16]. The overall finding indicates that all body areas were less at risk of experiencing discomfort frequently and to a lesser degree. Although combining a static and

dynamic standing working system and changing your leg position when standing can help to lessen the discomfort of working while standing, not all standing operators found this to be true [17]. The objective of this work is to provide a design technique for preventive ergonomics and comfort assessments of Human-Machine-Interface (HMI) [18].

2 Methods and Material

The power-loom industry located at MIDC Solapur is the site of this research study (Maharashtra). For the study of average stature for men of 166.52 cm + 2.47 S.D., average weight of 61.9 kg + 3.01 S.D., and average stature for females of 155.45 cm + 2.42 S.D., average weight of 50.7 kg + 2.85 S.D., the 60 workers with an average age of 31.81 years + 3.83 S.D., average experience of 11.6 years + 4.2 S.D., and M/F Ratio of 9:1. The RULA and REBA procedures are used to assess how the low back, neck, shoulders, and trunk move when engaged in threading department activities. The workers' movements during work were captured on film along with their postures. After recording the video, it was cropped to get still images for the worker's posture study 60 employees were photographed while they were at work. Score sheets for RULA and REBA were filled out using the analysis of the photos (Appendix).

Figure 1 displays the chosen images of employees at the manufacturing facility engaged in their work. The collected films and observational data have undergone a thorough investigation. The ErgoMaster™ software was used to calculate the RULA and REBA scores, and the computation for posture 1 is shown here as an example. The results were also checked using the ErgoMaster™ software, whose input and output screen shots are depicted in Figs. 2 and 3, respectively. Then, using this tool to examine the results, ergonomic risk factors were discovered. Using the RULA score sheet, which breaks down the range of motion for each body site into sections, the posture of the upper limbs, primarily the arm and wrist, was evaluated. The range of motion or working posture with the fewest risk factors present receives a score of 1 in these sections. Sites of the mobility range with more extreme postures receive higher scores, representing an augmented frequency of risk issues that place load on the structures of the body part. 4 exposure classes—negligible, low, medium, and high—were created using the RULA exposure scores: 0, 1, 2, and 3. To lessen the level of exposure to risk variables, urgent attention should be given to medium and high risk acts. The REBA approach, which is also a pen-and-paper method, was utilized for those activities where the motion of the entire body and limbs needed to be evaluated. Each body part is scored in REBA according to its range of motion and is separated into portions. Body parts with more risk factors are given higher ratings, while those with fewer risk factors are given lower ratings. Five categories were used to group the REBA scores: insignificant, low, medium, high, and extremely high (0, 1, 2, 3, and 4). For levels of medium, high, and very high, quick intervention was required to prevent any musculoskeletal disorders.



Fig. 1 The positions taken while working (threading depart)



Fig. 2 How the RULA score is assigned based on the position of the body component. *Source* ErgoMasterTM software

3 Results and Discussion

The RULA worksheet assessment is included in the appendix. The various risk level groups that were discovered during posture analysis are shown in Table 1.

Figure 4 demonstrated that 41% of the workforce is at high risk and requires immediate investigation, and 46% of the workforce was found to be at medium risk and requires more investigation and change shortly. Approximately 12% of the workforce is employed by Continue to investigate. The findings of the posture analysis using RULA are shown in Table 1. These findings show that all risk level categories are present in job postures. The table indicated that 41% of the workers’ postures while engaging in the tasks are high-risk. These employees were advised to conduct additional research and make an immediate change. Additionally, the data



Fig. 3 REBA Score assignment based on body component position *Source* ErgoMasterTM software

Table 1 Classification in RULA level of thread formation tasks performed by employees in power-loom industry

RULA action level				
Body parts with more risk factors are given higher ratings, while those with fewer risk factors are given lower ratings	The span of RULA score	Description	RULA risk grade	Percentage of employee
0	1–2	The job is of almost safe	Negligible	–
1	3–4	The job is of reasonably safe	Low	12
2	5–6	The job is of risky	Medium	46
3	7	The job is of highly risky	High	41

demonstrates that no worker is at a level of negligible risk. Workers from several industry sectors who participated in the study had their actions classified into many categories. By following the same order of RULA and REBA for these exercises, the posture analysis was completed [19]. The majority of the workers were found to be working at high risk levels and in unsatisfactory postures using the REBA analysis approach.

Fig. 4 Percentage of employee in RULA Level

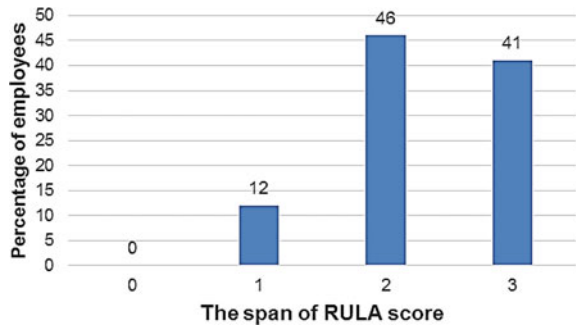


Figure 5 and Table 2 demonstrated that a little more than 52% of the employees were engaged in dangerous jobs. It was found that if the workers kept up their current posture, they would soon experience wrist, neck, and back MSDs. It was suggested that we begin the necessary remedial activity straight away. Although the majority of the female thread formation workers were found to be working in a suitable posture as compared with male workers, REBA analysis of these units showed that they could need to adjust. The necks, trunks, and wrists of almost 52% of the workers were subjected to considerable physical stress and required prompt help. Nearly 34% of the employees needed a necessary change and were at medium risk in their careers. Figure 6 and Table 3 demonstrate average RULA and REBA scores. The upper arms of many of the workers performing tread formation jobs were under extreme pressure, and some of them were bending their trunks in an inappropriate way. The operator was instructed to keep their trunks straight while working. In addition, some jobs needed more trunks bending than others, which was unsatisfactory and called for a change. The workers had good posture for the other activities, albeit they might have needed to do something [20].

Fig. 5 Percentage of employee in REBA level

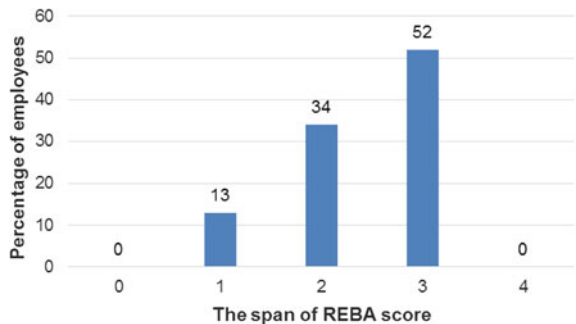


Table 2 Classification in REBA level of thread formation tasks performed by employee in power-loom industry

REBA action level				
REBA level	The span of REBA score	Description	REBA risk grade	Percentage of employee
0	1	The job is of almost safe	Negligible	–
1	2–3	The job is of reasonably safe	Low	13
2	4–7	The job is of medium safe	Medium	34
3	8–10	The job is of highly risky	High	52
4	11–15	The job is of very highly risky	Very high	–

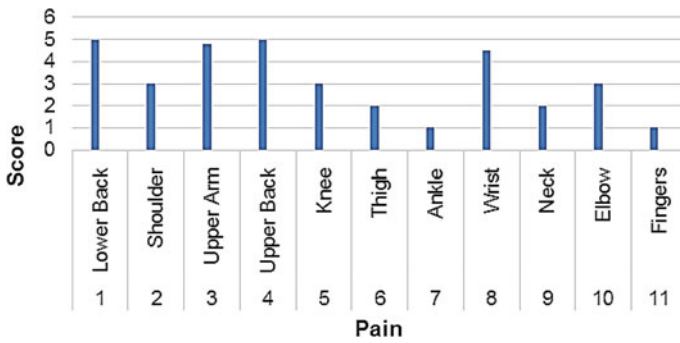


Fig. 6 Average RULA and REBA scores

Table 3 Average RULA and REBA scores of thread formation tasks performed by employee in power-loom industry

S. No.	1	2	3	4	5	6	7	8	9	10	11
Pain	Lower back	Shoulder	upper arm	Upper back	Knee	Thigh	Ankle	Wrist	Neck	Elbow	Fingers
RULA and REBA score	5	3	4.8	5	3	2	1	4.5	2	3	1

4 Conclusion

RULA and REBA tools have evaluated the body posture for this specific thread formation power loom unit. According to the studies' findings, a sizable share of the workforce is likely to be in painful and uncomfortable working positions. This is because the power-loom sector lacks understanding and awareness of ergonomics. According to the REBA and RULA risk classifications; these workers are at a moderate to high risk of musculoskeletal problems. Since there is a moderate to high risk of musculoskeletal issues among the workforce, many interventions are employed to avoid WMSDs or their symptoms, such as training, ergonomic adjustments, rest relief, and exercises. This study suggests that ergonomics treatments be implemented right away with the appropriate understanding among workers and health education on common postural changes. It is advised that legislation be implemented and enforced across industries to lower morbidity from musculoskeletal disorders.

Appendix

RULA Employee Assessment Worksheet Based on RULA, a scoring method for the identification of work-related upper limb disorders, Haslegrave & Corlett, Applied Ergonomics 1993, 24(2), 30-34

A. Arm and Wrist Analysis

Step 1: Locate Upper Arm Position: **Score:** 0-4

Step 2: Locate Lower Arm Position: **Score:** 0-4

Step 3: Adjust: **Score:** 0-4

Step 4: Wrist Flexion: **Score:** 0-4

Step 5: Ulnar/Radial Deviation: **Score:** 0-4

Step 6: Add Muscles Use Score: **Score:** 0-4

Step 7: Add Force/Load Score: **Score:** 0-4

Step 8: Final Row in Table C: **Score:** 0-4

SCORES

Table A: Upper Arm Position

Upper Arm	0	1	2	3	4
1	0	1	2	3	4
2	0	1	2	3	4
3	0	1	2	3	4
4	0	1	2	3	4
5	0	1	2	3	4
6	0	1	2	3	4

Table B: Neck, Trunk and Leg Position

Neck	0	1	2	3	4
1	0	1	2	3	4
2	0	1	2	3	4
3	0	1	2	3	4
4	0	1	2	3	4
5	0	1	2	3	4
6	0	1	2	3	4

Table C: Final Score

Neck	0	1	2	3	4
0	0	1	2	3	4
1	0	1	2	3	4
2	0	1	2	3	4
3	0	1	2	3	4
4	0	1	2	3	4
5	0	1	2	3	4
6	0	1	2	3	4

B. Neck, Trunk and Leg Analysis

Step 9: Locate Neck Position: **Score:** 0-4

Step 10: Adjust: **Score:** 0-4

Step 11: Locate Trunk Position: **Score:** 0-4

Step 12: Adjust: **Score:** 0-4

Step 13: Leg: **Score:** 0-4

Step 14: Adjust: **Score:** 0-4

Step 15: Add Muscles Use Score: **Score:** 0-4

Step 16: Add Force/Load Score: **Score:** 0-4

Step 17: Final Column in Table C: **Score:** 0-4

Scoring: Final score from Table C

0 = no discomfort
1 = acceptable posture
2 or 3 = further investigation, change may be needed
4 or 5 = further investigation, change needed
7 = investigate and implement change

Task name: _____ **Reviewer:** _____ **Date:** _____

This tool is provided without warranty. The author has provided this tool as a simple means for applying the concepts provided in RULA. © John Haslegrave, Inc. Provided by Practical Ergonomics

Source McAtamney, L. and Corlett, E.N. (1993)

REBA Employee Assessment Worksheet

Based on: Practical Ergonomics: Rapid Risk Post Assessment (1993), Revised, Hutchinson, Applied Ergonomics 24 (2000) 201-207

A. Neck, Trunk and Leg Analysis

Step 1: Locate Neck Position

Neck Score:

Step 2: Locate Trunk Position

Trunk Score:

Step 3: Legs

Leg Score:

Step 4: Look-up Posture Score in Table A

Table A:

Neck	Trunk	Legs	Score
1	1	1	1
1	1	2	2
1	1	3	3
1	2	1	2
1	2	2	3
1	2	3	4
1	3	1	3
1	3	2	4
1	3	3	5
2	1	1	2
2	1	2	3
2	1	3	4
2	2	1	3
2	2	2	4
2	2	3	5
2	3	1	4
2	3	2	5
2	3	3	6
3	1	1	3
3	1	2	4
3	1	3	5
3	2	1	4
3	2	2	5
3	2	3	6
3	3	1	5
3	3	2	6
3	3	3	7

Step 5: Add Posture + Load Score

Table B:

Score A	Score B	Score
1	1	1
1	2	2
1	3	3
2	1	2
2	2	3
2	3	4
3	1	3
3	2	4
3	3	5

Step 6: Score A, Find Row in Table C

Table C:

Score A	Score B	Score
1	1	1
1	2	2
1	3	3
2	1	2
2	2	3
2	3	4
3	1	3
3	2	4
3	3	5

B. Arm and Wrist Analysis

Step 7: Locate Upper Arm Position

Upper Arm Score:

Step 8: Locate Lower Arm Position

Lower Arm Score:

Step 9: Locate Wrist Position

Wrist Score:

Step 10: Look-up Posture Score in Table B

Table B:

Upper Arm	Lower Arm	Wrist	Score
1	1	1	1
1	1	2	2
1	1	3	3
1	2	1	2
1	2	2	3
1	2	3	4
1	3	1	3
1	3	2	4
1	3	3	5
2	1	1	2
2	1	2	3
2	1	3	4
2	2	1	3
2	2	2	4
2	2	3	5
2	3	1	4
2	3	2	5
2	3	3	6
3	1	1	3
3	1	2	4
3	1	3	5
3	2	1	4
3	2	2	5
3	2	3	6
3	3	1	5
3	3	2	6
3	3	3	7

Step 11: Add Coupling Score

Table D:

Score B	Score C	Score
1	1	1
1	2	2
1	3	3
2	1	2
2	2	3
2	3	4
3	1	3
3	2	4
3	3	5

Step 12: Score B, Find Column in Table C

Table C:

Score B	Score C	Score
1	1	1
1	2	2
1	3	3
2	1	2
2	2	3
2	3	4
3	1	3
3	2	4
3	3	5

Step 13: Activity Score

Activity Score:

Final REBA Score:

Task name: Reviewer: Date:

This tool is provided without warranty. The author has provided this tool as a simple means for applying the concepts provided in REBA. © 2000 by Practical Ergonomics. Reprinted by permission of the publisher.

Source Hignett and McAtamney, L. (2000)

References

- Metgud, D. C., Subhash Khatri, M. G., Mokashi, P. N., & Saha. (2008). An ergonomic study of women workers in a woolen textile factory for identification of health related problems. *Indian Journal of Occupational and Environmental Medicine*, 2(1), 14–19.
- Kolgiri, S., & Hiremath, R. (2019). Sustainable postural research for women workers from power-loom industry Solapur City, Maharashtra, India. *International Journal of Innovative Technology and Exploring Engineering*, 8(11s), 377–382.
- McAtamney, L., et al. (1993). RULA: A survey method for the investigation of world-related upper limb disorders. *Applied Ergonomics*.
- Hignett, S., & McAtamney, L. (2000). REBA: A survey method for the investigation of work-related upper limb disorders. *Applied Ergonomics*.
- Kolgiri, S., Hiremath, R., & Kolgiri, V. (2021). Ergonomic analysis tools for power-loom industry. In P. M. Pawar, R. Balasubramaniam, B. P. Ronge, S. B. Salunkhe, A. S. Vibhute, & B. Melinamath (Eds.), *Techno-Societal 2020* (Vol. 2, pp. 623–636). Springer.
- Halim, I., & Omar, A. R. (2011). A review on health effects associated with prolonged standing in the industrial workplaces. *International Journal of Research and Review in Applied Science*, 8(1).
- Agrawal, D. N., et al. (2011). Study and validation of body postures of workers working in small scale industry through Rula. *International Journal of Engineering Science and Technology*, 3(10).
- Maldonado-Macias, A., et al. (2008). Ergonomic evaluation of work stations related with the operation of advanced manufacturing technology equipment: Two cases of study. XV Congreso Internacional de Ergonomia SEMAC.
- Sachdeva, A., et al. (2011). Minimizing musculoskeletal disorders in lathe machine workers. *International Journal of Ergonomics*, 1(2).
- Iqbal, M., et al. (2011). Ergonomics and design. In *International Conference on Industrial Engineering and Operations Management Kuala Lumpur, Malaysia*.
- Parimalam P., et al. (2006). Ergonomic interventions to improve work environment in garment manufacturing units. *Indian Journal of Occupational and Environmental Medicine*, 10(2).

12. Javier Antonio Lom Holguín, M. C. I., et al. (2008). Ergonomics and its relationship to the design of production processes. Ponencia Conergo.
13. Singh, L. P. (2012). An investigation work posture of workers engaged in casting industry: A study in India. *Asian Journal of Managerial Science*, 1(1).
14. Zaheer, A., et al. (2012). Ergonomics: A work place reality in Pakistan. *International Posture Journal of Science & Technology*, 2(1).
15. Singh, L. P. (2010). Work posture assessment in forging industry: An exploratory study in India. *International Journal of Advanced Engineering Technology*, 1(3).
16. Halim, I., et al. (2011). Posture, muscle activity and oxygen consumption evaluations among metal stamping operators: A pilot study in Malaysian small and medium industries. *Journal - The Institution of Engineers, Malaysia*, 72(4).
17. Taha, Z., et al. (2008). Frequency and level of discomfort of male operators in standing work posture. In *The 9th Asia Pacific Industrial Engineering & Management Systems Conference*. APIEMS.
18. Naddeo, A., et al. (2010). Postural analysis in HMI design: An extension of OCRA standard to evaluate discomfort level. *Journal of Achievements in Materials and Manufacturing Engineering*, 39(1).
19. Kolgiri, S. G., et al. (2018). Work related musculoskeletal disorders among power-loom industry women workers from Solapur City, Maharashtra, India. *IJETSR* 5(3), 1002–1008.
20. Robert, N., & Richard, W. (1998). Ergonomic interventions for reducing musculoskeletal disorders: An overview, related issues and future directions, for the institute for work and health to the royal commission on worker's compensation in British Columbia.

Experimental Investigation on Injection System of Diesel Engine for Material Compatibility with Waste Cooked Oil Biodiesel



Rajesh Gurani, Malikasab Bagawan, and Prashant Tadalagi

Abstract Presently the whole globe is concerned about the effect of environmental pollution by the automobile vehicles. Biodiesel is the only alternative for diesel fuel due to its environment-friendly properties and easy availability. Biodiesel can be used directly in diesel engines without modifying the design of present engine but automotive companies are not ready to implement because of less research available about material compatibility issues of biodiesel. In this, experimental investigation is carried to study impacts of waste cooked oil biodiesel and diesel fuels on the injection system of diesel engine. This is done on fuel filter, fuel injectors, and fuel pump with both fuels i.e. diesel fuel and WCO biodiesel, engine was run for 100 h test period. Wear and pitting corrosion is observed around the needle tip after 100 h test run with diesel but not in case of waste cooked oil biodiesel and nozzle holes were affected nearly similar in both fuels.

Keywords Material compatibility · Waste cooked oil · Injection system · WCO biodiesel

1 Introduction

In this present scenario, there is a lot of development in the engine and is widely being used in every aspect of human life. But presently we are going to face many challenges also. In this fast-growing world, every country requires a lot of energy for development works and also for making human's life easier and more comfortable. So world needs the energy and then for this energy the whole world is depending

R. Gurani (✉) · P. Tadalagi
Department of Mechanical Engineering, KSGB'S Bharat Ratna Indira Gandhi College of Engineering, Kegaon, Solapur, Maharashtra, India
e-mail: rajeshgurani91@gmail.com

M. Bagawan
Department of Automobile Engineering, Matushri Venkata Subba Rao (M.V.S.R) Engineering College, Hyderabad, India

on petroleum products like coal, petrol, diesel, and petroleum gases. But wide usage of these sources, they are becoming obsolete in upcoming days. So we are in the situation that we should think about the alternative energy sources.

1.1 Biodiesel

Biodiesel is a combined product of long-chain monoalkyl esters of fatty acids derived feedstocks like plant seeds or animal fats. This produced by the transesterification process [1]. There are plenty of resources available for biodiesel production. The most common feedstock for biodiesel productions are rapeseed, canola, palm, soybean, coconut, peanut, rapeseed, linseed, safflower, jatropha seed, pongamia seed and animal fats.

1.2 Waste Cooked Oil Biodiesel

The waste cooked oil methyl ester is called as waste cooked oil biodiesel. This is a suitable source for the production of biodiesel because of a million tonnes of used/cooked oil is available worldwide a day. Reusing of this used oil causes many health hazards and disposal of it, is also challenging task because it pollutes soil and water.

Because once the cooking oil is heated, it undergoes thermal degradation leading to the formation of free radicals which cause oxidative stress that in turns cause destruction at the cellular and molecular levels in the body that increases the risk of colon cancer and colitis [2, 3]. When this oil introduced to the soil its cause clayey soil compaction because of its toxic contaminates, it's also pollutes the water [4]. This low cost, highly available waste can be converting as a wealth by producing a biodiesel. This also helps the world to go green and save human health from this waste.

1.3 Problem Facing by Automobile Sector While Using Biodiesel

Biodiesel is having many similarities with regular diesel fuel but it is eco-friendly with low pollutant emission compared to diesel. But presently the automobile sector is not fully accepting biodiesel as a complete fuel for the vehicle. Many vehicle manufacturers say that biodiesel is highly viscous and having low calorific value, but many researchers proved that the viscosity may be reduced in the production process.

In spite of lesser calorific value of biodiesel compared to diesel, many researchers show the way of using biodiesel as a blend with regular fuel. Plenty of work has been done on studying the performance and emission characteristic of blends from 5 to 90% blend combination. Results shows that up to 20% blend are showing better performance and emission characteristics [5–7]. But still, the automobile industry is not ready to accept it. Some European manufacturer's tried a lot on to implementing the biodiesel as a fuel for their vehicles. They allow them to run on higher biodiesel blends but later they stopped allowing usage of biodiesel for their vehicles and suggested that there is a need to be work more on it for modification in engine design then only they will allow biodiesel for their vehicles [8].

2 Literature Review

It is important to know how biodiesel affects the fuel flow system during engine run. On this, some researchers worked on material compatibility [9, 10]. Peterson et al. Conducted a static engine test for a thousand hours. They used engine manufacture association recommended engine for testing and used soy biodiesel. Run engine according to engine manufacture association recommended cycles. Observed smother engine run and lighter wear. Agarwal et al. conducted a static engine test for a longer time period to known engine tolerance. They used engine manufacture association recommended direct injection diesel engine for testing and used twenty percentage linseed biodiesel blends. They observed low carbon deposits and slight wear in parts.

Up to here we just observed positive results with biodiesel in engine test and field run test. But below some researchers shows negative side of it. How biodiesel has impact on engine parts by causing wear and corrosion. Similarly, NBB has concluded that in a thousand hour's test on the motor with twenty percent soybean biodiesel mixed fuel caused genuine specialized issues like problems in engine pump, degrades elastomers, sludge on engine parts.

3 Methodology

3.1 *Static Engine Test*

In this experiment, an investigation is done on the impacts of both pure biodiesel and commercial diesel fuel on the fuel flow system of IC engine parts like a fuel filter (top and bottom sealing, sealing ring), fuel injectors (Nozzle, needle, nozzle house, washer, plunger, spring, return fuel line), fuel pump (element, spring, washer, shims, push road, housing). For all these parts, the fuel flow system is studied for material compatibility and feasibility.

3.2 Engine Test Procedure for Conducting the Experiments

A single-cylinder Kirloskar diesel engine was used as the test engine (Fig. 1).

Before any startup, the fuel pump was calibrated and injectors tested for any leakage and also for chatter. The engine was fitted with a new set of gaskets, fuel pipes, fuel filters, fuel injectors, fuel pump and reassembled the engine properly for diesel and biodiesel tests. Engine was run for 100 h test period for both commercial diesel fuel and 100% WCO biodiesel separately. This 100 h. engine test is followed the engine running at various load conditions.

According to the engine manufacturers association, recommendation cycles are like (1) Half an hour at low idle condition (2) 1 h at rated power condition (3) 1 h at peak torque (4) half an hour at 80% speed and 25% load. The engine was run repeatedly based on these cycles with different time period like early morning, afternoon, evening, and night. Engine was run in maximum power in initial, middle & end of each 100 h cycles.

In order to understand the impacts of diesel fuel and biodiesel fuel on the injectors after running 100 h were analyzed by using a compound microscope. Many photos of the injector's parts like injector nozzle body, nozzle tip, needle, washer, plunger, spring and all three holes of nozzles with hole areas were studied. Then the surface of every part of each injector carefully observed for any surface damage or wear from compound microscopic images are compared with that of before run data. Wear in the parts are recorded by wearied surface area through EMZ -13TR trinocular compound microscope.

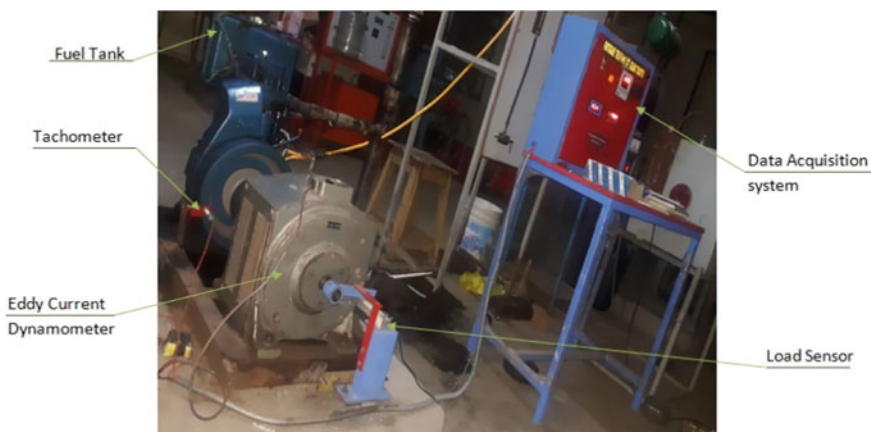


Fig. 1 Engine setup

4 Results and Discussion

4.1 Injector Wear

The fuel flow system plays an important role in the performance of an engine. According to many researchers, after using biodiesel (because of its properties and contaminations), most affecting part in the engine is the fuel injector. Hence, the automotive manufacturing companies are more bothered about how to alter fuel injectors, fuel pumps and more durable fuel filters are to be tested with biodiesel because these are very expensive parts and their damage also affects the cost of maintenance.

In Fig. 2 it is observed that the injector body, nozzle body and nozzle holes were not much covered with slurry but nozzle body covered with carbon deposits. Similarly, it is observed in the Fig. 2 that the injector body, nozzle body and nozzle holes were covered with slurry.

Similarly, it is observed in the Fig. 5 that, the injector nozzle is covered with slurry. Biodiesel contains unsaturated fats and has altogether different physical characteristics contrasted with oil diesel fuel. Waste cooked oil biodiesel has higher surface tension, higher thickness, lubricity and lower volatility properties. This low volatile biodiesel requires longer vaporizing after post-injection in the ignition process. This leads to deposition on injectors and cylinder walls during the fuel combustion (Figs. 3 and 4).

In order to estimate the impacts of diesel and biodiesel fuel on the injectors after running for 100 h, the samples were analyzed by the compound microscope. The optical surface photos of the injector's parts like injector nozzle body, nozzle tip, needle, washer, plunger, spring and all three holes of nozzles with hole areas were taken. Wear and pitting corrosion is observed around the needle tip after 100 h test run with diesel but not observed after similar kind of wear and pitting corrosion at the needle tip surrounding after 100 h test with waste cooked oil biodiesel. With the help of a compound microscope, the perimeter of the wear area of the needle is calculated. Figure 5 shows that wear area is on the tip of 100 h test run with diesel



Fig. 2 Injectors condition after 100 h. test run with diesel fuel and with WCO biodiesel

Fig. 3 New injector nozzle



Fig. 4 Injector nozzle after 100 h test run with diesel



fuel needle one side its perimeter is $2147.11 \mu\text{m}$ and on the other side is perimeter $4155.12 \mu\text{m}$. But no wear is observed on the needle tip after 100 h.

The presence of abrasive particles and reaction by corrosive acids during the fuel combustion process are the main reasons for wear. The lubricant transports protective chemicals to the sites where they are needed and transports waste products away from those sites. Many works reported that soot is the main reason for engine wear as it interacts with oil additives and reduces the effectiveness of anti-wear additives. Deposit formation relates to the formation of total insoluble. However, 100% waste cooked oil biodiesel does not produce significant insoluble (Fig. 6).

Fig. 5 Injector nozzle after 100 h test run with WCO biodiesel



4.2 Fuel Filter Clogging

In the fuel flow system fuel filter is the first part that is going to be affected by the fuel quality. In case of biodiesel, many researchers clearly mentioned similar things that biodiesel clogs the fuel filter and reduce the life of the filter. So after 100 h test run with both diesel fuel and waste cooked oil biodiesel fuel filter is disassembled and observed.

Elastomers were used in these fuel filters for sealing purposes. Fig. 7 shows the filter sealing ring after 100 h. Run with diesel and WCO biodiesel. The hardness of each sealing rubber of fuel filter (top seal, bottom seal and seal ring) was checked before and after the test. The very less change in hardness is exhibited for Biodiesel than diesel. These sealing rubbers are compatible with biodiesel.

4.3 The Major Findings of the Engine Test

1. During 100 h test run waste cooked oil biodiesel runs engine more smoothly than diesel fuel because biodiesel is having good lubricant properties than petroleum diesel.
2. Waste cooked oil biodiesel has higher surface tension, higher viscosity, lubricity and lower volatility properties. This low volatile biodiesel requires longer vaporizing after post-injection in the combustion process. This leads to deposition on injectors and cylinder walls during the fuel combustion.
3. The most important component of the injector is a nozzle and especially nozzle holes. These holes' size and shape are playing an important role in the combustion



Fig. 6 Nozzle holes radius like top hole, side hole 1, side hole 2 of new injector, 100 h run with diesel and 100 hr run with biodiesel

process. That can also affect the engine performance and emissions stability over the engine life time durability of the injectors. If any changes in hole size and shape directly affect engine performance. So in the results it is observed that injector nozzle holes size and shape with the help of a compound microscope and nozzle holes were affected nearly similar in both fuels.



Fig. 7 Condition of fuel filter bottom cup after 100 h test run with **a** diesel fuel and **b** WCO biodiesel fuel

References

1. Knothe, G., & Razon, L. F. (2017). Biodiesel fuels. *Progress in Energy and Combustion Science*, 58, 36–59.
2. Gurani, R., & Kurbet, S. N. (2021). A detailed experimental investigation on IC engine using alternate fuels for material compatibility of piping and fitting system. *Advanced Aspects of Engineering Research*, 5(2021), 111–117.
3. Venkata, R. P., & Subramanyam, R. (2016). Evaluation of the deleterious health effects of consumption of repeatedly heated vegetable oil. *Toxicology Reports*, 3, 636–643.
4. Gurani, R., & Kurbet, S. N. (2019). *CO emissions for CIDI engine using blends of combinations of biodiesel with diesel fuel* (pp. 8602–8607)
5. Tadalagi, P. B., Gurani, R., & Bagawan, M. (2018). Smoke emission levels for CI DI engine using blends of combinations of biodiesel and diesel fuel. *IOP Conference Series: Materials Science and Engineering*, 376(1).
6. Gurani, R., Tadalagi, P. B., & Bagawan, M. (2017). Emission characteristics of CI DI engine using blends of biodiesel (waste cooking oil) and diesel fuel. *IJERT*, 6(8).
7. Shafer, A. (1994). Biodiesel research Mercedes Benz-engine warranty policy. *Commerce Biodiesel Establishing Engine Warranties, University Idaho National Center Advantage Transplantation Technology*, 1994, 125–141.
8. Gurani, R., & Kurbet, S. N. (2018). Experimental investigation on IC engine using alternate fuels for material compatibility of piping and fitting system. *IOP Conference Series: Materials Science and Engineering*, 376(1).
9. Gurani, R. (2018). *Experimental investigation on compatibility of elastomeric materials with biodiesel % change in volume for % change in weight* (Vol. 6, no. 16, pp. 1–4).
10. Peterson, A., Lee, P.-I., Lai, M.-C., Wu, M.-C., & DiMaggio, C. (2009). *Impact of biodiesel emission products from a multi-cylinder direct injection diesel engine on particulate filter performance*.

Traffic Sign Recognition System Using YOLO: Societal System for Safe Driving



Kuldeep Vayadande, Rohit Patil, Ayush Patni, Pavankumar Bhadane, Siddhant Pawar, Rahul Ponnuru, and Varad Ingale

Abstract One of the primary criteria for autonomous cars and most advanced driving assistance systems is the capacity to perceive and interpret all static and dynamic objects around the vehicle under diverse driving and climatic circumstances (ADAS). Convolutional neural networks have the potential to give safe ADAS in current vehicles (CNN). In this research, we describe a YOLO based traffic sign identification system that has been enhanced using a CNN. As real-time detection is necessary for safe driving, the YOLO network utilized in this study was pre-trained to identify and classify just five items, which are divided into categories such as automobiles, trucks, people, traffic signs, and traffic lights.

Keywords Machine learning · Traffic sign · YoloV4 · Safe driving

1 Introduction

Traffic sign recognition has a lot of promise in intelligent autonomous vehicles and driver assistance systems, and traffic quality and safety can't be improved without properly applying and maintaining road traffic signs, signals, and road markings. Because of the benefits, such a system may give traffic sign detection and recognition has become more important with developments in image processing. The benefits that such a system might give have also risen as a result of recent breakthroughs and interest in self-driving automobiles. The interest in self-driving automobiles has grown as a result of recent breakthroughs and interest.

K. Vayadande · R. Patil · A. Patni · P. Bhadane · S. Pawar (✉) · R. Ponnuru · V. Ingale
Vishwakarma Institute of Technology, Pune, Maharashtra, India
e-mail: siddhant.pawar20@vit.edu

2 Problem Statement

The following objectives are expected.

- To implement a method to extract the image frames from the video segment.
- To implement an algorithm to identify the regions of interest.
- To implement a method to extract the symbol of the traffic warning sign.
- To implement a method to identify the symbol of the traffic warning sign.

3 Literature Review

This study provided ten additions to the current state-of-the-art methodologies in the Traffic Sign Detection and Recognition system. The investigations were carried out based on color behavior in response to changes in lighting and other environmental circumstances. It also compared the color properties of a source picture and a candidate image using a color matching model. This model is inaccurate [1].

The detecting module, comprises color and form analysis. SVM classifier and edge detection are included in the classification module, which improves results. It is vital to use the best procedures in order to achieve the greatest results, which will increase driving safety and comfort greatly. It worked with the German Dataset rather than a bespoke dataset [2].

In the training and testing dataset, over 2728 sign samples were collected for 24 different traffic signs. The dataset was pre-processed before being put into the network. It was broken down into three sections: training, testing, and validation. The final Deep CNN architecture presented in this study consists of two convolutional layers, two max pooling layers, one dropout layer, and three thick layers. For epoch 150, 100% accuracy was attained for all batch sizes [3].

The objectives of this research is to find and categorize indications initially. The localization U-Net is identified using CNN with the encoder-decoder architecture. To eliminate salt and pepper noise from the image, we may use image pre-processing techniques like the median filter, followed by contrast normalization across all channels. Although SqueezeNet may be used for classification, the HOG classifier can enhance accuracy [4].

4 Methodology

In this project, YOLO is used which is a CNN based network to detect objects. It performs real-time object detection. YOLO doesn't consider detection as several classification problems but it considers detection as a regression problem. It is a single-stage detection network that takes input as image pixels and predicts bounding box coordinates with class probabilities. With YOLO, the entire object identification



Fig. 1 Traffic symbols

procedure is completed in a single image assessment. YOLO splits the input picture into grids and predicts bounding boxes, box confidence, and class probability all at the same time.

4.1 Data Collection

All the images used for this project are collected randomly from different sites of the dataset like Kaggle, machine learning repositories, etc. While collecting this dataset care has been taken about the inclusion of almost all types of traffic signs from different locations get into the dataset. As of now for the demonstration and testing purposes, we have used 5 classes for the recognition.

Following are some of the images from the dataset (Fig. 1).

4.2 Data Preprocessing

To prepare the dataset, we need to create annotations for the corresponding image of the traffic sign. We have created a text file with the same name for each image file in the same directory Each text document contains the explanations for the comparing picture record, that is object class, object directions, level and width.

The model of the YOLOv4 consists of Bounding Box Pre-Processor. In this extraction and preparation of the detected traffic sign image takes place for classification. The regressed bounding box's center is then established. The box is then enlarged by 25% to correct for any regression errors and to guarantee that the traffic sign is completely included in the zone. After being cropped and resized to 48*48 size, the expanded boxes are handed up to the classifier system for detection of the traffic sign class.

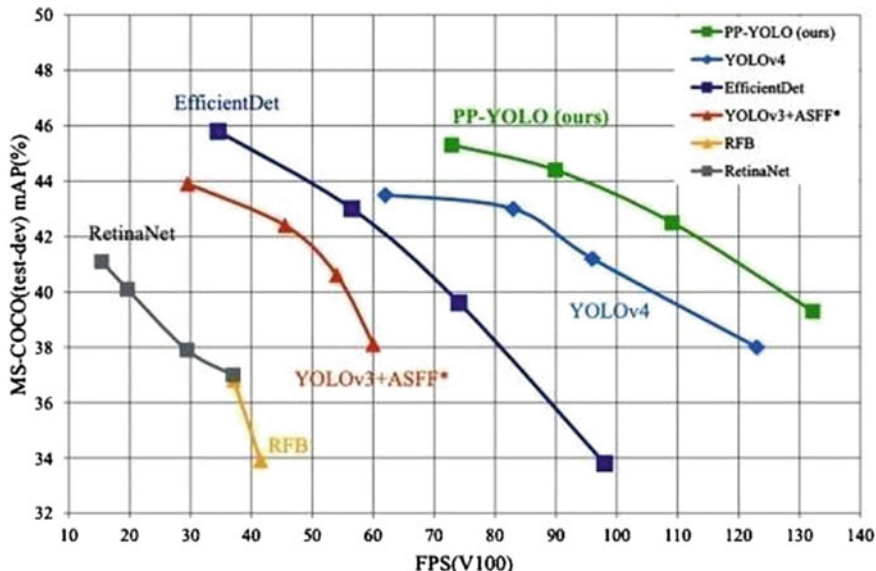


Fig. 2 Comparisons of accuracies

5 Overview of the Proposed Model

5.1 YOLOv4 for Traffic Sign Recognition

For our Traffic Sign Recognition System, we employed the YOLOv4 model. YOLOv4 is an object detection model that works in real time. It’s an updated version of the YOLOv3 model that includes several additional tricks and modules. The traffic sign recognition system has a YOLOv4 detector trained to recognize potential traffic signs, a boundary box Pre-Processor that expands the detected boundary box, trims and resizes the candidate traffic sign box, and candidate traffic which consists of a CNN-based classifier that classifies. A sign that belongs to one of five classes. These are for demonstration purposes and can be expanded in the future as needed.

Below is Fig. 2 which represents the comparison of accuracies obtained by respective models on MS-COCO Dataset.

5.2 Activity Recognition Phase

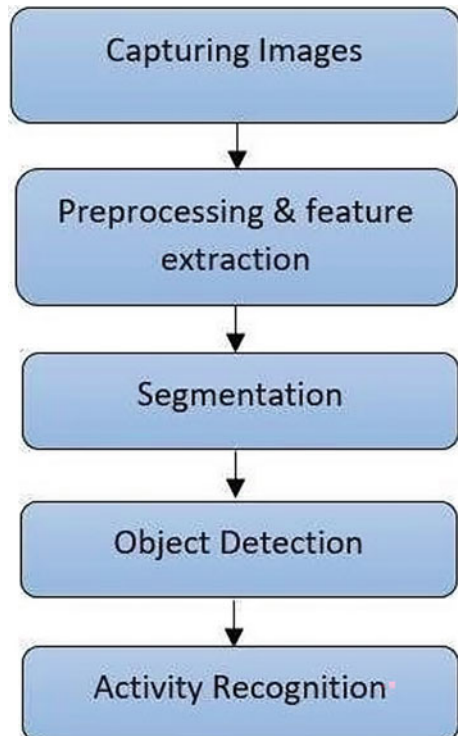
As shown in Fig. 2., In the first step, the image is captured by the model. Then the captured image is pre-processed by the Bounding Box Pre-Processor where the image is enlarged, cropped and resized to be fitted into the region. To make the image analysis easier, segmentation is done by the model itself after that object is detected.

After the detection of a traffic sign, the model throws the output of the recognized Traffic signs with its class.

6 YOLOV4 Architecture

YOLOv4 is a design based on CSPDarknet53 which is considered as a most important factor, Path Aggregation Network and the Spatial pyramid pooling which are mainly referred as a Neck and for the Head YoloV3. CSPNet is an optimization strategy that envisions segmenting the base layer feature map into two sections and shuffling them in order between stages, as shown in Fig. 3. The Spatial Pyramid Pooling is a method which is mainly used for acquiring both coarse data and the fine data by the pooling with different sizes of Kernel at the same time. PAN (Path Aggregation Network) is a method of using the data of the layer near the post by passing various backbone level elements to the detector (Fig. 4).

Fig. 3 Activity recognition phase



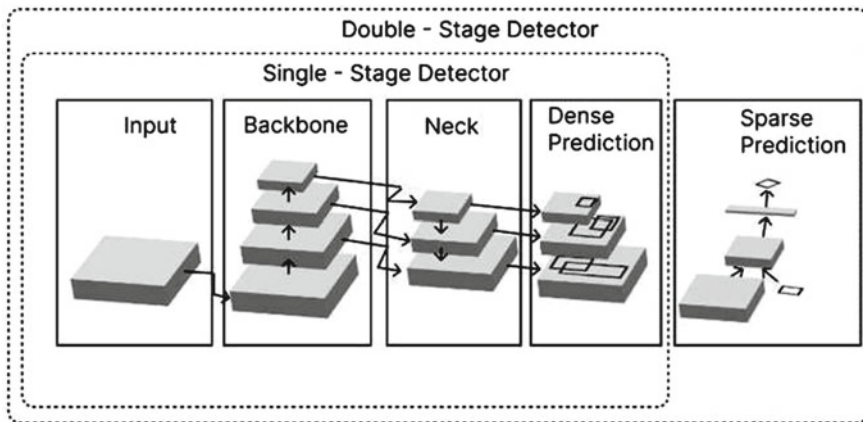


Fig. 4 YOLOv4 architecture [6]

7 Data Analysis

Data would be collected from various sources like Kaggle and would be working on a variety of images, by customizing the dataset for better accuracy. Firstly, we would acquire a video through a particular medium source and extract the images from a video segment would perform a few image filtration processes eventually by detecting the traffic symbol. As soon as the symbol is extracted it would perform computation to get the appropriate result for the extracted image and return the result (Figs. 5 and 6).

8 Results

The existing systems have very less accuracy whereas we have worked on enhancing the accuracy of our system. We have worked on the YOLO algorithm which is latest than the other algorithms that exist and are used for traffic sign recognition. To achieve better accuracy, we have used customized dataset (Figs. 7, 8 and 9).

9 Scope of Research

The YOLO algorithm helps to classify the classes at real time as well as with better accuracy. The particular research would elaborate the better use of convolutional neural network thus providing better results as well as learning techniques.

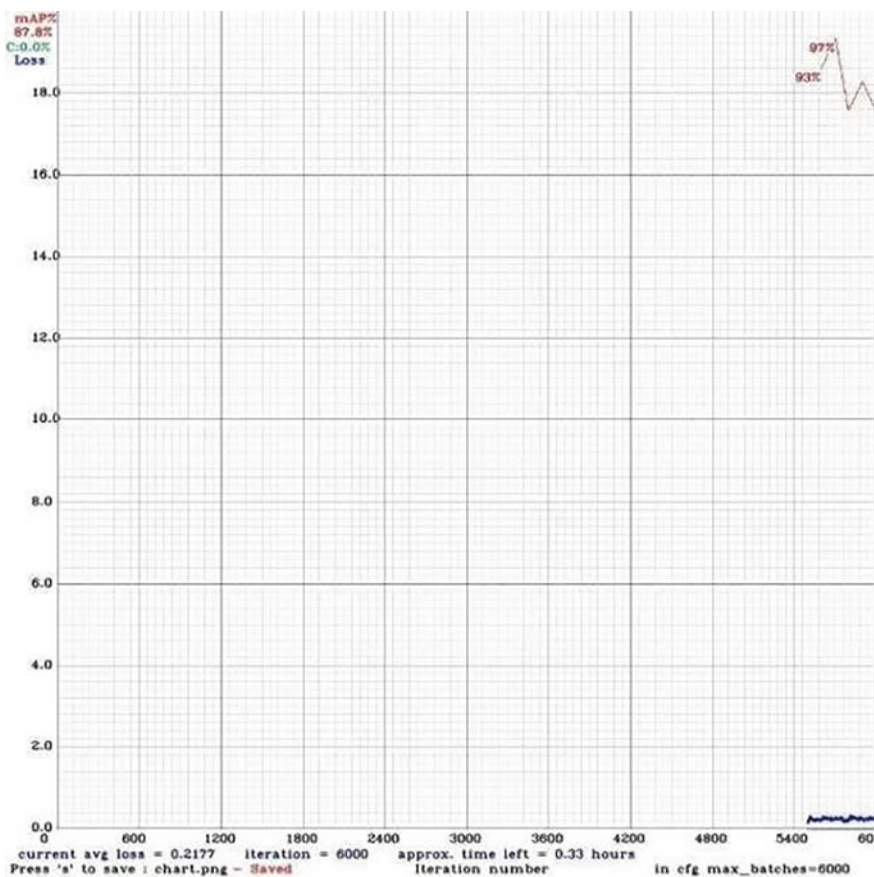


Fig. 5 mAP graph

10 Limitations

- (1) Data is directly proportional to the accuracy. Hence more data is expected.
- (2) Data needs to be annotated before training.
- (3) Model training requires a GPU.
- (4) Takes lots of time to train models.

Fig. 6 Zoomed image



Fig. 7 Results



11 Future Scope

The particular project could be integrated with the application to detect at real time with better accuracy for the road signs also further voice assistant could be the especially abled persons using special hardware. The application further could be used for driver less vehicles in upcoming days.

Fig. 8 Accuracy of the model

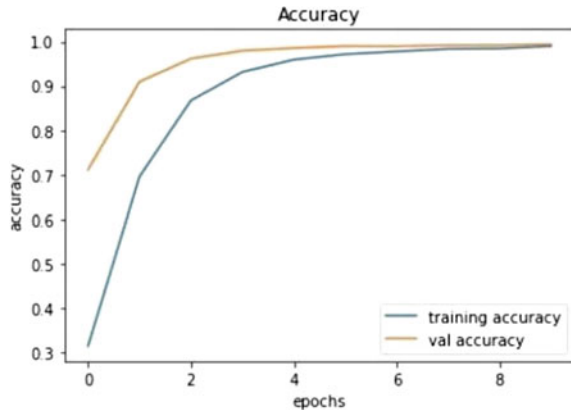
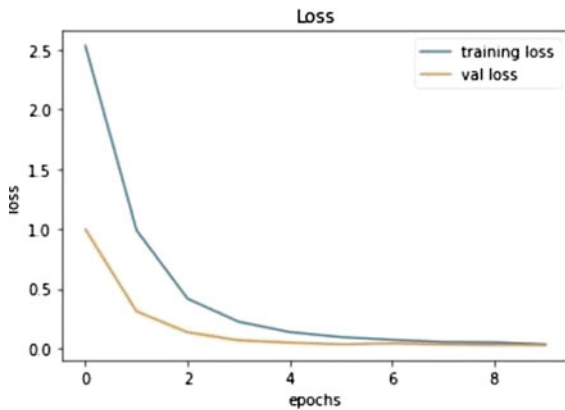


Fig. 9 Training loss in the model



12 Conclusion

The traffic sign recognition system using you only look once (YOLO) comes up with better results at real time, the better version of the convolutional neural network has made things easier in terms of accuracy. The model would be beneficial in upcoming days as the expected technology would be YOLO thus aiming to have better results rather than the other models. The model would easily recognize traffic signs out from the input videos, images and provide the most accurate result.

References

1. Dandil, E., Selvi, A. O., Çevik, K. K., Yildirim, M. S., & Süleyman, U. Z. U. N. (2021). A hybrid method based on feature fusion for breast cancer classification using histopathological images. *Avrupa Bilim ve Teknoloji Dergisi*, 29, 129–137.

2. Fu, M. Y., & Huang, Y. S. (2010). A survey of traffic sign recognition. In *2010 International Conference on Wavelet Analysis and Pattern Recognition* (pp. 119–124). IEEE.
3. Liang, Z., Shao, J., Zhang, D., & Gao, L. (2020). Traffic sign detection and recognition based on pyramidal convolutional networks. *Neural Computing and Applications*, *32*(11), 6533–6543.
4. De la Escalera, A., Armingol, J. M., & Mata, M. (2003). Traffic sign recognition and analysis for intelligent vehicles. *Image and Vision computing*, *21*(3), 247–258.
5. Hoferlin, B., & Zimmermann, K. (2009). Towards reliable traffic sign recognition. In *2009 IEEE Intelligent Vehicles Symposium* (pp. 324–329). IEEE.
6. Stallkamp, J., Schlipsing, M., Salmen, J., & Igel, C. (2011). The German traffic sign recognition benchmark: A multi-class classification competition. In *The 2011 International Joint Conference on Neural Networks* (pp. 1453–1460). IEEE.
7. Garcia-Garrido, M. A., Sotelo, M. A., & Martin-Gorostiza, E. (2006). Fast traffic sign detection and recognition under changing lighting conditions. In *2006 IEEE Intelligent Transportation Systems Conference* (pp. 811–816). IEEE.

A Review on Performance of Annular Raft Foundation



Ajay Pratap Singh Rathor and Jitendra Kumar Sharma

Abstract This study dedicates a literature review on the performance of annular raft foundations which depend on various parameters such as type of loading and soil, size of footing, bearing capacity factors. Annular raft foundation is used in structures such as silos, water tanks, chimneys, etc. which are often axisymmetric structures. A number of researchers studied the bearing capacity and settlement of annular raft. Both parameters significantly affect the stability and design of the annular raft foundation. It is found that the ratio of the radius of the annular raft is a key factor which governs the design criteria of annular raft.

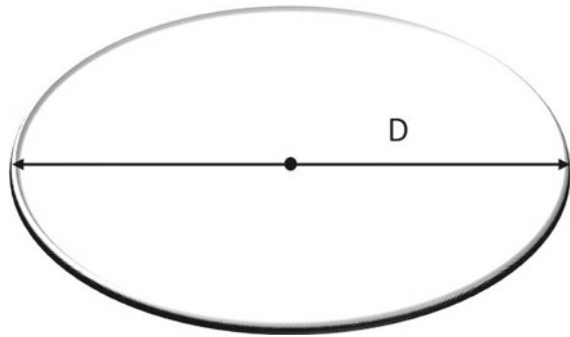
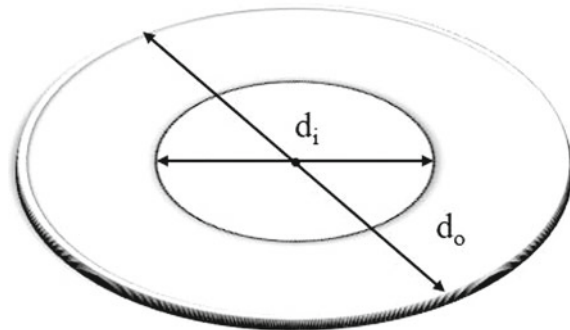
Keywords Annular raft · Ring footing · Annular ratio · Radius ratio · Settlement of ring footing · Settlement influence factor

1 Introduction

Structures like water towers, chimneys, TV towers, silos, etc. typically built on annular footings. Typically, such structures transfer the load using columns, and through the shells of different shapes such as cylindrical or cone. Due to its affordability and suitability for particular types of structures, this sort of foundation is becoming more and more popular. When the two requirements of complete utilization of bearing capacity of soil and no strain beneath foundation are to be achieved, circular footing is frequently the sole option in addition to being cost-effective. The most recent information on the subject is critically examined in the paragraphs that follow. The following paragraphs provide a critical analysis of the most recent information on the topic. Some researchers investigated the settlement and bearing strength of unreinforced soil and reinforced soil and compared the results.

The stress analysis in the annular raft is also done in various studies and it is found that the stresses in annular raft depend upon the size of the raft and the inner and outer diameter of the annular raft. The stress variation can be studied from various

A. P. S. Rathor (✉) · J. K. Sharma
Rajasthan Technical University, Kota, Rajasthan 324010, India
e-mail: apsrathor.phd19@rtu.ac.in

Fig. 1 Solid raft**Fig. 2** Representative diagram of annular raft

studies with radius ratio of annular raft. Most of the researchers adopted the FEM to analyze load settlement response of the annular raft. A few studies are performed to assess settlement and bearing capacity of annular raft numerically or experimentally (Figs. 1 and 2).

Fischer [1] investigated the annular raft and suggested a process to determine settlement of annular raft on elastic semi-infinite medium. Egorov [2] proposed an equation for the evaluation of the settlement of the annular raft. The results are compared of solid raft and annular raft foundation and several relationships are developed to find out the bearing strength of annular raft and settlement of the annular raft.

2 Annular Raft Foundation Over Unreinforced Soil

The soil which is in its natural condition is called unreinforced soil. If the natural unreinforced soil has adequate geotechnical properties, then it can be used for the structure without providing reinforcement. Number of researchers performed the analysis on annular raft on unreinforced soil.

Nasari et al. [3] investigated the settlement of annular raft lying over an elastic half space by performing computations by adopting finite difference approach. The settlement of annular raft is computed in the form of settlement influence factor (SIF). The study’s influencing variables were the shape of ring, embedment, stiffness of footing, and soil non-homogeneity parameters. It is assumed that the elastic modulus of soil increase linearly with depth.

Ismael [4] examined the behaviour of annular raft experimentally on very dense cemented sands. The load settlement response (LSR) for annular plates and solid plates were obtained, within the range of elastic settlement and ultimate bearing strength. The results show that there is less settlement in flexible ring plate in comparison to rigid plate. Figure 3 illustrates the annular ratio and the settlement influence factor variation. The outcomes were verified by Fischer’s outcomes (1957).

Al-sanad et al. [5] performed plate load test on the sand that was very dense in nature. A ring plate having outside and inside diameter of 1.28 and 0.68 m, as well as circular solid plates of diameter 0.3, 0.61, and 1.28 m, were used. A number of factors affecting settlement of foundation such as dry wet condition, load cycling, and loaded area size were examined. The LSR of the solid plate and ring plates was compared. The measured settlement was below the predictions and the measured value of settlement was in good agreement with empirical method based on standard penetration test.

Jadhav et al. [6] estimated the settlement of rigid ring footing on two layered soils. Computations have been carried out with PLAXIS 2D. Settlement influence factor is calculated and presented in the form of graphs for circular solid plate and ring plate. The study reveals that SIF decreases with increasing the width of top layer and the settlement increases as the annular ratio increases.

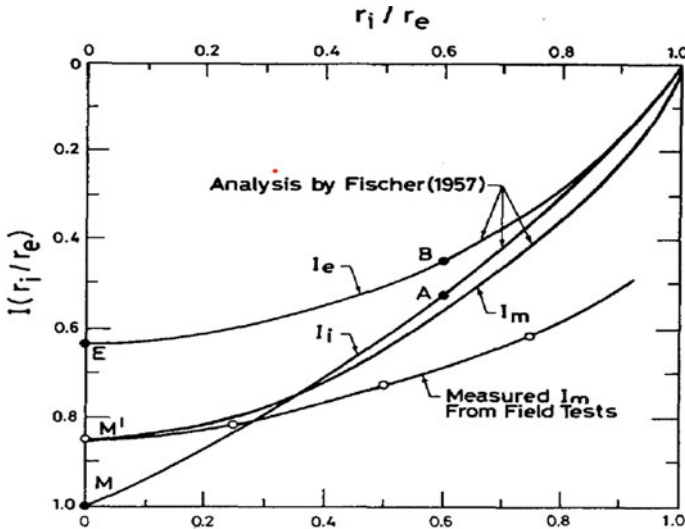


Fig. 3 Settlement influence factor variation with annular ratio. Source Nabil Ismael

3 Annular Raft Foundation Over Reinforced Soil

The loose soil has poor geotechnical properties and cannot be used for construction purpose. Hence in order to make the soil suitable for construction purpose the soil is reinforced and treated with various methods to improve the strength characteristics of the soil.

There are various approaches to reinforce the weak soil but use of geosynthetic material becomes an effective method now a day. Numerous researches performed to determine the efficiency of various geosynthetic materials in order to provide the weak soil the most strength possible. The numbers of geosynthetic layers and embedment depth as well as the use of geosynthetics all have an impact on the settlement and bearing strength of the annular raft foundation [7–10]. It is found in the studies that the bearing strength of the soil increased as the no. of geosynthetic layers increased [11] till the radius ratio 0.4, after the radius ratio 0.4 the bearing strength decreases. The studies show that the use of geosynthetic layers within soil provides significant increment in the capacity of the soil. It can be concluded from the above studies that the optimum results are obtained for 3 no. of geosynthetic layers. By increasing the no. of geosynthetic layers more than 3, there are no significant changes in the bearing strength and it remains approximately steady. If the eccentric loading is applied on the annular raft footing lie on compacted sand bed, the results show that the maximum capacity is obtained for 3 no. of geosynthetic layers and the results represents good agreement with the previous study conducted by Dhattrak [11].

Some scientists investigated the impact of footing reinforcement and embedment on the soil's ability to support load. Lavasan and Shana [12] discovered that one and two layers of geogrid at depths of 0.32 and 0.3 Do, respectively, obtained the best results for bearing capacity and settlement. The key values of a geogrid layer's diameter are found to be around 4 Do, and for sand reinforced with two layers of geogrid, the critical value of vertical spacing is roughly equivalent to 0.32 Do. However, Abbas and Al-Dorry [8] investigated that the ideal depth ratio was 0.5–0.53 Do for a top layer geogrid, and Laman and Yildiz [13] found the ideal size was about 3D. The variation in the optimum results is due to the different geogrid material and soil properties and loading conditions over annular raft.

4 Radii Ratio of Annular Raft

Radii ratio of annular raft is defined as the ratio of inner and outer diameter of the annular raft. The annular ratio of the annular raft is the key factor which affects the capacity and settlement of the annular raft foundation. Various studies were performed to find out the optimum radius or annular ratio for the maximum strength and the minimum settlement of the annular raft. The no. of studies found that the optimum value of bearing strength of annular raft foundation is obtained at the

annular ratio (radius ratio) 0.4 and for the values greater than 0.4, the bearing capacity decreases. Some researchers evaluated the effect of radius ratio numerically and experimentally on the dense sand and found that the optimum bearing strength of annular raft is recorded at annular ratio 0.35, and for the greater values of annular ratio, the bearing strength of annular raft foundation decreases linearly.

Ahmad et al. presented a study to evaluate the settlement and bearing strength of the solid raft and annular raft resting over the anisotropic soil and evaluated the significant value of annular ratio i.e., 0.6 that shows the good agreement with the previously performed studies such as Ohri et al. [14], Boushehrian and Hataf [10].

It is found from the previously performed studies that as the annular ratio (radius ratio) is kept less than 0.4, the surface area of the annular raft become more which leads the raft to carry more load because the contact area of the annular raft with soil is more for smaller annular ratio. If the annular ratio is kept more than 0.4, the area of annular raft decreases and the bearing strength of the foundation decreases. However, the optimum value of annular ratio is given different by many researchers but generally it is considered 0.4 or in the range of 0.4–0.6.

5 Bearing Capacity Factors of the Soil N_c , N_q , and N_γ

There is very less studies available comparatively on the bearing strength factors and their effects on the capacity of the foundation [15–24]. The bearing strength factors N_c , N_q , and N_γ depends upon the dilatancy angle of the soil beneath the foundation Chavda and Dodagoudar [25]. Various researchers evaluated the bearing strength factors numerically and observed that the value of bearing strength factors is different for various annular ratio. The bearing capacity factors depend upon the annular ratio and for higher value of annular ratio the bearing capacity factors are less [26–31].

Hosseininia [30] found that amongst all the bearing capacity factors, the N_γ factor mostly depends upon the annular ratio. As the annular ratio changes there is significant change recorded in the value of the factor N_γ . Chavda and Dodagoudar [25] examined that the bearing strength factors N_c , N_q , and N_γ depends upon the angle of internal friction of the soil beneath the foundation. It can be concluded from the above studies that the bearing strength factors increases as the value of annular ratio decreases for the annular raft having the base both rough and smooth. It is also found from the above studies that the value of N_γ remains less while the annular ratio is in the range of 0–0.9 and for the annular ratio 1, the value of N_γ attains the same value as the strip footing. Zhao and Wang [32] evaluated the value of N_γ using FLAC and the findings were similar with previous studies.

All the above studies state that bearing strength factors N_c , N_q , and N_γ remain more for the smaller annular ratio. Basically, the smaller annular ratio provides more surface area hence the value of these factors obtained more for the smaller annular ratio and specially the N_γ factor depends upon the value of friction between raft and soil, hence the value of N_γ is recorded more for smaller annular ratio as the area

increases for smaller annular ratio. If the base of the raft foundation is rough than N_γ obtained is even more.

Above studies conclude that the maximum values of bearing strength factors are recorded for annular ratio 0.25. Keshavarz and Kumar [33] evaluated the bearing strength of annular raft foundation with the help of stress characteristic method (SCM) and evaluated the value of bearing strength factors is maximum for the rough raft in comparison to smooth surface raft having the convincing annular ratio usually ranges between 0.1–0.5. The value of N_c , and N_q decreases for the smooth surface raft when the annular ratio increases. In case of smooth surface raft, the value of N_γ slightly changes with change in annular ratio because this factor depends upon the friction between surface of the annular raft and the soil.

6 Conclusions

The following conclusive statements can be made based on the above review of literature. The bearing strength and settlement of the annular raft severely depends upon the annular ratio. Annular ratio governs the major criteria of the design of the annular raft foundation. The Bearing strength factors depend upon the annular ratio and the surface of the footing whether it is smooth surfaced or rough surfaced. It can be concluded that the bearing strength of the foundation increases if the soil beneath the raft is reinforced. The reinforcement of soil can be done by using various geosynthetic materials and improve the load bearing strength and reduces the settlement of the annular raft significantly. It can also be concluded that the value of bearing strength factor is less for higher annular ratio as the surface area of the annular raft becomes less. The reinforcement of the soil using 3 geosynthetic layer is beneficial in order to provide strength to the foundation and minimize the settlement of the foundation. The suitable range of annular ratio is 0.4–0.6 for which the minimum settlement can be achieved.

References

1. Fisher, K. (1957). Zur Berechnung der setzung Von Fundamenten in der form einer Kreisformigen Ringflache. *Der Bauingenieur*, 32(5), 172–174.
2. Egorov, K. E. (1965). Calculation of bed for foundation with ring footing. In *Proceeding 6th International Conference of Soil Mechanics and Foundation Engineering* (Vol. 2, pp. 41–45).
3. Naseri, M., & Hosseininia, E. S. (2015). Elastic settlement of ring foundations. *Soils and Foundations*, 55(2), 284–295.
4. Ismael, N. F. (1996). Loading tests on circular and ring plates in very dense cemented sands. *Journal of Geotechnical Engineering*, 122(4), 281–287.
5. Al-Sanad, H. A., Ismael, N. F., & Brenner, R. P. (1993). Settlement of circular and ring plates in very dense calcareous sands. *Journal of geotechnical engineering*, 119(4), 622–638.
6. Jadhav, A. K., Madhav, M. R., & Padmavathi, V. (2019). Settlements of rigid ring-footings on two-layered soil. In *Conference on Geotechnical Applications Geoapps*.

7. Naderi, E., & Hataf, N. (2014). Model testing and numerical investigation of interference effect of closely spaced ring and circular footings on reinforced sand. *Geotextiles and Geomembranes*, 42(3), 191–200.
8. Abbas, J. K., & Al-Dorry, M. K. (2013). Bearing capacity of ring footing on geogrid reinforced sand. *IRECE Journal*, 4, 240–246.
9. El Sawwaf, M., & Nazir, A. (2012). Behavior of eccentrically loaded small-scale ring footings resting on reinforced layered soil. *Journal of Geotechnical and Geoenvironmental Engineering*, 138(2), 376–384.
10. Boushehrian, J. H., & Hataf, N. (2003). Experimental and numerical investigation of the bearing capacity of model circular and ring footings on reinforced sand. *Geotextiles and Geomembranes*, 21(4), 241–256.
11. Dhattrak, A. I., & Mishra, P. C. (2016). Performance of ring footing resting on reinforced multi-layered soil using plaxis 2d. *International Journal of Research in Engineering and Technology*, 7(4), 103–114.
12. Lavasan A., & Schanz, T. (2013). Bearing capacity and settlement of an isolated ringfooting on sand reinforced with geogrid. In *International symposium on Design and Practice of Geosynthetic-Reinforced Soils Structures, Bologna, Italy*.
13. Laman, M., & Yildiz, A. (2007). Numerical studies of ring foundations on geogrid-reinforced sand. *Geosynthetics International*, 14(2), 52–64.
14. Ohri, M. L., Purhit, D. G. M., & Dubey, M. L. (1997). Behavior of ring footings on dune sand overlaying dense sand. In *Proceedings of International Conference of Civil Engineers, Tehran, Iran*.
15. Israa, H. G. R. A. S., & Al-Tikrity, S. H. (2013). Experimental investigation of the bearing pressure for circular and ring footings on sand. *Tikrit Journal of Engineering Sciences*, 20(3), 64–74.
16. Hataf, N., & Fatolahzadeh, A. (2019). An experimental and numerical study on the bearing capacity of circular and ring footings on rehabilitated sand slopes with geogrid. *Journal of Rehabilitation in Civil Engineering*, 7(1), 174–185.
17. Sudhakar, A. R., & Sandeep, M. N. (2019). Static and incremental cyclic loading of ring and circular footings on coir geocell-reinforced sand. In *Geotechnical Applications* (pp. 69–77). Springer, Singapore.
18. Sharma, V., & Kumar, A. (2017). Strength and bearing capacity of ring footings resting on fibre-reinforced sand. *International Journal of Geosynthetics and Ground Engineering*, 3, 1–17.
19. Thomas, L. M., & Philip, J. G. (2017). Experimental and numerical analysis of load carrying capacity of ring footing on sand reinforced with geonet. *International Journal of Engineering and Management Research (IJEMR)*, 7(2), 345–350.
20. Shankar, D., & Kumar, V. (2018). A comparative study on experimental and theoretical bearing capacity of ring footings. *i-Manager's Journal on Structural Engineering*, 7(2), 63.
21. Mehrjardi, G. T. (2008). Bearing capacity and settlement of ring footings. In *The 14th World Conference on Earthquake Engineering* (pp. 12–17).
22. Rupani, H., & Bhoi, M., Experimental study of load settlement behaviour of ring footings for different internal diameter keeping the contact surface area same.
23. Zhu, F. (1998). *Centrifuge modelling and numerical analysis of bearing capacity of ring foundations on sand* (Doctoral dissertation, Memorial University of Newfoundland).
24. Tang, C., & Phoon, K. K. (2018). Prediction of bearing capacity of ring foundation on dense sand with regard to stress level effect. *International Journal of Geomechanics*, 18(11), 04018154.
25. Chavda, J. T., & Dodagoudar, G. R. (2019). Finite element evaluation of vertical bearing capacity factors N_c , N_q and N_y for ring footings. *Geotechnical and Geological Engineering*, 37(2), 741–754.
26. Choobbasti, A. J., et al. (2010). Numerical evaluation of bearing capacity and settlement of ring footing; case study of Kazeroon cooling towers. *International Journal of Research and Reviews in Applied Sciences*, 4(2).
27. Lee, J. K., Jeong, S., & Shang, J. Q. (2016). Undrained bearing capacity of ring foundations on two-layered clays. *Ocean Engineering*, 119, 47–57.

28. Lee, J. K., & Jeong, S. (2018). Immediate settlement of ring footings resting on inhomogeneous finite stratum. *Applied Sciences*, 8(2), 255.
29. Kumar, J., & Chakraborty, M. (2015). Bearing capacity factors for ring foundations. *Journal of Geotechnical and Geoenvironmental Engineering*, 141(10), 06015007.
30. Hosseininia, S. E. (2016). Bearing capacity factors of ring footings. *Iran Journal of Science Technology Transaction on Civil Engineering*, 40, 121–132.
31. Benmebarek, S., Remanda, M., Benmebarak, N., & Belounar, L. (2012). Numerical evaluation of the bearing capacity factor $N\gamma'$ of ring footings. *Computers and Geotechnics*, 44, 132–138.
32. Zhao, L., & Wang, J. H. (2008). Vertical bearing capacity for ring footings. *Computers and Geotechnics*, 35(2), 292–304.
33. Keshavarz, A., & Kumar, J. (2017). Bearing capacity computation for a ring foundation using the stress characteristics method. *Computers and Geotechnics*, 89, 33–42.

A Novel Intelligence System for Accident Prevention, Detection, and Reporting System for Smart City



Poornima Mallur, Shree Umarani, Shree Umarani, and Salma S. Shahapur

Abstract In this Project Accident Prevention, detection and reporting system is designed and implemented. The concept of our project is to help people in emergency time by giving instructions to us and third person before the occurrence of an accident due to Alcohol consumption (Drink and Drive) and Drowsiness. To implement this project, we have used sensors which detect Alcoholic consumption, Sleepiness. We are adding sensors such as flame sensor, Alcohol detecting sensor, panic button, tilt sensor for the safety of the people inside the car. We have used an MQ-3 sensor which detects alcohol presence in the surrounding, if the driver has consumed alcohol, the alcohol sensor fixed in the system detects the alcohol and then it sends a warning message through GSM, Driver drowsiness detection to prevent accidents from happening because of Driver fatigue and sleepiness. Dashing sensor is used to detect whenever a vehicle is being stroked by another vehicle or any object. If something crashes or strikes the car hard enough then through the dashing sensor we get a message via GSM, flame sensor is used in the system to detect flame or smoke coming out of the engine due to overheating or whenever a car catches fire in an accident. Tilt sensor is used detect the position of the driver while driving, if driver is falling asleep, he/she tends to face downwards or upwards, if the position of driver changes from the range of standard position, then relay installed in system gets triggered and the buzzer gets turned on and it makes sound in order to wake or alert the driver. To overcome the accidents due to the above causes we are creating a project to make lives aware and secure.

Keywords Accident prevention · Detection system · Reporting system

P. Mallur · S. Umarani · S. Umarani · S. S. Shahapur (✉)
Jain College of Engineering, Belagavi, India
e-mail: salma.jce@gmail.com

1 Introduction

Being reliant on others to take him to a local hospital, the victim. The majority of the time, it takes hours after an accident for someone to arrive and assist the injured party. All of these factors contribute to the high death rate of accident victims. Due to the increased risk of the accident victim dying due to the ambulance's delayed arrival at the hospital and accident site [1]. In the context of our project, we have used more sensors, electronic modules, and microcontroller units that help us in providing prevention from accidents, detects the accident if it occurs even after the preventive measures, and reports the accident to the ambulance services and third party. People travel frequently, reckless driving can cause accidents. The usage of autos has increased in the modern generation. Traffic has grown due to heavy automotive use, which has led to an increase in traffic accidents. Due to a lack of timely preventative and safety facilities, this damages the property and results in human life loss. Even while we cannot completely prevent accidents, we can at least adopt mitigation measures. The accident that will happen can be avoided with our built-in embedded system if the appropriate precautions are taken. The ambulance service and police station can identify the place quickly thanks to the position and a link to a Google map that will be sent to their mobile devices. Since the position and a link to a Google map will be given to their mobile devices, the ambulance service and police station can quickly locate the area. Our system includes a buzzer, LED, flame sensor, tilt sensor, alcohol sensor, GPS module, GSM module, and other components. And the core microcontroller unit connects all of these devices (Adriano Uno) [2]. By establishing a certain angle on the tilt sensor, we will be able to identify slumber and alert the driver if necessary. With the use of a flame sensor, we can measure engine heat and alert the driver if the engine is running hotter than usual. Alcohol sensors assist us in determining whether or not a motorist is intoxicated. The car offers protection if the driver is too intoxicated [3].

2 Literature Survey

The System is not reliable when it comes to more than one parameter. The major disadvantage of the products available in the market is that they are designed for specific one main purpose like accident, detection and reporting systems. Although the system has its own advantages as the devices lack in performing multitasking. This device, sensors increase the functionality by adding features to it and thus increases the system redundancy. In order to overcome these disadvantages we are building a system such that it increases both functionality and reliability such that it is able to prevent accident occurrence and detect the accident and also reports about it to third person or ambulance [4]. Accidents are detected by the dashing sensor, which then alerts the microcontroller to continue working. The GPS module gives us real-time access to the location, speed, time, and date of the specific spot

where the car is. In the event of an accident, the GPS position is sent to the police, emergency service, and other parties with the use of a GSM module [5–8]. After a minor collision, everything can be fine, in which case the driver can update the ambulance service, police station, and, in this instance, family members. Territorial areas. First generation (1G) analogue cellular network was replaced by the second generation (2G) network [9]. The third generation (3G) UMTS standard, the fourth generation (4G) LTE Advanced standard, and the fifth generation (5G) standards—all independent of the ETSI GSM standard—were later created by the 3GPP [10].

3 Block Diagram of Proposed Model

Because of the high usage of vehicles there is a high possibility of occurrence of accidents, in order to prevent and reduce accidents due to alcoholism and drowsiness, engine heating, we have developed a system which alerts us. Upon detecting a vehicle accident, the third person or ambulance or any contact programmed in the system gets a message through the GSM module so that time and life will be saved. We can install the system in the vehicles, as a preventive, detecting and reporting system for vehicle safety. In this system (Fig. 1) we have used MQ-3 alcohol sensor, Flame sensor, Tilt sensor, dashing sensor and panic button. GPS and GSM modules are used for detection of location and for alert messages. Dashing sensors are used for detection of vehicle accidents. Here we will be using a central microcontroller (Arduino Uno) unit. All the devices are interfaced to Arduino Uno, which has the capacity to control all the sensors. Our system detects the alcohol concentration around it, so if a driver has consumed alcohol, it detects and alerts him and sends a message through GSM. Tilt sensor is used to detect the position of the driver while driving, if driver is falling asleep, he/she tends to face downwards or upwards, if the position of driver changes from the range of standard position, then relay installed in system gets triggered and the buzzer gets turned on and it makes sound in order to wake or alert the driver. Flame sensor is used to detect when a car catches fire or there is any occurrence of detection of fire. Flame sensor senses the fire and sends a message through GSM. When an accident occurs, the Dashing sensor delivers a signal to the microcontroller. Panic button, whenever a driver is under some health issues or getting panic attacks or under some situations where he/she is not able to use his/her mobile he/she can press the panic button and call for help. The real-time position, velocity, period, and duration of a specific spot where the car is located are all provided by the GPS module. If an accident happens, the dashing notices it, uses GPS to determine its position, and then uses a GSM module to communicate the information to the police and medical service. The message received on a mobile device includes the position of the accident site link in the form of a google map, which will assist emergency services including ambulance services, police stations and family members in quickly reaching the casualty and saving lives.

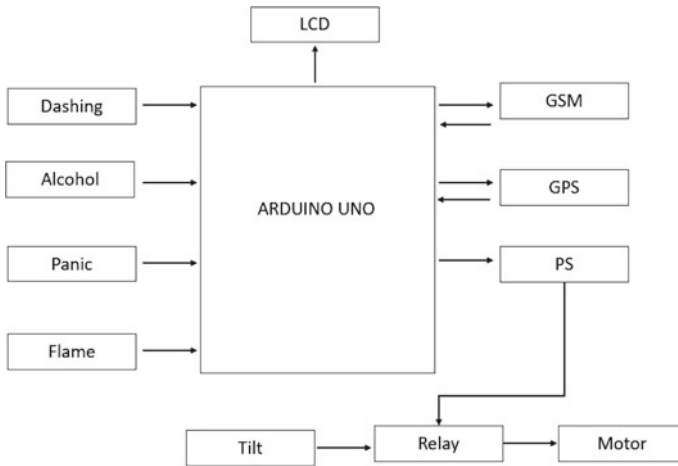


Fig. 1 Block diagram of proposed model

4 Results and Discussion

In Fig. 2 Panic button, whenever a driver is under some health issues or getting panic attacks or under some situations where he/she is not able to use his/her mobile he/she can press the panic button and call for help.

In Fig. 3 Dashing sensor senses the accident which has occurred and then sends a message to the third person (Fig. 4).

In Fig. 5 By testing all our components and performing the procedure we were able to get the outcomes of the project which we have done on “Accident Prevention Detection and Reporting system” and the final output of our project is shown above. In this generation due to increasing the usage of vehicles, accident rate increased by Drunk drivers, drowsiness and overheating of engines causing fire. It’s our duty to prevent, detect and report the system. This system is fast, low cost and easy to use, power efficient, which makes the person install this system in an easy manner. In this project the GPS exact location is reported to emergency units like family, friends and hospitals using the GSM module. It serves to save many survivors by reporting



Fig. 2 Result of panic button



Fig. 3 Result of dashing sensor



Fig. 4 Result of flame sensor

and extricating the person in time. Overall, this system is economic, which can be implemented in all vehicles.

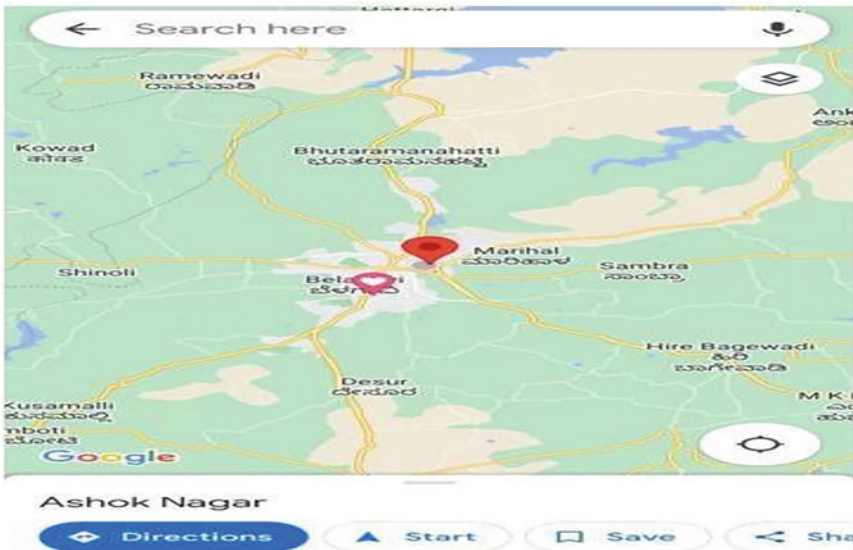


Fig. 5 Output in the form of map

5 Conclusion

In the twenty-first century science and technology has developed a lot in various fields such as automation. In this era vehicle usage has increased a lot, because of high usage of vehicles there is a high possibility of occurrence of accidents, in order to prevent and reduce accidents due to alcoholism and drowsiness, engine heating; we have developed a system which alerts us. Our system detects the alcohol concentration around it, so if a driver has consumed alcohol it detects and alerts him and sends a message through GSM. We have used a dashing sensor in our system which activates when someone/something strikes our vehicle hard enough and it even sends a message with location. Our system has a panic button, whenever a driver is under some health issues or getting panic attacks or under some situations where he/she is not able to use his/her mobile he/she can press the panic button and call for help. Our system even includes a Flame sensor; it gets activated whenever it senses fire. For drowsiness we have used a Tilt sensor in our system, which detects whenever the driver falls asleep. Our system works automatically and it is easy to use and low cost, safe to install in vehicles. By using GPS and GSM, the module system detects the location of the accident spot and sends a message for help.

References

1. Raosaheb Patil, V., & Suresh Pardeshi, S. (2022). Mechanism for accident detection, prevention and reporting system. *Materials Today: Proceedings*. <https://doi.org/10.1016/j.matpr.2022.11.215>
2. Accident Prevention, Detection and Reporting for Two Wheeler Safety System. (2020). *Regular Issue*, 9(5), 230–234. <https://doi.org/10.35940/10.35940/ijeat.d8369.069520>
3. Rathor, S., Dubey, P., & Samadhiya, S. (2022). Smart Automatic Accident Detection & Information System. In *2022 International Conference on Computational Intelligence and Sustainable Engineering Solutions (CISES)*. <https://doi.org/10.1109/cises54857.2022.9844371>
4. Lakshmi Devi, R., Saravanan, G., Sangeetha, K., Pavithra, S., & Thiyagarajan, S. (2021). Smart train accident detection and prevention system using IoT technology. In *2021 International Conference on System, Computation, Automation and Networking (ICSCAN)*. <https://doi.org/10.1109/icscan53069.2021.9526413>
5. Mehta, G., Mishra, Y., Ashraf, U., Dubey, S., Singh, M., & Khanam, R. (2021). Accident prevention using an auto braking system and accident detection using internet of things. *Smart Computing*, 142–148. <https://doi.org/10.1201/9781003167488-19>
6. Nanda, S., Joshi, H., & Khairnar, S. (2018). An IOT based smart system for accident prevention and detection. In *2018 Fourth International Conference on Computing Communication Control and Automation (ICCUBEA)*. <https://doi.org/10.1109/iccubea.2018.8697663>
7. Kulkarni, K. S., Shettar, C., Chowdhary, A., Kulkarni, N., & Doddamani, P. K. (2021). Vehicle accident detection, life-saving and smart reporting system. In *2021 6th International Conference on Communication and Electronics Systems (ICCES)*. <https://doi.org/10.1109/icc51350.2021.9488970>
8. Vidya, M. J., Veena Divya, K., & Rajasree, P. M. (2020). An IOT-based accident detection and rescue system – a prototype. *Augmented Intelligence Toward Smart Vehicular Applications*, 161–174. <https://doi.org/10.1201/9781003006817-12>

9. Jot based live streaming of vehicle, position accident prevention and detection system. (2017). *International Journal of Recent Trends in Engineering and Research*, 3(3), 52–55. <https://doi.org/10.23883/ijrter.conf.20170331.011.frelj>
10. Bhatti, F., Shah, M. A., Maple, C., & Islam, S. U. (2019). A novel internet of things-enabled accident detection and reporting system for smart city environments. *Sensors*, 19(9), 2071. <https://doi.org/10.3390/s19092071>

Waste Water Treatment by Using Constructed Wetlands



Anil Shirgire, Hemchandra Pawar, Satyawan Jagdale, and Ravikant Sathe

Abstract Constructed wetlands are wastewater treatment systems consisted of one or more treatment cells in a building designed and constructed to provide wastewater treatment. Constructed wetlands are classified into two types: free water surface (FWS) wetlands (also known as surface flow wetlands) closely resemble natural wetlands in appearance because they contain aquatic plants that are rooted in a soil layer on the bottom of the wetland and water flows through the leaves and stems of plants. Subsurface flow wetlands (SSF) or known as a vegetated submerged bed (VSB) systems do not resemble natural wetlands because they have no standing water. They contain a bed of media (such as crushed rock, small stones, gravel, sand, or soil) that has been planted with aquatic plants. When properly designed and operated, wastewater stays beneath the surface of the media, flows in contact with the roots and rhizomes of the plants, and is not visible or available to wildlife. Constructed wetlands are an appropriate technology for areas where inexpensive land is generally available and skilled labor is less available. In this paper, a study was done on covered types, characteristics, design variation and considerations, limitations, and the advantages and disadvantages of constructed wetlands.

Keywords Wastewater treatment · Constructed wetlands · Ecology · Environmental protection

1 Introduction

Water quality deterioration created pressure on decision-makers to adopt stringent regulations to find new means of cost-efficient water treatment methods in order to create healthy ecological conditions. Constructed wetlands being in use since

A. Shirgire (✉)
Dr D Y Patil Institute of Technology, Pimpri, Pune, India
e-mail: anil.shirgire@gmail.com

H. Pawar · S. Jagdale · R. Sathe
SVRI'S College of Engineering, Pandharpur, India

the '50s and provide better treatment for different kinds of wastewater such as (urban runoff, municipal wastewater, industrial wastewater, agricultural waste, and acid mine drainage by mimic biological, physical, and chemical processes that happen in natural wetland systems. The use of constructed wetlands for wastewater treatment has drastically increased over the last 40 years. Constructed wetlands are considered as an "eco-friendly" system to replace conventional secondary and tertiary municipal and industrial wastewater treatment processes. Constructed wetlands are fast gaining ground and became practical water resource management strategy in many developing countries. The flow in constructed wetlands is controlled and the water spreads consistently among the wetland plants. Constructed wetlands mimic the optimal treatment conditions which could be found in natural wetlands, with supreme flexibility of being constructible at almost any location and different conditions. Constructed wetlands with developing macrophytes are well known used to treat municipal wastewater, representing a tertiary treatment stage.

2 Constructed Wetlands Characteristics

2.1 Substrates

Wetland substrates physically are the support the wetland vegetation, which offer sites where biochemical and chemical transformations processes occur, and provide sites for storage of removed pollutants and waste. Usually, substrates include soil type, sand, gravel, and organic materials. Most soils are suitable for constructed wetlands. But for design considerations, different soil properties should be considered in selecting soils to comprise cation exchange capacity (CEC), soil pH, electrical conductivity (EC), soil texture, and soil organic matter. It is recommended to have a constructed substrate of sand or gravel when the receiving domestic and agricultural wastewaters are highly loaded with nutrients, such as can be built with. It was reported that soils that contain more than 15% clay are generally suitable for constructed wetland substrate.

2.2 Hydrologic Characteristics

Periods of inundation and saturation created in the wetlands are due to the hydrologic regime of the wetlands. Hydrologic conditions affect the soils and nutrients conditions and characteristics, which in turn influence the status of the biota. The flow and storage volume determine the length of time that water spends in the wetland and, thus, the opportunity for interactions between waterborne substances and the wetland ecosystem. Hydrological characteristics of wetlands include retention time,

water depth, flow velocity through the wetland, and the number of days per year in which the wetland is inundated is among the most important aspects of the wetlands.

3 Constructed Wetlands Types

Constructed wetlands are classified into various parameters. The most significant parameters are a water flow regime (surface and sub-surface) and the type of macrophytic growth (as emergent, submerged, free-floating, and floating-leaved plants). The quality of the final effluent from the systems improves with the complexity and the improvement of the system.

3.1 Free Water Surface Flow Wetlands

A free water surface (FWS) wetland is designed to comprise a shallow basin, soil, or another medium to support the roots of vegetation, and a water control structure that maintains a shallow depth of water (Fig. 1).

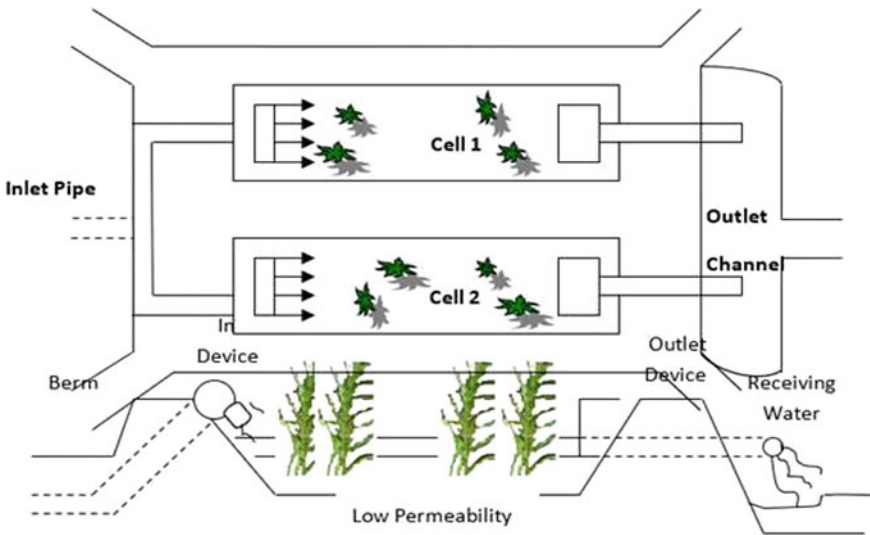


Fig. 1 Plan and profile of a typical free water surface wetland

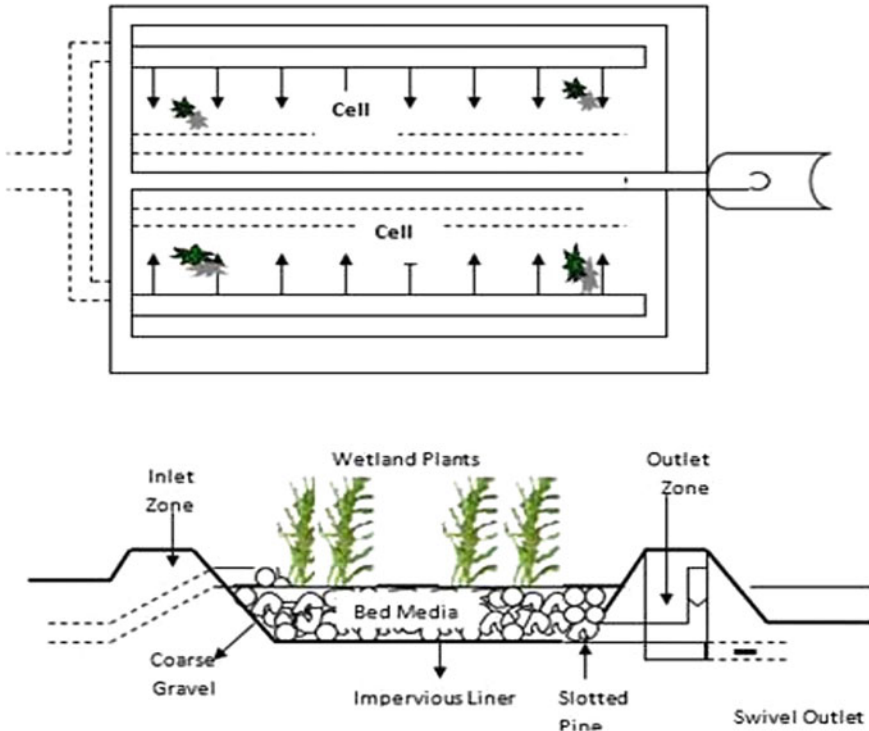


Fig. 2 Plan and cross-sectional view of a subsurface flow wetland

3.2 Subsurface Flow Wetlands

The first subsurface flow pilot-scale wetland was designed in the 50's 1950s in Germany. Constructed wetlands with the sub-surface flow may be classified according to the direction of the water flow either horizontal HF or vertical flow VF.

SSF constructed wetlands are best suited to treat wastewaters with relatively low solids concentrations and under relatively uniform flow conditions. Because of the hydraulic constraints imposed by the substrate (Fig. 2).

4 Design Variations

Design variations of constructed wetland affect shapes and sizes to fit match the site characteristics and optimize construction, operation, and enhance performance. Constructed wetlands typically are fitted with liners to prevent infiltration, which depends on local soil conditions and regulatory requirements [3]. A large number of

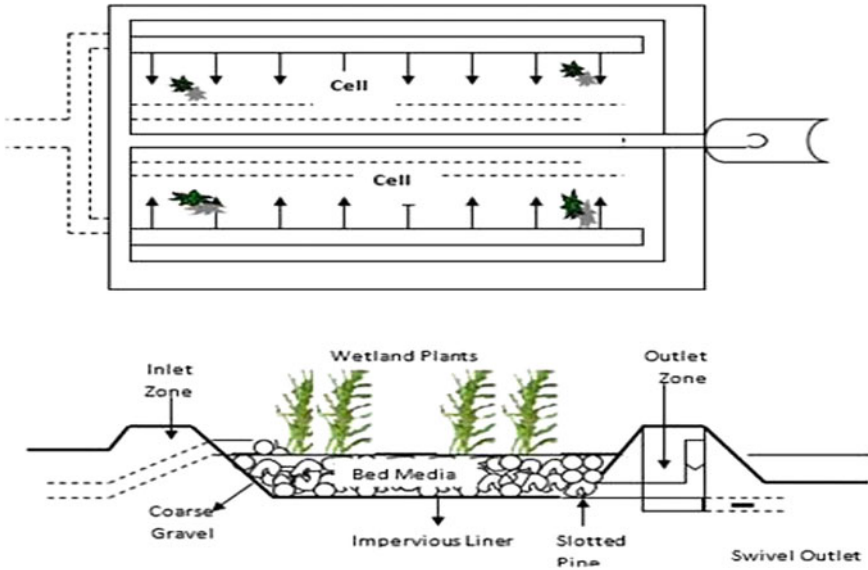


Fig. 3 A sectional view of wetland controls and Liner

researches and studies have been published about constructed wetlands, nevertheless; the optimal design of constructed wetlands is still undetermined due to the absence of adequate monitoring systems and inadequate operating time to provide appropriate data for analysis.

Constructed wetlands require four components: liner, distribution media (substrate), vegetation, an under-drain system. The liner prevents water leakage and keeps the wastewater away from reaching the surrounding environment and groundwater. Generally, the liner is manufactured from a number of materials, and among the most common and reliable materials are polyvinyl chloride (PVC) (Fig. 3).

The inlet consists of a distribution medium which is usually coarse rock that is 2 to 5 cm in diameter. The first section of the distribution system spreads the wastewater influent across the width and the cross-section of the wetland. The filter contains a pea gravel media which is 1–2 cm in diameter. The pea gravel depth varies and it is usually in the range of 45–60 cm. The under-drain system at the outlet of the wetland is a slotted 10 cm pipe covered with rock. The under-drain transfers the treated effluent out of the wetland and maintains the effluent level below the gravel surface to avoid direct contact with people and prevent mosquitoes from breeding in the wetland. Moreover, the water level stays high enough in order to sustain plant growth. Figures 4 and 5 depict the most common constructed wetland system design types.

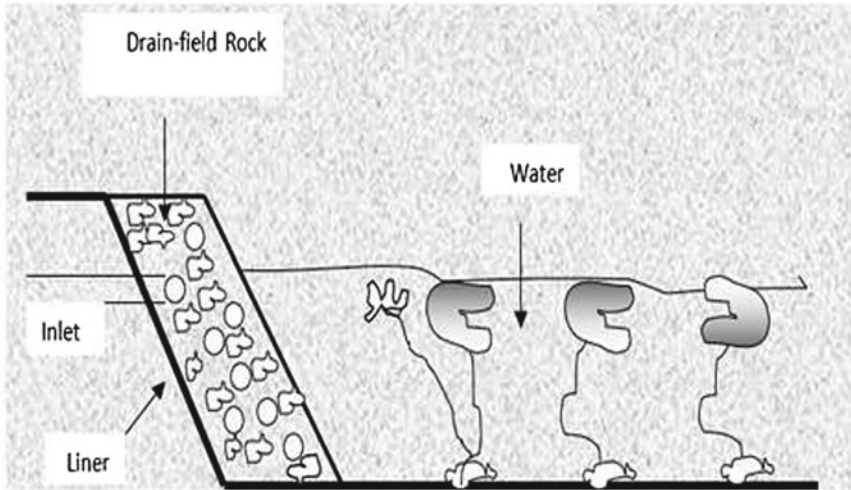


Fig. 4 A free water surface flow wetland Sketch

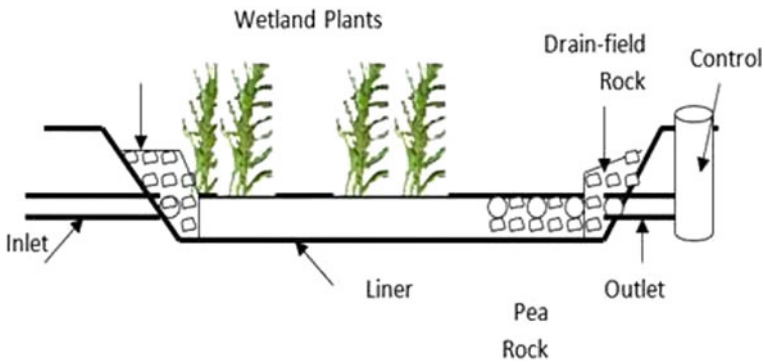


Fig. 5 A subsurface flow constructed wetland Sketch Vymazal (2001)

The designing criteria for both systems are different as can be shown in (Table 1).

Table 1 Design criteria for constructed wetlands

Design parameter	Unit	Surface wetland	Subsurface wetland
Retention time	d	5–14	2–7
Water depth/media depth	M	0.1–0.8	0.3–0.6
Hydraulic loading rate	mm d-1	15–65	80–300
Volume flow rate	m3 d-1	200–75,000	5–13,000

1. Surface area: (10–20) m². 60 g-1.d-1.dof total BOD5;
2. Water depth: 10–50 cm;
3. Hydraulic retention time: minimum 10 days;
4. $\tau = L \times W \times D/Q$ (Volume of water m³ and the Flow m³/d);
5. Length/Width = minimum 4/1.

Subsurface Horizontal Flow Wetland:

1. Surface area: 5–10 m² 60 g-1. D-1 of total BOD5;
2. Minimum Length is 6 m; max Length is 15 m;
3. The slope of the reed bottom is (1%) from the top surface level;
4. Depth of the inlet: ± 0.6 m; depth of the outlet: maximum depth 0.8 m; minimum depth 0.3 m.

5 Design Considerations

In constructed wetlands, hydrology is considered the most important design parameter because it connects all of the functions and it is responsible for the success or failure of a constructed wetland. Hydrology influences different components of the wetlands such abiotic components include water and nutrient availability, aerobic or anaerobic conditions of the soil, depth of water and velocity, and pH. Also, hydrology could affect biotic factors as water budget and gains through the interference of precipitation and losses through evapotranspiration through plants.

Velocity is controlled by a sloping bed that maintains an adequate hydraulic gradient through the wetland to achieve the desired velocity.

Hydrological considerations include climate and weather, hydro-period, hydraulic retention time, hydraulic loading rate, groundwater exchanges (infiltration and deep percolation), losses to the atmosphere (evapotranspiration), and overall water balance.

6 Limitations of Wetland Processes

Biochemical and biological processes rate dependent on environmental factors, these factors include light period, temperature, dissolved oxygen, and pH. Hydrology and hydraulics are the main driving forces behind the presence and functions of a constructed wetland. hydrology describes the quantity and temporal distribution of the flow from a watershed into a constructed wetland while, hydraulics is related to the patterns and velocities of water movement within a constructed wetland Braskerud (2002).

6.1 Hydrology

Hydrology or the water processes that occur in the wetland are important to the design and maintain the successful operation of the constructed wetlands.

There are two main considerations are:

Water balance—FWS wetlands are subjected to water loss due to evapotranspiration and seepage and subjected to gains (rainfall) which cause a fluctuating in water volumes and levels within the wetland.

Retention time—the period of time that wastewater is retained inside the wetland is critical to the various treatment processes that occur. Required retention times vary depending on the concentration of the pollutants and the desired level and the target of the treatment. It was suggested that the best retention times for BOD removal are 2 to 5 days and it was recommended for BOD and SS removal between 7 to 10 days. Moreover, it was recommended 1 to 3 days for coliform removal, and 7 to 14 days for nitrogen removal while P removal is unpredictable at any retention time.

6.1.1 Water Balance

Water balance for a constructed wetland is an account of the total inflow, storage, and outflow of water. The inflow consists of either surface water (the wastewater or storm-water), groundwater infiltration (in unlined wetlands), and rainfall. Outflow comprises surface water evaporation, evapotranspiration by plants, effluent discharge, and infiltration into groundwater. Effluent concentrations can be diluted by rainfall or increased by loss due to evaporation. During design and operation, the constructed wetland water balance is important for determining conformance with desired limits for hydraulic loading rate, hydro-period range, hydraulic retention time (HRT), and mass balances. The water balance equation for a constructed wetland can be expressed as:

$$S = Q + R + I - O - ET$$

Where: S = net change in storage.

Q = surface flow, including wastewater or storm-water inflow.

R = contribution from rainfall.

I = net infiltration (infiltration less exfiltration).

O = surface outflow.

ET = loss due to evapotranspiration.

Constructed wetlands are appropriate for tools for measuring water balance and ET due to having distinct inflow and outflow, and homogeneous substrate and vegetation Drexler et al. (2004).

6.1.2 Hydraulic Retention Time (HRT)

Water treatment processes depend on the period of time that wastewater physically resides within the wetland boundaries [1]. This period is known as retention time or could be defined in literature as hydraulic retention time, or detention time. Retention time can be obtained from the following equation:

$$t = \frac{nv \cdot d \cdot A}{Q_{av}}$$

where, t = average retention time (days) = (t_n) = nominal retention time.

nv = void ratio or porosity, corresponding to proportion of typical wetland cross section not occupied by vegetation. Typically, equal to 0.65–0.75.

d = wetland water depth (m).

A = wetland surface area (m^2).

Q_{av} = average discharge (m^3/day) or equal to the average of Q_i and Q_o to water balance transit of the bed.

The effectiveness of (biological, chemical, and physical) processes vary with the water retention time. It was reported that longer retention times accelerate the removal of more contaminants, though too-long retention times can have negative effects. It was mentioned in the literature and based on empirical experiences that it should be at least 3–5 days during normal high-water periods. Moreover, some reported that constructed wetlands with average retention times of less than 2 days should not be made if the purpose is nitrogen removal. In practice, water balance changes (e.g., varying influent discharges, rainfall, and evaporation conditions that combine to change effluent discharges) fluctuate retention time. In practice, t is the period during which all of the water flowing into the wetland at a specific time and with an equal flow velocity.

6.1.3 Hydraulic Loading Rate (HLR)

Hydraulic loading is a measure of the volumetric application of wastewater into the wetland. It is often used to make comparisons between wetland systems and indicates their potential to be overloaded by wastewater Dong et al. (2011). The hydraulic loading rate can be calculated by the following equation.

$$HLR = Q/A$$

Where: HLR = hydraulic loading rate (m/day).

Q_i = influent wastewater flow (m^3/day).

In some cases, Q_{av} is used instead of Q_i , A = wetland surface area (m^2).

Both HLR and HRT play a major role in the extent of the interaction between wastewater and the constructed wetland system. In natural wetlands, HLR must be

in the range of 1–2 cm/day to minimize vegetative changes and enhance treatment to reach maximum treatment efficiency. on the other hand, hydraulic loading between 2.5–5 cm/day was optimal for FWS wetland and 6–8 cm/day for SSF wetlands.

6.2 *Precipitation Impacts*

Precipitation and snowmelt can increase the flow in constructed wetland systems. It is very important to determine and estimate the runoff in areas with extended periods of precipitation and must be included in the design flow. Precipitation dilutes pollutants and washes out the chemical in the system, which raises the water level and decreases the HRT which deteriorate the efficiency of the wetland.

6.3 *Evapotranspiration*

Evapotranspiration (ET) is the water loss to the atmosphere from the water surface and from the soil (evaporation) and the loss of water from the vegetation of the wetland plants (transpiration). ET is an important factor in wetland design. It affects the overall water balance of a waste treatment system, thus decreasing efficiency. Usually, evaporation slows the water in the system, and that could significantly increase in retention time of the wetland. Due to high evaporation, the accumulation of concentrated pollutants could reach toxic levels if the water loss from the wetland exceeds the inflow.

7 *How Wetlands Improve Water Quality*

Wetland is a complex and sophisticated system with combinations of water, substrate, plants and plants debris and litter, invertebrates, and microorganisms [2]. Many physical, chemical, and biological processes occurred within treatment wetlands. The processes vary in simplicity and in complexity which makes them not fully understood in terms of the contribution to the treatment process. Normally, the driving factor in determining the limiting pollutant for which the wetland should be designed is the treatment level which must be very efficient to reach discharge permit requirements. Treatment performance of the wetlands could be judged by the capabilities and the percentage of mass removal of contaminants and depends on the contaminant concentration in the wetland outflow. It is important that the selected criteria accurately reflect the actual performance of the wetland relative to the objectives and intended uses of the wetland treatment system. However, justification conducted on experimental results obtained from a sub-surface flow constructed wetland showed that the first few years of the constructed wetland performance is related to the initial

operating stage. Immobilization and/or transformation of pollutants in constructed wetlands usually occur due to some physical, chemical, and biological processes which take place in the substrate-water matrix and in the plant rhizosphere. This could be a cheap way to improve the performance, sustainability, and durability of constructed wetlands or could be used to minimize the wetland area for a given level of treatment. Constructed wetland plants showed 80 to 90% removal efficiency of COD was shown at temperatures greater than 12° C. Moreover, emergent plants have shown high ammonia and phosphate removal efficiency. Only planted wetland cells exhibited significant long-term phosphate removal suggested that plant growth and development of fine root biomass were associated with the removal efficiency in SFW wetlands. The same author concluded that selecting highly effective wetland plants significantly depends on the development of fine roots biomass [2].

8 Conclusion

Constructed wetlands are among the recently demonstrated technologies to have a great potential for efficient wastewater treatment and management in rural and developed areas. When properly designed and operated, constructed wetlands have great advantages over conventional treatment systems for their relatively low cost, easy operation, and maintenance.

References

1. Almuktar, S. A. A. N., Abed, S. N., & Scholz, M. (2018). Wetlands for wastewater treatment and subsequent recycling of treated effluent: a review. *Environmental Science and Pollution Research*. 25(24), 23595–23623. Retrieved from <https://doi.org/10.1007/s11356-018-2629-3>.
2. Stein, O. R., et al. (1998). Performance data from model constructed wetlands for wastewater treatment. *Engineering Approaches to Ecosystem Restoration*, 949–954. Retrieved from [https://doi.org/10.1061/40382\(1998\)158](https://doi.org/10.1061/40382(1998)158)
3. Hadidi, L. A. (2021). Constructed wetlands a comprehensive review -Directorate of water and soil researches, National Agricultural Research Center, P.O. Box 639, Baq'a 19381, Amman, Jordan. <https://doi.org/10.29121/granthaalayah.v9.i8.2021.4176>

Seismic Analysis of Water Tank with Different Configuration to Find Optimal Solution



Sandip Nirmal, Prashant M. Pawar, and Ravikiran P. Jadhav

Abstract A Water tank means a container to store water in a huge amount of capacity. As known from experience, liquid storage tanks collapsed or are heavily damaged during earthquakes all over the world. The economic lifetime of ESR is generally around 40–65 years. Damage or collapse of the tanks causes some unwanted events such as shortage of drinking and utilizing water, uncontrolled fires, etc. Therefore, to avoid all those disadvantages numerous or various studies are being carried out regarding tanks. In this study, I have compared reinforced cement concrete Elevated Service Reservoir (E.S.R) of Square and Circular shape of 1 lakh capacity and a total height of 12.6 m with 3 m staging in Earthquake Zone II, III, IV, and V by Equivalent static analysis using ETABS software for base shear and deflection guidelines for the design of the tank and IS 1893-2016 code. It can be seen that a Circular water tank is more economical and preferable.

Keywords ESR—elevated service reservoir · Max displacement · Base shear · ETABS

1 Introduction

An elevated water tank is viewed as a global water storage container that is built to supply water at a specific height for the water distribution system. Municipalities and industries employ a variety of liquid storage methods, including underground, ground-supported, and raised storage. As a result, water tanks are critical for both public utility and industrial structures. Elevated water tanks have a large water mass at the top of a slender staging, and are the most important factor in the tank's failure during earthquakes. These are the most important and unique structures, and their destruction during earthquakes could affect the supply of drinking water, fail to prevent big fires, and result in significant financial damage. Water is one of the most basic human requirements. The design of a water tank determines how much

S. Nirmal (✉) · P. M. Pawar · R. P. Jadhav
Shree Vital Education and Research Institute, Pandharpur, Solapur, India
e-mail: sandipnirmal1997@gmail.com

water is distributed in different areas. In our country, water storage is provided by overhead water tanks since the required pressure in the water delivery process is achieved by gravity in elevated tanks rather than the use of large pumping systems. The Indian subcontinent is extremely vulnerable to natural calamities such as earthquakes, droughts, floods, and cyclones. More than 60% of India is vulnerable to earthquakes, according to the seismic code IS 1893 (Part 2)-2002. The fact that a large water mass is at the top of a slender stage during an earthquake is the most critical aspect of the failure of elevated water tanks. Elevated tanks are commonly employed in seismically active areas; thus, their seismic behavior must be thoroughly examined.

(1) Square Water Tanks

- Rectangular tanks are mostly in the square plan for economic purposes.
- It is also notable that the longer side not be greater than twice the smaller side. Moments are caused in both the way/direction of the wall i.e. vertical and horizontal.
- For small capacities, a circular tank is undesirable because of curved shuttering's. therefore, rectangular tank is preferable.

(2) Circular Water Tanks

- Mainly circular water tank possesses or shows the properties of the cylinder.
- The base of the circular water tank has a flexible joint.
- On account of its circular shape, it can be made watertight easily as there are no sharp corners.

2 Literature Survey

Lodhi et al. [1] designed and seismic loading of an intze type water tank was examined. These Intze type water tanks were created in accordance with IS: 3370, or the Code of Practice for Concrete Structures for Liquid Storage. The Intze water tank has been developed and examined under two different circumstances—without taking seismic impacts into account, and considering seismic effects. The reinforcing needs were increased when the Intze water tank was designed using the New IS Code: 3370-2009 and taking into account the influence of seismic forces, which were computed using the Draft IS Code: 1893-2005. Singh et al. [2] based on Indian codes, examined the water tank and came to a decision regarding the appropriate type of water tank for various wind and earthquake zones. Study was done on the seismic and wind forces affecting the water tank. The raised structure was built to withstand a range of wind speeds, and the same was double-checked with various earthquake zones. The conclusion reached was that for a given bearing capacity, concrete volume and steel quality both rose as wind speed and seismic zone increased. Each time, there is a 4–5% difference between the wind moment computed manually and the analysis performed using Staad Pro software as the wind speed changes or increases. Aware and Mathada

[3] finite modelling techniques are used to analyses. This essay examines the seismic performance of elevated water tanks in India at various heights and seismic zones. This research used analysis of 20 models with the same parameters to show the impact of water tank height and seismic zones on nodal displacement. STAAD-PRO, a finite element programme, is used to conduct the analysis. The conclusion reached was that maximum nodal displacement increases as water tank height increases. Madahvi et al. [4] RCC elevated liquid storage tank seismic analysis and earthquake characteristics with various bracing and staging systems are shown. With STAAD Pro V8i software, the behaviour of the supporting system was improved under various earthquake characteristics or earthquake zones. Here, a basic supporting system and two different staging patterns, such as radial bracing and cross bracing, were examined for varied fluid filling circumstances. Zone-III and Zone-V seismic zones as well as the associated earthquake characteristics were obtained from IS 1893 (PART 1)-2002 and draught code IS 1893. (Part 2). The outcome demonstrates that the features of the earthquake and the presence of water had a significant impact on the structure reactions. The study also highlights the significance of having a staging arrangement that can withstand the failure of an elevated water tank during seismic events. Gandhi et al. [5] conducted on circular raised water tanks with various bracing and staging for earthquake resistance. The primary goal of this study is to better understand how various staging patterns behave when bracing in order to reinforce the traditional kind of staging and provide better performance during an earthquake. STAAD Pro is used to perform equivalent static analysis for staging with various bracing systems applied to the staging of the elevated circular water tank in zone V. The circular water tank's base shear and maximum displacement in X, Y, and Z directions were compared. Various bracing designs were used in the staging of an elevated water tank for the parametric investigation. It was evident from the base shear for the various bracing patterns that the base shear value decreases for alternative bracing patterns in staging. This study concluded that cross bracing in staging is the most efficient way to reduce displacement caused by lateral loading. Cross bracing efficiently reduced displacement by 81.09% in the X direction and 92.98% in the Z direction compared to a structure without bracings.

3 Scope of the Project

This work aimed to investigate the impact of earthquake on a tank under different water tank conditions. Utilizing the software ETABS, the tank's finite element model was created, and seismic analysis was performed. Peak displacements and base shear were compared based on the study.

4 Methodology

The methodology includes fixing the dimension of a selected type of water tank and performing linear dynamic analysis using IS 1893-2002 (part2). In this study, 1 lakh liter water tank Switch circular and square shapes are considered for analysis. It is analyzed for the base shear and the deflection using ETABS software. Peak displacement and base shear obtained from the analysis are compared [6–8].

5 FEM Analysis Using ETABS Software

The details of the 100 m³ circular overhead water tank considered for seismic analysis are listed: Internal diameter—5 m, Height—3.6 m (Including FB-0.4 m), Tank Bottom slab thickness 150 mm, Tank top slab thickness 150 mm, Column size—0.3 × 0.4 m, Beam size—0.3 × 0.3 m, Steel Grades—Fe415, Fe500, Type of soil—Hard, medium and Soft [9, 10].

Seismic zones considered—II, III, IV, V.

6 Modeling

See Fig. 1.

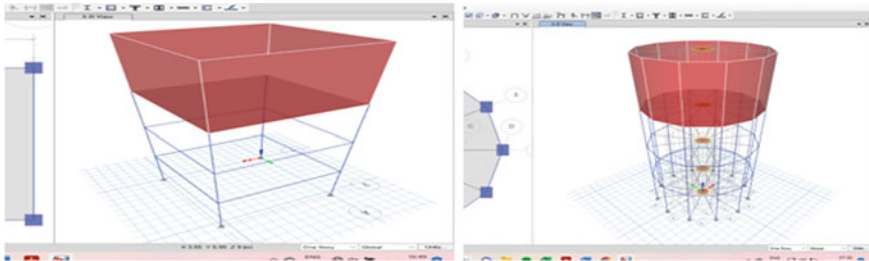


Fig. 1 Typical 3D View of circular and square water tank modeled on ETAB

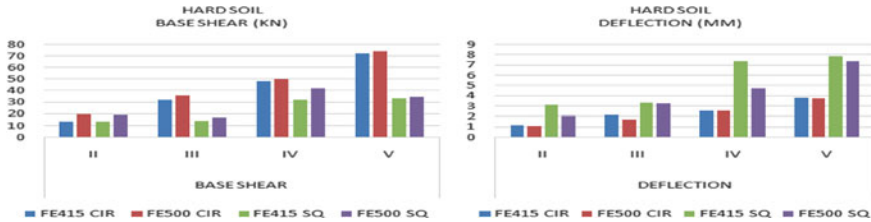


Fig. 2 Base shear values and the deflection values for the hard soil condition

7 Observations

7.1 For Hard Soil Condition

In the graph variation of the base shear in hard soil condition with seismic zones it can be observed that it's increasing from low seismic zone to high seismic zone. Base shear variation for the for Fe415 and Fe500 steel are increasing linearly in each seismic zone as shown in Fig. 2. The deflection given by the Fe500 steel are comparatively less than the Fe415 steel as shown in Fig. 2

7.2 For Medium Soil Condition

In the graph variation of the base shear in medium soil condition with seismic zones it can be observed that its increasing from low seismic zone to high seismic zone. Base shear variation for Fe415 and Fe500 steel are increasing linearly in each seismic zone as shown in Fig. 3. The deflection given by the Fe500 steel are comparatively less than the Fe415 steel as shown in Fig. 3.

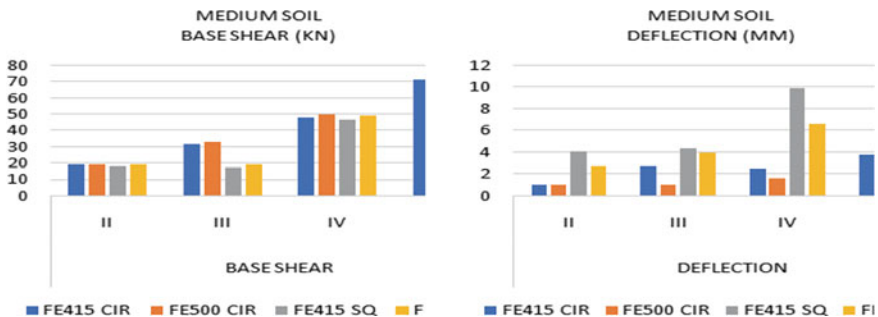


Fig. 3 Base shear values and the deflection values for the medium soil condition

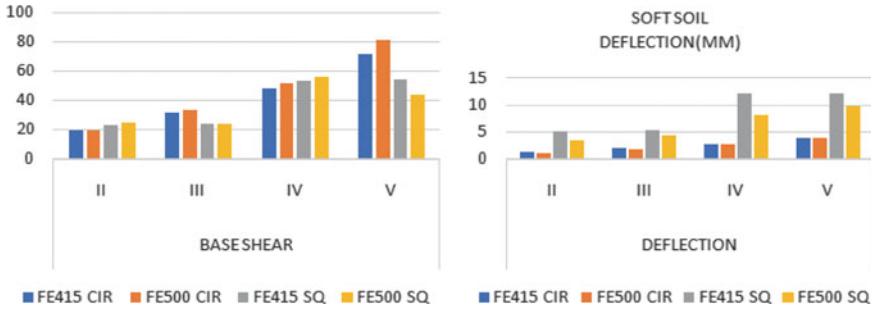


Fig. 4 Base shear values and the deflection values for the soft soil condition

7.3 For Soft Soil Condition

In the graph variation of the base shear in soft soil condition with seismic zones it can be observed that its increasing from low seismic zone to high seismic zone. Base shear variation for the for Fe415 and Fe500 steel are increasing linearly in each seismic zone as shown in Fig. 4 The deflection given by the Fe500 steel are comparatively less than the Fe415 steel as shown in Fig. 4.

8 Result

In this study, the analysis of water tanks with different grades of steel in each seismic zone was investigated by using ETAB Software. The circular and square shapes of the water tank with Fe415 and Fe500 in each seismic zone were modeled in soft, medium, and hard soil conditions, and the base shear and deflection of the water tank were obtained. According to the obtained result, the variation of base shear increases from seismic zone II to seismic zone V in each soil condition, so it is concluded that corresponding base shear would increase if the water tank is located in a higher seismic zone. Based on the observed base shear values in the various soil conditions, it can be concluded that in each seismic zone, steel grade Fe500 produces baser shear values than steel grade Fe415. It is concluded that the deflections produced by the water tank with the Fe500 grade are significantly lower than those produced by the steel of the Fe415 grade. In each seismic zone and soil condition, the base shear for a circular reservoir is greater than that of a square water tank when the same tank’s capacity is taken into consideration in the parametric study of the tank. It is concluded that the optimal solution for all other models looked at is to suggest a water tank with a circular shape made of Fe500 steel.

References

1. Lodhi, R. S., Sharma, A., & Garg, V. (2014). Design of Intze Tank in perspective of revision of IS: 3370. *International Journal of Scientific Engineering and Technology*, 3(9), 1193–1197.
2. Singh, N. J., & Ishtiyaque, M. (2015). Design analysis & comparison of intze type water tank for different wind speed and seismic zones as per Indian codes. *International Journal of Research in Engineering and Technology*, 4(09).
3. Aware, R. J., Vageesha, S., & Guide, M., Seismic performance of circular elevated water tank. *Shri Vitthal Education & Research Institute College of Engineering, Pandharpur International Journal of Science and Research (IJSR)*, ISSN (Online), 2319–7064.
4. Madhavi, K. D., et al., Seismic analysis and earthquake characteristics of RCC elevated liquid storage tank with different bracings and staging patterns.
5. Gandhi, M. N., & AncyRajan. (2016). Earthquake resistant analysis of circular elevated water tank with different bracings in staging. *IJISSET-International Journal of Innovative Science, Engineering & Technology*, 3(11), 255–259.
6. Bansode, P. A., & Datye, V. P. (2018). Seismic analysis of elevated water tank with different staging configuration. *Journal of Geotechnical Studies*, 3(1).
7. Shylaja, N., et al. (2018). Performance of RC elevated water tank under seismic effect. *International Journal of Applied Engineering Research*, 13(7), 46–49.
8. Ahirwar, S. K., Jain, S. K., & Pande, M. M. (2008). Earthquake loads on multistorey buildings as per is: 1893–1984 and is: 1893–2002: a comparative study. In *14th Conference on Earthquake Engineering*.
9. Lohade, S., & Kulkarni, S. (2016). Shape effects of wind induced response on tall buildings using CFD. *International Journal of Engineering and Applied Sciences*, 3(6), 257650.
10. Babu, B. G. (2017). Seismic analysis and design of G+ 7 residential building using STAADPRO. *International Journal of Advance Research, Ideas and Innovations in Technology*, 3(3).

Low Cost Housing Structure Using Bamboo as Reinforcement



Aishwarya S. Ingawale, Prashant M. Pawar, Sonali P. Patil,
and Ravikiran P. Jadhav

Abstract The need for the use of green technologies in the construction industry has arisen due to the depletion of natural resources. Bamboo is a strong, lightweight, environmentally friendly material with good tensile properties. Bamboo has a strength-to-mass ratio that is 20 times greater than steel. As a highly resilient and strong alternative material, bamboo is frequently mentioned as being as strong as steel reinforcement for concrete. Due to its strong strength to weight ratio and excellent flexural strength in tension, Bamboo has been utilized in construction since ancient times. All of this necessitates a thorough analysis of bamboo reinforced concrete's suitability as a structural material for the construction of affordable housing units. An important matter is housing. As a strong, resilient, and lightweight roofing material, bamboo is ideal. As businesses grow and rural areas are transformed, bamboo will continue to play a significant role in both of these processes. The stiffness, strength, and stability of the building are investigated using structural design. Construction of a structure that can withstand all applied loads without failing for the duration of its planned life is the primary goal of structural analysis and design. There are several stages in the structural design process, including the calculation of loads, member design, details, and many others. The traditional approach to structural design and analysis results in several difficulties and time-consuming, repetitive calculations. Fast software is now used to efficiently execute design and analysis tasks.

Keywords Bamboo · Low cost material · Structural analysis · Computer aided design

1 Introduction

Modern visualization tools, a STAAD PRO has advanced finite element technology, dynamic analysis capabilities, and a well-built analysis and design programme. Everything from tools for visualization and result verification to model development,

A. S. Ingawale (✉) · P. M. Pawar · S. P. Patil · R. P. Jadhav
SVRI's College of Engineering Pandharpur, Pandharpur, Maharashtra 413304, India
e-mail: aishwaryaingawale030@gmail.com

© The Author(s), under exclusive license to Springer Nature Switzerland AG 2024
P. M. Pawar et al. (eds.), *Techno-Societal 2022*,
https://doi.org/10.1007/978-3-031-34648-4_21

203

analysis, and design. STAAD PRO is frequently used for the design of multistory buildings, factories, tunnels, bridges, and other structures made of steel, concrete, aluminum, and cold-formed steel. However, we are employing STAAD PRO analysis to reinforce the building with wood. STAAD PRO computer-aided design of a residential structure, which includes: Creating a structural frame plan obtaining a model an examination of structure.

Materials like cement and steel are having a significant impact on the construction scene in rural India since they give things a long life. The current study recommends using bamboo as a building material in rural construction along with cutting-edge material technologies.

In many tropical areas, bamboo is highly recognized as a dependable, renewable, and adaptable building material. The plant is among the oldest naturally occurring building materials in use today and is a valuable source for eco-friendly construction. We'll talk about using bamboo as a steel substitute in this piece. Ferrocement, often known as Ferrocete, is a lightweight building material with thin walls that uses fine wire mesh. Bamboo is a sustainable, affordable, and widely accessible material. For non-permanent structures, bamboo can be used as reinforcement material in place of steel.

The research study focuses on creating affordable housing and replacing.

2 Objectives

Objectives of the current research are summarized below:

- To study the concept of ferrocete and its properties for the applications related to construction work.
- To research bamboo's mechanical and physical characteristics for use as a reinforcing material.
- To check the suitability of bamboo as a reinforcement material in ferrocete as replacement of steel.
- To carry out cost analysis for bamboo reinforced ferrocete in comparison with steel reinforced concrete.

2.1 Literature Review

The use of bamboo in the building of affordable homes was the result of the efforts of numerous national and international researchers. The following is a summary of the research on bamboo with ferrocete technology. To comprehend the idea of low-cost housing and how bamboo and ferrocete are used for low-cost construction, a thorough literature review is conducted. The effectiveness of bamboo in concrete as a steel substitute is assessed using a variety of strength, durability, and other criteria. We are conducting this research utilizing IS-AITC 1994. Research gaps are

then determined using the literature review. The research articles' specifics are as follows:

Kumar et al. [1] evaluated bamboo's mechanical and structural capabilities in comparison to steel. Numerous researches came to the conclusion that bamboo has pretty exceptional mechanical qualities. A helpful and significant asset to investigate that could change the building business, bamboo revealed startling similar findings to the alternative steel in tests addressing the compressive, tensile, and flexural strength. Salim et al. [2] made research physical and mechanical behavior of the bamboo/flax hybrid fiber-reinforced epoxy matrix composite affected by humidity was the subject. Epoxy resin-reinforced composites produced from bamboo and flax fibres were submerged in water for 60 days at 25 °C and 2 days at 85 °C. At high temperatures (85 °C), the composite showed structural and microstructural changes over the course of 25 h. Composites treated with NaOH (9% of the total) exhibited the maximum level of swelling at both temperatures, with both untreated and treated composites having lower swelling behavior. The weak link between the fibres and matrix had an increasing impact on water absorption in the biocomposite. The outcomes demonstrated a difference in maximum tensile strength between the two circumstances. Al-fasih et al. [3] carried out a series of tests on untreated species of *Bambusa Vulgaris Vittata* (BV), *Bambusa Heterostachya* (BH), and *Schizostachyum Brachycladum* Yellow to ascertain the effects of strip shape, bamboo type, and moisture content on the tensile strength of bamboo strip (SB). The efficiency of four different cutting shapes—strip-cut (S), strip-cut-side curve (SS), double curve (DC), and single curve (SC)—was assessed while accounting for the presence of bark and nodes in the strip. The results showed that the specimen in the SS shape with bark had a higher tensile strength. The strength was greatly reduced by the node's presence. The type of bamboo had a big effect on its tensile strength. The perfect amount of moisture for bamboo. Dey and Chetia [4]. This research compared different frictional qualities concrete beams strengthened with bamboo. The bamboo reinforcements are rolled in sand, wire, and coir. The frictional properties of bamboo reinforced concrete beams were accomplished. For rural projects, simple, effective, and cost-effective concrete beams made of bamboo were explored. The main component of the web material was steel stirrups, which helped prevent the shearing concrete beams strengthened with bamboo. According to the four-point bend test, eighteen such beams had been tested to failure. For comparison purposes, Flexural strength has been considered at 28, 45, and 60 days. It was found that during failure, beams with a longer curing time and larger reinforcement size function well. Four-point loading on a bamboo-reinforced concrete beam was assessed by Bhonde et al. [5] plotting the curve of load elongation and studying at first the load fracture and the point of failure's maximum bending moment. Maximum bending stress values at the most concrete fibres at the extremes surrounding reinforcement for concrete was discovered. Design stresses and ultimate experimental stresses were contrasted. The experimental plan and analytical findings of the bamboo-reinforced concrete beam are presented in this work. Agarwal [6] presented the findings of axial compression and transverse loading experiments performed on unreinforced, steel, and bamboo columns in order to ascertain the load carrying capacity, lateral deflection, and failure mode pattern. Beams were also put

through a two-point load test to see how they would respond to being bent. By using TMT rod stirrups and bamboo stirrups to strengthen treated and untreated bamboo beams, these trials demonstrated that bamboo, with the proper treatment, was capable of taking the place of steel in beam and column members. Quarry dust has replaced sand as the fine aggregate in concrete because sand was insufficient. Additionally, the usual steel reinforced concrete beam was compared and analysed with treated and untreated bamboo reinforced concrete beams. Stewart [7] examined the quantity and size of reinforcing bars, the depth at which steel reinforcing is effective, the width of the beam, and the quality of the concrete mix. Each of these micro tasks was explained together with human performance models. It has been discovered that human error causes a serious loss in structural safety. It was also demonstrated that structural dependability was greatly boosted by engineering inspections, although the actual structural reliability was still orders of magnitude less than “nominal” estimates of structural reliability.

Ghavami [8] analysed and presented the results of a few recent experiments on the microstructure of bamboo as a material with a functional gradient. These studies established the bamboo’s composite behaviour through the law of mix. A brief overview of columns, concrete slabs with permanent shutters, and bamboo-reinforced concrete beams is provided. Then, some recommendations for further research are made with reference to global sustainable development without damaging our planet, in the hope that the recently discovered information may be helpful. Utilizing bamboo concrete composites (Bamcrete), Sudhakar [9] has created a number of structural elements and tested them out by using them to construct homes. This study shows the first experimental confirmation of one of the Sudhakar-proposed structural arch forms employing bamboo as a structural component. In this instance, two vertically separated bamboo arches are joined together using ferro-cement band ties to create a bow beam arch that serves as a load-bearing element. The bow beam arch’s production specifications and preliminary experimental findings are presented in this study.

3 Methodology

In this study bamboo is used as reinforcement in structure with a replacement of steel. Analysis has been made with STAAD PRO software with all loading and boundary conditions. Following methodology is followed for the analysis:

- A timber beam analysis is performed in STAAD PRO, and this is the methodology used in STAAD PRO for a timber beam analysis.
- The geometry of the bamboo-material beam is formed into the STAAD PRO through modeling, as shown in Fig. 1.
- Dimension: According to the modelling, the timber beam has an inner diameter of 25 mm and an outside diameter of 30 mm. The cross sectional area of the beam is calculated.

Fig. 1 Bamboo beam



- Support condition: Using the model, we assigned fixed supports to the beam, and the analysis of that beam is based only on fixed a supports.
- For this analysis, the loading condition according to the beam dead load (self weight) and live loads is taken into account.
- After analysis post processing is done in that deflection, share force and bending moment in the member of frame is observed (Figs. 2 and 3).

Material and Properties

Timber

- Young’s Modulus (E) = 500,000 KN/m²
- Poisson’s ratio = 0.20

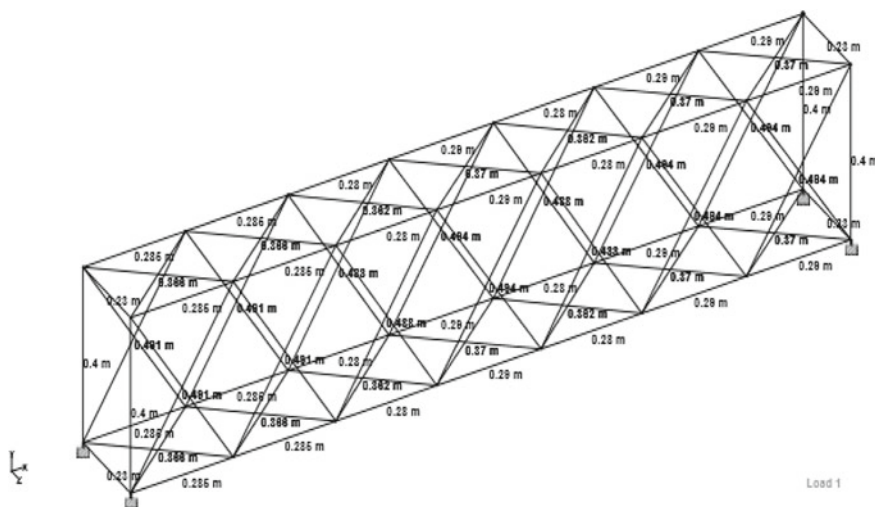
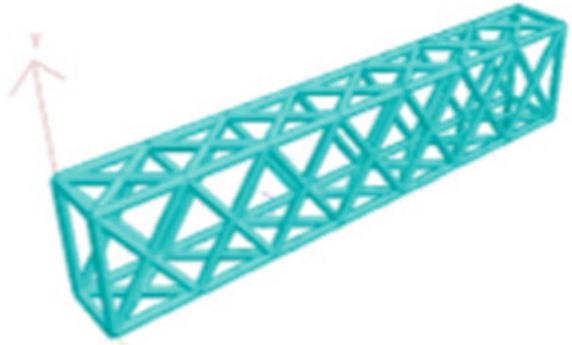


Fig. 2 Geometry of beam

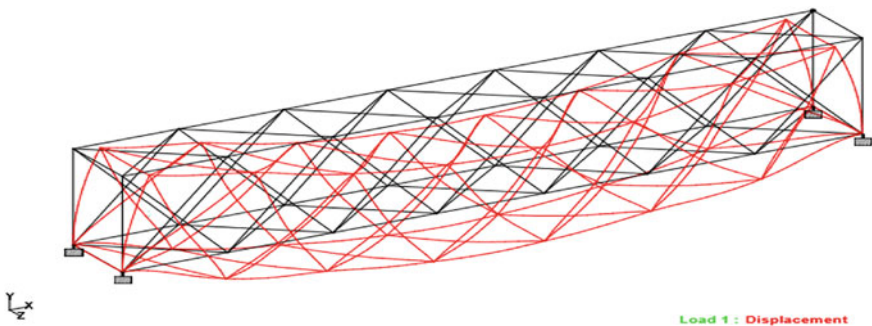
Fig. 3 3D rendered view

- Density = 5.88K N/m³
- Thermal Coefficient = $1.073 \times 10^{-5}/^{\circ}\text{C}$
- Critical damping = 0.0130
- Yield Stress = 50×10^3 KN/m²
- Tensile Strength = 95×10^3 KN/m²
- Yield Strength ratio = 0.52
- Tensile Strength = 1
- After importing this all properties we got the good results.

4 Results

Post processing in STAAD PRO is performed with giving all conditions of loading and boundary conditions. All loads and boundary conditions are given and results about the shear force, bending moment and deflection is calculated. The all boundary conditions are given to truss and calculated bending movement is 0KN and deformation is also very less around 1 mm (Fig. 4).

In the post processing we have got shear force which is shown in Fig. 5

**Fig. 4** Deflection

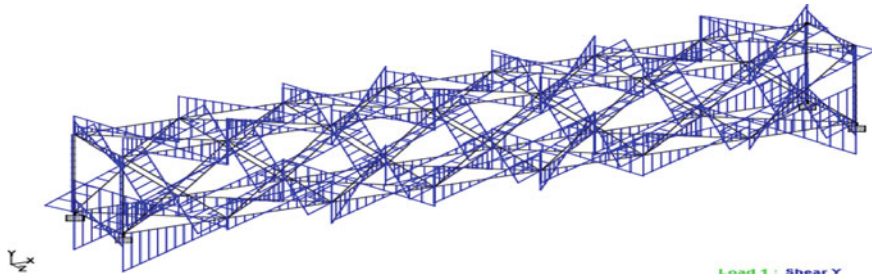


Fig. 5 Shear force

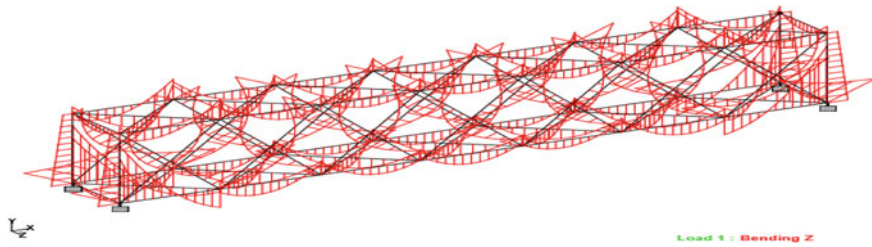


Fig. 6 Bending moment

In the post processing we have got bending moment which is shown in Fig. 6

5 Conclusion

Based on the application of such loading circumstances and the professional analysis of the bamboo frame, we found that there was a minimum deflection, shear force, and bending moment during loading. As a result, bamboo is a good material for low-cost housing of any kind.

References

1. Kumar, P., Gautam, P., Kaur, S., Chaudhary, M., Afreen, A., & Mehta, T. (2021). Bamboo as reinforcement in structural concrete. *Materials Today: Proceedings*, 46, 6793–6799.
2. Salim, S., Rihayat, T., Riskina, S., & Safitr, A. (2021). Physical and mechanical properties of bamboo/flax fibre reinforced epoxy composite water absorption behaviour and high-temperature conditions. *Macromolecular Engineering*, 50, 415–424.
3. Al-Fasih, M., Hamzah, S., Ahmad, Y., Ibrahim, I., & Mohd Ariffin, M. (2021). Tensile properties of bamboo strips and flexural behaviour of the bamboo reinforced concrete beams. *European Journal of Environmental and Civil Engineering*, 41, 510–516.

4. Deya, A., & Chetia, N. (2018). Experimental study of bamboo reinforced concrete beams having various frictional properties. *Materials Today: Proceedings*, 5, 436–444.
5. Bhonde, D., Nagarnaik, P., Parbat, D., & Waghe, U. (2014). Experiment analysis of bending stresses in bamboo reinforced concrete beam. In *3rd international conference on recent trends in engineering & technology* (Vol. 64, pp. 345–356).
6. Agarwal, A., Nanda, B., & Maity, D. (2014). Experimental investigation on chemically treated bamboo reinforced concrete beams and columns. *Construction and Building Materials*, 71, 610–617.
7. Stewart, M. (2007). A human reliability analysis of reinforced concrete beam construction. *Civil Engineering Systems*, 9, 227–250.
8. Ghavami, K. (2005). Bamboo as reinforcement in structural concrete elements. *Cement & Concrete Composites*, 27, 637–649.
9. Sudhakar, P. Visiting Professor, Center for Rural Development and Technology; Indian Institute of Technology, Delhi; New Delhi, 110016.

Techniques to Share and Store Large Data in Used System to Reduce Network Traffic and Cost



Punam S. Kamble and Namdev M. Sawant

Abstract CHARON is a cloud-based storage system that can reliably and efficiently store and share large amounts of data using multiple cloud storage repositories to meet regulatory requirements for sensitive personal data services. An efficient system that reduces network traffic costs. Design a new intermediate DataSubscriber schema. MapReduce types simplify large-scale processing of suite data, but a lot of effort is put into maximizing the performance of MapReduce operations. The hash capacity used in the intra-session topology minimizes the task, while the network topology appreciates moving notes. Finally, the reproducible results exhibited by the proposed algorithm can minimize network costs.

Keywords Cloud storage · Network traffic · Map reduction · Network cost · Data caching

1 Introduction

Now a days, Map Reduce is more famous framework of computing to huge amount of data processing. Hadoop language is based on java programming language. Map and Hadoop with Hadoop Distributed File System. Map Reduce breaks the parts into Map and Reduce, in this eachans every parts is performed by moew than one Map and Reduce tasks. Inbetween the mapping phase, equal mapping tasks are started to transfer the original input splits into inbetween data in the form of key-value pairs. These all key-value pairs are stored on the local computer and organized into various data partitions. Each truncated task gets its own share of the data partition from all mapping tasks to create the final result. There is a shuffle step between the map and reduce phases. The data produced by the Map stage is per-ordered and

P. S. Kamble (✉)

Department of Computer Science and Engineering, Korti, Pandharpur 413304, India
e-mail: punam29junkamble@gmail.com

N. M. Sawant

Punyashlok Ahilyadevi Holkar Solapur University, Sholapur, India
e-mail: namdev.sawant@sknscoe.ac.in

sent to the appropriate engine implementing the Reduce stage. Because network traffic patterns assign each task to each reduction task, which can generate a large amount of network traffic, the efficiency of data analysis applications must be tightly controlled. By default, intermediate data is shuffled according to Hadoop's hash function. This ignores the network topology and data size associated with each key, resulting in excessive network traffic. She manipulates the data for her own purposes immediately after issuing her card and does not use the option of aggregating the data across multiple tasks on different computers. The purpose of Map Reduces jobs is to minimize overall network traffic. MapReduce has become the more famous computing framework to process big data because its easy programming model and automatic management of parallel execution.

2 Related Works

In now a days, data has become one of the more essential part that needs to be handled and use correctly. The new social media platforms that have emerged over the past decade have vast amounts of data at their disposal. Data complexity is another big problem that traditional programming models haven't been able to solve. This is why Map Reduce was introduced. This is one of the useful models for a various of tasks involving huge amounts of data that cannot be performed by traditional methods. MapReduce uses the map() and Reduce() user-defined functions to perform their functions. The former processes key-value pairs, the latter produces a series of key-value pairs that are used for merging. The runtime system is also responsible for input splitting, scheduling, and error handling. MapReduce is now widely used [1]. Figure 1 clearly shows the flow of the map-reduce process.

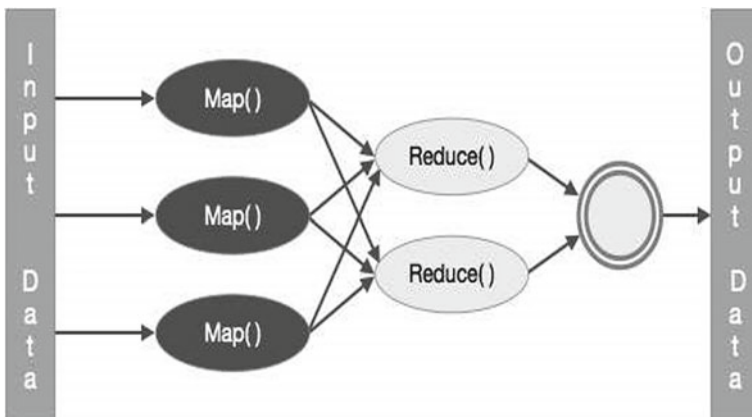


Fig. 1 Map reduce process flow

Cloud computing enables users to store data remotely in the cloud and deliver on-demand applications and services from a shared pool of configurable computing resources [2–4]. The security of outsourced data in the cloud depends on the security of the cloud computing system and network. Although many efforts have been made to protect data on cloud computing systems, assessing the security of data on networks between cloud providers and their users remains a daunting task [5].

Maximizing the use and efficient management of cloud storage resources has become one of the major themes in cloud computing. If the cloud storage space is limited or the size of a single file is limited, users can rent more cloud computing storage services.

Data partitioning and distributed storage technologies focus on solving the problem of limiting the size of large datasets in cloud storage. We present a model for partition-based data storage in the cloud and discuss its availability. Starting with the discussion of fragment partitions, three algorithms are designed based on the model. The first algorithm is about splitting and storing data, the second algorithm is about retrieving and combining data, and the last algorithm is about updating fragments and subdividing them again. Experimental results show that the model is applicable to the situation of multiple cloud storage services and large datasets or files [6].

Ensuring data availability in distributed computing may require the use of basic techniques such as: B. Various replications as shown in Fig. 2. Such an approach can improve overall system availability.

Cloud storage Drive HQ is used as cloud storage in this work. Drivehq: DriveHQ is the first cloud IT service provider. Founded in 2003 with the goal of becoming a one-stop shop for all cloud IT services. Since then, DriveHQ has been an industry leader in: Drive mapping is the easiest way to access cloud storage. The basic service is free and comes with 5 GB of storage. Individual and family plans start at \$4/month. Our business services are over 40% cheaper than our competitors. 256-bit SSL have DriveHQ to transfer secure data [7]. Files can be transferred using HTTPS or FTP over TLS (FTPS). DriveHQ supports to data security for client-side data encryption. Your data is encrypted locally before reaching our servers. Therefore, the data can only be decrypted using your private encryption key. Much more secure than server-side encryption [8, 9].

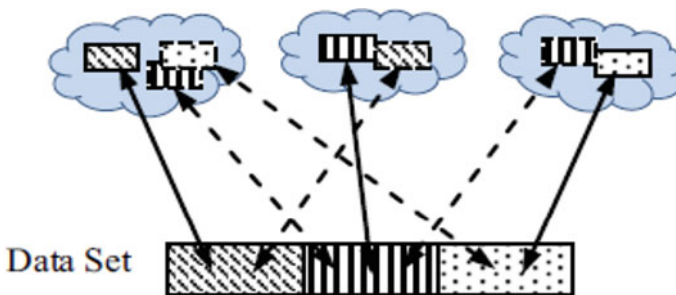


Fig. 2 Data fragment with multiple copies in the cloud

3 Proposed System

Overall, the system allows you to split and aggregate data for MapReduce jobs with the goal of minimizing overall network traffic. In particular, we propose distributed algorithms for big data applications by decomposing the original big problem into multiple subproblems that can be solved in parallel. In addition, online algorithms must dynamically handle data splits and aggregations. Finally, large-scale experimental results show that our proposal can significantly reduce network traffic costs in hybrid cloud systems. The advantages of the proposed system are:

- Design and implement a practical cloud-based storage system for storing and sharing big data.
- Reduce network traffic costs both offline and online.

In Fig. 3 the proposed system architecture is mentioned. The gateway server that runs this application contains four main functions.

1. **Server Details**, this function maintain the intermediate cloud server and storage space IP address and connection details.
2. **LBA**: Logical Block Addressing This function is used to identify blocks within a file.
3. **File Details**: When a user uploads a file, the file is split into blocks and LBAs are created and stored in the top cloud. These details are preserved in this function.
4. **Lookup**: This is an IP lookup function based on the client IP address that this system should redirect to the native IP cloud server.

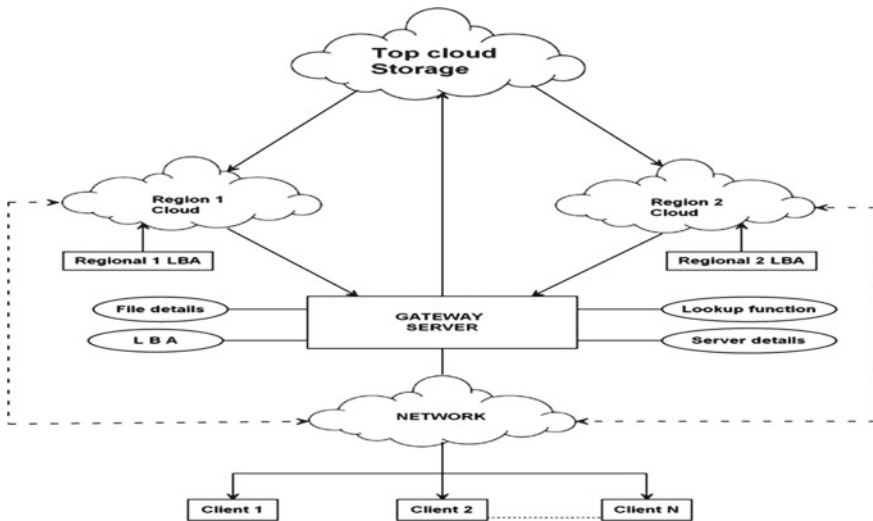


Fig. 3 Proposed system architecture

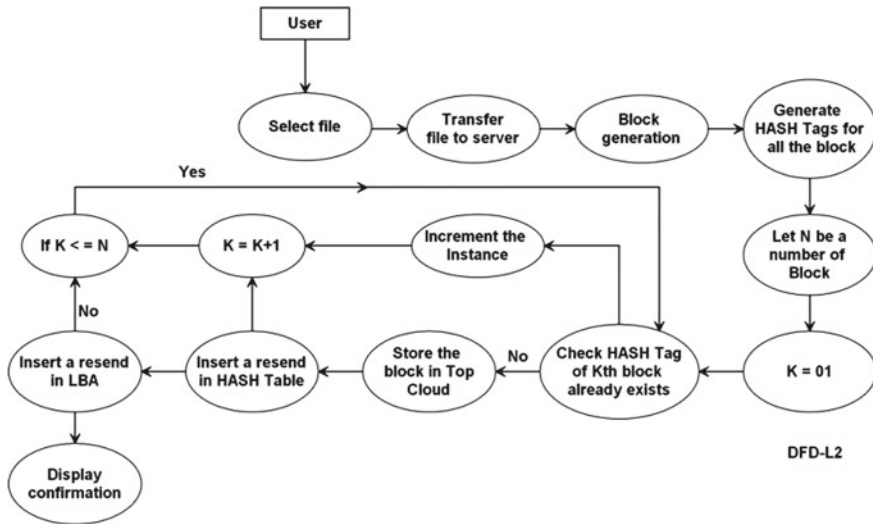


Fig. 4 File upload flow

Once a file is uploaded by a user, it must go through various processes described below. Figure 4 shows the data flow for the file upload process

A. File Upload Process

- First user compulsory selects a file from the system and click the upload option.
- Files are split into small blocks (500 bytes per block).
- Generate hashtags for all blocks.
- Compares the generated hash block with existing hash tags in the database if the hash tags match. In this case, do not upload this block to the cloud and increase the number of instances of this block in your database table.

When a user downloads a file, it must go through various processes described below and Fig. 5 shows the data flow for the File Upload Process.

B. Process for file downloading

- The user have to select a file for downloading.
- Send a request to the server. The server must obtain her IP address of the client system and use a lookup function to determine the region of her IP address, which is the Selected Region (SR).
- Each region has a location and a map area. All downloaded block data is available in your storage space, and details of downloaded blocks are available in the map section.
- LBA server needs to find block number in selected file.

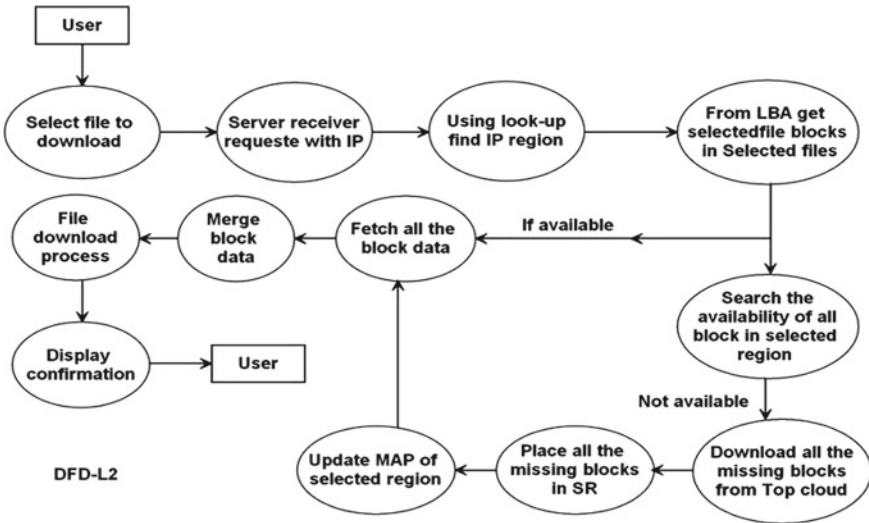


Fig. 5 File download process flow

- The server should check the availability of all blocks required by the file within the allocated space of the SR. Once all blocks are available in the SR section, download the blocks, merge them, and make them available to users. If there are few blocks available and some blocks are missing, grab the missing blocks from the top panel and place them on the SR panel to update the SR card detail.

4 Evaluation

This system has been deployed and tested in a hybrid cloud configuration and meets all requirement specifications. All four user functions work fine. Figure 5 shows a comparison of block upload and download times, and Fig. 6 shows block verification time requirement [10–12].

The system requires uploading about 30 files and splitting each file into blocks to store in cloud storage. Without the map-reduce technique, the total number of blocks would be 900. Using the map-reduce concept, they are reduced to 417 blocks (Fig. 7 and Table 1).

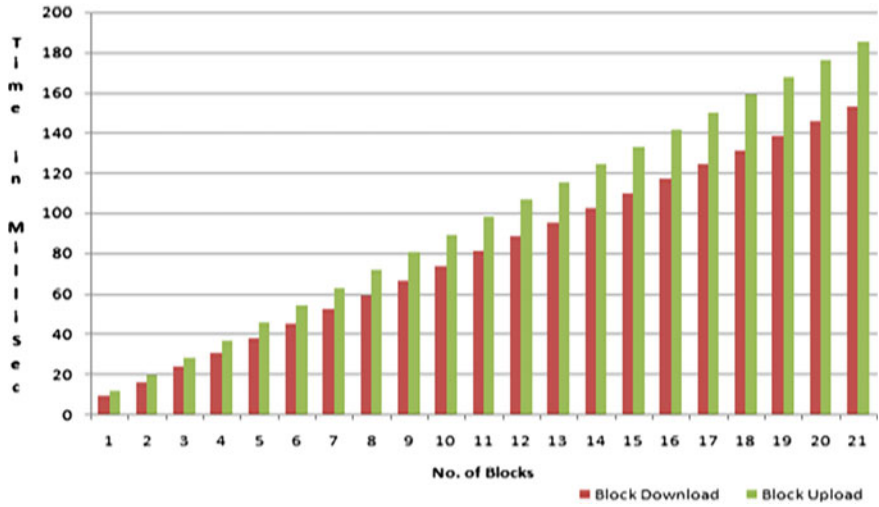


Fig. 6 File upload and download diagram

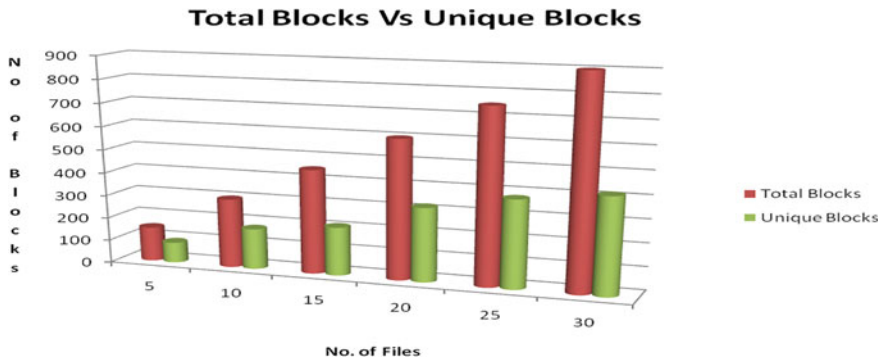


Fig. 7 Total blocks versus unique block

Table 1 Comparison of total blocks versus unique block

No. of files	Total blocks	Unique blocks
5	150	89
10	300	176
15	450	210
20	600	320
25	750	380
30	900	417

5 Conclusion

Proposed were focuses on minimizing general network traffic by data partitioning and aggregation technique for map reduce job. Proposed distributed algorithm which is executed in parallel by decomposing optimal problem in multiple sub problems over sample big data application. Algorithm also handle various function dynamically such as data splits and aggregations whenever required. Simulated result shows that, proposed model help to significantly reduce network traffic in both the cases in online as well as offline [13].

References

1. Kour Siledar, S., Deogaonkar, B., Panpatte, N., & Pagare, J. (2021). Map reduce overview and functionality. In *2021 6th international conference on communication and electronics systems (ICCES)* (pp. 1560–1566). IEEE.
2. Lane, M., Shrestha, A., & Ali, O. (2017). *Managing the risks of data security and privacy in the cloud: A shared responsibility between the cloud service provider and the client organisation*.
3. Dekker, M. (2012). *Critical cloud computing—A CIIP perspective on cloud computing services*. White paper.
4. Gunawi, H. S., Hao, M., Suminto, R. O., Laksono, A., Satria, A. D., Adityatama, J., & Eliazar, K. J. (2016). Why does the cloud stop computing? Lessons from hundreds of service outages. In *Proc. of the SoCC*.
5. Shetty, S., Biswal, B., & Maziku, H. (2014). Auditing and analysis of network traffic in cloud environment. *IEEE Ninth World Congress on Services*, 260–267. <https://doi.org/10.1109/SERVICES.2013.42>
6. Zhao, Y., & Wang, Y. (2012). Partition-based cloud data storage and processing model. In *2012 IEEE 2nd international conference on cloud computing and intelligence systems* (Vol. 1, pp. 218–223). IEEE.
7. Ponaganti, A., Mounika, K., & Student, M. C. A. *MUR CHARON a secure cloud of clouds system for storing and sharing big data*.
8. Delfino, R. (2020). European Union legislation and actions. *European Review of Contract Law*, 16(1), 206–211.
9. Gaskell, G., & Bauer, M. W. (2013). *Genomics and society: Legal, ethical and social dimensions*. Routledge.
10. Verissimo, P. E., & Bessani, A. (2013). E-biobanking: What have you done to my cell samples? *IEEE Security & Privacy*, 11(6), 62–65.
11. Burton, P. R., Hansell, A. L., Fortier, I., Manolio, T. A., Khoury, M. J., Little, J., & Elliott, P. (2009). Size matters: Just how big is BIG? Quantifying realistic sample size requirements for human genome epidemiology. *International journal of epidemiology*, 38(1), 263–273.
12. Haussler, D., Patterson, D. A., Diekhans, M., Fox, A., Jordan, M., Joseph, A. D., Ma, S., Paten, B., Shenker, S., Sittler, T., & Stoica, I. (2012). *A million cancer genome warehouse*. California University Berkeley Department of Electrical Engineering and Computer Science.
13. Watson, R. W. G., Kay, E. W., & Smith, D. (2010). Integrating biobanks: Addressing the practical and ethical issues to deliver a valuable tool for cancer research. *Nature Reviews Cancer*, 10(9), 646–651.

14. Bessani, A., Brandt, J., Bux, M., Cogo, V., Dimitrova, L., Dowling, J., Gholami, A., Hakimzadeh, K., Hummel, M., Ismail, M., Laure, E., Leser, U., Litton, J.-E., Martinez, R., Niazi, S., Reichel, J., & Karin, Z. (2015). BiobankCloud: A platform for the secure storage, sharing, and processing of large biomedical data sets. In *Biomedical data management and graph online querying* (pp. 89–105). Springer.
15. Gottweis, H. (2012). *Biobanks for Europe: A challenge for governance: Report of the expert group on dealing with ethical and regulatory challenges of international Biobank Research*. EUR-OP.

Ultra-Fast Charging Challenges in Grid Connected Charging Station: A Review



Nilam S. Patil and Rajin M. Linus

Abstract Electric Vehicles (EVs) and available charging infrastructures are unable to provide long distance trips without interruption due to the necessity of waiting long time to recharge the battery and moderate speed range. Charging time of EV has been a major factor that influences the customer to not attract much towards EVs. The ultra-fast charging (UFC) provides solution for such issue which charges EV with minimum time. Nevertheless, it is quite challenging and complicated to realize UFC due to the developments of battery cells, charging methods and impact on electric grid. The widespread of EV usage and necessitates to increase the charging demand have a number of effects on the electric grid. This paper aims to review analysis UFC in EV by including basic concepts, charging levels, types of chargers, positive and negative impacts of UFC on electric grid. Different fast charging strategies and power converter topologies for EV are presented and compared in this article.

Keywords SDG7 · Clean energy · Electric Vehicle · Ultra-fast charging

1 Introduction

Currently, Electric Vehicles (EVs) have been gaining popularity around the world due to economic and environmental benefits and development based on achieving Seventh Sustainable Development Goals (SDG7) in the year 2030. Demand for EVs has been increasing continuously day by day [1]. As per the global reports, IC engine-based vehicle contribute huge amount of pollution worldwide. Nevertheless, EVs are environment friendly and the possibilities of regenerative braking will increase the vehicle efficiency [2]. The overall global EV sales have been rising day by day from the year 2010–2020 as shown in Fig. 1a. Mostly, EVs can also be referred as Plug-in

N. S. Patil (✉)
PVPIT, Budhgaon, Sangli, Maharashtra, India
e-mail: nilamspatil.ale@pvpitsangli.edu.in

N. S. Patil · R. M. Linus
Sanjay Ghodawat University, Kolhapur, Maharashtra, India

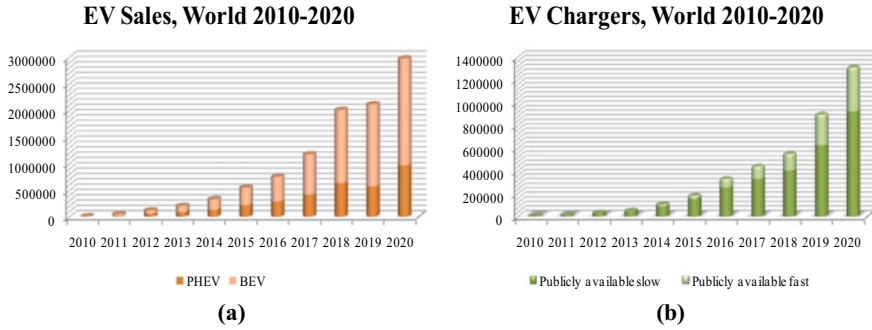


Fig. 1 a EV sales in world, 2010–2020. b EV chargers in world, 2010–2020

Hybrid Electric Vehicles (PHEVs) and Battery Electric Vehicles (BEVs). As EV sales are growing, there will be increase in number of charging stations worldwide from the year 2010–2020 as in Fig. 1b. Chargers have a charging power of greater than 22 kW are known as fast chargers whereas, the charging power of slow chargers is less than 22 kW [3]. As per the global report, in the year 2020, more than 90% of new vehicle registrations was EV based [4].

Among the different type of chargers for EV, DC fast chargers are more efficient in instances where the charging time is the constraints especially when commuting over a long distance with in short span of time. However, charging a battery at high power levels on a regular basis may reduce the battery’s life expectancy [5].

The EV sector has experienced rapid growth in recent years [6]. On the other hand, in order to achieve the predicted EV market penetration with respect to range anxiety, cost, charging infrastructure and most importantly charging time, some significant social constraints must be overcome [7]. Industry is working in tandem to lower charging time, as the range of EV increases. The charging method used for this purpose is known as quick, fast or ultra-fast charging and it uses power levels up to 120 kW [8].

EV owners demand for charging stations with characteristics that meet their need. They should recharge the vehicle’s on-board battery in less than 10 min. The researchers have been examining UFC to charge the battery within minimum time [9]. As stated, UFC for EV impacts on electric grid are addressed in this article.

2 Ultra Fast Charging Stations

The capability to recharge EVs when compared with regular petrol refueling is less than 20 min, is named as Ultra-fast charging [10]. The design of an off-board UFC is shown in Fig. 2. AC to DC converter is the first stage which is used to absorb the proper amount of electricity from the grid while maintaining input sinusoidal current shape (minimal distortion and harmonics) [11]. High-frequency DC/DC converter

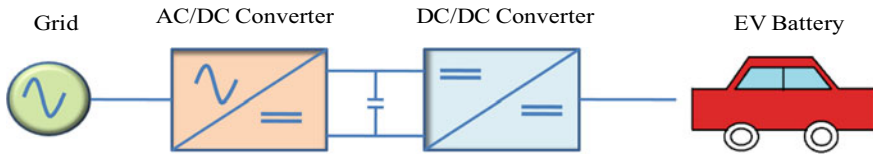


Fig. 2 Schematic diagram of DC fast charger

is the second stage, which provides controlled DC output current (battery charging process regulation) as well as grid galvanic isolation [12]. Both converter stages can be made to work in either a unidirectional or bidirectional mode.

2.1 Fast Charging Topologies

DC fast charger includes specifically two stages namely front end rectification followed by chopping operation. Accordingly, the topologies are classified as follows:

2.1.1 Topology 1: 3-Phase Fully Controlled Rectifier

In this topology, the battery is charged using a 3-phase, 6-pulse SCR rectifier with filter circuit. To isolate the 3-phase supply from the power converter, a 3-phase transformer is used as shown in Fig. 3. It has the benefits such as simplicity, no requirement for a DC-DC converter stage, design robustness, handle high voltage and current. SCR firing reduces the complexity of switching the rectifier. However, it suffers from drawbacks such as battery current ripple of almost 3% and poor input power factor [13].

2.1.2 Topology 2: 12 Pulse Diode Rectifier Followed by 3-Phase Inverter and 3-Phase Diode Rectifier

3-phase transformer with two secondary windings is feeding 12 pulse diode rectifier as shown in Fig. 4.

Total current is shared by two diode bridges. The DC output is now given to 3-phase inverter. It is passed to high frequency transformer and then rectified by diode rectifier. The LC filter is used to reduce ripples in DC current and voltage [14]. Due to higher switching frequency of IGBT based inverter, ripple in currents is decreased to 0.5% in this topology. Due to the incorporation of a 12-pulse diode rectifier, input current harmonics are also minimal. However, the use of a high frequency transformer, high frequency diodes and two transformers increase the cost of the system.

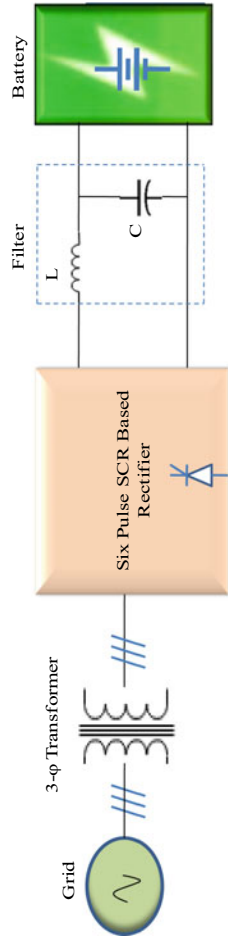


Fig. 3 3-Phase fully controlled rectifier

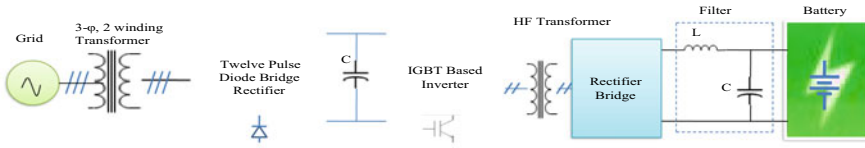


Fig. 4 12 Pulse diode rectifier followed by 3-phase inverter and 3-phase diode rectifier

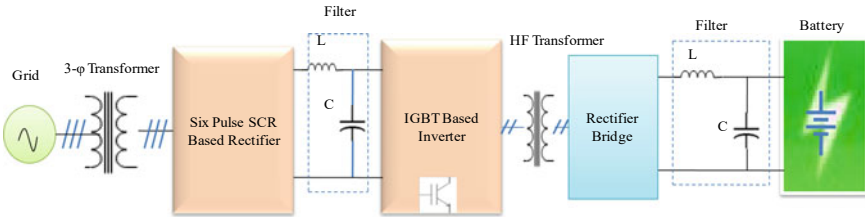


Fig. 5 6 Pulse diode rectifier followed by 3-phase inverter and 3-phase diode rectifier

2.1.3 Topology 3: 6 Pulse Diode Rectifier Followed by 3-Phase Inverter and 3-Phase Diode Rectifier

Here, the 12 pulse diode rectifier is replaced by controlled rectifier as emphasized in Fig. 5. It allows to supply variable DC voltage by adjusting the firing angle. The remaining part is same as that of previous technique. Due to less number of switches, the current and voltage stress is increased. Also input AC current has higher % THD and poor power factor [15].

2.1.4 Topology 4: 12 Pulse Diode Rectifier Feeding 3-Level Midpoint Clamped Buck Converter

12 Pulse diode rectifier is used to feed 3-level buck converter as shown in Fig. 6.

It consists of two mid-point clamped capacitors, which helps to reduce voltage stress on switches by 50%. It has benefits like higher input power factor, use of less switches in subsequent stages, reduced voltage and current stress [16].

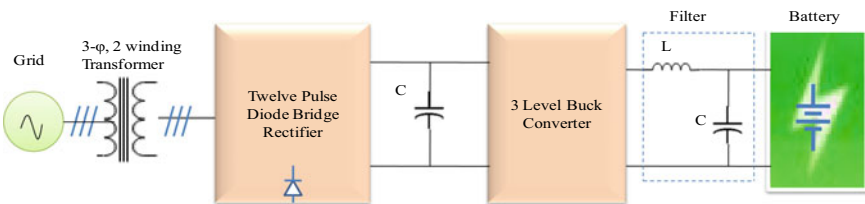


Fig. 6 12 Pulse diode rectifier feeding 3-level midpoint clamped buck converter

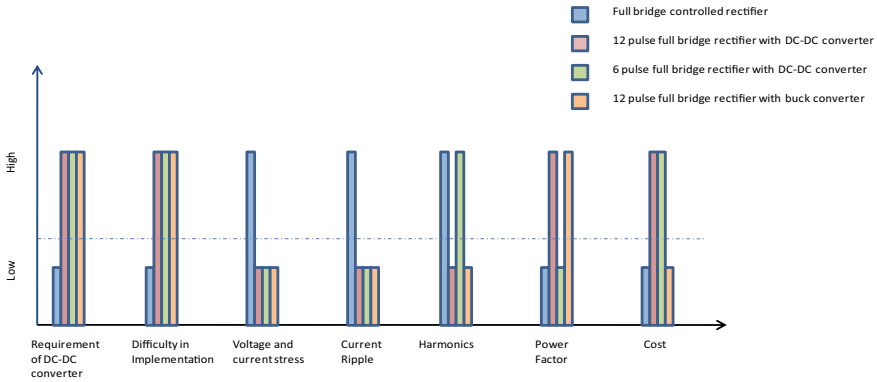


Fig. 7 Comparison between pros and cons of charging topologies

Figure 7 compares and summarizes the charging topologies with respect to number of factors as previously described. Harmonics are high in topology 1 and topology 3 owing to the use of a 6-pulse SCR-based rectifier, resulting in a lower power factor, whereas harmonics are low in topology 2 and topology 4 owing to the use of a 12-pulse SCR-based rectifier, resulting in a higher power factor. Topology 1 is the simplest and most cost-effective among the four topologies since it employs less converters and switches than topologies 2, 3, and 4. Current ripple is reduced in topologies 2, 3, and 4 as it uses DC-DC converter as compared with topology 1. Topology 2 and topology 3 requires high frequency (HF) transformer which makes them costlier than topology 1 and topology 4. Based on assessment of all topologies, topology 4, which consists of a 12 pulse diode rectifier feeding 3-level midpoint clamped buck converter is the best fit for EV charging due to lower voltage and current stress, reduced harmonics, high power factor and cost effectiveness.

3 Impacts of UFC on Electric Grid

Generation, transmission, and distribution are the three basic components of the utility system. Despite the fact that EVs would require a large amount of electricity, when installed in large numbers. According to the study, EVs will consume 95% of overall electrical load by the year 2050 [17]. The wide use of EVs necessitates have been increasing the charging demand, which can have a number of adverse effects for the electric grid [18]. The positive and negative effects of EV charging on the electric grid will be explored below.

3.1 *Negative Impacts*

Transformer overloading: As EVs are increasing day by day, a new peak demand may emerge, it implies pressure on power transformers and perhaps overloading them. Increase in temperature due to overloading may reduce the life time of transformer [19].

Voltage Stability: Since EVs can consume much more power in a short period and the load characteristics are non-linear when differs from those of household and industrial loads. Such load characteristics would have fixed impedance, also system can handle a large number of vehicles, but predicting the EV load in advance is not feasible, the power consumption is unpredictable; when charging multiple EVs at a time, distribution variables may be violated. To overcome this issue, solution has proposed in [20]. Voltage instabilities can be addressed by modifying the transformer's taping as investigated in [21].

Voltage Sag: Voltage sag occurs when there is an decrease in voltage for the duration of half cycle to one minute. It usually happens as a result of overloading and inrush currents when electrical equipment is turned on for the first time [22].

Harmonic Injection: As battery discharges, it needs to charge to propel EV. While charging and discharging, it inject harmonics in grid. Total harmonic distortion (THD) of source voltage shall not exceed 8% in accordance with global standards (EN 50160). The usage of inductor capacitor inductor (LCL) filters helps to reduce THD distortion as discussed in [23].

Phase and voltage unbalance: Since EV chargers are single-phased, when multiple EVs are powered along with the same phase, phase unbalance can occur [24]. Voltage imbalances can be caused by current imbalances. EV grid integration will also cause a voltage loss and variation at EV charger connectivity sites [25].

Power loss: The extensive usage of EVs in the grid results in a large increase in real power demand, resulting in power failure in the distribution system [26]. Coordinated charging can reduce power losses, however increases the load factor of the power grid. The proper location and capability of charging stations help to decrease the grid power losses [27].

3.2 *Positive Impacts*

Renewable energy sources (RES) support: The combination of EV and RES opens up the possibility of installing solar photovoltaic (PV) panels on roof of the vehicle. As a result, EV charges continuously when sun rays are available and owner of the vehicle is engaged in other activities. A number of benefits using PV to charge EV are

discussed [28]. Using EVs as a renewable energy barrier able to decrease emissions and save money [29].

Vehicle to Grid (V2G) technology: V2G is a concept in which parked or idle EV can operate as energy storage devices (ESDs), which delivers energy at the correct time. EVs can be used as an ESD to provide an energy buffer. EVs function as a load during periods of high energy output, but act as dynamic storage during periods of low energy production by delivering power back to the electrical grid [30].

4 Discussion

Topology 1 is the simplest to implement and the most reliable, although it has a higher battery current ripple and a lower power factor. Topology 2 provides better control and a higher power factor, but it is more expensive due to the use of high frequency transformers and diodes. The 12 pulse diode rectifier is replaced by controlled rectifier in topology 3. Topology 4 features a lower voltage and current stress, low harmonics, a higher power factor, and is more cost-effective. FCS's impact on the distribution MV grid can be minimized [31] by energy storage systems (ESSs), which helps to reduce high power consumption as well as provide extra network functions. Furthermore, ESS can boost the voltage level when there is a high voltage drop in transmission lines. However, voltage control is used for this purpose. The combination of RES and FCS helps to reduce the FCS's impact on the grid even more [32]. In fact, using solar PV panels, batteries of EV can be charged in a day under normal operation which reduces the risk of the MV network being overloaded. On the other hand, at night, when sun rays are not available, grid helps to charge EV batteries. If needed, EVs can also assist the grid during peak load demand [33].

5 Conclusion

This article explores the newest development and significant challenges in the field of EV charging infrastructure, different levels of charging, types of EV chargers and various fast charging topologies. According to review study, EVs have potential to entirely replace traditional gasoline-powered automobiles. The most widely used charging method for EV is conductive charging. On-board chargers (also called as AC chargers or slow chargers) and off-board chargers (also called as DC chargers or fast chargers) are main two types of conductive charging systems. Even though AC chargers have simple access for charging, they are unable to charge battery rapidly and also have power constraints. DC chargers, on the other hand, feature a high power output and help to reduce charging time. Many regions are installing UFC along roads which charges EV with minimum time, yet they are still insufficient to alleviate EV consumers' concerns about range. Furthermore, the wide uses of

EVs necessitates increased charging demand, which can have a number of positive and negative consequences on electric grid based on the topologies. However, as per these review negative consequences can be mitigated using coordinated charging or smart charging as discussed.

References

1. Gonzalez, L., Novella, H., Gutierrez, E., Ventura, J., & Mogas, P. (2013). EVIC (electric vehicle intelligent charging). In *2013 World Electric Vehicle Symposium and Exhibition (EVS27)* (pp. 1–8). Barcelona, Spain.
2. Cikanek, S. R., & Bailey, K. E. (2002). Regenerative braking system for a hybrid electric vehicle. In *Proceedings of the 2002 American Control Conference (IEEE Cat. No. CH37301)* (Vol. 4, pp. 3129–3134). Anchorage, AK, USA.
3. <https://www.iea.org/articles/global-ev-data-explorer>
4. Global EV Outlook. (2021). p. 101.
5. Srdic, S., & Lukic, S. (2019). Toward extreme fast charging: Challenges and opportunities in directly connecting to medium-voltage line. *IEEE Electrification Magazine*, 7(1), 22–31.
6. Muñoz, J., Martin, S., Ostermeier, D., Stadlbauer, Hummitzsh, U., & Arkadiy, A. (2017). (LION SMART) Analysis of the state of art on BMS-everlasting project.
7. Hosseinpour, S., Chen, H., & Tang, H. (2015). Barriers to the wide adoption of electric vehicles: A literature review based discussion. In *2015 Portland international conference on management of engineering and technology (PICMET)* (pp. 2329–2336). Portland, OR, USA.
8. Cabeza, T., Sanz, J. F., Calavia, M., Acerete, R., & Cascante, S. (2013). Fast charging emulation system for electric vehicles. In *2013 World Electric Vehicle Symposium and Exhibition (EVS27)* (pp. 1–6). Barcelona, Spain.
9. Pasquale, F., Pasquale, A. D., Iannuzzi, D., & Pagano, M. (2021). *Electric ultra fast charging stations: A real case study*. IEEE Xplore.
10. Meyer, D., & Wang, J. (2018). Integrating ultra-fast charging stations within the power grids of smart cities: A review. *IET Smart Grid*, 1(1), 3–10.
11. Tu, H., Feng, H., Srdic, S., & Lukic, S. (2019). Extreme fast charging of electric vehicles: A technology overview. *IEEE Transactions on Transportation Electrification*, 5(4), 861–878.
12. Cittanti, D., Gregorio, M., & Bojoi, R. (2020). Digital multi-loop control of a 3-level rectifier for electric vehicle ultra-fast battery chargers. In *2020 AEIT International Annual Conference (AEIT)* (pp. 1–6). Catania, Italy. <https://doi.org/10.23919/AEIT50178.2020.9241196>
13. Cittanti, D., Gregorio, M., Armando, E., & Bojoi, R. (2020). Digital multi-loop control of an LLC resonant converter for electric vehicle DC fast charging. In *2020 IEEE Energy Conversion Congress and Exposition (ECCE)* (pp. 4423–4430). Detroit, MI, USA. <https://doi.org/10.1109/ECCE44975.2020.9236177>
14. Ahmadi, M., Mithulananthan, N., & Sharma, R. (2016). A review on topologies for fast charging stations for electric vehicles. In *2016 IEEE international conference on power system technology (POWERCON)* (pp. 1–6). Wollongong, Australia.
15. Aggeler, D., Canales, F., Zelaya-De La Parra, H., Coccia, A., Butcher, N., Apeldoorn, O. (2010). Ultra-fast DC-charge infrastructures for EV-mobility and future smart grids. In *2010 IEEE PES Innovative Smart Grid Technologies Conference Europe (ISGT Europe)* (pp. 1–8). Gothenberg.
16. Srilatha, A., Pandian, D. A., & Varma, D. P. S. *Review of different methods and topologies for fast charging of electric vehicles* (p. 13).
17. Tan, L., Wu, B., Yaramasu, V., Rivera, S., & Guo, X. (2016). Effective voltage balance control for bipolar-DC-bus-fed EV charging station with three-level DC–DC fast charger. *IEEE Transactions on Industrial Electronics*, 63(7), 4031–4041.

18. Kasten, P., Bracker, J., Haller, M., & Purwanto, J. (2016). Electric mobility in Europe—Future impact on the emissions and the energy systems. <http://www.oeko.de/fileadmin/oekodoc/Assessing-the-status-of-electrification-of-the-road-transport-passengervehicles.pdf>
19. Yao, L., Lim, W. H., & Tsai, T. S. (2017). A real-time charging scheme for demand response in electric vehicle parking station. *IEEE Transactions on Smart Grid*, 8(1), 52–62.
20. Shareef, H., Islam, Md. M., & Mohamed, A. (2016). A review of the stage-of-the-art charging technologies, placement methodologies, and impacts of electric vehicles. *Renewable and Sustainable Energy Reviews*, 64, 403–420.
21. Mwasilu, F., Justo, J. J., Kim, E.-K., Do, T. D., & Jung, J.-W. (2014). Electric vehicles and smart grid interaction: A review on vehicle to grid and renewable energy sources integration. *Renewable and Sustainable Energy Reviews*, 34, 501–516.
22. Qian, K., Zhou, C., Allan, M., & Yuan, Y. (2011). Modeling of load demand due to EV battery charging in distribution systems. *IEEE Transactions on Power Systems*, 26(2), 802–810.
23. Go, H.-S., Cho, I.-H., Kim, G.-D., & Kim, C.-H. *A study on EV charging scheme using load control* (p. 9).
24. Alhamrouni, I., Wahab, W., Salem, M., Rahman, N. H. A., & Awal, L. (2019). Modeling of micro-grid with the consideration of total harmonic distortion analysis. *Indonesian Journal of Electrical Engineering and Computer Science*, 15(2), 581.
25. Pappalardo, C. M., Lombardi, N., Dašić, P. V., & Guida, D. (2019). Design and development of a virtual model of an electric vehicle of category L7. *IOP Conference Series: Materials Science and Engineering*, 568(1), 012114.
26. Cheng, S., Wei, Z., Shang, D., Zhao, Z., & Chen, H. (2020). Charging load prediction and distribution network reliability evaluation considering electric vehicles' spatial-temporal transfer randomness. *IEEE Access*, 8, 124084–124096.
27. Ahmadian, A., Mohammadi-Ivatloo, B., & Elkamel, A. (2020). A Review on plug-in electric vehicles: Introduction, current status, and load modeling techniques. *Journal of Modern Power Systems and Clean Energy*, 8(3), 412–425.
28. Sadeghi-Barzani, P., Rajabi-Ghahnavieh, A., & Kazemi-Karegar, H. (2014). Optimal fast charging station placing and sizing. *Applied Energy*, 125, 289–299.
29. Clement-Nyns, K., Haesen, E., & Driesen, J. (2010). The Impact of charging plug-in hybrid electric vehicles on a residential distribution grid. *IEEE Transactions on Power Systems*, 25(1), 371–380.
30. Habib, S., Khan, M. M., Abbas, F., Sang, L., Shahid, M. U., & Tang, H. (2018). A comprehensive study of implemented international standards, technical challenges, impacts and prospects for electric vehicles. *IEEE Access*, 6, 13866–13890.
31. Nguyen, H. N. T., Zhang, C., & Mahmud, M. A. (2015). Optimal coordination of G2V and V2G to support power grids with high penetration of renewable energy. *IEEE Transactions on Transportation Electrification*, 1(2), 188–195.
32. Bertini, D., Mauri, G., Fasciolo, E., & Fratti, S. (2013). The impact of EV'S fast charging stations on the MV distribution grids of the Milan metropolitan area. In *22nd International Conference and Exhibition on Electricity Distribution (CIRED 2013)* (pp. 1266–1266). Stockholm, Sweden.
33. Shiramagond, T., & Lee, W.-J. (2018). Integration of renewable energy into electric vehicle charging infrastructure. In *2018 IEEE international smart cities conference (ISC2)* (pp. 1–7). Kansas City, MO, USA.

Sustainable Integrated Renewable Energy System for a Cluster of Remote Villages in Indian Context



Naveen Rayaral and Prashanth P. Revankar

Abstract The primary concern of the Nations worldwide has been the growing energy demand. The present study has identified cluster of remote villages nearby Sringeri place, chickmagalur district of Karnataka state, India, for the assessment of Resources and their sustainability. HOMER based Simulation were carried out on PV-WIND-MH-HK systems considering the Two different Load strategies as Development side Load strategy and Demand side Load strategy. The possible resources combinations were investigated on the basis of Net Present Cost (NPC) and Cost of Energy (COE) for obtaining the optimal results. The results showed that Development side load strategy was optimal for PV-MH-HK combination with \$218,191.5 and \$0.167/kWh for NPC and COE values. On the contrary, Demand-side Load strategy yielded values of NPC and COE as \$121,825 and \$ 0.159/KWh respectively. From the results it has shown that the WIND resource is not a suitable option for the integration due to low wind energy Potential. Multiyear year simulations taking 10 year period shows that 4.46% increase in the COE and the energy production is dropped by 4.64%.

Keywords Simulation · Load strategies · Optimization studies · Cost of energy · Net present cost · Multiyear simulation

1 Introduction

Energy availability is the primary criteria for any development of any location/area/remote sites [1]. India has renewable energy potential of 900 GW from resources wind-12%, solar-83%, Bio energy-3% and small hydro by 2.2% [2]. Rural electrification and remote area electrification is one of the revolutionary development

N. Rayaral (✉)

Proudhadevaraya Institute of Technology, Hospet, Karnataka, India

e-mail: naveenganesh@pdit.ac.in

P. P. Revankar

KLE Technological University, Hubballi, Karnataka, India

which poses many challenges to provide the electricity to the villages. There are many socio-economic challenges need to overcome and provide the Grid extension [3]. It is found to be uneconomical to provide the grid extension to the remote hilly areas and another reason is that it affects the flora and Fauna of the place [4, 5]. The remote areas are usually found with one or more potential resources. Utilizing the available resources is far better than passing the Grid extension. The resources are sustainable for their livelihood and assessing the resources available at the site will be able to meet their energy demand. The optimization process for better integration selection of the systems is to be carried out to assess the feasibility and suitability of the system [6]. A study on 9 villages was carried out using HOMER [7] were investigated to obtain the values of NPC and COE taking MHG/BGG/PV/DG components for all possible combinations. Study on DSM strategy for standalone IRES [8] in the remote area is made taking PV/WIND/MHG/BGG/BMG configuration was made to assess the cost of COE and NPC using the Genetic algorithm approach. Optimal Modeling analysis of IRES for the remote area electrification [9, 10] in Chamaraja Nagar District, Karnataka is studied for obtaining the optimal results.

From the various literatures, it can be inferred that the integration of the Renewable energy systems is feasible and sustainable for the Remote areas. The studies related to Biomass–Biogas with Diesel generator is of more concern and found less literature on the part of Integrating the Micro-Hydro and Hydro-Kinetic turbine. This study is carried out in sringeri Taluka of Karnataka state, India to obtain the possible optimal results for various combinations on PV-WIND-MH-HK systems.

2 Objectives and Methodology

Motivation for this study is that to ascertain the sustainable integrated system for the remote cluster of villages identified. Investigate on the available resources for their feasibility and sustainability and to get the optimal results for NPC and COE for the each combination of the renewable energy system. This study is first carried out by assessing the resources of Micro Hydro by using the Google save location Mobile app to get the exact geographical coordinates of the location, and then it is plotted in Google earth app and obtains the elevation contours using ArcGis software. Load demand for the villages is calculated by considering Four quarters of a year. The load demand is calculated by taking the information from the local people and the members of the Gram Panchayat by preparing the questionnaire. The HOMER simulation tool is used to get the optimal results for each combination. Optimal results are obtained on the basis of two Load strategies as Development side Load strategy and Demand side Load strategy.

3 Load Demand and Resource Assessment of the Study Area

The Remote villages are identified within the radial distance of 1–2 km and study location is having the geographical coordinates as Longitude 75.152837 E and Latitude 13.470276 N.

Table 1 shows the demography of the villages identified and these people originally belong the scheduled tribes and living here for so many years in the mid of the wild life sanctuary.

The load demands are assessed based upon their living style and their usage of energy during various seasons. These are divided into four quarters. Load point are estimated for each house and their consumption are assessed in each quarter of a year as shown in Table 2. Development side load strategy is one which loads are estimated on the basis of Developments required at the villages such as hospitals, schools, community halls etc. Demand side load strategy is one which loads are calculated with the present situation at the villages. They do have only residential facilities and lack of various government facilities. These estimations are shown in Figs. 1 and 2 respectively.

3.1 Wind (WIND) and Solar Energy (PV) Potential Assessment

The Data of 10 years from 2008 to 2018 [11] is retrieved from the Typical Meteorological year (TMY) data. The wind data is also collected from the local IMD (Indian Meteorological Department) center at Karwar, Karnataka. The difference of IMD Data and TMY is noted and the wind patterns are observed in each case. The wind velocity is observed high during June–September from the Data. Typical meteorological data for wind speed generated and mean wind speed was found to be 4.2 m/s.

Solar energy assessment is carried out using Metronome 7.3 software by giving the Geographical coordinates and other factors of azimuth angle, tilt angle are given as input. Then the solar intensity in KWh/m²/day is calculated. The average solar

Table 1 Demography of the villages

Name of village	No. of houses	No. of population
Tarulli Kodige	27	132
Anukulli bylu	15	45
Bylubaru	6	25
Shunti hakkalu	6	18
Kote	25	112
Total	79	332

Table 2 Load points for estimation of hourly demand

Appliances	Quantity
<i>Domestic loads</i>	
CFL LIGHT (40 W)	4 Points in each House Hold
LCD TV (70 W)	1 Point in each House Hold
Radio (25 W)	1 Point in each House Hold
Fan (75 W)	2 Points in each HH
<i>Community loads</i>	
CFL LIGHT (40 W)	3 points for Hospital,4 points for School Building
Refrigerator (1000 W)	1 Point for Hospital Usage
Fan (75 W)	3 points for Hospital, 4 points for School Building
<i>Commercial loads</i>	
CFL LIGHT (40 W)	2 shops having 1 point for 79 HH
Street light (60 W)	1 pole for every 3 HH
Fan (75 W)	2 shops having 1 point for 79 HH
Pumping water (3.76 KW)	3 water pumps for 79 HH
Flour mill (5 KW)	1 Point having 5 KW for 79 HH

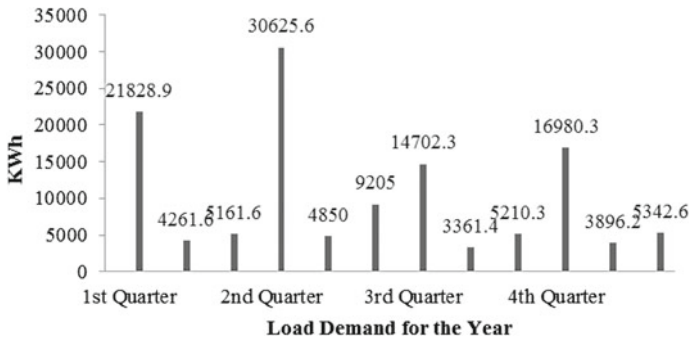


Fig. 1 Load demand for development side load strategy

intensity is found to be 5.44 KWh/m²/day for 10 years of solar intensity data. The solar intensity is found to be high during the month February–June from the Data. Table 3 shows the calculation of Rainfall Data by CN method.

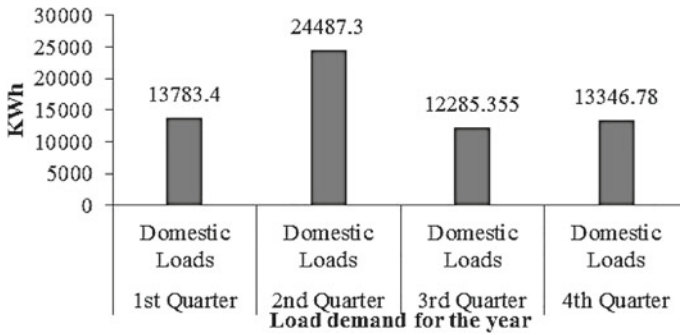


Fig. 2 Load estimation for demand side load strategy

Table 3 Rainfall data in mm and calculation of discharge (Q) by CN method

Months	2009–12	2013–16	2017–20	CN	Avg Q (m ³ /s)
January	6.11	2.84	6.76	52	0.835
February	3.42	9.175	4.96	52	0.845
March	10.89	15.83	16.75	52	0.745
April	65.5	41.9	62.42	52	0.130
May	92.61	67.69	200.32	52	3.898
June	99.94	69.54	190.63	52	3.706
July	123.31	85.74	214.75	52	5.265
August	122.25	76.7	220.76	52	5.342
September	125.37	76.6	237.24	52	6.0451
October	129.41	71.47	442.15	52	15.175
November	103.07	32.77	87.19	52	0.93592
December	19.19	8.92	62.89	52	0.0570

3.2 Micro-hydro (MH) and Hydro-kinetic (HK) Resource Assessment

In order to assess the Hydro potential at the site, Curve number (CN) method developed by the soil conservation services, USA in 1969 is used to estimate the actual run off depth based on the ten year Rainfall data.

Actual run off depth is calculated by the Eq. 1 as [12]

$$Q_D = \frac{(I - 0.2S)^2}{(I + 0.8S)} \quad I > 0.2S \tag{1}$$

$$S = \frac{25,400}{CN} - 254 \tag{2}$$

where Q_D is the direct surface run off depth (mm), I is the monthly rainfall (mm) and S is the Maximum potential retention in watershed (mm) and CN is curve number ranging from 48 to 58 for dense forest. The peak rate of run off or discharge are calculated by the equations as follows

$$T_P = 0.6T_C + \sqrt{T_C} \quad (3)$$

$$T_C = 0.0195 \left[\sqrt{L_w^3 / H_{net}} \right]^{0.77} \quad (4)$$

$$Q = \frac{0.0208 \times A \times Q_D}{T_P} \quad (5)$$

where Q is the rate of runoff or discharge in m^3/s , T_P is the time to peak run off (hour), T_C is the time of concentration (hour), L_w is the length of the water shed and A is the area of the Water shed (Figs. 3 and 4).

The study site is identified with water stream suitable for generating the power using the Hydrokinetic turbine. Figure 6 shows the sketch of Hydro resource available at the site. The data is recorded to assess the possibility of power generation. This velocity is obtained using the Electro-Mechanical current meter device. Figure 5 shows the Average monthly Data, in which the current meter is used to get the velocity readings for mid-day of the month for 12 h, by keeping the device at 0.5, 1 and 2 m depth from the surface level of water.

Fig. 3 Elevation contours from ArcGIS



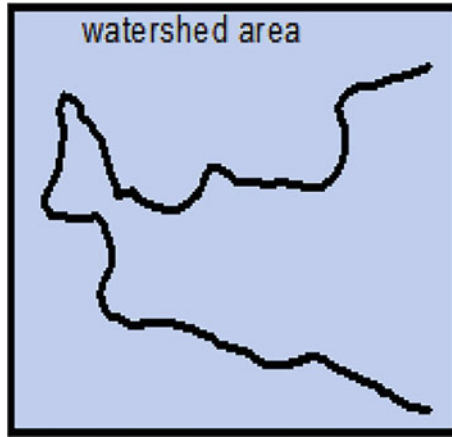


Fig. 4 Water shed area

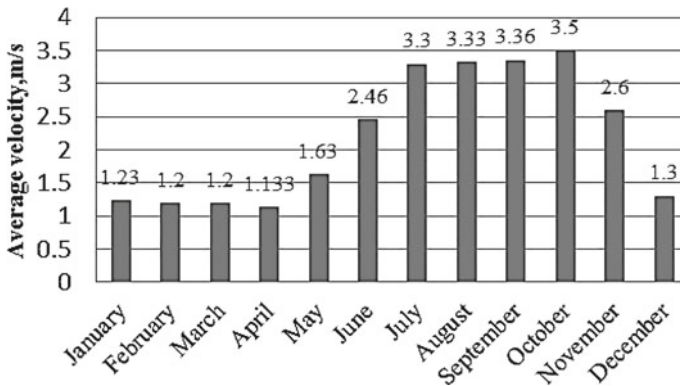


Fig. 5 Average velocity of stream velocity for hydro-kinetic resource recorded at the site

4 Optimization Studies

This study is made to assess the optimization of the different combination of integrations of renewable energy using HOMER tool developed by NREL, USA for the simulation of Hybrid renewables system. The NPC (Net Present cost) and COE (cost of energy) are the two parameters used for obtaining the optimal combination suitable as sustainable resources.

In economic analysis, NPC is calculated by Eq. 7 [13] as

$$NPC = \frac{C_{Totalyear}}{CRF}$$

$$C_{Totalyear} = C_{FCyear} + C_{RCyear} + C_{OMyear}$$

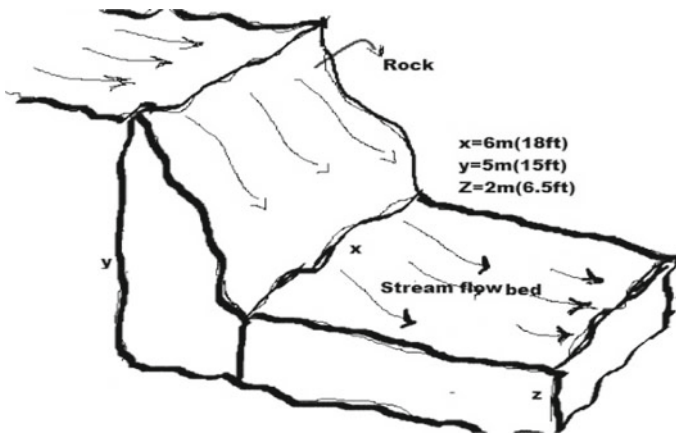


Fig. 6 Hydro-kinetic resource model at the site

$$CRF = \frac{i(1+i)^N}{(1+i)^N - 1} \tag{6}$$

Cost of Energy (COE) is the annualized Total cost of producing the Energy generation to the Total energy served by the Renewable energy systems given by Eq. 7 as

$$COE = \frac{C_{Totalyear}}{E_{served}} \tag{7}$$

E_{served} is the Total energy served in KWh.

5 Results and Discussions

Tables 4 and 5 shows the individual simulations for possible integration of systems.

Simulation results shows that for the integrated combination of MH-HK-BATT having the least optimal result of NPC \$167,816 and COE of 0.154\$/KWh from all the possible combinations of systems in case of Development side Load strategy. In case of Demand Load strategy the combination for least optimal result is also MH-HK-BATT with a NPC value of \$121,825 and COE of \$0.159\$/KWh. Therefore from the simulations results it can be inferred that this combination is sustainable at the site. It is also been observed that the combination of PV-MH-HK with battery is also suitable and more feasible than the later combination.

From Fig. 7 shows the leveled cost of energy \$/KWh is increased by 4.46% and PV production is decreased by 4.55% in the 10 year simulation study to one of the optimal result.

Table 4 Simulations results on development side load strategy annual average-342.68 KWh/day-65 KW

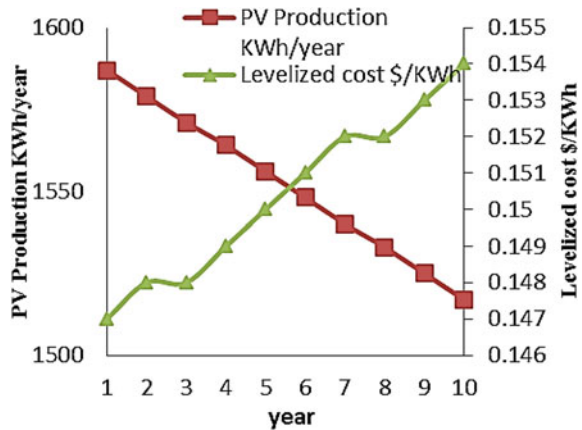
S. No	RE system	PV (KW)	WIND (Nos)	MH	HK (Nos)	Converter	Batt	NPC (\$)	COE \$/kWh
1	PV-BATT	116				48.7	729	\$987.814	0.686
2	PV-WIND-BATT	115	1			44.0	643	\$1.01 M	\$0.693
3	WIND-BATT		14			46.3	318	\$2.6 M	1.77
4	MH-HK-BATT			57.7	2	10.7	46	\$167.816	0.154
5	WIND-MH-HK-BATT		1	57.7	2	10.9	32	\$784.769	0.692
6	PV-MH-HK-BATT	1.8		49.4	2	26.6	129	\$218.191	0.167
7	PV-WIND-MH-HK-BATT	1.78	1	49.4	2	33.2	151	\$817.281	0.587

Table 5 Simulation results on demand side load strategy 176 KWh/day and 46 KW peak demand

S. No	RE system	PV (KW)	WIND	MH	HK	Converter	Batt	NPC (\$)	COE \$/kWh
1	PV-BATT	76				43.3	476	\$626.489	0.820
2	PV-WIND-BATT	11.7	1			35.3	245	\$818.623	1.08
3	WIND-BATT		2			25.2	168	\$1.4 M	1.9
4	MH-HK-BATT			57.7	2	1.72	8	\$120.841	0.155
5	WIND-MH-HK-BATT		1	57.7	2	0.87	2	\$697.170	0.875
6	PV-MH-HK-BATT	1		57.7	2	1.74	5	\$121.825	0.159
7	PV-WIND-MH-HK-BATT	0.4	1	57.7	2	0.173	1	\$697.049	0.877

System combination involves PV-BATT/PV-WIND-BATT/WIND-BATT/MH-HK-BATT/WIND-MH-HK-BATT/PV-MH-HK-BATT and PV-WIND-MH-HK-BATT.

Fig. 7 Multiyear simulation results



6 Conclusions

This study presents the feasibility of optimal Integration of various combinations of resources available at the remote cluster of villages in place of sringeri, Karnataka state, by considering the values of NPC (\$) and COE (\$/KWh). It is found from the resource assessments and simulations that the integration of PV-MH-HK is more sustainable and feasible to meet their energy demand. The two strategies are considered for the simulation of seven combinations of integrated renewable systems. In both the strategies it was observed that the optimal result of PV-MH-HK gives NPC values of \$218,191 and \$121,825, COE values of 0.167\$/KWh and 0.159\$/KWh. From the study it is concluded that integration with WIND system is not a feasible option. Multiyear simulations give increase of 4.5% and decrease of 4.5% linearly with respect to the value of COE and PV degradation. In overall the PV-MH-HK combination is more sustainable and feasible for the remote cluster of villages.

References

1. Code, E. C. B. (2017). Bureau of energy efficiency, Energy conservation Building code, Bureau of energy efficiency, New Delhi, India.
2. Cuce, E., & Cuce, P. M. (2013). A comprehensive review on solar cookers. *Applied Energy*, *102*, 1399–1421.
3. Dugoua, E., Liu, R., & Urpelainen, J. (2017). Geographic and socio-economic barriers to rural electrification: New evidence from Indian villages. *Energy Policy*, *106*, 278–287.
4. Ellabban, O., Abu-Rub, H., & Blaabjerg, F. (2014). Renewable energy resources: Current status, future prospects and their enabling technology. *Renewable and Sustainable Energy Reviews*, *39*, 748–764.
5. Hub, E. S. (2018). The European Commission's science and knowledge service. <https://ec.europa.eu/jrc/en/pvgris>
6. Naveen, R., Revankar, P., & Rajanna, S. (2020). Integration of renewable energy systems for optimal energy needs—A review. *International Journal of Renewable Energy Research (IJRER)*, *10*(2), 727–742.
7. Patel, A. M., & Singal, S. K. (2018). Economic analysis of integrated renewable energy system for electrification of remote rural area having scattered population. *International Journal of Renewable Energy Research*, *8*(1), 258–265.
8. Rajanna, S. (2016). *Integrated renewable energy system for a remote rural area* [Ph. D. thesis]. Alternate Hydro Energy Center, IIT Roorkee.
9. Rajanna, S., & Saini, R. (2014). Optimal modeling of Solar/Biogas/Biomass based IRE system for a remote area electrification. In *2014 6th IEEE Power India International Conference (PIICON)* (pp. 1–5). IEEE.
10. Rajanna, S., & Saini, R. (2016a). Selection of suitable strategy with peak load shifting based DSM strategy of standalone integrated renewable energy system for a remote rural area. In *2016 IEEE 1st international conference on power electronics, intelligent control and energy systems (ICPEICES)* (pp. 1–6). IEEE.
11. Rajanna, S., & Saini, R. (2016b). Optimal modeling of an integrated renewable energy system with battery storage for off grid electrification of remote rural area. In *2016 IEEE 1st international conference on power electronics, intelligent control and energy systems (ICPEICES)* (pp. 1–6). IEEE.
12. Ramesh, M., & Saini, R. P. (2020). Effect of different batteries and diesel generator on the performance of a stand-alone hybrid renewable energy system. *Energy Sources, Part A: Recovery, Utilization, and Environmental Effects*, 1–23.
13. Varshney, N., Sharma, M., & Khatod, D. (2013). Sizing of hybrid energy system using HOMER. *International Journal of Emerging Technology and Advanced Engineering*, *3*(6), 436–444.

Overview of Autonomous Vehicle and Its Challenges



Chinmay Amrutkar, Anushka Satav, Puskaraj D. Sonawwanay, and Ashish H. Pawar

Abstract The autonomous vehicles (AVs) are an intelligent mode of transport which can perceive their surroundings and perform autonomous actions without human control. The advanced driver assistance systems (ADAS) technology is considered as the future of transportation systems. The main aim of autonomous driving is to implement a safe transport system for people of all ages, minimize accidents and congestion on roads and make use of resources more efficiently. As the performance of AV will not be affected by emotions, distraction, fatigue compared to humans, it makes them more reliable and safer. Along with the advantages, there are various challenges faced by the AVs which need to be resolved before they can be fully commercialized. This paper presents a comprehensive overview of autonomous vehicles including its development, review challenges faced and future presence.

Keywords Autonomous vehicles · Intelligent vehicles · Object detection · Sensor technology · Advanced driver assistance systems · Challenges

1 Introduction

In today's society, the autonomous vehicles (AVs) are becoming more distinguished in the field of research as well as for commercial use. AV is able to navigate and operate independently without human intervention, by its ability to analyze the environment and control independently. They aim to provide safer mobility especially for the elderly, reduce the number of accidents and avoid traffic [1]. About 1.3 million casualties per year are caused due to road crashes, as per the World Health Organization's report on road traffic injuries (Feb-2020) [2]. Most of the casualties are caused due to distractions, over-speeding, drinking, etc. The society needs a more structural and safer system of transportation which can be achieved by AVs on a larger scale [3]. Various companies and researchers working on AVs realize the several challenges

C. Amrutkar · A. Satav · P. D. Sonawwanay (✉) · A. H. Pawar
School of Mechanical Engineering, Dr. Vishwanath Karad MIT World Peace University, Pune,
India
e-mail: puskarajdsonawwanay@gmail.com

which need to be solved for building reliable AVs. Accuracy in obstacle detection and decision control are few of the challenges faced [1]. The environment perceptions as well as large-scale network guided technologies are important for vehicle safety [4]. Based on the literature survey it is seen that various reviews have been conducted related to AV development, social impact, sensors used, etc. [3, 5–7]. Our work presents a comprehensive overview of autonomous vehicles and focuses on the working, challenges faced and the future scope.

2 Development of Autonomous Vehicles

2.1 Levels of Automation

Society of Automotive Engineers (SAE) defined the classification of intelligent vehicles in 2014, which is accepted worldwide and shown in Fig. 1 [8]. The six levels of automation are based on the allotment of driving tasks between vehicle and the driver [9]. Level 0 involves no automation and the vehicle is monitored by the driver, whereas level 5 vehicles achieve complete autonomous driving. Here, vehicles can responsibly run on any roads [1]. Similarly, the National Highway Traffic Safety Administration (NHTSA) has also categorized autonomous vehicle technologies in 6 levels (0–5) [10].

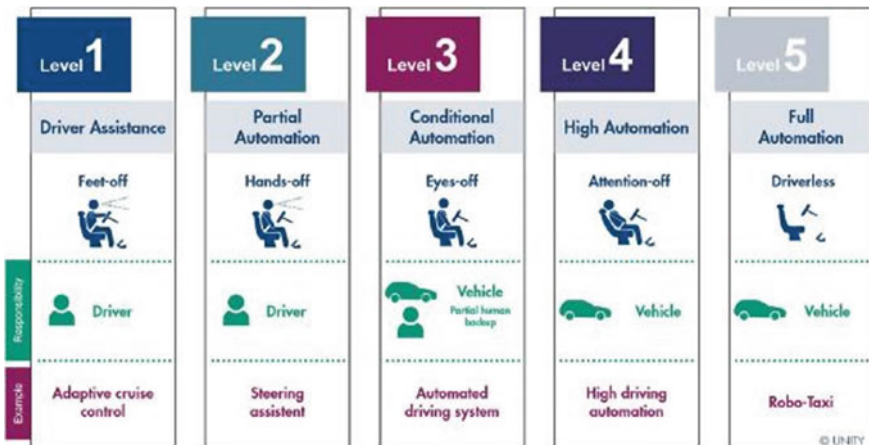


Fig. 1 Levels of vehicle automation according to SAE [8]

2.2 *Sensor Technologies for Environment Perception*

The sensing system of AV is responsible for surrounding data collection in real-time which helps them function autonomously. They provide information to the vehicle for object detection, lane occupancy, traffic flow, pedestrian detection, path planning and collision avoidance. The various sensors along with their drawbacks are as follows:

1. Ultrasonic sensor—Reliable to various light conditions but cannot be used at high speed with maximum range of 2 m [11].
2. Image Sensors—Generate images which are processed for object detection. Cameras are used in Tesla cars for complete self-driving features [12].
3. RADAR sensor—Emits radio waves which echo after hitting obstacles and the object position and speed is calculated but causes false alarms due to metal objects.
4. LIDAR sensors—Light Detection and Ranging (LIDAR create a real time virtual 3D environment but are affected by weather and are expensive [13, 14].
5. GNSS—Helps to determine the speed and location of a vehicle. It describes the layout of satellites and provides information like navigation, and traffic.
6. GPS—In this system, GPS provides longitude, latitude, and altitude and is a crucial part of path planning in autonomous vehicles [15].

Sensor data is organized efficiently by selecting suitable sensors and can be classified based on specifications, mode, and data type [16]. In a study, using LiDAR and thermal infrared cameras, an object detection algorithm was built which worked efficiently in day as well as night period [17].

2.3 *Algorithms for Object Detection and Path Planning*

Machine learning, Deep Learning, and Reinforcement learning algorithms are used for pedestrian detection [18], path planning [19], like:

1. CNN: CNN can be applied to AVs for pedestrian detection and path planning as this algorithm works best for image processing.
2. RCNN: It provides greater accuracy than CNN. It is used for traffic signs and pedestrian detection [20].
3. SLAM: Simultaneous localization and mapping (SLAM) estimates the body's relative position in a surrounding [21]. RADAR-SLAM provides velocity and LiDAR-SLAM is used for pedestrian detection, motion control and path planning [22].
4. YOLO: It is used for real-time object detection as it is fast and user-friendly.

Using DL and RL methods by learning their advantages and challenges can be used, which can remove the use of lengthy ML methods [19].

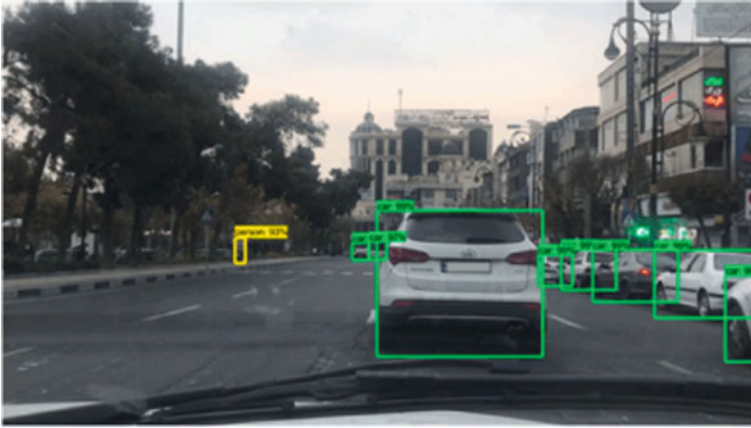


Fig. 2 Object detection using R-CNN [27]

Object detection: Object detection locates the roads, traffic signs, pedestrians, etc. It is becoming more accurate and reliable with time [19]. Pedestrian detection in real-time can be implemented in AVs using CNN [23]. Figure 2 shows object detection using R-CNN. In the design of ADAS, various algorithms are used to get surround and forward-view data fusion images to make AVs safer [24]. Semi-supervised 3D target detection can also be used with a fast 3D object detector; this needs only a small amount of labeled data [25]. A brief review of the 3D object detection techniques, for various scenarios faced during autonomous driving, is required for safety of the passengers [26].

Trajectory generation and Motion planning algorithms: The first step in navigation knows the location of a vehicle with respect to its surroundings. The next step is to follow the simplest path towards the required goal, followed by motion planning. It calculates steering angle, acceleration, and braking control, while path prediction consists of short-term path calculations of AV and future states. Various models and control methods can be used to choose a suitable path to reach a desired location [28]. SLAM method is used for navigation and localization of the AVs. Visual SLAM is being preferred over LiDAR sensors as they are cheaper and easy to install [22]. To change lanes on a highway, an approach including CNN and RNN can be effectively used [29].

2.4 Control System of AV

The decision made by the AVs is controlled by a Control Unit which is of two types: Direct control system, uses PC and needs controllers for different actuators and sensors, and Electric control unit (ECU), along with PC controls the AV. There are

some maneuvering systems that can be used without ECU (as they are expensive) [30]. The accuracy of navigation of AVs, calculating steering angles and vehicle speed, can be improved using CNN and results show that cars can drive automatically follow the lane stably with accuracy of 98.23% [31]. To improve steering and acceleration mechanisms, approaches using various types of control systems can be used [19].

Advanced Driver Assistance Systems (ADAS) in AVs: ADAS are active and passive systems designed to eliminate human error and assist while driving to improve driver’s performance. It uses various sensors to perceive the surrounding and it helps AV to take action when necessary [32]. It should be prepared to control the AV in worst case scenarios with utmost safety. ADAS is a bright application of AI and the availability of huge datasets is improving its performance. The Crash Avoidance and Overtaking Advice (CAOA) subsystems take decisions for AV’s overtaking on road [33]. Safeties on roads, reducing pollution, and efficient travel are benefits of new AI algorithms with ADAS. Figure 3 shows integration of sensors with ADAS systems in AVs.

Impact of AVs on Society: AVs are considered as the future of the transport system as they can make mobility more accessible for people unable to drive, like senior citizens, people with disabilities and children. Safer road travel will help reduce accidents. Impact of AVs can be predicted with the help of various simulation software [35]. To study the impact of AV on safety, environment and safety, various traffic simulation models can be used [10, 35, 36]. One study of traffic simulation of city Duisburg in 2020, 2030, and 2050 shows that, under the same traffic flow, increasing AVs can improve traffic flow and shorten the average travel time [37]. Network traffic matrix prediction can predict future network traffic behavior to improve

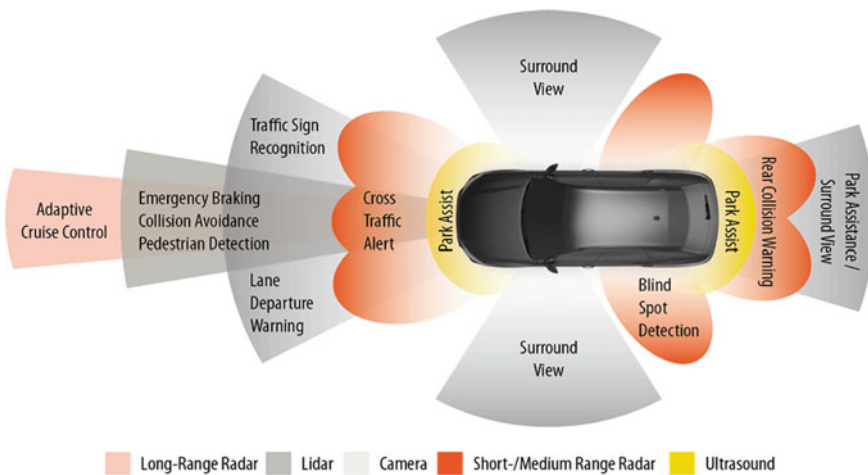


Fig. 3 ADAS integrated with sensors in modern AVs [34]

network management and planning [38]. A review of Agriculture autonomous vehicles (AAVs) was done by Hokkaido University from 1990 to 2018, where various aspects of AAVs development, future scope are discussed in detail [39].

3 Challenges of Autonomous Vehicles

AVs provide many advantages over conventional transport systems but implementation in today's world poses several challenges and issues that need to be solved. This can be done by analyzing those challenges and through extensive research and development, providing solutions for the same. Various challenges faced by the AVs are discussed.

1. Several challenges and their solutions in [33], have been described as follows:
 - (a) Driving AVs in dim light, glare and weather like rain, snow, fog, etc.
 - (b) To prevent vehicle collisions hidden in blind areas, when making lane changes for turning on bends, overtaking, etc.
 - (c) In AVs, tackling roads with mud, oil, sand, grease, ice, dust, food waste, glass, and accidents, can cause a car to lose control and roll over.
2. Congested metropolitan streets with heavy traffic and arriving pedestrians.
3. To change the law and traffic regulations to address AV ownership and operation.
4. Human decision-making is influenced by a variety of circumstances. A person might ethically think about crashing the car to save a pedestrian. For AVs, this sort of moral thinking and appropriate decision-making is essential.
5. Prior to each ride, an AV's sensors and systems must be checked and verified. And a cut-off mechanism must always be provided for safety purposes.
6. Traffic forecasting for autonomous vehicles is a difficult problem due to complex spatial modeling of the road network and non-linear temporal dynamics [40].
7. Development of a human-machine interface (HMI) system that assists passengers while complete automated driving uses the information continuously provided to enhance the mode awareness (i.e., their mental model about the current status and liability of the automated driving system) [41].
8. For AVs to function successfully, extremely high-quality, specialized maps may be needed. Planning is challenging since the best route between collection and drop-off places in AVs is dynamic.
9. A number of monetary problems, including expensive initial, service, maintenance, and spare cost, hinder the adoption of AV [2].
10. Cyber security is the main barrier in commercializing AVs in India. By turning off the safety features, it is possible to alter the software and computer system of the car, just as it is possible to purposefully cause an accident [2].

4 Conclusions

The paper gives an overview of the current scenario of working, development, challenges faced and the scope of AVs in the future. The key aspects related to the development of AVs such as AV's working, implementation, algorithms, intelligence, safety, impact on society, and study of various researches being conducted are discussed in this work. It shows the ability of AVs to make mobility in the future more efficient, safer, cleaner and more comprehensive. Based on this research we can highlight these challenges which require more efficient solutions:

1. Making ethical decisions for any kind of circumstances faced while driving.
2. Accurate detection of obstacles, pedestrians, mapping surroundings when vehicle is driving at high speeds.
3. Cyber-attacks on the AV can cause casualties, injuries, damage to property, etc.
4. Use of various sensors, their availability and costs can make AVs very expensive.

Many challenges faced in implementation of AVs make commercializing fully autonomous intelligent vehicles non-feasible and portrays the need for extensive research on AVs.

References

1. Martínez-Díaz, M., & Soriguera, F. (2018). Autonomous vehicles: Theoretical and practical challenges. In *Transportation research procedia* (pp. 275–282). Elsevier B.V.
2. Kumar, G., James, A. T., Choudhary, K., Sahai, R., & Song, W. K. (2022). Investigation and analysis of implementation challenges for autonomous vehicles in developing countries using hybrid structural modeling. *Technological Forecasting and Social Change*, 185, 122080.
3. Singh, S., & Saini, B. S. (2021). Autonomous cars: Recent developments, challenges, and possible solutions. In *IOP conference series: Materials science and engineering*. IOP Publishing Ltd.
4. Bimbraw, K. (2015). Autonomous cars: Past, present and future: A review of the developments in the last century, the present scenario and the expected future of autonomous vehicle technology. In *Proceedings of ICINCO 2015—12th international conference on informatics in control, automation and robotics* (pp. 191–198). SciTePress.
5. Raza, M. (2018). Autonomous vehicles: levels, technologies, impacts and concerns. *International Journal of Applied Engineering Research*, 13(16), 12710–12714.
6. Rajasekhar, M. V., & Jaswal, A. K. (2015). Autonomous vehicles: the future of automobiles. *IEEE International Transportation Electrification Conference (ITEC)*, pp. 1–6.
7. Van Brummelen, J., O'Brien, M., Gruyer, D., & Najjaran, H. (2018). Autonomous vehicle perception: The technology of today and tomorrow. *Transportation Research Part C: Emerging Technologies*, 89, 384–406.
8. Avoci, U. M., Marco, C., Antonio, P., & Consolatina, L. (2021). Enhanced sensor coverage for autonomous vehicles with a preliminary integration of fault detection scheme. In *Measurement: Sensors*. Elsevier Ltd.
9. Parekh, D., Poddar, N., Rajpurkar, A., Chahal, M., Kumar, N., Joshi, G. P., Cho, W. (2022). A review on autonomous vehicles: Progress, methods and challenges. *Electronics (Basel)*, 11, 2162.

10. Tyagi, A. K., & Aswathy, S. U. (2021). Autonomous intelligent vehicles (AIV): Research statements, open issues, challenges and road for future. *International Journal of Intelligent Networks*, 2, 83–102.
11. Budisusila, E. N., Arifin, B., Prasetyowati, S. A. D., Suprpto, B. Y., & Nawawi, Z. (2020). Artificial neural network algorithm for autonomous vehicle ultrasonic multi-sensor system. In *ECCIS 2020–2020 10th electrical power, electronics, communications, controls, and informatics seminar* (pp. 128–131). Institute of Electrical and Electronics Engineers Inc.
12. Autopilot | Tesla. Retrieved October 11, 2022, from <https://www.tesla.com/autopilot>
13. Zamanakos, G., Tsochatzidis, L., Amanatiadis, A., & Pratikakis, I. (2021). A comprehensive survey of LIDAR-based 3D object detection methods with deep learning for autonomous driving. *Computers and Graphics (Pergamon)*, 99, 153–181.
14. Ahangar, M. N., Ahmed, Q. Z., Khan, F. A., & Hafeez, M. (2021). A survey of autonomous vehicles: Enabling communication technologies and challenges. *Sensors*, 21, 706
15. Rahiman, W., & Zainal, Z. (2013). An overview of development GPS navigation for autonomous car. In *IEEE 8th conference on industrial electronics and applications (ICIEA)* (pp. 1112–1118).
16. Ignatious, H. A., El-Sayed, H., & Khan, M. (2021). An overview of sensors in autonomous vehicles. In *Procedia computer science* (pp. 736–741). Elsevier B.V.
17. Choi, J. D., & Kim, M. Y. (2022). A sensor fusion system with thermal infrared camera and LiDAR for autonomous vehicles and deep learning-based object detection. *ICT Express*, 9, 222–227.
18. Sha, M., & Boukerche, A. (2021). A novel visibility semantic feature-aided pedestrian detection scheme for autonomous vehicles. *Computer Communications*, 179, 50–61.
19. Elallid, B., Benamar, N., Hafid, A. S., Rachidi, T., & Mrani, N. (2022). A comprehensive survey on the application of deep and reinforcement learning approaches in autonomous driving. *Journal of King Saud University—Computer and Information Sciences*. 34, 7366–7390.
20. Carranza-García, M., Lara-Benítez, P., García Gutierrez, J., & Riquelme, J. C. (2021). Enhancing object detection for autonomous driving by optimizing anchor generation and addressing class imbalance. *Neurocomputing*, 449, 229–244.
21. Bresson, G., Alsayed, Z., Yu, L., & Glaser, S. (2017). Simultaneous localization and mapping: A survey of current trends in autonomous driving. *IEEE Transactions on Intelligent Vehicles*, 2, 194–220.
22. Cheng, J., Zhang, L., Chen, Q., Hu, X., & Cai, J. (2022). A review of visual SLAM methods for autonomous driving vehicles. *Engineering Applications of Artificial Intelligence*, 114, 104992.
23. Pranav, K. B., & Manikandan, J. (2020). Design and evaluation of a real-time pedestrian detection system for autonomous vehicles. In *2020 zooming innovation in consumer technologies conference, ZINC 2020* (pp. 155–159).
24. Yang, J., Liu, S., Su, H., & Tian, Y. (2021). Driving assistance system based on data fusion of multisource sensors for autonomous unmanned ground vehicles. *Computer Networks*, 192, 108053.
25. Zhang, J., Liu, H., & Lu, J. (2022). A semi-supervised 3D object detection method for autonomous driving. *Displays*, 71, 102117.
26. Ghasemieh, A. & Kashef, R. (2022). 3D object detection for autonomous driving: methods, models, sensors, data, and challenges. *Transportation Engineering*, 8, 100115. <https://doi.org/10.1016/j.treng.2022.100115>
27. Khosravian, A., Amirkhani, A., Kashiani, H., & Masih-Tehrani, M. (2021). Generalizing state-of-the-art object detectors for autonomous vehicles in unseen environments. *Expert Systems with Applications*, 183, 115417.
28. Bacha, S., Saadi, R., Ayad, M.Y., Aboubou, A., & Bahri, M. (2017). A review on vehicle modeling and control technics used for autonomous vehicle path following. In *2017 International Conference on Green Energy Conversion Systems (GECS)* pp. 1–6.
29. Xing, Y., Lv, C., Wang, H., Cao, D., & Velenis, E. (2020). An ensemble deep learning approach for driver lane change intention inference. *Transportation Research Part C: Emerging Technologies*, 115, 102615.

30. Choi, J. H., Lee, H. J., Oh, S., & Nam, K. (2022). Development of vehicle maneuvering system for autonomous driving. *Mechatronics*, 85, 102798.
31. Duong, M.-T., Do, T.-D., Le, M.-H. (2018). *Navigating self-driving vehicles using convolutional neural network*. IEEE.
32. What is ADAS (Advanced Driver Assistance Systems)? | Dewesoft. Retrieved October 11, 2022, from <https://dewesoft.com/daq/what-is-adas>
33. Perumal, P. S., Sujasree, M., Chavhan, S., Gupta, D., Mukthineni, V., Shingekar, S. R., Khanna, A., & Fortino, G. (2021). An insight into crash avoidance and overtaking advice systems for autonomous vehicles: A review, challenges and solutions. *Engineering Applications of Artificial Intelligence*, 104, 104406.
34. Types of ADAS Sensors in Use Today | Dewesoft. Retrieved October 10, 2022, from <https://dewesoft.com/daq/types-of-adas-sensors>
35. Orfanou, F. P., Vlahogianni, E. I., Yannis, G., & Mitsakis, E. (2022). Humanizing autonomous vehicle driving: Understanding, modeling and impact assessment. *Transportation Research Part F: Traffic Psychology and Behaviour*, 87, 477–504.
36. Miglani, A., & Kumar, N. (2019). Deep learning models for traffic flow prediction in autonomous vehicles: A review, solutions, and challenges. *Vehicular Communications*, 20, 100184
37. Ma, X., Hu, X., Weber, T., & Schramm, D. (2021). Effects of automated vehicles on traffic flow with different levels of automation. *IEEE Access*, 9, 3630–3637.
38. Aloraifan, D., Ahmad, I., & Alrashed, E. (2021). Deep learning-based network traffic matrix prediction. *International Journal of Intelligent Networks*, 2, 46–56.
39. Roshanianfard, A., Noguchi, N., Okamoto, H., & Ishii, K. (2020). A review of autonomous agricultural vehicles (The experience of Hokkaido University). *Journal of Terramechanics*, 91, 155–183
40. Miglani, A., & Kumar, N. (2019). Deep learning models for traffic flow prediction in autonomous vehicles: A review, solutions, and challenges. *Vehicular Communications*, 20, 100184.
41. Bellet, T., Cunneen, M., Mullins, M., Murphy, F., Pütz, F., Spickermann, F., Braendle, C., & Baumann, M. F. (2019). From semi to fully autonomous vehicles: New emerging risks and ethico-legal challenges for human-machine interactions. *Transportation Research Part F: Traffic Psychology and Behaviour*, 63, 153–164.

Identification and Protection of Landslide Prone Areas in Karul Ghat Region



Rohan Sawant

Abstract Landslides are amongst the most damaging natural hazards in the mountainous terrain. The area surrounded by pre-occurred landslide in Karul Ghat near Vaibhavwadi, Maharashtra is chosen as study area. Google Maps, Cartosat, and other satellite image services together with topographical sheets from the Survey of India, baseline data on a variety of parameters like slope, relative relief, drainage density, and geology are derived from these sheets. The aim of study is to discuss the role of mapping geological ligaments and terrain parameters like streams, slope and aspect. The main factors of landslide is rainfall. Any remedial measure used must include one or both of the above parameters. Soil samples are collected and physical, and engineering properties of the soil were tested in the laboratory. Thus, the slope characteristics are found. From this the most economical and feasible preventive measure can be used on site to prevent further landslides in the Karul Ghat region.

Keywords Cartosat · Hazardous zone map · Landslide · Remedial measures · Innovation

1 Introduction

“The movement of a mass of rocks, earth, or debris down a slope” is the definition of the term “landslide” [1]. Slope stability and typical patterns of landslide incidence will forever be affected by the dynamic climate as a result of human activity raising the global average temperature [2]. The primary actuation for a landslide is gravity, with other factors shifting the initial slope stability. The materials might fall, tip over, slide, spread out, or flow [3]. Due to dynamic precipitation designs, underwater immersion and pore pressure rise most of the time; Due to the frequency of high-intensity precipitation events at northern high latitudes [4, 5], total precipitation is also likely to rise as average temperatures rise [6–8]. To reach the present goal, which involves enhancing the quality of life and minimizing the danger trade-off among

R. Sawant (✉)

Department of Civil Engineering, Dr. D. Y. Patil Institute of Technology Pimpri, Pune, India
e-mail: rohan.sawant@dypvp.edu.in

fundamentally different decisional techniques [6–8], a technically improved strategy to landslide risk mitigation is necessary. Unlike landslides, mudflows are a type of mass waste that occur when an excessive amount of water is added to the source material. Mudflows are caused by a terrible to terrible fast flow of garbage that has liquefied to some extent or the other. Avalanches can be brought about by human action or by geography, and they can happen in created, lacking, or any region where the ground has been adjusted for streets, houses, utilities, or structures [9, 10].

2 Dams and Hydro-electricity Projects

Since it involves water as its fuel, hydropower is a spotless energy source that doesn't dirty the air like power establishes that utilization petroleum derivatives like coal or flammable gas. Compared to fossil fuels, which are not renewable and are rapidly depleting the environment, hydropower is a renewable energy source that is also more dependable and cost-effective. Hydropower is powered by the sun, making it a renewable energy source. The details about Dam are shown in Table 1.

2.1 Study Area-Karul Ghat

The research regions situated between latitudes 16.5435° N and 16.3352° N and longitudes 73.8316° E and 73.7419° E. These areas include the city of Gaganbawada

Table 1 Information of dam in study region

Dam Name	Kumbhi Dam
River Name	Kumbhi river
Year of construction	2007
Village	Katali
Location	16° 31' 36'' N 73° 51' 28'' E
Capacity	4 TMC
Submergence area	503 hectors
Length of dam	887 m
Height of dam	42.5 m
Catchment area	21.20 Sq km
Uses	Agricultural, industrial, domestic, hydroelectric project
Capacity of power generation	4 megawatts
Benefitted villages	Gaganbavda tehsil
Affected villages	3 villages

in the Kolhapur district and the village of Karul in the Sindhudurg district near Vaibhavwadi. The area is on top sheets 47 L/4, 47 H/15, and 47 H/16 of the Survey of India. Ghat is 55 km from Kolhapur and has a length of 11 km. It is in the Western Ghats or Sahyadri range. Talere-Kankavali now features Karul Ghat. Karul Ghat begins 1 km to the left of the bus stop. In the direction of the northern part of Sindhudurg District, Karul Ghat leads. The Sindhudurg tehsil of Vaibhavwadi is in charge of this Ghat.

2.2 Karul Ghat-Why Karul Ghat

1. Karul Ghat is the one of the major and important Ghat region due to its infra-structural important as Ghat joins two major region Deccan plateau (Kolhapur) region to costal region (vaibhavwadi) As a result, new highways across the Ghats portion are being built to transport commodities and commercial services.
2. Karul Ghat also is the one of the major and important Ghat region due to its political important as authority of Karul Ghat region going to change from public work department to National Highway authority of India.
3. Karul Ghat also is the one of the major and important Ghat region due to its sensitivity towards the landslide

2.3 Karul Ghat-Climate

It is very important to know about the climatic conditions of the region, as it helps in understanding the proper environment of the region. The elevated region of the Western Ghats records the temperate climate having low temperature while the climate is tropical and humid in the lower parts. Having approximately minimum 22–23 °C and maximum 30–31 °C temperature (Table 2). Minimum and maximum temperature average nearest to the 27 °C because this tehsil is the nearest to the Arabian Sea. In our study region rainfall is measure factor considered having average rainfall 4432 mm.

Table 2 Temperature in study region

Sr. No	Tehsil	Minimum in °C	Maximum in °C	Average in °C
1	Gaganbawada	19.83	29.34	24.39
2	Vaibhavwadi	23.32	30.82	27.18
3	Kankavli	22.24	31.27	26.76

Table 3 Percentage of forest area in study region

Sr. No	Tehsil	Forest	Total geographical area	% of Forest area to total area
1	Gaganbawda region	11,378.1	2822	40.31
2	Vaibhavwadi region	8631.85	41,612	20.74
3	Kankavli region	11,932.42	77,339	15.43

2.4 Karul Ghat-Vegetation

There are a variety of forest types in the region, ranging from evergreen deciduous forests to arid tracts, shrubs, and timber forests. The region's rainfall distribution, drainage pattern, topography, soil conditions, biotic factors, and degree of human interference are all influenced by natural vegetation. The following types of vegetation can be found in the area under study (Table 3).

2.5 Karul Ghat—Geology

In this lava flows are major, having thickness each of average of 15 ft. Youngest layer is having less thickness affected by weathering. Lowermost lava flow seen at Karul Ghat has 15 m thick. Each lava flow shows mural joints and columnar joints. Each lava flow is separated by local unconformity by red bole zone fallowed downward. Zeolitic basalt of varied thickness along with columnar and mural joint flow passes oblique and inclined joints which facilities for landslide. Thickness of wethered zone is also more around the surface. It has steep slopes (85–90) because of heavy rainfall it causes landslide immediately after rainfall.

2.6 Karul Ghat—Geomorphology

The Western Maharashtra Upland is formed by the Karul Ghat, which is a part of the Sahaydri Mountains and has a variety of local relief. The Ghat's typical height anywhere between 550 and 600 feet above sea level. In Table 4 given information of the Karul Ghat and in Table 5 information of western Ghat. The eastern portion of the region descends between 450 and 600 m, while the central portion is generally 650 m high. River basins and undulating topography in the middle, as well as mountain and hill ranges in the west.

Table 4 Information of Karul Ghat in study region

Sr. No	Name of the Ghat	Distance	Connected area	Type of road	Sensitivity
1	Karul Ghat	9 km	Gaganbawada to Vaibhavwadi	State highway	Sensitive

Table 5 Western Ghats

Sr. No	Name of the Ghat	Distance (km)	Connected area	Type of road	Sensitivity
1	Ambenali Ghat	35	Satara to Poladpur	State highway	Highly sensitive
2	Kas-Bamnoli road	75	Satara to Mahabaleshwar	District road	Sensitive
3	Kumbharli Ghat	48	Karad to Chiplun	State highway	Sensitive
4	Amba Ghat	31	Ratnagiri to Kolhapur	State highway	Highly sensitive
5	State Highway No. 111	24	Kolhapur to Rajapur	State highway	Sensitive
6	Bhuibawda Ghat	22	Gaganbavda to Kharepatan	State highway	Sensitive
7	Karul Ghat	18	Gaganbawada to Vaibhavwadi	State highway	Sensitive
8	Phonda Ghat	41	Kankavali to Kolhapur	State highway	Highly sensitive
9	Amboli Ghat	23	Kolhapur to Sawantwadi	State highway	Highly sensitive
10	Tillari Ghat	14	Tillari to Belgaum	State highway	Moderately sensitive

2.7 Western Ghats

3 Results and Discussion

The results of the tests conducted on samples is given in Table 6.

3.1 Field Test

The core cutter was used for the thumb penetration test. The thumb was found to easily penetrate the soil, indicating that the highest layer is sandy-clay. Soil was categorized texturally by the United States Department of Agriculture, with sandy-clay, salty-clay, and loosely clayey soils at the top, middle, and bottom, respectively

Table 6 Results of Tests carried out on the samples

Sr. No	Tests		Results			
			1st Sample	2nd Sample	3rd Sample	4th Sample
1	Determination of water content		6.55	7.07	5.46	4.31
2	Determination of specific gravity		2.54	2.60	2.516	2.65
3	Sieve analysis		Coarse sand	Coarse sand	Gravel	Coarse sand
4	Liquid limit (%)		51.51	55.30	52.48	56.20
5	Standard proctor test	Dry density	1.769	2.291	2.220	1.949
		Water Content	21.62	25.32	23.52	20.63
6	Direct shear stress	Cohesion (c)	0.637	0.5515	1.6425	0.807
		Angle of friction (ϕ)	52.580	44.500	34.1760	59.4750
7	Factor of safety (F.O.S.)		0.5			

(Table 7). Similar to this, a core cutter examination reveals that the soil’s typical dry density was 1.27 g/cc at the top, 1.33 g/cc at the middle, and 1.24 g/cc at the bottom, respectively. The core cutter’s evaluation of the results is supported by the crumble test’s conclusion that the pressure essential to crumble the soil was slight [11]. Field observations indicate that during the rainy season, land on top of the Head (the Hill) was suddenly used for rice and other crop plantations. We determined that the hill’s average slope angle from bottom to top was 35° using a surveyor’s level.

Table 7 Field test findings for three hill slope locations

Sample no	Specific gravity	Water content	Dry density	Liquid limit	Plastic limit	Plasticity Index	Cohesion	Internal friction
	SG	WC (%)	DD (g/cc)	LL (%)	PL (%)	PI	C (kg/cm ²)	ϕ (°)
Low	2.60	36.52	1.36	52.3	32.25	22.43	0.15	5.23
	2.50	38.12	1.28	50.6	29.86	22.6	0.12	6.21
	2.02	28.65	1.09	53.2	28.6	20.56	0.15	9.23
Middle	1.95	40.32	1.36	52.6	33.5	15.8	0.42	23.25
	2.21	35.25	1.27	49.5	29.2	23.66	0.45	38.65
	2.16	32.58	1.36	49.9	28.4	22.55	0.36	45.23
Top	2.15	39.58	1.22	47.8	32.33	14.56	0.41	25.23
	2.32	41.25	1.25	52.8	27.36	18.23	0.42	15.20
	2.68	25.62	1.35	45.3	33.5	24.63	0.44	36.52

Results of soil properties.

Internal friction angle— 17.52°

Cohesion— 0.45 kg/cm^2

Bulk density— 0.65 g/cm^3

Plasticity Index—17%

Specific gravity—1.84

Plastic limit—16%

Liquid limit—29%

Dry density— 0.04 g/cm^3 .

3.2 Geotechnical Parameters

The mean specific gravity of a typical soil specimen from top, middle, and bottom was 2.38, 2.10, and 2.37, correspondingly. These values suggested that the soil had a lot of sand particles, while the results for the water content classified the soil as sandy clayey [12]. According to the PI results, the liquid limit of the top soil sample is higher than that of the bottom hill soil sample. The top and middle hill slope soils, as shown in Table 7, were both unstable and prone to liquid state. Both samples produced identical results for other soil parameters like the plastic limit and the liquid limit. Because of this, top soil is more susceptible to microbial growth and required less water to reach the liquid and plastic limits.

3.3 Shear Strength Soil

Undrained cohesion and the internal friction angle of descriptive soil samples were examined. It found that the FOS for an endless incline is short of what one, demonstrating that the slope's slant was shaky during weighty precipitation when leakage was lined up with the slant [11]. The exploratory perusing prompted the underlying end that the dirt's lower opposing power than its main thrust makes the slant unsound. The representative soil's shear strength parameters are shown in Table 7.

4 Conclusions

The soil analysis that was done in the Karul Ghat region revealed that the FOS was less than one (1), which indicates that the slope is unstable. This is because the driving force was greater than the soil's resisting force. Zeolitic basalt (Manjra) was found to be the primary soil contributing to the landslide in all laboratory tests. The Core Cutter test indicated similar outcomes, with the top, center, and bottom of the soil having an average dry densities of 1.27 g/cc, 1.33 g/cc, and 1.24 g/cc, correspondingly. A

representative soil sample taken from the top, middle, and bottom had an average specific gravity of 2.38, 2.10, and 2.37, respectively. These values suggested that the soil contained a lot of sand, while the water content results described the soil as sandy clayey. An Indian study has found that hill slope monitoring is necessary for the Karul Ghat region to prevent landslides near residents. The major cause of sloping ground collapse was shown to be an inadequate sewage system at the top and centre of the hill. Unplanned agricultural land formation and deforestation, as indicated by the map of land use and land cover, were the other major causes of this landslide.

References

1. Cruden, D. M. (1991). A simple definition of a landslide. *Bulletin of the International Association of Engineering Geology*, 43, 2729.
2. Gariano, S. L., & Guzzetti, F. (2016). Landslides in a changing climate. *Earth-Science Reviews*, 162, 227–252. <https://doi.org/10.1016/j.earscirev.2016.08.011>
3. USGS Of USA. Lynn Highland. (2004). landslide types and processes. <http://Pubs.Usgs.Gov/Fs/2004/3072/Fs-2004-3072.html>
4. Orłowski, B., & Seneviratne, S. I. (2012). Global changes in extreme events: Regional and seasonal dimension. *Climatic Change*, 110, 669–696. <https://doi.org/10.1007/S10584011-0122-9>
5. Kharin, V. V., Zwiers, F. W., Zhang, X., & Wehner, M. (2013). Changes in temperature and precipitation extremes in the CMIP5 ensemble. *Climatic Change*, 119, 345–357. <https://doi.org/10.1007/S10584-013-0705-8>
6. Dai, F. C., Lee, C. F., & Ngai, Y. Y. (2002). Landslide risk assessment and management: An overview. *Engineering Geology*, 64, 65–87.
7. Cascini, L. (2014). Cascini, Criteri di analisi e gestione del rischio da frana: Dal governo centrale alle comunità locali. General report. In I. Baveno (Ed.), *XXV National Geotechnical Conference, AGI* (pp. 103–150).
8. Cascini, L. (2015). Geotechnics for urban planning and land use management. *Italian Geotechnical Journal*, 4, 7–62.
9. Chowdhury, A. A., Raul, M. G., & Khan, M. M. K. (2007). Numerical simulation of building performance under different low energy cooling technologies. *International Journal of Energy and Environment*, 1(1), 28–36.
10. Flentje, P., & Chowdhury, R. (1999). Quantitative landslide hazard assessment in an urban area. In *Proceedings of 8th Australia New Zealand conference on geomechanics: Consolidating knowledge*. Australian Geomechanics Society.
11. Shah, C. R., Sathe, S. S., Bhagawati, P. B., & Mohite, S. S. (2019). A hill slope failure analysis: A case study of Malingoan village, Maharashtra, India. <https://doi.org/10.1080/24749508.2019.1695714>
12. Sathe, S. S., Goswami, L., & Mahanta, C. (2019) Integrated factors controlling arsenic mobilization in an alluvial floodplain. *Environmental Technology & Innovation*, 17C, 100525. <https://doi.org/10.1016/J.Eti.2019.100525>

Indian Scenario of Electric Vehicles—A Review



Niket B. Adhia, Shikhar R. Takke, and Puskaraj D. Sonawwanay

Abstract Over the past few years, the global automotive sector has benefited greatly from electric vehicles. According to projections from 2020, there were over 12 million electric vehicles in use worldwide. China sold 90% of them, with Europe, the United States, and other nations following. In India, EV development is still in its infancy. In India, 3.8 lakh electric vehicles were sold in the 2019–20 year. Passenger vehicles generate the largest portion of EV sales in India, followed by commercial vehicles and two-wheelers. Numerous government policies and programmes, including FAME-India, NEMMP 2020, and many others, are mandated by the National Automotive Board, National Board for Electric Mobility, and National Council for Electric Mobility. This paper covers a review of Indian Scenario of Electric Vehicles, Statistics and different government policies associated with EV's, in detail. Electric Vehicles, Indian EV Scenario, Government Policies, FAME-India, EVs in India.

Keywords Electric vehicles · Indian EV scenario · Government policies · FAME-India · EV's in India

1 Introduction

The Indian electric vehicle market, which was estimated at USD 5.47 billion in 2020, is anticipated to grow to USD 17.01 billion by 2026, with a CAGR of 23.47% (2021–2026). The COVID-19 epidemic had an impact on the auto industry, which led to a decline in demand for electric cars, two-wheelers, and three-wheelers. The total number of electric vehicle registrations decreased by 20% in FY21 to 236,802 units from 295,683 in FY20, according to the Society of Electric Vehicle Manufacturers (SMEV). But because EV sales are increasing, the market is anticipated to grow favorably over the course of the forecast period. According to a Car Dekho OMG survey,

N. B. Adhia · S. R. Takke · P. D. Sonawwanay (✉)
School of Mechanical Engineering, Dr. Vishwanath Karad MIT World Peace University, Pune,
Maharashtra, India
e-mail: puskarajdsonawwanay@gmail.com

more Indian consumers are willing to purchase electric cars. The top auto technology company, Car Dekho, in collaboration with the advertising and marketing firm OMG (Omnicom Media Group), released the Electric Vehicle Customer Awareness Study [1–3].

2 Survey of Electric 4-Wheelers in Indian Market

EVs currently make up less than 1% of all vehicles sold, but they could increase to 5% within a few years. A total of 3.8 lakh electric vehicles, of which 58% were low-speed E3W and 40% were E2W, were sold in India in 2019–20. The survey found that 66% of consumers were willing to purchase electric vehicles, and 53% of those consumers indicated that they were very likely to do so. 13% of those surveyed feel they are not yet prepared for the change, while 19% are undecided. In addition, 68% of customers expressed concern for the environment and said they thought switching to EVs would help reduce air pollution, while 11 and 6% of respondents said driving pleasure and lower maintenance costs were the main factors in their decision to consider EVs [2] (Fig. 1).

The government is encouraging the use of electric-powered vehicles across various states, which is increasing demand for electric buses in India. This is due to the growing need to control GHG (Greenhouse gases) emissions emitted by vehicles.

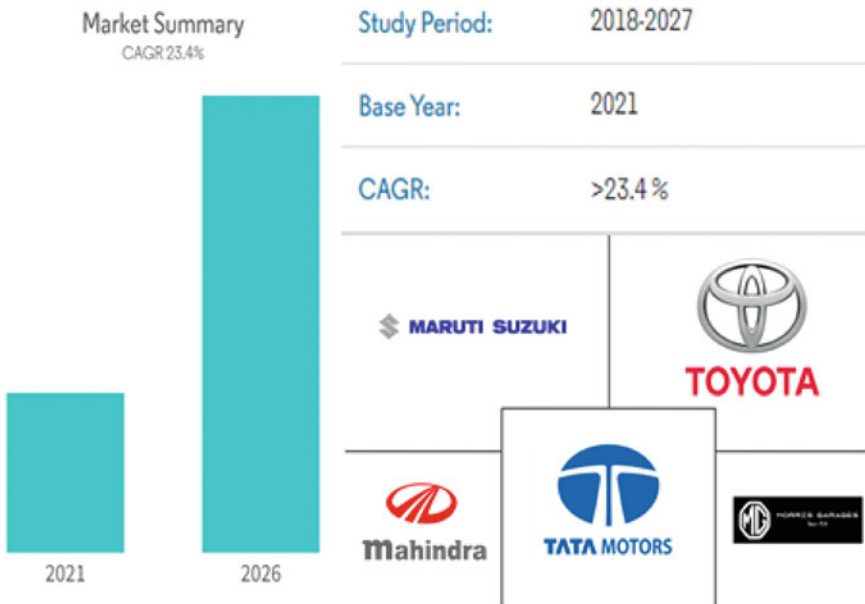


Fig. 1 EV market survey (India) [4]

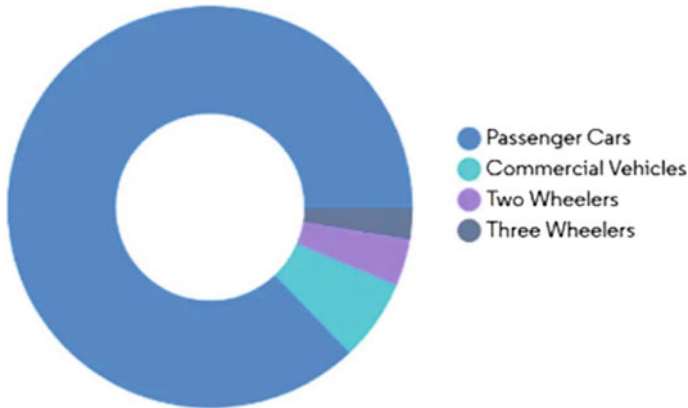


Fig. 2 Indian EV market revenue share (%), by vehicle type, 2020 [4]

Increased domestic manufacturing, rapid urbanisation, and a rise in environmental awareness are some of the factors driving the market [3, 5, 6]. With an investment of more than Rs 600 crores, Olectra Greentech, India’s largest producer of electric buses, announced the establishment of the nation’s largest electric bus factory in Hyderabad, with a capacity of 10,000 units [7, 8].

Original equipment manufacturers (OEMs) are growing their facilities to maximise revenue from the rapidly expanding Indian electric scooter and motorcycle market. Hyundai India announced in December 2021 that it intended to spend Rs 4000 crore on research and development in order to increase the number of battery-electric vehicles in its line-up [3]. To support its EV ambitions, Tata Motors established a wholly-owned company, Tata Passenger Electric Mobility Limited (TPEML), in December 2021. TPEML’s initial capital is Rs 700 crore [9]. Tata Motors introduced the new Tigor EV in August 2021. It features Tata’s cutting-edge Ziptron high-voltage architecture and a permanent magnet synchronous electric motor with 75 horsepower and 170 Nm of torque. With these output numbers, 5.7 s from 0 to 60 kph is possible [5] (Figs. 2 and 3).

3 Government of India Policies for EVs

The National Mission on Electric Mobility launched the Faster Adoption and Manufacturing of (Hybrid and) Electric Vehicles in India (FAME-India) Scheme in 2011 and the National Electric Mobility Mission Plan 2020 was unveiled in 2013. The programme seeks to promote the gradual introduction of dependable, cost-effective, and efficient electric and hybrid vehicles (xEV). The first two years of the scheme’s First Phase, beginning on April 1, 2015, were initially approved. It is covered by the Demand Incentive Disbursement Mechanism framework. For each type of vehicle,

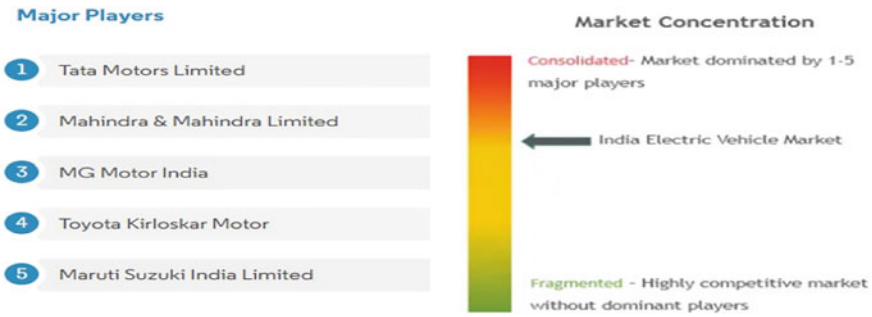


Fig. 3 Major Players and Market Concentration of Indian EV Market [4]

including those with Pure Electric, Plug-in Hybrid, Strong Hybrid, and Mild Hybrid technologies, an incentive amount has been determined (Fig. 4).

Under D/o Heavy Industry, the National Automotive Board is in charge of its implementation and oversight. It falls under the in-kind mode category and is one of the DBT schemes. The FAME India portal has been launched at <http://fame-india.gov.in/index.aspx> as part of the digitalization of the schemes to bring efficiency, transparency, and effective monitoring. In this online portal, the entire process life cycle of the scheme has been digitalized [9].

Currently, this scheme is registered for 30 Original Equipment Manufacturers (OEM) and one hundred thirty-seven Models of all types of vehicles. For 2.8 lakh vehicles, the total incentive sum that has been paid out to date is approximately Rs 359 crores. About 50 million litres of fuel are expected to be saved overall as a result of electrification, or about 52,700 L per day. The daily CO₂ reduction in litres is approximately 1.3 lakh kg, and the overall CO₂ reduction is approximately 129 million kg. Online Demographic Aadhaar Authentication of the beneficiaries

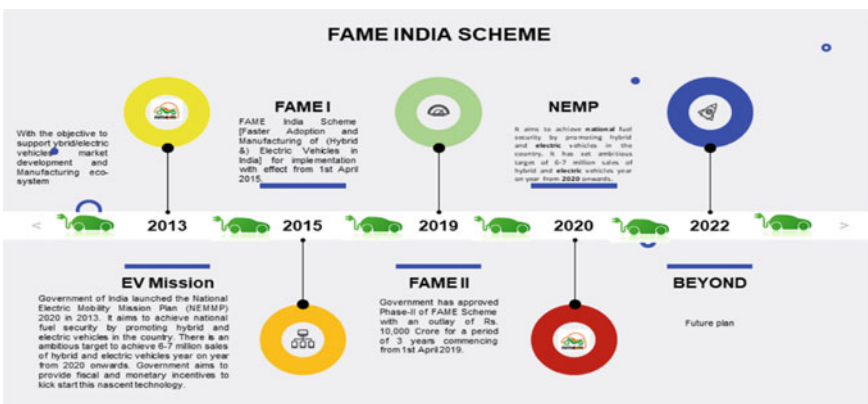


Fig. 4 FAME India scheme [9]

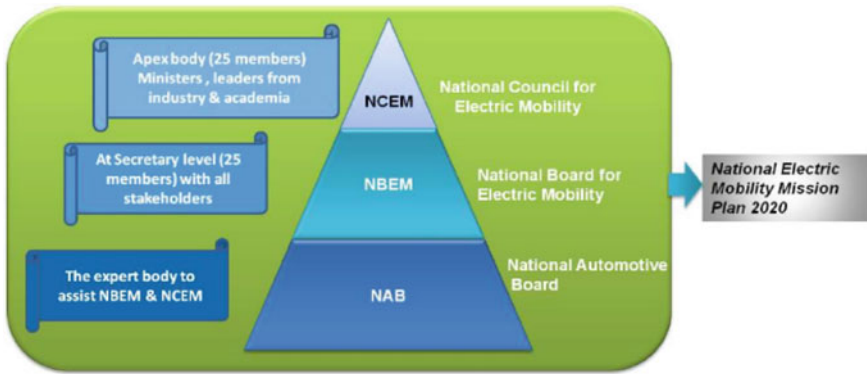


Fig. 5 National mission for electric mobility structure [9]

is also being enabled in accordance with DBT compliance. Phase-II of the FAME Scheme, which will cost Rs. 10,000 crore and run for three years starting on April 1, 2019, has received government approval [10]. By supporting 7000 electric buses (e-bus), 5 lakh electric three-wheelers (e-3W), 55,000 electric four-wheel passenger cars (including strong hybrids), and 10 lakh electric two-wheelers, this phase aims to create demand (e-2W). However, due to the inclusion of provisions for both inter- and intra-segment fungibility, these numbers may change depending on the off-take of various categories of xEVs. Additionally, the Scheme will support the development of charging infrastructure. Only advanced chemistry battery-equipped vehicles that meet the minimum Technical Criteria and are registered as “Motor Vehicles” according to the CMVR are eligible for the incentive under the programme (Fig. 5).

The scheme will be applicable primarily to vehicles used for public transportation or those registered for commercial purposes in the e-3W, e-4W, and e-bus segments, with a greater emphasis on providing affordable and environmentally friendly public transportation options for the masses. However, as a mass segment, privately owned registered e-2Ws are also protected by the programme [11].

The National Electric Mobility Mission Plan (NEMMP) 2020 is a National Mission document that lays out the goals and a plan for accelerating the use of electric vehicles and the nation’s production of them. This strategy has been developed to increase national fuel security, offer accessible, environmentally friendly transportation, and help India’s automotive sector take the lead in global manufacturing. The ambitious goal set forth in the NEMMP 2020 is to sell 6–7 million hybrid and electric vehicles by the year 2020. A sufficient number of charging infrastructure is needed to achieve the expected results of the plan, according to experience gained in Phase-I of the FAME India Scheme. This issue is currently being addressed in Phase-II of the FAME Scheme [12].

Central as well as State governments have been promoting adoption of EVs by providing fiscal as well as non-fiscal incentives. Some of the incentives being provided on purchase of EVs are:

- a. Upfront capital subsidy under FAME India Scheme Phase II
- b. Goods and Services Tax (GST) on EVs has been reduced from 12 to 5%,
- c. Income tax deduction can be claimed on the interest paid on loans taken for purchase of EVs [13].

4 EV’s in a Global Scenario—At a Glance

After a decade of explosive growth, there were 10 million electric cars on the roads of the world by the year 2020. Despite the worldwide auto sales slump brought on by the pandemic, which saw a 16% decline in global auto sales, the number of electric car registrations rose by 41% in 2020. Around 3 million electric vehicles were sold globally (a 4.6% sales share), and for the first time, Europe surpassed the People’s Republic of China (“China”) as the largest market for EVs.

After ten years of explosive growth, the number of electric cars sold worldwide reached 10 million in 2020, an increase of 43% over 2019 and a 1% stock share. In 2020, battery electric vehicles (BEVs) made up two-thirds of the stock and all new electric car registrations. China has the largest fleet with 4.5 million electric vehicles, but in 2020, Europe saw the largest annual increase to reach 3.2 million [12] (Figs. 6 and 7).

New car registrations decreased by about a third in the first quarter of 2020 compared to the previous year. Stronger activity in the second half helped to offset this to some extent, but overall, there was a 16% decline year over year. Notably, global

Global electric vehicle stock by region, 2010-2020

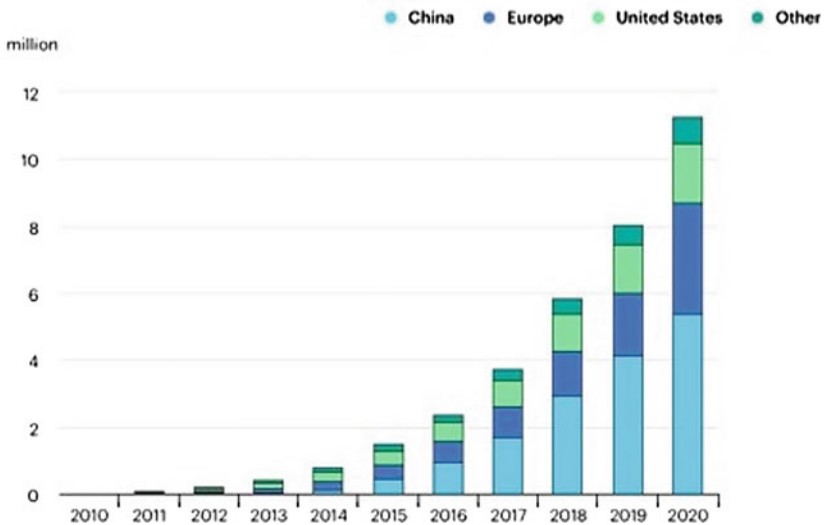


Fig. 6 Global electric vehicle stock by region [14]

Global electric vehicle stock by transport mode, 2010-2020

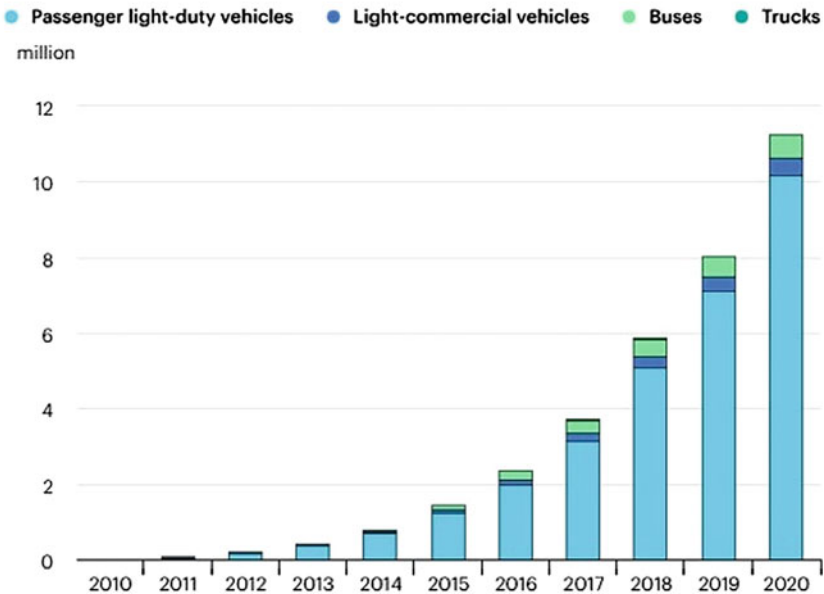


Fig. 7 Global electric vehicle stock by transportation mode [14]

electric car sales share increased 70% to a record 4.6% in 2020, despite conventional and overall new car registrations declining. In 2020, there were about 3 million new electric vehicle registrations. With 1.4 million new registrations, Europe took the lead for the first time. China registered 1.2 million new electric cars after the United States registered 295,000 (Figs. 8 and 9).

In 2030, it is anticipated that the demand for electricity for EVs will be 525 TWh in the scenario of stated policies and 860 TWh in the scenario of sustainable development. In both cases, LDVs make up about two-thirds of the demand. In both scenarios, the global final consumption of electricity for EVs by 2030 will be at least 2% of the total.

In the Stated Policies Scenario for 2030, India’s EV sales share across all modes (including two- and three-wheelers) is above 30%. According to FAME II’s goals, the main way that EV deployment is accomplished in India is through the electrification of two- and three-wheelers, which account for almost 50% of all sales. Less than 15% of buses and light duty vehicles will be electric by 2030. According to the Sustainable Development Scenario, sales of electric vehicles will increase in India across all road vehicle modes by 30% by 2030 (excluding two- and three-wheelers). Nearly 60% of all two- and three-wheeler sales as well as about 30% of LDVs and buses will be electric by 2030.

Electric car models available by region, 2020

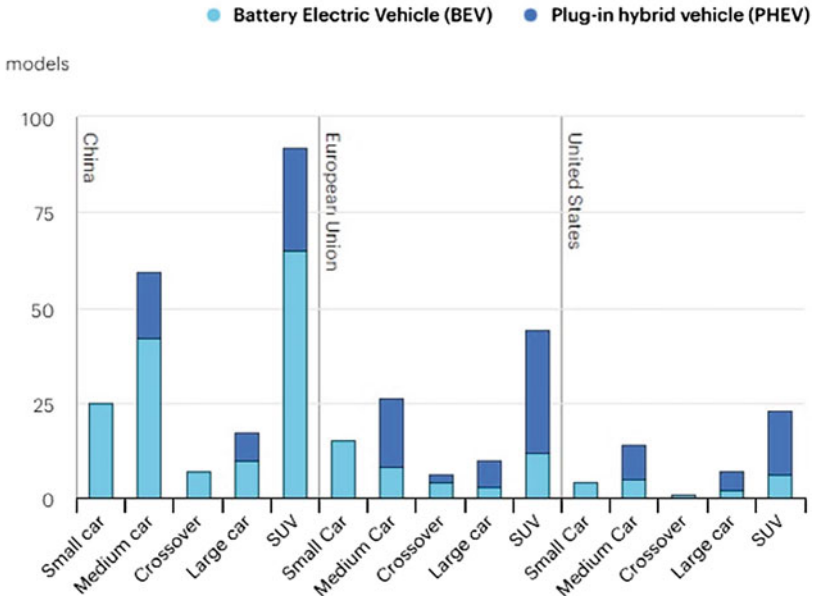


Fig. 8 Electric car models available by region [14]

Electric car models available globally and average range, 2015-2020

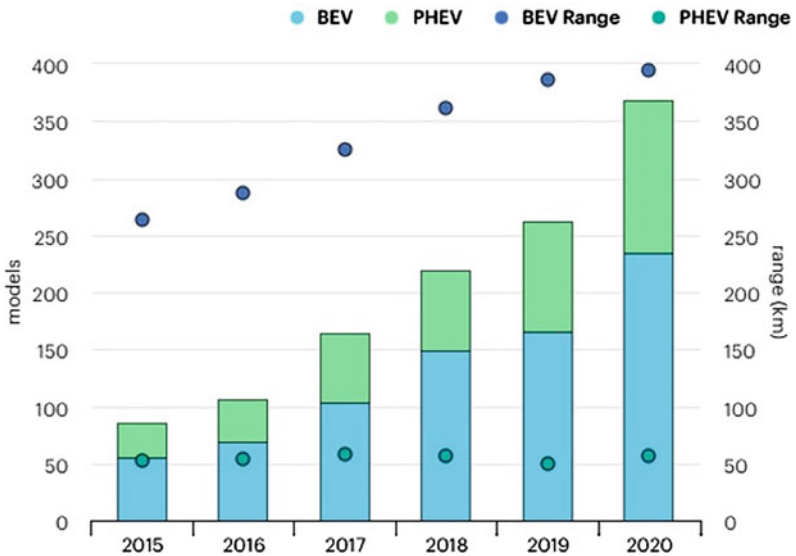


Fig. 9 Electric car models available globally and average range [14]

References

1. Ahmad, F., Alam, M. S., & Shahidehpour, M. (2018). *Optimal placement of electric, hybrid and plug-in hybrid electric vehicles (xEVs) in Indian power market*. IEEE.
2. Gupta, A. K., Kartik, V., & Ramanarayanan, C. P. (2015). *Design, development and performance evaluation of a light diesel hybrid electric pickup vehicle using a new parallel hybrid transmission system*. IEEE Xplore.
3. Chhikara, R., Garga, R., Chhabrab, S., Karnataka, U., & Agrawala, G. (2021). Factors affecting adoption of electric vehicles in India: An exploratory study. *Elsevier*, 100, 103084.
4. Javkhedkar, S. R., & Ashfa, B. (2021). Future of electric vehicle in India. *IRJEdT*, 02(02), 1–7.
5. Grackova, L., & Oleinikova, I. (2014). *Economic motivation for electric vehicles participation in power market*. IEEE Xplore.
6. Sachs, C., Burandt, S., & Mandelj, S. (2016). *Assessing the market of light electric vehicles as a potential application for electric in-wheel drives*. IEEE.
7. Cortezón, I. A., Borrull, R. S., López, A. Q., & Roig, V. F. (2014). *The impact of fully electric vehicles demands in the spot market*. IEEE Xplore.
8. Warweg, O., & Hartung, P. (2014). *Cost-utility analysis to evaluate business cases for electric vehicle market integration*. IEEE Xplore.
9. Vidhi, R., & Shrivastava, P. (2018). A review of electric vehicle lifecycle emissions and policy recommendations to increase EV penetration in India. *Energies*, 11, 483 (Multidisciplinary Digital Publishing Institute).
10. Gupta, S., & Sainai, P. (2018). Electric mobility in India: Potential and policy imperatives. In *International conference on recent advances in transport infrastructure* (pp. 1–10).
11. Shalender, K., & Yadav, R. K. (2017). Promoting e-mobility in India: Challenges, framework, and future roadmap. *Environment, Development and Sustainability*, 28, 2587–2607.
12. Bibra, E. M., Connelly, E., Gorner, M., Lowans, C., Paoli, L., Tattini, J., & Teter, J. (2021). *Global EV outlook 2021: Accelerating ambitions despite the pandemic, transportation research board*. International Energy Agency.
13. James, A. T., Kumar, G., Pundhir, A., Tiwari, S., Sharma, R., & James, J. (2022). Identification and evaluation of barriers in implementation of electric mobility in India. *Research in Transportation Business & Management*, 43, 100757.
14. IEA. (2021). *Global EV outlook 2021*. IEA.

Enhancement of Power Quality Approach Using Unified Power Quality Conditioner



Buddhapriy B. Gopnarayan and Vijay A. Sawant

Abstract The connection of a three-unified power quality conditioner is an effective and economical control approach for compensating for harmonics and Load-Q energy usage (UPQC). This paper proposes a control approach for a unified power quality conditioner as a dual control in the distribution system to reduce power quality issues. End-user-polluted loads are always at the heart of power quality problems. UPQC systems are employed in this study to regulate operations and series power conditioning. The filters convert non-sinusoidal electrical quantities into sinusoidal electrical values by injecting current and voltage at a large phase angle. This is referred to as dual compensation. The proposed UPQC system is compatible with both 3P3W and 3P4W distribution systems.

Keywords UPQC · PQ · THD · Nonlinear load

1 Introduction

Power quality refers to the consistency of the waveforms of current (I), voltage (V), and frequency (Hz) within the accepted sinusoidal range (PQ). Power quality problems include things like voltage flickering, notching, unbalance, interruption, frequency shifts, and transient disturbances. These PQ problems cause a wide variety of electrical problems, such as the tripping of relays and circuit breakers when they shouldn't, the malfunctioning of sensitive electrical devices, inaccurate metre readings, excessive heating and noise generation from electric machinery, and erratic motor speeds. The primary sources of harmonic currents are power (Q) and unbalanced loads resulting from huge inductive loads [1–3]. The voltage drops when switching large loads, but the voltage rises when there is a single LG failure in the power distribution system. Power quality problems can be alleviated with the use of P power-line conditioning equipment including UPQCs, series filters, shunt

B. B. Gopnarayan (✉) · V. A. Sawant
Department of Electrical Engineering, SVERI College of Engineering, Pandharpur, India
e-mail: bbgopnarayan@coe.sveri.ac.in

filters, hybrid P power filters (APFs), dynamic voltage restorers (DVRs), and static synchronous compensators (STATCOMs) [4].

There is a great idea to use APFs to fix PQ issues. Shunt APFs limit current-related issues like harmonics and Q current, while series APFs correct voltage-related issues including imbalance, voltage sag, voltage swell, and voltage harmonics. UPQC refers to a device that has both of these filters and compensates for the 3-phase power system. Problems with current and voltage in the three-phase power system are both addressed by the UPQC at once [9]. Key advantages are as follows. The idea of employing APFs to solve PQ problems is sound; the load is balanced, and harmonic current and voltage have been eliminated. While series P power filters tend to be heavy on voltage issues like voltage unbalance, voltage sag, voltage swell, and voltage harmonics, shunt APFs restrict concerns with current like current harmonics, Q current, and current unbalance. The term “UPQC” is used to describe the device that incorporates both of the aforementioned filters in order to achieve 3-power system balance. UPQC addresses voltage and current issues in the 3-power system at once [9]. That’s where you’ll find the most advantages. The load is compensated for Q power, harmonic current and voltage are removed, voltage and current are balanced at a 120-degree angle, continuous power (in Watts) is delivered, and flicker is eliminated.

Locating the unit vector’s coordinates using SRF-based controllers is possible. The 3-PLL strategy for UPQC systems employs a self-tuning filter to eliminate harmonic currents and load imbalances. The STF sits in the circuit between the 3pPLL and the bus voltage. The 3pPLL modifies the STF cut off frequency based on the initial angular frequency computation. Therefore, the STF’s characteristics can shift depending on the bus frequency. Due to its flexibility, the UPQC may be integrated into a three-phase three-wire or three-phase four-wire distribution system to mitigate line losses and improve power quality for consumers and generators alike. At the plant site, UPQC normally uses 3P3W, and loads require the neutral wire for operation. Having complete digital command over all three phases.

2 Foundational Ideas of UPQC

Its basic block architecture, which includes a 3-series and shunts APF, is depicted in Fig. 1 for the UPQC system. Injecting current and voltage into the system is what the filter is for. The series-P filter lessens voltage imbalance, voltage control, and harmonic compensation between utilities and consumers at the point of common connection (PCC).

Shunt filters regulate the dc-link voltage between the two P filters, dampen current harmonics, and equalize Q power and negative sequence current. When P power filters in series and shunt are combined, the resulting circuit is called a UPQC [12]. A sizeable amount of Q and P power would be consumed by the series inverter. Incorporating a voltage in series into the system creates a phase angle mismatch between the source and load voltage without raising the total load voltage. The need

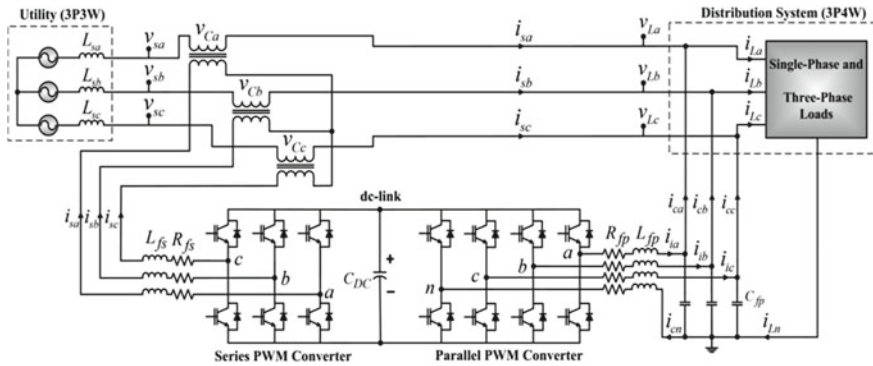


Fig. 1 A 3P3W power system is coupled to a P4W distribution system based on UPQC

for Load-Q power could be reduced using a series P power filter if the phase angle between the source and load voltage is appropriately managed [8].

2.1 Control Strategy for UPQC

In Fig. 1, three-legged and four-legged PWM converters with equal DC linkages are shown, representing the dual compensation technique used by the UPQC in this study. The UPQC links a 3P3W power distribution system to a 3P4W plant site that can handle 3P3W and 1P1S loads. One-phase appliances are assumed to be powered by the neutral wire. In this case, the loads must be supplied by a 3P4W distribution system, which uses three live wires to carry power and a neutral wire to keep the system grounded. Remember that in the UPQC-based 3P4W distribution system shown in Fig. 1, the neutral current flows through the wire conductor coupled to the fourth leg of the shunt 4-Leg PWM.

2.2 Managing the Series Active Power Filter

Unit Vector Templates (UVTs) are used in the series APF control approach (UVT). It is the imbalanced supply that creates the UVT [11]. Method of generating a sinusoidal wave of uniform frequency and amplitude. Series APF creates a balanced voltage at the load side by inserting voltages opposite to any distortion or imbalance existing in the source voltage (Fig. 2).

This controlling method employs a hysteresis controller to produce a load reference voltage for comparison with the load voltage signals in order to produce the necessary gating signal for the series inverter. The hysteresis band controller regulates the inverters' switching frequency. Such control is driven by such an error

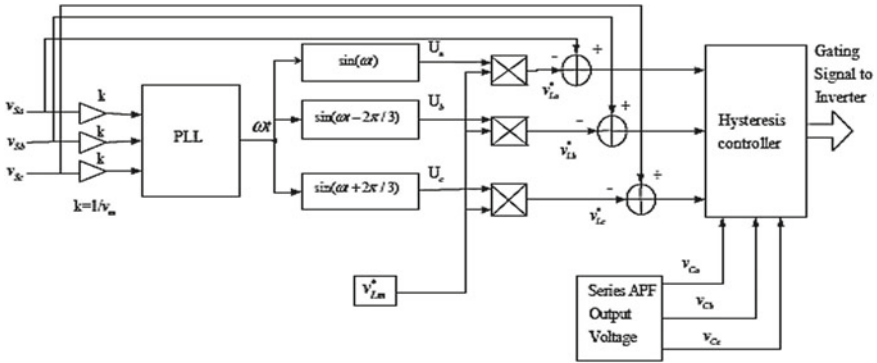


Fig. 2 APF series control block diagram

signal derived from comparing instantaneous load voltage signals to a load reference voltage [5].

2.3 Control of Shunt APF

The shunt P power filter relies on reference signals derived from the idea of sinusoidal Q power. It is depicted in Fig. 3 how the shunt APF is controlled. Considering Eqs. (1) and (2), this theory implies that instantaneous measurement of three-phase voltages and currents can be obtained (2) [5].

$$\begin{bmatrix} v_0 \\ v_\alpha \\ v_\beta \end{bmatrix} = \sqrt{\frac{2}{3}} \begin{bmatrix} 1/\sqrt{2} & 1/\sqrt{2} & 1/\sqrt{2} \\ 1 & -1/2 & -1/2 \\ 0 & \sqrt{3}/2 & -\sqrt{3}/2 \end{bmatrix} \begin{bmatrix} v_{sa} \\ v_{sb} \\ v_{sc} \end{bmatrix} \tag{1}$$

$$\begin{bmatrix} i_0 \\ i_\alpha \\ i_\beta \end{bmatrix} = \sqrt{\frac{2}{3}} \begin{bmatrix} 1/\sqrt{2} & 1/\sqrt{2} & 1/\sqrt{2} \\ 1 & -1/2 & -1/2 \\ 0 & \sqrt{3}/2 & -\sqrt{3}/2 \end{bmatrix} \begin{bmatrix} i_{sa} \\ i_{sb} \\ i_{sc} \end{bmatrix} \tag{2}$$

Equation depicts the zero-sequence elements of the load, the imaginary Q, and the P. A quick calculation of the source side’s real and imaginary power can be made using the Eq. (3) source currents and phase-neutral voltages.

$$\begin{bmatrix} p \\ q \end{bmatrix} = \begin{bmatrix} v_\alpha & v_\beta \\ -v_\beta & v_\alpha \end{bmatrix} \begin{bmatrix} i_\alpha \\ i_\beta \end{bmatrix} \tag{3}$$

The real and imaginary power is,

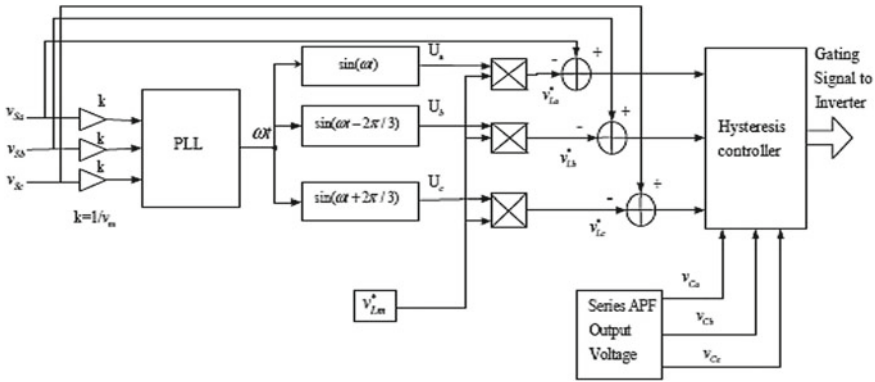


Fig. 3 Control block diagram of shunt APF

$$p_0 = v_0 * i_0; p = \bar{p} + \tilde{p} \tag{4}$$

In order to decrease the neutral current, p_0 is calculated using average and oscillating components.

$$\begin{bmatrix} i * s\alpha \\ i * s\beta \end{bmatrix} = \frac{1}{v_\alpha^2 + v_\beta^2} \begin{bmatrix} v_\alpha & -v_\beta \\ v_\beta & v_\alpha \end{bmatrix} \begin{bmatrix} \bar{p} + p_0 + \bar{p}_{loss} \\ 0 \end{bmatrix} \tag{5}$$

the shunt APF reference currents $i * (s)$, $i * (s)$, and $i*(s_0)$ in $- 0$ coordinates. These currents experience a 3-system transition, as represented in Eq. (6).

$$\begin{bmatrix} i * sa \\ i * sb \\ i * sc \end{bmatrix} = \sqrt{\frac{2}{3}} \begin{bmatrix} \frac{1}{\sqrt{2}} & 1 & 0 \\ \frac{1}{\sqrt{2}} & -\frac{1}{2} & \sqrt{\frac{3}{2}} \\ \frac{1}{\sqrt{2}} & -\frac{1}{2} & -\sqrt{\frac{3}{2}} \end{bmatrix} \begin{bmatrix} i * s0 \\ i * s\alpha \\ i * s\beta \end{bmatrix} \tag{6}$$

Adjustments to the neutral current, harmonics and Q power on the load side can be made once the reference current has been determined. After the reference current has been generated, it is used to compare incoming signals to a known value and any discrepancies are then processed by a hysteresis band PWM controller to form the necessary switching signals for the shunt APF switches [6, 7].

3 Simulation Model

We used MATLAB to create this design. This concept intends to investigate harmonic, Q power correction and other PQ difficulties under different operation situations. Figure 4 depicts the connection of the 1- and 3-nonlinear loads from across 3-supply.

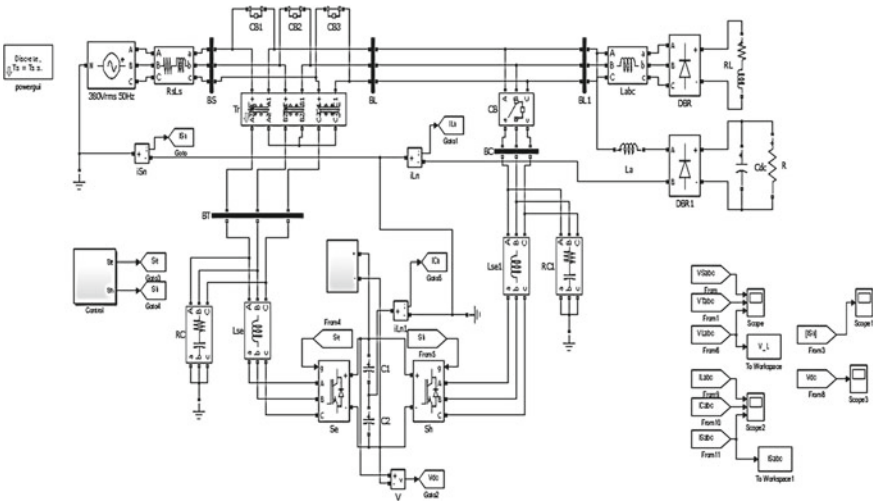


Fig. 4 Simulation model of the UPQC

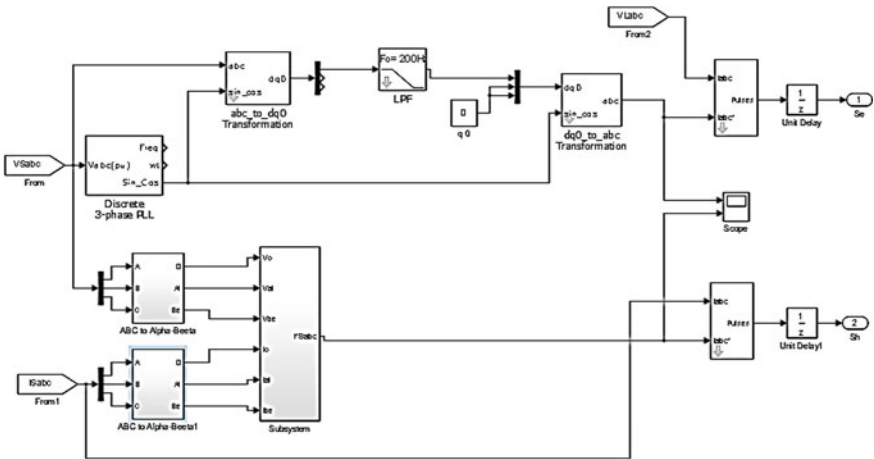


Fig. 5 Series and shunt APF controller

The P power filter can be either shunt or series, with the former connecting across the loads with a shunt transformer and the latter connecting in series with the line using series transformers. Series and shunt APF control Q power by maintaining a large phase difference between the voltage and current.

A converter and circuitry shown in Fig. 5 are part of the combined series and shunt power filter controller etc.

4 Result

MATLAB is used to analyse the performance of a suggested control system for UPQC given in figures that is grounded on p-q theory and designed to compensate for distortional and unbalanced load currents under the influence of distortional as well as unbalanced source voltages as shown in Fig. 6.

The 3-source voltage, terminal voltage, and load voltage waveforms are shown in Fig. 7; before 0.2 s, the UPQC is not connected to the system. After 0.2 s, there is minimal distortion throughout the board from the source voltage, terminal voltage and load voltage. The UPQC system achieves its findings in both steady-state and variable-load operations [10].

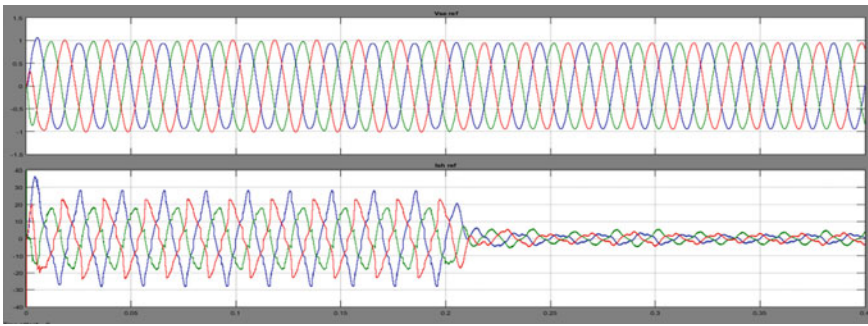


Fig. 6 Series and shunt APF waveforms of V_{ref} and I_{ref}

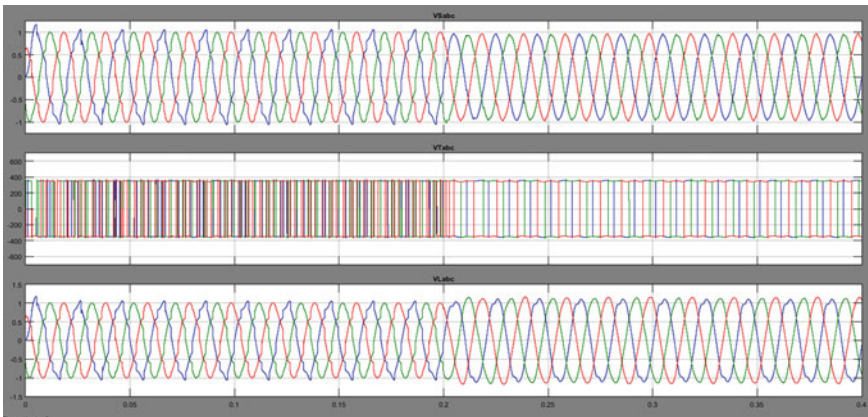


Fig. 7 $V_{S_{abc}}$, $V_{T_{abc}}$ and $V_{L_{abc}}$ waveforms

5 Conclusion

In this work, we show how the dual control scheme of a UPQC can help lessen PQ problems. For the purpose of Q power compensation, UPQC has been shown coupled to a three-phase bus. In addition, it lessens the voltage and current harmonics in contaminated loads. Reference signals for shunt and series power filters are derived from the power quality concept. The study of the effectiveness in terms of %THD reduction according to IEEE Standard is demonstrated in the outcome of the simulation aforesaid.

References

1. Campanhol, L. B. G., Silva, S. A. O., & Goedel, A. (2014). Application of shunt active power filter for harmonic reduction and reactive power compensation in three-phase four-wire systems. *IET Power Electronics*, 7(11), 2825–2836.
2. Dhagate, D. R., & Dhamaal, S. S. (2020). Design and performance evaluation of 3-phase photovoltaic integrated UPQC. In *2020 international conference on power, energy, control and transmission systems (ICPECTS)* (pp. 1–7). <https://doi.org/10.1109/ICPECTS49113.2020.9337053>
3. Ribeiro, R. L. A., de Azevedo, C. C., & de Sousa, R. M. (2012). A robust adaptive control strategy of active power filters for power-factor correction, harmonic compensation, and balancing of nonlinear loads. *IEEE Transactions on Power Electronics*, 27(2), 718–730.
4. Gidd, A. R., & Gore, A. D. (2019). Modelling, analysis and performance of DSTATCOM for voltage sag mitigation in distribution system. In *Proceedings of the 3rd IEEE international conference on trends in electronics and informatics (ICOEI 2019)*. Tamil Nadu, India.
5. Ucar, M., Ozdemir, S., & Ozdemir, E. (2011). A four-leg unified series–parallel active filter system for periodic and non-periodic disturbance compensation. *Electric Power Systems Research*, 81, 1132–1143.
6. Hadpe, S. S., & Shrivastava, R. G. (2021). The architecture of a 24 pulse dynamic voltage restorer for voltage enhancement incorporating vector control methodologies (July 10, 2021). In *2nd international conference on IoT based control networks and intelligent systems (ICICNIS 2021), proceedings of the international conference on IoT based control networks & intelligent systems ICICNIS 2021*. <https://doi.org/10.2139/ssrn.3883846>
7. Modesto, R. A., Oliveira da Silva, S. A., de Oliveira Junior, A. A., & Bacon, V. D. (2015). Versatile unified power quality conditioner applied to three-phase four-wire distribution systems using a dual control strategy. *IEEE Transaction on Power Electronics*, 31, 5503–5514.
8. Thakre, M. P., Borse, P. S., Patil, M. D., et al. (2022). Measurement and compensation of voltage sag employing open-loop single-phase dynamic voltage restorer. *Mapan*, 37, 107–118. <https://doi.org/10.1007/s12647-021-00494-6>
9. Hembram, M., & Tudu, A. (2015). Mitigation of power quality problems using unified power quality conditioner (UPQC). In *IEEE 3rd international conference on computer, communication, control and information technology*.
10. Thakre, M. P., & Matala, N. P. (2020). Alleviation of voltage sag-swell by DVR based on SVPWM technique. In *2020 international conference on power, energy, control and transmission systems (ICPECTS)* (pp. 1–6). Chennai, India. <https://doi.org/10.1109/ICPECTS49113.2020.9336972>
11. Maurya, D. S., Jadhav, P. D., & Joshi, R. S. (2020). A detailed comparative analysis of different multipulse and multilevel topologies for STATCOM. In *2020 international conference on electronics and sustainable communication systems (ICESC)* (pp. 1112–1117). Coimbatore, India. <https://doi.org/10.1109/ICESC48915.2020.9155708>

12. Kadam, R. S., & Thakre, M. P. (2021). Assessment of an improved voltage flicker remediation treatment method employing VSC-Based STATCOM. In *2021 5th international conference on trends in electronics and informatics (ICOEI)* (pp. 267–272). Tirunelveli, India. <https://doi.org/10.1109/ICOEI51242.2021.9452840>

Design and Analysis of GFRP and Chicken Mesh Confined Brick Masonry Columns



Mrunal M. Pawar, Mukund M. Pawar, and Sonali P. Patil

Abstract Unreinforced masonry is used as the load-bearing element still, its low strength and ductility make it prone to earthquakes, extreme wind actions, foundation settlement and deterioration due to environmental effects. Brick columns are mostly used as load-bearing elements. So the failure of a column can have significant to the entire structure. In this paper, different strengthening techniques such as Fibre Reinforced Polymer (FRP) and Fabric Reinforced Cementitious Matrix (FRCM) have been developed to improve masonry's strength and deformation characteristics structures. The proposed study helps to identify the best suitable method to enhance the strength and structural performance of brick masonry columns. A total of 3 masonry column specimens were produced with Bricks and Mortar. The columns with 1200 mm height and cross-sectional dimensions of 210 mm × 210 mm were constructed. Out of 3, 2 specimens of columns were confined by using different composite materials like Glass-FRP and Chicken mesh FRCM. All column specimens have been tested under Loading Frame Facility, and the column tests' outcomes have been evaluated in terms of strength and failure characteristics. GFRP confined brick masonry column showed confinement of 62.41% over unconfined brick masonry column whereas chicken mesh confined brick masonry column showed confinement of 26.62% over unconfined brick masonry column.

Keywords Confinement · Masonry columns · GFRP · Chicken mesh · Experimental testing · Analytical models

1 Introduction

Old buildings rehabilitation is more economical than rebuilding them. That's why the behaviour of strengthening techniques should be understood to make the best decision for rehabilitation in order to save time and cost. Brick is one of the oldest building materials and it is extensively used for load-bearing walls in low-rise buildings and

M. M. Pawar (✉) · M. M. Pawar · S. P. Patil
Civil Engineering Department, SVERI's College of Engineering, Pandharpur, Maharashtra, India
e-mail: mrunal.pawar2016@gmail.com

© The Author(s), under exclusive license to Springer Nature Switzerland AG 2024
P. M. Pawar et al. (eds.), *Techno-Societal 2022*,
https://doi.org/10.1007/978-3-031-34648-4_29

281

for partition walls in high-rise buildings. Encasing the brick masonry columns with composite materials develops a small increase in cross-sectional area and therefore due to this a large increase in strength can be achieved. It appears that these techniques are more cost effective than other techniques. Several research works studied the capabilities of these strengthening techniques—Cascardi et al. [1] studied reversible techniques for FRP-confinement of masonry columns. A reversible technique for FRP confinement of masonry columns has been proposed for three different techniques of FRP Confinement. The analysis of the confined column was carried out and study results were evaluated by comparing the compressive strength and deformability with the unconfined specimens [1]. Shahzada et al. [2] did an experiment on retrofitting of brick masonry columns by Ferrocementing. Retrofitting of masonry columns has been made by application of Ferro cement coatings using expanded wire mesh. The analysis of unretrofitted and retrofitted columns was carried out. This shows that the strength was recovered and the column become stronger due to retrofitting [2]. Yilmaz et al. [3] investigated experimentally the method of External Confinement of Brick Masonry Columns with Open Grid Basalt Reinforced Mortar. The analysis is made between experimental results and theoretical predictions made using analytical models and results are evaluated in terms of strength, deformability and failure characteristics [3]. Kanchidurai et al. [4] used special methods for the assessment of brick masonry strengthening practice. An assessment of Brick Masonry Strengthening practice by special methods has been proposed to strengthen the existing and new masonry structures. The study result shows that the durability of the structure increases drastically [4]. Thamboo [5] studied the performance of masonry columns confined with composites under axial compression. The performance of masonry columns has been improved using three different confinement techniques that are fibre reinforced polymer wrapping, fabric reinforced cementitious matrix application and confinement of mortar joints by steel grinds. Results are evaluated in terms of the strength and ductility of structural members [5]. Joshi [6] had done an experiment on masonry columns with fibre-reinforced polymer confinement. Confinement of masonry columns has been proposed to the type of masonry units, types of mortars, types of FRP used for strengthening, amount of FRP reinforcement and strengthening techniques. The analysis of FRP confined masonry column was carried out and the results show that there is a large increase in load carrying capacity of column specimens [6]. Thamboo [7] studied monotonic and cyclic compression characteristics of CFRP confined masonry columns. An attempt has been made to experimentally characterise the confined masonry columns under monotonic and cyclic axial compression. Results are presented in terms of observed failure modes, compressive strengths and stress–strain curves [7]. Adnan et al. [8] checked Performance of solid masonry columns after strengthening. This study proposed to use the two types of wire mesh i.e. steel and fibreglass on the wall and dry mortar sprayed on it. The analysis of the Ferro cement encased column was carried out and the Ferro cement system showed a good improvement than fibreglass mesh in increase the load capacity of column specimens [8]. Aiello et al. [9] did theoretical and experimental investigations on the confinement of masonry columns with the FRCM system. An experimental and theoretical investigation has been made by considering the kind

of Mortar, the number of layers and strengthening configuration i.e. continuous or discontinuous. The analysis of an experimental and analytical investigation on the performances of clay brick masonry columns with a square cross-section confined by FRCM systems was carried out and FRCM confinement systems improved the axial strength of the columns with respect to the unconfined specimens [9]. Cascardi et al. [10] focused on the study of discontinuous CFRP-confinement of masonry columns. This study has proposed to use of discontinuous FRP Confinement. Results show an increase in ultimate load and axial strain [10]. Maddaloni et al. [11] carried out an experiment on the confinement of full-scale masonry columns with FRCM systems. The use of fibrous nets embedded in a matrix has been developed and investigated. The analysis of Full-scale masonry columns with an FRCM system was carried out and the results show an increase in load carrying capacity and ultimate axial strain [11]. Minafo et al. [12] studied the effect of FRP wraps on the compressive behaviour of slender Masonry columns. This study proposed to external use of the Fibre reinforced polymer wrapping confinement technique. The analysis of FRP confined slender column was carried out and due to FRP wrapping compressive strength and ductility of the member increased [12].

2 Problem Statement

Unreinforced masonry is a common type of construction used throughout the world for hundreds of years and is commonly used for new construction projects. However, this type of construction is prone to damage from earthquakes. Therefore, the Column is one of the essential elements of the structure. In low-rise buildings, columns are considered the critical load- Bearing element, and research has been done to protect columns against external hazards. Techniques used to confine brick masonry columns are wrapping GFRP and Chicken Wire Mesh coatings to the unconfined brick masonry columns. The main objective of this study is to evaluate the capability of the confinement of the unconfined brick masonry columns and to make the confinement process more effective, safe and economical.

3 Analysis

ANSYS simulates structural analysis, including linear, nonlinear, and dynamic studies. Additionally, Finite Element Analysis models of structural components can provide a great alternative solution. Once developed FE model results are validated with that of experiments, a wide range of parametric studies can be performed through modelling simulation. This Study uses a static structural analysis tool to analyse brick column specimens. The sequence of operations done in the static structural analysis is Engineering Data, Geometry, Modelling, Setup, Solution, and Result.

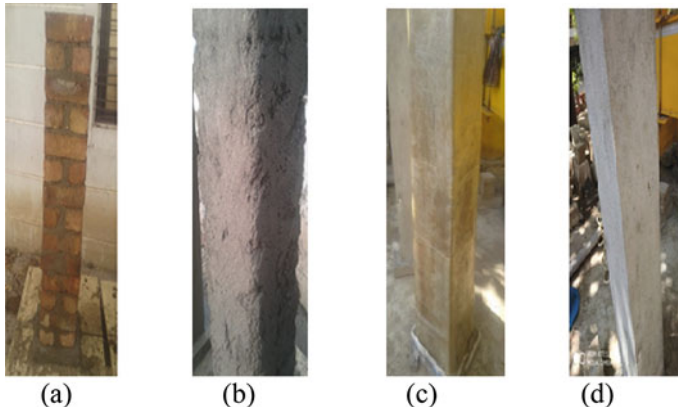


Fig. 1 a Brick column, b brick column with plaster, c GFRP confinement of brick masonry column and d chicken wire mesh FRCM confinement of brick masonry column

Model Description: ANSYS Workbench 17.2 is used to construct the Finite Element Model for Unconfined and Confined Brick Column, shown in figure. The fixed end conditions are used for the analysis of columns.

4 Results and Discussion

4.1 Experimental Analysis

4.1.1 Construction of Specimen

A total of three masonry column specimens with a square cross-section are constructed using bricks taken from a brick kiln available in a nearby village. The mortar used for casting brick masonry was 1:4 (Cement: Sand). The bricks used are 210 mm in length, 95 mm in breadth, and 60 mm in height. The nominal size of each column was 1200 mm and with nominal cross-sectional dimensions of 210 mm × 210 mm without plaster. The nominal thickness of mortar was 20 mm for the bed and head joint. Each masonry column includes 15 rows bonded with 15 beds and several head mortar joints (as shown in Fig. 1a).

4.1.2 Strengthening of Specimen

First, three brick masonry square column specimens with 210 mm sides and 1200 mm heights were cast. One brick masonry column was prepared as a control specimen without confinement. Two of the three were confined externally using Composites

like GFRP and Chicken wire mesh FRCM techniques. For plastering, apply a mortar layer of thickness of 15 mm over the prepared brick masonry column. Composites were used on the plastered surface of the column. The Strengthening procedure will be different for each composite. For GFRP composite, there will be two layers of Glass Fibre wrapping over the plastered brick masonry column. To properly bond Glass Fibre to column surface, Epoxy Resin with hardener is used in 2:1 proportion. It acts as bonding as well as strengthening material. This process should be done after the completion of 28 days of curing. After completion of all procedures of GFRP Confinement, dried the GFRP confined brick masonry column for 5–6 days before testing the column specimen. The GFRP column specimen is shown in Fig. 1c. For the Chicken Mesh FRCM composite, apply the chicken mesh of 1 mm over the rough plastered surface (see in Fig. 1b) of the column by using screws. The mesh used was in two layers. And after that, apply mortar of 1:4 (Cement: Sand) on the mesh surface for proper bonding, as shown in Fig. 1d. All of these specimens were water cured for 28 days. Curing of all samples was done with jute bags covered around all the models as the temperature was high during the casting.

4.1.3 Material Characterisation and Test Setup

Material characterization has been performed for the masonry and its constituents. The Compressive strength of the Brick was 4.511 MPa which is experimentally calculated by using Compression Testing Machine (CTM) instrument. The density of Brick was 1923.97 kg/m³. The Compressive strength of the mortar cube was 4.1 MPa, and the density was 2132 kg/m³. All the column specimens were tested under axial compression load using a structural loading frame machine. A steel plate of size 210 mm × 210 mm was used for uniform load distribution. The load was applied using a Hydraulic Loading Jack with a load capacity of 200 tonne. The load cell records the applied load. Throughout the test, the control system and its associated DAS software (Digital Data Acquisition System) record the readings of the applied load (Fig. 2).

Two of the three specimens of brick masonry columns were confined by composites. After 28 days of curing, all the column specimens were tested up to failure load. The failure loads of unconfined and confined brick masonry columns are presented in Table 1. Three columns were tested for compressive strength by applying axial load through a loading frame machine of 200-tonne capacity. Observations during tests of unconfined and confined brick masonry columns are:

- (1) For the Unconfined Brick Column, the average failure load was 89.4 kN. Significant cracks were vertical and which was observed on the plastered surface of the column, and a few horizontal cracks were also observed. The vertical cracks passed through the joints and bricks (see Fig. 2a). The cracks widening and propagation were quite fast after their first appearance. Near failure, i.e. below the point of load application, the specimen demonstrated outward bulging on all four faces.

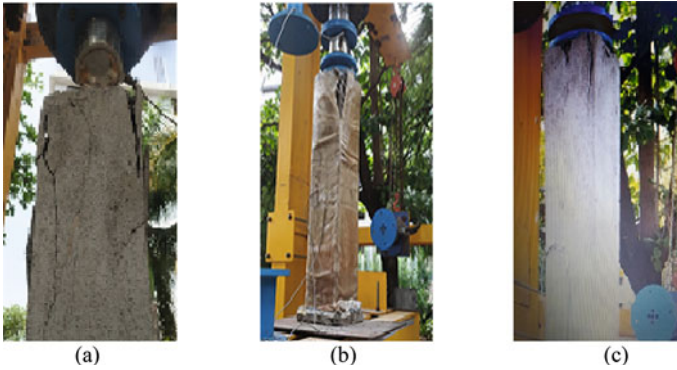


Fig. 2 Failure patterns: **a** unconfined brick masonry column, **b** GFRP confined brick masonry column and **c** chicken mesh confined brick masonry column

Table 1 Comparison of load increment in failure due to confinement effect

Sr. No	Specimen designation	Failure load (kN)	Load increment due to confinement effect (kN)	Effect of confinement (%)
1	Unconfined brick masonry column (210 mm × 210 mm)	89.4	–	–
2	GFRP confined brick masonry column (234.6 mm × 234.6 mm)	145.2	55.8	62.41
3	Chicken mesh FRCM confined brick masonry column (252 mm × 252 mm)	113.2	23.8	26.62

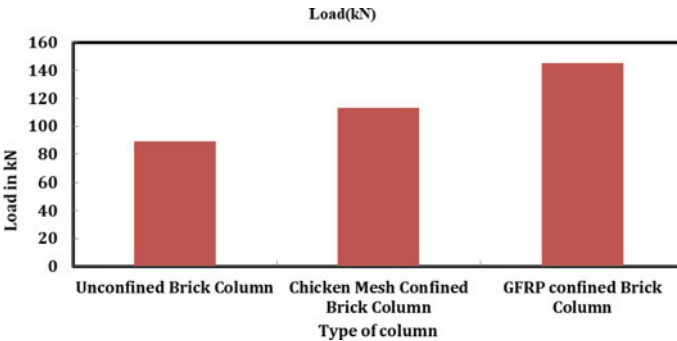


Fig. 3 Loads of unconfined and confined brick column

- (2) For Confined Brick Columns, both GFRP confined and Mesh Confined Brick Columns failed at a failure load of 145.2 and 113.2 kN, which was higher than Unconfined Brick Masonry Columns. Most cracks were initiated from the top and corner refers to Fig. 2b and c. But crack growth was relatively stable and much slower compared to the widening rate to the Unconfined Brick Column. This slow rate of crack growth is due to the presence of Chicken wire mesh and GFRP coatings, which helped arrest the cracks during the propagation process. Due to the outward bulging of material, there will be rupture of Glass Fibre sheet at top corner, but Chicken Wire Mesh inside was good in shape.

Confinement effect of composite materials on brick columns

Under compressive stresses in the transverse direction, the load carrying capability of the brick masonry column is increased by a considerable amount. When brick masonry columns are subjected to axial load, they are compressed in the vertical direction and tend to expand in the lateral direction due to the Poisson's ratio effect. So in the case of columns, the provision of Glass Fiber wrapping with Epoxy Resin and Chicken Wire mesh coatings opposes the lateral expansion of unconfined brick columns and imparts compressive stresses on columns. This process is known as the confinement effect. The structural behavior of the brick masonry column changes due to this confinement effect.

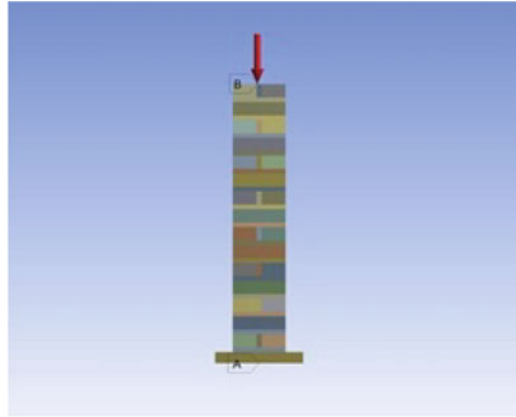
To obtain the strength increment of brick masonry columns due to the confinement effect, the Unconfined and Confined Brick Masonry Columns were tested individually up to failure. From Table 1 it can be seen that the failure load of the column having GFRP confinement was 60–62% higher than the Unconfined Brick Column and the Failure load of the column having Chicken Wire Mesh confinement was 20–27% higher than Unconfined Brick Column. So, it can be concluded that there is an increase in failure loads of brick masonry columns due to the confinement effect imparted by various composite materials.

4.2 Numerical Analysis

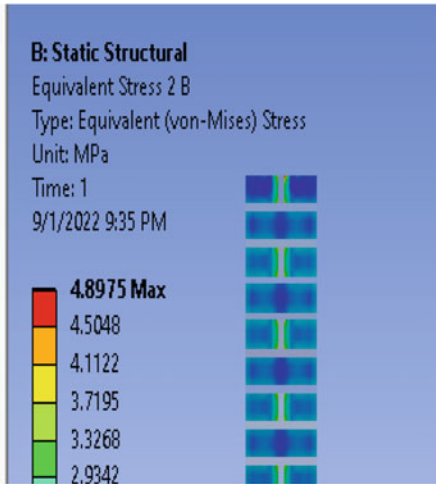
Analysis of Confined and Unconfined Brick Columns were performed by using ANSYS Workbench 17.2. From Analysis, the results of Equivalent stresses on different materials of unconfined and confined brick columns are shown in Table 1. And models of unconfined and confined brick columns are shown below.

4.2.1 Unconfined Brick Masonry Column with 89.4 kN Axial Load

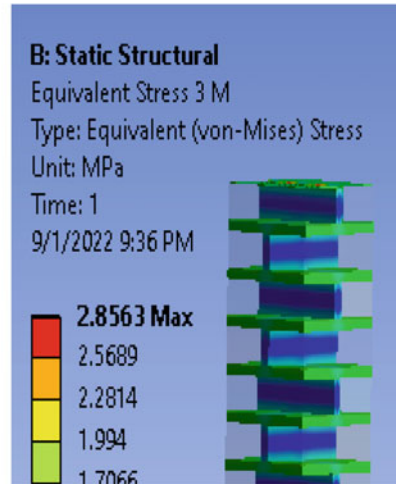
The results of Unconfined Brick Masonry Column in terms of Equivalent Stresses on Brick and Mortar are shown in Figs. 4 and 5.



(a)



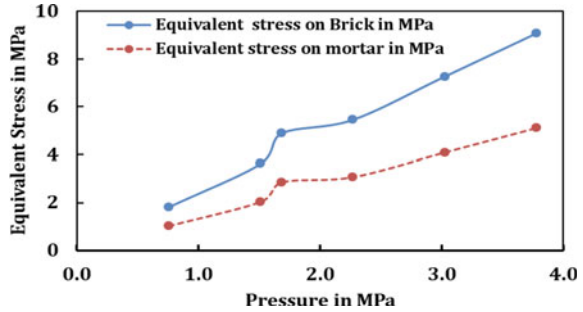
(b)



(c)

Fig. 4 Modelling of unconfined brick masonry column. **a** Application of load and boundary conditions, **b** equivalent stress on brick and **c** equivalent stress on mortar

Fig. 5 Pressure versus equivalent stress on different materials of unconfined masonry column



4.2.2 Chicken Mesh Confined Brick Masonry Column with 113.2 kN Axial Load

The results of Chicken Mesh Confined Brick Masonry Column in terms of Equivalent Stresses on Brick, Mortar and Chicken Mesh are shown in Figs. 6 and 7.

4.2.3 GFRP Confined Brick Masonry Column with 145.2 kN Axial Load

The results of GFRP Confined Brick Masonry Column in terms of Equivalent Stresses on Brick, Mortar, Glass Fibre and Epoxy Resin are shown in Figs. 8 and 9.

4.3 Comparative Analysis of Experimental and Analytical Results

It can be seen that for GFRP and Chicken Mesh confined column load carrying capacity was higher compared to unconfined brick column. Due to increase in load carrying capacity, there is increase in equivalent stresses. So from results, confinement using GFRP is very efficient and economical.

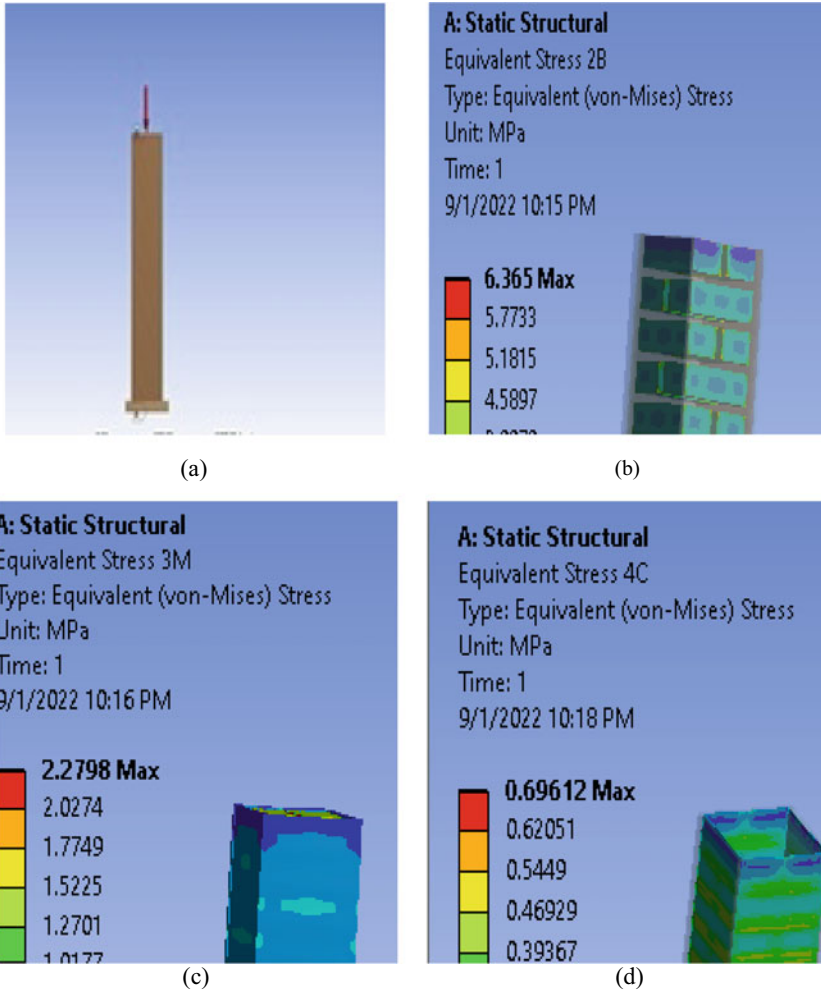
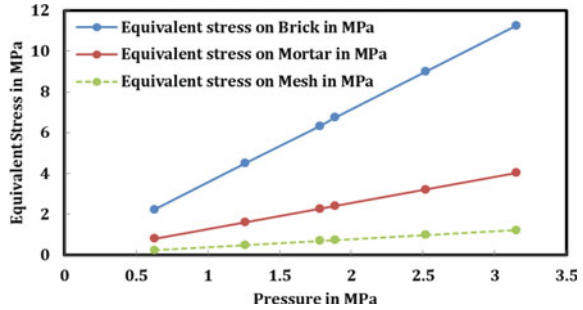


Fig. 6 Modelling of chicken mesh confined brick masonry column. **a** Application of load and boundary condition, **b** equivalent stress on brick, **c** equivalent stress on mortar and equivalent stress on mesh

Fig. 7 Pressure versus equivalent stress on different materials of chicken mesh confined masonry column



5 Conclusions

The experimental and analytical investigation of the performance of unconfined and confined brick columns with square cross-sections has been carried out. The strengths of both types of brick columns have been studied. Based on experimental investigations, the following conclusions are made.

1. Found the load carrying capacity of the Confined Brick Masonry column to be much higher than that of the Unconfined Brick Masonry column.
2. Load bearing capacity vastly increases in the case of specimens provided with a minimal volume of composites.
3. Applying GFRP and Chicken wire mesh coating on Unconfined Brick Masonry columns increases the confinement effect. Wrapping of composites around column shows an increase in Failure load up to 20–70% compared to Unconfined Brick Masonry column.
4. In the Unconfined Brick Masonry column, failure is sudden, and cracks widen rapidly compared to Confined Brick Masonry columns.
5. This study concludes that confinement using GFRP is very efficient and economical and increases compressive strength compared to chicken mesh FRCM confinement.
6. Stress analysis results by finite element method show similar failure patterns as compared to experimental.
7. The 0.2–0.3% variation in ANSYS stress result and the stress results of theoretical calculations.

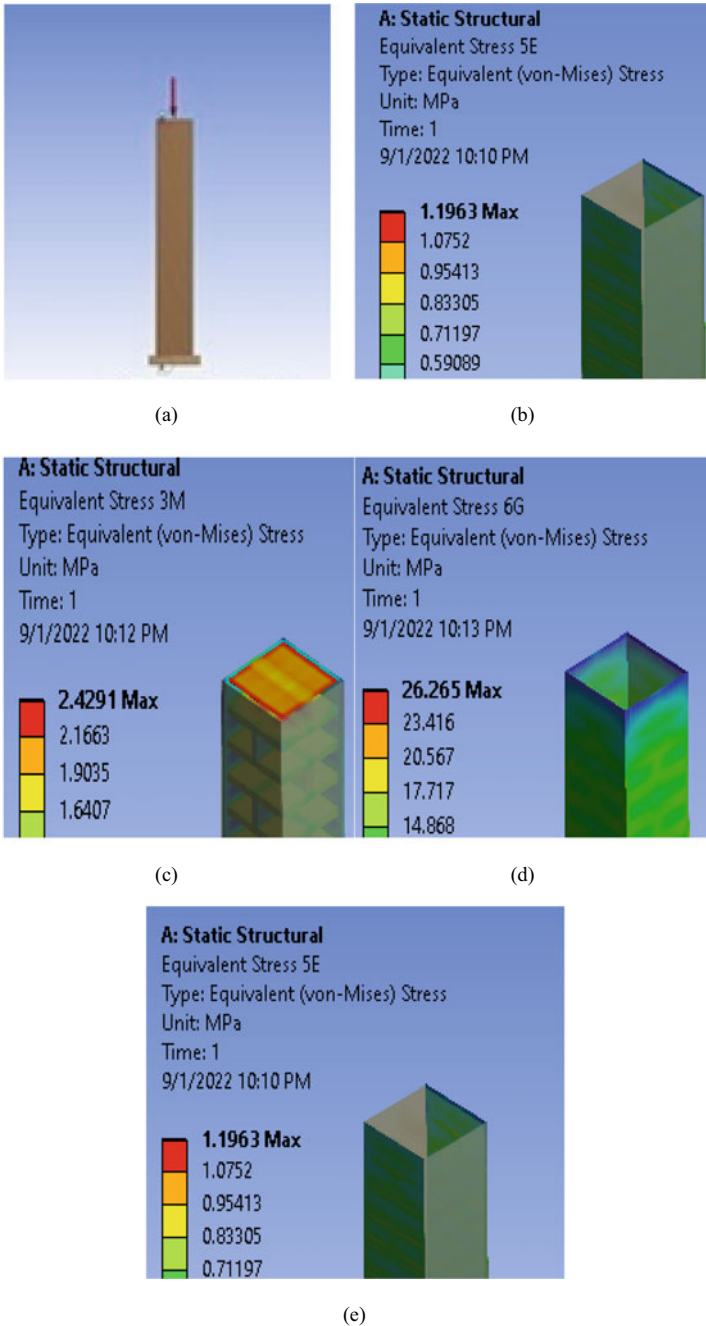


Fig. 8 Modelling of GFRP confined brick masonry column. **a** Application of load and boundary condition, **b** equivalent stress on brick, **c** equivalent stress on mortar, **d** equivalent stress on glass fibre and **e** equivalent stress on epoxy resin

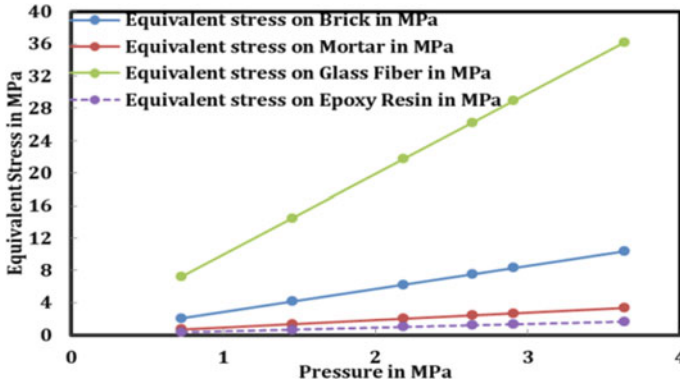


Fig. 9 Pressure versus equivalent stress on different materials of GFRP confined masonry column

References

- Cascardi, A., Dell'Anna, R., Micelli, F., Lionetto, F., Aiello, M. A., & Maffezzoli, A. (2019). Reversible techniques for FRP-confinement of masonry columns. *Construction and Building Materials*, 225, 415–428.
- Shahzada, K., Alam, B., Javed, M., Ali, Z., Khan, H., & Shah, S. S. A. (2012). Retrofitting of brick masonry columns by ferocementing. *International Journal of Advanced Structures and Geotechnical Engineering*, 01, 50–54.
- Yilmaz, I., Mezrea, P. E., Ispir, M., Binbir, E., Bal, I. E. & Ilki, A. (2013). External confinement of brick masonry columns with open-grid basalt reinforced mortar. In *Proceedings of the fourth Asia-Pacific conference on FRP in structures (APFIS 2013), Melbourne, Australia* (pp. 11–13).
- Kanchidurai, S., Krishnan, P., & Baskar, K. An assessment of brick masonry strengthening practice by special methods. *International Journal of Recent Technology and Engineering (IJRTE)*, 8, ISSN: 2277-3878.
- Thamboo, J. (2021). Performance of masonry columns confined with composites under axial compression: A state-of-the-art review. *Construction and Building Materials*, 274, 121791.
- Joshi, D. A. (2017). Confinement of masonry columns with fiber reinforced polymers, experimental research work: A state of the art. 8, 1077–1088.
- Thamboo, J., Zahra, T., & Asad, M. (2021). Monotonic and cyclic compression characteristics of CFRP confined masonry columns. *Composite Structures*, 272, 114257.
- Adnan, M. Q., Hatem, H. H., Alghazali, H. H., Mahdi, W. H., Mahdi, A. H., Mohammed, M. W., & Numan, M. A. (2021). Performance of solid masonry columns after strengthening. In *Journal of physics: Conference series* (Vol. 1973, No. 1, p. 012175). IOP Publishing.
- Aiello, M. A., Cascardi, A., Ombres, L., & Verre, S. (2020). Confinement of masonry columns with the FRCM-system: Theoretical and experimental investigation. *Infrastructures*, 5(11), 101.
- Cascardi, A., Lerna, M., Micelli, F., & Aiello, M. A. (2020). Discontinuous FRP-confinement of masonry columns. *Frontiers in Built Environment*, 5, 147.
- Maddaloni, G., Cascardi, A., Balsamo, A., Di Ludovico, M., Micelli, F., Aiello, M.A. & Prota, A. (2017) Confinement of full-scale masonry columns with FRCM systems. In *Key engineering materials* (Vol. 747, pp. 374–381). Trans Tech Publications Ltd.
- Minafò, G., D'Anna, J., La Mendola, L., Monaco, A., & Amato, G. (2017). Effect of FRP wraps on the compressive behaviour of slender masonry columns. In *Key engineering materials* (Vol. 747, pp. 85–92). Trans Tech Publications Ltd.

Effect of Fly Ash and Ground Granulated Blast Furnace Slag on Fracture Parameters of Sustainable Concrete



Sudhanshu S. Pathak and Gaurang R. Vesmawala

Abstract The knowledge of fracture mechanics has a great importance for numerous structural applications for structures like dams, nuclear power projects etc. This paper concentrated on study of fracture parameters on concrete using Fly ash (FA) and ground granulated blast furnace slag (GGBS) as a supplementary cementitious material (SCM) to make concrete sustainable. The FA and GGBS were partially replaced with cement with percentage of 10, 20, 30 and 40. The water to cement (w/c) ratio kept constant 0.38 for all mixes. The three point bend test was conducted on notched beams according to RILEM recommendation. The crack mouth displacement (CMOD) opening rate was maintained 0.05 mm/min. The mechanical and fracture parameters were studied, the results stated that the GGBS has shown improvement in fracture energy, fracture toughness and mechanical properties compared with FA. The presented result of research shows the usefulness of SCM in concrete.

Keywords Fracture energy · Fracture toughness · Sustainable concrete · Mechanical properties

1 Introduction

The supplementary cementitious materials (SCM's) are playing key role in making concrete sustainable, as these material will get replaced partially with cement. This will helps to make concrete green/sustainable concrete without compromising on strength factor of concrete. The various SCM's are used in research such as fly ash (FA), ground granulated blast furnace slag (GGBS) etc. as these are waste products generated from industries and having low cost [1]. The limestone powder is commonly used material having wide availability and low price. The use of limestone

S. S. Pathak (✉) · G. R. Vesmawala
Department of Civil Engineering, Sardar Vallabhabhai National Institute of Technology (SVNIT),
Surat, Gujrat, India
e-mail: pathaksudhanshu@yahoo.com

S. S. Pathak
Department of Civil Engineering, D Y Patil College of Engineering, Akurdi, Pune, India

powder in self- compacting concrete shown improvement in mechanical properties [2]. According to [3] the use of FA and TiO_2 nano powder (NT) will enhance the strength parameter of SCC, the rheological characteristics and workability enhanced with use of FA and NT. Moreover the consistency has been improved and accelerate the C–S–H gel formation. The use of NT leads to improve the pore structure and more refined microstructure has been observed. Bharatkumar et al. [4] mentioned about the effect on fracture properties using FA and slag replaced by 25 and 50% respectively with cement in high performance concrete (HPC). The addition of FA results into decrease in fracture energy for the mix having water to binder ratio and inverse condition was observed for fracture toughness, which increases with addition of FA and slag. According to [5] the use of GGBS in polymer concrete with alkaline solution to binder ratio (Ai/Bi) (0.65, 0.75 and 0.85) leads to improve in fracture energy, fracture toughness with increase in Ai/Bi ratio from 0.65–0.85. The all mixes are observed improvement in compressive strength with use of GGBS. Šejnoha et al. [6] observed that the use of 30% FA fulfil the strength parameter, while the higher volume FA failed to meet the requirement of strength. Moreover the fracture properties are improved around 60% compared with reference mix. Karamloo et al. [7] studied the fracture parameters with various water to cement (w/c) ratios changing from 0.35 to 0.5, it has been observed the fracture energy significantly decreased with increase in w/c ratio from 0.35 to 0.5 of SCC and same is the case for fracture toughness. The fracture parameters are analysed using size effect method (SEM). Beygi et al. [8] is also used SEM to study the fracture parameters of SCC and observed that the 0.4 w/c ratio showed maximum fracture energy, the characteristic length (*Lch*) which represents the brittleness of material, decreases with decrease in w/c ratio from 0.7 to 0.35 and fracture energy. The fracture properties are depend upon various factors such as w/c ratio, w/b ratio, aggregate size, volume of coarse aggregate etc. Beygi et al. [9] studied the fracture properties with various aggregate size (9.5, 12.5 and 19 mm). The fracture energy is strongly affected by size of coarse aggregate, the content of coarse aggregate increases, the fracture energy increases, while fracture toughness increased by 20% for 9.5 mm aggregate compared with 19 mm. Beygi et al. [10] observed the drop in fracture energy in SCC from size of coarse aggregate 19–9.5 mm in SEM and work of fracture (WFM) methods and *Lch* increased with increase in size of coarse aggregate. Eskandari et al. [11] observed maximum peak load in SCC beams without notch compared with beams with notch, it has been observed, the more is compressive strength more will be the fracture energy increases.

Table 1 Physical properties of cement

Particulars	Fineness (m ² /kg)	Standard consistency (%)	Setting time (min)		Soundness (mm)
			Initial	Final	
Observed values	322	27	125	230	0.55

Table 2 Physical properties of FA

Particulars	% moisture	Fineness: 45 micron	Sulphuric unhydride %	Chloride iron %	Relative density	Water requirement %
Observed values	< 0.1	82	0.1	0.0006	1.89	94.5

Table 3 Physical properties of GGBS

Particulars	CaO	Al ₂ O ₃	Fe ₂ O ₃	SiO ₂	MgO
Observed values (%)	37.67	15.42	1.21	36.32	7.71

2 Experimental Program

2.1 Materials

The 53 grade of Ultratech cement was used, India, according to IS 4031:1996 Part 1 [12]. Class 'F' FA was used and GGBS was obtained from the industry located in the region of Mumbai. The physical properties of cement, FA and GGBS are shown in Tables 1, 2 and 3 respectively. The maximum size of coarse aggregate was used 20 mm and river type fine aggregate was used with maximum size 4.75 mm conforming to IS 2386 Part 1 [13]. The polycarboxylic-ether type super plasticizer was used having specific gravity of 1.12–1.18.

2.2 Preparation of Specimens and Mix Design

A total nine numbers of mixes were prepared as shown in Table 4 conforming to IS 10626:2009 [14]. The cement was used 350 kg/m³, the w/c ratio was used same for all mixes is 0.38. FA and GGBS was replaced 10, 20, 30 and 40% by weight of cement. Mixing was done at specific proportion in drum mixer to prepare the concrete by mixing cement, CA, fine aggregate, admixture, water, SCM's.

To study the fracture properties of concrete using FA and GGBS, the 27 beams with notch of different sizes 38.2 × 76.4 × 204 mm³, 38.2 × 152.8 × 408 mm³,

Table 4 Mix proportions

No	Mix ID	w/c	Cement (kg/m ³)	FA (kg/m ³)	GGBS (kg/m ³)	Fine aggregate (kg/m ³)	CA (kg/m ³)
1	CC	0.38	350	35	–	845	1122
2	FA10	0.38	315	70	–	845	1122
3	FA20	0.38	280	105	–	845	1122
4	FA30	0.38	245	140	–	845	1122
5	FA40	0.38	210	35	–	845	1122
6	GGBS 10	0.38	315	–	35	845	1122
7	GGBS 20	0.38	280	–	70	845	1122
8	GGBS 30	0.38	245	–	105	845	1122
9	GGBS 40	0.38	210	–	140	845	1122

38.2 × 305.6 × 816 mm³ (width × depth × length) were prepared according to recommendations of RILEM TC-89, 1985 [15]. Figure 1 shows the beam specimens.

According to [15] the span to depth ratio 2.5 and length to depth ratio was considered 2.67. The depth of notch to beam depth ratio was taken 0.25. The 3 mm thick notch was made by using the M S plate in the beam molds. The M S plate was inserted in notch which was made in beam mold and this plate was removed while demolding of specimens. In addition to notched beams the 150 mm dia. × 300 mm height cylinders, 150 mm × 150 mm × 150 mm cubes and 150 mm × 150 mm × 700 mm beams were casted to study the split tensile strength, compressive strength and flexural strength respectively. The beams, cubes and cylinders were kept in water for curing. The 50 kN capacity closed loop servo control universal testing machine

**Fig. 1** Beam specimens



Fig. 2 Experimental setup

was used (Fig. 2). All the test was conducted under crack mouth opening displacement (CMOD), the displacement, CMOD, load and time are acquired through data acquisition system. The SEM was used as per the RILEM TC 89 FMT, to calculate the fracture properties the specimen weight is taken into account, based on dimensional properties of specimens the corrected peak load is calculated according to [15].

3 Result and Discussion

As per the RILEM recommendations, the SEM method is to evaluate the fracture parameters in which the weights of specimens are need to consider and corrected peak load need to calculate the as mentioned in Table 5. Table 6 shows the details of fracture parameters and strength parameters obtained from SEM. Figures 3 and 4 indicates the fracture energy of entire proportions and fracture toughness of entire specimens respectively. The fracture energy of FA 20 mix found highest amongst all the mixes, it is noted that fracture energy increased from FA 10 to FA 20 and thereafter significant drop has been decreased. The same is the case of GGBS, the GGBS 20 found highest fracture energy and thereafter significant drop is observed. As per Table 6 we may conclude that compressive strength and fracture energy has relation, as compressive strength increases the fracture energy also increases. About fracture toughness for FA and GGBS it has been observed that the fracture toughness increases with increases in percentage from 10 to 40 and FA 40, GGBS 40 observed highest in their respective series of mix and FA40 found highest amongst all the mixes.

Table 5 Corrected maximum load of all mixes

Specimen Ids	f_c (MPa)	a_o/d	Depth (d) mm	Corrected maximum P^o (N)			Average
				Beam 1	Beam 2	Beam 3	
CC	40.55	0.25	57.1	3820	3745	3850	3805
			114.3	4245	4358	4375	4326
			228.6	5005	5123	5127	5085
FA10	42.55	0.25	57.1	4285	4194	4156	4212
			114.3	5050	5180	4985	5072
			228.6	6375	6279	6285	6313
FA20	45.88	0.25	57.1	5045	4899	4987	4977
			114.3	6223	6275	6279	6259
			228.6	7375	7266	7295	7312
FA30	41.05	0.25	57.1	3185	3265	3207	3219
			114.3	4665	4852	4797	4772
			228.6	5115	5200	5205	5174
FA40	40.33	0.25	57.1	3535	3585	3625	3582
			114.3	4395	4495	4500	4464
			228.6	5850	5800	5885	5845
GGBS10	41.76	0.25	57.1	4215	4985	4532	4578
			114.3	5585	5698	5789	5688
			228.6	5945	6223	6187	6118
GGBS20	42.52	0.25	57.1	4945	4923	4900	4923
			114.3	6223	6235	6270	6243
			228.6	6801	6956	7025	6928
GGBS30	42.36	0.25	57.1	3185	3265	3207	3219
			114.3	3785	4052	3997	3944
			228.6	3985	4101	4098	4063
GGBS40	41.32	0.25	57.1	3355	3410	3501	3422
			114.3	4185	4298	4378	4287
			228.6	5875	5700	5752	5775

Figure 5 shows the load versus CMOD plot of FA and GGBS, the corrected peak load calculated with reference to Table 5 are plotted. In the plot S, M and L indicated the small, medium and large size beam specimens. The CMOD data is obtained through data acquisition system.

Table 6 Fracture parameters obtained from SEM

Specimen Ids	f_c (MPa)	f_t (MPa)	f_r (MPa)	G_F (N/m)	KIc (MPa m ^{0.5})
CC	41.55	3.65	7.25	92.61	0.75
FA10	42.55	3.92	8.15	95.53	0.68
FA20	45.88	4.02	8.95	98.35	0.78
FA30	41.05	3.83	7.45	89.37	0.80
FA40	40.33	3.14	7.35	88.56	0.90
GGBS 10	41.95	3.85	7.85	94.85	0.64
GGBS 20	42.22	3.92	7.56	94.94	0.72
GGBS 30	41.36	3.65	7.25	90.05	0.64
GGBS 40	41.32	3.21	7.02	89.54	0.88

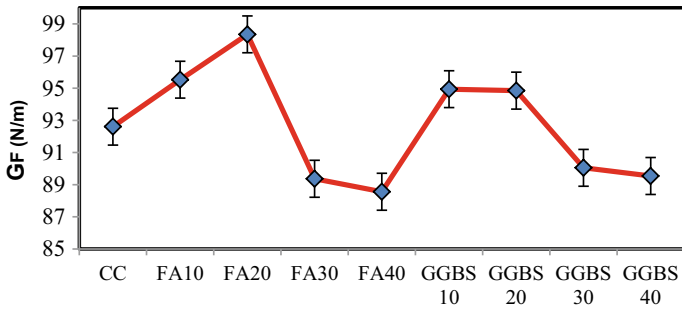


Fig. 3 Fracture energy of all mixes

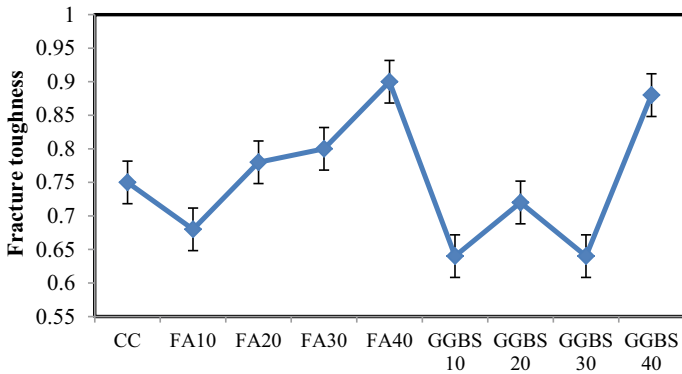


Fig. 4 Fracture toughness of all mixes

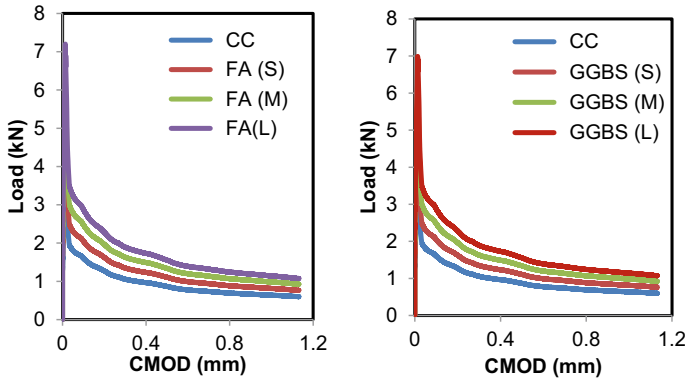


Fig. 5 Plot of Load versus CMOD

4 Conclusions

Following are the conclusion of present study.

1. The fracture energy of FA and GGBS has been improved when compared with control mix. Moreover the FA 20 show the maximum fracture energy amongst the all the mixes.
2. The fracture energy of GGBS observed highest at GGBS 20 mix, but it is slightly less compared to FA20 mix.
3. It has been observed the use of SCM up to 20% can improve the fracture energy component and after that it declines.
4. The SCM percentage increase from 10 to 40 the fracture toughness of both mixes (FA and GGBS) increases.
5. It is noted, the use of SCM improves the compressive strength up to specific extent and fracture energy increases with increase in compressive strength.

Acknowledgements The authors would like thank Mr. Ajay Vaghela, Mr. Atul Patane, Mr. Mallikarjun Hulgabali of SVNIT Surat for cooperation.

References

1. Salla, S. R., Modhera, C. D., & Babu, U. R. (2021). An experimental study on various industrial wastes in concrete for sustainable construction. *Journal of Advanced Concrete Technology*, 19, 133–148. <https://doi.org/10.3151/jact.19.133>
2. Nikbin, I. M., Davoodi, M. R., Fallahnejad, H., Rahimi, S., & Farahbod, F. (2016). Influence of mineral powder content on the fracture behaviors and ductility of self-compacting. *Concrete*, 28(3), 04015147. [https://doi.org/10.1061/\(ASCE\)MT.1943-5533.0001404\(2016\)](https://doi.org/10.1061/(ASCE)MT.1943-5533.0001404(2016))

3. Jalal, M., Fathi, M., & Farzad, M. (2013). Effects of fly ash and TiO₂ nanoparticles on rheological, mechanical, microstructural and thermal properties of high strength self compacting concrete. *Mechanics of Materials*, 61, 11–27. <https://doi.org/10.1016/j.mechmat.2013.01.010>
4. Bharatkumar, B. H., Raghuprasad, B. K., Ramchandramurthy, D. S., Narayanan, R., & Gopalkrishnan, S. (2005). Effect of fly ash and slag on the fracture characteristics of high performance concrete. *Materials and Structures*, 38, 63–72. <https://doi.org/10.1617/14107>
5. Mousavinejad, S. H. G., & Gashti, M. F. (2021). Effect of alkaline solution/binder and Na₂SiO₃/NaOH ratios on fracture properties and ductility of ambient curing GGBFS based heavyweight geopolymer concrete. *Structures*, 32, 2118–2129. <https://doi.org/10.1016/j.istruct.2020.04.008>
6. Šejnoha, M., Brouček, M., Novotná, E., Keršner, Z., Lehký, D., & Franti, P. (2013). Fracture properties of cement and alkali activated fly ash based concrete with application to segmental tunnel lining. *Advances in Engineering Software*, 62–63, 61–71. <https://doi.org/10.1016/j.advengsoft.2013.04.009>
7. Karamloo, M., Mazloom, M., & Payganeh, G. (2016). Effects of maximum aggregate size on fracture behaviors of self-compacting lightweight concrete. *Construction and Building Materials*, 123, 508–515. <https://doi.org/10.1016/j.conbuildmat.2016.07.061>
8. Beygi, M. H. A., Kazemi, M. Y., Nikbin, I. M., Javad, N., & Amiri, V. (2013). The effect of water to cement ratio on fracture parameters and brittleness of self-compacting concrete. *Materials and Design*, 50, 267–276. <https://doi.org/10.1016/j.matdes.2013.02.018>
9. Beygi, M. H. A., Kazemi, M. T., Amiri, J. V., Nikbin, I. M., Rabbanifar, S., & Rahmani, E. (2014). Evaluation of the effect of maximum aggregate size on fracture behavior of self-compacting concrete. *Construction and Building Materials*, 55, 202–211. <https://doi.org/10.1016/j.conbuildmat.2014.01.065>
10. Beygi, M. H. A., Kazemi, M. T., & Nikbin, I. M. (2014). The influence of coarse aggregate size and volume on the fracture behavior and brittleness of self-compacting concrete. *Cement and Concrete Research*, 66, 75–90. <https://doi.org/10.1016/j.cemconres.2014.06.008>
11. Eskandari, H., Muralidhara, S., Raghu Prasad, B. K., & Venkatarama Reddy, B. V. (2010). Size effect in self-consolidating concrete beams with and without notches. *Sadhana*, 35(Part 3), 303–317.
12. Indian Standard Method of physical tests for hydraulic cement part 1 determination of fineness by dry sieving (IS 4031:1996).
13. Indian Standard Method of test for aggregate for concrete, part 1 particle size and shape (IS 2386:1997).
14. Indian Standard Method Concrete mix proportion-guidelines (IS 10626:2009).
15. RILEM draft recommendations, TC-89 FMT. (1991). Size effect method for determining fracture energy. Fracture mechanics of concrete—Test methods. *Material and Structures*, 23, 461–465.

Trip Generation and Trip End Modal Split Modelling for East Zone of Surat City



Omkar Bidkar, Ravikiran Jadhav, Prashant Bhaganagare,
Ravikant S. Sathe, and Mangesh Survase

Abstract The demand for transportation in urban areas is influenced by the decisions people make about where to live in relation to their places of employment, shopping, entertainment, educational institutions, and other vital activities. Rapid urbanization in Indian cities contributes to an increase in population, congested traffic, noise pollution, and air pollution in the cities. In order to predict travel demand in urban areas, a four-stage model is used. Trip based approach is the conventional method to determine travel demand in cities. Surat is the fast growing metropolitan city with industrial hub. East zone of Surat city is major zone whose population is about 25% of total city. So, in present study, the study area is taken as East zone of the city. Data collection involves collection of socio-economic details of Surat at Household levels and Person levels. Trip Generation model is developed by using SPSS Software. Trip end modal split model is applied after trip generation by using NLOGIT Software.

Keywords Congestion · MNL · NL · NLOGIT · Urbanization

1 Introduction

Urban area development is mostly dependent on transportation. By allowing access and mobility, it promotes efficient urban area functioning. One of the most important components, especially in metropolitan areas, is the planning and development of the system's infrastructure for transportation. Urbanization is accelerating in metropolitan areas, which is contributing to a number of transportation-related issues. Traffic congestion, Noise and Air pollution, Delay at intersection. Growth rate of private vehicles is increasing in cities with reduction in public transport. Lack of efficient, commuter-friendly and sustainable mass transportation systems are forcing commuters to shift to private and intermediate means of transport, thereby inducing an imbalance in modal split and burdening the entire road network. There are so many factors which influence in choice of the mode such as Travel characteristics,

O. Bidkar (✉) · R. Jadhav · P. Bhaganagare · R. S. Sathe · M. Survase
SVERI's College of Engineering Pandharpur, Pandharpur, Maharashtra 413304, India
e-mail: osbidkar@coe.sveri.ac.in

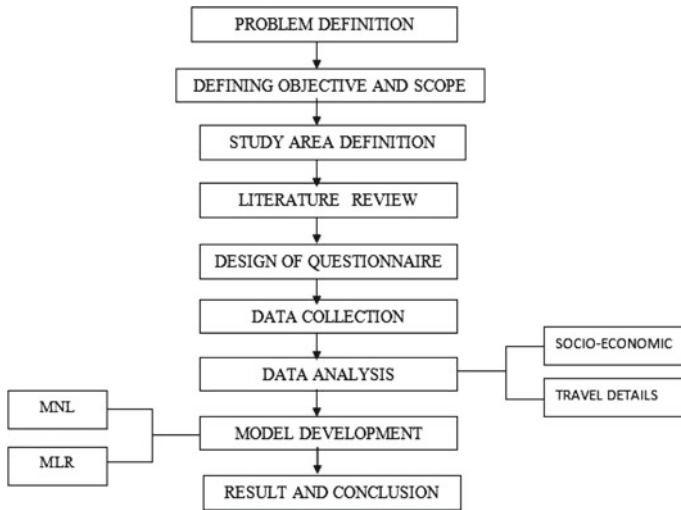


Fig. 1 Detailed methodology of the paper

Personal characteristics and Household characteristics. So, it is very necessary to study factors which affect modal split and to arrive and particular travel demand.

2 Methodology

See Fig. 1.

3 Literature Review

Literature review section focuses on basic theory related to travel demand modelling approaches and various literatures in the section of travel demand modelling approach. Sarkar et al. [1] developed four stage travel demand modelling is the typical procedure adopted by every person to arrive at various travel decisions. Trip Generation and distribution are the simple steps but, modal split is very complex phenomenon and affected by various factors such as accessibility measures, travel details, socio-economic factors and destination characteristics. There are various types literatures available on four stage demand modelling and mode choice modelling which are listed below [2] discussed attitude behaviour relationship in travel demand modelling. He found two types of variables which are affecting travel demand. One is the commuter variables and second one is the attitudes and perceived availability

constraints. Ghasri et al. [3] studied the transferability modelling framework to calculate the trips and attributes of trips in tour at disaggregate level. Heinrichs et al. [4] focuses on the introduction of Car-sharing into existing car fleets in microscopic travel demand model. According to the author, microscopic demand modelling considers only trip and personal attributes in modelling. Car-sharing is the old concept in demand modelling which enables people to use nearby car in Car-fleet in order to optimize the travel time and cost making the transportation system more sustainable. Hasnine and Habib [5] has demonstrated dynamics in the daily travel mode choices and dynamic discrete choice approach is used for tour-based mode choice modelling. The model is applied for the university students of Toronto. It is found that dynamic model is dynamic modelling is best fitted model and it is good for sensitivity analysis also. Kaewklungklom et al. [6] investigated influence of psychological factors on mode choice behaviour. Study area is considered Khon Kaen city, Thailand. A key finding from the paper is that the main intention to use BRT is governed by the subjective norm. It is also found from the paper that choice of BRT is not only governed by travel characteristics but also socio-economic characteristics. Heinen [7] focused on the changing behaviour of multimodal people. From the cross-sectional analysis, it is found that there is no relationship between multimodality and the intention to change mode choice. Mehdizadeh et al. [8] studied the role of socio-economic, built environment and psychological factors of mode choice behaviour of children of Iran. The mixed logit model is developed to study the behaviour of children in mode choice. The results of the model showed that several psychological, socio-economic and built environments affect the mode choice of children. Bajracharya [9] studied Transportation Mode Choice Behaviour of Individuals with Different Socio-Economic Status. The result showed that upper class people are more inclined to the private transport system than middle and lower class people. Sathe et al. [10–12] studied the settlement of pile by varying its size and shapes [13] proposed study on mode choice using nested logit model in travel towards Chennai city. It is found from the research that all the modes are not direct substitute of each other and nested structure is the best fitted structure to capture behaviour of people. Wong et al. [14] found effect of wearable fitness trackers and smartphone pedometer apps on the mode choice in transit oriented city. Binary Logit model is used to investigate mode choice decision between waking and travelling by public transport. Various policies are implemented to increase public share from private share. Wang et al. [15] explored the effects of the built environment mode choice of public transport from nearby public transport stations. Structural Equation modelling and discrete choice models are developed. The result showed that there is significance influence of built environment on mode choice of public transport. Kumagai and Managi [16] finds the impact of pro-environmental behaviour on the choice of commuting mode in Tokyo, Beijing, Shanghai and Singapore. The multinomial logistic regression is used to study the impact. The result showed that in most of the cities are affected by environmental factors so that there is great influence on the mode choice of individual.

4 Model Development

Model development is the post stage of data collection. Trip generation is carried out firstly with socio-economic data and then trip end modal split model is applied.

4.1 Trip Generation by Regression Analysis Technique

Multiple linear regression analysis is the statistical technique most often used to derive the estimates of future trip generation, where two or more independent factors are assumed to be simultaneously affecting the amount of travel. This technique measures the separate influence of each factor acting in association with the other factors. The aim of the analysis is to develop an equation in the following form to estimate the future trips from any zone, given the values for a set of land use and socio-economic parameters:

$$Y = a_0 + b_1X_1 + b_2X_2 + b_3X_3 + \dots + b_nX_n$$

where, Y is dependant variable and X1, X2, X3 Xn are independent variable. So, in this study, four independent variables are considered which are X1 (Total Vehicles), X2 (Gross Income), X3 (No. of Working Members) and X4 (No. of Members). Multi-linear regression is applied with dependent variables as Number of trips. Tables 1 and 2 show the results for Multilinear Regression.

Where R- Square is given by 0.695, which is suitable for MLR model analysis. So, explained error 69.5% of total error. Where the most influencing parameters is vehicle ownership. As more the number of vehicles in Household, the number of trips generated will be more and the least influencing parameter is gross income. So,

Table 1 Model validation for regression

Model	Unstandardized coefficient		Standerdized coefficient		
	B	Std. error	Beta	t	Sig.
Constant	- 0.567	0.245		- 2.315	0.021
X1	1.095	0.093	0.437	11.834	0
X2	0.026	0.006	0.169	4.487	0
X3	0.086	0.136	0.022	0.636	0.525
X4	0.634	0.062	0.37	10.257	0

Table 2 Model validation for regression

Model	R	R-square	Adjusted R-square	Std. error of the estimate
1	0.834	0.695	0.692	1.4877

Eq. 1 is for trip generation which becomes as follows:

$$Y = (-0.567) + (1.095)X1 + (0.026)X2 + (0.086)X3 + (0.634)X4 \quad (1)$$

Average trip rate is calculated from above equation by putting average value of X1, X2, X3 and X4. Average trip rate for zone is found to be 6.4. Total number of trips are calculated by multiplying the average trip rate by total population. Total number of trips are found to be 1,499,693.

5 Modal Split by Logistic Regression

From data collection, it is found that there are 5 modes in choice set of each person namely 2W,4W, 3W, City Bus and BRTS. There are 3 types of variables considered for modal split namely travel characteristics, personal characteristics and accessibility measures. Movement attribute involves Travel time, Travel cost as variables, Personal characteristics involves Income and age, Household characteristics involves Vehicle ownership and Car ownership as variables and accessibility measures involves Waiting Time at Transit stop, Nearest Transit stop distance and Time reach to transit stop as variables. Multinomial Logit and Nested Logit model is applied by using NLOGIT Software.

5.1 Model Validation (MNL)

Model validation for MNL is shown in Table 3.

5.2 Utility Equations for MNL

Utility equations for MNL are shown in Table 4.

5.3 Nested Logit (NL)

Model Validation for Nested Logit is shown in Table 5.

Table 3 Model validation for MNL

Variable	Coefficient	Standard error	b/St. Er.	P[Z >z]
A1	- 0.17729313	0.45066032	- 0.393	0.069
A2	- 0.04491952	...(Fixed Parameter)...		
A3	2.20675363	...(Fixed Parameter)...		
A4	0.73526888	0.830283D - 05	*****	0.0000
A5	0.51007269	0.24335862	2.096	0.0361
A6	- 0.02596863	0.00060387	- 43.003	0.0000
A7	0.550998D - 04	0.15784525	0.000	0.0020
B0	- 7.04027757	...(Fixed parameter)...		
B1	- 0.24033634	0.25246263	- 0.952	0.0341
B2	- 0.53483885	0.26019192	2.056	0.0398
B3	2.50277536	...(Fixed parameter)...		
B4	0.69464518	0.00086250	805.390	0.0000
B5	0.50408947	0.34272275	1.471	0.0141
B6	- 0.18981316	0.07265188	- 2.613	0.0050
B7	0.421453D - 04	1.08465444	0.000	0.0010
B8	1.62109668	...(Fixed parameter)...		
C0	3.03636052	...(Fixed parameter)...		
C1	- 0.32297944	0.48432468	- 0.667	0.0050
C2	- 0.21509284	...(Fixed parameter)...		
C3	1.47602647	...(Fixed parameter)...		
C4	0.50334505	...(Fixed parameter)...		
C5	0.86517415	...(Fixed parameter)...		
D0	54.4563001	...(Fixed parameter)...		
D1	- 1.20285994	...(Fixed parameter)...		
D2	- 0.41073062	...(Fixed parameter)...		
D3	- 6.09537277	...(Fixed parameter)...		
D4	- 1.64669461	...(Fixed parameter)...		
D5	- 1.39034287	...(Fixed parameter)...		
D6	- 0.00023978	...(Fixed parameter)...		
E0	43.2919368	...(Fixed parameter)...		
E1	- 0.46225103	...(Fixed parameter)...		
E2	- 0.13590413	...(Fixed parameter)...		
E3	- 0.09018269	...(Fixed parameter)...		
E4	- 0.28656450	...(Fixed parameter)...		
E5	- 0.48899344	...(Fixed parameter)...		
E6	- 0.00013982	...(Fixed parameter)...		

Table 4 Utility equations for MNL

Utilities	Equations
U(2W)	$(- 0.1772) * TT - (0.0449) * TC + (2.2067) * NTSD + (0.7352) * TRTS + (0.5100) * WT - (0.02596) * AGE + (0.550998D-04)*INCOME$
U(4W)	$(- 7.0402) - (0.2403) * TT - (0.5348) * TC + (2.5027) * NTSD + (0.6946) * TRTS + (0.5040) * WT - (0.1898) * AGE + (0.421453D - 04) * INCOME + (1.6210) * CARO$
U(3W)	$(3.0363) - (0.3229) * TT - (0.2150) * TC + (1.4760) * NTSD + (0.5033) * TRTS + (0.8651) * WT$
U(C.B.)	$(54.45) - (1.2028) * TT - (0.4107) * TC - (6.0953) * NTSD - (1.6466) * TRTS - (1.3903) * WT - (0.00024) * INCOME$
U(BRTS)	$(43.2919) - (0.4622) * TT - (0.1359) * TC - (0.0901) * NTSD - (0.2865) * TRTS - (0.4889) * WT - (0.00014) * INCOME$

Table 5 Model validation for nested logit

Variable	Coefficient	Standard error	b/St. Er.	P[Z >z]
A1	- 0.04082364	358,213.125	0.000	0.0010
A2	- 0.03717230	589,401.253	0.000	0.0010
B0	- 10.3922487	2.14197853	- 4.852	0.0000
B1	- 0.03391175	358,213.125	0.000	0.0010
B2	- 0.55671981	589,401.253	0.000	0.0010
B3	1.42659879	0.43769061	3.259	0.0011
C0	1.11276345	0.88965930	1.251	0.0211
C1	- 0.12492859	358,213.125	0.000	0.0010
C2	- 0.37262686	589,401.253	0.000	0.0010
D0	- 6.49050064	2.21475050	- 2.931	0.0034
D1	- 0.11803091	358,213.125	0.000	0.0010
D2	- 0.12113079	589,401.253	0.000	0.0010
E0	- 4.36593010	1.81903314	- 2.400	0.0164
E1	- 0.142065D - 04	358,213.125	0.000	0.0010
E2	- 0.10013446	589,401.253	0.000	0.0010
<i>IV parameters</i>				
PRIVATE	0.50000000	...(Fixed parameter)...		
PUBLIC	0.50000000	...(Fixed parameter)...		

5.4 Utility Equations

Table 6 shows utility equations for Nested Logit Model.

Table 6 Utility equations for nested logit model

Utilities	Equations
U(2W)	$(- 0.04082) * TT - (0.03717) * TC$
U(4W)	$(- 10.39225) - (0.03391) * TT - (0.55672) * TC + (1.42659) * CARO$
U(Auto-Rickshaw)	$(1.11276) - (0.12493) * TT - (0.37262) * TC$
U(City-Bus)	$(- 6.49050) - (0.11803) * TT - (0.12113) * TC$
U(BRTS)	$(- 4.36593) - (0.142065D - 04) * TT - (0.10013) * TC$
U (PUBLIC)	$0.5[e^{U(Rickshaw)} + e^{U(City-Bus)} + e^{U(BRTS)}]$
U (PRIVATE)	$0.5[e^{U(2W)} + e^{U(4W)}]$

6 Conclusion

From above study, it is found that urbanisation in Surat city is increasing with increase in vehicle ownership, decrease in Household size. Mode choice of person is affected by not only travel characteristics (Travel Time, Travel Cost) but also Individual characteristics (AGE), Household characteristics (Income, Car Ownership) and accessibility measures (Nearest transit stop distance, Time reach to transit stop, Waiting time at transit stop etc. Transportation policies are to be applied considering individual, personal and accessibility characteristics to reduce private transport and to increase public transport.

References

1. Sarkar, P. K., Maitri, V., & Joshi, G. J. (2017). *Transportation planning: Principles, practices and policies*. PHI Learning Pvt. Ltd.
2. Golob, T. F., Horowitz, A. D., & Wachs, M. (1977). Attitude-behavior relationships in travel demand modelling (No. GMR-2398).
3. Ghasri, M., Rashidi, T. H., & Waller, S. T. (2017). Developing a disaggregate travel demand system of models using data mining techniques. *Transportation Research Part A: Policy and Practice*, 105, 138–153.
4. Heinrichs, M., Krajzewicz, D., Cyganski, R., & von Schmidt, A. (2017). Introduction of car sharing into existing car fleets in microscopic travel demand modelling. *Personal and Ubiquitous Computing*, 21(6), 1055–1065.
5. Hasnine, M. S., & Habib, K. N. (2018). What about the dynamics in daily travel mode choices? A dynamic discrete choice approach for tour-based mode choice modelling. *Transport Policy*, 71, 70–80.
6. Kaewkluengkrom, R., Satiennam, W., Jaensirisak, S., & Satiennam, T. (2017). Influence of psychological factors on mode choice behaviour: Case study of BRT in Khon Kaen City, Thailand. *Transportation Research Procedia*, 25, 5072–5082.
7. Heinen, E. (2018). Are multimodals more likely to change their travel behaviour? A cross-sectional analysis to explore the theoretical link between multimodality and the intention to change mode choice. *Transportation Research Part F: Traffic Psychology and Behaviour*, 56, 200–214.

8. Mehdizadeh, M., Nordfjaern, T., & Mamdoohi, A. (2018). The role of socio-economic, built environment and psychological factors in parental mode choice for their children in an Iranian setting. *Transportation*, 45(2), 523–543.
9. Bajracharya, A. (2018). A study on the transportation mode choice behaviour of individuals with different socio-economic status. In *Advances in system dynamics and control* (pp. 476–493). IGI Global.
10. Sathe, R. S., Sharma, J. K., & Suneja, B. P. (2020). Top settlement analysis of single circular floating stepped pile. *Techno-Societal* 2018.
11. Sathe, R. S., Sharma, J. K., & Suneja, B. P. (2020). *Settlement analysis of single circular hollow pile. Construction in geotechnical engineering*. Lecture Notes in Civil Engineering (Vol. 84, pp. 703–712).
12. Sathe, R. S., Sharma, J. K., & Suneja, B. P. (2021). Estimation of settlement of stepped pile in granular soil. In *Indian geotechnical conference 2019*. Lecture Notes in Civil Engineering (Vol. 137, pp. 537–544).
13. Shanmugam, L., & Ramasamy, M. (2021). Study on mode choice using nested logit models in travel towards Chennai metropolitan city. *Journal of Ambient Intelligence and Humanized Computing*, 1–9.
14. Wong, R. C. P., Yang, L., & Szeto, W. Y. (2021). Wearable fitness trackers and smart-phone pedometer apps: Their effect on transport mode choice in a transit-oriented city. *Travel Behaviour and Society*, 22, 244–251.
15. Wang, X., Shao, C., Yin, C., & Dong, C. (2021). Exploring the effects of the built environment on commuting mode choice in neighborhoods near public transit stations: Evidence from China. *Transportation Planning and Technology*, 44(1), 111–127.
16. Kumagai, J., & Managi, S. (2020). Environmental behaviour and choice of sustainable travel mode in urban areas: Comparative evidence from commuters in Asian cities. *Production Planning & Control*, 31(11–12), 920–931.

Improving Conversion Efficiency of Solar Panel by Cooling System



Suryaji S. Kale, S. S. Gawade, and B. R. Birajdar

Abstract Conversion of solar energy into electricity through PV cells is varying between 7 and 20% and determined primarily by the type of semiconductor material from which the cells are manufactured. The increase in cell operating temperature has a negative impact on the electrical efficiency of PV cells. The efficiency of photovoltaic modules decreases with heating and also the photovoltaic cells will exhibit long-term degradation if the temperature exceeds a certain limit. In this work, active water cooling is utilized to reduce the operating temperature of the PV module. Without active water cooling, it was observed that the PV module's temperature was high and solar cells could only convert energy upto 8–9%. However, the temperature reduced dramatically when the PV module was used with active water cooling, increasing the efficiency of the solar cells to between 12 and 14%.

Keywords Photovoltaic modules · Cooling techniques for photovoltaic cell · Solar energy · Efficiency of solar panel

1 Introduction

PV cell is one of the most popular renewable energy products. It can directly convert the solar radiation into electricity which can be utilized to power household appliances. However, only about 15% of solar energy is converted to electricity and the remaining 85% is converted to heat during the operation of the PV cell [1–3].

Also at high temperatures, the light induced degradation of a PV module gets accelerated Therefore deterioration in the performance of a PV module can be minimized if it is operated at relatively lower temperatures, which can be achieved by extracting out the extra heat associated with it [4].

S. S. Kale (✉) · B. R. Birajdar
N K Orchid College of Engineering and Technology, Solapur, India
e-mail: kaless@gmail.com

S. S. Gawade
RIT Rajaramnagar Affiliated to Shivaji University, Kolhapur, India

PV cells absorb up to 80% of the incident solar radiation, however only small part of the absorbed incident energy is converted into electricity depending on the conversion efficiency of the pv cell technology used [5]. The remainder energy is dissipated as heat and the PV module [6] can reach temperatures as high as 40 °C above ambient.

For crystalline silicon PV cells, a drop in the electrical power output of about 0.2–0.5% was reported for every 1 °C rise in the PV module temperature [7] principally due to the temperature dependence of the open-circuit voltage of the cell depending on the PV technology. Such property of PV cells is known as the Temperature Coefficient of the PV cell [8].

2 Experimental System

A test set up is designed to investigate electrical performances of the Photovoltaic thermal system [9]. This experimental set up consists of four sub set up for analysis purpose as follows

- Conventional Photovoltaic System.
- Conventional Photovoltaic System with Reflector.
- Conventional Photovoltaic System with Reflector and with Cooling system.
- Conventional Photovoltaic System without Reflector and with Cooling System.

The current experiment is designed to investigate how the temperature affects the electrical efficiency and power output during the operation. Polycrystalline solar panels are used in the experiment to generate the electricity.

The experiments are performed for four different sets. The detailed experimental procedure for each set is discussed below.

2.1 *Conventional Photovoltaic System*

Figure 1 shows the experimental set-up of conventional photovoltaic system. This system consists a photovoltaic module tilted towards south direction. A K-type thermocouple is mounted on photovoltaic surface for measuring surface temperature. A digital multimeter is used for measuring output of photovoltaic module. A photovoltaic panel is kept outdoor for experimentation. The different readings like voltage, ampere, solar intensity, panel surface temperatures are taken for every half interval of time. From these readings photovoltaic efficiency and photovoltaic power determined.



Fig. 1 Conventional photovoltaic system

2.2 Conventional Photovoltaic System with Reflector

Figure 2 shows the experimental set-up of conventional photovoltaic system with reflector. In this experimental set up a pair of reflectors is fabricated from Aluminum sheet with its size equal to module dimensions and reflectors are mounted along the longest side of photovoltaic panel for increasing solar radiation falling on it [10]. An anodized aluminum sheet of 0.5 mm thickness, available in market is used for fabrication of flat reflectors. The amount of solar radiation reflected from reflectors on module surface is strongly influenced by its concentration ratio and reflector angle normal to module surface. Due to improved concentration ratio, electrical power and efficiency of module is enhanced drastically over a day.

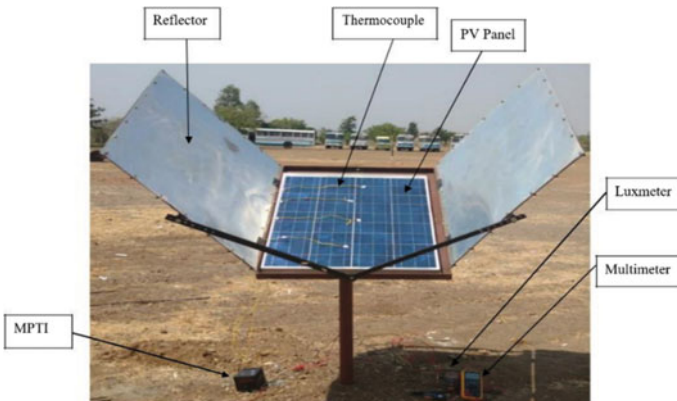


Fig. 2 Conventional photovoltaic system with reflector



Fig. 3 Conventional photovoltaic system with reflector and with cooling system

Experiments are conducted on PV [11] module by changing orientations of reflectors manually from 100° to 150° normal to PV surface with an interval of 10° on distinct days.

2.3 Conventional Photovoltaic System with Reflector and with Cooling System

Figure 3 shows the experimental set-up of conventional photovoltaic system with reflector and with cooling system. In this set up a cooling system is incorporated for reducing panel surface temperature and increasing panel output. A cooling system mainly consists of pump, rotameter, inlet pipe, water tray, inlet water tank, outlet water tank [12, 13].

2.4 Conventional Photovoltaic System Without Reflector and with Cooling System

Figure 4 shows the experimental set-up of conventional photovoltaic system without reflector and with cooling system. In this set up reflectors are removed for analysis purpose.

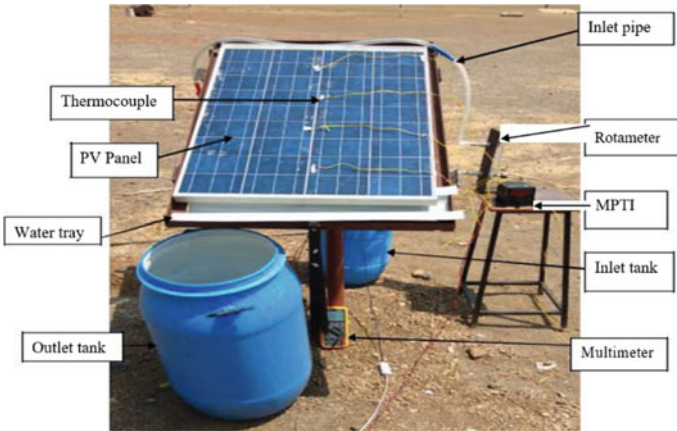


Fig. 4 Conventional photovoltaic system without reflector and with cooling system

3 Results

3.1 Results of Convective Photovoltaic System

The system is kept in outdoor at 10.30 AM. The photovoltaic panel is tilted at an angle of latitude and at 29° facing south direction. Different readings are taken for both inclinations for every half interval of time. The maximum efficiency is obtained during peak period for which the intensity of solar radiation is maximum. The temperature of photovoltaic panel is increased due to increased solar radiation falling on photovoltaic surfaces [14].

Figures 5 and 6 represents the comparison of electrical power and efficiency for a photovoltaic system tilted at latitude and 29° . From this figure it shows that maximum efficiency and maximum power is obtained for a photovoltaic system tilted at 29° . From these observations a photovoltaic panel is kept at 29° for subsequent experimentation for which a photovoltaic panel getting maximum solar radiation for any position of sun.

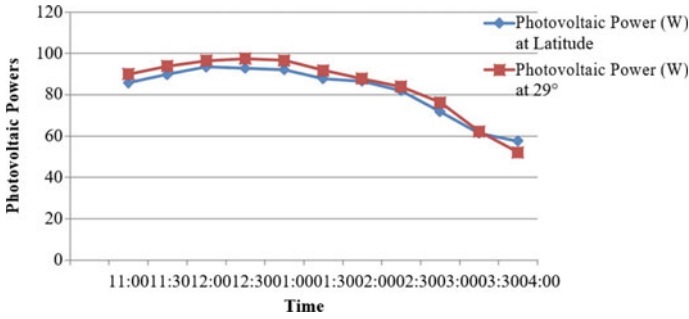


Fig. 5 Photovoltaic powers at latitude and 29°

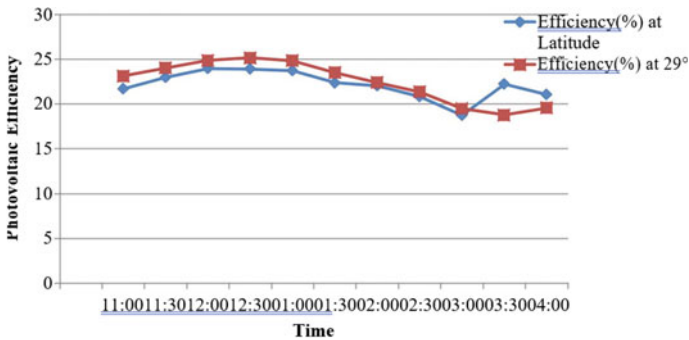


Fig. 6 Photovoltaic efficiency at latitude and 29°

3.2 Results of Convectonal Photovoltaic System with Reflector

A photovoltaic system is integral with reflector tilted normal to the surface of panel. The reflector angle is changed for finding the optimum angle of inclination for which system parameters are maximum. The reflector angel is changed from 90° to 150° for finding optimum angle. Different readings are taken for every reflector angle and from these observations an optimum angle of reflector is selected and it is kept for further experimentation.

Figure 7 is plotted between average electrical efficiency of photovoltaic system and reflector angle. This graph shows that reflector angle 120° is an optimum orientation of reflector for which average electrical efficiency and photovoltaic power is maximum.

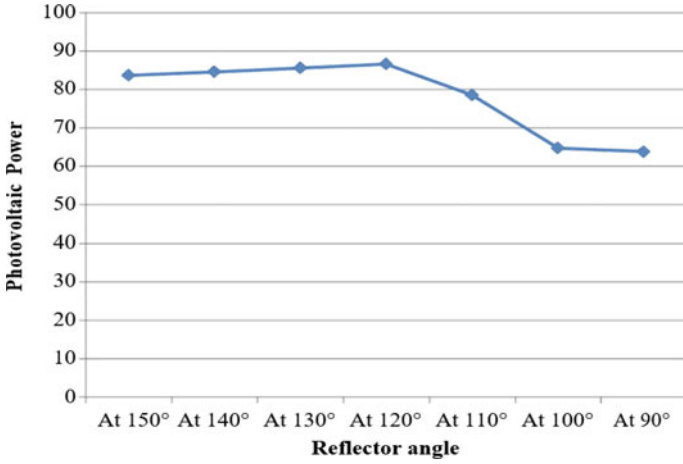


Fig. 7 Comparison of photovoltaic efficiency (%) for reflector at different orientational photovoltaic system with reflector

For this reflector angle maximum sun rays are falling on panel while for other reflector angle the sun rays are interrupted by reflector for falling on panel (Fig. 8).

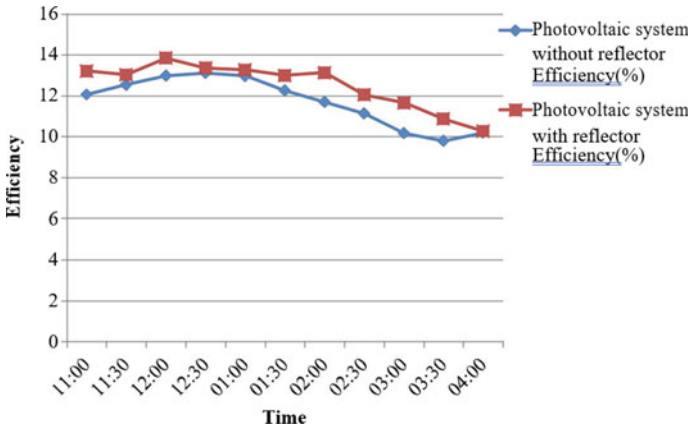


Fig. 8 Efficiency of photovoltaic system with and without reflector

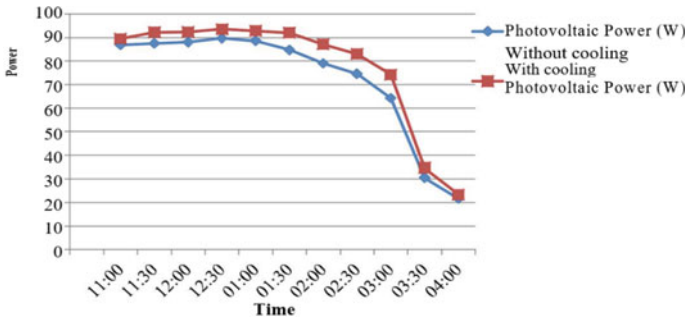


Fig. 9 Power of photovoltaic system with reflector with cooling and without cooling

3.3 Result of Conventional Photovoltaic System with Reflector and with Cooling System

The analysis is performed for other PV panels [15] under any different conditions. The output energy is calculated for two cases using different maximum allowable temperature namely 40–50 and 50–60 °C. The solar PV panel is left to overheat till the maximum temperature is reached in each case, and then, the panel is cooled to the normal operating temperature range as given above. Following table is for case I that is maximum allowable temperature of panel is maintained between 40 and 50 °C by using cooling system.

A comparison is made between Conventional photovoltaic system with reflector and Conventional photovoltaic system with reflector and with cooling system. This comparison is made for finding out the effect of using reflector with cooling system on photovoltaic power and photovoltaic efficiency (Fig. 9).

From the observations of experiments conducted following tables are prepared. From these table it concludes that average photovoltaic power is increased by 8.15% and average photovoltaic efficiency is increased by 7.73% due to the use of reflector with cooling system.

The graph is also plotted between powers of photovoltaic system with reflector with cooling and without cooling and time. The graph is also plotted between efficiency of photovoltaic system with reflector with cooling and without cooling and time. This graph shows that efficiency and power is increased due to use reflector with cooling system as compared with without cooling system.

Figure 10 shows the variation of Electrical efficiency as a function of PV temperature. The graph shows that as temperature of the solar panel increases the efficiency drops. For the temperature range of 34–50 °C the efficiency is in the range of 10–12%. After 50 °C the efficiency drops suddenly (Fig. 11).

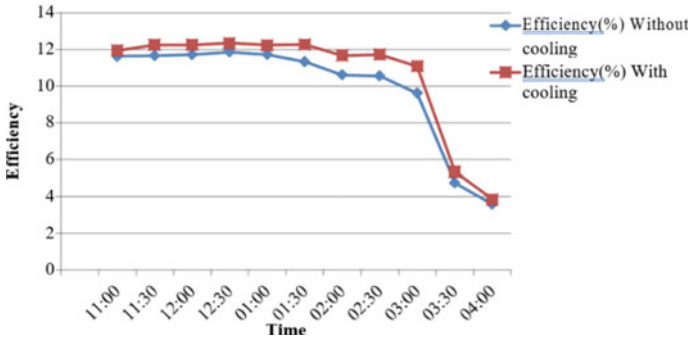


Fig. 10 Efficiency of photovoltaic system with reflector with cooling and without cooling

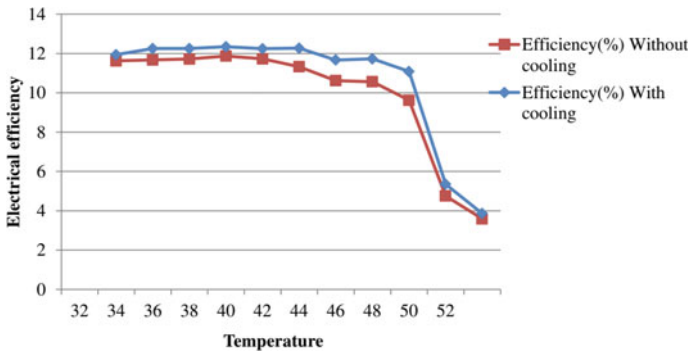


Fig. 11 Electrical efficiency as a function of PV temperature

4 Conclusion

The works done and presented the main conclusions drawn are:

- (1) This study compares the performance of simple cooled module with hybrid solar system [16–19] fitted with aluminum flat reflectors to module sides. The electrical power of the water cooled module with reflectors compared with the simple cooled module is improved by 7% and percentage increase in electrical power 9.52% by fitting reflectors with small increase in cost of the hybrid system. At the same time the percentage efficiency of water cooled module with reflectors increased by 12.01%.
- (2) This study also compares the performance of conventional photovoltaic system with photovoltaic system fitted with aluminum flat reflectors to module sides. The electrical power of photovoltaic system fitted with reflectors compared with conventional photovoltaic system is improved by 5.53% by fitting reflectors with small increase in cost of the hybrid system. At the same time the percentage

electrical efficiency of photovoltaic system fitted with reflectors compared with conventional photovoltaic system is improved by 7.02% by fitting reflectors.

- (3) Experimentation shows that for the temperature range of 34–50 °C the efficiency is in the range of 10–12%, after 50 °C the efficiency drops drastically.

References

1. Tabaei, H., & Ameri, M. (2012). The effect of booster reflectors on the photovoltaic water pumping system performance. *Journal of Solar Energy Engineering*.
2. Hosseini, N. H., & Khorasanizadeh, H. (2011). An experimental study of combining a photovoltaic system with a heating system. In World renewable energy congress Sweden, 8–13 May 2011, Linkoping, Sweden.
3. Duffie, J. A. B., & Beckman, W. A. (1974). *Solar energy thermal processes*. Wiley.
4. Teo, H., Lee, P., & Hawlader, M. (2012). An active cooling system for photovoltaic modules. *Applied Energy*, 90, 309–315.
5. Ceylana, I., Gurelb, A., Demircanc, H., & Aksu, B. (2014). Cooling of a photovoltaic module with temperature controlled solar collector. *Energy and Buildings*, 72, 96–101.
6. Gaur, A., & Tiwari, G. (2014). Performance of a-Si thin film PV modules with and without water flow: An experimental validation. *Applied Energy*, 128, 184–191.
7. Sukhatme, S. P., & Nayak. (2008). *Solar energy (principles of thermal collection and storage)* (3rd ed.). Tata McGraw-Hill Publishing Company Limited.
8. Palaskar, V. N., & Deshmukh, S. P. (2013). A critical review on enhancement in system performance of a hybrid solar flat plate PV/T collector system. *International Journal of Energy Science (IJES)*, 3(6), 395–403.
9. Tripanagnostopoulos. (2007). Aspects and improvements of hybrid photovoltaic/thermal solar energy systems. *Solar Energy*, 81(9), 1117–1131.
10. Kostic, T. P., & Pavlovic, Z. (2009). Influence of physical characteristics of flat aluminum concentrators on energy efficiency of PV/T collector. *Proceedings of the Tenth Annual Conference of the Materials Research Society of Serbia*, 115(4).
11. Huang, B. J., Lin, T. H., & Hung, W. C., et al. (2001). Performance evaluation of solar photovoltaic/thermal systems. *Solar Energy*, 70, 443–448.
12. Ameri, M., & Abdolzadeh, M. (2009). Improving the effectiveness of a photovoltaic water pumping system by spraying water over front of photovoltaic cells. *Renewable Energy*, 34, 91–96.
13. Bahaidarah, H., & Subhan, A. (2013). Performance evaluation of a PV (photovoltaic) module by back surface water cooling for hot climatic conditions. *Solar Energy*, 59.
14. Solanki, C. S. (2011). *Solar photovoltaic (fundamentals, technologies and applications)* (2nd ed.). PHI Learning Pvt. Ltd.
15. Moharram, K., Abd-Elhady, M., Kandil, H., & Sherif, H. (2013). Enhancing the performance of photovoltaic panels by water cooling. *Ain Shams Engineering Journal*, 4, 869–877.
16. Makki, A., Ormer, S., & Sabir, H. (2015). Advancements in hybrid photovoltaic systems for enhanced solar cells performance. *Renewable and Sustainable Energy Reviews*, 41, 658–668.
17. Palaskar, V. N., Deshmukh, S. P., Pandit, P. (2013). Performance analysis of an oscillatory flow design heat exchanger used in solar hybrid water system. *International Journal of Mechanical Engineering and Technology (IJMET)*, 4(6), 91–99.
18. Tripanagnostopoulos, M. S., Battisti, R., & Corrado, A. *Application aspects of hybrid PV/T solar systems*. Physics Department, University of Patras, Patras 26500, Greece and Dept. of Mechanics and Aeronautics, University of Rome “La Sapienza”, Rome 00184, Italy.

19. Garg, H. P., Agarwal, R. K., & Joshi, J. C. (1994). Experimental study on a hybrid photovoltaic-thermal solar water heater and its performance predictions. *Energy Conversion Management*, 35, 621–33.
20. Palaskar, V. N., & Deshmukh, S. P. (2012). Design configurations of hybrid solar photovoltaic/thermal collector technology a review. *Proceeding of Indian National Science Academy (INSA)*, 78(4), 725–734.

Influence of Accessibility Factors on Travel Mode Choice in an Emerging Metropolitan City, Surat



Yogesh Survase, Omkar Bidkar, Nitin More, Girish Falmari, Satyawar Jagdale, and Ravikant Sathe

Abstract Urbanization in Indian cities increasing rapidly causing increase in population of cities, traffic congestion, noise pollution and air pollution of cities. Trip based four-stage travel demand modelling is commonly used tool to forecast travel demand in urban areas. This paper focuses on the trip rate as well as mode preference behavior of travelers from Surat city in Indian State of Gujarat. Study area is the East zone among the seven administrative zones of Surat city because population of East zone is 25% of city population and residential density is 18,961 persons per km². Home interview survey technique is carried out with designed questionnaire. Sample size considered is 0.05% of total population of zone. Trip rate model is calibrated by using Multilinear Regression and Logit model is applied for mode choice. It is found that accessibility measures will affect the mode choice for particular zone.

Keywords Travel mode · Surat · Work-Zone

1 Introduction

The demand for transportation in urban area is linked to the residential location choices that people make in relation to places of work, shopping, entertainment, schools and other important activities. Increasing demand for transportation is an inevitable outcome of urban growth. These conditions bring about a number of traffic related issues in the city like traffic congestion. Most of the metropolitan cities in India are having less modal share for public transport with increased vehicle ownership. So, it is very important to forecast transportation planning requirement for city and to study the factors which affect the modal share for city.

Y. Survase (✉) · O. Bidkar · N. More · G. Falmari · S. Jagdale · R. Sathe
SVERI's College of Engineering, Pandharpur, India
e-mail: ybsurvase@coe.sveri.ac.in

2 Literature Review

Residential trip generation was investigated by Mary Diaz G. and Angela Quintero P. [1]. In this study, it is established that home social and economic characteristics influence trip generation, but nonresidential land use raises the possibility of other factors. Public, semi-private, and private schools, as well as travel generator poles, have not been researched in Venezuela. The Institute of Transportation Engineers' (ITE), EE.UU., TGMs presentations are frequently utilised but may not be appropriate. High correlation coefficients were found by utilising stepwise regression and data processing, and the variability of the data from various schools was also significantly reduced. The Ibero-American Network of travel attractor poles allows for comparison of the trip generation rates (TGRs) for various modes of transportation, including walking, motorcycling, taking public transportation, and driving.

According to Karo [2], This article presents travel demand and transportation supply modelling for conurbation areas without transportation models. The methodology's four-stage modelling with trip-based travel demand models is the foundation of the proposal. The Polish Upper-Silesian Conurbation has been used as an example to demonstrate the methodology. An overview of trip demand modelling for transportation planning was provided by Zala [3]. The trip generation, trip distribution, modal split, and trip assignment are the four main stages of the model. The selection of routes when creating a transportation plan depends on a number of factors, including cost, comfort, comfort level, and safety. The literature assessment and logical arrangement of the numerous models utilised in urban transportation planning are included in the study's scope.

3 Model Development

When two or more independent factors are considered to be influencing the quantity of travel at the same time, multiple linear regression analysis is the statistical technique that is most frequently employed to produce predictions of future trip generation. This method assesses each factor's individual impact as it interacts with the other elements. The objective of the analysis is to create an equation in the following format to predict future trips from any zone given the values for a number of socioeconomic and land use criteria:

$$Y = a_0 + b_1x_1 + b_2x_2 + b_3x_3 + \dots + b_nx_n$$

where, Y is dependent variable and X1, X2, X3, ..., Xn are independent variable. So, in this study, four independent variables are considered which are X1 (Total Vehicles), X2 (Gross Income), X3 (No. of Working Members) and X4 (No. of Members). Multilinear regression is applied with dependent variables as Number of trips. Tables 1 and 2 show the results for Multilinear Regression.

Table 1 Results of MLR

Model	Unstandardized coefficient		Standardized coefficient	t	Sig.
	B	Std. error	Beta		
Constant	- 0.567	0.245	-	- 2.315	0.021
X1	1.095	0.093	0.437	11.834	0
X2	0.026	0.006	0.169	4.487	0
X3	0.086	0.136	0.022	0.636	0.525
X4	0.634	0.062	0.037	10.257	0

Table 2 Results of MLR

Model	R	R-square	Adjusted R-square	Std. error of the estimate
1	0.834	0.695	0.692	1.4877

$$Y = (-0.567) + (1.095)X1 + (0.026)X2 + (0.086)X3 + (0.634)X4$$

Average trip rate is calculated from above equation by putting average value of X1, X2, X3 and X4. Average trip rate for zone is found to be 6.4. Total number of trips are calculated by multiplying the average trip rate by total population. Total number of trips are found to be 1,499,693.

3.1 Modal Split by Logistic Regression

From data collection, it is found that 5 modes are major modes in choice set of person namely 2W, 4W, 3W, City Bus and BRTS etc. Logistic Regression is applied for data by considering Travel Time, Travel Cost, Waiting Time at Transit stop, Nearest Transit stop distance and Time reach to transit stop as variables by using NLOGIT software. Utility equations framed for model are as follows-

$$\begin{aligned}
 U(2W) &= a1 * TT + a2 * TC + a3 * NTSD + a4 * TRTS + a5 * WTU(4W) \\
 &= b0 + b1 * TT + b2 * TC + b3 * NTSD + b4 * TRTS + b5 * WTU(3W) \\
 &= c0 + c1 * TT + c2 * TC + c3 * TRTS + c5 * WTU(CITY-BUS) \\
 &= d0 + d1 * TT + d2 * TC + d3 * NTSD + D4 * TRTS + D5 * WTU(BRTS) \\
 &= e0 + e1 * TT + e2 * TC + e3 * NTSD + e4 * TRTS + e5 * WT
 \end{aligned}$$

The results obtained from model are shown in Table 3.

Table 3 Validation of MNL

Variable	Coefficient	Standard error	b/St. Er.	P[Z >z]
A1	- 0.01786	0.44869	0.040	0.9682
A2	- 0.13859	0.04235	- 3.272	0.0011
A3	2.26384	0.13343	16.965	0.00
A4	0.84073	0.44907	1.872	0.0612
A5	0.88633	(Fixed parameter)		
BO	- 2.69386	(Fixed parameter)		
B 1	- 0.10415	(Fixed parameter)		
B2	- 0.63444	0.01986	31.931	0.00
B3	2.39837	0.44537	5.38S	0.00
B4	0.27606	(Fixed parameter)		
B5	0.93821	0.44624	2.102	0.0355
C0	31.13834	(Fixed parameter)		
C1	- 0.08220	(Fixed parameter)		
C2	- 0.21039	(Fixed parameter)		
C3	1.25849	(Fixed parameter)		
C4	0.03888	(Fixed parameter)		

3.2 Utility Equations

Table 4 shows utility equation for various modes of transport.

Table 4 Utility equations

Utilities	Equations
U(2W)	$= (- 0.01786 * TT) - (0.13859 * TC) + (2.26384 * NTSD) + (0.84073 * TRTS) + (0.88632 * WT)$
U(4W)	$= (- 2.6938) - (0.1041 * TT) - (0.6344 * TC) + (2.3983 * NTSD) + (0.2760 * TRTS) + (0.9382 * WT)$
U(3W)	$= 31.138 - (0.08220 * TT) - (0.21039 * TC) - (4.37918 * NTSD) + (0.03888 * TRTS) - (0.80275 * WT)$
U(C.B.)	$= (46.58) - (0.04598 * TT) - (0.11269 * TC) - (4.37918 * NTSD) - (0.55236 * TRTS) - (0.80275 * WT)$
U(BRTS)	$= (44.6059) - (0.08580 * TT) - (0.17275 * TC) - (1.54152 * NTSD) - (0.603322 * TRTS) - (0.60625 * WT)$

3.3 Sensitivity Analysis

Sensitivity of model is checked by applying different policies. There are totally 5 policies applied.

DO Nothing: In this case, no any transportation policies are applied and probabilities for different modes are calculated for Do Nothing condition. Table 5 shows Probabilities for Do Nothing Condition.

Policy-1-Travel cost of Car increase by 20%: In this Transportation Policy, travel cost of car increase by 20% by increasing fuel price for Car and by congestion Pricing. Then, there is reduction in use of Private vehicle by 4% and increase in use of transit also by 4%. Table 6 shows Probabilities when Travel cost of Car increase by 20%.

Policy-2-Time Reaches to BRTS and City-Bus Decrease by 15% (Improvement of Accessibility)

In this transportation policy, Improvement of accessibility is done by providing dense transit network and more transit stops so that time reach to transit stop decreases. Then, there is decrease in Private vehicle by 4.66% and increase in use of transit by 4.66%. Table 7 shows Probabilities when Time to reach to BRTS and City-Bus decrease by 15%.

Table 5 Probabilities for do nothing condition

Mode	P (do nothing)
2W	0.88
4W	0.0018
3W	0.09
City bus	0.0144
BRTS	0.012

Table 6 Probabilities when travel cost of car increase by 20%

Mode	P (do nothing)	P (policy-2)	Difference (%)
2W	0.88	0.806	7.4
4W	0.0018	0.031	2.92
3W	0.09	0.079	1.1
City bus	0.0144	0.072	5.76
BRTS	0.012	0.012	0

Table 7 Probabilities when time to reach to BRTS and city-bus decrease by 15%

Mode	P (do nothing)	P (policy-1)	Difference (%)
2W	0.88	0.86	2
4W	0.0018	0.0016	2
3W	0.09	0.11	2
City Bus	0.0144	0.0144	0
BRTS	0.012	0.014	2

4 Conclusion

From above study, it is found that accessibility measures for zone will affect the mode choice for that particular zone. If accessibility measures like time reach to transit stop, Nearest transit stop distance is more for particular household then, probability of choosing private transport is more. But, if transit stations are accessible then people will shift to the public transit and modal share of public transit will increase causing less congestion on major roads.

References

1. Angela Quintero, P., Mary Diaz, G., & Moreno, E. G. (2016). Trip generation by transportation mode of private school, semi-private and public. Case Study in Merida-Venezuela. In *XII conference on transport engineering*, CIT 2016, 7–9 June 2016, Valencia, Spain.
2. Ewing, R., & Cervero, R. (2010). Travel and the built environment: A meta-analysis. *American Planning Association*, 76(3), 265–294.
3. Zala, L. B., & Modi, K. B. Transportation planning models: A review. In *National conference on recent trends in engineering & technology*.

Categorizing and Ranking Comfort Design Requirements of Transportation Buses in India



A. B. Rathod and R. T. Vyavahare

Abstract Buses are the one of the main sources of public transportation in Rural and Urban India of mass use. Main intention of this study was to survey the customers of transportation buses and recognize their problems and needs. Around 150 consumers participated in the survey with age group of 18–60 years who use to travel a distance up to 100 km Range. All concerns and needs are then arranged in a manner to categories and ranked which will be useful for resolution. The study revealed that, there are while few problems which were observed with specific class of occupant while others are global is-sues. Based upon the study corrective actions were proposed to provide comfort design to facilitate uplift the travel experience with safety.

Keywords Comfort design · Road transportation · Public transport

1 Introduction

In India when public transportation modes are considered and discussed then Bus transport is considered as one of most widely used and popular option. Though it is Urban or Rural Public Transport passengers' common choice is Bus for road transport. The Passenger and bus get connected right from bus identification, when he enters the bus, moves inside the bus, the trip and ends post he leaves the bus. Comfort and safety is very important for user during all these interactions. All these interactions between passenger and bus have Satisfaction requirements these are recognized and summarized as follows.

1. Outside Appearance/Condition
2. Sitting Ergonomics and Space
3. Hygiene

A. B. Rathod (✉)

Walchand Institute of Technology, Solapur, Maharashtra 413006, India

e-mail: rathodamit2100@gmail.com

R. T. Vyavahare

N B Navale Sinhgad College of Engineering, Solapur, Maharashtra 413255, India

© The Author(s), under exclusive license to Springer Nature Switzerland AG 2024

P. M. Pawar et al. (eds.), *Techno-Societal 2022*,

https://doi.org/10.1007/978-3-031-34648-4_34

4. Safety
5. Simplicity of ingress/egress
6. Inner environment and
7. Expense of Travel.

1.1 Background

India is second largest country worldwide in terms of population after Republic of China. Public transportation is very important role in daily movement. Majority of public transport in Indian cities relied on buses. Local State and Municipal government own and operates most of buses. Compared to urban households, more rural households preferred using buses. Many working personnel commute to work and back home by the staff transportation buses. The travel time, comfort and safety is very important for most of these travelers. Hence, the bus travel needs to be very comfortable and reliable. Transportation portrays a crucial part in the expansion of a nation's financial structure; in defining total constructiveness, superiority of citizens living, approach to goods and facilities. An operational and well-developed conveyance structure performs a substantial role in the economic growth of a country. Figure 1 shows the transport systems in India, which comprises several different types and facilities, especially road and rail network, docks, domestic aquatic transportation, sea carriage, air transport etc.

Road is chosen as Transportation medium in India for lengthy and little trips.

India holds a massive setup of road of more than 6,215,797 km that signals the reality that highway carriage is the utmost prevalent form Indian transportation system. As per the NHAI, the roads bring more than 50% of cargo and 77% passenger traffic. When referred to Government official documents, highway carriage conveys about 90% of the total commuter transport and 67% cargo transportation. Figure 2

Fig. 1 India's different modes of transport services



shows the portion of types of Transport Facilities in the transportation industry, it clearly spells how the road transport is dominant over other modes of transport system,

India positions 3rd in terms of number of buses and coaches after Indonesia and China among the 192 nations described across globe refer to Fig. 3. Table 1 shows the buses awareness proportion of India is only 1 per thousand public which is very less as compared to other countries. Figure 4 shows the Portion of Cargo and Commuter transportation by Street in India.

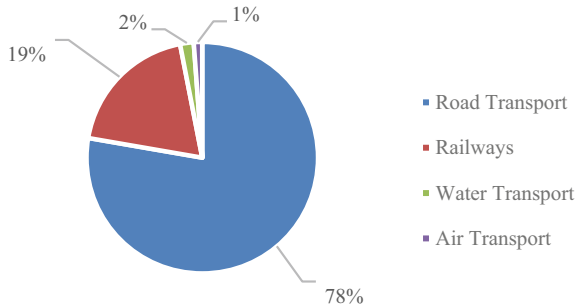


Fig. 2 Distribution of types of transport facilities

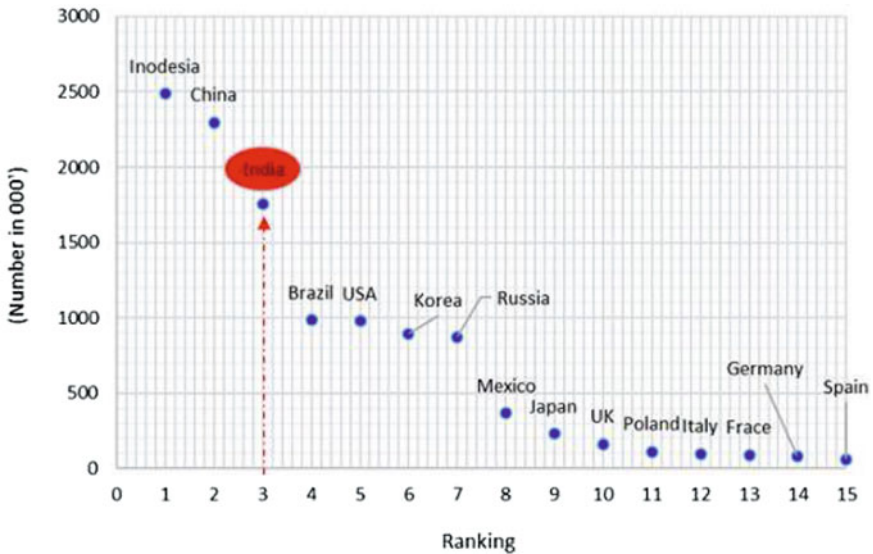


Fig. 3 Nation wise share of figure of bus as well as coaches

Table 1 Particulars of overall vehicles in application, classification across chief 15 nations

Country	Total vehicles in use	World rank	Total Vehicle penetration per 1000 people	Passenger cars			Buses and motor cars			Motor cycle and mopeds		
				Total	Rank	Penetration per 1000 people	Total	Rank	Penetration per 1000 people	Total	Rank	Penetration per 1000 people
United States	260,119,703	1	804	112,961,266	2	349	976,161	5	3	8,679,380	7	27
China	187,501,356	2	134	160,483,935	1	116	2,298,484	2	2	68,261,220	3	50
Japan	77,301,798	3	609	60,831,892	3	779	230,603	9	2	11,215,300	5	88
Brazil	68,511,508	4	330	52,004,134	4	250	984,847	4	5	25,311,251	4	122
Russia	52,337,486	5	363	45,163,201	6	313	874,382	7	6	2,266,183	12	16
Germany	50,964,751	6	619	45,803,560	5	556	78,949	14	1	43,144,936	8	52
Italy	43,323,517	7	715	38,515,701	7	635	98,623	12	2	9,740,471	6	161
India	42,515,000	8	32	30,242,000	10	23	1,757,000	3	1	168,975,000	1	128
Mexico	39,945,510	9	313	29,164,157	11	229	365,419	8	3	2,987,057	10	23
France	39,118,000	18	585	32,390,000	8	484	91,000	13	1	NA		NA
United Kingdom	35,287,562	11	538	30,850,440	9	470	161,500	10	2	1,248,074	14	9
Spain	28,895,046	12	622	22,876,830	12	492	61,838	15	1	3,211,474	9	69
Poland	25,329,863	13	667	21,675,388	13	571	113,139	11	3	2,647,825	11	70
Indonesia	24,130,997	14	92	14,580,666	15	56	2,486,898	1	10	105,150,082	2	403
Korea	21,722,872	15	424	17,338,160	14	338	892,339	6	17	2,180,688	13	43

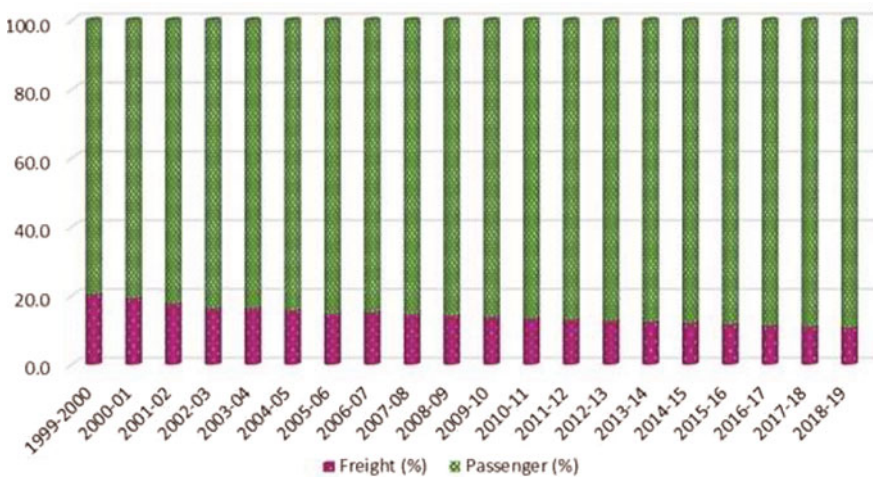


Fig. 4 Portion of cargo and commuter transportation by street in India

1.2 Objectives

The study conducted with below objectives:

1. Determine the discomfort and delight spots related commuting through bus.
2. Identify the possible causes of good or bad reactions to the survey questions.
3. Order the discomfort spots based on the importance rankings given to each of the satisfaction measures.
4. Establish the additional requirement in terms of features so that the passenger journey will be more pleasant.

2 Literature Review

Intra city buses are used for public transportation from house to working location and back. Márquez et al. [3] studied comfort requirement of buses used in the urban public transport in San Cristóbal city. The study was organized covering Senior Citizen, Children with all age group and gender, physically disabled group also. Munshi [2] explained about a good seat's ideal features. Srinivasan [5] recommended application of spring box to reduce the vibrations and improve seat ergonomic. Ramani [4] established a system used in case of theft the vehicle can be tracked and get locked in order to prevent further damage and prevent loss. Ben Barkow [1] investigated transit bus requirements in terms of interior feature.

The demands of the commuters are determined in the study are useful for Categorizing and Ranking Comfort Design Requirements of Transportation Buses in India.

Old Age senior citizens, children, and physically disabled people are not included in the survey. The bus seats are characterized by ergonomic principles. The security buzzer system is used for commuter safety in case of theft while journey.

3 Methodology

Quantitative and Qualitative methods of surveys are rigorously used in this research work. The outcome of this work was successfully filtered and administered to recognize the issues associated and suggest way forward with probable answers.

3.1 Survey Methodology

The interview techniques tools are used in qualitative survey and website tools were used in quantitative survey. Individual information, grading of satisfaction index as per the significance, present happiness and discomfort opinions and further add on requirements were included in questionnaire.

3.2 Data Processing

Each satisfaction experiences have been given separate weightages. Least weightage was given to most vital experience. Overall ranking was determined using Weighted average method. These contentment measures were arranged in ascending order to rank them. To understand the root cause of negative feedback in details all the question were further scrutinized, considering the appropriate factors. It was surfaced out there were three type factors i.e., Participant demographics (height, mass, age, gender, type of service, type of industry) Bus transport particulars (bus type) and travel aspects (duration, activity in the course of journey). All these factors were filtered and showcased in Tables 2 and 3 along with the percentage of participants in each segment. To address the issues faced by commuters the pain points were priorities as per ranking. The high priority discomfort points were answered to satisfy the commuter journey.

Table 2 Commuter information

Parameter	Groups				
	height (cm)	< 164.65	164.65–178.25	178.25–185.65	> 185.65
% participant	21	42	15	22	
mass (kg)	< 53	53–64	64–74	74–87	> 87
% participant	12	24	33	20	11
age	18–28	28–38	38–48	48–60	
% participant	12	15	29	44	
Gender	Male	Female			
% participant	62	38			

Table 3 Bus and travel information

Parameter	Groups			
	Kind of facility	Paid	Free	
% participant	100	0		
Form of bus	Large-bus	Small-bus		
% participant	52	48		
Period (min)	< 60	60–90	90–120	> 120
% participant	30	25	21	24
Pastime	Read	Sleep	Chat	Listen to music
% participant	10	65	15	10

4 Results

According to the negative responses generated during the interactions with commuters the overall discomfort issues were identified. To arrive at these discomfort issues the data collected through survey methods, commuters details, type of bus, travel time were used appropriately and ranked according to weightages were given.

4.1 Satisfaction Measures Score

All the commuters participated in the survey rated the happiness index based upon their interaction while bus travel in scale 1–7. Weightages for each of happiness measures were calculated based on the individual ratings. The happiness indicators were tabulated in Table 4 according to order and its preferred importance.

Table 4 Weightages for happiness measure

Parameters	Weightage							Weighted average
	1	2	3	4	5	6	7	
Exterior appearance of bus/state of bus	41	27	25	25	17	12	3	6.36
Hygiene	66	21	16	22	10	8	7	13.96
Inside atmosphere	42	29	29	22	16	9	3	15.36
Price of traveling	44	19	22	22	19	15	9	17.29
Seat ergonomics and individual area	27	19	19	16	17	28	24	21.68
Comfort of ingress/egress	21	10	15	12	15	32	45	25.57
Well-being	9	9	9	15	25	34	49	28.07

4.2 Inferences

A through data analysis was done to derive at the inferences and it is tabulated in Table 5. All these inferences are tabulated in the order of importance of the happiness actions.

All the feedback received during the survey were thoroughly studied against the questionnaire which are used for generation of commuter satisfaction and discomfort. Commuter sitting ergonomics safety and cleanliness were turned out to be extremely crucial and these were identified to be major pain points. The passengers were happy with rest of the satisfaction measures.

5 Recommendations

Response from participants showed safety, sitting ergonomics and cleanliness are the very crucial parameters, hence changes were proposed to enhance these parameters which is tabulated in Table 6.

Above mentioned recommendations will enhance the happiness of commuters while using the public transport. Bus manufacturers also can make use of this study to develop their products.

Table 5 Inferences

Happiness parameters	Participant feedback				
Protection features	Adequate	Inadequate			
% participant	41	59			
General sitting ergonomics	Poor	Fair	Good	Very good	Excellent
% participant	21	48	29	2	0
Hygiene	Very clean	Moderately clean	Dirty		
% participant	11	32	57		
Inside atmosphere	Roomy	Moderately roomy	Cramped		
% participant	26	44	30		
Comfort of ingress/egress	Difficult	Neutral	Easy		
% participant	35	26	39		
Price of traveling	Very high	Comparable			
% participant	43	57			
Exterior appearance of bus	Modern	Traditional			
% participant	14	86			

Table 6 Recommendations

Satisfaction measures	User's recommendations	Expert recommendations
Safety	(1) Armrests to be provided at passage side	(1) Every seat to be provided with seat belts
	(2) Roof side of bus supports to be given	(2) Security alarm with GPS provision
	(3) Ample handholds to be provided	(3) Speed limiting device to be provided
Sitting comfort and personal space	(1) Sufficient luggage storage	(1) Low-cost adjustable backrest provision to be given
	(2) More leg space required	(2) Footrests and armrests to be provided
	(3) Seat should be wider	(3) Lumbar support on seat to be provided
	(4) Seat spacing should be more	
Cleanliness	(1) Bus should be clean from inside	(1) Bus should be provided with waste material collection bags

References

1. Barkow, B. (1991). *Customer perspectives on the interior design of urban buses*.
2. Munshi, K. Chairs the human factor.
3. Márquez Jesús, M. A., & Garcia, M. (2004). Ergonomics of urban public passengers transport.
4. Ramani, R., Valarmathy, S., Suthanthira Vanitha, N., Selvaraju, S., Thiruppathi, M., & Thangam, R. (2013). Vehicle tracking and locking system based on GSM and GPS. *International Journal of Intelligent Systems and Applications*, 09, 86–93. <https://doi.org/10.5815/ijisa.2013.09.10>
5. Srinivasan, S., Prasanna, S., & Sambasivam, S. M. (2014). Passenger bus—seat modification to avoid accident damages and for comfort level. *International Journal of Scientific & Engineering Research*, 5(1), 1518. ISSN 2229–5518.

Use of Poly Contrast Interference Photography (PIP) for Energy Field Analysis of Concrete Pavement



Dipak M. Kolekar, Sunil S. Pimplikar, Rohit R. Salgude, Rohan R. Yadav, and Ashlesha S. Deshmukh

Abstract Energy analysis is the way of understanding variations of energy on the earth surface due to various activities occurring beneath the earth surface. This creates Geopathic stress, which is the phenomena evolves large amount of change in energy fields at specific locations. It disturbs the normal functioning of biotic and abiotic components of environment. Present study aims to investigate the energy field using Poly Contrast Interference Photography (PIP) mainly on concrete pavement. PIP hypothesizes that the manner with which light waves, both visible and non-visible are observed and reflected off the physical and energetic bodies can be used to access the molecular health state of the body under consideration. In the present study, PIP has been conducted on the road section from chainage 50 km to chainage 94 km on the Mumbai–Pune expressway i.e. rigid pavement and on major accident spots located at Khadki and Hadapsar, on the old Mumbai-Pune road i.e. flexible pavement located in India. Present research investigation proves that use of PIP hypothesis technique is extensively used to identify electromagnetic field which further helps to define geopathic stress.

Keywords Energy field analysis · Geopathic stress · Poly contrast interference photography · Road pavement

D. M. Kolekar (✉)

Research Scholar, School of Civil Engineering, Dr. Vishwanath Karad MIT World Peace University Kothrud, Pune, India 411038
e-mail: dmkolekar.scoe@sinhgad.edu

Assistant Professor, Sinhgad College of Engineering Vadgaon, Pune, India 411041

S. S. Pimplikar

Professor and Program Head M.Tech. Construction Engg. and Management Program, School of Civil Engineering, Dr. Vishwanath Karad MIT World Peace University Kothrud, Pune, India 411038

R. R. Salgude

Assistant Professor, School of Civil Engineering, Dr. Vishwanath Karad MIT World Peace University Kothrud, Pune, India 411038

R. R. Yadav · A. S. Deshmukh

M.Tech Construction Engg. and Management Program Student, School of Civil Engineering, Dr. Vishwanath Karad MIT World Peace University Kothrud, Pune, India 411038

© The Author(s), under exclusive license to Springer Nature Switzerland AG 2024

343

P. M. Pawar et al. (eds.), *Techno-Societal 2022*,
https://doi.org/10.1007/978-3-031-34648-4_35

1 Introduction

Roads are important asset in faster and socioeconomic growth of any nation. Road design along with maintenance plays major role in maintaining good condition and effective use of road network. There are many parameters such as crack pattern, aggregate structure, subgrade characteristics, soil structure, and climatic conditions.

Characteristics which needs to be considered for better serviceability. Recent studies related to these parameters suggest; Preventing pavement from crack is one of the main objective of regular maintenance, as crack length along with surface condition play key role in propagation of crack [1]. Advance crack detection model using vehicle vibration response, use of road video and local binary pattern with support vector machines and analytical approach to calculate number of cracks and width of cracks are recent development in crack detection approach [2–4]. (Jiaolong Ren et al.) studied aggregate structure, gradation and its significance in pavement. Aggregate structure plays key role in smooth performance of pavement and proper gradation enhance pavement performance. References [5, 6] introduced artificial neural network for evolution of strength of subgrade [7]. Climatic conditions plays important role in design of pavement as it control the material characteristics [8]. Partial replacement of cement by ecofriendly materials like mineral admixtures and natural fibers not only helps in quality enrichment but it also helps in achieving economy in road construction [9, 10]. All parameters related to road like cracks, subgrade characteristics, soil structure, climatic conditions are influenced by geopathic stress, so it is important to study geopathic stress aspect in design of road. The energy emitted by the earth surface at a specific location which affects the normal human body function is termed as geopathic stress [11]. It has some sort of subtle energy which affects human system, On such zone there is change in body voltage, skin resistance, blood pressure and heart rate and also reaction time of driver changes which leads to accidents [12–15]. It has been observed that there is increase in atmospheric pressure and temperature under influence of such zone [16]. Geopathic stress is responsible for the change in the soil properties like water content, density, specific gravity, liquid and plastic limit, pH value conductivity, electrical Resistivity [17, 18]. Under influence of such energies distress occurs on road and abrupt change in magnetic field has been occurred [19, 20]. Therefore geopathic stress is threat to build environment and should be part of planning aspect in engineering projects [21]. Detection of geopathic stress is successfully carried out by various methods like dowsing and geo-resistivity meter as under such zone copper rods get deflected and electrical resistivity decreases [22]. Use of light interface techniques suggests that it may be effect of concentrated low energy at particular location [23]. Also it can be attenuated by using NAAVRAJ technique [24]. Present study intend to investigate such zones with help of a technique called as Poly contrast interference photography (PIP) which covers micro analysis of field variations at location based on light patterns which other methods do not provide.

Basically Harry Oldfield invented PIP in the late 1980s, using microchip technology, for studying health aspect of human body. Energy field analysis is the process

of determining the light energy emitted by any physical body and then analyse it based on the spectrum pattern obtained. Poly contrast interference photography (PIP) is a scanning system showing the interference between the light reflected from any physical body and the full spectrum light, which is made to fall on it. The system comprises of a scanning environment including full spectrum lighting, a digital video camera to capture the image and computer capable of running the PIP software [25]. Focus of present study is to identify and study energy field variations using PIP, which enable researchers to study energy field using colour patterns; based on which it may be emerge as one the approach for investigation related geopathic stress and its variations.

2 Objective

Present study includes an investigation related to the effect of geopathic stress on the road environment associated with highways and expressways with following two main objectives.

- A. To analyse the condition of built environment at accident spots on the expressway and on national highways; where there are accidents but the cause for these accidents do not fall, under the typically known reasons, such as poor geometry, curves, gradients etc.
- B. To determine the response from the materials used for constructing rigid pavement mainly the concrete when exposed to light interference; also to observe the response at few locations on bituminous pavements.

3 Methodology

For conducting empirical investigation, an instrument system is necessary. Considering the general instrument system, the components for the empirical investigations that are carried out in the present study are as follows: The moving underground water zone would be the stimulus which is one of the primary reason for occurrence of geopathic stress; The subject would be the part of road subjected to the geopathic stress; The transducer is any device capable of converting on form of energy into a signal. In the present set, the copper L rods and poly contrast interference photography (PIP) are used as transducers. The set-up is used on the non-stress zones as well as on the various stress zones of the road for observing the difference.

The empirical sets devised in the present study as shown in Fig. 1 are simple. Initially, for detecting the empathically stressed zones, the system used is the healthy bio locator with two copper L rods as transducers. The position of the bio locator during bio location and on detection of the stress zones is as shown in the Figs. 2, 3, 10, 13 and 16.

Fig. 1 Model for identification of geopathic stress

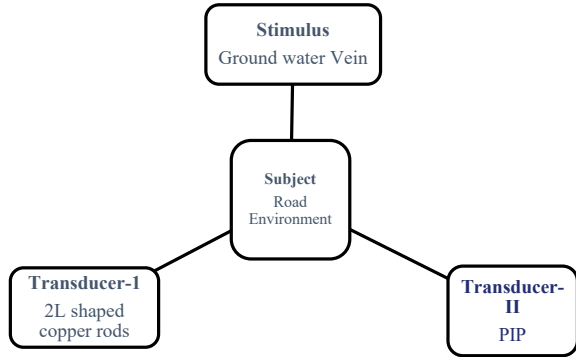


Fig. 2 Bio locator is taking his position to detect stress zone



Fig. 3 Bio locator is seen entering the stress zone at khadki railway station



The empirical setup for investigations related to the road environment, adopted in the present study comprises of two sets of observations. In the first set the procedure for on-site observations of accident spots is formulated in the following manner.

- i. The accident spots on the expressway and on national highways are selected where there are accidents but the cause for these accidents do not fall, under the typically known reasons, such as poor geometry, curves, gradients etc.
- ii. Thorough bio location is carried out at such spots, using 2 copper L rods to detect the presence of underground water zones.

- iii. For few sample initial spots, the existence of the water zones is also confirming using ground resistivity technique.
- iv. In addition to the above, visual clues such as thorny trees, diseased trees, presence of beehives, anthills, existence of a well or a bore-well are also recorded.

The second set considers the use of the Poly contrast interference Photography (PIP) technique. The system comprises of a scanning environment including full spectrum lighting, a digital video camera to capture the image and a computer capable of running the PIP software. The set-up is used on the non-stress zones as well as on the various stress zones of the road as aforementioned.

4 Results and Discussions

4.1 Analysis of Condition of Built Environment of Road Subjected Accidents and Geopathic Stress

An interesting feature is observed from the visual clues which are recorded along existence of heavily distressed pavement surfaces at the accident spots involving geopathic stress as the primary cause. These distresses are noticed in pavements which are newly constructed both in the flexible and rigid types. When moving at high speeds, tire bursting has been identified as a basic factor for cause of any accident. It is imperative that a very badly deteriorated pavement surface location is more prone to accidents, especially for vehicles moving at high speeds. Needless to mention, the economic maintenance of expressways and highways is also at stake. In Table 1 the basic details as mentioned above are highlighted.

4.2 Energy Field Analysis Using Poly Contrast Interference Photography (PIP)

Energy field analysis using Poly Contrast Interference Photography (PIP) has been conducted throughout the test road section from chainage 50 km to chainage 94 km on the Mumbai-Pune expressway and also at the few accident spots located at Khadki and Hadapsar and on old Mumbai-Pune road. The principle followed is the translation of the electromagnetic radiation into the visible spectrum. Brighter colours indicate higher energy levels whereas the darker colours indicate lower energy levels because of existence of geopathic stress. PIP hypothesizes that the manner with which light waves, both visible and non –visible are observed and reflected off the physical and energetic bodies can be used to access the molecular health state of the body under consideration. Figures 2, 3, 4, 5, 6, 7, 8, 9, 10, 11, 12, 13, 14, 15, 16, 17, 18, 19, 20,

Table 1 On-site observations of accident spots on Mumbai- Pune expressway

S. No.	Location of accident spot or Chainage (km)	Number of accidents averagely occurring per year	Visual clues recorded	Approximate length of the stress zone (m)	Intensity of stress as felt by the bio locator
1	50 bridge above canal	24	Thorny trees, very severely distressed concrete road, undergoing frequent repairs	Entire length of the bridge	Very strong
2	56	32	Discontinuity in vegetation	10	Very strong
3	56.7 railway overbridge	17	Thorny trees, state transport bus had fallen on the railway track on the day of observation	Entire length of the bridge	Strong
4	60	12	Anthills	12	Medium
5	63	16	Thorny trees, road surface showing cracks	20	Strong
6	65	21	Discontinuity in hedges, thorny trees	30	Medium
7	66	12	Poor riding quality of concrete road	20	Strong
8	67	6	Discontinuity in hedges	15	Medium
9	68	8	Anthills	22	Medium
10	70	15	Accident occurred on the day of observation	15	Very strong
11	73	12	Discontinuity in hedge	10	Medium
12	74	12	Asphaltic road severely distressed	22	Strong
13	75	13	Concrete exhibiting severe cracks	28	Strong
14	76 Baur	9	Anthills	15	Medium

(continued)

Table 1 (continued)

S. No.	Location of accident spot or Chainage (km)	Number of accidents averagely occurring per year	Visual clues recorded	Approximate length of the stress zone (m)	Intensity of stress as felt by the bio locator
15	76 near V. M. jog crusher plant		Thorny trees, anthills, diseased trees	53	Medium
16	81 near Kiwale junction	16	Asphalt patches on L.H.S. and R.H.S. of the road removed after repairs also the similar distress are seen	53	Strong
17	82 near Kiwale junction	12	Hair cracks visible on newly constructed road	15	Medium
18	83.1	20	Various types of distresses in concrete pavement, anthills, thorny trees, side railings broken	116	Very strong
19	85.3	8	Diseased vegetation	20	Medium
20	86.2 ahead of somatna bridge	20	Thorny trees	55	Medium
21	87	11	Discontinuity in vegetation, new road	15	Strong
22	88	7	Anthills	21	Medium
23	90.7	14	Thorny trees, asphaltic road repaired in patches	23	Strong
24	92	8	Side railing broken	15	Medium
25	93	9	Deceased trees	20	Medium
26	Near Wadgaon–Maval police station	7	Anthills, discontinuity in vegetation	30	Medium

21, 22, 23, 24, 25, 26, 27, 28, 29, 30 and 31 are the various PIP scans obtained at the various spots which are enlisted in Table 3.1.

PIP scans of the road ways:

The observations and inferences derived based on the research done using the PIP scans presented below:

At locations where the geopathic stress does not exist, the energy field scan shows uniform, coherent colour patterns of green, greenish blue, violet spectrum. Green colour with 584 trillion oscillations per second, blue with 658 trillion oscillations per second, violet with 732 trillion oscillations per second represent fast

Fig. 4 Moderately distressed road surface at Khadki railway station



Fig. 5 Hand pump is visible at the Khadki railway station



Fig. 6 Normal zone at Khadki railway station



Fig. 7 Black spot at the Khadki railway station



Fig. 8 Contrasting colour hues and strong magnetic polarity exhibited on a black spot at Khadki



Fig. 9 A combination of very bright and dull colour in the PIP scan at an accident spot



Fig. 10 The bio locator in position to detect the geopathic stress zone



Fig. 11 Road test 2_29 PIP scan showing contrasting red and green colour at an accident spot

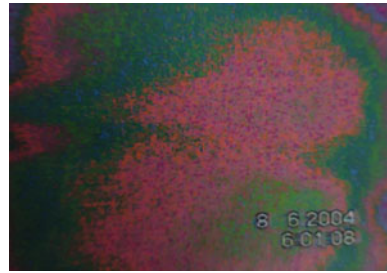


Fig. 12 Road test 2_34 A very strong geopathic stress zone, damaging the ground at site in hadapsar



Fig. 13 Road test 2_47 the bio locator is seen entering the stress zone with 2 L rods in deflected position



Fig. 14 Road test 2_52 A PIP scan of the expressway at a location where weak geopathic stress exists

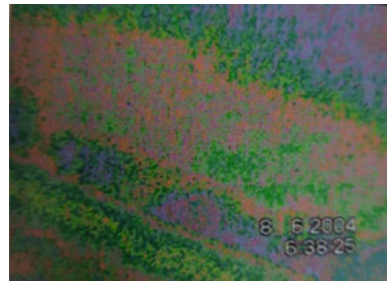


Fig. 15 Road test 2_57 A
PIP scan of the expressway
at an accident spot



Fig. 16 Road test 2_65 PIP
scan showing the bio locator
at an accident spot



Fig. 17 Road test 2_70 PIP
scan of the expressway at a
location unaffected by
geopathic stress



Fig. 18 Road test 2_85 PIP
scan showing existence of
strong quartz crystals close
to an accident spot



Fig. 19 Road test 2_89 PIP scan showing significant colours variations on geopathic stress zone.



Fig. 20 Road test 2_130 PIP scan at another accident spot on the expressway

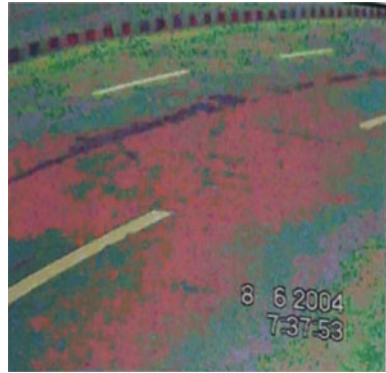


Fig. 21 Road test 2_143 Chainage showing location of accident spot



vibrating colours, indicating energetic material condition and balance in general. Colour uniformity and gradual change in the colour pattern indicate good physical health of the pavement. Figures 16, 20 and 21 show that where the accident has occurred, there is a predominance of red colour at the stress zone and the colour directly changes to red from greenish blue. Red has the lowest vibrations at 437 trillion oscillations per second. The sudden change of colour in the PIP scan is indicative

Fig. 22 Road test 2_144 PIP scan at a distressed road surface on the expressway



Fig. 23 Road test 2_146 A PIP scan showing possibility of a magnetic polarity as is evident from the horse-shoe shapes

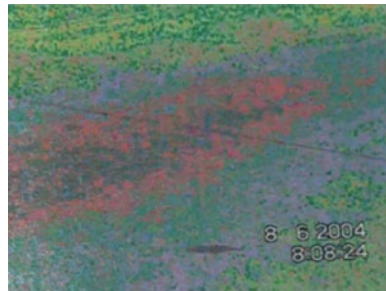


Fig. 24 Road test 2_147 A PIP scan at chainage 70 km, wherein the accident had occurred on the day of observation



Fig. 25 On site PIP hadapsar_100 A very strong geopathic stress location at an accident spot in hadapsar

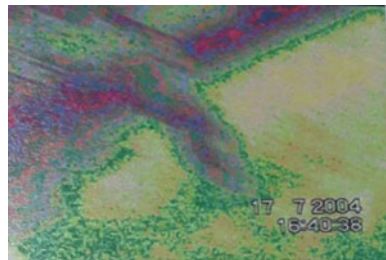


Fig. 26 On site PIP hadapsar_101 A PIP scan of the surface below which a moving underground water vein exists



Fig. 27 On the site PIP hadapsar_102 A PIP scan of the good site unaffected by geopathic stress, at hadapsar



Fig. 28 On site PIP hadapsar_103 A PIP scan inside the well at hadapsar

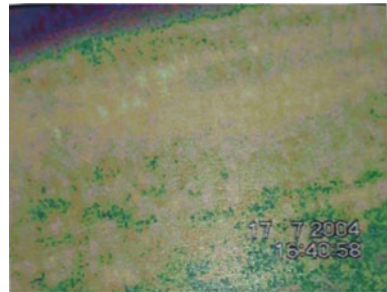


Fig. 29 On site PIP hadapsar_104 A PIP scan inside the well at hadapsar



Fig. 30 on site PIP
hadapsar_105 A PIP scan
inside the well at hadapsar



Fig. 31 On site PIP
hadapsar_106 A PIP scan
close to the well but at a
location where there is no
underground water vein



of a significant difference in the energies of the various particles, though they are of the same material. This, therefore indicates that the pavement material is being subjected to differential stresses, because of the geopathic energy. This is metaphorically termed as a diseased condition of the materials, which in turn is responsible for distresses on new pavements.

The contrasting colour patterns of red and green are more clearly visible in Figs. 4, 7, 8, 10, 11, 12, 15, 16 and 19 which also co-relate with the detection of geopathic stress using copper L rods, which are seen in the deflected position when entering the stress zone. Also Figs. 11, 16 and 20 show a predominant red colour on the stress zone. Figures 7, 8, 9, 20, 23 and 25 show the effect of electromagnetic polarity at very strong stress zones as indicated from the twisting energy bands. In these figures, it can be visualized that, at a cross section, the molecules of the pavement materials are being subjected to varying frequencies, nearly covering entire light spectrum. This, in turn is leading to the various distresses in both type of pavements, flexible as well as rigid (Table 2).

Table 2 Zone and respective colour pattern observations

Zone	Colour
Non-geopathic stress	Uniform, coherent colour patterns of green, greenish blue, violet spectrum
Geopathic stress zone	Red
Electromagnetic polarity (strong geopathic stress)	Contrasting colour

5 Conclusion

From the present investigation on expressway and Based on the observations, it is safe to conclude that

- A. Discontinuity in vegetation, Thorny tress, discontinuity in hedge, cracks in pavement and pavement distress on accident spots indicate geopathic stress influence normal functioning of both biotic and abiotic components of environment.
- B. Energy field analysis using PIP technique enables the researcher to visualize and analyse the molecular state of the pavement materials, based on the vibrational characteristics. A significant contrast is evidenced in the PIP scans of the same material, whether it is that of the flexible pavement or of the rigid pavement with respect to a continuous exposure to geopathic stress.

It may therefore be prudent to include the geopathic stress as an additional design parameter. Further investigations involving the measurement as well as determination of strains in the rigid and flexible pavement which are vulnerable to the earth energies, may open an entire innovative approach for designing of roads, so as to improve functional and economic performance of the sector.

References

1. Wang, X., Li, K., Zhong, Y., et al. (2019). Investigation of thermal reflective cracking in asphalt pavement using XFEM coupled with DFLUX subroutine and FILM subroutine. *Arabian Journal for Science and Engineering*, 44, 4795–4805. <https://doi.org/10.1007/s13369-018-3554-y>
2. Chen, C., Seo, H., & Zhao, Y. (2021). A novel pavement transverse cracks detection model using WT-CNN and STFT-CNN for smartphone data analysis. *International Journal of Pavement Engineering*. <https://doi.org/10.1080/10298436.2021.1945056>
3. Chen, C., Seo, H., Jun, C. H., & Zhao, Y. (2022). Pavement crack detection and classification based on fusion feature of LBP and PCA with SVM. *International Journal of Pavement Engineering*, 23(9), 3274–3283. <https://doi.org/10.1080/10298436.2021.1888092>
4. Ouzaa, K., & Benmansour, M. B. (2014). Cracks in continuously reinforced concrete pavement. *Arabian Journal for Science and Engineering*, 39, 8593–8608. <https://doi.org/10.1007/s13369-014-1442-7>

5. Ren, J., & Yin, C. (2022). Investigating mechanical characteristics of aggregate structure for road materials. *International Journal of Pavement Engineering*, 23, 2, 372–386. <https://doi.org/10.1080/10298436.2020.1748189>
6. Hafeez, I., Kamal, M. A., Ishaq, M. A., et al. (2015). A Laboratory-based research study to investigate the aggregate packing characteristics and its influence on asphaltic mixture's performance. *Arabian Journal for Science and Engineering*, 40, 3119–3134. <https://doi.org/10.1007/s13369-015-1804-9>
7. Raja, M. N. A., Shukla, S. K., & Khan, M. U. A. (2021). An intelligent approach for predicting the strength of geosynthetic-reinforced subgrade soil. *International Journal of Pavement Engineering*. <https://doi.org/10.1080/10298436.2021.1904237>
8. Bayraktarova, K., Eberhardsteiner, L., Zhou, D., & Blab, R. (2022). Characterisation of the climatic temperature variations in the design of rigid pavements. *International Journal of Pavement Engineering*, 23(9), 3222–3235. <https://doi.org/10.1080/10298436.2021.1887486>
9. Saini, S. K., Ransinchung, R. N. G. D., & Kumar, P. (2022). Effect of different mineral admixtures on the performance of pavement quality concrete containing the optimum amount of Jarosite as partial replacement of cement. *Arabian Journal of Science Engineering* <https://doi.org/10.1007/s13369-022-06892-5>
10. Farooqi, M. U., & Ali, M. A. (2022). Study on natural fibre reinforced concrete from materials to structural applications. *Arabian Journal for Science and Engineering*. <https://doi.org/10.1007/s13369-022-06977-1>
11. Freshwater, D. (1997). Geopathic stress. *Complement Therapies Nursing Midwifery*, 3, 160–162.
12. Dharmadhikari, N. P., Meshram, D. C., Kulkarni, S. D., Kharat, A. G., & Pimplikar, S. S. (2011). Effect of geopathic stress zone on human body voltage and skin resistance. *Journal of Engineering and Technology Research*, 3(8), 255–263. ISSN 2006-9790.
13. Dharmadhikari, N. P., Rao, A. P., & Pimplikar, S. S. (2010). Effect of geopathic stress on human heart rate and blood pressure. *Indian Journal of Science and Technology*, 3(1), 54–57.
14. Kharat, A. G. (2000). *Theoretical and empirical investigations on built environment*. Ph.D. thesis. Relator: Pune University, India.
15. Pimplikar, S. S., & Salgude, R. R. (2017). Road accident prediction models based on geopathic stress. *IJERMCE*, 77–75. ISSN (online): 2456-1290.
16. Pimplikar, S. S. (2011). *Empirical and theoretical investigations of accidents on expressways and national highways*. Ph.D thesis. Relator: Pune University, India.
17. Dharmadhikari, N. P., Muthekar, V. V., Mahajan, C. S., Basavaiah, N., Kharat, A. G., Barade, S. I., Sharma, A. K., & Laxminarayana, M. (2019). Vein width measurement of groundwater on earth surface using semiconductor lessor light and proton precession magnetometer. *Journal of Applied Geophysics*, 171(2019), 103864.
18. Sorate, R. R., Kharat, A. G., Dharmadhikari, N. P., & Bhagwat, S. (2013). Effect of geopathic stress zone on soil properties. *Elixir Geoscience*, 54C(2013), 12365–12367.
19. Rohit, S., Sunil, P., & Gaurav, S. (2020). Geopathic stress: A possible cause for pavement distresses and road accidents. *IJITEE*, 9(6), 850–854. ISSN: 2278-3075.
20. Chafekar, B. H., Jarad, G. P., Pimplikar, S. S., Dharmadhikari, N. P., Kharat, A. G., & Sorate, R. R. (2013). Effect of geopathic stress on pavement distresses. *IOSR Journal of Mechanical & Civil Engineering (IOSR-JMCE)*, 01–08. ISSN: 2278-1684.
21. Sorate, R. R., Kharat, A. G., Dharmadhikari, N. P., Pimplikar, S. S., Narang, G., Deshmukh, D., Bhagwat, S., & Sorate, S. (2012). Geopathic stress aspect for sustainable development of built environment. *International Journal of Scientific and Research Publications*, 2(12).
22. Dharmadhikari, N. P., Meshram, D. C., Kulkarni, S. D., Kharat, A. G., Sorate, R. R., & Pimplikar, S. S. (2011). Use of dowling and geo-resistivity meter for detection of geopathic stress zone. *International Journal of Modern Engineering Research (IJMER)*, 1(2), 609–614.
23. Dharmadhikari, N. P., Kharat, A. G., & Pimplikar, S. S. (2010). A study of geopathic stress using light interface techniques. *Research Communications—Current Science*, 98(5), 695–697.

24. Sorate, R. R., Kharat A. G., Shivshette, M., Desai A., & Sontakke, P. (2015). Attenuation of geopathic stress by using NAAVRAJ attenuation technique. *International Journal of Engineering and Computer Science*, 4(6), 12563–12567.x. ISSN:2319-7242.
25. PIP Manual Innovation. (2007). Technologies and energy medicine (ITEM) and centre for bio field sciences.

Energy Generation System Through Solar and Fast-Moving Vehicles



Basavraj R. Birajdar and Suryaji S. Kale

Abstract Now a days Energy is an important aspect in our every day's life. The resources available are limited, whereas the population consuming the energy is increasing day by day. The world continues to search for innovative solutions for harnessing clean energy; there is an emerging need for research in improving the efficiency of existing renewable energy conversion methods. Wind and Solar are two major renewable energy resources that are easily available and can be harnessed easily. This research aims to design and develop a mini vertical axis wind turbine (VAWT) along with the solar panel which can be installed on the road dividers. Our aim is to capture wind from the fast-moving vehicles on the highways and use the solar energy simultaneously. Vertical Axis Wind Turbine also abbreviated as VAWT is one such design which captures wind from all directions and will be using VAWT in this research work. The electricity will be generated from both VAWT and Solar panels and can be either stored into batteries or it can be supplied to the grid. The major components of the project are blades, shaft, strut, bearings, structural members, motor, gearbox, solar panel, and batteries. Maximum speed achieved by wind turbine is 300 rpm. This research aims to innovate and redesign the existing models and collaborate it with solar panels to increase the overall efficiency and to develop a sustainable model.

Keywords Wind turbine · Solar panel · Clean energy · Renewable energy

1 Introduction

A wind turbine can generate and store power with minimum to no pollution. The common person can considerably decrease their electricity costs if the efficiency of the conventional wind turbine is increased. People have been using the wind energy to simplify their life cycles since the seventh century [1, 2]. However, the initial wind turbines were neither very dependable nor energy effective. Only a portion

B. R. Birajdar (✉) · S. S. Kale

N. K. Orchid College of Engineering and Technology Solapur, Solapur, Maharashtra, India

e-mail: birajdar.basav@gmail.com

© The Author(s), under exclusive license to Springer Nature Switzerland AG 2024

P. M. Pawar et al. (eds.), *Techno-Societal 2022*,

https://doi.org/10.1007/978-3-031-34648-4_36

361

of the sail cycle was used. They were useful for torque even though they were typically sluggish and had a low tip speed ratio. Man has been working to advance the wind turbine ever since it was invented. As a result, the number of blades on wind turbines has diminished over time. While earlier wind turbines had 4–8 blades, the majority of modern wind turbines have 5–6 blades [3]. Modern wind turbines have the ability to automatically turn into the wind, unlike earlier models that required operator direction. Over time, changes have also been made to the materials and sail design. The effectiveness of the rotor is often directly related to its altitude. A recent wind turbine should be located at minimum twenty feet high and three hundred feet away from any obstacle, however thirty feet high and five hundred feet away from any impediment is ideal. We are aware that there must be wind for wind turbines to function, but how do they operate? The horizontal axis wind turbine (HAWT) and the vertical axis wind turbine (VAWT) these are the two different type of wind turbines. The horizontal rotor of the horizontal axis wind turbine is like that of the traditional Dutch four-arm wind turbine.

The wind's lift is what the horizontal axis wind turbines largely rely on. A fluid will move from higher pressure to a lower pressure, according to Bernoulli's Principle. Additionally, it claims that "a fluid's density falls as its velocity increases." Using this as a foundation, the top of horizontal axis wind turbine blades has been curled to resemble an airplane wing. With this design, the air above the blade will moves more quickly, which lowers its density and causes the air below the blade to rise the lift.

1.1 History

Drag, as opposed to lift, is used by vertical axis wind turbines like the Savonius (built in 1930). Drag is wind resistance, similar to a brick wall. The blades of vertical axis wind turbines are pushed by the wind because they are made to resist the wind [1]. There are many applications for wind turbines, both horizontal and vertical axis. Some of these are hydraulic pumps, motors, air pumps, oil pumps, churning, friction-producing devices, heat-directing devices, electric generators, and centrifugal pumps. There are many different types of wind turbines. Some wind turbines, like the sail wind turbine, are a very gradual moving, having a low tip speed ratio, and are not especially energy effective compared to cyclo-turbine, but are considerably cheaper and money is the major equalizer. Over time, the wind turbine has undergone numerous improvements. To control speed in heavy gusts, air brakes have been added to wind turbines. To avoid the stresses at high-level wind speeds, vertical axis wind turbines have been fitted along with hinged blades. To regulate the shaft speeds, gearboxes have been added to wind turbine generators. Most wind turbines begin to produce energy at 11 m/s and stops at speed near to 32 m/s. The swept area of the wind turbine is another factor in determining its efficiency. The wind speed is another factor that affects a wind turbine's production (Fig. 1).

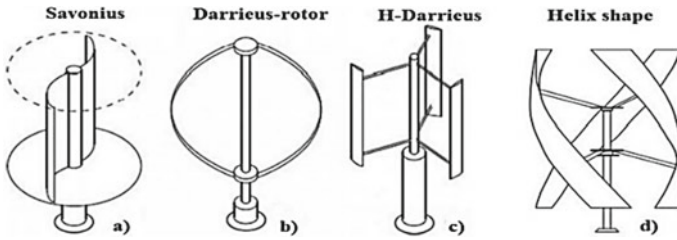


Fig. 1 Types of VAWT [4]

Movements of air in the atmosphere that are primarily caused by temperature variations are the source of winds. Uneven solar heating is the cause of the temperature gradients. As a result, the equatorial region's warmer and lighter air rises to the atmosphere's outer layers and travels in the direction of the poles. The Coriolis forces connected to the Earth's rotation also have an impact on this air circulation. The geotropic winds are large-magnitude air fluxes that exist throughout the whole atmosphere. The surface layer, which is the lowermost part of the atmosphere, is 100 m high. In this layer winds are prolonged by frictional forces and obstructions, changing both their speed and direction. Turbulent flows, which create fluctuations in wind speed over a broad range of amplitudes and rates, originate from these processes.

1.2 Small Scale Vertical Axis Wind Turbine Design (Castillo 2011)

A small-scale vertical axis wind turbine that will be constructed with components found around. The rotor blades are constructed of wood and are produced using standard workshop equipment [5]. The different factors like rotor's sweep area, power, power coefficient, tip speed ratio, blade chord, minimum number of blades were considered when designing the rotor for a wind turbine. Turbines typically had a power coefficient of between 0.2 and 0.3. The NACA 0021 airfoil was chosen because it exhibits superior self-starting behavior than the NACA 0015 [6].

1.3 Development of Small H—Darrieus Wind Turbine for Small Applications

To create a powerful, affordable wind turbine [7]. To produce power at relatively low wind speeds, they constructed a vertical axis rotor with three blades [8]. For the wind turbine, they used an open-source Q blade. To produce a rotor blade prototype, the design parameters were optimized. A NACA 0021 airfoil and a rotor with a diameter

of 2 m and a length of 1.6 m made up the final prototype design specifications. The depth (21% of the chord) and self-starting characteristics of the airfoil were important factors in the selection [4]. For experimental validation, an actual size turbine was built depending upon the final prototype design. Plastics with glass fiber reinforcement was the substance used (GFRP). Making the master blade for the moulds that would be used to create duplicate blades was a step in the blade manufacture process [9]. The sequenced steps of laminating, drying, trimming, and smoothing were applied to the blade copies. A wind fan was used to test the turbine’s power coefficient while exposing it to winds with speeds varying between 4 and 15 m/s [10].

1.4 Wind Survey

This section details the basic measurement parameters for wind resource measurement.

1.5 Wind Speed

In Wind turbine speed is the most important factor, which is directly proportional to the power output of a wind turbine. Wind speed is measured by anemometers. The data gathered are affected because of anemometer height, the exposure with the surroundings, the human error while reading the wind speed and the quality of the anemometer. Our team did the survey on the available wind speed at the corner of highways. We went to three highways in Solapur. These surveys were taken at the height of 1.7 m from ground (Figs. 2, 3, and 4).

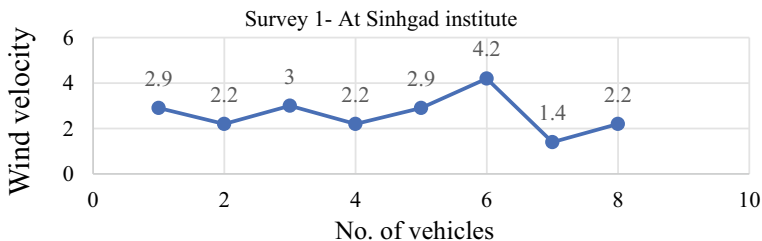


Fig. 2 Survey-1

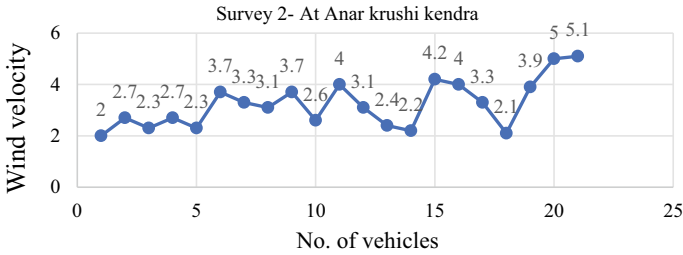


Fig. 3 Survey-2

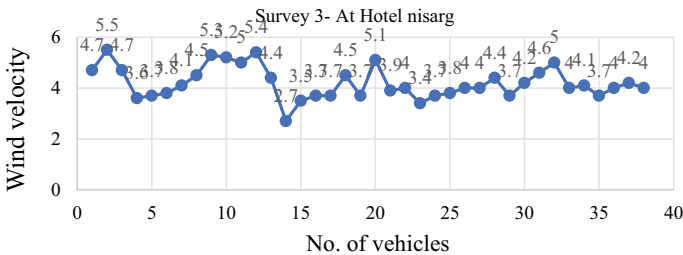


Fig. 4 Survey-3

Overall, an average of 5.5 m/s of wind speed was obtained at the corner of the highways. So, the velocity of 11 m/s was finalized for the design.

1.6 Wind Turbine Parameters

Power: The power produced from wind for a vertical axis wind turbine can be obtained from the formula $P = \frac{1}{2} \times \rho \times A \times V_{\infty}^3$.

Where, P is power (W), ρ is density of air, A is swept area and V_{∞} is ambient wind velocity.

Power coefficient: Power coefficient is the ratio of captured mechanical power by the rotor to the wind power offered in the wind [10]. It can be referred as efficiency of the turbine. There is a theoretical efficiency limit in wind turbine determined by the deceleration of the wind. It is known as Betz limit which is 59.3%.

Blade swept area: turbine blade swept area can be calculated by the expression $S = D \times L$.

Where, S is swept area (m^2), D is rotor diameter (m) and L is blade length (m).

Number of blades: The number of blades has direct effect in the efficiency of rotor function. The optimum number of blades for Straight blade vertical axis wind turbine

is three based on the review of literature. Three bladed turbines tend to run more effortlessly since the energy variations are lower in each revolution compared to other number of bladed turbines. More precisely, the changes in both torque and resultant force acting on the rotor are much lesser in turbine with three blades.

Airfoil selection: The most important factors for an efficient design of vertical axis wind turbine is the blade cross sectional shape. There majorly two types of airfoils Symmetrical and Asymmetrical. The profile will be selected symmetrical airfoils like NACA 0012, NACA 0015, NACA 0018, NACA 0021 [11]. Symmetrical airfoils are easy to fabricate. Based on various literature and ease of fabrication, NACA 0018 airfoil was finalized as it has overall better performance over other airfoil [12], and it is relatively thicker than the other airfoil which gives an added advantage.

Mechanism: When DC voltage is delivered to the terminals of a stepper motor, the motor rotates constantly. This motor is well known for its ability to transform a series of input pulsations into an exact increment in the rotational position of the shaft. The shaft rotates through a fixed angle with each pulse. Stepper motors really consist of several “toothed” electromagnets arranged as a stator revolving around a central iron rotor. An external driver circuit or a microcontroller powers the electromagnets. One electromagnet is powered to magnetically attract the gear teeth and turn the motor shaft. The teeth of the gear are somewhat offset from the next electromagnet when they are lined up with the first electromagnet. The method is then again repeated. Each of those rotations is referred to as a “step,” and a whole rotation is made up of an integer number of steps. This allows for accurate angle turning of the motor.

Charge controller: A solar charge controller is a piece of technology that controls how much power from the solar array enters the battery bank. It avoids power from running back to the solar panels during the night and prevents the deep cycle batteries from being overloaded during the day. Currently PWM and MPPT are the two available methods for solar charge controllers with additional features. An MPPT charge controller costs more money but is very effective.

Selected type: One charge controller can manage power from both solar as well as wind as the power does not exceeds the desired limit. Now for this we have calculated the maximum ampere from solar which is 6 A and maximum ampere from motor is 4 A. Hence PWM charge controller of 20 A was selected.

Solar panel selection: Loom solar 75 W mono panel provide a higher efficiency (20–25%) even in bad light and cloudy conditions and are constructed with A grade mono crystalline cells and ultra-clear tempered panels. The sole business in India that manufactures mono panels with eight cells and a 12-V configuration is Loom Solar.

Shaft calculation: ASME code for shaft design

Material used—Mild steel (AISI 1018).

Yield strength (S_{yt}) = 370 MPa.

Ultimate tensile strength (S_{ut}) = 440 MPa.

$$\tau_{\max} = 0.3 S_{yt} \text{ Or } 0.18 S_{ut}$$

$$\therefore \tau_{\max} = 79.2 \text{ MPa.}$$

• **Bending moment (M_b)**

Design speed of air = 30 m/s.

$$M_b = F_b \times r$$

$$M_b = \rho \times A \times V \times (V - u) \times r$$

$$M_b = 1.225 \times 0.85 \times 0.6 \times 30 \times 15 \times 0.875$$

$$M_b = 245 \text{ Nm}$$

• **Torque (T)**

$V = r \times \omega$	$P = T \times \omega$
$11 = 0.3 \times \omega$	$100 = T \times 36.67$
$\omega = 36.67 \text{ rad/s}$	$T = 2.72 \text{ Nm}$
$T_d = 10T = 27.2 \text{ Nm}$	

• $\tau_{\max} = \frac{16}{\pi d^3} \sqrt{(k_b \times M_b)^2 + (k_t \times T_d)^2}$

For minor shock $k_b = k_t = 1.5$

$d = 0.0287 \text{ m}$	$d \approx 3 \text{ cm}$
------------------------	--

Bearing Calculation

Area of turbine = $H \times D = 0.85 \times 0.6$	Equivalent dynamic load (p) = $\rho \times A \times V \times (V - u)$
Design velocity (V) = 30 m/s	Equivalent dynamic load (p) = $1.225 \times 0.85 \times 0.6 \times 30 \times 15$
No of hours = 10,000 h	Equivalent dynamic load (p) = 285 N
RPM = 1000	
$\therefore P \approx 300 \text{ N}$	Selected bearing = 61,806
$L_{10} = \frac{60 \times n \times L_{10h}}{10^6} \quad L_{10} = \frac{60 \times 1000 \times 10000}{10^6}$	Inner diameter (mm) = 30
$L_{10} = 600 \text{ million rev.}$	Outer diameter (mm) = 42
$C = P \times \sqrt[3]{L_{10}} \quad C = 2530.3 \text{ N}$	Width (mm) = 7
From catalogue	

Gear Calculations

Gear specification:	Dia of gear = 90 mm
Module = 1.5	Dia of pinion = 30 mm
Gear ratio = 3:1	Pressure angle (ϕ) = 20°
Teeth on pinion = 20	
Teeth on gear = 60	

Solar Panel Calculation

Daily output: formula for calculating solar panel's power output.

Solar panel watts x average hours of sunlight $\times 75\%$ = daily watt-hours.

$75 \text{ W} \times 8 \text{ h} \times 0.75 = 450$ daily watt hours.

$450/1000 = 0.450$ kWh per solar panel is obtained daily.

Annual Output

Global formula: $E = A \times r \times H \times PR$, Where, **E** is energy (kWh), **A** is total solar panel Area (m^2), **R** is solar panel yield (%), **H** is Annual average irradiation on tilted panels and **PR** is Performance ratio, coefficient for losses (ranges in between 0.9 and 0.5, default value is = 0.75).

$$E = A \times r \times H \times PR.$$

$$E = \{[H \times W] (\text{m}^2)\} \times 20\% \times 2000 \text{ kWh/m}^2 \times 0.75.$$

$$E = [0.775 \times 0.665] \times 0.20 \times 2000 \times 0.75$$

$$E = 0.5153 \times 0.2 \times 2000 \times 0.75.$$

$$E = 154.6 \text{ kWh/an}$$

Approximately, 154.6 kWh is obtained yearly, from 75W to 12 V Monocrystalline Solar Panel.

Battery Calculations

Total watt hour = 650 Wh.

Battery size = $650/12 \text{ Ah}$, = 55 Ah, 12 V.

- **Depth of Discharge (DOD)**

It is used to determine how deeply the battery is discharged.

For lead acid batteries DOD is 50%.

2 Modelling of Components

All the components are modelled in Fusion360 software which is a cloud-based software (Figs. 5, 6 and 7).

Fig. 5 Plywood assembly



Fig. 6 Electrical assembly

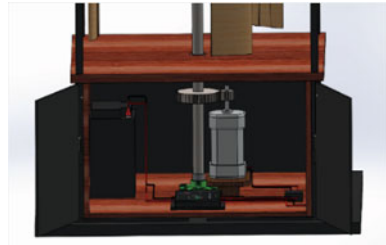


Fig. 7 Assembly of model



2.1 *Prototype Testing*

We had completed our first stage of prototyping. Now in order to test the prototype we went for the wind tunnel as we didn't find any nearby, so our idea was to go for Jumbo cooler. The advantage of this cooler is wind speed can be changed easily, area of the cooler is large, easy to transport, higher wind speed achievable (up to 9 m/s). In order to simulate like tunnel, we were using cardboard box in front of cooler to have similarity (Figs. 8 and 9).

As shown in above figure, this is how we carried out our testing. There were two important parameters that we were measuring (1) wind speed (2) rotation of shaft (RPM). To measure wind speed, we were using anemometer and to measure rotation of shaft tachometer was used. To increase, the self-starting ability of the turbine we

Fig. 8 Cooler with cardboard tunnel



Fig. 9 Two cooler with cardboard tunnel



were also using Drag blades (Basically pipe cut in halves) to get that initial drag force.

So now we can compare the values between just normal 3 bladed Darrius turbine and Darrius and savonius both combined turbines. As the Drag blades were a quick addition into the testing part so the fitting arrangement of blades to arms is on a temporary basis. We had kept the distance between cooler and the turbine constant. We also measured the velocity of the wind closest to the blades (Table 1).

Table 1 Prototype testing results (speed)

S. No.	Cooler	Drag blades	Self-started	Self-starting wind speed	Min (RPM)	Max (RPM)
1	Single	Without	No	–	0	0
2	Double	Without	Yes	7	–	50
3	Single	With	Yes	2.5	57.7	145
4	Double	With	Yes	5	64	300

3 Conclusion

A increasing number of signs indicate to a rapid energy transition that might have significant effects on energy demand and supply in the decades to come. Darrieus and Drag blade combination extremely good. It self-started at 2.5 m/s and as the wind speed increased, we saw a good amount of increase in RPM of shaft. At 9 m/s for single cooler 145 RPM of shaft was recorded. We were also using two coolers in opposite direction to simulate the condition on the highways and the results are quite promising as the turbine started to rotate at 5 m/s with an RPM of 64 and as the wind speed increased the maximum RPM was recorded as 300. Were able to draw a number of significant conclusions from our research and make several valuable recommendations that will aid in the further development of personal vertical axis wind turbines. Compared to the prior project, we were able to create a VAWT system that increased power output. We were able to suggest new design elements to enhance the system and efficiency based on our findings. Renewable energy sources might account from 15% in 2015 to 63% of all primary energy production in 2050.

4 Future Scope

- (1) In future this system can be used as charging station for Electric vehicles.
- (2) This system can be used to drive all the streetlights on the Highway.
- (3) This system can be used to collect various data like pollution on the highway, number of vehicles on the highway, etc.
- (4) This system can be used to indicate the location of some point with either barcode system or by numbering the poles.

References

1. Tong, W. (2010). *Wind power generation and wind turbine design*. WIT Press; Letcher, T. M. *Wind energy engineering*. Academic Press.
2. Rosato, M. A. (2018). *Small wind turbines for electricity and irrigation: Design and construction*. CRC Press.
3. Claessens, M. C. (2006). *The design and testing of airfoils for application in small vertical axis wind turbines*.
4. Battisti, L., Brighenti, A., Benini, E., & Castelli, M. R. (2016, September). Analysis of different blade architectures on small VAWT performance. *Journal of Physics: Conference Series*, 753(6), 062009.
5. Castillo, J. (2011). *Small-scale vertical axis wind turbine design*. Tampere University of Applied Sciences.
6. Bos, R. (2012). *Self-starting of a small urban Darrieus rotor: Strategies to boost performance in Low-Reynolds-number flows*.
7. Haroub, H. A. (2016). *Development of a low cost H-Darrieus rotor blade for a small vertical axis wind turbine* (Doctoral dissertation, JKUAT COETEC).

8. Jain, S., & Saha, U. K. (2020). The state-of-the-art technology of H-type darrieus wind turbine rotors. *Journal of Energy Resources Technology*, 142(3).
9. Alex, B., Guzman, D., Mayote, B., Reyes, K., Tiu, M. A., & Lawrence, R. (2014). *Development of a Darrius-type, straight-blade vertical axis wind turbine prototype with self-starting capability*. Bachelor Thesis, School of Mechanical and Manufacturing Engineering Mapua Institute of Technology.
10. Brusca, S., Lanzafame, R., & Messina, M. (2014). Design of a vertical-axis wind turbine: How the aspect ratio affects the turbine's performance. *International Journal of Energy and Environmental Engineering*, 5, 333–340.
11. Hameed, M. S., & Afaq, S. K. (2013). Design and analysis of a straight bladed vertical axis wind turbine blade using analytical and numerical techniques. *Ocean Engineering*, 57, 248–255.
12. Bhutta, M. M. A., Hayat, N., Farooq, A. U., Ali, Z., Jamil, S. R., & Hussain, Z. (2012). Vertical axis wind turbine—A review of various configurations and design techniques. *Renewable and Sustainable Energy Reviews*, 16(4), 1926–1939.

Machinability of Carbon Fiber Reinforced Silicon Carbide Composite Material—A Review



Sunilkumar Harsur, Ramdas Biradar, Pallavi Jadhav, Shital Waware, Kamalkishor Maniyar, and Pushparaj Warke

Abstract Carbon fiber reinforced silicon carbide is a comparatively new category of structural material. In the last, some years new materials and manufacturing techniques have been developed. Originally for the applications of space and military C/SiC composites have been developed. In addition to elevated thermal stability with high mass specific properties, functional properties like good tribological and low thermal expansion performance plays a growing significance for new commercial applications such as pads and brake disks clutches, calibration plates or furnace charging devices. This paper reviews some of the recent previous work on machining of carbon fiber reinforced silicon carbide.

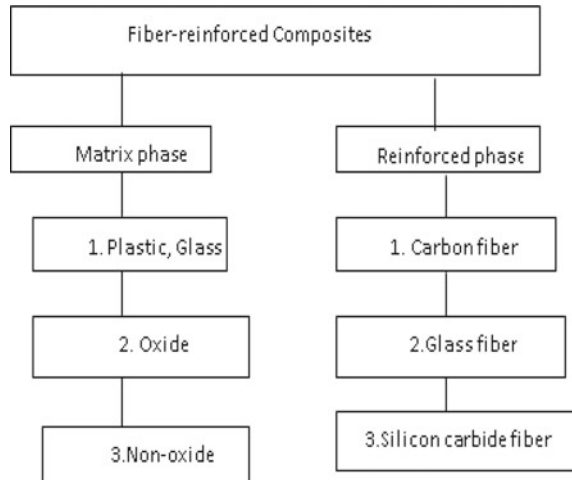
Keywords Fiber-reinforced composite material · CFRSC · Machining

1 Introduction

Fascinating properties of carbon fibers are higher modulus, lower density, lesser coefficient, of thermal expansion, higher strength etc. [1, 2]. These fibers are usually included with ceramic resin or metal like a matrix to shape a structural composite. Presently, the fiber strengthened composites are generally used in numerous areas. Figure 1 depicts the diagrammatic of fiber reinforced composites. One of the hot beds is the carbon fiber reinforced ceramic matrix composites and carbon fiber reinforced polymer matrix composites [3, 4]. CFRP is extensively utilised as resistant to high-temperature excision material and structural fabric in the aviation business, because of its brilliant qualities, for example, resistance to corrosion and thermodynamic phenomenal properties etc. The CFRC is widely used in aviation business [5], modern framework, brake set-up [6] sport products, and applicable in defence field [7, 8] and has numerous magnificent properties of chemical stability, lower weight, resistance to corrosion, specific strength, wear resistance, and fatigue resistance, etc.

S. Harsur (✉) · R. Biradar · P. Jadhav · S. Waware · K. Maniyar · P. Warke
Department of Mechanical Engineering, Dr. D. Y. Patil Institute of Technology Pimpri,
Pune, India
e-mail: sunil.harsur@gmail.com

Fig. 1 The schematics of fiber reinforced composite



Because of higher reluctance to corrosion, excellent temperature, and its higher creep reluctance, silicon carbide is predominantly appropriate as a material for matrix. Practically, the same manufacturing methods could be adopted for the creation of the silicon carbide matrix of composites as for the production of carbon/carbon composites. Carbon fiber-reinforced silicon carbide composites have rigidity and eminent levels of hardness. When exposed to high temperatures, they show high thermal and chemical steadiness, high mechanical strength, and a lower thermal expansion coefficient, making them the absolute for high-temperature structural materials for use in territories like the creation of airborne vehicles, electromagnetic shielding, and automotive components.

Particularly, the machinability and surface uprightness of CFRC can generate an undeviating impact on its accomplishment; this is one of the major concerning issues in the manufacture and utilization. The seriousness of the tool erodes and generation of residual stresses has been seen while machining these composites and the delamination is produced typically due the draw out of the carbon fibers. Consequently, its auxiliary application will be restricted. Even though researchers from various nations have been attempting new machining advances, a little attainments have been created in the facets of the mechanism creation of flaw, the mechanism of material infinitesimal elimination, the assessment of surface excellence and the categorization of the machining of these composites, along with newer machining techniques have also been identified. Tackling the composite machining problem has become one of the eye-catching topics for researchers around the world [9].

2 Literature Survey

2.1 Laser-Supported Fabrication of Carbon Fiber Reinforced Silicon Carbide

In this paper, the LAM of C/SiC spotlights choosing the ideal machining boundaries. In this investigation, the Taguchi strategy is utilized to get significant boundaries for the examination of cutting energy and surface unpleasantness within the different machining conditions. Prior to machining tests, a limited component investigation is carried out to decide the viable profundity of the cut. The cutting boundaries of C/SiC during LAM are the profundity of cut, feed rate, initial heating temperature, and shaft speed. The sign to commotion (S/N) proportion and change investigation (ANOVA) of the cutting power and surface unpleasantness is broken down, and the reaction streamlining strategy is utilized to propose the ideal machining boundaries [10]. To decide ideal machining circumstances for the laser supported machining of C/SiC composites plan of the test was done. The item capacities are chosen as cutting power and surface harshness. The boundaries, for example, the profundity of cut, initial heating warmth, spindle speediness, as well as feed pace are chosen. The limited component examination results grant the profundity of cut. Figure 2 shows the stream diagram of the plan of investigations of the laser supported fabricating of C/SiC composite [10].

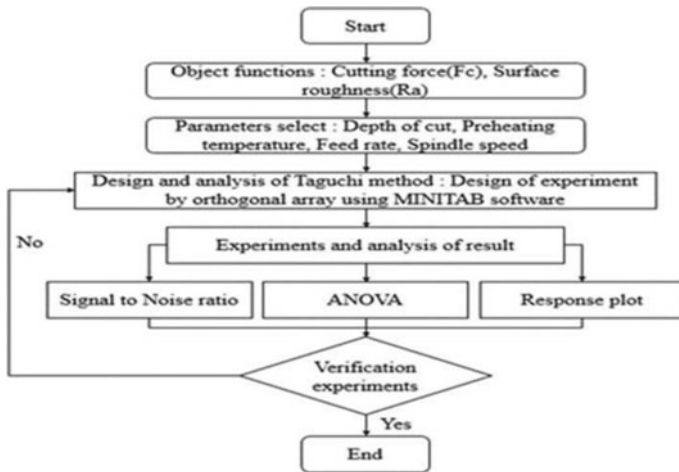


Fig. 2 Flow diagram of the design of laser-supported fabrication (LAM). Empiricals for the carbon fiber reinforced silicon carbide composite [10]

2.2 Machining Circumstances

The 5-axis machining centre is used to perform the LAM process with a laser component. The laser component is a powerful diode laser by a frequency scope of 940–980 nm. To quantify the initial heating hotness, a pyrometer by a scope of 400–3000 °C was utilized. The ordering table’s dynamometer was utilized to gauge the wounding powers. A dynamometer quantifies the three symmetrical parts of a power utilizing the quartz three-segment estimation. The estimation variety is – 5 to 5 kN, along with the inflexibility is 1–2 kN/μm. The surface harshness estimation gadget as well as field emanation filtering electron magnifying lens were utilized to quantify the surface unpleasantness. The surface unpleasantness estimation gadget was a test type with a goal of 32,000 focuses/16 chomp. The surface harshness estimation gadget utilized the Gaussian profile channel to isolate the lengthy and small floods of a surface contour, plus a break-off estimation of 0.25 mm was utilized for this investigation. Figure 3 indicates the empirical unit and Table 1 manifests fabrication circumstances [10].

The surface probity was checked by the surface irregularity estimation gadget plus scanning electron microscope. The cutting forces in the machining of the C/SiC composite substance were calculated by means of a tool dynamometer. The superlative machining circumstances for LAM of the Carbon fiber reinforced silicon carbide composite matter were attained as feed rate (200 mm/min), spindle speed

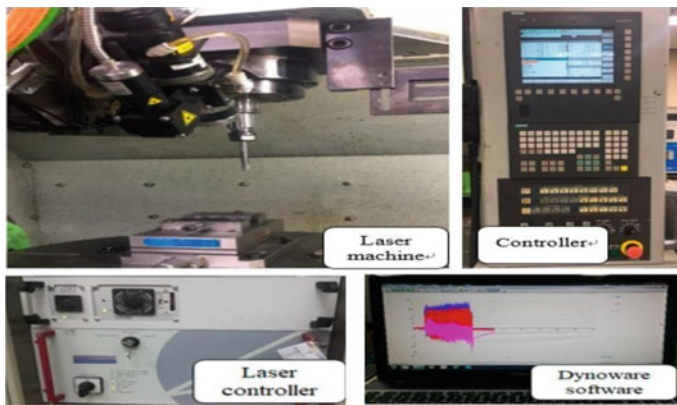


Fig. 3 The empirical setup

Table 1 The machining circumstances [10]

Substance	Carbon fiber reinforced silicon carbide composite
Substancel dimension	(T × W × L, mm) 15 × 15 × 60
Machining technique	Slot milling
Wounding tool	D8 CBN flat end-mill 2F, 70L

(5000 rpm), DOC (0.3 mm), and preheating hotness (1100 °C) was produced by the response optimization. once the test was conducted by superlative machining circumstances, the wounding force was estimated to be 34.55 N and surface irregularity was estimated to be 0.95 m [10].

2.3 Material Removal Mechanisms via Single-Abrasive Scratch Tests for Grinding Carbon Fiber Reinforced Silicon Carbide Composites

The material abolition process of carbon fiber reinforced silicon carbide composites have not yet been completely explained, although surface grinding has been broadly helpful in the machining of CMC composites [11]. “In two traditional cutting directions, solitary-abrasive scratch tests were planned and performed,, In the grinding of chemical vapour infiltration-manufactured C/SiC composites to unveil the material removal mechanisms” [11]. The empirical parameters, mainly the wounding speed, satisfied to the process of true grinding. “The outcomes illustrate that the grinding parameters (feed rate, spindle speed, depth of cut, and cutting direction) having considerable impacts on the surface integrity, grinding forces, and exaggerated subsurface section” [11]. “The normal force is usually smaller relatively the tangential force at the similar depth of cutting. In the longitudinal cutting direction, both the normal and tangential forces are too bigger relative to those in the transverse cutting direction.” [11]. The removal of material is mainly triggered by the impacts and abrasive events at the tooltip. Rigid breakage is one of the main material subtraction methods in the grinding of single directional carbon fiber reinforced silicon carbide composites since the impair deportments of the carbon fiber reinforced silicon carbide are mostly the fiber breakage, union of matrix fracturing, and fiber/matrix conjugation bounding [11]. In the scratching operation, the wounding forces rises with decreasing spindle speed and increasing depth of cut. Likewise, the cutting force in the transverse path was greater relatively that in the longitudinal route. In comparison, the lateral forces enlarged from 1.1 to 11 N in the lengthwise route and from 0.7 to 10.3 N in the crossways direction at a spindle speed of 500 rpm when the wounding depth amplified from 10 to 100 μm . As the spindle speed amplified from 500 to 1000 rpm, the usual cutting forces reduced respectively from 2.6 N to 1.3 N in the crossways route and from 3 N to 1.9 N in the lengthwise route at a cutting depth of 50 μm . There were similar uniformities in the tangential cutting forces. “To determine woven CMCs grinding force, the orientation of the fibre is an important parameter” [12] (Figs. 4 and 5).

The morphologies of the surface plus the subsurface in the lengthwise and crossways directions were furnished. “The result manifest that rigid breakage is the major approach to material deduction in the grinding of composites of C/SiC. The number of damage behaviours such as extensive rigid breakage of the matrix, fibre breakage,

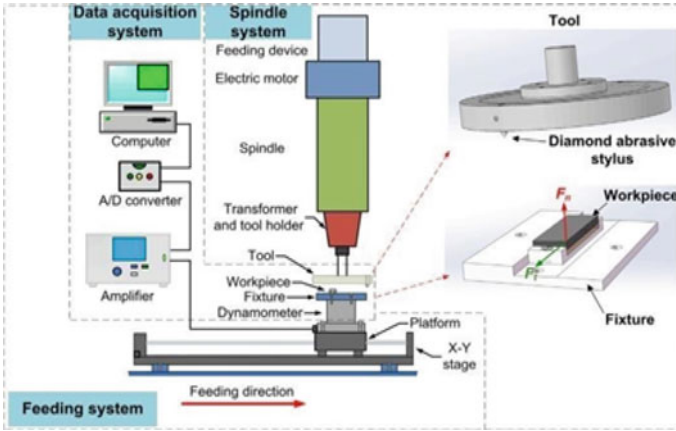


Fig. 4 Empirical setup of scratch test

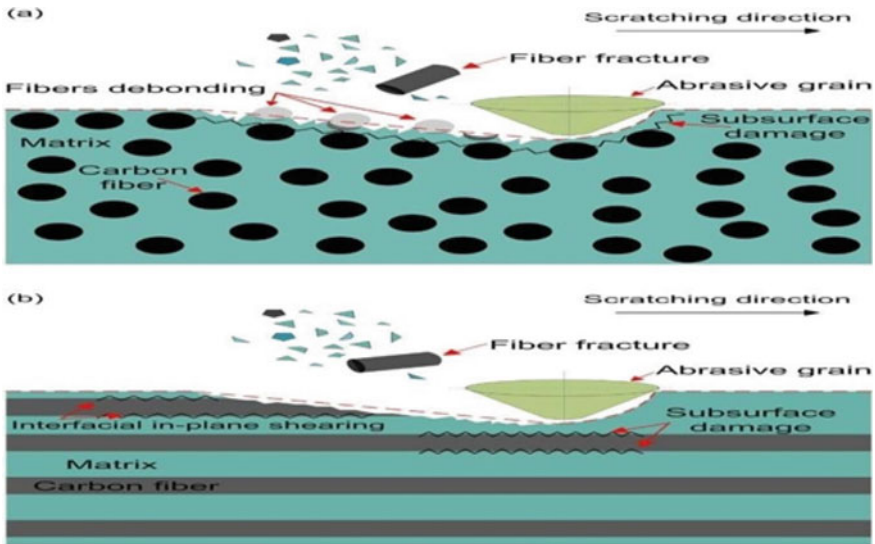


Fig. 5 Scratching process of carbon fiber reinforced silicon carbide composites in particular scratching a transverse cutting direction and b longitudinal wounding route

“The phenomenon showed that the cutting direction and the cutting force can affect the modes of material breakdown and the exaggerated regions of the subsurface” [11].

2.4 Experimental Analysis on Milling Performance Using Polycrystalline Diamond Tools for 2D C/SiC Composites

The present paper concerns the polycrystalline diamond (PCD) tools were used to evaluate the 2D C/SiC composites milling machinability. Empirical results exhibit that cutting forces differing significantly in a milling process because of the unexpected fibre cutting angle shifts cutting forces and surface irregularity declined as the cutting velocity amplified. As the feed rate enlarged cutting forces and surface irregularity both rised. Three major material removal mechanisms were matrix damage, fibre fracture, and fiber-matrix bounding in the slot milling method. Two dimensional carbon fiber reinforced silicon carbide composites were utilized here as workpieces and chemical vapour infiltration was the manufacturing process (CVI). The goal of this study is to determine the efficiency and feasibility of PCD tools for slot milling two dimensional carbon fiber reinforced silicon carbide composites. A test was performed with a two-edged straight flute PCD tool to take into account cutting speed and feed rate. Surface integrity, cutting forces and defects of the machined side edges of the machined ground surface were measured and examined [14] (Table 2).

Slot milling tests were performed on this system with the HURCO VMX42 5-axis upright machining centre that had a utmost spindle speed of 12,000 rpm. The empirical arrangement is furnished in Fig. 2a. The specimen dimension was 200 mm × 160 mm × 6 mm, plus the specimen was fastened, a fixture fixed on a four-component force dynamometer for network evaluate of the cutting force (Kistler, 9272). The angle of direction of the fibre is defined anticlockwise in the path of the tool feed, as shown in Fig. 6b [13]. There were two types of fibre orientation angles in the workpiece: 90° and 0°, and the tool's feed direction was beside with the 0° fibre orientation. Complete variables of the experiment are presented in Table 3 [13]. In this paper, an experimental study of the achievement of PCD tools in the milling process of two dimensional carbon fiber reinforced silicon carbide composites was carried out. Surface unification of ground surfaces and machined side edge flaws, wounding forces have been measured and assessed. During slot milling, alteration of fibre. Cutting angles can cause the cutting forces to fluctuate. Wounding forces decreased by the rise in cutting speed, along with by means of the rise in feed rate, wounding

Table 2 2D C/SiC composites material properties [14]

Fiber volume (%)	30
Porosity (%)	15
Density (g/cm ³)	2.0
Tensile strength (MPa)	200
Bending strength (MPa)	400
Young's modulus (GPa)	40
Coefficient of thermal expansion (×10 ⁻⁶ K)	1.8
Thermal conductivity (W/m K)	14
Maximum service temperature (°C)	1500

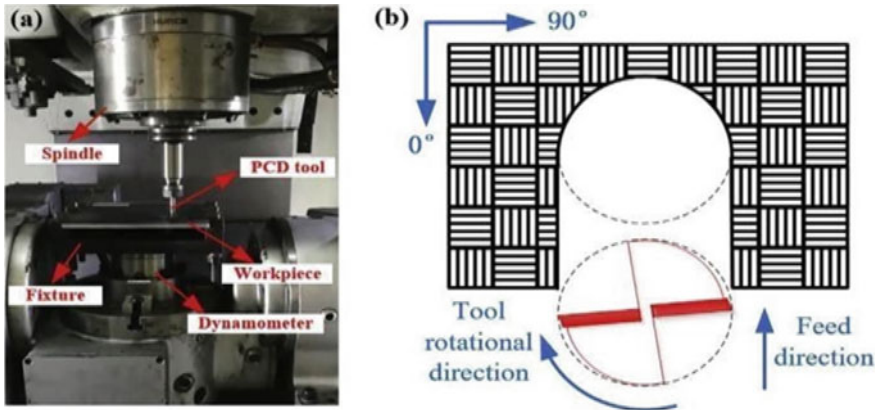


Fig. 6 Experimental setup: **a** experimental site for the slot milling of C/SiC Composites and **b** a system representing the milling path of PCD tool [16]

Table 3 Empirical variables [14]

Cutting speed, v_c (m/min)	20, 40, 60, 80
Feed per tooth, f_z (mm/z)	0.01, 0.02
Depth of cut, a_p (mm)	0.5
Milling length, l (mm)	20
Milling type	Slot milling
Coolant	Dry milling

forces increased. Three major material deduction methods during milling were on ground surfaces, fibre breakage, matrix destruction, and fiber-matrix debonding. Fiber breakage and matrix destruction predominate in increased cutting speed. With the rise in cutting speed, the unevenness of ground surfaces decreased and rised with the rise in feed rate. For ground surfaces, ditches and fractures were major surface flaws. Aside from, the integrity of the machined surface of 90° fibre direction was superior than that of 0° fibre orientation on ground surfaces. The amount and size of surface destruction were much larger than the fibre bulge, for the imperfections of side edges. By means of the rise in feed rate, the surface damage and fibre bulge of the side edge together rised. A elevated cutting/z speed can dramatically reduce the fibre bulge of the side edges [14].

3 Conclusion

It has been inferred, from the literature survey that by using laser-supported Carbon Fiber Reinforced Silicon machining, the most affirmative cutting force with high surface roughness can be found. The primary mode of material deduction for the

grinding of carbon fiber reinforced silicon carbide composites is rigid breakage, as well as numerous damage department counting substantial matrix rigid destruction, fiber fracture, fiber draw out, along with interfacial bounding helps to comprehend matter deduction methods. In the milling process of two dimensional carbon fiber reinforced silicon carbide c composites, the performance of PCD tools shows that, at the ground surfaces, fiber breakage, fiber-matrix debonding, along with matrix damage were three major material deduction process during milling. Increased cutting speed predominates fiber fracture and matrix damage.

References

1. Krenkel, W. (2005). Carbon fibre reinforced silicon carbide composites (C/SiC, C/C-SiC). In N. P. Bansal (Ed.), *Handbook of ceramic composites* (pp. 117–148). Springer.
2. Chung, D. D. L. (2017). Carbon fibers, nano fibers, and nanotubes (pp. 1–87). Elsevier Inc. Cambridge, 2.
3. Chung, D. D. L. (2017). Ceramic-matrix composites. In D. D. L. Chung (Ed.), *Carbon composites: Composites with carbon fibers, nano fibers and nano tubes* (pp. 467–531). Elsevier Inc.
4. Che, D. M., Saxena, I., Han, P. D., Guo, P., & Ehmann, K. F. (2014). Machining of carbon fiber reinforced plastic/polymers: A literature review. *Journal of Manufacturing Science Engineering Transactions of ASME*, 136(3).
5. Padture, N. P. (2016). Advanced structural ceramics in aerospace propulsion. *Nature Materials*, 15(8), 804–809.
6. Fan, S. W., Zhang, L. T., Cheng, L. F., Tian, G. L., & Yang, S. J. (2010). Effect of braking pressure and braking speed on the tribological properties of C/SiC aircraft brake materials. *Composites Science and Technology*, 70(6), 959–965.
7. Schmidt, S., Beyer, S., Knabe, H., Immich, H., Meistring, R., & Gessler, A. (2004). Advanced ceramic matrix composite materials for current and future propulsion technology applications. *Acta Astronautica*, 55(3), 409–420.
8. Ahmad, J. (2009). *Machining of polymer composites*. Springer.
9. Du, J., Zhang, H., Geng, Y., Ming, W., He, W., Ma, J., Cao, Y., Li, X., & Liu, K. (2019). A review on machining of carbon fiber reinforced ceramic matrix composites. *Elsevier Ceramics International*, 45, 18155–18166.
10. Erdenechimeg, K., Jeong, H.-I., & Lee, C.-M. (2019). A study on the laser-assisted machining of carbon fiber reinforced silicon carbide, 31 May 2019. Accepted June 26, 2019. Published: 27 June 2019.
11. Li, Y., Ge, X., Wang, H., Hu, Y., Ning, F., Cong, W., & Ren, C. (2019). Study of material removal mechanisms in grinding of C/SiC composites via single-abrasive scratch tests, March 2019.
12. Huang, L., Bonifacio, C., Song, D., van Benthem, K., Mukherjee, A. K., & Schoenung, J. M. (2011). Investigation into the microstructure evolution caused by nanoscratch-induced room temperature deformation in M-plane sapphire. *Acta Materialia*, 59(13), 5181–5193.
13. Lopez, L. N., Lamikiz, A., Campa, F. J., Valdivielso, A. F., & Etxeberria, I. (2009). Design and test of a multitooth tool for CFRP milling. *Journal of Composite Materials*, 43, 3275–3290.
14. Hu, M., Ming, W., An, Q., & Chen, M. (2019). Experimental study on milling performance of 2D C/SiC composites using polycrystalline diamond tools. *Elsevier-Ceramics International*, 45, 10581–1058.

Electric Vehicle Industry-Challenges and Opportunities



Asmita Saravade, Megha Burungal, Laxmi Brungi, Kiran Lakkam, and Amitkumar Shinde

Abstract Present automotive industry has come up with many latest technologies to increase the energy efficiency and cut down cost of manufacturing. With having tremendous advantages over IC engine vehicles, Electric vehicles are showing remarkable growth in Automobile market with helping in improving environmental conditions. In this present study an effort is made to understand and showcase the challenges and opportunities EV's have for mass production and increase the demand in market. Study reveals that the main challenges EV facing to enter into the market is insufficient technologies, social awareness, lack of infrastructure, and range anxiety. Recommendations are being provided to enhance EV market with better range, reliability and performance, thus moving towards an imperishable future to EV market.

Keywords Electric vehicles · Hybrid electric vehicles · EV batteries · Market penetration · Range anxiety

1 Introduction

As we see in the present scenario increase in global warming i.e. raise in environmental pollution is mainly because of extensive use of gasoline vehicles. On the other hand depleting of fossil fuels is also an alarming thing. These two are the main reasons why the car industry all over the world is tending towards electric vehicles (EV's) and their infrastructure [1].

We can also observe that the global prices of crude oil are increasing at a faster rate which is influencing to increase the electric vehicle market. Even though there is a shortage of supply, the electric vehicle market is growing steadily [2]. Governments

A. Saravade (✉) · M. Burungal · K. Lakkam · A. Shinde
SVERI's College of Engineering, Pandharpur, India
e-mail: asmitadsaravade@gmail.com

L. Brungi
Jain College of Engineering, VTU Belagavi, Belagavi, India

are supporting to this raise in use of electric vehicles and setting higher targets of use of EV's in upcoming years. EV's are setting a milestone for cleaner energy and lower driving costs.

However still many researches are going on for reducing the high initial cost of electric vehicles and also avoiding range anxiety. Lot of challenges the electric car manufacturing companies are facing and trying hard to overcome them.

2 EV's Market Scenario in India

Electric vehicles market for the first time made a remarkable hike in sales by launching many successful models into the market. Especially the 2 wheeler sales were into an exponential growth. When Tata launched Nexon EV, which was one of the first successful products in the EV market. Many start-up's started entering into the EV market like Ola, Ather, Pure EV, Hero electric etc. This brought up the EV market and it is into a succeeding path.

But still analysis say that only about 2% population have accepted Electric vehicles as an alternative to gasoline vehicles in India till 2020–21 [3]. This figure is extremely low. However the growth percentage says that EV's penetration is growing aggressively at a greater pace of about 200% every year. With this acceptance of EV by Indian costumers, it is expected that a 30% of penetration of EV's in Indian market can be achieved till this decade. As compared to other countries, such as Norway, China, they are a decade ahead of us in terms of adopting EV. Now there is a need of study about the limitations that are hampering the electric vehicles from replacing gasoline vehicles [4]. Few of them are discussed here in the present work.

3 Problems with Electric Vehicles

3.1 EV Cost

The cost is one of the major concerns for a person when it comes for purchasing an electric vehicle. Initial buying cost is more for electric vehicles as compared to gasoline vehicles. However, government is promoting the sales of electric vehicles by providing subsidies, incentives, tax benefits etc. [5]. Still the problem doesn't overcome because these schemes are limited to specific number of vehicles. After applying all the government schemes, still the electric vehicle feels unaffordable while any costumers wishes to buy it.

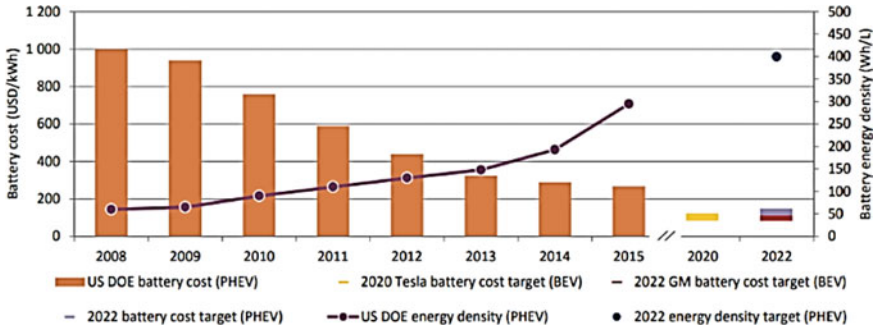


Fig. 1 Development of battery energy density and changes in cost [8]

3.2 Battery Cost

It cannot be hidden that the life span of a Li-ion battery used in most of the electric vehicles is maximum upto 6–7 years. Even researches show that after 5 years these batteries require more maintenance. When it comes for replacing the batteries, it costs approximately 3/4th of the complete vehicle cost. Battery cost is another major problem for the EV customers, because EV’s are newborn to market and costumers [6]. It needs still another minimum 5 years to relay on these systems (Fig. 1).

3.3 Beta Version of Vehicles

Presently both the technologies and companies are new in the market and customers are facing their products for the first time. In the first go it’s nearly impossible for companies to give customers a perfect automobile. It has to go through many complex designs. After customers feedback and reviews, many companies had to update their EV’s like RV400, EPluto 7G, Nexon etc.

Many companies like PureEV made a lot of revisions in the policies, hardware, and software’s. Because of lot of complaints from customers, even Tata Motors upgraded their Regenerative system and Battery Management System software [7]. Hence there is a set back from the customers to buy an Electric vehicle from a company who is manufacturing it for the first time which may lead to a bad experience.

3.4 Poor Infrastructure and Range Anxiety

When people think of opting electric vehicles, poor infrastructure is the major hurdle for them. Poor infrastructure includes unavailability of public charging stations along

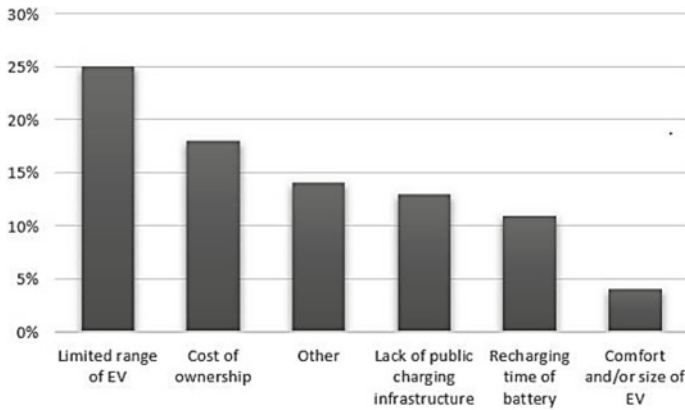


Fig. 2 Survey results of disinterest in EVs from the public [9]

with lack of proper charging setup in their home. For a EV car owner it will be major task to charge a heavy electric car if he/she doesn't have proper setup [8].

Figure 2 shows the negative impact on customers regarding range of EV's. Because of the range problem, customers do not prefer EV's. But on the other side, with a survey it can be seen that almost many people ride or drive for a maximum of 65 km a day or even lesser then it. On an average present EV's can provide a range of 300 km in four wheeler and 120 km in 2 wheeler segments. Still it is challenging one in emergency or to plan a journey in shorter time relaying in EV's.

Range anxiety is another problem depends on infrastructure. It creates a fear among the EV driver while driving for longer distances because of unavailability of charging stations (infrastructure). Yes of course there is an improvement subsequently but still a long way to go for completely depending on it. Many manufacturing companies of EV are offering ranges of the vehicles like 150–200 km. but these ranges are of ideal conditions and achieving them is extremely impossible in actual riding conditions. If a vehicle is specified of 150 km range then with city riding conditions, the rider must be satisfied with 100 km riding range. Here in four wheeler segment the loading capacity may not have more impact, but in 2 wheelers, a small increase in load can impact the EV range.

3.5 Non Availability of Universal Charger (Need of Standardization)

In present EV market, individual companies have their own specific charging ports which are becoming a major hurdle in building up a public charging station. Even my customers have complained regarding this that they face a heavy trouble in charging their electric vehicles any where available. Standardization of chagrining ports is

very much essential. Otherwise it may become a curse to Electric vehicles market in India. As for every second electric scooter a different charging station cannot be provided in every charging infrastructure.

Just as electric vehicles get a standard charging port (CCS-2), electric 2 wheelers and 3 wheelers should have a similar standard to reach more number of customers depending on EV's.

3.6 Temperature Issues

Temperature is one of the major things that affect the performance of Electric vehicle batteries. When these vehicles are used in too cold regions like Utrarakand, Meghalaya or rigorous hot regions like Rajasthan, Kerala, and the properties of batteries very and hamper the performance of it. Ideal performance of batteries can be achieved when it is used at a temperature range of 15–40°.

3.7 Academic Inclusion and Skill Development Programmes

Upcoming generations must be given the awareness regarding use of EV's and advantages of using EV's on environment conditions. Production of Spares and providing services easily is a challenging task for EV industries at present scenario. When an IC Engine vehicle gets breakdown, they can easily find a service or assistance for it. But on the other side for EV's still lot of infrastructure development is needed in terms of service providing to completely depend on EV's.

4 Conclusion

EV's are inevitable and IC vehicle technology needs to completely vanish if not today then someday for sure. But what is more important is opting for EVs smartly. Be a smart investor and user of this growing goldmine industry. One or another day fossil fuels may get exhaust and the time comes where almost complete transportation start depending on EV's. But in this regard opting for EV needs a smart decision. A lot of scope for research and opportunities for industrials is there in the field of EV's to invest and bring the market of EV's to the present world.

References

1. Faizal, M., Chelvan, R. K., & Amirah, A. (2017). Energy, economic and environmental impact of wind power in Malaysia. *International Journal of Advanced Scientific Research and Management*, 2, 81–87.
2. Zhang, Q., Li, H., Zhu, L., Campana, P. E., Lu, H., Wallin, F., & Sun, Q. (2018). Factors influencing the economics of public charging infrastructures for EV—A review. *Renewable & Sustainable Energy Reviews*, 94, 500–509.
3. Kihm, A., & Trommer, S. (2014). The new car market for electric vehicle and the potential for fuel substitution. *Energy Policy*, 73, 147–157.
4. Peng, T., Ou, X., & Yan, X. (2018). Development and application of an electric vehicle's life-cycle energy consumption and greenhouse gas emissions analysis model. *Chemical Engineering Research and Design*, 131, 699–708.
5. Faizal, M., Wardah, Y. H., Husna, M. A., Amirah, A., & Tan, Y. H. (2018). Energy, economic and environmental impact of waste-to-energy in Malaysia. *Journal of Mechanical Engineering Research and Developments*, 41, 109–113.
6. Marshall, B. M., Kelly, J. C., Lee, T. K., Keoleian, G. A., & Filipi, Z. (2013). Environmental assessment of plug-in hybrid electric vehicles using naturalistic drive cycles and vehicle travel patterns: A Michigan case study. *Energy Policy*, 58, 358–370.
7. Jaunky, V. C. (2011). The CO₂ emissions-income nexus: Evidence from rich countries. *Energy Policy*, 39(3), 1228–1240.
8. Global EV Outlook. (2016). International Energy Agency, Paris.
9. Noel, L., Zarazua de Rubens, G., Sovacool, B. K., & Kester, J. (2019). Fear and loathing of electric vehicles: The reactionary rhetoric of range anxiety. *Energy Research & Social Science*, 48, 96–107.

3D Printing in Construction Industry: A State of Art



Pruthviraj Zadbuke, Yogesh Patil, Nishad Sheje, Sahil Nachane,
and Rohan Sawant

Abstract The development of the 3D printer led to the development of a novel construction method known as “3D printing building technology.” There are a number of potential outcomes, including time and cost savings, less pollution of the environment, and fewer accidents and fatalities on construction sites. The conclusions provide a summary of our concerns, despite the numerous benefits and advantages of this new technology. 3D printing technology is getting a lot of attention because it is quicker than traditional construction. Structures with intricate designs and miniature versions of a variety of products are both achievable. In 3D printers, improved concrete-based mortar material is used. In buildings constructed with this technology, sustainable building materials are given special consideration. In addition, research is done to ensure that no materials are wasted. The goal of this research is to review the literature and present this new generation method.

Keywords 3D printing · Construction automation · Sustainability · Digital construction · Cementations material

1 Introduction

The development business is additionally under the strain of progress because of mechanical turns of events. In order to remain competitive in the variable industry, it is essential to keep up with the new ageing order. Technologies for 3D printing make it possible to optimize designs and offer advantages over more conventional manufacturing processes. As a result, the construction industry is focusing a lot on it as a new strategic challenge [1]. The primary objective of this paper is to briefly discuss the construction industry’s use of 3D printing technology. The studies talk about the future of 3D printing technology and offer ideas for possible applications in the construction industry.

P. Zadbuke · Y. Patil · N. Sheje · S. Nachane · R. Sawant (✉)
Department of Civil Engineering, Dr. D. Y. Patil Institute of Technology, Pimpri, Pune, India
e-mail: rohan.sawant@dyvpv.edu.in

Traditional concrete cannot be used in 3D printing because each layer must first be sufficiently hardened. Layering successive layers over one another until the top layer is reached is how the component is built. It might only take a few days to build, as opposed to months. A Chinese company announced in 2014 that it had constructed ten homes entirely from recycled waste in less than 24 h. This construction method was utilized in numerous nations in addition to South Africa, India, Canada, Japan, Russia, Australia, and India. Win Sun has conceived a procedure to develop structures that are all the more harmless to the ecosystem, remembering one of the biggest 3D printers for the world. It is able to build homes with materials obtained from local sources by utilizing hydroelectricity, wind energy, or solar energy. Finishing work in remote areas without electricity for a while is easier with this.

2 3D Printing Technology

Traditional production methods are based on the idea that material must be removed from raw material during component production. One of the most recent and significant manufacturing techniques is additive production, which stands in contrast to conventional methods of production that are entirely dependent on cloth discount strategies from the component. The events are produced simultaneously from the material in additive manufacturing. The tool used in production produces the component layer through the use of layer by following a device course that is derived from the component's geometry. It is feasible to supply components with challenging geometries due to this one-of-a-kind function of additive production, and there is minimal cloth loss throughout the production process [2]. The method of additive manufacturing was developed in the 1980s. It is believed that the primary 3D printer system was the SLA-1 tool from the 3D System Company [3]. One of the cutting-edge production techniques that has gained recognition in recent years is additive manufacturing. By layering powders into tubes, this manufacturing method creates three-dimensional designs using geometric information [4]. Plan, projection, and execution are critical stages in building fabricating underway [5]. In the planning and projection phases of a structure, advanced assembling has been utilized for some time. With the help of digital modeling techniques, architects, designers, and engineers have been able to easily make the necessary adjustments to their projects. Because it grants design freedom, interest in the technology has grown over the past few years.

This review focuses on concrete printing and contour crafting as examples of 3D printing with material extrusion [6–8]. Layers of recent concrete that are either made up of materials that are already in use within the company or that are available commercially are used in contour crafting. Concrete print is a type of wet extruded in which a nozzle spreads out layers of cement-based mortar or pre-mixed concrete to construct a structure without the use of moulds. When technology progresses, most studies simply make hypothetical predictions about the future applications of 3D-printed structures. With two trowels, it shapes the edges and tops of the layers as they

are extruded to produce smooth, precise surfaces [9]. Nevertheless, unlike contour crafting, it does not use polishing processes, giving the printed pieces a single-bedded look [10]. One of the most common uses is to assist disaster victims and construct emergency shelters. The autonomous 3D-printed construction technology may even be revolutionary in dangerous or remote areas. In areas with harsh climates, inhospitable environments, or rugged parcels of land, this technology may be useful. However, very few studies examine the feasibility of 3D printing in underdeveloped or rural areas.

3 Literature Review

The 3D printer machine includes a nice guide with a printer head with an estimation of 15 mm. cellulose fiber and additives were used to create a brand-new cement mortar. The printed layer surface absorbs the most moisture when the utilized mixture is pumped [11, 12]. Geopolymer binder materials for powder-based 3D printers were only made with slag mixtures [13]. As a result of the research, geopolymer materials that are suitable for use in powder-based 3D printers have had mixtures of fly ash and slag added to them. To determine how much fly ash was added, the geopolymer mixture's compressive strength and 3D printability were examined. According to the study, increasing the quantity of fly ash had a negative effect on the mixture's compressive strength and wettability, but not on its ability to settle. It was decided that the examples with half slag and half fly debris were the best blend [13]. A study compared the production of ultra-high-performance fiber-reinforced concrete (UHPFRC) made with a 3D printer to that of UYPFRB made by hand. It discovered that the one that was poured into the standard mold had a higher compressive strength in addition to being printable and stable in shape. The stability of four different types of printing mixtures was significantly improved when Nano-clay and silica fume were utilized [14–16].

4 3D Printing Methods

The steps involved in 3D printing are the focus of the following section.

1. Selective Laser Melting (SLM)

A technique known as selective laser melting (SLM) involves sintering to produce a three-dimensional object. Sintering is the process of making solid objects without melting the powder by compressing it with heat and pressure. This method is advantageous because it does not necessitate a great deal of additional sanding or modifications after an object has been completed.

2. Fused Deposition Modeling (FDM)

Stratasys is a company that specializes in additive manufacturing and 3D printing. In 1988, S. Scott Crump created the technology known as fused deposition modeling (FDM) When ductile material is forced through a double-headed nozzle, FDM results. The material begins to cool and harden as soon as it is pumped through the nozzle.

3. Contour Crafting (CC)

Contour crafting was developed by Professor Behrokh Khoshnevis of the University of Southern California (CC). This is a method of additive manufacturing. By piling material on top of one another, the process produces an item with a smooth surface. This approach offers several benefits, including quicker manufacturing speed, a larger choice of materials, and enhanced surface quality.

4.1 3D Printing Materials

The following are the materials required for 3Dprinting according to method of construction.

1. Selective Laser Melting (SLM)

Powders with a metallic base that have been fused together are the materials that are most frequently utilized in SLM. SLM is now able to process aluminum, copper, and tungsten thanks to recent advancements in fiber optics and high power lasers.

2. Fused Deposition Modeling (FDM)

The most frequently utilized materials in FDM are thermoplastics like polylactic acid (PLA) and acrylonitrile butadiene styrene (ABS). ABS comes in a wide range of colors. PLA is made of biodegradable materials like cornstarch or sugar cane. Fused deposition modeling is the most common 3D printing technique.

3. Contour Crafting (CC)

The wet mix of 3D printable materials goes through a number of steps, like mixing, pumping, and layer-by-layer deposition. Materials like concrete and sand, which set quickly, are used in contour crafting. The researchers have successfully utilized a variety of cement-based materials, including conventional mortar mix.

4.2 Process of Construction

3D Concrete Printing Engineers and builders have recently become interested in printing cementitious items and concrete. At the time of their creation, Form Casting



Fig. 1 3D printing in construction

(University of Southern California), D Shape (Enrico Dini), and Concrete Printing (Loughborough College) were the most well-known major printing companies. The contour crafting method of layered manufacturing makes use of a polymer and ceramic slurry. Large structures with a smooth surface finish are constructed with cement and a variety of other components and blends. Smooth expulsion is accomplished by limiting the expelled stream in both the vertical and flat tomahawks to scoop surfaces. The side trowel's orientation is dynamically altered to accommodate the surface's slope. Additionally, large aggregates and additives like reinforcing fibers may be used in a wide range of materials used in CC (Fig. 1).

4.3 Advantages

Although still in its infancy, 3D printing has the potential to provide the following advantages:

1. Assuming items are imprinted nearby, they can be moved for less cash (however shipping the printer can be exorbitant given the size of printers as of now expected for development).
2. Applications in factories or on-site.
3. Products that are printed only require as much material to form as necessary. This implies less assets are required and less waste is created.
4. Potential for designing in a way that is both more effective and more interesting because 3D printing can create shapes that traditional methods cannot.
5. Reduce labor expenses.

6. Customized design at a lower cost (with 3D printing, producing one item costs the same as producing thousands of them.)
7. In the event that 3D printing can be utilized to make congregations that would some way or another require unique hardware and wellbeing measures, there will be less dangers to wellbeing and security.

Current challenges to be overcome include:

1. In order to produce the digital model that will lead to products that are secure and affordable, 3D printing incurs higher initial costs.
2. Despite the fact that they can be used seven days a week, twenty-four hours a day, printers currently operate at a slower pace than conventional construction.
3. Due to the high cost of the 3D printer and the lack of industry familiarity with its technologies and applications, it is more expensive than traditional construction.
4. Currently, only a few materials have been used, but printers that can use multiple materials to make more complicated assemblies are being tested.
5. It can be difficult and costly to install large 3D printers on site.

4.4 3D Printing Applications

1. Built 10 3D Printed Houses

Win Sun Decoration Design Engineering, based in Shanghai, constructed ten 3D-printed homes at the beginning of 2015 in less than 24 h. According to them, building each house only cost \$5000. A similar structure was also constructed by the Russian firm Apis Cor. Using their enormous 3D printers, they were able to spray a cement and recyclable raw materials mixture that cured quickly. The blocks were then moved to the building site, where they were assembled, from an off-site location.

2. Development of Contour Crafting Process

Russian researchers have used a 3D printer to construct both the interior and exterior walls of a house. A method known as contour crafting was developed by Professor Behrokh Khoshnevis. These tracks were to support the gantry crane that stretched the length of the whole building area.

4.5 Buildings Printed in Three Dimensions for the Construction of Sustainable Homes

Architects will be able to develop structures that can transcend the limits imposed by traditional building processes. House construction can benefit from the material life cycle, which can be utilized to assess the environmental sustainability of construction materials. Building erection processes produce less dust and waste material than traditional methods because wet construction processes are minimized.

4.6 Building Disaster Relief Shelters

A project-specific 3D printer was used to print an eco-friendly house. Solar panels have been installed on the roof of the pod-like house. The energy is stored and used to power the house throughout the day and night by an integrated battery system. It could also be useful in resolving housing issues following disasters.

4.7 Printing of 3D Bridge and Canal

1. Building the First Pedestrian 3-D Bridge in the World

The world's first 3D printed pedestrian bridge was opened in Madrid, Spain on December 26, 2016. A company by the name of ACCIONA built the bridge in Alcobendas, which is in the Castillo-La Mancha urban park. The bridge only has a width of 1.75 m and a length of 12 m.

2. Building a Canal

3D technology was used to construct a canal in Amsterdam in addition to a bridge. In 2014, the project was finished. The project required a distinct 3D printer. The canal was built with 3D plastic created by this printer. The best way to describe the 3D printer is as a massive printing arm that looks like a crane. It received the name "Kamermaker," which translates to "Room Builder," as a result.

3. Metal Frames for Solid Structures

The WAAM system for 3D printing was developed by the Dutch company MX3D. Wire Arc Additive Manufacturing, or WAAM, is its acronym. In order to accomplish this, a unique six-axis robot was developed. A nozzle and a welder are included in the robot's kit. It adheres to the pre-programmed design as it welds metal rods layer by layer.

4.8 Difference Between Conventional Construction and 3D Printing

1. Conventional Construction

As can be seen, traditional construction necessitates the utilization of human resources at multiple stages, which is not only time-consuming but also costly. Additionally, the finished product contains a significant amount of construction debris. The formwork, which includes a significant amount of execution time, accounts for 25–35% of the structural work cost, even for a straightforward geometrical layout. Formworks are used extensively in traditional building, resulting in increased expenses for Labour, equipment, materials, and Labour, as well as material waste.

2. 3D Printing Construction

Then again, 3D printing is generally robotized and prints structures from a PC helped plan (3D-computer aided design) with less individuals included and no tooling, bites the dust, or installations required. As a result, many manual processes, the need for labor, and material waste are reduced by this approach. Endlessly showcases report says that 3D printing can slice development squander by 30–60%, work costs by 50–80%, and development time by 50–70%. 3D printing is also better for the environment than traditional printing systems, which mostly use automated technologies and large 3D printers to print large construction elements. In the field of construction, automated technologies and robotics have made significant progress.

5 Case Study

‘India’s First’ 3D Printed House.

Tvasta Manufacturing Solutions, a deep tech startup founded by three former IIT Madras students, constructed India’s first 3D-printed house. This one-story home on campus has a single bedroom, a hall, and a kitchen. India’s affordable housing project is bolstered by the single-story IBHK project. It takes a computerized three-dimensional design file from the user and prints a layer-by-layer 3D structure out of a specialized type of concrete made for this purpose. The built-up area of the structure is about 600 square feet (Fig. 2).



Fig. 2 TVASTA

6 Conclusion

3D printing has the potential to benefit both the economy and the environment. One of the most significant benefits for the majority of architects may be the ability to construct buildings with intricate shapes. While 3D printing may revolutionize architecture, it should be developed with sustainability issues in mind. New filament materials are currently being developed to ensure various properties such as transparency, thermal insulation, or strength. Powder bed fusion (PBF) and directed energy deposition (DED) are the most effective 3D printing techniques. Cost, time, and the size of the elements limit these methods, but they do make it possible to properly construct structures. By using a detailed BIM system, a plan of action can be more precisely defined, and design details can also be improved.

References

- Ozturk, G. B. (2018) The future of 3D printing technology in the construction industry: a systematic literature review. *Eurasian Journal of Civil Engineering and Architecture*, 2(2), 10–24.
- Lou, A., & Carol, G. (2012). *Selective laser sintering, birth of an industry* (p. 8). University of Texas.
- Bourell, D., Kruth, J. P., Leu, M., Levy, G., Rosen, D., Beese, A. M., & Clare, A. (2017). Materials for additive manufacturing. *CIRP Annals*, 66(2), 659–681.
- Özsoy, K., & Burhan D. (2017). Eklemeli İmalat (3 BoyutluBaskı) Teknolojilerinin Eğitimde Kullanılabilirliği. *International Journal of 3D Printing Technologies and Digital Industry*, 1(1), 36–48.
- Çelik, İ, Karakoç, F., Çakır, M. C., & Duysak, A. (2013). Hizliprototipleme teknolojileri ve uygulama alanları. *Journal of Science and Technology of Dumlupınar University*, 031, 53–70.
- Mueller, R. P., Fikes, J. C., Case, M. P., Khoshnevis, B., Fiske, M. R., Edmunson, J. E., Kelso, R., Romo, R., Andersen, F. (2017). Additive construction with mobile emplacement (ACME). In Proceedings of International Astronautics Congress, IAC, International Astronautical Federation, IAF, pp. 10311–10320. <https://www.scopus.com/inward/record.uri?eid=2-s2.0-85051385926&partnerID=40&md5=6758e18905f4362d57efd9e0f65a1482>. Accessed September 25.
- Perkins, I., & Skitmore, M. (2015). Three-dimensional printing in the construction industry: A review. *International Journal of Construction Management*, 15, 1–9. <https://doi.org/10.1080/15623599.2015.1012136>
- Smith, D. (2012). Printed buildings: An international race for the ultimate in automation. *Construction Research and Innovation*, 3, 26–31. <https://doi.org/10.1080/20450249.2012.11873838>
- Bosscher, P., Williams, R. L., II., Bryson, L. S., & Castro-Lacouture, D. (2007). Cable-suspended robotic contour crafting system. *Automation in Construction*, 17, 45–55. <https://doi.org/10.1016/j.autcon.2007.02.011>
- Di Carlo, T., Khoshnevis, B., & Chen, Y. (2013). Manufacturing additively, with fresh concrete. In *ASME international mechanical engineering congress exposition proceedings*. American Society of Mechanical Engineers (ASME). <https://doi.org/10.1115/IMECE2013-63996>
- Hojati, M., Nazarian, S., Duarte, J. P., Radlinska, A., Ashrafi, N., Craveiro, F., & Bilén, S. (2018). 3D printing of concrete: A continuous exploration of mix design and printing process. In *42nd IAHS world congress the housing for the dignity of mankind*.

12. Ma, G., Salman, N. M., Wang, L., & Wang, F. (2020). A novel additive mortar leveraging internal curing for enhancing interlayer bonding of cementitious composite for 3D printing. *Construction and Building Materials*, 244, 118305.
13. Xia, M., Behzad, N., & Jay, S. (2019). Printability, accuracy and strength of geopolymer made using powder-based 3D printing for construction applications. *Automation in Construction*, 101(2019), 179–189.
14. Marchment, T., & Jay, S. (2020). Mesh reinforcing method for 3D concrete printing. *Automation in Construction*, 109, 102992.
15. Kazemian, A., Yuan, X., Cochran, E., & Khoshnevis, B. (2017). Cementitious materials for construction-scale 3Dprinting: Laboratory testing of fresh printing mixture. *Construction and Building Materials*, 145, 639–647.
16. Arunothayan, A. R., Nematollahi, B., Ranade, R., Bong, S. H., & Sanjayan, J. (2020). Development of 3D-printable ultra-high performance fiber-reinforced concrete for digital construction. *Construction and Building Materials*, 257, 119546.

Optimization of Car Tie Rod with the Help of Finite Element Analysis



Pramod Navale and Sameer Katekar

Abstract The FEA examination of Checks are made on the tie rod's natural frequency, study of the maximum stress, and deformation. The suspension system bears the majority of the vehicle's weight, yet tie rods are susceptible to failure because of forces that change as the car is being driven and bumped. When the car is in its static condition, the steering forces are also taken into account. Tie rod exhaustion and vibration have long been issues that, if the strains and vibrations involved are too great, could lead to structural failure. To fully comprehend the structural aspects of this important work, further research is necessary dynamic action. The study of a typical automotive tie rod using finite elements (FE) is presented in this paper and is the main topic.

Keywords Finite element analysis · Natural frequency · Tie rod · Optimization

1 Introduction

In a McPherson steering system, the tie rods additionally join the rack and the driving knuckle in addition to linking the central link and the steering knuckle in a regular suspension system. Tie rod typically transfers force from the rack to the turn the wheels, use the steering knuckle. Having both an outer and an inner threaded end, a tie rod is a circular rod. Alloy steel constitutes the majority of a tie rod (Figs. 1 and 2).

The car could become unstable and crash if the tie rod fails. Therefore, determining the tie rod's strength is essential. The tie rod is under compressive load the majority of the time. Moving the automobile requires less work than standing still does. The permitted working stress multiplied by the tie rod's working strength yields the least area of the cross section. Tie rods are often constructed with thicker ends to avoid deterioration when the threads are cut into them. Numerous methods can be used

P. Navale (✉) · S. Katekar

Department of Mechanical Engineering, SKN Sinhgad College of Engineering, Korti, Pandharpur, Maharashtra, India

e-mail: pramodnavale182@gmail.com

© The Author(s), under exclusive license to Springer Nature Switzerland AG 2024

P. M. Pawar et al. (eds.), *Techno-Societal 2022*,

https://doi.org/10.1007/978-3-031-34648-4_40

399

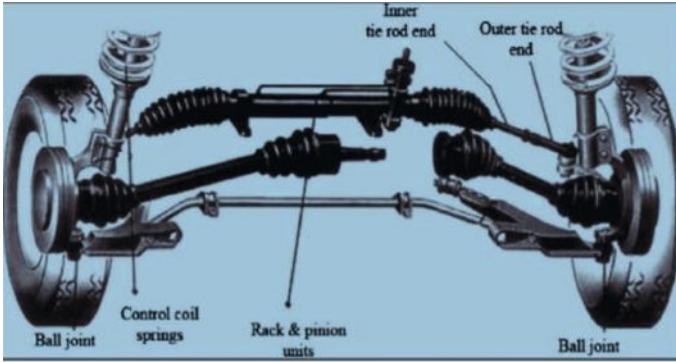


Fig. 1 McPherson suspension system with rack and pinion (source IJMIE [7])



Fig. 2 Tie rod

to join tie rods at their ends. However, it is preferred that the connection's strength be at least as strong as the rod. Drill holes or shackles can be used as entry points for the ends once they have been threaded. The spacing between the loading points could change if both the left and right hands are used when threading the ends. To change the tension in tie rods, a turnbuckle is a tool. Forging an eye or hook into the rod is another way to join any ends. Regular maintenance is required for your car's suspension and steering systems, ideally once a year, as well as a full wheel alignment. Wandering, erratically steering, and significant tyre wear are all caused by a worn tie rod. A wheel align is necessary if a tie rod is needed since altering the tie rod would alter the alignment's settings.

2 A Summary of Some Research

Joshi et al. [1] as practicable as we have to reduce the likelihood not only shear as well as bending failure happening in the meshed threaded tooth when the rod is in use. When the connection's nominal diameter exceeds 80 mm, the trapezoidal threaded

connection is strongly advised. Falah et al. [2] in this study an SUV's broken tie rod end was the subject of a research. The defective component was made of AISI 8620 steel, as determined by spectral analysis and hardness testing. The hardness and composition did not meet the required standard. Lagomarsino et al. [3] Examined was the axial tensile properties of metal tie-rod are used in brick vaults and arches. Tie-first rod's three modal frequencies, as determined by a dynamic test, are used in the identification process. A beam with a uniform cross section that is spring-hinged at both ends and is subject to an axial tensile force makes up the reference structural system.

Campbell and Ting [4] Tie rod huge finite element models testing using NASTRAN Version 68. A tie rod's static buckling load is examined. The results of the trials and the FEM are compared. Kaiser [5] has notably enhanced the technique by using variations in slope rather than absolute time to more accurately coordinate the stress and strain pulses. He also created a method for optimizing specimen diameter based on the destructive interference that emerges at the boundary between used materials. Patil et al. [6] have noted that while the suspension system carries the majority of the weight of the automobile, tie rods are vulnerable to failure because of forces that change when the car is driven and bumped, according to their study titled "FEA of Tie Rod of Steering System of Car". Ghorpade et al. [7] have researched automotive engine mounting systems, which are crucial for understanding several elements of vehicle performance. Without a vehicle authorization sample, the construction of the engine mounting system needs to be quickly examined and accurately studied. The researchers came to the conclusion that the number of engaged thread turns on a steel tie rod should be kept as low.

3 Proposed Methodology

First, tie-rods are the subject of a theoretical investigation. The two roles of tie-rods are to convey motion from the guiding arms to the wheel and also to absorb the stresses and vibrations brought on by tyre shocks on uneven roads. The key areas that require improvement are listed. The major aims of this project are to determine the deformation and stresses in tie rods and optimize them for various material combination. For the 3-D model, the tie-rod is ready to Ansys FEM software is used to conduct the inquiry. There are many different materials designated. The results are compared to outcomes from the real world.

4 Theoretical Calculation for Mass

Now we can find value of mass for each material of tie.

So, $\text{Mass} = \rho \times \text{volume}$ Mass.

$$= \rho \times \pi/4 \times D^2 \times L.$$

1. Mass of Aluminium

$$\begin{aligned} \text{Mass} &= 2700 \times \pi/4 \times 0.04^2 \times 0.381 \\ &= 1.29 \text{ kg.} \end{aligned}$$

2. Mass of Cast Iron

$$\begin{aligned} \text{Mass} &= 7200 \times \pi/4 \times 0.04^2 \times 0.381 \\ &= 3.44 \text{ kg.} \end{aligned}$$

5 Analysis of Tie-Rod

One of the most often used engineering analytical techniques for nonlinear issues is finite element analysis (FEA). FE mesh is needed as a geometric input for FEA. Directly from a solid model, a detailed component model may be produced in 3D CAD system. A precise solid model must be idealized properly in order to be simplified because it is too complex to analyze well as is. This can entail altering the FE model's material and mesh size. Steel alloy is used to make the tie rod. It is necessary to use a particular meshing strategy for thin bodies. Hex Dominant Quadrilateral and Triangular components were used to extract and mesh the mid-surface for the tie rod component. Figure 10 shows the finite element method model of the current design. The threaded portion is fixed, while the remaining half has a compressive force of 5738.9 and 611.0 N. Both steering force and bumping force contribute to the generation of this force. Self-weight is an additional choice (g). FE analysis makes use of nonlinear material. The six degrees of freedom in the FEM model include rotations and translations regarding the x, y, z axes of the nodes.

5.1 FEA Model Procedure is Follows;

Tie rod 3D model creation with CATIA software (Fig. 3).

For additional examination, this model is imported into the ANSYS programme (Fig. 4).

Meshing of Tie Rod (Fig. 5).

On the tie rod, various boundary conditions such as fixed support and forces are applied (Fig. 6).

As meshing and applying constraints, this issue is resolved by ANSYS, which also calculates various deformation and stress values (Figs. 7 and 8).

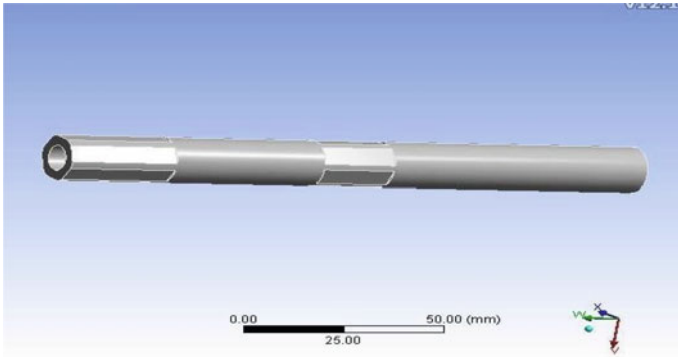


Fig. 3 Create 3D model in CATIA software

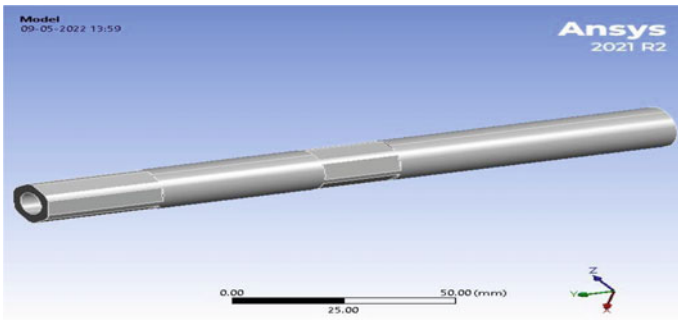


Fig. 4 3-D model of tie rod of steering system in Ansys software

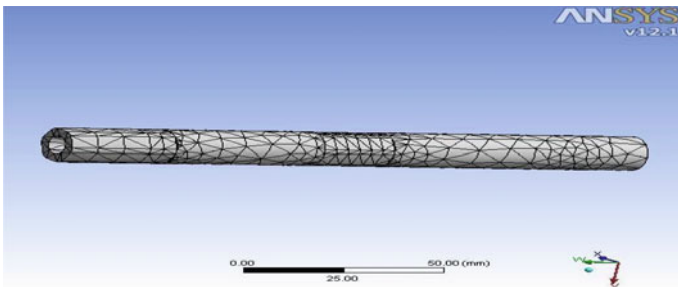


Fig. 5 Tie rod steering system mesh model in Ansys software

After the static analysis is finished, we perform a modal analysis to determine the natural frequency (Fig. 9).

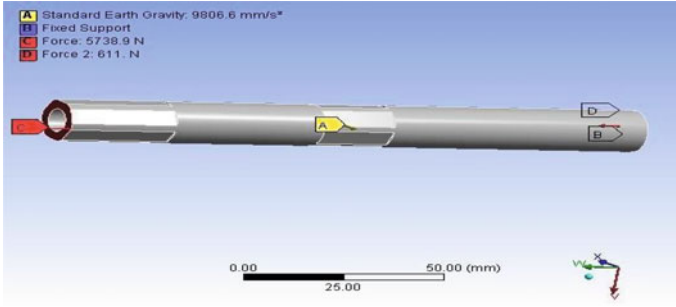


Fig. 6 Applying boundary constraints to the tie rod model in Ansys software

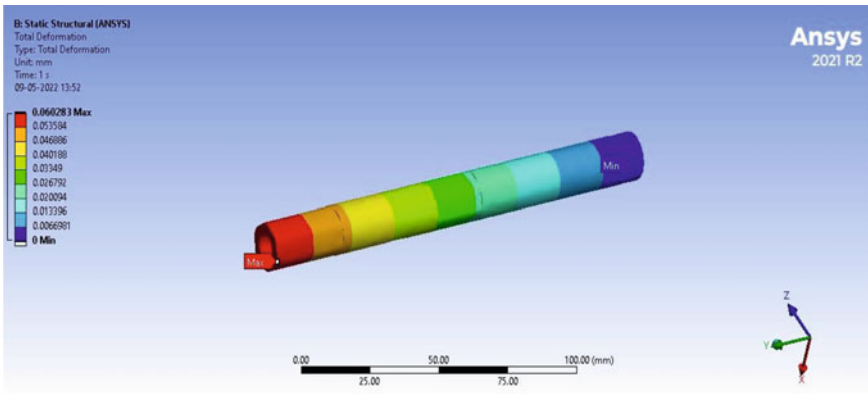


Fig. 7 Total deformation of tie rod in Ansys software

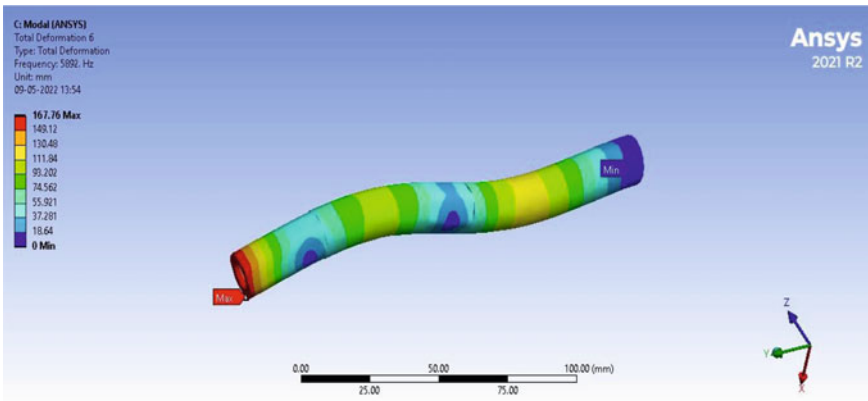


Fig. 8 The tie rod stresses are equivalent to the von misses stresses

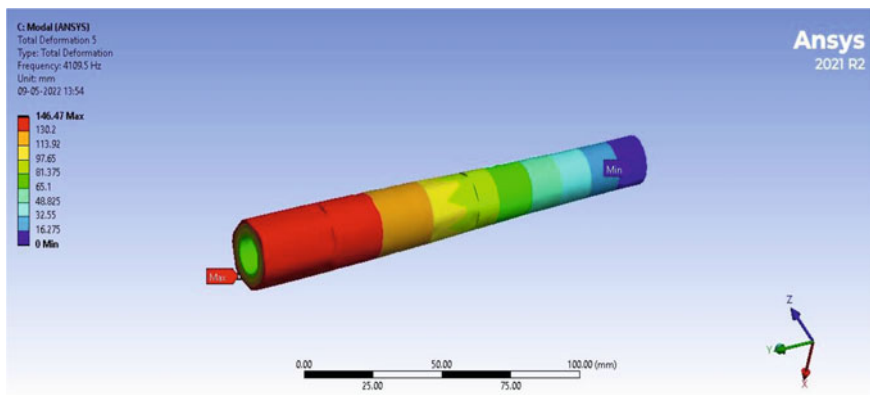


Fig. 9 Natural frequency of tie rod in Ansys soft

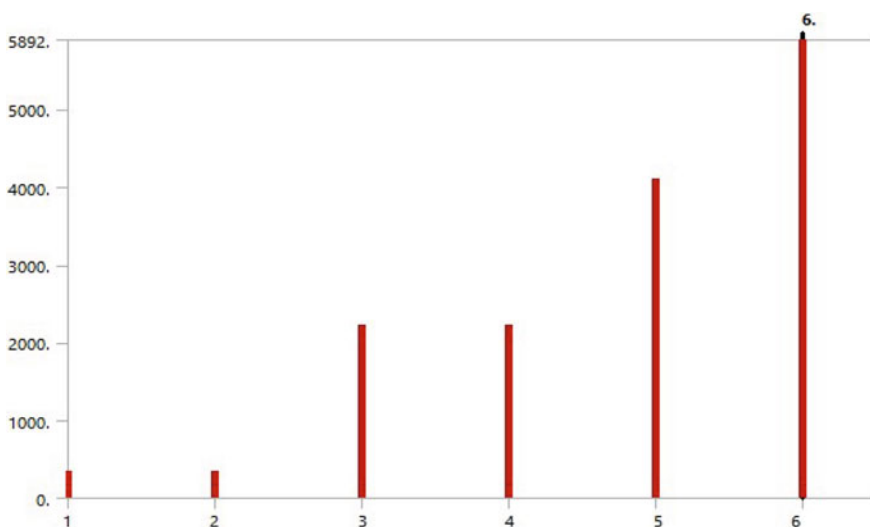


Fig. 10 Graph of natural frequency versus modes

6 Results

Static analysis outcome (Fig. 10; Table 1).

Modal Analysis outcome (Table 2).

Table 1 Result table for static analysis

S. No.	Deformation	Equivalent (von misses) stresses
01	0.060257 M	52.135 MPa

Table 2 Result table for modal analysis

S. No.	Modes	Natural frequency (Hz)
01	1	350.74
02	2	350.75
03	3	2223.7
04	4	2223.9
05	5	4109.5
06	6	5892.0

7 Conclusion

Creation of a roughly accurate multi-body 3D-CAD solid model served as the project's initial starting point. Next, a solid mesh was built, with the assumption that every mesh component was entirely rigid. Finally, using the Ansys software suite, finite element analysis was performed. From the results shown, we can consequently, it may be said that neither the distribution of deformation nor the stress exceeds the yield strength value. Neither tie rod failure nor damage. The choice still affects the precision and correctness of computed results. Pertaining to different modelling parameters Boundary conditions, the proper mesh, and the kind of elements are a few of the most crucial factors that play a crucial role in getting the right results. Using ANSYS software, a tie rod study reveals a deformation of 0.060257 mm and an equivalent stress of 52.135 MPa, both of which are less than the 572 MPa tensile and compressive yield strength. When the engine is operating, the tie rod experiences constant vibrations. In Ansys software, Natural Frequency is therefore determined, and its result is 350.74 Hz. Based on the aforementioned findings, the tie rod that was removed for analysis is secure. The mass for cast iron is found maximum as compared to aluminium.

References

1. Duan, W., & Joshi, S. (2011). Failure analysis of threaded connections in large-scale steel tie rods. *Engineering Failure Analysis*, 18(8).
2. Falah, A. H., Alfares, M. A., & Elkholy, A. H. (2007). Failure investigation of a tie rod end of an automobile steering system. *Engineering Failure Analysis*, 14(5), 895–902.
3. Lagomarsino, S., & Calderini, C. (2005). The dynamical identification of the tensile force in ancient tie-rods. *Engineering Structures*, 27(6), 846–856.
4. Campbell, G., & Ting, W. (2006). *Buckling and geometric nonlinear analysis of a tie rod in NASTRAN VERSION68*. Light Truck Division, Ford Motor Company, 14.
5. Kaiser, M. A. (1998). *Advancements in the split Hopkinson bar test* (Doctoral dissertation, Virginia Tech.).
6. Patil, M. A., Chavan, D., & Ghorpade, M. K. U. S. (2013). FEA of tie rod of steering system of car. *International Journal of Application or Innovation Engineering and Management*, 2(5), 222–227.

7. Ghorpade, U. S., Chavan, D. S., Patil, V., & Gaikwad, M. (2012). Finite element analysis and natural frequency optimization of engine bracket. *International Journal of Mechanical and Industrial Engineering (IJMIE)*.

Calculative Study for Fuel Cell Based Vehicle Propulsion



Siddharth Gandhi and Abhijeet Chavan

Abstract Considering the recent shift in technology for the automotive development, electrical energy based vehicles were designed. The advanced transition from IC engine based technical aspects migrated to motor based aspects required for vehicle propulsive action. This reduced the polluting environmental rate drastically, but it came with certain disadvantages and certain challenge. Change in power source generation lead to development of further avenues like battery powered, fuel cell powered, hybrid etc. with individual source based its advantages and disadvantages. Vehicle range is the major frictional topic to continue further development. As an immediate alternative, fuel cell is considered to pose as possible solution. This study suffices detailed calculative approach for the fuel cell powered vehicles powertrain. Towards the end, considerable revamping of the vehicle parameters is optimizable taking propulsive energy requirement into primary considerations.

Keywords Powertrain · Size · Calculations · Vehicle etc.

1 Introduction

Recent exponential rise in the electric energy powered vehicles displays the encouragement of the industry and the people supporting it. Looking at the severe environmental challenging threat posed to the current and future generations of living beings, this technological change was the need of the hour for all the nations. Developing nations contributing to the most of the world's pollution were supposed to thrive on this major trend change so as to curb or bring drastic change in its contribution [1]. Nevertheless, the harmful gaseous emissions are not only emitted by the Automotive sector, but numerous other energy sectors are contributing at the highest level,

S. Gandhi (✉) · A. Chavan
Mechanical Engineering, MITADT University, Pune, Maharashtra, India
e-mail: siddharthgandhi@live.com

A. Chavan
e-mail: abhijeet.chavan@mituniversity.edu.in

but Automotive sector considering and reducing its contribution in the polluting ranking, it took the sudden steps in curbing the same. Several newer technologies were introduced for betterment of all beings [2].

Electrical energy was identified and developed in the recent half decade and is currently leading the change. Several sources of electrical energy are explored and optimized. Mainly hybridization of the current and new vehicles reducing CO₂ contribution. Several categorization in vehicle hybridization has been developed. Next being the battery powered vehicles in which energy can be stored via grids, generators etc. Fuel cell being the latest technical advancement posing as a great alternative to the roadblocks and challenges emerged in the currently sold electrical vehicles. One of the major challenge posed is the short vehicle range with fully charged battery and the other being the electricity generation required to recharge the already drained sources [3]. For the short vehicle range, additional options needed to be developed to avoid the fading of technological change initiated by the industry. Keeping the same in mind, fuel cells were developed. Fuel cells are nothing but electrical energy producers by burning some sort of fuel. Fuel to be used had to be emission free and that point was very challenging. Hence, different types of fuels were explored for viability checks and some of the types of fuel cells were finalized for further developmental research and advances based on encouraging methodology and advantages [4]. Most common being the Hydrogen powered fuel cells. In this, hydrogen is used as major fuel source. To avoid the same, entities are devising the safety protocols which needs to be established during hydrogen generation, refilling, storage and usage. In line with fuel cells, certain organizations are developing and some have already developed Hydrogen powered engines. Entities also need to explore the option of converting the existing fuel vehicles for conversion similar to the hybridization.

The structure of the study is categorized as: In Sect. 1, the harm provided to climatic conditions by conventional fuels used, major challenges in the Battery electric vehicles and recent development on the fuel cell technology and development of engines powered by harmless fuel [5]. Several studies define the development of Battery electric vehicle as stop gap arrangement for hybridization start. To further attract customers to shift to alternate energy form, innovative energy generation devices need to be looked upon to eliminate the challenges faced by battery based vehicle electrification [6]. Section 2 details the fuel cell technology and different types of fuel cells and their respective powertrain components. Section 3 describes the calculative approach study involving thorough calculations required to design optimum vehicle to satisfy the organizations and customer considering power and range. Lastly, conclusion is expressed in Sect. 4.

2 Fuel Cell—Fundamental

Device designed for electrochemical energy conversion to electric energy is termed as Fuel Cell. Output of the fuel cell is DC, powering the motor. Multiple kinds of fuel cells are available as Polymer Electrolyte Membrane, Solid fuel, Ethanol, Methanol,

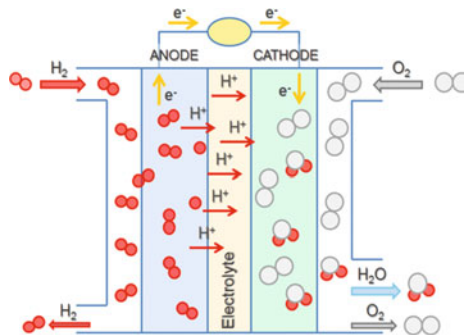
Phosphoric acid, Reversible fuel etc. [7]. With multiple modelling techniques available for system design, actual deviations considering testing is quite different. To suffice and reduce the modelling and testing gaps, the present study assists same and develop perfect powertrain combination.

2.1 Hydrogen Fuel Cell

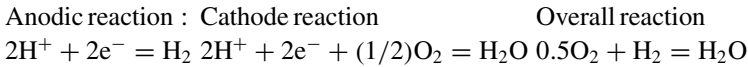
Overall, fuel cells comprises of two terminals, Anode and Cathode. Both the terminals are separated by electrolytic solution termed electrolyte and the circuit is connected externally. As shown in Fig. 1, the oxidation of fuel (fuel depends on type of fuel cell being used) is carried at the anode and the reduction of oxygen is carried at cathode. Ions induced due to the oxidation of fuel migrates via the electrolyte medium and electrons voyage through the connected external circuit causing electric current. In comparison with the internal combustion engines powered by conventional fuels, the fuel cell efficiency is not limited by Otto or Carnot cycle and is definitely higher than the IC engine or some other device used for electrochemical energy conversion to electrical energy [2, 4]. Similar to the engine functionality, energy is generated till the uninterrupted supply of fuel and air is available, likewise, for continuous fuel cell operation, hydrogen and oxygen (air) need to be supplied continuously for energy generation. In hydrogen fuel cell, hydrogen is oxidized at anode, releasing electrons and protons. Electrons are transported across the electrical circuit and transportation of protons across membrane. Both travel to the cathode, where supplied oxygen is reduced to water. Water is the only exhaust byproduct for the fuel cell functionality [5].

Due to the functionality, heat is also produced and is dissipated to the environment. Classification of fuel cells is based on temperature (High and Low) and is differentiated based on the temperature threshold conditions. High temperature fuel cells operate above 600 °C whereas low temperature fuel cells operate lower than 250 °C. Many organizations prefer low temperature fuel cells as they have several advantages, the one being faster start-up times and effective for mobile applications

Fig. 1 Fuel cell working [8]



like vehicle with peppy responsiveness [1, 3]. Also, fuel cells are further classified based on fuel and electrolyte used as mentioned earlier. In line for the usage of hydrogen in fuel cell (low temperature), other fuels such as alcohols, formic acid, hydrazine or sodium borohydride etc. are used. Generally, single fuel cell produces lower amount of energy and have to be used in multiple quantities depending on the operating system requirement. Several fuel cells are connected in series and parallel combination and are joint as fuel stack. Several hundreds of fuel cells are used in critical application. Based on the fuel cell size comprising stack, area requirement is determined. Major challenge in the hydrogen based fuel cell is the generation, carrying and stockpiling of hydrogen. It is the most unstable and has extremely flammable chemical properties [6, 7]. For mobile applications, that is best suitable considering higher energy density. The oxidation reaction involves either homolytic or heterolytic electrochemical absorption of hydrogen, followed by hydrogen oxidation and release of ions/protons. The reactions occurring in the hydrogen fuel cells are expressed as [9].



3 Calculative Approach for Fuel Cell Sizing

3.1 Fuel Cell Calculations

Fuel cell is considered the heart of vehicle as it is the energy production house similar to the IC engine. Its sizing is of utmost importance to suffice the power requirement and the vehicle space available.

3.2 Thermodynamic Voltage

Since, 1 MJ = 0.28 kWh, Energy is calculated as [9]

$$\left(E = E_0 - \frac{RT}{nF} \ln \frac{[\text{H}_2\text{O}]}{[\text{H}_2][\text{O}_2]} \right) \quad (1)$$

where,

E_0 = Thermodynamic voltage under standard operating conditions, R = Gas Constant, T = Temp, n = no. of electrons transferred (2 in case of H_2O)

F = Faradays Constant = 96,485 C/mol

Now, Gibbs free energy is expressed as (under standard conditions)

$$E_0 = \frac{\text{gibbs Energy}}{nF} \tag{2}$$

Under standard conditions, Gibbs Free energy is 237.2 kJ/mol for production of liquid water at 250C for HHV and 228.6 kJ/mol considering LHV.

$$E_0 = \frac{237200}{2 * 96485} = 1.229 \text{ V (HHV)} \text{ and } E_0 = \frac{228600}{2 * 96485} = 1.18 \text{ V(LHV)}$$

Thermodynamic voltage under prevailing conditions

$$E = 1.229 - \left\{ \frac{8.314 * 298.15}{2 * 96400} \ln \left[\left[\frac{1}{350} * (1 * 0.21) \right]^{\frac{1}{2}} \right] \right\} \tag{3}$$

$$E = 1.294 \text{ V (HHV)} \text{ and } E = 1.245 \text{ V (LHV)}$$

For efficient air flow, different air cleaners and filter elements can be designed. New study of Turbocharger usage in the air requirement in the fuel cell operation is necessary with exhaust flow calculation and its benefits are to be reaped to improve the acceleration performance of the vehicle [9, 10]. Based on the reactions, water is the only byproduct. Byproduct form either in the form of water or vapour can be considered depending on the lower and higher heating value. Both heating values are defined as High Heating Value (HHV): Exhaust water is in fluidic state and Low Heating value (LHV): Exhaust water is in vapour state.

Most of the times, water produced is in the vapour form itself. For further calculations, LHV is considered and corresponding thermodynamic output voltage. Consider a system of 400 V and total peak power requirement as 65 kW [11].

3.3 Current Requirement

$$I = \frac{P}{V} = \frac{65 \text{ kW}}{400 \text{ V}} = 162.5 \text{ A} \tag{4}$$

3.4 Area Requirement

$$\begin{aligned} \text{Area} &= \frac{\text{Current}}{\text{Current Density}} = \text{Area} = \left[\frac{162.5}{2000 \left(\frac{\text{mA}}{\text{cm}^2} \right)} \right] * \left[\frac{1000 \text{ mA}}{1 \text{ A}} \right] \\ &= 81.25 \text{ cm}^2 = 0.008125 \text{ m}^2 \end{aligned} \tag{5}$$

Table 1 Energy modes comparison

Sr No	Energy modes current requirement		
	Description	Value	Unit
1	Sports	162.5	A
2	Normal (35% reduction)	105.625	A
3	Eco (50% reduction)	81.25	A
4	Eco + (65% reduction)	56.875	A

No significant voltage difference is observed in either of both series and parallel combinations [12].

Considering Sports, Normal, Eco, Eco+ driving modes as per Table 1, current consumption is restricted with eventual torque restriction to improve the fuel economy and range extension. For the described modes, current is restricted as 0%, 35%, 50% and 65% respectively. Depending on the driving requirement, customers are made deciders to utilize the amount of electrical energy they intend to use for propulsion [13].

Now, for given system of 400 V and each fuel cell efficiency as 75%,

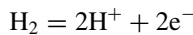
$$\begin{aligned} \text{Total Cells} &= \frac{\text{System Voltage}}{\text{Each Cell Voltage}} \\ \text{Total cells} &= \frac{400}{1.245} \approx 322 \text{ cells} \end{aligned} \quad (6)$$

$$\begin{aligned} \text{Total Fuel Stack} &= \frac{\text{Total Cells}}{\text{Cells in 1 stack}} \\ \text{Total Fuel Stack} &= \frac{322}{161} \approx 2 \end{aligned} \quad (7)$$

Combining all the small output voltages of individual fuel cells suffice the propulsion requirement [14, 15].

3.5 Fuel Flow Rate

As each hydrogen molecule contains two hydrogen atoms, at the fuel cell anode, two electrons are released. The passage of released electrons through the externally connected circuitry arrangement powers up the system. The functional principle is very simple, diffusion of electrons and combining with oxygen at the cathode via electrolytic solution producing exhaust. Pressure variations for the supplied fuel changes the energy density and storage capacity in the tank. Also, altering the temperature conditions hamper the density factor [16, 17].



Number of moles released to produce one ampere current is calculated,

$$n_{H_2} = (1 \text{ A}) \left[\frac{(1 \frac{\text{coulomb}}{\text{sec}})}{1 \text{ A}} \right] \left[\frac{1 \text{ equivalence of } e^-}{96487 \text{ coulombs}} \right] \left[\frac{(1 \text{ g mol of } H_2)}{2 \text{ equivalent of } e^-} \right] \left[\frac{3600 \text{ sec}}{1 \text{ hr}} \right] \quad (8)$$

$$n_{H_2} = H_2 \frac{[0.018655] \text{ g mol}}{\text{A hr}}$$

$$m_{H_2} = \left\{ 0.018655 \left[\frac{(\text{gmol})}{\text{hr} - \text{A}} \right] H_2 \right\} \left[\frac{2.1058 \text{ g}}{1 \text{ gmol } H_2} \right] \left[\frac{1 \text{ kg}}{1000 \text{ g}} \right] * 10^3$$

$$m_{H_2} = 37.605 \times 10^{-3} \frac{\text{kg } H_2}{\text{hr} - \text{A}}$$

Hydrogen consumption in fuel stack to deliver maximum power is calculated

$$\begin{aligned} m_{H_2} \text{ consumed} &= (162.5 \text{ A}) \left[37.605 \times 10^{-3} \frac{\text{kg } H_2}{\text{hr} - \text{A}} \right] \\ &= 6.11 \frac{\text{kg } H_2}{\text{hr}} = 13.55 \frac{\text{Lb } H_2}{\text{hr}} \end{aligned} \quad (9)$$

Fuel usage in fuel cell (Input Fuel)

$$\begin{aligned} U_f &= \frac{H_2 \text{ consumed}}{H_{2in}} = H_{2in} = \frac{H_2 \text{ consumed}}{U_f} \\ &= \frac{0.0135}{0.8} = 16.875 \frac{\text{Lb } H_2}{\text{hr}} = 7.6 \frac{\text{kg } H_2}{\text{hr}} \end{aligned} \quad (10)$$

3.6 Oxygen Flow Rate

For correct oxygen requirement estimation, air fuel ration should be considered. In this case, 2 to 1 is considered for H₂O. Thus, oxygen moles requirement for fuel cell operation is determined

$$\begin{aligned} n_{O_2 \text{ consumed}} &= \left[0.0135 \frac{\text{lb } H_2}{\text{hr}} \right] \left[\frac{1 \text{ lb mol } H_2}{2.0158 \text{ lb } H_2} \right] \left[\frac{1 \text{ lb mol } O_2}{2 \text{ lb mol } H_2} \right] \\ &= 0.0335 (\text{lb mol } O_2)/\text{hr} \end{aligned} \quad (11)$$

Considering 25% air utilization, to suffice complete requirement, almost 4 times of additional air is required

$$\begin{aligned} n_{O_2 \text{ supplied}} &= \left[0.0335 \frac{\text{lb mol } O_2 \text{ consumed}}{\text{hr}} \right] \left[\frac{1 \text{ lb mol } O_2 \text{ supplied}}{0.25 \text{ lb mol } O_2 \text{ consumed}} \right] \\ &= 0.134 \frac{\text{lb mol } O_2}{\text{hr}} \end{aligned} \quad (12)$$

As air is made up of 21% oxygen by volume, accordingly, air consumption to deliver maximum power is calculated as

$$\begin{aligned} n_{\text{air supplied}} &= \left[0.134 \frac{\text{lb mol } O_2 \text{ supplied}}{\text{hr}} \right] \left[\frac{1 \text{ lb mol air}}{0.21 \text{ lb mol } O_2} \right] \left[\frac{28.85 \text{ lb mol dry air}}{1 \text{ lb mol of air}} \right] \\ &= 18.41 (\text{lb dry air})/\text{hr} = 8.35 (\text{kg dry air})/\text{hr} \end{aligned} \quad (13)$$

For efficient air flow, different air cleaners and filter elements can be designed. New study of Turbocharger usage in the air requirement in the fuel cell operation is necessary and its benefits are to be reaped to improve the acceleration performance of the vehicle [11, 18, 19].

3.7 Gas States and Constants

At the prevailing conditions, various values are taken from the thermodynamic tables to perform constant values calculations. Thus, constants a and b are [1, 9, 20]

$$a = \frac{0.4275 \cdot R^2 \cdot \vartheta c^{\frac{2}{3}}}{pc} = a = \frac{0.4275 * R^2 * 32.97^{0.4}}{1.293 * 10^6} = a = 9.251 * 10^{-5} \quad (14)$$

$$b = \frac{0.08664 \cdot R \cdot \vartheta c}{pc} = b = \frac{0.08664 * 8.314^2 * 32.97}{1.293 * 10^6} = b = 1.837 * 10^{-5} \quad (15)$$

When $p_1 = 350 * 10^5$ Pa and $t_1 = 300$ K

$$\begin{aligned} p &= \frac{R \cdot \vartheta}{V - b} - \frac{a}{\sqrt{\vartheta} \cdot V \cdot (V + b)} = 350 * 10^5 \\ &= \frac{8.314 * 300}{V_1 - 1.837 * 10^{-5}} - \frac{9.251 * 10^{-5}}{\sqrt{300} * V_1 * (V_1 + 1.837 * 10^{-5})} \end{aligned} \quad (16)$$

Volume $V_1 = 8.963 * 10^{-5} \text{ m}^3/\text{mol} = 0.08965 \text{ L}$.

Mass of hydrogen/molecule = 2 g = $2 * 10^{-3}$ kg and Gas Density = $\rho = M/V = 22.31 \text{ kg/m}^3$

To store 5 kg of compressed gaseous hydrogen,

$$\text{Volume (For 5kg } H_2) = \frac{5 * 0.08965}{2 * 10^{-3}} = 224 \text{ L} \quad (17)$$

Table 2 Hydrogen consumption comparison

Sr No	Energy modes current requirement		
	Description	Value	Unit
1	Sports	6.11	kg/hr
2	Normal	3.97	kg/hr
3	Eco	3.055	kg/hr
4	Eco+	2.14	kg/hr

3.8 Weight of Hydrogen and Tank

Assuming Tank weight as 100 kg and 2 tanks, Total Full Tank weight = 210 kg.

Thus total GVW considered is 1080 kg.

Thus, as per Table 2, fuel consumption is estimated for the different energy modes for the vehicle and depending on the requirement, mode is to be selected for balanced approach between efficient fuel consumption and vehicle performance.

4 Conclusions

1. Present study suffices the overall scenario of the parameters to be considered for the optimum fuel cell based propulsion system design. Considering major challenge for the battery electric vehicle as very limited range, fuel cell technology is being explored on much larger scale. Electrical energy generation from hydrogen is one of the core development. Energy generation can be possible from both fuel cells as well as hydrogen based engines.
2. This study deals with the detailed calculative approach for designing hydrogen fuel cell based powertrains beneficial for organizations.
3. Various energy modes are studied with the mileage estimation to encourage consumer for the benefits of using hydrogen energy.

References

1. Larminie, J., Dicks, A., & McDonald, M. S. (2018). *Fuel cell systems explained*. Wiley.
2. Arruda, B. A., Santos, M. M., & Keshri, R. K. (2016). A comparative study of performance for electric vehicles for wheel traction configurations. *IEEE*.
3. Behling, N., Williams, M. C., & Managi, S. (2015). Fuel Cells and the hydrogen revolution: Analysis of a strategic plan in Japan. *Economic Analysis Policy*, 48.
4. Brey, J. J., Carazo, A. F., & Brey, R. (2018). Exploring the marketability of fuel cell electric vehicles in terms of infrastructure and hydrogen costs in Spain. *Renewable and Sustainable Energy Reviews*, 82.
5. Brown, L. F. (2001). A comparative study of fuels for on board hydrogen production for fuel cell powered automobiles. *International Journal of Hydrogen Energy*, 26.

6. Das, H. S., Tan, C. W., & Yatim, A. H. M. (2017). Fuel Cell hybrid electric vehicles: A review on power conditioning units and topologies. *Renewable and Sustainable Energy*, 76.
7. Demirbas, A. (2005). Hydrogen and Boron as recent alternative motor fuels. *Energy Sources*, A27.
8. María, E. E. (2011). Electrocatalysis and surface nano structuring: Atomic ensemble effects and non-covalent interactions. Catalan Institute of Nano Science and Nano Technology.
9. EG&G Technical Services (2004). *Fuel cell handbook*, US Department of Energy.
10. Gherairi S (2019). Hybrid electric vehicle: Design and control of a hybrid system supplied by hydrogen. *Energies* 76.
11. Kendall, M. (2018). Fuel cell development for new energy vehicles and clean air in China. *Progress in Natural Science: Materials International*, 28.
12. Kordesch, K. (1979). Survey of carbon and its role in phosphoric acid fuel cells, BNL 51418, Brookhaven Laboratory.
13. Lattin, W. C., & Utgikar, V. P. (2007). Transition to hydrogen economy in the United States: A 2006 status report. *International Journal of Hydrogen Energy*, 32.
14. Fan, L., Tu, Z., & Chan, S. H. (2021). Recent development of hydrogen and fuel cell technologies.
15. Balat, M. (2008). Potential importance of hydrogen as a future solution to environmental and transportation problems. *International Journal of Hydrogen Energy*.
16. Manoharan, Y., Hosseini, S. E., Butler, B., Alzahrani, H., Senior, B. T. F., Ashuri, T., & Krohn, J. (2019). Hydrogen fuel cell vehicles: Current status and future prospect, *Applied Science Base*, 19.
17. Kolavennu, P. K., Telotte, J. C., & Palanki, S. (2006). Design of a fuel cell power system for automotive applications. *Journal of Chemical Reactor Engineering*, 4.
18. Sulaiman, N., Hannan, M. A., Mohamed, A., Majlan, E. H., & Daud, W. W. (2015). A review of energy management system for fuel cell hybrid electric vehicle: Issues and challenges. *Renewable and Sustainable Energy Reviews*, 52.
19. Hirschenhofer, J. (1992) Latest progress in fuel cell technology. *IEEE Aerospace and Electronic systems*.
20. Hirschenhofer, J. (1993, April). Status of fuel cell commercialization efforts. In *American power conference*, Chicago.

Design Interventions Towards Optimization of Drive Features in Electric Bicycle in Adherence to ISO 4210



Theodore Mohandas Tatpati, Jeevith Arambooru, Krishnaraja Kodancha, and P. P. Revankar

Abstract The bicycle promises to become an important mobility device that promotes green solution to pollution menace in domestic short distance travel. Its structural design involves the frame as the vital part that gets subjected to severe fatigue loading that has led to accidents and expensive product recalls. The frame is the key load bearing member that decides user safety, demanding a stringent design, appropriate weld process and base material adoption. This study develops baseline model using BikeCAD Open-Source tool for component selection and design. The material selection coupled to fatigue test based on ISO 4210 helps to simulate failures and behavior of weld affected heat-zone. The iterative method checks various gauge of steel to identify safe thickness for bottom tube. In the final stage, results of standard frame were subjected to suitable design interventions leading to modified version that are safe with additional features of enhanced range and durability.

Keywords ISO 4210 · Electric bicycle · Interventions · Finite element analysis

Abbreviations

ARAI	Automotive Research Association of India
BIS	The Bureau of Indian Standards
BLDC	Brushless Hub Motor
BSD	Bead Seat Diameter
EN	European standard

T. M. Tatpati

MTech Programme, Design Engineering, KLE Technological University, Hubli, Karnataka, India

J. Arambooru

Vidyuthyaan Private Limited, Hunsur, Karnataka, India

K. Kodancha · P. P. Revankar (✉)

Faculty, KLE Technological University, Hubballi, Karnataka, India

e-mail: pp_revankar@kletech.ac.in

EPAC	Electronically Power Assisted Cycles
LFP	Lithium Iron Phosphate battery
NiMH	Nickel metal hydride battery

1 Introduction

The Pedal Electric Cycle (Pedelec) or Electronic Power Assisted Cycle (EPAC) or low-powered E-Bicycle adopt low power electric motor along with electronic controller to cut-off power to limit drive speed to 25 kmph [1, 2]. The rear hub motor driven by battery placed in frame structure assists in uphill drive or against headwinds. In 1989 bicycle with hub- motor, controller and battery was conceptualized and marketed as Dolphin in 1992 [3]. The Swiss start-up BKTech AG introduced first Flyer E-Bicycle in small production through e-business in 1995 [4]. Pedelec are handy owing to technological benefits and unique qualities not available in traditional bicycles as explained in this section.

Power compensation: is primary external power from motors that augment to pedal work generating higher traction. This supports user especially during crucial and work continuous work for extended periods [5].

Speed: is adjusted through combined power from pedal and motor optimized by the controller that understands pedaling behavior. The Pedelec reach the destination faster compared to standard bicycle at reduced effort [5].

Accessibility: People in hilly area cannot use standard bicycles due to tough terrain that needs motorized drives like Pedelec. The accessibility in this area improves on adopting E-Bikes regardless of age, gender, strength, skill, health, or athletic ability, may ride this.

Effort: for E-Bicycle is lesser than that for any other type of bicycle due to motor provided torque that assists the user to push wheels.

Eco-friendly: features E-Bicycle as top listed drive owing to 30 times lower CO₂ than conventional automobile making it a quiet transport mode [6].

Health: regular cycling strengthens heart, lungs and circulation, lowering risk of heart disease due to improved cardiac muscle strength [7].

2 Literature Study

Cycling, a popular recreational and sport activity is now significant for its eco-friendly nature, escalating cost and associated pollution menace of fossil fuels. A wide range of bicycles are now in market with more innovative designs developed by industry.

Literature on bicycle frame design indicates that horizontal, vertical, and pedalling fatigue stresses are critical loads to assess fatigue safety factor. Its minimum value is greater than unity and fatigue test research findings pointed that the bottom and top parts of down tube had substantial impact on its magnitude [8]. Forrest Dwyer et al., developed material, heat treatment process, frame design, and fatigue behaviour for mountain bike using Al-6061-T6. The weld that joins top and bottom tube region of bicycle is prone to fracture [9]. The bicycle frame Pedal test (EN 14764) indicated pedal axle force led to down tube connect zone stresses beyond material yield stress. The higher wall thickness was suggested or use of better mechanical grade steel [10]. The area of bicycle frame failure was observed at each joint closer to weld [11]. Tomaszewski showed that major stress occurred away from weld that was stronger than base material with respect to fatigue failure mode [12]. The Pedelec distinguished from regular bicycle in terms presence of battery, electric motor, and electronic control system apart from display panel for operation detailing. Battery comes in various types and capacities, but most common are NiMH, Li-ion [13] with storage of around 400 Wh and 400–800 (NiMH) or 1000 (Li-ion) cycles [14]. Motors used in Pedelec include brushed and brushless motors with latter preferred due to durability. Controller are compatible to brushed and brushless motor, with the latter having higher efficiency, longevity and lower prices. The brushed motors are still employed for their more accessible controller.

3 Design Requirements

Fatigue failures can be more damaging to product life cycle especially while cruising tough mountain terrain. The bicycle frame modelled in 3D with structural steel adopted as frame material and steel used for front forks, bar, rigid mount, vertical link, vertical arm and tie-rod. The boundary condition based on ISO 4210 is applied in Ansys Workbench to identify appropriate material qualities and minimum fatigue factor of bicycle frames subjected to horizontal, vertical and pedalling fatigue test simulations. The bottom tube gauge is finalised and tested for fatigue loading.

The standards to follow in design of E-Bicycle covers motor, battery and controller. The motor specification and wheel size help calculate RPM to be within ARAI standards (25 kmph) and later battery size is decided to suit motor capacity.

Motor RPM Calculation Wheel Specification: 26" × 1.25/2.1".

Tyre diameter ϕ = 680 mm Bead Seat Diameter (BSD) = 630 mm

$$\text{Speed} = \text{RPM} \times L \tag{1}$$

$$L(\text{Length}) = \pi \times D$$

$$L = \pi \times (680) = 2136.56 \text{ mm} = 2.136 \text{ m}$$

$$\text{RPM} = \text{Speed}/L|25 \text{ km/h(ARAI Std.)}$$

$$\text{RPM} = (25 \times 1000)/(2.136.56) = 195.068$$

The minimum RPM required is 195, and motor of 250 W and 36 V is selected [15].

Battery Selection and Calculation

A lithium iron phosphate battery LFP batteries are suitable for hot climates of because of their high thermal resistance [16].

Battery Specification: LiFePO_4

Working voltage = 3.0–3.2 V Working Current = 6 Ah

The maximum efficiency of Motor by Technical Data [X] is 36 V and 12 A.

Therefore, the combination of battery module is

11S (In Series): $11 \times (3.2) = 35.2 \text{ V}$; 2P (In Parallel): $2 \times (6) = 12 \text{ Ah}$

Frame Baseline Design

The e-bicycle frame was designed in BikeCAD [17] Tool developed by Brent Curry. It provides all design dimensions of bicycle frame including wheels base, seam distance, head tube bearing, bottom bracket bearings, seat height, gear system and tolerances before designing the frame.

Material Selection

The material used for analysis is structural steel has its properties of Youngs modulus: 200 GPa, Poisson ratio: 0.3, yield strength: 250 GPa and ultimate strength: 460 GPa. The bicycle frame tube is made of steel due to its balanced mechanical properties, weight and price; this material is widely used in bicycle frame components. Design parameters and standards were adopted in model developed using Solid-Works tool.

4 Loading and Boundary Conditions

Loading and boundary conditions are used to ensure rider safety. Bicycle frames must pass three fatigue tests to fulfil the ISO 4210 bicycle testing standard (2016) that include Horizontal fatigue test, Vertical fatigue test and Pedalling test.

Horizontal Fatigue Test: in Fig. 1 includes 1200 N horizontal force in forward and 600 N in reverse for 10^5 cycles in front fork of wheel axles. The dropouts on rear axles are fixed with front fork vertically constrained but move back and forth [8].

Vertical Test: Fig. 2 has frame assembled and secured to rear dropout to prevent rotation with roller attached to front axle allowing back and forth motion. An equivalent to seat stem is inserted to 75 mm depth into seat tube top. A dynamic vertical downward force (0–1200 N) is applied at 70 mm for test cycle of 5×10^4 [8].

Fig. 1 Horizontal fatigue test

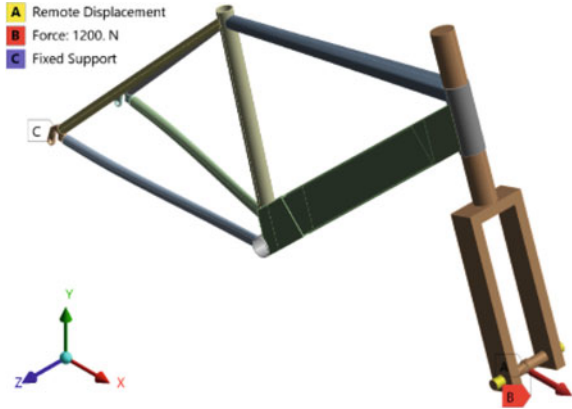
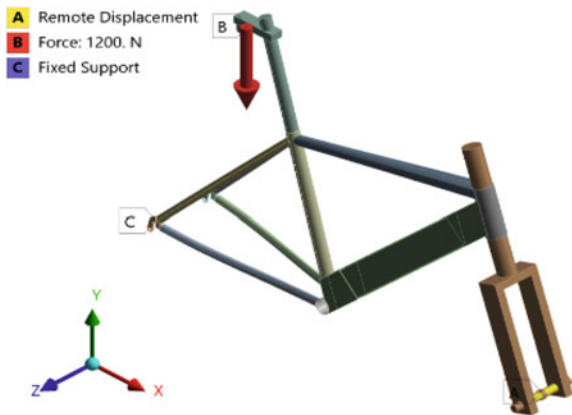


Fig. 2 Vertical fatigue test



Peddalling Test: Fig. 3 has frame assembly base mounted and dummy fork at rigid bracket on its axle and hub is free to rotate on the axle. Each pedal axle is tilted 7.5° to frame vertical section at a position of 150 mm, subject to repeated downward forces of 1200 N in vertical cross-section. Test forces are applied for 10^5 cycles [8].

5 Results and Discussions

The fatigue tests based on ISO 4210 for frame fatigue using Ansys Workbench are summarized in Table 1 exhibiting Fatigue Safety Factor (FSF). The results lead to modifications and network convergence analysis to establish accuracy in the results obtained. The maximum von Mises stress value converges at element size 4 mm and smaller as shown in Fig. 6 for pedalling fatigue analysis.

Fig. 3 Pedalling test

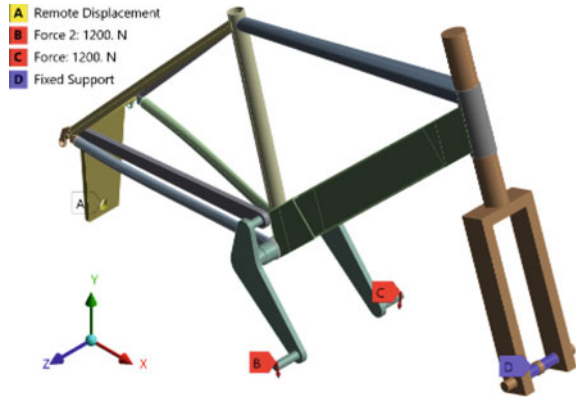


Table 1 Fatigue safety factor for standardised and modified model

Fatigue safety factor					
Model	Standardized			Modified	
Thickness	1.6 mm	1.8 mm	2.0 mm	1.8 mm	2.0 mm
Horizontal	0.75001	0.80491	0.85946	0.81466	1.0551
Vertical	1.802	1.8039	1.8064	1.8047	2.4606
Pedalling	0.53931	0.54243	0.54526	1.3434	1.4934

The Frame is analysed with quadratic mesh 4 mm element having bottom tube designed to fit battery pack dimensions. The 85 × 85 mm bottom tube cross-section adopted optimized wall thickness among trail values of 2 mm, 1.8 mm and 1.6 mm (14, 15 and 16 gauge). The minimum fatigue factor of safety using Goodman theory for frame indicated in Fig. 4 shows fatigue safety factor distribution as 0.8594.

In vertical fatigue test an external vertical downward force is applied to a point 70 mm behind intersection of solid steel rod. The rollers attached to front fork can move freely in horizontal direction. Figure 5 shows minimum fatigue factor of safety for bicycle frames to be 1.8064.

Fig. 4 FSF for E-Bicycle frame (Gauge 14) in horizontal fatigue test

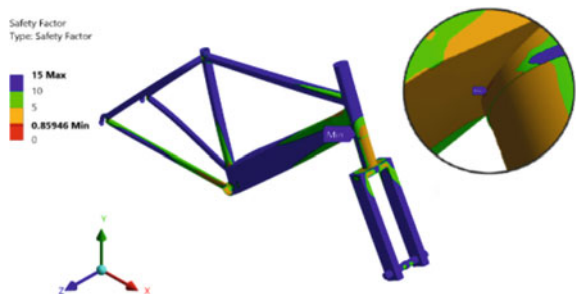


Fig. 5 FSF for E-Bicycle frame (Gauge 14) in vertical fatigue test

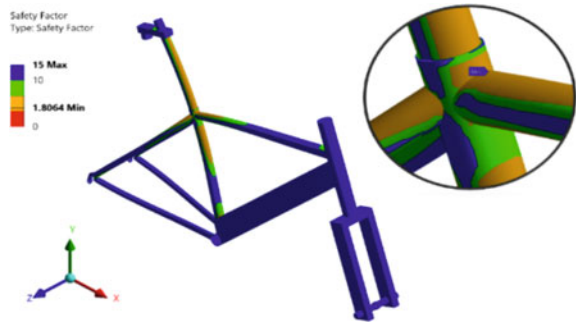
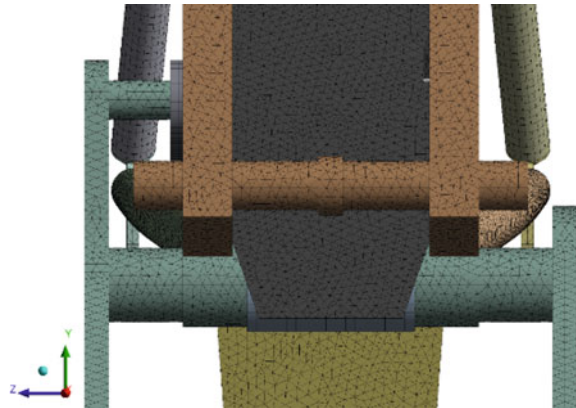


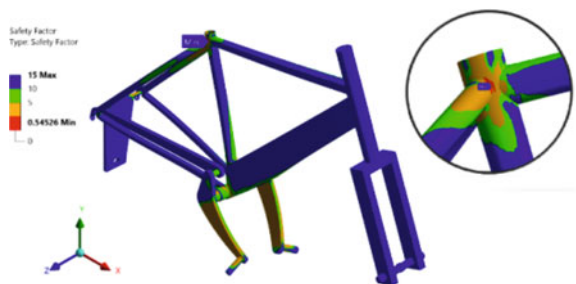
Fig. 6 Meshing of E-Bicycle model



For the pedalling fatigue test shown in Fig. 7, bicycle frame, vertical arms and tie rods are meshed for pedal fatigue test simulations. The x, y and z boundary conditions for the rear dropout and front fork are fixed. A vertical cross-section is tilted 7.5° to vertical, to apply 1200 N force 150 mm from frame centre line. The distribution of fatigue factor based gave minimum frame fatigue factor of safety as 0.54526.

The standard based frame analysed for various thicknesses is summarized in Table 1.

Fig. 7 FSF of E-Bicycle (Gauge 14) frame in pedalling test



6 Modifications and Analysis

The significant changes were made at the top joint of the seat stay and the area of the top tube was increased at the head tube region as these were observed as the failed regions from Table 1. A modified CAD version of the E-Bicycle is shown in Fig. 8.

The mesh quality was maintained for 4 mm in size and quadratic mesh order for better result. Again, the horizontal, vertical and pedalling fatigue test was conducted based on the ISO standard. The testing was conducted to understand the proper thickness of the bottom tube. The previous experiments showed that gauge 14 (2 mm thick) for bottom tube would be safe for the E bicycle and decrease the chances of fatigue fracture failure. Figures 9, 10 and 11, show the fatigue fracture failure result for horizontal, vertical and paddling fatigue tests, respectively.

Table 1, shows that apart from the vertical fatigue test, all 3 gauge of steel fail in horizontal and pedalling fatigue tests. Later after modification there was an improvement in the result as shown in Table 1. From the result gauge 14 which is of 2.0 mm thickness for the bottom tube will give a safe life.

Fig. 8 Modified CAD model of E-Bicycle

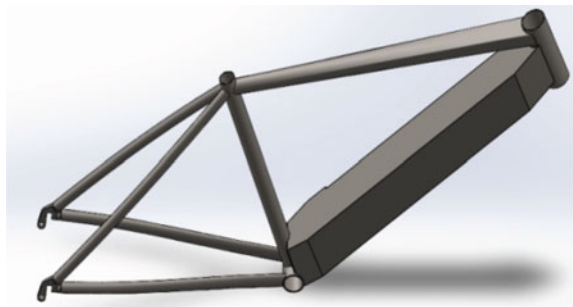


Fig. 9 FSF of E-Bicycle (Gauge 14) frame in horizontal fatigue test

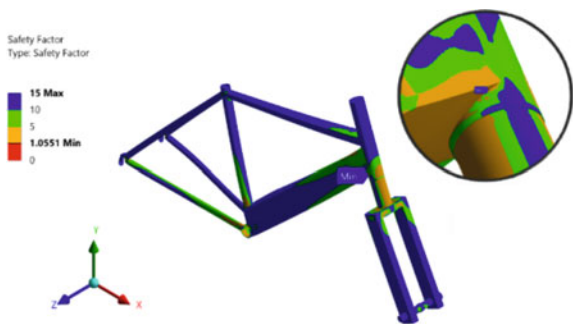


Fig. 10 FSF of E-Bicycle (Gauge 14) frame in vertical fatigue test

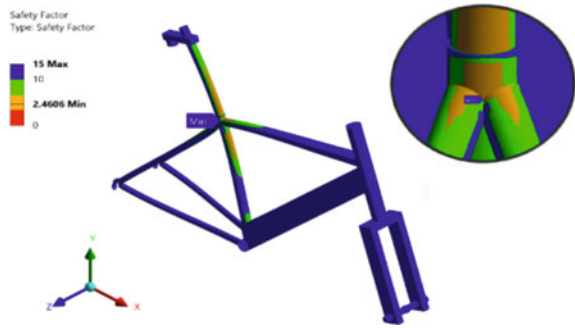
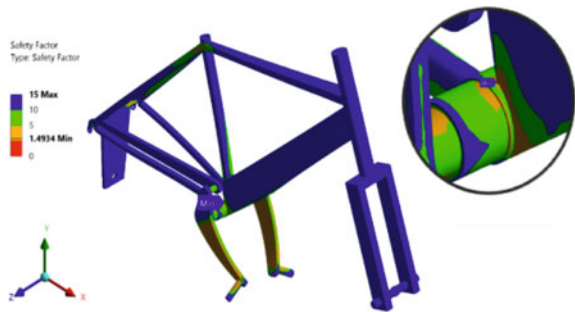


Fig. 11 FSF of E-Bicycle (Gauge 14) frame in pedalling fatigue test



7 Conclusions

In this study, we used finite element simulation for Electric bicycle frame. The road bicycle frame model has undergone horizontal, vertical and pedalling fatigue testing. For users with average height, [15, 18] Electric bicycle frame was designed to be rendered to a standardised bicycle frame and tested for fatigue according to ISO 4210:6.

- Fatigue test simulations under ISO 4210 loading conditions have shown that 1.2 mm gauge and 2.0 mm gauge for bottom tube fail at horizontal and Pedalling fatigue tests. Therefore, it was necessary to redesign for electric bicycle frame. The redesigned frame gave a safer result and amplified the frame life.
- The new model proposed by thorough investigations of the failure region resulted in an improvement in factor of safety by 14.05% in horizontal fatigue test, 23.47% in vertical fatigue test and 63.48% in pedalling fatigue test.
- Most of the failure regions are at the joints of frame caused due to heat-affected zone. This can be overcome by implementing an automated welding system in a controlled environment.
- The results obtained from the study can lead to design of safer Pedelec and thereby expand the user base nationwide, making a path to eco-friendly mobility.

References

1. Automotive Research Association of India. https://www.araiindia.com/faqs_electric_vehicle.asp
2. Pedelec. <https://en.wikipedia.org/wiki/Pedelec>
3. Dolphin EBike. <https://web.archive.org/web/20130330101103/http://www.dolphin-EBike.ch/mainnav/story/>
4. BKTech AG. <https://www.experience-online.ch/en/>
5. Altoumaimi, R., Altoumaimi, T., & Upadhya, B. P. (2014). *Characteristics and control of the motor system in E-Bikes*. Bachelor Thesis Electrical Engineering.
6. Conserve Future Energy. <https://www.conserve-energy-future.com/environmental-benefits-electric-bike.php>
7. UPMC. <https://share.upmc.com/2018/11/pedaling-to-a-healthier-heart/>
8. Cheng, Y. C., Lee, C. K., & Pornteparak, P. (2020). An improved design of an on-road bicycle frame under fatigue testing simulations. *Journal of the Chinese Institute of Engineers*, 43(4), 319–327.
9. Dwyer, F., Shaw, A., & Tombarelli, R. (2012). Material and design optimization for an aluminum bike frame—project report. Worcester Polytechnic Institute.
10. Zaimović-Uzunović, N., Bešlagić, E., & Porča, A. (2019). Numerical analysis of material fatigue impact on bicycle frame safety in accordance with EN 14764. In *New Technologies, Development and Application 4* (pp. 41–49). Springer International Publishing.
11. Covill, D., Allard, P., Drouet, J. M., & Emerson, N. (2016). An assessment of bicycle frame behaviour under various load conditions using numerical simulations. *Procedia Engineering*, 147, 665–670.
12. Tomaszewski, T. (2021). Fatigue life analysis of steel bicycle frame according to ISO 4210. *Engineering Failure Analysis*, 122, 105195.
13. Fetcenko, M., Koch, J., & Zelinsky, M. (2015). Nickel–metal hydride and nickel–zinc batteries for hybrid electric vehicles and battery electric vehicles. In *Advances in battery technologies for electric vehicles* (pp. 103–126). Woodhead Publishing.
14. Battery Stuff. <https://www.batterystuff.com/kb/articles/battery-articles/proper-care-and-feeding-of-a-nimh-battery.html>
15. EMF Innovation Pvt. Ltd. BL-05-36-250-210. <https://bit.ly/3JOsj00>
16. DAO EV. <https://www.daoev.com/blog/lfp-battery-need-in-india/>
17. BikeCAD. <https://www.bikecad.ca/>. Accessed on February 28, 2022.
18. Mamidi, R. S., Kulkarni, B., & Singh, A. (2011). Secular trends in height in different states of India in relation to socioeconomic characteristics and dietary intakes. *Food and Nutrition Bulletin*, 32(1), 23–34.
19. Mutyala, S., & Tech, M. (2019). Design and development of electric motor bike. *IRJET*, 6, 19–29.

Solar Thermal Energy Storage Technology: Current Trends



Pravin Prabhu and Sanjay Sawant

Abstract Energy security has major three measures: physical accessibility, economic affordability and environmental acceptability. For regions with an abundance of solar energy, solar thermal energy storage technology offers tremendous potential for ensuring energy security, minimizing carbon footprints, and reaching sustainable development goals. Global energy demand soared because of the economy's recovery from the COVID-19 pandemic. By mitigating the adverse effects of solar energy uncertainties, solar thermal energy storage provides an opportunity to make the power plants economically competitive and reliable during operation. Solar thermal power plant technology is still in the early stages of market introduction, with about six gigawatts of installed capacity globally in 2020 compared to PV technology. In a developing economy, the potential for cost reduction through invention, mass production, and growing competitiveness is far from being exhausted. The objective of this review paper is to access the progress of solar thermal energy technology in India compared to world and its potential to accomplish the clean energy goals.

Keywords Solar energy · Thermal energy storage · Concentrated solar power · Phase change materials · Carbon emission

1 Introduction

The goals outlined in the 2030 Agenda for Sustainable Development are under threat as the globe deals with interrelated and cascading global crises and wars. The war in Ukraine is intensifying the food, energy, humanitarian, and refugee problems while also contributing to the COVID-19 epidemic, all against the context of a declared

P. Prabhu (✉)

Department of Technology, Shivaji University, Kolhapur, Maharashtra, India
e-mail: pap_tech@unishivaji.ac.in

S. Sawant

Sant Gajanan Maharaj College of Engineering, Mahagaon, Gadhinglaj, Kolhapur, Maharashtra, India

climate emergency. The world is moving further toward its sustainable energy goals. However, with the current rate of development, Goal 7 of affordable and sustainable energy cannot be met by 2030 [1].

Economic growth has always been highly linked to growing energy use and GHG emissions. Solar energy breaks up this link, promoting sustainable development and climate action. Three important technological breakthroughs are required for such separation: shifting to solar energy in place of fossil fuels; reducing energy consumption on the demand side, and increasing electrical generation efficiency. An indicator of diminishing poverty and improved economic growth, in emerging countries, is increased together with power consumption. Renewable solar energy enhances rural poor people’s ability to access electricity and reduces poverty.

One of the most significant challenges confronting humanity today is global warming. To address the problem of global warming, solar thermal systems (STs) have seen a surge in the recent two decades on the international market. Solar thermal systems would be a better choice to replace existing energy systems. By functioning as thermal storage batteries, phase change materials (PCMs) have emerged as an alternative to improve the efficiency of solar heating systems [2] (Fig. 1).

Utilizing thermal energy storage (TES) enables the efficient use of clean energy sources, reduction of energy consumption, and improvement of energy system performance. The primary step to minimize the effects of climate change is now generally acknowledged to be reducing carbon emissions into the atmosphere. As a result, the majority of countries invested many resources in search of effective techniques for reducing energy usage and the amount of energy generated by fossil fuels [4].

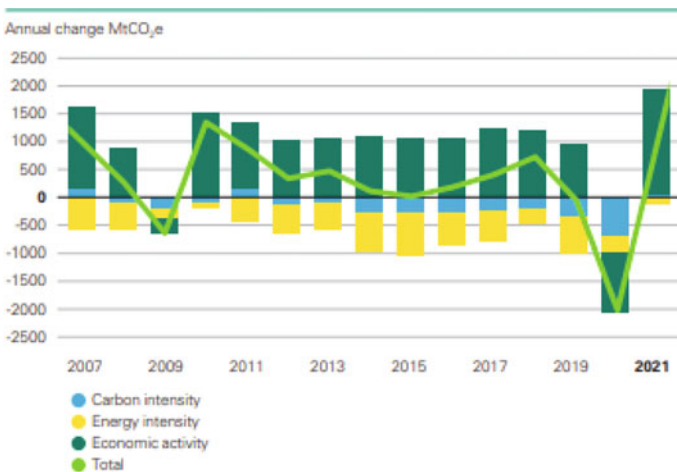


Fig. 1 Increase in carbon emissions in 2021, driven by the rebound in economic growth [3]

2 Thermal Energy Storage

Thermal energy storage is a technique that stores thermal energy by heating or cooling a storage medium so that the energy can be used later for power generation, heating and cooling systems, and other purposes. In order to balance energy demand and supply on a daily, monthly, and even seasonal basis, Thermal energy storage systems are used. They can also improve the overall effectiveness of energy systems by minimizing peak demand, energy consumption, carbon dioxide emission, and cost [5].

There are two distinct types of TES systems: (A) sensible heat storage, which utilizes heating or cooling a solid or liquid storage medium (such as water, rock, sand, or molten salts), and (B) latent heat storage, which utilizes phase change materials or PCMs. Energy storage system prefers to utilize PCM with the latent heat of fusion of 300 kJ/kg and higher at operating temperatures of 180 °C [6].

It is predicted that India receives more than 5000 trillion kWh of solar energy each year, with the majority of areas receiving 4–7 kWh/m². Presently, India consumes over 1.13 trillion kWh per year while producing roughly 1.38 trillion kWh per year, indicating that production capacity is just a little bit more than actual demand. India now has roughly 40 GW of installed solar capacity out of 100 GW of installed renewable energy potential [7].

2.1 World

The world has installed 6313.9 MW by the end of 2021, with Spain and the United States dominating the market. Figure 2 represents the total installed CSP capacity globally from 2011 to 2021 and illustrates the percentage of CSP capacity across all nations as of the end of 2021. The completion and operation of numerous large-scale commercial CSP plants in developing nations like China, Morocco, South Africa, India, Israel, and UAE significantly increased the installed capacity of CSP globally in 2021 [8].

More than 35% of the world's total energy consumption is made up of process heat in industrial applications. Fossil fuel is used for industrial process heat applications, providing 10% of the energy for the metal industry, 23% for the refining of petroleum, 80% for the pulp and paper industry, and 60% for the food processing industry. Applications for industrial process heating account for 32% of overall energy consumption in countries like India. Flat plate collectors and evacuated tube collectors may be employed for low-temperature applications (120 °C), whereas concentrated solar power technology is appropriate for medium- and high-temperature applications (400 °C) [9]. For regions with an abundance of solar resources, solar thermal technology is extremely promising for ensuring energy security, minimizing carbon footprints, and ultimately achieving sustainable development goals. The introduction of

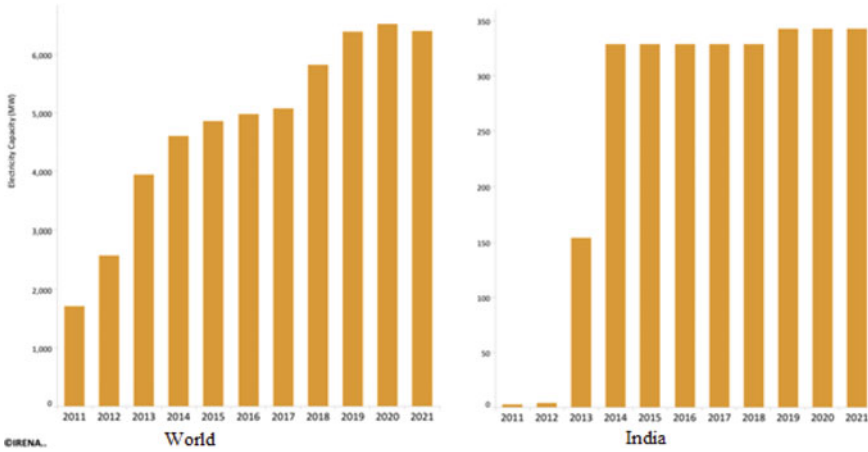


Fig. 2 Electricity capacity (MW)–CSP technology [14]

thermal energy storage (TES) to CSP plants could balance the supply and demand of energy by minimizing the adverse effects of solar energy intermittency [10].

Increased use of irregular RES has an impact on grid stability. Systems for storage of electricity (EES) offer a potential solution for grid stability problems [11] (Table 1).

Table 1 WORLD: percentage of renewable technologies [12]

Parent-technology	Sub-technology	Percentage (%)	Generation: GWh
Bioenergy	Biogas	1.3	96,564.82
Solar	Concentrated solar power	0.2	13,113.42
Geothermal	Geothermal energy	1.3	94,949.10
Bioenergy	Liquid biofuels	0.1	7932.64
Marine	Marine energy	0.0	957.47
Renewable hydropower	Mixed hydro plants	0.0	115.29
Wind	Offshore wind energy	1.3	1,00,114.07
Wind	Onshore wind energy	19.9	14,88,471.96
Renewable hydropower	Renewable hydropower	58.3	43,55,819.74
Bioenergy	Renewable municipal waste	1.0	73,239.19
Solar	Solar photovoltaic	11.1	8,30,741.44
Bioenergy	Solid biofuels	5.4	4,06,038.84

2.2 India

In India, Solar power generation has grown at an accelerating rate from 0.07 GW in 2010 to 50 GW in 2021. India is in an active position to accelerate toward its goal of 280 GW by 2030, a six-fold increase over present levels. As a result of solar Power generation, India has saved US\$4.2 billion in fuel expenditures in the first half of 2022. It also eliminated the requirement for 19.4 million tonnes of extra coal, which would have put even more burden on the already constrained domestic supply [13].

According to the Global Trends in Renewable Energy Investment 2020 report, India's renewable energy projects and programs attracted investments of US\$64.2 billion between 2014 and 2019. (Rs 4.7 lakh crore). Since April 2014, solar tariffs have also dropped significantly, from Rs. 6.47 per kilowatt-hour in 2013–14 to Rs. 1.99 in December 2020 [15] (Table 2).

India's Nationally Determined Contributions (NDC) under the Paris Agreement for the period 2021–2030 include the following goals: To achieve about 40% of the total installed capacity of electric power from non-fossil fuel-based energy resources by 2030 with the aid of technology transfer and inexpensive international financing. By 2030, India aims to reduce the emissions intensity of its GDP by 33 to 35% from 2005 levels. India is on track to accomplish these goals.

India has a total installed capacity for renewable energy of 92.54 GW (excluding large hydro), of which 5.47 GW was added from April 2020 to January 2021. India's installed RE capacity expanded by two and a half times between April 2014 and January 2021, while installed solar energy capacity increased by 15 times within the same time frame. India currently ranks fourth in the world for RE power capacity, fourth for wind power, and fifth for solar power capacity. One of the world's fastest rates of growth for renewable energy is seen in India.

In order to ensure the objectives of energy security and climate protection, there is a need for definite policies. In order to fulfil peak electricity demand and ensure grid stability without any severe environmental impact, solar thermal energy storage is an important step forward in sustainable energy production [17] (Table 3).

The most effective option for India is to implement a system that is entirely dependent on renewable energy. India's future energy system will be mostly comprised of

Table 2 INDIA: percentage of renewable technologies [12, 16, 17]

Parent-technology	Sub-technology	Percentage (%)	Generation: GWh
Bioenergy	Biogas	0.01	31.89
Solar	Concentrated solar power	0.10	360.3
Wind	Onshore wind energy	21.20	63,522.27
Renewable hydropower	Renewable hydropower	53.30	1,59,728.81
Bioenergy	Renewable municipal waste	0.30	931.62
Solar	Solar photovoltaic	18.10	54,305.90
Bioenergy	Solid biofuels	7.00	21,023.86

Table 3 INDIA: list of solar thermal plants [8]

No	Power_station	Capacity (MW)	CSP technology	Owner
1	ACME solar tower	2.5	Power tower	ACME Group
2	National solar thermal power facility	1	Parabolic trough	IIT Bombay
3	Godawari solar project	50	Parabolic trough	Godawari Green Energy
4	Dhursar	125	Linear fresnel	Reliance power
5	Megha solar plant	50	Parabolic trough	Megha Engg. and Infra
6	Dadri ISCC plant	14	Linear fresnel	NTPC
7	KVK energy solar project	100	Parabolic trough	KVK Energy Ventures Ltd

solar PV and batteries, with other technologies acting as a control mechanism [18]. India's constructive and cooperative climate commitment is reflected by the foundation of the International Solar Alliance (ISA) in November 2015. The alliance was established during the Paris Agreement negotiations jointly by India and France. It is a treaty-based, member-driven forum aimed at trans-regional solar energy cooperation to both minimize the reliance on fossil fuels and create a more just and sustainable energy system.

The ISA was established during the 2015 UN Conference of Parties 21 (COP21) in Paris as a result of Indian Prime Minister Narendra Modi's ambitious "One World, One Sun, One Grid" initiative. The establishment of ISA underlined India's position as a major global player in the difficult issues of climate change. On December 6, 2017, ISA's multilateral treaty status, as granted by the UN, became effective. A multi-country partnership organization called ISA was proposed, with members from the "sunshine belt" nations located entirely or in part between the Tropics of Cancer and Capricorn [19].

3 Discussion

India's power sector is the largest contributor to its CO₂ emissions, and coal-fired power plants are responsible for the great majority of power sector emissions [20].

The key reasons for the moderate growth of the CSP technologies are a number of constraints, including inadequate DNI data, inappropriate policies, a complex system of land acquisition, a scarcity of water, approval complications, low investor confidence, and a lack of long-term planning. A key challenge to promoting CSP is the lack of funding and the rapid decline in the price of PV modules.

Table 4 summarizes the results of a SWOT analysis that has been conducted based on the opinions of various researchers.

In addition to this, several technical factors are listed below.

Table 4 SWOT analysis of CSP technology [21]

Strength	Weakness	Opportunity	Threats
Significant efficiency	Excessive investment cost	Room for high concentration ratio	Remarkable reduction in PV price
Completely recyclable working medium	Production cost of a reflector	More efficient reflector	Focused radiation, harmful for flying species
Storage	Heat transfer losses	New material for storage	Possibilities of leakage may hamper the system
Longer duration span than batteries	Controlling high-temperature working medium	Thermochemical storage with minimum loss of heat	Environmental pollution by chemicals

Capacity factor

Traditional thermal power plants have a capacity factor of 90%. The majority of CSP power plants have capacity factors of under 25% and can reach up to 80% with an expensive storage system.

High capital cost

The capital cost of the CSP-based technology is multiplied due to the necessity of highly complicated components and land. Based on a lifecycle study, the lifespan of CSP-based power plants is longer than that of traditional thermal power plants.

Low level of technological development

CSP technology is still in its initial phases. The industrial infrastructure for the production of components has not yet been built to meet the demand for CSP deployments in DNI-exposed countries like India.

Materials and component availability

The CSP includes components like absorbers and reflectors. Due to the lack of a developed market for the availability of these components, they are costly. The addition of a unique design and sun tracking so the deployment of CSP is complicated.

The development of heat and power generation employing Rankine cycles, research on supercritical CO₂ power cycles in CSP plants, performance analysis of calcium looping, and thermochemical energy storage on CSP systems are further study topics [22]. In India, a country with typically 300 bright days per year and 220 MW of solar radiation per square kilometer, coal-fired power plants produce enormous amounts of carbon dioxide emissions. As a result, solar-based power generation has the ability to both reduce emissions and meet the growing demand for energy [23]. The government of India has set an ambitious goal of increasing the contribution of manufacturing output to 25% of gross domestic product (GDP) by 2025, which would be a 9% increase from the current level of 16%. The International Solar Alliance (ISA), a platform initiated by the government of India, encourages trade among its 121 members positioned in tropical regions with abundant solar radiation [24].

4 Conclusion

India is now the third-largest carbon dioxide emitter in the world when combined with the industry, transportation, and service sectors. The National Solar Mission has encouraged future growth of the solar thermal sector with ambitious goals in terms of installation targets. India's solar business has extensive experience with large-scale projects; approximately 78,000 m² of concentrating projects have been implemented.

Barriers to the growth of renewable energy sources include a lack of transmission infrastructure, land availability, overvalued resource assessments, and, policy instability brought on by various political interests. In a competitive market, low-cost imports and inadequate standards might constrain market expansion.

Solar thermal energy storage technology is a promising field with advancements and setbacks in a national scenario. Although this technology currently involves some technical risks and high electricity costs, with ongoing technological advancements and the gradual localization of core equipment, it will undoubtedly become the sustainable energy solution of the future. Further technological advancements are required to overcome the stated hurdle and a comprehensive policy encouraging solar thermal power generation is essential for the deployment of solar thermal energy storage-based CSP power plants in India. CSP technology is expected to grow quickly because of its numerous benefits, including efficiency, a long life cycle, negligible environmental effects, etc. By 2024, it is estimated that CSP's total installed capacity would increase to 1.3 GW.

References

1. The sustainable development goals report: 2022
2. Palacios, A., Barreneche, C., Navarro, M. E., & Ding, Y. (2020). Thermal energy storage technologies for concentrated solar power—A review from a materials perspective. *Renewable Energy*, 156, 1244–1265. <https://doi.org/10.1016/j.renene.2019.10.127>
3. BP. Statistical Review of World Energy 2022.
4. Cabeza, L. F., de Gracia, A., Zsembinszki, G., & Borri, E. (2021). Perspectives on thermal energy storage research. *Energy*, 231. <https://doi.org/10.1016/j.energy.2021.120943>
5. Solar thermal power plants Heat, electricity and fuels from concentrated solar power, German Aerospace Center (DLR) Institute of Solar Research. www.dlr.de/st/en/
6. Kalidasan, B., Pandey, A. K., Shahabuddin, S., Samykano, M., Thirugnanasambandam, M., & Saidur, R. (2020). Phase change materials integrated solar thermal energy systems: Global trends and current practices in experimental approaches. *Journal of Energy Storage*, 27. <https://doi.org/10.1016/j.est.2019.101118>
7. Pandey, A., Pandey, P., & Tumuluru, J. S. (2022). Solar energy production in India and commonly used technologies—An overview. *Energies*, 15(2). <https://doi.org/10.3390/en15020500>
8. <https://solarpaces.nrel.gov/>
9. Ravi Kumar, K., Krishna Chaitanya, N. V. V., & Sendhil Kumar, N. (2021). Solar thermal energy technologies and its applications for process heating and power generation—A review. *Journal of Cleaner Production*, 282. <https://doi.org/10.1016/j.jclepro.2020.125296>

10. Achkari, O., & el Fadar, A. (2020). Latest developments on TES and CSP technologies—Energy and environmental issues, applications and research trends. *Applied Thermal Engineering*, 167. <https://doi.org/10.1016/j.applthermaleng.2019.114806>
11. Shyam, B., & Kanakasabapathy, P. (2018). Large scale electrical energy storage systems in India- current status and future prospects. *Journal of Energy Storage*, 18, 112–120. <https://doi.org/10.1016/j.est.2018.04.018>
12. Global Energy Perspective 2022 Executive Summary. 2022.
13. The sunny side of Asia, Centre for Research on Energy and Clean Air (CREA) Institute for Energy Economics and Financial Analysis (IEEFA), Publication date: November 10, 2022.
14. <https://www.irena.org/Energy-Transition/Technology/Solar-energy>
15. G. of I. Ministry of New and Renewable Energy. Annual Report 2020–21. [Online]. Available: <https://www.mnre.gov.in/>
16. Cea Annual Report 2020–21 Central Electricity Authority Ministry of Power Government of India.
17. <https://mnre.gov.in/solar/current-status>
18. Gulagi, A., Bogdanov, D., & Breyer, C. (2018). The role of storage technologies in energy transition pathways towards achieving a fully sustainable energy system for India. *Journal of Energy Storage*, 17, 525–539. <https://doi.org/10.1016/j.est.2017.11.012.91>
19. Issue Brief speech or electronic media without prior written approval from ORF. India and the Global Commons: A Case Study of the International Solar Alliance OluwaseunOguntuase. 2022.
20. I. Energy Agency. (2021). India Energy Outlook 2021 World Energy Outlook Special Report. [Online]. Available: www.iea.org/t&c/
21. Bijarniya, J. P., Sudhakar, K., & Baredar, P. (2016). Concentrated solar power technology in India: A review. *Renewable and Sustainable Energy Reviews*, 63, 593–603. <https://doi.org/10.1016/j.rser.2016.05.064>
22. Shahabuddin, M., Alim, M. A., Alam, T., Mofijur, M., Ahmed, S. F., & Perkins, G. (2021). A critical review on the development and challenges of concentrated solar power technologies. *Sustainable Energy Technologies and Assessments*, 47. <https://doi.org/10.1016/j.seta.2021.101434.915>
23. Akhtar, I., Kirmani, S., Jameel, M., & Alam, F. (2021). Feasibility analysis of solar technology implementation in restructured power sector with reduced carbon footprints. *IEEE Access*, 9, 30306–30320. <https://doi.org/10.1109/ACCESS.2021.3059297>
24. Solar heat for industry, Solar Payback INDIA, German Solar Association, Solar Thermal Federation of India (STFI).

A Review on Material Compatibility on the Fuel Flow System of a Diesel Engine with Waste Cooked Oil Biodiesel



Rajesh Gurani, B. J. Patil, Malikasab Bagawan, and Prashant Tadalagi

Abstract Presently the whole globe is concerned about the effect of environmental pollution by the automobile vehicles. The use of fossil fuel is considered as a major contribution to it. The second aspect of fossil fuel is the depletion of fuel which leads to thinking of alternative fuel for running the automobiles. Biodiesel is the only alternative for diesel fuel due to its environment-friendly properties and easy availability. Biodiesel can be used directly in diesel engines without modifying the design of present engine. Even biodiesel is the best replaceable alternative for petroleum diesel but automotive companies are not ready to implement because of less research available about material compatibility issues of biodiesel.

Keywords WCO biodiesel · Injection system · Fuel filter · Metal erosion · Elastomer

1 Introduction

In this present scenario, there is a lot of development in the engine and is widely being used in every aspect of human life. But presently we are going to face many challenges also. In this fast-growing world, every country requires a lot of energy for development works and also for making human's life easier and more comfortable. So world needs the energy and then for this energy the whole world is depending on petroleum products like coal, petrol, diesel, and petroleum gases. But wide usage of these sources, they are becoming obsolete in upcoming days. So we are in the situation that we should think about the alternative energy sources.

R. Gurani (✉) · B. J. Patil · P. Tadalagi
Department of Mechanical Engineering, KSGB'S Bharat Ratna Indira Gandhi College of Engineering, Kegaon, Solapur, Maharashtra, India
e-mail: rajeshgurani91@gmail.com

M. Bagawan
Department of Automobile Engineering, Matushri Venkata Subba Rao (M.V.S.R) Engineering College, Hyderabad, India

Table 1 The main parts and their materials of diesel engine fuel flow system

Main parts	Components	Materials
Fuel tank	Housing	Steel, plastic, paint, coating
	Gasket	Elastomer, paper, cork, copper
Fuel feed pump		Aluminum alloy, iron based alloy, copper based alloy
Fuel lines	High pressure	Steel
	Low pressure	Plastics, rubber
Fuel filter	Filter cartridge	Paper
	Housing	Aluminum, plastic
Fuel pump	–	Aluminum alloy, iron based alloy, copper based alloy
Fuel injector	–	Stainless steel

Use of petroleum products in engines, will emits very harmful emission gases like CO, CO₂, HC, NO_x, SO_x, particulate matters to the environment. The earth is being polluted highly and the Ozone layer is depressing rapidly day by day. This is directly affecting human health, so there is a serious need to find alternative energy sources, which are like eco-friendly, easily replaceable and easily available energy sources. For this solar energy wind energy, fuel cells and biofuels are the best replacements. Especially being of less weight and non harmful biodiesel is easily replaceable for the automotives in place of fossil fuels.

1.1 Waste Cooked Oil Biodiesel

The waste cooked oil methyl ester is called as waste cooked oil biodiesel. This is a suitable source for the production of biodiesel because of a million tonnes of used/cooked oil is available worldwide a day. Reusing of this used oil causes many health hazards and disposal of it is also challenging task because it pollutes soil and water. This low cost, highly available waste can be converting as a wealth by producing a biodiesel. This also helps the world to go green and save human health from this waste. Below Table 1 provides the cooking oil yield for different crops [1–3].

1.2 Problem Facing by Automobile Sector While Using Biodiesel

Biodiesel is having many similarities with regular diesel fuel but it is eco-friendly with low pollutant emission compared to diesel. But presently the automobile sector is not fully accepting biodiesel as a complete fuel for the vehicle. Many vehicle manufacturers say that biodiesel is highly viscous and having low calorific value,

but many researchers proved that the viscosity may be reduced in the production process.

In spite of lesser calorific value of biodiesel compared to diesel, many researchers show the way of using biodiesel as a blend with regular fuel. Results shows that up to 20% blend are showing better performance and emission characteristics [4–6]. But still, the automobile industry is not ready to accept it. Some European manufacturer's tried a lot on to implementing the biodiesel as a fuel for their vehicles. They allow them to run on higher biodiesel blends but later they stopped allowing usage of biodiesel for their vehicles and suggested that there is a need to be work more on it for modification in engine design then only they will allow biodiesel for their vehicles [7].

Because biodiesel can degrade the rubber products, engine components, rubber seals and pipes. This causes fuel leaks and the other problems around the plumb seal. Also biodiesel is more corrosive, thus it may corrode the entire fuel flow system.

1.3 Fuel Flow System of Diesel Engine

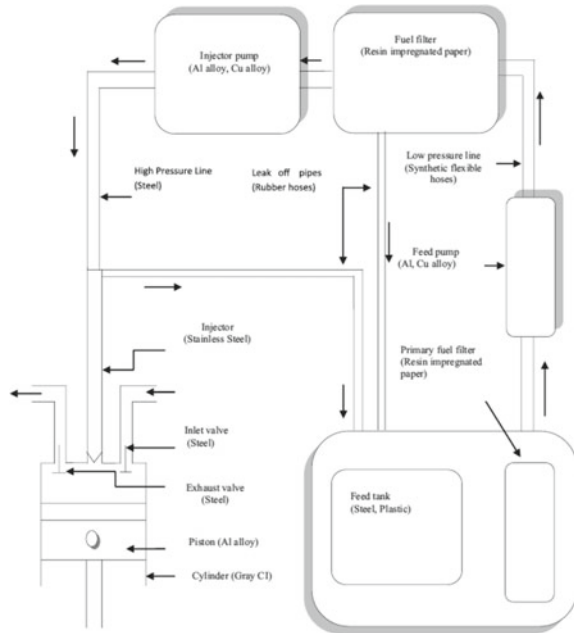
In a diesel vehicle, fuel comes into contact with a wide range of materials. Material flexibility in biodiesel may not be the same as that in diesel. Diesel is a blend of hydrocarbons, while biodiesel is a blend of unsaturated fat esters. The flexibility of seal, gaskets, hose materials generally utilized in car fuel frameworks utilizing regular diesel fuel has for quite some time been built up. It is realized that biodiesel is more destructive than customary diesel fuel. Destructive qualities of biodiesel are significant for the long haul sturdiness of motor parts. Corroding of metals parts can likewise trigger or catalyze other unwanted responses in biodiesel and it might lead to the debasement of biodiesel.

There is a lack of research and knowledge about fuel flow system material compatibility with waste cooked oil biodiesel. Present work is concentrating on the effects of waste cooked oil biodiesel by experimentally investigating the fuel flow system materials of the diesel vehicle and suggesting compatible materials to diesel engine fuel flow system (Fig. 1).

1.4 Components of Fuel Flow System of Diesel Engine that Comes in Contact with Biodiesel

Fuel is stored in the fuel tank; from this tank, fuel is provided to initial filters by gravity flow to remove impurities. The pump sucks the fuel from the initial filter and supplies it to the injector pump via the main filter. Pressurized fuel is provided by the injector pump to injectors via metal pipes. Injectors inject the atomized fuel to the engine combustion chamber with high pressure. During this fuel flow path biodiesel

Fig. 1 Flow diagram of fuel in diesel engine



comes in contact with many metals and non-metal materials. So in Table 1 shows the main parts of fuel flow system materials.

Generally, in compression ignition engine low-pressure fuel flow lines are made up of synthetic rubber and whereas in high pressure, fuel flow lines are made up of steel metal material. Gaskets and seals are made from elastomer. The commonly used elastomers are NBR rubber, EPDM rubber, Chloroprene rubber, SR rubber and natural rubber. Fuel tank and injectors are made up of steel or stainless steel. Fuel pumps are made by aluminium alloy, iron alloy or copper alloy.

2 Literature Review

2.1 Elastomer Degradation

Generally, in compression ignition engine low-pressure fuel flow lines are made up of synthetic rubber and whereas high pressure fuel flow lines are made up of steel material. Gaskets and seals were manufactured by the elastomer. The normally used elastomers are NBR rubber, Polyvinyl Chloride (PVC), polychloroprene, Fluoroviton A, HNBR rubber, Terpolymer FKM rubber, Buna rubber, EPDM rubber, CR rubber, SR Rubber and PTFE rubber [8]. Haseeb et al. [9] Studied the breakdown nature of elastomers in biodiesel. NBR, CR, Fluoro-Viton are immersed in diesel and palm

oil methyl ester biodiesel for investigation. Conducted immersion test for different biodiesel blends like B0, B10, B100 at 25 and 50 °C with a time period of 500 h. They studied properties like volume, weight and hardness. It was observed that degradation is higher in CR rubber and nitrile rubber but fluoro-Viton showed little changes. So they concluded that fluoro-Viton rubber had good resistance to degradation.

Compatibility of elastomer depending on the biodiesel sources, on these Lei Zhu et al. [10] studied Nitrile Butadiene Rubber degradation behavior with few types of biodiesels. They studied the properties of Nitrile Butadiene Rubber. They concluded by telling, biodiesel compatibility sequence for Nitrile Butadiene Rubber (NBR) is soybean biodiesel, used oil biodiesel, palm biodiesel. Impurities present in biodiesels so need of optimizing the production of biodiesel.

Haseeb et al. [11] investigated the compatibility of elastomers like ethylene propylene diene monomer rubber, SR rubber, CR rubber, Polytetrafluoroethylene rubber, Nitrile Butadiene elastomer in palm oil biodiesel. Tests were conducted on static immersion with B0, B10, B20, B50, and B100 at 25 °C with the time period for 1000 h. They suggested compatibility sequence for this biodiesel as Polytetrafluoroethylene rubber > SR rubber > Nitrile Butadiene elastomer > ethylene propylene diene monomer rubber > CR rubber.

The elastomer's degradation behavior was studied by many with different techniques but static immersion tests were suggested by most. Trakarnpruk and Porn-tangjitlikit [12] did the same test with 10% palm oil biodiesel fuel for a time period of 1008 h at 100 °C. They found that volume and mass were increased with an increase in time period for all specimens but except Nitrile Butadiene elastomer and NBR/PVC. NBR and PVC/NBR showed a decrease in mass and volume with time interval.

Raitisrudbohs et al. [13] conducted experimental research on elastomer compatibility with rapeseed oil biodiesel. They selected EPDM, NBR, HNBR, Fluorocarbon material (FKM), also 2 polyamide materials PA10.10 and PA12 elastomer for their study. Static immersion was conducted for different biodiesel blends like B0, B30, B100 at 20 °C with time period of 1000 h. Frame et al. [14] also studied the degradation behavior of elastomers in diesel fuels. In this, they chose different rubbers like peroxide-cured NBR, NBR, high aceto-nitrile contenting elastomer with and without carbon black fluorocarbon elastomer in regular diesel and 20% soy methyl ester biodiesel. They found that all types of rubbers were highly suitable for B20 and regular diesel.

Baranescu [15] worked for biodiesel research engine warranty policy. They concluded that many elastomers were swells in diesel fuel because of the absorption of aromatic contains. They suggested that normally biodiesel rich in aromatics so need to work more on it. Bessee et al. [16] studied the effect of soybean biodiesel and commercial diesel on the physical and mechanical properties normally using elastomers in automobile engines like NBR, Nylon rubber, Teflon-Viton, Viton GFLT and high-density polypropylene rubber. They observed that NBR, nylon, and polypropylene showed changes in elongation, volume and also in hardness but Teflon-Viton and Viton-GFLT were unaffected.

Shafer [7] worked for Mercedes Benz for its biodiesel-engine warranty policy. They studied different types of elastomers with different types of biodiesels [17]. In this, they mentioned that fatty acids are causing swelling of NBR rubber. Similar results were observed even in lighter blends of hydrogenated acrylonitrile butadiene rubber also [12]. They also observed shrinking of NBR during the immersion. But [14] reported opposite results for different methyl ester biodiesel blends for NBR rubber, which gains its volume up to 20% in B20 soybean methyl ester biodiesel blend [18].

Alves [19] also studied biodiesel compatibility with automotive elastomers using palm oil biodiesel and soybean oil biodiesel. They choose NBR and FKM rubbers for tests and they studied hardness by applying 200 bar pressure during the test. They found that FKM showed good resistance to degradation compared to another elastomer.

2.2 *Metal Corrosion*

It is very well known that biodiesels are more corrosive compared to normal diesel fuel. Corrosion attributes of biodiesel are significant for longer life of vehicle parts. Erosion of metals parts can likewise trigger or catalyze other unwanted responses in biodiesel and it might lead to the degradation of biodiesel. The acidic number of biodiesel identified with a free unsaturated fat substance inside it and it is straightforwardly consequences for metal erosion. Haseeb et al. [20] studied corrosion behaviors of metals in PME biodiesel. They had chosen copper and bronze for their static immersion test [21–23]. They observed copper corroding more compared to bronze in PME biodiesel. Copper easily reacts with dissolved oxygen of biodiesel.

Geller et al. [24] conducted a static immersion test at room temperature for ten months to study the corrosion characteristics of metals. They had chose copper, cast iron, brass, stainless and carbon steel for experiments. Finally, they concluded that due to the corrosive nature of biodiesel brass and copper corrode more in biodiesel. Some researchers [25, 26] conducted a similar static immersion test for different metals in different biodiesel and observed corrosion rates. Then added anti-corrosive additives to biodiesel and conducted the same test. Biodiesel easily reacts with the surrounding environment and absorbs oxygen and degrades itself by converting methyl esters back to free fatty acids with some water like impurities. This causes corrosion of engine. There is a less research available on corrosion of fuel flow system materials in methyl ester fuels and less data accessible about fuel flow system, real working influences dependent on which certain choices may be made. The destructive nature of biodiesel under a wide range of structural, ecological and working factors ought to be explored.

2.3 Engine Test and Injector Wear

It is important to know how biodiesel affects the fuel flow system during engine run. On this, some researchers worked and are discussed below. Peterson et al. [27] conducted a static engine test for a thousand hours. They used engine manufacture association recommended engine for testing and used soy biodiesel. Run engine according to engine manufacture association recommended cycles. Observed smother engine run and lighter wear. Ziejewski et al. [28] investigated wear and corrosion in a turbo engine. They run engine with sunflower biodiesel for 200 h and compared with diesel run impacts. They also observed smother engine run and lighter wear in injector parts. A small amount of carbon deposits and slurry were observed on engine surface.

Chase et al. [27] studied the wear and corrosion of field running. They run their vehicle nearly three lakh kilometers with a lower biodiesel blend (20% biodiesel). They observed no wear in engine parts. They also concluded that lower biodiesel blends are suitable and compatible with existing diesel engines Up to here we just observed positive results with biodiesel in engine test and field run test. But below some researchers shows negative side of it. How biodiesel has impact on engine parts by causing wear and corrosion.

3 Conclusion

From the review of literature, it is observed that limited work has been recorded in the material compatibility of diesel engine components with biodiesel; there exists a problem of compatibility of the biodiesel fuel used with the parts involved in fuel flow system of an IC engine. The materials of which the parts are made used to play an important role as regards the performance of the engine used. So there exists a scope for research to investigate the effects of biodiesel fuel on the parts of fuel flow systems and the need for their change.

References

1. Haseeb, A., Fazal, M. A., Jahiril, M. I., & Masjuki, H. H. (2011). Compatibility of automotive materials in biodiesel: A review. *Fuel*, 90(3), 922–931.
2. Murugapopathi S., & Vasudevan, D. (2020). *Experimental investigation on variable compression ratio engine using rubber seed oil biodiesel*. Anna University, Ph.D Thesis, 2020. <https://hdl.handle.net/10603/342583>
3. Gurani, R., & Kurbet, S. N. (2019). *CO emissions for CIDI engine using blends of combinations of biodiesel with diesel fuel* (pp. 8602–8607).
4. Gurani, R., & Kurbet, P. R. S. N. (2019). Performance characteristics of CI DI engine using blends of biodiesel (WCO) and diesel fuel. *IOSR Journal of Engineering*, 09(9), 7–10

5. Tadalagi, P. B., Rajesh, G., & Bagawan, M. (2018). *Smoke emission levels for CI DI engine using blends of combinations of biodiesel and diesel fuel. IOP conference series: Materials science and engineering* (Vol. 376. No. 1). IOP Publishing.
6. Shafer, A. (1994). Biodiesel research-Mercedes Benz-engine warranty policy. *Journal of Commercialization of Biodiesel: Establishment of Engine Warranties, 01*, 125–141.
7. Sorate, K. A., Bhale, P. V., & Dhaolakiya, B. Z. (2015). A material compatibility study of automotive elastomers with high FFA based biodiesel. *Energy Procedia*, 75, 105–110.
8. Haseeb, A., Jun, T. S., Fazal, M. A., & Masjuki, H. H. (2011). Degradation of physical properties of different elastomers upon exposure to palm biodiesel. *Energy*, 36(3), 1814–1819.
9. Gurani, R., Tadalagi, P. B., & Bagawan, M. (2017). Emission characteristics of CI DI engine using blends of biodiesel (waste cooking oil) and diesel fuel. *International Journal of Innovative Research in Science, Engineering and Technology*, 6(8), 16461–16465. <https://doi.org/10.15680/IJRSET.2017.0608219>
10. Haseeb, A., Masjuki, H. H., Siang, C. T., & Fazal, M. A. (2010). Compatibility of elastomers in palm biodiesel. *Renewable Energy*, 35(10), 2356–2361.
11. Trakarnpruk, W., & Porntangjitlikit, S. (2008). Palm oil biodiesel synthesized with potassium loaded calcined hydrotalcite and effect of biodiesel blend on elastomer properties. *Renewable Energy*, 33(7), 1558–1563.
12. Rudbahs, R., & Smigins, R. (2014). Experimental research on biodiesel compatibility with fuel system elastomers. *Engineering for Rural Development*, 13, 278–282.
13. Terry, B. (2005). Impact of biodiesel on fuel system component durability. *Technical report CRC project no. AVFL-2a* (Vol. 44, pp. 1–149).
14. Chandran, D., Ng, H. K., Lau, H. L. N., Gan, S., & Choo, Y. M. (2016). Investigation of the effects of palm biodiesel dissolved oxygen and conductivity on metal corrosion and elastomer degradation under novel immersion method. *Applied Thermal Engineering*, 104, 294–308.
15. Chaudhari, J., & Patel, M. G. M. (2013). Experimental investigation on material compatibility of biodiesel fuel. *IJERT*, 6(1), 95–103.
16. Gurani, R., & Kurbet, S. N. (2018). Experimental investigation on compatibility of elastomeric materials with biodiesel. *International Journal of Engineering Research & Technology (IJERT) RDME*, 06(16)
17. Gurani, R., & Kurbet, S. N. (2018). Experimental investigation on IC engine using alternate fuels for material compatibility of piping and fitting system. *IOP Conference Series: Materials Science and Engineering, Vol. 376(1)*, 012004 (IOP Publishing).
18. Alves, S. M., Mello, V. S., & Medeiros, J. S. (2013). Palm and soybean biodiesel compatibility with fuel system elastomers. *Tribology International*, 65, 74–80.
19. Gurani, R., & Kurbet, S. N. (2021). A detailed experimental investigation on IC engine using alternate fuels for material compatibility of piping and fitting system. *Advanced Aspects of Engineering Research*, 5(2021), 111–117.
20. Haseeb, A., Masjuki, H. H., Ann, L. J., & Fazal, M. A. (2010). Corrosion characteristics of copper and leaded bronze in palm biodiesel. *Fuel Processing Technology*, 91(3), 329–334.
21. Geller, D. P., Adams, T. T., Goodrum, J. W., & Pendergrass, J. (2008). Storage stability of poultry fat and diesel fuel mixtures: Specific gravity and viscosity. *Fuel*, 87(1), 92–102.
22. L. Díaz-Ballote, López-Sansores, J. F., Maldonado-López, L., & Garfias-Mesias, L. F. (2009). Corrosion behavior of aluminum exposed to a biodiesel. *Electrochemistry Communications*, 11(1), 41–44.
23. Kamiński, J., & Kurzydłowski, K. J. (2008). Use of impedance spectroscopy to testing corrosion resistance of carbon steel and stainless steel in water-biodiesel configuration. *Journal of Corrosion Measurement*, 5, 35.
24. Fazal, M. A., Haseeb, A., & Masjuki, H. H. (2010). Comparative corrosive characteristics of petroleum diesel and palm biodiesel for automotive materials. *Fuel Processing Technology*, 91(10), 1308–1315.
25. Sgroi, M., Bollito, G., Saracco, G., & Specchia, S. (2005). BIOFEAT: Biodiesel fuel processor for a vehicle fuel cell auxiliary power unit: Study of the feed system. *Journal of Power Sources*, 149, 8–14.

26. Kaul, S., Saxena, R. C., Kumar, A., Negi, M. S., Bhatnagar, A. K., Goyal, H. B., & Gupta, A. K. (2007). Corrosion behavior of biodiesel from seed oils of Indian origin on diesel engine parts. *Fuel Processing Technology*, 88(3), 303–307. <https://doi.org/10.1016/j.fuproc.2006.10.011>
27. Maleque, M. A. (2000). Effect of mechanical factors on tribological properties of palm oil methyl ester blended lubricant. *Wear*, 239(1), 117–125.
28. Kalam, M. A., & Masjuki, H. H. (2002). Biodiesel from palmoilan analysis of its properties and potential. *Biomass and Bioenergy*, 23(6), 471–479.

Boosting Performance with the Integration of Stochastic Energy Storage into Hybrid Electric Vehicles



Dipti Tamboli, Mohan Thakre, and Pranali Thakre

Abstract Power Electronics includes power interface circuits and low-level switching functionality. A power and energy management system for a dual-source electric vehicle with lead-acid batteries and ultra-capacitors demonstrates this unique framework. Energy system macro models are verified with practical experiments to determine system configuration. Those metrics have been employed to design concepts to assess power and energy management to validate the conceptual platform. Deployment of the individual blocks that make up the system architecture focuses on power electronics infrastructure design. The design-implementation-oriented modular framework helps unify the energy's significant challenges.

Keywords SVPWM control · Energy storage system (ESS) · Electric vehicle (EV) · Distributed energy sources (DES) · Ultracapacitor (UC)

1 Introduction

Electric vehicle (EV) dependability and safety depend on battery state-of-health (SOH) supervision. SOH battery evaluation using Independent Component Analysis (ICA). For Grey Relational Analysis (GRA), entropy-weighted health indicators from partial incremental capacity curves were assessed [1]. The SOH battery has been evaluated using the grey connection between reference and comparative patterns [1, 2]. ICA and GRA has been assessed two identical batteries. GRA ordered referral sequences. The SOH model maximizes battery and Ultracapacitor (UC) SOH,

D. Tamboli (✉) · M. Thakre

Department of Electrical Engineering, SVERI, College of Engineering, Pandharpur, Solapur, MS, India

e-mail: datamboli26@gmail.com

P. Thakre

Department of Master of Computer Application, SVERI, College of Engineering, Pandharpur, Solapur, MS, India

weight, and cost, according to [3]. The author in [4] employed multi-objective optimization to find the ideal HESS size, for example, an electric car, to reduce ESS cost and maximize battery life. A SOH battery model quantifies how component sizing impacts battery life.

This study analysis has been performed in many non-isolated bidirectional, multi-level, and multipulse converter topologies [5–7], including the half-bridge, cuk, sepic/cuk, and sepic/Luo combined converters [8, 9]. Inductors place major role in the performance of the dc-dc converter. The author developed [10] covered batteries and the UC model in MATLAB simulation software. Peak current is supplied by the battery and UC. Energy source size, cost, and efficiency are crucial. UC cannot store much energy. Therefore, hybrid source operation with UC and the battery delivers adequate storage and peak current characteristics, decreasing energy management system size and cost [11].

The research was carried out in [12, 13] to build a HESS (battery) connected to a fraction via a dc-dc converter. The dc link switches the loading UC during peak. In the urban driving cycle dc-link, UC responses during propulsion system peak power and regenerative braking were dynamically linked. UC-based distributed energy sources (DES) with or without grid interaction hybrid system were studied, to improved transient and steady-state performance [14]. DES devices strengthen them, enabling them to quickly meet smart grid demands. In [15], the author designed dc microgrid-based charging and discharging, where a board-mounted bidirectional dc-dc converter regulates direct power flow from an EVs storage system to a microgrid and increases storage EV batteries and UCs system performance. Microgrids using renewable power sources would have specific battery and UC energy management concepts. The professional elaborated on the differences between low-frequency batteries and high-frequency UC power sources. When a multisource is linked to a dc connection, solar radiation can penetrate deeply [16–18].

Changing the design to accommodate greater voltages, such as those used by plug-in electric automobiles, is discussed in Sect. 2. In Sect. 3, we go over the criteria for choosing a time constant and the results of our analysis. In Sect. 4, we go through the prototype development of the proposed technique and its modes of operation, including a detailed flowchart, and in the last section, Sect. 5 provides the conclusion.

2 Methodology and Design Approach

Due to simplicity and precise parameter controllers, existing vehicles equipped with three-phase induction motors are now available in the market. As the operating voltage of the ac link is decided based on the propulsion motor's rating, the minimum system operating voltage is selected as 230 V. Transient currents will be caused because of the hybridization of sources [19]. UC has rapid dynamics with high power density; the heavy current will be taken from the battery during hybrid operation, which heavily affects the battery's life. This inrush current can be controlled by (a)

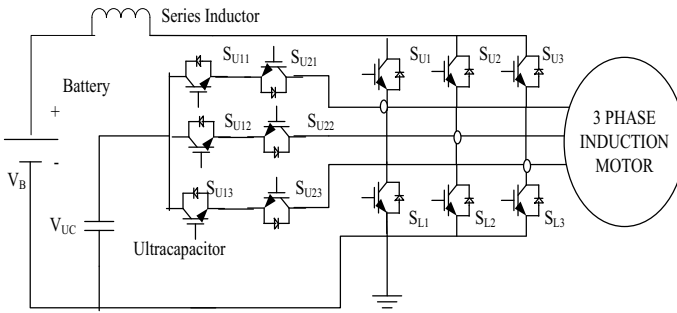
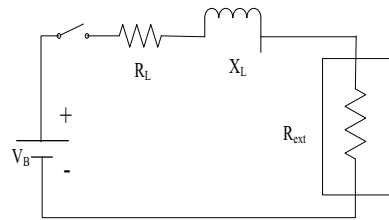


Fig. 1 Series inductor at the inverter output (dc side)

Fig. 2 Series inductor with load



inverter control utilizing pulse width modulation synchronized PI controllers having dc and ac elements and feedback controllers. (b) Using series inductor at inverter input (dc side) and (c) using series inductor at inverter output (dc side). Figure 1 shows the series inductor at the inverter output (dc side), such a method is simple and more effective as compared to another method that can be preferred for an open-loop system. Figure 2 describes an equivalent circuit of a series inductor with a load.

By applying KVL to the equivalent circuit using Eq. (1) and (2)

$$V_B - (R_{ext} + R_L)i(t) - V_L(t) = 0 \tag{1}$$

$$V_B = (R_{ext} + R_L)i(t) + L \frac{di(t)}{dt} = 0 \tag{2}$$

where V_B = Applied voltage, R_L = Resistance of coil, R_{ext} = Load resistance = $R_L + R_{ext}$

Using Eq. (3) to find the classical method solution of a standard first-order equation,

$$i(t) = i_n(t) + i_f(t) = A_1 e^{\alpha t} + A \tag{3}$$

$i_n(t)$ is a natural solution of the first-order differential equation.

$i_f(t)$ is a particular integral solution due to $f(t) = V_B$.

A provides a solution for a steady-state response and current growth with time is calculated by using Eq. (4)–(9)

$$\alpha = \frac{d}{dt} \tag{4}$$

Characteristic relation is

$$\begin{aligned} R + \alpha L &= 0 \\ \alpha &= -\frac{R}{L} \end{aligned} \tag{5}$$

At the final condition $t = \infty$

$$V_B = Ri_f(t) + L \frac{di_f(t)}{dt} \tag{6}$$

where $i_f(t) = A = \text{constant}$

$$\begin{aligned} V_B &= RA + L \frac{dA}{dt} \\ A &= \frac{V_B}{R} \end{aligned} \tag{7}$$

At $t = 0^-$ $i = 0$

$$\begin{aligned} i(0) &= i(0^-) = i(0^+) = A_1 + A \\ i(0) &= i(0^-) = i(0^+) = A_1 + A \\ A_1 &= -A = -\frac{V_B}{R} \end{aligned} \tag{8}$$

The current expression is

$$i(t) = -\frac{V_B}{R} \left[1 - e^{-\frac{R}{L}t} \right] \tag{9}$$

where $\tau = \frac{L}{R}$; The growth of current concerning time as shown in Table 1.

It is seen that as time rises, the growth of current also increases, at $t = \infty$ inductor current reaches 99.3% of its steady-state value, and the voltage across the load R_{ext} . Equations (10)–(12) are expressed as

$$V_{R_{ext}} = i(t)R_{ext} = \frac{V_B}{R} \left[1 - e^{-\frac{R}{L}t} \right] R_{ext} \tag{10}$$

The voltage across the coil is $V_L(t) = V_B - V_{R_{ext}}(t)$

Table 1 Current growth with time

Time in second (t)	Growth of current
$t = 0$	$i(0) = 0$
$t = \tau$	$i(\tau) = 0.632 * V_B/R$
$t = 2\tau$	$i(2\tau) = 0.865 * V_B/R$
$t = 3\tau$	$i(3\tau) = 0.950 * V_B/R$
$t = 4\tau$	$i(4\tau) = 0.982 * V_B/R$
$t = 5\tau$	$i(5\tau) = 0.992 * V_B/R$

$$V_L(t) = V_B - \frac{V_B}{R} (R_{ext}) \left[1 - e^{-\frac{R}{L}t} \right] \quad (11)$$

At $t = 0^- i(t) = i(0) \neq 0$

$$i(t) = \frac{V_B}{R} \left[1 - e^{-\frac{R}{L}t} \right] - \left[i_0 e^{-\frac{R}{L}t} \right] \quad (12)$$

3 Selection of Parameters

A steady voltage, the current through the inductor i_0 , is assumed to be zero. As time t increases, the current through the inductor increases as shown in Eq. (14). A smaller time constant gives a quick response to reach its steady state, whereas a larger time constant provides a slow response and required a longer time to reach a steady state. The time constant is given in Eq. (13) as

$$\tau = \frac{L}{R} \quad (13)$$

$$i(t) = \frac{V_B}{R} \left[1 - e^{-\frac{R}{L}t} \right] \quad (14)$$

During a sudden rise or fall in current, the inductor opposes the flow of current based on Lenz law and provides regulated current. During hybridization of UC with battery, series inductor limits the inrush current requirements of the UC taken from the battery.

4 Prototype Development

Improving the driving cycle of an EV, the suggested scheme integrates multiple dc voltage sources to enhance the transient performance acquired from the ESS. Thus, one has a parallel link that connects two dc sources, the battery as well as the UC.

The suggested topology's primary benefit is that it requires fewer components between the load (motor) and the source. Thus, authors achieve a better reaction to EVs by increasing power and energy supply to meet demand. With this concept, sources of the EVs are directly connected to the load without any additional boost/buck stage. Power density gets affected due to the inductor present in the dc-dc converter. In multisource dc/ac called an inverter, the inductor is eliminated. Also, the volume and weight of the converter are reduced. Overall efficiency, performance, and power density are improved using a simple architecture dc/ac inverter. Multisource inverter topology fundamentally connected with two different dc sources gives ac output with a single stage.

Power demands from the grid or an EVs acceleration, cruising, and braking are used to choose modes in a controller. In this case, source-sharing features under dynamic conditions of loading have been seen by selecting modes having open-loop monitoring. Here is now an overview of the circuit's control method, illustrated by a flowchart as shown in Fig. 3. The proposed method verifies the power/energy exchange under dynamic loads by having the batteries as well as UC drive the loads concurrently. The experiments are conducted for various modes of operation.

4.1 Modes of Operation

With hardware, the analogy is validated with different cases with combinations of modes. Figure 4 illustrate the power circuit of study system. The 3 modes of potential switching regions as described in the following section.

In mode 1: The IGBT valves S_{U1} , S_{U2} , and S_{U3} discharge the battery to power the RL load such as the motor, bypassing the need for a UC. During closed-loop control, valves S_{U21} , S_{U22} , and S_{U23} sense the I_L and V_i of the UC to charge the UC from the battery as seen in Fig. 5.

Mode-2: Valves S_{U1} , S_{U2} , S_{U3} , and S_{U11} , S_{U12} , S_{U13} allow the battery to feed the motor. While discharging UC as mode 2 circuitry operation is shown in Fig. 6.

The V_{LL} (V_{AB} , V_{BC} , V_{AC}) and V_{ph} (V_{AN} , V_{BN} , V_{CN}) are calculated by using Eq. (15) and (16).

$$\begin{aligned} V_{AB} &= V_{AN} - V_{BN} \\ V_{BC} &= V_{BN} - V_{CN} \\ V_{CA} &= V_{CN} - V_{AN} \end{aligned} \tag{15}$$

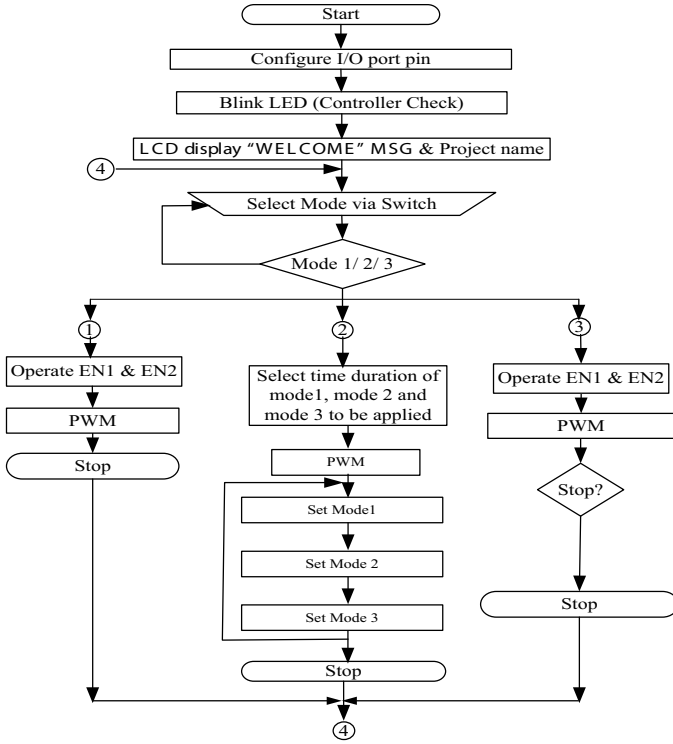
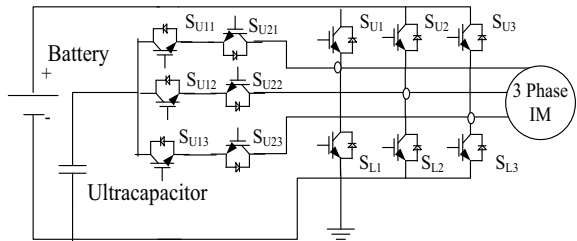


Fig. 3 Flowchart of proposed work

Fig. 4 Power circuit



$$\begin{bmatrix} V_{AN} \\ V_{BN} \\ V_{CA} \end{bmatrix} = \frac{1}{3} \begin{bmatrix} 2 & -1 & -1 \\ -1 & 2 & -1 \\ -1 & -1 & 2 \end{bmatrix} X \begin{bmatrix} V_{AO} \\ V_{Bo} \\ V_{Co} \end{bmatrix}. \tag{16}$$

From the Eq. (16), the voltages (V_{AO} , V_{Bo} , V_{Co}) can be derived as a function of the gate signal of the switches and dc bus voltage as given in Eq. (17).

$$V_{AO} = S_{U1} \cdot V_{dc1} + S_{U21} \cdot V_{dc2} - Z_a i_a$$

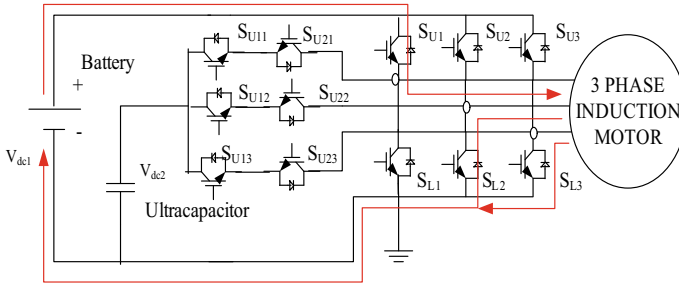


Fig. 5 Mode-1 circuitry operations

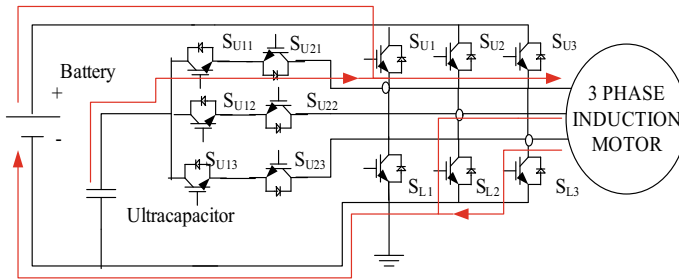


Fig. 6 Mode-2 circuitry operations

$$\begin{aligned}
 V_{BO} &= S_{U2} \cdot V_{dc1} + S_{U22} \cdot V_{dc2} - Z_b i_b \\
 V_{CO} &= S_{U3} \cdot V_{dc1} + S_{U23} \cdot V_{dc2} - Z_c i_c
 \end{aligned}
 \tag{17}$$

Z_k is the phase impedance of the load and S_{U1} , S_{U21} is the switching mechanism.

Mode 3: Valves S_{L1} , S_{L2} , S_{L3} , and S_{U11} , S_{U12} , and S_{U13} allow the UC to power the RL load (motor) without the battery shown in Fig. 7. Such a mode isolates the battery from the load.

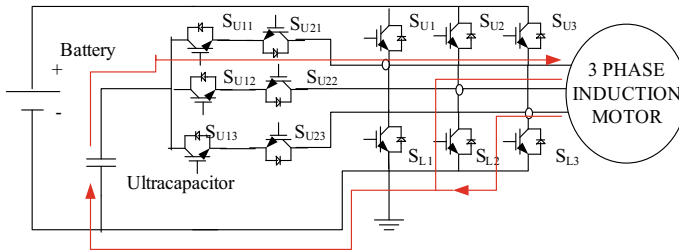


Fig. 7 Mode-3 circuitry operations

A buffer IC (74HC244) controls modes with such a regulated duty cycle utilizing the latch-enabled pulse. EN1 controls upper switches $S_{U1}-S_{U3}$. EN2 regulates S_{L1}, S_{L2}, S_{L3} , while EN1* and EN2* govern $S_{U11}, S_{U12}, S_{U13}$ as well as $S_{U21}, S_{U22}, S_{U23}$.

A latch-enabled signal digital zero (low state) permits latch output-input as shown in Fig. 8. Proteus software simulates. As can be seen from Fig. 9, the Space Vector Pulse-Width-Modulation (SVPWM) method is used to do the control switching.

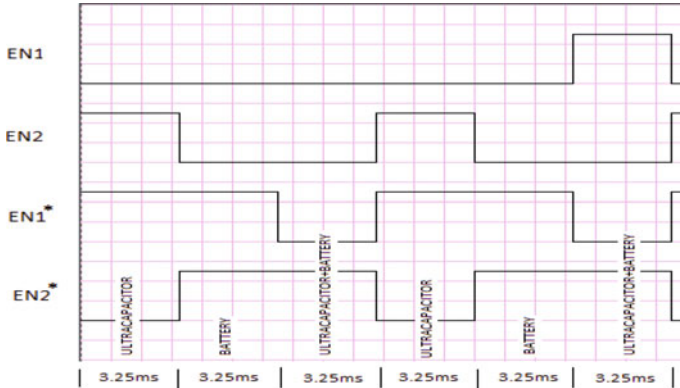


Fig. 8 Mode control using a buffer

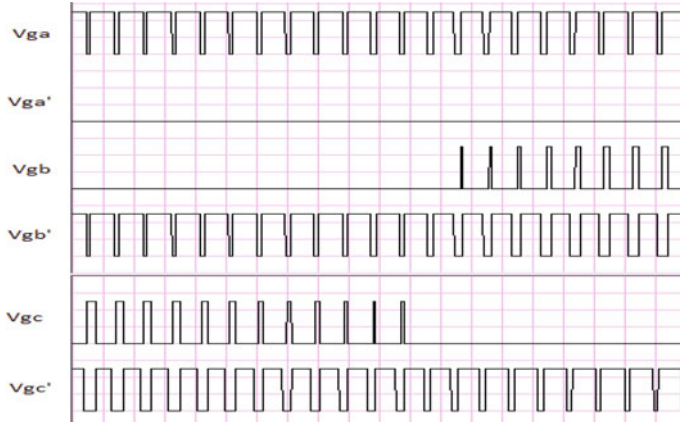


Fig. 9 SVPWM control signal generation in protease

5 Conclusion

A proposed model demonstrated a multi-source inverters structure. A power and energy management system for a dual-source electric vehicle with lead-acid batteries and UC demonstrated this unique framework. The outcome shows that multisource configuration increases driving range, reduces the average current by 27%. It also reduces size, improves thermos-stability, as well as extends energy storage systems' lifespan. Phase lock loop analysis and real-time control using the phasor measuring unit can be used to coordinate power exchange throughout the smart grid in a future study.

References

1. Cosgrove, D. (2017). Energy consumption in GCC countries. Power on, power up. In *4th IEEE international conference on engineering technologies and applied sciences (ICETAS)* (pp. 1–6). Salmabad, Bahrain. <https://doi.org/10.1109/ICETAS.2017.8277862>
2. Abubakr, H., Vasquez, J. C., Mahmoud, K., Darwish, M. M. F., & Guerrero, J. M. (2022). Comprehensive review on renewable energy sources in Egypt-current status, grid codes and future vision. *IEEE Access*, *10*, 4081–4101. <https://doi.org/10.1109/ACCESS.2022.3140385>
3. Mehrabani, A., & Mardani, H. (2022). Optimal energy management in smart home considering renewable energies, electric vehicle, and demand-side management. In *9th Iranian conference on renewable energy & distributed generation (ICREDG)* (pp. 1–5). Mashhad, Islamic Republic of Iran. <https://doi.org/10.1109/ICREDG54199.2022.9804525>
4. Thakre, M. P., & Kumar, N. (2022). Design, development, and simulation modeling of hybrid electric vehicles incorporating with BLDC Drive. In *Planning of hybrid renewable energy systems, electric vehicles and microgrid. Energy systems in electrical engineering*. Springer, Singapore. https://doi.org/10.1007/978-981-19-0979-5_20
5. Jha, R. R., & Dubey, A. (2020). Distributed algorithm for Volt-VAr optimization in unbalanced distribution system. In *IEEE power & energy society innovative smart grid technologies conference (ISGT)* (pp. 1–5). Washington, DC, USA. <https://doi.org/10.1109/ISGT45199.2020.9087698>
6. Thakre, M. P., & Gaidhani, T. S. (2019). VSC-HVDC bipolar grid based on novel distance protection scheme. *International Journal of Recent Technology and Engineering (IJRTE)*, *8.3*, 1527–1532.
7. Zhang, Y., Wang, X., Wang, J., & Zhang, Y. (2021). Deep reinforcement learning based volt-VAR optimization in smart distribution systems. *IEEE Transaction on Smart Grid*, *12*(1), 361–371. <https://doi.org/10.1109/TSG.2020.3010130>
8. Li, X., & Wang, S. (2021). Energy management and operational control methods for grid battery energy storage systems. *CSEE Journal of Power and Energy Systems*, *7*(5), 1026–1040. <https://doi.org/10.17775/CSEEJPES.2019.00160>
9. Mohan, T., & Kumar, N. (2021). Evaluation & control propoective of VSM based Multilevel STATCOM for distributed energy systems. *MAPAN Journal of Metrology Society of India* (Springer). <https://doi.org/10.1007/s12647-021-00481-x>
10. Asuhaimi, F. A., Nadas, J. P. B., & Imran, M. A. (2017). Delay-optimal mode selection in device-to-device communications for smart grid. *IEEE International conference on smart grid communications Dresden, Germany* (pp. 26–31). <https://doi.org/10.1109/SmartGridcomm.2017.8340710>

11. Sendin, A., & Matanza, J. (2021). *Smart grid applications and services. Smart grid telecommunications: Fundamentals and technologies in the 5G era* (pp.137–177). IEEE. <https://doi.org/10.1002/9781119755401.ch5>
12. Thakre, M. P., & Matala, N. P. (2020). Alleviation of voltage sag-swell by DVR Based on SVPWM Technique. *International conference on power, energy, control and transmission systems (ICPECTS)* (pp. 1–6). Chennai, India. <https://doi.org/10.1109/ICPECTS49113.2020.9336972>
13. Ostadi, A., & Kazerani, M. (2015). A comparative analysis of optimal sizing of battery-only, ultracapacitor-only, and battery-ultracapacitor hybrid energy storage systems for a city bus. *IEEE Transaction on Vehicular Technology*, 64(10), 4449–4460. <https://doi.org/10.1109/TVT.2014.2371912>
14. Chen, B., Chen, L., Tan, Y., & Kuang, X. (2021). Investigations on communication and management techniques for electric internet of things applications in smart grid. In *China international conference on electricity distribution (CICED)* (pp. 515–518). Shanghai, China. <https://doi.org/10.1109/CICED50259.2021.9556838>
15. Dusmez, S., & Khaligh, A. (2014). A supervisory power-splitting approach for a new ultracapacitor-battery vehicle deploying two propulsion machines. *IEEE Transaction on Industrial Informatics*, 10(3), 1960–1971. <https://doi.org/10.1109/TII.2014.2299237>
16. Guntuk, V. S., & Bakle, U. V. (2019). A novel 4-level converter for switched reluctance motor drive in plug-in HEVs. In *International conference on intelligent computing and control systems (ICCS)* (pp. 626–631). Madurai, India. <https://doi.org/10.1109/ICCS45141.2019.9065527>
17. Bhatt, J., Jani, O., & Harish, V. S. K. V. (2021). Wireless communication technologies for Indian smart grid: Fitness evaluation and optimal decision-making. In *9th IEEE international conference on power systems (ICPS)* (pp. 1–6). <https://doi.org/10.1109/ICPS52420.2021.9670197>
18. Thakre, M. P., & Borse, P. S. (2020). Analytical evaluation of FOC and DTC induction motor drives in three levels and five levels diode clamped inverter. In *International conference on power, energy, control and transmission systems (ICPECTS)* (pp. 1–6). <https://doi.org/10.1109/ICPECTS49113.2020.9337015>
19. Chowdhary, P. K. (2020). MMC based SRM drives for hybrid EV with decentralized BESS. In *4th international conference on electronics, communication and aerospace technology (ICECA)* (pp. 319–325). Coimbatore, India. <https://doi.org/10.1109/ICECA49313.2020.9297508>

Implications of Multiple Energy Source Integration for Electric Mobility



Dipti Tamboli, Mohan Thakre, and Pranali Thakre

Abstract This article optimizes electric mobility energy sources for power and energy. An electric vehicle installation cloud powers the smart grid. Energy storage devices can extend the EV driving range. Manage energy and power expenditures, proportionate distribution, and energy sector interfacing controls to meet driving cycle needs. This study provides a new electric vehicle (EV) power and energy optimization method for all demands. Energy management principles underpin the solution. Driving requires long-term and short-term energy. Power Management operations make immediate power-splitting ratio decisions among several energy sources, while a smart energy layer makes long-term energy usage judgments based on longitudinal vehicle dynamics. This interdisciplinary challenge can be addressed systematically using the offered strategy.

Keywords Electric vehicle (EV) · MATLAB and PSIM software · Remaining useful life (RUL) · SVPWM control · Ultracapacitor (UC)

1 Introduction

Concerns about the safety of electric vehicles are exacerbated by design at the core of EVs, which utilize various strategies for energy storage, power distribution, and exchange. Concerned with finding methods to go beyond the cost–benefit thresholds of competing energy sources to meet the needs of various vehicle propulsion load and weight profiles. Several types of energy storage devices can exploit crucial features of perfect systems when used in concert. However, these energy storage devices necessitate controlled power distribution from many energy storage sources to a single

D. Tamboli (✉) · M. Thakre

Department of Electrical Engineering, SVERI, College of Engineering, Pandharpur, Solapur, MS, India

e-mail: datamboli26@gmail.com

P. Thakre

Department of Master of Computer Application, SVERI, College of Engineering, Pandharpur, Solapur, MS, India

load. Famous authors' electric vehicle objectives inspired the study. Zhao [1] created a hybrid Remaining Useful Life (RUL) prediction model using Long Short-Term Memory (LSTM) and Elman neural networks to track long-term battery degradation with more significant cycle numbers and short-term capacity recovery at certain cycles. Considering the heat manufacturing system and thermal battery characteristics, the author analyzed [2], lithium-ion battery thermal safety issues, including thermodynamic behaviour, thermal runaway modeling, and battery pack security management regulations. Thermal runaway avoidance requires heat, electrical, and mechanical model additives in several material refining engineering methods. Hybrid Energy Storage System (HESS) optimization for RUL estimation. During propulsion system transient load demands, peak current demands reduce system quality and safety [3].

The authors [4–7] focused on a hybrid electric car with a fuel cell and battery source connected by dc-dc or dc-ac power electronics converters to control power exchange between source and load according to the current requirements. The operation of the Ultracapacitor (UC) and battery power management with an improved hybrid power storage system have been explained [8, 9]. Dc-dc converters manage power exchange with different topologies. Two bidirectional input converters provide the best performance and flexibility. Passive control estimates future driving patterns to triple battery power. EV propulsion capacity and combining two or more energy storage devices to provide better power sources can increase it been discussed [10]. Batteries or fuel cell-connected UCs have excellent power density, low cost, and extended life. In [9], closed-loop control of dc-dc bidirectional converters is utilized for simple dynamics, reasonable regulation, reduced Electromagnetic Interference (EMI), low source current ripple, and easy control with bidirectional power flow. Many authors discussed [11, 12] hybrid EV range extenders. HEVs should use fuel-based or renewable range extenders. Through a dc-dc converter, solar arrays extend their range.

Introduced the concept of EV using a combination of several energy sources. Multiple battery, UC, and PV panel usage situations were analyzed and compared [13, 14]. It has been discovered that urban use necessitates the hybridization of sources, which can be tailored to meet individual client requirements. Long-term goals (specific energy demand) and short-term goals (specific power demand) from the load inform energy management activities [15]. Hybridization extends the ESS's helpful life, stops thermal runaway, keeps people healthy, and minimizes the system's footprint. These improvements to battery life and EVs' driving cycle reduce the system's overall cost. The literature supports the recommendation of a hybrid source inverter-based system over the conventional one. A new perspective and increased storage system efficiency are discussed in this research, which provides a framework for studying power and energy management. This article summarizes the findings of a study on EV workforce and energy management.

Section 2 delves into the hybrid electric vehicle, its classification, and the new HEV technology. Section 3, explains the different strategies of HEVs and the reliability of EVs for transportation, as well as the performance of the ESS. The comparison of energy storage systems is explained in Sect. 4. Section 5 proposes Parallel HEV

(PHEV) as an active power source, and Sect. 6 presents simulation results and a detailed discussion followed by the conclusion.

2 Hybrid Electric Vehicle (HEV)

A subset of these vehicles, called “battery EVs,” gets their energy from an electrical source. HEVs, on the other hand, can run on various types of power, including those from an ICE, a fuel cell, or sustainable sources [16]. Again, HEV is classified into two types.

2.1 Series and Parallel HEV

In series HEV, driving is obtained with the electric motor alone, which is faded by different energy sources, e.g., battery, engine-driven generator, etc., through the converter. Figure 1 shows the block diagram of the series HEV. The converter provides electric control to the electric propulsion motor.

Parallel HEV (PHEV) is shown in Fig. 2; it consists of a battery-sourced electric motor and engine as a mechanical driving system. In such a system, the motor is used as a driving system along with the engine.

For momentary load, the battery acts as an energy buffer. Plug-in pure EV, in contrast to HEV, can indeed be charged from an external source, such as a charging station or a standard household electrical outlet. In a smart-grid environment, where PHEVs are feasible, the EVs ESS can function as either a sink or a source when interacting with the electric grid [17].

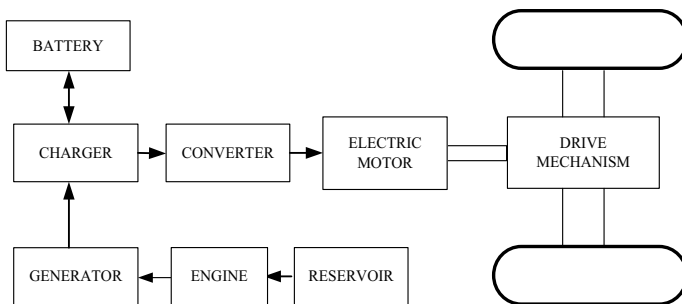


Fig. 1 Series HEV

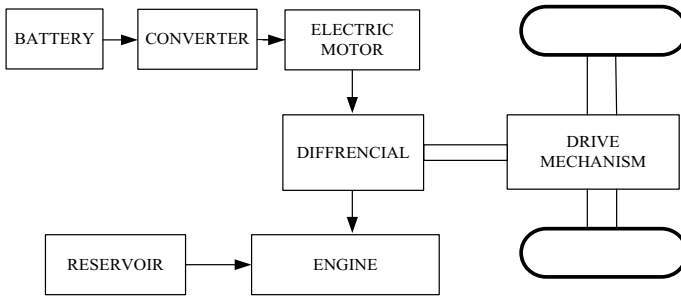


Fig. 2 Parallel HEV

2.2 HEV Technology

A battery, fuel cell, UC, or PHEV could provide electricity to the grid through V2G power while parked and/or idle.

In extreme crises, such as a significant decline in oil supplies or a sudden surge in oil costs, cars might benefit from the utility reserve’s stored or underutilized energy in use at night or off-peak times. Compared to internal combustion engine cars, electric propulsion systems are about 70% efficient; a first-generation plug-in hybrid, for example, can go only around 3–4 miles/kWh. Each PHEV will have an onboard control and metering system and a control or logical link required for interaction with the grid operator. Power transfers from generators to end customers throughout the grid while reversing good energy flow from the PHEV to the electrical grid. The idea of a PHEV is described in Fig. 3 as an interconnection of PHEV with smart grids.

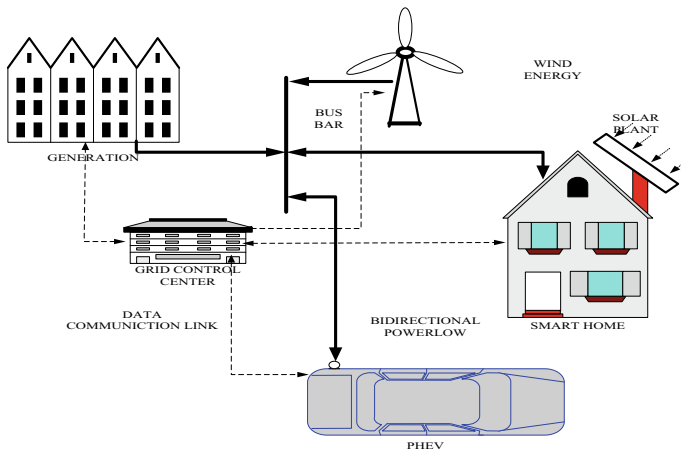


Fig. 3 Interconnected smart grids

3 Strategies of Hybrid Energy Sources

The reliability of EVs for transportation depends upon the performance of the ESS. Although significant developments have been done in the last twenty years in the ESS, progress is ongoing in the EVs. The lead-acid battery, Nickel Cadmium (Ni–Cd), Nickel Metal Hydride (Ni MH), Zebra battery, lithium polymer/ion, and Nitrium nickel chloride are most widely used in an EV.

There are various compromises to be made among several criteria. For example, the lead-acid battery provides the value of low price and elevated specific power but the demerits of comparatively short cycle life, heavyweight, and low specific energy, whereas the nickel-metal hydride battery has relatively high particular energy but is very expensive [18]. All batteries generally compromise between particular power, particular energy, weight, and price. For contemporary EVs, lithium-based batteries such as lithium-ion and lithium-polymer have excellent opportunities. On the other side, emerging sources of energy, including UC, provide promising features required by the load. EVs are driven by a battery. Reusable (secondary) batteries have commonplace in automobiles.

Metal air batteries provide elevated specific energy due to the oxygen in the air surrounding the cathode. NiCd, nickel-metal hydride, lithium-ion, Li-ion polymer, and less frequently used zinc-air and molten-salt batteries are included in the EVs battery. Due to their elevated energy-to-weight ratio, modern electric cars are fitted with lithium-ion and lithium-polymer batteries. Ampere hours are used to measure the amount of energy stored in batteries. The battery makes up for the high cost of EVs. The optimum sizing of an ESS can reduce EV costs. With a new era, batteries are used with high power density sources called hybridization of ESS. With the advancement in ESS in 2018, a few electric cars cross the driving range of 500 km (the Tesla Model S) but are in the luxury segment [19]. Compared to the cost of fossil fuel-based vehicles, the price of electricity to operate an EV is a tiny fraction, validating greater energy effectiveness. Popularly used batteries for EVs are lead acid, Nickel metal hydride, Zebra (Sodium Battery), Lithium-ion, and UC, also known as a supercapacitor (SC).

4 Comparative Analysis of Energy Sources

A comparative assessment is performed as a case study that can clarify the efficacy of source hybridization. Based on the maximum power demands of an EV propulsion scheme, an ESS is designed. A conventional energy storage scheme comprises batteries that supply peak power requirements as well as energy requirements. The Ragone plot provides an understanding of the power and energy densities of different sources. Some researchers [18] used three cases (i) a battery, (ii) an UC, and (iii) combined the two sources, to perform a comparative analysis. In the entire driving cycle, peak energy requirements are regarded to be 20%. Consider the total energy

requirement of an EV with 150 kW, from which 120 kW is the average energy requirement and 30 kW is the highest energy requirement.

A single-source battery-based power storage system is intended for 150 kW, making the system voluminous (100 kg). According to the specifications document with Ragone plot, a UC's peak power consumption approves ultimately 6800 W/kg, although its energy rating is rather small (4.1 Wh/kg), hence a single UC (22.05 kg) cannot supply a vehicle's continuous energy demands. As a solution, a combination of batteries and UC gives fruitful results for any driving requirement. To put it another way, an UC can store and release a significant amount of energy at 6800 W/kg (but only 4.1 Wh/kg of energy). This effectively minimizes the average W/kg of the system by downplaying the cost, weight, and lifespan while simultaneously improving vehicle performance due to swift UC dynamics [12]. The weight and price of the new hybrid ESS were reduced by 15.59% and 15.53%, respectively [19]. The use of UC leads to maintenance and replacement cost savings.

4.1 Modeling of Ultra-Capacitor (UC)

UC is modelled based on usable energy that can transfer by UC. The power capacity of the UC is decided from the driving cycle requirement during peak power (fast discharging). The fundamental equations of capacitors are present, Eq. (1).

$$i = C \frac{dv}{dt} \text{ and } E = \frac{1}{2} CV^2 \quad (1)$$

The magnitude of voltages decays over time scale is given by Eq. (2)

$$E|_k^{k+1} = \frac{1}{2} C (V_k^2 - V_{k+1}^2) \quad (2)$$

Usable energy depends on the voltage discharge ratio i.e.

$$V_{dr} = \frac{V_{min}}{V_{max}} * 100 \quad (3)$$

Usable energy derived as per Eq. (4),

$$E_u = \frac{1}{2} CV_{max}^2 - \frac{1}{2} CV_{min}^2 = \frac{1}{2} CV_{max}^2 \left(1 - \left(\frac{V_{dr}}{100} \right)^2 \right) \quad (4)$$

Total usable energy for n number of UCs is given in Eq. (5)

$$E_T = nE_u = \frac{1}{2} nCV_{max}^2 \left(1 - \left(\frac{V_{dr}}{100} \right)^2 \right) \quad (5)$$

The number of UCs (n) is calculated by the Eq. (7)

$$n = \frac{2E_T}{CV_{max}^2 \left(1 - \left(\frac{V_{dr}}{100}\right)^2\right)} \quad (6)$$

Battery and UC are characterized as per the electrical load requirements. Different sources are available with power and energy densities. Penetration of a source with a high power density and a source with optimum energy density extends the driving range of vehicles with a great reduction in the weight and cost of the energy storage system.

5 Proposed Works

The ESS has two inverters-batteries, and UC is connected to the sources. A multi-source inverter connects the battery and UC to the three-phase ac connection (smart grid) for controlling electrical behavior with Space Vector Pulse-Width-Modulation (SVPWM) technique. When idle, sources sink or inject power into the smart grid, and the HES system links to the load during propulsion without a dc-dc converter. Eliminating dc-dc converters makes ESS compact and cheaper. Peak load current determines battery life. Integrating the UC into a battery meets these peak necessities. The advantages of this new topology of the battery/UC have reduced the size and thus the general price of the ESS, together with enhanced system life, effectiveness, and endurance. The HESS model was thoroughly researched and evaluated using a simulation based on the PSIM environment, whose results are discussed below.

6 Simulation Finding

To comprehend the UC charging/discharging features and electrical behavior, a simulation is conducted in MATLAB and PSIM environments. The proposed innovative inverter is coupled to an ac connection in the PSIM model of an ac load such as an induction motor. Figure 4 shows the inverter output of voltage and current.

The battery supply voltage is 24 V and is connected to inverter-1, and the UC rating is 300 F, 24 V, and is connected to inverter-2. The simulation illustrates how the battery as well as UC divides up the workload when the load fluctuates in real-time. Figure 5 mentions reference versus calculated active and reactive power.

In propose configuration, the UC is used instead of the battery to power the motor. In such a mode, the ultra-power-sharing capacitor's dynamics are rapid. When connecting a motor, an UC can be used as a variable power source. During hybrid source operation, power is distributed in a way that can be characterized as in Fig. 6.

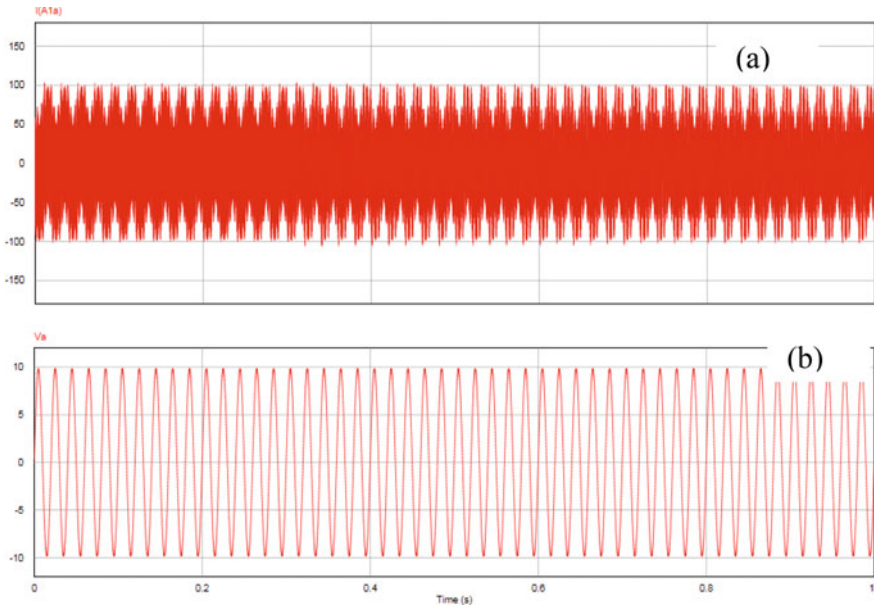


Fig. 4 The inverter output **a** inverter current and **b** inverter voltage

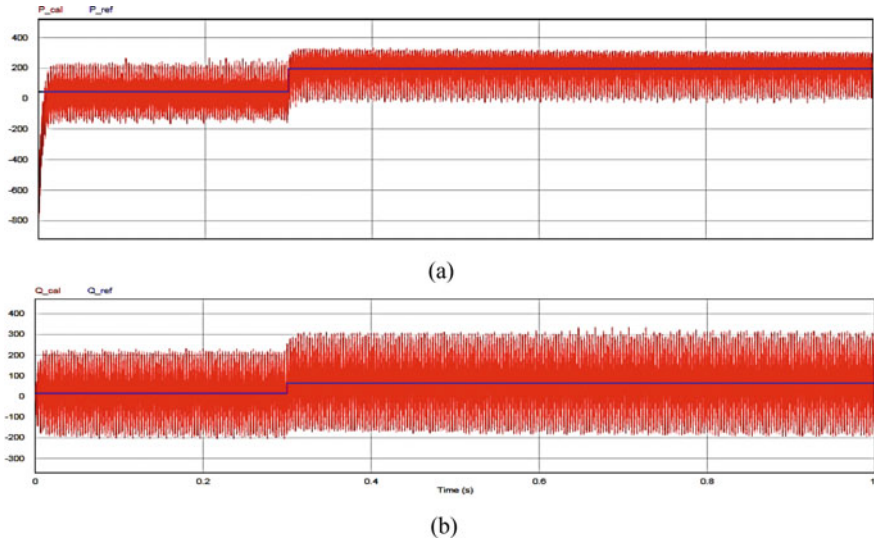


Fig. 5 Reference versus calculated **a** active and **b** reactive power

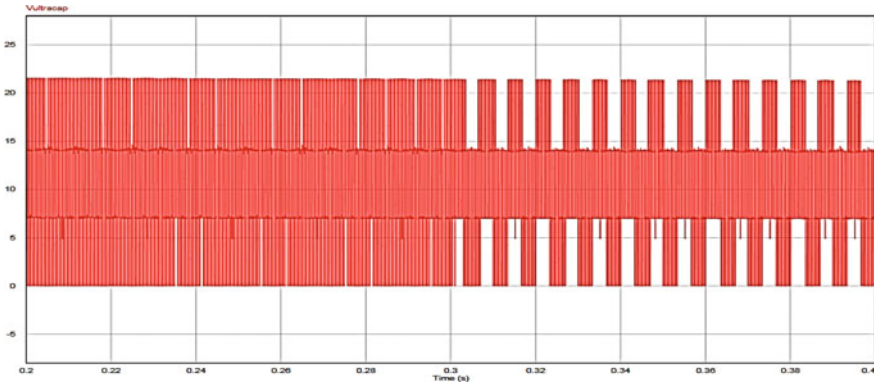


Fig. 6 UC terminal voltage [the voltage drop indicates power infusion by UC (at 0.3 s)]

At 0.3 s, a change in the load reference initiates the UC and battery-shared dynamic power delivery.

This mode minimizes battery stress with such a UC, according to simulations. A modest experiment combining a battery and UC operated by a unique hybrid category inverter validates a hybrid source inverter based on battery management energy management storage system.

7 Conclusion

The said investigation suggested a multisource multilevel inverter. Such structure eliminates steps between the grid/motor and energy storage systems, which is its main benefit. Innovative multi-source interface improves system load requirement fulfilment and electric vehicle economy. Multisource inverters provide smoother current exchange and lower overall currents. However, the batteries could directly control the load via boost operation like a dc-dc conversion, decreasing the converter’s size and expense and enhancing ESS effectiveness. An SVPWM-based controlling method allows active power and energy exchange across various resources during dynamic load requirements of driving conditions, improving load power consistency in the induction motor/power system.

References

1. Zhao, G., Li, S., Li, Y., Duan, B., Shang, Y., & Zhang, C. (2021). Capacity prediction and remaining useful life diagnosis of lithium-ion batteries using CNN-LSTM hybrid neural network. In *2021 China automation congress (CAC), Beijing, China* (pp. 2179–2183). <https://doi.org/10.1109/CAC53003.2021.9727496>

2. Zhou, Y., Li, H.-X., & Xie, S.-L. (2022). Space-decomposition-based spectral modeling for distributed battery thermal dynamics. *IEEE Transaction on Transportation Electrification*, 8(2), 1634–1641. <https://doi.org/10.1109/TTE.2021.3124894>
3. Chiodo, E., De Falco, P., & Di Noia, L. P. (2022). Probabilistic modeling of li-ion battery remaining useful life. In *IEEE transaction on industry applications* (Vol. 58, no. 4, pp. 5214–5226). <https://doi.org/10.1109/TIA.2022.3170525>
4. Hadke, V. V., & Thakre, M. P. (2019). Integrated multilevel converter topology for speed control of SRM drive in plug in-hybrid electric vehicle. In *3rd international Conference on trends in electronics and informatics (ICOEI)* (pp. 1013–1018). Tirunelveli, India. <https://doi.org/10.1109/ICOEI.2019.8862524>
5. Ponnaluri, S., Linhofer, G. O., Steinke, J. K., & Steimer, P. K. (2005). Comparison of single and two stage topologies for interface of BESS or fuel cell system using the ABB standard power electronics building blocks. In *2005 European conference on power electronics and applications* (p. 9). Dresden, Germany. <https://doi.org/10.1109/EPE.2005.2195202>
6. Chowdhary, P. K., & Thakre, M. P. (2020). MMC based SRM drives for hybrid EV with decentralized BESS. In *4th international conference on electronics, communication and aerospace technology (ICECA)* (pp. 319–325). Coimbatore, India. <https://doi.org/10.1109/ICECA49313.2020.9297508>
7. Umre, B. S., Junghare, A. S., et al. (2016). Fractional-order PI based STATCOM and UPFC controller to diminish subsynchronous resonance. *Springerplus*, 5, 1599. <https://doi.org/10.1186/s40064-016-2727-y>
8. Passalacqua, M., & Lanzarotto, D. (2019). Fuel economy and EMS for a series hybrid vehicle based on supercapacitor storage. *IEEE Transactions on Power Electronics*, 34(10), 9966–9977. <https://doi.org/10.1109/TPEL.2019.2895209>
9. Buticchi, G., Costa, L., & Liserre, M. (2017). DC/DC conversion solutions to enable smart-grid behavior in the aircraft electrical power distribution system. In *IECON 2017—43rd annual conference of the IEEE industrial electronics society* (pp. 4369–4374). Beijing, China. <https://doi.org/10.1109/IECON.2017.8216752>
10. Thakre, M., & Kale, V. (2015). Study and mitigation of subsynchronous oscillations with SSC Based SSSC. *Journal of Power and Energy Engineering*, 3, 33–43. <https://doi.org/10.4236/jpee.2015.39003>
11. Kumar, B. V., Singh, R. K., & Mahanty, R. (2016). A modified non-isolated bidirectional DC-DC converter for EV/HEV's traction drive systems. In *IEEE international conference on power electronics, drives and energy systems (PEDES)* (pp. 1–6). Trivandrum, India. <https://doi.org/10.1109/PEDES.2016.7914345>
12. Kaneko, T., Nomura, A., Yang, W., Daisho Y., Kamiya Y., Sawada N., Yasukawa M., Takekoshi F., & Tsushima R. (2013). Optimization of engine control methods for range extender-type plug-in hybrid vehicles. In *2013 world electric vehicle symposium and exhibition (EVS27)* (pp. 1–8). Barcelona, Spain. <https://doi.org/10.1109/EVS.2013.6914827>
13. Mane, J. A. (2021). Significant affect of EV charging on grid with renewable technologies (May 25, 2021). In *Proceedings of the international conference on smart data intelligence (ICSMDI 2021)*, <https://ssrn.com/abstract=3852716> or <https://doi.org/10.2139/ssrn.3852716>
14. Sakamoto, S., Okada, A., Sasaki, K., & Kato, T. (2022). Study on power source properties suitable for volume minimization in electric vehicle hybrid power-source system. In *2022 international power electronics conference (IPEC-Himeji 2022- ECCE Asia)* (pp. 1935–1939). Himeji, Japan. <https://doi.org/10.23919/IPEC-Himeji2022-ECCE53331.2022.9807043>
15. López-Ibarra, J. A., Lucu, M., Goitia-Zabaleta, N., Gaztañaga, H., Herrera, V. I., & Camblong, H. (2019). Battery aging conscious intelligent energy management strategy for hybrid electric buses. In *2019 fourteenth international conference on ecological vehicles and renewable energies (EVER)* (pp. 1–7). Monte-Carlo, Monaco. <https://doi.org/10.1109/EVER.2019.8813567>
16. Shahverdi, M., Mazzola, M. S., Grice, Q., & Doude, M. (2017). Bandwidth-based control strategy for a series HEV With light energy storage system. *IEEE Transaction on Vehicular Technology*, 66(2), 1040–1052. <https://doi.org/10.1109/TVT.2016.2559949>

17. Shahverdi, M., Mazzola, M. S., Grice, Q., & Doude, M. (2016). Pareto front of energy storage size and series HEV fuel economy using bandwidth-based control strategy. *IEEE Transaction on Transportation Electrification*, 2(1), 36–51. <https://doi.org/10.1109/TTE.2015.2508000>
18. Jawad, A., Nahid-Al-Masood, & Munim, S. (2021). Optimal sizing of BESS for attaining frequency stability under high PV penetration. In *International conference on technology and policy in energy and electric power (ICT-PEP)* (pp. 348–353). Jakarta, Indonesia. <https://doi.org/10.1109/ICT-PEP53949.2021.9601074>
19. Laghari, G. F., Umar, A., & Abdullah, S. (2015). Comparative analysis of multi-input DC/DC converter topology for hybrid renewable energy systems. In *Power generation system and renewable energy technologies (PGSRET)* (pp. 1–5). Islamabad. <https://doi.org/10.1109/PGSRET.2015.7312254>

Advances in Pharmacy, Nutraceuticals and Traditional Medicines

Design, In Vitro Evaluation of Sustained Release Matrix Tablet of Enalapril Maleate Employing Natural Polymer-Olibanum Gum and Its Resin Component



Pravin B. Awate, Mahesh K. Gupta, Dipak P. Kardile, Vishwas C. Bhagat, and Rajkumar V. Shete

Abstract In order to offer a sustained release of tablets containing Enalapril Maleate by employing olibanum gum were tested as matrix components that could control release rate. Enalapril was chosen due to its short half-life and limited oral bioavailability (41%). In order to confirm the chemical interaction between drugs and polymers, FTIR and DSC investigation was conducted. Matrix tablet of Enalapril Maleate was formulated using varied concentrations of HPMC K 100 M, olibanum, its resin, and its carbohydrate component. The tablet was evaluated for pre- and post-compression studies. Within low concentrations ranging from one to 2% w/w, the resinous component of olibanum and olibanum gum has a retarding effect on release rate of drug from matrix tablets. Enalapril Maleate was released slowly and systematically over a period of more than 24 h by Enalapril Maleate matrix tablets formulated with olibanum and its resin component. Release rate and % polymer relation was found to be linear in each case. Enalapril Maleate matrix tablet exhibited good controlled release characteristics and found suitable for once, a day oral controlled release products.

Keywords Enalapril Maleate · Matrix tablet · Olibanum gum and its resin and carbohydrate fraction

P. B. Awate (✉) · M. K. Gupta
School of Pharmacy, Career Point University, Kota, Rajasthan, India
e-mail: kumarawate007@gmail.com

D. P. Kardile · V. C. Bhagat · R. V. Shete
Department of Pharmaceutics, Rajgad Dnyanpeeth's College of Pharmacy Bhor, Pune, MS, India

1 Introduction

Oral drug delivery is one of the preferred popular drug delivery, especially compared to parenteral. The goal of oral drug products is to gradually release the active ingredient over an extended period after administration. These products offer notable advantages over conventional orally administered products, including a reduction in side effects, an increase in safety, and an improvement in patient compliance through decreased dosing and drug plasma concentration variations [1, 2].

It is simple to formulate dosage forms for sustain release by using a matrix system of various control release excipients, such as hydrophilic polymers like HPMC, insoluble gum, and waxes, which are employed as matrix-forming elements in solid dosage forms (to prolong the release of pharmaceuticals) [3].

As a hydrophilic matrix forming, HPMC has been widely used to create oral controlled-release dosage forms for a variety of medicines. Its non-toxic properties, minimal influence of processing factors on drug release, relief from compression, ability to accommodate high levels of drug loading, and propensity to swell upon jellification when in contact with water are all factors that contribute to the polymer's reputation [4, 5].

Due of their benefits over synthetic materials, polymers are increasingly being used by researchers. Olibanum is a gum resin made from the *Boswellia serrata*, Roxburgh, and other *Boswellia* species. It is made up of gum (30–36%), acid resin (50–60%), and volatile oil (2–8%). The resin is mostly composed of resin acids (boswellic acid and olibanoresine in equal amounts) [6–8].

Enalapril Maleate is the salt form of the drug. It is used to treat hypertension and functions as an ACE inhibitor on the Renin–Angiotensin–Aldosterone pathway. In contrast to ethanol and methanol, where it is easily soluble, it is sparingly soluble in water. Therefore, when administered in the customary manner, the clinically appropriate sustained release dose form of Enalapril Maleate manufactured using traditional technology will not meet the needs of the patient [4].

Enalapril Maleate sustained-release tablets provide stable plasma concentration with fewer repeated administrations and, to a limited extent, lessen side effects. This might increase patient compliance and secure administration. In order to determine how well olibanum gum and olibanum resin HPMC K100 support the sustained release of Enalapril Maleate from the matrix system, the goal of the current study was to evaluate their strengths. The effect of type of polymer and its concentration on the pattern of Enalapril Maleate release was also assessed.

2 Materials and Method

Enalapril Maleate was obtained as a gift sample from Wockhardt, Pvt. Ltd, Aurangabad. olibanum gum was purchased from Girijan co-operative society, Vishakapatnam (AP), HPMC K 100 M from Goa Antibiotics, Pvt. Ltd, Goa, PVP

K 30 from Balaji Amines, Solapur, Micro crystalline cellulose from Yogi Chem. Mumbai, and Magnesium stearate, Talc, Sodium Hydroxide (NaOH), Potassium dihydrogen phosphate (PDP), Petroleum Ether, Methanol, and Conc. HCl purchased from Loba Chem. Pvt. Ltd, Mumbai.

2.1 Formulation of Enalapril Maleate Matrix Tablet

In the current study, Enalapril Maleate matrix tablets were made using the direct compression method, and the following polymers were employed [4, 13]: Hydrophilic swellable polymer, HPMC K100M. olibanum gum, olibanum resin, carbohydrate fraction.

2.2 Methodology for Isolation of Olibanum Resin and Carbohydrate Fraction [6–9]

Olibanum powder (10 gm) was repeatedly extracted using solvent ether in amounts ranging from 4 × 50 ml. To obtain the resin fraction, the ether extracts were collected on a porcelain dish and dried out at 40 °C. The dry bulk was ground into a powder and then sieved through a 200-mesh screen. Following ether extraction of the resin, the carbohydrate fraction was recovered, dried at 60 °C for 4 h, and the size was decreased to 200 mesh.

2.3 Procedure for Preparation of Matrix Tablets [6–8]

The composition was chosen taking into account the drug-polymer ratio. The weights of each item were precise. A sieve no. 60 was used to filter the corresponding particles (drug, polymer, and additives). In a polythene bag, the desired amounts of the previously weighed medication, polymer, and diluent were combined, transferred these blend for compression to cadmach tablet punching machine (Table 1).

2.4 Pre-formulation Studies

Physical characteristics: The substance was identified by visual inspection based on its color, texture, odor, and other physical properties.

Table 1 Formulation chart of Enalapril Maleate matrix tablet

Ingredients	FH1	FH2	FH3	FG1	FG2	FG3	FR1	FR2	FR3	FC1	FC2	FC3
Enalapril Maleate	10	10	10	10	10	10	10	10	10	10	10	10
HPMC K 100 M	5	10	15	–	–	–	–	–	–	–	–	–
Olibanum gum	–	–	–	1.2	2.4	4.8	–	–	–	–	–	–
Olibanum resin	–	–	–	–	–	–	1.2	2.4	4.8	–	–	–
Carbohydrate fraction	–	–	–	–	–	–	–	–	–	1.2	2.4	4.8
Microcrystalline cellulose	92	88	83	96.8	95.6	93.2	96.8	95.6	93.2	96.8	95.6	93.2
PVP K30	10	10	10	10	10	10	10	10	10	10	10	10
Magnesium stearate	1	1	1	1	1	1	1	1	1	1	1	1
Talc	1	1	1	1	1	1	1	1	1	1	1	1

2.5 Melting Point Determination

The drug's melting point was determined by using the open capillary method.

2.6 FTIR Spectroscopy

FTIR spectroscopy was used to identify Enalapril Maleate in relation to a marker chemical. It was confirmed using the IR spectrum results in accordance with the specifications. FTIR Spectrophotometer used to record FTIR spectra on KBr disc. In a glass mortar and pestle, the sample powder was thoroughly mixed with KBr before being compacted into discs in a hydraulic press. All of the materials' FTIR spectra were captured using 20 scans with a resolution of 4 cm^{-1} , covering a spectral range from 4700 to 400 cm^{-1} .

2.7 Construction of Calibration Curve of Enalapril Maleate in Phosphate Buffer pH 7.2

2.7.1 Primary Stock Solution

To formulate 100 ml of solution, 100 mg of Enalapril Maleate were precisely weighed and dissolved in phosphate buffer pH 7.2. Then, using phosphate buffer with a pH of 7.2, extract 2 ml of this solution and dilute it to 100 ml.

2.7.2 Secondary Stock Solution

The primary stock solution in increments of 1 ml, 2 ml, 3 ml, 4 ml, and 5 ml was diluted to 10 ml in phosphate buffer pH 7.2 to get concentrations of 2 g/ml, 4 g/ml, 6 g/ml, 8 g/ml, and 10 g/ml. Using a Spectrophotometer Systronics-2203, the absorbance of these solutions measured at wavelength of 204.4 nm using phosphate buffer pH 7.2 as a blank. The concentration in g/ml was then plotted on the X-axis and the absorbance on the Y-axis to create a calibration curve.

2.7.3 Evaluation

Pre-compression Parameters

- Bulk and tapped density.
- Carr's index
- Hausner's ratio.
- Angle of repose.

Post-compression Parameters (Evaluation of Compressed Tablets)

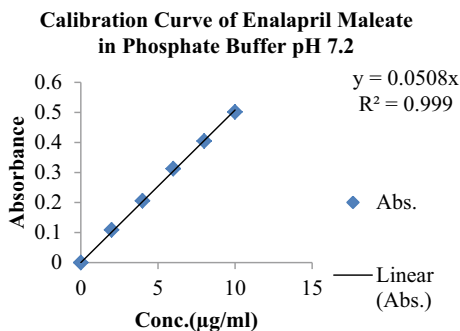
- Thickness and appearance.
- Hardness.
- Friability.
- Weight variation.
- Uniformity of drug content.
- In-vitro dissolution studies.

3 Results and Discussion

3.1 Description and Melting Point

The preformulation parameter indicates their organoleptic properties and Melting point found to be white, crystalline, odorless powder and 142 °C respectively. It is exactly same as the standard monograph mentioned in the EP.

Fig. 1 Calibration curve of Enalapril Maleate in phosphate buffer pH 7.2



3.2 Calibration Curve

Enalapril Maleate curve was plotted for concentrations between 2 and 10 g/ml ranges in phosphate buffer with an R^2 value of 0.99. Enalapril Maleate's standard curve revealed that the medication follows Beer's law in the concentration range of 2–10 g/ml in phosphate buffer pH 7.2. The derived linear regression equation was applied to determine the medicine dosage (Fig. 1).

3.3 Drug-Excipient Compatibility Study

3.3.1 Infrared Spectroscopy

Drug-excipient compatibility is a crucial factor in formulation development and is well investigated by FTIR. The KBr disc pellet technique was used to evaluate samples of the pure medication Enalapril Maleate, polymers, and physical mixes corresponding to formulations. The resulting spectra were analyzed to look for or investigate any potential drug-polymer interactions (Figs. 2, 3 and 4).

3.3.2 DSC Study

The thermal properties of produced Formulation FR1 and Enalapril Maleate are shown in Figs. 5 and 6. The DSC thermogram of Enalapril Maleate clearly showed an endothermic peak at 159.81 °C, which corresponded to its melting point. The usage of pure crystalline Enalapril Maleate is indicated by the strong endothermic peak. The thermogram of Formulation FR1 with optimizations revealed an endothermic peak at 193.43 °C.

The absence of any notable changes in the endothermic peak of the drug in the DSC thermogram of the optimized formulation indicated that there was no interaction between the drug and excipients. Reduced peak intensity on the thermogram could

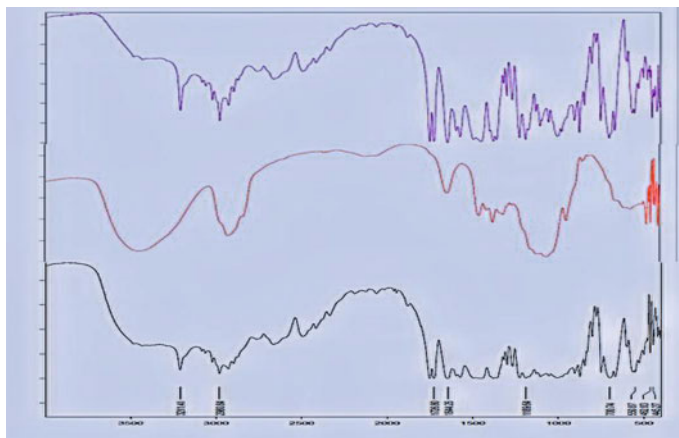


Fig. 2 FTIR spectra of **a** Enalapril Maleate, **b** HPMC K 100 M and **c** formulation FH1

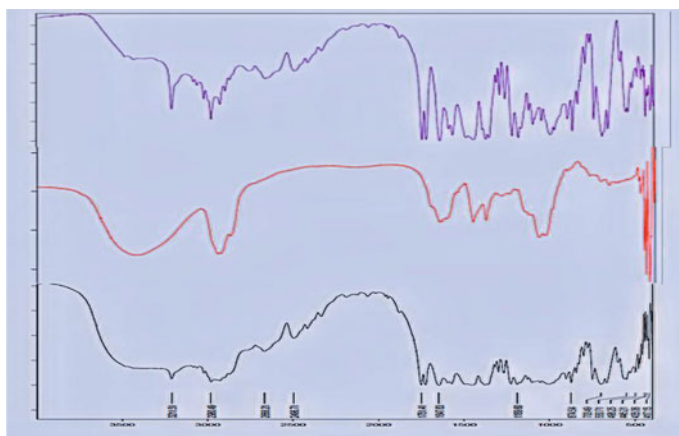


Fig. 3 FTIR spectra of **a** Enalapril Maleate **b** olibanum gum and **c** formulation FG1

be the result of a change in the drug's thermal properties without any excipient interaction.

3.3.3 Pre-compression Studies

All formulations showed acceptable flow properties.

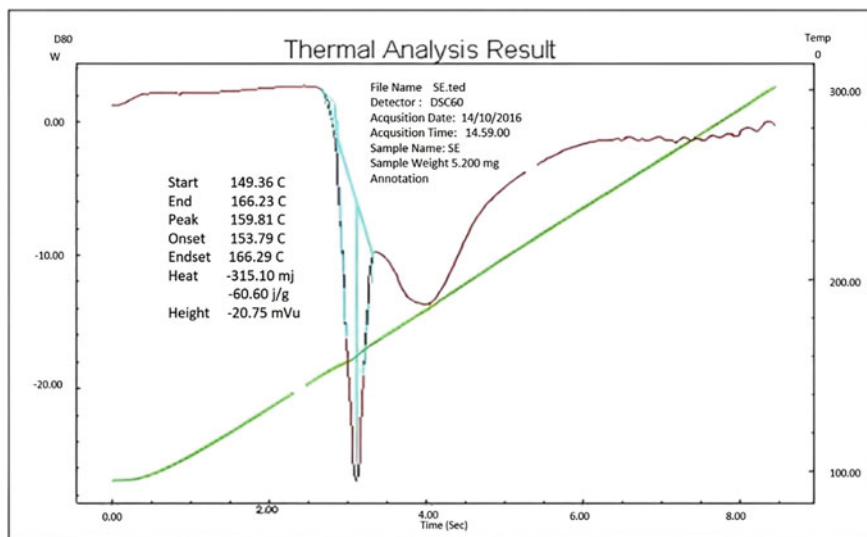


Fig. 4 DSC spectra of Enalapril Maleate

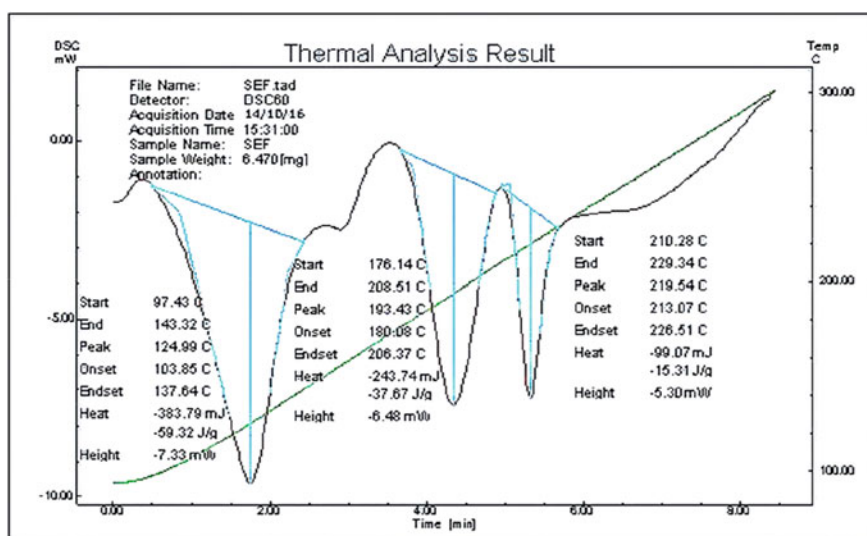


Fig. 5 DSC spectra of optimized formulation FR1

3.3.4 Post-compression Study

Thickness of tablets ranged from 2.52 ± 0.11 to 2.64 ± 0.16 mm. Formulations FH1, FH2, FH3 showed hardness 5.4 ± 0.22 , 5.3 ± 0.27 , 5.2 ± 0.27 respectively.

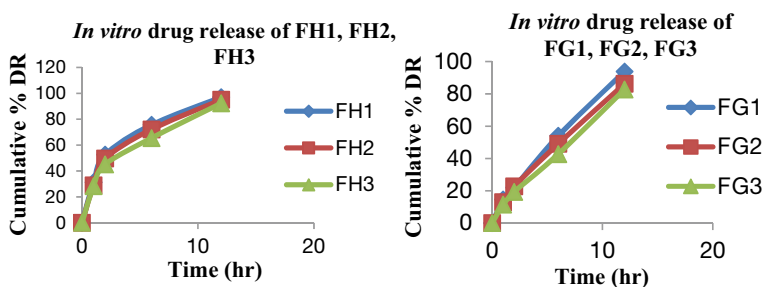


Fig. 6 a In vitro drug release of Enalapril Maleate through HPMC K 100 M (FH1, FH2, FH3). **b** In vitro drug release of Enalapril Maleate through olibanum gum (FG1, FG2, FG3)

Formulations FG1, FG2, FG3 showed hardness 4.4 ± 0.22 . Formulations FR1, FR2, FR3 showed hardness 5.3 ± 0.27 , 4.3 ± 0.27 , 4.9 ± 0.27 respectively. Formulations FC1, FC2, FC3 showed hardness 5.1 ± 0.22 , 4.7 ± 0.27 , 4.6 ± 0.22 respectively. The results of a weight variation test showed that all tablet formulations fell within the range of Pharmacopeial requirements. All formulations showed % friability less than 1%. The drug content of all matrix system found to be within the limits.

3.3.5 In Vitro Drug Release Studies

To determine the release profiles, the in vitro cumulative % amount of drug released at various time intervals was plotted versus time. The dissolution test for in vitro release of all the formulation, were carried out using USP Type-II (paddle). A revolving at 50 rpm with phosphate buffer pH 6.8 dissolution media was used. The study carried out at 37 ± 0.5 °C. All the Formulation FH1, FH2, FH3, FG1, FG2, FG3, FR1, FR2, FR3, FC1, FC2 and FC3 showed cumulative % DR 96.99 ± 0.643 , 95.06 ± 0.502 , 92.34 ± 1.605 , 93.89 ± 4.037 , 86.30 ± 1.895 , 82.75 ± 1.605 , 91.533 ± 0.58 , 82.22 ± 1.958 , 76.46 ± 0.078 , 97.13 ± 1.400 , 93.42 ± 1.612 , 91.65 ± 0.707 respectively. The formulations FH1, FH2, FH3 are formulated with different concentrations of HPMC K 100 M with 15%, 25%, and 35% respectively. In FH1, formulation $96.99 \pm 0.643\%$ of the drug release was within 12 h.

The formulations FG1, FG2, and FG3 are formulated with different concentrations of olibanum gum with 1%, 2%, and 3% respectively. In FG1 formulation $93.89 \pm 4.037\%$ of the drug release was released in 12 h.

The formulations FR1, FR2, and FR3 are formulated with different concentrations of olibanum resin with 1%, 2%, and 3% respectively. In FR1, formulation $91.533 \pm 0.58\%$ of the drug release was released in 24 h. The release was highly sustaining as the concentration of the polymer is increasing.

The more appreciating drug release was observed with the formulations FH1, FG1 and FR1. In comparison to the formulation FH1, the FG1 and FR1 had a stronger sustaining effect, while the FR1 formulation had a greater delaying effect on drug release. In very low concentration 1% w/w, FR1 showed a very high sustaining effect

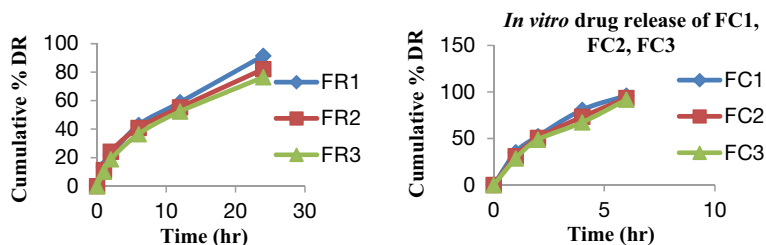


Fig. 7 a In vitro drug release of Enalapril Maleate through olibanum resin (FR1, FR2, FR3). b In vitro drug release of Enalapril Maleate through Carbohydrate Fraction (FC1, FC2, FC3)

up to 24 h in comparison to FH1 and FG1 formulation having drug release up to 12 h. From results, it was concluded that, for drugs having high dose the olibanum resin was better polymer to sustain a drug release and to minimize a drug concentration (Fig. 7).

4 Conclusion

As reported by research findings, it can be concluded that, Enalapril Maleate matrix tablets can be prepared successfully using HPMC K 100 M, olibanum gum, its resin and carbohydrate fraction by direct compression technique. It was found to be good without tableting defects. The drug content was uniform in all the formulations of tablets prepared. Low standard deviation values suggest a uniform distribution of the drugs within the matrices. The FTIR study confirmed that no chemical interaction took place during formulation process. All formulations showed acceptable flow properties and tableting properties like Hardness, Tablet dimensions, Weight variation, Friability, and Drug content. It was discovered that the drug release from the formulations was influenced by the drug-polymer ratio. Drug release rates were observed to decrease as polymer concentration increased. The FG1 and FR1 had a more sustaining effect as compared to the formulation FH1 while the formulation FR1 had the more retarding effect on drug release than FG1. In very low concentration 1% w/w, FR1 showed a very high sustaining effect up to 24 h in comparison to FH1. Release kinetic study showed that drug release followed Anomalous transport. Thus, olibanum gum and its resin was found suitable as controlled release polymer and the olibanum matrix tablet of Enalapril Maleate exhibited good sustained release characteristics and were found suitable for oral sustained release products. Olibanum is reported as non-toxic. Since the resin is of natural origin, it is biocompatible and economic.

References

1. Sivanewari, S., Hemalatha, G., Jayasree, J., Mounika, B., Murthy, S. V., & Preethi, N. (2014). Role of various natural, synthetic and semi-synthetic polymers on drug release kinetics of losartan potassium oral controlled release tablets. *International Journal of Pharmaceutical Investigation*, 4(4), 183. <https://doi.org/10.4103/2230-973x.143118>
2. Patel, K. N., Patel, S. S., Trivedi, H. J., Patel, B. A., & Patel, M. M. (2018). Design and characterization of Donepezil hydrochloride sustained release matrix tablets. *Journal of Drug Delivery and Therapeutics*, 8(3), 64–74. <https://doi.org/10.22270/jddt.v8i3.1769>
3. Tazri, J., Moghal, M. M., Dewan, S. M., Noor, W., & Mohammad, N. (2014). Formulation and quality determination of indapamide matrix tablet: A thiazide type antihypertensive drug. *Advanced pharmaceutical bulletin*, 4(2), 191–195. <https://doi.org/10.5681/apb.2014.028>
4. Nair, A. B., Vyas, H., & Kumar, A. (2010). Controlled release matrix uncoated tablets of enalapril maleate using hpmc alone. *Journal of basic and clinical pharmacy*, 1(2), 71–75. <https://www.ncbi.nlm.nih.gov/pmc/articles/PMC3979173/>
5. Nair, A., Gupta, R., & Vasanti, S. (2007). In vitro controlled release of alfuzosin hydrochloride using HPMC-based matrix tablets and its comparison with marketed product. *Pharmaceutical Development and Technology*, 12(6), 621–625. <https://doi.org/10.1080/10837450701563277>
6. Chowdary, K. P. R., & Rama Reddy, G. (2012). Formulation and evaluation of diclofenac-controlled release tablets employing olibanum resin. *International Journal of Pharmaceutical Sciences and Research*, 3(4), 1090–1095. [https://doi.org/10.13040/IJPSR.0975-8232.3\(4\).1090-95](https://doi.org/10.13040/IJPSR.0975-8232.3(4).1090-95)
7. Chowdary, K. P. R., Mohapatra, P., & Murali Krishna, M. N. (2006). Evaluation of olibanum and its resin as rate controlling matrix for controlled release of Diclofenac. *Indian Journal of Pharmaceutical Sciences*, 68(4), 497–500. <https://doi.org/10.4103/0250-474x.27826>
8. Chowdary, K. P. R., Mohapatra, P., & Murali Krishna, M. N. (2006). Evaluation of olibanum resin as microencapsulating agent for controlled drug delivery. *Indian Journal of Pharmaceutical Sciences*, 68(4), 461–464. <https://doi.org/10.4103/0250-474x.27818>
9. Uddin, M., Halde, S., Kumar, U., & Shara Shamsur Rouf, A. (2012). Design and evaluation of once daily losartan potassium sustained release matrix tablet. *International Journal of Pharmaceutical Sciences and Research*, 5(2), 519–525. [https://doi.org/10.13040/IJPSR.0975-8232.5\(2\).519-25](https://doi.org/10.13040/IJPSR.0975-8232.5(2).519-25)

Optimization of Thermo-reversible Nasal Gel of Carbamazepine for Better Control in Chronic Epilepsy



Utkarsha S. Shivsharan, Avinsah H. Hosmani, and Yogesh S. Thorat

Abstract The aim of present work was to formulate thermosensitive in situ gel of carbamazepine (CBZ), an anti-epileptic agent. In situ nasal gel of CBZ was formulated by cold method using Pluronic F68 and Pluronic F127 as thermoreversible stimuli sensitive polymer along with two different grades of hydroxypropyl methyl cellulose as mucoadhesive polymer. It is thought that the thermo-reversion and mucoadhesion would synergistically enhance the residence time of the drug in the nasal cavity and also impart better penetration of the drug to brain for the site-specific activity. The sustained release obtained from the viscous gel makes the treatment even better especially in the chronic epileptic conditions like tonic–clonic seizures. The prepared formulations were evaluated for pH, clarity, in vitro gelation, gelling strength, mucoadhesion, in vitro drug release and accelerated stability studies. Results have shown that final batches of in situ gels were having desired gelation temperature to provide pourable ‘Sol’ form at room temperature and ‘Gel’ form in the nasal cavity with a good gel strength and mucoadhesion required for nasal retention. Formulations showed polymer concentration dependent drug release retardation over a period of 6 h.

Keywords Thermoreversible gel · Stimuli sensitive · HPMC · Pluronic · Carbamazepine · Epilepsy

1 Introduction

Carbamazepine is an anticonvulsant and/or anti-epileptic drug which also relieves neuropathic pain and also used in case of Schizophrenia. Carbamazepine reduces sodium channel activity by binding with it. Carbamazepine is metabolized by

U. S. Shivsharan (✉) · A. H. Hosmani
DSTSM’s College of Pharmacy, Solapur, Maharashtra, India
e-mail: utkarsha.shivsharan@gmail.com

Y. S. Thorat
Government College of Pharmacy, Karad, Maharashtra, India

CYP3A4 system in liver [1]. This leads to increase in drug clearance and reduced half-life as well, increasing its frequency of administration. In case of patients with brain disorders, oral drugs administration is more challenging due to presence of lipophilic tight junctions of blood brain barrier [2]. To avoid these difficulties, bypassing oral route could be better option. Nasal administration of Carbamazepine can lead to efficiency of it, by maintaining drug levels in brain through brain targeted drug delivery [3]. Drug delivery through nasal route gives better bioavailability and pharmacological action too. Nasal mucosa provides drug absorption at higher levels at faster rate due to higher permeability and low enzymatic environment. As there is direct contact between brain and nasal route, it is preferred route to enhance pharmacological effects of drug [4, 5]. The present work describes formulation of thermoreversible nasal in situ gel of carbamazepine for better control in chronic epilepsy and evaluation thereof.

2 Materials and Methods

Carbamazepine was obtained from Sun Pharmaceuticals Ltd., Mumbai complying with USP monograph supplied as a gift sample. HPMC (Methocel K4M, K15M, and K100M grades) suitable for use in the present study was supplied by Colorcon, Mumbai. Pluronic was obtained from Noveon Ltd, Mumbai. All other excipients used were of pharmaceutical grade.

2.1 *Thermoreversible In Situ Gels Preparation*

The drug-loaded thermoreversible in situ gels were prepared by cold method [6]. The drug was dissolved in sufficient quantity of distilled water. Pluronic F127/F68 was added slowly with continuous stirring. The dispersions were refrigerated at 8 °C until clear solution was obtained and finally volume was adjusted. Optimization was done by varying the polymer concentrations for gelation temperature. Batch containing optimized concentration was used for preparation of mucoadhesive gel. The final combinations are depicted in Table 1.

2.2 *Evaluation of Thermoreversible Gel*

2.2.1 pH

For the pH determination, calibrated pH meter was used. 1 ml of formulation was diluted to 10 ml with distilled water and pH was determined.

Table 1 Formulation code and quantities

Ingredients	Formulation code and quantities								
	CF ₁	CF ₂	CF ₃	CF ₄	CF ₅	CF ₆	CF ₇	CF ₈	CF ₉
Carbamazepine (mg)	200	200	200	200	200	200	200	200	200
Pluronic F68 (mg)	1000	1000	1000	1000	1000	1000	1000	1000	1000
Pluronic F127 (mg)	1500	1500	1500	2000	2000	2000	2500	2500	2500
HPMC K4M (mg)	50	75	100	50	75	100	50	75	100
Distilled water (ml)	10	10	10	10	10	10	10	10	10

2.2.2 Clarity

Visual Inspection was carried out in by using black and white background in order to check the clarity.

2.2.3 In-Vitro Gelation Studies [7]

Inflection Point

As the temperature of the formulations was increased from 4 °C, a point reached where drastic change in the viscosity was observed, that point was considered as Inflection point.

2.2.4 Gelation Temperature

It was determined by using method described by Miller and Donovan technique. A 2 ml aliquot of solution was transferred to a test tube, immersed in a water bath. The temperature of water bath was increased slowly. The sample was then examined for gelation, which was said to have occurred when the meniscus would no longer moves upon tilting through 90°.

2.2.5 Gelling Strength

The gelling strength of the formulation was determined by using 50 g of formulation in 100 ml measuring cylinder. 1 g weight was placed on top of the formulation and time taken for the 5 cm movement of weight was noted.

2.2.6 Mucoadhesion Study [8]

The mucoadhesive force can be determined by measuring the force required to detach the formulation from biological membrane. The biological membrane was fixed onto the platform of modified apparatus. The nasal mucosa of goat was soaked in Phosphate buffer pH 7.4. overnight. Accurately 1 ml gel was placed on the biological membrane. A preload of 50 g was placed on to glass slide for 5 min (preload time) to establish adhesion bonding between gel and biological membrane.

2.2.7 Determination of Drug Content

Drug content analysis was used to determine the uniform distribution of carbamazepine in the gels. The gels were diluted using pH 6 phosphate buffer with dilution factor of 100 (gel:phosphate buffer = 1:100) prior to the drug content analysis. The drug content of gel formulation was determined by using UV Spectrophotometer Lab India mech at 284 nm.

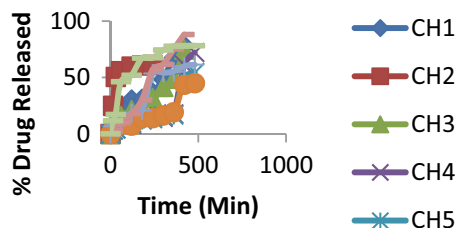
2.2.8 In Vitro Drug Release Study

The nasal diffusion cell was fabricated in glass. The water-jacketed recipient chamber has total capacity of 60 ml and a flanged top of about 3 mm; the lid has 3 openings, each for sampling, thermometer, and donor tube chamber. The 10 cm long donor chamber tube has internal diameter of 1.13 cm. The nasal mucosa of goat was separated from sub layer bony tissues and stored in distilled water containing few drops of gentamycin sulfate injection. After the complete removal of blood from mucosal surface, it was attached to donor chamber tube. The receptor chamber was filled with phosphate buffer (pH 6) and agitated continuously using a magnetic stirrer. The cell was equilibrated at 3.7 ± 2 °C. The donor chamber tube was lowered to just touch the diffusion medium in recipient chamber. The drug formulations were placed on the dorsal surface of nasal mucosa. 1 ml aliquot was withdrawn at predetermined intervals and estimated for the drug concentration at 284 nm spectrophotometrically [9].

2.2.9 Accelerated Stability Studies

Stability testing of drug product being a part of drug discovery and ends with the commercial product, to assess the drug and formulation stability, stability studies were done. The stability study was carried out for the most satisfactory formulation. The most satisfactory formulation was sealed in a glass vial and kept at 4 ± 2 °C for 3 months. At the end of each month, the samples were analyzed for the parameters like pH, viscosity, drug content and in vitro diffusion study [10].

Fig. 1 Drug release profile for in-situ gel with HPMC K4M



3 Results and Discussion

3.1 Melting Point of Carbamazepine

Melting point of Carbamazepine was found to be 189–192 °C. The result was in good agreement with the literature.

3.2 IR Interpretation of Carbamazepine

FTIR spectra interpretation for drug is as given in Fig. 1 shows all the characteristics peaks which authenticate the drug as pure substance.

3.3 Physical Appearance and pH

All formulations were evaluated for the presence of any physical particles. pH of all formulations was measured using a digital calibrated pH meter. Table 2 depict the evaluation of in situ gels for pH.

3.4 In Vitro Gelation Study

In these studies, the gelling capacity (gelling speed and extent of gelation) for all formulations were determined. Gelation characteristics were assessed. The gelation of all the batches was observed at the nasal temperature. It can be seen from the results that the gel strength is dependent on the concentration of HPMC. The increase in the gel strength can be attributed to the concentration dependent swelling property of celluloses as well as viscosity building characteristics of HPMC. The results of inflection points, gelation temperature and gel strength are tabulated in Table 2.

Table 2 Evaluation of in-situ thermoreversible gels

Formulation code	pH	Gelling capacity	Inflection point (°C)	Gelation temperature (°C)	Mucoadhesion (dyne/cm ²)
CF ₁	5.91	+	48	50	3678 ± 104
CF ₂	5.94	++	45	51	4885 ± 86
CF ₃	6.2	+++	44	52	5320 ± 73
CF ₄	5.84	+++	38	41	4557 ± 89
CF ₅	5.96	+++	30	40	7854 ± 29
CF ₆	6.2	+++	35	38	9567 ± 57
CF ₇	6	+++	29	35	5431 ± 94
CF ₈	5.94	+++	32	33	5885 ± 84
CF ₉	6.7	+++	29	32	9875 ± 11
CH ₁	6.78	+	Heated upto 50	No gel formation	
CH ₂	6.5	+	Heated upto 50	No firm gel formation	
CH ₃	6.3	++	49	50	4720 ± 73
CH ₄	6.5	+	38	44	4537 ± 98
CH ₅	6.5	++	40	43	6845 ± 49
CH ₆	6.4	+++	39	45	8567 ± 83
CH ₇	6.2	++	32	37	4256 ± 74
CH ₈	6.4	++	31	36	5684 ± 92
CH ₉	6.3	+++	30	35	8798 ± 96

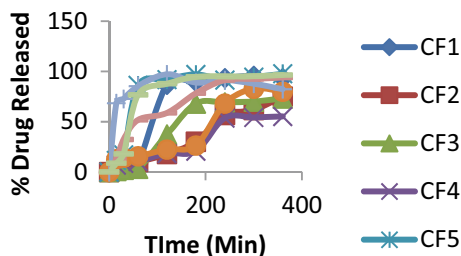
3.5 Mucoadhesion Study

HPMC and other celluloses are well known as mucoadhesive polymers due to their ability to swell in aqueous conditions and forming cross-linked bonds with the mucin molecules present in the mucous membrane. This enables the gel to reside at the desired membrane for long period of time. In the prepared formulations, mucoadhesion was found to be satisfactory ranging from 9875 to 3678 as depicted in Table 2. It can be understood from the results that the mucoadhesion is dependent on the concentration of the polymer.

3.6 In-Vitro Drug Diffusion Study

The in vitro diffusion rate of Carbamazepine was performed using modified Franz Diffusion Cell at 37 ± 0.5 °C using pH 7.4 Phosphate Buffer as a diffusion medium. It can be observed from the results that the drug release from the batches with HPMC

Fig. 2 Drug release profile for in-situ gel with HPMC K4M



K4M is almost complete while that of HPMC K100M is not complete. This can be due to the higher viscosity of the gels as well as gel strength with HPMC K100M compared to HPMC K4M owing to the different molecular weight and chain length of the polymer. The release was found to be sustained upto approximately 6 h in the formulations with HPMC K4M (Fig. 2).

3.7 Accelerated Stability Study

Stability studies were carried for the most satisfactory formulation CF₅, with temperature 5 °C for three months. At the end of three months, samples were evaluated for pH, clarity and drug contents. It was observed that there was no significant change in the values of evaluation parameters.

4 Conclusion

The present work describes formulation of thermoreversible nasal in situ gel of carbamazepine for better control in chronic epilepsy and evaluation thereof. Pluronic F68 and F127 were used as thermosensitive polymers along with two grades of HPMC as mucoadhesive agents. The formulations were found to be efficient to cause thermoreversible gelation at the nasal temperature with a good gel strength and mucoadhesion which can lead to increased residence of the drug delivery system at the nasal mucosa which is required to deliver the drug to brain for the control of chronic epilepsy. The technique can be industrially viable and useful in the effective therapy of chronic epilepsy with Carbamazepine.

References

1. Mandal, S., et al. (2010). Design and development of carbamazepine mucoadhesive microemulsion for intranasal delivery. *International Journal of Pharmaceutical Sciences Review and Research*, 3(1), 56–60.
2. Gaikwad, M. V., et al. (2015). Development and evaluation of carbamazepine loaded transferosomal in-situ gel for nose to brain delivery. *Indo American Journal of Pharmaceutical Research*, 5(05).
3. Serralheiro, A., et al. (2014). Intranasal administration of carbamazepine to mice: A direct delivery pathway for brain targeting. *European Journal of Pharmaceutical Sciences*, 5(05), 2047–2053.
4. Almeida, H., et al. (2012). Temperature and pH stimuli-responsive polymers and their applications in controlled and self regulated drug delivery. *Journal of Applied Pharmaceutical*, 02(06), 01–10.
5. Gil, E. S., et al. (2004). Stimuli-responsive polymers and their bioconjugates. *Progress in Polymer Science*, 29(12), 1173–1222.
6. Sudhakar, Y., et al. (2013). Thermoreversible nasal gel of carvedilol using methanol precipitated solids of Aloe vera and yellow mustard mucilage. *Indo American Journal of Pharm Research*, 3(8).
7. Raj, A., et al. (2015). Formulation and evaluation of nasal in-situ gel of bupropion hydrochloride. *World Journal of Pharmacy and Pharmaceutical Sciences*, 4(1), 595–614.
8. Nair, A. B., et al. (2022). Intranasal delivery of Darunavir-loaded mucoadhesive in situ gel: Experimental design, in vitro evaluation, and pharmacokinetic studies. *Gels*, 8, 342.
9. Morsi, N., et al. (2016). Ketorolac tromethamine loaded nanodispersion incorporated into thermosensitive in situ gel for prolonged ocular delivery. *International Journal of Pharmaceutics*, 506(1–2), 57–67.
10. Gadad, A. P., et al. (2016). Thermosensitive in situ gel for ocular delivery of lomefloxacin. *Indian Journal of Pharmaceutical Education and Research*, 50, S96–S105. <https://doi.org/10.5530/ijper.50.2.24>

Antimicrobial Activities of Organic Solvent Extracts of *Citrus aurentifolia*, *Eucalyptus globulus* and *Jasmine grandiflorum* Against Certain Microorganisms



Vaibhav Gaikwad, Anil Landge, Dharba Sastry, and Rushikesh Shelke

Abstract Bioassays for antimicrobial activities were carried out using peels, leaves & flowers of *Citrus aurentifolia*, *Eucalyptus globulus* and *Jasmine grandiflorum* respectively. Various organic solvents extract of these plants were evaluated for antimicrobial activity against clinically important organism viz. *Escherichia coli* ATCC25922, *Klebsiella pneumoniae* NCIM2719, *Pseudomonas aeruginosa* ATCC27853 and *Saccharomyces cerevisiae* ATCC9763. The plants Extracts were isolated by means of a Soxhlet device and as per accordance to polarity of solvents. The in vitro antimicrobial activity was performed by agar well diffusion method The Minimum Inhibitory Concentration MIC of the plant extracts were 20 μ l. The organic solvents extract of all the plants were active against all the investigated bacterial strains while ethanolic extracts were showing considerable activity. Accelerated gradient chromatography (AGC) gave fractions of the extract that were also active as antimicrobial crude extract fractions.

Keywords Bioassays · Ethanolic extract · Antimicrobial activity · Agar diffusion · Minimum inhibition concentration (MIC)

1 Introduction

Plants have a great potential for producing new drugs of great benefit to mankind. There are many approaches to the search for new biologically active principles in higher plants [1]. Many efforts have been done to discover new antimicrobial compounds from various kinds of sources such as soil, microorganisms, animals and plants. One of such resources is folk medicine and systematic screening of them

V. Gaikwad (✉) · A. Landge · R. Shelke
SVRI's College of Pharmacy, Pandharpur, Maharashtra, India
e-mail: vaibhavgaikwad055@gmail.com

D. Sastry
KLE College of Pharmacy, Belagavi, Karnataka, India

may result in the discovery of novel effective compounds [2]. Further, scientific investigation and information of the therapeutic potential of the plant material is limited. Despite the existence of potent antibiotic and antifungal agents, resistant or multi-resistant strains are continuously appearing, imposing the need for a permanent search and development of new drugs [3]. There is an urgent need to systematically evaluate the plants used in traditional medicine. Such research could lead to new drug discovery or advance the use of indigenous herbal medicines for orthodox treatment. Now a day a renewed interest in traditional medicine is observed and there has been an increasing demand for more and more drugs from plant sources. This revival of interest in plant-derived drugs is mainly due to the current widespread belief that “green medicine” is safe and more dependable than the costly synthetic drugs many of which have adverse side effects [4].

Presently in the developing countries, synthetic drugs are not only expensive and inadequate for the treatment of diseases but are also often with adulterations and side effects [5]. There is therefore the need to search for plants of medicinal value. The plants used in the present study are *Citrus aurentifolia*, *Eucalyptus globulus* and *Jasmine grandiflorum* which are used traditionally varieties of ailments with which the test organisms are routinely associated. The main objective of this study is to examine the antimicrobial activities of the organic solvents extracts of *Citrus aurentifolia*, *Eucalyptus globulus* and *Jasmine grandiflorum* with varying polarity of organic solvents. The antimicrobial activities of the active fractions of the extracts were also determined. **Materials and methods** Collection of plant material. *Citrus aurentifolia*, *Eucalyptus globulus* and *Jasmine grandiflorum* were collected from hilly and city areas of Vellore, Tamil Nadu, India. The plants were duly authenticated by Dr. C. Rajasekaran at the Department of Biotechnology and Chemical Engg. VIT University, Vellore (Tamil Nadu, India).

2 Materials and Method

2.1 Source of Microorganisms

The organisms used were *Escherichia coli* ATCC25922, *Klebsiella pneumoniae* NCIM2719, and *Pseudomonas aeruginosa* ATCC27853 and *Saccharomyces cerevisiae* ATCC18824. The organisms were obtained from the Microbiology Laboratory, VIT University, Vellore.

Table 1 Solvent system used for Soxhlet extraction

Solvents (in order of non-polar to polar)	Temperature (°C)	Time (h)
Petroleum ether	30	3
Hexane	30	3
Benzene	30	5
Ethyl acetate	30	5
Ethanol	30	5

2.2 Standardization of Microorganisms

Exactly 0.2 ml of overnight cultures of each organism was dispensed into 20 ml of sterile nutrient broth and incubated for 3–5 h to standardize the culture to 10^6 cfu/ml. A loopful of the standard cultures were used for the antimicrobial assay [6].

2.3 Preparation of Plant Materials and Extract

Both dried and fresh plants were used for extraction of crude materials. Plant parts were dried for three days followed by removal of citrus peels, further cleaned, dried in shade and ground at controlled temperature [7]. Eucalyptus leaves were separated from stem and ground [8]. Jasmine petals were dried in shade and ground. Grinding carried out at cold rooms to avoid loss of volatile residues at room temperature [9, 10].

2.4 Preparation of Crude Plant Extract

The moderately fine powdered plant material about 60 g was processed for continuous hot extraction method (Soxhlation) by using 200 ml of different solvents based on polarity criteria as follows (Table 1).

Each extract was evaporated to dryness under reduce pressure using rotary evaporator. The standard extracts were then stored at refrigerator at 4 °C for further uses [11].

2.5 Phytochemical Screening of Crude Extracts

The phytochemical components of the medicinal plants were screened for using the methods of [12, 13]. The components analyzed for are saponins, saponin glycosides, steroid, glycosides, anthraquinones, tannins, flavonoids alkaloid, volatile oils, phenols and balsam (gum).

2.6 Antimicrobial Assay

The antimicrobial assay was performed by agar well diffusion method [14] for solvent extract. McFarland 0.5 standard was prepared [15]. The molten Mueller Hinton Agar was inoculated with inoculum (1×10^8 cfu) and poured into the Petri plate (Hi-media). For agar well diffusion method, a well was prepared in the plates with the help of a cork-borer (0.85 cm). 20 μ l of the test compound was introduced into the well. The plates were incubated overnight at 37 °C. Microbial growth was determined by measuring the diameter of zone of inhibition [16]. For each bacterial strain controls were maintained where pure solvents were used instead of the extract. The result was obtained by measuring the zone diameter.

3 Results and Discussion

Different plant metabolites are extracted into different organic solvents, depending on their polarities. To ensure that plant organic acids or bases are extracted into organic solvents at this stage, the pH of an alcohol-water extract can be raised or lowered with a water-soluble acid or base to convert dissociated analytes into their non-dissociated forms, which are then soluble in neutral organic solvents [17, 18]. The organic phase can then be evaporated under reduced pressure or under nitrogen and adjusted to the desired volume for TLC. The pH of the extract is unlikely to be lethal to bioassay microorganisms due to the partitioning of analytes into neutral solvents, small final volume, and evaporation of the extract on the TLC plate prior to separation [19].

3.1 Separation of Extracts Using Accelerated Gradient Chromatography (AGC)

About 5 ml of extract of the plants were dissolved in small quantity of distilled methanol. 5 g of silica gel (Qualigens, Mumbai) was added to the mixture and stirred thoroughly after which it was transferred to a mortar and mixed thoroughly with pestle. The components of the mixture were then separated using AGC machine.

Gradient elution chromatography starts from a composition of mobile phase rich in organic constituent (e.g. methanol), and the concentration of the polar (aqueous buffer) component is increased in time. The high initial methanol content in the mobile phase will assure sufficient retention for the analytes with low affinity for the stationary phase. Running the gradient toward a high-water concentration (e.g., 90%) favors the desorption of strongly retained analytes on the stationary phase [17].

The fractions were collected in sterile test tubes for further analysis. For the gradient separations with the initial mobile phase with no buffer and with the buffer

content increasing during the run, changes in the retention mechanism may occur [18].

3.2 Separation of Components of Fractions Using Thin Layer Chromatography (TLC)

TLC plates were prepared and spotted with fractions of the medicinal plants separated by the AGC. Plant extracts are frequently screened for antimicrobial compounds with this method, often referred to as bioautography. The protocols described herein apply to bioautography of thin-layer chromatograms. TLC is widely used because it is relatively rapid and can be performed on different adsorbents (e.g. silica, starch, alumina), as well as providing good resolution and sensitivity [20]. The spotted plates were then placed in TLC tank containing the solvent system—Toluene:Ethyl acetate in the ratio 9:1 for all fractions. The separated components on the TLC plates were viewed using ultraviolet light at 365 nm wavelength and by using Anisaldehyde solution as visualizing agent. Fractions from the AGC with similar components on TLC were combined and used for antimicrobial assay. Many different combinations of test microorganism and media can be used for bioautography. However, several factors must be considered when selecting microorganism and media. The media should be tested to determine that there are no components that reduce the tetrazolium salt and cause a nonbiological color change [21]. The agar should also be light enough in color to provide contrast between the stained cells and unstained zones of inhibition. A microorganism that can only grow on the surface of agar can be removed along with the TLC band or washed off during staining. Additionally, the selection of microorganism/medium combination that minimizes gas production will reduce bubbles in the agar [22]. Tables 2, 3 shows zone of inhibitions presented by different extracts ensuring major inhibitory zones were observed in extreme non-polar and extreme polar solvents. The overall result indicates the functional groups in specific extracts are responsible for their antimicrobial activities. Hence, its ultimate to understand their biochemical characterization by use of molecular biomarkers. Perhaps the most common use of TLC plate bioassays is to narrow the range of possible antimicrobial compounds in a plant extract. After inhibitory zones are identified by a bioassay, the corresponding regions on a duplicate TLC plate can be eluted with a solvent, such as methanol or ethyl acetate, and analyzed by HPLC with ultraviolet spectroscopy detection to begin characterizing bioactive compounds [19].

Table 2 Zone of inhibition shown by *Citrus aurentifolia* extracts

Microorganisms	Crude extracts zone diameter (in mm)									
	Pet. Ether		Hexane		Benzene		Ethyl acetate		Ethanol	
	Ctrl	Test	Ctrl	Test	Ctrl	Test	Ctrl	Test	Ctrl	Test
<i>Escherichia coli</i> ATCC25922	0	0	0	0	0	0	0	2	0	2
<i>Pseudomonas aeruginosa</i> ATCC27853	0	0	0	0	0	0	0	11	0	2
<i>Klebsiella pneumoniae</i> NCIM2719	0	6	0	5	0	4	0	2	0	5
<i>Saccharomyces cerevisiae</i>	0	10	0	9	0	5	0	2	0	2

Table 3 Zone of inhibition shown by *Eucalyptus globulus* extracts

Microorganisms	Crude extracts zone diameter (in mm)									
	Pet. ether		Hexane		Benzene		Ethyl acetate		Ethanol	
	Ctrl	Test	Ctrl	Test	Ctrl	Test	Ctrl	Test	Ctrl	Test
<i>Escherichia coli</i> ATCC25922	0	6	0	0	0	0	0	0	0	1
<i>Pseudomonas aeruginosa</i> ATCC27853	0	10	0	3	0	6	0	6	0	13
<i>Klebsiella pneumoniae</i> NCIM2719	0	11	0	2	0	6	0	2	0	7
<i>Saccharomyces cerevisiae</i> ATCC9763	0	6	0	2	0	9	0	4	0	7

4 Conclusion

In the current investigation, the organic solvent extract of *Citrus aurentifolia*, *Eucalyptus globulus* and *Jasmine grandiflorum* was found to be active on most of clinical isolates of *Escherichia coli* ATCC25922, *Pseudomonas aeruginosa* ATCC27853, *Klebsiella pneumoniae* NCIM2719 and *Saccharomyces cerevisiae* ATCC9763. Phytochemical test confirms the presence of flavonoids alkaloid, volatile oils, phenols. In most cases higher concentration will be necessary to show the maximum activity. AGC isolated fraction's structural study will prove the activity relationship as far as antimicrobial activity concern. Thus, it is reasonable to expect that these terpenoidal and flavonoidal derivatives would be therapeutically useful for

not only on topical skin infection but also to enhance fragrance in formulations like antiseptic lotions, liniments, deodorants, soaps, and hand washers.

References

1. Farnsworth, N. R., & Loub, W. D. (1983). Information gathering and data bases that are pertinent to the development of plant-derived drugs in plants: The potentials for extracting protein, medicines, and other useful chemicals. In *Workshop Proceedings* (Vol. 1, pp. 178–195). OTA-BP-F-23. U.S. Congress, Office of Technology Assessment, Washington, D.C.
2. Janovska, D., Kubikova, K., & Kokoska, L. (2003). Screening for antimicrobial activity of some medicinal plant species of traditional Chinese medicine. *Czech Journal of Food Sciences*, *21*, 107–111.
3. Silver, L. L. (1993). Discovery and development of new antibiotics: The problem of antibiotic resistance. *Antimicrobial Agents and Chemotherapy*, *37*, 377–383.
4. Parekh, J., & Chanda, S. (2006). In-vitro antimicrobial activities of extracts of *Launaea procumbens* Roxb. (Labiatae), *Vitis vinifera* L. (Vitaceae) and *Cyperus rotundus* (Cyperaceae). *African Journal of Biomedical Research*, *9*, 21–30.
5. Shariff, Z. U. (2001). *Modern herbal therapy for common ailments. Nature Pharmacy Series* (Vol. 1, pp. 9–84). Spectrum Books Limited, Ibadan, Nigeria in Association with Safari Books (Export) Limited, United Kingdom.
6. Collins, C. H., Lynes, P. M., & Grange, J. M. (1995). *Microbiological methods* (Vol. 7, pp. 175–190). Butterworth-Heinemann Ltd.
7. Farahmandfar, R., Tirgarian, B., Dehghan, B., & Nemati, A. (2019). Changes in chemical composition and biological activity of essential oil from Thomson navel orange (*Citrus sinensis* L. Osbeck) peel under freezing, convective, vacuum, and microwave drying methods. *Journal of Food Science and Nutrition*, *8*(1), 124–138.
8. Jean-Paul, L., Julio, C. R., Gonçalves, J. L. M., et al. (2009). Influence of nitrogen and potassium fertilization on leaf lifespan and allocation of above-ground growth in *Eucalyptus* plantations. *Tree Physiology*, *29*(1), 111–124.
9. DeFilipps, R. A., & Krupnick, G. A. (2018). The medicinal plants of Myanmar. *PhytoKeys*, *102*, 1–341.
10. Zhang, Q. W., Lin, L. G., & Ye, W. C. (2018). Techniques for extraction and isolation of natural products: A comprehensive review. *Chinese Medicine*, *13*, 20.
11. Phuyal, N., Jha, P. K., Raturi, P. P., & Rajbhandary, S. (2020). Total phenolic, flavonoid contents, and antioxidant activities of fruit, seed, and bark extracts of *Zanthoxylum armatum* DC. *The Scientific World Journal*, *8*(7), 807–811.
12. Harbone, J. B. (1984). *Phytochemical methods: A guide to modern technique of plant analysis* (Vol. 2, pp. 37–168). Chapman and Hall.
13. Trease, G. E., & Evans, W. C. (1989). *Pharmacognosy* (Vol. 13, pp. 386–480). English Language Book Society, Bailliere Tindall.
14. Perez, C., Paul, M., & Bazerque, P. (1990). An Antibiotic assay by the agar well diffusion method. *Acta Biologicae et Mediciniae Experimentalis*, *15*, 113–115.
15. Balouiri, M., Sadiki, M., & Ibsouda, S. K. (2016). Methods for *in vitro* evaluating antimicrobial activity: A review. *Journal of Pharmaceutical Analysis*, *6*(2), 71–79.
16. Coban, A. Y., Darka, O., Taşdelen Fişgin, N., Aksakal Tanyel, E., Cetinkaya Sensoy, E., Hepsert, S. A., Birinci, A., & Durupinar, B. (2007). Kisa bildiri: Short communication: Use of cefoxitin disc diffusion method for the detection of methicillin resistance in *Staphylococcus aureus* clinical isolates. *Mikrobiyoloji Bulletin*, *41*(1), 109–113.
17. Zhang, M. T., Ye, X. X., Lan, W., et al. (2018). Strategic combination of isocratic and gradient elution for simultaneous separation of polar compounds in traditional Chinese medicines by HPLC. *Journal of Analytical Methods in Chemistry*, *2018*, 7569283.

18. Altemimi, A., Lakhssassi, N., Baharlouei, A., Watson, D. G., & Lightfoot, D. A. (2017). Phytochemicals: Extraction, isolation, and identification of bioactive compounds from plant extracts. *Plants (Basel)*, *6*(4), 42–49.
19. Kagan, I. A., & Flythe, M. D. (2014). Thin-layer chromatographic (TLC) separations and bioassays of plant extracts to identify antimicrobial compounds. *Journal of Visualized Experiments*, *85*, 51411.
20. Suleimana, M. M., McGaw, L. J., Naidoo, V., & Eloff, J. N. (2009). Detection of antimicrobial compounds by bioautography of different extracts of leaves of selected South African tree species. *African Journal of Traditional, Complementary and Alternative Medicines*, *7*(1), 64–78.
21. Bonnet, M., Lagier, J. C., Raoult, D., & Khelaifia, S. (2019). Bacterial culture through selective and non-selective conditions: The evolution of culture media in clinical microbiology. *New Microbes and New Infections*, *34*, 100622.
22. Wang, M., Zhang, Y., Wang, R., Wang, Z., Yang, B., & Kuang, H. (2021). An evolving technology that integrates classical methods with continuous technological developments: Thin-layer chromatography bioautography. *Molecules*, *26*, 4.

Evaluation of Phytochemical, Antioxidant of *Fumaria parviflora* (Lam.) Methanolic Extract of Whole Plant by HPTLC Analysis



Madhu Singh, Shamshad Ather, Himanshu Gupta, Kapil Singh Thakur, and Mansee Thakur

Abstract Plants play a crucial role in contemporary medication and the Indian traditional medical system is well known for its use of *Fumaria parviflora*. Analysis using HPTLC showed the presence of alkaloids, phenols, flavonoids, tannins, and bitter principles in the plant's methanolic extract. The HPTLC system also revealed its excellent antioxidant activity. The study concludes that *F. parviflora* has a wide range of phytoconstituents that contribute to its medicinal potential, confirming its traditional use in India.

Keywords *Fumaria parviflora* · Phytoconstituents · Chromatogram · Antioxidant · Densitometry · HPTLC

1 Introduction

New drugs have been influenced by plants, improving human health. Traditional medicine includes plant-derived meds, manual and spiritual treatments. Nearly 75% of the world relies on traditional medicine, mostly herbal remedies. Many civilizations have used herbal medicine, including Indian, Chinese, Western, Japanese, Egyptian, and Unani/Tibb [1] In India, herbal medicine is widely used with over 178 species of plants used in large quantities [2]. Herbs can correct imbalances and restore balance in the body through phytochemicals. Medicinal plants are used to make well-known drugs such as ephedrine, morphine, and digoxin [3, 4].

Fumaria parviflora var. *indica*, also known as *Fumaria indica*, is a common plant in the Indian subcontinent known for its therapeutic possessions, including hepatoprotective activity [5, 6], anti-inflammatory activity [7], antimicrobial activity

M. Singh · S. Ather · H. Gupta · M. Thakur (✉)
Department of Medical Biotechnology, MGMCR & MGMSBS, MGMIHS, Navi Mumbai, India
e-mail: mansibiotech79@gmail.com

K. S. Thakur
Nuvox Healthcare Pvt, Ltd., Navi Mumbai, India

[7], spasmolytic effect [8], chemo preventive effect [6], fever [9] and laxative as well as, diuretic, detoxification and diaphoretic [10] effects. Bioactive phytochemicals in the plant cause these effects and identifying them is important due to rising drug resistance and limited treatments for many diseases. The WHO emphasizes quality research to validate traditional plant-based remedies [11]. Technology allows accurate recognition and isolation of active components, including with HPTLC which generates precise data. HPTLC “fingerprint analysis” helps standardize plant matter, especially for unprocessed plant extracts [12]. The objectives of this work included the description and development of HPTLC analysis for the confirmation of phytoconstituents in extract of *F. parviflora* and its antioxidant activity.

2 Materials and Method

2.1 Physicochemical Evaluation

According to the procedure outlined in The Ayurvedic Pharmacopoeia of India, several physicochemical characteristics, including extractive values, ash values, and moisture content were estimated [13].

2.2 Extraction

Fumaria parviflora Lam. whole plant powder was acquired from Azamdeal, a certified vendor in Pune, Maharashtra, and carrying FSSAI ID 21520368000053. Plant powder was macerated in a closed flask for 24 h with of 90% ethanol, using the maceration method by evaporating the excess solvent the extract was then obtained.

2.3 Instrumentation and Chromatographic Conditions

To prepare the sample of 100 $\mu\text{g/ml}$, 300 mg of extract was weighed and dissolved in 3 ml HPTLC grade methanol, sonicated for 10 min in ultrasonic bath and at 25,000 rpm it was centrifuged for 10 min and used the supernatant as the test solution for the study. The CAMAG HPTLC system was used for the study. The sample was applied to a pre-coated silica gel aluminum HPTLC 60 F254 plate using a micro syringe and dried. The plate was then developed using a twin trough chamber and photo documented using a CAMAG TLC Visualizer 2 at visible light, UV 254 and 366 nm. Densitometric scanning was performed using deuterium (254 nm), mercury (366 nm), and tungsten (540 nm) lamps and analyzed using winCATS software to ensure separation reliability.

2.4 HPTLC Fingerprint of *Fumaria parviflora* Lam. Plant Extract

The sample bands were applied in volumes of 2, 5, and 10 μl of concentration 100 $\mu\text{g}/\text{ml}$ on the TLC plate by using ATS 4 syringe. The sample-applied plate was saturated in the Twin trough chamber with Toluene: Chloroform: Ethanol in proportion of 4:4:1 (v/v/v) as mobile phase followed by derivatizing with 10% Methanolic Sulphuric acid. The clean and developed plates were visualized for bands at visible light, at UV 254 and 366 nm followed by densitometer scanning at 254, 540, 366, 190–400 nm for spectra [14].

2.5 Qualitative Phytochemical Investigation

For the prepared extract, qualitative HPTLC phytochemical investigations were conducted. These phytochemical screens comprised examinations for bitter principle, alkaloids, tannins, flavonoids, and phenols [15].

2.6 In-Vitro Antioxidant Activity Investigation

A 25 ml syringe was used by ATS 4 to dispense 2, 4, 6, 8, and 10 μl of the sample onto the TLC plate. The sample-loaded plate was saturated in a Twin trough chamber with mobile phase Ethyl acetate: Methyl ethyl ketone: Formic acid: Water, 5:3:1:1 (v/v/v). The plate was derivatized using DPPH reagent in the dark after visualisation at R white. The plate was incubated in the dark for five minutes before being checked for a white fluorescent zone [16].

3 Results and Discussion

3.1 Physicochemical Evaluation

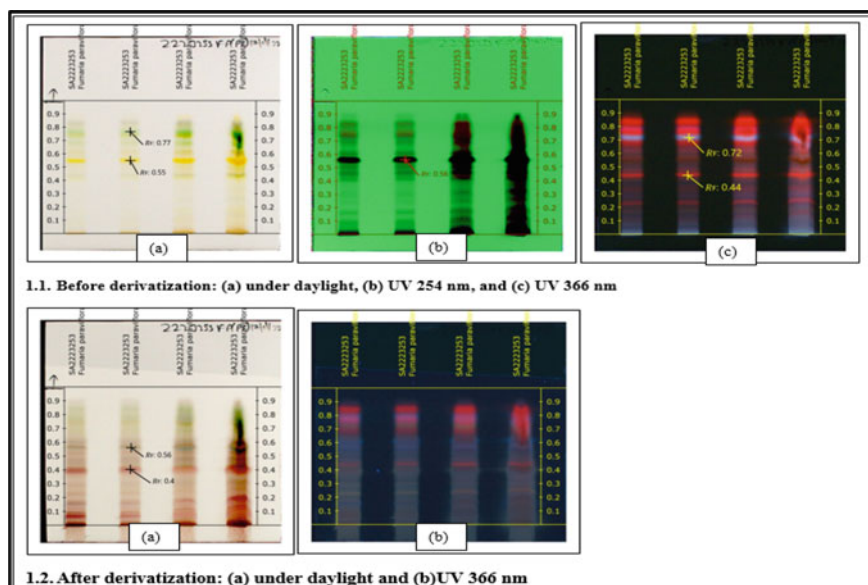
Herbal drug evaluation of physical constants is important to check for adulteration or poor management. Low moisture content prevents growth of microorganisms, while ash and extractive values determine purity [17, 18]. Average values as a percentage of air-dried material are given in Table 1.

Table 1 Physicochemical studies result

Particulars	% w/w \pm SD (at 90% C.I.; $n = 3$)
Moisture content	77 \pm 1.89
Total ash	23.7 \pm 0.54
Acid insoluble ash	6.4 \pm 1.45
Water soluble ash	7.4 \pm 1.45
Alcohol soluble extractive value	8.7 \pm 0.548
Water soluble extractive value	31 \pm 0.95

3.2 HPTLC Fingerprinting

In the current study, phytochemical fingerprint profiles created by HPTLC and methanolic extracts of *F. parviflora* Lam. are optimised. As shown in the figures and tables below, it reveals the presence of different phytochemicals. At 366 nm, two prominent bands were observed at Rf 0.44 (red) and 0.72 (blue) in the chromatograms of Fig. 1 when they were examined at visible light, UV 254 nm, and 366 nm. Following derivatization, at 540 nm scanning a densitogram was produced Fig. 2 and peak table, in Table 2. The 10 peaks in the densitogram from the well-resolved HPTLC profiles corroborate the traditional therapeutic usage of this species.

**Fig. 1** Fingerprinting profile of *F. parviflora*

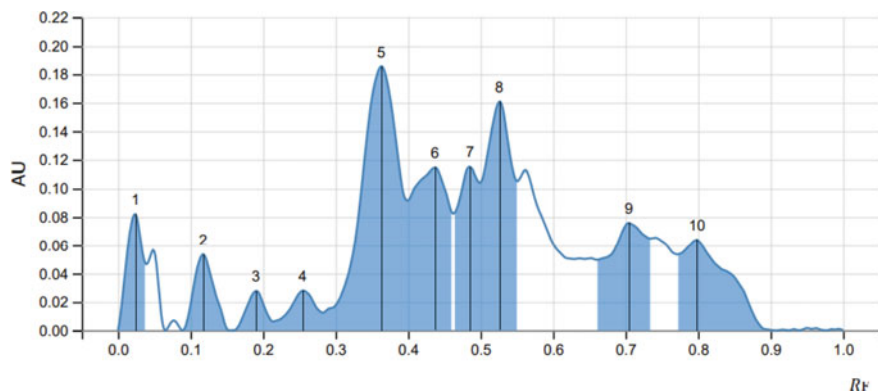


Fig. 2 Densitogram of methanolic extract of *F. parviflora* Lam. at 540 nm, depicting the various peaks (bands)

Table 2 Peak table of methanolic extract of *F. parviflora* Lam. at 540 nm (track 2)

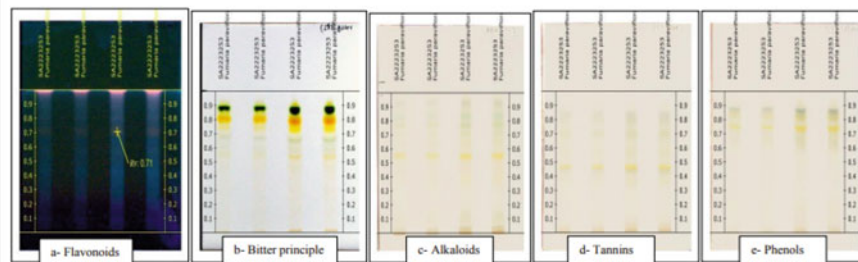
Peak	Start R_f	Start H	Max R_f	Max H	Max %	End R_f	End H	Area	Area %
1	0.000	0.0000	0.0240	0.0818	9.03	0.039	0.0467	0.00207	4.8
2	0.089	0.0000	0.1180	0.0536	5.91	0.153	0.0000	0.00169	3.91
3	0.160	0.0000	0.1900	0.0277	3.06	0.215	0.0063	0.00081	1.87
4	0.215	0.0063	0.2550	0.0280	3.09	0.282	0.0124	0.00117	2.71
5	0.282	0.0124	0.3630	0.1856	20.47	0.398	0.0916	0.01111	25.69
6	0.398	0.0916	0.4370	0.1145	12.63	0.461	0.0826	0.00649	15
7	0.463	0.0825	0.4850	0.1150	12.69	0.498	0.1041	0.00366	8.46
8	0.498	0.1041	0.5260	0.1606	17.72	0.550	0.1053	0.00682	15.78
9	0.661	0.0496	0.7050	0.0757	8.35	0.734	0.0647	0.00462	10.68
10	0.773	0.0535	0.7980	0.0638	7.040	0.905	0.0000	0.00479	11.09

3.3 Qualitative Phytochemical Investigation

Methanolic extract of *F. parviflora* showed the presence of flavonoids, alkaloids and bitter principle in phytoconstituent analysis. HPTLC chromatogram showed various proportions of mobile phase and derivatizing reagents, with changes in color (Fig. 3(3.1)) after derivatization presented in Table 3.

The confirmation of flavonoids detected under 366 nm derivatized as fluorescent compounds at R_f 0.71 (Fig. 3(3.2a)). The bitter principles were detected as yellow band at R_f 0.51 and 0.84 respectively (Fig. 3(3.2b)). The alkaloid was detected as orange bands at R_f 0.32 (Fig. 3(3.2c)). Whereas tannins and phenols were not identified in the *F. parviflora* Lam. methanolic extract (Fig. 3(3.2d)) and (Fig. 3(3.2e)) respectively. The sample extract was scanned at 540 nm for densitograms to validate

3.1 HPTLC developed chromatograms of phytochemicals before derivatization:



3.2 HPTLC developed chromatograms of phytochemicals after derivatization

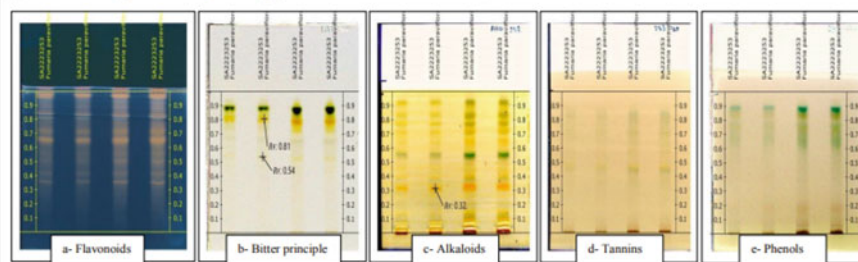


Fig. 3 HPTLC Chromatograms of phytoconstituents at 366 nm (3.1a) and R White (3.1b–e) before derivatization; at 366 nm (3.2a) and R White (3.2b–e) after derivatization

Table 3 Phytoconstituent analysis of *F. parviflora* Lam. methanolic extract by HPTLC

Compounds	Mobile phase	Derivatizing reagent	R White light	UV 366 nm
Flavonoids	Ethyl acetate:water:formic acid:glacial acetic acid, 10:2.6:1.1:1.1 (v/v/v)	10% Methanolic sulphuric acid + heating of plate	–	Yellow florescent compound, red fluorescent-chlorophyll
Bitter principle	Ethyl acetate:methanol:water, 7.7:1.5:0.8 (v/v/v)	Vanillin sulphuric acid reagent + heating of plate	Yellow bands	–
Alkaloids	Toluene:ethyl acetate:diethyl amine, 7:2:1 (v/v/v)	Dragendorff reagent + 10% methanolic sulphuric acid	Orange bands	–
Tannins	Toluene:ethyl acetate:formic acid, 6:4:0.3 (v/v/v)	Alcoholic ferric chloride	No dark blue bands	–
Phenols	Cyclohexane:ethyl acetate:formic acid, 4:6:1 (v/v/v)	Alcoholic ferric chloride	No dark blue bands	–

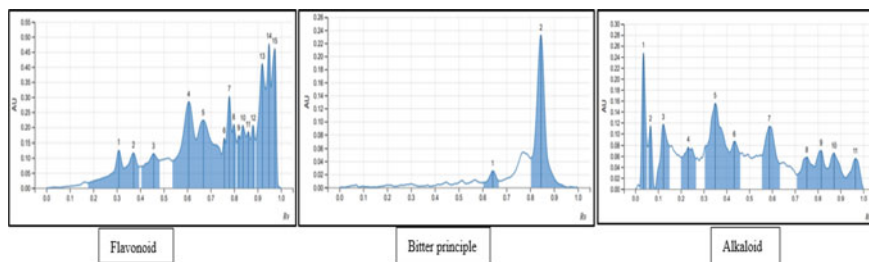


Fig. 4 HPTLC densitograms at 540 nm of *F. parviflora* Lam. methanolic extract, showing different peaks of phytoconstituents in concentration of sample 100 mg/ml

the presence of flavonoids, bitter principle and alkaloids from chromatograms after derivatization (Fig. 4).

Alkaloids are amino acids present in plants, used for therapeutic purposes like pain relief, disease resistance, stress tolerance, and disorder treatment [19]. Four types of alkaloids were found in methanolic extracts of *F. parviflora* Lam with different Rf values. Medical research is focusing on flavonoids for their beneficial properties, such as anti-inflammatory, enzyme inhibition, antibacterial, anticancer, anti-allergenic, and antioxidant effects [20]. The bitter principle of the plant can be used for detoxification and spasmolytic effects [21]. *Fumaria* species have been shown to have antifungal [22], antibacterial [23], and anti-inflammatory properties [24] due to the presence of phytochemicals such as alkaloids, polyphenols, and flavonoids.

3.4 *In-Vitro* Antioxidant Activity

F. parviflora extract showed excellent to significant antioxidant activity at 2–10 μ l with DPPH reagent. The plant was moderate in polyphenols, with antioxidant activity observed at Rf 0.34 and 0.56 with white fluorescent zones. (Fig. 5).

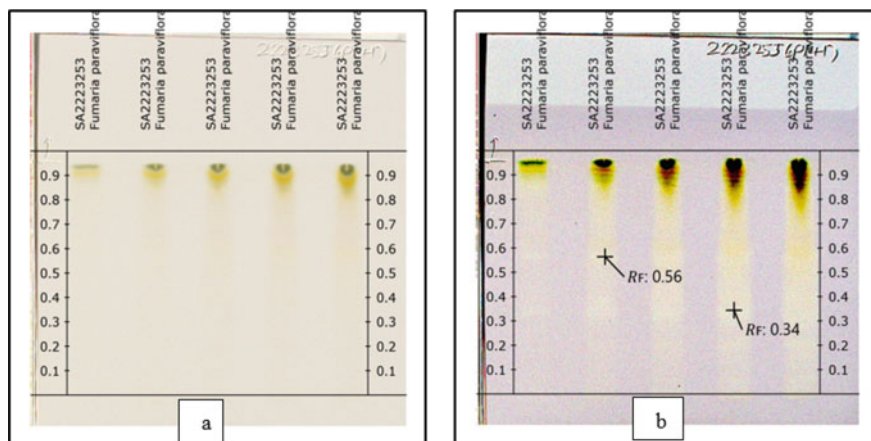


Fig. 5 HPTLC antioxidant analysis-DPPH chromatograms at R White (**a** before derivatization, **b** after derivatization)

4 Conclusion

The study contends that various phytoconstituents of therapeutic importance are present in the methanolic extracts of the *F. parviflora* Lam. plant, which supports their use in medicine. These factors also aid in defining pharmacopoeia standards, which are desperately needed both for the survival of the conventional, age-old medical system and because it is becoming increasingly important on a worldwide scale.

Acknowledgements Authors thank MGMIHS, Navi Mumbai and Anchrom, Mumbai for encouragement and technical aid during the study.

References

1. Fokunang, C. N., Ndikum, V., Tabi, O. Y., Jiofack, R. B., Ngameni, B., Guedje, N. M., Tembe-Fokunang, E. A., Tomkins, P., Barkwan, S., Kechia, F., Asongalem, E., Ngoupayou, J., Torimiro, N. J., Gonsu, K. H., Sielinou, V., Ngadjui, B. T., Angwafor, F., III, Nkongmeneck, A., Abena, O. M., ... Kamsu-Kom. (2011). Traditional medicine: Past, present and future research and development prospects and integration in the National Health System of Cameroon. *African Journal of Traditional, Complementary and Alternative Medicines*, 8(3).
2. Sen, S., & Chakraborty, R. (2017). Revival, modernization and integration of Indian traditional herbal medicine in clinical practice: Importance, challenges and future. *Journal of Traditional Complementary Medicine*, 7(2), 234-244.
3. Heinrich, M. (2010). Ethnopharmacology in the 21st century-grand challenges. *Frontiers in Pharmacology*, 1, 8.
4. Latha, P. S., & Kannabiran, K. (2006). Antimicrobial activity and phytochemicals of *Solanum trilobatum* Linn. *African Journal of Biotechnology*, 5(23).

5. Kooshki, F., Niazkari, H. R., Shirazi, S., Asghari Azar, V., Moghimian, M., & Karimi, A. (2020). *Fumaria parviflora* improves liver damage and lipid profile changes in STZ-induced diabetic rats. *Physiology and Pharmacology*, 24(3), 221–229.
6. Rezaeikia, Z., Saeidi-Sar, S., Malakijoo, N., & Mousavi, Z. (2019). Chemoprotective effect of *Fumaria parviflora* L. extract against vincristine induced hepatotoxicity in male rats. *Medical Science*, 29(2).
7. Bhargava, A., Shrivastava, P., & Tilwari, A. (2022). Investigation of antioxidant and antimicrobial activity of *Fumaria parviflora* Lam. *Journal of Advanced Scientific Research*, 13(03), 146–150.
8. Bashir, S., Al-Rehaily, A. J., & Gilani, A. H. (2012). Mechanisms underlying the antidiarrheal, antispasmodic and bronchodilator activities of *Fumaria parviflora* and involvement of tissue and species specificity. *Journal of Ethnopharmacology*, 144(1), 128–137.
9. Anonymous, A. (2004, August 24). The ayurvedic pharmacopoeia of India. In: *The ayurvedic pharmacopoeia of India*. Retrieved January 23, 2023, from <http://www.ayurveda.hu/api/API-Vol-4.pdf>
10. Khare, C. P. (2007). *Indian medicinal plants*. Springer.
11. World Health Organization. (2004). Guidelines for the regulation of herbal medicines in the South-East Asia region (No. SEA-Trad. Med.-82). WHO Regional Office for South-East Asia.
12. Shanthi, P., Sownthariya, C., & Sundari, U. T. (2022). HPTLC profiling and antibacterial efficacy of *Melia azedarach* Linn. leaf extracts against secondary bacterial pathogens of Dermatophytosis. *Biomedical & Pharmacology Journal*, 15(2), 1013–1024.
13. New Delhi: Govt. of India, Ministry of Health and Family Welfare, Dept. of Ayush. (2008). *The ayurvedic pharmacopoeia of India*. Retrieved January 23, 2023.
14. Merck | life science | industrial & lab chemicals | eshop. (n.d.). Retrieved January 23, 2023, from <https://www.merckmillipore.com/INTL/en>
15. Gasparic, J., & Churáček, J. (1978). *Laboratory handbook of paper and thin-layer chromatography*. E. Horwood.
16. Islam, M. K., Sostarić, T., Lim, L. Y., Hammer, K., & Locher, C. (2021). Antioxidant HPTLC-DPPH fingerprinting of honeys and tracking of antioxidant constituents upon thermal exposure. *Foods*, 10(2), 357.
17. Modi, K., Amin, A., & Shah, M. (2016). A pharmacognostical study on *Fumaria parviflora* Lamk. *Journal of Natural Remedies*, 16, 1–6.
18. Kumar, S., Kumar, V., & Prakash, O. M. (2011). Pharmacognostic study and anti-inflammatory activity of *Callistemon lanceolatus* leaf. *Asian Pacific Journal of Tropical Biomedicine*, 1(3), 177–181.
19. Yan, M. H., Cheng, P., Jiang, Z. Y., Ma, Y. B., Zhang, X. M., Zhang, F. X., Yang, L. M., Zheng, Y. T., & Chen, J. J. (2008). Periglaucines A-D, anti-HBV and -HIV-1 alkaloids from *Pericampylus glaucus*. *Journal of Natural Products*, 71(5), 760–763.
20. Harborne, J. B., & Williams, C. A. (2000). Advances in flavonoid research since 1992. *Phytochemistry*, 55(6), 481–504.
21. The bitter principle. *The naturopathic herbalist* (March 15, 2014). Retrieved January 23, 2023, from <https://thenaturopathicherbalist.com/plant-constituents/the-bitter-principle/>
22. Moghtader, M. (2013). In vitro antifungal effects of *Fumaria vaillantii* Loisel. essential oil on *Aspergillus flavus*. *Journal of Yeast and Fungal Research*, 4(2), 21–25.
23. Khamtache-Abderrahim, S., Lequart-Pillon, M., Gontier, E., Gaillard, I., Pilard, S., Mathiron, D., Djoudad-Kadji, H., & Maiza-Benabdesselam, F. (2016). Isoquinoline alkaloid fractions of *Fumaria officinalis*: Characterization and evaluation of their antioxidant and antibacterial activities. *Industrial Crops and Products*, 94, 1001–1008.
24. Brihi, N., Algieri, F., Rodriguez-Nogales, A., Vezza, T., Garrido-Mesa, J., Utrilla, M. P., Del Mar Contreras, M., Maiza, F., Segura-Carretero, A., Rodriguez-Cabezas, M. E., & Gálvez, J. (2016). Intestinal anti-inflammatory effects of total alkaloid extract from *Fumaria capreolata* in the DNBS model of mice colitis and intestinal epithelial CMT93 cells. *Phytomedicine*, 23(9), 901–913.

Treating Fungal Infections by Herbal Transdermal Patches



Sonam Toraskar, Vijay Chakote, Shweta Bahire, and Pooja Patil

Abstract Innovations in transdermal drug delivery system (TDDS) have made important contributions to medical practice by providing advances in the delivery of treatment with existing and novel drugs. Today about 74% of drugs are taken orally and are found not to be as effective as desired. To improve such character transdermal drug delivery system was emerged. Drug delivery through the skin to achieve a systemic effect of a drug is commonly known as transdermal drug delivery system. The study aimed to formulate herbal transdermal patch and to evaluate its physicochemical properties. The Herbal transdermal patch was formulated by adding the extract of neem in the form of oil and ginger powder. Physicochemical tests viz. visual inspection, pH, thickness, weight variation, folding endurance etc. were performed to determine overall efficiency of patches. The antifungal efficacy was investigated with marketed antifungal patch and found reasonably comparable. The related parameters also were estimated in specified limits.

Keywords Transdermal · Herbal patch · Neem oil · Ginger powder · Patch · Antifungal

1 Introduction

Discovering a new medicine is a very expensive and time-consuming undertaking. However, re-designing the modules and means to transport medicine into the body is a less demanding and more lucrative task. The design of dosage form, whether a tablet, an injection or a patch; to deliver the right amount of medicine at the right time to the right target site becomes complicated if each medication were to be delivered in an optimal and preferred manner to the individual patient. The medication may not be absorbed if it is released too slowly. If it is delivered too rapidly, the patient may suffer untoward effects and its desired effects may not last if needed. If patient is expected to take the medicine more than two times a day,

S. Toraskar (✉) · V. Chakote · S. Bahire · P. Patil
Department of Pharmaceutics, SVERI's College of Pharmacy, Pandharpur, India
e-mail: sdtoraskar@cop.sveri.ac.in

© The Author(s), under exclusive license to Springer Nature Switzerland AG 2024
P. M. Pawar et al. (eds.), *Techno-Societal 2022*,
https://doi.org/10.1007/978-3-031-34648-4_51

513

compliance will be adversely affected. One of the solutions develop is transdermal drug delivery system which can deliver medicines via the skin portal to systemic circulation at a predetermined rate and maintain clinically effective concentration over a prolonged period. This route of drug administration avoids the hazards and discomfort associated with parental therapy and improves patient compliance, as it is easy to apply a patch. Controlled drug release can be targeted by transdermal drug delivery systems (TDDS) which supplies medicines through the skin portal over an extended tenure of time. A lot of sensation has been achieved by TDDS during the last decade as it furnished several merits over the traditional delivery systems and oral controlled release delivery systems, including better patient conformity [1–5].

2 Materials and Methods

Drug substance i.e. Ginger Powder and Neem Oil purchased from Pandharpur. Polyvinyl pyrrolidone and polyvinyl alcohols, is collected from the Loba Chem Pvt. Ltd, Mumbai. Other excipients methanol, Propylene glycol, Dimethyl sulfoxide, is collected from the Loba Chem Pvt. Ltd, Mumbai.

2.1 Preparation of Antifungal Herbal Transdermal Patch

The equal amount of water and methanol taken and make the solution of solvent. The given quantity of PVP of 2 mg and PVA 3 mg polymers are taken, dissolve and clear solution is produced. To dissolve polymers and make clear solution heated at 60 °C. Add 5 ml of neem oil and 2 mg of ginger powder. At the end add polyethylene glycol 400 in a quantity 0.2 ml and dimethyl sulphoxide 0.2 ml. Apply glycerin to petri plate. Pour solution into petri plate at all equal thickness. Place petri plate in hot air oven for 20 min. After drying, striped patch with the help of knife. Place petri plate without disturbance in hot air oven for 20 min. Cut the patches into 2 * 2 cm. The herbal transdermal patches were prepared (Fig. 1).

3 Results and Discussion

3.1 Percentage Moisture Content

The prepared films were weighed individually and kept in desiccators containing fused calcium chloride at room temperature for 24 h. After 24 h, the films were re-weighed and percentage moisture content was determined [6].



Fig. 1 Extraction of sample and conversion into formulation

3.2 Thickness

The thickness of the film was measured using a screw gauge.

3.3 Weight Uniformity

The prepared patches were dried at 60 °C for 4 h before testing. A specified area of patch was cut in different parts of the patch and weighed on digital balance. The average weight and standard deviation values were calculated from the individual weights [7].

3.4 Percentage Elongation Break Test

The percentage elongation break was determined by measuring the length just before the break point.

3.5 Flatness Test

Three longitudinal strips were cut from each film at different portion like one from the center, other one from the left side, and another one from the right side. The length of each strip was measured and the variation in length because of non-uniformity in flatness was measured by determining percent constriction, with 0% constriction equivalent to 100% flatness [8-10].

3.6 Statistical Analysis

Each patch formulations were prepared in duplicate and each analysis was duplicated. Evaluation test of all the batches were tested for significance by using independent t-test with the aid of SPSS-12.0. Difference was considered significant when $p < 0.05$.

3.7 In Vitro Release

Dissolution studies Herbal transdermal film measuring 2.8 cm² were subjected to in vitro diffusion testing using Keshary-Chien diffusion cell. Mesh (60) was clamped between the donor and receptor compartments and the film was placed over the mesh. The receptor compartment contained Phosphate buffer/methanol (9:1). The amount of drugs diffusing into the receptor compartment across the mesh was determined by withdrawing 0.5 ml samples over the duration of experiment and an equivalent amount of diffusion medium was added to the receptor compartment to maintain a constant volume. The samples were filtered through injection millipore filter of 0.45 μ . These samples were analyzed by HPLC. The cumulative amount of drug permeating through the mesh was then calculated [11, 12].

3.8 Folding Endurance Test

Developed patch was taken and subjected to repetitive folding at same point until it gets sever. Instances of time when patch folded without breaking was noted down.

4 Conclusion

Today about 74% of drugs are taken orally and are found not to be as effective as desired. To improve such character transdermal drug delivery system was emerged. Drug delivery through the skin to achieve a systemic effect of a drug is commonly known as transdermal drug delivery system. The study aimed to formulate herbal transdermal patch and to evaluate its physicochemical properties. The Herbal transdermal patch was formulated by adding the extract of neem in the form of oil and ginger powder. Physicochemical tests viz. visual inspection, pH, thickness, weight variation, folding endurance etc. were performed to determine overall efficiency of patches. The antifungal efficacy was investigated with marketed antifungal patch and found reasonably comparable. The related parameters also were estimated in specified limits (Fig. 2).

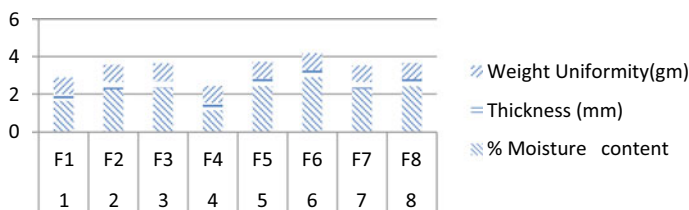


Fig. 2 Weight uniformity test

References

1. Vyas, S. P., & Khar, R. K. (2002). 1st ed., p. 411. Vallabh Prakashan.
2. Vyas, S. P., & Roop, R. K. (2005). *Controlled drug delivery concepts and advances*. Vallabh Prakash Publishers.
3. Sanap, G. S., Dama, G. Y., Hande, A. S., Karpe, S. P., Nalawade, S. V., & Kakade, R. S. (2008). Preparation transdermal monolithic systems of solvent casting method of indapamide and the use of vegetable oil as permeation enhancer. *IJGP*, 2, 129–133.
4. Patel, R. P., Patel, G., & Baria, A. (2009). Formulation and evaluation of transdermal patch of aceclofenac. *International Journal of Drug Delivery*, 1, 41–51.
5. Devi, K. V., Saisivam, S., Maria, G. R., & Deepti, P. U. (2003). Design and evaluation of matrix diffusion controlled transdermal patches of verapamil hydrochloride. *Drug Development and Industrial Pharmacy*, 29, 495–503.
6. Suryadevara, P. K. (2010). *Formulation and evaluation of antiemetic patch comprising ondansetron hydrochloride*. KLE University.
7. Dhiman, S., Singh, T. G., & Rehni, A. K. (2011). Transdermal patches—A recent approach to new drug delivery system. *Indian Journal of Pharmaceutical Sciences*, 3(Suppl 5), 26–34.
8. Lec, S. T., Yac, S. H., Kim, S. W., & Berner, B. (1991). One way membrane for transdermal drug delivery systems/system optimization. *International Journal of Pharmaceutics*, 77, 231–237.
9. Ansari, K., Singhai, A. K., & Saraogi, G. K. (2011). Recent advancement in transdermal drug delivery system. *Indian Journal of Pharmaceutical Sciences*, 3(Suppl 5), 52–59.
10. Gupta, R., & Mukherjee, B. (2003). *Drug Development and Industrial Pharmacy*, 29, 1–7.
11. Bhalla, H. L., & Bhate, A. S. (1994). *Indian Drugs*, 31(7), 328–333.
12. Reddy, R. K., Muttalik, S., & Reddy, S. (2003). Once daily sustained release matrix tablets of nicorandil: Formulation and in-vitro evaluation. *AAPS PharmSciTech*, 4, 480–488.

Current Advances in Tablet in Tablet as Drug Delivery System: A Review



Satish Vasant Mandave and Narendra Kumar Pandey

Abstract Tablets are the most frequently used oral dosage form amongst the patient because of their simplicity, accuracy in the administration of dose, stability, and economy. Coating of the tablet is one of the most important techniques to mask the bitter taste, unpleasant odor and also for a better quality of tablets like color and texture. Commonly used coating techniques are aqueous or organic coating which has its limitations. As compared to other coating techniques tablet in tablet (Compression coating) is one of the first non-solvent coating techniques and it is also known as a dry coating or press coating. The present review consolidates and broadens on introduction, classification, recent advancement, and characterization of tablet in tablet technology. The one-step dry coating (OSDrC[®]) technology which is used to manufacture tablet in tablet is based on three compression processes. It does not require a separate procedure for the production of the core tablet as both the layer (core layer and surrounding compressed coating layer) are formed into the same tablet press on one turret. Compression coating technology is not only used to preserve the drug from the atmosphere but also to attain the desired release of the drug at a specific site.

Keywords Tablet in tablet · OSDrC · Compression coating · The core layer · Nonsolvent coating

S. V. Mandave (✉)

Faculty of SVERI's College of Pharmacy (Poly.), Pandharpur, Solapur, Maharashtra 413304, India
e-mail: svmandave@cop.sveri.ac.in

S. V. Mandave · N. K. Pandey

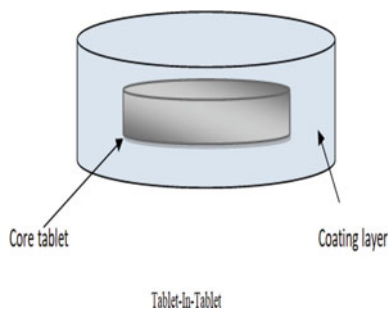
School of Pharmaceutical Sciences, Lovely Professional University, Phagwara, Punjab 144411, India

1 Introduction

Now a day's oral dosage form is extensively used amongst all other available dosage forms. From all the oral dosage forms, the tablet is the most commonly used oral dosage form as 70% of prescriptions are dispensed in the form of tablets. Pharmaceutical tablets became most popular amongst the patient due to their simplicity, accuracy in the administration of dose, stability, and economy [1]. Many pharmaceutical drugs are bitter with an unpleasant odor and they may cause gastric irritation when given in tablet form. Various tablet coating techniques are used to ensure the masking of taste and odor, physical and chemical protection of drug, and also to protect the active pharmaceutical ingredient from the gastric environment [2]. Frequently used coating techniques in pharmaceutical industries are aqueous or organic coating. However these coating technologies are also having some limitations and pitfalls like it as a very costly, tedious, and time-consuming process, highly skilled persons are required for coating, also it may hamper the pharmacodynamic properties of the active pharmaceutical ingredient. To defeat these drawbacks, one of the best options is tablet into tablet or compression coating drug delivery system. Compression coating is among the first complete dry coating technique of tablets without solvent and exceeds the limitations of the organic coating technique [3].

1.1 *Tablet-in-Tablet Technology*

Tablets are the most accepted solid dosage form compare to other available dosage forms due to their advantages like ease of administration, relatively low cost of production, and attractive appearance. From all categories of tablet formulations, controlled or modified release formulations are having significant importance due to their various benefits [4]. Now a day's importance of tablet-in-tablet technology is increased for producing modified-release products. The tablet-in-tablet technology was initially recommended by Noyes in the year 1896. As compared to other coating techniques this was among the first solvent-free coating technology also named a dry coating or press coating [5]. Tablet-in-tablet is also known as a compression-coated tablet which has two types; a centralized part is an inner drug core and another surrounding part is an outer coating sheath (Fig. 1). The core is innermost part contains a small permeable tablet with active pharmaceutical ingredients (API) which is compressed with different adjuvant compatible with API. The outer coat consists of coating material that surrounds the internal core to modify the drug release and controls the stability [6]. The inner core is nothing but a tiny tablet that is formulated using a relatively smaller die as compared to the die by which the surrounding coat is formulated. Then formulation of the inner tablet core is shifted to (placed in the center) other somewhat bigger dies which consist of coating powder. From the top of the core tablet, a sufficient quantity of coating powder is filled and the resultant material is compressed once again to form a tablet within the tablet. This is a complex

Fig. 1 Tablet in tablet

process, as there are chances of tilting of core tablet while shifting to another die cavity. To obtain an immediate-release formulation, mostly the surrounding coat of tablet is water-soluble and disintegrates rapidly when it is administered orally [7]. The tablet in tablet drug delivery system can be used for the formation of a repeat action tablet in which the surrounding coat rapidly disintegrates and gives the immediate release of the drug whereas the interior core portion releases afterward. However, when the core tablet present in the tablet in tablet dosage form immediately releases the drug, an altogether distinct blood level is obtained which shows the chances of toxicity due to overdose of the drug. To avoid the release of drugs from the two layers at the same time, the core tablet is coated with various polymers which will give an extended-release of a drug in the intestine while the surrounding coat releases immediately in the stomach [8].

1.2 Core Tablet

Core tablet is small porous central part of compression coated tablet dosage form which contains active pharmaceutical ingredient (API). The other polymers and additives which are compatible with API are added during formulation of core table. Polymers are selected on the basis of release profile required for the drug. The drug is released as per the nature of the polymer like immediate release, controlled release etc. The release rate of core tablet is modifying by making the layer of coated material above core tablet [9] (Fig. 2).

Method of preparation of core tablet:

The core tablet is prepared by wet granulation method or direct compression method by mixing active drug with polymers and some additives and compresses them together. In granulation method the drug and all other additives are mixed thoroughly and granules are prepared from the mixer by appropriate method of granulation and dry it. All the granules are finally loaded into the hopper. The tablets are compressed with required compression force with punch which is having smaller diameter as

Fig. 2 Flexible double-punch framework

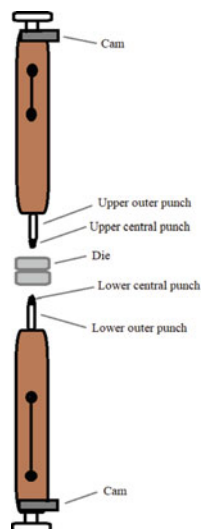


Table 1 Frequently used polymers in the core tablets

Sr. No.	Name of polymer	Use	References
1.	Xanthan gum	Suspending, thickening, emulsifying and stabilizing agent	[11]
2.	Hydroxypropylmethyl cellulose	Thickening agent, binder, film former	[12]
3.	Ethyl cellulose	Coating agent, binder	[13]
4.	Carbopol	Bioadhesion, and good binding	[14]
5.	Polyvinylpyrrolidone	As binder	[15]
6.	Hydroxypropyl cellulose	Binder, thickening agent	[16]
7.	Microcrystalline cellulose	Excellent compressibility and binding properties	[17]
8.	Compritrol	Coating agent	[18]

compared to the diameter of the coating tablet [10]. Various polymers used in core tablet of compression coating tablets are mentioned in Table 1.

1.3 Coat Tablet

Coating tablet concerned with coating material which surrounds the formed core tablet. It doesn't need any solvent to make coat on inner core tablet. It consists of polymers and additives which may or may not contain active drug. It is called as coat tablet because it is generally used to coat the inner core tablet. Sometimes coat tablet immediately releases initial dose of drug and core tablet releases the drug in

Table 2 Frequently used polymers in the coat tablets

Sr. No.	Name of polymer	Use	References
1.	Crospovidone	Excellent swelling characteristics, disintegrant	[21]
2.	Croscarmellose sodium	Superdisintegrant	[22]
3.	Sodium starch glycolate	As dissolution excipient	[23]
4.	Sodium alginate	Disintegrating agent	[24]
5.	Sodium carboxymethyl cellulose	Adhesion and film-forming agent	[25]

extended release pattern. Also many compression coating tablet consist of same drug in core and coat layer, it gives loading and maintenance dose in single formulation [19].

1.3.1 Method of Preparation of Coat Tablet

Coat or final compression coating tablet is prepared by inserting 50% of coating material in the larger die cavity compared to diameter of core tablet. The core tablet is placed at the center of the die cavity and remaining space is filled by other 50% of coating material which covers the upper part of core tablet. The power is compressed by applying the required compression force. The entire process is done either manually or automatically by double press automatic compression machine [20]. Various polymers used in preparation coat tablet of compression coating tablets are mentioned in Table 2.

2 Merits of Tablet in Tablet Technology [26, 27]

- This method is very simple and economic.
- Tablet in tablet is completely dry coating technique, free from solvent and heat.
- Core and surrounding coat are used to separate incompatible drugs.
- This method is generally used for drugs that require extended-release action which releases the drug in the intestine.
- Hygroscopic and thermo-labile drugs are protected with the help of tablet in tablet technology.
- It is used to avoid drug-drug interaction (pharmacokinetic) in between the drugs which are administered at the same time by forming the time gap between the drug releases.

3 Classification of Tablet in Tablet Dosage Form Based on Coating

Various polymers have been used to make compression coats on the tablets to improve the release pattern and pharmacological effect of the drug and to minimize side effects. The discharge of the drug could be controlled or modified by coating the core tablet surface with different types of polymers [28]. A tablet in tablet is a drug delivery system in which the inner core of the table is covered by a coat of various polymers. The drug is released from the core only when the outer coat is breakdown completely [29].

3.1 Controlled Release System

Tablet in tablet technology consists of an immediate release or controlled release core. The core is compression coated which could contain various polymeric excipients, diluents, and active pharmaceutical ingredients (Drug) [24]. The coating protects the inner drug as well as modifies the drug release profile. Based on this concept, the drug could be released in a modified or extended manner and has been used in the pharmaceutical sector for various purposes like preparation of the modified release, pulsatile release, colon targeting release, etc. [30].

3.2 Multiphasic Release

This class of drug delivery system is used in various clinical significance where a disease conditions show circadian rhythm and also as per the pathophysiological requirement of the disease [31]. In such disease conditions concentration of drugs needs to change throughout the day. In this system, the drug is entrapped in both the core and coat layer to form biphasic drug release from a single tablet. The core layer is surrounded by various polymers which give an extended-release of the drug. While the outer coat gives an immediate release of the drug. Extended-release and immediate release of the drug could be obtained by variation in the concentration of the drug and polymer [32].

3.3 Delayed-Release

The delayed-release is designed to extend the release of the drug after a predetermined lag time. In this system, the drug is delivered immediately and completely at the right time and the right site. The system depends on a drug reservoir that is surrounded by

a different soluble barrier layer. The release of the drug could be controlled by using barrier layers of different polymers so that the drug release into the small intestine and more absorption takes place due to more surface area [33].

3.4 Time Controlled Release

The drug core of compressed coated tablets is formulated to delay the release of the drug by coating with various erodible polymers in a different ratio. This controlled drug release is helpful in the treatment of circadian rhythmic diseases. The compression coating method which controls the release of the drug from the core depends on the various polymer coating. The drug releases from the core as per the lag time, after the complete rupture of the polymer coat [34]. The coating layer of erodible polymers could be carried out by using hydrophilic polymer like hydroxypropyl methylcellulose, hydroxypropyl cellulose, polyvinylpyrrolidone, etc. as well as hydrophobic polymers like ethylcellulose, wax, etc. Propranolol hydrochloride tablets of time-controlled pulsatile release properties were formulated with compression coating techniques by using hydroxypropyl methylcellulose and ethylcellulose as a press coated polymer [35].

3.5 pH-Controlled Release

A pH-controlled release system is used to release the drug in desired pH medium with the help of various polymers. pH-sensitive polymers are safe and important additives for site-specific drug delivery system which releases the drug at specific pH depending on the physiological condition of our body. This is achieved by making a coat of pH-sensitive polymers on the core tablet [36]. Depending on various functional groups present in the polymers the material may erode in presence of surrounding pH. The various pH-sensitive polymers like cationic polymers can mask the bitter taste of drugs that respond to acidic pH and release the drug in the stomach while anionic polymers respond to basic pH and the drug liberates in the intestine.

4 Conclusion

Tablet in tablet consists of combined features of sustained-release as well as an immediate-release tablet in the single dosage form. There are many advantages of this technique as compared to traditional coating methods, as it does not require separate procedures for the production of core and therefore no transfer mechanism of the core is required. To improve the release pattern of the drug various polymers with different ratios have been used in the core and coat. To obtain site-specific drug

delivery in a controlled release system, different steps like lag phase and release phase might be regulated by adjusting the different parameters which control the release rate of compressed coating tablet such as various forms of polymer and its particle size, compression force used, the thickness of coating layer.

Acknowledgements Authors would like to thanks Lovely professional University, Punjab, India and SVERI's College of Pharmacy (Poly.), Pandharpur, Solapur, Maharashtra, India, for giving an opportunity to work and publish this review article.

References

1. Harbir, K. (2012). Processing technologies for pharmaceutical tablets: a review. *Int Res J Pharm*, 3(7), 20–23.
2. Ankit, G., Ajay, B., Kumar, K. M., & Neetu, K. (2012). Tablet coating techniques: concepts and recent trends. *Int Res J Pharm*, 3(9), 50–58.
3. Rohit P, Manish J, Bhupendra SC, Sanjay KS (2014) Compression coated tablets as drug delivery system (tablet in tablet): a review. *Int J Pharm Res Dev* 06(01):21–33
4. Nagashree K (2015) Research and reviews. *J Pharm Anal Solid Dosage Forms Tablets* 4(2):60–71
5. Prasanthi, D., Prashanti, S., & Meghana, G. (2019). Formulation and evaluation of press coated tablets of lansoprazole. *Int J Appl Pharm*, 11(4), 49–56.
6. Patil PR, Bobade VD, Sawant PL, Rajendra P (2016) Emerging trends in compression coated tablet dosage forms: a review 7(3):930–938
7. Modi, D., Amaliyar, P., Kalal, Y., Gangadia, B., & Chaudhary, S. (2013). Novel approach in compressed-coated tablet dosage form: core-in-cup (in lay) tablet with geometrically altered drug delivery concept. *Br Biomed Bull*, 1(2), 90–102.
8. Gaikwad, S. S., & Kshirsagar, S. J. (2020). Review on tablet in tablet techniques. *Beni-Suef Univ J Basic Appl Sci*, 9(1), 7–14.
9. Ubhe, S. T., & Gedam, P. A. (2020). A brief overview on tablet and it's types. *J Adv Pharmacol*, 1(1), 21–31.
10. Hadi MA, Rao NGR, Rao AS (2013) Formulation and evaluation of compression coated tablets of lornoxicam for targeting early morning peak symptoms of rheumatoid arthritis 12(2):109–117
11. Niranjan, K., Shivapooja, A., Muthyala, J., & Pinakin, P. (2013). Effect of guar gum and xanthan gum compression coating on release studies of metronidazole in human fecal media for colon targeted drug delivery systems. *Asian Journal of Pharmaceutical and Clinical Research*, 6(suppl 2), 310–313.
12. Mamani PL, Ruiz-Caro R, Veiga MD (2012) Matrix tablets: the effect of hydroxypropyl methylcellulose/anhydrous dibasic calcium phosphate ratio on the release rate of a water-soluble drug through the gastrointestinal tract I. in vitro tests. *AAPS PharmSciTech* 13(4)
13. Wasilewska K, Winnicka K (2019) Ethylcellulose-a pharmaceutical excipient with multidirectional application in drug dosage forms development. *Materials* 12(20)
14. Mehta, T. J., Rajput, S. S., Patel, M. R., Patel, K. R., Patel, N. M., & Mothilal, M. (2011). Formulation, development and optimization of metronidazole compression coated tablets. *Der Pharmacia Lett*, 3(5), 94–103.
15. Giri, P., & Singh, I. (2020). Development and evaluation of mucoadhesive tablets of cinnarizine using carboxymethylated guar gum by compression coating technique. *Biointerface Res Appl Chem*, 10(5), 6365–6376.
16. Patel RR, Patel JK, Rajput GC (2009) Novel coating techniques for pharmaceutical dosage form 2(1):756–761

17. Mohapatra, S., Murthy, K. V. R., & Si, S. C. (2016). Formulation and evaluation of chrono modulated time release tablets of metoprolol tartrate. *Journal of Pharmaceutical Sciences and Research*, 8(12), 1367–1369.
18. Hamza, Y. E. S., & Aburahma, M. H. (2010). Innovation of novel sustained release compression-coated tablets for lornoxicam: formulation and in vitro investigations. *Drug Development and Industrial Pharmacy*, 36(3), 337–349.
19. Zaid, A. N. (2020). A comprehensive review on pharmaceutical film coating: past, present, and future. *Drug Des Dev Therapy*, 14, 4613–4623. <https://doi.org/10.2147/DDDT.S277439>
20. Jariwala, D. M., Patel, H. P., Desai, C. T., Shah, S. A., & Shah, D. R. (2016). A review on multiple compressed tablets. *J Pharm Sci Biosci Res*, 6(3), 371–379.
21. Desai, P. M., Liew, C. V., & Heng, P. W. S. (2016). Review of disintegrants and the disintegration phenomena. *Journal of Pharmaceutical Sciences*, 105(9), 2545–2555.
22. Bala BP, Madhavi BLR (2015) Formulation of taste masked, compression coated, immediate release tablets of oseltamivir phosphate—a preliminary investigation 9(4):255–263
23. Wasimul Hasan, M., Someshwar, K., Chaitanya, P., Mohd, A., Pratyusha, A., & Rao, V. U. (2014). Formulation and evaluation of press coated tablets of salbutamol sulphate for time controlled release. *Asian J Pharm*, 8(3), 161–170.
24. Rane, A. B., Gattani, S. G., Kadam, V. D., & Tekade, A. R. (2009). Formulation and evaluation of press coated tablets for pulsatile drug delivery using hydrophilic and hydrophobic polymers. *Chemical & Pharmaceutical Bulletin*, 57(11), 1213–1217. <https://doi.org/10.1248/cpb.57.1213>
25. Bajpai, M., Singh, D. C. P., Bhattacharya, A., & Singh, A. (2012). Design and in vitro evaluation of compression-coated pulsatile release tablets of losartan potassium. *Indian Journal of Pharmaceutical Sciences*, 74(2), 101–106. <https://doi.org/10.4103/0250-474X.103839>
26. Nawle, R. B., & Tadvee, A. A. (2014). Formulation and evaluation of time-release compression coated tablet containing acebrophylline for chronotherapy of asthma. *International Journal of Pharmacy and Pharmaceutical Sciences*, 6(9), 231–237.
27. Sateesh Kumar, V. (2017). Compression coating—an approach to colon-specific drug delivery: review. *Mod Appl Bioequivalence Bioavailab*, 1(3), 1–5.
28. Himaja, V., Sai, K. O., Karthikeyan, R., & Srinivasa, B. P. (2016). A comprehensive review on tablet coating. *Austin Pharmacol Pharm*, 1(1), 1–8.
29. Tang, Y., Teng, H., Shi, Y., He, H., Zhang, Y., Yin, T., Cai, C., & Tang, X. (2018). Tablets of paliperidone using compression-coated technology for controlled ascending release. *Asian Journal of Pharmaceutical Sciences*, 13(2), 143–154.
30. Maity, S., & Sa, B. (2016). Compression-coated tablet for colon targeting: impact of coating and core materials on drug release. *Off J Am Assoc Pharm Sci*, 17(2), 504–515.
31. Arpit, M., Aadesh, K., Manoj, B., & Vaseem, F. (2015). Formulation and in vitro evaluation of dry coated floating pulsatile drug delivery system of enalapril maleate. *Indian J Pharm Sci Res*, 6(5), 2005–2012.
32. Jain, D., Raturi, R., Jain, V., Bansal, P., & Singh, R. (2011). Recent technologies in pulsatile drug delivery systems. *Biomatter*, 1(1), 57–65.
33. Subramaniam, K., Rangasamy, M., Ayyasamy, B., & Natesan, S. K. (2010). Formulation and evaluation of aspirin delayed release tablet. *International Journal of Comp Pharm*, 01(04), 01–03.
34. Vlachou, M. (2016). An account of modified release of melatonin from compression-coated, uncoated and bilayer tablets. *Journal of Pharma & Pharmaceutical Sciences*, 1(4), 10–14.
35. Prajapati, B. G., Patei, G. N., & Solanki, H. K. (2010). Formulation and statistical optimization of time controlled pulsatile release propranolol hydrochloride compressed coated tablet. *Design*, 9–19.
36. Hadi, M. A., Raghavendra Rao, N. G., & Srinivasa Rao, A. (2014). Formulation and evaluation of pH-responsive mini-tablets for ileo-colonic targeted drug delivery. *Tropical Journal of Pharmaceutical Research*, 13(7), 1021–1029.

Design and Optimization of Novel Floating Agent *Saccharomyces boulardii* Probiotic Formulation Based Floating Tablet of Valsartan



Chittam Suvarna and Bhosale Ashok

Abstract *Saccharomyces boulardii* is the unique yeast probiotic which can grow under aerobic or anaerobic conditions and generates CO₂. In present investigation this property of yeast used to develop floating drug delivery system by entrapping generated in situ CO₂ gas. Valsartan is a highly selective and orally active antihypertensive drug which has absorption window in the acidic environment of stomach. Central composite design response surface methodology technique used, so as to explore the effect of formulation variables such as amount of *Saccharomyces boulardii* preparation and calcium hydroxide on floating lag time and % drug release after 12 h. An optimal formulation selected using numerical and graphical optimization technique Valsartan formulation containing this novel floating agent is suitable for gastro retention and it increases its bioavailability. The experimental values and predicted values of an optimized batch are in compliance with each other.

Keywords *Saccharomyces boulardii* · Valsartan · Response surface methodology · Sodium lauryl sulfate

1 Introduction

Yeasts are eukaryotic microorganisms prevalent in natural environments including the normal microbial flora of humans, on plants. In aerobic respiration yeast produces CO₂ and H₂O and in anaerobic alcoholic fermentation it generates ethanol and CO₂. In present investigation this property of yeast used to generate carbon dioxide in floating tablet [1].

C. Suvarna (✉)

PDEA'S Seth Govind Raghunath Sable, College of Pharmacy, Saswad, Pune, Maharashtra, India
e-mail: cssgrs@gmail.com

B. Ashok

PDEA'S Shankarrao Ursal College of Pharmaceutical Sciences and Research Centre, Pune, Maharashtra, India

Saccharomyces boulardii, is the unique yeast probiotic that has been effectively used to prevent and/or treat variety of gastrointestinal diseases. *Saccharomyces boulardii* is generally directed in lyophilized powder form [2]. *Saccharomyces boulardii* retains many properties that make it an imminent probiotic agent, i.e. it survives during GI transit, it grows healthy at temperature 37 °C, both in vitro and in vivo [3], its high acceptance to gastric acidity, proteolysis enables it to attain high populations in the GI tract. They can forever colonise in the colon and do not easily translocate out of the intestinal tract [4]. They can also be perceived alive throughout the GIT, if they are given in lyophilized form. [5]. *Saccharomyces boulardii* is facultative anaerobe so that it can cultivate under aerobic or anaerobic conditions [6].

Valsartan is a potent vasoconstrictor used in hypertension and heart attack, it is an angiotensin-II receptor, type I antagonist. This is a weak acidic drug has absorption window in the acidic environment of stomach. It is rapidly absorbed orally but unfortunately its bioavailability is 23%. Hence different types of formulations in the form of solid dispersions. B cyclodextrin complexes, microcapsules etc., have been fabricated by many scholars in order to improve its low bioavailability and low solubility. But no attempt has been made to address the retention of valsartan near to its absorption window. So, in the present study an attempt was made to develop floating dosage form to increase the bioavailability of drug by taking the advantage of its primary absorption in the stomach region [7].

Sodium lauryl sulfate (SLS) is an anionic surfactant commonly used in pharmaceutical formulations used as an emulsifier, solubilizer and wetting agent. When used as a wetting agent, above the critical micelle concentration (CMC), SLS monomers aggregate to form micelles that can solubilize hydrophobic drugs [8].

2 Materials and Methods

Valsartan was purchased from Destination Pharmagens Aurangabad, Hydroxy propyl methyl cellulose was gifted by Loba Chemie Pvt. Ltd., *Saccharomyces boulardii* probiotic preparation purchased from local market, Hydrochloric acid was gifted by Themis Research lab, Mumbai.

2.1 Preparation of Floating Tablet of ANOVA Batches of Valsartan

Floating tablets of valsartan were prepared by direct compression technique using polymer like HPMC E 15 LV and other ingredients like calcium hydroxide, SLS, magnesium stearate, and *Saccharomyces boulardii* probiotic formulation. All ingredients were passed through sieve no # 40, except yeast preparation. First HPMC E

15 LV, SLS, calcium hydroxide and valsartan were first mixed in mortar and pestle to get a uniform tablet blend. Finally, *Saccharomyces boulardii* preparation and magnesium stearate were mixed delicately to above prepared mixture blend. The mixture was then weighed accurately according to the formula and compressed into tablets using Rotary tablet compression machine (Model: MINI PRESS-II MT) (Karnavati) to obtain tablets of desired specifications [9, 10].

2.2 Evaluation Test

2.2.1 Hardness Test

Monsanto hardness tester used for evaluate hardness [10].

2.2.2 Thickness

Vernier caliper was used for evaluating of thickness of tablets [10].

2.2.3 Friability

For determination of friability Roche friabilator [11].

2.2.4 Drug Content

About 10 tablets were weighed individually and crushed using motor pestle. The crushed powder put in 100 ml 0.1 N HCl solution for complete extraction of drug and stirred continuously, and diluted with 0.1 N HCl solution and the drug content was determined spectrophotometrically [12].

2.2.5 Uniformity of Weight

Twenty tablets were selected randomly weighed individually and the average weight was calculated. The % weight variation was calculated and checked for weight variation as per IP [13].

$\% \text{Weight variation} = \frac{\text{Average weight} - \text{Individual weight}}{\text{Individual weight}} \times 100$

2.2.6 Tablet Floating Behavior

The floating lag time and total floating duration were determined using USP type II (paddle) apparatus at speed 50 rpm in 900 ml 0.1 N HCl at 37 ± 0.5 °C to simulate in vivo conditions on the basis of visual inspection time were recorded [14].

2.2.7 In Vitro Dissolution Studies

In vitro dissolution studies were conducted by using paddle dissolution apparatus (Electrolab) at 50 rpm using 900 ml of 0.1 N HCl, (pH 1.2) as a dissolution medium at 37 ± 0.5 °C and the absorbance of the sample solution was recorded using UV spectrophotometer at 249 nm. The in vitro dissolution study calculation conducted using disso software (PCP disso V3). The in vitro release profile was determined [15].

2.2.8 Determination of Swelling Index

Swelling degree define the change of dimension or weight gain of dosage form. First a tablet was weighed (W_1) and placed in a glass beaker containing 0.1 N HCl solution, having temp 37 ± 0.5 °C. Tablets were removed at intervals of 1, 2, 3, 4, 6 and 8 h, excess solution was carefully removed using filter paper and tablets were again weighed. The % swelling index (SI) was measured by following formula [16].

$$\%SI = \frac{\text{Final Weight of tablet}(W_2) - \text{Initial weight of tablet}(W_1)}{\text{Initial weight of tablet}(W_1)} \times 100$$

2.2.9 Drug Release Mechanism and Model Fitting

In the present study, several mathematical models such as zero-order, first-order, matrix, Higuchi's, peppas and Hixson–Crowell model can be tested to determine the best fit model [17, 18].

2.2.10 Statistical Analysis and Optimization

Design Expert version 13 software used for statistical analysis of the data and optimization polynomial models. The best fitting model was selected on the basis of comparisons of several statistical parameters. ANOVA used to ascertain significant

Table 1 Composition of Valsartan ANOVA formulations (mg/tablet)

Formulation code	Ingredients (mg)					
	Valsartan	HPMC E 15 LV	<i>Saccharomyces boulardii</i> preparation	Calcium hydroxide	SLS	Magnesium stearate
F1	80	125	60	30	5	5
F2	80	135	50	30	5	5
F3	80	145	40	30	5	5
F4	80	135	60	20	5	5
F5	80	145	50	20	5	5
F6	80	155	40	20	5	5
F7	80	145	60	10	5	5
F8	80	155	50	10	5	5
F9	80	165	40	10	5	5

effect of factors on responses. The relationship between the dependent and independent factors was further clarified using response surface plots. Subsequently, a numerical optimization technique used to engender best optimized solution [19] (Table 1).

3 Results and Discussion

The prepared FDDS tablets were evaluated and data enclosed in Table 2. From this data it was clear that evaluation parameters of all ANOVA batches were in acceptable range.

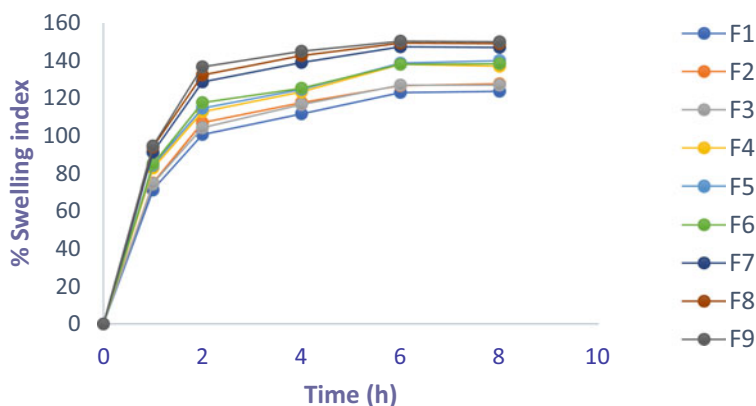
The percentage swelling index which expressed in terms of weight gain of all batches shown in Fig. 1. Formulation F9 shows higher swelling index and formulation F1 shows lower swelling index. Floating is achieved due to hydration of swelling material like polymer Hydroxy propyl methyl cellulose and carbon dioxide gas [20] generation from *saccharomyces boulardii* formulation when it come in contact with water from acidic media.

From data of factorial design, it was clear that floating lag time changes as amount of *Saccharomyces boulardii* preparation and calcium hydroxide changes. As amount of *Saccharomyces boulardii* preparation is changed from 40 to 60 mg the floating lag time decreased because more amount of floating agent contain more Colony Forming Unit of *Saccharomyces boulardii* which produce more amount of carbon dioxide gas, but as concentration of calcium hydroxide changed from 10 to 30 mg floating lag time increased because swellability and viscosity of polymer layer also effect on floating lag time hence as quantity of calcium hydroxide increased it effect on viscosity of HPMC layer. The decrease in viscosity at acidic pH is mainly because of the more coiling nature of HPMC due to increased ionic strength increased. At the lowest pH

Table 2 Evaluation of parameters of Valsartan ANOVA formulations

Batch code	Hardness (kg/cm ²) Mean ± SD	Thickness (mm) Mean ± SD	Friability (%) Mean ± SD	Weight variation	Drug content uniformity (%) Mean ± SD	Total floating time (h)
F1	5.1 ± 0.10	5.04 ± 0.13	0.58 ± 0.05	307.2 ± 3.65	98.80 ± 0.78	> 12
F2	5.2 ± 0.10	5.07 ± 0.11	0.50 ± 0.02	308. ± 3.2	99.70 ± 0.68	> 12
F3	5.06 ± 0.12	5.13 ± 0.10	0.44 ± 0.16	307.6 ± 3.85	100.84 ± 0.39	> 12
F4	4.96 ± 0.28	5.14 ± 0.12	0.50 ± 0.08	306.4 ± 3.50	99.48 ± 0.39	> 12
F5	4.86 ± 0.21	5.10 ± 0.10	0.38 ± 0.10	299.7 ± 3.25	100.57 ± 0.88	> 12
F6	5.1 ± 0.26	5.13 ± 0.08	0.46 ± 0.01	306.15 ± 4.5	101.06 ± 0.69	> 12
F7	5.03 ± 0.25	5.11 ± 0.09	0.52 ± 0.08	304.9 ± 4.77	102.20 ± 0.41	> 12
F8	5.06 ± 0.11	5.13 ± 0.14	0.46 ± 0.09	302.35 ± 4.0	102.65 ± 0.39	> 12
F9	5 ± 0.2	5.14 ± 0.11	0.53 ± 0.21	306.1 ± 3.65	101.74 ± 0.68	> 12

Represents mean ± SD (n = 3)

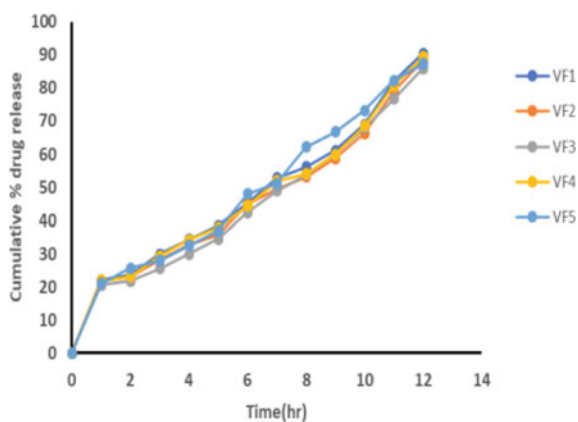
**Fig. 1** Maximum % swelling index of all the Valsartan ANOVA formulations

i.e. in acidic pH of stomach medium, the coiling of polymer molecules proceeds which favored HPMC-water interaction and the possibility for polymer-polymer contact is less prominent [20] (Table 3).

From regression coefficient (R^2) of release data of formulation from F1 to F9 found by curve fitting method displays zero order model is best fit model for formulation. In Krosmeier–Peppas model release exponent i.e. n value of is in range from 0.45 to 0.85 for all batches (Figs. 2 and 3; Tables 4, 5 and 6).

Table 3 Experimental design and observed response of the formulation in central composite design

Std	Run	Factor 1	Factor 2	Response 1	Response 2
		A: floating agent (mg)	B: pH modifier (mg)	FLT (min)	R (%)
4	13	60	30	15.5	91.5
8	2	50	30	17	88.23
3	10	40	30	18.8	85
6	4	60	20	11.3	90
9	5	50	20	12.8	87
13	7	50	20	13.5	87.31
11	8	50	20	14	87.13
10	11	50	20	13.6	87.5
12	12	50	20	14.2	88
5	9	40	20	16	84.5
2	3	60	10	8.5	83
7	1	50	10	10.3	80
1	6	40	10	12.2	78

**Fig. 2** Drug release profiles of Valsartan ANOVA formulations VF1–VF5

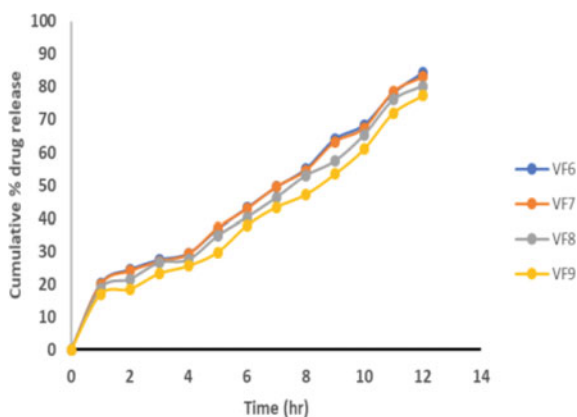


Fig. 3 Drug release profiles of Valsartan ANOVA formulations VF6–VF9

Table 4 ANOVA for linear model for Response 1: floating lag time

Source	Sum of squares	Df	Mean square	F-value	p-value	
Model	91.50	2	45.75	264.28	< 0.0001	Significant
A- <i>Saccharomyces boulardii</i> preparation	22.82	1	22.82	131.80	< 0.0001	
B-Calcium hydroxide	68.68	1	68.68	396.77	< 0.0001	
Residual	1.73	10	0.1731			
Lack of fit	0.5630	6	0.0938	0.3214	0.8959	Not sig
Pure error	1.17	4	0.2920			
Cor total	93.23	12				

4 Response Surface Analysis

3D surface plot for floating lag time shown in Fig. 4 indicate that floating lag time increases with decreasing amount of floating agent and it increases with an increasing amount of pH modifier.

3D surface plot shown in Fig. 5 demonstrates the relation of % drug release after 12 h with floating agent and pH modifier. The effect of floating agent (*Saccharomyces boulardii* preparation) and pH modifier (calcium hydroxide) was found to be in an ascending manner i.e. increasing the amount of both increases the response.

By using numerical and graphical optimization techniques best solution found. The statistically optimized formulation selected contained 60 mg of A (*Saccharomyces boulardii* preparation) and 19.50 mg of B (calcium hydroxide) as shown in overlay plot Fig. 6. The observed value for floating lag time and cumulative % drug release after 12 h were 11.3 min and 89.77%. Model predicted value of floating lag time was 11.70 min, % drug release after 12 h was 90.20%. The experimental values

Table 5 ANOVA for quadratic model for Response 2: cumulative % drug release after 12 h

	Sum of squares	Df	Mean square	F-value	p-value	
Model	172.85	5	34.57	296.13	< 0.0001	Significant
A-Saccharomyces boulardii preparation	48.17	1	48.17	412.61	< 0.0001	
B-Calcium hydroxide	93.85	1	93.85	803.96	< 0.0001	
AB	0.5625	1	0.5625	4.82	0.0642	
A ²	0.0081	1	0.0081	0.0693	0.7999	
B ²	26.22	1	26.22	224.57	< 0.0001	
Residual	0.8172	7	0.1167			
Lack of fit	0.2069	3	0.0690	0.4520	0.7299	Not significant
Pure error	0.6103	4	0.1526			
Cor total	173.66	12	34.57			

Table 6 Statistical summary of response

Fit statics	Floating lag time (min)	% Drug release after 12 h
Std. dev	0.4161	0.3417
Mean	13.67	85.94
C.V. %	3.04	0.3976
R ²	0.9814	0.9953
Adjusted R ²	0.9777	0.9919
Predicted R ²	0.9721	0.9849
Adeq precision	53.3689	58.4905

and predicted values of an optimized batch are in adjacent with each other, which approve the predictability and validity of the model.

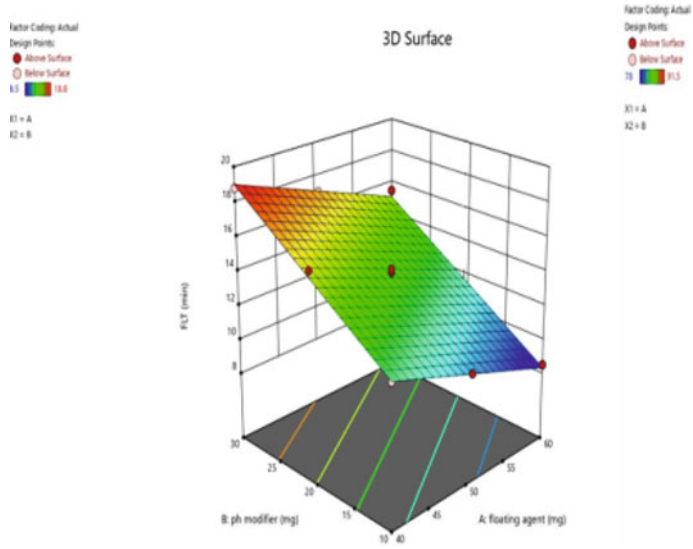


Fig. 4 Response surface plot showing the effect of the amount of *floating agent* and pH modifier on floating lag time

Fig. 5 Response surface plot showing the effect of the amount of *floating agent* and pH modifier on % drug release after 12 h from floating tablet

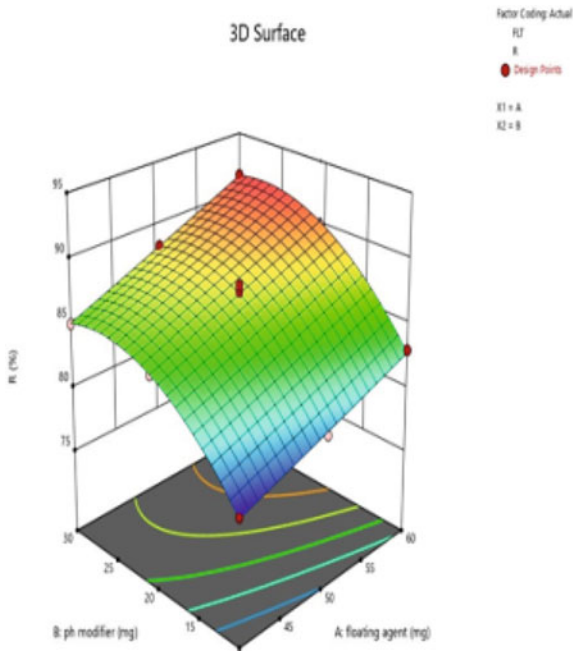
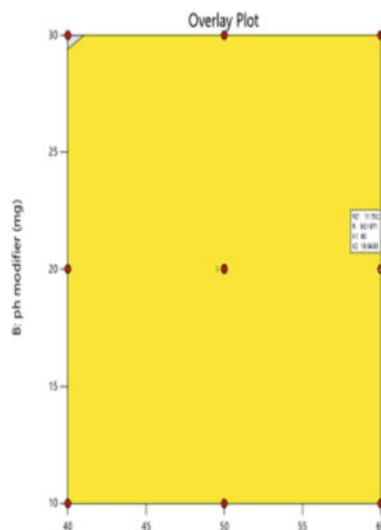


Fig. 6 Optimization of Valsartan floating tablet's overlay plot



5 Conclusion

We conclude that *Saccharomyces boulardii* formulation was good floating agent and its very easy to prepare tablet using this novel floating agent. The response variables of the formulation were optimized by response surface methodology technique. The optimized formulation (O) shows 89.77% cumulative drug release after 12 h and 11.3 min floating lag time. In vitro and in vivo buoyancy studies and in vitro % drug release study indicate that the formulation is suitable for gastroretention.

References

1. Elghandour, M. M. Y., Tan, Z. L., Abu Hafsa, S. H., Adegbeye, M. J., Greiner, R., & Ugboju, E. A. (2019). *Saccharomyces cerevisiae* as a probiotic feed additive to non and pseudo-ruminant feeding: A review. *Journal of Applied Microbiology*, 128, 658–674.
2. Czerucka, D., Piche, T., & Rampal, P. (2007). Review article: Yeast as probiotics—*Saccharomyces boulardii*. *Alimentary Pharmacology & Therapeutics*, 26, 767–778.
3. Boyle, R. J., Roy, M. R. B., & Tang, M. L. (2006). Probiotic use in clinical practice: What are the risks? *The American Journal of Clinical Nutrition*, 83, 1256–1264.
4. Dixit, K., & Gandhi, D. N. (2006). Biotherapeutic properties of probiotic yeast *Saccharomyces* in fermented dairy products. Available from <https://www.dairyscience.info/index.php/probiotics/232-yeast-probiotics.html>. Accessed March 21, 2021.
5. Sindhu, S. C., & Khetarpaul, N. (2002). Effect of probiotic fermentation on antinutrients and in vitro protein and starch digestibilities of indigenously developed RWGT food mixture. *Nutrition and Health*, 16, 173–181.
6. Available from: <https://www.verywellhealth.com/the-benefits-of-saccharomyces-boulardii-89509>

7. Prasanthi, S., & Vidyavathi, M. (2017). Formulation and optimization of buoyant in situ gelling system of valsartan using natural polymer. *International Journal of Pharmacy and Pharmaceutical Sciences*, 9(10), 128–136.
8. Guo, Y., Wang, C., Dun, J., Du, L., Hawley, M., & Sun, C. C. (2019). Mechanism for the reduced dissolution of ritonavir tablets by sodium lauryl sulfate. *Journal of Pharmaceutical Sciences*, 108, 516–552.
9. Pawar, H. A., Gharat, P. R., Dhavale, R. V., Joshi, P. R., & Rakshit, P. P. (2013). Development and evaluation of gastro retentive floating tablets of an antihypertensive drug using hydrogenated cottonseed oil. *ISRN Pharmacology*, 2, 1–9.
10. Aswatha Ram, H. N., Lachake, P., Kaushik, U., & Shreedhara, C. S. (2010). Formulation and evaluation of floating tablets of liquorice extract. *Pharmaceutical Research*, 2(5), 304–308.
11. Chauhan, Y. S., Kataria, U., & Dashora, A. (2018). Formulation and evaluation of floating tablet for indomethacin. *Journal of Drug Delivery Therapeutics*, 8(4), 338–345.
12. Oussama, M., Ghenwa, I., Mostafa, I., & Mais, A. (2016). Assessment of physicochemical properties of valsartan (40 mg) tablets marketed in Syria. *Journal of Chemical and Pharmaceutical Sciences*, 9(4), 2879–2881.
13. Puthoori, H., Murthy, T., Kaushik, A., & Murthy, K. (2012). Formulation and evaluation of floating tablets of niacin for sustained release. *Asian Journal of Pharmaceutics*, 6, 31–37.
14. Chittam, S., Bhosale, A., & Chavan, R. (2022). Development and evaluation of floating tablet using novel floating agent *Saccharomyces boulardii* and hydrophilic polymers. *IJBPAS*, 11(8).
15. Tiwari, S. B., Murthy, T. K., Pai, M. R., Mehta, P. R., & Chowdary, P. B. (2003). Controlled release formulation of tramadol hydrochloride using hydrophilic and hydrophobic matrix system. *Official Journal of American Association of Pharmaceutical Sciences*, 4(3), E31.
16. Shaikh, S. A., Shaikh, S. N., Patel, S. M., Khalifa, M. Y., Makrani, S. I., Siddiqi, H. A., et al. (2021). Design expert supported formulation development, mathematical optimization and predictability study of floating tablets of bisoprolol fumarate. *International Journal of Applied Pharmaceutics*, 13, 242–248.
17. Rashmitha, V., Madhusudan Rao, Y., & Pavani, S. (2021). Formulation and evaluation of fenoverine floating tablets. *Asian Journal of Pharmaceutical and Clinical Research*, 14, 175–180.
18. Siepmann, J., & Siepmann, F. (2008). Mathematical modeling of drug delivery. *International Journal of Pharmaceutics*, 364, 328–343.
19. Mohapatra, S., Barik, B., Kar, R. K., Sahoo, S. K., & Barik, B. B. (2013). Design, development and optimization of gastro retentive floating tablets of cefixime trihydrate. *Asian Journal of Chemistry*, 25, 7599–7606.
20. Chittam, S., & Bhosale, A. (2021). Novel floating agent *saccharomyces boulardii* formulation based floating drug delivery system. *International Journal of Pharmaceutics*, 13(5), 223–229.

Isolation and Characterization of Bioactive Compound from *Euphorbia pulcherrima* (Wild) Leaves



Prashali Shinde and Gurdeep Singh

Abstract Medicinal plants have played vigorous role in life of humans also used to treat several diseases. Poinsettia is a popular ornamental crop, mostly during the Christmas season also known as the Christmas Flower. The dried powder of *Euphorbia pulcherrima* was subjected to soxhlet extraction by using solvent like water, methanol and petroleum ether. This extracts yielded terpenoids, flavonoids, alkaloids, saponin, and steroids, triterpenes. These were identified as germanicol acetate, germanicol, brain, beta-sitosterol, beta-sitosteryl 3-D-glucoside, and rutin. The isolated beta-sitosterol from fraction of ether extract has been characterized by thin-layer chromatography, ultraviolet–visible spectroscopy, Fourier transform infrared spectroscopy, Nuclear magnetic resonance. Therefore, it is needed to isolate and detect more bioactive constituents and clarify their structure, activity, with this plant. It is also highlighted for more detailed research and clinical trials to explore its pharmacological activity and clinical efficacy.

Keywords *Euphorbia pulcherrima* · Phytoconstituents · Isolation · Characterization

1 Introduction

Medicinal plants comprise various phytochemicals and secondary metabolites in one or more parts of the plant. The plant poinsettia (*Euphorbia pulcherrima*) is a commercially important plant species of the diverse spurge family [1]. It is also termed Christ blossom [2]. Phytomedicine refers to the use of any herbal seeds, roots, leaves, bark, flowers for curative purposes. Plants are used medicinally in diverse countries and are the source of many dominant and potent drugs [3–6]. Plant drugs

P. Shinde (✉) · G. Singh

School of Pharmaceutical Sciences, Lovely Professional University, Kapurthala, Punjab, India
e-mail: prashali.shinde@gmail.com

G. Singh

e-mail: gurdeep.26222@lpu.co.in

could be effective and have fewer or no side effects. These classes in this genus are commonly used in traditional medicine for the management of diseases [7]. It has been accounted for that *Euphorbia* has antiarthritis, anticancer, anticonvulsant, antidiabetic, dermatitis, against skin inflammation, antitumor, antimicrobial, antispasmodic, antitussive properties, hormonal and myelopoietic properties [2] Some species of Euphorbiaceae have been documented for numerous pharmacological potentials such as central nervous system, inflammation, fever, neuropharmacological, and hypnotic [8]. The phytochemical analysis of petroleum ether and methanolic and aqueous extracts revealed the presence of tannins, related polyphenols, terpenes, anthocyanins, alcohols, steroid-like β -sitosterol [9].

The broad range and diversity of biological activities in the *Euphorbia* genus may be due to the presence of various components in the plants with different modes of action [10] steroid-like β -sitosterol, has been experimentally confirmed to show various pharmacological properties, such as anti-diabetic, ameliorative, anti-inflammatory, antiatherosclerotic, hepatoprotective, immune modulating, and lipid-lowering, protection against oxidative damage. Due to its ability, low toxicity, and good safety profile beta—sitosterol has attracted major consideration from researchers in recent years. From pharmacological investigation, β -sitosterol has been found to exhibit extensive anti-tumor activity and is a prospective drug for the treatment of various tumors [11]. The aim of the present study was to identify various classes of chemical constituents responsible for the traditional claim that plant are used in breast cancer chemotherapy.

2 Materials and Methods

2.1 Collection of Plant

Leaves of *Euphorbia pulcherrima* were collected in the month of February 2022 from the botanical garden of the University of Pune (Maharashtra). Collected leaves of a plant sample was identified and authenticated by the Botanical Survey of India—Pune (Maharashtra) Voucher specimen number (PGSEP3).

The dust particles were removed by washing the leaves under fresh tap water. The leaves of *Euphorbia pulcherrima* were dried at in air at 40 °C and made into fine powder using the mixer grinder and fine powder was used for the extraction procedure.

2.2 *Phytochemical Test*

The fresh aqueous, methanol and ether extract were subjected to various phytochemical screenings for the detection of various plant constituents, characterized for their possible bioactive compounds [12, 13]. All the parameters are tested as per Ayurvedic pharmacopoeia results are within the limit.

2.3 *Physico-chemical Studies*

All the parameters are testing as per Ayurvedic pharmacopoeia and results are within the limit.

2.4 *Extraction and Isolation*

Soxhlet extraction apparatus was used for extraction. One hundred grams of leaves powdered were placed in a thimble of the apparatus in the upper chamber. The flask containing two hundred and 50 ml of extracting solvent was heated by using a heating mantle which is controlled by a thermostat. Different solvents were filled in the round-bottom flask, and the temperature was set up to the boiling point of the solvents. Then this solvent was heated to reflux and extracted. The material in the thimble was extracted with various solvents like methanol, water, Petroleum ether successively till colorless extract was collected on the top of the extractor. Then this extracted solvent was collected and concentrated separately under the reduced pressure. After complete evaporation of the solvent from the extract, all solvent extracts were weighed and stored in airtight bottle at 40 °C until further use [14].

2.5 *General Analysis*

The Petroleum ether extract of *E. pulcherrima* (L) leaves was subjected to thin layer chromatography (TLC) using normal TLC precoated silica gel G microslides from MERCK (Germany). The spots were manually applied using a capillary tube, the plates were dried with a hot air blower, and the spots were developed in a Shandon chromatography tank at room temperature. Various solvent systems consisting of hexane and ethyl acetate in a ratios of 9:1, 4:1, 7:3, 3:2, and 1:1 were used at different concentrations to determine the solvent system that provided maximum separation of compounds when the slides were sprayed with p-anisaldehyde and visualized under UV light (254 and 366 nm) hexane:ethyl acetate in ratio 7:3 used to separate the components of extract.

2.6 Column Chromatography

A glass column of length 30 cm and width 3 cm packed with column silica was used for the partitioning of the ethereal extract of *E. pulcherrima* (L). The weight of the extract used was 4 g, hexane:ethyl acetate in a ratio 7:3 was finalized as a system for TLC and this system was extended for column chromatography in ratio of 17.5:7.5 first and then with varying ratios of hexane:ethyl acetate via increasing polarity 25 eluents were collected at intervals and similar compounds were pooled together after TLC.

3 Results and Discussion

3.1 Results of Phytochemical Screening

The fresh aqueous, methanol and Petroleum ether extract was subjected to various phytochemical screening for the detection of various plant constituents like Steroids, Alkaloids, Glycosides, Carbohydrate, Protein, Tannin, Saponin, Terpenoids as shown in Table 1 and Foreign matter, Total ash value, Acid insoluble ash value, Water soluble ash value, Loss on drying, Alcohol soluble extractive value, Water soluble extractive value shown in Table 2.

Table 1 Phytochemical analysis for different solvent extracts

Phytochemical compounds	Aqueous extract	Methanol extract	Petroleum ether extract
Steroids	—	+	+
Alkaloids	+	+	+
Glycosides	+	+	+
Flavonoids	+	+	+
Carbohydrate	+	+	+
Protein	+	+	+
Tannin	—	—	—
Saponin	—	+	+
Anthroquinone glycosides	—	—	—
Terpenoids	+	+	+

Table 2 Phytochemical parameter of powdered leaves *Euphorbia pulcherrima*

Parameters	<i>Euphorbia pulcherrima</i> observed value (in %)
Foreign matter	00
Total ash value	3
Acid insoluble ash value	1
Water soluble ash value	0.9
Loss on drying	0.28
Alcohol soluble extractive value	4
Water soluble extractive value	6.9

3.2 Results of Spectroscopic Analysis

The pure β -sitosterol was eluted with hexane:ethyl acetate and isolated as white powder (15 mg) with melting point 134–135 °C, molecular mass 414 g, UV–Visible spectra of the β -sitosterol. is at 285 nm, (Fig. 1) FTIR (cm^{-1}) 3406.85, 3598.65, 3665.14 (stretching vibration of OH), 2877.74 (stretching vibration of CH alkane), 2945.55 (stretching vibration of CH alkene), 1651.78 (stretching vibration of C=C), 1454.28 (bending vibration of OH), 1368.78 (bending vibration of isopropyl), 1053.70 (bending vibration of C–O of alcohol), 1368.78 (bending vibration of CH₃), 1053.70 (bending vibration of C–O of alcohol), 1368.78 (bending vibration of CH₃), 1454.28 (bending vibration of CH₂) (Fig. 2).

Data Set: S1 120922 - RawData

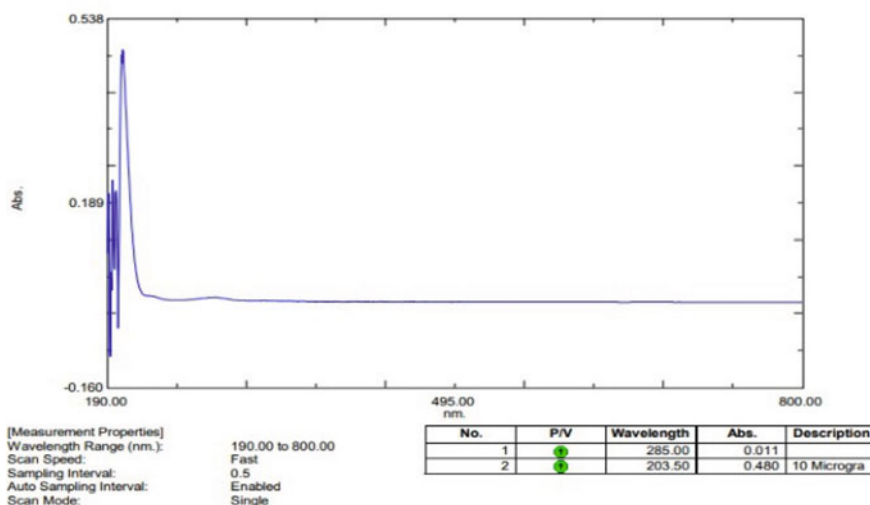


Fig. 1 UV–visible spectra of the β -sitosterol. Its λ max in ethanol is at 285 nm

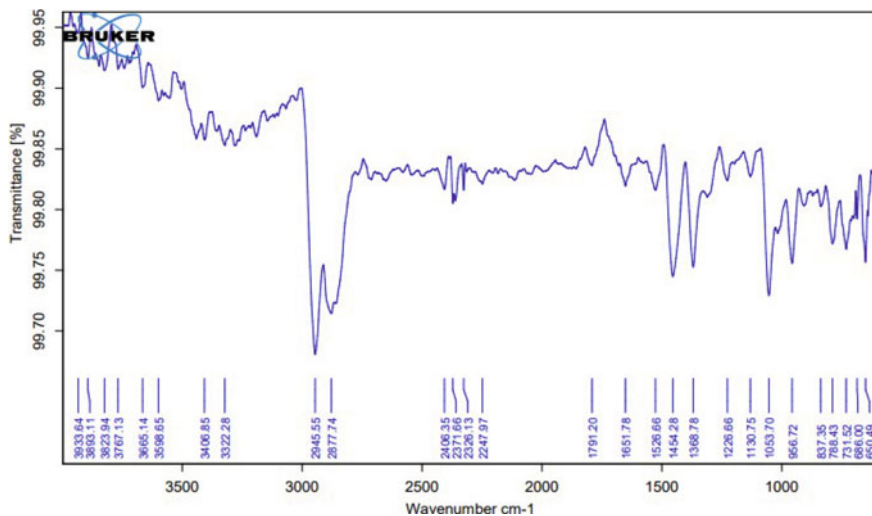


Fig. 2 Fourier transform infrared (FTIR) of the β -sitosterol

3.3 *Fourier Transform Infrared (FTIR)*

FTIR identified chemical bands in molecules, the range of scanning $4000\text{--}400\text{ cm}^{-1}$. IR radiation is passed through a sample. Some of the IR radiation is absorbed by the sample, and some is transmitted.

3.4 *NMR*

NMR spectral data of this compound shows the existence of six methyl groups, eleven methylene and three quaternary carbons together with hydroxyl group. The olefinic carbons are appeared at 140.7 (C-5) and 121.7 (C-6) ppm. The number of carbons, extracted from ^{13}C -NMR, may reveal the structure of a sterol with 27 carbons Figs. 3 and 4.

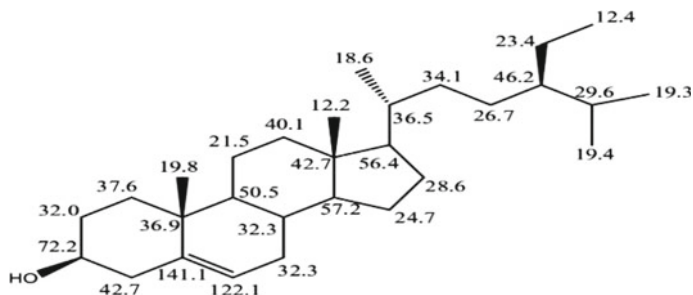


Fig. 3 NMR spectral data of this compound

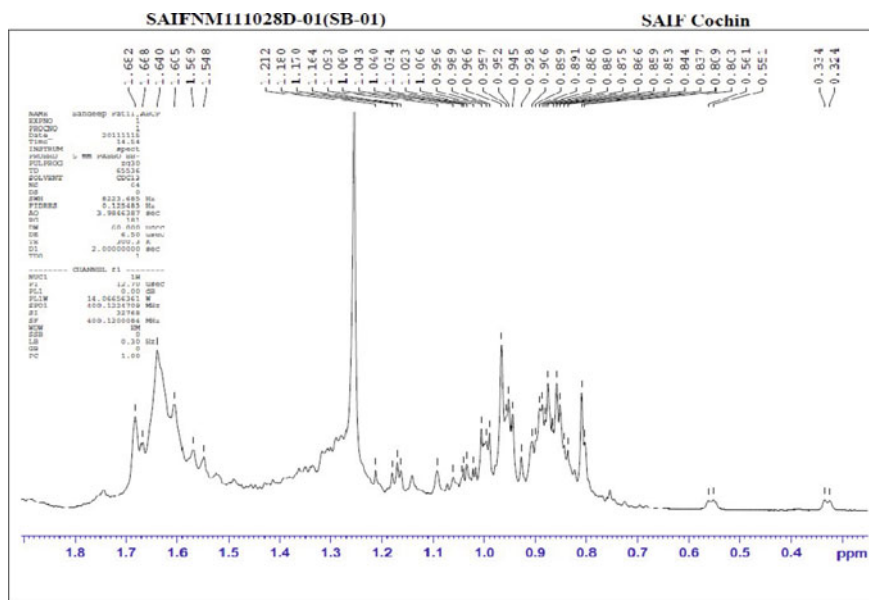


Fig. 4 NMR spectrometry of β -sitosterol

4 Conclusion

As per our aim powdered extract were characterized by using physical, chemical and modern spectral analysis. The extract was identified as presence of various phytochemicals such as glycosides, terpenoids, flavonoids, alkaloids, saponin, and steroids, triterpenes and after fractionating of ether extract by mention solvent system beta-sitosterol isolate. These compound show various pharmacological activities and antioxidant property leading to anticancer activity. In the future, the active medicaments can be studied further for their pharmacological and biological activities. In an in-depth pharmacological examination, beta sitosterol has been found to exhibit

considerable anti-tumor activity and is a prospective drug for the treatment of various tumors. The research progress on the anti-tumor mechanism of beta –sitosterol is summarized to provide new visions into solving the current problems of treatment traditional anti-tumor drugs with maximum efficacy, low toxicity, and low drug resistance.

References

1. Kunal, K., & Singh, K. (2021). Antimicrobial and antioxidant studies and Gc-MS analysis of leaf and stem extracts of *Euphorbia pulcherrima*. *Gis Science Journal*, 8(2), 488–510.
2. Shlini, P., & Mary Clare, H. (2020). Isolation and purification of Rutin from *Euphorbia pulcherrima*. *International Journal of Pharmaceutical Sciences Review and Research*, 64(1), 45–49, Article No. 08.
3. Singla, A. K., & Pathak, K. (1990). Phytoconstituents of Euphorbia species. *Fitoterapia*, 61(6), 483–516.
4. Alves, C. Q., David, J. M., David, J. P., Bahia, M. V., & Aguiar, R. M. (2010). Methods for determination of in vitro antioxidant activity for extracts and organic compounds. *Química Nova*, 33, 2202–2210.
5. Tayade, A. B., Dhar, P., Kumar, J., Sharma, M., Chauhan, R. S., Chaurasia, O. P., & Srivastava, R. B. (2013). Chemometric profile of root extracts of *Rhodiola imbricata* Edgew. with hyphenated gas chromatography mass spectrometric technique. <https://doi.org/10.1371/journal.pone.0052797>
6. Balandrin, M. F., Kinghorn, A. D., & Farnsworth, N. R. (1993). Plant-derived natural products in drug discovery and development: An overview. In *Human Medicinal Agents from Plants: American Chemical Society Symposium* (Vol. 534, pp. 2–12), Washington, D.C.
7. Douglas, K., & Xolani, P. (2020). A review of the ethnomedicinal uses, biological activities, and triterpenoids of Euphorbia species. *Molecules*, 25, 4019.
8. Aljohani, A. S. M., & Alhumaydhi, F. A. (2022). In vivo anti-inflammatory, analgesic, sedative, and muscle relaxant activities and molecular docking analysis of phytochemicals from *Euphorbia pulcherrima*. *Hindawi Evidence-Based Complementary and Alternative Medicine*, Article ID 7495867.
9. Jayalakshmi, B., Raveesha, K. A., & Amruthesh, K. N. (2021). Isolation and characterization of bioactive compounds from *Euphorbia cotinifolia*. *Future Journal of Pharmaceutical Sciences*, 7(9).
10. Abdur, R., & Muhammad, N. (2013). Phytochemical and pharmacological evaluation of aerial parts of *Euphorbia pulcherrima* L. *Wudpecker Journal of Pharmacy and Pharmacology*, 2(2), 015–020.
11. Xingxun, B., Yanan, Z., Hairong, Z., & Xia, L. (2022). Molecular mechanism of β -sitosterol and its derivatives in tumor progression. *Frontiers in Oncology*, 12, Article 926975. www.frontiersin.org
12. Deepa, P., Kaleena, P. K., Valtivittan, K., & Girish Kumar, C. P. (2011). Phytochemical screening and antimicrobial activity of *Sansevieria roxburghiana* Schult and Suhult. *Middle-East Journal of Scientific Research*, 10, 512–518.
13. Savithramma, N., Lingarao, M., & Suvrulatha, D. (2011). Screening of medicinal plant for secondary metabolites. *Middle-East Journal of Scientific Research*, 8, 579–584.
14. Beretz, A., Joly, M., Stoclet, J., & Anton, R. (1979). Inhibition of 3',5'-AMP phosphodiesterase by biflavonoids and xanthenes. *Planta Medica*, 36(7), 193–195, 19.

High Performance CeO₂ Nanoparticles for Real-Time NO₂ Detection



R. N. Dhanawade, N. S. Pawar, G. M. Hingangavkar, Y. M. Jadhav, T. M. Nimbalkar, M. A. Chougule, R. N. Mulik, and V. B. Patil

Abstract Cerium oxide (CeO₂) nanoparticles (NPs) were prepared via cost-effective sol–gel route. XRD, SEM, and EDAX techniques was utilized to the crystallographic, morphological, and compositional analysis. Gas sensing characteristics of CeO₂ sensor were investigated through customly invented gas sensing unit. CeO₂ NPs annealed at 500 °C delivers admirable selectivity towards NO₂ gas. CeO₂ sensor examined at distinctive working temperatures (150, 200, and 250 °C) and gases such as NO₂, CO₂ and CO. CeO₂ NPs sensor presents prominent sensitivity (33%) towards oxidizing NO₂ gas at 200 °C with remarkable stability (75.7%).

Keywords CeO₂ NPs · Sol–gel · SEM · Sensitivity · NO₂

1 Introduction

In recent days, due to the fast industrialization growth and modern lifestyle emission of harmful gases in the surrounding by numerous ways. Nitrogen dioxide (NO₂) is most hazardous air pollutant, which can strongly affected on human health. High level concentration of NO₂ causes damaging human cells and critical health complications. Consequently, for the environment safety and better human life, recognizing and controlling of the poisonous NO₂ gas is necessary [1–4].

Semiconducting metal oxides are inexpensive and ease to synthesis. Among them cerium oxide (CeO₂) is n-type, ample and attracting rare earth metal oxide. Also, CeO₂ have great electrical properties and displays better oxidation/reduction characteristics. It shows significant applications in several areas like gas sensing, thermal coatings, anticorrosion, optical, and photochemistry respectively [5–9]. It shows +

R. N. Dhanawade · N. S. Pawar · G. M. Hingangavkar · Y. M. Jadhav · T. M. Nimbalkar · M. A. Chougule · V. B. Patil (✉)

Functional Materials Research Laboratory, School of Physical Sciences, PAH Solapur University, Solapur, Maharashtra, India

e-mail: drvbpatil@gmail.com

R. N. Mulik

Department of Physics, DBF Dayanand College of Arts & Science, Solapur, Maharashtra, India

3 and + 4 oxidation states correspondingly, while more rare earth semiconducting metal oxides have + 3 oxidation state [10, 11]. For the synthesis of CeO_2 in powder as well as thin film form distinct methods are applied such as sol–gel, hydrothermal, thermal evaporation, and co-precipitation techniques respectively. Amongst these preparation methods, sol–gel technique have great interest in obtaining the pure product.

Here, we synthesized sol–gel prepared CeO_2 NPs thin films at annealing temperature of 500 °C. CeO_2 sensor exhibit significant gas response to oxidizing NO_2 at 200 °C as compared with other test air pollutants.

2 Materials and Method

2.1 Chemicals

Cerium nitrate hexahydrate [$\text{Ce}(\text{NO}_3)_3 \cdot 6\text{H}_2\text{O}$], ethanol ($\text{C}_2\text{H}_5\text{OH}$), methanol (CH_3OH), and m-Cresol [$\text{CH}_3\text{C}_6\text{H}_4\text{OH}$].

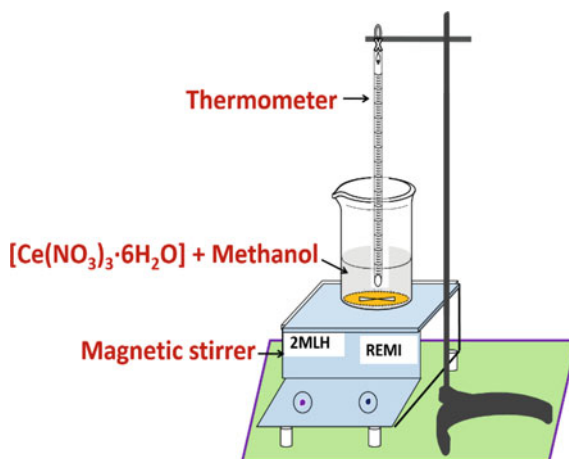
2.2 Preparation of CeO_2

Cerium oxide (CeO_2) NPs were prepared using facile sol–gel route technique. Firstly, 2.82 g $\text{Ce}(\text{NO}_3)_3 \cdot 6\text{H}_2\text{O}$ mixed in 40 ml methanol and vigorously stirred for 1.5 h at 60 °C. Subsequently, obtained residue was rinsed with ethanol and distilled water number of times and then dried at 60 °C for 2 h on a hot plate. At the end obtained powder was annealed at a temperature of 500 °C in zone furnace for 1 h and grinded it in smooth agate mortar for 3 h. For thin film preparation of CeO_2 , powder was mixed in 5 ml m-cresol with constant stirring for 10 h at RT. Finally thin films were prepared using simple drop cost technique. The obtained thin films were dried under IR lamp for 20 min (Fig. 1).

2.3 Characterizations

The structural crystallography of cerium oxide NPs thin film was revealed by Ultima IV Rigaku diffractometer ($\lambda = 1.5406 \text{ \AA}$). Scanning electron microscope (Model: JEOL-6300F) depicted surface morphological structure of CeO_2 NPs annealed at 500 °C. Energy dispersive X-ray spectroscopy (EDAX) was demonstrated element mapping study of CeO_2 NPs.

Fig. 1 Schematic of as-prepared CeO₂ NPs



2.4 Gas Sensing Study

The sensing performance of cerium oxide (CeO₂) thin film was studied by utilizing custom fabricated high temperature gas sensing set-up. The electrical contacts of silver paste were 2 mm wide and 1 cm apart. In gas sensing evaluation process, film is mounted in gastight chamber of 250 cc volume and maintained at 200 °C in fresh air. The electrical resistance of gas sensing film was calculated in ambient air and in target gas correspondingly with interfacing the digital electrometer (Keithley 6514). The gas sensing response (S) was calculated by following equation [12],

$$\text{Response, } S (\%) = \frac{|R_a - R_g|}{R_a} \times 100$$

Here, R_a be the resistance of sensor in ambient air and R_g be the resistance of sensor in NO₂ correspondingly.

XRD was utilized to characterize the crystallinity structure of as-prepared CeO₂ NPs. Figure 2 exhibit XRD pattern of as prepared CeO₂ NPs. Numerous diffraction peaks are observed in displayed XRD pattern. The CeO₂ NPs containing diffraction peaks at $2\theta = 28.54, 32.99, 47.53, 56.26, 59.06, 69.58, 76.88,$ and 79.17° consistent with (111), (200), (220), (311), (222), (400), (331), and (420) planes, correspondingly [13, 14]. All the diffraction peaks of CeO₂ NPs are well suited with standard JCPDS card no. 34–0394. It shows fluorite pure cubic structure with lattice parameters of $a = b = c = 5.12 \text{ \AA}$. No any additional diffraction peaks are displayed in X-ray diffraction pattern, approving that sol gel synthesized CeO₂ NPs powder is pure. The average crystalline size of cerium oxide NPs annealed at 500°C was calculated using Debye-Scherrer's relation,

$$D = \frac{0.9\lambda}{\beta \cos \theta} \quad (1)$$

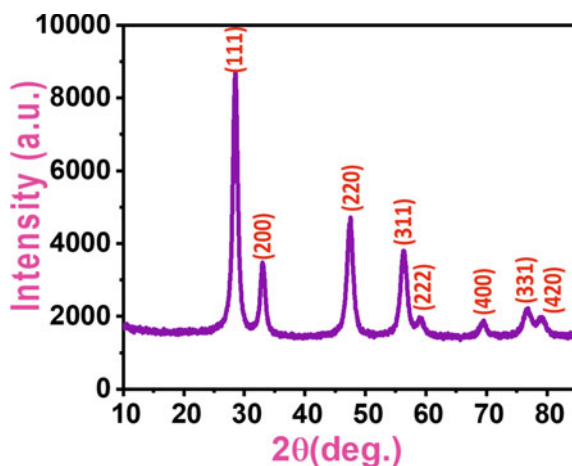


Fig. 2 X-ray diffractometry pattern of as-prepared CeO₂ NPs

Table 1 Microstructural parameters of CeO₂ NPs

Material	Crystallite size (D) (nm)	Micro-strain (ϵ)	Dislocation-density (δ) (cm ⁻²)	Stacking fault (SF)
CeO ₂	14.1639	0.2447	0.004984	0.5530

The microstructural properties of CeO₂ NPs like microstrain (ϵ), stacking fault (SF), and dislocation density (ρ) were calculated using well known relations [15] and illustrated in Table 1.

2.5 Surface Morphology Study

Scanning electron microscopy technique was used to characterize the surface morphology structure of CeO₂ nanoparticles displayed in Fig. 3a. Cerium oxide NPs shows a randomly nanospheres. The gas sensing performance was affected by surface morphology and adsorption rate of gas molecules on the sensor surface, which enhances gas sensitivity behavior.

The energy dispersive analysis X-ray spectroscopy (EDAX) represents the compositional study of as synthesized product. Figure 3b shows EDAX spectra of CeO₂ NPs annealed at 500 °C, containing Ce, and O elements with atomic weight of 44.74% and 55.26% respectively [16].

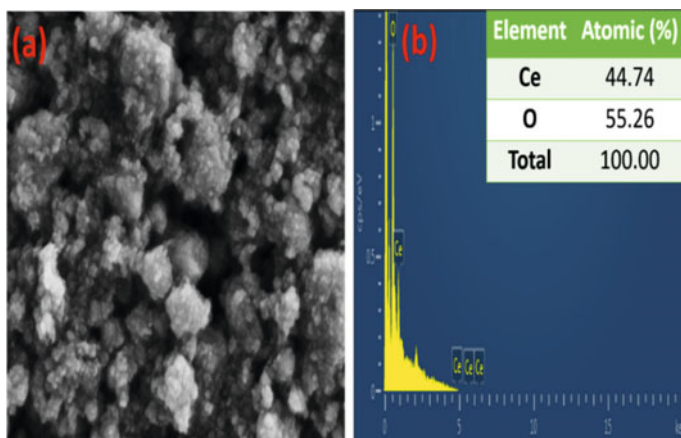


Fig. 3 Typical **a** high resolution SEM, and **b** EDAX images CeO₂ NPs

2.6 Gas Sensing Characteristics

To study the practical operation in convoluted atmosphere, we observe the effect of NO₂, CO₂, and CO gases on the sensitivity of the CeO₂ based sensor film, as demonstrated in Fig. 4a. The CeO₂ sensor shows highest response 33% towards 100 ppm NO₂ at 200 °C as compared to other test gases, which confirms that CeO₂ sensor have excellent selectivity towards NO₂ gas [17].

In the sensing performance, working temperature is most notable aspect, which control the adsorption/desorption rate of gas molecules on the sensor surface at equilibrium. The sensing behavior of CeO₂ sensor was evaluated by utilizing custom fabricated gas sensing unit at distinct working temperatures of 150–250 °C. In the

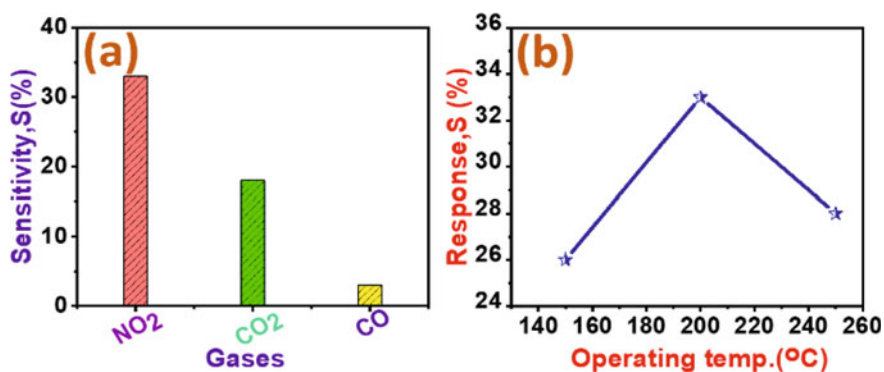


Fig. 4 **a** Selectivity and **b** operating temperature images CeO₂ sensor

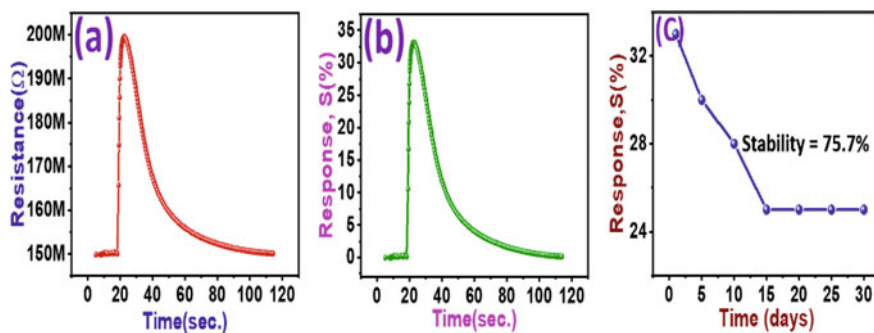


Fig. 5 a Resistance versus time, b response versus time and c stability curve of CeO₂ sensor

current work, CeO₂ sensor reveals the higher NO₂ sensitivity at 200 °C. This temperature was found as an optimum working temperature for CeO₂ gas sensor depicted in Fig. 4b [18].

CeO₂ gas sensing response was significantly dependent on adsorption and desorption process rate of NO₂ gas molecules on the sensor surface. Figure 5 shows resistance vs. time and response versus time curves of CeO₂ sensor at 200 °C. As prepared CeO₂ gas sensor represents excellent gas sensitivity of 33% to 100 ppm oxidizing NO₂ at 200 °C.

To find the stability performance of CeO₂ sensor, gas response was measured at 200 °C towards 100 ppm oxidizing NO₂ gas for 30 days with an interval of 5 days. Firstly, NO₂ sensor displayed higher gas response to NO₂, after 30 days it dropped down from 33 to 23% with stability performance 75.7% [19].

3 Conclusions

In the present research work, CeO₂ NPs were effectively prepared using simple sol-gel route technique at annealing temperature of 500 °C. The synthesized CeO₂ NPs were displayed fluorite cubic structure with an average crystalline size of 14.1639 nm. Furthermore, it shows spherically shaped CeO₂ NPs and notable elemental mapping. The CeO₂ sensor demonstrated excellent selectivity and higher sensitivity towards NO₂ at 200 °C. Moreover, this sensor displays 75.7% stability performance confirming that CeO₂ sensor is propitious for manufacturing NO₂ sensor.

Acknowledgements Prof. Vikas B. Patil was thankful to Rajiv Gandhi Science and Technology Commission, Mumbai Grant ID: RGSTC/File-2019/PAHSUS/CR-91 dated 23/12/2019 and Punyashlok Ahilyadevi Holkar Solapur University, Solapur for financial support.

References

1. Navale, Y. H., Navale, S. T., Galluzzi, M., Stadler, F. J., Debnath, A. K., Ramgir, N. S., Gadkari, S. C., Gupta, S. K., Aswal, D. K., & Patil, V. B. (2017). Rapid synthesis strategy of CuO nanocubes for sensitive and selective detection of NO₂. *Journal of Alloys and Compounds*, *708*, 456–463.
2. Chougule, M. A., Navale, S. T., Navale, Y. H., Ramgir, N. S., Stadler, F. J., Khuspe, G. D., & Patil, V. B. (2019). Processing temperature dependent chemiresistive performance of spin coated cerium oxide films. *Materials Chemistry and Physics*, *224*, 85–92.
3. Husain, A., Ahmed, S. A., Al Otaibi, A., Khan, H., Ali Khan, M. M., Alosaimi, A. M., Khan, A., Hussein, M. A., Asiri, M., & Jawaid, M. (2021). Fabrication of reproducible and selective ammonia vapor sensor-pellet of polypyrrole/cerium oxide nanocomposite for prompt detection at room temperature. *Polymers*, *13*, 1829.
4. Kulkarni, S. B., Navale, Y. H., Navale, S. T., Ramgir, N. S., Debnath, A. K., Gadkari, S. C., Gupta, S. K., Aswal, D. K., & Patil, V. B. (2017). Enhanced ammonia sensing characteristics of tungsten oxide decorated polyaniline hybrid nanocomposites. *Organic Electronics*, *45*, 65–73.
5. Navale, Y. H., Ramgir, S. T., Stadler, N. S., Gupta, F. J., Aswal, D. K., & Patil, V. B. (2017). Zinc oxide hierarchical nanostructures as potential NO₂ sensors. *Sensors and Actuators B*, *251*, 551–563.
6. Choi, S. W., Jung, S. H., & Kim, S. S. (2011). Significant enhancement of the NO₂ sensing capability in networked SnO₂ nanowires by Au nanoparticles synthesized via γ -ray radiolysis. *Journal of Hazardous Materials*, *193*, 243–248.
7. Navale, S. T., Chougule, M. A., Mane, A. T., & Patil, V. B. (2014). Highly sensitive, reproducible, selective and stable CSA-polypyrrole NO₂ sensor. *Synthetic Metals*, *189*, 111–118.
8. Montemor, M. F., Pinto, R., & Ferreira, M. G. (2009). Chemical composition and corrosion protection of silane films modified with CeO₂ nanoparticles. *Electrochimica Acta*, *54*, 5179–5189.
9. Venkadesan, G., & Muthusamy, J. (2019). Experimental investigation of Al₂O₃/8YSZ and CeO₂/8YSZ plasma sprayed thermal barrier coating on diesel engine. *Ceramics International*, *45*, 3166–3176.
10. He, G., Fan, H., Ma, L., Wang, K., Liu, C., Ding, D., & Chen, L. (2016). Dumbbell-like ZnO nanoparticles-CeO₂ nanorods composite by one-pot hydrothermal route and their electrochemical charge storage. *Applied Surface Science*, *366*, 129–138.
11. Pikalova, E. Y., Murashkina, A. A., Maragou, V. I., Demin, A. K., Strekalovsky, V. N., & Tsiakaras, P. E. (2011). CeO₂ based materials doped with lanthanides for applications in intermediate temperature electrochemical devices. *International Journal of Hydrogen Energy*, *36*, 6175–6183.
12. Hingangavkar, G. M., Navale, Y. H., Nimbalkar, T. M., Mulik, R. N., & Patil, V. B. (2022). Hydrothermally engineered WO₃ nanoflowers; a selective detection towards toxic NO₂ gas. *Sensors and Actuators B: Chemical*, *371*, 132584.
13. Umar, A., Kumar, R., Akhtar, M. S., Kumar, G., & Kim, S. H. (2015). Growth and properties of well-crystalline cerium oxide (CeO₂) nanoflakes for environmental and sensor applications. *Journal of Colloid and Interface Science*, *454*, 61–68.
14. Zhang, C., Meng, F., Wang, L., Zhang, M., & Ding, Z. (2014). Morphology-selective synthesis method of gear-like CeO₂ microstructures and their optical properties. *Materials Letters*, *130*, 202–205.
15. Ingole, S. M., Navale, S. T., Navale, Y. H., Bandgar, D. K., Stadler, F. J., Mane, R. S., Ramgir, N. S., Gupta, S. K., Aswal, D. K., & Patil, V. B. (2017). Nanostructured tin oxide films: Physical synthesis, characterization, and gas sensing properties. *Journal of Colloid and Interface Science*, *493*, 162–170.
16. Yang, A., Li, W., Chu, J., Wang, D., Yuan, H., Zhu, J., Wang, X., & Rong, M. (2020). Enhanced sensing of sulfur hexafluoride decomposition components based on noble-metal-functionalized cerium oxide. *Materials & Design*, *187*, 108391.

17. Chang, J., Zhang, X., Wang, Z., Li, C., Hu, Q., Gao, J., & Feng, L. (2021). Polyaniline-reduced graphene oxide nanosheets for room temperature NH₃ detection. *ACS Applied Nano Materials*, 4(5), 5263–5272.
18. Kim, H. J., & Lee, J. H. (2014). highly sensitive and selective gas sensors using p-type oxide semiconductors: Overview. *Sensors and Actuators B: Chemical*, 192, 607–627.
19. Navale, S. T., Bandgar, D. K., Nalage, S. R., Khuspe, G. D., Chougule, M. A., Kolekar, Y. D., Sen, S., & Patila, V. B. (2013). Synthesis of Fe₂O₃ nanoparticles for nitrogen dioxide gas sensing applications. *Ceramics International*, 39, 6453–6460.

Achieving Germ-Free Rejuvenation of Skin by Medicated Beauty Soap with Richness of Essential Oils



Pooja Patil, Mithun Maniyar, Pradnya Mane, Bhagyashree Yadav, and Pratiksha Mali

Abstract The herbal soap was formulated using the Essential oils and fruit extract of *Carica papaya*, *Azadirachta indica*, *Ocimum sanctum*, *Prunus amygdalus* and *Aloe barbadensis*. Ayurvedic ingredients are well known that limited or do not have any side effect on the human body. The work was aimed to formulate a medicated soap for dermal infections using the leaf extract of *Azadirachta indica*, *Ocimum sanctum*. The work was initiated with extraction of active constituents by Soxhala-tion. Medicated Soap was formulated using three types of oils: Coconut, Almond and lemongrass oil. The medicated soaps were further evaluated for their physiochemical tests appearance, pH, the determined % free alkali content was 0.08%, moisture content about 5.8%, and total fatty matter was determined about 2.80%. The alcohol insoluble content was investigated as 1.02 g. The microbial and stability tests were found to comply with specified limits and as per ICH guidelines.

Keywords Herbal soap · Formulation · *Azadirachta indica* · *Ocimum sanctum*

1 Introduction

Herbal soap preparation is an herb based medicine which contains Antibacterial and Antifungal agents and it mainly uses different parts of plants like leaves, stem, roots and fruits to treatment for an injury or disease or to maintain good health [1, 2]. This preparation possess antimicrobial property are administered topically and available to apply in various forms like creams, lotion, gel, soap, solvent extract, or ointment.

The varieties of creams and soap properties have been used to treat various skin disorders. Mostly skin infection is caused by Fungi, *Staphylococcus aureus* and *Streptococcus* species. Ethnomedical, juice and extract from leaves of the plants are topically applied as antimicrobial and anti-inflammatory agents in treatment of skin disease including eczemas, ringworm and pruritus [2].

P. Patil (✉) · M. Maniyar · P. Mane · B. Yadav · P. Mali
SVERI's College of Pharmacy, Pandharpur, Maharashtra, India
e-mail: papatil@cop.sveri.ac.in

Soap is an important surface-active agent, and it is chemically the alkaline metal salt of long-chain fatty acids. The most common used fat or oils for production of soap through saponification reactions are animal tallow, coconut oil, clove oil, eucalyptus oil and lemongrass oil. Soap is an anionic surfactant used in conjunction with water for washing and cleaning, which historically comes either in solid bars or in the form of a viscous liquid [3].

Soap essentially includes an important surface-active agent, and it is chemically the alkaline metal salt of long-chain fatty acids. The most common used fat or oils for production of soap through saponification reactions are animal tallow, coconut oil, palm oil, kernel oil and linseed oil [4].

2 Material and Methods

2.1 Selection of Herbal Essential Oil

Neem oil was selected by its Antifungal properties, so it is very effective against verities of fungi. These oils are cold pressed and available in their purest form that contains the essence of the herb/ingredient they are prepared from. Some essential oils also have anti-aging benefits. Some essential oils also have anti-cancer benefits and help treat skin infections.

Tulsi has a unique combination of actions that include: Antimicrobial (including antibacterial, antiviral, antifungal, antiprotozoal, antimalarial, anthelmintic), mosquito repellent, anti-diarrheal, anti-oxidant [5, 6].

2.2 Neem Oil Extraction Process

The oil was obtained through pressing or crushing of the seed kernel through a process incorporating temperature control 40–50 °C.

Around 40, 50, and 60 g of Neem seeds, leaves and barks were collected from local market at Pandharpur (Maharashtra, India), weighed accurately and placed into the thimble of the Soxhlet extractor. The ethanol was used as solvent and taken 300 ml and poured into the round bottom flask of the Soxhlet extractor, the apparatus was then coupled, and the condenser unit was connected to an overhead water tank to cool rising solvent vapor. The head source was a Bunsen burner operating at a temperature of 68 °C. The process was repeated severally for about nine refluxes in three hours after which the extraction process was completed. The temperature was regulated using a thermometer [7].

2.3 Lemongrass Oil Extraction Process

Lemongrass oil is derived from the steam distillation of the fresh or partly dried leaves. Lemongrass oil is collected by distillation unit of the herbage for 1.5–2 h. The distillation on cooling separates out into a layer of oil, floating over the bulk of water which is composed by decantation. The lemongrass is distilled either fresh or after wilting [8].

2.4 Hydro-distillation

In this process, the herb is packed in a vessel and partly filled with water. The unit vessel is heated by direct fire without an external boiler. This method of distillation is less efficient, but the unit is simple and cheaper [9].

2.5 Preparation of Soap Solution

A sterilized razor blade was used to scrape flakes of each glycerin-soap base into sterile Petri dishes. A chemical balance was used to weigh out each sample which was subsequently introduced into a universal bottle, it was followed with the addition of Coconut oil, Olive oil, Castor oil accurately according to their amounts. This was stirred with a glass rod and then placed in a water bath at about 60 °C to aid dissolution of the soap. This mixture was introduced with stearic acid and sodium lauryl sulphate. Neem oil and Essential oils are added at the end. The overall mixture was poured into soap mould and allowed to set down. It was followed with the refrigeration, for about 2–4 h. the prepared soap was packed into a suitable container box, labeled, and used for further studies [10]. The formula for the preparation of herbal soaps is shown in Table 1.

2.6 Characterization and Evaluation Studies

2.6.1 Physiochemical Parameters

The formulated medicated soaps were evaluated for certain physio-chemical tests. The appearance, clarity and color were checked by naked eyes against white background, and the odor was examined.

Table 1 Formula for the preparation of herbal soaps

Sr. No.	Ingredients	Quantity (F1)	Quantity (F2)	Quantity (F3)
1	Stearic acid	1 g	1 g	1 g
2	Coconut oil	1 ml	1 ml	1 ml
3	Olive oil	1 ml	1 ml	1 ml
4	Neem oil	10 ml	10 ml	10 ml
5	SLS	1 g	1 g	1 g
6	Sodium stearate	0.5 g	0.5 g	0.5 g
7	Tulsi	1 g	1 g	1 g
8	Aloe vera gel	q. s	q. s	q. s
9	Almond oil	5 ml	5 ml	5 ml
10	Lemongrass	12 ml	12 ml	12 ml
11	Papaya	q. s	q. s	q. s
12	Mentha oil	–	2 ml	–

2.6.2 pH

The pH of all the prepared formulations was determined by using digital pH meter and pH paper. The formulations were dissolved in 100 ml of distilled water and stored for two hours. The measurement of pH of formulation was done in previously calibrated pH meter.

2.6.3 Foam Retention and Height

About 25 ml of the 1% soap solution was taken in to a 100 ml graduated measuring cylinder. The cylinder was covered with hand and shaken 10 times. The volume of foam at 1-min intervals for 4 min was recorded. The height retained by soap foam was also determined [11].

2.6.4 Alcohol Insoluble Matter

In a conical flask 5 g of sample was taken. To this 50 ml of warm ethanol was added and it was shaken vigorously, until a sample dissolved completely. The solution was filtered through a filter paper along with 20 ml warm ethanol and a dried it at 105 °C for 1 h. The weight of dried paper was taken [11].

2.6.5 Total Fatty Matter

TFM was estimated by reacting soap with acid in the presence of hot water and calculating the fatty acid obtained. 10gm of the formulated soap was dissolved in 150 ml distilled water and heated. To this, 20 ml of 15% H₂SO₄ added while heating until a clear solution was obtained. Fatty acids that are present on the surface of the resulting solution are solidified by adding 7 g beeswax and heated again. Then it was allowed to cake [11].

2.6.6 Determination of Percentage Free Alkali

About 5 g of sample was taken in a conical flask and added to it into 50 ml of neutralized alcohol. It was boiled under reflux on water bath for 30 min, cooled and 1 ml of Phenolphthalein solution was added it was then titrated immediately with 0.1 N HCL [11].

2.6.7 Media Preparation

Sabouraud Dextrose Agar (SDA) is a selective medium for fungal cultivation and primarily used for the cultivation of *Candida albicans* MTCC I83.

The readily available media was accurately weighed and dispersed in distilled water and further autoclaved. The sterile medium was allowed to cool up to 50 °C and quickly poured into sterile Petri plates under aseptic conditions. The medium was allowed to cool and to produce solid agar plates [12].

2.6.8 Agar Well Diffusion Method

Agar well diffusion method is widely used to evaluate the antimicrobial activity. The agar plate surface was inoculated by spreading a volume of the microbial inoculum over the entire agar surface. Then, a hole with a diameter of 6–8 mm was punched aseptically with a sterile corn borer or a tip, and volume (20–100 µL) of previously diluted soap solution (100 mg/ml) was introduced into the well [12].

Fig. 1 Prepared essential oil soaps using moulds



3 Results and Discussion

3.1 *Physiochemical Parameters*

The overall appearance of all three different soaps were pleasant and attractive. The color with three different soap formulation was observed to be greyish-cream (F1), yellowish-brown (F2) and pink (F3). The odor detected as pleasant (Fig. 1).

3.2 *pH*

The pH of all the prepared formulations were determined in the range of 6.5–7.2 by using digital pH meter.

3.3 *Foam Retention*

Foam Retention was performed by using soap solution is about 5 min.

3.4 *Foam Height*

Foam height was observed to be 10.5 cm by using graduated measuring cylinder.

The other results are obtained were as given in Tables 2 and 3.

The results revealed that despite variations in the inhibition zones produced by corresponding concentrations of the four soaps in the agar-well diffusion assay, none of the soaps seemed to be significantly better than the other in terms of antibacterial

Fig. 2 Zone of inhibition of soap solution on *Candida albicans*

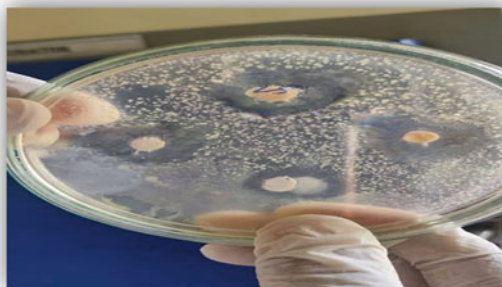


Table 2 Physiochemical parameters of soap solution

Sr. No.	Physiochemical parameters	Herbal soap	Standard
1	pH	6	6.5–7.5
2	Foam height (cm)	10 cm	2.5–3.0
3	Foam retention (min)	5 min	0.5–2.5
4	% Free alkali	0.36	0.25
5	Alcohol insoluble matter	28.0	18–28
6	High temperature stability	Soap melts above 45 °C	45 °C

activity. In general, soap in this study seemed to perform equally well as soap base in the agar-well diffusion assay (Fig. 2).

4 Conclusion

The present work indicates herbal soap containing neem aloe vera, tulsi, lemongrass as natural plant ingredients and this content gives or shows antibacterial antifungal and anti-inflammatory activity. In this soap, neem is main compound, and shows medicinal properties. The main antifungal activity of Tulsi serves to be beneficial in soap formulation. Neem is an exceptional cleanser. Its perfect substitute for soap and face wash due the presence of saponin. It is also good for use on sensitive skin. A combination of Neem and Tulsi gives a gentle and experience to the skin it has conditioning properties; therefore, it keeps skin moisturized and cool. The prepared formulation when tested for different test gave good results. Furthermore, the prepared soap was standardized by evaluating various physiochemical properties such as pH, appearance, odour in which the exhibit satisfactory effect. The present study suggested that choice of soap should be on basis of effectiveness against disease causing bacteria in small amount. The study proved that three soaps have antibacterial

Table 3 Minimum inhibitory concentration (MIC) values of soap solution

Organisms	MIC							
	A	B	C	D	E	F	G	H
<i>Candida albicans</i> MTCC 183	6.5 ± 0.32	2.8 ± 0.10	2.4 ± 0.13	6.7 ± 0.20	7.4 ± 0.14	16.7 ± 0.10	62.5 ± 0.20	2.0 ± 0.04

activity against bacterial strain but essential oil soap was found to be most effective in Chapped skin, Withered Skin, Sensitive skin, Acne.

References

1. Bochare Vaishnavi, K., Shelke Dipali, S., Belhekar Archana, B., Bodake Ravina, S., & Vidhate Prajwal, G. (2022). Formulation and evaluation of antifungal *Pelargonium graveolens* soap. *International Journal of Advanced Research in Science, Communication and Technology (IJARSCT)*, 2(2) 519–532.
2. Amrutkar, S. V., Patil, A. R., & Ishikar, S. K. (2022). A review on herbal soap. *Research Journal of Topical and Cosmetic Sciences*, 13(1), 49–54.
3. Adigun, O., Manful, C., Prieto Vidal, N., Mumtaz, A., Pham, T. H., Stewart, P., Nadeem, M., Keough, D., & Thomas, R. (2019). Use of natural antioxidants from newfoundland wild berries to improve the shelf life of natural herbal soaps. *Antioxidants*, 8(11), 536.
4. Asiagwu, A. K. (2013). Kinetics of saponification of *Treulia africana* oil using a locally sourced alkaline. *IJRRAS*, 14(3).
5. Alzohairy, M. A. (2016). Therapeutics role of *Azadirachta indica* (neem) and their active constituents in diseases prevention and treatment. *Evidence-based complementary and alternative medicine: ECAM*, 2016, 738–2506.
6. Cohen, M. M. (2014). Tulsi—*Ocimum sanctum*: A herb for all reasons. *Journal of Ayurveda and Integrative Medicine*, 5(4), 251–259.
7. Swapna Sonale, R., Ramalakshmi, K., & Udaya Sankar, K. (2018). Characterization of neem (*Azadirachta indica* A. Juss) seed volatile compounds obtained by supercritical carbon dioxide process. *Journal of Food Science and Technology*, 55(4), 1444–1454.
8. Koula, V. K., Gandotraa, B. M., Koula, S., Ghosha, S., Tikooa, C. L., & Gupta, A. K. (2004). Steam distillation of lemon grass (*Cymbopogon* spp.). *Indian Journal of Chemical Technology*, 11, 135–139.
9. Irshad, M., Subhani, M., Ali, S., & Hussain, A. (2019). Biological importance of essential oils. <https://doi.org/10.5772/intechopen.87198>
10. Ghanwat, A., Wayzod, S., Divya, V., & Nerkar, A. (2020). Formulation and evaluation of herbal soap 02.
11. Betsy, K. J., Jilu, M., Fathima, R., & Varkey, J. T. (2013). Determination of alkali content & total fatty matter in cleansing agents. *Asian Journal of Science and Applied Technology*, 2(1), 8–12.
12. Mohammed Haneefa, K. P. (2019). Formulation and evaluation of medicated soap of *Ixora coccinea* root extract for dermal infections. *Journal of Pharmaceutical Sciences and Research*, 11(8), 3094–3097.

In Silico Prediction and Screening of Potential Immunomodulators Using Autodock Vina



Snehal Kashid, Ashish Suttee, and Prasad Kadam

Abstract The recent drug discovery emphasizes new targets, compound efficiency, and safety in pharmacological models. The main objective of the study is to identify the immunomodulatory potential of *Pimpinella anisum* phytoconstituents using in silico approach. With the provision of autodock vina, we consider a protein–ligand interaction approach to drug discovery based on the screening of small molecules and a protein at the atomic level. Position and orientation of ligand and binding affinities are basic steps in docking. The current protocol encompasses, ligand selection, protein preparation, target, ligand optimization, analysis of target active binding sites, and binding affinity. Pharmacokinetic parameters were evaluated using SwissADME and drug likeness by using Lipinski’s rules. The present study, anethole, anisaldehyde, trans-anethole, cisanethole, estragole, and linalool were docked with nitric oxide (NOs). Molecular docking exposed the remarkable binding affinity between – 9.4 and – 5.9 kcal/mol. Author conclude that, bioactive compounds from *Pimpinella anisum* can be used as immunomodulatory agents.

Keywords Molecular docking · Immunomodulatory · Protein–ligand · *Pimpinella anisum* · Nitric oxide

1 Introduction

The word immunity was derived from the Latin term ‘immunitas means exemption form military services’. To protect the host from infectious disease there is strong defence mechanism in body known as immunity. It has adaptive immunity (more specific) and innate immunity (less specific) components [1]. From ancient times, herbal plants have been exploited in indigenous as well as conventional medicines to

S. Kashid (✉) · A. Suttee

School of Pharmaceutical Sciences, Lovely Professional University, Phagwara, Punjab, India
e-mail: snehalkashid1231@gmail.com

P. Kadam

Marathwada Mitra Mandal College of Pharmacy, Savitribai Phule Pune University, Pune, India

battle against diseases [2]. Natural products are ‘Gifted Gods’ for curing, supporting and rehabilitate patients. Plants primary and secondary metabolites like alkaloids, glycosides, terpenoids and polyphenols, fatty acids, volatile oils, and probiotics, also are implicated in the regulation of immune function. The ayurveda, siddha, unani, Chinese systems are the oldest traditional system of medicine plays a crucial role in combating and pleasing the needs of the universal healthcare system. *Pimpinella anisum* (aniseed) one of the oldest spices and important medicinal herb mentioned by Unani, Greek and Roman physicians [3]. Aniseed being cultivated in Egypt and later in Greece, Rome, and the Middle East mainly used as stimulant, carminative, flavoring agent, coughs, flatulence, respiratory infections, diuretic, expectorant, asthma, menopause [4]. *P. anisum* consist of several active constituents such as *trans*-anethole, estragole, (E) methyleugenol, α -cuparene, α -himachalene, β -bisabolene, *p*-anisaldehyde, phenylpropanoid, and *cis*-anethole [5–7]. In recent years molecular docking becoming the fundamental computer-aided drug design for analysing novel ligands, Position and orientation of ligands, binding affinity, and behavior of small molecules at the binding site of the target protein [8–11]. The binding interaction between protein–ligand represented in the form of docking score (kcal/mol) [9, 10]. The present study aimed to explore in silico interaction of selected five phytoconstituents with protein 5UO1 (NOs). 5UO1 possesses a total structure weight of about 48.78 kDa with 421 amino acids chains length (chain A and B).

2 Materials and Methods

2.1 Molecular Docking

Molecular docking is a significant computer-assisted drug design tool to recognize the binding interaction at the target site and elucidate biochemical process.

2.1.1 Software

Autodock_vina version 4.2.6 (<https://vina.scripps.edu>) software was used to envisage the in-silico interaction between active compounds of *Pimpinella anisum* and immunomodulatory proteins 5UO1. The active pocket site of protein encompass amino acids was observed by the CASTp tool in Fig. 1 [12, 13]. For visualization purpose BIOVIA Discovery Studio was downloaded from <https://discover.3ds.com> [14]. Open bable 3.1.1 was used to convert SDF to PDB format downloaded from <http://openbabel.org> [15]. The calculations were performed on Windows 10 operating system.



Fig. 1 Binding pockets of protein 5UO1 along with amino acid sequence

2.1.2 Ligand Sélection

Five phytoconstituents i.e. anisaldehyde, trans-anethole, *cis*-anethole, estragole, linalool are selected as the ligand (Table 1). The 2D and 3D structures of these ligands in SDF format were downloaded from <https://pubchem.ncbi.nlm.nih.gov/to> dock against nitrous oxide while, natural phytoconstituent curcumin was selected as standard. The ligands were converted into PDB format.

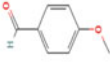
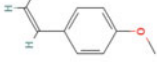
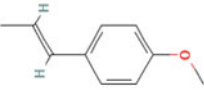
2.1.3 Preparation of Protein

The three-dimensional (3D) structure of the protein PDB ID: 5UO1 was extruded from the protein data bank (PDB) (<http://www.rcsb.org>) observed in Fig. 2. For the purpose of protein preparation and observation of protein chain, active pockets, ligand groups BIOVIA Discovery Studio was utilized [14]. Het-atoms, water molecules were deleted which ultimately responsible for elevation of resolution.

2.1.4 Identification of Conserved Active Régions of Proteins

Subsequent to protein preparation, a particular ligand is chosen, and the receptor-ligand interaction between small molecules and proteins was analyzed. The binding site was analyzed and the SBD site sphere size was edited as 20 Å for PDB ID: 5UO1. Later the ligand group was deleted, Polar hydrogen atoms and the Kollman charges were added, and the final file was saved in PDB format using BIOVIA Discovery Studio [16, 17].

Table 1 List of selected immunomodulatory compounds and their details

Name	Structure	Pubchem CID	Molecular wt (g/mol)	Molecular formula	Canonical smiles
Anisaldehyde		31244	136.15	C ₈ H ₈ O ₂	<chem>COC1=CC=C(C=C1)C=O</chem>
Cis-anethole		1549040	148.20	C ₁₀ H ₁₂ O	<chem>CC=CC1=CC=C(C=C1)OC</chem>
Trans-anethole		637563	148.20	C ₁₀ H ₁₂ O	<chem>CC=CC1=CC=C(C=C1)OC</chem>

(continued)

Table 1 (continued)

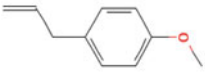
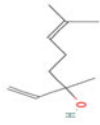
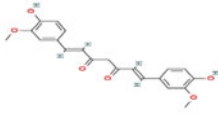
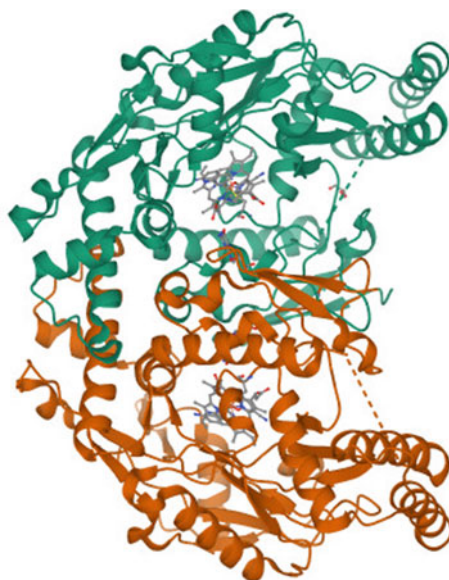
Name	Structure	Pubchem CID	Molecular wt (g/mol)	Molecular formula	Canonical smiles
Estragole		8815	148.20	C ₁₀ H ₁₂ O	COC1=CC=C(C=C1)CC=C
Linalool		6549	154.25	C ₁₀ H ₁₈ O	CC(=CCCC(C)(C=C)O)C
Curcumin		969516	368.40	C ₂₁ H ₂₀ O ₆	COC1=C(C=CC(=C1)C=CC(=O)CC(=O)C=CC2=CC(=C(C=C2)O)OC)O

Fig. 2 3D structure of 5UO1

2.1.5 Dockings Protein and Ligand Molecules

At the final protein was converted into PDBQT format using AutodockVina tool. Ligand was embedded with protein and configuration file were prepared. Later on molecular docking was carried out using command prompt along with nine binding modes and exhaustiveness was set as eight which was globally accepted. Further analysis of interaction between protein and ligand was determined with the help of Biovia Discovery Studio.

2.2 Pharmacokinetic Profiling of Ligand

Swiss ADME (<http://www.swissadme.ch/index.php>) used to compute pharmacokinetic properties of any compound using its conical smiles or its structure [18, 19]. Five phytoconstituents from *Pimpinella anisum* anisaldehyde, trans-anethole, cis-anethole, estragole, linalool were targeted against protein estimated for its ADME prediction with the help of Swiss ADME.

2.3 Drug-Likeness of Ligand

Lipinski rule of five predict probability of success or failure of any compound from natural or synthetic origin. The drug likeness of active compounds from *Pimpinella*

anisum were analyzed using Lipinski rule of five. Input file of ligand in SDF format was added and submit file ultimately results would be revealed [20].

3 Results

Numerous protein structures were available at RCSB to screen immunomodulatory potential of compound. PDB ID: 5UO1 (Structure of human neuronal nitric oxide synthase heme domain in complex with 3-[(2-aminoquinolin-7-yl)methoxy]-5-((methylamino)methyl)benzonitrile) [area (SA) Å²3859.237 and (SA) Å³ volume 3296.295] was downloaded from protein data bank (<https://www.rcsb.org>) and considered for determination of immunomodulatory potential. Five active compounds from *Pimpinella anisum* such as screened against PDB ID: 5UO1 to determine binding affinities in kcal/mol. Active binding pockets and amino acid sequence was observed in Fig. 1.

Figure 1 indicates the binding pockets of protein 5UO1 in red color and highlighted residue sequence outlined the binding pocket achieved from the CASTp tool. Molecular docking was a striking scaffold to recognize the interaction of small molecules and pharmacophore for rational drug design and discovery. Place ligand into the preferred binding sites of specific regions of protein target which may form ligand-receptor complex. 3D crystal structure of protein 5UO1 was observed in Fig. 2. Five phytoconstituents from *Pimpinella anisum* i.e. anisaldehyde, *trans*-anethole, *cis*-anethole, estragole, linalool were selected as immunomodulatory ligand while curcumin was selected as natural standard and its molecular details was mentioned in Table 1.

Nitrous oxide is synthesized from L-arginine by the enzyme Nitrous Oxide Synthase in the presence of two cofactors viz. NADPH and oxygen [21]. Nitrous oxide has a wide range of biological functions counting immunomodulation, inflammation, microbial and tumour abolition. Considering its immune function nitrous oxide promotes Th2 cytokine response escorts to humoral immunity and allergic responses while down regulate Th1 cytokine [22]. Nitrous oxide regulates the growth, function, and death of several immune and inflammatory cell types counting macrophages, neutrophils, T lymphocytes, mast cell, NK cells, and antigen-presenting cells [23]. NOs at low concentration have vital role in immune function while at higher concentration shows immunosuppressive action [22] (Fig. 3).

The present study, the five phytoconstituents of *Pimpinella anisum* bind individually to chain A of protein 5UO1 comprising a number of amino acids such as TRP414, PHE589, LEU429, ILE464, PHE709, ALA417, MET575, PHE709, CYS420, TRP592, GLY591, ILE424, GLU597, and SER590. The binding of energy of Anisaldehyde to NOs was - 6.2 kcal/mol involves TRP414, PHE589 amino acids via hydrophobic bond. *Trans*-Anethole chief constituent of *Pimpinella anisum* interact with 5UO1 via several amino acids such as TRP414, PHE589, LEU429, ILE464, PHE709 with - 6.5 kcal/mol binding affinity. Molecular docking utilized for virtual screening and calculation of binding affinity. It is used for visualizing

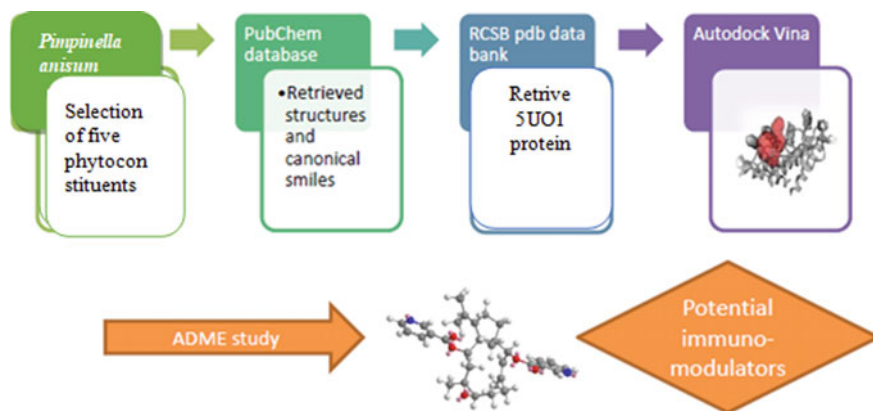


Fig. 3 Schematic representation of methodologies implemented in the current protocol

diverse types of bonded and non-bonded interaction between the protein 5UO1 and ligands (Table 2).

Cis-anethol binds hydrophobically to NOs via amino acid residue TRP414, PHE589, ALA417, LEU429, MET575, PHE709, and CYS420 shows -7.2 kcal/mol binding affinity. Among all Estragole shows highest binding affinity -9.4 kcal/mol interact via hydrogen Bond and hydrophobic bond shows amino acid residue TRP592, GLY591, TRP414, PHE589, and ILE424. Furthermore, Linalool interacts with protein 5UO1 hydrophobically via TRP414, PHE589, PHE589, and PHE709 shows -7.4 kcal/mol binding affinity observed in Table 3.

Nitric oxide (NO) has been eminent role in the immune system, it significantly involved in the pathogenesis and control of infectious diseases, tumors, autoimmune processes and chronic degenerative diseases as defense molecule [24]. The bar diagram drawn below (Fig. 4) for better distinction of binding affinities, where curcumin was considered as natural standard and anisaldehyde, *trans*-anethole, *cis*-anethole, estragole, and linalool were serve as ligands.

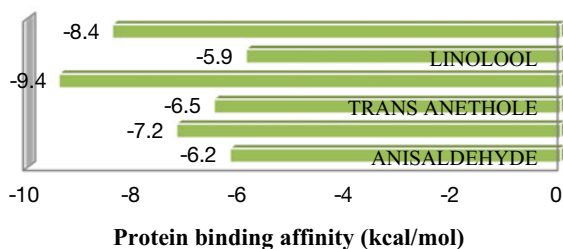
Furthermore, after molecular docking study we performed in silico pharmacokinetic study by using Swiss ADME. For screening of its absorption, distribution, metabolism, and excretion of selected phytoconstituents as shown in Table 4. According to Swiss ADMET anisaldehyde, *trans*-anethole, *cis*-anethole, estragole, and linalool shows no cytotoxicity and metabolic interferences with membrane receptors or Cyps. All the ligands pass Lipinski rule for five, shows high GI absorption, BBB permeation and good solubility these criteria make them perfect fit candidate as drug with good pharmacokinetic profile [25].

Table 2 Interactions of active phytoconstituents with protein 5U01

Interaction (5u01)	2D structure	3D structure
<p>Anisaldehyde (6.2 kcal/mol)</p> <ul style="list-style-type: none"> Pi-Pi Stacked Pi-Alkyl 		
<p>Trans-anethole (anethole) (6.5 kcal/mol)</p> <ul style="list-style-type: none"> Alkyl Pi-Pi Stacked Pi-Alkyl 		
<p>Cis-anethole (-7.2 kcal/mol)</p> <ul style="list-style-type: none"> Alkyl Pi-Pi Stacked Pi-Alkyl 		
<p>Estragole (9.4 kcal/mol)</p> <ul style="list-style-type: none"> Conventional Hydrogen Bond Carbon Hydrogen Bond Pi-Sigma Alkyl Pi-Pi Stacked 		
<p>Linalool (5.9 kcal/mol)</p> <ul style="list-style-type: none"> Unfavorable Acceptor-Accept Pi-Sigma Pi-Alkyl 		
<p>Curcumin (8.4 kcal/mol)</p> <ul style="list-style-type: none"> Conventional Hydrogen Bond Pi-Anion Pi-Pi Stacked Pi-Alkyl 		

Table 3 Type of interactions and interacting amino acid residues of 5UO1

Compound name	Binding energy (kcal/mol)	Bond	Amino acid residues
Anisaldehyde	- 6.2	Hydrophobic	TRP414, PHE589
<i>Trans</i> -anethole	- 6.5	Hydrophobic	TRP414, PHE589, LEU429, ILE464, PHE709
<i>Cis</i> -anethole	- 7.2	Hydrophobic	TRP414, PHE589, ALA417, LEU429, MET575, PHE709, CYS420
Estragole	- 9.4	Hydrogen bond Hydrophobic	TRP592, GLY591, TRP414, PHE589, ILE424
Linalool	- 7.4	Hydrophobic	TRP414, PHE589, PHE589, PHE709
Curcumin	- 8.4	Hydrophobic	GLU597, SER590, TRP414

Fig. 4 Protein binding affinity (kcal/mol) of phytoconstituents**Table 4** Cytotoxicity and drug ability profiling of selected ligands

Compound name	Acute toxicity (<i>Daphnia magna</i>)	Toxicity profiling		Lipinski rule of five
		Carcinogenicity (mouse)	Mutagenicity (<i>Salmonella typhimurium</i>)	
Anisaldehyde	2.65 mg/L	Carcinogenic	Non-mutagenic	Pass
<i>Trans</i> -anethole	3.7 mg/L	Non-carcinogenic	Mutagenic	Pass
<i>Cis</i> -anethole	0.0031–284 mg/L	Non-carcinogenic	Mutagenic	Pass
Estragole	1.24 mg/L	Carcinogenic	Non-mutagenic	Pass
Linalool	-	Not predictable	Non-mutagenic	Pass
Curcumin	-	Non-carcinogenic	Non-mutagenic	Pass

4 Conclusion

The current study scrutinizes the immunomodulatory potential of five active compounds of *Pimpinella anisum* on immunomodulatory target protein 5UO1 through in-silico studies, including molecular docking utilizing Autodock Vina,

ADME by Swiss MADE and toxicity profiling via Lazar toxicity predictions. The phytoconstituents were anisaldehyde, *trans*-anethole, *cis*-anethole, estragole, and linalool while curcumin serve as standard. In the middle of the all compound estragole shows promising results and shows highest binding affinities against protein 5UO1. All the compounds can be served as novel immunomodulatory agent. However, further *in vitro* and *in vivo* animal activity will be suggested for better interpretation of novel safe and potential immunomodulatory compound.

References

1. Viikari, L., Suurnäkki, A., Grönqvist, S., Raaska, L., Ragauskas, A., & Moselio, S. (2009). *Encyclopedia of microbiology*.
2. Khanna, K., Kohli, S. K., Kaur, R., Bhardwaj, A., Bhardwaj, V., Ohri, P., Sharma, A., Ahmad, A., Bhardwaj, R., & Ahmad, P.: Herbal immune-boosters: Substantial warriors of pandemic Covid-19 battle. *Phytomedicine: International Journal of Phytotherapy and Phytopharmacology*, 85.
3. Ali, K., Hasan, A., Parray, S., & Ahmad, W. (2017). Anisoon (*Pimpinella anisum* L.): A review of pharmacological activities and clinical effects. *Hippocratic Journal of Unani Medicine*, 12, 31–46.
4. Ibrahim, D. (2017). Medicinal benefits of anise seeds (*Pimpinella anisum*) and thymus vulgaris in a sample of healthy volunteers. *International Journal of Research in Ayurveda & Pharmacy*, 8, 91–95.
5. Shojaii, A., & Abdollahi Fard, M. (2012). Review of pharmacological properties and chemical constituents of *Pimpinella anisum*. *ISRN Pharmaceutics*.
6. Balasubramanian, D., Wongwuttanasatian, T., Venugopal, I. P., & Rajarajan, A. (2022). Exploration of combustion behavior in a compression ignition engine fuelled with low-viscous *Pimpinella anisum* and waste cooking oil biodiesel blends. *Journal of Cleaner Production*, 331.
7. Campana, R., Tiboni, M., Maggi, F., Cappellacci, L., Cianfaglione, K., Morshedloo, M. R., Frangipani, E., & Casettari, L. (2022). Comparative analysis of the antimicrobial activity of essential oils and their formulated microemulsions against foodborne pathogens and spoilage bacteria. *Antibiotics*, 11(4), 447.
8. Pagadala, N. S., Syed, K., & Tuszynski, J. (2017). Software for molecular docking: A review. *Biophysical Reviews*, 9(2), 91–102.
9. Taguchi, Y. H., & Turki, T. (2020). A new advanced *in silico* drug discovery method for novel coronavirus (SARS-CoV-2) with tensor decomposition-based unsupervised feature extraction. *PLoS One*, 15(9).
10. Prabhu, D. S., & Rajeswari, V. D. (2018). *In vitro* and *in silico* analyses of *Vicia faba* L. on peroxisome proliferator-activated receptor gamma. *Journal of Cellular Biochemistry*, 119(9), 7729–7737.
11. Dhameiliya, T. M., Nagar, P. R., & Gajjar, N. D. (2022). Systematic virtual screening in search of SARS CoV-2 inhibitors against spike glycoprotein: Pharmacophore screening, molecular docking, ADMET analysis and MD simulations. *Molecular Diversity*, 1–8.
12. Trott, O., & Olson, A. J. (2010). AutoDock Vina: Improving the speed and accuracy of docking with a new scoring function, efficient optimization, and multithreading. *Journal of Computational Chemistry*, 31(2), 455–461.
13. Tian, W., Chen, C., Lei, X., Zhao, J., & Liang, J. (2018). CASTp 3.0: Computed atlas of surface topography of proteins. *Nucleic Acids Research*.
14. BIOVIA. (2016). Dassault Systèmes: Comprehensive modeling and simulations for life sciences. Biovia Discovery Studio, 1.

15. O'Boyle, N. M., Banck, M., James, C. A., Morley, C., Vandermeersch, T., & Hutchison, G. R. (2011). Open Babel: An open chemical toolbox. *Journal of Cheminformatics*, 3(1), 1–4.
16. Xue, Q., Liu, X., Russell, P., Li, J., Pan, W., Fu, J., et al. (2022). Evaluation of the binding performance of flavonoids to estrogen receptor alpha by Autodock, Autodock Vina and Surflex-Dock. *Ecotoxicology and Environmental Safety*, 233.
17. Xia, B., Luo, M., Pang, L., Liu, X., & Yi, Y. (2021). Lipopeptides against COVID-19 RNA-dependent RNA polymerase using molecular docking. *Biomedical Journal*, 44(6), S15-24.
18. Daina, A., Michielin, O., & Zoete, V. (2017). SwissADME: A free web tool to evaluate pharmacokinetics, drug-likeness and medicinal chemistry friendliness of small molecules. *Science and Reports*, 7(1), 1–3.
19. Daina, A., & Zoete, V. (2016). A boiled egg to predict gastrointestinal absorption and brain penetration of small molecules. *ChemMedChem*, 11(11), 1117–1121.
20. Maunz, A., Gütlein, M., Rautenberg, M., Vorgrimmler, D., Gebele, D., & Helma, C. (2013). Lazar: A modular predictive toxicology framework. *Frontiers in Pharmacology*, 4, 1–10.
21. Omer, N., Rohilla, A., Rohilla, S., & Kushnoor, A. (2012). Nitric oxide: Role in human biology. *International Journal of Pharmaceutical Sciences and Drug Research*, 4(2), 105–109.
22. Shreshtha, S., Sharma, P., Kumar, P., Sharma, R., & Singh, S. P. (2018). Nitric oxide: It's role in immunity. *Journal of Clinical and Diagnostic Research*, 12(7), 1–5.
23. Tripathi, P. (2007). Nitric oxide and immune response. *Indian Journal of Biochemistry & Biophysics*, 44(5), 310–319.
24. Christian, B. (2001). Nitric oxide and the immune response. *Nature Immunology*, 2, 907–916.
25. (2022). An in-silico studies for immunomodulatory potential of phytoconstituents from a naturally occurring herb nigella sativa. *Pharmacophore*, 13(5), 14–26.

Phytochemical Studies and Anticariogenic Activity of Some Folklore Plants for Dental Care



M. I. Mujawar, E. N. Gaviraj, and S. P. Ghunaki

Abstract Oral diseases are a major health problem worldwide. The increasing failure of chemotherapeutics and antibiotics resistance exhibited by pathogenic micro-organisms has led to the screening of several medicinal plants for their anticariogenic activity (Indrani and Kalpesh in Asian Journal of Traditional Medicines 11:88–98, 2016) [1]. The present study was undertaken to evaluate the anticariogenic activity of some folklore plants for dental health. *Argemone mexicana*, *Pongamia pinnata*, *Solanum virginianum* and *Thevetia peruviana* were tested against the bacteria that cause dental carries. Ethanolic extracts were prepared by maceration and soxhlet methods and they studied for phytoconstituents by chemical tests. *A. mexicana* seed extract produced greater zone of inhibition when compared other extracts. The MIC of *A. mexicana* seeds extract was found to be lower hence; it was decided to study the antimicrobial constituents of the *A. mexicana* extract by TLC-bio autography. Our findings of anticariogenic activity on the plant extracts against selected bacteria and phytochemical analysis revealed that these plants possess antimicrobial substances.

Keywords Anticariogenic · Folklore plant · Dental care

1 Introduction

Oral health is integral to general well-being and relates to the quality of life that extends beyond the functions of the craniofacial complex. Dental caries and periodontal diseases are among the most important global oral health problems, although conditions such as oral and pharyngeal cancers and oral tissue lesions are also significant health concerns [2]. According to WHO, dental caries is defined as localized

M. I. Mujawar (✉)

College of Pharmacy (Poly.), Shri Vitthal Education and Research Institute, Pandharpur, Maharashtra, India

e-mail: mimujawar@cop.sveri.ac.in

E. N. Gaviraj · S. P. Ghunaki

B.L.D.E.A's. SSM College of Pharmacy and Research Centre, Vijayapur, Karnataka, India

© The Author(s), under exclusive license to Springer Nature Switzerland AG 2024

579

P. M. Pawar et al. (eds.), *Techno-Societal 2022*,

https://doi.org/10.1007/978-3-031-34648-4_58

post eruptive pathological process of external origin involving softening of the hard tooth tissue. It is an infectious disease caused by microbe's results in decalcification and destroying particular infected tooth. It develops by complicated mechanism such as interaction of tooth or saliva with acidogenic bacteria [3]. The pH of a healthy mouth is between 6.2 and 7.0. When the pH is < 5.5 the tooth is in acid environment and start demineralization. As the enamel losses its minerals, it starts to breakdown, resulting into formation of cavity [4]. Medicinal plants and their products used as a primary source of many drugs from several thousands of years. These plants play a significant role in prevention, diagnosis and treatment of various diseases in humans. Herbal plants used in medicine are a traditional way to maintain spiritual, physical and mental health. Folklore plants are defined as, the traditional beliefs, customs and stories of a community about medicinal plants, passed through the generations by word of mouth. *Lactobacillus acidophilus*, *Lactobacillus casei*, *Streptococcus mutans* and *Staphylococcus aureus* were the bacteria used to produce cariogenic effect.

As a result some bacterial infections are now essentially untreatable with antibiotics. In a 2003, Institute of medicine report, microbial threat to health, antimicrobial resistance was noted as a paramount microbial threat of the twenty first century, some strain of bacteria are now resistant to essentially available antimicrobial drugs and some remain susceptible to only one. The lack of new drug classes is a consequence of difficulties in discovery of new compounds that has persisted for many years [5]. The present study was taken up to conduct phytochemical and anticariogenic activity studies of some folklore plants viz. seeds of *Argemone mexicana*, Tender leaf twigs of *Pongamia pinnata*, fruits of *Solanum virginianum*, Latex of *Thevetia peruviana*.

2 Material and Methods

2.1 Collection of Plant Material

Argemone Mexicana Seeds, *Pongamia pinnata* tender twigs, *Solanum virginianum* Fruits and *Thevetia peruviana* Latex were collected between June and July were collected from the surrounding fields of Bijapur and Solapur. All plants and their products were identified and authenticated by botanist.

2.2 Extraction of Plant Material

The selected plant materials were shade dried and coarsely powdered. The coarse powder was first extracted by maceration and then by soxhlet extraction method. About 50 gm. of *Argemone mexicana* *Argemone Mexicana* Seeds, *Pongamia pinnata*

tender twigs and *Solanum virginianum* Fruits powder was subjected to cold maceration with 200 ml of 80% aqueous ethanol for 24 h [6]. 50 gm of milky white latex was obtained by incising the fruits. The latex was air dried and treated with petroleum ether eliminate any chlorophyll pigments and rubber materials that were present. The air dried latex was then extracted by maceration using 80% aqueous ethanol [7].

2.3 Bacterial Strains for Anticariogenic Activity

A group of bacteria that cause tooth caries were selected. *Lactobacillus acidophilus* (NCIM 5306), *Lactobacillus casei* (NCIM 5303), *Streptococcus mutans* (MTCC 890) and *Staphylococcus aureus* were used in present study to study the antimicrobial activity of the prepared extracts. *L. acidophilus* and *L. casei* were procured from National Collection of Industrial Microorganism (NCIM), CSIR-National Chemical Laboratory, Dr. Homi Bhabha Road, Pune-411008, India. *S. mutans* was procured from Microbial Type Culture and Gene Bank (MTCC), Institute of Microbial Technology, Shanti Path, 39A, Sector 39, Chandigarh, 160036, India. *S. aureus* procured from BLDE Shri B. M. Patil Medical College Hospital and research Centre, Solapur road, Vijayapur 586103.

2.4 Preparation of Bacterial Inoculum

Broth cultures of the selected bacteria were prepared by inoculating a loopful of bacteria into organism-specific media and incubated at optimal temperature. MRS media was used for *L. acidophilus* and *L. casei*. Enriched infusion heart media for *S. mutans* and Nutrient broth media for *S. aureus* were employed respectively. The bacterial suspension was compared with 0.5 McFarland turbidity standards, which is equivalent to approximately 1×10^8 bacterial cell count per ml. Such prepared bacterial suspensions were used for antimicrobial studies [8].

2.5 Bioassay for Anticariogenic Activity of Plant Extracts

2.5.1 Agar Well Diffusion Method

The anticariogenic activity of extracts of *Argemone mexicana* (seed), *Pongamia pinnata* (tender leaf), *Solanum virginianum* (fruit) and *Thevetia peruviana* (latex) were studied by agar well diffusion method. The plant extracts were dissolved in dimethyl sulfoxide and were tested at three concentrations viz. 10, 50 and 100 mg/ml. The agar plates were prepared and labeled for specific bacteria and extract. A fresh bacterial culture of 100 μ l having 1×10^8 CFU/ml was spread on

agar plates using sterile cotton swab. 6 mm diameter well was made with a sterile borer. The prepared wells were filled with 100 μ l of respective plant extracts. Plates were placed in the refrigerator for 30 min for diffusion of extracts. Then plates were incubated at 37 °C for 24 h. The zone of inhibition was measured. Tetracycline (100 μ g/ml) was used as a standard drug for comparison [9].

2.5.2 Determination of Minimum Inhibitory Concentration (MIC) of Plant Extracts

MIC was done by broth dilution method. The plant extracts were tested at 30, 40, 50, 60, 70 80, 90 and 100 mg/ml.

100 μ l of bacterial suspension was added to each tube. The tubes were incubated for 24 h at 37 °C. 100 μ l of 0.1% growth indicator 2,3,5-triphenyl tetrazolium chloride was added to each tube to find out bacterial growth inhibition. Tubes were incubated for 30 min under dark condition. Bacterial growth was determined when colorless growth indicator converted into red color [10].

2.5.3 Thin Layer Chromatography

Stationary phase silica gel 60 F 254, Mobile Phases: (i) toluene:ethyl acetate (90:10, v/v), (ii) chloroform:methanol (90:10, v/v), (iii) chloroform:ethyl acetate (90:10, v/v) and (iv) chloroform:ethyl acetate:ammonia (90:9:1, v/v/v) 0.10 μ l of *A. mexicana* seed extract (100 mg/ml in ethanol) was spotted on TLC plates and developed with the above mobile phases. After air-drying, the plates were visualized with iodine vapor.

2.5.4 Bioautography

Direct bioautography was used for the localization of antimicrobial compounds in the seed [11]. After applying seed extract, the TLC plate was developed using chloroform:methanol (90:10, v/v) and then air dried completely. The plate was placed over sterile nutrient agar and pressed gently. Overnight broth cultures of bacteria viz. *L. acidophilus*, *L. casei*, *S. mutans* and *S. aureus* were made and the turbidity of the suspension was adjusted to that of Mac Farland's standard.

The plate was incubated overnight at 37 °C, sprayed with a 2% w/v aqueous solution of 2,3,5-triphenyl tetrazolium chloride and incubated for further 4 h. Zone of inhibition appeared as transparent area against reddish background.

3 Result and Discussion

In present study, the anti-cariogenic assay of plant material extract formulation against oral pathogenic organism was carried out for the purpose of checking of sensitivity of cariogenic bacteria. Plant material were extracted by using 80% aqueous Ethanol and used for further anti cariogenic activity.

The results of anticariogenic activity of the plant extracts and their efficacy were quantitatively assessed by measuring the zone of inhibition. Four plants were used for the evaluation of anticariogenic activity. The plant extracts were tested for anticariogenic activity by agar well diffusion method. They were tested at three concentrations viz. 10, 50 and 100 mg/ml. Dimethyl sulfoxide was used to dissolve the plant extracts. The result of sensitivity of cariogenic organisms was assessed by recording the presence or absence of Zone of inhibition in diameter. The results are summarized as under Table 1. At 10 mg/ml concentration, all the plant extracts showed no zone of inhibition. The zone of inhibition was observed at 50 and 100 mg/ml concentration of all four ethanolic plant extracts. Among the four plants extracts, *Argemone mexicana* showed maximum zone of inhibition compared to other plants. *Pongamia pinnata* and *Thevetia peruviana* showed comparatively same zone of inhibition. *Solanum virginianum* showed anticariogenic activity but the zone of inhibition was smaller compared to other three plant extracts in Fig. 1.

Table 1 Anticariogenic activity plant extracts at 100 mg/ml concentration

Zone of inhibition (mm) at 100 mg/ml concentration				
S. No.	Plant name	<i>L. acidophilus</i>	<i>L. casei</i>	<i>S. mutans</i>
1	<i>Argemone mexicana</i>	19	16	17
2	<i>Pongamia pinnata</i>	13.4	14	11
3	<i>Solanum virginianum</i>	7	10.2	9
4	<i>Thevetia peruviana</i>	13	11.2	13
5	<i>Tetracycline</i>	24.4	27	24.2

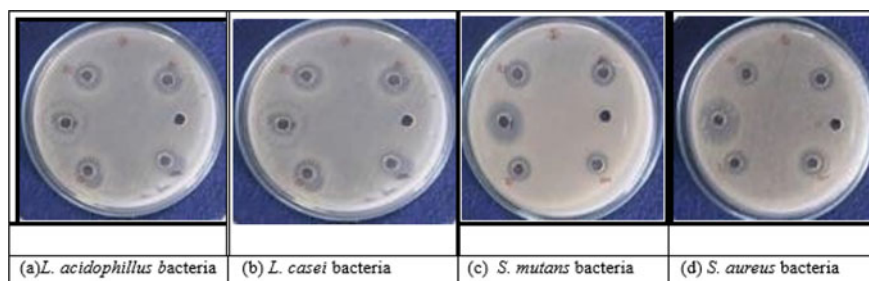


Fig. 1 Anticariogenic activity of plant extracts at 100 mg/ml concentration using

The Minimum Inhibitory Concentration (MIC) values of different formulation of leaves extracts of all the selected plants showing highest activity against selected organisms was assessed and summarized in Table 2. Examining the MIC values of nine samples of various extracts generated the data where the maximum MIC value was found to be all the plant extracts showing highest anticariogenic activity against selected bacteria. The plants extracts showed significantly remarkable anticariogenic activity against all four bacteria, *L. acidophilus*, *L. casei*, *S. mutans* and *S. aureus* with their MIC values ranging from 40 to 90 mg/ml.

Argemone mexicana seed extract was found to be the most active extract in the agar well diffusion and MIC studies. Thin layer chromatography of *Argemone mexicana* seed extract done by using 4 different mobile phases viz. toluene:ethyl acetate (90:10, v/v), chloroform:methanol (90:10, v/v), chloroform:ethyl acetate (90:10, v/v) and chloroform:ethyl acetate:ammonia (90:9:1, v/v/v) were used for TLC studies. After air-drying, the plates were visualized with iodine vapour. The mobile phase toluene:ethyl acetate (90:10, v/v) gave 3 spots. Chloroform:methanol (90:10, v/v) produced good separation and 5 spots were visible. Separation was not satisfactory with the remaining mobile phases viz. chloroform:ethyl acetate (90:10, v/v) and chloroform:ethyl acetate:ammonia (90:9:1, v/v/v) and 2 spots were seen with each mobile phase in Fig. 2.

Direct bio autography was performed to localize the antimicrobial compounds on TLC plate. *A. mexicana* seed extract was applied to the TLC plate and then developed with chloroform:methanol (90:10, v/v) as it gave good separation. Overnight

Table 2 MIC values of all plants ethanolic extracts in mg/ml

Minimum Inhibitory Concentration (MIC) in mg/ml				
S. No.	Plant name	<i>L. acidophilus</i>	<i>L. casei</i>	<i>S. mutans</i>
1	<i>Argemone mexicana</i>	40	50	50
2	<i>Pongamia Pinnata</i>	70	90	60
3	<i>Solanum virginianum</i>	60	70	80
4	<i>Thevetia peruviana</i>	70	80	60

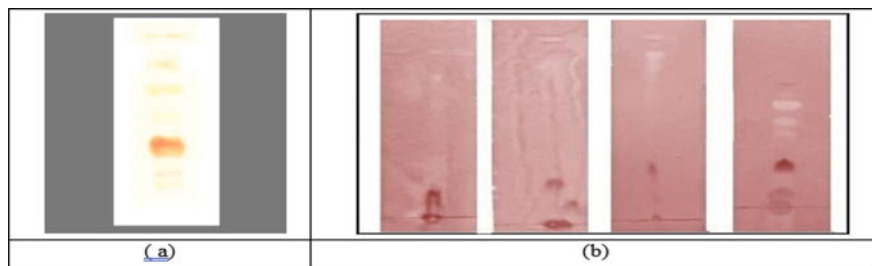


Fig. 2 *Argemone mexicana* seed extract **a** TLC, **b** bioautographic study with *L. acidophilus*, *L. casei*, *S. mutans*, and *S. aureus*

broth cultures of bacteria viz. *L. acidophilus*, *L. casei*, *S. mutans* and *S. aureus* were prepared. About 8–10 ml of bacterial suspension in molten agar media was distributed as a thin layer over TLC plate, which solidified within a few min. The plate was incubated overnight at 37 °C, sprayed with a 2% w/v aqueous solution of 2,3,5-triphenyl tetrazolium chloride and incubated for further 4 h. Zone of inhibition appeared as transparent area against reddish background.

Out of the 5 spots, spot with an Rf value of 0.25 showed activity with *L. acidophilus*. The spot with an Rf value of 0.78 showed activity with *L. casei*. The spot with an Rf value of 0.78 showed activity with *S. mutans*. Out of the 5 spots, spots with Rf values of 0.34, 0.46 and 0.6 showed activity with *S. aureus* in Fig. 2.

4 Conclusion

The extract of different plant material has good sources of as anticariogenic compound against pathogenic microorganisms, which can be used to treat the infectious diseases. The very good activity of plant extracts formulation useful for future development of drug for control of dental caries.

References

1. Indrani, B., & Kalpesh, I. (2016). In vitro anticariogenic activity of some Indian medicinal plants towards human oral pathogen. *Asian Journal of Traditional Medicines*, 11(4), 88–98.
2. Susheela, A. K. (2003). Dental fluorosis. In: *A treatise on fluorosis* (pp. 43–57). Fluorosis Research and Rural Development Foundation.
3. Veiga, N., Aires, D., Douglas, F., Pereira, M., Vaz, A., & Rama, L. (2016). Dental caries: A review. *Journal of Oral Dent Health*, 3(1), 1–3.
4. Freeth, C. (1999). Ancient history of trips to the dentist. *British Archaeology*, 1999(1999), 43.
5. Parmar, B., & Ishnava, K. B. (2019). Exploring of anticariogenic activity of herbal formulation from selected five medicinal plants leaves. *International Journal of Pharmacognosy and Chinese Medicine*, 3(4), 0003.
6. Panigrahi, S., & Mahapatra, S. (2016). Evaluation of antibacterial activity of *Pongamia pinnata* against *Staphylococcus aureus*. *International Journal of ChemTech Research*, 9(02), 205–212.
7. Shobowale, O. O., Ogbulie, N. J., Itoadon, E. E., Oresegun, M. O., & Olatope, S. O. (2013). A phytochemical and antimicrobial evaluation of aqueous and organic extract of *Calotropis procera* ait leaf and latex. *Nigerian Food Journal*, 31(1), 77–82.
8. Perilla, M. J. (2003). *Manual for the laboratory identification and antimicrobial susceptibility testing of bacterial pathogens of public health importance in this developing world* (pp. 209–214). WHO.
9. Agbor, A. M., & Naidoo, S. (2016). A review of the role of African traditional medicine in the management of oral diseases. *African Journal of Traditional, Complementary and Alternative Medicines*, 13(2), 133–142.

10. Dash, T. R., Singh, N., Gupta, D., Panwar, E., & Ramisetty, S. (2014). Role of medicinal herbs in oral health management. *International Journal Dental and Medical Sciences Research*, 2014, 113–119.
11. Bhattacharjee, I., Chatterjee, S. K., & Chandra, G. (2010). Isolation and identification of antibacterial components in seed extracts of *Argemone mexicana* L. (Papaveraceae). *Asian Pacific Journal of Tropical Medicine*, 3(7), 547–51.

Evaluation of Ondansetron Hydrochloride Interactions with Mannitol



Mangala J. Khandekar, Swarup R. Lahoti, Ravindra G. Kulkarni, and Aasiya N. Choudhary

Abstract The present study is to evaluate Ondansetron Hydrochloride (OND) interaction with Mannitol. Attempt has been made to prepare physical mixtures of OND with Mannitol in different proportions. The mixture was subjected to room temperature and accelerated temperature as per ICH guideline 1996. The interaction was studied by IR, UV Absorbance, TLC, Dissolution and DSC. From the study it was clear that C = O is the major site for interaction and more interaction is observed in case of accelerated condition than the room temperature. From the data obtained, it is observed that Mannitol showed the interaction with OND. Mannitol causes significant reduction in dissolution of OND.

Keywords OND · Stability · DSC

1 Introduction

To build quality, safety and efficacy in the drug formulation stability testing of pharmaceutical products is required. Capacity of drug substance or drug product to maintain its identity, quality, strength, and purity throughout the expiration or retest period is called as stability [1]. Stability testing is complex procedures involving scientific expertise, considerable time and cost. During the drug development process stability testing is most essential step [2]. Stability testing assures the identity, potency and purity of ingredients during all stages of drug developments [3]. As per WHO the stability of pharmaceutical products depends on humidity, light, ambient temperature, physical and chemical properties of active substance, excipient, diluents, composition of dosage form, manufacturing process, packaging material, container closure system etc. [4]. OND is a 5-HT₃ receptor antagonist used to prevent post and preoperative

M. J. Khandekar (✉) · R. G. Kulkarni · A. N. Choudhary
SVERI's College of Pharmacy, Gopalpur, Pandharpur, India
e-mail: khandekarmandal@gmail.com

S. R. Lahoti

Y. B. Chavan College of Pharmacy, Rauza Bagh, Dr. Rafiq Zakaria Campus, Aurangabad 431001, India

nausea and vomiting associated with cancer chemotherapy, radiotherapy. Excipients can join with the drug molecule in physical and chemical interactions which can lessen the usefulness of the drug. The rate of dissolution of a solid dosage form can be affected by physical interaction of excipients. Some excipients can adsorb APIs, which ultimately leads to slower dissolution rates, resulting in less bioavailability of the drug. Diluent is one of the important excipient used in different formulations. To increase weight and improve content uniformity diluents can act as fillers in pharmaceutical tablets. In this communication we report the interaction D-Mannitol with OND stored at two different proportions and stored at two different temperatures, all of these protected from the light.

2 Materials and Methods

OND received as gift sample from Wockhardt Ltd. (Aurangabad). Mannitol was purchased from Merck Ltd. (Mumbai). All other chemicals and solvents used were of analytical research grade. Distilled water was used as per need.

2.1 Preparation of Mixtures

OND and Mannitol were passed through 100# sieve. Concentrations of OND and diluents in 1:5 and 1:9 ratio were prepared by gently blending in an glass mortar with a spatula for 10 min at room temperature (25 ± 1 °C). Samples were stored in Thermolab, Mumbai Stability Chamber at 40 °C \pm 2 °C/ $75\% \pm 5\%$ RH and 25 °C \pm 2 °C/ $60\% \pm 5\%$ RH in glass bottles and analyzed after 0, 3, 6, 9, 12 Weeks [7].

2.2 Physical Stability Study

The physical stability was determined by visual inspection of each sample for change in color and formation of lumps or particle agglomeration [8].

2.3 Infrared Spectrophotometer

IR was recorded on **Jasco/FT/IR-4100, Japan** spectrophotometer in KBr pellet over the $400\text{--}4000$ cm^{-1} at the resolution of 2 cm^{-1} . For IR spectroscopy KBr powder was dried at 60 °C for one hour in hot air oven. The dried KBr powder was uniformly mixed with samples and IR spectra was taken for mixture [9].

2.4 Thin Layer Chromatography

TLC was performed on pre-coated silica gel F₂₅₄ (Merck) by using chloroform:methanol (4:1) as mobile phase. The sample to be analyzed were dissolved in the methanol and spots were given with the help of capillary tube. This plate was then put into the saturated chamber of mobile phase and mobile phase was allowed to run over the plate. The plates then put into the iodine chamber for activation and position of spot was identified [10].

2.5 Dissolution Studies

In Vitro dissolution study were carried out using Electrolab USP dissolution apparatus Type II at 37 ± 0.5 °C at a speed of 50 rpm. 500 ml of 0.01N HCL were used as dissolution medium. 10 ml of sample were withdrawn after 5, 10, 15, 30, 45 and 60 min and filter through Whatman filter paper No. 41. 1 ml of filtrate was diluted up to 10 ml with dissolution medium [9] (U.S. National Library of Medicine, 2007). From the absorbance value, the dilution factor is calculated by using Hayton and Chen equation [11].

2.6 Differential Scanning Colorimeter

DSC Measurements were Conducted Using Shimadzu W70 Thermal Analyser, Japan. High purity sample of indium was used to calibrate the system. Samples were scanned at the heating rate of 20 °C/min over a temperature range of 60–240 °C (Table 1).

Table 1 OND and Mannitol interactions on the basis of IR study

S. No	Conc. of OND:Mannitol	Storage condition	Interaction observed during period (week) (X = No interaction, ✓ = Interaction)				
			0	3	6	9	12
1	1:5	Room temp.	X	X	✓	✓	✓
		Accelerated	X	✓	✓	✓	✓
2	1:9	Room temp.	X	X	✓	✓	✓
		Accelerated	X	X	✓	✓	✓

3 Results and Discussion

3.1 Physical Interaction

Physical Interaction reveals that there is no color change as well as no lumps formation takes place up to 12 weeks in any sample.

3.2 Infra-Red Studies

Ondansetron has shown intense bands at 1699, 1638, 2975, 3124, 1480, and 1281 cm^{-1} corresponding to presence of functional groups $-\text{C}=\text{O}$, $-\text{C}=\text{N}$, $-\text{CH}$ (aliphatic), $-\text{CH}$ (aromatic), $-\text{C}=\text{C}$ and $-\text{C}-\text{N}$. The IR spectral pattern of the two different proportion mixture of Ondansetron with Mannitol was prepared and studied at time intervals 0, 3, 6, 9 and 12 weeks (Figs. 1, 2, 3 and 4).

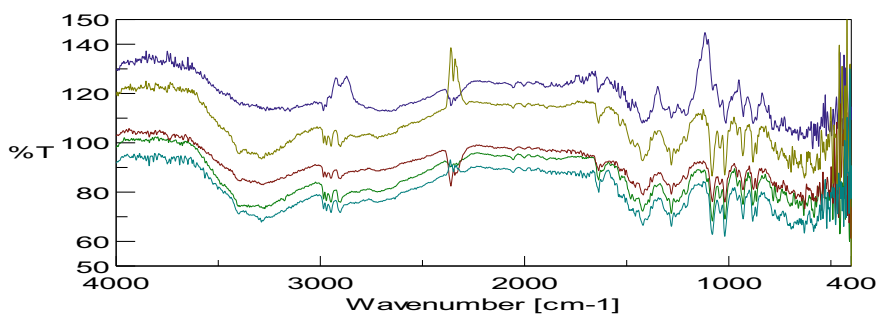


Fig. 1 OND and Mannitol (1:5) room temp

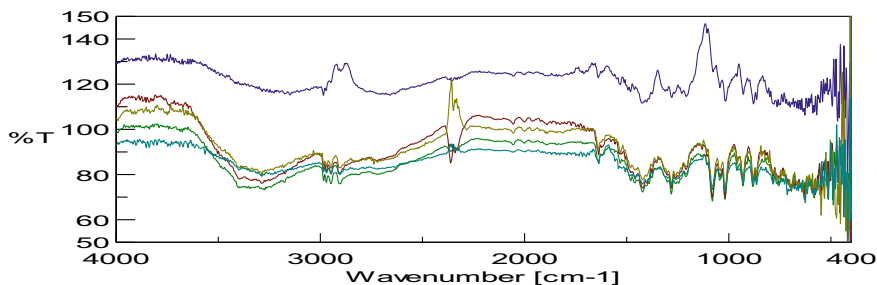


Fig. 2 OND and Mannitol (1:5) accelerated

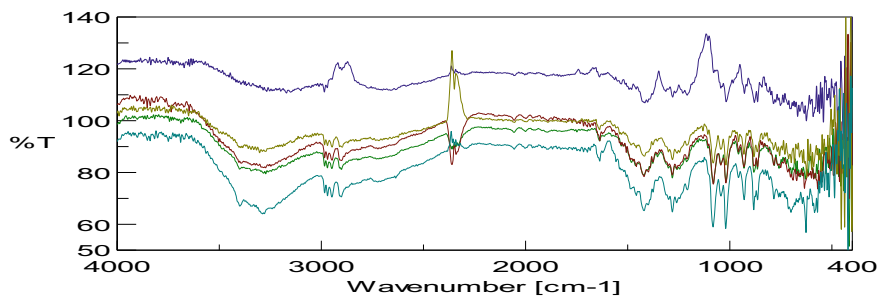


Fig. 3 OND and Mannitol (1:9) room temp

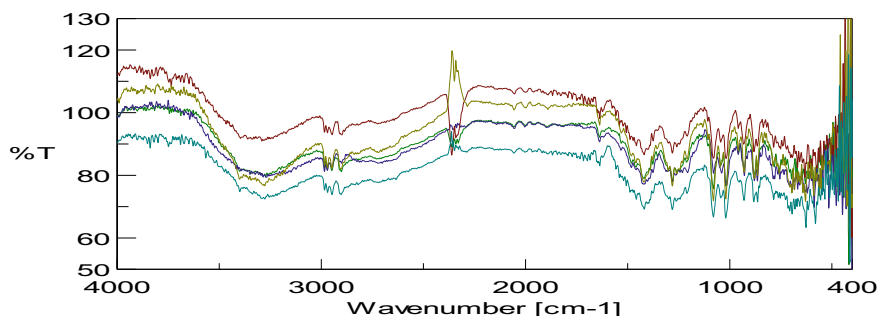


Fig. 4 OND and Mannitol (1:9) accelerated

3.3 Thin Layer Chromatography

TLC was used as a primary tool for interaction studies. In all the samples there is continuous change in the R_f value (Table 2). Slight increase R_f value were observed in case of the samples which were stored at accelerated condition than the samples stored at room temperature.

Table 2 OND + Mannitol R_f value (week)

OND + Mannitol					
Ratios and storage condition	Rf value (week)				
	0	3	6	9	12
1:9 Accelerated	0.65	0.67	0.68	0.71	0.72
1:9 Room temp.	0.66	0.65	0.67	0.70	0.71
1:5 Accelerated	0.64	0.66	0.67	0.69	0.72
1:5 Room temp.	0.66	0.68	0.69	0.70	0.73

3.4 *Dissolution Studies*

The dissolution study is an important parameter in identifying the drug excipient interaction. The change in the release rate of the sample will give some indications of interaction between drug and excipient. If the drug was get interacted with excipient it will form a new complex which will affect the dissolution performance of the mixture. This will lead to increase and/or decrease in drug release from the samples. The data from dissolution study shows that % drug dissolved with Mannitol was significantly reduced (Tables 3 and 4).

3.5 *Differential Scanning Colorimeter*

DSC thermogram from Fig. 5 reveals sharp endotherm between 178 and 179.5 °C which corresponds to melting point of ODN and Fig. 6 shows melting point of mannitol between 168 and 169 °C. Figure 7 shows endothermic peak between the range 150–180 °C a range in which both i.e., ODN and mannitol has the melting endotherm. The comparison of the two concentration shows that a broad peak was observed in case of 1:9 concentration and a sharp endothermic peak was observed in case of 1:5 concentration. DSC studies of the sample confirm the interactions between the OND and Mannitol.

4 Conclusion

From the data obtained, it is observed that Mannitol showed the interaction with OND. Mannitol cause significant reduction in dissolution of OND. The interaction was more at accelerated condition as compare to room temperature.

Table 3 Percent drug dissolved from OND and Mannitol mixture (1:5)

Time (min)	% Drug dissolved (weeks) (Avg \pm Std. deviation) (N = 3)											
	1:5 Room temp.						1:5 Accelerated temp.					
	0	3	6	9	12	0	3	6	9	12		
5	67.59 \pm 0.66	70.90 \pm 0.05	67.77 \pm 0.41	63.86 \pm 0.82	59.23 \pm 0.91	67.59 \pm 0.66	72.90 \pm 0.65	68.86 \pm 0.05	63.68 \pm 0.45	58.23 \pm 0.01		
10	79.27 \pm 0.14	74.51 \pm 0.26	70.56 \pm 0.05	68.35 \pm 0.10	63.94 \pm 0.06	79.27 \pm 0.14	74.51 \pm 0.02	70.45 \pm 0.03	65.46 \pm 0.14	60.42 \pm 0.06		
15	80.44 \pm 0.23	80.13 \pm 0.35	74.85 \pm 0.01	70.23 \pm 0.03	68.42 \pm 0.03	80.44 \pm 0.23	76.13 \pm 0.09	73.63 \pm 0.02	68.35 \pm 0.05	63.91 \pm 0.03		
30	83.87 \pm 0.59	85.31 \pm 0.13	81.93 \pm 0.02	76.42. \pm 0.33	70.34 \pm 0.06	83.87 \pm 0.59	79.63 \pm 0.04	75.36 \pm 0.03	70.24. \pm 0.34	67.92 \pm 0.06		
45	87.74 \pm 0.63	88.05 \pm 0.12	83.68 \pm 0.06	79.51 \pm 0.12	71.12 \pm 0.51	87.74 \pm 0.63	83.56 \pm 0.02	79.03 \pm 0.03	74.02 \pm 0.01	70.66 \pm 0.51		
60	90.33 \pm 0.10	70.90 \pm 0.05	67.77 \pm 0.41	63.86 \pm 0.82	59.23 \pm 0.91	90.33 \pm 0.10	89.34 \pm 0.12	86.42 \pm 0.22	76.24 \pm 0.51	73.02 \pm 0.23		

Table 4 Percent drug dissolved from OND and Mannitol mixture (1:9)

Time (min)	% Drug dissolved (weeks) (Avg ± Std. deviation) (N = 3)											
	1:9 Room temp.						1:9 Accelerated temp.					
	0	3	6	9	12		0	3	6	9	12	
5	66.49 ± 0.82	71.90 ± 0.55	65.86.81 ± 0.07	61.98 ± 0.45	56.13 ± 0.02		66.49 ± 0.82	69.230.63	66.86. ± 0.27	63.52 ± 0.05	48.32 ± 0.52	
10	77.1260.04	74.50 ± 0.52	67.02 ± 0.85	65.33 ± 0.14	60.24 ± 0.04		77.1260.04	70.12 ± 0.02	67.02 ± 0.08	64.91 ± 0.04	50.12 ± 0.94	
15	79.44 ± 0.24	78.10 ± 0.19	70.12 ± 0.18	69.12 ± 0.05	65.03 ± 0.02		79.44 ± 0.24	73.51 ± 0.09	69.72. ± 0.13	66.12 ± 0.45	55.42 ± 0.12	
30	82.30 ± 0.57	80.65 ± 0.84	75.24 ± 0.10	71.23 ± 0.64	68.37 ± 0.05		82.30 ± 0.57	76.93 ± 0.14	74.24 ± 0.61	73.12 ± 0.04	59.27 ± 0.05	
45	88.12 ± 0.05	83.0.23 ± 0.12	78.23 ± 0.03	75.93 ± 0.81	70.61 ± 0.67		88.12 ± 0.05	80.34 ± 0.02	78.36 ± 0.07	75.34 ± 0.01	61.03 ± 0.07	
60	92.89 ± 0.15	89.88 ± 0.32	80.34 ± 0.22	78.21 ± 0.51	76.02 ± 0.81		92.89 ± 0.15	91.03 ± 0.42	79.02 ± 0.21	76.12 ± 0.01	70.25 ± 0.51	

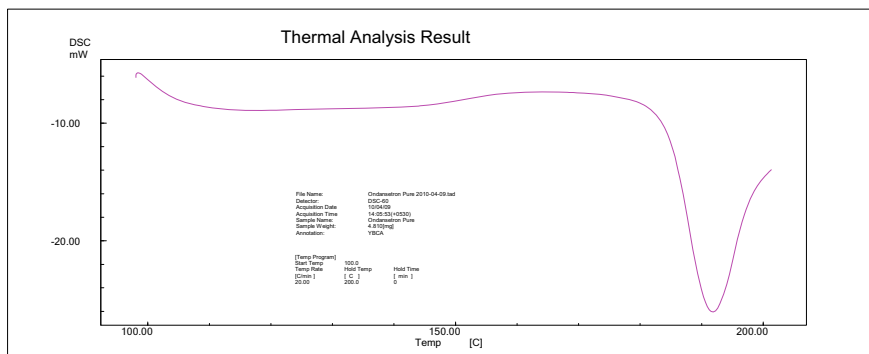


Fig. 5 DSC thermogram of OND pure

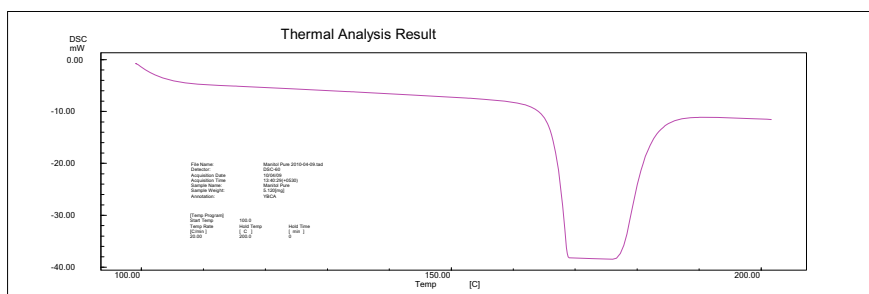


Fig. 6 DSC thermogram of Mannitol pure

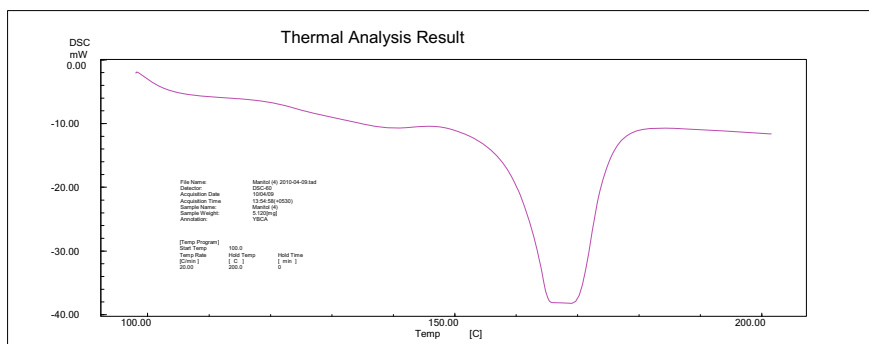


Fig. 7 DSC thermogram of OND and Mannitol 1:5

References

1. Bardin, C., Astier, A., Vulto, A., Sewell, G., Vigneron, J., Trittler, R., Paul, M., Tronjniak, M., & Pinguet, F. (2011). Guidline for the practical stability studies of anticancer drugs. In *A European Consensus Conference* (Vol. 69, pp. 221–231)
2. Singh, S. (2000). Stability testing during product development in Jain NK Pharmaceutical product development (pp. 272–293). CBS Publisher and Distributors, India.
3. Pranshu, T., & Bisht, B. B. (2012). Who role and guidelines in stability study of pharmaceuticals: A regulatory perspective. *International Journal of Research in Pharmaceutical and Biomedical Science*, 3(3).
4. Kaur, M., Kaur, G., Kaur, H., & Sharma, S. (2013). Overview on stability studies. *International Journal of Pharmaceutical, Chemical and Biological Sciences (IJPCBS)*, 3(4), 1231–1241.
5. Kulkarni, M. S., & Kandive, S. (2005). Stability of solid dosage form a global prospective. *Pharma Times*, 37(5).
6. ICH Q1C Stability Testing for New Dosage Forms (1996).
7. Misra, M., Misra, A. K., & Panpalia, G. M. (2007). Interaction study between Pefloxacin mesilate and some diluents using DSC supported with isothermal method. *Journal of Thermal Analysis and Calorimetry*, 89, 803–808.
8. Indian Pharmacopoeia, Govt. of India, Ministry of health and family welfare. Published by controller of publication Delhi (Vol. 1, p. 13) (1985).
9. U S P-30, NF-25. (2007). The official compendia of standards (p. 2800).
10. Kulkarni, S., Kale, S., Tambe, S., & Chhajed, S. (2004). HPTLC analysis of ondansetron in oral solid dosage forms. Abstract No. GP-15, IPC 56th.
11. <http://en.wikipedia.org/wiki/Ondansetron> (surf on date 08/05/09).

Phytochemical Screening, Isolation, Characterizations of Stem Extract of *Parkinsonia Aculeate* Linn



Snehal Patil, Sunil More, Sneha Ghule, and Shweta Bahire

Abstract Stem of *Parkinsonia aculeate* was extracted with ethyl acetate. The extracts were screened for the active components present. The ethyl acetate extract showed the presence of Flavonoids, Saponin, Tannin, and Carbohydrate. Ethyl acetate was chromatographed. The flavonoid fraction was isolated using Column Chromatography over Silica gel Column (230–400 mesh) and eluted with the solvent mixture of CH₃Cl:CH₃OH in the ratio (9:1 V/V). The Flavonoid fraction collected was purified using re-crystallization method and a small amount of yield was obtained.

Keywords Isolation · Flavonoids · *Parkinsonia aculeata*

1 Introduction

Parkinsonia aculeate Linn may be a spiny shrub or a small tree. Synonym of *Parkinsonia aculeate* Linn is vedi bhamat (Marathi), Mexican Palo verde (English). Family-Fabaceae [1]. It grows 2–8 m (6.6–26.2 ft) high, with a maximum height of 10 m (33 ft). Palo verde may have single or multiple stems and many branches with pendulous leaves. The leaves and stems are hairless. The leaves are alternate and pennate (15–20 cm long). The flattened petiole is edged by two rows of 25–30 tiny oval leaflets; the leaflets are soon deciduous in dry weather (and during the winter in some areas) leaving the green petioles and branches to photosynthesize. The branches grow double or triple sharp spines 7–12 mm (0.28–0.47 in) long at the axils of the leaves [2]. The flowers are yellow–orange and fragrant, 20 mm (0.79 in) in diameter, growing from a long slender stalk in groups of eight to ten. They have five sepals

S. Patil (✉) · S. More · S. Ghule · S. Bahire
Department of Pharmaceutical Chemistry, SVERI College of Pharmacy, Pandharpur, Solapur,
Maharashtra, India
e-mail: sp.snehalpatil97@gmail.com

S. More
Emcure Pharmaceuticals Ltd. Research and Development, Hinjewadi, Pune, Maharashtra 411057,
India

and five petals, four of them clearer and rhomboid ovate, the fifth elongated, with a warmer yellow and purple spot at the base. The flowering period is in the middle months of spring (March–April or September–October). The flowers are pollinated by bees. The fruit is a seedpod, leathery in appearance, light brown when mature [3, 4].

2 Materials and Methods

The Stems of *Parkinsonia aculeate* Linn was collected from Sangola Village in Solapur, Maharashtra, India. The Stems were dried under shade for 15 days, grounded into fine powder and sieved using a laboratory test sieve of 212 mm aperture.

2.1 Extraction

The fine powder of *Parkinsonia aculeate* Linn was defatted with ethyl acetate as solvent using Soxhlet extraction. The extraction was carried out for about 4 days at a temperature between 65 and 70 °C Pre-Phytochemical screening:

Phytochemical examinations were carried out for above extract as per the standard methods.

2.2 Detection of Alkaloids

Extracts were dissolved individually in dilute Hydrochloric acid and filtered.

- a. **Mayer's Test:** Filtrates were treated with Mayer's reagent (Potassium Mercuric Iodide). Formation of a yellow coloured precipitate indicates the presence of alkaloids.
- b. **Wagner's Test:** Filtrates were treated with Wagner's reagent (Iodine in Potassium Iodide). Formation of brown/reddish precipitate indicates the presence of alkaloids.
- c. **Dragendroff's Test:** Filtrates were treated with Dragendroff's reagent (solution of Potassium Bismuth Iodide). Formation of red precipitate indicates the presence of alkaloids.
- d. **Hager's Test:** Filtrates were treated with Hager's reagent (saturated picric acid solution). Presence of alkaloids confirmed by the formation of yellow coloured precipitate.

2.3 Detection of Carbohydrates

Extracts were dissolved individually in 5 ml distilled water and filtered. The filtrates were used to test for the presence of carbohydrates.

2.3.1 Molisch's Test

Filtrates were treated with 2 drops of alcoholic α -naphthol solution in a test tube. Formation of the violet ring at the junction indicates the presence of Carbohydrates.

2.3.2 Benedict's Test

Filtrates were treated with Benedict's reagent and heated gently. Orange red precipitate indicates the presence of reducing sugars.

2.3.3 Fehling's Test

Filtrates were hydrolysed with dil. HCl, neutralized with alkali and heated with Fehling's A and B solutions. Formation of red precipitate indicates the presence of reducing sugars.

2.3.4 Detection of Glycosides

Extracts were hydrolysed with dil. HCl, and then subjected to test for glycosides.

2.3.5 Modified Borntrager's Test

Extracts were treated with Ferric Chloride solution and immersed in boiling water for about 5 min. The mixture was cooled and extracted with equal volumes of benzene. The benzene layer was separated and treated with ammonia solution. Formation of rose pink colour in the ammoniacal layer indicates the presence of anthranol glycosides.

2.4 Detection of Saponins

2.4.1 Froth Test

Extracts were diluted with distilled water to 20 ml and this was shaken in a graduated cylinder for 15 min. Formation of 1 cm layer of foam indicates the presence of saponins.

2.4.2 Foam Test

0.5 gm of extract was shaken with 2 ml of water. If foam produced persists for ten minutes, it indicates the presence of saponins.

2.5 Detection of Phytosterols

2.5.1 Salkowski's Test

Extracts were treated with chloroform and filtered. The filtrates were treated with few drops of Conc. Sulphuric acid, shaken and allowed to stand. Appearance of golden yellow colour indicates the presence of triterpenes.

2.5.2 Liebermann Burchard Test

Extracts were treated with chloroform and filtered. The filtrates were treated with few drops of acetic anhydride, boiled and cooled. Conc. Sulphuric acid was added. Formation of brown ring at the junction indicates the presence of phytosterols.

2.6 Detection of Phenols

2.6.1 Ferric Chloride Test

Extracts were treated with 3–4 drops of ferric chloride solution. Formation of bluish black colour indicates the presence of phenols.

2.7 Detection of Tannins

2.7.1 Gelatin Test

To the extract, 1% gelatin solution containing sodium chloride was added. Formation of white precipitate indicates the presence of tannins.

2.8 Detection of Flavonoids

2.8.1 Alkaline Reagent Test

Extracts were treated with few drops of sodium hydroxide solution. Formation of intense yellow colour, which becomes colourless on addition of dilute acid, indicates the presence of flavonoids.

2.8.2 Lead Acetate Test

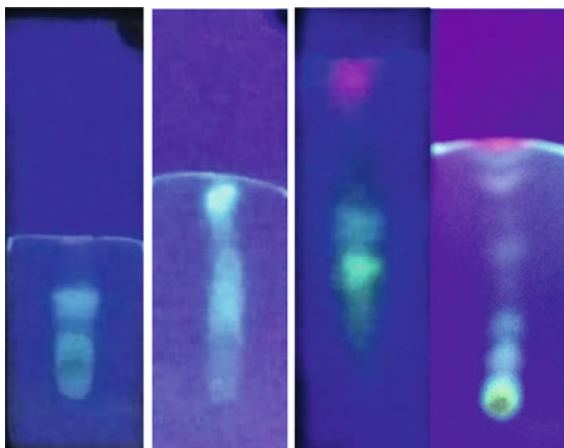
Extracts were treated with few drops of lead acetate solution. Formation of yellow colour precipitate indicates the presence of Flavonoids [5–7].

2.9 Thin Layer Chromatography Study of Ethyl Acetate Extract of *Parkinsonia aculeate* Linn Sample Preparation

Thin layer chromatography (TLC) is increasingly used in the fields of chemistry, biochemistry, and molecular biology. Advantages such as speed, versatility, and low cost make it one of the leading techniques used for locating and analyzing bioactive components in plants. Thin layer chromatography in Phytochemistry is the first source devoted to supplying state-of-the art information on TLC as it applies to the separation, identification, quantification, and isolation of medicinal plant components. Renowned scientists working with laboratories around the world demonstrate the applicability of TLC to a remarkable diversity of fields including plant genetics, drug discovery, nutraceuticals, and toxicology. For TLC study Ethyl acetate extract of *Parkinsonia aculeate* was dissolved in ethyl acetate. This solution was applied as spot with capillary on TLC plate.

Various solvents and mixture of solvents were tried to optimize mobile phase to use an optimized mobile phase in column chromatography. Following are the mobile phases that were tried (Fig. 1).

Fig. 1 Thin layer chromatography of sample



1. Chloroform: ethyl acetate (7:3)
2. Toluene: ethyl acetate (9:1)
3. Methanol: Chloroform (7:3)
4. Methanol: Chloroform (7:3)
5. Chloroform: Methanol (9:1)
6. Stationary phase: Normal TLC plate with silica gel (for TLC)
7. Detection: UV chamber at 253 nm.

After TLC it was concluded that Chloroform:Methanol (9:1) showed best separation proportion of which can be increased gradually.

3 Results and Discussions

Ethyl acetate extracts showed the presence of the following active ingredients: Flavonoids, Tannin, Saponins and Carbohydrate are shown in Table 1. The results for phytochemical screening of the extracts isolated from the Column Chromatography are shown in Table 1. The seven different components were isolated through the column chromatography where one of the components gave the Flavonoid and after recrystallization a small amount of yield was obtained.

Table 1 Results for the phytochemical screening

S. No	Components	Ethyl acetate extract
1	Alkaloids	–
2	Carbohydrates	+
3	Glycosides	–
4	Legal's test	–
5	Saponins	+
6	Phytosterols	–
7	Phenols	–
8	Tannins	+
9	Flavonoids	+

Hints: “+” indicates presence, “–” indicates absence

4 Conclusion

The *Parkinsonia aculeata* is a good source of Flavonoids which has an important antioxidant Property.

References

1. Mohammed, S. Y., Suleiman, H., Abubakar, M., et al. (2017). Preliminary phytochemical screening of *Parkinsonia aculeata* leaf extracts. *International Journal of Chemical Studies*, 5(2), 86–88.
2. Singh, P., Shrivastava, R., Saxena, R. C., et al. (2011). Phytochemical screening and evaluation of antioxidant activity of *Parkinsonia aculeata* L. leaves extract. *International Journal of PharmTech Research*, 3(4), 1952–1957.
3. Kamba, A. S., & Hassan, L. G. (2010). Phytochemical and microbial screening of *Parkinsonia aculeata* L. leaves. *International Journal of Drug Development and Research*, 2(1), 1–7.
4. Sharma, S., & Vig, A. P. (2014). Preliminary phytochemical screening and in vitro antioxidant activities of *Parkinsonia aculeata* Linn. *BioMed Research International*, 2014, 1–8. Article ID 756184
5. Cushine, T. P., & Lamb, A. J. (2011). Recent advances in understanding the antibacterial properties of flavonoids. *International Journal of Anti-microbial Agents*, 38(2), 99–103.
6. Edeoga, H. O., Okwu, D. E., & Mbaebie, B. O. (2005). Phytochemical constituents of some Nigerian medicinal plants. *African Journal of Biotechnology*, 4(7), 685–688.
7. Kamal, R., & Mathur, N. (2007). Rotenoids from *Parkinsonia aculeata* L and their in vitro amoebicidal activity. *Asian Journal of Experimental Sciences*, 21(1), 122–128.
8. Devika, R., & Koilpillai, J. (2015). Column chromatographic separation of bioactive compounds from *Tagetes erecta* Linn. *International Journal of Pharmaceutical Sciences and Research*, 6(2), 762–766.

Chemical and Physical Processes

Tailored Synthesis of CuO/2D-BiVO₄ for Enhanced CO₂ Photoreduction to Methanol



Prasad Kulkarni, Aniruddha Chatterjee, Ganesh Kotiye, and Shravanti Joshi

Abstract Herein, we report on the one-pot synthesis of CuO/2D-BiVO₄ nanostructures for natural sunlight induced CO₂ reduction to CH₃OH. The crystal structures, morphological features, and band gap values were carefully examined using XRD, FESEM, and UV-DRS techniques. The heterogeneous catalysis experimentation revealed that CuO/2D-BiVO₄ nanostructures with an optimum concentration of 10 mol% CuO decoration showcased excellent catalytic conversion of CO₂ gas to CH₃OH throughout 8 h. A comparison of various light sources such as ultraviolet, visible, white light, and natural sunlight is presented. Among the various light sources employed for photocatalytic activity, the maximum CH₃OH production yield of 27.435 μmolg⁻¹ h⁻¹ was observed in the presence of natural sunlight. Tailored CuO/2D-BiVO₄ nanostructures with conveniently formed heterojunctions depicted enhanced activity when compared to pristine BiVO₄ nanosheets. It is anticipated that the work presented here will provide deeper insights into the ever-growing field of renewable energy generation and carbon neutral technology.

Keywords Photoreduction · Hydrothermal · Catalysis · Nanosheets · Methanol

1 Introduction

The last few decades have witnessed unmonitored fossil fuels usage leading to increased levels of CO₂ emissions thus triggering extreme climate variations [1]. Photosynthesis and deep ground mineralization effected naturally are excellent options for reducing harmful CO₂ emanations. But these endeavors by nature go in vain as the man-made emissions are greater and hence more rigorous methods

P. Kulkarni (✉) · G. Kotiye · S. Joshi
Functional Materials Laboratory, G. S. Mandal's Marathwada Institute of Technology,
Aurangabad, Maharashtra 431010, India
e-mail: prasad.kulkarni.pgk@gmail.com

A. Chatterjee
Centre for Advanced Materials Research and Technology, Maharashtra Institute of Technology,
Aurangabad, Maharashtra 431010, India

based on principles of sustainable technology need to be developed [2]. A convenient route is to harvest natural sunlight for artificial photosynthesis-mediated CO₂ conversion to value-added fuels like CH₃OH, CH₄, and so on. The technology has the full potential to solve environmental and energy concerns. However, the catalytic CO₂ conversion requires high bond dissociation energy to necessitate the chemistries involving C–O, and C–H bonds which is tedious to achieve in traditional set-ups. To resolve the concern, recent studies displayed different synthesis approaches emphasizing the semiconductor-governed CO₂ conversion in overcoming the higher energy potential required for such reactions [3, 4]. In this context, materials such as copper oxide (CuO) and bismuth vanadate (BiVO₄) are currently being touted as potential candidates owing to their lower bandgap in the visible range, ability to form *p-n* heterostructure in type I, chemical elements are widely available, and economic to procure. Recently, Zhu et al. reported on 0.5 wt.% Cu/BiVO₄ photocatalysts effectiveness in converting CO₂ gas to methane (CH₄), carbon monoxide (CO) and methanol (CH₃OH) [5]. Previously, Chen et al. documented BiVO₄ quantum dots capability to photoreduce CO₂ to CH₄ and CO [6]. Albeit several such novel reports, there still lay ample opportunities for materials development from viewpoints of energy and environmental applications.

The major novelty of the current work lies in the type I fabrication of *p-n* heterostructure wherein, the 3D CuO nanoparticles are decorated over 2D BiVO₄ nanosheets. The heterostructured 3D CuO/2D-BiVO₄ nanomaterial in a 1:10 mol ratio was prepared using a facile route involving molten mixed salts in specific ratio (NaOH and KOH) as a reaction medium in a high pressure hydrothermal reactor at 200 °C meant for 24 h. The as-synthesized material was compared with pure BiVO₄ and CuO for CO₂ photoreduction capabilities to value-added products in the presence of four different lamp sources, such as, ultra-violet, simulated solar, light emitting diode in white light, and direct sunlight.

2 Experimental Section

2.1 Chemicals

Copper(II) nitrate trihydrate (Cu(NO₃)₂·3H₂O) and bismuth (III) nitrate pentahydrate (Bi(NO₃)₃·5H₂O) were procured from Sigma-Aldrich. Sodium hydroxide (NaOH) and potassium hydroxide (KOH) were procured from Finar Chemicals. The chemicals were used as received. Water distilled twice with its temperature at 32 °C was employed for experiments purpose.

2.2 Preparation of Heterostructured CuO/BiVO₄ Nanomaterial

The standard route that was followed for the current work, *ca.* 5 g of each sodium hydroxide and potassium hydroxide were mixed in a dry state and transferred to a Teflon container with an overall capacity of 150 mL. Further, 4.832 mg (0.5 mmol) of copper(II) nitrate trihydrate and 97.014 mg (5 mmol) of bismuth (III) nitrate pentahydrate were added to the container and mixed vigorously with a glass rod for 15 min to achieve uniformity. Thereafter, the Teflon container was placed inside the high pressure hydrothermal reactor and kept in oven at 200 °C. The reaction was continued for 24 h. Then the residue was suspended in double distilled water and sonicated for 30 min followed by centrifugation. The final product that is, heterostructured CuO/2D-BiVO₄ nanomaterial in a 1:10 ratio was achieved by oven aeration at 80 °C for 12 h. Similarly, pure BiVO₄ and pure CuO nanomaterials were synthesized and tested for CO₂ photoreduction application.

2.3 Materials Characterization

X-ray diffractograms were recorded on Bruker AXS diffractometer (D8 ADVANCE). Electron micrographs were imaged using JEOL JSM-7610F (JEOL Inc. Japan) in a scanning mode. Ultraviolet diffuse reflectance spectra were recorded using a AvaSpec-ULS2048 Starline fiber optics spectrophotometer. The CO₂ conversion experiments were executed from 25th January to 10th February 2022 with coordinates of the place as 19.8762° N, 75.3433° E.

2.4 Catalytic CO₂ Conversion to Methanol

The catalytic CO₂ reduction to methanol (CH₃OH) was executed in an indigenously designed quartz apparatus with a total volume of 125 mL. Before each cycle, nanopowder (that is, independently pure BiVO₄, pure CuO, and heterostructured CuO/2D-BiVO₄ in 1:10 mol ratio) in a known amount of 50 mg was distributed in 100 mL water used as reaction medium. The quartz apparatus was unceasingly cleansed with N₂ for 45 min at 200 sccm to make sure undesired moieties were eradicated. The homogeneously dispersed mixture was then cleansed with CO₂ for 45 min to fill the container. Subsequently, the rate of flow was reduced to 25 sccm and continuously monitored by an MFC. Thereafter, the apparatus was fully wrapped with a septum to prevent seepage of CO₂ gas or hydrocarbon fuels. The light source was switched ON upon stabilization of the flow rate followed by monitoring the composition of products produced as a function of irradiation time. Four irradiation mediums, such as ultra-violet, white light emitting diode, simulated and natural

solar were employed. The apparatus was outfitted with an assembly for cool reaction medium distribution to preserve lower temperatures near the light medium in addition to increasing the solubility of CO_2 in the reaction medium during the experiments. Under similar circumstances, the blank reactions without CO_2 gas, catalyst, or lamps were executed to corroborate that the product produced owing to the CO_2 conversion in the existence of a nanocatalyst. The experiment was systematically examined by extracting the calculated amount of supernatant every single 1 h through the plunger. The composition of the end products generated from the apparatus was estimated utilizing a Shimadzu GC-MS analyzer.

3 Results and Discussion

Figure 1a illustrates X-ray diffractograms for as-synthesized BiVO_4 , CuO , and $\text{CuO}/2\text{D-BiVO}_4$ heterostructured samples. X-ray diffraction (XRD) peaks of pure BiVO_4 pattern matches monoclinic scheelite structure (JCPDS card no.: 14-0688) with the absence of impurities arising due to the formation of intermediate compounds further suggesting high phase purity of the prepared sample. Pure CuO pattern revealed highly crystalline peaks matching monoclinic tenorite structure (JCPDS card no.: 74-1021). The heterostructured CuO/BiVO_4 nanomaterial in a 1:10 mol ratio showed peaks belonging to both BiVO_4 and CuO , thus confirming *p-n* nanointerfaces presence in heterostructured $\text{CuO}/2\text{D-BiVO}_4$ sample. Figure 1b shows the UV-DRS data of the nanostructured samples. Here, the bandgaps were found to be 2.46, 1.70, and 2.15 eV for pure BiVO_4 , CuO , and $\text{CuO}/2\text{D-BiVO}_4$, respectively. The electron micrographs in scanning mode for pure BiVO_4 sample depicted the formation of randomly oriented thin sheets with thickness ~ 15 nm (Fig. 2a).

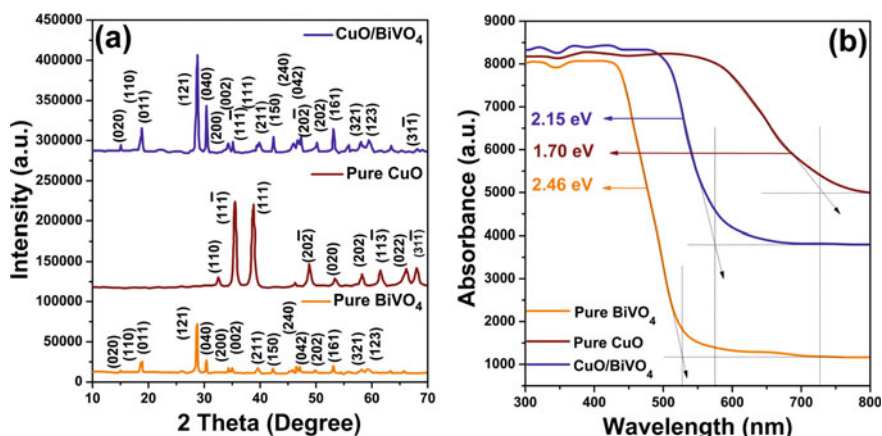


Fig. 1 a XRD patterns and b UV-DRS data for as-synthesized nanomaterials. Here, the heterostructured $\text{CuO}/2\text{D-BiVO}_4$ nanomaterial is in a 1:10 mol ratio

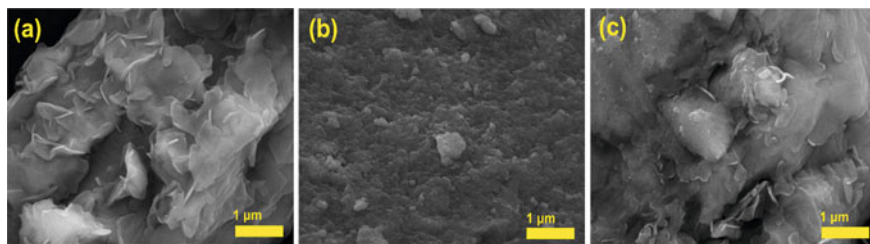


Fig. 2 Electron micrographs in scanning mode for **a** pure BiVO₄, **b** pure CuO, and **c** CuO/2D-BiVO₄ in a 1:10 mol ratio

Interestingly, pure CuO displayed the formation of nanoparticles ranging from 20 to 50 nm (Fig. 2b). However, the heterostructured sample showed CuO particles decorated over BiVO₄ thin sheets forming discreet *p-n* nanointerfaces (Fig. 2c). The presence of such morphological features is indeed lucrative since they enhance the active sites to carry out rapid catalytic reactions in presence of appropriate nanocatalysts and light source over a longer period with a reduced $e^- - h^+$ recombination rate. Thus, it is anticipated that CuO/2D-BiVO₄ in 1:10 mol ratio sample will show excellent CO₂ photoreduction outcomes in comparison to pristine BiVO₄ and CuO nanomaterial.

Initially, 3 reference experiments were carried out using water as a standard medium at ambient conditions. At the end of the experiments, the evolution of valuable products in the form of hydrocarbons was not observed, thus hinting that CO₂ gas, photocatalysts, and light sources are imperative for photoreduction studies (Fig. 3a). In this study, methanol (CH₃OH) generation is based on the specific ambient conditions, materials and methods detailed in Sect. 2. Natural sunlight-mediated CO₂ reduction experiments supervised at each hour for 8 h relating to methanol evolution validated the superior catalytic capacities of the heterostructured nanomaterial in comparison to the pure BiVO₄ and CuO (Fig. 3b). Additionally, the product quantity went up with an increased exposure to direct sunlight till 8 h, further than the value, a saturation was noted. Due to this, the experimentation proved that the optimal light exposure should be for 8 h. It is widely understood the fact that the light source is imperative from heterogeneous catalysis point of view and to corroborate it, herein we used 4 diverse light sources, namely ultra-violet, white light emitting diodes, simulated solar and direct sunlight in natural form (Fig. 3c). The maximum evolution of products was noticed in the existence of natural sunlight then simulated solar source, and in each case, the CuO/2D-BiVO₄ in 1:10 mol ratio depicted highest photoconversion efficiency, when compared to pure BiVO₄ and CuO. The CH₃OH evolution in existence of natural sunlight as displayed by pure BiVO₄, pure CuO, and CuO/2D-BiVO₄ in 1:10 mol ratio was calculated to be 9.179, 17.246, and 27.435 $\mu\text{mol g}^{-1} \text{h}^{-1}$, respectively. Poor response was noticed upon exposure to UV and white cold floodlight (Fig. 3c). The repeatability was verified by performing three successive runs of CO₂ photoconversion to CH₃OH in existence of natural sunlight (Fig. 3d). Post 3 cycles, a minimal degradation of 0.36, 0.28, and 0.06% during the

photoconversion was shown by pure BiVO_4 , pure CuO , and $\text{CuO}/2\text{D-BiVO}_4$ in 1:10 mol ratio, respectively. The aforementioned data is motivating from commercialization point of view results as a direct conversion to hydrocarbons is effectuated. Furthermore, absence of other organic species can be attributed to inconsequential intake of H^+ and e^- throughout the photo conversion experiments.

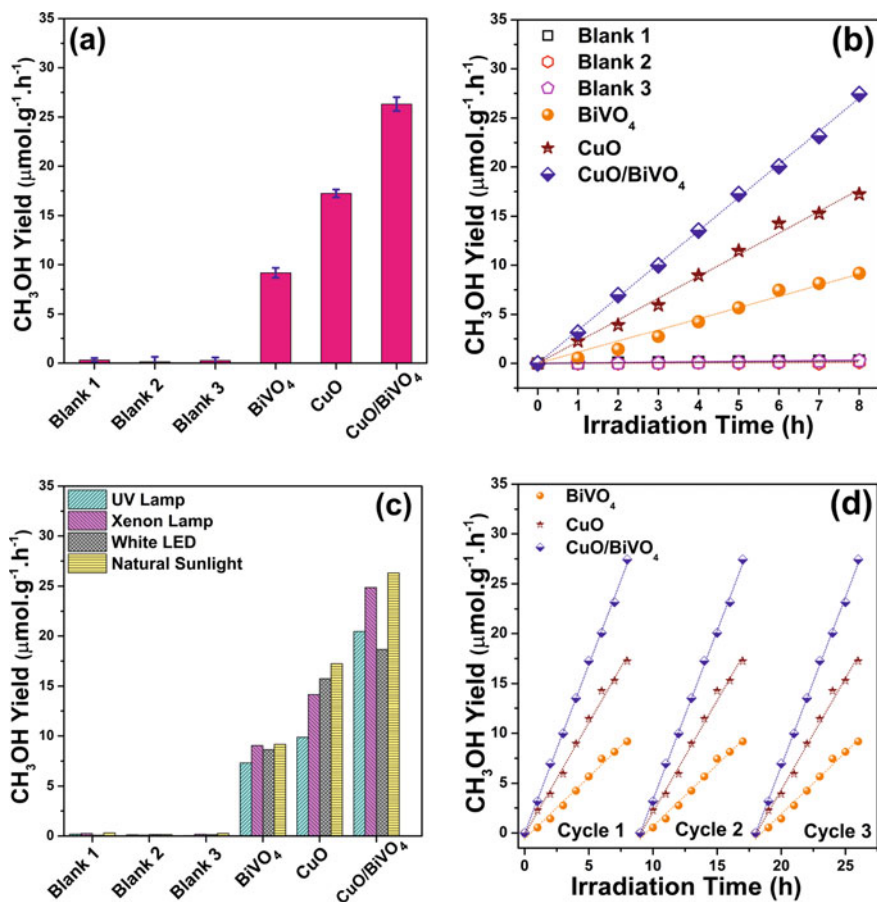


Fig. 3 a Photocatalytic conversion from CO_2 to CH_3OH under different conditions and nanocatalysts for 8 h. b Photoreduction studies conducted in existence of direct sunlight. c Photoreduction data versus various lamp mediums used over nanocatalysts at ambient conditions. d Repeatability data depicting the use of various as-synthesized nanocatalysts for CO_2 photoreduction to CH_3OH . Here, the heterostructured $\text{CuO}/2\text{D-BiVO}_4$ nanomaterial is in a 1:10 mol ratio

4 Conclusion

In summary, a convenient one-pot hydrothermal methodology was developed for the synthesis of *p-n* heterostructured CuO/2D-BiVO₄ nanomaterial in a 1:10 mol ratio. The as-synthesized nanomaterial depicted high crystallinity, tailored morphological features, and bandgap in the visible range. The photocatalysts prepared were experimented for CO₂ photoreduction in existence of different lamp mediums. The heterostructured CuO/2D-BiVO₄ nanomaterial displayed CH₃OH evolution of 27.435 and 24.86 $\mu\text{mol g}^{-1} \text{h}^{-1}$ in direct sunlight and simulated artificial irradiation, respectively. A reasonably stable and high yield of CH₃OH was observed in presence of natural sunlight when compared to artificial solar and ultra-violet illumination. Lastly, heterostructured samples performed better compared to pristine nanomaterials and this could be attributed to well-structured morphology in the form of CuO nanoparticles decorated over BiVO₄ nanosheets, giving access to numerous *p-n* junctions at discrete levels enhancing the photoconversion efficiency.

Acknowledgements Shravanti Joshi acknowledges the Department of Science and Technology, Ministry of Science and Technology, Government of India for the funds sanctioned.

References

1. Xu, Y. F., Yang, M. Z., Chen, B. X., Wang, X. D., Chen, H. Y., Kuang, D. B., & Su, C. Y. (2017). A CsPbBr₃ perovskite quantum dot/graphene oxide composite for photocatalytic CO₂ reduction. *Journal of the American Chemical Society*, *139*, 5660–5663.
2. Kulkarni, A., Satbhai, M., Li, W., Bornare, D. T., Syed, K., & Joshi, S. (2022). Oleic acid induced tailored morphological features and structural defects in CuO for multifunctional applications. *Materials Advances*, *3*, 418–436.
3. Joshi, S. (2021). Solar induced CO₂ reduction achieved by halide tuning in cesium titanium (IV) mixed perovskite. In *21st IEEE International Conference on Nanotechnology (NANO)* (pp. 299–302). IEEE Xplore.
4. Joshi, S. (2021). Hierarchical faceted cesium tin iodide superparticles for solar based CO₂ reduction. In *21st IEEE International Conference on Nanotechnology (NANO)* (pp. 100–103). IEEE Xplore.
5. Zhu, Z., Yang, C. H., Hwang, Y. T., Lin, Y. C., & Wu, R. J. (2020). Fuel generation through photoreduction of CO₂ on novel Cu/BiVO₄. *Materials Research Bulletin*, *130*, 110955.
6. Chen, L., Zhang, M., Yang, J., Li, Y., Sivalingam, Y., Shi, Q., Xie, M., & Han, W. (2019). Synthesis of BiVO₄ quantum dots/reduced graphene oxide composites for CO₂ reduction. *Materials Science in Semiconductor Processing*, *102*, 104578.

Synthesis and Evaluation of Some Fused Ring System of Thiazole for Their Antimicrobial Activity



Ramdas Naiknaware, Ravi Ajudia, Hemant Bansode, and Sweta Bahire

Abstract A series of novel N-2 [2-chloro-4(3,4,5-trimethoxy phenyl azetidine-1-yl)-N4(substituted aryl)-1,3-thiazole-2,4-diamine(4a-j)] were synthesized starting from 3,4,5-trimethoxy benzaldehyde thiosemicarbazone(1). The compound (1) was obtained by condensing 3,4,5-trimethoxy benzaldehyde with thiosemicarbazide in methanol. 3,4,5-trimethoxy benzaldehyde thiosemicarbazone(1) on treatment with chloroacetyl chloride afforded 4-chloro [2-(3,4,5-trimethoxy benzylidene)hydrazinyl]-1,3-thiazole(2). Compound 2 was reacted with chloroacetyl chloride and triethylamine to obtain the corresponding 4-chloro-N[2-chloro-4(3,4,5-trimethoxy phenyl)azetidine-1-yl]-1,3-thiazole-2-amine(3). Various substitution on compound(3) with secondary amines yielded series of compounds (4a-j). The newly synthesized compounds were characterized by IR, ¹H NMR, Elemental analysis and Mass spectral studies. All the compounds were screened for their antimicrobial properties. Disc diffusion values of compound 3 and 4(a-j) revealed that some of the synthesized compounds were showing potent antibacterial activity.

Keywords Thiazoles · Antimicrobial activity · Disc diffusion

R. Naiknaware (✉) · S. Bahire
Department of Pharmaceutical Chemistry, SVERI'S College of Pharmacy, Pandharpur,
Maharashtra, India
e-mail: ram777pharma@gmail.com

R. Ajudia
School of Pharmacy, RK University, Rajkot, Gujarat, India

H. Bansode
Department of Pharmaceutics, SVERIS College of Pharmacy, Pandharpur, Maharashtra, India

1 Introduction

Heterocyclic compounds containing five membered rings recently occupied the vast area. One nitrogen and one sulphur atom in a molecule represent a very important group of organic compound may exhibit significant biological activity, including anti-microbial and pharmacological effects. Among these five membered heterocyclic compounds, thiazole is a very important ring system. In this situation there is a need for rapid and effective target validation and for accelerated lead discovery procedures. Organic chemists are increasingly directing their attention towards synthetic aspects of biomolecules and biologically active compounds, biosynthesized by plants and animals. They have been proven for their anti-inflammatory, antitubercular and antimicrobial activities [1]. Bleomycin antibiotics which have antitumor [2] properties are complex aminoglycosidic structures containing thiazole units. Nitro-thiazoles have been used in the preparation of antiparasitic agents [3]. Condensation of 6-nitro-2-aminothiazole with ethylisocyanate yields the antiprotozoal agent Nithiazole. Whilst many heterocycles are isolated in trace amounts from crude oil, thiazoles are not within this, they are however found in nature, generally in peptidic compounds [4–7]. There are a number of different types of thiazole natural products, perhaps the most well known are the Epothilones [8–9], originally isolated from soil bacteria *Sorangium cellulosum*, they are microtubule polymerization promoters and have a similar mechanism of action to Taxol [4–7].

Thiazoles are convenient bio-isosteres for carbonyl or aromatic groups in the Pharmaceutical industry [10]. Carbonyl and aromatic groups can be quickly metabolized the body, so replacement offers a better pharmacokinetic profile and increasing the concentration of drug reaching its point of action. As such, thiazole has been incorporated into Ritonavir, an HIV1 protease inhibitor [11]. Dasatinib was developed as an ABL/SCR family tyrosine kinase inhibitor for the treatment of chronic myelogenous leukemia and Philadelphia chromosome-positive acute lymphoblastic leukemia [13].

It is currently being assessed for use in the treatment of metastatic melanoma. Cefotaxime is a third generation cephalosporin antibiotic with broad spectrum activity against both gram positive and gram negative bacteria [15]. Whilst there are a variety of drugs currently on the market with thiazole moieties if they are far outnumbered by agrochemicals, preservatives and flavorings [17]. A number of agrochemicals like thiabendazole, metsulfovax and ethaboxam are fungicides used to treat mould and blight. Clothianidin and Thiamethoxam are neonicotinoid insecticides both are used as seed treatments and to treat juvenile and mature crops [17]. The use of thiazoles in flavorings is widespread. They are used in the food industry to provide meaty and roasted flavors.

From the observation based on above discussion, it is clear that the thiazoles are acquiring greater importance because of their useful biological activities and synthetic utility. This led us to undertake the present study of synthesis and characterizations of some fused ring system of thiazole and various antibacterial and

antioxidant activity. Recently many thiazoles reported to possess antibacterial, anti-cancer, antitubercular, cytotoxic, analgesic and anti-inflammatory activity. In course of investigation on thiazole, Prakash Karegoudar and co-workers developed a convenient single step method for synthesis of thiazole. In view of this we thought of synthesizing corresponding thiazole and further this reacted to formation of fused azetidine ring. In our present thesis work we are synthesizing new compounds i.e. thiazole with fused azetidine ring. The entire newly synthesized compounds in the present investigation were screened for antibacterial activity.

We have chosen 3,4,5-trimethoxy benzaldehyde and condensed with thiosemicarbazide, forming corresponding thiasemicarbazone, this thiasemicarbazone on reaction with chloroacetyl chloride cyclize and gives corresponding thiazole. Then we were reacted thiazole with chloroacetyl chloride and triethyl amine gives corresponding fused azetidine ring with cyclization. We used 3,4,5-trimethoxy benzaldehyde and 3-ethoxy, 4-hydroxy benzaldehyde as starting material. Finally, this synthesized thiazole is connected with azetidine ring by reacting with various secondary amines. The reaction is stepwise observed by thin layer chromatography, with suitable mobile phase and the R_f value is noted the detailed procedure is discussed in experimental section. To give confirmation to the reaction IR spectra of compound followed, we have taken under consideration of following some point of objective in all over the thesis work. To establish the method of synthesis for the proposed thiazole with fused azetidine and carry out the preliminary tests such as physical constant determination, solubility, TLC. Confirmation of the structures of the synthesized compounds by IR, ^1H NMR and mass spectral analysis and evaluate the proposed compounds for their antimicrobial activity.

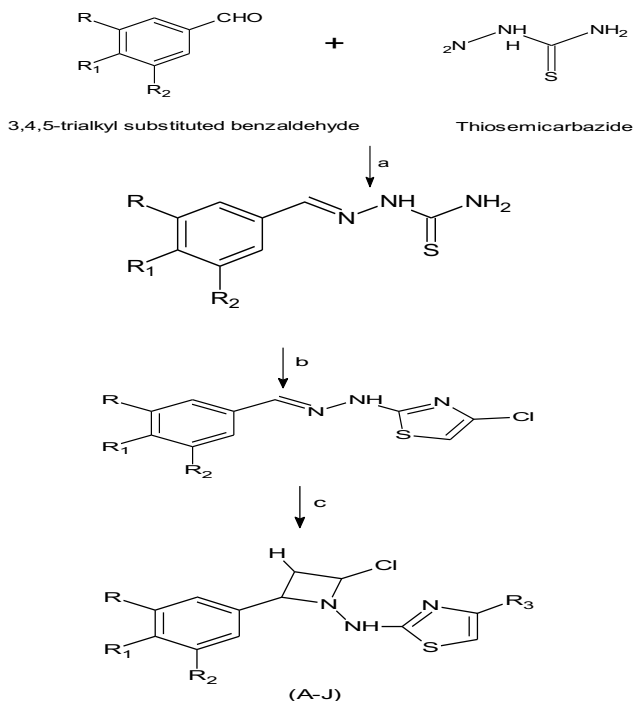
2 Materials and Method

2.1 Physical Method

Melting points of the synthesized compounds were determined using the microcontroller-based melting point apparatus and were found uncorrected.

2.2 Analytical Techniques

Purity of the compounds was checked by thin layer chromatography using silica gel—G as stationary phase and various combinations of Chloroform: methanol as mobile phase. The spots resolved were visualized as brown-coloured spots by using iodine chamber. The IR spectra of the synthesized compounds were recorded using KBr pellets in range of $4000\text{--}400\text{ cm}^{-1}$ on a Fourier transform IR spectrometer (Shimadzu 8700, SAC College of Pharmacy, B.G. Nagara) and the frequencies were



Scheme 1 2-amino-[2-chloro-4(3,4,5-trimethoxy phenyl azetidine), 4-chloro]-1,3-thiazole-2-yl. a—Methanol, b—Chloroacetyl chloride, methanol, c—Triethyl amine, Chloroacetyl chloride, methanol

recorded in wave numbers. ^1H —NMR (400 MHz) spectra were recorded in chloroform-d in Amx-400 liquid state NMR spectrometer (University Science Instrument Center, Dharwad). Chemical shifts (δ) are reported in parts per million downfield from internal reference Tetra methyl Silane (TMS). Mass spectra were recorded on GCMS in dimethyl sulphoxide (University Science Instrument Center, Dharwad) (Scheme 1; Table 1).

2.3 Experimental Procedure

2.3.1 Preparation of 3,4,5-trialkyl substituted benzaldehyde thiosemicarbazone (1)

An equimolar mixture of 3,4,5-trialkyl substituted benzaldehyde (0.143 mol) and thiosemicarbazide (0.164 mol) in methanol (50 ml) and catalytic amount of con. Sulphuric acid was refluxed for 5 h. Then the mixture cooled and solid separated

Table 1 Various substitutions on thiazoles

Code	R	R ₁	R ₂	R ₃
a	-OCH ₃	-OCH ₃	-OCH ₃	-Cl
b	-OCH ₃	-OCH ₃	-OCH ₃	-NHC ₆ H ₅ NO ₂
c	-OCH ₃	-OCH ₃	-OCH ₃	-NHC ₆ H ₅ NO ₂
d	-OCH ₃	-OCH ₃	-OCH ₃	-NHC ₆ H ₅ COOC ₂ H ₅
e	-OCH ₃	-OCH ₃	-OCH ₃	-NHC ₆ H ₅ OH
f	-OCH ₃	-OCH ₃	-OCH ₃	-NHC ₆ H ₅ COOH
g	-OCH ₃	-OCH ₃	-OCH ₃	-NHC ₆ H ₅ C ₂ H ₅
h	-OCH ₃	-OCH ₃	-OCH ₃	-NHC ₆ H ₅
i	-OCH ₃	-OH	-H	-Cl
j	-OCH ₃	-OH	-H	-NHC ₆ H ₅ NO ₂

was filtered, dried and recrystallized using chloroform/methanol mixture. Yield 70%, M.P. 160–163 °C. Completion of reaction is observed by TLC.

2.3.2 Preparation of 4-chloro-2-(3,4,5-trialkylsubstitutedphenyl) thioazoles (2)

An equimolar mixture of 3,4,5-Trialkyl substituted benzaldehyde thiosemicarbazone (0.01 mol) and chloroacetyl chloride (0.01 mol) in methanol is refluxed for 4 h. After completion of reaction, the reaction mixture was allowed to cool. The solid thus separated was collected by filtration and recrystallized with chloroform. Completion of reaction is observed by TLC.

2.3.3 Preparation of 4-chloro-2-(3,4,5-trialkylsubstituted phenyl, azetidene) thioazoles (3)

The equimolar mixture of corresponding 4-chloro-2-(3,4,5-trialkyl substituted phenyl) thioazoles (0.01 mol) and it mixed with mixture of chloroacetyl chloride and triethylamine at 0–5 °C. Mixed well and kept for 3 h at the room temperature. Then the mixture is refluxed for 8 h then the reaction mixture was poured in to ice cold water. The white colored solid is separated which is collected by filtration, dried and recrystallized with methanol.

2.3.4 General Procedure for Synthesis of Various Derivatives of 4-amine substituted-2-(3,4,5-trialkyl substituted phenyl) thiazoles azetidinones

An equimolar mixture of 4-chloro-2-(3,4,5-trialkyl substituted phenyl) thiazoles azetidine (0.01 mol) and corresponding secondary amines (0.01 mol) were refluxed in ethanol for 4–5 h. Then resulting reaction mixture was evaporated and the residue is recrystallized with methanol. Completion of reaction is observed by TLC.

2.3.5 Antimicrobial Activity

After the development of desired new drug molecules, with different structure, an antimicrobial screening programme is necessary to uncover the interesting activity of the compounds. The inhibition of the microbial growth under standard may be utilized for demonstrating the therapeutic efficacy of the synthesized compounds. The following two are the methods available for screening the antimicrobial substances.

- Turbidimetric/photometric/tube dilution method.
- Agar diffusion/cup-plate/cylinder plate method.

2.3.6 Agar Diffusion Method

This method gives the extent of growth of the microorganism, inoculated into a solid nutrient agar bed by the antimicrobial substance. The test substance is kept in a cup made of agar bed, diffuses into it and inhibits the growth of microorganism. The diameter of the zone of inhibition is measured in comparison with suitable drug substance, is considered as potency of that substance. The diameter of zone of inhibition is directly proportional to the concentration of the drug substances added into the cup, thickness of the agar bed, diffusion coefficient of the antimicrobial substance into the agar cup, sensitivity of the microorganism to the test substance and the temperature. The appropriate media is sterilized and cooled to 42 °C, incubated with the test organism, mixed uniformly and poured into petri plates and cooled. Bores are made into it; specified test solution is added and left at room temperature for 30 min. Incubate at 37 °C for 24 h. The zone of inhibition is measured in mm.

Stock solution of the synthesized compounds and standard drug used were prepared in dimethyl sulfoxide taken in the concentration of 100 µg/ml.

Standard cultures of *Bacillus subtilis*, *Staphylococcus aureus*, *Escherichia coli* and *Klebsiella pneumoniae* species were obtained from Adichuncunagiri Institute of Biotechnology and cancer research center B. G. Nagara. Staining technique and biochemical reaction identified the microorganism. The microorganisms, which were maintained by sub culturing, were used at regular intervals in nutrient agar medium.

The Petri plate were washed thoroughly and sterilized in autoclave at 12 °C for one hour. 30 ml of sterile nutrient agar medium was poured into sterile Petri dishes and allow to solidify. The petri plates were incubated at 37 °C for 24 h to check for

sterility. The medium was seeded with the organism by spread plate method using sterile cotton swabs. Sterilized pepper disk was placed on media and compound samples of various concentration were placed on the disk. 0.1 ml of streptomycin at a concentration of 100 ug/ml was taken as standard reference. A control having only DMSO in on the disk was maintained in each plate. The petri plates were kept in refrigerator at 4 °C for 15 min, allowing diffusion to take place. The petri plate was incubated at 37 °C for 24 h and zone of inhibition were observed and measured using a scale. Antibacterial activity of all the compounds was carried out against all four microorganisms. The zone of inhibition is as shown in table the media was used for both sub culturing and also for estimating antibacterial activity.

2.3.7 Antifungal Activity

The antifungal activity of the compounds was carried out against following strains of microorganism *Candida albicans* and *Aspergillus flavus*. Agar diffusion method was used for antifungal activity. Stock solution of the synthesized compounds and standard drug used were prepared in dimethyl sulfoxide taken in the concentration of 100 ug/ml.

Standard cultures of *aspergillus flavones* and *candida albicans* and species were obtained from Adichuncunagiri Institute of Biotechnology and cancer research center B. G. Nagara. Staining technique and bio-chemical reaction identified the fungus, which were maintained by sub culturing, were used at regular intervals in nutrient agar medium.

3 Results and Discussion

3.1 Chemistry

The synthetic route of the compound is outlined in scheme-1,3,4,5-Trimethoxy benzaldehyde was condensed with thiosemicarbazide to obtain corresponding 3,4,5-trimethoxybenzaldehyde thiosemicarbazone (1). Cyclization of (1) with chloroacetyl chloride yielded corresponding thiazolyl hydrazine (2). Compound (2) was cyclized with chloroacetyl chloride and triethyl amine to obtain corresponding 4-chloro-N [2-chloro-4(3,4,5-trimethoxy phenyl) azetidene-1-yl]-1,3-thiazole-2-amine (3). Various substitution on compound (3) with secondary amines yielded series of compound (4a-j). The structure of synthesized compounds was confirmed by analytical and IR, ¹H NMR and Mass spectra.

3.2 Antimicrobial Activities

The antibacterial property of thiazole derivatives were screened in disc diffusion method using various concentration and microorganisms as shown in Table 2. The compound 4e has shown average antibacterial activity against *E. coli* and *B. subtilis*. All other compounds showed low antibacterial activity against all bacteria.

3.3 Antifungal Activity

The antifungal property of thiazole derivatives were screened in disc diffusion method using various concentration and microorganisms as shown in Table 3 the compound 4d, 4g and 4e has showed moderate antifungal activity against *A. flavus* and *C. albicans*, all other compounds showed low antifungal activity against both microorganisms.

4 Conclusion

Molecules prepared for the biological testing do not always turn out as potential new compounds but may be intended to serve as models for evaluation of hypothesis. The thiazole contained moieties independently are antibacterial agents. The present work is to synthesize certain derivatives of thiazole fused with azetidine ring and were studied for their antibacterial activity. Here when these moieties are screened for antibacterial studies showed good antibacterial and also good antifungal properties. Thus an expected substituted thiazole azetidine exhibited antibacterial activity of some derivatives showed potent activity when compared to the standard. Some of thiazole derivatives showed potent antibacterial activity, some found good activity, and the other derivatives showed moderate antibacterial activity. There is no such a thing as completely safe drug. Drugs are powerful tools which alter physiological processes for the better or for the worse. A society which wishes to benefit from them will not achieve all the benefits open to it, if it ignores the fact and seeks for impossible standards of harmlessness. The antibacterial testing showed that few compounds have promising activity at low dosage levels.

Among these derivatives 2-amino-[2-chloro-4(3,4,5-trimethoxyphenyl)azetidine], 4-amino-4-hydroxy phenyl]-1,3-thiazole-2-yl showed good antibacterial activity. Derivatives of thiazole are responsible for antibacterial activity. Above results establish the fact that thiazole with fused azetidine can be a rich source for exploitation. Hence, in search of new potent biodynamic agent, it may be worthwhile to explore the possibility in this area by fusing different azetidine with thiazole.

Table 2 Screening of compounds 4 (a-j) at different concentration by disc diffusion method (values are in mm) - Antimicrobial Activity

Compound	<i>E. coli</i>					<i>B. Subtilis</i>					<i>K. Pneumonia</i>					<i>S. Typhy</i>				
	25 µg	50 µg	100 µg	25 µg	50 µg	100 µg	25 µg	50 µg	100 µg	25 µg	50 µg	100 µg	25 µg	50 µg	100 µg	25 µg	50 µg	100 µg		
Control	00	00	00	00	00	00	00	00	00	00	00	00	00	00	00	00	00	00		
Streptomycin	19	20	21	18	20	22	18	20	22	19	21	23	19	21	23	19	21	23		
4a	02	04	06	04	05	06	02	03	05	06	03	03	03	03	03	03	03	03		
4b	00	00	08	02	04	08	00	01	07	03	05	06	03	05	06	03	05	06		
4c	02	04	07	09	11	13	01	04	07	00	02	03	00	02	03	00	02	03		
4d	03	05	08	04	09	11	00	01	03	04	06	07	00	04	06	04	06	07		
4e	11	13	14	02	14	16	00	07	09	16	08	11	00	08	09	08	09	11		
4f	05	06	11	09	11	16	06	08	10	16	06	07	06	06	07	05	06	07		
4g	06	09	14	08	12	15	00	00	00	15	00	01	00	00	01	00	01	01		
4h	02	05	07	08	09	11	00	00	00	11	00	02	00	00	02	00	02	02		
4i	00	01	03	09	11	13	04	05	05	13	04	05	04	05	05	02	03	05		
4j	02	03	05	07	09	11	04	08	05	11	04	08	04	08	05	00	00	01		

Table 3 Screening of compounds 4 (a-j) at different concentration by disc diffusion method (values are in mm) - Antifungal Activity^a

Compound	Candida albicans				Aspergillus flavus			
	25 µg	50 µg	100 µg	150 µg	25 µg	50 µg	100 µg	150 µg
Control	00	00	00	00	00	00	00	00
Amphotericin	04	05	07	09	05	07	09	12
4a	01	03	03	04	01	02	03	06
4b	01	02	03	03	02	03	04	05
4c	00	01	03	03	01	02	02	06
4d	02	02	03	04	00	00	01	03
4e	00	01	02	04	01	03	04	06
4f	00	01	02	03	01	02	03	04
4g	01	02	02	06	01	03	02	07
4h	02	03	04	04	01	02	04	06
4i	00	00	01	02	02	03	05	06
4j	02	02	03	04	01	02	04	06

^aAverage of three determinations

References

1. John, J., Bobade, A. S., & Khadse, B. G. (2001). Synthesis and antimicrobial activity of substituted thiazole derivatives containing 1,2,4-triazole ring systems. *Indian Journal of Heterocyclic Chemistry*, 10, 295–298.
2. William, D. A., & Lemke, T. L. (2002). *Foye's principles of medicinal chemistry*. Lippincott Williams and Wikins Philadelphia.
3. Lednicer, D., & Mitscher, L. A. *The organic chemistry of drug synthesis* (Vol. 2, pp. 241–69). Wiley.
4. Jin, Z. (2005). Muscarine, Imidazole, Oxazole and Thiazole alkaloids. *Natural Products Reports*, 22, 196–199.
5. Jin, Z. (2003). Muscarine, Imidazole, Oxazole and Thiazole alkaloids. *Natural Products Reports*, 20, 584–591.
6. Jin, Z., Li, Z., & Huang, R. (2002). Muscarine, Imidazole, Oxazole, Thiazole, Amarylidaceae and selenium alkaloids. *Natural Products Reports*, 19, 454–464.
7. Jin, Z. (2006). Muscarine, Imidazole, Oxazole and Thiazole alkaloids. *Natural Products Reports*, 23, 464–469.
8. Mann, J. (1997). Myxobacterial bounty. *Nature*, 385, 117–121.
9. Zhu, B., & Panek, J. S. (2000). Total synthesis of Epothiline A. *Organic Letters*, 2, 2575.
10. Dalvie, D. K., Kalgutkar, A. S., Khojasteh-Bakht, S. C., Obach, R. S., & O'Donnell, J. P. (2002). A practical two step synthesis of 1-alkyl-4-aminopyrazoles. *Chemical Research in Toxicology*, 15, 269–274.
11. Kempf, D. J., Sham, H. L., Marsh, K. C., Flentge, C. A., Betebenner, D., Green, B. E., McDonald, Vasavanonda, S., Saldivar, A., Wideburg, N. E., Kati, W. M., Ruiz, L., Zhao, C., Fino, L., Patterson, J., Molla, A., Plattner, J. J., & Norbeck, D. W. (1998). Discovery of ritonavir, a potent inhibitor of HIV protease with high oral bioavailability and clinical efficacy. *Journal of Medicinal Chemistry*, 41, 602–08.
12. Struengmann, A., Freudensprung, B., & Klokckers, K. (1999). Novel NSAID, S Meloxicam (Vol. 40, pp. 112–121). PCT International Application (Hexal A.-G., Germany). Wo. 1999.

13. Shah Neil, P., Tran, C., Lee Francis, Y., Chen, P., Norris, D., & Charles, S. (2004). Overriding imatinib resistance with a novel ABL, kinase inhibitors. *Life Science*, 305, 399–408.
14. Jung, F. H. (1984). Discovery of novel and potent thiazoloquinazolines as selective Aurora A and B-kinase Inhibitors (pp. 138–44). European Patent Application (ICI-Pharma S. A., Fr.). Ep; 1984.
15. Ryan, C. W. (1984). The biosynthesis of Thiazole phosphate moiety of thiamine (Vitamin B1): The early step catalyzed by Thiazole synthase (p. 4). British UK Patent Application (Eli Lilly and Co., USA). Gb. 1984.
16. Grayson, I. (2001). Palladium and copper-mediated direct C-2 arylation of azoles including free (NH)-imidazole, benzimidazole and indole under base free and ligandless condition. *Speciality Chemicals Magazine*, 21, 10.
17. Rowe, D. (2001). Flavoring properties of novel thiazoles. *Speciality Chemicals Magazine*, 21, 17–30.
18. Masui, K., Mori, A., Okano, K., Takamura, K., Kinoshita, M., & Ikeda, T. (2004). Palladium and copper mediated direct C-2 arylation of azoles. *Organic Letters*, 6, 2011–2018.
19. Sharma, S., Ray, J. K., & Chatterjee, B. G. (1982). Review on synthesis of some novel β -lactum derivative. *Journal of the Indian Chemical Society*, 541–61.
20. Karegoudar, P., Karthikeyan, M. S., Prasad, D. J., Mahalinga, M., Holla, B. S., Suchetakumari, N. (2008). Synthesis of some novel 2,4-disubstituted thiazoles as possible antimicrobial agent. *European Journal of Medicinal Chemistry*, 43, 261–67.
21. Sonwane, S. K., Shrivastava, S. D., & Shrivastava, S. K. (2008). Synthesis and antimicrobial activity of 2-(2'-arylidine-hydrazo-acetyl-amino)-4-phenyl-1,3-thiazoles and 2-[2'-(4''-substituted-aryl-3''-chloro-2''-oxo-azetidine)-acetyl-amino]-4-phenyl-1,3-thiazoles. *47B*, 633–36.
22. Pattan, S. R., Dighe, N. S., Nirmal, S. A., Marekar, A. N., Laware, R. B., Shinde, H. V., & Musade. (2009). Synthesis and biological evaluation of some substituted amino thiazole derivatives. *Asian Journal of Research in Chemistry*, 2(2), 196–201.
23. Usha Rani, P., Chandra Sekhar, B. V. V. N., Rameshkumar, N., Mahendra, R. S., & Kalian, C. A. (2008). Synthesis and antimycobacterial activity of thiazole derivative. *Asian Journal of Chemistry*, 20(1), 718–722.
24. Holla, B. S., Malini, K. V., Rao, S. B., & Sarojini, B. K. (2003). Synthesis of some new 2,4-disubstituted thiazoles as possible antibacterial and anti inflammatory agents. *European Journal of Medicinal Chemistry*, 38(3), 313–318.

Experimental and CFD Analysis of Heat Transfer Enhancement in Channel



Vaibhav H. Bansode and Munna Verma

Abstract Energy is necessary for economic progress, which is beneficial for emerging nations. The connection between rising energy consumption and economic development is not necessarily a simple linear one, though. The high levels of energy consumption in industrialized nations are responsible for their high standards of life. Experiments were conducted in the current work to improve heat transfer in channel with various rib arrangements, and a technique for heat transfer and fluid flow analysis in a channel with rib utilizing CFD tool. Average wall temperatures for steady state conditions were computed for the various mass flow rates and compared to test findings. The findings of the experiment demonstrate that as the mass flow rate of the flowing fluid increases, so does the rate of heat transfer from the test surface. It also demonstrates how the addition of ribs to the test surface improves forced convection heat transfer.

Keywords Heat transfer enhancement · Channel · Parametric study · CFD

1 Introduction

Round, square, or rectangular channels are frequently utilised to transport air. In terms of air volume handled per perimeter distance, a circular channel performs the best. For the same capacity as a square or rectangular channel, less material is required. These channels cross sections might be either orthogonal (rectangular or square) or non-orthogonal (trapezoidal), in which case the resultant flow is exceedingly complicated. To facilitate a quicker transition to turbulence, the channels may occasionally be wavy or corrugated in the stream-wise direction and may even be built with ribs [1].

To improve heat transmission between the fluid and the surface, turbulent flows can be produced by inserting geometrical components into the channel at irregular intervals. Temperature regulation along the channel is possible with turbulent flow. This need for better predictive performance also applies to turbulent channel

V. H. Bansode (✉) · M. Verma

Department of Mechanical Engineering, Bhagwant University, Ajmer, Rajasthan 305023, India
e-mail: bansode.vaibhav@gmail.com

flows, which are common in many industrial applications, including inter-coolers, recuperates, cooling channels in combustion chambers, gas turbine cooling systems, compact heat exchangers, and nuclear reactors [2]. For a wide range of industrial and transportation applications, as well as in other technical disciplines like microelectronics and biotechnology, the research of heat transfer enhanced surfaces is of great interest. Enhanced surfaces are typically employed as the fundamental component of a compact heat exchanger. To increase the rate of heat transfer of the fluid running in a channel, artificially roughening the surface or adding turbulence boosters works well [3].

2 Experimental Set-Up and Experimentation

The heat exchange module, air flow bench, test plates, thermocouple wires, temperature indicator, and water-manometer make up the experimental setup. The key component of the entire experimental apparatus, the heat exchange module, is where heat is pushed convectively transferred from a heated test surface to a cool fluid. The heat exchange module consists of a $500\text{ mm}^3 \times 50\text{ mm}^3 \times 50\text{ mm}^3$ galvanised iron channel that was lined with plain test plates and ribbed test plates. Three scenarios were taken into consideration: a channel with a simple plate, a channel with ribs attached in line, and a channel with ribs attached staggered. The ribs have a square cross section ($w = e$), a rib height to duct height ratio of 0.2, and a ratio of 10 between the rib pitch and rib height. With the aid of a screw, a rectangular strip heater (measuring $500\text{ mm}^3 \times 50\text{ mm}^3 \times 2\text{ mm}^3$) was fastened to the top and bottom of the test plate. To regulate the electric power provided to the heater, connections were established to the power socket using wattmeters. The test plate has insulation and a heater connected to the top and bottom.

The test plates also had insulation on the other two non-roughened surfaces. Glass wool was used as insulation. Thus, only the test plate's ribbed surface where convective heat transfer to the air stream occurs was exposed to the air stream. On the top and bottom surfaces of the heat exchanger module, aluminium ribs were riveted. In order to perform the tests for the forced convection heat transfer measurements, the heat exchange module was developed. An adequate air flow bench was created with the needs of testing forced convection heat transfer in mind. In the open area above the test surface, it was necessary to push the air to flow there at the necessary rate. A blower, a flow control valve, an orifice metre, and a pipe that carries forced air from the blower outlet to the intake of the heat exchange module make up the bulk of an air flow bench. The blower with a 1.0 HP motor was employed in the current task. Using a manually operated regulating valve, the air flow rate across the test surface was controlled. Orifice metres were created to measure the volume flow rate of air next to the regulating valve. To measure the pressure differential across the orifice metre in centimetres of water column difference, a U-tube water manometer was attached. The air was transported from the blower outlet to the heat exchange module's input via a metal pipe (made of mild steel). Because the blower's exit was

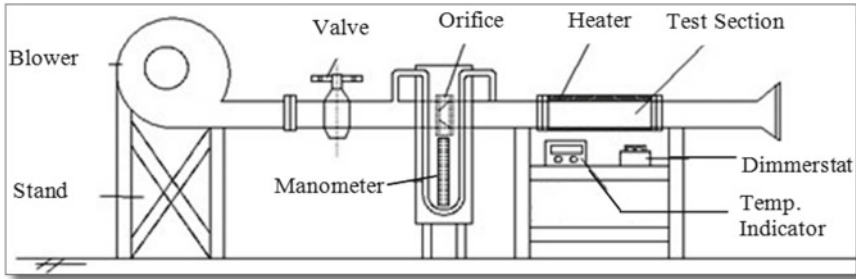


Fig. 1 Schematic of the experimental set-up

round, the pipe that was utilised had a circular cross section. The experimental set-up is schematically depicted in Fig. 1, which provides a clear understanding of the air flow bench ready for the forced convection heat transfer measurements.

The temperatures were measured by temperature indicators at eight separate locations on the test surface for a different air flow rate and heat input. Air temperatures at the heat exchange module’s input and output were recorded. Newton’s rule of cooling, which stated that the heat flow from the surface to fluid was proportional to the temperature differential between the surface and fluid, was used to determine the heat transfer coefficient. To transport the forced air from the blower to the heat exchange module in the air flow bench, a pipe was employed to link the blower output and the heat exchange module. A flow controlling valve was attached to the pipe right next to the blower output to control the airflow. To provide fully developed flow, air was transported through a conduit of around 2 m in length before approaching the heated test part. In order to monitor the controlled air flow rate in the pipe, an orifice metre was installed next to the regulating valve. The orifice metre was coupled to a water manometer. The pressure difference across the orifice metre is shown by a water manometer in centimetres of water column difference. The air flow bench was attached to the heat exchange module created as indicated in the previous section in order to drive the air parallel to the ribbed test surface. The wattmeter was used to connect the strip plate heater, which was mounted to the top and bottom test plates, to the power socket. To provide the test plate with the necessary heat input, wattmeter readings were changed. Temperature measurements were performed using calibrated Copper-Constantan thermocouple wires. On the test surface, provisions are established to secure the thermocouple connection. Additionally, air temperature readings at the heat exchange module’s input and output were taken. The picture of the experimental setup is shown in Fig. 2.



Fig. 2 Experimental set-up

2.1 Experimental Results and Discussion

The results based on the test's observations are presented in this in graphical style. The experimental findings regarding heat transport in a duct with various rib layouts were given. The outcomes are displayed in terms of the average wall temperature and Nusselt number computed for various Reynolds numbers. The experiment's findings are represented graphically in Figs. 3 and 4, which demonstrate how the average wall temperature and Nusselt number for various duct arrangements vary with Reynolds number and Reynolds number, respectively. For all test surfaces taken into consideration, it has been noted that as Reynolds number rises, average wall temperature values fall and Nusselt number values rise. In comparison to the other two arrangements, the average wall temperature values for the inline attached rib arrangement were lower and their Nusselt numbers were higher. For the same operating conditions, the average wall temperature values for plain channel were also higher. It demonstrates that a channel with an inline connected rib configuration performs more effectively at heat transmission.

Fig. 3 Variation of average wall temperature with Reynolds number

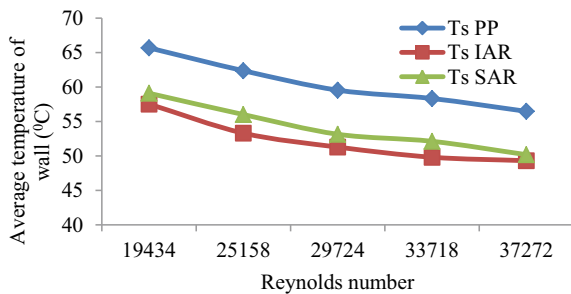
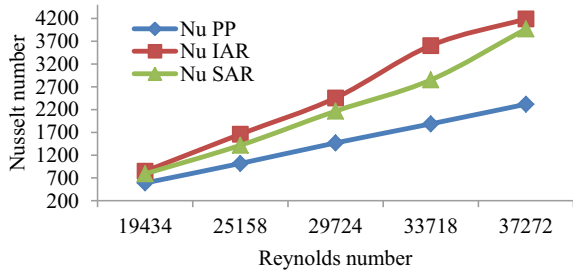


Fig. 4 Variation of Nusselt number with Reynolds number



3 Numerical Solution

CFD code was used for the analysis. The development of the geometry, meshing, assigning of boundary conditions, solution, and post-processing were the processes in the analysis. The channel was designed and separated into tiny elements during the development and meshing of the geometry. Assignment of boundary conditions and domain definition follow. The system is then imported into a suitable solver to be solved using various physical models. To obtain additional information about the outcomes, several parameters are anticipated during post-processing. The present system was analysed using above steps with proper model as follows.

3.1 Computational Model

The 3D axi-symmetric square duct was taken into account as a continuum in order to investigate the fluid flow and heat transfer properties of the square channel. The rectangular computational domain of geometry was utilised to simulate the square channel using GAMBIT, and a hexahedral element with map meshing technique was employed for effective surface meshing. Once the boundary conditions had been assigned, the model was imported into Fluent.

3.2 Initial and Boundary Conditions

In the current study, 0 gauge pressures was taken into account at the exit and the velocity at the entrance was inputted as derived from the mass flow rate. The top and bottom walls were thought to provide a continual source of heat flow. Different solver models, including those for turbulence, radiation, and phase change, are included in the commercial code. The reference velocity in the current research suggests more turbulent flows. Therefore, analysis was conducted using the usual K-ε model.

3.3 Numerical Results and Discussion

The X-Velocity contour plot for a simple plate in the middle part of the channel is displayed in Fig. 4. It shows that velocity drops off close to the wall because to boundary layer generation. The centre segment of the channels X-Velocity contour plot is seen in Fig. 5. It shows how turbulence is produced between the ribs and a negative velocity zone is generated behind the ribs. Negative velocity signifies the formation of the recirculation zone behind the ribs. The X-Velocity contour plot for a channel with staggered connected ribs in the centre part of the channel is shown in Fig. 6. It shows how turbulence is produced between the ribs and a negative velocity zone is generated behind the ribs.

Figures 7 and 8 depict the relationship between average wall temperature and Reynolds number as well as the relationship between Nusselt number and Reynolds

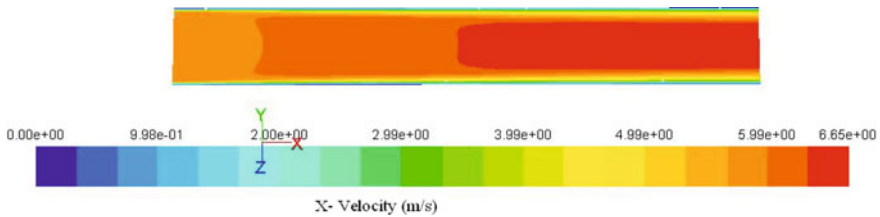


Fig. 5 X-Velocity contour plot for Plain duct with no ribs at Re = 19,434

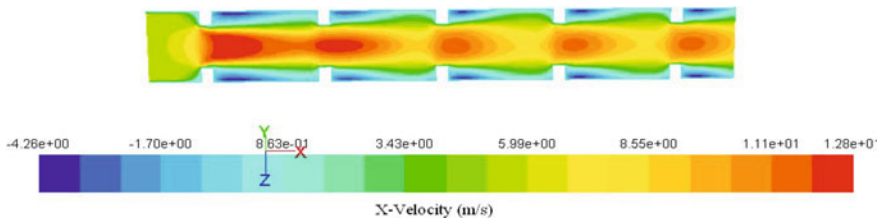


Fig. 6 X-Velocity contour plot for Inline Ribbed duct at Re = 19,434

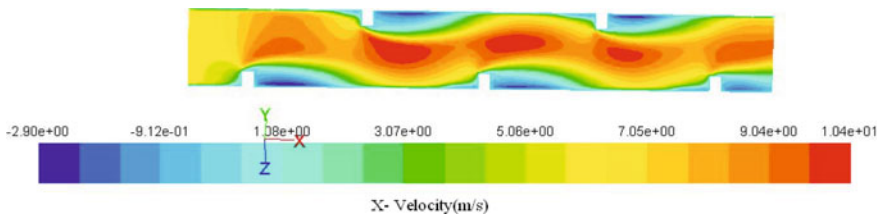


Fig. 7 X-Velocity contour plot for staggered Ribbed duct at Re = 19,434

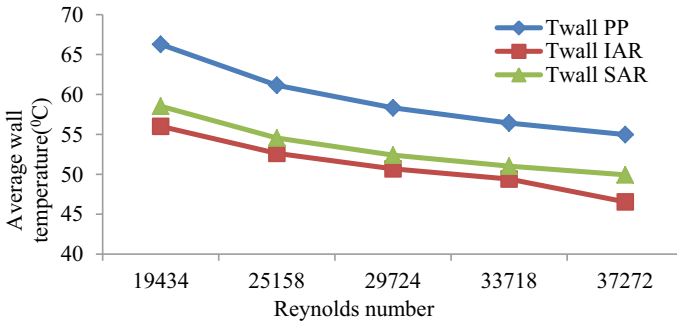


Fig. 8 Variation of average wall temperature with Reynolds number

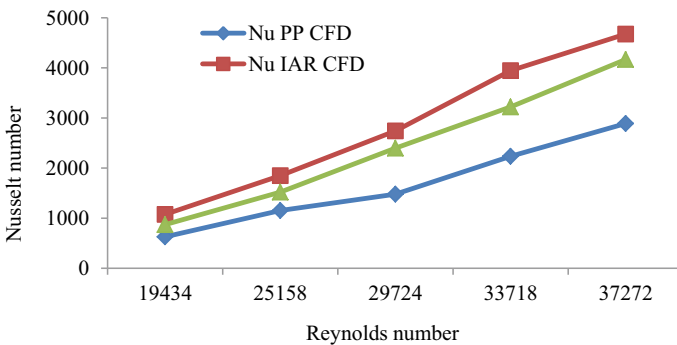


Fig. 9 Variation of Nusselt number with Reynolds number

number for various channel configurations. For all test surfaces taken into consideration, as Reynolds number rises, average wall temperature values fall and Nusselt number values rise. The average wall temperature values are lower and the Nusselt numbers are higher for the inline attached rib configuration than for the other two arrangements for the same heat input, while the average wall temperature values are higher for plain channel. It demonstrates that a channel with an inline connected rib configuration performs more effectively at heat transmission.

4 Comparison of CFD Results with Experimental Results

The CFD findings are compared with the outcomes of experiments. The average wall temperature versus the Reynolds number and the Nusselt number versus the Reynolds number for the three examples are shown in Figs. 9 and 10, respectively. It demonstrates that the findings of the experiments and the CFD are in good agreement.

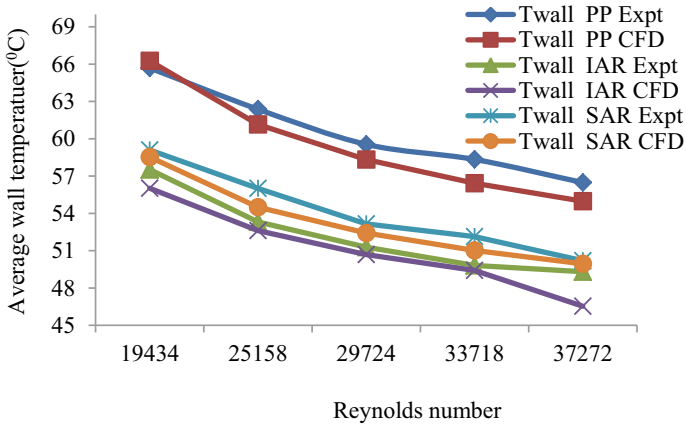


Fig. 10 Average wall temperature versus Reynolds number

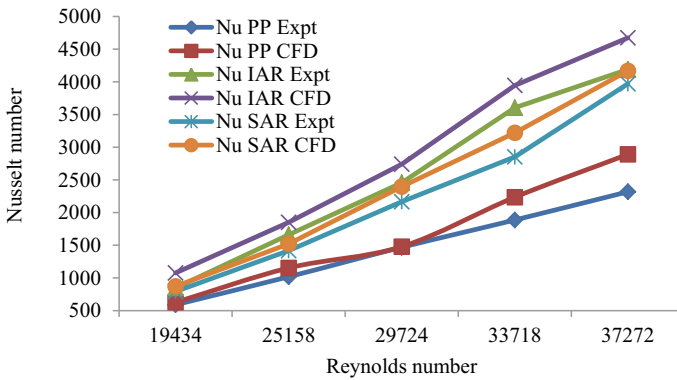


Fig. 11 Nusselt number versus Reynolds number

In terms of average wall temperature and Nusselt number, the maximum errors are 2.34% and 2.25%, respectively.

5 Conclusion

CFD approach is used to analyse various channel unit types and forecast velocity distribution, temperature distribution, and flow pattern. To build the analytical process, CFD findings are compared to experimental data. The findings of the experiment demonstrate that as the mass flow rate of the flowing fluid increases, so does the rate of heat transfer from the test surface. It also demonstrates how the addition of ribs to the test surface improves forced convection heat transfer. CFD results show

a good agreement with experimental results. According to the results of the three-dimensional square channel, the recirculation zone immediately behind the ribs in both the inline and staggered arrangements grows as the Reynolds number rises. In contrast to the staggered attached ribs, the inline attached ribs have a stronger recirculation zone.

References

1. Mushatet, K. S., & Mehdi, G. S. (2008). Analysis of turbulent flow in a duct roughened with attached and detached ribs. *Emirates Journal for Engineering Research*, 13(1), 61–69.
2. Han, J. -C., & Wright, L. M. Enhanced internal cooling of turbine blades and vanes. Turbine Heat Transfer Laboratory, Department of Mechanical Engineering, USA.
3. Gao, X., & Sunden, B. (2004). Effects of inclination angle of ribs on the flow behavior in rectangular ducts. *ASME*, 126.
4. Kucuk, H., Avci, M., Aydin, O., & Asan, H. (2008). Analysis of heat and fluid flow in concentric annular square ducts. *Journal of Thermal Science and Technology*, 1300–3615.
5. Razak, A. A., Yaakob, Y., & Ramli, M. N. (2009). Computational simulation of turbulence heat transfer in multiple rectangular ducts (p. 53). World Academy of Science, Engineering and Technology.
6. Jung, Y., Choi, S. -U., & Choi, J. -I. (2007). Direct numerical simulation of turbulent flow in a square duct: Analysis of secondary flows. *Journal of Engineering Mechanics*.
7. Han, J. C. (1960). Hydrodynamic entrance lengths for incompressible laminar flow in rectangular ducts. *Journal of Applied Mechanics*, 27, 403–409.
8. Morini, G. L. (2000). Analytical determination of the temperature distribution and Nusselt numbers in rectangular ducts with constant axial heat flux. *International Journal of Heat Mass Transfer*, 43(17), 741–755.
9. Shin, L. K. (1993). Numerical study of laminar heat transfer with temperature dependent fluid viscosity in a 2:1 rectangular duct. *International Journal of Heat Mass Transfer*, 36(18), 4365–4373.
10. Anderson Jr, J. D. *Computational fluid dynamics*. Publication McGraw-Hill, Inc.
11. Su, C. C., & Lin, R. H. (1997). Experimental studies on flow in converging and divergent ducts of rectangular cross section. *International Journal of Energy Research*, 21, 77–86.
12. Manglik, R. M. Heat transfer enhancement techniques.
13. Hans, V. S., Saini, R. P., & Saini, J. S. (2009). Performance of artificially roughened solar air heaters—A review. *Renewable and Sustainable Energy Reviews*, 13, 1854–1869.
14. Aharwal, K. R., Gandhi, B. K., & Saini, J. S. (2007). Experimental investigation on heat-transfer enhancement due to a gap in an inclined continuous rib arrangement in a rectangular duct of solar air heater. *Renewable Energy*, 33, 585–596.
15. Banerjee, M. K., & Banerjee, R. (2006). Application of variational method for analysis of velocity and temperature distribution of a fluid flowing through a duct.
16. Facao, J., & Oliveira, A. C. (2005). Modeling laminar heat transfer in a curved rectangular duct with a computational fluid dynamics code. *Numerical Heat Transfer, Part A*, 48, 165–177.
17. Kamali, R., & Binesh, A. R. (2009). Heat transfer and friction characteristics optimization with compound turbulators in roughened ducts. *Journal of Mechanics*, 25, 3.
18. Karmare, S. V., & Tikekar, A. N. (2007). Heat transfer and friction factor correlation for artificially roughened duct with metal grit ribs. *International Journal of Heat and Mass Transfer*, 50.
19. Fluent 6.3.26 documentation, Fluent Inc.

Heat Transfer Augmentation in Forced Convection with Regularly Spaced Inserts—A Review



Suryaji S. Kale and S. S. Gawade

Abstract Heat transfer augmentation techniques are widely used to enhance performance in the Process industries, Thermal Power Plants, Heat Exchangers, Air conditioning, Refrigeration industries, Automobiles etc. In heat transfer enhancement basically two types of techniques are used, Passive technique and Active technique. Out of these techniques Passive technique used widely used, as it does not consume energy to operate it. Researcher have investigated the performance parameters with different type of twisted tape. In this paper the detailed review of regularly spaced insert is discussed. In the regularly spaced inserts attempt is made to reduce pumping power by reducing obstacles in the flow. All the researcher has used twisted tape insert for study of regularly spaced inserts. In some of the research work special type of tube section is used like convergent divergent tube. Some of the researcher has found that regularly spaced insert helps for the enhancing overall performance ratio whereas some of them found that it affects adversely. Overall Enhancement Factor found to be improved between 1 and 1.66 at various Reynolds numbers.

Keywords Inserts · Heat transfer enhancement technique · Regularly spaced

Nomenclature

D	Inner tube diameter, mm
f	Friction factor, dimensionless
h	Convective heat transfer coefficient, $\frac{W}{m^2k}$
L	Length of test tube, m
Nu	Nusselt number, dimensionless
Nu ₀	Nusselt number in plain tube, dimensionless

S. S. Kale (✉)
Department of Technology, Shivaji University, Kolhapur, India
e-mail: kaless@gmail.com

S. S. Gawade
RIT Rajaramnagar Affiliated to Shivaji University, Kolhapur, India

OER	Overall enhancement ratio, dimensionless
Pr	Prandtl number, dimensionless
P	Pitch of twisted tape, dimensionless
ΔP	Pressure drop, Pa
Re	Reynolds number, dimensionless
s	Space ratio, dimensionless
T	Temperature, K
TEF	Total enhancement factor, dimensionless
Y	Twist ratio, dimensionless
η	Performance evaluation factor, dimensionless

1 Introduction to Augmentation

Heat Transfer Augmentation (HTA) is very important as per as the process industry is concerned. In HTA effort is made for the increasing heat transfer with minimum increase in the pumping power. Heat transfer is measured by measuring heat transfer coefficient or by measuring Nusselt Number. As per Newtons cooling law heat transfer by convection can be calculated by multiplying Heat transfer coefficient with Surface area and Temperature difference. Surface area is limited by the space available in the actual equipment and temperature difference is limited by operating conditions, so heat transfer increase by the increase of surface area and temperature difference has lot of limitations. The economical, feasible solution is to improve the heat transfer coefficient. HTA has many advantages, it reduces size of equipment considerably, it reduces pumping power, in some cases it helps for reducing operating temperatures. HTA reduces the operating cost of the equipment. Heat transfer enhancement techniques are practically used in many industrial applications, its widely used in the refrigeration, process industry, automotive applications. Now a days HTA techniques are playing vital roll in the electronic applications. Day by day the size of electronic equipment are reducing considerably, which create need of the heat transfer enhancement. HTA technique also used in the Solar collector, Chemical industry.

Heat transfer enhancement technique can be classified in to three types as Active, Passive and Compound method. Active method uses external power to enhance heat transfer. These are simplest methos and enhance heat transfer considerably but as it takes external power heat enhancement factor is less. Another method is passive method in which no external power is required. In this method surface variations, inserts like twisted tape, wire coils etc. are used, in this methos enhancement factor is quite high and ample amount of research is present. Most widely insert used in the passive method is Twisted tape. Twisted tapes are easy to manufacture and fittings. Third method of heat transfer enhancement is Compound method, in this methos combination of active and passive technique is used, this method is also known as

hybrid technique. As this method is combination of two methods, it considered to be complex method.

2 Performance Measurement Parameters

Performance of any Heat transfer enhancement method is measured by various parameters like Nusselt number, friction factor, Enhancement factor. Nusselt number is measure of increase of heat transfer coefficient. Nu is heat transfer coefficient multiplied by characteristic length and divide by thermal conductivity of respective fluid. In the heat transfer enhancement Nu number increases. All the heat transfer enhancement technique increases the friction factor and pumping power required for the fluid. Enhancement factor is given as

$$\text{Overall Enhancement Ratio(OER)} = \frac{\left(\frac{Nu}{Nu_0}\right)}{\left(\frac{f}{f_0}\right)^{\frac{1}{3}}}$$

In the above equation Nu is Nusselt number with insert and Nu_0 is the Nusselt number without insert. f is friction factor with insert and f_0 is the friction factor without insert. Overall Enhancement ratio (OER) gives idea about how much heat transfer enhancement has occurred with how much consumption of pumping power. Ideally OER should be more than 1 and higher enhancement factor will be more advantageous.

3 Review of the Research

Twisted tape is one of important passive insert. It is simple in construction and easy to manufacture. Twisted tape is called as flow divider type of insert as it divides flow in to separate parts. Twisted tape works on the basic principle of disturbing boundary layer near the wall and converting laminar flow in to turbulent flow. Many researchers have worked on the twisted tape. Researcher have used different kind of twisted tape like dimpled tape, perforated tape, notch tape, helical screw type, serrated twisted tape, spiky twisted tape, dimpled twisted tape, square cut twisted tape, V cut twisted tape, classic twisted tape. In this paper regularly spaced inserts or broken inserts are considered for the review. Regularly spaced inserts are insert in which inserts are not continuous, it will have space in between. This space can be varied for the evaluating of performance. There are various terms used for the performance. In that twist ratio (γ) is the ratio of twist pitch to the diameter. Spacer length (S) is the space between two conjugative inserts. In the regularly spaced inserts friction factor and pumping power required is less compared to the continuous insert.

4 Comparative Table

Table 1 shows the summary of the results various regularly spaced inserts (RSI).

Researchers have studied regularly spaced inserts/twisted tape experimentally as well as theoretically. Experimental work available is more compared to the theoretical work. In this paper review of experimental as well as theoretical is discussed in detail.

5 Experimental Study on Regularly Spaced Inserts

In the Regularly spaced inserts almost all the research available on the twisted tape. Table 1 shows comparative summary of the research work.

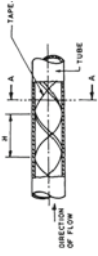
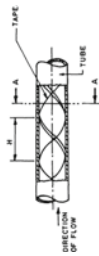
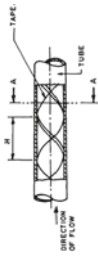
Date and Gaithonde [2] the axial momentum equation for flow in a tube containing regularly spaced twisted tape elements has been integrated to yield a correlation for friction factor that reflects the influences of secondary flows and wall shear. This was accomplished by extracting relationships for relevant parameters from previous numerical predictions of laminar flow in a tube containing a full-length twisted tape. Similarly, a correlation for the Nusselt number is established by assuming the existence of a mixing length over a portion of the distance between consecutive twisted-tape elements. For Pr 5, the correlations and the experimental data are compared and found to be in good agreement. To identify promising areas for future research, the correlations are extended to parametric values outside of the range of previous experiments.

Shah et al. [3] experimental research has been done on the properties of heat transfer and pressure loss in a tube with components made of twisted tape spaced regularly. They studied a viscous fluid with an intermediate Prandtl number range's in laminar swirl flow. The swirl was made of single-twist twisted tape pieces equally spaced out and linked by thin circular rods. Both the rod diameter and the tape width were variable. Studies have been done on the effects of sequential tape components with higher-than-zero phase angles. Data on the heated and isothermal friction factors have been produced.

Eiamsa-ard et al. [4] experimental research is done on the improvement in heat transferred by helical tapes inside a tube. In order to create swirl flow, which aids in boosting the tube's rate of heat transmission, a helical tape is introduced within the tube. The Reynolds number range for the tube's flow rate is between 2300 and 8800.



In compared to a plain tube, the maximum mean Nusselt number may be enhanced by 160% for a full-length helical tape with a centered rod, 150% for a full-length helical tape without a rod, and 145% for a full-length helical tape with normal spacing ($s = 0.5$). The mean Nusselt number is around 15% lower when employing a tiny spacing ratio of 0.5 than when using a full-length helical tape with a centered rod, but the decrease in pressure drop is about 63%. In contrast to space ratio $s = 0.5$, the longer free-spacing length, $s = 2.0$, offers lower values of heat transfer rate and pressure loss reduction of around 16% and 17%, respectively.

Table 1 Summary of the research on regularly spaced inserts

S. No	Author and year	Parameters	Insert type	Insert arrangement	Major findings
1	Shah et al. [1]	Re—500 to 2300 Twist ratio—3.18 to ∞ Space ratio—2.5 to 10 Pr—4 to 5.5	Regularly spaced twisted tape		Friction factor and Nusselt number for $s > 0$ can be both greater and smaller than for $s = 0$. For $s > 7.5$, the measured friction factor is always found to be less than the value for $s = 0$
2	Date and Gaithonde [2] Numerical study	Re—500 to 2300 Twist ratio—3.18 to ∞ Space ratio—2.5 to 10 Pr—4 to 5.5	Regularly spaced twisted tape		The correlations for Fr and Nu predict the experimental data of Saha et al. [13] within 15%. They also predict the effects of s in that they show that the case of $s = 0$ is not a limiting case of finite spacing between the tape elements
3	Shah et al. [3]	Reynold number— $45 < Re < 1150$ Twist ratio (y) $2.5 \leq y \leq 5$ Space ratio (s) $0 \leq s \leq 5$	Regularly spaced twisted tape		Difference between heated friction factor and isothermal friction factor for regularly spaced twisted tape is significantly less than that of plain tube

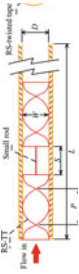

(continued)

Table 1 (continued)

S. No	Author and year	Parameters	Insert type	Insert arrangement	Major findings
4	Eiamsa-ard et al. [4]	Reynolds number between 2300 and 8800 Space ratio = 0.5, 1, 1.5, 2	Regularly-spaced Helical tape swirl generators		When using a small space ratio of 0.5, the mean Nusselt number is around 15% lower than the full-length helical tape with centered-rod but the reduction of pressure drop is about 63%. The larger free-spacing length, $s = 2.0$ provides lower values of heat transfer rate and pressure loss reduction around 16% and 17%, in comparison with space ratio $s = 0.5$
5	Eiamsa-ard et al. [5]	Reynolds number between 2000 and 12,000	Regularly spaced twisted tape elements		For both the Nusselt number and the friction factor, the results were compared with the experimental data. It was discovered that the friction factor's Nusselt number was between 15 and 10%

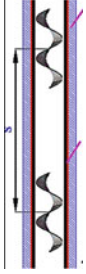
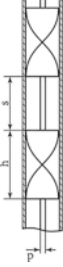
(continued)

Table 1 (continued)

S. No	Author and year	Parameters	Insert type	Insert arrangement	Major findings
6	Eiamsa-ard et al. [6]	Reynolds number between 5000 and 12,000 Twist ratio = 6, 8 Space ratio = 1, 2, 3	Regularly-spaced twisted tapes		Full length twisted tapes (s/40) provided higher heat transfer rates, friction factors, and thermal performance factors than RS-TT ones (s/41.0, 2.0 and 3.0) under identical conditions because they consistently created swirling flows, which in turn increased turbulence
7	Samruaisin et al. [8]	Re—6000 to 24,000 Space ratio = 0.5, 1, 1.5, 2 Twist ratio = constant 2.5			In all configurations, RS-QTTs provide lower heat transfer rates (Nu) and result in less friction loss than QTTs. Heat transfer rate (Nu), friction loss, and TEF for RS-QTTs all rise with a falling free space ratio

(continued)

Table 1 (continued)

S. No	Author and year	Parameters	Insert type	Insert arrangement	Major findings
8	Du and Hong [9]	Re—6000 to 18,000 Pitch length ratio = 1.03 to 1.724 Module distance ratio = 5.69 to 14.224	Transverse rib tube fitted with regularly spaced helical tapes		The heat transfer rate and flow resistance are respectively augmented by 35.3–49.4% and 1.48–1.70 times. By further fitting RSHTs into the TRT, the heat transmission performance and friction loss are increased by about 108.1–177.0% and 5.97–15.31 times, respectively
9	Liu et al. [10]	Re—10,000 to 35,000 Twist ratio—2.0, 3.3, 4.6 Length ratio = 0.3, 0.5, 0.7	Segmented Twisted Tape Insert		It is shown that a segmented tape insert can increase the overall heat transfer rate by 23.5% and the friction factor by 235%, while local improvement along the tube can be 2.8 times more than the plain tube

Eiamsa-ard et al. [6] the impacts of the regularly-spaced twisted tape (RS-TT) on the heat transfer, friction factor, and thermal performance factor behaviours in a heat exchanger are shown along with those of a full-length twisted tape. For the comparative study, full length (or normal) twisted tapes with two different twist ratios ($y=146.0$ and 8.0) were employed alongside regularly-spaced twisted tape (RS-TT) with three different free space ratios ($s=1.0, 2.0, \text{ and } 3.0$) research along with full length (or usual) twisted tapes with two different twist ratios ($y=14P/W=146.0$ and 8.0). The use of a mathematical model for numerical modelling of the swirling flow in a tube caused by the insertion of regularly-spaced twisted tape (RS-TT) is also covered in the article.

At the constant twist ratio, the tapes with $s=1.0, 2.0, \text{ and } 3.0$ enhanced heat transmission by $56.8\%, 46.2\%, 30.5\%, \text{ and } 22.6\%$, respectively. These tapes also had higher friction factors than the plain tube, which were $4.22, 3.78, 3.17, \text{ and } 2.63$ times higher. Figure 1 shows relationship between Reynolds number and thermal performance factor for a tube fitted with twisted tapes at different ratios and open space ratio.

Samruaisin et al. [8] it has been shown that as the pitch of the twisted tape decreases, so does the rate of heat transmission. When the pitch ratio is less, $s/D = 4.5$, the rate of heat transmission is more comparable to that of full-length twisted tape.

In comparison to the QTTs, the The RS-QTTs with s/y values of $0.5, 1.0, 1.5, \text{ and } 2.0$ yield heat transfer rates that are, respectively, around $6.2\%, 8.13\%, 10.6\%, \text{ and } 12.8\%$ lower. For RS-QTTs, the heat transfer rate, friction loss, and TEF all increase with decreasing s/y . The heat transfer rate of the RS-QTTs in cross-arrangement with $s/y = 0.5$ is up to 6.6% higher than that of the QTTs over the indicated range, with a maximum TEF of 1.27 .

Fig. 1 Relationship between the Reynolds number and the thermal performance factor for twisted tape tubes with different free space ratios [6]

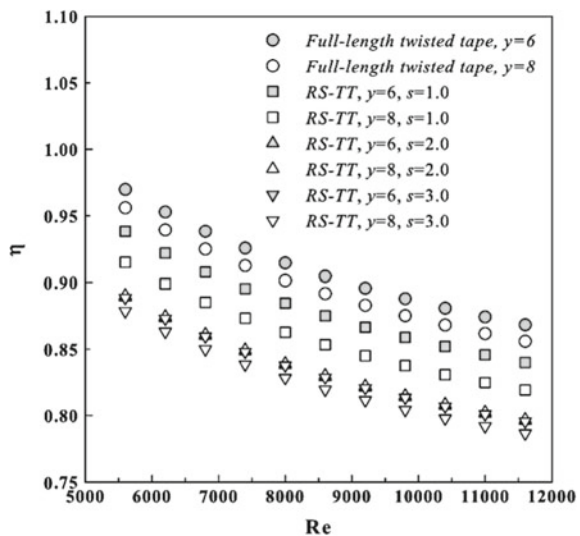


Figure 2 shows influence of the QTTs and RS-QTTs with different free space ratio and tape arrangement on the thermal enhancement factor.

Du and Hong [9] in order to improve the thermal performance of heat exchangers and boost energy efficiency, a transverse rib tube (TRT) and regularly spaced helical tapes (RSHTs) were combined. Under continuous heat flow and isothermal settings, air flow heat transfer and pressure drop experiments were conducted by analysing several factors, including Reynolds numbers, pitch length ratios, and space ratios. The obtained findings in the sole application of TRT demonstrate that the heat transfer rate and flow resistance are, respectively, increased by 35.3–49.4% and 1.48–1.70

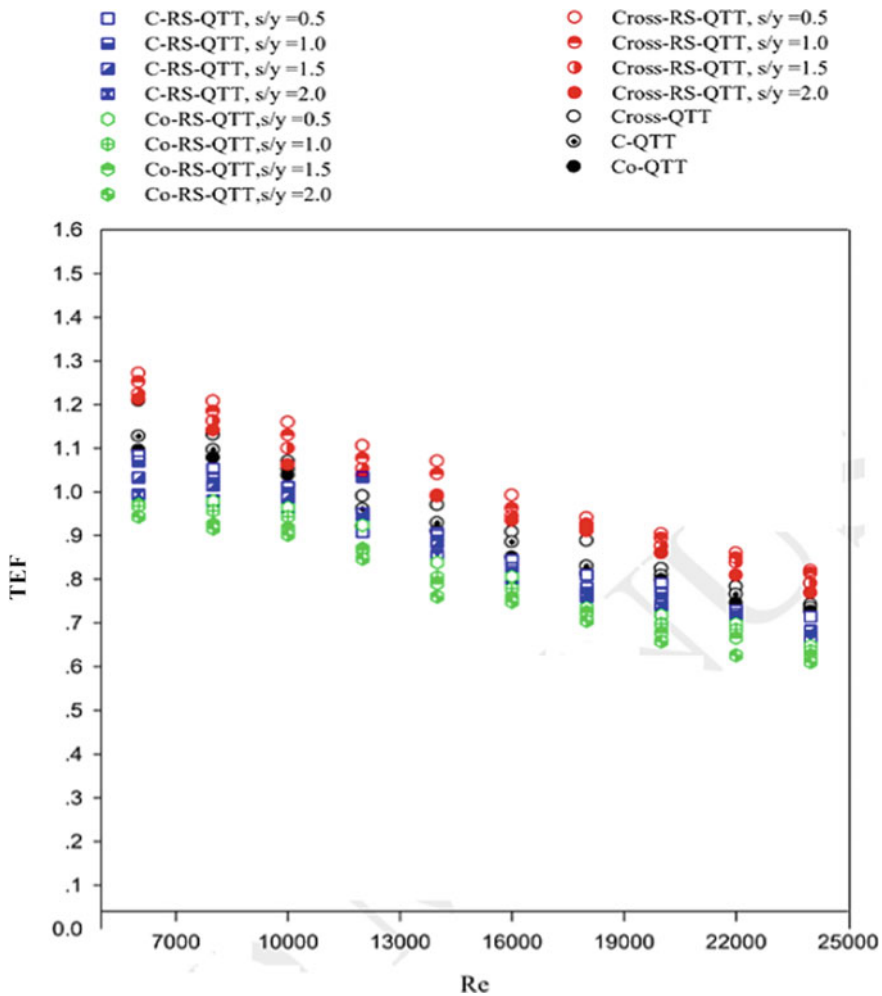


Fig. 2 Influence of the QTTs and RS-QTTs with different free space ratio and tape arrangement on the thermal enhancement factor [8]

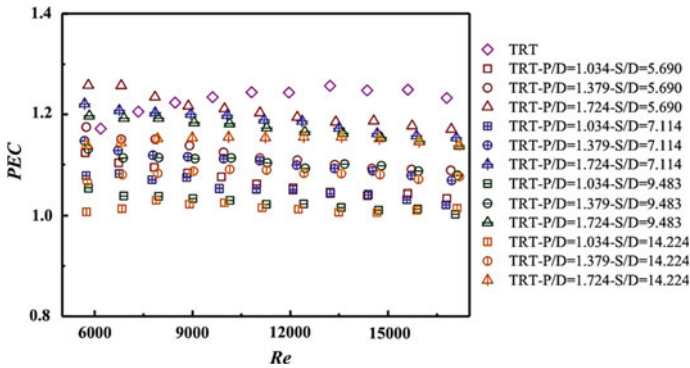


Fig. 3 Variation of PEC versus Re for the TRT fitted with different RSHTs [9]

times over the plain tube. The heat transfer performance and friction loss are raised by approximately 108.1–177.0% and 5.97–15.31 times, respectively, by adding more RSHTs to the TRT.

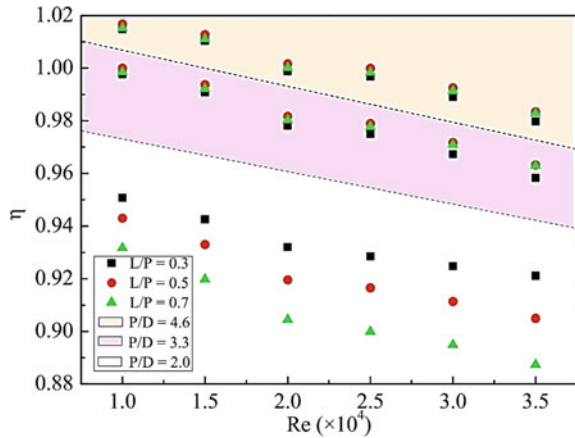
Figure 3 shows variation of PEC versus Re for the TRT fitted with different RSHTs. From the its clear that Performance Evaluation Criterion (PEC) of Traverse Rib Tube (TRT) is highest.

Liu et al. [10] a heat exchanger is a machine that moves waste heat from one area to another, where it may be entirely recycled to increase energy efficiency. Numerous research and investigations on automation technologies have been conducted to support this beneficial procedure. Since they can disrupt the boundary layer and facilitate heat exchange, inserts are frequently employed in pipe flow to improve heat transmission. Segmented twisted tape is a new insert that may be used in 3D printing and has the potential to improve heat transmission. This research includes a numerical analysis of vortex flow and heat increase in pipes with a single segmented twisted element to clarify its benefits and drawbacks. It has been demonstrated that a segmented tape insert may boost local heat transmission along the tube by 2.8 times more than a plain tube, while also increasing the friction factor and total heat transfer rate by 23.5% and 23.5%, respectively (Fig. 4).

6 Conclusions

In the literature it has been found that different researchers have different finding for the regularly spaced inserts. Majority of the researchers have used twisted tape as insert. Researcher basically found results for the different Reynolds number with variation the space between the inserts. The general trend is that with increase in the space between the inserts reduces the pumping power required, also it reduces friction factor of the inserts. This is due to reduction of the obstacles in flow path. In some of the research Overall enhancement factor increases with increase of space

Fig. 4 Relationship between η and Reynolds number [10]



between the inserts but some research shows adverse results. Enhancement factor found to be improved between 1 and 1.66 at various Reynolds number.

References

1. Saha, S. K., Gaitonde, U. N., & Date, A. W. (1989). Heat transfer and pressure drop characteristics of laminar flow in a circular tube fitted with regularly spaced twisted-tape elements. *Experimental Thermal and Fluid Science*, 2, 310–322.
2. Date, A. W., & Gaitonde, U. N. Experimental thermal and fluid science, development of correlations for predicting characteristics of laminar flow in a tube fitted with regularly spaced twisted-tape elements.
3. Saha, S. K., Dutta, A., & Dhal, S. K. (2001). Friction and heat transfer characteristics of laminar swirl flow through a circular tube fitted with regularly spaced twisted-tape elements. *International Journal of Heat and Mass Transfer*.
4. Eiamsa-ard, S., & Promvong, P. (2005). Enhancement of heat transfer in a tube with regularly-spaced helical tape swirl generators. *Solar Energy*, 78, 483–494.
5. Eiamsa-ard, S., Thianpong, C., & Promvong, P. (2006). Experimental investigation of heat transfer and flow friction in a circular tube fitted with regularly spaced twisted tape elements. *International Communications in Heat and Mass Transfer*, 33, 1225–1233.
6. Eiamsa-ard, P., Piriyaungroj, N., Thianpong, C., & Eiamsa-ard, S. (2014). A case study on thermal performance assessment of a heat exchanger tube equipped with regularly-spaced twisted tapes as swirl generators. *Case Studies in Thermal Engineering*, 3, 86–102.
7. Kumbhar, D. G., & Sane, N. K. (2015). Exploring heat transfer and friction factor performance of dimple tube equipped with regularly spaced twisted tape inserts. In *International Conference on Computational Heat and Mass Transfer*.
8. Samruaisin, P., Changcharoen, W., Thianpong, C., Chuwattanakul, V., Pimsarn, M., & Eiamsa-ard, S. (2018). Influence of regularly spaced quadruple twisted tape elementson thermal enhancement characteristics. *Chemical Engineering and Processing*.
9. Du, J., & Hong, Y. (2020). Experimental investigation on thermal-hydraulic characteristics in a traverse rib tube fitted with regularly spaced helical tapes. *International Journal of Heat and Mass Transfer*, 154.

10. Liu, G., Yang, C., Zhang, J., Zong, H., Xu, B., & Qian, J. (2020). Internal flow analysis of a heat transfer enhanced tube with a segmented twisted tape insert. *Energies*.
11. Kumar, P., & Judd, R. L. (1970). Heat transfer with coiled wire turbulence promoters. *Canadian Journal of Chemical Engineering*, 48, 378–383.
12. Pak, B. C., & Cho, Y. I. (1998). Hydrodynamic and heat transfer study of dispersed fluids with submicron metallic oxide particles. *Experimental Heat Transfer*, 11, 151–170.
13. Xuan, Y., & Li, Q. (2000). Heat transfer enhancement of nanofluids. *International Journal of Heat and Fluid Flow*, 21, 58–64.
14. Pavel, B. I., & Mohamad, A. A. (2004). An experimental and numerical study on heat transfer enhancement for gas heat exchangers fitted with porous media. *International Journal of Heat and Mass Transfer*, 47, 4939–4952.
15. Qian, J.-Y., Li, X.-J., Wu, Z., Jin, Z.-J., & Sunden, B. (2019). A comprehensive review on liquid–liquid two-phase flow in microchannel: Flow pattern and mass transfer. *Microfluidics and Nanofluidics*, 23, 207.
16. Qian, J., & Wu, Z. (2019). Heat transfer analysis on dimple geometries and arrangements in dimple jacketed heat exchanger. *International Journal of Numerical Methods for Heat and Fluid*, 29, 2775–2791.
17. Xue, Y., Ge, Z., Du, X., & Yang, L. (2018). On the heat transfer enhancement of plate fin heat exchanger. *Energies*, 11, 1398.
18. Bayram, H., & Sevilgen, G. (2017). Numerical investigation of the effect of variable baffle spacing on the thermal performance of a shell and tube heat exchanger. *Energies*, 10, 1156.
19. ERG. (1999). Duocel aluminum foam data sheet. In *ERG material and aerospace*. ERG.
20. Webb, R. L. (1987). Enhancement of single-phase heat transfer. In *Handbook of single-phase convective heat transfer*. Wiley.

Thermoluminescence Studies in Europium Doped KSr_2Br_5 and CsBa_2I_5 Halide Phosphors



Chhagan D. Mungmode, Dhananjay H. Gahane, Chetan V. Chanmal, and Sanjiv V. Moharil

Abstract Divalent Europium (Eu^{2+}) doped alkali halides KSr_2Br_5 and CsBa_2I_5 phosphors are synthesized by wet chemical method. These phosphors are characterized for Thermoluminescence (TL) properties. Different γ -dose using Co^{60} source are used to irradiate the samples. For $\text{CsBa}_2\text{I}_5:\text{Eu}^{2+}$, thermoluminescence curve shows maxima at 207.5°C and for $\text{KSr}_2\text{Br}_5:\text{Eu}^{2+}$, TL maxima peaks around 261.74°C which are related to the defects at trap depths. Kinetic parameters of the peak are calculated. The activation energy value for KSr_2Br_5 and CsBa_2I_5 are 1.5 eV and 0.811 eV respectively, suggest a possible good stability of the trapped charges produced during irradiation. Hence, Eu (0.5%) doped KSr_2Br_5 and CsBa_2I_5 phosphors could be used for possible TL Dosimetry applications.

Keywords Thermoluminescence · Eu^{2+} · Kinetic order · Trap depth

1 Introduction

Thermoluminescence dosimetry has found numerous applications [1, 2] which includes areas of health science and other biological sciences, radiation protection and personnel monitoring. The phosphors show thermoluminescence phenomenon when it is illuminated by ionizing radiations; traps are created and electrons get trapped into it. These trapped electrons are released due to application of temperature and recombine with hole to emit radiation. Specifically tuned phosphor materials which

C. D. Mungmode (✉)

M. G. Arts, Science and Late N. P. Commerce College, Armori 441208, India
e-mail: mungmode.prashant@gmail.com

D. H. Gahane
Nevjabai Hitkarini College, Bramhapuri 441206, India

C. V. Chanmal
D.B.F. Dayanand College of Arts and Science, Solapur 413002, India

S. V. Moharil
Department of Physics, RTM Nagpur University, Nagpur 440033, India

are used in TLD badges has found wide applications in environmental and personnel radiation monitoring. New TLD phosphors have been established by researchers [3–7].

Thermoluminescence study can be efficiently used for the measurement of radiation dose and to study the electronic trap levels in crystals. Very large number of phosphor materials exhibits thermoluminescence but very few of them possesses all the perfect characteristics of an ideal TLD [8]. Also, defects and impurities present in solids can be studied with the help of Thermoluminescence. In thermoluminescence study, ionizing radiations are used to irradiate a phosphor material for a particular time period. This phosphor is then annealed at a fixed rate and the emitted light output is measured as a function of temperature of the phosphor. The curve of emitted light intensity versus temperature is plotted.

The energy depth of the trapped electrons is given by the position of the peaks on the scale of temperature. How many numbers of electrons are transferred to these traps by the exciting radiations can be measured by area under the curve. The exciting radiations used for this purpose may be UV rays, Gamma rays, alpha particles, ion beams, electrons, neutrons, etc. TL studies give the distribution of traps in the band gap of solids.

Many Sulfides, Sulfates and fluorides of alkali and alkaline earth elements are extensively studied and widely used for Thermoluminescence Dosimetry (TLD). Phosphates and halo-phosphates of alkali and alkaline-earth metal elements were synthesized [9, 10] and also explored for their suitability as TLD materials (Welker 1991; Band et al. 1997; Kottaiswamy et al. 1997; Sanayee et al. 1997; Dhabekar et al. 2002). Schipper et al. (1993) studied X-ray storage phosphor $\text{Ba}_3(\text{PO}_4)_2:\text{Eu}$ for trapping of electrons, Seshagiri et al. (1992) studied the thermally stimulated luminescence (TSL) and electron paramagnetic resonance (EPR) properties of calcium chlorophosphates doped with actinide [11].

Very few Eu^{2+} activated alkali halide materials are studied for thermoluminescence. In this work, synthesis and characterization of bromide and iodide-based phosphor is discussed. $\text{KSr}_2\text{Br}_5:\text{Eu}^{2+}$ and $\text{CsBa}_2\text{I}_5:\text{Eu}^{2+}$ are prepared using wet chemical synthesis method and their thermoluminescence study is discussed in this paper.

2 Experimental

All the reagents used in this work were of analytical purity manufactured by Merck and were used without further purification. $\text{CsBa}_2\text{I}_5:\text{Eu}^{2+}$ sample was prepared using wet chemical method. Initially stoichiometric composition of metal carbonates and Eu_2O_3 were dissolved in HI. This solution was then heated on magnetic stirrer to boil off excess amount of acid and to get dry compound. This whole process was carried out in a glass distillation assembly which consists of a glass flask placed on hot plate with magnetic stirrer. One neck of the flask is connected to condenser unit, so that the evaporated acid can be cooled and collected in a receiving vessel at the lower end. The remaining compound was crushed to get fine powder and dried for 2 h in air.

After that the powder annealed for 1 h at 925 k in a reducing atmosphere provided by burning activated charcoal. Similarly, $\text{KSr}_2\text{Br}_5:\text{Eu}^{2+}$ phosphor was also prepared. Thermally stimulated glow curves were recorded at room temperature. Phosphors under examination were irradiated with gamma dose of 23 kGy.

3 Result and Discussion

KSr_2Br_5 and CsBa_2I_5 has TlPb_2Cl_5 structure ($\text{P2}_1/\text{c}$, monoclinic) as shown in Fig. 1. In KSr_2Br_5 , there are four formula units per unit cell. K^+ and half the Sr^{2+} cations are in a trigonal prismatic coordination of Br^- with three additional Br^- ions capping the polyhedron. Such tricapped trigonal prisms are joined along $[1\ 0\ 0]$ by common triangular faces, and they contain K^+ and Sr^{2+} alternatively. K^+ and half the Sr^{2+} ions are in a $[6+2(+1)]$ coordination based on the geometry of a trigonal prism and the remaining half of the Sr^{2+} ions are in a $[6 + 11]$ coordination of an extended octahedron [12].

Figure 2 shows TL glow curve observed in $\text{KSr}_2\text{Br}_5:\text{Eu}^{2+}$ (0.5 mol%) phosphor and Fig. 3 shows TL glow curve observed in $\text{CsBa}_2\text{I}_5:\text{Eu}^{2+}$ (0.5 mol%) phosphor irradiated with gamma dose of 23 KGy (75 min) recorded in the temperature range between room temperature to 400 °C. Heating rate was 0.11 °C/s. A dominant TL peak is observed at 261.74 and 213 °C.

Fig. 1 Crystal structure of KSr_2Br_5

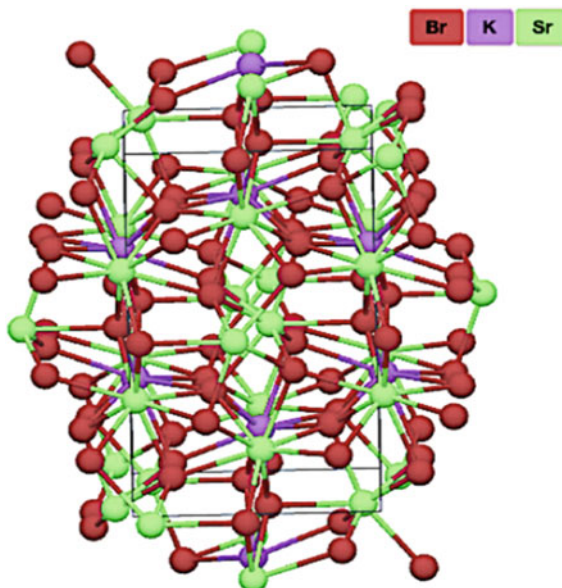


Fig. 2 Thermoluminescence glow curve of γ -irradiated $\text{KSr}_2\text{Br}_5:\text{Eu}^{2+}$ phosphor

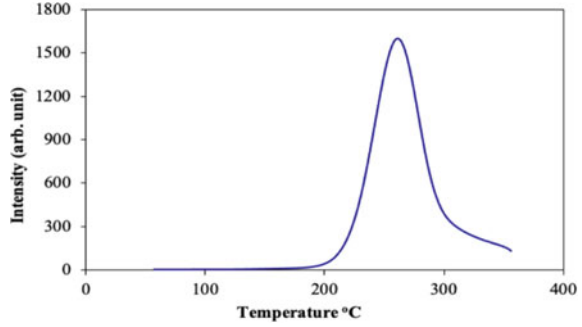
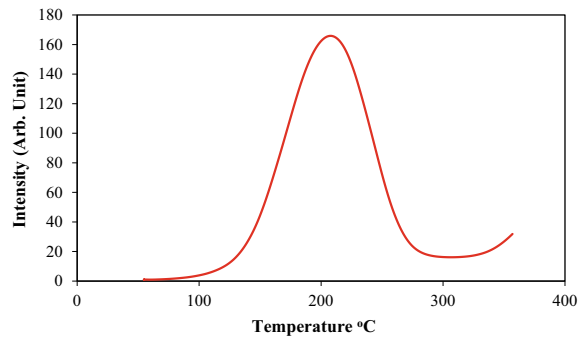


Fig. 3 Thermoluminescence glow curve of γ -irradiated $\text{CsBa}_2\text{I}_5:\text{Eu}^{2+}$ phosphor



The nature of the TL glow curve is decided by the order of kinetics. Half-width methods in which the temperatures T_m , T_1 and T_2 are the highest temperature, temperatures on the lower and upper sides related to half the highest intensity respectively and relied on the form of the glow curve, are utilized to make equations to relate E to all or any or a number of these temperatures.

The order of kinetics was calculated by Chen’s Method [13] measuring the geometrical factor $\mu_g = \delta/\omega$, where δ is half width towards fall-off side of glow curve and ω is full width at half maximum of glow curve. These are calculated as $\delta = T_2 - T^m$, $\omega = T_2 - T_1$ and $\tau = T_m - T_1$, where T_m is peak temperature related to maximum intensity, T_1 and T_2 are temperature on either side of T_m corresponding to half of maximum intensity.

The calculated values of geometrical factor for $\text{KSr}_2\text{Br}_5:\text{Eu}^{2+}$ is $\mu_g = 0.48$ which corresponds to the kinetic order (l) 1.4 and that for $\text{CsBa}_2\text{I}_5:\text{Eu}^{2+}$ is $\mu_g = 0.4756$ which is less than 1 corresponds to the kinetic order (l) 1.38, shows that the kinetic order is first order estimated by the employment of Figs. 2 and 3 given by Chen [13].

The trap depth (E_τ) was calculated from the height parameters by the Chen’s equation

$$E_\tau = C_\tau(kT_m^2/\tau) - b_\tau(2kT_m)$$

Table 1 Kinetic parameters of $\text{KSr}_2\text{Br}_5:\text{Eu}^{2+}$ and $\text{CsBa}_2\text{I}_5:\text{Eu}^{2+}$ phosphors calculated by the peak shape method

Material	Peak temp. T_m (K)	Geometric factor (μ_g)	Kinetic order (l)	Activation energy (E (eV))			Freq. factor ($s(s^{-1})$)
				E_τ	E_δ	E_ω	
$\text{KSr}_2\text{Br}_5:\text{Eu}^{2+}$	534.74	0.48	≈ 1.4	1.52	1.55	1.54	3.4×10^{12}
$\text{CsBa}_2\text{I}_5:\text{Eu}^{2+}$	480.57	0.4756	≈ 1.38	0.638	0.716	1.08	3.8×10^{12}

where,

$$C_\tau = [1.51 + 3(\mu_g - 0.42)] \text{ and } b_\tau = [1.58 + 4.2(\mu_g - 0.42)]$$

$$E_\delta = [0.976 + 7.3(\mu_g - 0.42)]kT_m^2/\delta$$

$$E_\omega = [2.52 + 10.2(\mu_g - 0.42)](kT_m^2/\omega) - 2kT_m$$

where, C_τ and b_τ are constants of Chen's equation, k is Boltzmann's constant and temperature is taken in kelvin. After determination of the trap depth and also the order of kinetics, the frequency factor s , in general, is estimated using the relation.

$$s = [(kT_m^2/\beta E) e^{(-E/kT_m)} (1 + (l-1)2kT_m/E)]^{-1}$$

The calculated kinetic parameters for peak of $\text{KSr}_2\text{Br}_5:\text{Eu}^{2+}$ and $\text{CsBa}_2\text{I}_5:\text{Eu}^{2+}$ phosphors by the peak shape method are given in Table 1.

An important factor for a long-lasting phosphor is to supply an appropriate trap depth within the host. Due to too low trap depth, the electrons within the trap can return to the energy of the excited state easily, thus leading to a brief afterglow lifetime and if the trap depth is just too deep, the transition probability of electrons in the traps to the excited state is extremely low. In such a state, the after glowing is weakly intense. As per Sakai's report, a trap depth between 0.6 and 0.7 eV is suitable for an extended afterglow [14]. The frequency factor is also another important parameter that affects the lifetime of electrons in the traps. In this case, when the frequency factor is increased, the lifetime of the electrons in the traps is decreased.

4 Conclusion

We have synthesized the $\text{KSr}_2\text{Br}_5:\text{Eu}^{2+}$ and $\text{CsBa}_2\text{I}_5:\text{Eu}^{2+}$ phosphors using simple wet chemical method. TL of the $\text{KSr}_2\text{Br}_5:\text{Eu}^{2+}$ phosphor shows a maximum at 261.74 °C and for $\text{CsBa}_2\text{I}_5:\text{Eu}^{2+}$ phosphor TL maxima is around 207.57 °C. It shows linear response up to 23 kGy. Glow curve deconvolution and peak shape methods are used to find out the kinetic parameters. The activation energy value for $\text{KSr}_2\text{Br}_5:\text{Eu}^{2+}$ is 1.5 eV and for $\text{CsBa}_2\text{I}_5:\text{Eu}^{2+}$ is 0.811 eV, suggest a possible good stability of the

trapped charges produced during irradiation. $\text{KSr}_2\text{Br}_5:\text{Eu}^{2+}$ phosphor with a trap depth higher than 0.75 eV, a frequency factor of the order of 10^{12} s^{-1} .

References

1. Marwaha, G., Singh, N., & Mathur, V. (1980). *Radiation Effects and Defects in Solids*, 53, 25.
2. Marwaha, G., Singh, N., Vij, D., & Mathur, V. (1979). *Materials Research Bulletin*, 14, 1489.
3. Banerjee, D., & Murthy, K. (2000). In *Proceedings of International Conference on Luminescence and its Applications (Baroda)*. M.S. University of Baroda.
4. Ekambaram, K., & Patil, K. (1995). *Bulletin of Materials Science*, 18, 921.
5. Joshi, R., Joshi, T., Mahajan, O., Kathuria, S., & Nehate, A. (1984). *Journal of Luminescence*, 31–32, 142.
6. Kar, S., Bairagi, S., Debnath, C., Verma, S., & Bartwal, K. (2012). *Applied Physics Letters*, 101, 071904.
7. Tiwari, G., Bramhe, N., Sharma, R., Bisen, D., & Sao, S. (2015). *International Research Journal of Engineering and Technology*, 2, 591.
8. Madhukumar, K., et al. (2007). *Bulletin of Materials Science*, 30, 527.
9. Mungmode, C., et al. (2022). *Journal of Optics*, 51, 1065–1070. <https://doi.org/10.1007/s12596-022-00882-4>
10. Mungmode, C., et al. (2019). *Materials Today: Proceedings*, 15, 555–559. <https://doi.org/10.1016/j.matpr.2019.04.120>
11. Seshagiri, T., Natrajan, V., & Sastry, M. (1992). *Pramana—Journal of Physics*, 39, 131.
12. Gahane, D., et al. (2009). *Journal of Alloys and Compounds*, 484, 660.
13. Chen, R. (1969). *Journal of the Electrochemical Society*, 116, 1254.
14. Sakai, R., Katsumata, T., & Kumuro, S. (1999). *Journal of Luminescence*, 85, 149.

Deployable Environment or Health Care Technologies

Analysis and Design of Pyrolysis System for Islampur City



Shridhar Kumbhar and Priyanka Bamane

Abstract Plastic waste has enduring life and currently, Islampur Municipality does not have any treatment technology for the disposal of plastic waste. 1.2 tons of plastic waste is dumped in the dumping yard every day. The 16 acres of dumping yard are 85% filled with earlier dumped Municipal solid waste. There are 6 technologies invented by researchers for effective plastic waste disposal. In this paper, these methods are compared and the suitability of pyrolysis technology is analyzed and designed for Islampur City. The main goal is to find methods of getting rid of plastic trash without harming the environment, and to replace that trash with environmentally safe items.

Keywords Plastic waste · Refused derived fuel (RDF) · Pyrolysis

1 Introduction

In the early days, several options were used for disposing of municipal and industrial plastic garbage, including land filling, incineration, recycling, and recovery [2]. As far as I know, this was the greatest rate of recycling ever recorded. Comparatively, it is 7% in Europe, 12% in Japan, 10% in China, and 16% in South Africa. Rates of plastic trash disposal and recovery were almost identical throughout Europe in 2006. Where we now have a recycling/dumping ratio of 50% each. Energy recovery is now at 30.3%, up from 29% in 2005; while recycling is at 19.7%, up from 18% that year. In 2006, the rate of recycling total materials was 19.7%; this included 19.1% from mechanical recycling and 0.6% from recycled feedstock.

The infrastructure in India, especially in urban areas, is insufficient for the safe disposal of municipal solid garbage [6]. A study of the issue shows that a blanket

S. Kumbhar (✉) · P. Bamane
Rajarambapu Institute of Technology, Islampur, Maharashtra, India
e-mail: shridhar.kumbhar@ritindia.edu

P. Bamane
e-mail: priyankabamane0049@gmail.com



Fig. 1 Location of Islampur city

ban on plastic shopping bags would not be effective. There is a need to take strong steps for disposal of waste.

Islampur is the city located in Sangli District of Maharashtra state, India with a population of 69,743 holdings a municipal council of over 14,376 houses (according to the 2011 census) and is forecasted to reach 1, 15, and 127 (by incremental increase method) in 2021. The city facing a problem of 1.2 tons of plastic waste generated per day does not have proper treatment technology (Fig. 1).

2 Modern Technologies for Disposal of Plastic Waste

The plastic disposal becomes the most challenging work for everyone. Despite, researchers find several methods listed below. From listed methods, a suitable method is found by comparing them with each other.

Gasification

In order to create fuels or combustible gases from plastic trash, gasification is used [2]. The gasification agent in this process is air. One major benefit is the ability to save money by using air instead of oxygen. Negative aspects of gasification include releasing nitrogen into the atmosphere. The best method for turning plastic trash into useful energy is gasification. It is thermo-chemical process which transforms carbon containing material into gaseous product creating carbon di-oxide, carbon mono-oxide, and hydrogen and methane gas.

Bioremediation

In that process where micro-organisms decompose wastes. Microorganism development necessitates the establishment of optimal conditions for the culture medium, which includes nutrients, enzymes, pressure, and temperature. Polyvinyl chloride and other plastics break down into phthalate monomers such as vinyl monomers, dioxins, and CFCs during natural deterioration. These methods have a negative impact on the natural world.

Photo-Reforming

In this method, plastic trash is combined with a photo catalyst that turns solar energy into chemical energy [11]. We exposed the plastic and catalyst mixture to sunlight and alkaline solution, which broke down the plastic and released hydrogen gas in the form of bubbles. Gas formation amount is not significant.

Hydrogenation

It is recycling method. Plastic waste is mixed with hydrogen and coal liquefaction [2]. It converts into naphtha and oil gas. The product is condensed. To remove the chlorine, the condensate is pumped through a device called a hydrocracker. The principal byproducts of plastic waste hydrogenation include hydrochloric acid, halogenated solid residue, and gas.

Re-Extrusion

According to [9], this technique is a closed-loop primary recycling technology that uses discarded plastic in an extrusion process. Plastic trash that has not been polluted by other substances is utilized in this method. The recovered plastic is remade into other products made from the same material. It is ineffective and inefficient as it demands clean and strict sorting which increase cost of processing.

Pyrolysis

At high temperatures and in the absence of oxygen, pyrolysis breaks down polymers [14]. Plastics are derived from crude oil. The progressive depletion of renewable fossil fuels is a major long-term concern since it may take millions of years to replenish these resources, if they can be replenished at all. The value-added gases and carbon residue are also formed. Above mentioned methods are modern technologies used worldwide. It is simpler method and has efficient in complete decomposition of gases. The whole process carried out in anaerobic condition; that's why whole process is done without hampering environment.

Pyrolysis Process

Pyrolysis word is derived from the "Greek" where pyro means "fire" and lysis means "Decomposition". There is a liquid component, a gaseous component, an ion, and a solid residue that remain after pyrolysis [1]. Several different types of reactor systems, including batch semi-batch reactors, tubular beds, rotary kilns, fixed beds, and fluidized beds, have been designed and put into use. There is a large market for fixed bed reactors. The issue is solved by using catalytic pyrolysis [12]. Catalytic agents reduce reaction temperatures, promote breakdown reactions, and improve the overall quality of the products.

Methodology

The project aims to design a pyrolysis system for Islampur city. Hence, the methodology is structured along-wise. The data collection and literature review were carried out to find the scope suitable for the city. Then dry waste sample is collected from

Islampur Municipal Corporation Material Recovery Centre. The purpose of sample collection is to analyze the content of the waste sample. In the end, the collected sample is cleaned i.e., removal of dust soil, or other content like food are removed. Then the waste is segregated into papers, plastic, organic dry waste, foam, and clothing waste and their respective weights are noted. The stated methodology is as below:

- Data Collection and Literature Review
- Sample Collection of Waste from Solid waste management plant of Islampur City
- Preprocessing of sample collected
- Analysis of waste Sample Collected
- Shredding of Plastic Waste
- Pyrolysis of Plastic Waste
- Oil Generation.

2.1 *Materials and Methods*

2.1.1 Experimental Analysis of Dry MSW Sample

The dry waste sample of MSW is collected from the per day household collection of solid waste of Islampur city. The pre-processing involves cleaning and sorting of waste. The sample consists of paper, cloths, organic dry waste, plastic, and foam. In that, paper 53%, cloths 5%, organic dry waste 14%, plastic 22%, and foam 6%. Plastic content is considerable.

2.1.2 Experimental Setup for Pyrolysis Process

The plastic used in this study was MPW. A laboratory-scale model is prepared which has a fixed bed reactor schematic diagram shown in Figs. 2 and 3. The pyrolysis apparatus incorporates a pyrolysis chamber, thermostat, condenser, temperature sensor, heating coil, insulator, storage tank, valves, and gas outlet line [10].

Plastic waste is cleaned and allowing it to sundry. There are four plastic waste samples taken, PE, PP, PS, and MPW. Each waste sample of 1.5 kg was taken for the pyrolysis process. The plastic waste sample is shredded to 300–500 mm size. The effective length is 38 cm and the diameter is 15 cm of the stainless steel-made reactor. The reactor with plastic waste is heated with NZ catalyst heated up to 380 °C. To obtain temperature readings, a sensor is inserted into the pyrolysis area. In the combustion chamber, a 1:1 ratio of catalyst to plastic was required. The procedure took place in the reactor between 350 and 450 °C for a total of 160 min. Figure 4 displays the oil yield. The results of the pyrolysis process are listed in Table 3.

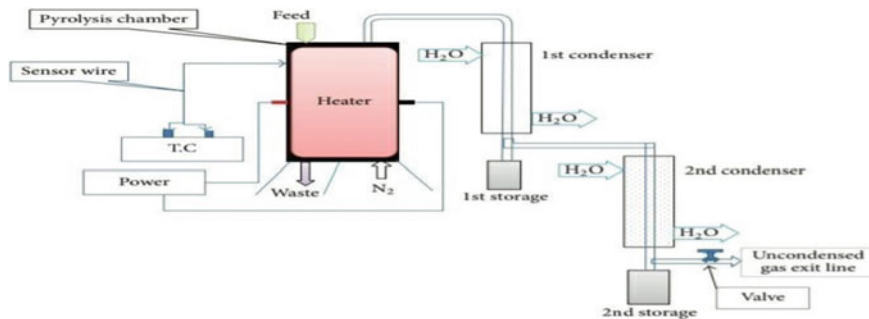


Fig. 2 Schematic diagram of pyrolysis setup



Gas Chamber



Reactor



Oil Collector

Fig. 3 Laboratory scale model



Fig. 4 Sample obtained in process

2.1.3 Results of Pyrolysis Process

The results of pyrolysis process tabulated in following Table 1.

The results of the pyrolysis process are stated above in percentage. It is seen that oil yield is comparatively higher in PS and MPW than in PE and PP (both having nearly equal results). Gas yield is significantly higher for PE and PP averagely near

Table 1 Product yield of different types of plastic waste

S. No	Sample	Oil in%	Gases %	Carbon residue%
1	PE	40	47	13
2	PP	39.88	41.1	19.02
3	PS	70	14.2	15.8
4	MPW	60	17.5	22.5

45% while in the case of PS and MPW it is lesser. The properties of oil produced from MPW are summarized in Table 2 as follows.

As per the report of tested oil, the oil is the best quality fuel for furnaces, and boilers and it is applicable for all applications which have a requirement of the same with a calorific value. It is also a lower cost. It has a very small amount of Sulphur emission and near to zero-carbon residue. Pyrolysis oil is the best alternative available at a lower cost than natural oil. Table 3 shows a comparison between pyrolysis oil, light diesel oil (LDO), and furnace oil (FO). As shown in Table 3, properties of pyrolytic oil are seen well than LDO and FO. The calorific value of pyrolytic oil (10,400) is lesser than LDO (10,450). It is not much significant. Other properties are better than other two oils.

Table 2 Product yield of mixed plastic waste

1	Color	Orange to dark brown
2	Calorific value	10,450
3	Specific gravity	0.81
4	Sulphur content	0.167%
5	Water content	0.05%
6	Flash point	< 40 °C

Table 3 Comparison between LDO, FO and Pyrolytic

So. No	Technical specification	LDO	FO	Pyrolyze
1	Calorific value	10,450	9500	10,400
2	Ash	0.02–0.04	0.02–0.04	0.0028
3	Carbon residue	1.5	2.0	0.0068
4	Density	0.84	0.92	0.81
5	Kinetic viscosity	2.5–5	80–125	1.5
7	Sulphur	1.8	4	0.167
8	Water content	0.25	10	0.05

3 Design of Pyrolysis System

As can be observed from the reviews of plastic, population, trash creation in Islampur, and pyrolysis technology that have already been presented, and the pyrolysis system will be useful for the city. A census never was taken because of covid-19. Hence, population forecasted in 2021 is 115,127. According to the latest data from the Central Pollution Control Board (2019), daily per capita plastic waste production was 10.41 g. Therefore, Islampur produces 1.2 tons of plastic waste per day. The pyrolysis plant's capacity is hence 2 tonnes while taking future scope into account.

3.1 Details of Pyrolysis Plant

Type of Pyrolysis Plant: Continuous Pyrolysis Plant Type of Pyrolysis Process: Catalytic Pyrolysis Reactor Used: Fixed bed reactor Cycle Time: 12 h.

3.2 Estimation of Pyrolysis Plant

- Cost of Plant: Rs. 18,750,000/-
- Erection and Installation Charges: Rs. 275,000/-
- Transportation Charge: At actual Sub Total = Rs. 19,025,000/-
- Pre-processing Machine:
 - (1) Shredding Machine: Rs. 240,000/-
 - (2) Grinding Machine: Rs. 370,000/-
 - (3) Aglow Machine: Rs. 550,000/-
 - (4) Dust Cleaning Machine: Rs. 17,500/- Sub Total = Rs. 1,335,000/-
- Land Required
 - (1) Plot: 8500 ft²
 - (2) Shed: 5500 ft².

Total Cost = Rs. 194,954,500/-
- Manpower Requirement
 - (1) Plant Operators = 4 = 4*15,000 Per Month = Rs. 60,000/-
 - (2) Pre-processing Labour = 4*7800 = Rs. 31,200/- 3) Supervisors = 3 = 3*23,000 = Rs.69,000/-.
- Miscellaneous Requirement
 - (1) Water: 3000 L per month = Rs. 27,000/-
 - (2) Electricity: 35 HP per month = Rs. 51,000/-
 - (3) Catalyst: 26000 kg = Rs. 520,000/-.

Table 4 One cycle requirement

S. No	Description	Quantity	Cost
1	Water required	112 L	1008
2	Electricity Required	1.3 HP	1970
3	Catalyst Required	1000 kg	20,000
4	Total manpower	11	6161.540

Total cost required for 1100-L = Rs. 29,140

Total Cost Required Per Month = Rs.758,200/-

- Cost Estimation Per Liter:

Oil generated by plant = 1100 L in one cycle (in one day) (Table 4).

4 Conclusion

Islampur City produces 1.2 tonnes of domestic plastic waste. From the analysis of the dry waste sample of MSW, it is seen that plastic content is 22% which is much higher. Pyrolysis involves combustion in a controlled environment and the resulting products are so much beneficial in maintaining the harmony of the environment and human health. The designed pyrolysis plant capacity is 2 tonnes per day. It has the efficiency to produce 1100 L of oil. The production cost of oil is much lesser than naturally producing oil. One liter of oil produced in Rs. 27/- is so much lesser. As stated above, the technology proves best in all ways.

References

1. Nakhate, A. S., & Sahasrabudhe, O. (2017). Grade analysis of pyrolysis oil by step distillation. *International Journal of Mechanical and Production Engineering*, 5(6), 120–124.
2. Dwivedi, A. K., Yadav, M. Kr., Kumar, A., Singh, G., & Singh, S. (2020). Design analysis and manufacturing of plastic fuel pyrolysis. *International Journal for Scientific Research and Development*, 8(7), 612–614.
3. Ayanoglu, A., & Yumrutas, R. (2016). Production of gasoline and diesel-like fuels from waste tire oil by using catalytic pyrolysis. *Energy*, 103, 456–468.
4. Acevedo, B., Barriocanal, C., & Alvarez, R. (2016). Pyrolysis of blends of coal and tire wastes in a fixed bed reactor and a rotary oven. *Fuel*, 113, 817–825.
5. Fekhar, B., Zsinka, V., & Miskolczi, N. (2020). Thermo-catalytic co-pyrolysis of waste plastic and paper in batch and tubular reactors for in-situ product improvement. *Journal of Environmental Management*, 269, 110–741.
6. Kumbhar, S. S., & Bamane, P. R. (2022). Effective plastic waste management and oil production by using pyrolysis process for Islampur city: A review. *International Journal of Research Publication and Reviews*, 3, 2392–2397.
7. Siddiqui, J., & Pandey, G. (2013). A review of plastic waste management strategies. *International Research Journal of Environment Science*, 2(12), 84–88.

8. Kumar, S., Prakash, R., Murgan, S., & Singh, R. K. (2013). Performance and emission analysis of blends of waste plastic oil obtained by catalytic pyrolysis of waste HDPE with diesel in CI engine. *Energy Conversion Management*, 74, 323–331.
9. Lee, K. (2009). Thermal and catalytic degradation of pyrolytic oil from pyrolysis of municipal wastes. *Journal of Analytical and Applied Pyrolysis*, 85, 372–379.
10. Ncube, L. K., Ude, A. U., Ogunmuyiwa, E. N., Zulkifli, R., & Beas, I. N. (2021). An overview of plastic waste generation and management in food packaging industries. *Recycling*, 6(12), 1–25.
11. Syamsiroa, M., Saptoadi, H., Norsujianto, T., Noviasria, P., Cheng, S., Alimuddin, Z., & Yoshikawa, K. (2014). Fuel oil production from municipal plastic wastes in sequential pyrolysis and catalytic reforming reactors. *Energy Procedia*, 47, 180–188.
12. Quadri, M. W., & Dohare, Er. D. (2020) A study to optimise plastic to fuel technology—A review. *International Journal of Engineering Research and Technology*, 9(4), 192–222.
13. Khan, M. Z. H., Sultana, M., Al-Mamun, M. R., & Hasan, M. R. (2016). Pyrolytic waste plastic oil and its diesel blend: Fuel characterization. *Journal of Environmental and Public Health*, 2016, 1–6.
14. Evode, N., Qamar, S. A., Bilal, M., Barcelo, D., & Iqbal, H. M. N. (2021). Plastic waste and its management strategies for environmental sustainability. *Case Studies in Chemical and Environmental Engineering*, 4, 100–142.
15. Yadav, R. J., Solanki, S., Saharna, S., Bhardwaj, J., & Ramvijay. (2020). Pyrolysis of waste plastic into fuel. *International Journal of Recent Technology and Engineering*, 9(1), 2600–2606.
16. Wiriyaumpaiwong, S., & Jaemradloerdruk, J. (2017). Distillation of pyrolytic oil obtained from fast pyrolysis of plastic wastes. *Energy Procedia*, 138, 111–115.
17. Wang, Y., Wang, S., Leng, F., Chen, J., Zhu, L., & Luo, Z. (2015). Separation and characterization of pyrolytic lignin from the heavy fraction of bio-oil by molecular distillation. *Separation and Purification Technology*, 2015(152), 123–132.
18. Xue, Y., Zhou, S., Brown, R. C., Kelkar, A., & Bai, X. (2015). Fast pyrolysis of biomass and waste plastic in a fluidized bed reactor. *Fuel*, 156, 40–46.

Intermittent Water System—A Review of Literature



Nitin P. Sonaje and Mukund M. Pawar

Abstract This literature review tries to examines the concept of intermittent water distribution network systems, which provides the water to consumers for only a few hours in a day. The review explores the reasons for the widespread use of Intermittent Water Systems (IWS) in few countries, including cost-effectiveness and water conservation. However, it also discusses the negative impacts of IWS, such as increased health risks due to the proliferation of waterborne diseases and social inequality resulting from differential access to water, inoperative water meters, resulting in revenue loss. Overall, the literature suggests that while IWS may provide short-term benefits in terms of cost and water conservation.

Keywords Intermittent water systems · Genetic algorithm · Stochastic programming model · Auto-regressive model · EPANET

1 Introduction

The scarcity of potable water is an important issue for most of the countries in the world. Most cities will have to manage themselves with intermittent service wherein water is provided to residents for a limited number of hours per day. An intermittent water supply scheme provides water for a certain period, bringing uncertainty to the water supply. This uncertainty brings various drawbacks to the system, like storing a large quantity of water resulting in its wastage while collecting fresh water again and inoperative water meters, resulting in revenue loss, increased health risks due to the proliferation of waterborne diseases and social inequality resulting from differential access to water.

N. P. Sonaje (✉)
Government Polytechnic, Miraj, Maharashtra, India
e-mail: nitinsonaje@gmail.com

M. M. Pawar
SVRI's College of Engineering, Pandharpur, Maharashtra, India

In this paper various approaches have been reviewed. The previous researchers have studied various parameters such as flow rate, diameter and length of pipe, losses through the pipes, sustainability of water distribution network, average specific demand, peak factor, pipe condition, energy loss, and decanter efficiency.

2 Study Approaches

There are different approaches of water supply systems. Previous researchers have studied water supply systems, which can be grouped in as shown in Fig. 1.

2.1 Computer Tool

The different software like SCADA, Bently WaterGEMS, GIS based DSS, ArcGIS, AutoCAD, GPS and ERDAS 9.1, EPANET have been used by previous researchers to study water distribution system. They have studied water supply system for different parameters viz., demand factor, peak factors, pipe condition, design horizons, etc.

Grayman et al. [1], observed that the water distribution system changes with advanced technology in operation and water quality in the past 40 years. The desired area, which involves a future improvement in the method of water distribution, was

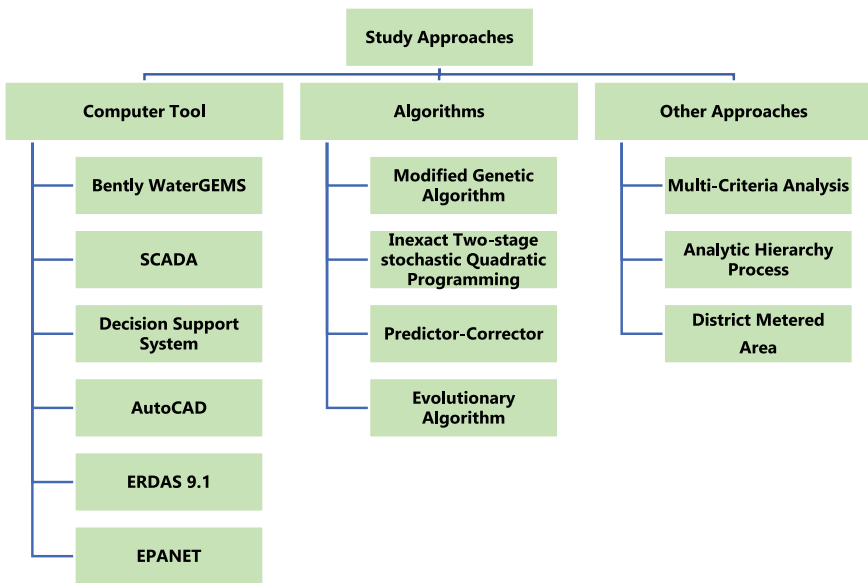


Fig. 1 Study approaches for water supply system

suggested. They demonstrated the future system, which will be completely regulated, tracked, and managed by a computer-funded system like SCADA from the customer's treatment plant. They also proposed the futuristic water distribution infrastructure by advancing the pipe techniques, operating, monitoring, asset control and construction.

Sumithra et al. [2], explored the water distribution network in Tirunelveli city of Tamil Nadu, India, and suggested the measures for improvement to the existing too aged, corroded CI pipes and incursion AC mains of large leakage distribution network. Two methods developed by LOOP and by Bentley WaterGEMS software were used to evaluate the future situation. The analysis indicates that the existing pipe network to be retabulated to cater the future demand after 36 years. WaterGEMS was found more efficient with graphical interface for varying demand pattern, peak factors, pipe condition and design horizons.

Eljamassi and Abeaid [3], examined and tested the existing operation and management of water distribution system network in the Rafah area in the Gaza strip, selected as a pilot study area with GIS based DSS. The study reveals that the advantage of man-aged water pipes' networks was the GIS and DSS modelling method for the assisted operation and maintenance system.

Chena and Boccelli [4], developed an integrated Time Series Forecasting Framework (TSFF) for prediction of statistically hourly demands in real-world and real-time scenarios with a Fixed Seasonal Auto-Regressive (FSAR) model and an Adaptive Seasonal Auto-Regressive (ASAR) model for evaluation. The performance of algorithm has been developed and evaluated to additional demand time series and compare the water consumption characteristics of different distribution systems for the medium-sized water supply system located in Florida, USA. Time Series Forecasting Framework (TSFF) interfaced with the SCADA infrastructure of water utilities. The TSFF was applied to additional demand time series for evaluation of the forecasted algorithm and compared the water consumption characteristics of different distribution systems.

Khadri and Pande [5], utilized GIS, GPS and RS technology for visualization, network planning, and mapping. This study aimed to develop the subject maps, monitor the pipe network, digitalize the water supply networks in the city of Chalisgaon in the state of Maharashtra, India and map the existing water distribution system. The programme used in this paper was ArcGIS, AutoCAD, GPS and ERDAS 9.1. This research's key emphasis was the use of remote detection and GIS to classify the current structures of water distribution.

Ramana et al. [6], published the efficient design and pipe network distribution using EPANET software for Chowduru of Ptoddaturumandal in Kadapa District of Andhra Pradesh, India. EPANET was useful for calculating flow rates, friction head losses, bent failure, and demand trends. EPANET tool offers information on the water distribution network panel.

Parrod [7], described SCADA, and hydraulic models' constraints were overcome for operators and operation engineers by integrating SCADA and hydraulic models. This paper analyses SCADA-hydraulic modelling integrations software and techniques for Bentley, allowing operators and service engineers to enhance the water

supply system process. SCADA data can automatically be merged into simulation applications through the software, Water GEMS.

Lungariya et al. [8], observed that pipe failure in the system disrupted the water supply to the consumer and reduced the reliability of the system. The existing model must then be controlled effectively by the inspection, checks, repair and recovery programme. The measurement of the pressure and lift as well as many nodes and head losses on each pipe was done using EPANET tools.

From the above said approaches, it can be concluded that can be used suitably to enhance the water supply system.

2.2 Algorithms

This subsection gives a brief review about various studies for water supply systems which use various algorithms, including Modified Genetic Algorithm (MGA), Inexact Two-stage stochastic Quadratic Programming (ITQP), Predictor–Corrector (PC) with statistical data-driven (M5 Model Trees) algorithm and Evolutionary Algorithm (EA).

Montesinos et al. [9], had proposed a Modified Genetic Algorithm (MGA) to solve the problems associated with expanding the water distribution system for New York City. For improvement in the water supply system design, GA was modified by improving the basic GA selection and mutation operations. Optimum design of a looped network for a gravity system was obtained to minimize investment cost using a set of pipe sizes by configuring the hydraulic elements and a sequence of defined node specifications. A constant number of solutions were discarded in each generation and the chosen solutions were labelled as convergence solutions. The new solutions were subjected to a cumulative mutation. All these modifications significantly boosted the convergence of the algorithm. This paper proved that the MGA was the lowest-cost feasible solution than the previously known GA for mutation.

Li and Huang [10], developed an inexact two-stage stochastic quadratic programming (ITQP) model for water-quality management under uncertainty. The ITQP handled uncertainties expressed as probability distributions and interval values, and nonlinearities in the objective function. It was also useful in analyzing various scenarios linked with different levels of economic penalties or opportunity losses caused by improper policies. The ITQP was applied to water-quality management in the presence of uncertainties in probabilities and intervals, which reflected dynamic interactions between pollutant loading and water quality. Interactive and derivative algorithms were employed for solving the ITQP model. The solutions were presented as combinations of the deterministic, interval, and distributional information, thus facilitating communications for different uncertainties.

Preis and Allen [11], presented an on-line hydraulic model for urban water distribution system in Singapore. In this model they had identified demand zones with optimization tools and graph algorithms within the topology of homogenous clusters. The on-line Predictor–Corrector (PC) with statistical data-driven (M5 Model

Trees) algorithm were applied to predict the future hydraulic states. The evolutionary optimization technique was used to correct the predictions with real-time monitoring states. The Genetic Algorithms with a modified Least Squares (LS) fit method was used to minimize the residuals between predicted and measured pressure and flow rates with hourly variations in the zone demand. This model has proved to be more comprehensive and elaborate on-line hydraulic model of the water distribution system.

McClymont et al. [12] has given a practical method for assessment of Evolutionary Algorithm (EA) operator behavior in the context of specific WDN design features of pumps, tanks and loops. This method was proved to be useful for WDN for establishing a prior understanding of an operator's efficacy and aids for the development of new specialist operators and then selection of the most appropriate operators. This method is tested with six EA operators on 60 artificial networks containing specific features. The analysis of performance of the six operators shows, 1-Step mutation operator performs well across the different artificial networks compares to the operators specialised for dendritic systems. The research also confirms while solving the WDN problems, the mutation operators were more effective on the simpler dendritic systems compared to the looped systems in which combined operators were more effective.

Through the algorithms, water distribution network problems can be solved efficiently and also used for improving water-quality management.

2.3 Other Approaches

Other approaches include study for different site—specific and cost-effective techniques required to be made in infrastructure. Some of the studies focus on the relationship between reliability, resilience and sustainability, calculation of average specific demand and analysis of the water supply system regarding water flow rate, energy loss, and decanter efficiency.

Pramanik and Rahman [13], attempted to assess the gap between the existing water requirement and the supply condition of the research area, in Pabna Municipality of Bangladesh. This research indicates different site-specific and cost-effective techniques to be developed in infrastructure.

Butler et al. [14], developed the conceptual framework of new approach to water management i.e., 'Safe and Sure' which identifies the role of mitigation and adaption of new strategies. This study proposed a discussion of engineering, organization and social options which develop a degree of resilience and sustainability needed to deal with the threats of twenty-first century. This paper has tried to explore the relationship between reliability, resilience and sustainability.

Annus and Vassiljev [15], calculated hourly and daily demand based on various customer categories such as domestic households, hotels, hospitals, industrial or business areas, etc. of the District Metered Area (DMA) of WDS of Tallinn, Estonia. Water consumption for the extended duration was typically calculated, which

provides the average specific demand information. This research tried to use the Water Distribution System (WDS) model to achieve successful, accurate calculation decrease errors.

Gunthera et al. [16], presented an experimental water distribution system (EWDS-TUG) configured with a smart water network consisting of measurement and control devices, data collection and communication, data display, and management as well as data fusion and evaluation. The advantages of the smart water grid were projected to increase the quality and durability of buried infrastructures.

Pandit and Crittenden [17] proposed a novel index of network resilience (INR) for urban water distribution systems, embracing resilience as a sustainability indicator. The index included six network attributes for constructing a hybrid INR based on the topology of the water distribution networks. A Multi-Criteria Analysis (MCA) was used to assess alternative solutions that would satisfy demand and other hydraulic requirements using the Weighted Summation method. Analytic Hierarchy Process (AHP) was designed for two scenarios: efficacy to assign weights to the attributes. Using the original configuration of any town network as the base case scenario, four alternative designs were developed. This article presents the comparative performance results.

Haut and Viviers [18], simulated the flow of water in several elements of the water supply system of the city of Apamea, Syria. The studied elements were used in the sixth century AD. These simulations allowed a modern point of view analysis of the water supply system regarding water flow rate, energy loss, and decanter efficiency. This analysis provided a qualitative description of the city's water supply system, supplementing the field observations.

These problem specific approaches allowed a modern point of view analysis for different water supply systems in respect of various parameters viz., flow rate, energy loss, and decanter efficiency.

3 Conclusion

Expanding the water distribution system by Genetic Algorithm (GA) Model for water distribution network optimization; Simulations allowed a modern point of view analysis of the water supply system regarding water flow rate, energy loss, and decanter efficiency by simulating the flow of water in several elements of the water supply system for qualitative description of the city's water supply system; Presented a general water supply planning tool consisting of modular components viz. Water source, users, recharge facilities, and water and wastewater treatment plants by dynamics simulation environment to get general water supply planning model; Online hydraulic state predictor (PC) model by using predictive data-driven algorithm (Predictor-corrector (PC) technique) for predict the potential hydraulic condition; Calculating flow rates, friction head losses, bent failure, and demand trends for getting the efficient design and pipe network distribution using EPANET software.

References

1. Grayman, W. M., Murray, R., & Savic, D. A. (2009). Effects of redesign of water systems for security and water quality factors. In *World Environmental and Water Resources Congress 2009*, Great Rivers (pp. 1–11).
2. Sumithra, R., & Amaranath, J. (2013). Feasibility analysis and design of water distribution system for Tirunelveli corporation using loop and WATERGEM software. *International Journal on Applied Bioengineering*, 7(1), 61–70.
3. Eljamassi, A., & Abeaid, R. A. (2013). A GIS-based DSS for management of water distribution networks (Rafah city as case study).
4. Chen, J., & Boccelli, D. L. (2014). Demand forecasting for water distribution systems. *Procedia Engineering*, 70, 339–342.
5. Khadri, S. F. R., & Pande, C. (2014). Urban water supply systems—A case study on water network distribution in Chalisgaon City in Dhule District Maharashtra using remote sensing and GIS techniques. *IOSR Journal of Mechanical and Civil Engineering*.
6. Ramana, G. V., Sudheer, C. V., & Rajasekhar, B. (2015). Network analysis of water distribution system in rural areas using EPANET. *Procedia Engineering*, 119, 496–505.
7. Parrod, P. (2016). Water system operations made easier enriching SCADA data through hydraulic modeling. A Bentley Technical Paper Water System Operations Made Easier, Bentley.
8. Lungariya, P., Katharotiya, N., Mehta, D., & Waikhom, S. (2016). Analysis of continuous water distribution in Surat city using EPANET: A case study. *Global Research and Development Journal of Engineering*, 1–7.
9. Montesinos, P., Garcia-Guzman, A., & Ayuso, J. L. (1999). Water distribution network optimization using a modified genetic algorithm. *Water Resources Research*, 35(11), 3467–3473.
10. Li, Y. P., & Huang, G. H. (2009). Two-stage planning for sustainable water-quality management under uncertainty. *Journal of Environmental Management*, 90(8), 2402–2413.
11. Preis, A., Allen, M., & Whittle, A. J. (2010). On-line hydraulic modeling of a Water Distribution System in Singapore. In *Water distribution systems analysis 2010* (pp. 1336–1348).
12. McClymont, K., Keedwell, E., & Savic, D. (2015). An analysis of the interface between evolutionary algorithm operators and problem features for water resources problems. A case study in water distribution network design. *Environmental Modelling and Software*, 69, 414–424.
13. Pramanik, Md. A., & Rahman, M. M. (2013). Urban water supply network analysis: A case study on Pabna municipality. *Bangladesh*, 1(8), 121–126.
14. Butler, D., Farmani, R., Fu, G., Ward, S., Diao, K., & Astaraie-Imani, M. (2014). A new approach to urban water management: Safe and sure. *Procedia Engineering*, 89, 347–354.
15. Annus, I., & Vassiljev, A. (2015). Different approaches for calibration of an operational water distribution system containing old pipes. *Procedia Engineering*, 119, 526–534.
16. Günther, M., Camhy, D., Steffelbauer, D., Neumayer, M., & Fuchs-Hanusch, D. (2015). Show-casing a smart water network based on an experimental water distribution system. *Procedia Engineering*, 119, 450–457.
17. Pandit, A., & Crittenden, J. C. (2016). Index of network resilience for urban water distribution systems. *International Journal of Critical Infrastructures*, 12(1–2), 120–142.
18. Haut, B., & Viviers, D. (2007). Analysis of the water supply system of the city of Apamea, using Computational Fluid Dynamics. Hydraulic system in the north-eastern area of the city, in the Byzantine period. *Journal of Archaeological Science*, 34(3), 415–427.

Extraction of Cellulase from Soil Microorganisms by Using Banana Peels as Substrate



Samir Pachpute, Chetan Pawar, and Sanjana T. Philip

Abstract Higher production of essential food commodities and the lack of adequate methods and facilities for managing these, as well as their components, by-products and residues, have led to tremendous losses and waste. Bananas are one of the most widely consumed fruit and are available throughout the year. In this study, attempts were made to use Banana peels as a substrate for production and extraction of cellulase by *Bacillus subtilis*. Optimization and characterization studies were also carried out. On quantitative analysis, it was found that *B. subtilis* showed an activity of FPase 0.09 IU/ml and CMCase 0.182 IU/ml respectively. Further, partial purification of the extracted cellulase was also carried out. Enzyme activity of purified enzyme was 0.2144 IU/ml when assessed by DNS method. This method revealed a much easier and low expensive protocol for the production of extracellular enzyme cellulase by solid-state fermentation.

Keywords Cellulase · *B. subtilis* · Banana waste · Cellulose

1 Introduction

In our diet and human life, fruits and vegetables play a crucial role, and as a result of the world population and evolving dietary habits, demand for such essential food composites has increased quite significantly. Higher production and development, and the lack of adequate methods and facilities for managing these essential food commodities, as well as their components, by-products and residues, have led to tremendous losses and waste. For juice or pulp extraction, jams, and frozen pulp, many fruits and vegetables, such as banana, oranges, pineapples, peaches, apples,

S. Pachpute (✉) · C. Pawar
Department of Microbiology, MGM Medical College and Hospital, MGM Institute of Health Sciences, Sector 1, Kamothe, Navi Mumbai, Maharashtra 410209, India
e-mail: drsamirpachpute@gmail.com

S. T. Philip
Department of Medical Biotechnology, MGM School of Biomedical Sciences, MGM Institute of Health Sciences, Sector 1, Kamothe, Navi Mumbai, Maharashtra 410209, India

potatoes, carrots, green peas, onions, artichokes, and asparagus, are used, generating large quantities of waste [1].

Banana peels constitute about 35% of total banana as waste and losses. They contain 60–65% cellulose, 6–8% hemicellulose, and 5–10% lignin. Cellulose is a homo-polymer of β -1, 4 bond-linked d-glucose units. It is the most abundant biomass in the biosphere and a major structural part of plants and a renewable source of energy [2]. Therefore, the production of suitable methods for the successful treatment and use of cellulose-containing waste as a cheap source of carbon has become of significant economic interest. Cellulose is primarily degraded by the enzyme cellulase, usually produced by bacteria and fungi [3]. The most widely studied cellulase-producer are from the genera *Bacillus*, *Clostridium*, *Cellulomonas*, *Thermomonospora*, *Trichoderma*, and *Aspergillus*. In various industries, including pulp and paper, textiles, laundry, biofuel processing, food and feed, brewing, and agriculture, microbial cellulases have demonstrated their potential application [4].

Bananas are one of the most widely consumed fruits in the world, and India is one of the major banana producers. Farmers discard the majority of the residual wastes generated by banana cultivation into surrounding waterways, streams, and highways, creating a great environmental threat. Leaves and pseudo stems (flattened and modified stems) are leftover wastes from banana crops. This pseudo stem is rich in lignocellulose. Some bacteria use these lignocellulosic products as a source of cellulolytic enzymes, which have a wide variety of applications in various industries [5].

Gram-positive *Bacillus* species are among the top producers of secreted enzymes among bacteria. *Bacillus subtilis*, and *Bacillus licheniformis* have become the most common bacteria in biotechnological protein production processes due to their excellent fermentation properties, high product yields (20 to 25 g/L), and lack of toxic by-products. The high amenability of *B. subtilis* to genetic alteration and large-scale fermentation made it the organism of choice for agricultural applications [6].

This study was conducted at Microbiology Laboratory and Central Research Laboratory of MGM Medical College and Hospital, Navi Mumbai. The project was conducted to study the utilization of banana waste for the value-added byproduct such as cellulase enzyme using soil-based cellulase-producing bacteria. The usage of *Bacillus subtilis* in the study and its ability to produce cellulolytic enzyme such as endo-1, 4-D-glucanase via solid state fermentation of the substrate (banana peels) was assessed. Quantitative estimation of the cellulase was performed using Carboxy-methyl cellulase activity (CMCase) and Filter paper activity (FPAase) and the released reducing sugar was assessed by DNS method. The protein content in the extracted cellulase was estimated by Bradford method. Further, the crude enzyme was partially purified using the ammonium sulphate precipitation method and its enzyme activity and specific activity was determined.

2 Materials and Methods

25 gm of banana peel waste was collected from the fruit juice vendors from MGM Canteen, MGMIHS, Kamothe Navi Mumbai. Soil samples were obtained from MGM Medical College Ground, MGMIHS, Kamothe Navi Mumbai.

Analytical grade chemicals were used in the study, which are mentioned as- 1% Congo red, 1 M sodium chloride, crystal violet, gram's iodine, safranin, hydrogen peroxide, 0.01 M acetate buffer pH 6.5, of 0.05 M sodium citrate buffer pH 4.8, Bradford reagent, ammonium sulphate, sodium bicarbonate and distilled water. Sterile nutrient media such as Nutrient Broth, 1% Carboxy Methyl Cellulose Agar, were used.

Equipment and glassware such as autoclave, shaker, spectrophotometer, autoclave, pH-meter, thermometer, boiling water bath, glass pipette, Erlenmeyer flasks, glass beakers, glass spreaders, etc., were used.

2.1 Isolation and Primary Screening of Cellulolytic Bacteria

2.1.1 Isolation of Cellulase-Producing Bacteria

1 gm of soil was inoculated in sterile 5 ml of nutrient broth. This sample was serially diluted up to 10^{-6} in nutrient broth. And colonies were isolated using spread-plate technique, on Carboxy Methyl Cellulose Agar plate (containing 0.5 g KH_2PO_4 , 0.25 g MgSO_4 , 0.25 g cellulose and 2 g gelatin). These plates were incubated at 37 °C for overnight. Bacterial colonies were purified by repeated streaking [3].

2.1.2 Primary Screening/Qualitative Determination of CMC Case Activity

Primary screening of cellulase activity was carried out using Carboxy-Methyl Cellulase (CMCase) activity. The pure isolated colony was inoculated at the center of the CMC agar plate and kept for incubation at 37 °C for 24 h. On the next day, the incubated plate was flooded with the 1% Congo red and kept for 5 min. It was further washed with 1 M NaCl [3].

2.1.3 Identification of Isolated Bacteria

Morphological Characterization

The gram nature of the bacteria was determined using Gram's staining method. The presence of endospores was determined using Endospore staining by Schaeffer-Fulton method. The motility of the bacteria was observed using the hanging drop technique [3].

Biochemical Characterization

Further identification of isolated bacteria was done by various biochemical tests such as catalase test, oxidase test, Sugar fermentation test, Triple Sugar Iron (TSI) Agar test, IMVIC test, urease test, nitrate reduction test, phenylalanine deaminase test, and gelatin hydrolysis test, as per the standard methods [3].

2.2 *Preparation of Substrate by Solid State Fermentation Method*

25 g of Banana peels were collected from the fruit vendors. Peels were chopped into very small pieces and added into the 500 ml conical flask and moisten with 75 ml of distilled water. The flask was autoclaved for 2 h at 121 °C for sterilization. After sterilization flask was allowed to reach room temperature and then it was inoculated with the 20 ml of *Bacillus subtilis* inoculum and incubated at 32 ± 2 °C in a BOD incubator. The sample was collected after an interval of 40 days [5].

2.3 *Sampling and Extraction of Crude Cellulase Enzyme*

The crude enzyme was extracted from the 25 gm banana peel sample using 100 ml of 0.01 M cold Acetate buffer (pH 6.5). This homogenate was filtered through the 200 mesh nylon cloth. The filtrate was centrifuged at 6000–8000 rpm at 4 °C for 30 min. The supernatant was analyzed further for endo-1,4- β -glucanase (CMCase) and Exo-1, 4- β -glucanase (FPase) activity [5].

2.4 Quantitative Determination of Cellulase Activity

2.4.1 Filter Paper (FPase) Activity

Mendels and Weber method was used to determine the filter paper activity of the culture filtrate. Here, Whatman's filter paper (No. 1) strip of 50 mg weight was used as the substrate. It was suspended in 1 ml of 0.05 M sodium citrate buffer (pH 4.8) at 50 °C in water bath. 0.5 ml of enzyme aliquot was added to reaction mixture and incubated at 50 °C in the water bath for 1 h. A control was run simultaneously without enzyme [5]. After incubation, the reduced sugar was estimated using 3, 5-dinitrosalicylic acid (DNS) method [7]. One filter paper unit (FPU) was defined as the amount of enzyme releasing 1 mol of reducing sugar from filter paper /ml /h [5].

2.4.2 Carboxy Methyl Cellulose (CMCase) Activity:

Enzyme activity of endoglucanases in the culture filtrate was quantified by CMCase method. The reaction mixture with 1% carboxy methyl cellulose in 0.02 M acetate buffer (pH 5.0) was pre-incubated at 50 °C in water bath for 20 min. 0.5 ml of filtrate with appropriate dilutions was added to the reaction mixture and incubated at 50 °C in the water bath for 1 h. A control was run simultaneously without enzyme [5, 8]. Following incubation, DNS method was used to estimate the reducing sugars [7]. One unit of endo- β -1,4-glucanase activity was defined as the amount of enzyme that could hydrolyze CMC and release 1 μ mol of glucose within 1 min of reaction [3, 9].

2.4.3 Enzyme Activity (U/ml) for CMCase Activity and FPase Activity

= O.D at 540 nm \times μ M of glucose (from standard graph) \times dilution factor 0.1 \times Incubation time (min) \times aliquots of enzyme (ml) \times MW of glucose (gm) [5].

2.5 Determination of the Specific Activity

The protein concentration in the crude cellulase was determined by the Bradford method [10].

2.5.1 Specific Activity

Enzyme activity (Units/ml)/total protein concentration (mg/ml) [3].

2.6 *Partial Purification of Crude Cellulase*

The crude enzyme was precipitated using 70% ammonium sulphate and this mixture was incubated for 4 °C for 24 h. After incubation, the mixture was centrifuged at 10,000 rpm for 20 min and the pellet was dissolved in phosphate buffer (pH 7). The partially purified enzyme was dialyzed against phosphate buffer (pH 7) for 24 h, to remove salts [3]. The activity and the specific activity of partially purified cellulase were carried out as mentioned earlier.

2.7 *Characterization of Partially Purified Cellulase*

2.7.1 *Effect of Temperature on Cellulase Activity*

The partially purified cellulase was incubated with 1% CMC for 20 min at different temperatures i.e. 25, 30, 37, 40, 45 °C. The enzyme activity was determined by using DNS method [3, 11].

2.7.2 *Effect of pH on Cellulase Activity*

Phosphate buffer of different pH 5.8, 6.5, 7.0, 7.5, 8.0 were prepared. 1 ml of respective buffer was added to 1 ml of enzyme with substrate and incubated at RT for 20 min. The enzyme activity was determined by the DNS method [3, 11].

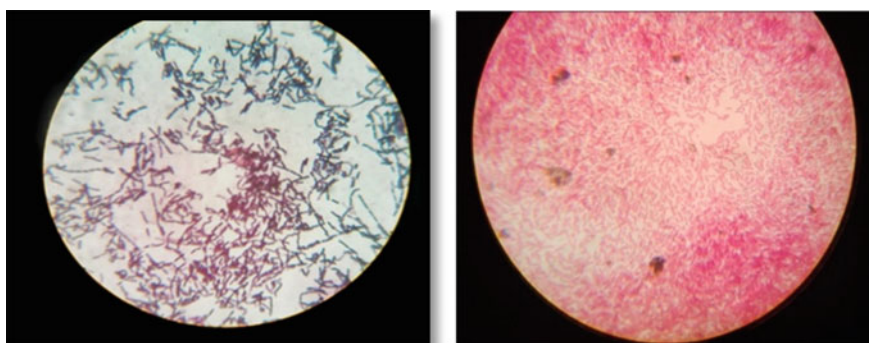
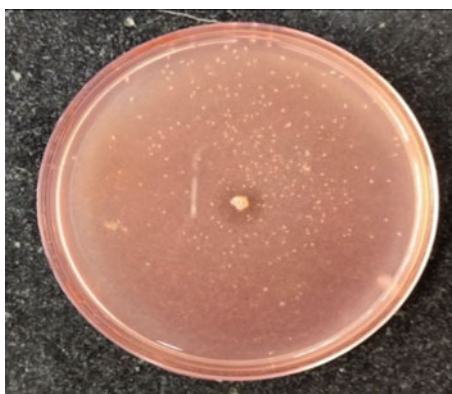
3 *Results and Discussion*

3.1 *Isolation, Primary Screening, and Identification of Cellulase-Producing Bacteria*

A clear halo zone of around 14 mm diameter was observed around pure colonies of isolated bacteria from soil, on the CMC agar plate after the addition of Congo red and 1 M NaCl. This indicates the hydrolysis of cellulose using cellulase enzyme. These colonies were further identified by using morphological and biochemical methods. Gram-positive bacilli of rod-shaped were observed upon Gram staining, during microscopic examination. Endospores were also observed. The biochemical characterization used for the identification of the isolated organism is mentioned in Table 1. Based on morphological and biochemical characterization, the isolated organism from the soil was identified to be *Bacillus subtilis* (Figs. 1 and 2).

Table 1 The activity and specific activity of partially purified cellulase

Sample	Enzyme activity (U/ml)	Amount of protein present (in mg/ml)	Specific activity (U/ml/mg protein)
Partially purified cellulase	0.2144	1.021	0.209

Fig. 1 1% CMC agar plate showing clear zone after addition of 1% Congo red**Fig. 2** a Gram staining b Endospore staining of isolated bacteria

3.2 Quantitative Determination of Cellulase Activity

Cellulase activity was determined quantitatively by DNS method. The activity was calculated using standard glucose curve by absorbance at 540 nm. The enzyme activity of CMCase and FPAse was found as 0.182U/ml and 0.09 U/ml respectively.

Table 2 Various biochemical tests used for identification of isolated bacteria

S. No	Biochemical test	Observation
1	Motility test	Motile
2	Catalase test	Positive
3	Oxidase test	Positive
4	Glucose	Pink coloration with no gas
5	Sucrose	Pink coloration with no gas
6	Lactose	No fermentation occur
7	Mannitol	Pink coloration with no gas
8	Triple sugar iron test	Alkaline/Acid (K/A)with no gas
9	Indole test	Negative
10	VP test	Positive
11	Citrate utilization test	Positive
12	Urease test	Negative
13	Nitrate reduction test	Positive
14	Phenylalanine deaminase test	Negative
15	Gelatin hydrolysis test	Negative

3.3 Determination of Specific Activity

The amount of protein present in the crude cellulase was calculated by the standard BSA curve using Bradford method, and it was found to be 16.807 mg/ml. The specific activity of the crude cellulase was calculated to be 0.0108.

3.4 Partial Purification of Crude Cellulase

Partial purification of the crude cellulase enzyme extract was carried out by ammonium sulphate precipitation method, followed by using dialysis. The activity and specific activity after partial purification is mentioned in Table 2.

4 Characterization of Partially Purified Cellulase

4.1 Effect of Temperature on Cellulase Activity

The partially purified cellulase was incubated with its substrate (carboxy-methyl cellulose) for 20 min at different temperatures i.e. 25, 30, 37, 40, 45 °C. Maximum enzyme activity (0.204 IU/ml) was found to be at 40 °C (Fig. 3).

Fig. 3 Effect of various temperatures on cellulase activity, as determined using DNS method

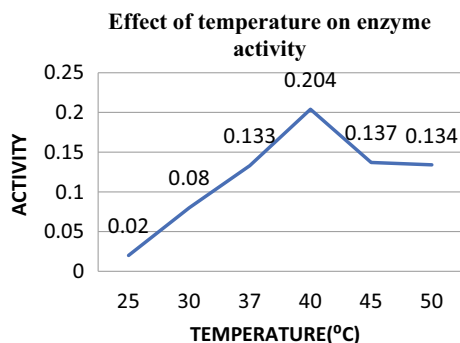
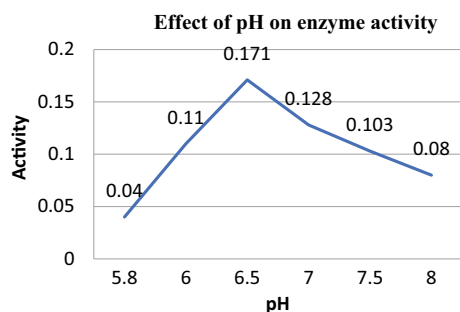


Fig. 4 Effect of various pH on cellulase activity, as determined using DNS method



4.2 Effect of pH on Cellulase Activity

Phosphate buffer of different pH 5.8, 6.5, 7.0, 7.5, 8.0 were prepared. 1 ml of respective buffer was added to 1 ml of enzyme with substrate and incubate at RT for 20 min. The optimum pH was found to be pH 6.5 (Fig. 4).

In the current study, banana waste was used as substrate for the cellulase enzyme production using *Bacillus subtilis*. *Bacillus subtilis* was isolated and identified by colony morphology on agar plate and by using various biochemical tests. Ability of *Bacillus subtilis* to produce cellulase enzyme was primarily determined by using CMC agar plate on which zone of clearance was observed (14 mm). Crude CMCase and FPase activity found was 0.182 U/ml and 0.09 U/ml respectively. Further partial purification of enzyme was done by ammonium sulphate precipitation method, followed by dialysis method. Enzyme activity of purified enzyme was 0.2144 $\mu\text{mol}/\text{min}$ i.e. IU/ml when assessed by the DNS method. Protein estimation enzyme of purified was found 1.021 mg/ml done by the Bradford method. Further the cellulase was characterized for its optimum temperature and pH for its activity and find out that enzyme activity was maximum at temperature 40°C i.e. 0.244 $\mu\text{mol}/\text{min}$ i.e. IU/ml and pH at 6.5 i.e. 0.171 IU/ml. Our results were comparable with previous studies described below. At the end of study it was found that optimum temperature and pH for the enzyme was 40 °C and pH 7 respectively, which is similar to our study [12].

It was found that cellulase activity was increased by increasing glucose significantly i.e. 0.475 ± 0.019 IU/ml/min. Nitrogen source including NH_4Cl and peptone in the medium results in the cellulase activity found as 0.450 ± 0.012 and 0.474 IU/ml/min. when incubated at 37°C for 48 h. Endoglucanase activity was maximum i.e. 0.451 ± 0.011 IU/ml/min. at optimum pH 7.5. Cellulase produced by the *Cellulomonas sp.* Showed optimum activity at 60°C . However, in our study, enzyme activity was maximum at 40°C , as *B. subtilis* was our cellulase producer. In the study performed by Rathnan, R.K. & Mechoor, Ambili, 10 isolates were collected from the different fruit waste. After extraction of the enzyme, the effects of various parameters like temperature and pH on enzyme activity was assessed and it was found that enzyme activity was maximum at pH 5 and at 50°C [13].

5 Conclusion

The bioconversion of cellulose to soluble sugars is important for global stabilization and sustainable human society. It is possible to degrade cellulose complex which is present in nature by using various microbial communities. Using the preliminary studies conducted by previous researchers, we formulated and conducted our study to extract cellulase enzyme from the banana peels as substrate using *Bacillus subtilis*, obtained from the soil. Therefore, the current study reveals that banana peel waste can be used as the substrate using the solid-state fermentation, instead of agro-industrial waste, and wheat bran/ straw, which are already in use for the production of cellulase enzyme. This method reduces the time required for degradation and no major foul odor is released. Cellulases are being commercially produced by many industries worldwide and are largely being used in food, animal feed, fermentation processes, agriculture field, paper, and textile industries, etc. Considering modern microbiological tools, novel enzyme applications will become available for various industries. This method revealed a much easier and cheaper protocol for the production of the extracellular enzyme Cellulase by Solid-state fermentation. Keeping this in mind, further study may be required to expand our work for possible future applications of this method.

Acknowledgements The authors wish to thank Hon'ble Vice Chancellor, MGM Institute of Health Sciences, Navi Mumbai for permitting us to conduct this study at MGMIHS. We would also acknowledge some of our MSc students from the Department of Microbiology, MGMIHS, Navi Mumbai, for their support to complete the study successfully.

References

1. Sagar, N., Pareek, S., Sharma, S., Yahia, E., & Lobo, M. (2018). Fruit and vegetable waste: bioactive compounds, their extraction, and possible utilization. *Comprehensive Reviews in Food Science and Food Safety*, 17(3), 512–531.
2. Widiastuti Agustina, E., & Elfi, S. V. (2018). Natural wrapping paper from banana (*Musa paradisiaca* Linn) peel waste with additive essential oils. *Journal of Physics: Conference Series*, 1022, 012032.
3. Islam, F., & Roy, N. (2018). Screening, purification and characterization of cellulase from cellulase producing bacteria in molasses. *BMC Research Notes*, 11(1).
4. Kuhad, R., Gupta, R., & Singh, A. (2011). Microbial cellulases and their industrial applications. *Enzyme Research*, 2011, 1–10.
5. Dabhi, B. K., Vyas, R. V., Shelat, H. N. (2014). Use of banana waste for the production of cellulolytic enzymes under solid substrate fermentation using bacterial consortium. *IJCMAS*, 3(1), 337–346
6. van Dijl, J., & Hecker, M. (2013). *Bacillus subtilis*: From soil bacterium to super-secreting cell factory. *Microbial Cell Factories*, 12(1), 3.
7. Miller, G. L. (1959). Use of dinitrosalicylic acid reagent for the determination of reducing sugars. *Analytical Chemistry*, 31, 426–428.
8. Sajith, S., Sreedevi, S., Priji, P., Unni, K., & Benjamin, S. (2015). Production and partial purification of cellulase from a new isolate, *Penicillium verruculosum* BS3. *British Microbiology Research Journal*, 9(1), 1–12.
9. Shanmugapriya, K., Saravana, P. S., Krishnapriya, M. M., Mythili, A., & Joseph, S. (2012). Isolation, screening and partial purification of cellulose from cellulose producing bacteria. *International Journal of Advanced Biotechnology and Research*, 3, 509–514.
10. Bradford, M. (1976). A rapid and sensitive method for the quantitation of microgram quantities of protein utilizing the principle of protein-dye binding. *Analytical Biochemistry*, 72(1–2), 248–254.
11. Irfan, M., Safdar, A., Syed, Q., & Nadeem, M. (2012). Isolation and screening of cellulolytic bacteria from soil and optimization of cellulase production and activity. *Turkish Journal of Biochemistry/Turk Biyokimya Dergisi*. 2012 Jul 1;37(3).
12. Sethi, S., Datta, A., Gupta, B. L., & Gupta, S. (2013). Optimization of cellulase production from bacteria isolated from soil. *International Scholarly Research Notices*, 2013
13. Rathnan, R. K. & Mechoor, A. (2011). Cellulase enzyme production by streptomyces Sp. using fruit waste as substrate. *Australian Journal of Basic and Applied Sciences*, 5, 1114–1118.

In Vitro Leaf Injection Method for Detecting the Pathogenicity of Pomegranate Bacterial Blight Pathogen



Mrudula M. Bendigeri, Girish R. Pathade, and Yasmin C. Attar

Abstract Pomegranate is called as ‘fruit of paradise’ due to its multiple uses. However, pomegranate yield is adversely affected by infection by various phytopathogens. One of the hazardous pathogens is *Xanthomonas axonopodis* pv *Punicae* causing bacterial blight, the disease commonly known as Telya disease. In current research work, the pathogen was isolated from infected pomegranate fruits and leaves. The pathogen was studied for its cultural, morphological, biochemical and genetic characters. The pathogenicity of the isolate was determined by in vitro pathogenicity test in petri plate. The fresh healthy leaves were removed from the plant. Those leaves were artificially injected with the isolate. The leaves were observed for development of symptoms.

Keywords Pomegranate · Telya disease · In vitro pathogenicity

1 Introduction

Pomegranate (*Punica granatum* L), belonging to family Lythraceae, is an ancient favourite fruit of tropical and subtropical countries of the world. It is one of the important commercial fruit crops of an Indian farmer. It is called as ‘fruit of paradise’. In India, it is mainly cultivated in Maharashtra, Karnataka and Andhra Pradesh. In Maharashtra, it is cultivated in Solapur, Beed, Jalana, Sangli, Nashik, Ahmednagar, Pune, Dhule, Aurangabad, Satara, Osmanabad, Wardha and Latur districts. Thus, pomegranate has occupied export market worldwide [1]. However, pomegranate is suffering from various phytopathogens. One of them is *Xanthomonas axonopodis* PV. *Punicae*. It produces a disease commonly known as bacterial blight of pomegranate. The pathogen affects leaves, twigs, stem, buds, flowers and fruits [2]. However, the

M. M. Bendigeri (✉) · G. R. Pathade
Krishna Institute of Allied Sciences, KVVDU, Karad, Maharashtra, India
e-mail: bendigerimrudula@yahoo.in

Y. C. Attar
Rajaram College, Kolhapur, Maharashtra, India

disease is more destructive when fruits are affected. On the plant parts, the pathogen produces small spots or lesions. The spots are initially small and round. They are surrounded by bacterial ooze. Under favorable conditions, the spots enlarge and get converted into dark brown water filled lesions with indefinite margins and then appear as oily spots. (Hence the disease is commonly known as Telya disease). It results into cracking of fruit, defoliation and sometimes drying and death of plants. It was a disease of minor economic importance till 1998. But the incidences of the disease were ever increasing. Bacterial blight has caused considerable economic losses to the pomegranate farmers. It may cause up to 90% reduction in yield. The disease is reported to cause 30–50% losses on an average. However, under favorable environmental conditions, 80 to 90% losses are reported [3]. Various measures are taken to control the disease. Whichever is the method of control, the first step is isolation of pathogen from infected pomegranate plant parts [4]. Here, bacterial blight pathogen was isolated from infected pomegranate leaves. The pathogen was studied for its morphological, cultural, biochemical and genetic characters. It was confirmed to be of *Xanthomonas* species. However, any organism cannot be declared as pathogen unless its pathogenicity is reconfirmed by applying on its own host [5]. Hence, the pure culture of isolated pathogen was applied to the healthy pomegranate leaves in petri plate. Another healthy leaf was kept as control. It was not inoculated with pathogen. During reconfirmation, the pathogen produced the black spots on the leaves. These spots were compared with the original spots. It was found that the pathogen produced the similar symptoms as those produced by Xap. Thus, the pathogenicity of the culture was reconfirmed by in vitro detached leaf assay.

2 Materials and Methods

2.1 Preparation of Bacterial Suspension

Initially, the suspension of the isolated culture was prepared in sterile saline. The cell density was adjusted to 10^7 cells per ml.

2.2 Preparation of Filter Assembly

Whatmann filter paper number 1 was cut in the form of a circular piece of 90 mm diameter. This paper was placed aseptically at the base of a sterile petri plate. The paper was soaked with sterile distilled water up to its holding capacity. The excess water was drained from the petriplate.

2.3 Collection of Pomegranate Leaves

The healthy pomegranate leaves were collected from pomegranate plant variety Ganesh from the pomegranate plants at Mohite Colony, Kolhapur, Maharashtra. The leaves were directly collected into a beaker containing sterile water. The leaves were rinsed in sterile distilled water twice to remove the surface dust and attached microorganisms.

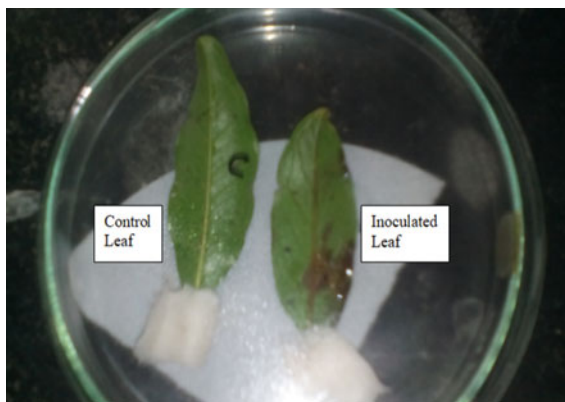
2.4 In Vitro Infection of Leaves

The leaves were placed in the above petri dish in such a manner that the lower side of the leaves were facing in upward direction. Two leaves were placed in a single petri plate. The petioles of the leaves were wrapped with moistened cotton swabs. Then fine pricks were made on the upper surface of the single leaf with the help of a sterile dissection needle. Immediately 15–20 ul of bacterial inoculum was aseptically drop inoculated with the help of sterile micropipette on the surface of this pricked leaf. The second leaf was kept uninoculated and used as control. The plate was covered with the lids. The plate was incubated at 28 °C for 5–7 days. The leaves were observed for development of symptoms.

3 Results and Discussion

After incubation of the pomegranate leaves in petri plate at 28 °C for 7 days, the inoculated leaf developed typical bacterial blight spots on its surface. The second uninoculated control leaf did not develop spots on its surface (Fig. 1).

Fig. 1 Development of spots on the surface of inoculated leaf



The appearance of water-soaked lesions on the lower surface of spray-inoculated leaves is the characteristic feature of bacterial blight of pomegranate [4]. The development of water-soaked lesions, initially transparent and greyish yellow that later on coalesce to form typical oil like spots is the characteristic feature of bacterial blight of pomegranate [6]. It indicated that the pathogenicity characters of isolated culture are similar to the pathogenicity characteristics of pomegranate bacterial blight pathogen. Considering the results of this experiment, this culture was later on studied for its genetic characters. After genetic characterization, this organism was identified as *Xanthomonas vasicola*. The genome sequence of this isolate was submitted to NCBI gene bank. The NCBI gene bank has provided the accession number MN658853 to this strain. The strain was labelled as *Xanthomonas vasicola* MY strain. This strain is also deposited at National Collection of Microbial Resources (NCMR) (Culture deposition accession number MCC 4830).

4 Conclusion

There are various techniques of detection of pathogenicity. Some techniques make use of whole plant while some techniques can be performed in laboratories. In vitro leaf injection method is the in vitro technique of detection of pathogenicity that can be performed in laboratory. The technique is simple, easy, less costly, requires minimum equipments and glasswares. Last but not the least, the technique is reliable, reproducible and can be applied for any plant pathogen.

Acknowledgements The entire work has been carried out in the laboratory of Rajaram College, Kolhapur. The current research work was not funded by any funding agency.

Conflict of Interest There is no any conflict of interest between the authors.

References

1. Ayyappan, S. (2015) Executive summary of vision 2015. *Vision 2050*, 1–15.
2. Asgary, S., Javanmard, S., & Zarfeshany, A. (2014). Potent health effects of pomegranate. *Advanced Biomedical Research*, 3(1), 100–110. <https://doi.org/10.4103/2277-9175.129371>
3. Raghuvanshi, K. S., Hujare, B. A., Chimote, V. P., & Borkar, S. G. (2013). Characterisation of *Xanthomonas axonopodis* PV. *punicae* isolates from western Maharashtra and their sensitivity to chemical treatments. *N Save Nature to Survive*, 8(3), 845–850
4. Doddaraju, P., Kumar, P., Gunnaiah, R., Gowda, A.A., Lokesh, V., Pujer, P., Anjunatha, G. (2019). Reliable and early diagnosis of bacterial blight in pomegranate caused by *Xanthomonas axonopodis* pv. *Punicae* using sensitive PCR techniques. *Scientific Reports*, 9(1). <https://doi.org/10.1038/s41598-019-46588-9>

5. Koch's postulated for plant pathogen. British Mycological Society, 1993–1994, (2007).
6. Sharma, J., Sharma, K., Aundy, K., Mondal, K., Thakor, S., Maity, A., Gharate, R., Chinchure, S., & Jadhav, V. (2017). Pomegranate bacterial blight: Symptomatology and rapid inoculation technique for *xanthomonas axonopodis* pv. *punicae*. *Journal of Plant Pathology*, *99*, 109–119. <https://doi.org/10.4454/JPP.V99I1.3825.S9>

Disha: The Facility Locator for the Disabled



Kuldeep Vayadande, A. Dhiwar, D. Khadke, R. Golawar, S. Khairnar, S. Wakchoure, S. Bhoite, and D. Prasad

Abstract With the advancements in digital and information technology, various kinds of maps are becoming a necessity for information and navigation technologies. Paper based maps can be easily read through even by a disabled person but such kind of maps lack some functions and facilities, that a normal disabled user is not able to access. For that easy road to road navigation, user interface, cognitive and voice assistive technology becomes a necessity for a disabled person. Furthermore, more advanced and optimal techniques must be considered to the disabled user's maximum benefit. Therefore, we have proposed android based system that will be beneficial for disabled human beings. So disabled human beings can easily find services which are offered to them easily.

Keywords Advancement · Navigation · User-interface · Assistive technology · Design

1 Introduction

Nowadays google maps has made it very easy for every Business owner or an organization to pin or upload their business land marks, like we can easily know where the Hospitals, Hotels, Theaters, School, Colleges etc. are located. For a non-disabled person, it's very easy to access the location as well as to visit and make use of all the facilities. However, for a disabled person its quite tough to access the location according to his need. Along with this, though the person manages to access the location, the person is completely unaware about the facilities provided for a disabled person by the respective Organization. So, to solve this issue we are developing a portal and an application where business owners can mention all the facilities provided by them for a disabled person, from which a disabled person can easily

K. Vayadande · A. Dhiwar · D. Khadke · R. Golawar (✉) · S. Khairnar · S. Wakchoure · S. Bhoite · D. Prasad
Artificial Intelligence and Data Science, Vishwakarma Institute of Pune, Pune,
Maharashtra 411037, India
e-mail: rohan.golawar21@vit.edu

figure out whether he/she can visit the place or not. We are also focusing on developing an application which could be easily handled by a disabled person by providing voice instructions.

2 Problem Statement

In the present situation one can get tons of information regarding map-based platforms using a web and android application. Example- Uber and Ola presenting cab location, Food Panda and Swiggy showing restaurant locations and other locations such as hotels, schools, theatres etc. are shown by Google Maps. Such locations have various facilities which includes—lifts, ramps, public toilets, stairs etc. These accessible features or provisions are not filtered for a disabled person currently. It would be helpful for a disabled user to get notified about all the facilities of the center provided by a regular user or by a business owner. This paper has a solution to this issue, a centralized platform is developed for storing and sharing information regarding such facilities only for the use of the disabled. Information concerning the provisions would be displayed to the disabled user and would let the user decide whether he/she should visit the center or not.

3 Literature Survey

- [1] “Accessibility Map” and “Social Navigator Services for Persons with Disabilities”, Describes common application architectures and technologies used. The android as well as the web application use the same model which contains information about road sections and road descriptions, object accessibility, stored in the database of the previously developed application “Accessibility Passport”. The “Social Navigator” service describes the route as a graph with the arrival rate of the route portion as a weighted edge.
- [2] “Accessible way finding and navigation: a systematic mapping study”, The purpose of this paper is to describe the characteristics and development of accessible way finding and navigation systems proposed in the literature, and to highlight the most interesting features and weaknesses that should be considered in the future development of similar systems.
- [3] “Assistive Technology for Disabled People”, Assistive technologies are intended to assist people with disabilities who cannot easily carry out their daily activities. Despite the emphasis on mechanics and the rapid adoption of modern devices, little is known about the specific applications of such devices being deployed today. Caregivers of the blind and disabled are indecisive when choosing the tools, they need. So, the main objective of this paper is in aiding the needy in choosing the widget that suits them best.

- [4] “Geographic Information Systems in the Context of Disabilities”, The goal of this work is to present an overview of research results and useful strategies for GIS applications in a context with disabilities. Their opinions demonstrate how well-established his GIS for space-related disability concerns is across several domains and thematic areas. The support for disaster and emergency management, wayfinding aids to help with orientation and navigation, and accessibility mapping and identification are the main areas of attention. Addressing specific audiences/disabilities, application usability/portability, data availability, accuracy, and cost are the main restrictions placed on the use of GIS.
- [5] “Mobile follow-up system for elderly and disabled people”, This research presents a prototype of a mobile app for planned care and after care for the elderly and disabled. This is equivalent to sensors in devices such as GPS, non-invasive control and tracking systems. It can also be integrated with Android and IOS Wear, making using this app more transparent, secure and less invasive.
- [6] “Speaking Map: An application for the visually impaired, in this paper to help the visually impaired people, the author has designed and implemented “Speaking Map” an android based application which informs the user’s current location, nearby places and direction of going from one place to another vocally. The author has devised and enhanced the system by using algorithms by adding more features such as intelligent obstacle detecting ability. In future, the author ends to adopt form or obstacles and different languages for getting instructions for the maps.
- [7] “Future Challenges in Next the Generation of Voice User Interface”, this paper mainly introduces the key elements and core techniques in VUI in terms of the disabled. Also, future challenges will be discussed from the perspective of empathy, ethics, and accessibility. This paper serves as a summary for future study in VUI.
- [8] “The route planning services approach for people with disability”, This paper describes the approach and methods used to develop location services for people with disabilities. This paper describes navigation methods and sophisticated algorithms developed for people with disabilities. Practical possibilities for services to assist persons with disabilities are also presented. The results of research and development work on the approach are also presented in this paper.
- [9] “Voice Helper: A Mobile Assistive System for Visually Impaired Persons”, The design and implementation of a system to help blind people use Android smartphones are the main topics of this research. Voice Helper (VH), the system, improves many of its functions while integrating open sources. To help the visually impaired carry out their daily activities, VH includes Message Reader, Text File Reader, OCR Reader, Voice Dialer, and Dialer for the Visually Impaired. It also provides a navigation player for walking and riding that is based on Google Maps and supports more thorough voice guidance for driving directions and distance to destination. Visually impaired people are integrated into and verified VH’s operating environment.

4 Process Flow Diagram of Our System

A. Diagram (Fig. 1).

B. Explanation

A group of users would be accessing our application (review user, business owner and disabled user) for use. After landing on the landing page, the user would be asked for his/her location to be accessed. When the permission is granted to the users their Aadhaar Card will be put to verification, after successful verification the users would be divided into three types. The reviewer, business owner and the disabled user as mentioned earlier. The reviewer or the survey user or the visitor may it be abled or disabled, if visited to a place or have some idea of that place whether the particular place has provisions for the disabled or not. Such users can simply fill out a survey form wherein they can add appropriate details and images regarding to those places that they have visited or plan to visit and can also give reviews and ratings. Adding images is mandatory for validation purpose and also agreeing to our terms and conditions. After filling out the survey form, the information would get stored in our database. Next are the business owners who act as a key entity of our model. They just have to pin their location of their store, building or any other business guid

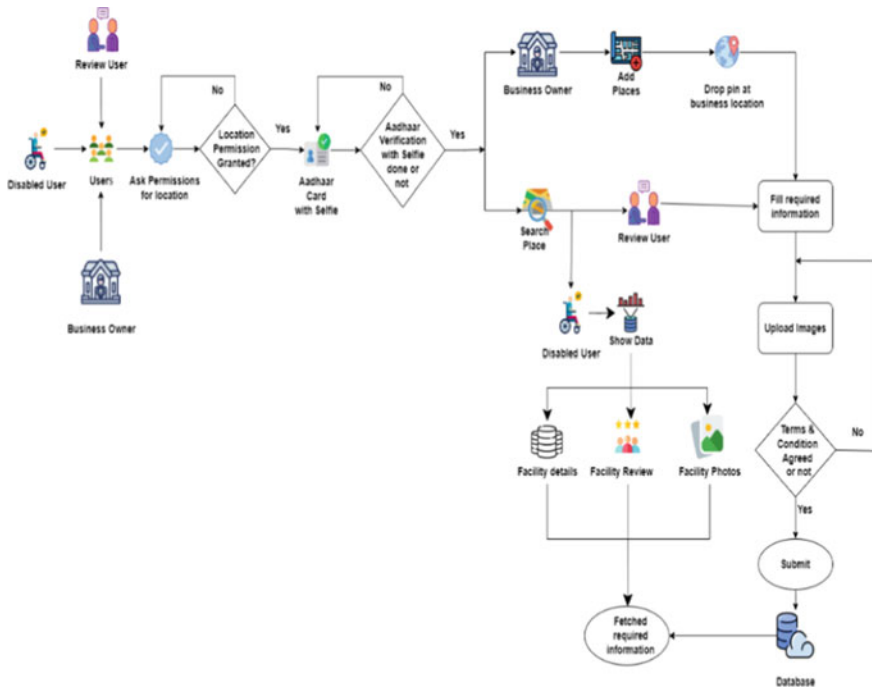


Fig. 1 Block diagram of our model

that they want to add. After this they have to fill up the survey form where they have to add necessary details regarding their business or organization. Upload of images is mandatory for validation purpose as well as agreeing to terms and conditions. After such steps the data will be stored in our database. And now the disabled user has the liberty to look for any place he/she wants to access just as google maps. The data will be fetched from our database and will be presented to the disabled user for use.

5 Idea

- Problems faced by specially-abled.
- Web and Mobile based solution.
- Three types of users (Business owners, Surveyor/Visitor, Disabled user).
- The impaired user will be shown lifts, wheelchairs, braille signage, ramps, public toilets, counters etc. with accompanying photographs.
- User will be able to search a place just like google maps and will get all information in a click.
- Voice based instructions will be provided on long click on options. Voice based location search will also be available
- Business owner will add location, details, images of place/business while registration.
- Information will be taken from business owner while registration.
- Information like ratings and images of services will be taken from visitors through surveys as a supporting information.
- For Navigation, Directions purpose we rely on Google Maps.

6 Approach

- For our main user who is especially abled, he/she just needs to search location to visit just like in google maps. All information will be displayed for that location with supporting images, ratings, comments etc.
- For Business Owner, user needs to drag pin at selected location just like Swiggy/ola. After user confirms the location, he/she needs to fill out complete details and add images required about business after successful submission the place will get added into the database and made available to user.
- User can give visitor's survey if he/she is at that place. For this user needs to select location to survey/rate. Then it will be checked with geo-fencing if user is at that location. Otherwise, to validate user adding images will be compulsory. If yes then, user will fill required information and submit it. Information will be added to Database.

7 Dependencies

- Our main problem is what if user using the app/website can't see. But to overcome this we will add voice-based feature to the app/website.
- Another show stopper is awareness. There is very less awareness about google maps, mobile phones, technology to the disabled users. We can run awareness sessions and campaigns to spread awareness regarding all these things.
- Internet connection is also one of the dependencies. Because, without internet connection location service can't work. The solution is also spreading awareness.

8 Impact

Person with disability will get the information about the place and its facilities before visiting. Reviewer will be satisfied in doing a good work. Also, awareness regarding problems of especially abled people will spread throughout youth. In result of this more such innovations will be done addressing such problems. This is a huge global problem everyone ignores about. Solution will have huge impact on this problem. People will start thinking about disabled. After this the solution, owners will also start thinking adding facilities that will help disabled people to visit that place. This will have a great impact on society.

9 Our Solution Versus Google Map

Our solution more precisely focuses on disabled people, their requirements etc. We don't really focus on navigation, directions, places, contacts etc. Instead, we rely on Google maps for this purpose. Because these features are already implemented in google maps. We provide information regarding pace to our main user who is a disabled person. We contribute to a social cause. A Google Map is a widely used technology nowadays. It provides features like nearby places, navigation, direction, location sharing, location saving and many more. It is an application with many useful features. It also provides information like timings, contact no, details of that place etc. But there is no information provided for disabled people. Also. Software is somewhat difficult to use for any disabled person. It's really a good software tech giant but it doesn't have information that we need for the disabled user.

10 Technology Stack

As we all know that to implement such huge technological system, we need a good variety of tech stack. For this very reason our project will be using the following:

- For android development we would be using Java/Kotlin/Flutter, Android SDK as it has a good community support.
- For creating beautiful UI applications: XML Jetpack Compose would be just fine.
- For integrating maps and related technologies in app and website related stuff we would like to use Maps SDK, Geo-coding, Places API.
- For database and real-time CRUD operations and scalability: Firebase.
- For the frontend of the web application: HTML, CSS, Java script. These are the entire technology stack we would need for the implementation of our system.

11 Results

See Figs. 2, 3, 4, 5, 6 and 7.

Fig. 2 Location request page

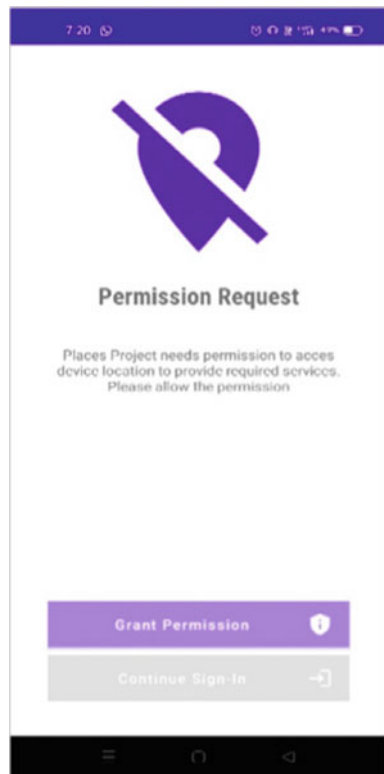
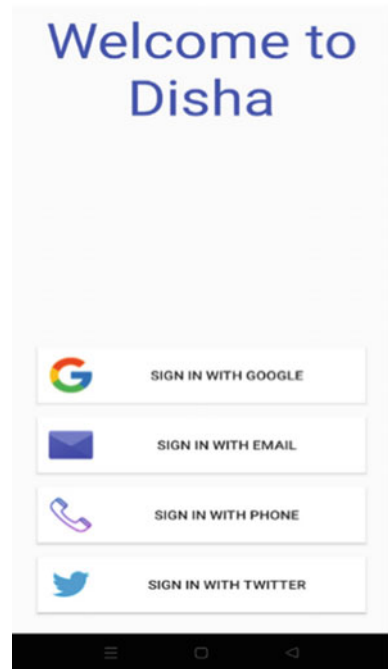


Fig. 3 Start up page

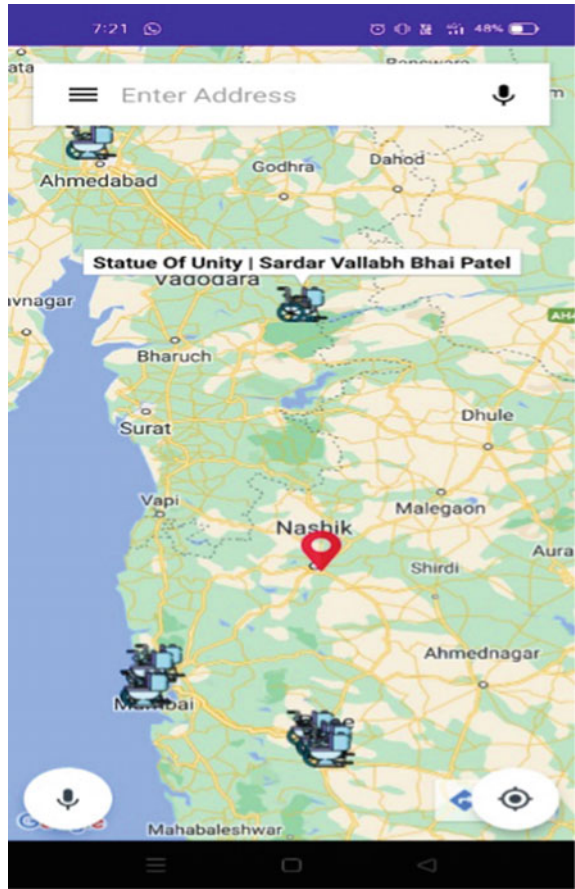
12 Future Work

There are some enhancements to be made in our application. Our future enhancements would not only focus on Computer/Informative related domains but would also give emphasis to Artificial Intelligence and Data Analytics. Thus, it would prove beneficial in providing better assistance to the disabled user and would make their journey in comfort and ease. These are some of the enhancements that we will be working on:

A. Security Advancements

Talking about security management, how can our application detect whether a user has uploaded any malicious content or a disturbing image on our application? We would like to propose a solution. To detect any malicious content in any android or web applications there are some reserved malware detection techniques. Such techniques rely upon Computer Vision, Machine Learning and Deep Learning algorithms. So, for instance if any user uploaded an unwanted image on our application, then such algorithms would help us in resolving such issues. These are the steps we would go through to train our model.

Fig. 4 Information about location



- I. Collecting some samples regarding unwanted/malicious/disturbing images.
- II. Next aspect would be training the model.
- III. After the model has been trained it would filter out and acknowledge us whether a malicious content is present or not.

B. Object Detection

Such a parameter was given importance for a better compatibility and for convenience of the disabled user. Our application would help the user in detecting various instances of objects around them so that they would have a better understanding about their surroundings. The application would scan a particular object, detect, verify it and

Fig. 5 Map showing facilities for disabled

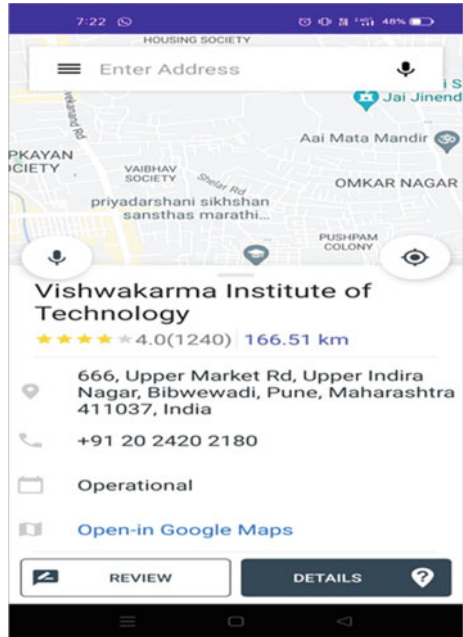


Fig. 6 Survey form (basic information)

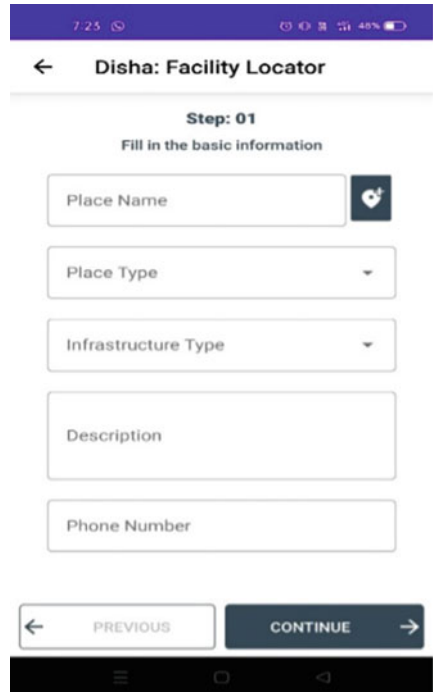
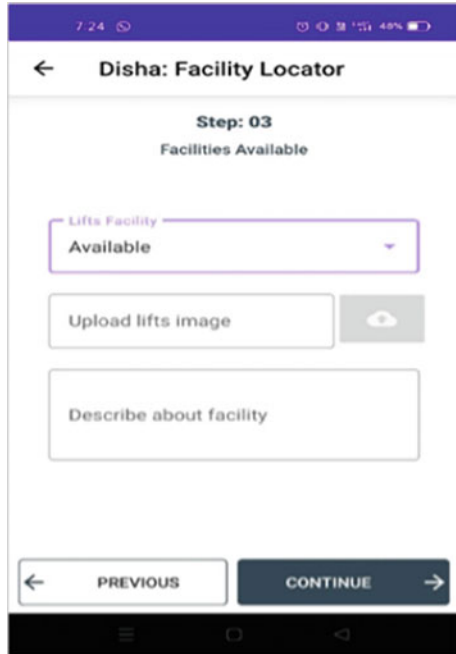


Fig. 7 Survey form



provide information about the object such as whether an object is a wheelchair or not or whether it is accessible or not. Such features would be implemented.

C. Geofencing

This feature would create a virtual fence involving a specific geographic location which would further help the disabled users to know about the components or objects surrounding them by getting instant notifications on their devices. If a disabled user is traveling from Point A to Point B, then whether any objects/components are present or not in such vicinity would be informed to the user.

These were some of our enhancements which we would be working on in the coming future.

13 Conclusion

We know have come to know that over 21 million people in India are suffering from some or the other kind of disability. The number is huge in rural areas than the urban areas. This system aims to foster and lend a hand to such kind of people seeking for help. Our system would prove to its very best for the disabled to navigate to their selected destination and enjoy their time in comfort. Not only this but we tend to encourage researchers and people to serve at this noble cause by developing and

enhancing such systems which are beneficial for such group of people. We look forward to see a better future with such people and be a part of their journey.

References

1. Kulakov, K. A., Apanasik, Y. A., Shabaev, A. I., & Shabalina, I. M. (2014). Accessibility map and social navigator services for persons with disabilities. In *Open innovations association FRUCT proceedings of 15th conference of IEEE* (pp. 69–76)
2. Tereschenko, V., Yanchik, D., & Pustovoitov, D. (2010). The optimal way searching task on obstacles multiplicity. In *Proceeding of 20th international conference on computer graphics and vision GraphiCon 2010* (pp. 280–284). [Online]. Available: <http://graphicon.ru/html/2010/conference/RU/Se6/34.pdf>
3. Puviarasi, R., Ramalingam, M., & Chinnavan, E. (2014). Self-assistive technology for disabled people–voice-controlled wheel chair and home automation system. *IAES International Journal of Robotics and Automation (IJRA)*, 3(1).
4. Zimmermann-Janschitz, S. (2018). Geographic information systems in the context of disabilities. *Journal of Accessibility and Design for All*, 8(2), 161–192. <https://doi.org/10.17411/jaces.v8i2.171>
5. Vera, P. M., Carrau, M. K., & Rodríguez, R. A. (2018). Mobile follow-up system forelderly and disabled people. In *2018 Congreso Argentino de Ciencias de la Informática y Desarrollos de Investigación (CACIDI)* (pp. 1–5). IEEE
6. Zaslavskiy, M., & Krinkin, K. (2012). Geo2tag performance evaluation. In *Proceedings of 12th conference of open innovations association FRUCT* (pp. 185–193). [Online]. Available: <https://fruct.org/publications/fruct12/files/Zas.pdf>
7. Wang, Z. (2020, August). Future challenges in the next generation of voice user interface. In *2020 International conference on computing and data science (CDS)* (pp.191–193). IEEE
8. Kulakov, K. A., Shabaev, A. I., & Shabalina, I. M. (2015). The route planning services approaches for people with disability. In *Proceeding 17th conference open innovations framework program FRUCT*. ITMO University (pp. 89–95), Apr 2015.
9. Liu, K. -C., Wu, C. -H., Tseng, S. -Y., & Tsai, Y. -T. (2015). Voice helper: A mobile assistive system for visually impaired persons. In *2015 IEEE international conference on computer and information technology; Ubiquitous computing and communications; dependable, autonomic and secure computing*. Pervasive Intelligence and Computing (pp. 1400–1405), IEEE.
10. Li, Y., Ng, A. S., Trinh, T., & McNamara, R. (2001). Text-to-speech based reminder system. Jan. 302001, uSPatent6, 182, 04.

Face Mask Detection and Recognition Using CNN Deep Learning Models



Aniket Muley, Tukaram Navghare, and Vinayak Jadhav

Abstract In the pandemic situation, the corona virus-2019 is unfortunately highly transmissible all over the world. To wear mask is one of the precautionary measures that reduces the risk level in the public place. In this study, our focus is classification of with mask and without mask peoples in public places. To deal with this problem deep learning technique is used here. We have used different algorithms for more precise classification of with mask and without mask dataset. The result of this study reveals that, the Admax algorithm showed 97.92 percent accuracy level as compared to other algorithms. In future, for similar kind of studies this algorithm is strongly recommended that can help to classify the image objects more precisely.

Keywords Convolutional neural network · Face mask · Adam algorithm

1 Introduction

Face recognition plays important role in identification, Interaction in every day understanding between two or more peoples. Corona virus disease (COVID-19) is due to the spread of the novel corona (SARS-CoV-2) virus. Initially, in epidemic situation, people commonly used face masks to protect themselves from air pollution [1] or hospital paramedical staff, or to maintain to secrete identity from community peoples. It is observed that wearing masks in public places is useful to prevent the spread of COVID-19. A preponderance of evidence from WHO [2], analysis [3] and research [4, 5] has shown that use of face mask declines the spread of COVID-19 by reducing the spread of tainted respiratory droplets [6–8]. So, it is one of the preventive measures used in number of countries. Also, to check person to person and screen

A. Muley (✉) · T. Navghare
School of Mathematical Sciences, Swami Ramanand Teerth Marathwada University, Nanded,
Maharashtra 431606, India
e-mail: aniket.muley@gmail.com

V. Jadhav
Shivaji Mahavidyalaya, Udgir, Maharashtra 413517, India

individuals in community areas for wearing face masks is a scary job. Consequently, there is a need to develop automatic mechanisms for facemask detection [9].

Recently, some studies [10–12] work on the same direction and it is observed that, they have least focus on the specific ones. It is due to unavailability of the standard dataset. [13–15] Many large and variety of the unmask data set is available, that containing thousands of people's face images. As per our review of similar studies we observed that, customary and large scale masked face data exists. It is observed that creating a masked face dataset requires images of people with various facial masks along with various other parameters [16]. Further, feature extraction is performed with DBN-SMO for facial expression recognition with MATLAB software [17, 18]. Proposed a face mask recognition system for still images and real time video. Their study is useful in identifying masked individuals. They have used a CNN model with different layers and calculated the performance based on processing time and accuracy [19–23]. Projected an IoT based smart assist system for monitoring activity venue occupancy and COVID 19 screening during the pandemic. Their system is distributed in three modules and functions are implemented using Python programming and thereafter, compared the proposed algorithm with existing algorithms and observed that the proposed algorithm is highly cost-effective and useful in reducing public transmission of COVID 19.

Our objective is to recognize images of normal people with and without face masks using different algorithms. The paper is structured as follows: Methodology. The result and discussion, conclusion is given in subsequent sections.

2 Methodology

2.1 Dataset

In this study, we have collected primary dataset consist of 65 with and without mask images. Specifically, our data includes image gender, mask type, face angle, occlusion, environment, shape, size and shape, etc.

2.2 Proposed Methodology

Step 1: Collect with and without mask primary dataset.

Step 2: Collected image dataset numbered with prefix with and without mask.

Step 3: Apply CNN deep learning neural network to identify the optimal solution with different types algorithms viz., Adadelta, Adagrad, Adam, AdamW, AdamaxASGD, NAdam, RAdam, RMSprop and Rprop.

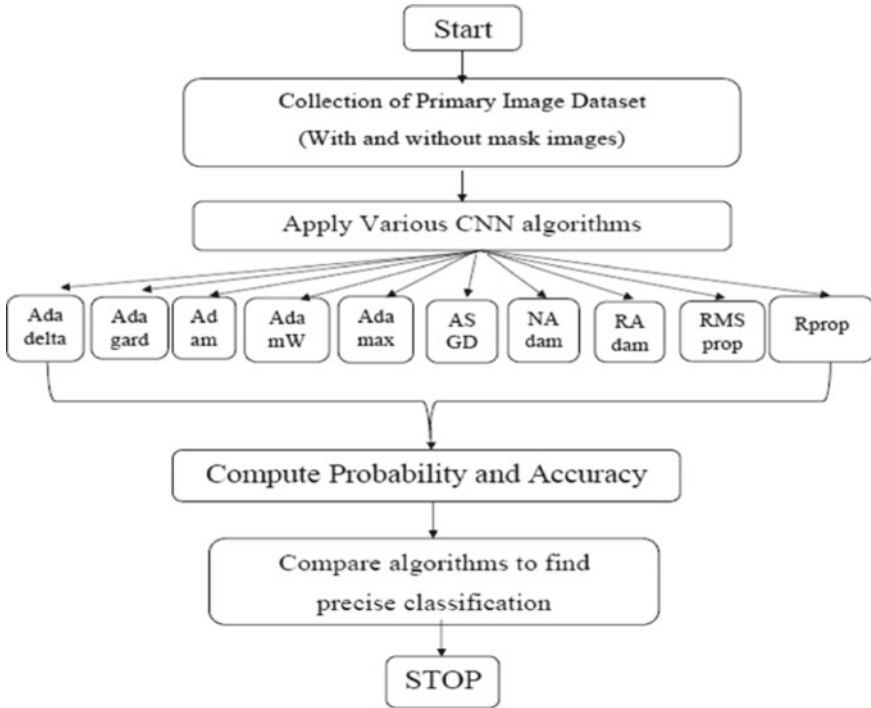


Fig. 1 Flow chart

Step 4: Use appropriate number of epoch that helps to the improve the accuracy.

Step 5: Compare the results obtained through step 3 and step 4 to check the performance measure (Probability with mask and without mask, accuracy) of the different algorithm (Fig. 1).

2.3 Analytical Tools

In this study, Python is used as analytical tool with some packages viz., Fastai, torchvision, fastai metrics, os, pandas, numpy, torchvision, torch.utils.data, torch.nn.functional, torchvision.transforms, matplotlib.pyplot.

3 Result and Discussion

The results obtained through the proposed methodology is elaborated in detailed below.

3.1 Evolution Matrix

Figures 2a, 3, 4, 5, 6, 7, 8, 9, 10, and 11b shows probabilities of with and without mask and their train loss of different algorithm (Tables 1 and 2).

4 Conclusions

The main focus of this study is to identification of images with and without facemask to the common people. In this study, we observed that the Admax algorithm gives approximately 97.92 accuracy as compared to other algorithms. We highly recommended that Adamax algorithm is best for face mask detection purpose. Adamax algorithm is beneficial for face detection or similar image detection analysis. Further, we will increase number and variety of dataset to get the more accurate results. In future this work can be use in various filed viz., school, hospitals, bank and airports and public or commercial locations.

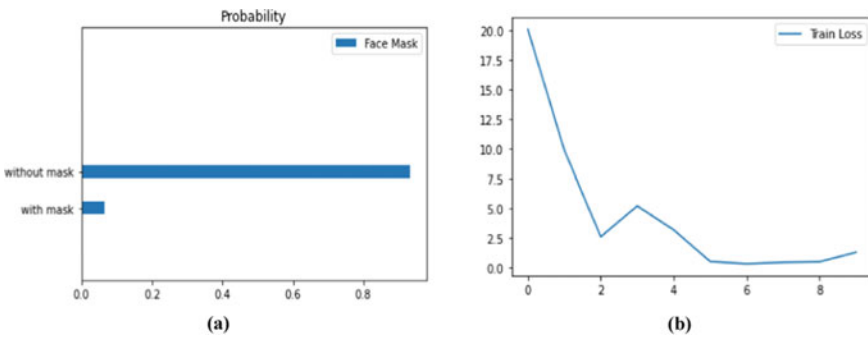


Fig. 2 a. Adadelta algorithm probability, b. Adadelta algorithm train loss

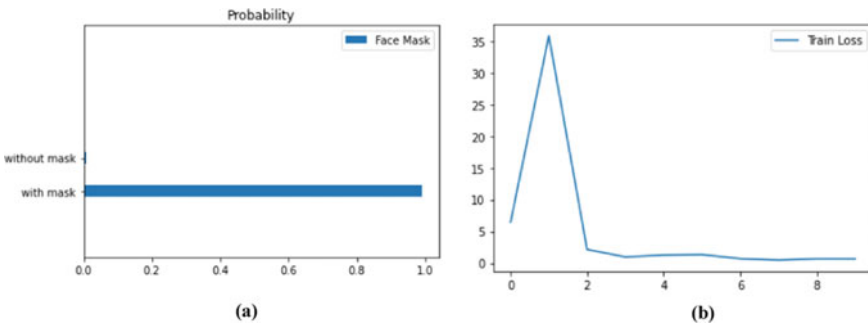


Fig. 3 a. Adagrad algorithm probability, b. Adagrad algorithm train loss

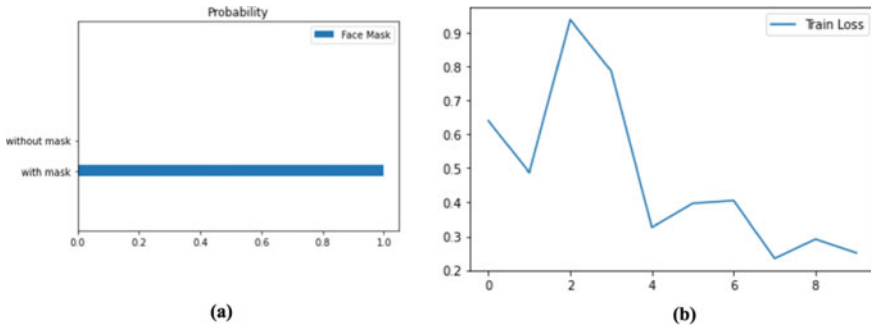


Fig. 4 a. Adam algorithm probability, b. Adam algorithm train loss

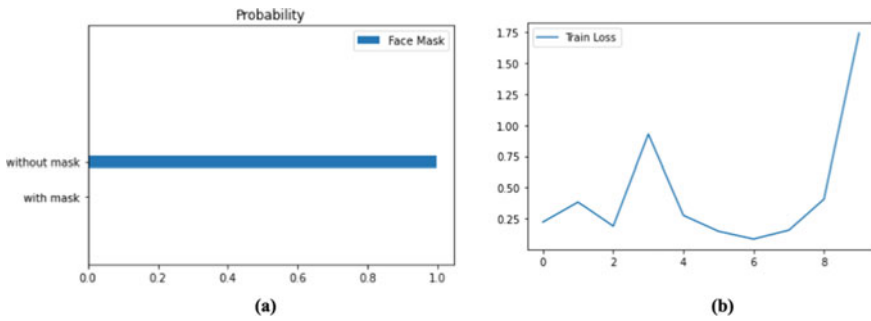


Fig. 5 a. AdamW algorithm probability, b. AdamW algorithm train loss

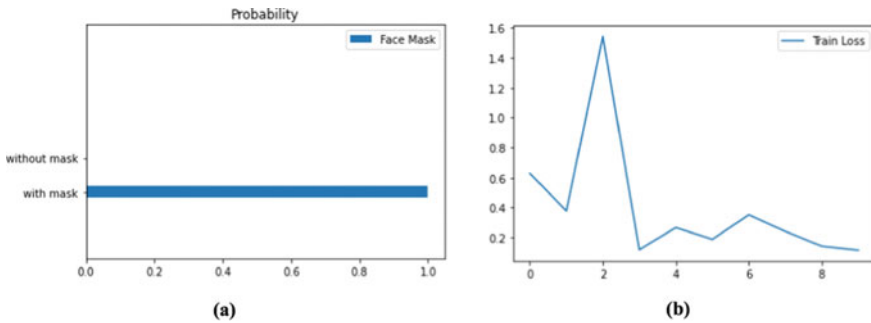


Fig. 6 a. Adamax algorithm probability, b. Adamax algorithm train loss

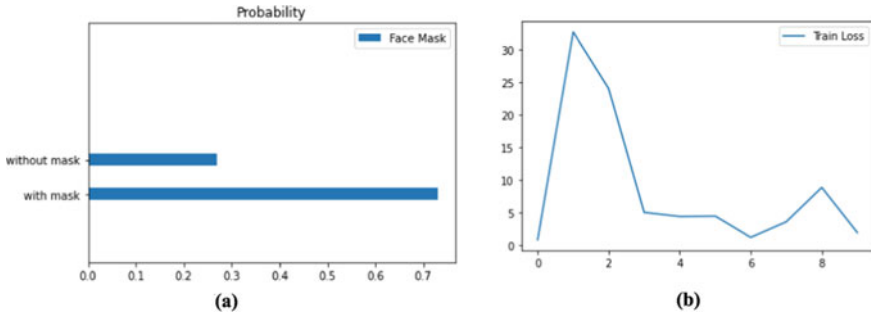


Fig. 7 a. ASGD algorithm probability, b. ASGD algorithm train loss

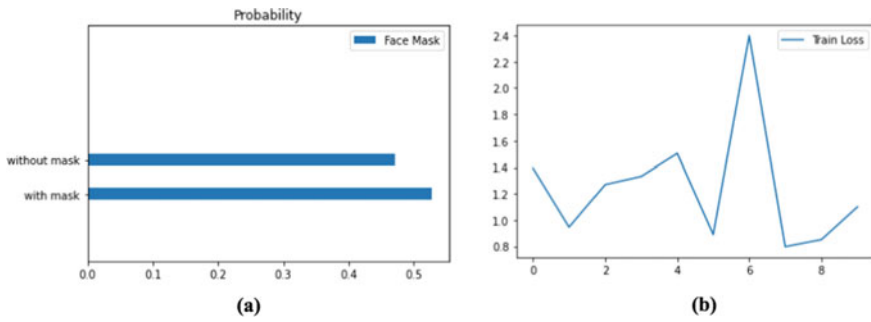


Fig. 8 a. NAdam algorithm probability, b. NAdam algorithm train loss

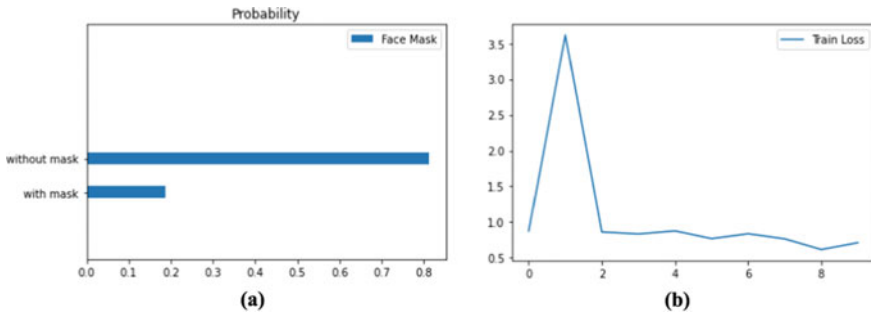


Fig. 9 a. RAdam algorithm probability, b. RAdam algorithm train loss

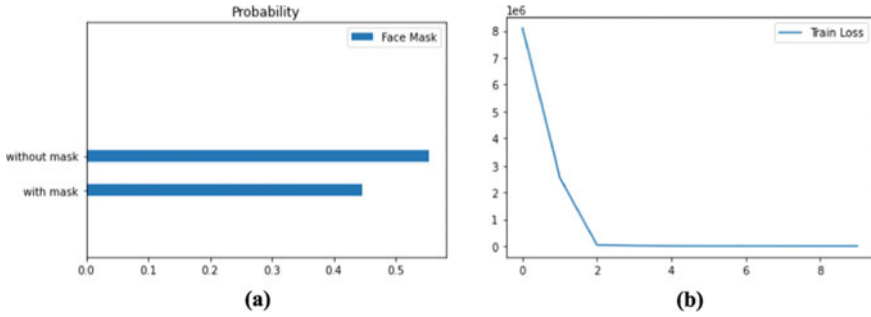


Fig. 10 a. RMSprop algorithm probability, b. RMSprop algorithm train loss

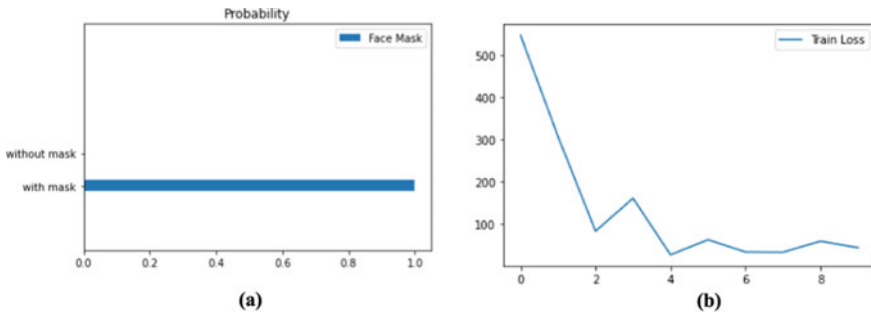






























































Fig. 11 a. Rprop algorithm probability, b. Rprop algorithm train loss

Table 1 Comparative results of CNN algorithms

Algorithm	Probability		Accuracy
	With mask	Without mask	
Adadelta	0.93351316	0.0664869	64.0625
Adagrad	0.99236554	0.00763444	81.2500
Adam	1.000000e + 00	7.3767864e-20	92.7083
AdamW	0.00276331	0.9972366	93.7500
Adamax	1.000000e + 00	2.1680032e-17	97.9167
ASGD	0.73120856	0.2687914	50.0000
NAdam	0.5285248	0.4714752	75.0000
RAdam	0.1872336	0.81276643	40.6250
RMSprop	0.4459279	0.55407214	50.5208
Rprop	1	0	46.3542

The significance of bold term is the reflection of more accurate results as compared with other method results

Table 2 Summary of sample data input and output

Algorithm	Sample Data					Output
convo						
Adazrad						
Adam						
AdamW						
Adamax						
ASGD						
NAdam						
RAdam						
RMSprop						
Rprop						

References

1. Al-Ramahi, M., Elnoshokaty, A., El-Gayar, O., Nasralah, T., & Wahbeh, A. (2021). Public discourse against masks in the COVID-19 era: Infodemiology study of Twitter data. *JMIR Public Health and Surveillance*, 7(4), e26780.
2. Greenhalgh, T., Schmid, M. B., Czypionka, T., Bassler, D., & Gruer, L.. Face masks for the public during the covid-19 crisis. *Bmj*, 369
3. Balotra, A., Maity, M., & Naik, V. (2019). An empirical evaluation of the COTS air pollution masks in a highly polluted real environment. In *2019 11th international conference on communication systems networks (COMSNETS)* (pp. 842–848). IEEE.
4. McDonald, F., Horwell, C. J., Wecker, R., Dominelli, L., Loh, M., Kamanyire, R., & Ugarte, C. (2020). Facemask use for community protection from air pollution disasters: An ethical overview and framework to guide agency decision making. *International Journal of Disaster Risk Reduction*, 43, 101376.
5. Zhao, W. (2017). Research on the deep learning of the small sample data based on transfer learning. In *AIP conference proceedings* (1864, No. 1, p. 020018). AIP Publishing LLC. (2017, August).
6. Eikenberry, S. E., Mancuso, M., Iboi, E., Phan, T., Eikenberry, K., Kuang, Y., & Gumel, A. B. (2020). To mask or not to mask: Modeling the potential for face mask use by the general public to curtail the COVID-19 pandemic. *Infectious disease modelling*, 5, 293–308.
7. Jayaweera, M., Perera, H., Gunawardana, B., & Manatunge, J. (2020). Transmission of COVID-19 virus by droplets and aerosols: A critical review on the unresolved dichotomy. *Environmental Research*, 188, 109819.
8. Razavi, M., Alikhani, H., Janfaza, V., Sadeghi, B., & Alikhani, E. (2022). An automatic system to monitor the physical distance and face mask wearing of construction workers in COVID-19 pandemic. *SN Computer Science*, 3(1), 1–8.
9. Can'ario, J. P., Ferreira, M. V., Freire, J., Carvalho, M., & Rios, R. (2022). A face detection ensemble to monitor the adoption of face masks inside the public transportation during the COVID-19 pandemic. *Multimedia Tools and Applications*, 1–26.
10. Ding, F., Peng, P., Huang, Y., Geng, M., & Tian, Y. (2020). Masked face recognition with latent part detection. In *Proceedings of the 28th ACM international Conference on multimedia* (pp. 2281–2289).
11. Du, H., Shi, H., Liu, Y., Zeng, D., & Mei, T. (2021). Towards NIR-VIS masked face recognition. *IEEE Signal Processing Letters*, 28, 768–772.
12. Geng, M., Peng, P., Huang, Y., & Tian, Y. Masked face recognition with generative data augmentation and domain constrained ranking. In *Proceedings of the 28th ACM international conference on multimedia* (pp. 2246–2254).
13. Cao, Q., Shen, L., Xie, W., Parkhi, O. M., & Zisserman, A. Vggface2. A dataset for recognising faces across pose and age. In *2018 13th IEEE international conference on automatic face gesture recognition (FG 2018)* (pp. 67–74). IEEE
14. Guo, Y., Zhang, L., Hu, Y., He, X., & Gao, J. (2016). Ms-celeb-1m: A dataset and benchmark for large-scale face recognition. In *European conference on computer vision* (pp. 87–102). Springer (2016, October).
15. Yi, D., Lei, Z., Liao, S., & Li, S. Z. (2014). Learning face representation from scratch. arXiv preprint [arXiv:1411.7923](https://arxiv.org/abs/1411.7923).
16. Zhang, J. P., Li, Z. W., & Yang, J. (2005). A parallel SVM training algorithm on large-scale classification problems. In *2005 international conference on machine learning and cybernetics* (vol. 3, pp. 1637–1641). IEEE. (2005, August).
17. Goyal, H., Sidana, K., Singh, C., Jain, A., & Jindal, S. (2022). A real time face mask detection system using convolutional neural network. *Multimedia Tools and Applications*, 81(11), 14999–15015.
18. Vedantham, R., & Reddy, E. S. (2020). A robust feature extraction with optimized DBNSMO for facial expression recognition. *Multimedia Tools and Applications*, 79(29), 21487–21512.

19. Abate, A. F., Cimmino, L., Mocanu, B. C., Narducci, F., & Pop, F. (2022). The limitations for expression recognition in computer vision introduced by facial masks. *Multimedia Tools and Applications*, 1–15.
20. Kaur, G., Sinha, R., Tiwari, P. K., Yadav, S. K., Pandey, P., Raj, R., & Rakhra, M. (2021). Face mask recognition system using CNN model. *Neuroscience Informatics*, 100035.
21. Li, et al. (2021). Cropping and attention based approach for masked face recognition. *Applied Intelligence*, 51(5), 3012–3025.
22. Li, X. (2022). Masked face detection and calibration with deep learning models. *Journal of Physics: Conference Series*, 2196(1), 012011. IOP Publishing. (2022, February).
23. Narayanan, K. L., Krishnan, R. S., & Robinson, Y. (2022). H.IoT based smart assist system to monitor entertainment spots occupancy and COVID 19 screening during the pandemic. *Wireless Personal Communications*, 1–20.

Ergonomics-Based Postural Assessment of Rural Water Fetcher



Sonali Patil, Sanjay More, K. K. Sangale, Rakesh Birajdar,
and Muntasim Bhaijan

Abstract The ergonomics tools REBA and RULA are used for evaluation and ergonomic assessment in carrying, handling, lifting and moving loads. A RULA and a REBA ergonomic tool are used to evaluate complex manual water fetching activities, and this study on water fetching activities mainly involved women from rural areas. Based on this ergonomic tool, observations, video recordings, and photographs of women fetching water were taken. The reviewed literature and postural activity guidelines were proposed for a summary analysis of women's water fetching activity and discomfort. The basic objective of the water fetching study is to determine the level of ergonomic strain in different water fetching activities. Another objective of water fetching activities is to determine the level of strain and musculoskeletal disorders in different body segments and to take corrective measures to reduce the health risk in water fetching activities.

Keywords Musculoskeletal disorder · Pain · Water fetching aid · RULA · REBA

1 Introduction

The heavy workload in construction and the activities associated with construction, where heavy loads are transported from one place to another, lead to MSD symptoms in the human body. Various industrial works with awkward posture lead to ergonomic health risks and serious injuries in the human body. In construction work, MSDs occur due to various activities such as carrying heavy loads, repetitive movements, awkward working postures and pain, stress [12]. In construction, workers work for a long period of time without any break, which leads to fractures and fatigue among construction workers. Therefore, it is necessary to take corrective measures to reduce the pain

S. Patil (✉) · S. More · R. Birajdar · M. Bhaijan
SVERI's College of Engineering Pandharpur, Gopalpur, India
e-mail: sppatil@coe.sveri.ac.in

K. K. Sangale
VJTI Matunga Mumbai, Mumbai, India

of workers. Since construction workers often perform their work repetitively, it is necessary to take the time to understand the stress and strain of construction workers, which affects the health of workers. Ergonomics is one of the tools that are helpful in assessing worker pain. Rapid whole body assessment (REBA) and rapid upper limb assessment (RULA) are the two tools ergonomics that are helpful in identifying disorders, fractures and discomfort related to the existing working conditions.

RULA analysis provides us with a RULA score associated with risk factors for upper limb disorders. The development of this ergonomic tool RULA is based on the repetitive actions and the awkward postures of the workers related to the upper body segment, and the development of the ergonomic tool REBA is based on the repetitive movements of the workers related to all body parts. The RULA and REBA assessment tool provides a RULA score or number calculated using the standard RULA score table. The RULA score is calculated based on the score of each body segment. Ergonomic tools such as RULA and REBA assess malposition without special equipment based on the standard RULA and REBA table. Ergonomic tools focus on direct observation methods such as video recordings and photographs of workers. In this paper, awkward posture during water fetching is evaluated using the REBA and RULA methods of ergonomics.

2 Materials and Methods

Literature review: In this article, the researcher describes an ergonomic tool that evaluates the entire human body. The ergonomics tool such as REBA and RULA is used by practitioners to assess awkward working postures found in health centers and industry [8]. REBA and RULA are ergonomic tools that assess the body without any equipment or machine. These ergonomics tools determine the score and based on the score we can predict the working postures of the human body. Based on the awkward posture while lifting and lowering loads, the ergonomics tool quantifies the fatigue and fractures in the human body. The RULA and REBA ergonomic tools evaluate postural activity during work by using the standard tables of RULA and REBA scores, which are useful to understand the awkward posture and quantify the risk during work and suggest changes in working posture. This assessment method is useful to identify the high pain and fatigue.

Another ergonomic tool is the Ovako Work Posture Analyzing System (OWAS), which is used to evaluate proper work posture in the construction industry. The Ovako Work Posture Analyzing System (OWAS) has several objectives, such as analyzing the posture according to the risk level and providing corrective actions to improve and reduce the risk level.

The biomechanical evaluation of manual handling of materials and lifting, pulling, and pushing of materials are all activities that pose a risk to the human body. The goal of biomechanical analysis is to understand the stresses and symptoms of musculoskeletal disorders in the various body segments that occur during construction work in Indian industry. Such biomechanical assessment is helpful for redesigning

products for construction workers that reduce pain, human body risks, fatigue, and musculoskeletal disorders and improve worker performance. The highlighted items (communication, ergonomic design, safety management, training and education, written program) correlate significantly with ergonomics. Risk control is complemented by proper ergonomic design, organizational training, and education. The OWAS method is based on the Posture, Activity, Tools and Handling method (PATH). The study shows that the different road construction workers, laborers have pain and spend a lot of time, i.e. 20% of the time, on manual material handling tasks [5]. Work details-: In a rural area, where the problem of water scarcity is greater, activities to obtain water are more pronounced. In this work, people from Solapur and Latur districts were used for the health assessment study. During summer season, fetching water becomes very difficult as people gather at the water source, wait in a queue and fetch the water. Sometimes rural women make deadly efforts to fetch water from the well. During the process of fetching water, there are processes such as filling the water into the pot, lifting the pot, and lowering the pot. Based on this activity, the analysis of body postures was conducted. When a woman is pregnant in the countryside, fetching water is very risky because the activities such as lowering, lifting, filling water into the pot and fetching water from the well are very dangerous. Water is one of the most important parts of human being, so rural people live in their house every day to fetch water and spend their time on it.

Some of the unfavorable postures are shown below. RULA and REBA scores are calculated for unfavorable postures using a standard table. The RULA ergonomics tool is used to analyze the upper limbs, while the REBA ergonomics tool is used to determine the RULA score for the entire body. RULA score and REBA score are calculated using the standard diagram based on this score, which is given as the standard diagram. Some of the awkward postures of rural women water fetchers were selected during water fetching. Rural women gather at a spring and fetch water in a group with 2–3 jugs on their head, hand and shoulder. The total load carried by rural women ranges from 10 to 30 L in a single trip with all awkward postures while fetching water. The journey to fetch water is also longer and the roads used by rural women to fetch water are very poor. So it becomes risky and painful for rural women.

3 Results

The ergonomic instruments used to measure the RULA and REBA scores of women's awkward posture while fetching water. The RULA score is shown in Table 1 and the REBA score is shown in Table 2, where the score was calculated for the different activities of fetching water such as filling water, draining water, and lifting water. The results of the assessment are the highest for both instruments, so an investigation is required, as shown in Tables 1 and 2. The highest score indicates the risk of repetitive activities and fatigue, fractures, and sometimes suffering that occurs in the body of

Table 1 REBA score awkward posture of women while water fetching activities

Rapid entire body assesment		India		
Activity description		Water filling	Water lifting	Water lowering
Neck, trunk and leg analysis	Neck score	3	3	3
	Trunk score	4	4	3
	Leg score	2	3	4
	Look posture score—A	7	8	8
	Fore load score	0	1	1
	Score A	7	9	9
Arm and wrist analysis	Upper score	4	3	3
	Lower arm score	2	2	2
	Wrist score	3	1	3
	Look up posture Score—B	7	4	5
	Coupling score	1	1	1
	score B	8	5	6
Activity score		1	1	1
Table score		10	10	10
Final REBA score		11	11	11
Recommendation		High risk, investigate and implement change	High risk, investigate and implement change	High risk, investigate and implement change

women. Therefore, the RULA and REBA score is different for different working conditions.

4 Discussions

The RULA and REBA ergonomic instruments (Tables 1 and 2) show that the shoulders, knees, legs, and lower back are at high risk when fetching water. Table 3 gives an idea of the understanding and interpretation of the RULA score in the basic mode of water fetching. The repetitive movements in the work, lifting and lowering cause severe pain in women during water fetching. The process to reduce the pain of women water haulers needs to be improved and changes need to be made to the water hauling activity by redesigning the equipment for water hauling. REBA's ergonomic tool identifies the awkward postures and the correlation between the severe pain and injuries and the awkward postures.

Table 2 RULA score awkward posture of women while water fetching activities

Rapid upper limb assesment		India		
activity description		Water filling	Water lifting	Water lowering
Neck, trunk and leg analysis	Neck score	3	3	3
	Trunk score	3	3	3
	Leg score	2	2	2
	Look up posture score—A	5	5	5
	Fore load score	2	2	2
	Score A	7	7	7
Arm and wrist analysis	upper score	3	3	3
	Lower arm score	2	2	2
	Wrist score	3	3	3
	Look up posture score—B	4	4	4
	Coupling score	2	2	2
	Score B	6	6	6
Activity score		1	1	1
Table score		7	7	7
Final RULA score		7	7	7
Recommendation		High risk, Investigate and implement change	High risk, investigate and implement change	High risk, investigate and implement change

Table 3 Interpretation of RULA score in basic mode





Sr.No	Score	Color	Meaning
1	1 and 2		The posture is acceptable if it is not retained or repeated for longer period
2	3 and 4		Further investigation is required and Changes may also be required
3	5 and 6		Investigation and changes are needed soon
4	7		Investigation and changes are needed immediatly



Fig. 1 Awkward posture of women while water fetching activities

5 Conclusion

Difficult water procurement has the highest score according to the standard sheet of RULA and REBA. The score from the standard tables is shown in the table of acceptable limits (Tables 1 and 2). Figure 1 shows the various unfavorable postures that pose a high risk and for which further investigation and modifications are required. After studying the ergonomics of water fetchers using RULA and REBA assessment, some suggestions were made to reduce the pain of water fetchers in rural areas:

A product design for water fetching is needed.

Redesigning the existing product or improving the existing design is important.

The water fetching aid should reduce the time of the water fetcher to fetch water.

The water fetching aid should fetch at least 50 L of water in one trip.

References

1. Abdul-Tharim, A. H., Jaffar, N., Lop, N. S., Mohd-Kamar, I. F. (2009). Ergonomic risk controls in construction industry—A literature review. In *Proceeding 2nd international build control conference*, 20, 80–88.
2. McA-Tamney. (2010). Postural analysis in HMI design: An extension of OCRA standard to evaluate discomfort level. *Journal of Achievements in Materials and Manufacturing Engineering*, 39(1), 117–129.
3. Maldonado-Macias, A., et al. (2009). Ergonomic evaluation of work stations related with the operation of advanced manufacturing technology equipment: Two cases of study. *XV Congreso Internacional De Ergonomia Semac.*, 49(3), 217–224.
4. Bhandare, A., Bahirat, P., Nagarkar, V., & Bewoor, A. (2013). Postural analysis and quantification of fatigue by using RULA and REBA techniques. *International Journal of Mechanical & Production Engineering.*, 1, 46–50.
5. Buchholz, B., Paquet, V., Punnett, L., Lee, D., & Moir, S. (1996). PATH: A work sampling based approach to ergonomic job analysis for construction and other non repetitive work. *Applied Ergonomics*, 27(1), 177–187.
6. Hedge, A. (2001a). *RULA: Employee assessment worksheet*. [Accessed April 22, 2017]. <http://ergo.human.cornell.edu/Pub/AHquest/RULAworksheet.pdf>
7. Hedge, A. (2001b). *Rapid entire body assessment (REBA)*. [Accessed April 22, 2017]. http://ergo.human.cornell.edu/Pub/AHquest/Cornell_REBA.pdf

8. Hignett, S., & McAtamney, L. (2000). REBA: A survey method for the investigation of work-related upper limb disorders. *Applied Ergonomics*, 39(1), 60–84.
9. Hignett, S., & McAtamney, L. (2000). Rapid entire body assessment (REBA). *Applied Ergonomics*, 31, 201–205.
10. Isa, H., & Omar, A. R. (2011). A review on health effects associated with prolonged standing in the industrial workplaces. *International Journal of Research and Review in Applied Science*, 8(1), 1–8.
11. Halim, I., Omar, A. R., Ismail, A. R., & Jaya, H. T. (2011). Posture, muscle activity and oxygen consumption evaluations among metal stamping operators: A pilot study in Malaysian small and medium industries. *Journal—The Institution of Engineers, Malaysia*, 72(4), 47–57.
12. Kulkarni, V. S., & Devalkar, R. V. (2017). Ergonomic analysis of building construction workers using RULA & REBA techniques. *National Institute of Construction Management and Research—Journal of Construction Management*, 32, 9–15.
13. McAtamney, L. (1993). RULA: A survey method for the investigation of world-related upper limb disorders. *Applied Ergonomics*, 19(2), 179–184.

Design and Implementation of Plastic and Microplastic Collection System



Abhishek N. Bhagat, Kashmira V. Dixit, and Amarnath D. Landge

Abstract Plastic trash contaminates the earth and its environment and has adverse effects on all living beings including humans. There is a need to devise plastic management strategies at a large scale as plastic manufacturing is rising and the current practices used for waste management are ineffective. Plastic is not biodegradable and it can move far in the aquatic environment. Scientists have started quantifying plastic waste in freshwater and plastic debris is now been observed on beaches, lakes, rivers, and riverbanks. There are numerous sources of plastic waste, and their introduction into the environment can occur at any point in the plastic product's life cycle. Current systems and machines to manage plastic contamination focus on large plastic contaminants. This project aims to bridge the gap between a separate system for macro and micro-plastics by trapping them both in a single system.

Keywords Plastic · Microplastic · Plastic pollution · Cleanup

1 Introduction

Given the versatility and usefulness of plastic, it is no wonder that many products available in the market are made of it; but, as this material's popularity grew, so did the amount of litter in the environment. Plastics serve numerous applications and are inexpensive to produce, therefore; they have become a common material in many commercial items in the 100 years after they were invented. In fact, over the past

A. N. Bhagat (✉)

EPC Division, Reliance Infrastructure, Mumbai, Maharashtra, India
e-mail: abhagat2000@gmail.com

K. V. Dixit

Department of Mechanical and Aerospace Engineering, California State University, Long Beach, California, USA

A. D. Landge

Department of Mechanical Engineering, Shree L.R. Tiwari College of Engineering, Thane, Maharashtra, India

seven decades, annual plastic output has increased from around 1.5 to 322 million tonnes [1, 2].

Consequently, the omnipresence and mass production of the product means that many plastics are improperly disposed which allow them to pollute nearby waterbodies and other habitats. Since 2010, an estimate of 4–12 million tonnes of plastic pieces have escaped into marine environments, causing trash to accumulate in the ocean and other waterbodies [1, 3, 4]. The plastics are subsequently broken down into tiny microplastics by ocean currents, making them difficult to remove from the environment.

Toxics Link, a Delhi-based NGO working for the environmental cause has discovered microplastic pollution along the reaches of River Ganga. They define microplastic pollution as solid synthetic particles ranging from 1 μm to 5 mm which cannot dissolve in water. River Ganga flows through five states and has been under vast effort for cleaning under the National Mission for Clean Ganga [5].

Microplastics are well acknowledged as a major source of aquatic pollution. Industrial waste, untreated sewage from cities and pooja offerings wrapped in non-biodegradable plastic are picked up as the river flows through multiple heavily populated areas. Plastic objects and waste materials that are released or dumped into the river degrade and eventually break down into microscopic particles, which the river then transports it in massive quantities into the ocean, which becomes a massive sink for all plastics used by humans. Microplastics fundamentally flow into the river system all along and reflect to a direct relationship with the bad state of waste management; hence, it is alarmingly important to initiate steps to rectify it [5].

Plastic particles are found in the environ in a very extensive range of sizes; researchers initially reported finding tiny pellets and pieces of polystyrene in the ocean in the early 1970s. The term ‘microplastic’ was coined in the year 2004 and it is extensively used to denote particles with a maximum size of 5 mm.

Microplastics have been shown to be absorbers and carriers of triclosan and polyvinyl chloride, two prevalent pollutants that may operate similarly to other pollutants. With a certain pH level and a higher salinity, microplastics adsorption capacities increase too and can aggravate the toxicity of other present pollutants. Since the particles are small, small fish are likely able to eat them, while most plastics can pass through the digestive system. This also applies to humans and the extent of the damage is largely unknown. Higher-ranking marine species may consume other organisms that have plastic particles in their tissue and can accumulate more and more plastic in their internal organs over time that can potentially clog the digestive tract of an animal it invades which may eventually lead to the death of the animal [6–8].

In a study done by Kirstein [9, 10], there was a high diversity of organisms living in the microplastic and many produced bacteria containing pathogens while prior studies showed that there were even harmful algae species found on plastic debris. Other potentially dangerous bacteria were also found in the biofilm that can cause harm in other species in the ocean and because of the ease that plastics can enter the environment; many marine species are subjected to the consequences of human pollution [11].

Plastic waste has accumulated in the Pacific Ocean, forming the Great Pacific Garbage Patch, where plastic particles from all over the world have congregated to form a mass of plastic weighing an estimated 1.15 to 2.41 million tonnes [12–14]. Other smaller patches exist where ocean currents aggregate them, plastic particles also accounted for 65% of the collected debris along the shoreline of the Tamar Estuary in the United Kingdom in the year 2010 [10, 15, 16].

Plastic simply wears down physically into tiny fragments while its molecular formula remains constant. A study done by Lisbeth Van Cauwenberghe showed that microplastics are not only limited at surface level but also at a depth of 4000 m and possibly on the ocean floor due to higher density where it mixes with the sediments [17–19].

Consumers are unaware of the microplastics that are present in day to day use items such as tooth-paste and skin care products like face wash and body wash, which are not typically filtered out during sewage treatment and end up being discharged into the oceans. Microplastics are also found in synthetic textiles; according to a study by Mark Anthony Brown [13, 15, 20], on an average around 2000 microplastic fibers can be released by synthetic materials during a single wash and the fibers were similar to those found in sewage treatment plants and shore lines of populated cities.

Although 99% of the microplastics can be filtered from wastewater it ends up being in a vicious cycle of being transformed into sludge, then using this sludge as fertilizers or green construction material which again ends up in the environment and is later washed away into the oceans [21]. A study shows that polyester fibers made up 79.1% of all microplastic-filled water collected from multiple sites and were described to be equally thick and bent [22, 23].

The proposed system aims to reduce the concentration of plastic and microplastic contaminants in water bodies by effectively trapping them with the help of conveyors and mesh of different sizes.

Table 1 Plastic and production rates [2]

Type of plastic	Product and origin	Production (%)
Low density polyethylene (LDPE)	Plastic bags, netting, drinking straws	21
High density polyethylene (HDPE)	Milk and juice jugs	17
Polypropylene (PP)	Rope, bottle caps, nettings	24
Polystyrene (PS)	Plastic utensils, cups, food containers	6
Poly-Vinyl Chloride (PVC)	Plastic films, pipe, cups	19

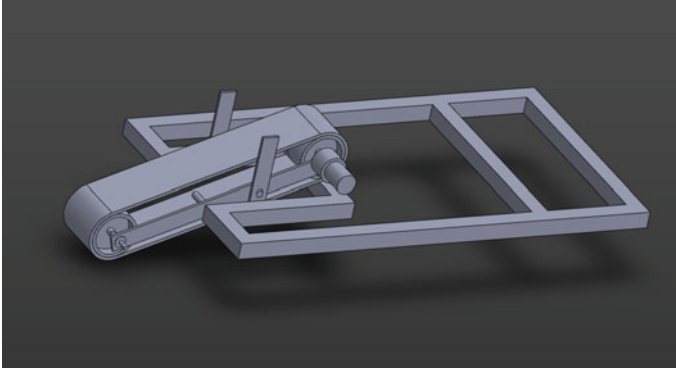


Fig. 1 Basic frame structure

2 Experimental Setup

To tackle plastic and microplastic contamination, we have come up with a system that not only collects plastic contaminants but also microplastic contaminants from water bodies such as rivers, lakes, and the ocean. Taking inspiration from The Ocean Cleanup, we set out to design a system capable of collecting contaminants of all sizes.

To achieve this, the system consists of conveyors and traps to collect macroplastic pollutants (see Fig. 1). To effectively catch the contaminants, angled guides are provided so that the pollutants can be guided to the conveyor belt. Coming to microplastic contaminants, a pump, which continuously sucks in water from the waterbody, is attached and the outlet is given to the filter. The filter consists of stainless steel mesh of varying mesh size in decreasing order of size so that it can trap microplastic contaminants easily and efficiently.

A separate provision in the form of frame is provided to facilitate the mounting of filters and conveyor. The prototype is of dimension $26'' \times 14''$, which when scaled for commercial use would be compact. In order to make the system float, multiple floats of EVA material are used. In order to propel the system, two motors are mounted on the sides that can work in both direction, forward and reverse. The major components used for the setup are shown in Table 2 with their usage.

3 Result and Discussion

The prototype system is efficient in cleaning plastic and micro-plastic contaminants up to 100 microns and is capable of cleaning out 500L of water per hour. Table 3 shows number of microplastic contaminants collected over a series of test runs.

Table 2 Major components and their usage


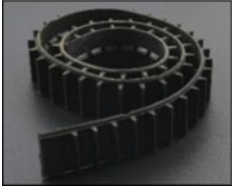
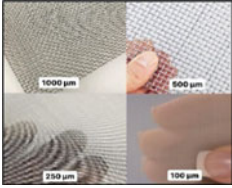

Sr. No.	Component	Image	Use
1	Jhonson's DC Motor specification- 12 V, 3.5A, 5 kg/cm torque		For powering conveyor and for propelling the entire system
2	Conveyor belt Material-Rubber size- 2" × 50 cm		For picking up macro plastic contaminants
3	Mesh arrangement a. 1000 micron b. 500 micron c. 250 micron d. 100 micron Material-SS304		For trapping microplastic contaminants
4	EVA floats Material-Ethylene Vinyl Acetate		To help keeping the system afloat

Table 3 Result

Mesh size	Particles introduced	Particles captured
1000 µ	150	100–115
500 µ	100	60–65
250 µ	100	45–55
100 µ	60	25–30

Figure 2 shows the microplastic particle collected on the different sizes of SS 304 mesh.

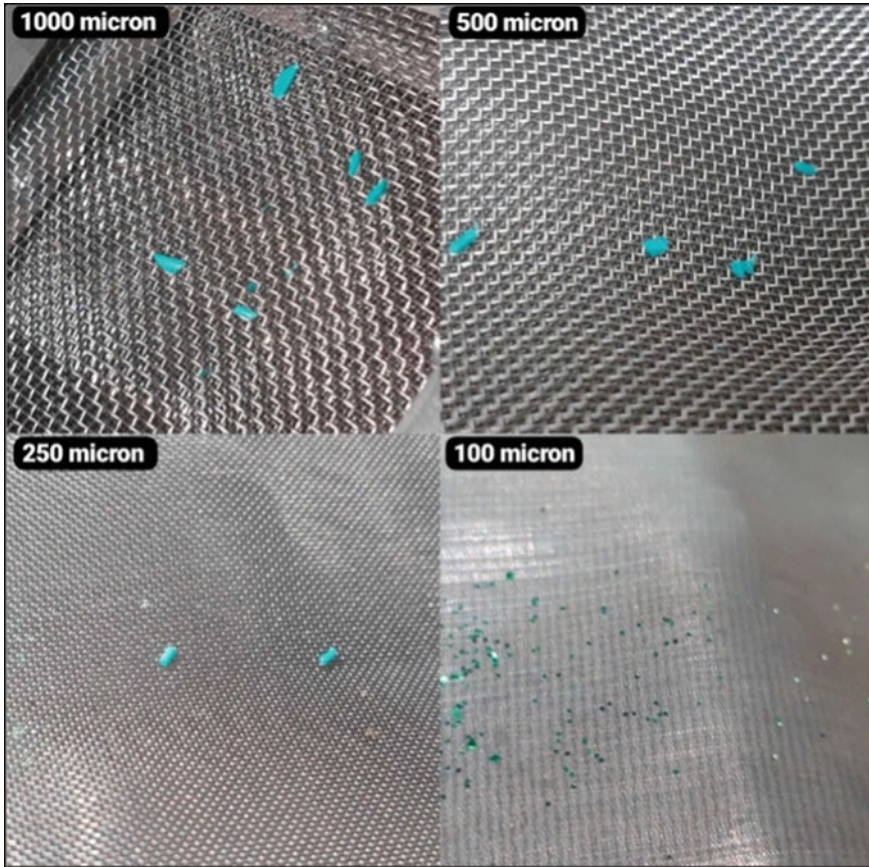


Fig. 2 Results in test conditions

4 Conclusion

The proposed system aims at reducing the concentration of plastic pollutants in the water bodies of our planet. The prototype permits the usage of pump and filter setting, which will not only filter out macro plastics, but also be able to separate out micro plastic debris from the water. This system can filter out plastic debris of up to 100 μ . As the mesh size decreases, number of particles captured also decreases due to the low concentration of microplastic of size less than 250 μ .

This project is a real prototype that is developed to test the feasibility of an actual, large-scale project. The major advantage of our system is that it can be fabricated in accordance to the requirement, and can be mounted on already existing water vessels, thus reducing the overall cost of construction.

References

1. Coppock, R. L., Cole, M., Lindeque, P. K., Queirós, A. M., & Galloway, T. S. (2017). A small-scale, portable method for extracting microplastics from marine sediments. *Environmental Pollution*, 230, 829–837. <https://doi.org/10.1016/j.envpol.2017.07.017>
2. Andrady, A. L. (2011). Microplastics in the marine environment. *Marine Pollution Bulletin*, 62(8), 1596–1605. <https://doi.org/10.1016/j.marpolbul.2011.05.030>
3. Cole, M., Lindeque, P., Halsband, C., & Galloway, T. S. (2011). Microplastics as contaminants in the marine environment: A review. *Marine Pollution Bulletin*, 62(12), 2588–2597. <https://doi.org/10.1016/j.marpolbul.2011.09.025>
4. Clark, J. R., Cole, M., Lindeque, P. K., Fileman, E., Blackford, J., Lewis, C., Lenton, T. M., & Galloway, T. S. (2016). Marine microplastic debris: A targeted plan for understanding and quantifying interactions with marine life. *Frontiers in Ecology and the Environment*, 14(6), 317–324. <https://doi.org/10.1002/fee.1297>
5. Quantitative analysis of microplastic along river Ganga: A report by Toxics Link (2021).
6. Ma, J., Zhao, J., Zhu, Z., Li, L., & Yu, F. (2019). Effect of microplastic size on the adsorption behavior and mechanism of triclosan on polyvinyl chloride. *Environmental Pollution*, 254, Part B.
7. Mai, L., Bao, L. J., Shi, L., Wong, C. S., & Zeng, E. Y. (2018). A review of methods for measuring microplastics in aquatic environments. *Environmental Science and Pollution Research*, 25(12), 11319–11332. <https://doi.org/10.1007/s11356-018-1692-0>
8. Nelms, S. E., Galloway, T. S., Godley, B. J., Jarvis, D. S., & Lindeque, P. K. (2018). Investigating microplastic trophic transfer in marine top predators. *Environmental Pollution*, 238, 999–1007. <https://doi.org/10.1016/j.envpol.2018.02.016>
9. Kirstein, I. V., Hensel, F., Gomiero, A., Iordachescu, L., Vianello, A., Wittgren, H. B., & Vollertsen, J. (2021). Drinking plastics?—Quantification and qualification of microplastics in drinking water distribution systems by μ FTIR and Py-GCMS. *Water Research*, 188, 116519. <https://doi.org/10.1016/j.watres.2020.116519>
10. Barnes, D. K. A., Galgani, F., Thompson, R. C., & Barlaz, M. (2009). Accumulation and fragmentation of plastic debris in global environments. *Philosophical Transactions of the Royal Society B: Biological Sciences*, 364(1526), 1985–1998. <https://doi.org/10.1098/rstb.2008.0205>
11. Alimi, O. S., Farnier Budarz, J., Hernandez, L. M., & Tufenkji, N. (2018). Microplastics and nanoplastics in aquatic environments: Aggregation, deposition, and enhanced contaminant transport. *Environmental Science & Technology*, 52(4), 1704–1724. <https://doi.org/10.1021/acs.est.7b05559>
12. Lebreton, L., Slat, B., Ferrari, F., Sainte-Rose, B., Aitken, J., Marthouse, R., Hajbane, S., Cunsolo, S., Schwarz, A., Levivier, A., Noble, K., Debeljak, P., Maral, H., Schoeneich-Argent, R., Brambini, R., & Reisser, J. (2018). Evidence that the great pacific garbage patch is rapidly accumulating plastic. *Scientific Reports*, 8(1). <https://doi.org/10.1038/s41598-018-22939-w>
13. Jambeck, J. R., Geyer, R., Wilcox, C., Siegler, T. R., Perryman, M., Andrady, A., Narayan, R., & Law, K. L. (2015). Plastic waste inputs from land into the ocean. *Science*, 347(6223), 768–771. <https://doi.org/10.1126/science.1260352>
14. Wong, C. S., Green, D. R., & Cretney, W. J. (1974). Quantitative tar and plastic waste distributions in the Pacific ocean. *Nature*, 247(5435), 30–32. <https://doi.org/10.1038/247030a0>
15. Browne, M. A., Crump, P., Niven, S. J., Teuten, E., Tonkin, A., Galloway, T., & Thompson, R. (2011). Accumulation of microplastic on shorelines worldwide: Sources and sinks. *Environmental Science & Technology*, 45(21), 9175–9179. <https://doi.org/10.1021/es201811s>
16. Browne, M. A., Galloway, T., & Thompson, R. (2007). Microplastic—an emerging contaminant of potential concern? *Integrated Environmental Assessment and Management*, 3(4), 559–561. <https://doi.org/10.1002/ieam.5630030412>
17. Van Cauwenbergh, L., Vanreusel, A., Mees, J., & Janssen, C. R. (2013). November). Microplastic pollution in deep-sea sediments. *Environmental Pollution*, 182, 495–499. <https://doi.org/10.1016/j.envpol.2013.08.013>

18. Thompson, R. C., Olsen, Y., Mitchell, R. P., Davis, A., Rowland, S. J., John, A. W. G., McGonigle, D., & Russell, A. E. (2004). Lost at sea: Where is all the plastic? *Science*, *304*(5672), 838–838. <https://doi.org/10.1126/science.1094559>
19. O’Brine, T., & Thompson, R. C. (2010). Degradation of plastic carrier bags in the marine environment. *Marine Pollution Bulletin*, *60*(12), 2279–2283. <https://doi.org/10.1016/j.marpolbul.2010.08.005>
20. Eriksen, M., Lebreton, L. C. M., Carson, H. S., Thiel, M., Moore, C. J., Borerro, J. C., Galgani, F., Ryan, P. G., & Reisser, J. (2014). Plastic pollution in the world’s oceans: More than 5 trillion plastic pieces weighing over 250,000 Tons afloat at sea. *PLoS ONE*, *9*(12), e111913. <https://doi.org/10.1371/journal.pone.0111913>
21. Lares, M., Ncibi, M. C., Sillanpää, M., & Sillanpää, M. (2018). Occurrence, identification and removal of microplastic particles and fibers in conventional activated sludge process and advanced MBR technology. *Water Research*, *133*, 236–246. <https://doi.org/10.1016/j.watres.2018.01.049>
22. Sun, X., Chen, B., Li, Q., Liu, N., Xia, B., Zhu, L., & Qu, K. (2018). Toxicities of polystyrene nano- and microplastics toward marine bacterium *Halomonas alkaliphila*. *Science of the Total Environment*, *642*, 1378–1385. <https://doi.org/10.1016/j.scitotenv.2018.06.141>
23. McCormick, A. R., Hoellein, T. J., London, M. G., Hittie, J., Scott, J. W., & Kelly, J. J. (2016). Microplastic in surface waters of urban rivers: concentration, sources, and associated bacterial assemblages. *Ecosphere*, *7*(11). <https://doi.org/10.1002/ecs2.1556>

Ward Assignment Prediction in Multi-speciality Hospital Using DDPGO Technique



Gajanan Krishna Bhoi, G. A. Patil, and U. L. Kulkarni

Abstract In a current crisis of pandemic hospitals are unable to allocate the ward to patients in efficient manner. Patients have to visit the Emergency Department and register their information and medical condition. Then the Emergency Department will run the deep learning algorithm with curriculum learning after that the process data is passed to DDPGO to find out the appropriate ward depending on the state and patient type to allocate the suitable ward to the approached patient. While carrying out this process the deep learning algorithm self-trains itself on curriculum data and improves itself each time the process is run. We have 7 different types of wards which can be allocated to the different patients requesting the services. This type of system will help hospitals to allocate wards whenever there is a huge health crisis just as a pandemic as well as it will help improve the process of ward allocation.

Keywords Deep deterministic policy gradient · Deep learning · Curriculum learning · Mahalanobis distance technique

1 Introduction

Pandemic situations or peak seasons of disease spreading puts a load on medical service providers to allocate the ward and necessary medical-care resources for the patient promptly and hence huge amounts of chaos happen that delays the treatment of patients to overcome this problem this paper put light on Deep learning method of predicting suitable ward for the patient who is approaching to the emergency department of a multi-speciality hospital. such early predictions will help the hospital to provide the required medical-care resources to the patient in an efficient manner.

Generally, patients with critical conditions and uncertain symptoms rush to the emergency department. Where the emergency department Nursing attendant checks

G. K. Bhoi (✉) · G. A. Patil · U. L. Kulkarni
Department of Computer Science and Engineering. DYPCET, Kolhapur, Maharashtra, India
e-mail: gajananbhoi@gmail.com

the patient and in order to decide the line of treatment prescribes some medical tests for further investigation. In pandemic circumstances or the Pinnacle periods of infections spreading the emergency department will get full in no time that is it will put a load on the clinical service framework.

We have designed a model that exploits the concept of learning via the curriculum and deep deterministic policy gradient optimization (DDPGO) that successfully predicts one of the seven wards available at a multi-speciality hospital for the initial admission of the patient who is approaching the emergency department of the hospital. We successfully predict the initial admission ward of the patient with accuracy ranging between 70 and 80% for the individual ward using the instance of test cases run at that particular time with some randomly picked records through the stored dataset. This optimal deep network learning framework will prove to be a helping hand to multi-speciality healthcare institutions by enabling the allocation of bed space as well as the planning of critical healthcare instruments well ahead of time.

2 Methodology

The work mainly covers the aspects of suitable ward allocation and required patient-care resources to a patient before his admission [1]. To cover this specific need of framework, a deep deterministic policy gradient is used which gradually learns as well as propagates the output in a way that will optimize the allocation in 7 different ward [2] types by keeping in mind the state of the patient that has to be admitted. For training, the system curriculum learning [3] is initially used to pass meaningful basic attributes like the state of the patient, increasing and the type of ward. This helpfully speeds up the rate of learning and gives multi-speciality hospitals an efficient ward-allocating capability. The system mainly consists of four modules that are Feature selection, batch preparation, learning with DDPGO (*Deep Deterministic Policy Gradient Optimization*), and ward prediction. Feature selection mainly involves datasets of the mixed type which are given as input to the system. Batch preparation consists of a distance calculation technique whereas learning and self-training of the system is done through DDPGO. In the end, we have clustering and suitable ward prediction for the patient.

Module 1: Feature Selection

Data of hospitals containing the number of admissions in each ward with the details of patients is a crucial asset for implementing such types of systems. The data needs to be gathered manually through multi-specialty hospitals. For testing out the developed model, we initially used the dataset named MIMIC-III Dataset (Medical Information Mart for Intensive Care dataset) as well as the local dataset of a local Multispecialty Hospital. The whole dataset is sectored into sets to train the model and test it out.

The dataset may have missing data or may include data of mixed type. Missing information (or missing qualities) is characterized as information with significance for the prediction of a suitable and correct ward. The reasons for the missing information are corrupted or truncated values, missing information, or sometimes unavailability of data. So, the mean-substitution technique is used to tackle the problem of missing feature problem; here mean is average of the sum of values in a column. This lets us employ the recorded data in a dataset that is incomplete due to missing information [4]. To solve the mixed data type problem, it is required to encode. This encoding is achieved using autoencoders. Label autoencoders are being used for cleaning the data and preprocessing it in a way that actual feature extraction receives more meaningful data from the versatile data provided in the dataset. we have exercised the method—**fit transform ()** function to achieve label autoencoding (Fig. 1).

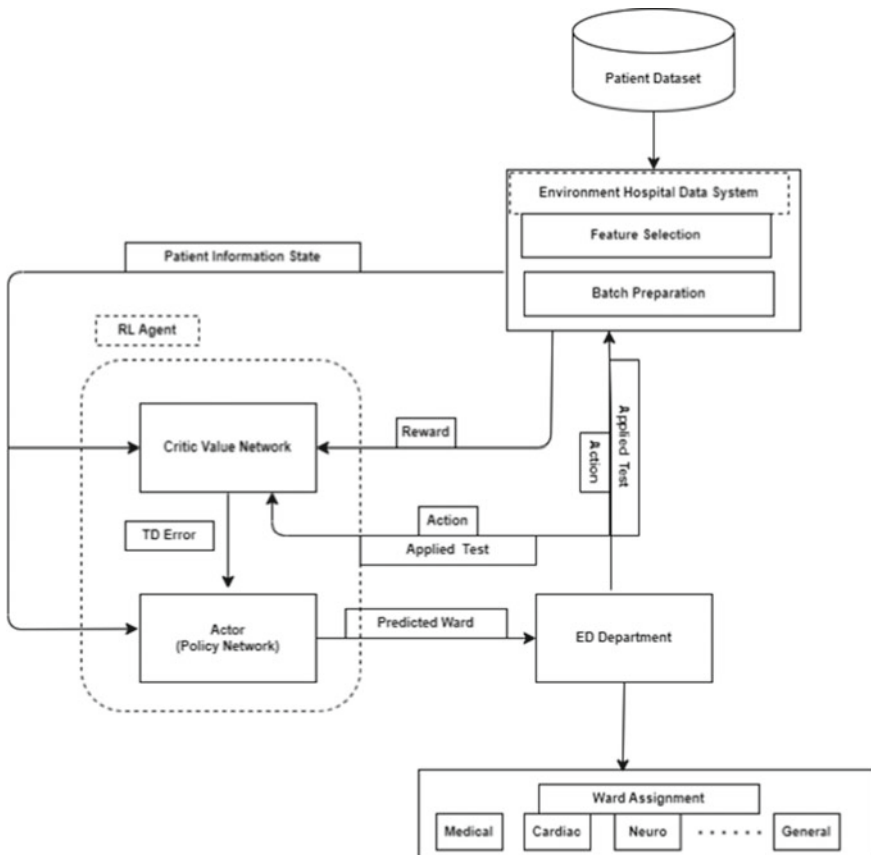


Fig. 1 Architecture diagram

Module 2: Batch Preparation

Noisy data is cleaned and encoded in a proper manner that is needed by the curriculum training phase. This encoded training dataset is represented by Z and it contains n data points so represented by Z_n . Each data point is represented as,

$$Z_i = \{x_i, y_i\} | i \in 1, 2 \dots n$$

where

x_i i^{th} feature

y_i i^{th} Label.

Like Humans, ML algorithms [5] also can learn effectively from intelligently organized experiences. If one first starts with easy activities of the task and then slowly over the period increasing the complexity of the task one can learn from the experience effectively. These intelligently organized experiences for the student are called curriculum. Similarly, the AI algorithm is presented with less complex data i.e. data with similarity is bunched together in a batch and fed to the network for training purpose so the AI algorithm will learn efficiently. The organization of the data into batches to form the curriculum for the curriculum learning [3] is accomplished with the Mahalanobis distance calculation technique. Mahalanobis distance calculation technique is used as a distance metric that measures the distance between feature and distribution. This distance is calculated as follows,

$$d_m = ((x_n - \mu)^T \alpha^{-1} (x_n - \mu))^{1/2}$$

Here,

x_n Input features

μ Feature vector contains the mean value of every feature set

δ Covariance matrix

T Timestamp.

The features are bunched up into batches depending on the Mahalanobis distance. The features with less Mahalanobis distance are bunched together to form the batch of the curriculum. So, to facilitate the easy learning form the batch contains features with similar values. For creating curriculum, we have arranged batches in ascending order of Mahalanobis distance.

Module 3: Model Learning with a DDPGO

DDPGO is an off-policy actor-critic algorithm that uses a user agent. We take into consideration the seven types of wards as reference classes to create datasets [6]. In this framework, we have carried out a method given a learning agent which is the kind of agent that can gain knowledge from its previous experiences or the agent has learning capacities [7]. It starts acting with fundamental information and afterward ready for acting and adjustment consequently due to learning.

From the given observation, it uses the most appropriate action. In the system, batches are given as input to DDPG. Here (S_t, a_t) denotes the state and action pair at time t. Here S_t is the batch set containing input feature i.e. prescribed tests for patients and a_t is the suitable ward predicted for the patient. The policy deterministic function, $a_t = \mu_0(S_t)$ will be used where μ_0 is a network that maps the state of a patient to the appropriate ward [8]. The policy is parametric conditional probabilistic distributions over space of possible actions inputted the state S_t with model parameter. It is represented as an actor network as follows

$$\Pi_{\theta}(S_t, a_t) = P(a_t|S_t\theta)$$

The objective is to search for a policy that amplifies the rewards with the equation.

$$R(S_t, a_t) = r_t + \gamma r_{t+1} + \dots + \gamma^{T-t} r_T$$

Here,

S_t State of Patient at time t

a_t Action taken at time t.

This reward is used for model prediction.

Module 4: Possible learning algorithm for Ward assignment prediction

In the developed system, the reward is calculated for state S_t for action a_t , critic network is updated from the gradient obtained. Then the algorithm executes a series of actions to get optimized results [9].

Critic network is calculated as

$$Q_w^{\mu}(S_t, \mu_0(S_t)) = E_u[R(S_t, \mu_0(S_t))]$$

Here,

S_t State of Patient at time t

R Replay set (i.e. Feature set)

$Q_w^{\mu}(St, \mu_0(St))$ Critic Network

E_u Equivalent Function.

The estimated treatment-ward assignment will be calculated as follows

$$E(\gamma(t)|X = x) = E[\gamma|T = t, X = x)$$

Here,

γ Outcome (Ward Assignment)

X Patient Vector

S_t State of Patient at time t

a_t Action taken at time t
 T Time.

3 Results Analysis

Accuracy

Classification models are evaluated on the basis of a metric called accuracy. Casually, Accuracy is the portion of total predictions our model got correct. Accuracy can be defined as follows:

$$Accuracy = \frac{\text{Number of right Predictions}}{\text{Total Number of predictions}}$$

For this system, we have calculated the accuracy by increasing the number of batches and we analyzed the performance. The accuracy is calculated with the following formula

$$Accuracy = \frac{TN + TP}{TN + TP + FN + FP}$$

Here,

TN True_Negative

FN False_Negative

TP True_Positive

FP False_Positive.

For illustration purpose, we have 7 different classes of wards to be predicted as the result of input prescribed tests for the patient. Namely, Cardiac, ICU, Medicine, Neuro, Surgical, Obstetrics & Gynecology, Trauma [2].

The calculation of accuracy is carried out on both the datasets i.e. the local dataset and MIMIC dataset. The accuracy is calculated against each ward allocation prediction percentage (Fig. 2).

Logarithmic Loss

Logarithmic loss is nothing but a parameter that helps predict and measure how closely we have achieved the results. Logloss is a metric that demonstrates how close real-world true values are to the probabilities of the prediction. It is explained as follows:

$$Logloss = \frac{-1}{N} \sum_{i=1}^N (\log(pi))$$

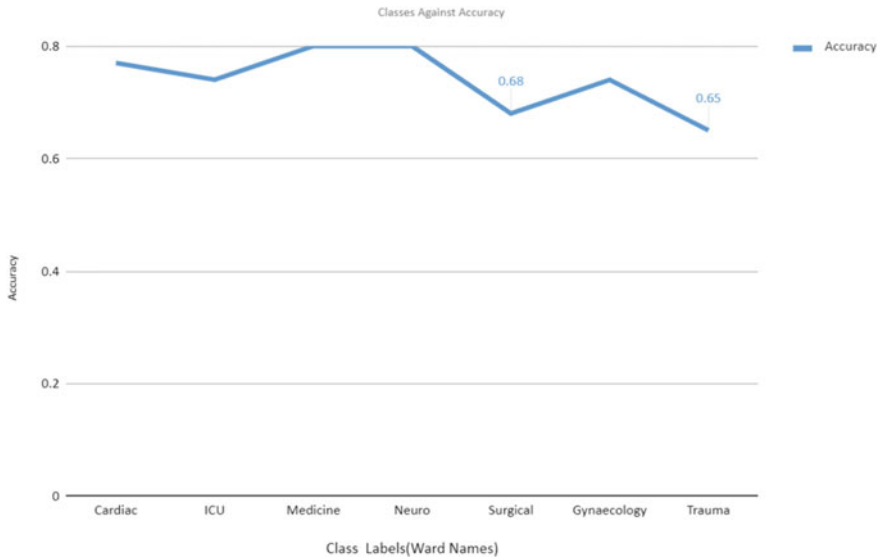


Fig. 2 Accuracy against each type of ward

where,

y_{ij} , Demonstrates if test i has a place with class j

p_{ij} , Demonstrates the likelihood of test i having a place with class j .

Test1 to test10 are nothing but randomly selected record sets from the local dataset as well as from the MIMIC-III dataset that we have used to test the system for prediction. It will calculate the correct probability out of the total set of results obtained against each correct class. The probability indicates how well the model is predicting the correct ward and the log of this probability can be considered as a loss of the correctly prediction functionality of a model. i.e. we can say that if the value of logloss is lower more accurately the model is predicting the suitable ward for the patient. We have values for Actual value, probability, and negative index related to the MIMIC-III dataset. Each value has its own significance in proving that our system which is using DDPGO is more efficient and has close results to the MIMIC dataset readings. Hence it proves that with different datasets the system works in a similar efficient manner as with our dataset. Hence, we have achieved the maximum amount of success in the prediction of wards. The less the log value more the accuracy and preciseness of results are proved. We have obtained very negligible values for the log and hence we have achieved maximum accuracy in ward prediction (Fig. 3).

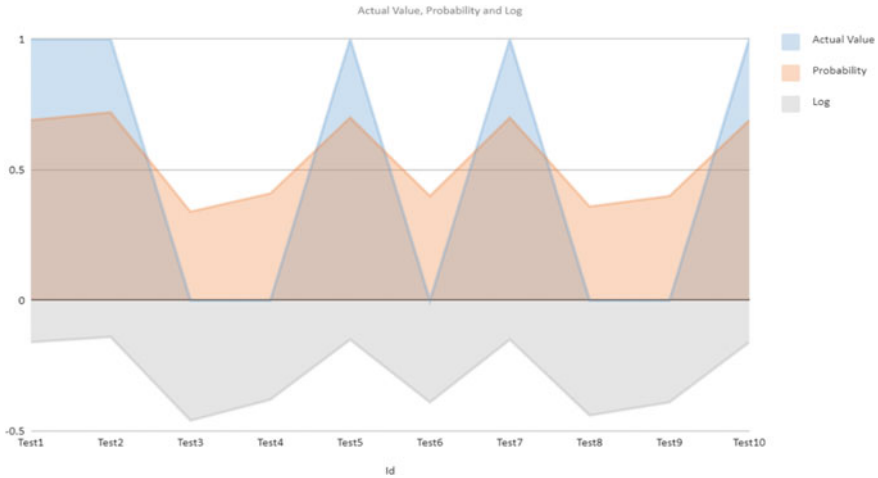


Fig. 3 Logarithmic loss against actual defined results and values

4 Conclusion

The dissertation work mainly involves the process of implementation and development of the ward prediction DDPGO. Thus, we have developed a novel framework that uses Curriculum learning and DDPGO technique to predict the suitable ward for patient more accurately.

The existing system had achieved AUC (Area under Curve) values between 0.60 and 0.78 for the individual ward types [2]. The developed model achieves 65–80% accuracy for the individual ward types with the Logloss of 0.33 for local dataset and 0.28 for MIMIC dataset, which signifies that model has improved prediction. The batch preparation has helped us obtain feature specific and appropriate data in the form of batches that can be easily used by DDPGO for training and analysis. We have observed that model achieves 65–80% accuracy of the system while allocating each ward based on local dataset. Similarly, we have fed the system with our dataset and MIMIC dataset and tested the results obtained achieves 71–83% accuracy.

However, we have a few enhancements that can improve the system implementation. Security-related issues are not taken into consideration and hence encryption can be implemented at the phase of data selection so as to preserve the privacy of data being used. Whereas we have carried out the implementation on the set of static datasets which will be replaced by dynamic data hence growing data will help us understand the system nature in a better way.

References

1. Staib, A., Sullivan, C., Prins, J. B., Burton-Jones, A., Fitzgerald, G., & Scott, I. (2017). Uniting emergency and inpatient clinicians across the ed–inpatient interface: The last frontier? *Emergency Medicine Australasia*, 29(6), 740–745.
2. El-Bouri, R., Eyre, D. W., Watkinson, P., Zhu, T., Clifton, D. A. (2021). Hospital admission location prediction via deep interpretable networks for the year-round improvement of emergency patient care. *IEEE Journal of Biomedical and Health Informatics*, 25(1), 289–300. Jan 2021. <https://doi.org/10.1109/JBHI.2020.2990309>
3. Matiisen, T., Oliver, A., Cohen, T., & Schulman, J. Teacher-student curriculum learning, [arXiv:1707.00183](https://arxiv.org/abs/1707.00183).
4. Zhai, H., et al. (2014). Developing and evaluating a machine learning based algorithm to predict the need of pediatric intensive care unit transfer for newly hospitalized children. *Resuscitation*, 85(8), 1065–1071.
5. Ma, F., Chitta, R., Zhou, J., You, Q., Sun, T., & Gao, J. (2017). Dipole: Diagnosis prediction in healthcare via attention-based bidirectional recurrent neural networks. In *Proceeding of the 23rd ACM SIGKDD international conference on knowledge discovery data mining* (pp. 1903–1911).
6. Liang, Z., Zhang, G., Huang, J. X., & Hu, Q. V. (2014). Deep learning for healthcare decision making with emrs. In *Proceedings IEEE international conference on bioinformatics biomed* (pp. 556–559).
7. Xu, H., Wu, W., Nemati, S., & Zha, H. (2017). Patient flow prediction via discriminative learning of mutually-correcting processes. *IEEE Transactions on Knowledge and Data Engineering*, 29(1), 157–171, Apr 2017.
8. Bishop, C. M. (2006). *Pattern recognition and machine learning* (p. 2006). Springer.
9. Samek, W., Wiegand, T., & Müller, K. -R. (2017). *Explainable artificial intelligence: Understanding, visualizing and interpreting deep learning models*, [arXiv:1708.08296](https://arxiv.org/abs/1708.08296).

Evaluation of Some Medicinal Plants as an Antimicrobial Agent for Drinking Water Treatment



Sachin G. Chonde and Sonal G. Chonde

Abstract Plants are the richest resource of drugs of traditional systems of medicine, modern medicines, nutraceuticals, food supplements, folk medicines, pharmaceutical intermediates and chemical entities for synthetic drugs. The use of plants and plant products as medicines could be traced as far back as the beginning of human civilization. In the present Study, Evaluation of Medicinal Plants *Ocimum tenuiflorum* (Tulsi), *Syzygium aromaticum* (Clove), *Azadirachta indica* (Neem) and *Aloe vera* (*Aloe*) was tested for drinking water treatment. Various doses of different selected medicinal plants powder were given on water sample and tested for antimicrobial capacity against the water borne pathogens. *Syzygium aromaticum* powder was found to be effective against human pathogenic bacteria like *S. typhi* and *E. coli*. Also, other selected medicinal plants show best results for drinking water treatment.

Keywords Medicinal plants · Drinking water treatment · Natural coagulants · Water borne pathogens

1 Introduction

Plants are the richest resource of drugs of traditional systems of medicine, modern medicines, nutraceuticals, food supplements, folk medicines. The “herbal drugs” or “phytomedicines” are generally single plant extracts and they digger from pure synthetic chemical medicines call “molecular drugs”. The herbal drugs are mainly use in the form of indigenous ayurvedic medicines while purely chemical molecular

S. G. Chonde

Department of Applied Sciences and Humanities, Ashokrao Mane Group of Institutions, Vathar, Kolhapur, Maharashtra, India

e-mail: sonalchonde@gmail.com

S. G. Chonde

e-mail: sgchonde2021@gmail.com

S. G. Chonde

Krishna Institute of Allied Sciences, Krishna Vishwa Vidyapeeth “Deemed to be University”, Karad, Maharashtra, India

drugs and synthetic drugs prepared after knowing the basic structure of herbal drug are used in the form of allopathic medicines.

India is rich in Variety of medicinal plants, unfortunately only few of them are used for their medicinal purposes from which some plants are under taken the study viz. *Ocimum tenuiflorum* (Tulsi), *Syzygium aromaticum* (Clove), *Azadirachta indica* (Neem), *Aloe barbadensis* (Aloe) etc. are used by the people for various ailments mainly for the relief in bronchitis, cold, cough, vomiting, skin diseases.

Traditionally in India various medicinal plants are used as primary health care. Medicinal plants are source of great economic value all over world. The earliest mention of medicinal use of plants in Hindu culture is found in 'Rig-Veda'. This is said to have been written between 4500 and 1600 BC. The ayurved is foundation of medicinal science of Hindu culture [3, 5].

Plants are richest source of drugs of traditional systems of medicine, modern medicines, nutraceuticals, food supplements, folk medicines, pharmaceutical intermediates and chemical entities for synthetic drugs [2, 6, 9] Plant medicines as alternatives to synthetic drugs [1].

Herbal medicine is still the mainstay of about 75–80% of whole population and the major part of traditional therapy involves the use of plant extract and their active constituents [7, 10].

Many infectious diseases have been known to be treated with herbal remedies throughout the history of mankind [5, 12, 13]. Naturally occurring substances of the plant origin have been reported to inhibit the growth of micro-organism [11].

The use of natural materials of plant origin to clarify turbid water is not a new idea [2, 7, 9]. *Moringa oleifera* seed powder was removed 90–99% turbidity [7, 8] act as antimicrobial agent against micro-organisms [1, 4] and also acts as removal hardness in water to increase with increasing dosage through adsorption and inter particle bridging [6, 11] Turbidity, hardness, Chloride, Acidity, TS, TDS, MPN and SPC reduced with increased dose of *Moringa oleifera* seed powder except Alkalinity and pH [7].

The antimicrobial activity has been attributed to the presence of some active constituent in the extracts *E. caryophyllata* (Clove) was found to be the most effective against *S. typhi*. *O. sanctum* (Tulsi), *E. caryophyllata* (Clove), *A. indica* (Neem), *A. bidentata* (Datiwan) was ineffective against *E. coli* and *K. pneumonia* (Joshi et al., 2011). Here some ZOI was observed is 5 cm. The MIC mg/ml value for *O. sanctum* (Tulsi) against *E. coli*, *S. typhi*, *P. vulgaris* is found to be 2 [8]. *E. coli* effectively inhibited by *E. caryophyllata* (Clove) and *O. sanctum* (Tulsi) also reduced MPN and bacterial count [12].

Recent studies on *O. gratissium* proved it to be a useful medication for people living with HIV and AIDS [8] and also antimicrobial activity carried out the using agar well diffusion method [5, 9].

2 Materials and Methods

Four plants were selected for study of their antimicrobial activity against two pathogenic bacteria namely, *E. coli* and *S. typhi*. The selected plants are: *Ocimum tenuiflorum* Linn (Tulsi), *Aloe barbadensis* Mill (Aloe), *Syzygium aromaticum* Linn. (Clove), *Azadirachta indica* A. Juss. (Neem).

The medicinal plant identified according to various literatures.

1. *Ocimum tenuiflorum* (Tulsi):- The Tulsi leaves stem, roots are collected from Local area and seeds are purchased from market of pethvadgaon, Dist. Kolhapur.
2. *Syzygium aromaticum* (Clove):- The clove buds were purchased from local market of Pethvadgaon, Dist. Kolhapur.
3. *Azadirachta indica* (Neem):- The Neem leaves and stem collected from local area of Pethvadgaon, Dist. Kolhapur.
4. *Aloe vera* (Aloe):- The *Aloe vera* leaves are collected from local area of Pethvadgaon, Dist. Kolhapur.

2.1 Collection of Water Sample for Study Purpose

For study purposes ground water sample was collected from Pethvadgaon area, Vathar, Dist. Kolhapur.

2.2 Selection of Micro-Organisms for Study Purposes

For study purpose two pathogenic bacteria namely, *Escherichia coli* (*E. coli*) and *Salmonella typhi* (*S. typhi*) are used. The Bacterial cultures were collected from Department of microbiology, Rajaram College, Kolhapur, Maharashtra.

2.3 Methodology

(A) Study of medicinal plant for water purification

All collected plant material was oven dried at 100 °C. then the oven dried plant materials are powdered by using mortar and pestle. This powder is directly used as coagulant. The different medicinal plants parts are used for treatment of collected water sample. Before the treatment of medicinal plant parts check the water quality by using different parameter. Requiring dosage of powder was added in the water sample.

The treatment was given with different time interval (6, 12, 24 h) with addition of powder of selected medicinal plants. After the treatment, water samples were settle

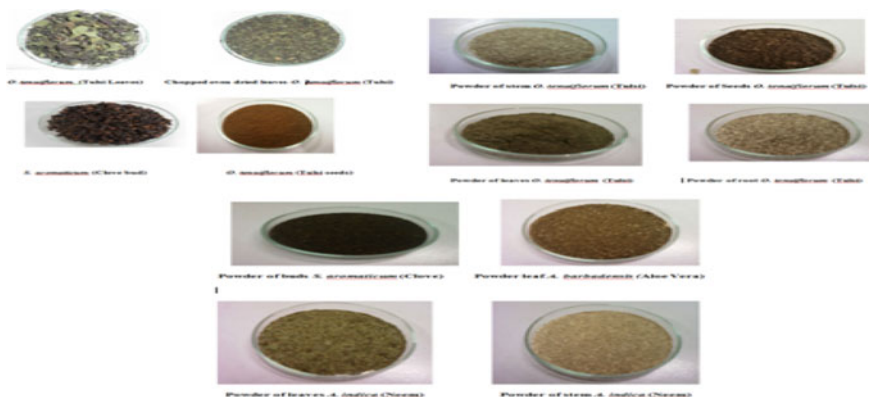


Fig. 1 Representation of photos of plant material collected for experiment

for the constant turbidity, then the water samples were filtered. The water samples were tested for physicochemical parameters.

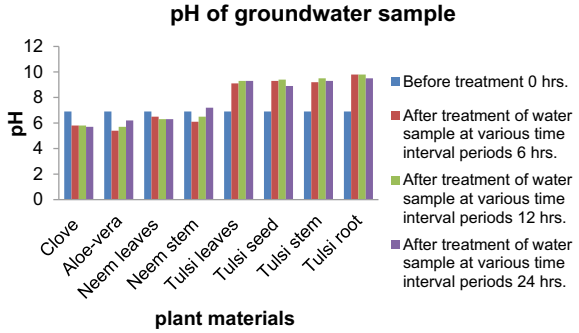
(B) **Zone of Inhabitation (ZOI) study**

The antimicrobial activity of the medicinal plant parts dose was tested by using Zone of Inhibition method. The nutrient media was inoculated with selected pathogens and with the cork borer the media was inoculated with the medicinal plant powder extract.

3 Study of Physical, Chemical and Biological Characteristics of Water

Before the treatment of water samples with the different medicinal plants powder the physic-chemical and biological parameters of the water were analyzed. These include pH, E.C., Chloride, Hardness, TS, TDS, TSS, MPN etc. (Figs. 1, 2, 3 and 4; Tables 1, 2, 3 and 4).

Fig. 2 Graphical representation of pH of water before and after treatment of selected medicinal plants



E. C. of groundwater sample

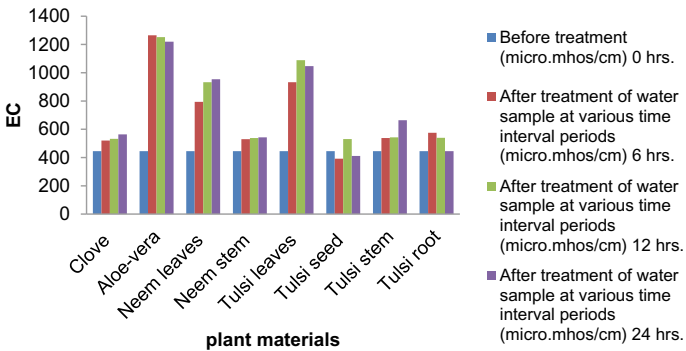


Fig. 3 Graphical representation of conc. of electrical conductivity of water before and after treatment of selected medicinal plants

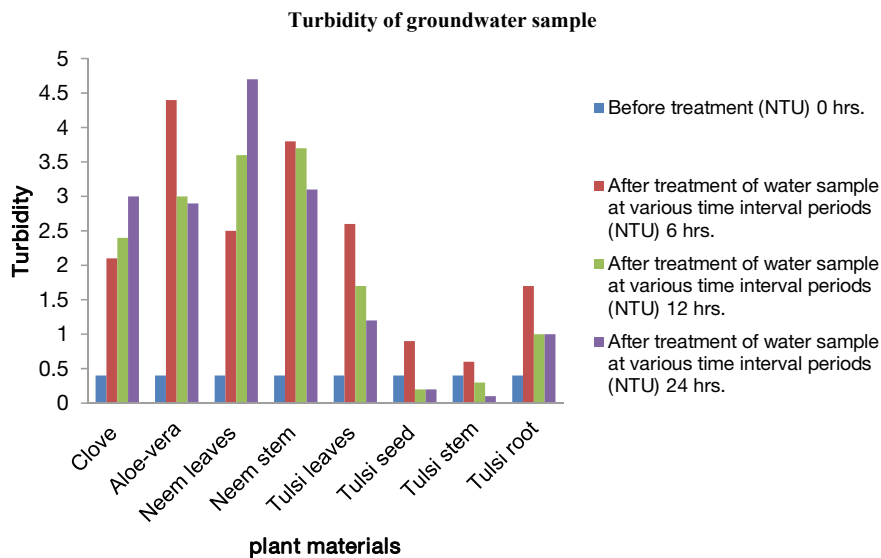


Fig. 4 Graphical representation of turbidity of water before and after treatment of selected medicinal plants

Table 1 Study of pH of groundwater before and after treatment of medicinal plant powder

Plant material	Before treatment	After treatment of water sample at various time interval periods		
	0 h	6 h	12 h	24 h
Clove	6.9	5.8	5.8	5.7
Aloe-vera	6.9	5.4	5.7	6.2
Neem leaves	6.9	6.5	6.3	6.3
Neem stem	6.9	6.1	6.5	7.2
Tulsi leaves	6.9	9.1	9.3	9.3
Tulsi seed	6.9	9.3	9.4	8.9
Tulsi stem	6.9	9.2	9.5	9.3
Tulsi root	6.9	9.8	9.8	9.5

Table 2 Study of electrical conductivity of groundwater before and after treatment of medicinal plant powder

Plant material	Before treatment (micro.mhos/cm)	After treatment of water sample at various time interval periods (micro.mhos/cm)		
	0 h	6 h	12 h	24 h
Clove	445	520	532	564
Aloe-vera	445	1265	1252	1220
Neem leaves	445	794	933	954
Neem stem	445	530	538	543
Tulsi leaves	445	933	1089	1047
Tulsi seed	445	392	531	411
Tulsi stem	445	538	543	664
Tulsi root	445	575	540	445

Table 3 Study of turbidity of groundwater before and after treatment of medicinal plant powder

Plant material	Before treatment (NTU)	After treatment of water sample at various time interval periods (NTU)		
	0 h	6 h	12 h	24 h
Clove	0.4	2.1	2.4	3
Aloe-vera	0.4	4.4	3	2.9
Neem leaves	0.4	2.5	3.6	4.7
Neem stem	0.4	3.8	3.7	3.1
Tulsi leaves	0.4	2.6	1.7	1.2
Tulsi seed	0.4	0.9	0.2	0.2
Tulsi stem	0.4	0.6	0.3	0.1
Tulsi root	0.4	1.7	1	1

Table 4 Study of chloride of groundwater before and after treatment of medicinal plant powder

Plant material	Before treatment (mg/lit)	After treatment of water sample at various time interval periods (mg/lit)		
	0 h	6 h	12 h	24 h
Clove	60.06	6	10	36
Aloe-vera	60.06	138.15	138.15	140.15
Neem leaves	60.06	50.05	52.05	56.06
Neem stem	60.06	56.06	56.06	60.06
Tulsi leaves	60.06	88.18	165.18	165.18
Tulsi seed	60.06	45.04	40.04	40.04
Tulsi stem	60.06	28.03	75.08	130.4
Tulsi root	60.06	54.05	65.07	74.08

4 Conclusion

Present study evaluated the use of medicinal plants for water purification and antimicrobial activity. From the study it can be concluded that, the medicinal plant shows antimicrobial activity against different micro-organism due to presence of their chemical constituents. *Syzygium aromaticum* (Clove) powder was found to be effective against human pathogenic bacteria like *S. typhi* and *E. coli*. with the effective dose. 0.5 mg. of powder conc. As the dose of medicinal plant powder increases then decrease in number of micro-organisms was observed in ZOI study. It was concluded that, the dose of (0.5) *Syzygium aromaticum* (Clove) and *Ocimum teuniflorum* (Tulsi leaves) powder shows effective result for given ground waster as it to decreases microbial load and MPN value of groundwater sample (Fig. 5).

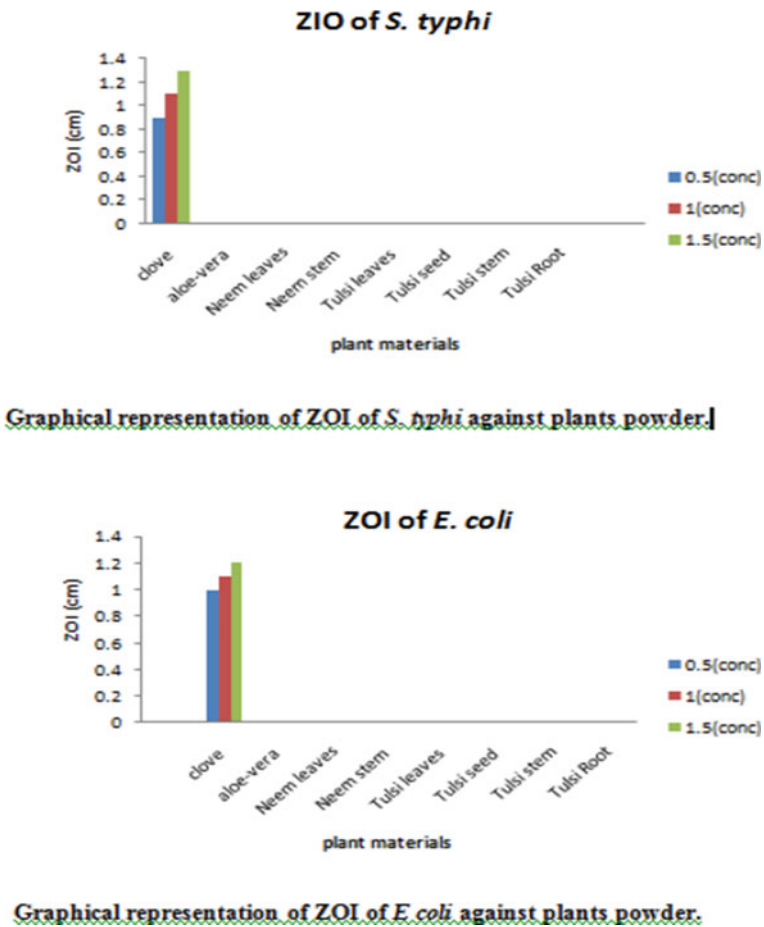


Fig. 5 Zone of inhibition of *S. typhi* and *E. coli* against all selected plants powder

pH of the sample becomes more acidic while the medicinal plant material is added into water. Also the electrical conductivity and turbidity of water sample was found to be increase after the addition of *Syzygium aromaticum* (Clove), *Ocimum tenuiflorum* (Tulsi seed) powder. Alkalinity < TS, TDS and TSS values of the water also decreases after the treatment with *Azadirachta indica* (Neem stem) and *Ocimum tenuiflorum* (Tulsi seed, stem and root). From the above results it can be concluded that all the selected plants show best results for water treatment, besides the *Ocimum tenuiflorum* was found to be best plant material for coagulation and antimicrobial treatment of water.

References

1. Bandyopadhyay, U., Chatterjee, R., & Bandyopadhyay, R. K. (1998). Process for the isolation of an active principle from *Azadirachta indica* useful for controlling gastric hyperacidity and gastric ulceration. US patent No. p. 5730986. Gastroprotective effect of Neem (*Azadirachta indica*) bark extract: Possible involvement of H⁺-K⁺ -ATPase inhibition and scavenging of hydroxyl radical. *Life Science*, 71, 2845–2865.
2. Ekhaise, F. O., Soroh, A. E., & Falodun, A. (2013). Antibacterial activity properties and preliminary phytochemical analysis of methanolic extract of *Occimum gratissimum* (Scent leaves). *Bayero Journal of Pure and Applied Sciences*, 3(2), 81–83.
3. Elujoba, A. A. (2000). *Studies on the antidiarrhoea activity of Ocimum gratissimum guavu* (p. 160). University of Ife Press.
4. Garrod, L. P., Lambert, H. P., & Grady, O. A. (1981). *Antibiotics and chemotherapy* (p. 385). Church-Hill, Livingstone Press London.
5. Hammer, K. A., Carson, C. F., & Riley, T. V. (1999). Antimicrobial activity of essential oils and other plant extracts. *Journal of Applied Microbiology*, 86(6), 985.
6. Hart, L. A., Nibbering, P. H., van den Barselaar, M. T., & van Dijk, H. (1990). van den Berg AJ and Labadie RP effects of low molecular constituents from 2398. *Journal of Medicinal Plants Resources*, 1, 61–69.
7. Mangale, S. M., Chonde, S. G., Jadhav, A. S., & Raut, P. D. (2012). Study of *Moringa oleifera* (Drumstick) seed as natural absorbent and antimicrobial agent for river water treatment. *Journal of Natural Product Plant Resource*, 2, 89–100.
8. Mangale, S. M., Chonde, S. G., & Raut, P. D. (2012). Study of *Moringa oleifera* (Drumstick) seed as natural absorbent and antimicrobial agent for ground water treatment. *Research Journal of Research Sciences*, 1(3), 31–40.
9. Mao, L., Jin, H., Wang, M., et al. (2020). Neurologic manifestations of hospitalized patients with coronavirus disease 2019 in Wuhan, China. *JAMA Neurology*, 77(6), 683–690.
10. Rastogi, R. P., & Mehrotra, B. N. (2002). *Glossary of Indian medicinal plants*. National Institute of Science Communication.
11. Joji, R. L., Spandana, G., Beena, J., Devi, J. R. (2012). 'Evolution of antibacterial and antioxidant activities of the leaf and bark extracts of *Azadirachta indica* A. Juss. *World Journal of Pharmaceutical Research*, 1(3), 661–672.
12. Parag, S., Vijayshree, N., Ranu, B., & Patil, B. R. (2010). Antibacterial activity of *Ocimum sanctum* Linn. and its application in water purification. *Research Journal of Chemistry and Environment*, 14(3), 46–50.
13. Kamkin, V., Kamarova, A., Shalabayev, B., Kussainov, A., Anuarbekov, M., & Abeuov, S. (2022). Comparative analysis of the efficiency of medicinal plants for the treatment and prevention of COVID-19. *International Journal of Biomaterials*, 2022, 1–14.

Identification and Analysis of Musculoskeletal Disorder Among Indian Truck Driver



A. B. Rathod and R. T. Vyavahare

Abstract Truck driving is one of growing and demanding profession in India, there are many people from Rural and Urban society engaged in Truck Driving. Indian Truck drivers face work related concerns and injuries due to musculoskeletal disorders. Truck driving is overstressed, stubborn and prolonged static postures while performing the duty while operating from limited space of truck cabin, which many times not designed as per Indian Anthropometry. During driving, driver faces numerous discomforts like continued sitting positions, considerable pressure to neck, upper, lower back and uneasy environment. Work related musculoskeleton disorders are observed due to these discomfort factors. Study was directed to identifying the problems concerned to musculoskeletal disorder among Indian Truck Drivers, its linked factors and their outcomes. A survey in questionnaire form was done which had Demographic, professional and data related to musculoskeletal disorders, their reasons and their consequences. Around 100 Truck drivers contributed to the study.

Keywords Indian truck driver · Musculoskeletal disorder · Ergonomics · Work posture

1 Introduction

While driving a truck in safe working posture it is very much essential to have good balance between back and neck of a truck driver. Musculoskeleton disorder are the result of unbalanced postures, and it can be prevented by optimizing driver seat position by keeping required height of seat, using comfort seat design, rest and relaxing while performing truck driver duty [1]. One of most important ergonomic aspect

A. B. Rathod (✉)

Walchand Institute of Technology, Solapur, Maharashtra 413006, India

e-mail: rathodamit2100@gmail.com

R. T. Vyavahare

N B Navale Sinhgad College of Engineering, Solapur, Maharashtra 413255, India

accountable for growth of MSD is uneven posture used for extended seating positions while driving. Monotonous movement of upper limb along with postural weight on neck and upper back during truck driving for long duration and mental pressure have significant role in attracting drivers with musculoskeletal warning sign. These working exposures result in absenteeism from work and ultimately decrease the superiority and yield of their duty [2]. The frequency, duration, and intensity of driver's exposure to these severe work conditions defines the level of risk causing WMSDs. Use of comfortable driver seat design, proper positioning of hand operated dashboard equipment's and cabin ergonomics are the means to reduce MSDs [3]. The Truck cabin design and the driving positions displayed by the drivers impact their well-being. Inappropriate work environment of truck cab such as the incorrect driver's seat design, insufficient air circulation and illumination. There are several positions that driver take such as working on one side, undue twisting, forward bending, shoulder joint flexed and abducted. The most important aim of Ergonomics is the prevention of MSDs. In driving profession, uneasy physical position promotes to musculoskeletal disorders, pressure, and loss of yield. Lower back ache can be lowered if the lower back arc is retained while sitting. To achieve highest ergonomic advantages, drivers should be cognizant about cabin seat adjustments. To have an easy reach to steering wheel, various cabin switch, control panel it is important for a driver to position himself before performing the truck driving [4–6]. The truck driver does neck bending and spine twisting during his duty. Ergonomically designed seat keeps his posture well maintained to do his job all the time [7]. Neck and lower back of truck driver are affected because of poor design of truck cabin and driver seat. Improper position of neck and back cause backache, which is commonly seen in truck drivers [8]. The study showed that, the driver postures were not acceptable as RULA (Rapid Upper Limb Assessment). A score of 5–6 was seen post ergonomic risk assessment through RULA method. It was suggested for modification, which can minimize ergonomic risks associated with drivers [9]. Occurrence of MSDs among truck drivers is very ordinary as observed in numerous investigation studies. The research revealed that 76.92% truck drivers were suffering from musculoskeleton disorders. Components that are noticed which are accountable for work related musculoskeletal discomfort in automobile motorists are oldness, driving experience, amount of driving, relaxation period, pose, anxiety, pulsation and inadequate situation of roads [10].

Truck motorists are more vulnerable to musculoskeletal disorders due to uncomfortable and prolonged static positions, monotonous activities, forward bending, unnecessary twisting, and shoulders stretched and captured. It can be lowered by keeping improved postures and using ergonomically designed seats. The purpose of the research was to find out that regardless of the progress in the innovative trucking industry work environment, drivers are still experiencing from musculoskeletal disorders and there is a necessity to enhance upon the features of existing truck driving environment and seats. A questionnaire was made, and information was gathered linked to truck driver seats.

2 Materials and Methods

In this assessment, questions were constructed to evaluate the bodily workload, body pain or work stress in the truck drivers and incidence of risk aspects conducive to discomfort due to WMSDs (Work-related Musculoskeletal Disorders), all the significant aspects regarding ergonomics were integrated. Truck drivers reacted to a questionnaire regarding their working model (years of duty, working hours, specialization etc.), their typical daily life including exercise, occurrence of MSDs (Musculoskeletal Disorders) and their general perception about MSDs (Musculoskeletal Disorders).

Questionnaire is dedicated on the information associated to musculoskeletal symptoms, Musculoskeletal disorders, driving habits initiating pain and tiredness, the years of service after which the drivers began experiencing discomfort and Musculoskeletal disorders was established.

The aim of the questionnaire was to discover the obstacles faced by the drivers. It was studied that majority of the drivers were innocent of the incidence of MSD. Some of them confirmed that it was a part and parcel of their employment, so they believed it for granted. And did not understand that this can be prevented if taken care of at the proper care.

One of the major problems coupled with MSD is that it gets manifested after a long period usually after 3 to 4 years when there is no opportunity for restorative action. Hence it is paramount needed to train the drivers and help them implementing appropriate posture while carrying truck driving duties. The replies were evaluated using pareto analysis showing the most substantial incidence.

Inclusion criteria

1. Work experience of at least 1 years of duration
2. Both Left-handed and Right-handed
3. Private and institutional drivers
4. All specializations of drivers
5. Different age, height, weight etc.

3 Results and Discussion

A total of 100 drivers from various places were contacted, 79 drivers responded as mentioned in Table 1, 95% were male and 5% were female. Age of the participants differed from 24 to 54 years. Height differed from 149 to 189 cm. Weight differed from 49 to 111 kg. Considering the BMI, 32 are overweight and 8 are obese. 73.41% of our respondents were in private transports industry alone, and 11.39% were in individual truck owners while 15.18% were both in transports industry and in individual truck owners. 94.9% of the respondents were right-handed, while 5.1% were left-handed. Years of duty wide-ranging from 1 to 30 years, 30% lies between 6 to 10 years.

Table 1 Truck driving specialization

Specialization	No. of respondents
Flatbed truckers	6
Dry van truckers	3
Tanker truckers	7
Freight haulers	5
Refrigerated freight drivers	5
Local drivers	6
Regional drivers	5
OTR drivers	6
Light freight truckers	2
Heavy freight truckers	8
Oversized load drivers	3
Vocational drivers	6
Bullrack drivers	7
Team drivers	5
Dry bulk pneumatic drivers	5

It was seen that the 59% truck drivers work minimum 8 h a day, 88% work 6 days a week. Now a days advanced technologies are seen in commercial trucks but still many truck drivers are experiencing lots of work-related health concerns. A high number of truck drivers are facing Musculoskeletal symptoms.

The consequences of MSD are discomfort, constant ache in the joints, muscular tissue, ligaments, produced by recurrent activities and persistent uncomfortable postures and overweightness. Based on the statistics accumulated, a Pareto chart was made Fig. 1 shows almost 70% of the difficulties are related to too much fatigue in shoulder, back, neck and joints. The primary emphasis thus requires to be on lowering the shoulder, back, neck and joints fatigue.

The Musculoskeletal Disorders like Intervertebral Disc Problem, Ankylosing Spondylitis, Sciatica is due to prolonged seating and are related to awkward positions of back and the repetitive work will lead to Carpel tunnel syndrome, Tennis. When truck drivers are in uncomfortable positions, the back is overburdened and there is extreme strain in upper body as shown in Fig. 2. There are pains affected in head and upper limb sides. Owing to MSD, discomfort is exasperated in several parts of the body consist of shoulders, neck, hands, lower back etc. This impacts the productivity of the work completed. The information gathered indicates that 55% of the drivers have decreased their driving hours due to the stimulated discomfort.

A lesser proportion of MSDs noticed in truck drivers of a greater age band; this could be recognized to their improved managing actions, given their larger knowledge as shown in Fig. 3. Additional thought could be that youthful truck drivers work more in their initial years of job, which advances to MSDs and the causing muscle stiffness. It was also seen that the drivers decreased their driving hours past a certain amount

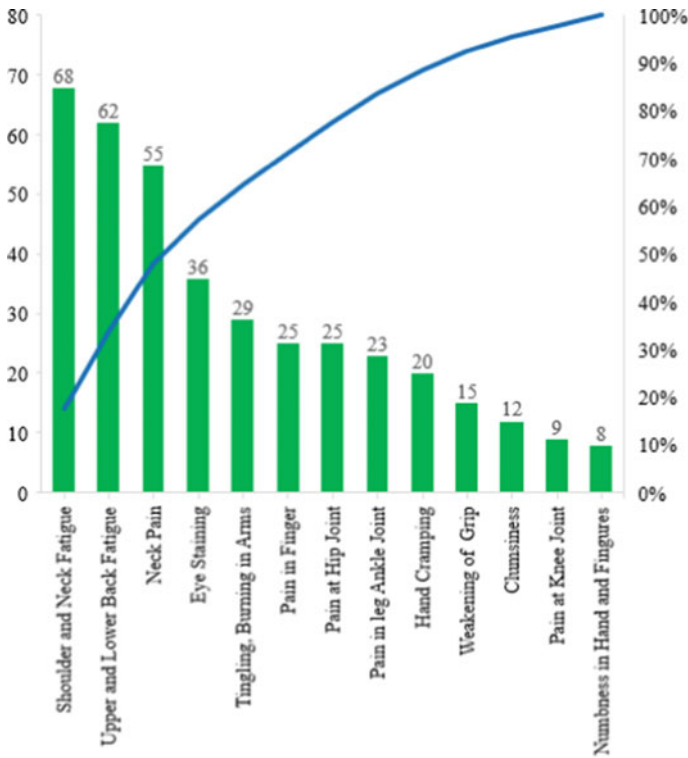


Fig. 1 Symptoms of musculoskeletal disorder in drivers

of years. Nature of driving is analyzed in Fig. 4, and it was found that long haul and highway driving are carried out regularly.

4 Conclusions

Due to work nature of Truck Driver Musculoskeletal disorder (MSD), discomfort or damage seen, and which is the major reason for absenteeism, loss of efficiency and productivity, higher rate of physical and mental ailments. The research had clearly indicated, the Musculoskeletal disorder are arising from prolonged seating, improper ergonomic design of truck cabin and seat, unbalanced seating postures used by drivers. Hence, most of truck drivers are facing high amount of tiredness and discomfort in neck, spinal, arm etc. It is also observed more than 60% drivers work in same driving posture for longer duration which again increases the risk of pain and discomfort. Hence the effective working hours of driver get reduced due to pain and discomfort. The Major Musculoskeleton disorders observed in driver are Intervertebral Disc Problem, Lower Back Pain, Ankylosing Spondylitis,

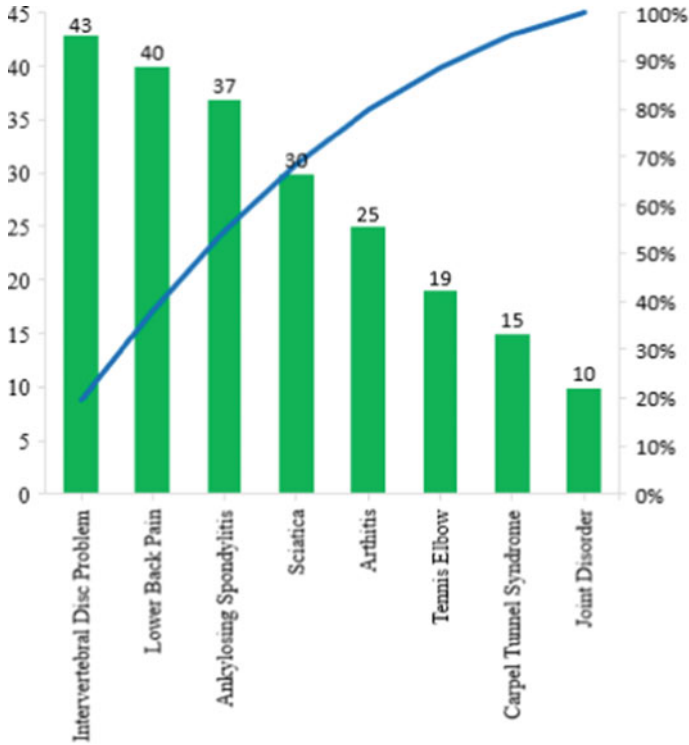


Fig. 2 Musculoskeletal disorder observed in drivers

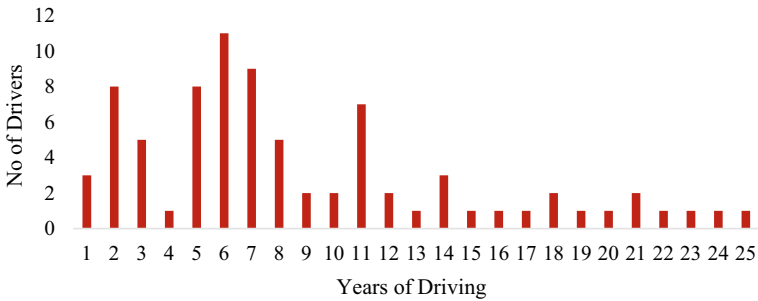


Fig. 3 Driver's feeling pain during years of driving

Sciatica, Arthritis, Tennis Elbow, Carpel Tunnel Syndrome, Joint Disorder. Long Haul Driving, Hilly region driving causes more inconvenience and tiredness due to prolonged seating which causes feel discomfort and exhaustion. It is seen that 48% of the drivers are experiencing extreme fatigue in the Back, shoulders, and neck, 55%

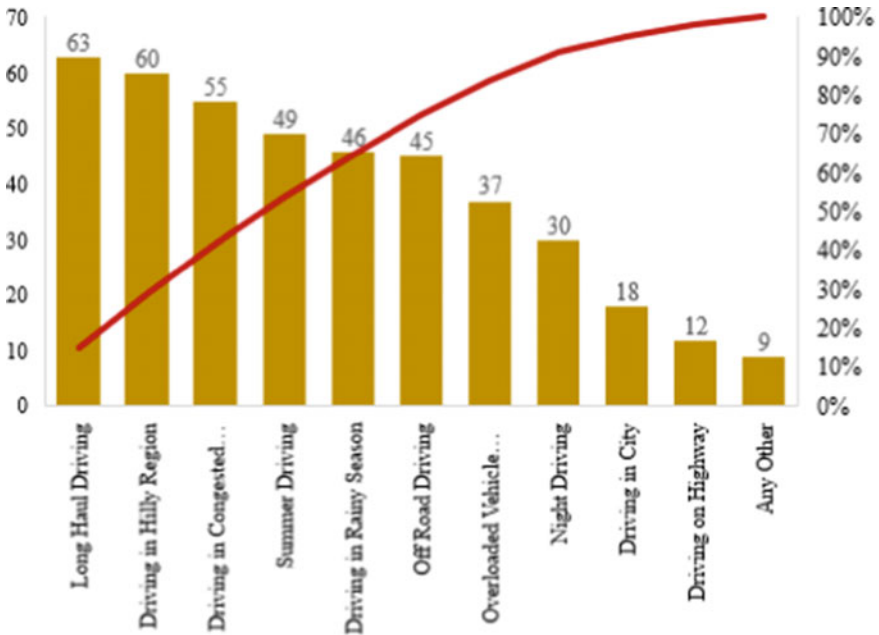


Fig. 4 Driving category causing driver fatigue and pain

are suffering from MSD like Intervertebral Disc Problem, Lower Back and Ankylosing Spondylitis. 73% of drivers are suffering from tiredness and discomfort due to common driving like Long Haul Driving, Driving in Hilly Region Congested Road, Off Road, Overloaded Vehicle, and different extreme weather conditions. Hence it is crucial to adopt appropriate ergonomic design Cabin and seats. Contemplating the physical work pressure and psychological pressure of the drivers it is further essential to prepare the working model and the duration of job. It is also necessary for the drivers to take care of their BMI as overweight beings are more susceptible to neck and back pain.

References

- Halder, P., Mahmud, T., Patel, S., Setiawan, A., & Shah, K. (2018). Ergonomic considerations for designing truck drivers’ seats: The case of Bangladesh. *Journal of Occupational Health*, 60(1), 64–73.
- Cardoso, M., McKinnon, C., Viggiani, D., Michel, J., & Wayne, A. (2017). Biomechanical investigation of prolonged driving in an ergonomically designed truck seat prototype. *Ergonomics*, 61(1), 1–35.
- Magnusson, M. L., Pope, Wilder, Areskoug (1996). Are occupational drivers at an increased risk for developing musculoskeletal disorders? *Spine*, 21(6), 710–717.

4. Reed, M. P., & Mirian, A. (2000). Effects of vehicle interior geometry and anthropometric variables on automobile driving posture. *Human Factors*, 42(4), 541–552.
5. Mahoney, J. M., Kurczewski, N. A., & Froede, E. W. (2015). Design method for multi-user workstations utilizing anthropometry and preference data. *Applied Ergonomics*, 2015(46), 60–66.
6. Ozsoy, B., Ji, X., Yang, J., Gragg, J., & Howard, B. (2015). Simulated effect of driver and vehicle interaction on vehicle interior layout. *International Journal of Industrial Ergonomics*, 2015(49), 11–20.
7. Wilder, D., Magnusson, M. L., Fenwick, J., & Pope, M. (1994). The effect of posture and seat suspension design on discomfort and back muscle fatigue during simulated truck driving. *Applied Ergonomics*, 25(2), 66–76.
8. Troup, J. D. (1978). Drivers back pain and its prevention: A review of the postural, vibratory and muscular factors, together with the problem of transmitted road-shock. *Applied Ergonomics*, 9(4), 207–214.
9. Agarwal, P. K., Kumar, V., & Banerjee, D. (2015). Ergonomic risk assessment and postural analysis of Indian Auto-Rickshaw drivers using RULA and REBA. *HWWE Conference Proceedings, 2015*, 562–567.
10. Mehta, A. S., & Sancheti, P. K. (2019). Prevalence of work-related musculoskeletal disorders in truck drivers and its associated risk factors. *IJCMPH*, 6, 2712–2717.

A Comprehensive Review of COVID-19 Detection and Prediction Using of ML/DL Method



Md. Sadab, Deepak Kumar, and Ved Parkash

Abstract COVID-19, a new coronavirus, causes severe acute respiratory syndrome (SARS-CoV-2). As of late, COVID-19 spread to more than 500 million individuals throughout 230 nations and territories, turning it into a pandemic. Traditional diagnosis methods are no longer effective due to the exponential rise in infection rates. Machine learning (ML) and Deep learning (DL), two intelligence techniques that have been developed by numerous researchers, can assist the healthcare industry in providing prompt and accurate COVID-19 detection. As a result, this work offers an in-depth analysis of most recently ML and DL methods for COVID-19 analysis. In-depth investigations are released between December 2019 and November 2022. Generally speaking, this document contains more than 200 studies that were carefully chosen from a variety of publications, including MPDI, ScienceDirect, Springer, Elsevier, and IEEE. For identifying COVID-19 and forecasting outbreaks, SVM is the most widely used machine learning method, and CNN is the most widely used deep learning algorithm. The most often utilized metrics in prior investigations were accuracy, sensitivity, and specificity. The research community will receive guidance from this review paper regarding the expected development of machine learning and deep learning for COVID-19 and motivation for their prospective work.

Keywords Coronavirus disease (COVID-19) · Machine learning · Deep learning · Detection · Prediction

Md. Sadab (✉) · D. Kumar · V. Parkash
Computer Science Engineering Department, State Institute of Engineering and Technology,
Nilokheri, India
e-mail: sadabalam0205@gmail.com

D. Kumar
e-mail: wadhwa123deepak@gmail.com

1 Introduction

The word “corona,” which refers to the outer, club- and crown-shaped spikes of the virus gets its name from the Latin word corona, which means “crown” Coronaviruses are large viruses that coexist with RNA viruses with positive strands. Coronavirus (COV) is a corona viridae family and Ortho corona variant subfamily member. Coronaviruses are classified into four generations: alpha, beta, gamma, and delta COVs, with the former infecting mammals and the latter infecting birds [1]. COV was discovered in the late 1930s after a severe respiratory virus was discovered in farm chickens infected with the Infectious Bronchitis Virus (IBV) [2]. Human Corona Viruses (HCOVs) were later found in the 1960s. SARS and MERS are both Beta COVs, which spread an infectious and fatal respiratory infection [3]. A new illness called COVID-19 first appeared three years ago.

Further difficulties in developing a vaccine for this virus are caused by the numerous genetic mutations it shows. From a technical point of view, Due to the shortage of imaging equipment and the multiple images required for a more precise diagnosis by professional radiologists, researchers have proposed and developed AI techniques for COVID-19 diagnosis to aid medical professionals in their work [3].

There are many deadly viruses in the world today, which can be divided into infectious and non-infectious groups. Different classes of microorganisms are the root cause of infectious diseases. These illnesses can spread by water, saliva, and air from affected individuals, as well as other foods. Flu, cold, cough, diarrhea, and mild to severe fever, and in very extreme situations, death may result from this. Infectious diseases are a major cause of death in developing nations because they are infectious and difficult to control. Many diseases still have no treatments available today. We don't have access to proper healthcare facilities in our country, which has a population of over 1 billion people. It gets worse as a result. Some mechanisms that are capable of forecasting such outbreaks could be used to stop such deadly situations. In this approach, machine learning has offered a light of hope. The study of the virus and the discovery of the specific medicine to fight it, together with the ability to predict various outbreaks and pandemics, were all made possible thanks to machine learning. It aids in the analysis of massive datasets as well as the potential outcomes. Accurate data analysis helps enhance disease detection and improve patient treatment. Prediction helps us predict events and make us aware of them.

A field called machine learning encourages the study of computer algorithms so that the system can develop the capacity for automated learning and enhance its performance based on prior knowledge. This attempts to develop computer programs that can access data and use it to conclude. The algorithms are primarily concerned with creating models from “training data,” or sample data. Predictive analysis, natural language processing, sentiment analysis, and many more disciplines use machine learning techniques. A. Samuel coined the term “machine learning” for the first time in 1959. There are three types of ML. In supervised learning, the algorithms are trained with labels, meaning that the matching output is known for a particular input.

In unsupervised learning, the learning algorithm is not given any labels. Input patterns must be discovered by the machine itself. In reinforcement learning, algorithms use their model of the solution to learn from a dynamic environment [4].

AI and (ML) [5] is well known efficient methods in the healthcare sector [6]. AI analyzing tools constantly adapt their methodologies to modify their behaviors. In the beginning, AI/ML identifies the relevant keys and then removes redundant features. It uses different models of machine learning the relative impact of the factors is then measured using random forest and gradient-boosted models [7]. A support vector Machine (SVM) is used to classify data. It selects features using a relief algorithm before deforestation. For accuracy calculation, a tenfold cross-validation method is used. Deep learning models are used to predict COVID-19 cases using time series data [8]. To find, analyze, and combine reliable publications, this study conducted an (SLR) systematic literature review. The study lists several ML/DL techniques used in the present pandemic, including imaging techniques, survival analysis, forecasting, challenges associated with geography and the economy, monitoring techniques, drug research, and hybrid apps. These applications mostly apply ML/DL techniques like CNNs, generative adversarial networks (GANs), random forests (RF), and long short-term memory networks (LSTMs). We used ML techniques to analyze almost all of the features for each categorization. The applied SLR describes the techniques and includes a variety of situations that could potentially occur anywhere [9].

2 The Models of Machine Learning

Machine learning is typically a group of automated data processing techniques that helps with performance improvement based on results and helps make decisions seem more natural. In this context, the ability of an algorithm to learn new information and perspectives without being explicitly programmed is referred to as “Learning”. Several numerous machine learning models are available. From those, the following major concepts are described [10].

2.1 *Supervised Machine Learning*

It is defined as the development of algorithms that can accurately categorize data or predict outcomes using labeled datasets. The weights are updated as fresh data are added to the model, and this process is repeated until the model is properly fitted.

2.2 Unsupervised Machine Learning

Because the inputs are unlabeled, these algorithms are capable of detecting patterns. We evaluate and cluster unlabeled datasets using machine learning techniques. Without the need for human intervention, these algorithms discover hidden patterns or data groupings.

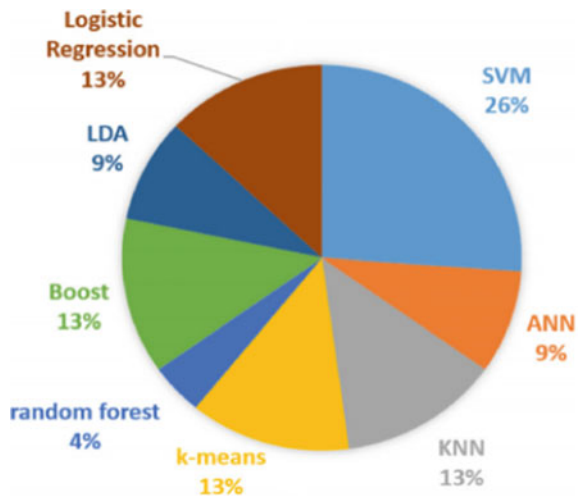
2.3 Reinforcement Machine Learning

Like supervised ML, however instead of a labeled output, in this case, there are rewards, and the algorithm’s objective is to maximize rewards. A machine learning training technique, reinforcement learning, encourage good actions while punishing bad ones.

2.4 Semi-Supervised Machine Learning

To organize, the model must learn structures of the mixed labeled and unlabeled input data to make predictions. Machine learning techniques such as semi-supervised learning aim to address problems involving both labeled and unlabeled data. Mathematical ideas like clustering and classification method features are used in semi-supervised learning [11] (Fig. 1).

Fig. 1 The percentage of COVID-19 machine-learning models used adapted from [20]



3 The Models of Deep Learning

Machine learning's deep learning subfield is based on a network of synthetic neurons that is organized similarly to the human brain [12, 13]. System disease diagnosis has been successful with deep learning models. Reinforcement learning, recurrent neural networks (RNN), deep belief networks (DBN), and convolutional neural networks (CNN) are the four most popular deep learning architectures.

3.1 Convolutional Neural Networks (CNN)

Convolutional neural networks (CNNs), a subclass of multilayer perceptron, have distinguished themselves in computer vision applications including image classification. [14]. The convolutional neural network architecture consists of three layers: a convolutional layer, a pooling layer, and a fully connected layer. In the CNN model, the convolutional layer is important. convolution uses various types of filters to a picture's edges, textures, and objects can all be extracted as features (kernels) [15].

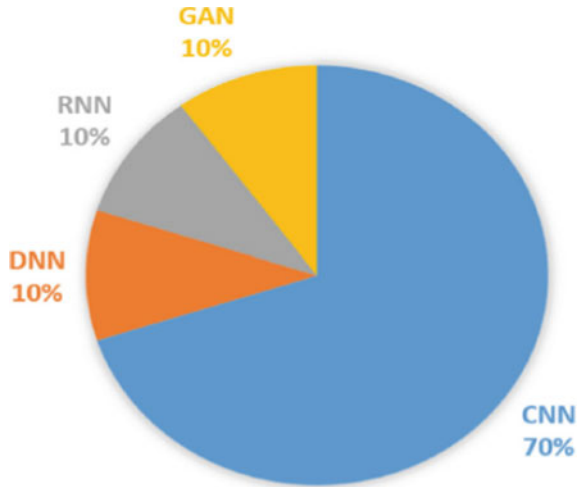
3.2 Recurrent Neural Network (RNN)

A class of neural networks known as "recurrent neural networks" (RNNs) uses time-series or sequential data and has recurrent connections. It is used to recognize patterns in streams of data, including text, handwriting, and speech. [16].

3.3 Deep Belief Networks (DBN)

DBNs are multiple-layered, probabilistic generative models containing hidden variables. They offer an effective solution to problems with the deep neural network, such as low velocity and overfitting in learning. A DBN is a combination of a stack of constrained Boltzmann machines [17]. The RBMs' layers are connected to their parent and child layers. Deep belief networks primarily exhibit two traits: (1) Top-down learning, and (2) single bottom-up learning [18].

Fig. 2 The percentage of COVID-19 models that use deep learning adapted from [20]



3.4 Reinforcement Learning

A type of machine learning called reinforcement learning automatically detects and fixes problems with goal-oriented learning and judgment. The collection of techniques known as reinforcement learning enables an agent to develop the ability to decide for itself what action to take. It has recently been applied to a range of sectors with outstanding outcomes [19] (Fig. 2; Table 1).

Table 1 Table of comparisons between the techniques and algorithms used for COVID-19

Sr. No	Problem	Algorithm/tech/method	Advantages	Conclusion	Year
1	Analysis of machine learning systems for covid-19	1. Data Augmentation 2. Segmentation 3. classification Mostly uses Methodology a. SVM b. CNN	COVID-19 diagnosis using chest X-ray or CT scan images	Early detection and radiologists' efforts at diagnosis can both benefit from COVID-19 screening	2022
2	Analysis of the Machine Learning Methodologies for Covid-19 Cases	I. Analyzing how the COVID-19 data II. Gain a better understanding III. Improving machine learning techniques IV. Analyzing the efficacy and impact	Machine learning has proven to be one of the best methods for identification	It's also vital to get over the COVID-19 data shortage issues to do a more in-depth study	2022
3	A Detailed Analysis of ML Used to Fight COVID-19	<ul style="list-style-type: none"> • CNN • ANN • Chest X-rays • SVM • LSTM 	CT imaging played a significant role in the decision-making process in the majority of the papers	Patient biomarkers differ from hospital infrastructure, this worldwide solution is nevertheless practical because of these similarities	2022
4	Outbreak management with machine learning	<ul style="list-style-type: none"> • (CNNs) • (LSTM) • (RNNs) • (GANs) • Autoencoders • Random forest 	Some application of ML in the battle against the COVID-19 outbreak by examining the research gaps and opportunities highlighted in this study	Its processes were examined, as well as imaging methods, survival analysis, forecasting, and challenges	2022

(continued)

Table 1 (continued)

Sr. No	Problem	Algorithm/tech/method	Advantages	Conclusion	Year
5	COVID-19 Infection Recovery and Mortality Rate Prediction in the Indian States	Decision Trees, Naive Byes, SVM, Random Forest, Bagging Hybrid Model, and AdaBoost, are examples of algorithms	The current study is confined to using epidemiologic expertise to assess the effectiveness of the diagnostic model	The proposed learning model is preferred since it requires less training time and processes information more quickly and accurately	2021
6	Complete analysis of machine learning techniques for predicting the emergence of Covid-19 cases	<ul style="list-style-type: none"> • SIRD Model • SEIR Model • ARIMA Model • SARIMA Model • ANN Model • RNN Model • NNAR Model 	ML algorithms for the prediction of epidemic diseases, which will aid the healthcare system in making wise medical decisions	More sophisticated machine learning methods are required to detect hidden patterns in huge and complicated datasets	2022
7	ML and DL, COVID-19 diagnosis models used in COVID-19	Machine learning methods 1. SL 2. USL Deep learning methods for COVID-19 <ul style="list-style-type: none"> • CNN • DNN • RNN • GAN 	This is consistent with earlier studies that used ML and DL techniques for the prediction process	SVM and CNN are the two most popular algorithms for identifying COVID-19 and forecasting outbreaks, respectively	2021

4 Conclusion

This study's main objective is to give an overview of earlier research and its COVID-19 detection and prediction outbreak. The examined studies were chosen from a variety of well-known public research sources, including MDPI, IEEE, Springer, ScienceDirect, Elsevier, and others. The selection of these publications goes through many filters, utilizing machine learning and deep learning methods, to weed out duplicate concepts with pertinent information connected to COVID-19. Two categories—supervised learning and unsupervised learning—are used to categorize machine learning studies. The deep learning investigations are further broken down into CNN, DNN, RNN, GAN, and Optimization using deep learning techniques. All of the listed research was utilized to either identify COVID-19 by analyzing CT scans and X-ray images. In conclusion, India and China have the most research on machine learning and deep learning that is based on COVID-19, whereas India has the most research

on machine learning that is based on COVID-19. The evaluation metrics for the machine learning and deep learning methods based on COVID-19 are compiled in this report. The most often utilized metrics in earlier research have been accuracy, sensitivity, and specificity.

References

1. Paules, C. I., Marston, H. D., & Fauci, A. S. (2020). Coronavirus infections more than just the common cold. *JAMA*, *323*(8), 707–708.
2. Estola, T. (1970). Coronaviruses, a new group of animal RNA viruses *Avian Dis.* *14*(2), 330–336
3. Alsaaidah, B., AL-Hadidi, M. R., AI-Nsour, H., Masadeh, R., & AIZubi, N. (2022). Comprehensive survey of machine learning systems for COVID-19 detection. *Journal of Imaging*, *8*, 267.
4. Santra, A., Dutta, A. (2022). A comprehensive review of machine learning techniques for predicting the outbreak of covid-19 case, MECS-Press I.J. *Intelligent Systems and Applications*, *3*, 40–53.
5. Silver, D., Schrittwieser, J., Simonyan, K., Antonoglou, I., Huang, A., Guez, A., Hubert, T., Baker, L., Lai, M., Bolton, A., et al. (2017). Mastering the game of go without human knowledge. *Nature*, *550*(7676), 354–359.
6. Chakraborti, S., Maiti, A., Pramanik, S., Sannigrahi, S., Pilla, F., Banerjee, A., & Das, D. N. (2021). Evaluating the plausible application of advanced machine learning in exploring determinant factors of a present pandemic. a case for continent-specific COVID-19 analysis. *Science Total Environment*, *765*, 142723.
7. Muammer, T. (2021). Covidetectionet COVID-19 diagnosis system based on X-ray images using features selected from pre-learned deep features ensemble. *Applied Intelligence*, *51*, 1213–1226.
8. Shahid, F., Zameer, A., & Predictions, M. M. (2020). For COVID-19 with deep learning models of LSTM, GRU, and BI-LSTM. *Chaos Solitons Fractals* *140*, 110212
9. Doewes, R. I., et al. (2022). An updated systematic review on the effects of aerobic exercise on human blood lipid profile. *Current Problems in Cardiology*. <https://doi.org/10.1016/j.cpcardiol.2022.101108>
10. <https://www.ibm.com/cloud/learn/supervised-learning>. Accessed October 26, 2021.
11. Abirami, R. S., & Kumar, G. S. (2022). Comparative study based on analysis of coronavirus disease (COVID-19) detection and prediction using machine learning models. *SN Computer Science*, *3*, 79.
12. Goodfellow, I., Bengio, Y., Courville, A., & Bengio, Y. (2016). *Deep learning*, vol 1. MIT Press.
13. Schmidhuber, J. (2015). Deep learning. *Scholarpedia*, *10*, 32832. [CrossRef].
14. Islam, Z., Islam, M., & Asraf, A. (2020). A combined deep CNN-LSTM network for the detection of novel coronavirus (COVID-19) using X-ray images. *Informatics in Medicine Unlocked*, *20*, 100412. [CrossRef] [PubMed].
15. Yang, B., Guo, H., & Cao, E. (2021). Chapter Two—Design of cyber-physical-social systems with forensic-awareness based on deep learning in AI and Cloud computing. In Hurson, A. R. and Wu, S (Eds.) Amsterdam, (vol 120, pp. 39–79), Elsevier.
16. Shamshirband, S., Fathi, M., Dehzangi, A., Chronopoulos, A. T., & Alinejad-Rokny, H. (2020). A review on deep learning approaches in healthcare systems: taxonomies, challenges, and open issues. *Journal of Biomedical Informatics*, *113*, 103627. [CrossRef] [PubMed].
17. Hua, Y., Guo, J., & Zhao, H. (2015). Deep belief networks and deep learning. In: *Proceedings of the 2015 international conference on intelligent computing and internet of things*, 17–Jan 18, 2015.

18. Hinton, G. E. (2009). Deep belief networks. *Scholarpedia*, 4, 5947. [CrossRef].
19. Zong, K., & Luo, C. (2022). Reinforcement learning-based framework for COVID-19 resource allocation. *Computers & Industrial Engineering*, 167, 107960. [CrossRef] [PubMed].
20. Alyasseri, Z. A. A., Al-Betar, M. A., Doush, I. A., Awadallah, M. A., Abasi, A. K., Makhadmeh, S. N., Alomari, O. A., Abdulkareem, K. H., Adam, A., Damasevicius, R., Mohammed, M. A., & Zitar, R. A. (2022). Review on COVID-19 diagnosis models based on machine learning and deep learning approaches. *Expert Systems*, 39(3), e12759. <https://doi.org/10.1111/exsy.12759>

Construction of Spreadability Testing Apparatus



Vrunal V. More, Prajakta K. Khule, Mithun G. Maniyar, Anil V. Landge, and Pradip A. Jadhav

Abstract Researchers always encounter a problem in the establishment of reliable technique for measurement of spreadability characterization of semisolid topical–mucosal preparations. The parallel-plate method is the most widely used method for determining and quantifying the spreadability of semisolid preparations. This method is less precise and sensitive, and the data it generates must be manually interpreted and presented. The present invention relates to an apparatus for measuring the spreadability of semisolid formulations. The apparatus works on the principle of centrifugation forces. The fixed amount of semisolid formulation (0.5–1 g) under evaluation is poured in the center of disc and rotated at 500–800 rpm for 30 s. The centrifugal force generated during disc rotation circularly spreads the semi solid preparation. The spreadability is evaluated based on the diameter of semisolid formulation spread on the circular plate. The present investigation is a reliable technique to evaluate spreadability characterization of semisolid preparations.

Keywords Spreadability · Semisolid · Centrifugal force · Parallel plate method

1 Introduction

The present invention relates to an apparatus for measuring the spreadability of semisolid formulations.

Semisolid preparations such as ointments, pastes, cream emulsions, gels and rigid foams are considered as important topical pharmaceutical formulation. Their common property is their ability to adhere to the applied surface for a reasonable period before they are washed off or worn off. Semisolid preparations usually serve as vehicle for topical drug delivery, as emollients, or as protective or occlusive dressings, or they may be applied to the skin and membranes [1]. These preparations are widely used as a means to alter the hydration state of applied topical area and deliver the incorporated drugs in it [2].

V. V. More (✉) · P. K. Khule · M. G. Maniyar · A. V. Landge · P. A. Jadhav
SVERI'S College of Pharmacy, Gopalpur-Pandharpur, Maharashtra 413304, India
e-mail: vvmore@cop.sveri.ac.in

© The Author(s), under exclusive license to Springer Nature Switzerland AG 2024
P. M. Pawar et al. (eds.), *Techno-Societal 2022*,
https://doi.org/10.1007/978-3-031-34648-4_78

771

The delivery of the correct dose of the drug depends highly on the spreadability of the semisolid topical formulations. As spreading the formulation in an even layer on the applied area to deliver a standard dose and optimum consistency of formulation ensure the suitable dose of the drug. A reduced dose would not deliver the desired effect and an excessive dose may lead to undesirable side effects. Hence, spreadability is an important parameter evaluated in the characterization of semisolid formulations [3].

Researchers always encounter a problem in the establishment of reliable technique for spreadability characterization of semisolid topical–mucosal preparations [2]. The parallel-plate method is the most widely used method for determining and quantifying the spreadability of semisolid preparations. This method is less precise and sensitive, and the data it generates must be manually interpreted and presented. Some techniques or instruments originally designed for other purposes also used for the measurement of spreadability of semisolids [2]. These include viscometers like cone-and-plate viscometers in which slippage between the rotating portion of the viscometer and the sample during measurement is a major disadvantage. Penetrometers, texture analyzers, spread meters are other instruments used for the assessment of spreadability of semisolids. These instruments are not economic and some require a mathematical manipulation to assess the spreadability [2, 3]. Parallel plate method is a technique used to measure the thermal conductivity of materials. It consists of two parallel plates, one of which is heated and the other is cooled. The temperature difference between the two plates is then measured and the thermal conductivity of the material between the plates is calculated. The parallel plate method works by measuring the amount of heat that is conducted through a material between two parallel plates. The two plates are held at different temperatures, with one plate being heated and the other being cooled. Heat is conducted from the hot plate to the cold plate and the temperature difference between the two plates is measured. The thermal conductivity of the material between the plates is then calculated using the equation: $k = q/(A\Delta T)$.

Where k is the thermal conductivity, q is the heat flux, A is the area of the plates, and ΔT is the temperature difference between the two plates. Based on these facts, the present study was planned to construct a simple, economical and reliable apparatus for the evaluation of spreadability character of various pharmaceutical semisolid preparations. The patent for apparatus is filed to Indian patent office (application No 201921010606, dated 2019/03/2019).

2 Material and Methods

Spreadability measurement apparatus is constructed using a circular plate (16 cm in diameter) made of acrylic material, electric motor (12 V) and power battery (12 V) as shown in Fig. 1. A circular plate is fixed on the shaft of an electrically driven motor connected to a power battery. The speed of motor rotation can be adjusted (up 1000 rpm) using the speed regulator knob. From center to periphery the plate

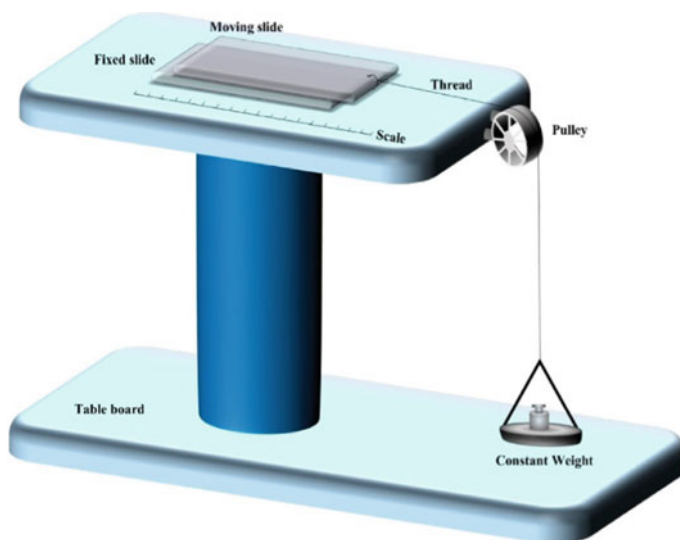


Fig. 1 Parallel plate method

is marked with circles of different diameter with 5 mm increment. The apparatus is equipped with a camera to capture the semisolid spreading diameter from the center of the plate.

The apparatus works on the principle of centrifugation forces. The fixed amount of semisolid formulation (0.5–1 g) under evaluation is poured in the center of disc and rotated at 500–800 rpm for 30 s. The centrifugal force generated during disc rotation circularly spreads the semi solid preparation. The spreadability is evaluated based on the diameter of semisolid formulation spread on the circular plate. We evaluated 15 marketed pharmaceutical semisolid preparations (0.5 g) at 800 rpm for 30 s showed spreading with a diameter of 2–4 cm.

Procedure for testing of semisolid.

1. Place a sample on circular plate at center of the disk.
2. Start machine with 500 to 800 rpm for 30 s.
3. Measure and mark the diameter of the sample.
4. Measure and mark the diameter of the sample again.
5. Observe the initial diameter and after the rotation for 30 s. If the diameter of the sample has increased, the sample considered to be highly spreadable.

3 Results and Discussion

Various samples of semisolid formulations are evaluated for the spreadability. The results are given in the table mentioned below. Figure 2 shows the apparatus used for evaluating the spreadability proposed in this study (Table 1).

Fig. 2 Apparatus for evaluating spreadability

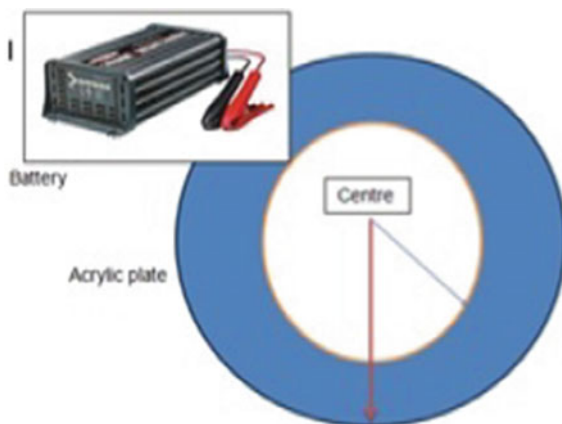


Table 1 Results of sample evaluated by spreadability machine

Sample code	Spreadability in cm	Remark
F1	2.20	Excellent
F2	2.27	Excellent
F3	2.33	Excellent
F4	1.98	Poor
F5	2.43	Excellent
F6	1.78	Poor
F7	2.97	Excellent
F8	3.12	Excellent
F9	3.24	Excellent

4 Conclusion

The present investigation is a reliable technique to evaluate spreadability characterization of semisolid preparations. The evaluation method is quick, easy and economical for the researchers working in the field of pharmaceutical semisolid preparations. This methodology can be implemented directly in pharmaceutical industries, testing laboratories and research institutes as per the requirement. This work has also been patented in India. [Indian Patent Application No 201921010606].

References

1. Chandakavathe, B. N., & Dhadde, S. B. (2019). *Textbook of industrial pharmacy*. 2019 Studium Press (India) Pvt. Ltd. ISBN 13: 978-93-85046-63-6.
2. Idson, B., & Lazarus, J. (1987). Semisolids. In L. Lachman, H. A. Lieberman, & J. L. Kanigs (Eds.), *The theory and practice of industrial pharmacy*, 2nd ed (pp. 215–244), Lea and Febiger.
3. Tamburic, S., Craig, D. Q. M., Vuleta, G., & Milic, J. (1996). A Comparison of electrical and rheological techniques for the characterization of creams. *International Journal of Pharmaceutics*, *137*(2), 243–248.

Elucidation: Reduction of Environment and Health Issues Due to Non-exhaust Pollution



S. P. Jadhav and S. H. Sawant

Abstract With concern environment and health, brake friction emission is a very hot issue that creates bad effects on the environment. The brake pad composition contains many metallic and other ingredients; some of them form toxic oxides and pollute the environment. The environment agencies of various countries have found the bad effect of brake pads emitted pollutants like Asbestos, Pb, Sb, Cu, etc. on plants, animals and human beings. The use of Asbestos is banned by the environment protection agency because it is found to be carcinogenic. To reduce the effects of harmful pollutants on the environment it is necessary to develop eco-friendly organic friction material. In the present work, friction material is developed with some natural ingredients. The physical, mechanical and tribological characterization is done as per ASTM standards. Thermal behavior and morphological properties are studied by thermo gravimetric analysis (TGA) and scanning electron microscope (SEM).

Keywords Environment and health issue · Natural ingredients friction material · TGA · SEM

1 Introduction

The brake friction material is intended to slow down and stop the vehicle or automobile as per driver need. The brake friction material classified in to metallic, semi-metallic and non-asbestos organic (NAO) [1, 2]. The manufactures of brake friction material added excess metallic ingredients in friction material composition to increase performance but its adverse effect is observed by various environmental agencies on plants, animals and human beings [3]. The ingredients like Cu, Pb, Sb, Ni, Zn, Cr, Cadmium, Asbestos etc. or other metallic ingredients produces toxic

S. P. Jadhav (✉)
DOT Shivaji University Kolhapur and SETI, Panhala, Maharashtra, India
e-mail: sachin.jadhav@seti.edu.in

S. H. Sawant
SGMCOE, Mahagaon, Maharashtra, India

oxides due to chemical changes that creates diseases related to respiratory track damage, lung cancer, kidney failure etc. the size of the wear debris emitted at time of braking operation has size less than 10 microns are remain in lungs [4–6]. The Senate bill 6757 passed in state of Washington (USA), the toxic elements and their percentage of weight concentration shown in Table 1. The sources of non-exhaust pollution are from the clutch, brake tyre. As the vehicle moves on road surfaces, the road also wear out and its dust is suspended and mixed with atmosphere. Mechanical parts get rusted when they are used in humid environment. The wear and tear of these parts also responsible for non-exhaust corrosion [7].

The brake friction material composition consists of binder, reinforcement, filler, friction additives and elastomer. In case of metallic brake friction material, the percentage of metals in friction material composition is more than 50% whereas it is 15–40% in semi-metallic and in case of non-Asbestos organic (NAO) it is less than 15%. The low metallic friction material is developed by using more organic or natural ingredients that play crucial role to reduce toxicity in non-exhaust pollution. The scope in reinforcement that used as natural fibers are classified as leaf, seed and fruit, some of the natural fibers are sisal, jute, flax, kenaf, hemp, abaca, pineapple, banana bamboo, wheat straw etc. the organic fillers are also used such as vermiculate, cashew shell powders, coconut shell powders, crab shell powder, cow horn particle etc. [8]. In present work, the friction material is fabricated by compression moulding method and its physical mechanical and tribological characterization is carried to study material behaviour according to ASTM standard methods. The process parameters such as load, sliding speed and sliding distances are varied to study material behaviour in different operating conditions. Thermal behaviour and surface characterization is done of friction material using thermo gravimetric analysis (TGA) and scanning electron microscope (SEM).

Table 1 Non-exhaust pollutant concentration and their effective dates (Washington State Senate Bill 6557)

Elements	Concentration (W _t %)	Effective date
Asbestiform fiber	< 0.1	January 1, 2014
Cadmium and its compounds	< 0.01	January 1, 2014
Chromium (VI)-salts	< 0.1	January 1, 2014
Lead and its compounds	< 0.1	January 1, 2014
Mercury and its compounds	< 0.1	January 1, 2014
Copper	< 5	January 1, 2021
Copper	< 0.5	January 1, 2023

2 Method and Materials

The friction material samples are prepared with 10 ingredients viz. epoxy resin modified with sodium silicate used as a binder whereas cashew shell powder, human nail and vermiculate are used as a filler material. Steel wool and glass fiber are used as reinforcement and boron carbide, zirconium oxide and rubber crumb are used as an abrasive, friction modifier and elastomer respectively. The composition ingredients and their volume percentage are shown in Table 2.

2.1 Manufacturing Method

2.1.1 Raw Material Preparation

The friction material samples are prepared by compression molding method. The first step is preparation of material in which raw materials powders are prepared by crushing with hammer mills or grinder and sieve of different mesh are used to obtain small size (micron) of materials powder.

2.1.2 Preparation of Friction Specimen

The manufacturing of specimen is done by preparing homogeneous mixture of various powders by ball mill machine; the ball mill machine reduces particle size and produces uniform mixture. The prepared homogeneous mixture put in to required mould. The cold compaction is done at room temperature. The homogeneous mixture is compressed at pressure 17–20 MPa by compression molding machine. The mould

Table 2 Composition ingredients and their volume percentage

Sr. No.	Material function	Material ingredients	Volume %
1	Binder	Epoxy resin	34
		Sodium silicate	7
2	Filler	Cashew shell powder	21
3		Vermiculate	12
4		Human nail powder	1
5	Reinforcement	Steel wool	3
6		Glass fiber	1
7	Abrasive	Boron carbide	13
8	Friction modifier	Zirconium oxide	5
9	Elastomer	Rubber crumb	3

is kept in a furnace for 6 h at temperature of 150–160 °C and cured for 24 h. The specimen is taking out from mould and kept ready for different experiment test.

2.2 Experimental Details

The characterization of samples is done as per ASTM standard procedure. The water and oil absorption test is conducted according to ASTM D570-98 method and density test by ASTM D792. The Rockwell hardness test is conducted by Rockwell hardness tester on S scale. The tribological behaviour of sample is studied by pin on disc wear monitor apparatus as per ASTM G99 standard. Thermal gravimetric analysis (TGA) is used to study thermal behaviour of friction material and for morphological study, the scanning electron microscope (SEM) is used.

2.2.1 Density Test

The density test is carried out by using Archimedes principal as per ASTM D792. The dry weight of sample measured by electronic balance and volume is measure by displacement method.

2.2.2 Water and Oil Absorption Test

Water and Oil absorption test is conducted by ASTM D570-98 method. The sample size of 50.8 mm diameter and 3.2 mm thickness is used to conduct a test. The specimen is immersed in water and oil for 24 h duration and its weight before and after immersion is noted. The percentage of water and oil absorbed by the specimen is estimated.

2.2.3 Rockwell Hardness Test

The Rockwell hardness test is conducted on S scale according to ASTM D785 standard. The 1/16-inch steel ball indenter is pressed against specimen by using minor and major load. The reading at three spots is taken and average hardness value is estimated.

2.2.4 Wear Test

The wear test is conducted to estimate and study tribological behaviour of friction material specimen. The test is conducted on pin on disc wear monitor apparatus (Ducom, Bangalore) as per ASTM G-99 standards. The 12 mm friction material pin

Table 3 Experimental design for wear test on pin on disc apparatus

Load (N)	Speed (rpm)	Sliding distance (m)	Velocity (m/s)	Time (min)	Friction force (N)	Wear in micron
9.81	900	1000	4.71	2.35	8.83	20.9
9.81	1100	2000	5.76	3.85	8.79	28.34
9.81	1300	3000	6.805	4.89	8.89	28.41
19.62	900	2000	6.805	4.89	8.86	48.64
19.62	1100	3000	4.71	2.35	9.08	41.38
19.62	1300	1000	5.76	3.85	8.99	37.3
29.43	900	3000	5.76	3.85	8.87	30.07
29.43	1100	1000	6.805	4.89	9.2	49.22
29.43	1300	2000	4.71	2.35	8.85	47.19

rub against 165 mm diameter cast iron disc. Speed, load and sliding distance are the process parameters selected for wear testing experiment. The mass of before test is noted. The monitor screen shows the behaviour friction pattern of pin. The graph is appeared on monitor screen viz. friction force (N) against time (s) and wear (micron) against time (s). The experimental design is shown in Table 3.

3 Result and Discussion

The results of parent friction material are compared with commercial friction material. The density of parent friction material 1.7355 g/cm^3 is slightly less than commercial friction material. The water and oil absorption results are better than parent friction material. The major factor is wear rate which found more efficient in parent friction material (0.00033–0.002 mg/m) as compared with commercial friction material (3.80 mg/m). The coefficient of friction is better found in case of parent friction material having range 0.3013–0.4627 as compared commercial coefficient of friction having range 0.3–0.4. Thermo gravimetric analysis of parent friction material is done under nitrogen atmosphere the rate of heating kept $10 \text{ }^\circ\text{C}$ per minute up to $200 \text{ }^\circ\text{C}$, the linear weight loss is obtained. The percentage of weight loss is 9.05 is shown in Table 3 and Fig. 1. After $200 \text{ }^\circ\text{C}$ the progressive loss is 30.95% found and weight loss percentage is also increased. The complete decomposition of sample friction material is found beyond temperature $900 \text{ }^\circ\text{C}$. The SEM images before and after test are shown in Fig. 2. The wear test is carried at 29.43 N load, 1300 rpm speed and 3000 sliding distance. The small cracks, wear debris and pit marks are observed in SEM image after conduction of test [9–12].

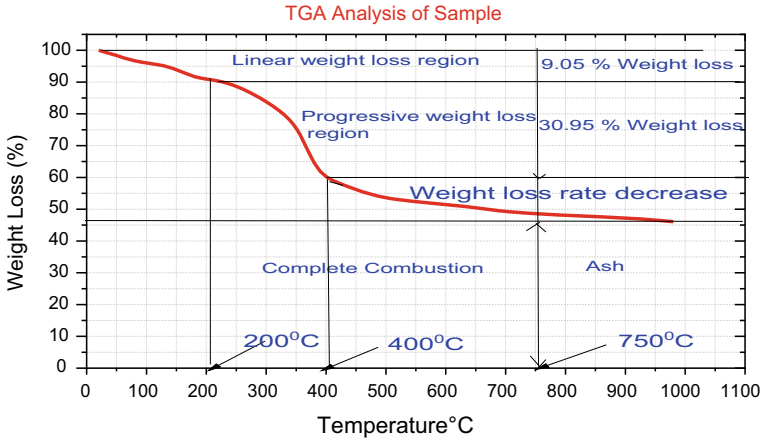


Fig. 1 TGA analysis of friction material

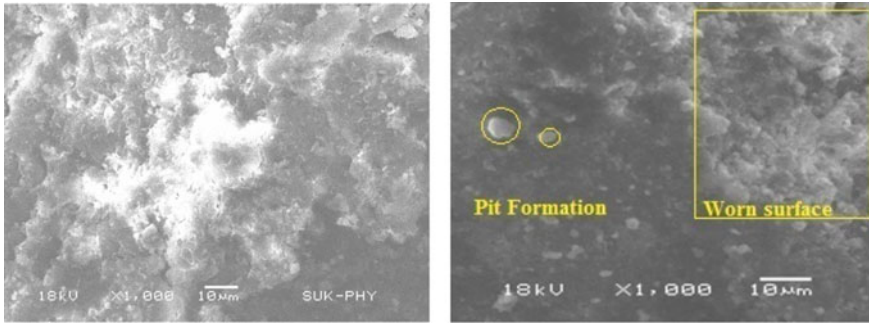


Fig. 2 SEM images of sample A9 a before wear test b after wear test (load of 29.43 N, 1300 rpm speed and 2000 m sliding distance)

4 Conclusions

The reduction in non-exhaust pollution because of brake friction material is possible by developing low metallic friction material having more natural or organic ingredients and low metallic ingredients. In present work the low metallic friction material is developed from more natural ingredient and has better or equivalent results as compared with commercial brake friction material. The following are the key points,

- The boron carbide significant effect on hardness of friction material.
- The process parameters viz. load, speed and sliding distance, significant effect on wear and coefficient of friction.
- As load and speed increases the wear rate and coefficient of friction decreases. This is due to low asperity contact of tribo-pair at high speed.

The coefficient of friction of parent friction material is 0.3013–0.4627 that equivalent commercial friction material coefficient of friction. The wear rate 0.00033–0.002 mg/m is obtained in parent friction material is better than commercial friction material. The TGA analysis shows 9.05% weight loss at 200 °C and it progresses to 30.95% at temperature 400 °C. A SEM analysis result shows pit marks and small cracks on surface of friction material after conducting wear test.

References

1. Akıncioğlu, G., Öktem, H., Uygur, I., & Akıncioğlu, S. (2018). Determination of friction-wear performance and properties of eco-friendly brake pads reinforced with hazelnut shell and boron dusts. *Arabian Journal for Science and Engineering*, 43, 4727–4737.
2. Xiao, X., Yin, Y., Bao, J., Lu, L., & Feng, X. (2016). Review on the friction and wear of brake materials. *Advances in Mechanical Engineering*, 8, 1–10.
3. Jadhav, S. P., & Sawant, S. A. (2019). A review paper: Development of novel friction material for vehicle brake pad application to minimize environmental and health issues. *Materials Today: Proceedings*, 19, 209–212.
4. Ciudin, R., Verma, P. C., Gialanella, S., & Straffelini, G. (2014). Wear debris materials from brake systems: Environmental and health issues. *Sustainable Cities and Society*, 2, 1423–1434.
5. Park, S. H. (2018). Types and health hazards of fibrous materials used as asbestos substitutes. *Safety and Health at Work*, 9, 360–364.
6. Maiorana, S. (2019). Phytotoxicity of wear debris from traditional and innovative brake pads. *Environment International*, 123, 156–163.
7. Lee, P. W., Lee, L., & Filip, P. (2012). Development of Cu-free brake materials. *SAE Technical Papers*, 7.
8. Asokan, P., Firdoous, M., & Sonal, W. (2012). Properties and potential of bio fibres, bio binders, and bio composites. *Reviews on Advanced Materials Science*, 30, 254–261.
9. Kumar, M., & Bijwe, J. (2010). Studies on reduced scale tribometer to investigate the effects of metal additives on friction coefficient—Temperature sensitivity in brake materials. *Wear*, 269, 838–846.
10. Idris, U. D., Aigbodion, V. S., Abubakar, I. J., & Nwoye, C. I. (2015). Eco-friendly asbestos free brake-pad: Using banana peels. *Journal of King Saud University—Engineering Sciences*, 27, 185–192.
11. Ikpambese, K. K., Gundu, D. T., & Tuleun, L. T. (2016). Evaluation of palm kernel fibers (PKFs) for production of asbestos-free automotive brake pads. *Journal of King Saud University—Engineering Sciences*, 28, 110–118.
12. Gunjal, S. S., & Chougule, N. K. (2022). Development of eco-friendly composite brake pad lining material by using agave fiber. *IOP Conference Series: Materials Science and Engineering*, 1248, 012103.

Mechatronics, Micro-nano Related for Bio and Societal Applications

Influence of Uneven Patch Zeta Potential on Electroosmotic Mixing Characteristics in a Heterogeneously Charged Micromixer



Sumit Kumar Mehta, Anindya Nath, and Sukumar Pati

Abstract The effects of unequal patch zeta potential modulation between walls on flow and mixing characteristics for the electroosmotically driven flow in a plane micromixer are examined utilising numerical analysis. To investigate the flow field, recirculation velocity (U_R), dimensionless flow rate (Q), mixing efficiency and dimensionless species concentration field, the ratio of the patch zeta potential of the top to bottom wall (ζ_r), diffusive Peclet number (Pe) and the patch zeta potential of the bottom wall ($\zeta_{P,bottom}$) are varied within the physically justified range. It's been found that U_R strengthens with $\zeta_{P,bottom}$. Interestingly, the value of U_R is insensitive with ζ_r up to $\zeta_r = 1$. and U_R enhances with ζ_r when $\zeta_r > 1$. Furthermore, as ζ_r and $\zeta_{P,bottom}$ rises, the flow rate decreases. The critical limit of Pe is obtained such that η is 100% and it increases with increasing ζ_r at higher $\zeta_{P,bottom}$ ($= 3$). Moreover, η drops with Pe and rises with increase in ζ_r for larger Pe .

Keywords Micromixing · Electroosmosis · Electric double-layer (EDL)

1 Introduction

The medical industry has witnessed increased applications of microfluidic devices recently where micromixing plays a vital role [1]. Numerous advantages of electric field-driven flow in electroosmotic micromixers have given it dominion over its other active counterparts [2].

When Biddiss et al. [3] examined the effects of surface charge heterogeneities on an electrokinetic micromixer, they discovered a 22–68% improvement in mixing

S. K. Mehta (✉) · A. Nath · S. Pati

Department of Mechanical Engineering, National Institute of Technology Silchar, Silchar 788010, India

e-mail: sumitkrmehta@md.iitg.ac.in

S. Pati

e-mail: sukumar@mech.nits.ac.in

quality over a micromixer that was uniformly charged in the range of applied electric fields of 70–555 V/cm. Hadigol et al. [4] explored the electroosmotic mixing of non-Newtonian fluids in a slit microchannel having non-uniform zeta potential and deduced that for shear-thinning fluids, electroosmotic mixing is preferred. The influence of slip-dependent zeta potential on mixing efficiency of a non-uniformly charged micromixer was recently investigated by Vasista et al. [2]. They identified a critical diffusive Peclet number, which was improved by slip length and Debye parameter, up to which mixing efficiency was 100%. Several latest studies on the impact of non-uniform surface charge on the mixing quality were also performed for micromixers with wavy walls [5, 6] and obstructions [7, 8].

After a relevant literature survey, the influence of the modulation of unequal zeta potential of patch along diffusive Peclet number change was found to be unexplored, hence this is decided as the focus of the current study.

2 Problem Formulation

The external electric field with magnitude E is exposed to a planar micromixer with the dimensions given in Fig. 1 [2]. Pure fluid and reagent with the same physical properties are two Newtonian fluids that enter via top and bottom half of the channel, respectively.

The top and bottom wall of channel are alternately covered with positively charged patches that have the same length as the channel half height H (see Fig. 1). The walls except the patches have a negative zeta potential resulting in a flow from left to right. The flow is considered to be two-dimensional, laminar, steady and incompressible. Joule heating is neglected as $O(E)$ is $\sim 10,000$ V/m [2]. Additionally, the ions Peclet number is substantially below unity, which limits the ionic distributions to being static [2]. For the symmetric (Z:Z) electrolyte, ions are considered as point charges [2].

The dimensionless governing equations viz. Poisson-Boltzmann, conservation of mass, momentum and species transport equations are given by [2]:

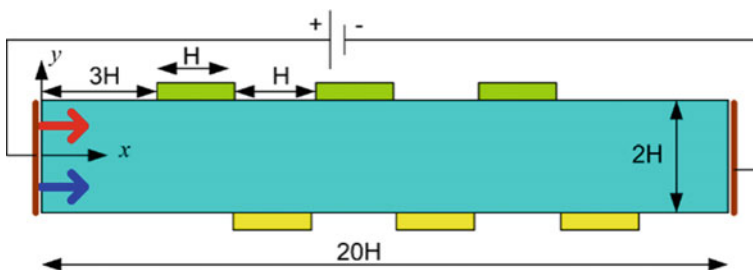


Fig. 1 Illustration of the electroosmotic micromixer's physical domain

$$\nabla^2 \psi = \kappa^2 \sinh \psi, \tag{1}$$

$$\nabla \cdot \vec{V} = 0, \tag{2}$$

$$Re(\vec{V} \cdot \nabla)\vec{V} = -\nabla P + \nabla^2 \vec{V} + \kappa^2 \sinh \psi, \tag{3}$$

$$Pe\vec{V} \cdot (\nabla C) = \nabla^2 C. \tag{4}$$

where, $X = x/H$, $Y = y/H$, $\nabla \equiv (\partial/\partial X, \partial/\partial Y)$ $\psi (= \bar{\psi}/\bar{\psi}_0)$ is the dimensionless electric double-layer (EDL) potential, $\bar{\psi}_0 = k_B T / Ze$, $\kappa (= H/\lambda_0)$ is the Debye parameter and $\lambda_0 (= (2n_0 Z^2 e^2 / \epsilon k_B T)^{-1/2})$ is the Debye length, where n_0 is the bulk ionic concentration. The absolute permittivity of the medium is ϵ . $\vec{V} (= (U\hat{i} + V\hat{j}) = (u\hat{i} + v\hat{j})/v_0)$ is the dimensionless velocity, $v_0 (= ((\epsilon E \psi_0) / \mu))$ is the reference velocity, μ is the dynamic viscosity, P is the dimensionless pressure whose scale is $\mu v_0 / H$, the dimensionless species concentration is $C (= c/c_0)$, D is the species diffusion co-efficient, the diffusive Peclet number and Reynolds number is expressed as $Pe (= v_0 H / D)$ and $Re (= \rho v_0 / H)$, respectively.

The following boundary constraints are imposed: At $X = 0$, $\hat{n} \cdot \nabla \psi = 0$, , for the upper part of inlet ($0 \leq Y \leq 1$), $C = 1$ and for the lower part of the inlet ($-1 \leq Y \leq 0$), $C = 0$; at $X = 20$, $\hat{n} \cdot \nabla \psi = 0$ and $\partial C / \partial X = 0$; at $Y = -1$, $\psi = \zeta_{P, \text{bottom}}$ for the patches, at $Y = 1$, $\psi = \zeta_r \zeta_{P, \text{bottom}}$ for the patches; at $Y = -1$ and $Y = 1$ $\psi = -\zeta$ for other walls except patches, $\vec{V} = 0$ and $\hat{n} \cdot \nabla C = 0$. Here, the dimensionless unit normal to a surface is denoted by \hat{n} . Further, $P_{atm} = 0$ at the inlet and outlet.

The dimensionless form of flow rate (Q) at the outlet is expressed as $\underline{Q} = \bar{Q} / \bar{Q}_0$. Here, the flow rate per unit width is \bar{Q} and flow rate per unit width is $\bar{Q}_0 (= v_0 H)$. Hence, Q is denoted as [2]:

$$Q = \int_{Y_1}^{Y_2} U dY \tag{5}$$

The mixing efficiency (η) is calculated from numerical simulated non-dimensional species concentration field at the outlet, which indicates the quality of mixing, is described by [2]:

$$\eta = \left[1 - \left(\int_{Y_1}^{Y_2} |C - C^*| dY \right) / \left(\int_{Y_1}^{Y_2} |\bar{C} - C^*| dY \right) \right] \times 100\% \tag{6}$$

Table 1 Grid independence test at $Pe = 1000$ by comparing mixing efficiency at different mesh system when $\kappa = 30$, $\zeta_{P, \text{bottom}} = 3$ and $\zeta_r = 1.5$

Number of elements	Mixing efficiency	Percentage difference in mixing efficiency w.r.t. extremely fine mesh
12,275	58.985	0.61
21,470	59.145	0.34
49,420	59.173	0.29
114,027	59.345	0

where, \bar{C} ($=0$ or 1) and C^* ($=0.5$) constitutes the fully unmixed fluid concentration and the pure mixed fluid concentration, respectively. $\eta = 0\%$ and $\eta = 100\%$ correspond to pure unmixed and mixed states, respectively.

3 Methodology for Numerical Simulation and Benchmarking

The software COMSOL Multiphysics, which uses the finite element technique, has been used to compute the related transport equations [9]. The governing transport partial differential equations are iteratively solved using non-uniform triangular elements until the relative residual is 10^{-6} for each transport variable. Additionally, the grid independence test was carried out by evaluating mixing efficiency in several mesh systems as presented in Table 1. After examination, the mesh system with 49,420 elements is chosen for all simulations because we obtained smaller percentage change in mixing efficiency in comparison to a very fine mesh system with 114,027 elements, which is 0.29%.

An attempt has been taken to compare the current work against the experimental work by Biddiss et al. [3] in order to validate the model as it is shown in Fig. 2. The non-dimensional species concentration is compared at the channel outlet when zeta potential is uniform with electroosmotic mobility, $-5.9 \times 10^{-4} \text{ cm}^2/\text{V s}$. The mass diffusion coefficient is kept as $4.37 \times 10^{-10} \text{ m}^2/\text{s}$. It should be noted that the strong agreement between experimental results from Ref. [3] and those from the present testifies to the accuracy of the numerical model employed in the present work.

4 Results and Discussion

By varying the ratio of patch zeta potential between the top and bottom wall (ζ_r), the diffusive Peclet number (Pe) and the dimensionless zeta potential of the patch at the bottom wall ($\zeta_{P, \text{bottom}}$) in the range of $0.5 \leq \zeta_r \leq 1.5$, $1 \leq Pe \leq 1000$ and $1 \leq \zeta_{P, \text{bottom}} \leq 3$, respectively [3, 8], we investigate the influence of uneven

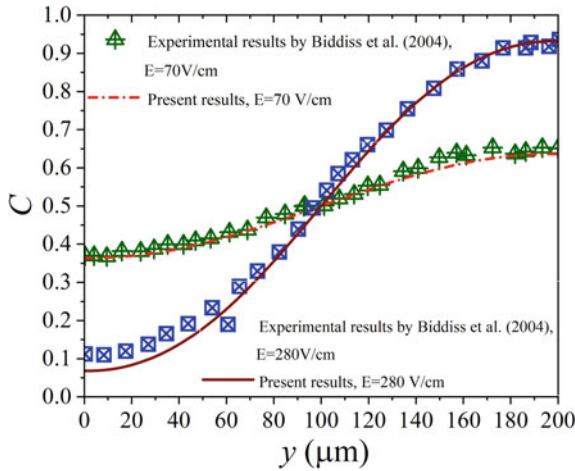


Fig. 2 Comparison of the normalised species concentration with Biddiss et al. [3] experimental findings at varied E

distribution of zeta potential on flow as well as mixing characteristics. The value of the non-dimensional Debye parameter is fixed as 30 [4, 7, 8, 10, 11].

First, an effort has been made to investigate the flow field inside the mixer at different ζ_r which is depicted in Fig. 3. A recirculation zone is generated near to the positively charged wall due to the generation of electroosmotic actuation from right to left direction by the interaction of positively charged surface and applied external electric field. Moreover, the alternate position of patches at the top and bottom wall causes undulated primary flow pattern inside the core region. Also, the increase in ζ_r augments the size and strength of bottom wall recirculation zone due to an increase in the patch zeta potential enlarges the reverse electroosmotic strength.

The variation of recirculation strength in terms of recirculation velocity (U_R) is illustrated in Fig. 4a. In this work, the maximum magnitude of the reversed flow velocity is used to represent the recirculation strength [7]. We observe that the value of U_R enhances with $\zeta_{p,bottom}$ as the strength of reversed electroosmotic flow actuation enhances. Interestingly, U_R is insensitive with ζ_r up to $\zeta_r = 1$. It is because the maxima reverse flow velocity exist close the bottom wall as the corresponding patch zeta potential magnitude is higher and constant for $\zeta_r < 1$. Hence, the larger reversed electroosmotic actuation strength at the bottom patch surface with constant zeta potential causes insensible variation of U_R with ζ_r . Whereas the higher patch zeta potential magnitude at the top wall when $\zeta_r > 1$ causes higher recirculation strength at the top patch wall. Hence, the rise in the magnitude of top wall patch zeta potential with increase in ζ_r enhances the recirculation strength, as well as U_R for $\zeta_r > 1$.

Further, Fig. 4b shows the change in non-dimensional flow rate (Q) with ζ_r is depicted in Fig. 4b at different $\zeta_{p,bottom}$. It is found that the value of Q reduces with ζ_r as the increase in recirculation size and strength at the top wall augmented resisting the main flow. Additionally, a higher bottom wall patch zeta potential improves the

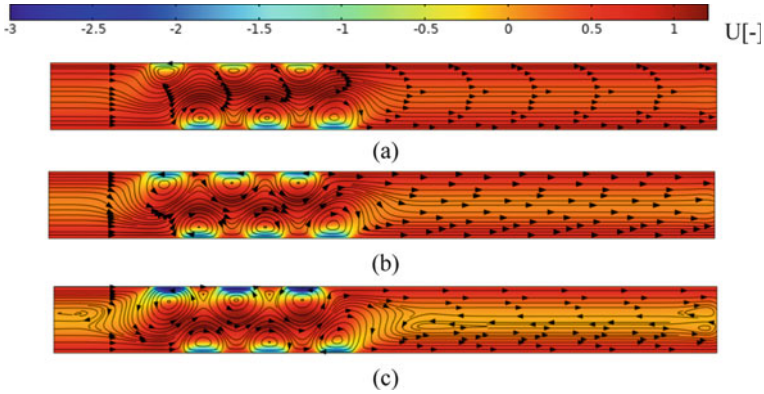


Fig. 3 Contours of flow velocity and streamlines at **a** $\zeta_r = 0.5$, **b** $\zeta_r = 1.0$ and **c** $\zeta_r = 1.5$ when $\kappa = 30$ and $\zeta_{P, \text{bottom}} = 3$

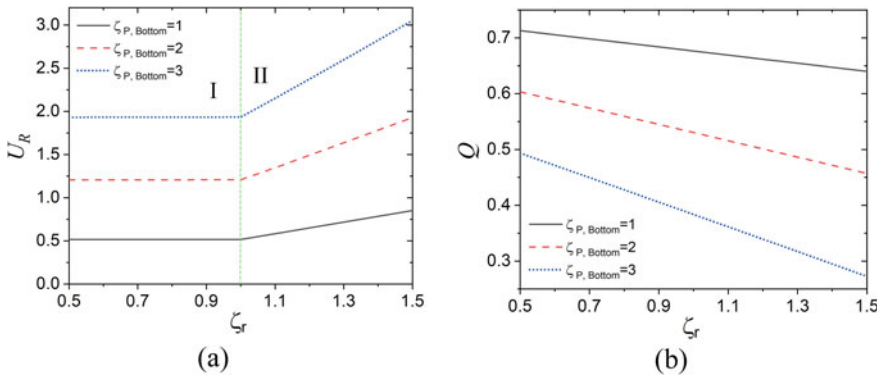


Fig. 4 **a** Dimensionless recirculation velocity and **b** dimensionless flow rate versus (ζ_r) at different $\zeta_{P, \text{bottom}}$ when $\kappa = 30$

strength of the recirculation, which lowers the flow rate with increase in the magnitude of $\zeta_{P, \text{bottom}}$.

The dimensionless species concentration contours are depicted in Fig. 5 at different ζ_r . We found that the homogeneity of the non-dimensional species concentration near the outlet approaches to 0.5 with increase in ζ_r . It is because of the increase in recirculation strength with ζ_r enhances the convective mixing strength and allows efficient mixing of the fluids. One can clearly see that the mixing is better when patch zeta potential at top and bottom wall is uneven with $\zeta_r = 1.5$ compared to the even distribution with $\zeta_r = 1$.

Figure 6a shows the change in mixing efficiency (η) with increase in Pe at different ζ_r for smaller bottom patch zeta potential ($\zeta_{P, \text{bottom}} = 1$). It is found the value of η in 100% for the smaller value of Pe up to a critical value ($=14.8$) for all ζ_r , which

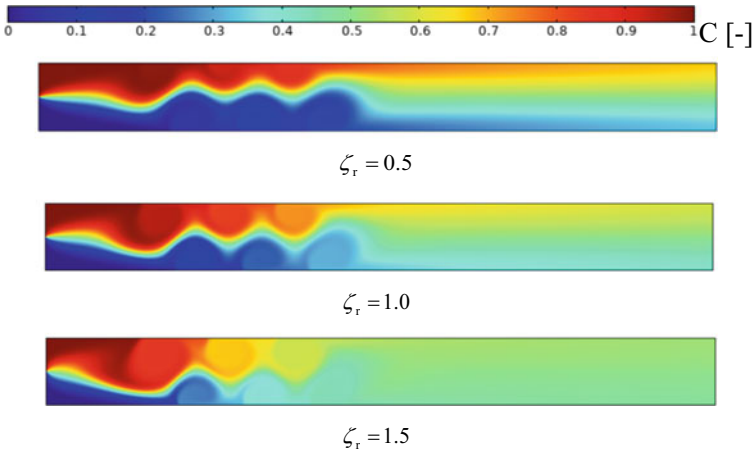


Fig. 5 Contours of dimensionless species concentration at different ζ_r when $\kappa = 30$, $\zeta_{P,bottom} = 3$ and $Pe = 100$

is attributed to the presence of sufficient convective mixing strength provided by recirculation zones near the patches. Whereas η decreases with Pe beyond the critical value ($Pe > 14.8$) because of the decrease in mass diffusion coefficient reduces the uniformity of species near the outlet. Moreover, η enhances with ζ_r due to the augmentation of species concentration uniformity by the increase in recirculation strength with ζ_r . Furthermore, effort has been made to identify the critical Pe up to which the micromixer length equal to mixing length based on 90% mixing efficiency. Notably that critical Pe augmented with ζ_r as the increase in recirculation strength with ζ_r augmented the convective mixing strength up to the greater Pe . Further, the change of η with Pe is depicted in Fig. 6b at different ζ_r for higher bottom patch zeta potential ($\zeta_{P,bottom} = 3$). Noted that the critical value of Pe up to which $\eta = 100\%$, is higher compared to the case of $\zeta_{P,bottom} = 1$. It is because of the higher recirculation strength owing to the higher patch zeta potential at $\zeta_{P,bottom} = 3$ (see Fig. 4a). Notably that critical value of Pe enhances with ζ_r at higher $\zeta_{P,bottom}$ ($= 3$) while constant for smaller $\zeta_{P,bottom}$ ($= 1$) due to the stronger convection mixing strength at higher $\zeta_{P,bottom}$.

Moreover, the critical Pe up to which the micromixer length behaves as mixing length based on $\eta = 90\%$, greatly augmented with ζ_r at higher $\zeta_{P,bottom}$ ($= 3$) owing to the greater strength of recirculation zone at higher $\zeta_{P,bottom}$ (see Fig. 4a). Also noted that η enhances with ζ_r at higher Pe due to the enhance in recirculation strength with ζ_r .

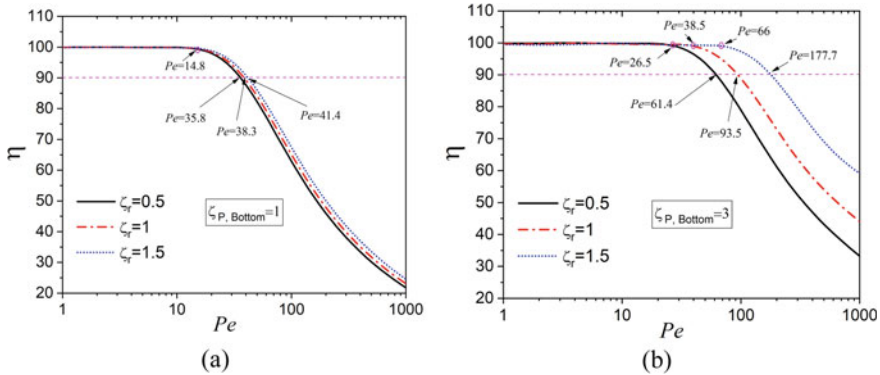


Fig. 6 Mixing efficiency at outlet versus diffusive Peclet number at different (ζ_r) when $\kappa = 30$ for **a** $\zeta_{P, \text{bottom}} = 1$ and **b** $\zeta_{P, \text{bottom}} = 3$

5 Conclusions

In this work, numerical investigation has been done to examine the flow as well as mixing characteristics of the electroosmotically actuated flow imposing the uneven modulation of patch zeta potential between the top and bottom walls. In order to study the flow field, recirculation velocity (U_R), non-dimensional flow rate (Q), non-dimensional species concentration field, and mixing efficiency (η), the ratio of the patch zeta potential of the top to bottom wall (ζ_r), patch zeta potential of the bottom wall ($\zeta_{P, \text{bottom}}$), and diffusive Peclet number (Pe) are varied in the physically reasonable range. It is found that the value of U_R enhances with $\zeta_{P, \text{bottom}}$. The value of U_R is insensitive with ζ_r up to $\zeta_r = 1$. Whereas the increase in top patch zeta potential magnitude with ζ_r enhances U_R when $\zeta_r > 1$. The value of Q reduces with ζ_r and $\zeta_{P, \text{bottom}}$. Further, the species concentration uniformity near the outlet approaches to 0.5 with increase in ζ_r . Interestingly, the species concentration is more uniform when patch zeta potential at top and bottom wall is uneven with $\zeta_r = 1.5$ compared to the even distribution with $\zeta_r = 1$. The value of η in 100% for the smaller value of Pe up to a critical value ($=14.8$) for all ζ_r when $\zeta_{P, \text{bottom}} = 1$. Whereas that critical value of Pe enhances with ζ_r at higher $\zeta_{P, \text{bottom}} (=3)$. η decreases with Pe at higher Pe and enhances with ζ_r . The critical Pe up to which the micromixer length behaves as mixing length based on $\eta = 90\%$, greatly augmented with ζ_r at higher $\zeta_{P, \text{bottom}} (=3)$.

References

1. Vasista, K. N., Mehta, S. K., & Pati, S. (2021). Numerical assessment of hydrodynamic and mixing characteristics for mixed electroosmotic and pressure-driven flow through a wavy microchannel with patchwise surface heterogeneity. *Proceedings of the Institution of Mechanical Engineers, Part E: Journal of Process Mechanical Engineering*. <https://doi.org/10.1177/09544089211051640>
2. Vasista, K. N., Mehta, S. K., & Pati, S. (2022). Electroosmotic mixing in a microchannel with heterogeneous slip dependent zeta potential. *Chemical Engineering and Processing—Process Intensification*, 176, 108940.
3. Biddiss, E., Erickson, D., & Li, D. (2004). Heterogeneous surface charge enhanced micromixing for electrokinetic flows. *Analytical Chemistry*, 76(11), 3208–3213.
4. Hadigol, M., Nosrati, R., Nourbakhsh, A., & Raisee, M. (2011). Numerical study of electroosmotic micromixing of non-Newtonian fluids. *Journal of Non-Newtonian Fluid Mechanics*, 166(17–18), 965–971.
5. Mondal, B., Mehta, S. K., Pati, S., & Patowari, P. K. (2021). Numerical analysis of electroosmotic mixing in a heterogeneous charged micromixer with obstacles. *Chemical Engineering and Processing—Process Intensification*, 168, 108585.
6. Mehta, S. K., Mondal, B., Pati, S., & Patowari, P. K. (2022). Enhanced electroosmotic mixing of non-Newtonian fluids in a heterogeneous surface charged micromixer with obstacles. *Colloids and Surfaces A: Physicochemical and Engineering Aspects*, 648(5), 129215.
7. Mehta, S. K., Pati, S., & Mondal, P. K. (2021). Numerical study of the vortex-induced electroosmotic mixing of non-Newtonian biofluids in a nonuniformly charged wavy microchannel: Effect of finite ion size. *Electrophoresis*, 42(23), 2498–2510.
8. Mehta, S. K., & Pati, S. (2022). Enhanced electroosmotic mixing in a wavy micromixer using surface charge heterogeneity. *Industrial & Engineering Chemistry Research*, 61(7), 2904–2914.
9. COMSOL Multiphysics® v. 5.2. COMSOL AB. www.comsol.com
10. Vasista, K. N., Mehta, S. K., Pati, S., & Sarkar, S. (2021). Electroosmotic flow of viscoelastic fluid through a microchannel with slip-dependent zeta potential. *Physics of Fluids*, 33(12), 123110.
11. Banerjee, D., Mehta, S. K., Pati, S., & Biswas, P. (2021). Analytical solution to heat transfer for mixed electroosmotic and pressure-driven flow through a microchannel with slip-dependent zeta potential. *International Journal of Heat and Mass Transfer*, 181, 121989.

Heat Transfer Enhancement in Micro-fin Tube Using Coil Wire Insertions of Different Lengths



Roheshkumar S. Lavate, K. B. Sutar, Avishi Saini, Ankita Shakshi, and Parth Sethi

Abstract Heat transfer augmentation techniques are generally employed in thermal power plants, refrigerators, radiators for space vehicles, automobiles, process industries, heating and cooling in evaporators, air-conditioning equipment, etc. Inserting coiled wire in microfin tubes are a typical technique that offers a higher heat transfer increase and, at the same time, only a mild pressure drop. One of the passive heat transfer augmentation techniques been used is coiled wire insert and are widely used tubes in several heat transfer applications. Flow conditions as well as Reynolds number directly affect the thermodynamic performance of heat exchange components. Rate of heat transfer, Heat Transfer Coefficient, Pressure drop in case of microfin tube with coil wire insertion is higher than that of without coil wire insertion. Friction factor decreases with the increment in mass flow rate of hot water for the microfin tube with and without coiled wire insert. Wire coils at a constant pumping power shows an increase in heat transfer at low Reynolds number.

Keywords Coil-wire insert · Microfin tube · Heat augmentation techniques

1 Introduction

1.1 Heat Exchanger

Heat exchanger is a system used to exchange heat between two or more fluids [1, 2]. Existing fluids can be either single phase or two phase and, in accordance with the type of heat exchanger, they may be in direct contact or separated to each other. Instruments having energy sources like nuclear fuel pins or fired heaters are not generally regarded as heat exchangers although many of the principle involved in their design are an equivalent. Fluid temperatures in food, beverage, sterilization,

R. S. Lavate (✉) · K. B. Sutar · A. Saini · A. Shakshi · P. Sethi
Department of Mechanical Engineering, Bharati Vidyapeeth (Deemed to be University) College of Engineering, Pune-Satara Road, Katraj, Pune 411043, India
e-mail: lavate.rohesh@gmail.com

clean-in-place and other hygienic operations are controlled with the help of heat exchangers. Heat exchangers can be classified in different ways, based on construction, phase of process fluids, degrees of surface compactness, pass arrangements, flow arrangements, mechanisms of heat transfer and transfer processes. The methodology for designing a heat exchanger is very complicated and sophisticated since it requires an accurate analysis of the rate of heat transfer, efficiency and pressure drop apart from aspects such as economy, performance of the system [3]. Heat exchangers are applied in various applications such as power plant generation, chemical processing plant, cryogenic, refrigeration and air conditioning, transportation, alternative fuels, food beverage and dairy, air processing, compressor cooling, pharmaceuticals and other industries. With the use of different heat transfer augmentation techniques along with the improvement in heat transfer rate, drop in pressure also increases substantially, which increases the cost of pumping. Therefore in order to apply any augmentation technique or device in to the heat exchanger it should be optimized between the improvement of heat transfer coefficient and higher pumping cost resulting in the high frictional losses. Heat transfer augmentation methods are generally classified in to three categories as:

(a) Active Method

It involves input from some external power source to enhance the heat transfer rate [4]. They are complicated in terms of design and application due to urge of external energy to control the flow of fluid. Various types of active techniques used are pulsation by cams and reciprocating plungers, fluid vibration, jet impingement, mechanical aids, electrostatic fields, suction or injection, etc. Supplying external energy in most applications is not easy, due to this, the necessity of active techniques is limited in scientific fields.

(b) Passive Method

Like active technique, power from any external source is not required, instead either geometry or surface of the flow channel is modified by incorporating inserts or additional devices to enhance the thermohydraulic performance of the system. For instances swirl flow devices, rough surfaces, extended surfaces, coiled wire inserts, treated surface are used. To upgrade the turbulence and mixing of fluid in the flow rough surfaces, inserts and ribs are used, resulting in the enhancement of overall heat transfer. These methods increase the heat transfer rate by altering the flow treatment resulting in increase in pressure drop [5].

(c) Compound Method

Combination of two or more heat transfer augmentation method (either active and/or passive) is required by the compound method to enhance the thermohydraulic performance of the system [6]. By applying these techniques both heat transfer rate and pressure drop increases but to improve the efficiency it is required to lower the pressure drop, done by varying the length of coil wire insert keeping the pumping power constant.

1.2 Heat Augmentation Techniques

(a) Coiled Wire Inserts

Coil wire inserts have been utilized as one of the passive method of heat enhancement techniques. Helical inserts are new addition for enhancement of heat transfer used in various heat transfer application such as cooling device, air conditioning, refrigeration system, preheater, good and dairy product etc. The swirl for helical taps moves unidirectionally along the helical and stimulate swirl within the flow, which increase their tension time of the flow and consequently provide better heat transfer performance in comparison to twisted tape inserts.

In comparison to other heat exchanger performance enhancement methods advantages of coil wire inserts are below [7]:

1. Easy installation and eviction
2. Simple manufacturing process with reduced cost
3. No change in the mechanical strength of original plain tube
4. Easy installation probability in an existing smooth tube heat exchanger.

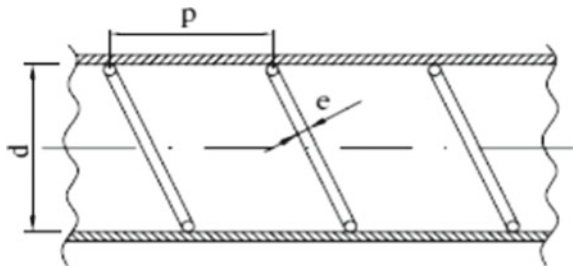
Wire-coil inserts enhances the heat transfer coefficient to almost 72%, while the frictional pressure drop increases up to 85% [8].

(b) Microfin Tubes

Internally grooved copper tubes also termed as “microfin tubes” are a small diameter coil technology applied in modern air conditioning and refrigeration systems, facilitate more efficient heat transfer rate than smooth coils. Small diameter coils offers better heat transfer rates than the conventional-sized condenser and evaporator coils having round copper tubes and copper or aluminium fin. Microfin tubes can sustain higher pressures required by the environmental friendly new generation refrigerants, having lower material costs requiring less refrigerant, coil materials and fin.

Copper is typically used for making microfin tubes having an outside diameter ranging from 4 to 15 mm, a single set of 50–70 fins with helix angle (β) from 6° to 30° , fin height (h) from 0.1 to 0.25 mm, trapezoidal or triangular fin shapes with an apex angle (g) from 25 to 90° [9] (Fig. 1).

Fig. 1 Diagram of a helical-wire-coil fitted inside a smooth tube [9]



Following parameters can be reduced to find the wire geometry in non-dimensional form. Dimensionless wire-diameter e/d pitch to wire-diameter ratio p/e and dimensionless pitch p/d .

2 Literature Review

Lavate [10] concluded that the heat transfer rates obtained from the microfin tube with coil wire insert are higher than those microfin tubes without coil wire insert. The average heat transfer coefficient improves with increase in hot water mass flow rate, pressure drop in microfin tube with coil wire insert is greater in comparison to microfin tube without coil wire insert at the same mass flow rate of hot and cold water. There is a slight decreasing tendency of friction factor with the increment in mass flow rate of hot water for the microfin tube with and without coiled wire insert. Ray [11] concluded that pressure drop in wire coiled tube is more in comparison to an empty tube. In transition and turbulent region flow wire coil insert performs better. Wire coil insert is not very effective in laminar flow and behave like a smooth tube heat exchanger as per the results. Gosavi [12] experimentally inquired that, fins are the method of improving heat transfer. The perforated fin may release about 50 to 60% more heat. Heat transfer becomes more uniform by providing the perforations. Perforated fin efficiency is higher than the solid fin. The perforated materials may have better strength. Richard [13] studied the temperature distribution in a simple pin fin for different materials, fin efficiencies of brass, aluminium and copper was achieved as 66%, 91% and 94% respectively. Copper has highest thermal conductivity among the materials analyzed. Kanojiya [14] reviewed different ways of improving the heat transfer rate by generating the swirl flow by using different types of inserts. Heat transfer rate increases in perforated twisted tape hence, with decrease in pressure drop heat transfer coefficient increases. In a perforated twisted tape inserts, the friction factor increases in the laminar region, increase the heat transfer coefficient in comparison to without perforated twisted tape inserts. Twisted tape insert performs better in laminar flow. Matani [15] found out the thermal characteristics in a tube fitted with twisted-tapes in co-swirl arrangement with wire coil. Results replicates that the wire coil having pitch ratio of 0.88 is more effective among all of the twisted tapes experimented. Again, in twisted tapes particularly the double twisted tape behaves like a counter swirl generator and exhibit better performance than the single twisted tape. Work being conducted in the turbulent flow condition, having Re number ranging between 5000 and 18,000 using air as the test fluid. Reference [16] experimentally investigated augmentation of heat transfer rates in heat exchanger by means of perforated twisted tapes. The results showed that the presence of wings and holes on perforated twisted tapes significantly influences heat transfer rate and friction factor. Gunes [17] investigated the pressure drop and heat transfer in a tube inserted with coil wire. Equilateral triangle cross section coiled wire inserted separately from the tube wall. The coiled wire inserts results a significant increase in both pressure drop and heat transfer in comparison with the smooth tube depending on

wire thickness and coil pitches. San [18] experimented the effect of wire diameter to tube diameter ratio and coil pitch to tube inner diameter ratio. Results concluded that the Nusselt number decreases with increase of wire diameter to tube diameter ratio whereas it improves with reduction in coil pitch to inner diameter ratio. Chang [19] obtained the effects of grooved and ribbed wire coils on thermal performance through the experiment. An unsteady partitioned flow was generated rewarding in enhanced thermal performance. The Thermal Performance Factor of 45° rib, 45° groove and 90° rib, 45° groove was higher than that of one. Martinez [20] performed experiments and concluded that adding nanoparticles to the de-ionized water enhances the single-phase heat transfer. Again there is almost no effect of the mass concentration of nanoparticles on single-phase heat transfer enhancement. Selvam [21] had used the wire coiled coil-matrix turbulator as an insert in the concentric tube heat exchanger. Again, determining the effect of bonding with and without bonding of wire coiled coil-matrix turbulator on heat transfer and friction factor characteristics. From this they concluded that the heat transfer rate improved with the reduction in the pitch. Wire coiled coil-matrix with and without center core rod was used as an insert in the concentric tube heat exchanger. Eiamsa-ard [22] concluded that the use of wire coil elements causes a high pressure drop. Nusselt number growth tends to decrease slightly with the rise in Reynolds number. In comparison to smooth duct, wire coils at a constant pumping power shows an increase in heat transfer at low Reynolds number. Application of tandem wire coil elements can significantly reduce the friction losses in the duct but the rate of heat transfer is also decreased. Garcia [23] compared the effect of corrugated tubes, smooth tubes and wire coil insert on heat transfer improvement in laminar flow. The wire coil inserts have no influence in heat transfer at $Re = 400$. But it becomes influential as turbulence is established. At $Re = 1800$, influence of wire coil insert in smooth tube is that heat transfer improved by 300% without increase in pumping power. Saha [24] performed experiments to study the effect of wire coil inserts and transverse ribs. Use of transverse rib with wire coil enhanced the thermal performance. Also, numerical investigation was performed to study the effect of wire coil insertion on laminar flow in rectangular micro channel heat sink using ANSYS. So, from the obtained results, they concluded that the wire coil insertion performs better only when there is lesser Re flow. Eiamsa-ard [25] concluded experiments to study the effect of combined non-uniform wire coil and twisted tape inserts on thermal performance characteristics. Wire coil was arranged in two other forms: (1) reducing the coil pitch ratio and (2) increasing–decreasing the coil pitch ratio. TPF of 1.25 was obtained with increasing–decreasing coil with least twist ratio. Nanan [26] found heat transfer by using helically twisted tapes to create counter swirl flow. Experimentation for several parameters was executed, it was found that co-swirl helically twisted tape have higher thermal performance factor in comparison to the counter-swirl tape. Also, thermal performance factor of the combined enhancement technique was better. Copetti [27] finalized that the microfins promote a major turbulence that intensifies the heat transfer. However, at the same time, they introduce an enhancement in the pressure drop. Thus, it is required to find the heat transfer coefficient and the friction factor for heat exchangers design, considering the various flow characteristics of the applications. Naphon [28] presented the drop in pressure

and heat transfer characteristics results of the horizontal double tubes with coil-wire insert. Mass flow rates of cold and hot water directly affects the heat transfer coefficient and heat transfer rates. Also, with the increase in Re the effect of coil-wire insert on the enhancement of heat transfer decreases. Fuskele [29] conducted the experimental work on heat transfer augmentation in double pipe heat exchanger with the use of a new type of insert known as twisted wire mesh. With the introduction of insert in a way of flow of liquid, more degree of turbulence is generated which resulted into higher heat transfer rate as well as pressure drop. Heat transfer coefficient and friction factor for two different twisted wire mesh type insert was calculated having twist ratio of $y = 5$ and $y = 7$. To confirm experiment result, standard correlation of heat transfer was used. The results obtained from experimentation for twisted wire mesh having distinct twist ratio when compared with result of smooth plain tube. For twisted mesh type insert friction factor improved from 4.0 to 4.3 times and the heat transfer coefficient were improved from 1.69 to 2.09 times in comparison to smooth tube value. In addition, researcher also found the impact of new wire mesh type of insert on heat transfer improvement efficiency. Results obtained leads to conclusion that with the insertion of insert, heat transfer rate improves with reasonable pressure drop. Wang and Sunden [30] did the comparison of coil wire inserts and twisted tapes. It was found that the solution to disturb the central core flow are twisted tapes but when the peripheral annular flow is to be mixed with core flow better performance is showed by the wire coil inserts. Eiamsa-ard [31] investigated the enhancement of the heat transfer in a tube fitted with delta-winglet twisted tapes which act as swirl generator and turbulator. Values of friction factor and Nusselt number in the delta winglet twisted tape test tube are higher than those in the plain tube. Also, the Nu and friction factor increases with decrease of twist ratio (y/w) and increase in depth of wing cut ratio (DR) for all Reynolds numbers was studied. Sapali [32] designed and developed the experimental test facility, used to determine the condensation heat transfer coefficient and pressure drop in microfin and smooth tubes for various hydrofluorocarbon refrigerants. Condensation heat transfer coefficient and the pressure drop shows increasing trend with increase in mass flux and decreases with increase in the condensation temperature for both type of tubes. Sonawane [33] concluded that by using treated surface we can enhance the rate of heat transfer which are applicable for condensing as well as boiling. Heat transfer can also be done by using extended surfaces in which copper has the higher thermal conductivity than aluminium and brass.

3 Experimental Apparatus

The shell is of mild steel material having diameter 80 mm and length 800 mm. Inside the shell 5 number of micro-fin tubes are provided. The copper tube having 8.92 and 9.52 mm be the inner and outer diameters of the micro-fin tube respectively. The length of micro-fin tube is 760 mm. Coiled wire insert is with coil diameter of 7 mm and length of coil wire is 750 mm per tube. The close loops of hot and cold water

contain the storage tanks, electric heaters. The hot water is set to the desired level and regulated by a temperature controller the temperature of hot water maintains in between 40 and 45 °C and water temperature is 25–30 °C. After the temperature of the cold and hot water are adjusted to get the desired level, the water of each loop is pumped out of the storage tank and is passed through a flow meter, test section, and returned to the storage tank. In this test rig two rotameters with the range of flow lies between 1 and 10 LPM, are used to measure flow of cold water and hot water. The flow of water is being controlled through ball valves. To measure pressure drop across the microfin test section the manometer is needed. To measure the different temperatures 6 thermocouples are used. T1, T2 be the temperature of hot water at inlet and outlet and T3, T4 be the temperature of cold water at inlet and outlet for microfin tube with coil wire insert. Similarly, T5, T6 be the temperature of hot and cold water storage tank. Experimentation is carried out by changing the length of coil wire insert (Fig. 2).

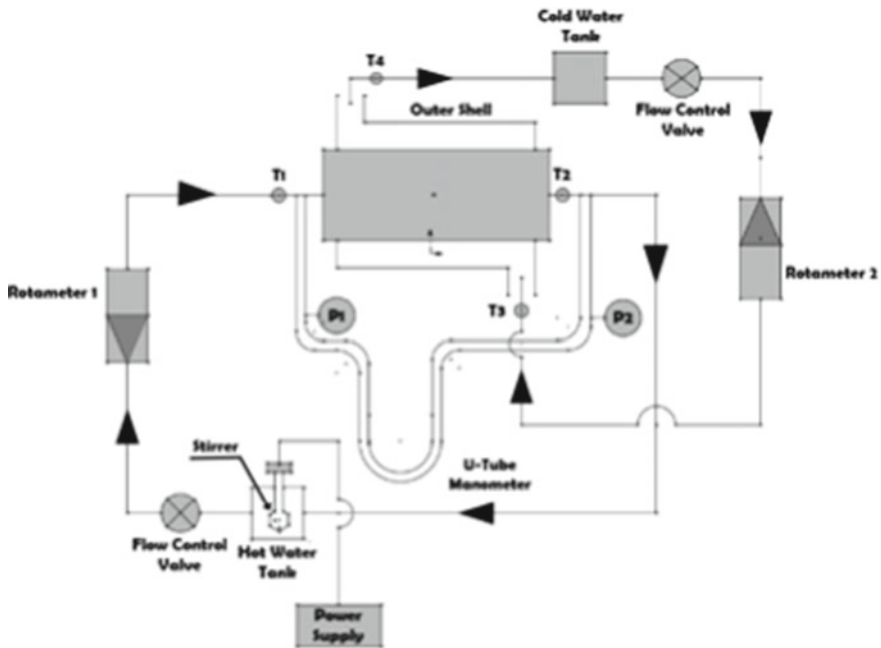


Fig. 2 Layout of the experimental set-up

4 Results and Discussion

1. Rate of heat transfer in case of microfin tube with coil wire insertion is higher than that of without coil wire insertion. Wire coils at a constant pumping power shows an increase in heat transfer at low Reynolds number. Full-length coil should be used in order to obtain higher rate of heat transfer and performance. Wire coil insertion performs better only when there is lesser Reynolds flow. Major turbulence is promoted by microfins, intensifies the heat transfer. Twisted tape results in high heat transfer rate in comparison to the wire coil inserts.
2. Mass flow rates of cold and hot water directly affects the heat transfer coefficient and heat transfer rates. With the increase in Reynolds number, the effect of coil-wire insert on the enhancement of heat transfer decreases.
3. Pressure drop in wire coiled tube is more when compared to an empty tube. The coiled wire inserts results a significant increase in both pressure drop and heat transfer in comparison with the smooth tube.
4. Friction factor decreases with the increment in mass flow rate of hot water for the microfin tube with and without coiled wire insert. Wire coil insert performs better in transition and turbulent flow region.
5. Nusselt number growth tends to decrease slightly with the rise in Reynolds number.

References

1. Hou, T. K. (2017). Industrial heat exchanger: Operation and maintenance to minimize fouling and corrosion. *Heat Exchangers-Advanced Features and Applications*.
2. Zohuri, B. (2016). *Heat exchanger types and classifications*. Springer.
3. Admane, A. A. (2013). A review of heat transfer augmentation technique for combined coiled insert and dimple tube approach. *International Journal of Engineering Research & Technology (IJERT)*, 2(11).
4. Dewan, A. (2004). Review of passive heat transfer augmentation techniques. *SAGE Journal*.
5. Sheikholeslami, M. (2015). Review of heat transfer enhancement methods: Focus on passive methods using swirl flow devices. *Renewable and Sustainable Energy Reviews*, 49, 444–469.
6. Keklikcioglu, O. (2018). A review of heat transfer enhancement methods using coiled wire and twisted tape inserts. *Heat Transfer-Models, Methods and Applications*.
7. Rathod, P. (2017). Heat transfer enhancement in pipe flow using wire coil inserts in forced convection. *International Journal of Engineering Research & Technology (IJERT)*, 6(08).
8. Sajadi, B. (2019). The effect of wire-coil inserts on the heat transfer and pressure drop of R1234yf flow boiling. *Applied Thermal Engineering*.
9. Doretti, L. (2013). Condensation flow patterns inside plain and microfin tubes: A review. *International Journal of Refrigeration*, 36, 567–587.
10. Lavate, R. S., & Patil, A. M. (2015). Experimental study on heat transfer and pressure drop in microfin tubes with and without coiled wire insert. *IJAIEEM*, 4.
11. Ray, P. (2014). A review paper on heat transfer rate enhancement by wire coil inserts in the tube. *International Journal of Engineering Sciences & Research Technology*, 3(6), 238–243.
12. Gosavi, G. D., Prayagi, S. V., & Narnaware, V. S. (2014). Use of perforated fins as a natural convection heat transfer—A review. *International Journal of Current Engineering and Technology*.

13. Richard, A. H. (2015). Experimental analysis of heat transfer enhancement using fins in pin fin apparatus. *International Journal of Core Engineering & Management (IJCEM)*.
14. Kanojiya, N. C., Kriplani, V. M., & Walke, P. V. (2014). Heat transfer enhancement in heat exchangers with inserts: A review. *International Journal of Engineering Research & Technology*, 3.
15. Matani, A. G., & Dahake, S. A. (2013). Experimental study on heat transfer enhancement in a tube using counter/co-swirl generation. *International Journal of Application or Innovation in Engineering & Management (IJAIEM)*, 2(3).
16. Promvong, P., & Eiamsa-ard, S. (2011). Effect of perforated twisted-tapes with parallel wings on heat transfer enhancement in a heat exchanger tube. In *Second International Conference on Advances in Energy Engineering (ICAEE)*.
17. Gunes, S. (2010). Heat transfer enhancement technique and their thermal performance factor. *Journal of Basic and Applied Sciences*.
18. Nguyen, D.-K., & San, J.-Y. (2014). Effect of solid heat conduction on heat transfer performance of a spiral heat exchanger. *Applied Thermal Engineering*, 76, 400–409.
19. Chang, S. W., Gao, J. Y., & Shih, H. L. (2015). Thermal performances of turbulent tubular flows enhanced by ribbed and grooved wire coils. *International Journal of Heat and Mass Transfer*, 90, 1109–1124.
20. Martinez, C. D. (2009). *Heat transfer enhancement of spray cooling with nanofluids*. Graduate Theses and Dissertations, Department of Mechanical Engineering, University of South Florida Scholar Commons.
21. Selvam, S. (2012). Effect of wire coiled coil matrix turbulators on the concentric tube heat exchanger. *Journal of Thermal Sciences*.
22. Eiamsa-ard, S. (2015). Water nano fluid heat transfer in heat exchanger equipped with double twisted tape inserts. *Journal of Material Science and Engineering*.
23. Garcia, A. (2010). Heat transfer enhancement in smooth tube with wire coil inserts in laminar flow. In *7th International Conference on Heat Transfer, Fluid Mechanics and Thermodynamics*.
24. Saha, S. K. (2012). Laminar flow heat transfer enhancement using transverse rib and helical tape inserts. *Journal of Thermo Physics and Heat Transfer*.
25. Eiamsa-ard, S. (2009). Heat transfer enhancement in a tube using delta-winglet twisted tape inserts. *Journal of Applied Thermal Engineering*.
26. Nanan, K. (2012). Heat transfer augmentation by helically twisted tapes as swirl and turbulence promoters. *Journal of Chemical Engineering and Processing*.
27. Copetti, J. B. (2004). Experiments with micro-fin tube in single phase. *International Journal of Refrigeration*.
28. Naphon, P., & Sriromrulp, P. (2006). Single-phase heat transfer and pressure drop in the micro-fin tubes with coiled wire insert. *International Communications in Heat and Mass Transfer*.
29. Fuskele, V., & Sarviya, R. M. (2009). Experimental investigation of heat transfer enhancement in double pipe heat exchanger using twisted mesh insert. *IJARS*, 1(II), 05–09.
30. Wang, L., & Sunden, B. (2002). Performance comparison of some tube inserts. *International Communications in Heat and Mass Transfer*, 29(1), 45–56.
31. Eiamsa-ard, S. (2009). Heat transfer enhancement in a tube using delta-winglet twisted tape inserts. *Applied Thermal Engineering*, 30.
32. Sapali, S. N. (2009). Two-phase condensation heat transfer coefficients and pressure drops of R-404a for different condensing temperatures in a smooth and micro-fin tube. *International Journal of Engineering Science and Technology*, 1(2).
33. Sonawane, T., Patil, P., Chavhan, A., & Dusane, B. M. (2016). A review on heat transfer enhancement by passive methods. *International Research Journal of Engineering and Technology (IRJET)*, 03.

Numerical Study of a Miniature Concentration Gradient Generators (CGGs) of Various Shapes



Sachin Gavali, Prashant M. Pawar, and Digvijay D. Ronge

Abstract Microfluidic devices in the miniaturized chip format are famous for performing laboratory functions and are used in a wide array of biomedical applications such as rapid clinical diagnosis, forensic science, flow cytometry, and analysis of blood chemistry, protein and DNA. In many biochemical applications studies of CGG helps to get the trends of cells and molecules in different samples such as extracting the maximum information of tumour cells in response to several drugs varying in concentration so as to obtain the minimal sample which is helpful for basic biomedical research in cancer treatment. This paper analyses concentration gradient generators (CGGs) of various shapes having two inlets and five outlets for water and ethanol fluids. The study resulted that the square-shaped CGG performed better than the other designs. It also demonstrates the no significant effect of Reynold number variation on the concentration gradient for Straight CGG.

Keywords Concentration Gradient Generator (CGG) · CFD · Concentration gradient · Reynold's number · R^2 value

1 Introduction

The Lab on Chips devices gives novel approaches for fluid control and manipulation. Concentration Gradient Generators (CGGs) are the most efficient devices for accurately generating different concentration gradients. The concentration of chemicals significantly affects cellular behaviour in most biosynthesis activities [1]. The

S. Gavali (✉) · D. D. Ronge
Department of Mechanical Engineering, SVERI's College of Engineering, Pandharpur,
Maharashtra State 413304, India
e-mail: srgavali@coe.sveri.ac.in

P. M. Pawar
Department of Civil Engineering, SVERI's College of Engineering, Pandharpur, Maharashtra
State 413304, India

microfluidic CGG is a vital element used in biochemical engineering to analyze the effect of various concentrations of drugs on cells or species [2]. Micro-miniature CGGs have emerged as important components in various applications like cell culture and organ-on-a-chip [3].

In cancer treatment, the optimized dose of medicine results in the best outcome. Cancer patients are treated with different concentrations of drugs, and the optimized dose is applied further [4]. It is also essential in studying cell biology, biochemistry, surface patterning and microfabrication. Many researchers worked on the CGGs to study and establish the analogy of electric circuits for the effective designing of microfluidic networks and the effect of different microchannels on the concentration gradients [5].

Tree-like CGGs generate more precise and stable concentrations and are mostly used in drug screening in microfluidic cell culture. Many researchers designed CGGs based on analytical models in respect of concentration and pressure [6].

Generally, low-cost, tree-like CGGs yield non-linear concentration gradients with multiple inlets to generate non-linear concentration gradients [7]. A non-linear concentration gradient is also generated in the applications like electroosmosis [8, 9]. It concentrates charged particles by fluid pumping.

This paper reports a numerical analysis of Concentration Gradient Generators of various shapes such as Straight, Square, Circular and Triangular at a particular Reynold number on the fluid mechanics' models and previous research using computational fluid dynamics (CFD) software. Also studied was the effect of the length of the generator on concentration gradient and time-to-gradient stability. The resulting mixing of a miniaturized gradient mixer mostly depends on parameters like viscosity, density, flow velocity and the characteristics and length of the flow. Reynold's equation (Re) involves all of these parameters.

In the current research, to understand the mixing process two different fluids having concentrations (0 and 1 mol/m³) are passed separately into two inlets. The objective is to find the concentration of two input fluids in different concentrations in the form of concentration gradients at five outlets of a CGG. The concentration gradient generators were drawn in AutoCAD software in the current research work. COMSOL Multiphysics version 6.0 was used to perform simulations of the designed CGGs. The concentrations of mixing of the two microfluidics at the five different outlets at Reynold's number of 50 with different shapes CGGs like Straight, Circular, Square and Triangular were simulated and studied for the Concentration gradients. The best-configured design was selected based on the good linearity of the concentration gradient and the basis of R square analysis. For an optimistic shape, the concentration gradient generator was simulated for different Reynold's Numbers, varying from 10 to 100. The objective was to find the optimistic CGG, which gives a linear variation of the concentration gradient and maximum R square value.

2 Methodology

2.1 Micro-miniature CGG Design

The design of a Straight shaped CGG consisting of two inlets and five outlets is shown in Fig. 1. The total length and width of the CGG are 54.2 mm and 18.5 mm respectively. The width of the channel is maintained at 0.5 mm. The total length is divided into five zones. The mixing inlet zone is 5.0 mm in length and the other four Tiers are 11.4 mm in length each as illustrated in Figs. 1 and 2. The illustration in respect of different arrangements of branching for various shapes of CGGs is shown in Fig. 3.

The other CGGs with circular, square and rectangular shapes also having two inlets and five outlets were designed and simulated at the Reynold number of 50. Schematics of their design are illustrated in Fig. 3.

Two-dimensional (2D) CGG was drawn in the AutoCAD software and then the Auto CAD file was converted into .dxf to import it into COMSOL Multiphysics software. Afterwards, the CGG applied the modelling equation to the applicable area of interest.

The optimistic shape CGG was selected based on the linearity of the concentration gradient and having a better R square value.

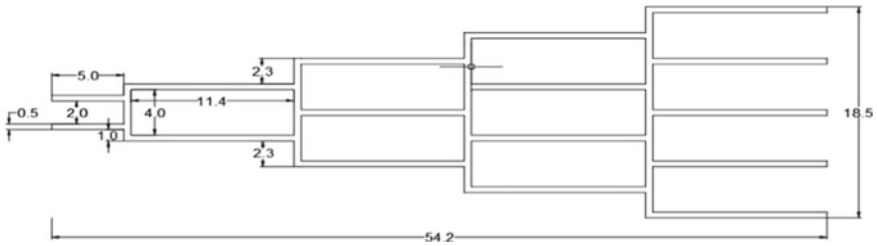


Fig. 1 Designed straight CGG produced in AutoCAD (all dimensions are in mm)

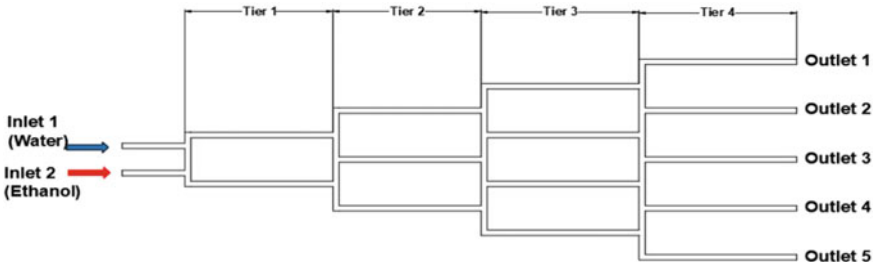


Fig. 2 Schematic for illustrating inlets, outlets and tier zones of straight CGG produced in AutoCAD

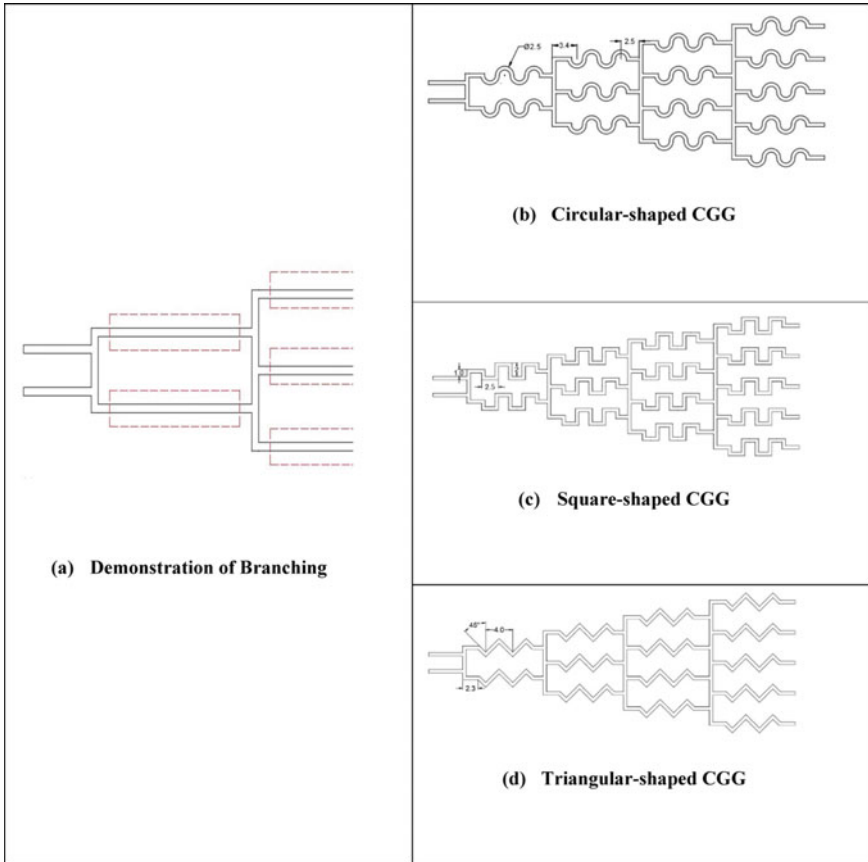


Fig. 3 Technical drawings of designed circular, square and triangular CGGs produced in AutoCAD

2.2 Numerical Simulation of CGG

The no-slip boundary condition was implied which represents the hydrophobic condition of the CGG. The simulations were performed by using water–ethanol-based fluids, the properties of these fluids are mentioned in Table 1.

The model in the COMSOL Multiphysics software was built by considering laminar flow was applied to generate the mesh. The inlets 1 and 2 of the model

Table 1 Fluid properties at 20 °C [10]

Property	Water	Ethanol	Unit
Density	998	780	kg/m ³
Dynamic viscosity	0.0009	0.0012	Pa s
Diffusion coefficient	1.2×10^{-9}	1×10^{-9}	m ² /s

were fixed after meshing. Water was allowed to flow through the Inlet 1 and Ethanol was passed through inlet 2. Different concentration gradients were indicated by the colour intensity. The fluid flow in input channels was desired to be identical and simultaneous. Further, the efficiency of mixing in terms of concentration gradients (mol/m^3) was examined to identify better-shaped CGG by identifying the optimum mixing of the fluids and yielding a linear range of concentration gradients at different outlets. Optimized CGG was tested by comparing the concentration gradients for Reynold numbers varying from 10 to 100. Various colour intensities were used to identify the mixing results by mixing two fluids of various concentrations produced at the outlets.

2.3 Mathematical Model and Governing Equations

Concentration Gradient Generator-based Micro-mixer generates a stable gradient during the flow. Laminar flow results in many cases due to low velocities and small dimensions, for which Reynold’s number is in the range of unity [11]. Diffusion and convective mass transfer are the responsible elements for the mixing in the case of laminar flow possessing low-Reynolds-number [12]. Hence to facilitate proper diffusive mixing, the channels should have sufficient length [13]. The mathematical model is based on the assumption of a steady flow of incompressible fluid.

The volume force in the microchannel is negligible and hence ignored, however it is considered that the flow is driven by pressure only. Hence the following governing equations such as the continuity equation, the Navier–Stokes’s equation, and the convection–diffusion equation are applied to the study [14].

The continuity equation,

$$\nabla \cdot u = 0, \tag{1}$$

the Navier–Stokes’s equation,

$$\partial u \partial t + u \cdot \nabla u = -1 \rho \nabla P + v \nabla^2 u, \tag{2}$$

the convection–diffusion equation,

$$\partial c \partial t + (u \cdot \nabla) c = D \nabla^2 c \tag{3}$$

where u is the velocity vector of the fluid, ρ is the density of the fluid, v is the kinematic viscosity of the fluid, c is the molar concentration of the component, and D is the diffusion coefficient of the component.

2.4 R-Squared Regression Analysis

The R-squared statistical method gives closeness of data to the fitted regression line and is applied to determine the linearity of a concentration gradient. Its value ranges between 0 and 100%. In general, the higher the R-square, the variable concerning a given benchmark index [15].

$$R^2 = \frac{SSR}{SST} = \frac{SST - SSE}{SST} \tag{4}$$

SSR represents the regression sum of squares, SSE means the minimum of the sum of squared residuals and SST indicates the total sum of squares.

3 Results and Discussion

CGGs of various shapes like Straight, Square, Circular and Triangular were simulated for studying the average concentration gradient at Reynold number 50. The average concentration at each outlet is recorded for finding out the linearity of the values. Tone scale representation for different shaped CGGs was represented in Figs. 4, 5, 6 and 7.

The average concentration values for different shaped CGGs were tabulated below to identify the optimistic shape of the CGG which yields linear relation of the average concentration gradient (Fig. 8).

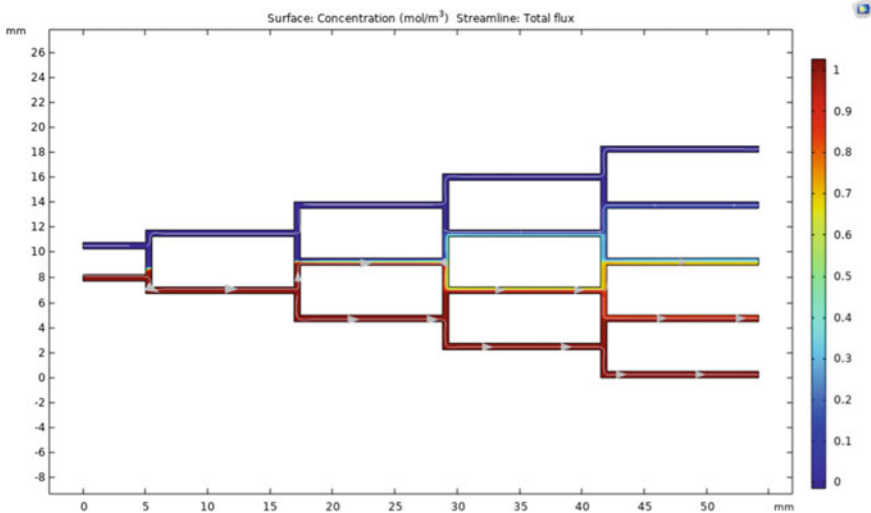


Fig. 4 Tone scale output for the concentration gradients of straight CGG for Re 50

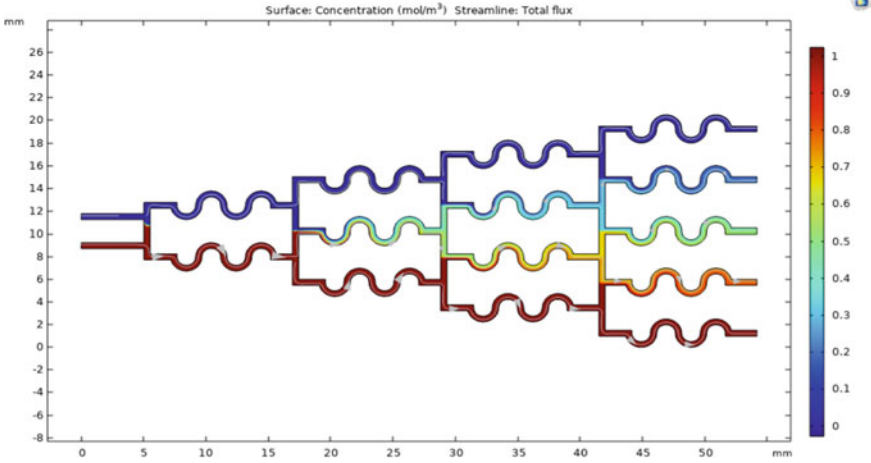


Fig. 5 Tone scale output for the concentration gradients of circular CGG for Re 50

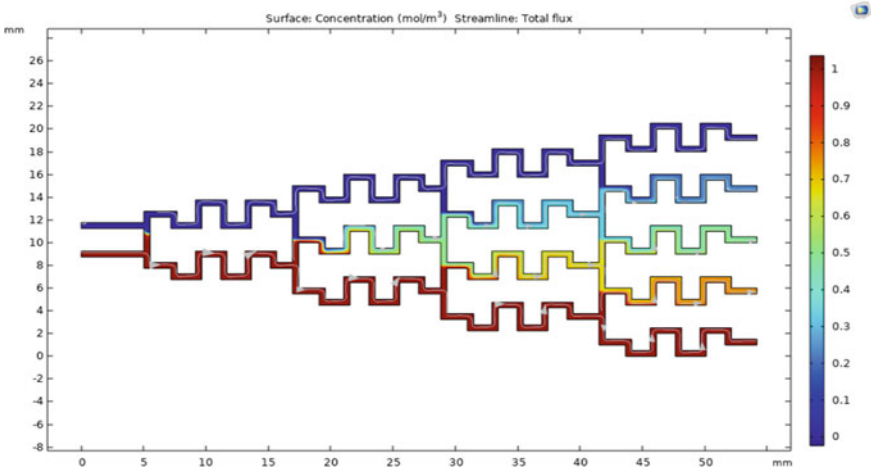


Fig. 6 Tone scale output for the concentration gradients of square CGG for Re 50

It is expected that the percentage average concentration values should vary from 0, 25, 50, 75 and to 100 for outlets 1, 2, 3, 4 and 5 respectively. The average concentration values for Square shaped CGGs show almost good linearity followed by Triangular and Circular CGGs as compared to other remaining shaped CGGs. It is almost closer to the expected value range of the concentration gradients.

The R^2 value of the average concentrations for all the designed CGGs was calculated and the same was tabulated in Table 3.

R^2 value is also better for Square shaped CGGs followed by triangular and Circular shaped CGGs. For getting the effect of Reynold's number on CGG, the Square

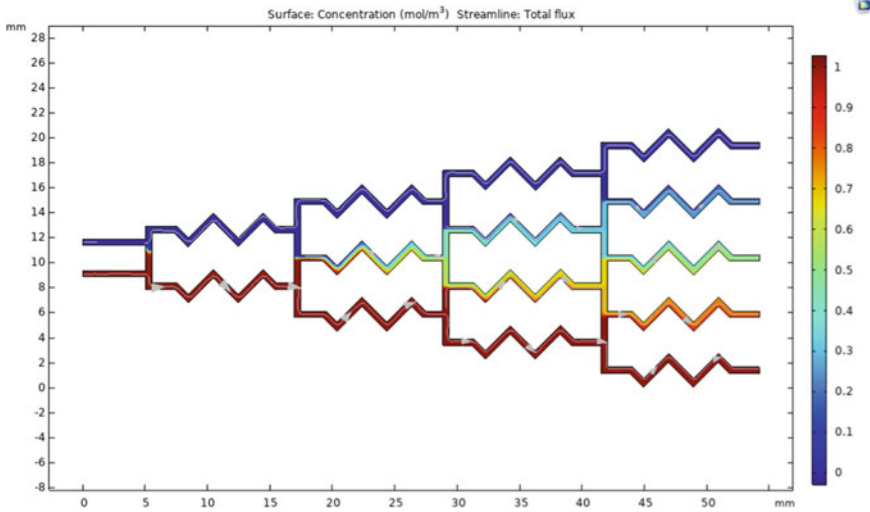


Fig. 7 Tone scale output for the concentration gradients of triangular CGG for Re 50

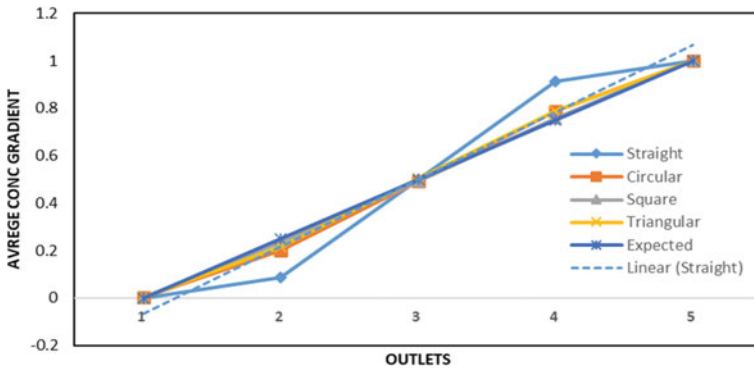


Fig. 8 Graph of average concentration gradients versus outlet position for different CGGs at Re 50

Table 3 R² values for different shapes CGG at Reynold's numbers of 50

CGG type	R ² value
Straight	0.9488
Circular	0.9954
Square	0.9996
Triangular	0.9966

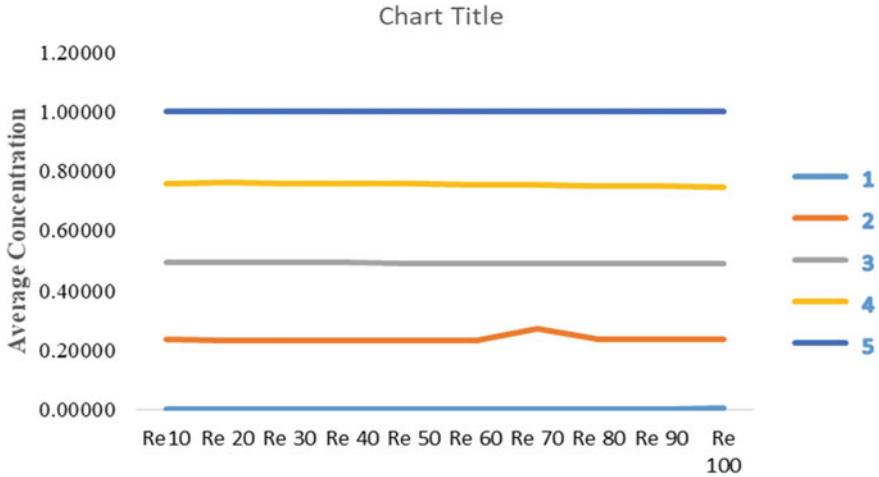


Fig. 9 Graph of average concentration gradients versus Reynold number for different outlets for square CGG

shaped CGG which has shown better linearity for concentration gradient was tested for different values of Reynold’s number varying from 10 to 100 (Fig. 9).

From the above-simulated result, it is clear that no significant effect in a variation of Reynold’s number on the concentration gradients. The average concentration gradient at corresponding outlets almost remains the same irrespective of Reynold Number.

4 Conclusion

The CGGs of different shapes viz. Straight, Circular, Square and Triangular have been designed and simulated to generate five different outlets of varying concentration gradients with two inlet fluids. All CGGs were simulated for Reynold’s Number of 50. For the designed CGGs sufficient time was found for mixing and diluting the two fluids owing to laminar flow with a low range of Reynold’s Number. The average concentration values for Square shaped CGGs followed by Triangular and Circular CGGs show almost good linearity as compared to other remaining shaped CGGs at Reynold Number of 50. Therefore, to obtain linear dilution, the resulting simulation suggests for Square shaped CGG applying at Reynold Number of 50. Square-shaped CGG also possesses a better R^2 value.

However, simulations were carried out with 2D models without involving the significant depth of the channels with low Reynolds numbers, representing a case of passive macromixing without applying external forces. For studying the effect of Reynold’s number on the design of CGG, Square shaped CGG was tested for

different values of Reynold's number varying from 10 to 100. Simulation results indicated that Reynold's number has not a significant effect on the concentration gradients.

References

1. Sundra, S., Soon, C. F., Zainal, N., & Tee, K. S. (2016). The effects of flow rates to the concentration gradients in a passive micromixer. IEEE Engineering in Medicine and Biology Society. Malaysia Chapter, IEEE Engineering in Medicine and Biology Society, and Institute of Electrical and Electronics Engineers. In *IECBES, IEEE-EMBS Conference on Biomedical Engineering and Science*.
2. Fink, G., Mitterramskogler, T., Hintermuller, M. A., Jakoby, B., & Wille, R. (2022). Automatic design of microfluidic gradient generators. *IEEE Access*, 10, 28155–28164. <https://doi.org/10.1109/ACCESS.2022.3158327>
3. Yahyazadeh Shourabi, A., Kashaninejad, N., & Saidi, M. S. (2021). An integrated microfluidic concentration gradient generator for mechanical stimulation and drug delivery. *Journal of Science: Advanced Materials and Devices*, 6(2), 280–290. <https://doi.org/10.1016/j.jsamd.2021.02.009>
4. Ruppen, J., et al. (2015). Towards personalized medicine: Chemosensitivity assays of patient lung cancer cell spheroids in a perfused microfluidic platform. *Lab on a Chip*, 15(14), 3076–3085. <https://doi.org/10.1039/c5lc00454c>
5. Ye, N., Qin, J., Shi, W., Liu, X., & Lin, B. (2007). “Cell-based high content screening using an integrated microfluidic device. *Lab on a Chip*, 7(12), 1696–1704. <https://doi.org/10.1039/b711513j>
6. Ebadi, M., Moshksayan, K., Kashaninejad, N., Saidi, M. S., & Nguyen, N. T. (2020). A tool for designing tree-like concentration gradient generators for lab-on-a-chip applications. *Chemical Engineering Science*, 212. <https://doi.org/10.1016/j.ces.2019.115339>
7. Toh, A. G. G., Wang, Z. P., Yang, C., & Nguyen, N. T. (2014). Engineering microfluidic concentration gradient generators for biological applications. *Microfluidics and Nanofluidics*, 16(1–2), 1–18. <https://doi.org/10.1007/s10404-013-1236-3>
8. Glawdel, T., Elbuken, C., Lee, L. E. J., & Ren, C. L. (2009). Microfluidic system with integrated electroosmotic pumps, concentration gradient generator and fish cell line (RTgill-W1)-towards water toxicity testing. *Lab on a Chip*, 9(22), 3243–3250. <https://doi.org/10.1039/b911412m>
9. Jain, M., Yeung, A., & Nandakumar, K. (2010). Induced charge electro-osmotic concentration gradient generator. *Biomicrofluidics*, 4(1). <https://doi.org/10.1063/1.3368991>
10. Gidde, R. R., Pawar, P. M., Gavali, S. R., & Salunkhe, S. Y. (2019). Flow feature analysis of an eye-shaped split and collision (ES-SAC) element-based micromixer for lab-on-a-chip application. *Microsystem Technologies*, 25(8), 2963–2973. <https://doi.org/10.1007/s00542-018-4271-x>
11. Keenan, T. M., & Folch, A. (2007). Biomolecular gradients in cell culture systems. *Lab on a Chip*, 8(1), 34–57. <https://doi.org/10.1039/b711887b>
12. Shames, I. H. (2003). *Mechanics of fluids*. McGraw-Hill.
13. Alciatore, D. D., & Anderson, J. D. *Computational fluid dynamics: The basics with applications*. McGraw-Hill Series in Mechanical Engineering.
14. Wu, Z., Li, Y., Xu, L., Bao, D., Zhang, X., & Zhang, T. (2022). Numerical study of the passive micromixer with the novel blocks. *AIP Advances*, 12(4). <https://doi.org/10.1063/5.0078400>
15. Figueredo Filho, D. B., Silva Júnior, J. A., & Rocha, E. C. (2011). What is R2 all about? *Leviathan (São Paulo)*, 3, 60. <https://doi.org/10.11606/issn.2237-4485.lev.2011.132282>

Computational Analysis of Fluid Flow in Split and Recombine Micro-channel with Circular Obstacles



Sanjay A. Pawar and Vimal Kumar Chouksey

Abstract The microchannel plays a vital role in the microfluidics and have vast application in different areas like Lab-on-a-chip, Micro reactors, micro electro mechanical system (MEMS) biological applications, etc. The mixing in microchannel governs the performance. The computational study of split and recombined micro channels with obstacles is presented in this paper. The computational study of arrow type microchannel is performed by using COMSOL Multiphysics software at different Reynolds number (Re). The sway of the Reynolds number, form, and size of the barriers is reported along with the suggestions regarding the future scope.

Keywords Microfluidics · Microchannel · Micro mixtures · Split and recombine micro channels

1 Introduction

Microfluidics is a word that refers to fluid control and actuation methods and components used for tiny size fluid transport phenomena. The fast-growing technology is microfluidic systems, and lab-on-a-chip (LOC) implementation benefits from microfluidics research. The LOC systems, also known as “micro total analysis systems” (TAS), are capable of carrying out the whole range of chemical and biological activities [1, 2]. They make it easier to miniaturize and combine many operations, which can automate arduous laboratory activities. The developing trends in point of care diagnostics are improved by LOC devices’ mobility, parallelization, and compactness properties. The field of microfluidics focuses on the design and creation of tiny apparatuses that can detect, mix, pump, monitor, and regulate extremely small

S. A. Pawar (✉)
Sardar Patel University, Balaghat, M.P, India
e-mail: sanjaypawardo@gmail.com

V. K. Chouksey
Mechanical Engineering Department, Sardar Patel University, Balaghat, M.P, India

amounts of fluid. Numerous sectors, including those in the cosmetic, pharmaceutical, biotech, and medical fields, as well as the physical sciences for control systems and heat management, employ microfluidics [3].

The study of fluid flow in geometries with micrometer-scale channel dimensions is known as microfluidics. A micro channel is a channel with width and height measurements that are on the order of micrometers. The fast development of microfluidic and MEMS devices has resulted in a substantial requirement for understanding liquid flows in micro channels or microchannel structures [1–3]. The technology of micro mixing has advanced quickly in recent years.

Pressure Drop

The Darcy-Weisbach equation [4] may be used to calculate the pressure drop in a straight, rectangular channel, which is mostly caused by friction. Its expression is pressure drop per square centimeter.

$$\Delta P = \left[\frac{f \times Re}{2} \right] \times \left[\frac{\mu \times u \times L}{(D_h)^2} \right] \quad (1)$$

where, ΔP is the pressure difference within the channel in Pa and L is channel length in mm.

Micro Mixture Performance Criteria

The mixing index is a statistical indicator that shows the uniform level of species intensity in a given fluid. The following equation is used to compute the mixing index of the species at any cross section in the micro channel [5]:

$$M = 1 - \sqrt{\frac{1}{N} \sum_{i=1}^N \left(\frac{C_i - \bar{C}}{\bar{C}} \right)^2} \quad (5)$$

where, M is the mixing index,

N is total number of grid points,

C_i is the normalized concentration at any cross section and,

\bar{C} is the average normalized concentration of the domain.

Mixing index ranges from 0 to 1 ($M = 0$ for no mixing and $M = 1$ for 100% mixing).

1.1 Computational Model Development of the Microchannel

Design Considerations for Split and Recombine Microchannel

A micro channel's mixing ability is frequently determined by its mixing duration and pressure drop. The diffusion coefficient, aspect ratio, breadth, height, and inlet

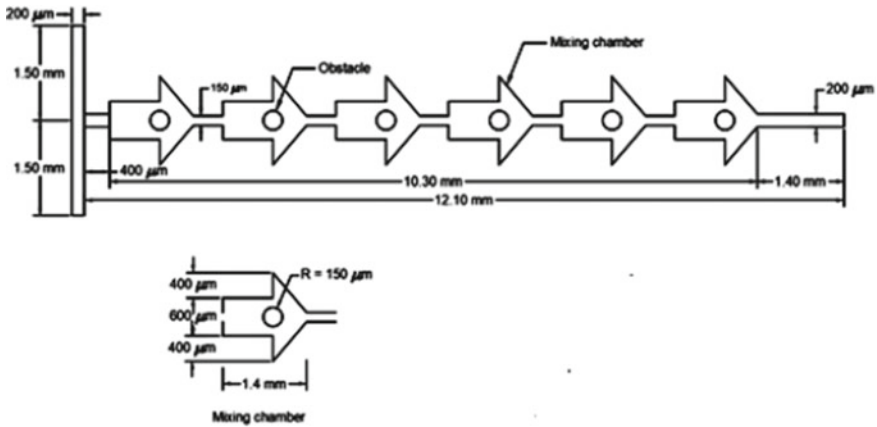


Fig. 1 Arrow SAR geometry with mixing chamber and circular ...

velocities of the fluids are all factors that affect the mixing length in the channel. The many methods used to improve the mixing performance for Micromixers include channels with obstacles, channels with different geometric forms, and split-and-recombine type channels [6–8].

Arrow Type SAR Micromixer Geometry

Figure 1 shows the innovative shape for the arrow-type SAR Micromixer. The geometry comprises of mixing chambers with barriers in the shape of arrows. The waterway is 200 μm wide at the entry, through the T-shaped intersection, and at the terminus. Figure 1 also shows a detailed view of the mixing chamber [9].

1.2 Computational Analysis of Arrow Type SAR Micromixer

Assumptions

In the Comsol Multiphysics 5.0 programme, the following hypotheses are taken into account for the computational study of the serpentine micro channels.

- Fluids are Newtonian.
- Fully developed fluid flow.
- Inlet cross sections are constant and inlet velocity is consistent.
- For the sake of simplicity in model ling, the effects of the fluid passing through the syringe, tubing elements, and the micro-fluidic chip’s intake port are neglected.
- The Comsol database is used to extract the characteristics of the fluids under consideration.
- Internal walls of micro channels are assumed to have negligible surface roughness.

- Because the micro channels are arranged horizontally, the effect of gravity is ignored.
- The micro-channel has constant and laminar flow [10–12].

2 Result and Discussion

2.1 *Mixing Performance Analysis for Arrow Type Split and Recombine Type Micromixer with Circular Shaped Obstacle*

2.1.1 Effect of Re on the Pressure Drop

COMSOL Multiphysics 5.0 software was used to conduct the mixing performance analysis research for arrow type split and Recombine type Micromixers with circular shaped obstacles. In the computational analysis, the Reynolds number (Re) is modified as 0.1, 1, 5, 10, 15, 30, 45, and 60 to investigate its impact on mixing performance.

Eight distinct considered Re locations capture the pressure decrease. Re is changed as 0.1, 1, 5, 10, 15, 30, 45, and 60 in order to examine the impact of the Reynolds number (Re) on pressure decrease. Figures 2 and 3, respectively, provide representative pictures for pressure drop contours [13–15].

With a rise in Re, the pressure drop rises. The obstructions in the direction of the flow cause constraints, which raises the pressure drop. The arrow type SAR with

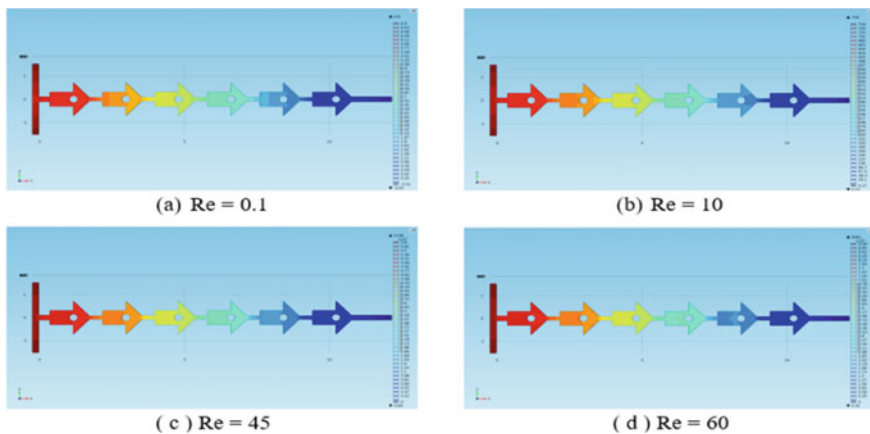


Fig. 2 Pressure drop contours for circular obstacle-based Micromixer having obstacles of size 150 μm

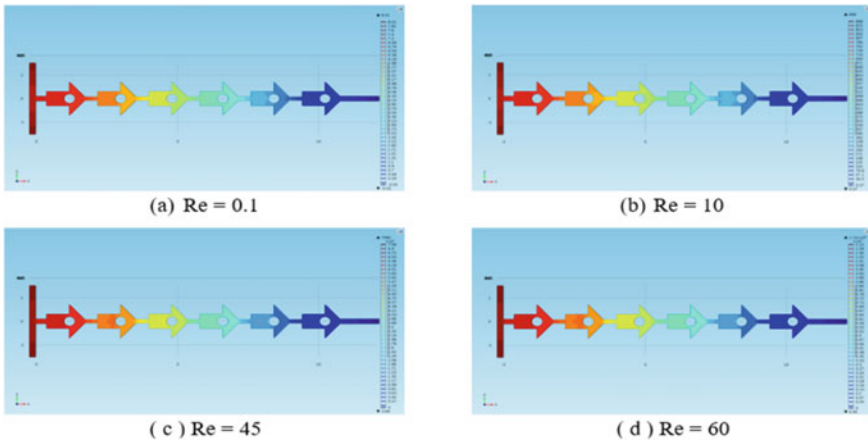


Fig. 3 Pressure drop contours for circular obstacle-based Micromixer having obstacles of size 200 μm

200 μm diameter circular obstacles has the most pressure decrease. This results in a greater pressure decrease as the size of the obstruction increases (Fig. 4).

Re is varied as 0.1, 1, 5, 10, 15, 30, 45, and 60 in the computational study to examine its impact on the mixing index. By noting the concentration at any specific site, the mixing index has been derived. Figure 5 and 6 shows the concentration profiles for arrow type SAR with 150 μm and 200 μm circular barriers for eight distinct Re, respectively. With an increase in Re from 10 to 60 (refer Fig. 7), it is seen that the mixing index is rising. Because the mixing is only caused by diffusion at this lower Reynolds number, this pattern is seen for both the arrow type SAR with circular barriers of diameters 150 and 200 μm . The fluid is given less time for diffusion in the Re range of 0.1–10, and there is also little noticeable advection and expansion of secondary flows [16, 17].

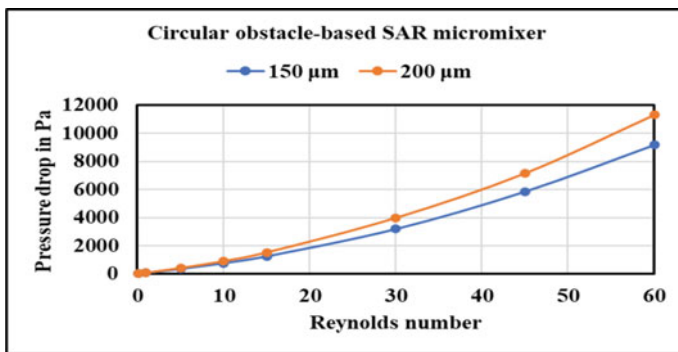


Fig. 4 Pressure drop as a function of Reynolds number for circular obstacle-based SAR micromixer

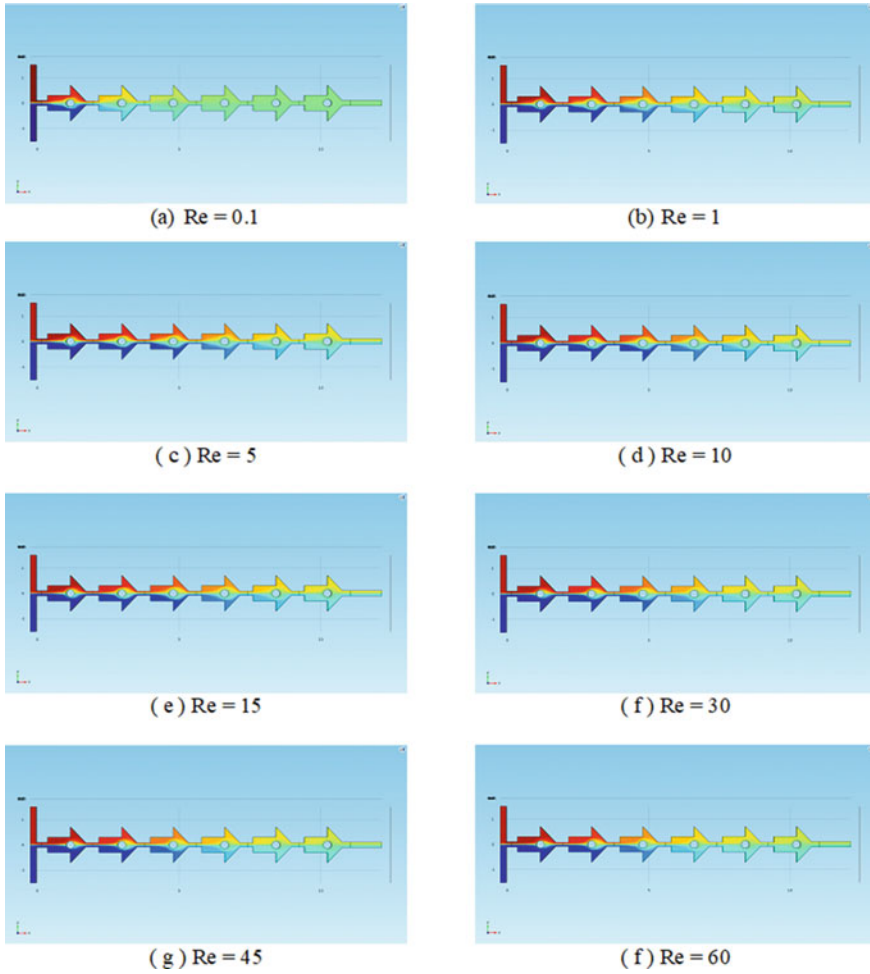


Fig. 5 Concentration profiles for circular-obstacle based arrow type SAR micromixer having obstacles of size $150 \mu\text{m}$

2.1.2 Effect of Re on the Mixing Index

See Figs. 5, 6 and 7.

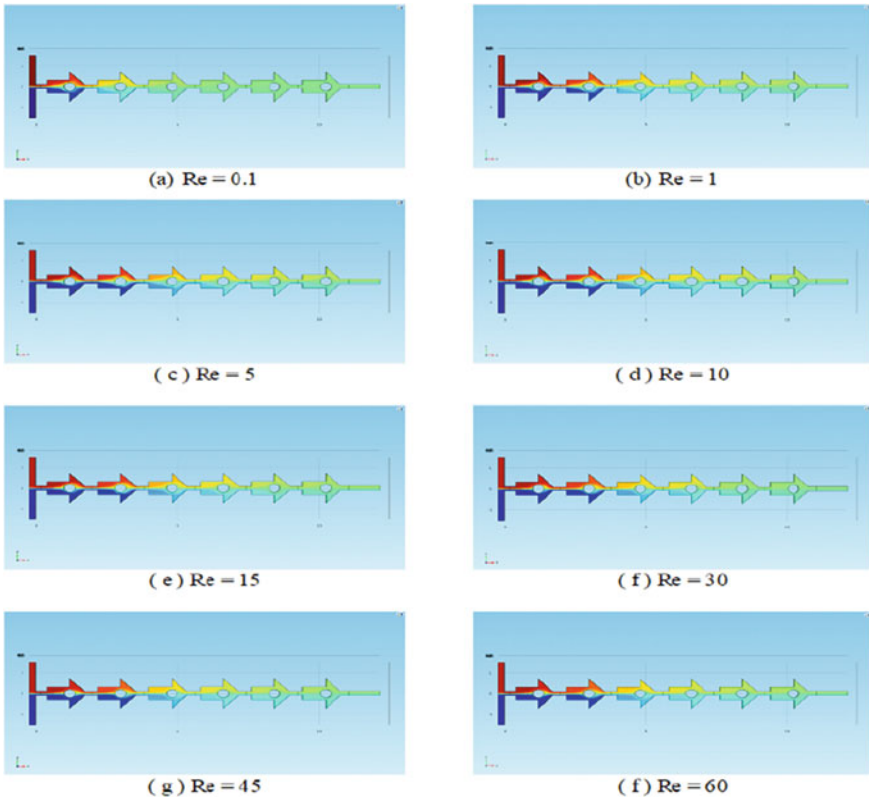
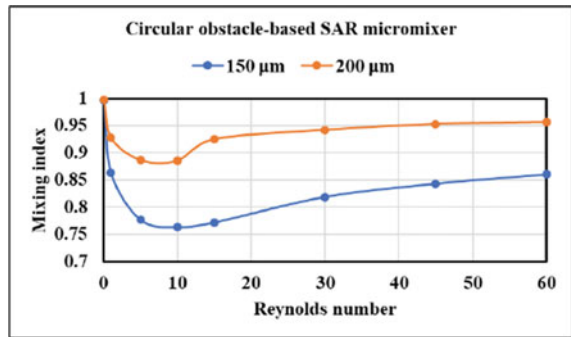


Fig. 6 Concentration profiles for circular-obstacle based arrow type SAR micromixer having obstacles of size 200 μm

Fig. 7 Mixing index as a function of Reynolds number for circular obstacle-based SAR micromixer



3 Conclusion

It has been thoroughly investigated how to create and analyze Micromixers with circular barriers. The mixing of arrow-type split-and-recombine-type Micromixers with circular-shaped obstacles has been computationally analyzed at eight different Reynolds numbers (Re), ranging from 0.1 to 60 [18, 19].

- For all the contemplated Micromixer designs, the pressure loss rises as Re grows.
- In comparison to other Micromixer designs, the pressure loss is seen to be reduced for arrow type split and recombine type Micromixers with circular shaped barrier of dimension 150 μm . In comparison with 200 μm -diameter circular obstacles.
- The arrow type split and recombines type Micromixers with circular shaped obstacles having size 200 μm gain a higher mixing index, as compared to that for 150 μm .
- The mixing index displays a lowering trend from Re 0.1 up to Re 10 and then follows a steady increasing trend from Re 10 up to Re 60 for the Micromixer setups taken into consideration.
- Better mixing (higher mixing index) is seen for Micromixers with obstacles as the size of the impediments increases.

References

1. Lee, C. Y., Wang, W. T., Liu, C. C., & Fu, L. M. (2016). Passive mixers in microfluidic systems: A review. *Chemical Engineering Journal*, 288, 146–160.
2. Lim, Y. C., Kouzani, A. Z., & Duan, W. (2010). Lab-on-a-chip: A component view. *Microsystem Technologies*, 16, 1995–2015.
3. Capretto, L., Cheng, W., Hill, M., & Zhang, X. (2011). Micromixing within microfluidic devices. *Microfluidics: Technologies and applications* (pp. 27–68).
4. Xia, G., Li, J., Tian, X., & Zhou, M. (2012). Analysis of flow and mixing characteristics of planar asymmetric split-and-recombine (P-SAR) micromixers with fan-shaped cavities. *Industrial & Engineering Chemistry Research*, 51(22), 7816–7827.
5. Song, H., Wang, Y., & Pant, K. (2012). Cross-stream diffusion under pressure-driven flow in microchannels with arbitrary aspect ratios: A phase diagram study using a three-dimensional analytical model. *Microfluidics and Nanofluidics*, 12, 265–277.
6. Bahrami, M., Yovanovich, M. M., & Culham, J. R. (2006). Pressure drop of fully developed, laminar flow in rough microtubes.
7. Ansari, M. A., Kim, K. Y., & Kim, S. M. (2010). Numerical study of the effect on mixing of the position of fluid stream interfaces in a rectangular microchannel. *Microsystem Technologies*, 16, 1757–1763.
8. Gobby, D., Angeli, P., & Gavriilidis, A. (2001). Mixing characteristics of T-type microfluidic mixers. *Journal of Micromechanics and Microengineering*, 11(2), 126.
9. Bothe, D., Stemich, C., & Warnecke, H. J. (2006). Fluid mixing in a T-shaped micro-mixer. *Chemical Engineering Science*, 61(9), 2950–2958.
10. Virk, M. S., & Holdø, A. E. (2016). Numerical analysis of fluid mixing in T-Type micro mixer. *The International Journal of Multiphysics*, 2(1).
11. Cortes-Quiroz, C. A., Azarbadegan, A., & Zangeneh, M. (2014). Evaluation of flow characteristics that give higher mixing performance in the 3-D T-mixer versus the typical T-mixer. *Sensors and Actuators B: Chemical*, 202, 1209–1219.

10. Lü, Y., Zhu, S., Wang, K., & Luo, G. (2016). Simulation of the mixing process in a straight tube with sudden changed cross-section. *Chinese Journal of Chemical Engineering*, 24(6), 711–718.
11. Naher, S., Orpen, D., Brabazon, D., Poulsen, C. R., & Morshed, M. M. (2011). Effect of micro-channel geometry on fluid flow and mixing. *Simulation Modelling Practice and Theory*, 19(4), 1088–1095.
12. Ansari, M. A. (2009). Parametric study on mixing of two fluids in a three-dimensional serpentine microchannel. *Chemical Engineering Journal*, 146(3), 439–448.
13. Liu, J., Li, S., & Mitra, D. (2015). Multiphysical phenomenon of air bubble growth in polydimethylsiloxane channel corners under microfluidic negative pressure-driven flow. *International Journal of Heat and Mass Transfer*, 91, 611–618.
14. Liu, R. H., Stremmer, M. A., Sharp, K. V., Olsen, M. G., Santiago, J. G., Adrian, R. J., & Beebe, D. J. (2000). Passive mixing in a three-dimensional serpentine microchannel. *Journal of Microelectromechanical Systems*, 9(2), 190–197.
15. Kuo, J. N., & Jiang, L. R. (2014). Design optimization of micromixer with square-wave microchannel on compact disk microfluidic platform. *Microsystem Technologies*, 20, 91–99.
16. Kuo, J. N., & Chen, X. F. (2016). Decanting and mixing of supernatant human blood plasma on centrifugal microfluidic platform. *Microsystem Technologies*, 22, 861–869.
17. Kuo, J. N., & Li, Y. S. (2017). Centrifuge-based micromixer with three-dimensional square-wave microchannel for blood plasma mixing. *Microsystem Technologies*, 23(7), 2343–2354.
18. Li, J., Xia, G., & Li, Y. (2013). Numerical and experimental analyses of planar asymmetric split-and-recombine micromixer with dislocation sub-channels. *Journal of Chemical Technology & Biotechnology*, 88(9), 1757–1765.
19. Tran-Minh, N., Dong, T., & Karlsen, F. (2014). An efficient passive planar micromixer with ellipse-like micropillars for continuous mixing of human blood. *Computer Methods and Programs in Biomedicine*, 117(1), 20–29.

Comparison of Experimental and Analytical Results of Impact of Various Geometrical Configurations on Pressure Drop Through Micro-channel



Sachin M. Kale, Digambar T. Kashid, Avinash K. Parkhe, Sandip S. Wangikar, Chetan C. Jadhav, and Sunil S. Gaikwad

Abstract Shape and size of micro-channel have remarkable effect on the heat transfer and the pressure drop performance. This paper mainly focuses on the effect of various geometrical configurations of micro-channel heat sink performance. The performance parameters considered for the study are Reynolds number, friction factor, uniformity of flow and pressure drop. In this study, the surface area of all micro channels is kept constant, so that the any performance variation can be attributed solely to the variation in geometry of the micro channel. Different geometrical configurations of micro channel considered in this study. Experimental analysis is carried out for different flow rates of coolant through the micro channels. In this work, the copper micro channel having hydraulic diameter as a $1340\ \mu\text{m}$ is used in experimental analysis. The experimental results obtained in this study are found to be in good agreement with the theoretical results from literature. This work is proposed to help in selecting suitable geometry for micro channels having the less pressure drop per unit length along with less pumping power and reduced weight and size of the device.

Keywords Micro-channel · Hydraulic diameter · Pressure drop · Reynolds number · Friction factor

1 Introduction

Shrinking size is the buzzword of the modern electronics industry. However, as component sizes shrink, various new issues such as heat dissipation become important and these devices can fail due to overheating. Therefore, it is very important to

S. M. Kale (✉) · D. T. Kashid · A. K. Parkhe · S. S. Wangikar · C. C. Jadhav · S. S. Gaikwad
Mechanical Engineering Department, SVERI's College of Engineering, Pandharpur, Maharashtra, India
e-mail: smkale@coe.sveri.ac.in

dissipate the heat generated by such small devices more quickly or in a very short time. The most promising solution to this problem is the incorporation of micro or mini-channels into the heat sink. The main purpose of introducing micro-channels or mini channels is to increase the surface area exposed to heat transfer. Microchannels are provided to increase surface area, which increases heat transfer from small electronic components.

In the field of micro-heat sinks, the majority of researchers are focusing on the improvement of its thermal performance. But along with thermal performance of micro-heat sink there are various other factors which are also affecting on its performance. Out of those the major one is the pressure drop, which interns affects the power required by the pump, flow uniformity through micro-channels and the weight and size of the device. The flow distribution between individual microchannels plays an important role in the performance of micro-channel reactors and heat exchangers. In micro-channel heat sinks used to cool electronic chips, uneven flow distribution can cause uneven heat transfer conditions, creating undesirable lateral temperature gradients that lead to poor performance. Hence it could be said that thermal efficiency is a natural requirement but pressure drop is a strong design constrain to be dealt with.

The concept of micro-channel heat sink cooling was first introduced by Tuckerman and Pease in the early 1980s [1]. Due to their inherent properties, micro-channel heat sinks have received considerable attention since the pioneering work of Tuckerman and Pease. A comprehensive review of the literature on heat sink optimization for heat transfer and pressure drop can be found in Khan et al. [2]. In this article, the author emphasizes the importance of considering these two effects in the practical engineering application of forecasting. A very detailed experimental study on pressure drop and heat transfer in micro-channels was published by Qu and Mudawar [3]. They identified an array of rectangular micro-channels 231 μm wide and 713 μm deep in the Reynolds number range considered 139–1672, two different heat flows: 100 and 200 W/cm^2 .

Till today, a large number of investigations have been conducted on the properties of flow in straight micro-channels. Wu and Little [4] used an experimental method to measure the friction coefficient of gases flowing through micro-channels with hydraulic diameters between 50 and 80 μm under both laminar and turbulent flow conditions. As a result, it was found that the coefficient of friction was higher than the conventional prediction. However, the trends obtained by Wu and Little [4] did not match those of Choi et al. [5]. They used nitrogen gas as the working medium in their study of flow through microtubes. The measured friction coefficients in both the laminar and turbulent regimes were found to be lower than those predicted by conventional correlations. Peng et al. [6] experimentally studied the flow properties of water flowing through rectangular micro-channels with hydraulic diameters of 133–367 μm and aspect ratios of 0.333–1. Their experimental results showed that they found that the frictional behavior of both laminar and turbulent flows deviated from those derived from conventional correlations. Geometric parameters such as hydraulic diameter and aspect ratio have been found to have important effects on fluid flow through rectangular micro-channels. Flockhart and Dhariwal [7] measured

the flow properties of distilled water in trapezoidal micro-channels with hydraulic diameters between 50 and 120 μm and Reynolds numbers < 600 .

Papautsky et al. [8] used numerical models based on micropolar fluid theory to predict the volume flow, pressure drop and Darcy friction coefficient of incompressible fluids at the microscale. Judy et al. [9] experimentally studied the flow properties of distilled water, methanol and isopropanol through circular and square microchannels made of fused silica and stainless steel. Kohl et al. [10] used an integrated pressure sensor to measure the pressure drop in micro-channels with hydraulic diameters of 25–100 μm . As reported by Kandlikar et al. [11] one of the major challenges in multi-channel configurations is achieving a uniform flow distribution among the channels, which affects the performance of micro heat exchangers report. Therefore, most researchers have focused on studying flow distributions in multi-channel configurations to obtain optimal designs for microdevices. For example, Tonomura et al. [12] performed a computational fluid dynamics (CFD) optimization study on a plate-and-fin micro device design consisting of five channels with a cross-sectional area of $0.1 \times 0.1 \text{ mm}$. A simulation was performed using water as the test liquid. Fluid entered and exited the micro device horizontally in a direction perpendicular to the channel (Z shape). Simulation results showed that, especially at very low flow rates ($\text{Re} = 10$), increasing the channel length resulted in a very uniform flow distribution across the channels. Balaji and Lakshminarayanan [13] modeled a two-dimensional microchannel plate to study the effect of the number and position of inlet and outlet ports on the flow distribution along the channels of a micro heat exchanger. Pan et al. [14] numerically examined the effects of geometric parameters such as length, width, manifold area and inlet/outlet port locations on the flow uniformity of a micro-channel plate consisting of 10 channels. The inlet/outlet manifold shape was rectangular. The channel length and width were varied from 10 to 50 mm and 0.1 to 0.7 mm, respectively. We found that the narrower the width and the longer the micro-channel, the better the flow uniformity.

Pfund et al. [15] determined the friction coefficient of water flowing through high-aspect-ratio channels with depths of 128–521 μm . They reported that the transition from laminar to turbulent flow occurred at Reynolds numbers lower than the critical Reynolds number of the macrochannel, and that the transition Reynolds number decreased with decreasing channel depth. The laminar flow coefficient of friction was significantly higher than that of classical values. Hegab et al. [16] found that the transition from laminar to turbulent flow occurs at Reynolds numbers between 2000 and 4000, and that the friction coefficient and Nusselt number results are macroscale correlations for rectangular channels in the range of hydraulic diameters reported lower values than suggested by 112–210 μm were predicted. Shea et al. [17] experimentally studied the pressure drop characteristics of water flow in a rectangular channel with a hydraulic diameter of approximately 146 μm and Reynolds numbers ranging from 50 to 1000. $\Delta P/L$ is claimed to exhibit linear behavior with $\text{Re} 200$.

Many researchers in this area have done numerical analysis to study the pressure drop in different configurations as numerical analysis of any configuration is competitively easy with wide variety of simulation tools. But very few have concentrated on experimental analysis. Moreover, since many parameters affect the pressure

drop performance, any change in one parameter affects the overall performance and analysis becomes more complicated. Taking these facts into consideration, experimental analysis of micro channels with different geometrical configurations are carried out in this study, so that they can be used in different applications like micro-electronic, Molecular analysis, Bio-defence, Molecular biology, Clinical diagnostics, Drug development etc.

2 Design of Micro Channels

Micro channels having different geometries such as rectangular, square, triangular and circular are designed by keeping its surface area, depth and cross section area as constant parameter. Water is used as cooling fluid which carries heat generated in micro channel. The material selected for preparation of different geometries of micro channel is copper which consists of following properties/geometries.

Thermal properties of copper

Melting temperature	1084.62 °C
Thermal conductivity	401 W/m K
Electric resistivity	16.78 nΩ m (at 20 °C)

Geometrical dimensions of copper micro channel

Size of plate	50 mm × 70 mm
Channel width	2 mm
Channel height	Channel height

2.1 Manufactured Geometries

See Figs. 1, 2, 3 and 4.

Fig. 1 Image of rectangular micro channel



Fig. 2 Image of triangular micro channel



Fig. 3 Image of square micro channel

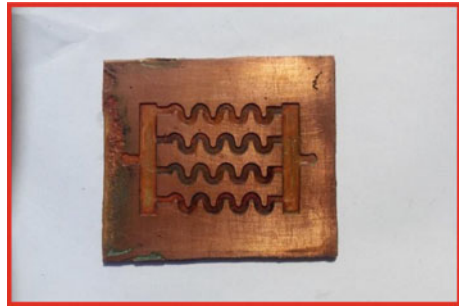


Fig. 4 Image of circular micro channel

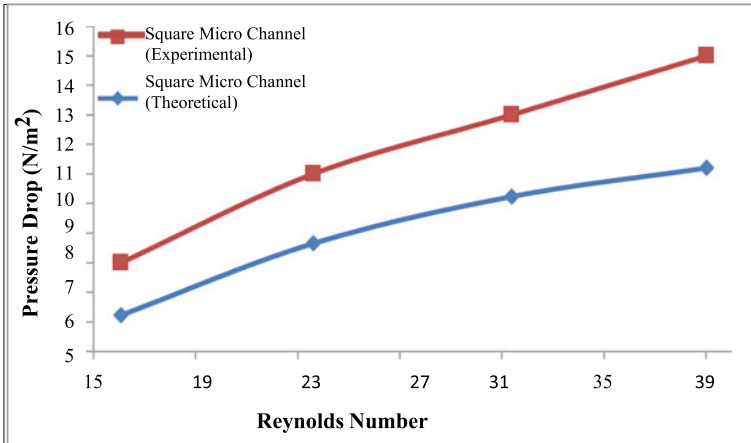


3 Result and Discussion

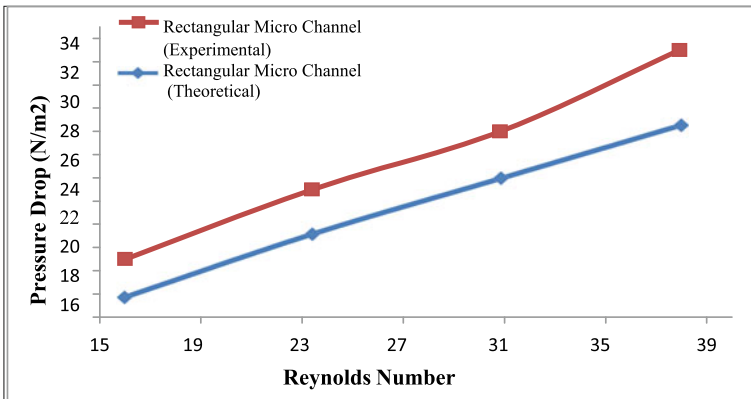
Graph 1 shows variation of experimental results from theoretical for square micro channel. It is observed that experimental results are quite higher than theoretical for square micro-channel. Experimental results are deviated in the range of 26–33% from theoretical.

From Graph 2 it is observed that for rectangular micro-channel experimental values for pressure drop are higher than that of theoretical in the range of 18–27%.

Graph 3 compares experimental results with theoretical for different Reynolds number in circular micro channel. It is observed that as Reynolds number goes on



Graph 1 Variation of experimental results from theoretical for square micro channel

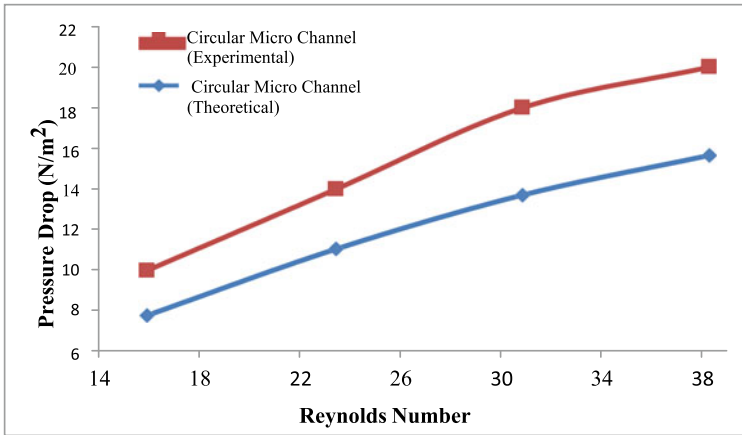


Graph 2 Variation of experimental results from theoretical for rectangular micro channel

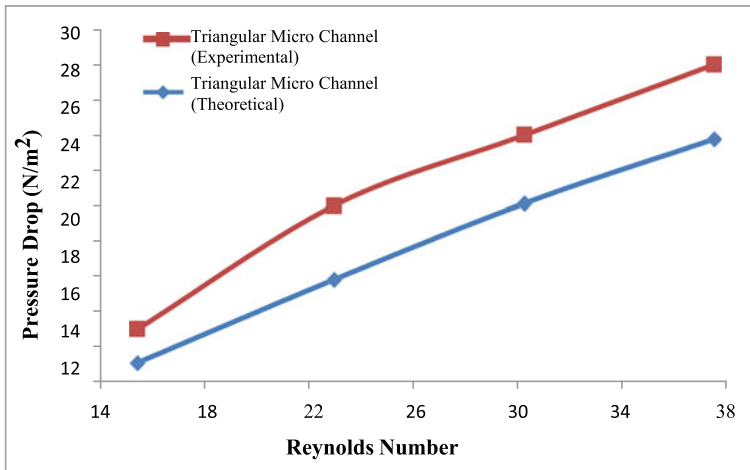
increasing pressure drop inside the microchannel also goes on increasing simultaneously. The percentage deviations of experimental results from theoretical are in the range of 26–31% for circular microchannel.

Variation of the experimental results from theoretical; for various Reynolds numbers for triangular micro-channels are shown in Graph 4. It is observed that as Reynolds number goes on increasing pressure drop inside the micro-channel also goes on increasing simultaneously. The percentage deviations of experimental results from theoretical are in the range of 17–26% for triangular micro-channel.

Graphs 5 and 6 are the graph of comparison of variation Experimental as well as Theoretical pressure drop w. r. t. change in Reynolds number for different Geometrical configurations. In both the graph increase in Reynolds number increases pressure



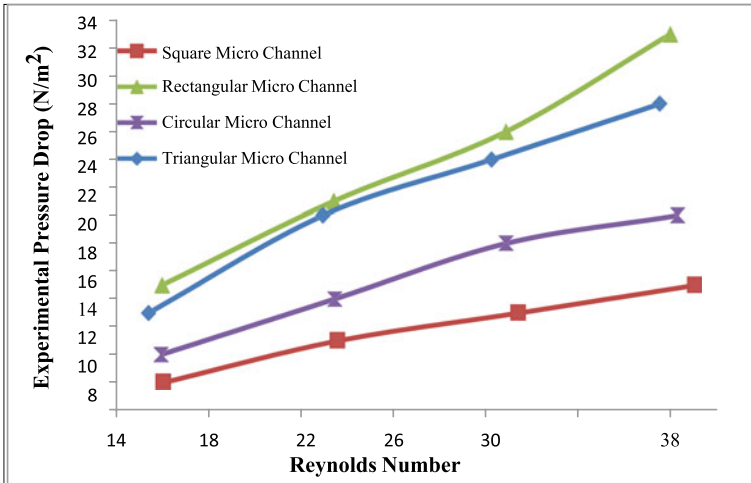
Graph 3 Variation of experimental results from theoretical for circular micro channel



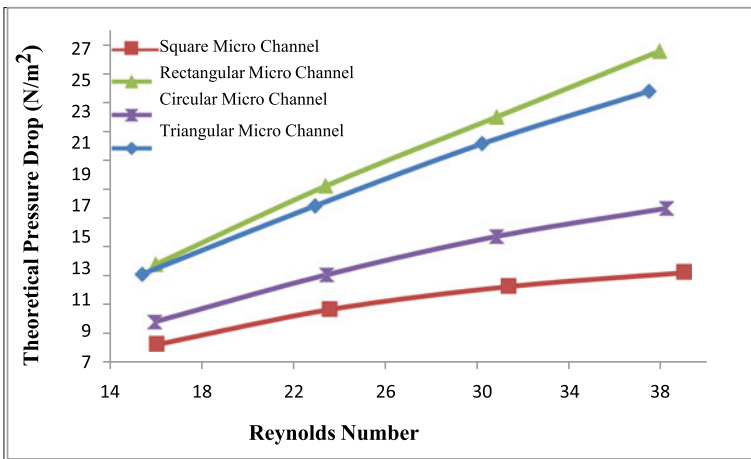
Graph 4 Variation of experimental results from theoretical for triangular micro channel

drop in the micro-channel. Experimentally as well as Theoretically Square Micro-channel is having lower pressure drop as compare to rest of three geometries. While Rectangular Micro-channel is having higher pressure drop as compare to rest of three geometries. Hence for more uniformity of flow and to reduce pumping cost as well as weight & size one should go for Square Micro-channel rather than rest of three configurations.

As variation of values for friction factor is in the range of 0.4–1.2 for various range of Reynolds number. Graph 7 Dissipate Variation of friction factor w. r. t. Reynolds number for different geometrical configurations of Micro channel. It is observed



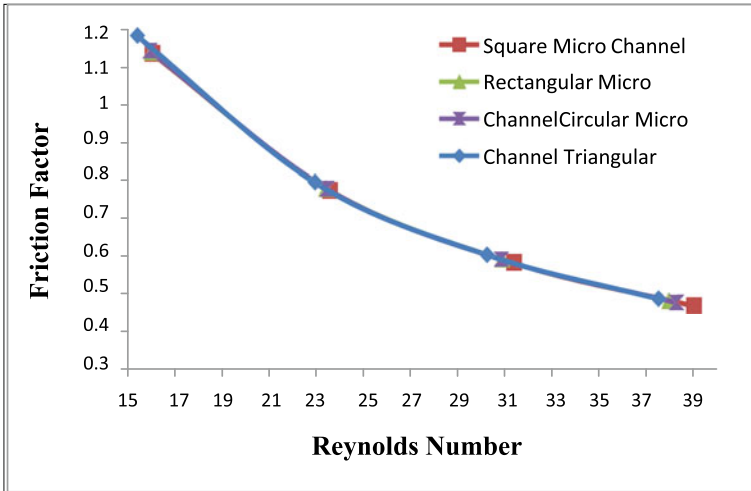
Graph 5 Variation of experimental pressure drop w. r. t. Reynolds number



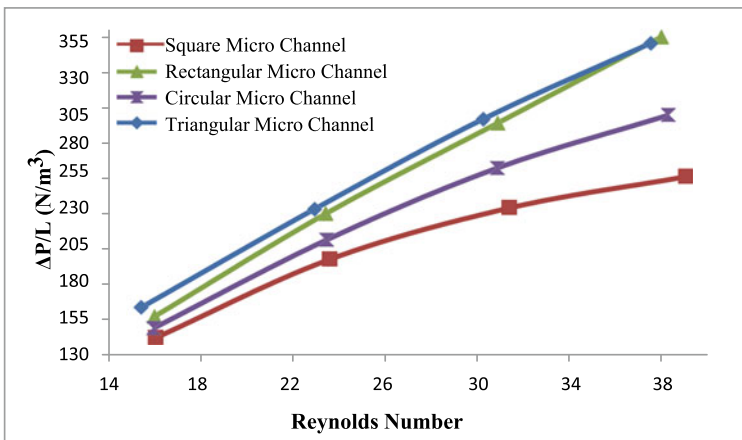
Graph 6 Variation of theoretical pressure drop w. r. t. Reynolds number

that friction factor goes on decreasing with increasing Reynolds number for all the geometrical configurations.

Variation of Pressure Drop per unit Length w. r. t. Reynolds Number is shown in Graph 8. From that it is clear that as Reynolds number goes on increasing pressure drop per unit length for different geometrical configuration also goes on increasing. For Square Micro-channel Pressure Drop per unit Length is less as compare to rest of three geometries.



Graph 7 Variation of friction factor w. r. t. Reynolds number



Graph 8 Variation of pressure drop per unit length w. r. t. Reynolds number

4 Conclusion

With the research and development of the miniaturized technologies, mini and micro-channel cooling systems have been widely used in the electronic devices. The channel studied in this work is of the range of 1340 μm hydraulic diameters which are suitable for different micro cooling applications. For single phase channels, in the fully developed, incompressible laminar flow regime the behaviour of fluid in micro-channel with hydraulic diameter several hundred micrometers obey classical theory.

Experimental as well as Theoretical results for pressure drop in Square Micro-channel is having lower value as compare to rest of three geometries. While Rectangular Micro-channel is having higher pressure drop as compare to rest of three geometries and Triangular Micro-channel is having highest pressure drop per unit length compare to rest of three geometries. Hence for more uniformity of flow as well as to reduce pumping cost one should go for Square Micro-channel rather than rest of three configurations.

References

1. Tuckerman, D., & Pease, R. (1981). High-performance heat sinking for VLSI. *IEEE Electron Device Letters*, 5, 126–129.
2. Khan, W. A., Culham, J. R., & Yovanivich, M. M. (2009). Optimization of microchannel heat sinks using entropy generation minimization method. *IEEE Transactions on Components and Packaging Technologies*, 32, 243–251.
3. Qu, W., & Mudawar, I. (2002). Experimental and numerical study of pressure drop and heat transfer in a single-phase micro-channel heat sink. *International Journal of Heat and Mass Transfer*, 45, 2549–2565.
4. Wu, P., & Little, W. A. (1983). Measurement of friction factors for the flow of gases in very fine channel heat exchangers used for micro miniature Joule-Thomson refrigerators. *Cryogenics*, 23, 273–277.
5. Choi, S. B., Barron, R. F., & Warrington, R. O. (1991). Fluid flow and heat transfer in microtubes. In *Micromechanical Sensors, Actuators, and Systems*. ASME DSC (Vol. 32, pp. 123–134).
6. Peng, X. F., Peterson, G. P., & Wang, B. X. (1994). Frictional flow characteristics of water flowing through rectangular micro-channels. *Experimental Heat Transfer*, 7, 249–264.
7. Flockhart, S. M., & Dhariwal, R. S. (1998). Experimental and numerical investigation into the flow characteristics of channels etched in h100i silicon. *Journal of Fluids Engineering*, 120, 291–295.
8. Papautsky, I., Brazzle, J., Ameel, T., & Frazier, A. B. (1999). Laminar fluid behavior in micro-channels using micropolar fluid theory. *Sensors and Actuators, A: Physical*, 73, 101–108.
9. Judy, J., Maynes, D., & Webb, B. W. (2002). Characterization of frictional pressure drop for liquid flows through micro-channels. *International Journal of Heat and Mass Transfer*, 45, 3477–3489.
10. Kohl, M. J., Abdel-Khalik, S. I., Jeter, S. M., & Sadowski, D. L. (2005). An experimental investigation of microchannel flow with internal pressure measurements. *International Journal of Heat and Mass Transfer*, 48, 1518–1533.
11. Kandlikar, S., Lu, Z., Domigan, W., White, A., & Benedict, M. (2009). Measurement of flow maldistribution in parallel channels and its application to ex-situ and in-situ experiment's in PEMFC water management studies. *International Journal of Heat and Mass Transfer*, 52, 1741–1752.
12. Tonomura, O., Tanaka, S., Noda, M., Kano, M., Hasebe, S. & Hashimoto, I. (2004). CFD-based optimal design of manifold in plate-fin microdevices. *Chemical Engineering Journal*, 101, 397–402.
13. Balaji, S., & Lakshminarayanan, S. (2006). Improved design of microchannel plate geometry for uniform flow distribution. *Canadian Journal of Chemical Engineering*, 84, 715–721.
14. Pan, M., Shao, X., & Liang, L. (2013). Analysis of velocity uniformity in a single microchannel plate with rectangular manifolds at different entrance velocities. *Chemical Engineering and Technology*, 36(6), 1067–1074.

15. Pfund, D., Rector, D., Shekarriz, A., Popescu, A., & Welty, J. (2000). Pressure drop measurements in a microchannel. *AIChE Journal*, *46*, 1496–1507.
16. Hegab, H. E., Bari, A., & Ameen, T. (2002). Friction and convection studies of R-134a in micro-channels within the transition and turbulent flow regimes. *Experimental Heat Transfer*, *15*, 124–259.
17. Hsieh, S. S., Tsai, H. H., Lin, C. Y., Huang, C. F., & Tsai, H. H. (2004). Liquid flow in a micro-channel. *Journal of Micromechanics and Microengineering*, *14*, 436–445.

Manganese Oxide Nanofibers for High Performance Supercapacitors



S. S. Gavande, A. C. Molane, A. S. Salunkhe, Y. M. Jadhav, T. M. Nimbalkar, R. N. Mulik, and V. B. Patil

Abstract Here we reported the facile electrospinning technique for the synthesis of MnO₂ nanofibers (NFs) electrodes envisaged in energy storage application. As-spun MnO₂ NFs are followed by annealing at 500 °C to remove polymer matrix. Rough and randomly oriented morphology of the fibers was confirmed through SEM analysis. Structural and wettability studies of synthesized electrodes were carried out using Raman Spectroscopy and Contact Angle Measurement respectively. While, electrochemical properties of MnO₂ NFs electrode were studied with the help of cyclic voltammetry as well as galvanostatic charge–discharge measurement, which revealed 336 F/g specific capacitance for 5 mV s⁻¹ scanning rate, 27.7 Wh/kg specific energy, 83.3 kW/kg specific power with a Coulombic efficiency of 98% in 1 M NaOH aqueous electrolyte solution.

Keywords Electrospinning · MnO₂ nanofibers · Pseudocapacitor · Hydrophilic · Electrochemical properties

Abbreviations

SC	Specific capacitance
NFs	Nanofibers
PVA	Polyvinyl alcohol
SEM	Scanning Electron Microscopy
SCE	Saturated Calomel Electrode

S. S. Gavande · A. C. Molane · A. S. Salunkhe · Y. M. Jadhav · T. M. Nimbalkar · V. B. Patil (✉)
Functional Materials Research Laboratory, School of Physical Sciences, Punyashlok Ahilyadevi
Holkar Solapur University, Solapur, Maharashtra, India
e-mail: drvbpatil@gmail.com

R. N. Mulik
Department of Physics, D. B. F. Dayanand College of Arts and Science, Solapur, Maharashtra,
India

1 Introduction

Flexible Supercapacitors, also known as ultracapacitors are playing a significant role as electrochemical energy storage devices with higher SC and greater power densities, also have attracted much interest in applications for various energy and power requirements [1]. The three categories of supercapacitor are electrical double layer capacitors (EDLCs), pseudocapacitors and hybrid type, based on energy storage mechanisms. Electrochemical performance strongly depends on the characteristics of electrode materials. Pseudocapacitor typically includes Transition Metal Oxides (TMO), conducting polymers. Until now, TMOs such as RuO_2 , Co_3O_4 , NiO , SnO_2 , V_2O_5 , MnO_2 and TiO_2 [2] have been investigated as electrode material due to delivery of higher SC and stability through charge–discharge cycling than EDLC and polymer-based materials, caused by reversible faradic redox reactions [3]. Amongst inexpensive TMOs, MnO_2 is one of the most promising candidates for supercapacitors, due to its theoretically high SC, natural abundance, eco-friendly and cost-effective nature [4]. Various techniques have been reported; sol–gel technique [5, 6], electrospinning [7], Hydrothermal [8, 9], Chemical Bath Deposition [10], electrodeposition [11] etc. for preparation of Manganese oxide electrodes with different morphologies as shown in Table 1. From these methods, electrospinning is arguably very facile and most cost-effective technique for preparation of nanofibers on a larger scale aiding in exact optimization of the NFs at uniform physical conditions which is highly challenging in other methods. Such electrospun NFs have unique properties viz. fabulous directional strength, large surface area, outstanding flexibility. So, NFs produced by this method make a novel combination of the electrode with deposition method, which can be reliably used in supercapacitors.

Table 1 Specific capacitance value by this proposed method as compared to other methods

Materials	Method	Capacitance F/g	Potential window V	References
Mn_2O_3	Sol–gel	230.5	0–1.0	[6]
MnO_2	Hydrothermal	202	0–0.8	[8]
$\text{Mn}_2\text{O}_3 @ \text{MnO}_2$	Hydrothermal	225	0–1.0	[9]
MnO_2	Chemical bath deposition	328	– 0.1 to 0.9	[10]
MnO_2	Electrodeposition	240	0–0.9	[11]
MnO_2	Electrospinning	336	– 1.3 to 0.3	Present

2 Experimental Details

The homogenous solution was prepared by mixing aqueous Mn acetate (MnAc) and aqueous PVA solutions, further stirred for 5 h. The viscous solution was used for electrospinning to prepare NFs. As-spun fibers were subjected to annealing in air at 500 °C for 1 h to develop MnO₂ NFs. The morphological and structural studies of MnO₂ NFs were done by Raman spectroscopy and Scanning Electron Microscopy. All the electrochemical studies like galvanostatic charge–discharge (GCD) and cyclic voltammetry (CV) of MnO₂ NFs electrode were done by a three-electrode system using CHI608E electrochemical workstation (CH instruments Inc., USA) in 1 M NaOH aqueous electrolyte.

3 Results and Discussion

3.1 Morphology Study of MnO₂ NFs

The morphology of surface of the as-spun and heat-treated electrospun fibres was analyzed from SEM. Figure 1a exhibits the images of SEM of as-spun MnAc/PVA nanofibers. It also reveals that the NFs are smooth and thick, having an average diameter of 225–435 nm. Figure 1b depicts the SEM images of annealed MnO₂ NFs at 500 °C. Annealed NFs are rough and thin as compared to the as-spun NFs, because the polymer matrix decomposes after annealing. After PVA completely degrades, the diameter of MnO₂ NFs is shrunk to the range of 211–340 nm. This enables the electrode to offer large specific area. Such kind of morphology is beneficial to enhance SC of electrochemical capacitors [12].

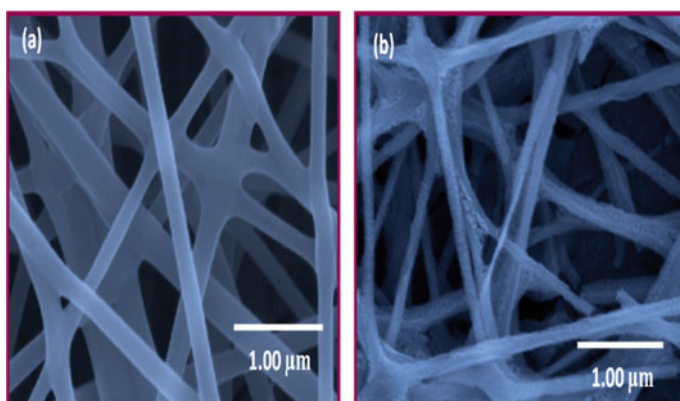


Fig. 1 SEM image of MnO₂ electrode **a** as-spun NFs **b** NFs annealed at 500 °C

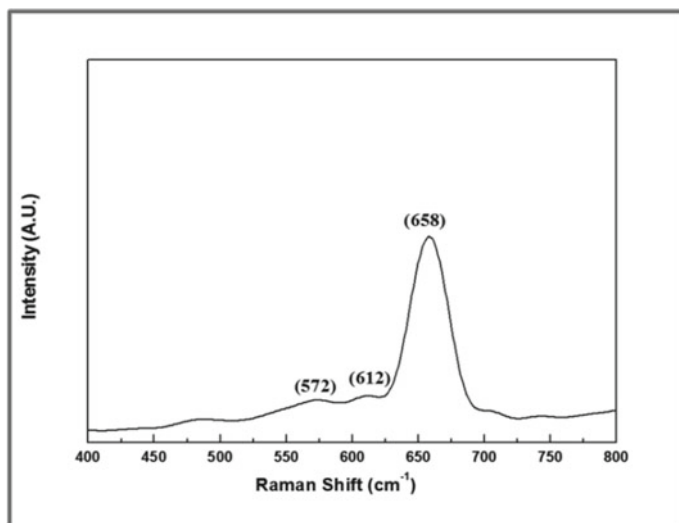


Fig. 2 Raman spectrum of MnO₂ NFs annealed at 500 °C

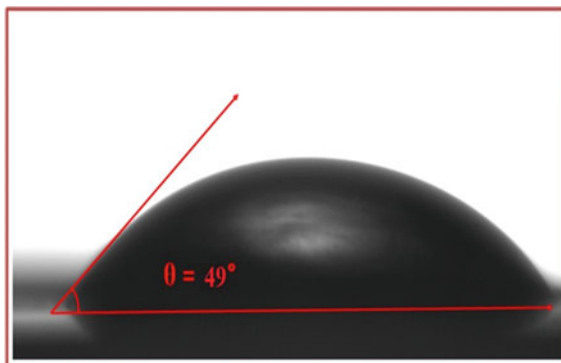
3.2 Structural Study

Raman spectroscopy is a useful analytical tool to investigate chemical structure and vibrational properties of the electrode material. Figure 2 highlights the Raman spectrum of electrospun MnO₂, displaying three prominent characteristic peaks at 572 cm⁻¹, 612 cm⁻¹, 658 cm⁻¹. The bands observed are assigned to the lattice vibrations and stretching vibration of Mn–O in MnO₂ [13].

3.3 Surface Wettability Study

To study wetting ability of electrolyte with the surface of electrode, the empirical mechanism such as water contact angle (CA) measurement is used. From this notable study, if CA measurement is diminutive (less than 90°), the sample surface is supposed to be hydrophilic with high wettability. On the other hand, less wetting of liquid with sample surface is referred to as hydrophobic in nature (CA is greater than 90°). Figure 3 displays CA of sample surface with measured angle to be 49°. Thus, the hydrophilic nature reveals that the aqueous electrolyte ions interact more with electroactive sites on electrode surface [14] and is regarded as a key point for the enhanced specific capacitance of supercapacitor electrode.

Fig. 3 Contact angle of MnO_2 electrode annealed at 500°C



3.4 Cyclic Voltammetry

To understand the supercapacitive property of electrospun MnO_2 , electrochemical measurement was performed by using CV analysis at various scanning rates. Figure 4a shows CV plot for 5 to 100 mV/s scan rate within -1.3 to -0.3 V potential window, examined in 1 M NaOH aqueous electrolyte. From CV curve it is clear that integral area of curve increases with rise in scan rate, which suggests the behaviour of an ideal capacitor, Fig. 4b depicts the variation of specific capacitance with respect to scan rate [7]. The decrease in SC value at higher scan rate owes to slow diffusion of ions to available sites of active material from electrolyte and reduction of efficient interaction between them [12].

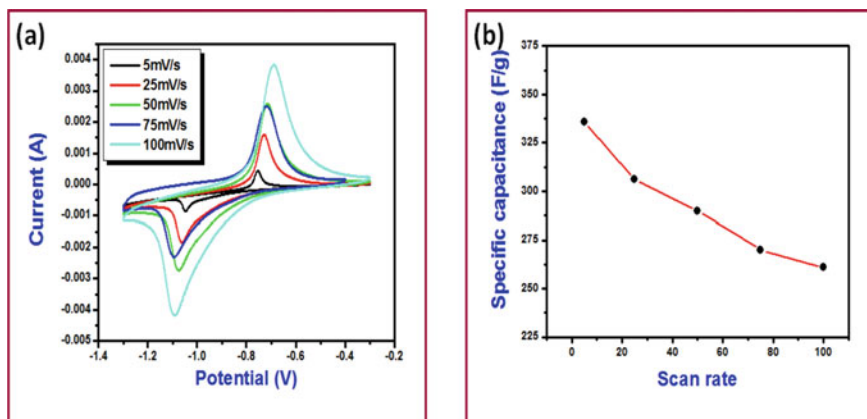


Fig. 4 **a** CV curves of MnO_2 electrodes at various scanning rates, annealed at 500°C and **b** plot of SC versus scan rate (5–100 mV/s) in 1 M NaOH electrolyte

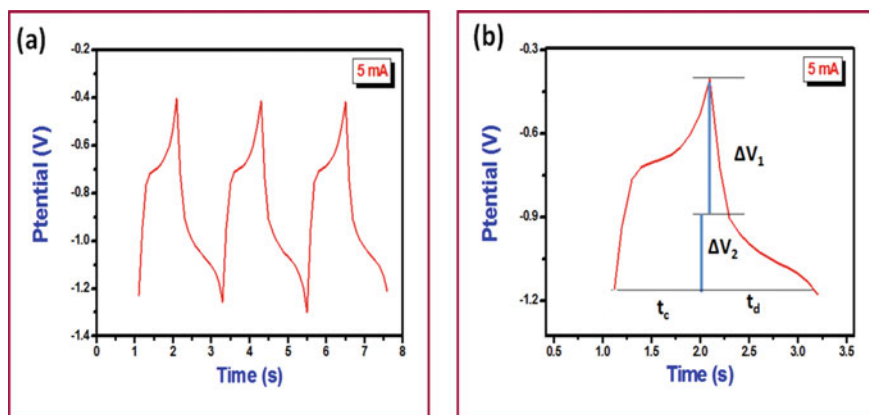


Fig. 5 **a** Charging-discharging curves at 5 mA/cm^2 and **b** a particular cycle at 5 mA/cm^2 in 1 M NaOH electrolyte

3.5 Galvanostatic Charge–Discharge Study

The GCD behaviour of electrode in 1 M NaOH aqueous electrolyte at 5 mA/cm^2 current density within the range of applied potential from -1.3 to -0.3 V versus SCE for the respective cycles, which is shown in Fig. 5a and it is clear that each charge–discharge profile is non-linear, close to an isosceles triangle, which indicates fine pseudo-capacitive behaviour [15]. From Fig. 5b it is visible that ΔV_1 falls quickly because of equivalent series resistance of supercapacitor and changes in ΔV_2 and t_d are the result of voltage decrement [16]. The electrode showed supercapacitive parameters viz. specific energy (SE) of 27.7 Wh/kg , specific power (SP) of 83.3 kW/kg with Coulombic efficiency of 98%.

4 Conclusion

MnO_2 NFs electrodes have been successfully prepared via electrospinning technique. The rough and thin surface morphology MnO_2 NFs were analysed by SEM. Their hydrophilic nature was confirmed through CA measurement with angle of 49° . The maximum specific capacitance achieved by MnO_2 nanofibers electrode annealed at 500°C is 336 F/g at 5 mV/s scan rate in 1 M NaOH aqueous electrolyte. The other supercapacitive properties such as specific power and energy, coulombic efficiency from GCD measurement were found to be 83.3 kW/kg , 27.7 Wh/kg and 98% respectively. It is believed that this study has implications in design to flexible metal oxide-based electrodes for supercapacitor application.

Acknowledgements Prof. V. B. Patil is grateful to Rajiv Gandhi Science and Technology Commission for supporting financially, Grant Id: RGSTC/file-2019/PAHSUS/CR-91 dated 23/12/2019.

References

1. More, P. D., Jadhav, P. R., Ghanwat, A. A., Dhole, I. A., Navale, Y. H., & Patil, V. B. (2017). Spray synthesized hydrophobic α -Fe₂O₃ thin film electrodes for supercapacitor application. *Journal of Materials Science: Materials in Electronics*, 28, 17839–17848.
2. Gavande, S. S., Kulkarni, P. S., Karche, B. R., Gavande, S. S., & Patil, V. B. (2021). An assay of electrodeposited cobalt oxide thin film as a supercapacitor electrode. *Macromolecular Symposium*, 393, 2000169–2000175.
3. More, P. D., Dhole, I. A., Navale, Y. H., Navale, S. T., & Patil, V. B. (2019). Impact of electrolyte concentration on the supercapacitive properties of spray pyrolyzed CdO thin film electrode. *Solid State Ionics*, 334, 56–64.
4. Lin, C.-K., Chuang, K.-H., Lin, C.-Y., Tsay, C.-Y., & Chen, C.-Y. (2007). Manganese oxide films prepared by sol-gel process for supercapacitor application. *Surface & Coatings Technology*, 202, 1272–1276.
5. More, P. D., Kadam, S. A., Ma, Y., Chen, Y., Tarwal, N., Navale, Y. H., Salunkhe, A. S., & Patil, V. (2022). Spray synthesized Mn-doped CuO electrodes for high performance supercapacitor. *Journal of Chemistry Select*, 7, 202202504–202202510.
6. Sarkar, A., Satpati, A., Kumar, V., & Kumar, S. (2015). Sol-gel synthesis of manganese oxide films and their predominant electrochemical properties. *Electrochimica Acta*, 167, 126–131.
7. Jiang, H., Zhao, T., Yan, C., Ma, J., & Lic, C. (2010). Ultrafine manganese dioxide nanowire network for high-performance supercapacitors. *The Royal Society of Chemistry*, 2, 2195–2198.
8. Zhu, Y.-P., Xia, C., Lei, Y., Singh, N., Schwingenschlogl, U., & Alshareef, H. N. (2019). Solubility contrast strategy for enhancing intercalation pseudocapacitance in layered MnO₂ electrodes. *Nano Energy*, 56, 357–364.
9. Lu, W., Li, Y., Yang, M., Jiang, X., Zhang, Y., & Xing, Y. C. (2020). Construction of hierarchical Mn₂O₃@MnO₂ core-shell nanofibers for enhanced performance supercapacitor electrodes. *ACS Applied Energy Materials*, 3, 8190–8197.
10. Dubal, D. P., Holze, R., & Kulal, P. M. (2013). Enhanced supercapacitive performances of hierarchical porous nanostructure assembled from ultrathin MnO₂ nanoflakes. *Journal of Materials Science*, 48, 714.
11. Chou, S., Cheng, F., & Chen, J. (2006). Electrodeposition synthesis and electrochemical properties of nanostructured γ -MnO₂ films. *Journal of Power Sources*, 162, 727–734.
12. Salunkhe, A. S., Navale, Y. H., Navale, S. T., Nadargi, D. Y., & Patil, V. B. (2021). Electrospun flexible 1D-MnO₂ nanofibres: A versatile material for energy storage application. *Journal of Materials Science: Materials in Electronics*, 32, 18028–18042.
13. Julien, C. M., Massot, M., & Poinignon, C. (2004). Lattice vibrations of manganese oxides. Part I. Periodic structures. *Spectrochimica Acta Part A: Molecular and Biomolecular Spectroscopy*, 60, 689–700.
14. Navale, Y. H., Navale, S. T., Dhole, I. A., Stadler, F. J., & Patil, V. B. (2018). Specific capacitance, energy and power density coherence in electrochemically synthesized polyaniline-nickel oxide hybrid electrode. *Organic Electronics*, 57, 110–117.
15. Liu, K.-Y., Zhang, Y., Zhang, W., Zheng, H., & Geng, S. U. (2007). Charge-discharge process of MnO₂ supercapacitor. *Transactions of the Nonferrous Metals Society of China*, 17, 649–653.
16. Navale, Y. H., Navale, S. T., Chougule, M. A., Ingole, S. M., Stadler, F. J., Mane, R. S., Naushad, M., & Patil, V. B. (2017). Galvanostatically electroplated MnO₂ nanoplate-type electrode for potential electrochemical pseudocapacitor application. *Journal of Colloid and Interface Science*, 487, 458–464.

A Critical Review of Recent Research on the Application of Nanofluids in Heat Exchanger



Shital Waware, Sunilkumar Harsur, Ramdas Biradar, Pallavi Jadhav, Kamalkishor Maniyar, and Pushparaj Warke

Abstract Heat exchangers (HEs) are the devices that are used to transfer heat from one medium to another. Heat is not mixed together in this type of heat exchanger. A number of research studies have been conducted in order to improve heat transfer through HEs. Nanofluids are used as a coolant in HEs to improve their effectiveness. The nanofluids have been used in HEs recently in various HEs such as pipe-in-pipe heat exchangers, shell and tube HEs, plate heat exchangers and many other heat exchangers. However, several novel developments in the use of HEs and nano-fluids have been made.

Keywords Plate heat exchangers · Double-pipe heat exchangers · Shell and tube heat exchangers · Compact heat exchangers · Nanofluids

1 Introduction

Energy conservation is one of the most significant issues of the twenty-first century. It is one of the most significant issues of the 21st As a result; scientists, engineers, and researchers are working very hard to solve this important problem. Industrial equipment's usable life is further extended by the improvements in heat transfer and energy efficiency brought about by better heating or cooling. Saving energy is made possible by effective energy use. Conversion, conservation, and recovery of energy are a few strategies for energy conservation.

HEs have previously proven to be essential parts of thermal systems in a variety of industrial areas. In order to improve HE efficiency, nanofluids are currently being employed as coolants. Recent years have seen a tremendous increase in research on the unique characteristics of nanofluids. Recently, a number of studies and reports have focused on the use of nanofluids in heat exchangers, including those on plate heat exchangers, double-pipe heat exchangers (DPHE), shell and tube heat exchangers (STHE), and compact heat exchangers (CHE).

S. Waware (✉) · S. Harsur · R. Biradar · P. Jadhav · K. Maniyar · P. Warke
Department of Mechanical Engineering, Dr. D.Y. Patil Institute of Technology, Pimpri, Pune, India
e-mail: shitalwaware@gmail.com

Different types of HEs are used in a variety of manufacturing industries for the aforementioned purposes, including power plants, nuclear reactors, the petrochemical industry, refrigeration, air conditioning, process industries, solar water heaters, food engineering, and chemical reactors. Utilizing a range of techniques enhances the efficiency of HEs. Long-term efforts have been made to improve heat transfer in HEs reduce the time needed for heat to exchange, and eventually boost system efficiency. To improve the area for heat transmission, fins are frequently employed. But this approach leads to heavier and bigger HEs. As a result, widely used techniques like the use of fins have indeed been exhausted.

Convective heat transmission in HEs may be increased along with geometrical changes if the thermal characteristics of the heat transfer fluids are improved. The addition of additives to the working fluids to modify their thermophysical properties is an attractive technique for improving heat transfer. Nanotechnology's most recent developments have given rise to a remedy for this. S.U.S.C. [1] used the phrase "nano-fluid" for the first time in 1995 to refer to a fluid with improved capabilities for heat transport compared to common fluids. Regular fluids and solid nanoparticles are combined to form a nanofluid. Nanofluids, a new class of high performance heat transfer fluids, may overcome the shortcomings of traditional fluids' poor thermophysical characteristics, such as low thermal conductivity. Nanofluids are advantageous due to their excellent thermal conductivity and suitable stability, according to research [2, 3].

The use of nanofluids is one of the more promising ways to improve heat transfer in heat exchangers. For this, a number of researchers have used nanofluids. This review article attempts to summarise the developments in the application of nanofluids for heat exchangers while also highlighting shortcomings and issues. The review first focuses on research done on various heat exchanger types employing nanofluids as coolants before introducing and delving into some fascinating aspects of this topic.

2 Plate Heat Exchangers

The Plate Heat Exchanger (PHE), created in 1921 for use in dairy technology, is utilized extensively in a variety of industries. PHE comes with a set of thin plates and a frame to hold them. The working fluid is the fluid that is flowing within the void between adjacent plates. The heat transfer surface can be easily changed, as well as the heat transfer rate, by adding or moving plates. As the need for energy conservation grows, PHEs now play a vital role in several industries. Energy waste may be considerably decreased with an extremely efficient PHE. PHEs are available in many different designs, including chevron, herringbone, and washboard. The one of these types that is most usually used is the chevron PHE.

A chevron plate may frequently produce a lot of turbulence, which helps heat transfer effectively. The heat transfer coefficients provided by PHEs can be equivalent to those of pipes with several times higher Reynolds numbers, according to study

by Morgan et al. [4]. As a result, several studies into PHEs with various geometries have been carried out.

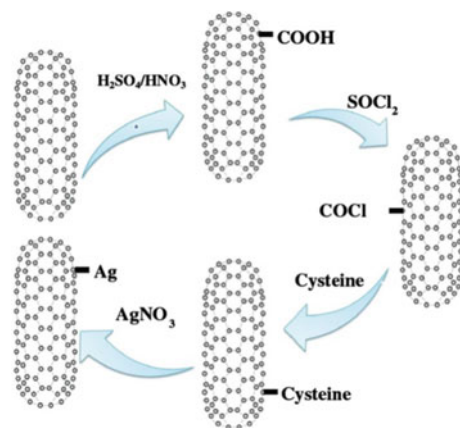
Ghosh et al. [5] examined the heat transmission and pressure drop properties in a chevron-type corrugated PHE while using CeO_2 /water nanofluid as the coolant. The experiments looked at how well heat transfer and pressure drop performed at various fluid flow rates (1–4 lpm) and operating temperatures across a wide concentration range (0.5–3 vol%). It was also determined at what CeO_2 /water nanofluid concentration heat transmission above base fluid improved the most. It was discovered that at an ideal concentration of 0.75 vol%, the nanofluid in PHE has a heat transfer coefficient that is up to 39% greater than water's. Additionally, when the volume flow rate of the hot water and nanofluid increased and dropped as the temperature of the nanofluid climbed, the heat transfer coefficient increased.

The largest increase in heat transfer coefficient was 13% for a 4% concentration. Furthermore, when the Reynolds number increased, both the required pumping power and the pressure decreased. The greatest pressure drop increase over the base fluid was determined to be 45% at a concentration of 4%. The schematic of the used chevron plate and the corrugation proportions are shown in Fig. 1.

The flow and convective heat transfer characteristics of nanofluids inside a PHE were investigated by Peng et al. [7]. They used Cu, Fe_2O_3 , and Al_2O_3 nanoparticles with a particle size of 50 nm. The outcomes showed that the inclusion of nanoparticles improves the total heat transfer coefficient and resistance coefficient. The convective heat transfer coefficient of the Cu-water nanofluid was the best because various nanoparticles had varied effects. The Cu-water nanofluid's maximum enhancement, which occurred at a concentration of 0.5%, was 34.55%.

For CeO_2 -water, Al_2O_3 -water, TiO_2 -water, and SiO_2 -water nanofluids, P. Ghosh et al. [8]'s optimization effort focused on the maximum heat transfer rate, convective heat transfer coefficient, total heat transfer coefficient, effectiveness, and performance index. Their work was unique in that it optimised the volume fraction of several

Fig. 1 Diagram of functionalization process of MWCNT with cysteine and Ag [6]



nanofluids using experiments in commercial PHE for a wide range of volume fractions. The findings show that various nanofluids function at various optimal concentrations for maximal augmentation of heat transfer properties. The ideal concentrations were 0.75%, 1%, 0.75%, and 1.25% for CeO₂-water, Al₂O₃-water, TiO₂-water, and SiO₂-water nanofluids, respectively. The relative maximum heat transfer improvements were approximately 35.9, 26.3, 24.1, and 13.9%.

SiO₂, TiO₂, and Al₂O₃ nanoparticle-containing nanofluids were used in a PHE by Sadeghipour et al. [9], and SiO₂, TiO₂, and Al₂O₃ nanoparticle-containing nanofluids were used in a PHE by Cengel et al. [10]. The results showed that the addition of nanoparticles increased the fluid's thermal conductivity, heat transfer coefficient, and heat transfer rate, and that TiO₂ and Al₂O₃ produced superior thermophysical qualities than SiO₂. The Al₂O₃ nanofluid had a total heat transfer coefficient of 308.69 W/m² K at a concentration of 0.2%, which was the highest ever recorded. Compared to SiO₂ nanofluid, the relevant heat transfer rate was increased by around 30%. SiO₂ demonstrated the lowest pressure drop when compared to TiO₂ and Al₂O₃, which was approximately 50% less.

The investigations mentioned above demonstrated that fouling may have a major impact on the properties of PHEs that function with nanofluids. However, there hasn't been much research done in this area, so much more research is needed to create applicable approaches to designing PHEs as effectively as possible.

There are two methodologies used in the literature for numerical studies on nanofluids: single-phase and two-phase. In the former, conservation equations are solved while taking into account the useful properties of nanofluids, and in the latter, solutions are applied to show how liquid and solid phases behave.

3 Shell and Tube Heat Exchangers

Shell-and-Tube Heat Exchangers have a wide range of uses in power plants, oil refineries, the food industry, and other industrial settings, making them one of the most widely used types of heat exchangers. Shell-and-tube heat exchangers account for more than 35–40% of all heat exchangers [11] due to their sturdy construction geometry, ease of maintenance, and upgradeability. Despite industrial developments in other types, these heat exchangers have continued to be engineers' first choice and are widely used as heat exchange devices because of their advantages.

Research on the forced convective heat transfer and flow properties of water-Al₂O₃ nanofluids flowing in a STHE under turbulence was published by Tayal et al. in [12]. The outcomes show that for the same mass flow rate and identical inlet, the nanofluid's heat transfer coefficient is marginally greater than that of the base liquid temperature. The nanofluid's heat transfer coefficient increased as the mass flow rate and concentration rose, but as the concentration rose, the viscosity and friction factor also rose. The total heat transfer coefficient of the nanofluid was 57% higher than that of plain water.

Abbassi et al. [13] studied Al_2O_3 nanofluid flow inside shell and helical tube heat exchangers for heat transfer. The findings showed that 0.2% and 0.3% volume concentration, respectively, increase the rate of heat transfer by approximately 14 and 18%. The outcomes also show that when concentration increases, so do the coil-side, shell-side, and total heat transfer coefficients. According to the data, the heat transfer rate of nanofluid improves considerably for the same mass flow rate compared to water and only a little with additional concentration increases. Additionally, it was discovered that increasing concentration, tube diameter, and coil diameter while reducing mass flow rate increases effectiveness.

Mahbubul et al. [14] evaluation of a nanofluid-operated STHE's performance. It was discovered that the convective heat transfer coefficient is 2–15% greater than that of water. Additionally, the nanofluid's energy effectiveness increased by roughly 23–52%. Maximum energy effectiveness was found for the ZnO -water nanofluid and the lowest one for the SiO_2 -water nanofluid because the density and specific heat of the working fluids substantially rely on each other.

4 Compact Heat Exchangers

Although considerable research has been done on employing nanofluids in small heat exchangers, this application has received less attention than that of other heat exchangers even though it is widely used in a variety of thermal system applications. Common examples of ground equipment are automotive thermal fluid systems, vehicle radiators, HVAC evaporators and condensers, oil coolers, and inter coolers.

Krishna et al. [15] used the -NTU approach and an Al_2O_3 /water nanofluid as coolant to examine the thermal design of a flat tube plain fin compact heat exchanger. It was discovered that the pressure drop of the 4% concentration nanofluid is nearly double that of the base fluid. The results of using nanofluids in vehicle radiators have been explored by several researchers. Car radiators are really thought of as little heat exchangers. A car's radiator is crucial in protecting the engine from overheating. A radiator with louvered fins has been constructed in order to transmit more heat from the surface area and disrupt the boundary layer that has developed nearby.

In an experiment conducted by Bakar et al. [16], TiO_2 and SiO_2 nanoparticles dispersed in water were used to study the enhancement of heat transfer in automobile radiators. The test setup was constructed using tubes and a container to resemble a vehicle radiator. The Reynolds number varied between 250 and 1750, and the volume fraction varied between 1.0 and 2.5%. The findings show that as volume percent increases, so does heat transmission. For TiO_2 and SiO_2 nanofluids, the enhancement values for the energy rate were 20 and 32%, and for effectiveness, they were 24 and 29.5%.

In a unique vehicle radiator, Saeed et al. [17] looked at the impact of nanofluid on pressure drop and friction factor at various concentrations. The base fluid was a 60:40 mixture of ethylene glycol and distilled water, and CuO nanoparticles were evenly scattered to create stable nanofluids. The findings showed that the presence of

nanoparticles increases pressure loss, which was aggravated by raising concentration as well as lowering inlet fluid temperature. Additionally, an empirical equation was created to forecast the pressure decrease via the radiator. Additionally, when the flow rate climbed, the performance index did too, showing that using nanofluid at larger flow rates is affordable.

The flow and heat transmission of two different nanofluids, Al_2O_3 and CuO , in an ethylene glycol and water mixture flowing through the flat tubes of an automotive radiator were examined by Namburu et al. [18]. With the flow of the nanofluid along the flat tubes, the convective heat transfer coefficient significantly outperformed that of the base fluid in both the developing and developed zones. For a 10% Al_2O_3 nanofluid and a 6% CuO nanofluid, respectively, the percentage increase in the heat transfer coefficient over the base fluid at Reynolds number 2000 was 94% and 89%, respectively. The pressure loss rose as the concentration grew, but the necessary pumping power decreased since a smaller volumetric flow was needed for the same amount of heat transfer.

The effectiveness of ethylene glycol and water-based TiO_2 nanofluids as automotive radiator coolants was determined experimentally by Reddy et al. [19]. In each experiment, air moved at a constant speed in a transverse direction between the radiator tubes, and nanofluids were created to flow through them. The findings showed that while the fluid intake temperature to the radiator had minimal impact on heat transfer efficacy, increasing fluid circulation rate may have. When compared to base fluid, the heat transfer rate was increased by the nanofluids studied in the current work by up to 37% at low concentrations.

5 Conclusions

The current contribution made an effort to give a thorough analysis of studies done on the subject of using nanofluids in heat exchangers. Numerous studies have been conducted to examine the performance of nanofluids in heat exchangers due to the suitable features of nanofluids. According to the majority of experimental and computational studies, nanofluids have an enhanced rate of heat transfer, which is significantly boosted by raising concentration and Reynolds number. From this review, the following crucial directions for future study and difficulties may be learned:

1. The cost of synthesising nanofluids and the stability of nanoparticles are two crucial aspects to take into account in order to advance the usage of nanofluids in heat exchangers. In the future of research, it is crucial to pay more attention to the financial aspects of using nanofluids as coolants. The applicability of nanofluids may be constrained if trade-offs between nanofluid performance increase and cost cannot be thoroughly confirmed. Therefore, taking into account performance optimization and cost analysis at the same time is crucial. However, there are relatively few publications that have looked into both hydrothermal optimization and cost analysis in heat exchangers.

2. The absence of consistency among diverse assessments is one of the key issues observed in research studies on the application of nanofluids in heat exchangers. This may be the primary cause of the discrepancies in the findings reported by the relevant research.
3. The properties of nanofluid heat exchangers can be significantly impacted by fouling. To build appropriate solutions for heat exchanger design optimization, however, considerably more investigation is required as there hasn't been much study done in this field. Because research on double-pipe heat exchangers is dependent on the type of nanofluids used, the findings from this study cannot be applied to all nanofluids.
4. One of the crucial design factors that significantly affect performance in STHEs is the baffle. However, there hasn't been much investigation into how the baffle configuration affects the properties of STHEs that operate with nanofluids.
5. Future applications of hybrid nanofluids as potential nano-fluids for heat transfer enhancement in heat exchangers are possible. It may pave the way for heat exchanger performance to be improved.

References

1. Choi, S. U. S. (1995). Enhancing thermal conductivity of fluids with nanoparticles. *ASME's International Mechanical Engineering Congress & Exposition*, 66, 99–105.
2. Agarwal, R., Verma, K., Agrawal, N. K., & Singh, R. (2017). Sensitivity of thermal conductivity for Al₂O₃ nanofluids. *Experimental Thermal and Fluid Science*, 80, 19–26.
3. Pryazhnikov, M. I., Minakov, A. V., Rudyak, V. Ya., & Guzei, D. V. (2017). Thermal conductivity measurements of nanofluids. *International Journal of Heat and Mass Transfer*, 104, 1275–1282.
4. Morgan, J. G., Troupe, R. A., & Prifti, J. (1960). *Chemical Engineering Progress*, 56, 124–128.
5. Tiwari, A. K., Ghosh, P., & Sarkar, J. (2013). Performance comparison of the plate heat exchanger using different nanofluids. *Experimental Thermal and Fluid Science*, 49, 141–151.
6. Amiri, A., Maghrebi, M., Baniadam, M., & Zeinali Heris, S. (2011). One-pot, efficient functionalization of multi-walled carbon nanotubes with diamines by microwave method. *Applied Surface Science*, 257(23), 10261–10266.
7. Sun, B., Peng, C., Zuo, R., Yang, D., & Li, H. (2016). Investigation on the flow ... the plate heat exchanger. *Experimental Thermal and Fluid Science*, 76, 75–86.
8. Tiwari, A. K., Ghosh, P., & Sarkar, J. (2015). Particle concentration levels of various nanofluids in plate heat exchanger for best performance. *International Journal of Heat and Mass Transfer*, 89, 1110–1118.
9. Javadi, F. S., Sadeghipour Saidur, S., BoroumandJazi, R., Rahmati, G. B., Elias, M. M., & Soheli, M. R. (2013). *International Communications in Heat and Mass Transfer*, 44, 58–63.
10. Cengel, Y. A., & Boles, M. A. (2015). *Thermodynamics: An engineering approach* (8th ed.). McGraw-Hill.
11. Bahiraei, M., Hosseinalipour, S. M., & Saeedan, M. (2015). Prediction of Nusselt number and friction factor of water-Al₂O₃ nanofluid flow in shell-and-tube heat exchanger with helical baffles. *Chemical Engineering Communications*, 202, 260–268.
12. Albadr, J., Tayal, S., & Alasadi, M. (2013). Heat transfer through heat exchanger using Al₂O₃ nanofluid at different concentrations. *Case Studies in Thermal Engineering*, 1, 38–44.

13. Abbassi, A., & Bahrehmand, S. (2016). Heat transfer and performance analysis of nanofluid flow in helically coiled tube heat exchangers. *Chemical Engineering Research and Design*, 109, 628–637.
14. Shahrul, I. M., Mahbulul, I. M., Saidur, R., & Sabri, M. F. M. (2016). Experimental investigation on Al_2O_3 -W, SiO_2 -W and ZnO -W nanofluids and their application in a shell and tube heat exchanger. *International Journal of Heat and Mass Transfer*, 97, 547–558.
15. Krishna, K. R., Vasu, V., & Kumar, A. C. S. (2008). *International Journal of Nanomanufacturing*, 2271–287.
16. Hussein, A., Bakar, R. A., Kadirgama, K., & Sharma, K. V. (2014). Heat transfer augmentation of a car radiator using nanofluids. *Heat and Mass Transfer*, 50, 1553–1561.
17. Samira, P., Saeed, Z. H., Motahare, S., & Mostafa, K. (2015). Pressure drop and thermal performance of CuO/ethylene glycol (60%)-water (40%) nanofluid in car radiator. *Korean Journal of Chemical Engineering*, 32(4), 609–616.
18. Vajjha, R. S., Das, D. K., & Namburu, P. K. (2010). Numerical Study of fluid dynamic and heat transfer performance of Al_2O_3 and CuO nanofluids in the flat tubes of a radiator. *International Journal of Heat and Fluid Flow*, 31(4), 613–621.
19. Sandhya, D., Reddy, M. C. S., & Rao, V. V. (2016). Improving the cooling performance of automobile radiator with ethylene glycol water-based TiO_2 nanofluids. *International Communications in Heat and Mass Transfer*, 78, 121–126.

CFD Analysis of Hydrodynamic Journal Bearing with Rectangular Top Inlet



Smeeta Ashar, Abhijeet Chavan, and Pradnya Patil

Abstract Journal bearings have wider range of applications owing to their theoretically infinite life span and high load carrying capacity at high speeds. An accurate performance prediction of journal bearing will lead to longer bearing life and reduced energy losses. In this work CFD analysis is used to simulate the fluid flow in a journal bearing. With help of advanced computational facilities and dedicated software tools hydrodynamic action of journal bearing can be predicted more accurately. This work simulates a journal bearing with a top inlet as close to the practical cases. Top inlet case for various eccentricities, operating speeds, and lubricants are simulated in this work. Pressure and temperature profiles and contours of the respective bearings are presented. Simulated results can be adopted for designing a bearing with top inlet.

Keywords Hydrodynamic journal bearing · CFD · Pressure profile · Temperature profile

1 Introduction

Journal bearings are one of the most used bearings due to their low maintenance, infinite life and higher load carrying capacities. Hydrodynamic bearings are bearings with a lubricant separating the two elements moving with respect to each other. In a stationary condition there is direct contact between the journal and shaft. When the shaft starts moving initially, the lubricant is pulled under the shaft due to viscosity and forms a wedge shape under it. The bearing performance is dependent on lubricant viscosity, shaft speed, film thickness, radius of shaft, load on shaft, etc. The growing

S. Ashar (✉) · A. Chavan
MIT School of Engineering, MIT ADT University, Pune, Maharashtra, India
e-mail: smeetaashar@gmail.com

P. Patil
SVRI's College of Engineering, Pandharpur, Maharashtra, India

tendency toward higher-speed, higher-performance, but smaller-sized machinery has pushed bearing working conditions toward superior versions, as well as numerous forms of research and study being done on them.

Relevant work has been done on the computational fluid dynamic analysis of journal bearings by various researchers. Most of the literature mentioned used a side-inlet, side-outlet model for simplicity of simulation. Sahu et al. [1] and Singla et al. [2] carried out thermo-hydrodynamic analysis of a journal bearing using CFD software. They used CFD to predict the performance and three-dimensional study has been done to get the pressure and temperature distribution circumferentially and axially. Manojkumar et al. [3] examined the pressure field and deformation of bearing coupling surfaces of an elastic hydrodynamic model using fluid dynamics and fluid surface interaction (FSI) methods. Dhande et al. [4] did a CFD analysis with multi-phase flow phenomena considering cavitation in the FSI model. Models with and without cavitation were simulated to find elastic deformation on the bearing with the results being analyzed numerically as well as experimentally. Some work considered different lubricants other than lubricating oils. Gertzoz et al. [5] use Bingham fluids to check non-Newtonian lubrication in journal bearing, where the analysis was done on ANSYS Fluent. Krykou et al. [6] presented a complete thermo-hydrodynamic analysis using CFD software. The authors used commercially available lubricants and environmentally friendly lubricants and compared the pressure and temperature plot, suggesting the latter gave a good pressure distribution on the bearing. Cupillard [7] studied surface texturing of different geometries and shapes on the inner bearing surface and their respective effects on the pressure distribution and load carrying capacities on bearings have been shown by using CFD.

This work deals with the CFD analysis of a rectangular inlet journal bearing to get a close look at the pressure and temperature profiles in the bearing. This can further help in designing better bearing for machinery in turn reducing failures and pollution in the society and moving forward to a better future.

2 Theoretical Background

The lubricant flow across the clearance space of journal bearing is determined by fluid flow characteristics. The basic laws associated with the flows of fluid are Conservation of momentum, Conservation of energy and Conservation of mass.

In order to get the solution for the Pressure, two-dimensional Reynolds equation is used but ANSYS Fluent solves Navier-Stokes equation of continuity and momentum to get the solution for a given CFD problem; here being the pressure distribution for the given fluid film profile. These equations are solved in fluent for momentum, mass and energy, considering steady state, laminar, incompressible flow. Additionally for the solution of temperature profile, energy conservation equation is solved.

Mass conservation Equation provided by Dhande [4] is represented by Eq. (1)

$$\frac{\partial \rho}{\partial t} + \nabla \cdot (\rho \vec{v}) = 0 \quad (1)$$

where, ρ and \vec{v} are the fluid density and fluid velocity, respectively.

The momentum equation is:

$$\frac{\partial(\rho \vec{v})}{\partial t} + \nabla \cdot (\rho \vec{v} \vec{v}) = -\nabla P + \nabla \cdot (\bar{\tau}) + \rho \vec{g} + \vec{F} \quad (2)$$

where, $\bar{\tau}$ is stress tensor, $\rho \vec{g}$ is gravitational force, P is the static pressure and F is external body force. Stress tensor [4] is written as:

$$\bar{\tau} = \mu \left[\left(\nabla \vec{v} + (\nabla \vec{v})^T \right) - \frac{2}{3} \nabla \cdot \vec{v} \bar{I} \right] \quad (3)$$

where, μ is fluid viscosity \bar{I} is unit tensor, and another term on right hand side is effect of volume dilation.

The energy equation for steady-state, Newtonian fluid and incompressible flow is given by [2]:

$$\rho C_p \left[\frac{\partial T}{\partial t} + u \frac{\partial T}{\partial x} + v \frac{\partial T}{\partial y} + w \frac{\partial T}{\partial z} \right] = k_h \frac{\partial^2 T}{\partial y^2} + \mu \left[\left(\frac{\partial u}{\partial y} \right)^2 + \left(\frac{\partial w}{\partial y} \right)^2 \right] \quad (4)$$

The term on the left hand side signifies heat transfer due to convection, and the terms on right hand side signify conduction and viscous damping respectively.

3 Modeling and Validation

Mainly two types of simulations can be performed with respect to viscosity of the lubricant used. The iso-thermal simulations, where viscosity as a function of temperature is not considered and the thermal simulations where the change in viscosity is considered. Latter is incorporated in the work. This work considers the thermal simulations where the viscosity data for the lubricant (5W-30) is calculated using ASTM D341 and put in tabular form, which can be directly loaded in the CFD software.

Two geometries are used for the simulation. A side inlet side outlet model generally simulated in various literatures [1–5] is simulated first for the purposes of validation. The model parameters for both the geometries are same and are stated in Table 1.

The top inlet model has a rectangular (5 mm × 10 mm) top inlet apart from the properties stated. The model has 80 elements along the axial direction, 600 elements along the circumference and the outlet faces have 11 elements in the thickness with a suitable bias to get inflation layer along the boundaries. Average skewness of 0.40 and an average orthogonal quality of 0.70 is found for the mesh which shows that the

Table 1 Model and analysis properties

Bearing inner radius	20 mm
Bearing length	40 mm
Clearance	0.25 mm
5W-30 viscosity (40 °C, 100 °C)	54.1 cP, 8.98 cP
5W-30 thermal conductivity	0.134 W/m K
5W-30 density	856 kg/m ³
5W-30 specific heat	2000 J/kg K

mesh is of good quality. A steady state, laminar CFD analysis is carried out on the bearing. The outer wall of the model is set as a stationary wall, and the inner wall as the moving wall with respective rotational speed. The rectangular face of the inlet is set as the inlet with zero gauge pressure and 40 °C as oil inlet temperature similarly the thin walls on the sides of the model are set as the outlet. Operating pressure and temperature was set to 101,325 Pa and 40 °C respectively. The convergence criterion was set to default value in the software with under-relaxation factors decreased by 0.1 for all equations to curb the divergence observed at the beginning of the calculations. SIMPLE algorithm was used with default controls for momentum and energy equations.

A user defined function (UDF) is added to apply the Christopherson's algorithm i.e. at points having negative pressure values are changed to zero after every iteration. This is to consider the cavitation effects in the divergent region of the bearing. Viscous Dissipation option is switched on for the heat generation calculation in the fluid film due to the viscosity of the moving liquid.

Grid independency study for the model is carried out at 0.8 eccentricity ratio (ϵ) running at 2000 rpm. Table 2 gives the difference % between consecutive results with changing grid parameters. Lastly the difference % comes down to 1% so the penultimate model is selected since the last model has higher number of elements thereby increasing the computation time.

Table 2 Grid independency study

No. of elements (axial, circum., radial)	Max. pressure (MPa)	Difference %
(60, 300, 5)	0.4096	–
(70, 300, 9)	0.4523	9.9
(80, 500, 9)	0.5065	11.3
(80, 600, 11)	0.5345	5.3
(80, 600, 13)	0.5399	1

The validation of the simulation is done by comparing the pressure results of a side-inlet side-outlet (SISO) model with the well-defined parameters in Raimondi-Boyd charts [8] for the given eccentricity and L/D ratio. The SISO model with eccentricity of 0.6 had a max pressure of 2.41×10^5 Pa whereas the max pressure from charts comes out to be 2.3×10^5 Pa which is a 4.5% difference. This validates the model.

4 Results and Discussion

4.1 Different Eccentricity Ratios

CFD analysis is performed on the model having different eccentricity ratios ranging from 0.4 to 0.9. The shaft speed is set constant to 2000 rpm and L/D ratio of all the models is 1. Same lubricant with same meshing in all the models is used, to keep all the other variables constant.

Pressure and temperature contour for eccentricity ratios 0.6 and 0.9 are shown from Figs. 1, 2, 3 and 4. Figure 5 shows a pressure distribution curve of all bearing eccentricity ratios along the inner wall of bearing. It can be noted from the plots that the maximum pressure increases exponentially as the eccentricity ratio increases. The difference between max pressure for $\epsilon = 0.6$ and $\epsilon = 0.4$ is 0.1 MPa, whereas that for $\epsilon = 0.9$ and $\epsilon = 0.8$ is 1 MPa. Bearings with high eccentricity ratios have very high load carrying capacities due to high pressure generated in lubricant.

The increase in temperature is observed to be proportional to increase in eccentricity ratio. The temperature contours in this work are generated by considering only the temperature rise in the lubricant due to its viscosity and not the effect of conduction in the bearing and shaft, which shows why the change in temperature has not been as high as rise in pressure.

Fig. 1 Pressure contour ($\epsilon = 0.6$)

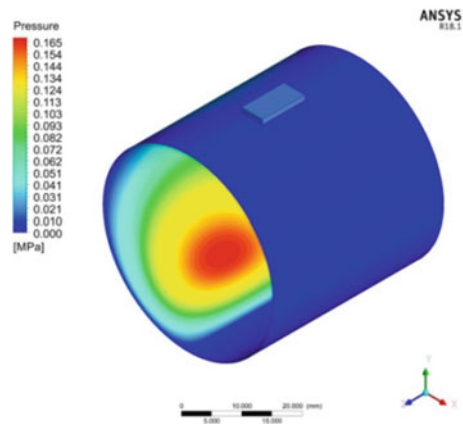


Fig. 2 Temperature contour ($\epsilon = 0.6$)

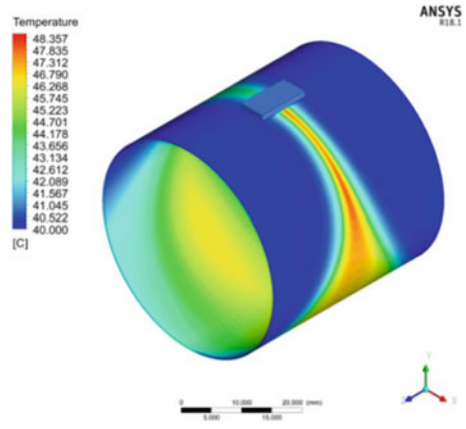


Fig. 3 Pressure contour ($\epsilon = 0.9$)

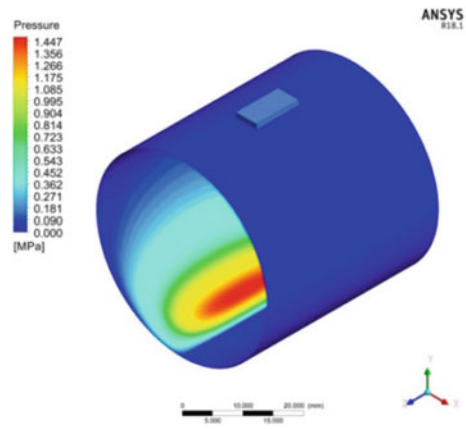


Fig. 4 Temperature contour ($\epsilon = 0.9$)

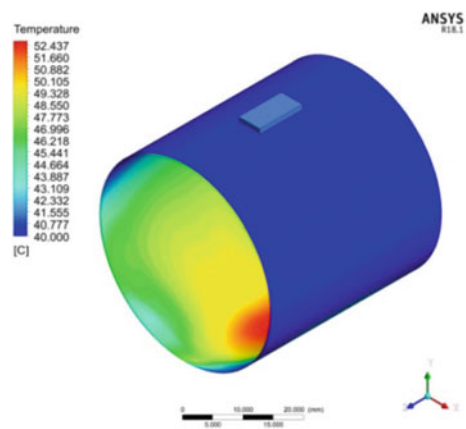
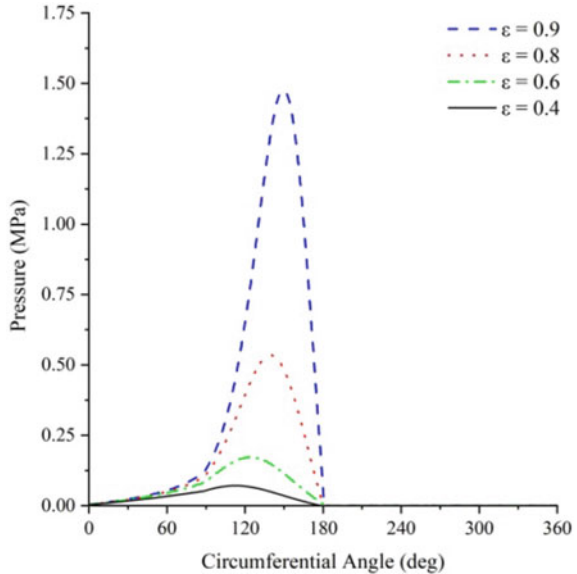


Fig. 5 Pressure versus bearing angle plot for different eccentricity ratios



4.2 Different Shaft Speeds

The model with 0.8 eccentricity ratio was simulated at different shaft speeds ranging from 1500 rpm through 3500 rpm for a comparison of pressure generated at different shaft speeds.

Figures 7 and 8 show the pressure and temperature contour for the model with shaft speed of 3500 rpm. Figure 6 shows a comparison of circumferential pressure distribution for different shaft speeds. It can be inferred from the plot that maximum pressure generated is directly proportional to shaft speed. The increase in pressure is not as prominent as it was for increase in eccentricity ratio, but is a significant change.

Bearings operating at high eccentricity ratios and at high speeds such as those in turbines generate tremendously high pressures, thereby having very high load carrying capacities.

4.3 Different Lubricants

Analyses on the 0.8 eccentricity ratio model were carried out at a constant speed of 2000 rpm while changing the lubricant properties for different lubricants. Table 3 gives all the details about the different lubricants used. These are ISO grade lubricants widely used in the industry with most of their physical properties readily available in catalogues.

Fig. 6 Pressure versus bearing angle plot for different shaft speeds

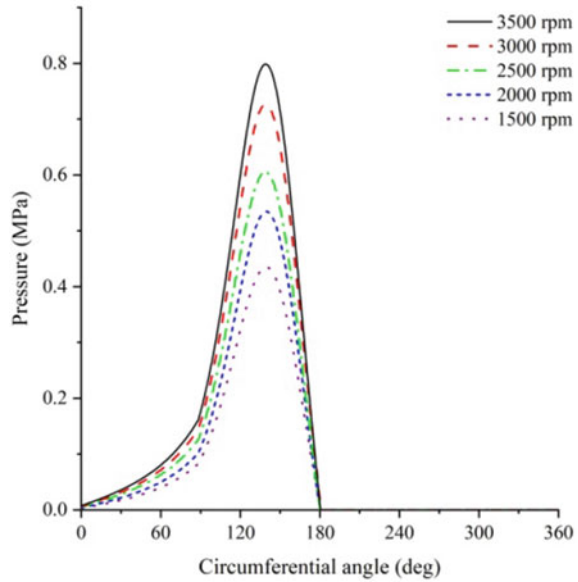
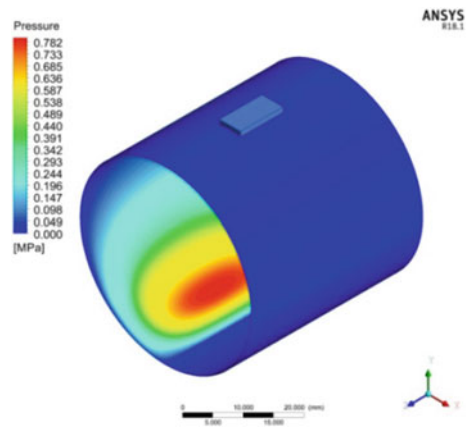


Fig. 7 Pressure contour (n = 3500 rpm)



Figures 9 and 10 show the pressure and temperature contour for one of the three lubricants simulated. Figure 11 shows the comparison of circumferential pressure distribution for different lubricants in a bearing with constant speed and eccentricity ratio. The increase in pressure with the change in lubricants can be attributed to increasing viscosity of the lubricants for a particular temperature. Using a viscous lubricant can lead to higher load carrying capacities but also higher inertial losses and high fluid temperature generation due to high shear stresses developed in moving the high viscosity fluid.

Fig. 8 Temperature contour
(n = 3500 rpm)

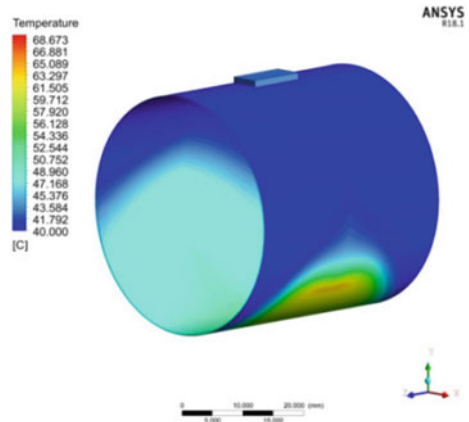


Table 3 Lubricant properties

Name	Density (kg/m ³)	Viscosity (cP)	Thermal conductivity (W/m K)	Specific heat (J/kg K)
		(40 °C, 100 °C)		
ISO vg 22	837.5	18.8, 3.7	0.134	1963
ISO vg 32	848.37	26.8, 4.6	0.132	1951
ISO vg 46	854.36	39.3, 5.8	0.132	1942

Fig. 9 Pressure contour
(ISO vg-46)

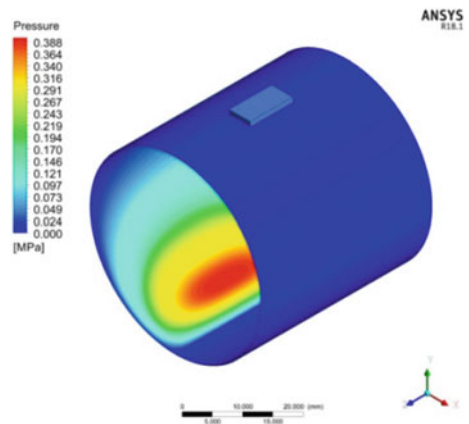


Fig. 10 Temperature contour (ISO vg-46)

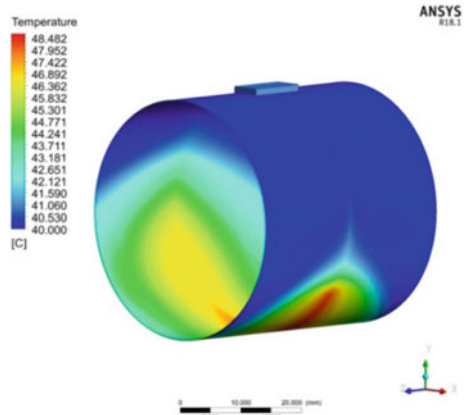
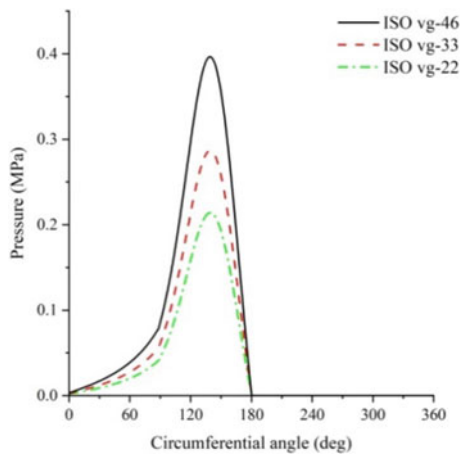


Fig. 11 Pressure versus bearing angle plot for different lubricants



5 Conclusion

In this work, CFD analysis of a journal bearing with top inlet is performed on suitable software. A 3 dimensional model is simulated for different eccentricity ratios, different shaft speeds, and different lubricants.

Analysis on bearings of different eccentricity ratios show that the increasing pressure is exponentially proportional to the increase in eccentricity ratio where the maximum pressure at 0.2 eccentricity ratio is around 10% of that at 0.9 eccentricity ratio.

Results on bearings operating at different speeds show that the increase in pressure is directly proportional to increase in the shaft speed. The pressure increase is not as high as the previous case but significant and can affect selection of a bearing system for a machine.

Lastly, a bearing running on different lubricants was simulated. Lubricants with higher viscosity produce more pressure thereby having more load carrying capacity but also generate higher temperatures which are an important parameter in selecting bearing lubricant. Higher accuracy for temperature analysis can be achieved by simulating solid bearing and shaft as well with the fluid film to consider the effects of conduction in them.

References

1. Sahu, M., Giri, A. K., & Das, A. (2012). Thermohydrodynamic analysis of a journal bearing using CFD as a tool. *International Journal of Scientific and Research Publications*, 2(9), 1–7.
2. Singla, A., Kumar, A., Bala, S., Singh, P., & Chauhan, A. (2014). Thermo-hydrodynamic analysis on temperature profile of circular journal bearing using computational fluid dynamics. In *Recent advances computational sciences (RAECS)* (pp. 1–6).
3. Udgire Manojkumar, N., Jagadish, H., & Kirankumar, B. (2020). CFD analysis of hydro-dynamic lubrication journal bearing using castor oil. In *Recent trends in mechanical engineering* (pp. 673–681).
4. Dhande, D. Y., & Pande, D. W. (2017). A two-way FSI analysis of multiphase flow in hydrodynamic journal bearing with cavitation. *Journal of the Brazilian Society of Mechanical Sciences and Engineering*, 39(9), 3399–3412.
5. Gertzos, K. P., Nikolakopoulos, P. G., & Papadopoulos, C. A. (2008). CFD analysis of journal bearing hydrodynamic lubrication by Bingham lubricant. *Tribology international*, 41(12), 1190–1204.
6. Kyrkou, M. E., & Nikolakopoulos, P. G. (2020). Simulation of thermo-hydrodynamic behavior of journal bearings, lubricating with commercial oils of different performance. *Simulation Modelling Practice and Theory*, 104, 102128.
7. Cupillard, S., Glavatskih, S., & Cervantes, M. J. (2008). Computational fluid dynamics analysis of a journal bearing with surface texturing. *Proceedings of the Institution of Mechanical Engineers, Part J: Journal of Engineering Tribology*, 222(2), 97–107.
8. Raimondi, A. A., & Boyd, J. (1958). A solution for the finite journal bearing and its application to analysis and design: III. *ASLE Transactions*, 1(1), 194–209.

Brain Tumour Segmentation Using cGAN with Residual (ResNet) Technique



Meenakshi M. Pawar, Suvarna D. Pujari, Swati P. Pawar,
and Anchit Narwadkar

Abstract A brain tumour is a malformed cell growth that can be either cancerous or non-cancerous. The most dangerous disease is a brain tumour, which can be detected. The tumour can be detected easily and reliably using automated techniques on MRI images. Many researchers have proposed several methods for effective tumour detection, including efficient diagnosis and segmentation of brain tumors. We propose conditional generative adversarial networks (cGAN)-based approach for brain tumour segmentation in this paper. cGAN is made up of two networks: the generator, which generates the brain tumour segmentation map, and the discriminator, which validates the generator output. Encoder-decoder architecture is used in the proposed generator. It encodes the input brain MRI slice into a set of features using the encoder network, and then uses the decoder network to generate the brain tumour segmentation map from the encoded features. To maintain structural consistency, feature maps generated by a specific encoder are shared with the corresponding decoder via skip connections i.e. ResNet. Unlike previous encoder-decoder architectures, we ran the encoder feature maps through a convolution layer before passing them to the appropriate decoder. It aids in the refinement of the encoded features. We trained the proposed network for brain tumour segmentation using the BraTS-15 training set. Its testing set, on the other hand, is used to validate the proposed network for brain tumour segmentation. The experimental analysis compares proposed and existing methods for brain tumour segmentation using the Dice similarity coefficient and the Jaccard index. When compared to existing methods, the proposed method outperforms them all for brain tumour segmentation.

Keywords Brain tumour · Deep learning · cGAN · Residual network

M. M. Pawar (✉) · S. D. Pujari

Department of Electronics and Telecommunication Engineering, SVERIs College of Engineering, Punyashlok Ahilyadevi Holkar Solapur University, Pandharpur, India
e-mail: mmpawar@coe.sveri.ac.in

S. P. Pawar

Department of Computer Science Engineering, SVERIs College of Engineering, Punyashlok Ahilyadevi Holkar Solapur University, Pandharpur, India

A. Narwadkar

Rubrics Softcon Pvt. Ltd., Pune, India

1 Introduction

The brain is one of the most complicated organs in the human body, working with a large number of cells. Brain tumours grow when cells divide uncontrollably, resulting in an irregular pattern. The group of cells will disrupt the normal functioning of brain activity and harm the healthy cell [1]. Support vector machine [2] and random forest have been widely used for automatic brain tumour segmentation as machine learning techniques have advanced. However, such approaches enable the collection of hand-crafted features for the learning of the corresponding machine learning model. Chattopadhyay et al. [3] proposed an algorithm to segment brain tumours from 2D Magnetic Resonance brain Images (MRI) by a convolutional neural network which is followed by traditional classifiers and deep learning methods. Ronneberger et al. [4] first presented a completely convoluted U-Net framework in 2015, inspired by a deep learning methodology. U-Net is comprised of a contractor path and a symmetrical expansion route, with skip connections in between. Mirror methods have been used to predict boundary pixels. Dipu et al. [5] proposed a YOLO V3 Pytorch, YOLO V4 Darknet, Scaled YOLO V4, YOLO V4 Tiny, YOLO V5, Faster-RCNN, and Detectron2. The network was less effective in segmenting the LGG cohort's enhancement area. Kong et al. [6] also present the hybrid Pyramid U-Net brain tumour segmentation model. They also improved the U-Net model, which presents global context knowledge in a variety of regional contexts. Alex et al. [7] proposed using a completely convoluted neural network to classify brain tumours from multimodal MR images (FCNN). They used a 23-layer voxel-based classification with a single forward pass followed by a false positive reduction using linked component analysis. On the BraTS dataset, Havaei et al. [8] improved brain tumour segmentation output. In their network, they used two-way and cascaded frameworks. For both local and global features, the two-way structure is used to identify two receptive fields. The pixel mark is determined by two factors: the visual characteristics of the marker and the location of the patch in the brain MRI scan. Wang et al. [9] generalised cascaded structure and used CNN for automated brain tumour segmentation. Hussain et al. [10] proposed a patch-based approach and used cascaded deep CNN for brain tumour segmentation.

The proposed encoder-decoder framework by Noh et al. [11] in the field of semantic segmentation of natural scenes consists of specific convolution and pooling layers and exhibits high-resolution features in low-level conspicuous edges. Badrinarayanan et al. [12] proposed SegNet, a redesigned encoder-decoder architecture that overcomes the shortcomings of [11]. The max-pooling indexes effectively retain all information without memorising the float-precision feature maps, and the following decoder displays the input feature map(s) using specific indices. Drozdal et al. [13] extended SegNet to segment brain tumours. The advantages of identity mappings (i.e. short skip connections) over long skip links (as used in U-Net) were used by the authors in [4]. Such identity mappings enable the creation of a deeper CNN without the gradient disappearing, as well as rapid network learning with proper recovery of spatial information lost during down sampling. Researchers

[14–16] used small kernel sizes to create a more complex network architecture. Deep CNN 3 3 kernels were added by Pereira et al. [16]. This model used fewer weights to generate feature maps, which reduced over-fitting. Different architectures are used for LGG and HGG. In the post-processing phase, a minimal volumetric restriction was used to eliminate the error caused by incorrect cluster classification. Kamnitsas et al. [17] include a fully-connected, conditional random field (CRF) 3D CNN for accurate brain lesion segmentation. The 3D CNN architecture has 11 layers and handles neighbouring image patches in a single pass while accounting for the inherent class disparity. For multi-scale feature extraction, they used a dual route architecture. Cui et al. [18] segment brain tumours using a deep cascaded NN, which combines a tumour detection network and an intratumor classification network. Lin et al. [19] also employ dense CRF-learning in conjunction with CNNs for segmentation refinement. Zhao et al. [20] used FCNN in conjunction with CRF to increase tumour segmentation activity. The approaches described above were all based on a patch-based approach in which medical scans were mostly separated into patches during training and testing. As a result, there is a need for a model that takes the entire medical scan as input and can be used to address the data imbalance class by integrating both local and global features.

2 Related Work

2.1 Related Studies

Most computer vision applications, such as image-to-image style transfer [21], image super-resolution [22], image depth estimation [23], image de-hazing [24–27], and moving object segmentation [28–33], have been investigated in recent years using an adversarial training approach (especially for image-to-image translation). In medical image segmentation, the robustness of adversarial training in image-to-image translation has been used. In medical image processing, adversarial techniques are frequently employed and have the potential to yield excellent results [34, 35]. An end-to-end adversarial network was introduced by Xue et al. [35] for the segmentation of brain tumours from the results of an MRI scan. The fundamental concept behind this segmentor (i.e. generator) network as an FCNN for producing segmentation label maps and a critical network (i.e. discriminator) for multi-scale L1 failure is the classic generative adversarial network (GAN) architecture. The vital network received two inputs: the ground truth label maps, which mask the real brain MRI images, and the predicted segmentor label maps, which mask the real brain MRI images. Segmentor learning aims to reduce multi-scale loss of L1, while critical training aims to optimise the same loss function. Segmentor and critical networks are alternately trained in a min-max manner. For the segmentation of brain tumours, the author of [36] proposed an unpaired conditional adversarial training approach. Rezaei et al.'s conditional GAN [21] was expanded for use in segmenting brain

tumours in MRI images in their study by Rezaei et al. For BraTS 2017, a semantic CNN and an adversarial network were suggested.

In this paper, we propose a conditional generative adversarial networks-based method for segmenting brain tumours, which is inspired by the existing methods. The following is a summary of the proposed work.

- A conditional generative adversarial network is suggested for segmenting brain tumours.
- Principles of encoder-decoder architecture and residual learning are used to design a generator and discriminator network.
- Before sharing them with the appropriate decoder feature maps, encoder feature refinement has been applied.

3 Material and Method

The proposed conditional generative adversarial networks (cGAN) A mapping from a random noise vector z to the output image y , known as $G: z \rightarrow y$, is learned by generative models called GANs. Conditional GANs, in contrast, learn a mapping from an observed image (x) and a random noise vector (z) to (y), where $G: x, z, y$. The generator G is specifically trained to produce a brain tumour segmentation map that cannot be distinguished from a brain tumour map created using the ground truth. Contrarily, discriminator D is taught to distinguish between the output of the generator and the true ground truth. Figure 1 depicts this training procedure in diagram form.

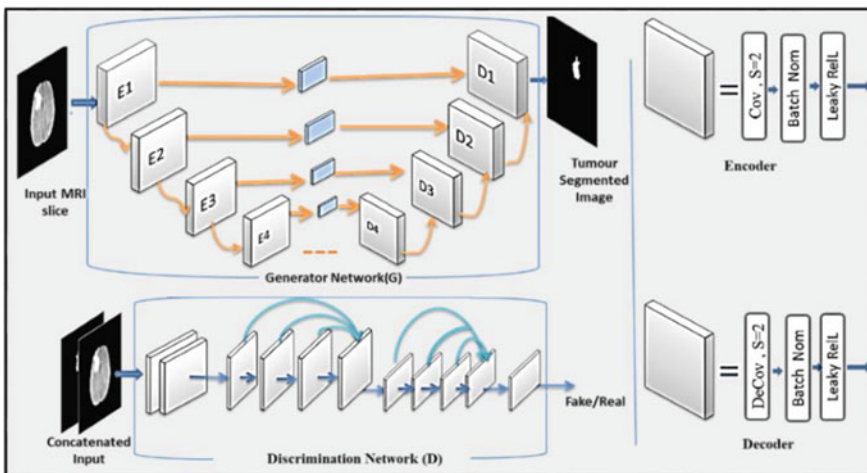


Fig. 1 The proposed approach for brain tumor segmentation—the proposed generator network and discriminator network using residual network

The a conditional GAN can be expressed as,

$$\text{lcGAN}(G, D) = \mathbb{E}_x, y[\log D(x, y)] + \mathbb{E}_x, z[\log(1 - D(x, G(x, z)))] \quad (1)$$

The proposed cGAN has two network (I) Generator Network; (ii) Discriminator Network.

3.1 Generator Network

The encoder-decoder architecture used in the proposed generator network. It uses an encoder network to convert the input brain MRI slice into a set of features, and then a decoder network to create a segmentation map of the brain tumour using the encoded features. Three components make up the proposed generator network: (1) Encoder and Decoder (2) Useful feature sharing strategy as demonstrated in Fig. 1.

3.1.1 Encoder and Decoder

The proposed generator network consists of eight encoder modules. Convolution layers, batch normalisation, and leaky rectified linear units make up each encoder module (leaky ReLU). Convolution layer is used in this context to extract features. While the leaky ReLU is intended to cause the network to become non-linear. To normalize the learned feature maps, batch normalization is used. In each convolution layer of the encoder module, Stride is maintained at 2. However, each leaky ReLU layer has a leaky factor of 0.2.

The path taken by the encoder modules is a straightforward one, consisting of feature extraction via a convolution layer, downsampling, and so forth. Eight encoder modules process the input 256×256 size brain MRI slice in this way, arriving at a feature vector that is $1 \times 1 \times 512$ size in total. Figure 1 depicts the proposed encoder module, while Fig. 1 illustrates how it would be used. The decoder module's job is to unravel the encoder feature maps and up-sample them. We have eight decoder modules that we have designed to keep the network symmetric. Every decoder module starts with a deconvolution layer with a stride/up-sampling factor of 2, then moves on to batch-normalization and leaky ReLU with a leaky factor of 0.02. Thus, the proposed generator network finally produces the brain tumour segmentation map using the trail of the eight decoder modules. Figure 1 depicts the proposed decoder module and illustrates how it would be used.

3.1.2 Feature Sharing Strategy

Sharing features observed at initial layers across the network is crucial, along with extracting multi-scale features. For instance, in [21], the author distributed across the

network the features learned at the initial layers for the image-to-image translation task. The feature sharing strategy proves successful in keeping the sharp edges in the desired output image map. As a result, feature maps produced by a specific encoder module are shared with the corresponding decoder module via skip connections to preserve structural consistency. Contrary to existing encoder-decoder architectures [4, 21, 37], we convolutional processed the encoder feature maps before passing them along to the appropriate decoder. It supports in fine-tuning the encoded features and proved successful in retaining the prominent edge information important to the segmentation of brain tumours. In Fig. 1, the modified feature sharing approach is indicated.

3.1.3 Discriminator Network

In order to differentiate between the actual brain tumor segmentation map and the one generated using the proposed generator network, we used the discriminator network proposed in [27]. For feature extraction, it consists of the residual block with complicated feature sharing. Figure 1 shows the discriminator network with the residual block.

4 Result and Discussion

From the BraTS-2015 dataset 90% of the brain MRI slices were taken into account. These 90% brain MRI slices show no overlap with the training data. Table 1 provides a quantitative evaluation of the suggested and existing methods. The second-best method [6] has a DICE similarity coefficient of 0.8993. While the DICE similarity coefficient for the proposed method, which is 0.9225, is the highest.

Brain tumour segmentation map obtained using proposed approach is mapped on the original brain MRI image. The Input brain MRI image, Proposed approach

Table 1 Performance comparison between the proposed method and existing state-of-the-art methods for the whole tumor segmentation on BraTS 2015 database

Method	Publication year	Testing data %	Sensitivity
Pereira et al. [16]	2016	15	0.87
Zhao et al. [20]	2018	18	0.81
Kamnitsas et al. [17]	2017	40	0.88
Cui et al. [18]	2018	10	0.87
Xue et al. [35]	2018	10	0.8
Kong et al. [6]	2018	30	0.9581
Proposed method		90	0.9653

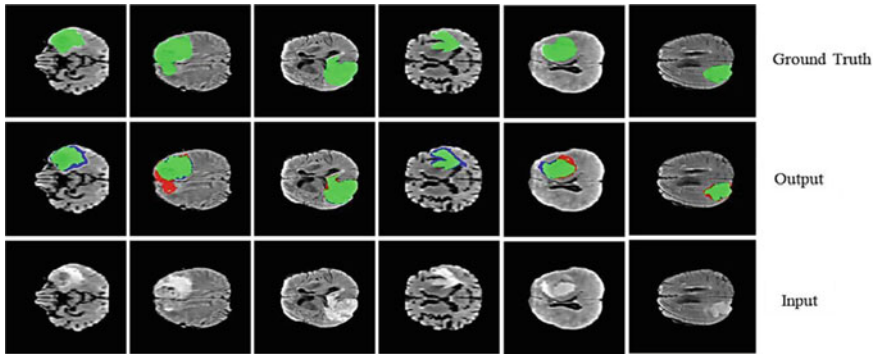


Fig. 2 Visual results of the proposed approach for brain tumour segmentation

and Ground truth. Green, red and blue color indicates the accurate segmentation, under-segmentation and over-segmentation respectively.

This is an interesting fact: while [6] validated their method on 30% of the brain MRI slices from the BraTS dataset, the proposed network was validated on 9% of the slices. Sensitivity is similar in this regard. On 30% of the test data, Method [6] achieves the highest Sensitivity value of 0.9653. While using 90% of the testing data, the proposed network achieves a sensitivity value of 0.9653. It is observed from Table 1 that the proposed method outperforms the other existing methods for brain tumour segmentation in terms of the evaluation parameters.

For the analysis, we used a sample set of brain MRI images. The segmentation map of a brain tumour created using the proposed methodology is shown in Fig. 2. It is obvious from 2 that the brain tumour segmentation maps produced by the suggested method converge on the actual segmentation maps of the tumours. We attribute this to the proposed generator network, which combines a modified feature-sharing approach with encoder-decoder architecture [38–43].

5 Conclusion

In this paper, we present a conditional generative adversarial network-based method for segmenting brain tumours. It has two networks that serve as the discriminator and generator. For the purpose of producing the brain tumour segmentation map for a given input brain MRI image, we have designed an encoder-decoder based generator network. In contrast to the conventional approach, we propose a modified feature sharing approach to transfer the features discovered at the encoder module to the appropriate decoder module over the network. To train and test the suggested network for brain tumour segmentation, we used the 10% and 90% brain MRI slices from the BraTS-2015 dataset, respectively. The proposed network for the segmentation of brain tumours has been validated through the use of both qualitative and quantitative

analysis. The experimental analysis proves that the proposed method for segmenting brain tumours performs better than the other ones currently in use.

References

1. Amin, J., Anjum, M. A., Sharif, M., Jabeen, S., Kadry, S., & Moreno Ger, P. (2022). A new model for brain tumor detection using ensemble transfer learning and quantum variational classifier. *Computational Intelligence and Neuroscience*, 2022.
2. Ayachi, R., & Ben Amor, N. (2009, July). Brain tumor segmentation using support vector machines. In *European Conference on Symbolic and Quantitative Approaches to Reasoning and Uncertainty* (pp. 736–747). Springer.
3. Chattopadhyay, A., & Maitra, M. (2022). MRI-based brain tumor image detection using CNN based deep learning method. *Neuroscience Informatics*, 100060.
4. Ronneberger, O., Fischer, P., & Brox, T. (2015, October). U-net: Convolutional networks for biomedical image segmentation. In *International Conference on Medical Image Computing and Computer-Assisted Intervention* (pp. 234–241). Springer.
5. Dipu, N. M., Shohan, S. A., & Salam, K. A. (2021, August). Brain tumor detection using various deep learning algorithms. In *2021 International Conference on Science & Contemporary Technologies (ICSCT)* (pp. 1–6). IEEE.
6. Kong, X., Sun, G., Wu, Q., Liu, J., & Lin, F. (2018, October). Hybrid pyramid u-net model for brain tumor segmentation. In *International Conference on Intelligent Information Processing* (pp. 346–355). Springer.
7. Alex, V., Safwan, M., & Krishnamurthi, G. (2017). Brain tumor segmentation from multi modal MR images using fully convolutional neural network. In *Medical Image Computing and Computer Assisted Intervention-MICCAI* (pp. 1–8).
8. Havaei, M., Davy, A., Warde-Farley, D., Biard, A., Courville, A., Bengio, Y., Pal, C., Jodoin, P. M., & Larochelle, H. (2017). Brain tumor segmentation with deep neural networks. *Medical Image Analysis*, 35, 18–31.
9. Wang, G., Li, W., Ourselin, S., & Vercauteren, T. (2018). Automatic brain tumor segmentation using cascaded anisotropic convolutional neural networks. In *Brainlesion: Glioma, Multiple Sclerosis, Stroke and Traumatic Brain Injuries: Third International Workshop, BrainLes 2017*, Held in Conjunction with MICCAI 2017, Quebec City, QC, Canada, September 14, 2017, Revised Selected Papers 3 (pp. 178–190). Springer.
10. Hussain, S., Anwar, S. M., & Majid, M. (2017, July). Brain tumor segmentation using cascaded deep convolutional neural network. In *2017 39th Annual International Conference of the IEEE Engineering in Medicine and Biology Society (EMBC)* (pp. 1998–2001). IEEE.
11. Noh, H., Hong, S., & Han, B. (2015). Learning deconvolution network for semantic segmentation. In *Proceedings of the IEEE International Conference on Computer Vision* (pp. 1520–1528).
12. Badrinarayanan, V., Kendall, A., & Cipolla, R. (2017). Segnet: A deep convolutional encoder-decoder architecture for image segmentation. *IEEE Transactions on Pattern Analysis and Machine Intelligence*, 39(12), 2481–2495.
13. Drozdal, M., Vorontsov, E., Chartrand, G., Kadoury, S., & Pal, C. (2016). The importance of skip connections in biomedical image segmentation. In *Deep learning and data labeling for medical applications* (pp. 179–187). Springer.
14. Soomro, T. A., Zheng, L., Afifi, A. J., Ali, A., Soomro, S., Yin, M., & Gao, J. (2022). Image segmentation for MR brain tumor detection using machine learning: A review. *IEEE Reviews in Biomedical Engineering*.
15. He, K., Zhang, X., Ren, S., & Sun, J. (2016). Deep residual learning for image recognition. In *Proceedings of the IEEE Conference on Computer Vision and Pattern Recognition* (pp. 770–778).

16. Pereira, S., Pinto, A., Alves, V., & Silva, C. A. (2016). Brain tumor segmentation using convolutional neural networks in MRI images. *IEEE Transactions on Medical Imaging*, 35(5), 1240–1251.
17. Kamnitsas, K., Ledig, C., Newcombe, V. F., Simpson, J. P., Kane, A. D., Menon, D. K., Rueckert, D., & Glocker, B. (2017). Efficient multi-scale 3D CNN with fully connected CRF for accurate brain lesion segmentation. *Medical Image Analysis*, 36, 61–78.
18. Cui, S., Mao, L., Jiang, J., Liu, C., & Xiong, S. (2018). Automatic semantic segmentation of brain gliomas from MRI images using a deep cascaded neural network. *Journal of Healthcare Engineering*, 2018.
19. Lin, G. C., Wang, W. J., Wang, C. M., & Sun, S. Y. (2010). Automated classification of multi-spectral MR images using linear discriminant analysis. *Computerized Medical Imaging and Graphics*, 34(4), 251–268.
20. Zhao, X., Wu, Y., Song, G., Li, Z., Zhang, Y., & Fan, Y. (2018). A deep learning model integrating FCNNs and CRFs for brain tumor segmentation. *Medical Image Analysis*, 43, 98–111.
21. Isola, P., Zhu, J. Y., Zhou, T., & Efros, A. A. (2017). Image-to-image translation with conditional adversarial networks. In *Proceedings of the IEEE Conference on Computer Vision and Pattern Recognition* (pp. 1125–1134).
22. Thawakar, O., Patil, P. W., Dudhane, A., Murala, S., & Kulkarni, U. (2019, September). Image and video super resolution using recurrent generative adversarial network. In *2019 16th IEEE International Conference on Advanced Video and Signal Based Surveillance (AVSS)* (pp. 1–8). IEEE.
23. Malik, R., Hambarde, P., & Murala, S. (2022, July). Depth estimation using sparse depth and transformer. In *Computer Vision and Image Processing: 6th International Conference, CVIP 2021, Rupnagar, India, December 3–5, 2021, Revised Selected Papers, Part II* (pp. 329–337). Springer.
24. Murala, S., & Dudhane, A. (2018). C2MSNet: A novel approach for single image haze removal.
25. Dudhane, A., & Murala, S. (2019). RYF-Net: Deep fusion network for single image haze removal. *IEEE Transactions on Image Processing*, 29, 628–640.
26. Dudhane, A., & Murala, S. (2019, January). Cdnet: Single image de-hazing using unpaired adversarial training. In *2019 IEEE Winter Conference on Applications of Computer Vision (WACV)* (pp. 1147–1155). IEEE.
27. Dudhane, A., Singh Aulakh, H., & Murala, S. (2019). Ri-gan: An end-to-end network for single image haze removal. In *Proceedings of the IEEE/CVF Conference on Computer Vision and Pattern Recognition Workshops* (pp. 0–0).
28. Patil, P. W., & Murala, S. (2018). MSFgNet: A novel compact end-to-end deep network for moving object detection. *IEEE Transactions on Intelligent Transportation Systems*, 20(11), 4066–4077.
29. Patil, P. W., Murala, S., Dhall, A., & Chaudhary, S. (2018, October). Msednet: Multi-scale deep saliency learning for moving object detection. In *2018 IEEE International Conference on Systems, Man, and Cybernetics (SMC)* (pp. 1670–1675). IEEE.
30. Patil, P., & Murala, S. (2019, January). Fggan: A cascaded unpaired learning for background estimation and foreground segmentation. In *2019 IEEE Winter Conference on Applications of Computer Vision (WACV)* (pp. 1770–1778). IEEE.
31. Patil, P. W., Thawakar, O., Dudhane, A., & Murala, S. (2019, September). Motion saliency based generative adversarial network for underwater moving object segmentation. In *2019 IEEE International Conference on Image Processing (ICIP)* (pp. 1565–1569). IEEE.
32. Patil, P. W., Dudhane, A., Murala, S., & Gonde, A. B. (2020). A novel saliency-based cascaded approach for moving object segmentation. In *Computer Vision and Image Processing: 4th International Conference, CVIP 2019, Jaipur, India, September 27–29, 2019, Revised Selected Papers, Part I 4* (pp. 311–322). Springer.
33. Patil, P. W., Biradar, K. M., Dudhane, A., & Murala, S. (2020). An end-to-end edge aggregation network for moving object segmentation. In *Proceedings of the IEEE/CVF Conference on Computer Vision and Pattern Recognition* (pp. 8149–8158).

34. Nie, D., Trullo, R., Lian, J., Wang, L., Petitjean, C., Ruan, S., Wang, Q., & Shen, D. (2018). Medical image synthesis with deep convolutional adversarial networks. *IEEE Transactions on Biomedical Engineering*, 65(12), 2720–2730.
35. Xue, Y., Xu, T., Zhang, H., Long, L. R., & Huang, X. (2018). SegAN: Adversarial network with multi-scale L1 loss for medical image segmentation. *Neuroinformatics*, 16(3), 383–392.
36. Nema, S., Dudhane, A., Murala, S., & Naidu, S. (2020). RescueNet: An unpaired GAN for brain tumor segmentation. *Biomedical Signal Processing and Control*, 55, 101641.
37. Zhu, J. Y., Park, T., Isola, P., & Efros, A. A. (2017). Unpaired image-to-image translation using cycle-consistent adversarial networks. In *Proceedings of the IEEE International Conference on Computer Vision* (pp. 2223–2232).
38. Li, Z., Wang, Y., Yu, J., Guo, Y., & Cao, W. (2017). Deep learning based radiomics (DLR) and its usage in noninvasive IDH1 prediction for low grade glioma. *Scientific Reports*, 7(1), 1–11.
39. Wu, Z., Paulsen, K. D., & Sullivan, J. M. (2005). Adaptive model initialization and deformation for automatic segmentation of T1-weighted brain MRI data. *IEEE Transactions on Biomedical Engineering*, 52(6), 1128–1131.
40. Liu, J., Chen, F., Pan, C., Zhu, M., Zhang, X., Zhang, L., & Liao, H. (2018). A cascaded deep convolutional neural network for joint segmentation and genotype prediction of brainstem gliomas. *IEEE Transactions on Biomedical Engineering*, 65(9), 1943–1952.
41. Menze, B. H., Jakab, A., Bauer, S., Kalpathy-Cramer, J., Farahani, K., Kirby, J., Burren, Y., Porz, N., Slotboom, J., Wiest, R., & Van Leemput, K. (2014). The multimodal brain tumor image segmentation benchmark (BRATS). *IEEE Transactions on Medical Imaging*, 34(10), 1993–2024.
42. Rezaei, M., Harmuth, K., Gierke, W., Kellermeier, T., Fischer, M., Yang, H., & Meinel, C. (2018). A conditional adversarial network for semantic segmentation of brain tumor. In *Brain-lesion: Glioma, Multiple Sclerosis, Stroke and Traumatic Brain Injuries: Third International Workshop, BrainLes 2017*, Held in Conjunction with MICCAI 2017, Quebec City, QC, Canada, September 14, 2017, Revised Selected Papers 3 (pp. 241–252). Springer.
43. Yi, D., Zhou, M., Chen, Z., & Gevaert, O. (2016). 3-D convolutional neural networks for glioblastoma segmentation. arXiv preprint [arXiv:1611.04534](https://arxiv.org/abs/1611.04534)

Effect of Patch Length on Electroosmotic Mixing Characteristics Inside a Heterogeneously Charged Micromixer



Anindya Nath, Sumit Kumar Mehta, and Sukumar Pati

Abstract The flow and mixing attributes within a micromixer with heterogeneous surface charge is investigated. The finite element approach is used to numerically compute the governing transport equations. By varying the patch lengths (H_P) and the diffusive Peclet number (Pe) in the physically reasonable span, the flow field, dimensionless flow rate, recirculation velocity (U_R), species concentration field, and mixing efficiency (η) are explored. It reveals that as patch length is increased, the size of the regions of recirculation and U_R both augment while an increment in patch length diminishes the flow rate. Moreover, as H_P increases, the homogeneity of the outlet dimensionless species concentration improves and gets closer to 0.5. There is a critical Pe ($Pe_{cri,1}$) over which mixing efficiency is 100% for all H_P and $Pe_{cri,1}$ increases as H_P increases. Contrarily, for $Pe > Pe_{cri,1}$, mixing efficiency decreases as Pe increases.

Keywords Micromixing · Electroosmosis · Diffusive Peclet number

1 Introduction

Micromixing has gained immense attention due to its numerous applications in the biomedical sector, chemical, and other fields [1]. An electroosmotic micromixer, where the flow actuation is accomplished by an external electric field, amongst other active mixers has countless expediency due to ease of design, inexpensive manufacturing, etc. [2].

A. Nath (✉) · S. K. Mehta · S. Pati
Department of Mechanical Engineering, National Institute of Technology Silchar, Silchar 788010, India
e-mail: anindyanath1457@gmail.com

S. Pati
e-mail: sukumar@mech.nits.ac.in

Biddiss et al. [3] studied the ramifications of surface charge heterogeneities on an electroosmotic micromixer and concluded that mixing efficiencies improved substantially for 70–555 V/cm external electric field range. The non-Newtonian fluid's electroosmotic mixing in a slit microscale mixer with a non-uniform zeta potential was studied by Hadigol et al. [4]. They observed that when fluid shows shear-thinning behavior, electroosmotic mixing is an appreciable mixing method. Vasista et al. [2] further examined the zeta potential slip dependence of the mixing traits in a heterogeneous charged 2-D micromixer. They claimed that up to the critical diffusive Peclet number, mixing efficiency is 100% and the slip length and Debye parameter results in augmented critical diffusive Peclet number. Recently, many researchers also examined the impact of surface charge non-uniformity on mixing performance for obstructed [5, 6] and wavy [7, 8] micromixers.

Upon careful relevant literature investigation, it is revealed that the effect of positively charged patch length by simultaneous variation in diffusive Peclet number remained unexplored, which forms the objective of the current study.

2 Problem Formulation

The external electric field intensity (E) is imposed across a micromixer with channel half-height, H and length, $20H$ [2] as depicted in Fig. 1. The flow is regarded to be steady, laminar, two-dimensional, and incompressible. Two working fluids viz. tracer fluid (fluid 1) and pure fluid (fluid 2) having same the thermo-physical properties enter through the upper and lower half of the inlet, respectively. Positively charged patches of length H_P are distributed in a staggered fashion on the upper and lower walls along the length of the channel with gaps $H_G (= H_P)$ (see Fig. 1). The other parts of the walls have a negative zeta potential resulting in a net flow in the positive x -direction. Moreover, the Peclet number for the ions is considered to be far less than unity ($Pe_i \ll 1$) [2] rendering the ionic distribution static. The electrolyte is assumed to be symmetric ($Z:Z$) while the finite ionic volume effect is disregarded as the zeta potential is less than 330 mV [2]. Further, the Joule heating effect is neglected as $E \sim 10,000$ V/m [2].

The EDL potential distribution is given by the solution of non-dimensional Poisson-Boltzmann equation and expressed as [2]:

$$\nabla^2 \psi = \kappa^2 \sinh \psi \quad (1)$$

Here, $\nabla \equiv (\partial/\partial X, \partial/\partial Y)$, $X = x/H$, $Y = y/H$, $\psi (= \bar{\psi}/\psi_{ref})$ is the normalized EDL potential, $\kappa (= H/\lambda)$ is the Debye parameter and $\lambda (= (2n_0 Z^2 e^2 / \epsilon_0 \epsilon_r k_B T)^{-1/2})$ is the Debye length, where n_0 is the bulk ionic bulk concentration, ϵ_0 is the absolute permittivity of free space, ϵ_r is the relative permittivity of the medium. The boundary conditions for the equation are $\mathbf{n} \cdot \nabla \psi = 0$ at $x = 0$ and at $x = 20H$; $\psi = \zeta$ for the patches and $\psi = -\zeta_w$ for other walls; \mathbf{n} being the non-dimensional unit normal

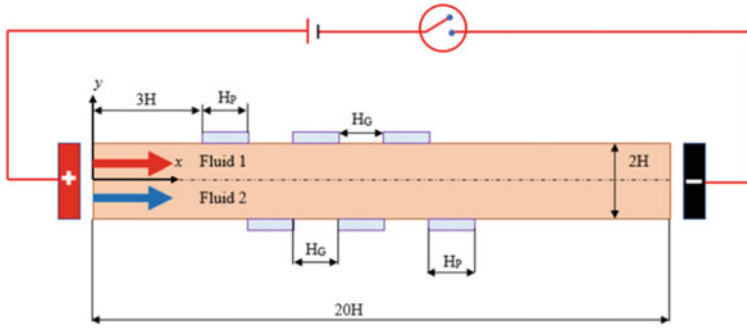


Fig. 1 Physical domain of the heterogeneously charged electroosmotic micromixer

to any surface, $\zeta (= \bar{\zeta} / \psi_{ref})$ and $\zeta_w (= \bar{\zeta}_w / \psi_{ref})$ are the non-dimensional zeta potentials at the patch surface and the other wall surface, respectively.

The continuity, momentum and the species transport equations in the dimensionless form are respectively [2]:

$$\nabla \cdot \mathbf{V} = 0, \tag{2}$$

$$Re(\mathbf{V} \cdot \nabla)\mathbf{V} = -\nabla P + \nabla^2 \mathbf{V} + \kappa^2 \sinh \psi, \tag{3}$$

$$Pe\mathbf{V} \cdot (\nabla C) = \nabla^2 C. \tag{4}$$

where $\mathbf{V} (= (U\mathbf{i} + V\mathbf{j}) = (u\mathbf{i} + v\mathbf{j})/v_{HS})$ is the dimensionless velocity vector, $v_{HS} (= ((\epsilon_0 \epsilon_r E \psi_{ref}) / \mu))$ is scale for velocity, P is the dimensionless pressure whose scale is $\mu v_{HS} / H$, μ is the dynamic viscosity, $C (= c/c_{ref})$ is the dimensionless species concentration, D is the species diffusion co-efficient, $Re (= \rho v_{HS} / H)$ is the Reynolds number and $Pe (= v_{HS} H / D)$ is the diffusive Peclet number.

The boundary conditions that are inflicted are the differential in external pressure across the micromixer ends is zero, $C = 1$ for the upper part of inlet ($0 \leq Y \leq 1$) and $C = 0$ for the lower part of inlet ($-1 \leq Y \leq 0$) at $x = 0$, $\partial C / \partial X = 0$ at $x = 20H$, $\mathbf{V} = 0$ and $\mathbf{n} \cdot \nabla C = 0$ at $Y = -1$ and $Y = 1$.

The non-dimensional flow rate per unit width for the micromixer at the outlet in normalized form is given by [2]:

$$\dot{V} = \int_{-1}^1 U dY. \tag{5}$$

The dimensionless flow rate (\dot{V}) is scaled as $\dot{V} = \bar{V} / \bar{V}_{ref}$, where \bar{V} is the flow rate per unit width and $\bar{V}_{ref} (= v_{HS} H)$ is scale for flow rate per unit width.

Further, the parameter, which measures the mixing performance, is the mixing efficiency (η) and is gauged at the outlet using the following equation [2]:

$$\eta = 100 \left[1 - \left(\int_{-1}^1 |C - C_{fm}| dY \right) / \left(\int_{-1}^1 |C_{um} - C_{fm}| dY \right) \right], \quad (6)$$

where, C_{um} ($= 0$ or 1) and C_{fm} ($= 0.5$) portray the pure fluid concentration and the fully mixed fluid concentration respectively. $\eta = 0$ and $\eta = 100$ correspond to pure fluid and fully mixed states, respectively.

3 Numerical Method and Validation

The transport variables are calculated using COMSOL Multiphysics [9], a finite element method-based software. By generating non-uniform triangular meshes, the computational domain is subdivided into the sub-domains. The transport equations are calculated iteratively until the residual criteria are met for all of the transport variables as 10^{-6} . After conducting the grid independency test (Table 1), grid with 49,387 elements has been chosen for simulations (Fig. 2).

The results of the current study have been validated by comparison with those of Biddiss et al. [3] at $E = 7000$ and 28000 V/m, where the micromixer is uniformly charged with electroosmotic mobility of -5.9×10^{-4} $\text{cm}^2/\text{V}^{-\text{s}}$. It is considered that the mass diffusion coefficient is 4.37×10^{-10} m^2/s . The precision of the current numerical model is attested to by the close agreement between the current and established data.

Fig. 2 Comparison of the outlet dimensionless species concentration profile for the uniformly charged micromixer outlet having inlet height $200 \mu\text{m}$ with the results of Biddiss et al. [3]

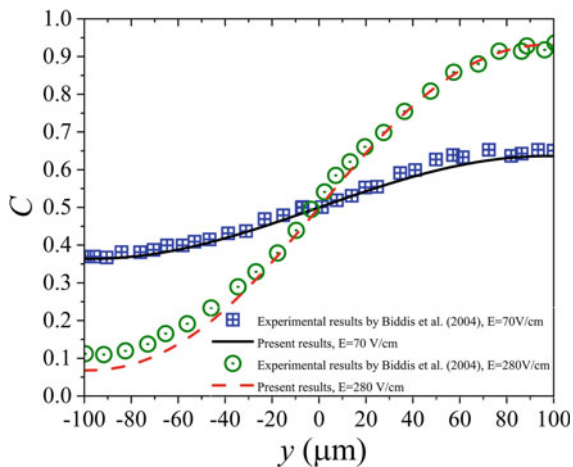


Table 1 Representation of grid independency test by calculating mixing efficiency when $\kappa = 30$, $H_P = 2$, $\zeta = 1.5$ and $Pe = 1000$

Number of elements	Mixing efficiency	Percentage difference in mixing efficiency w.r.t. mesh system M4
12,316	73.799	0.85
21,523	74.131	0.404
49,387	74.310	0.16
113,641	74.431	0

4 Results and Discussion

The flow field and mixing traits inside the heterogeneously charged micromixer have been investigated. The flow field, dimensionless flow rate, recirculation velocity, species concentration field and mixing efficiency are inspected by differing the patch length (H_P) and the diffusive Peclet number (Pe). H_P is assigned three discrete values— $H_P = H, 1.5H$ and $2H$, where H is the channel half height of the micromixer which is chosen as $20 \mu\text{m}$. Pe is varied in between 1 and 1000 [3, 8]. The Debye parameter (κ), dimensionless zeta potential for patches (ζ) and dimensionless wall zeta potential for other walls (ζ_w) are taken as $30 + 1.5$ ($= 37.5 \text{ mV}$) and -1 ($= -25 \text{ mV}$), respectively [4, 7, 8]. The value of Re is fixed as 0.0035 corresponding to $\varepsilon = 78$, $E = 10,000 \text{ V/m}$, $\mu = 0.001 \text{ Pa}^{-\text{s}}$, $\rho = 1000 \text{ kg/m}^3$ and $\psi_{ref} = 25 \text{ mV}$ [10, 11].

The flow field and streamlines are depicted in Fig. 3 for the three different values of H_P . Regions of recirculation are formed near the positively charged patches, which is due to interaction between the positively charged patches and the employed electric field from left to right causing electroosmotically impelled flow from right to left. Simultaneously, the opposite effect is observed at the negatively charged wall surface, where flow takes place from left to right. Since, the length of the negatively charged surface is greater than that of the gross length of the positively charged patches; the net flow is actuated from left to right. Further, immensity recirculation regions intensify with the increase in H_P , which is due to the augmented region of reverse flow with the increase in length of positively charged patches.

Recirculation strength in terms of dimensionless recirculation velocity (U_R) is also explored. Notably, U_R is the maximum reverse flow velocity in the domain [7]. The variation of U_R with H_P is presented in Fig. 4a. It is seen that U_R enhances with H_P , which is due to an increase in positively charged surface area and consequent region of reverse flow. The percentage increase in U_R is 31.21% as H_P increases from H to $2H$. Also, the dimensionless flow rate (\dot{V}) variation with H_P is depicted in Fig. 4b. It is seen that \dot{V} decreases with an increase in H_P as a larger recirculation zone at higher H_P causes higher flow resistance (see Fig. 3). The percentage decrease in \dot{V} is 60.4% as H_P increases from H to $2H$.

Figure 5 shows the contours of dimensionless species concentration (C) with change in H_P . C approaches 0.5 at a shorter length from the inlet as H_P increases.

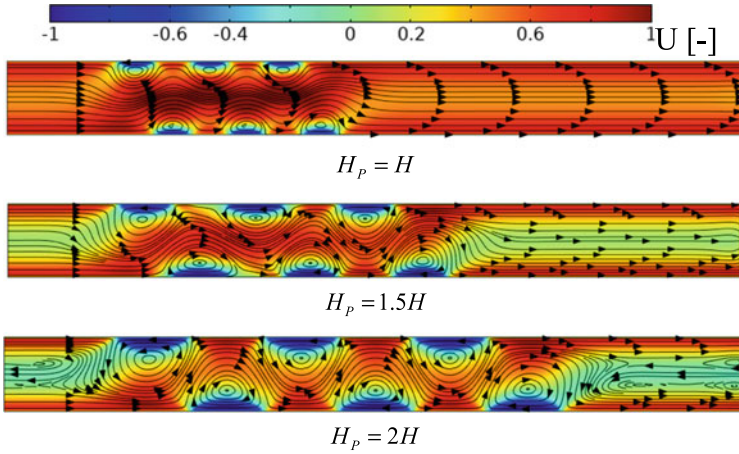


Fig. 3 Contours of flow velocity and streamlines at different patch length (H_p) when $\kappa = 30$ and $\zeta = 1.5$

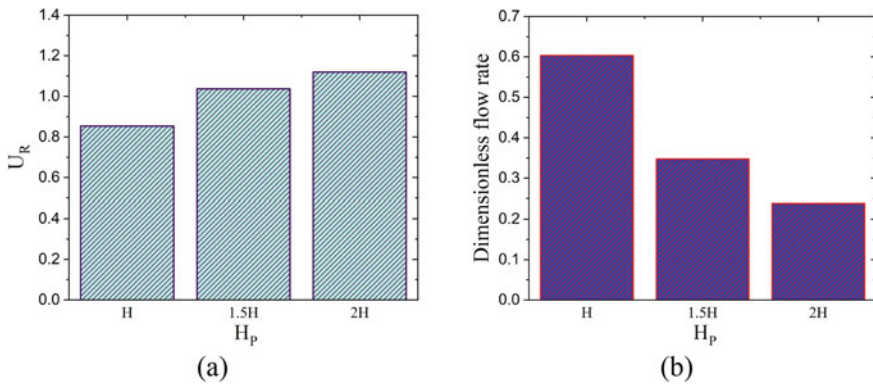


Fig. 4 a Dimensionless recirculation velocity and **b** dimensionless flow rate at different patch length (H_p) when $\kappa = 30$ and $\zeta = 1.5$

This is due to an increase in recirculation intensity with an increment in H_p , allows for greater convection mixing strength. In other words, uniformity in C at the outlet of the micromixer is higher and approaches to 0.5 for higher H_p .

The plot depicting the mixing efficiency (η) versus Pe for discrete values of H_p is presented in Fig. 6. It can be noted that η is almost 100% at lower Pe prior to a certain limit ($Pe_{cri,1}$) and these values of $Pe_{cri,1}$ increase with the increase in H_p . This is due to presence of recirculation zones capable of mixing the two fluids entirely. Since the recirculation strength is higher at higher H_p (see Fig. 4a), which allows 100% mixing efficiency at higher Pe and the corresponding value of $Pe_{cri,1}$ is higher at higher H_p . An important observation in this regard is that for $Pe > Pe_{cri,1}$, η decreases with Pe .

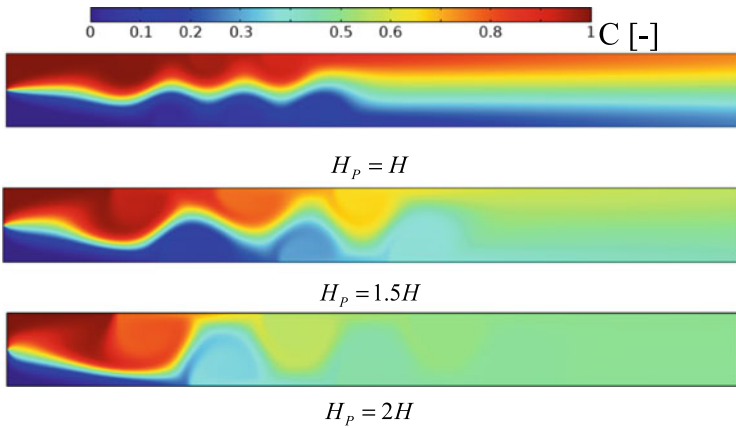
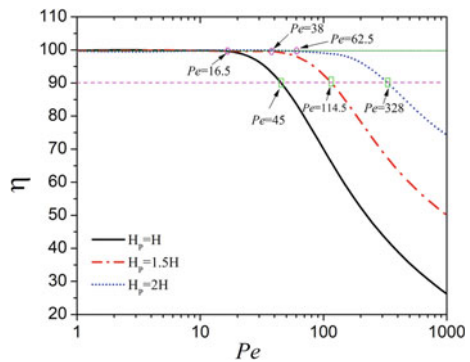


Fig. 5 Contours of dimensionless species concentration at different patch length (H_p) when $\kappa = 30$ and $\zeta = 1.5$

The reason behind this decreasing trend can be attached to the fact that an increase in Pe decreases the respective diffusion co-efficient and consequently weakens the tendency to mix the two fluids. Also, the increase in η with an increase in H_p at higher Pe is caused due to higher recirculation strength at higher H_p (see Fig. 4a) allowing better mixing quality. Further, for numerous applications regarding micromixers, the mixing length is defined as the length starting from the inlet where mixing efficiency approaches 90% [8]. Therefore, the Pe corresponding to $\eta = 90\%$ is identified as $Pe_{cri,2}$. The present micromixer achieves a fully mixed state up to $Pe_{cri,2}$, which also increases with the increase in H_p . This is also attributed to higher recirculation zone strength at higher H_p , which provides greater convective mixing strength.

Fig. 6 Mixing efficiency at outlet vs. diffusive Peclet number at different patch length (H_p) when $\kappa = 30$ and $\zeta = 1.5$



5 Conclusions

In this work, we analyze the flow and mixing attributes inside a micromixer with non-uniform surface charge distribution. The flow field, dimensionless flow rate, recirculation velocity (U_R), species concentration field and mixing efficiency (η) are studied varying the patch lengths (H_P) and the values of diffusive Peclet number (Pe) in the physically justified ranges. The salient observations are summarized below:

- The recirculation zone size and U_R enhances with an increase in patch length. Notably, the percentage increase in U_R is obtained as 31.21% when H_P increases from H to $2H$. In contrast, the increment in patch length reduces the flow rate.
- The dimensionless species concentration uniformity at outlet enhances with the increase in H_P and approaches to 0.5.
- The critical Pe ($Pe_{cri,1}$) is identified up to which the mixing efficiency is 100% for all H_P and $Pe_{cri,1}$ increases with the increase in H_P . Whereas for $Pe > Pe_{cri,1}$, mixing efficiency decreases with Pe .
- Another critical value of Pe ($Pe_{cri,2}$) is identified for which the micromixer length behaves as mixing length corresponding to 90% mixing efficiency. The value of $Pe_{cri,2}$ also follows the same trend as $Pe_{cri,1}$, which increases with an increase in H_P .

References

1. Vasista, K. N., Mehta, S. K., & Pati, S. (2021). Numerical assessment of hydrodynamic and mixing characteristics for mixed electroosmotic and pressure-driven flow through a wavy microchannel with patchwise surface heterogeneity. *Proceedings of the Institution of Mechanical Engineers, Part E: Journal of Process Mechanical Engineering*, 09544089211051640.
2. Vasista, K. N., Mehta, S. K., & Pati, S. (2022). Electroosmotic mixing in a microchannel with heterogeneous slip dependent zeta potential. *Chemical Engineering and Processing-Process Intensification*, 176, 108940.
3. Biddiss, E., Erickson, D., & Li, D. (2004). Heterogeneous surface charge enhanced micromixing for electrokinetic flows. *Analytical chemistry*, 76(11), 3208–3213.
4. Hadigol, M., Nosrati, R., Nourbakhsh, A., & Raisee, M. (2011). Numerical study of electroosmotic micromixing of non-Newtonian fluids. *Journal of Non-Newtonian Fluid Mechanics*, 166(17–18), 965–971.
5. Mondal, B., Mehta, S. K., Pati, S., & Patowari, P. K. (2021). Numerical analysis of electroosmotic mixing in a heterogeneous charged micromixer with obstacles. *Chemical Engineering and Processing-Process Intensification*, 168, 108585.
6. Mehta, S. K., Mondal, B., Pati, S., & Patowari, P. K. (2022). Enhanced electroosmotic mixing of non-Newtonian fluids in a heterogeneous surface charged micromixer with obstacles. *Colloids and Surfaces A: Physicochemical and Engineering Aspects*, 129215.
7. Mehta, S. K., Pati, S., & Mondal, P. K. (2021). Numerical study of the vortex-induced electroosmotic mixing of non-Newtonian biofluids in a nonuniformly charged wavy microchannel: Effect of finite ion size. *Electrophoresis*, 42(23), 2498–2510.
8. Mehta, S. K., & Pati, S. (2022). Enhanced electroosmotic mixing in a wavy micromixer using surface charge heterogeneity. *Industrial & Engineering Chemistry Research*, 61(7), 2904–2914.

9. COMSOL Multiphysics® v. 5.2. www.comsol.com. COMSOL AB, Stockholm, Sweden.
10. Vasista, K. N., Mehta, S. K., Pati, S., & Sarkar, S. (2021). Electroosmotic flow of viscoelastic fluid through a microchannel with slip-dependent zeta potential. *Physics of Fluids*, 33(12), 123110.
11. Banerjee, D., Mehta, S. K., Pati, S., & Biswas, P. (2021). Analytical solution to heat transfer for mixed electroosmotic and pressure-driven flow through a microchannel with slip-dependent zeta potential. *International Journal of Heat and Mass Transfer*, 181, 121989.

Breast Cancer Detection Using Deep Neural Network (DNN) on Histopathological Data



Suvarna D. Pujari, Meenakshi M. Pawar, Swati P. Pawar,
and Mohua Biswas

Abstract The leading cause of death for women in both developed and less developed nations is breast cancer (BC). It may be possible to treat cancer patients effectively by classifying the subtype of malignant (cancer) lesions. With the recent development in computer vision and deep learning, convolution neural networks (CNN) achieved enormous success in image classification and widely used in medical image processing. To recognize the subtype of cancer automatically of the whole slide images (WSI), which is computational impossible. The proposed Multi-Scale, Multi-Channel feature network for breast histopathological image classification follows the knowledge sharing strategy by sharing learned features at each stream across the network and the attention mechanism. The proposed module achieved accuracy for different magnification factors (MF) (40×, 100×, 200× and 400×) but the superior accuracy i.e. 99.25% for multi-class and 99.70% for binary at 200× MF. We observed that Deep Neural Network (DNN) model were better than existing models like VGG16, Xception and ResNet152, MuSCF-Net.

Keywords Histopathology · DDN · Multi-scale · Multi-stream

S. D. Pujari (✉) · M. M. Pawar · M. Biswas

Department of Electronics and Telecommunication Engineering, SVERIs College of Engineering, Pandharpur, India

e-mail: supujari94@gmail.com

S. D. Pujari · M. M. Pawar · S. P. Pawar · M. Biswas

Punyashlok Ahilyadevi Holkar Solapur University, Solapur, India

S. P. Pawar

Department of Computer Science Engineering, SVERIs College of Engineering, Pandharpur, India

1 Introduction

Breast cancer (BC) is the most common cancer type, especially in women, According to GLOBOCAN 2020, breast cancer in women left behind the lung cancer with 2,261,419 new cases and 684,996 deaths were recorded worldwide [1]. To improve survival rate in this disease, patients need to be identified at an early stage. Many tests are available, including physical examination, Mammography, tomosynthesis, magnetic resonance imaging (MARI), ultrasound and biopsy [2]. Out of them, biopsy serves as the gold standard for BC detection and further treatment; general pathologists make more diagnostic errors than experts [3] and overall disagreement between the individual pathologists' interpretations and the expert consensus [4]. Computer-assisted analysis can help to reduce the discrepancies in benign/malignant classification by providing an objective classification. Many researchers have started developing computer-aided detection tools to classify breast whole slide images as benign or malignant [5]. Some feature extraction techniques are used like wavelet-based, Haralick, intensity-based, and morphological features extracted from segmented nuclei and their surroundings to classify histopathological image [6]. Due to the complex structure of histopathological images, the hand crafted feature extraction technique is fruitless.

Breast cancer is not like a single disease; a cancer type usually includes multiple subtypes in different molecular pathogenesis and clinical features [7]. It is very crucial to identify cancer subtypes to facilitate the precision of cancer diagnosis and therapy. Recent developments in deep learning (DL) [8]. DL is a growing field in Machine learning. Supervised machine learning algorithms—Support vector machine (SVM), K-NN, Naïve Bayesian [9], and SVM [10] were used in breast cancer detection. When there is an intra-class and inter-class variation, the classical machine learning approaches degrade the system's performance regarding efficiency and accuracy [11]. The convolution neural network (CNN) based classifier networks like BCNN [12], DCNN [13] and ResNet152 [11] the Ensemble of MultiScale convolutional neural Networks (EMS-Net) [2] used for the automated classification of hematoxylin and eosin (H&E) stained breast histopathological microscopy images.

In this paper, we proposed a DNN based Multi-scale, Multi-stream feature network for classification of breast histopathological image. The proposed network processes the input H&E stained breast histopathological microscopy image patches through each of the multi-scale streams to extract the robust features.

2 Related Wok

2.1 Related Studies

In [12], Chaofeng Wang et al., proposed a deep learning-based Bilinear convolution neural network method to breast tissue images. Histopathological images decompose into H and E components and then applied convolution and pooling layers on both the decomposed images to fuse and learn more effective feature representation. The fivefold cross-validation strategy was performed for CNN-based algorithms. These two features were combined in a special way by bilinear pooling and achieved an average accuracy of $92.6 \pm 1.2\%$.

In another study by Toğaçar et al. [13], Three Deep Layer CNN (DCNN) Architectures were used for Breast Cancer Image Detection. they initially created a region of interest (RoI) from which Mitosis and non- Mitosis were selected of size $64 \times 64 \times 3$. These RoI's were given to DCNN, three different types of CNN Architecture were used for Mitosis and non-Mitosis detection, namely, 6-layer CNN, 13-layer CNN 17-layer CNN and 19-layer CNN. They achieved an accuracy of 84.49% by using 19-CNN layer which was highest among three CNN.

Another research study conducted by Sanaullah et al. [14] in this study, they came up with a deep learning model developed based on a convolutional neural network called BreastNet. BreastNet model had a convolutional block attention module, dense block, residual block and hypercolumn technique for histopathological image classification. They also trained the proposed model for different magnification factors ($40\times$, $100\times$, $200\times$ and $400\times$). The model was a multi-classification of breast [15, 16].

2.2 Contribution

In various medical image applications, CNN models have achieved promising results [11, 13]. The CNN is useful to get more robust, refined features and accurate performance. These studied motivated us to explore the performance of different DNNs and also to verify the accuracy and network parameters for breast cancer assessment from histopathological images.

Our main contributions of this study given below:

- A. We proposed a multi-scale filter bank with an attention mechanism for feature extraction.
- B. The proposed network consists of multi-streams for fine-level as well as course-level feature extraction.

- C. The proposed network follows a knowledge sharing strategy by sharing learned features at each stream across the network.
- D. The proposed network is trained and validated for histopathological hematoxylin–eosin stained breast digital slides on BreakHis dataset

3 Methodology

The proposed approach for the classification of breast cancerous image. Here we propose a Multi-scale; Multi-stream network for training of breast cancer images is described. As shown in Fig. 1 the block diagram of the proposed method. The proposed network made up of three streams belongs to a trail of convolution layer having filter size 1×1 , 3×3 and 5×5 respectively. Each convolution layer down-scales the feature maps by a factor of 2. Each convolution layer processes the input breast histopathological patch and extracts the features at a particular scale. This inspired by the [17, 18] work. Thus, the real-time use case of the proposed network, we use the element-wise addition operation to share the learned feature maps within the network streams. As shown in Fig. 1.

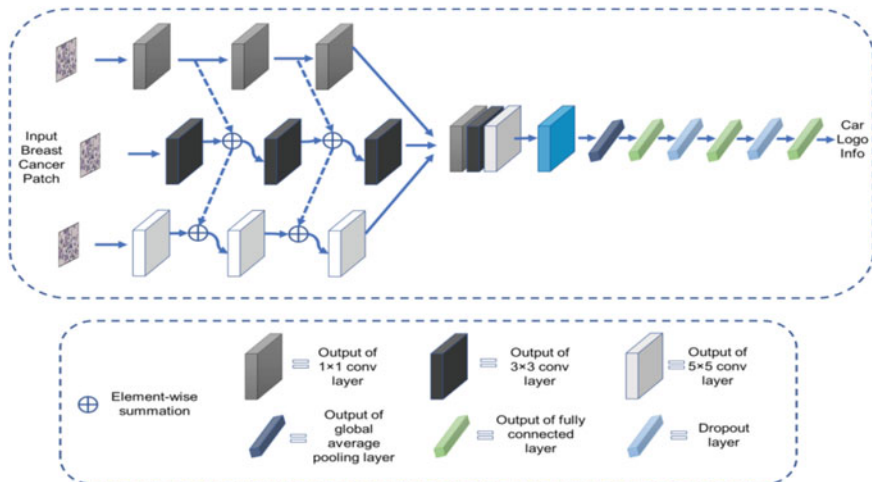


Fig. 1 Block diagram of the proposed deep neural network

3.1 Convolution of Filter Bank for Feature Extraction

We used the CNN's basic building block, such as convolution, Relu and batch normalization, for feature extraction with different filter size. Figure 1 shows the block diagram of the proposed multi-scale multi-stream deep neural network. Table 2 gives the details of network architecture and parameter details of the proposed network.

Choosing a filter size for a particular convolutional layer is very crucial, and there are no universal rules for choosing filter size. Thus, we choose filter size $(1 \times 1, 3 \times 3, 5 \times 5)$, multi-scale filter bank for feature extraction. This multi-scale filter bank helps tackle network design difficulties by letting the network decide the best route for itself.

Let, x and F represents input to the convolution layer's and output of the convolution layer's in the proposed network, respectively.

Thus,

$$F_{ijN} = \sum_{uvC} W_{uvCN} \times X_{i+u,j+v,C} \quad (1)$$

where, W_{uvCN} represents the filter bank having filters of spatial size $M \times N$ and locations $u \in \left[-\frac{(M-1)}{2}, \frac{(M-1)}{2}\right]$, $v \in \left[-\frac{(K-1)}{2}, \frac{(K-1)}{2}\right]$ The number of channels C and number of filters N . $(i; j)$ represent the image location. Instance normalization followed by ReLU activation are given as follows

$$\begin{aligned} F_{1ijk} &= \frac{F_{ij} - \mu_k}{\sqrt{\sigma^2 + \varepsilon}} \\ \mu_k &= \frac{1}{HW} \sum_{i=1}^W \sum_{j=1}^H F_{ijk} \\ \sigma_k^2 &= \frac{1}{HW} \sum_{i=1}^W \sum_{j=1}^H (F_{ijk} - \mu_k)^2 \end{aligned} \quad (2)$$

where, μ_k and σ_k represent the mean and variance of the k th feature map, W and H represent the width and height of the feature map.

$$F_{2ijN} = \max\{0, F_{1ijN}\} \quad (3)$$

3.2 Global Average Pooling Layer

In CNN [15], traditional fully connected layers replaced by global average pooling layers. The final multi perceptron convolutional layer (mlpconv) produces a feature map for each class. The resulting vector is fed directly into the softmax layer after each feature map has been averaged. Overfitting at this level is avoided because global average pooling has no parameters to optimize.

3.3 Dropout Layer

The dropout layer is used in CNN for regularization and to avoid overfitting. It temporarily disconnects some network units as well as all incoming and outgoing connections [19].

3.4 Dense Block Dense Layer

It is commonly used in neural networks to change the vector dimension. Every neuron in this layer receives input from all neurons in the previous layer. As a result, it is referred to as a deeply connected layer.

3.5 Training Details

Our proposed network [20] was trained on the BreakHis dataset. We create RoI's of size 64×64 image from a given dataset, from that 80% of the RoI's as training and 20% as validation for each class at each magnification level. The network is trained on an NVIDIA GeForce RTX 2060 super GPU with a learning rate ranging from 0.0001 to 0.001. To design and train the proposed network, we used the Keras library on Tensorflow.

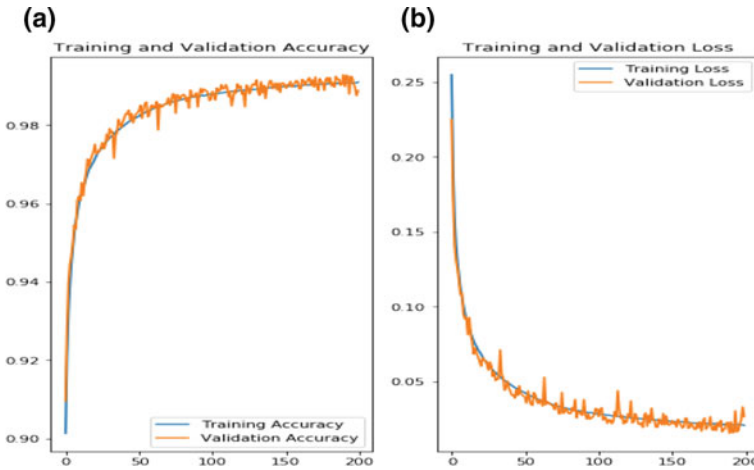


Fig. 2 **a** Accuracy distribution in the training process, **b** distribution of losses with the epoch number (validation phase)

4 Results and Discussion

In this section, we have discussed the experimental analysis of the proposed for a classification problem, accuracy and loss is calculated in this section. The accuracy & loss our proposed model have compared with existing models like VGG16, Xception model, and MuSCF-Net, as shown in Table 2, the DCNN model gives better results than existing CNN models. We trained our proposed model and obtained results at various MF ($40\times$, $100\times$, $200\times$, and $400\times$) of images, the best result at $200\times$ Fig. 2a shows the training and validation accuracy graph and Fig. 2b shows the training and validation loss graph.

5 Conclusion

We proposed multi-stream, multi-scale to get fine and robust feature. We enable a feature sharing in-between the multi-stream branches for effective feature learning. Our proposed model can classify eight sub-classes of benign and malignant breast cancer image, with the increasing depth of CNN model; more image data is required for the best generalization of the model (Table 1).

For that reason, after preprocessing the data, we enlarged the dataset through the patch creation. Model performances have been analyzed through comparison with few other models. We achieved classification Accuracy 99.25 for multi-classification and 99.70 for binary classification (Table 2).

Table 1 Layer wise details of our DCNN network

Input	Input image size	Output layer/ stride	Filter size	Output image size
Input image	$128 \times 128 \times 3$	Conv1_1/2	$1 \times 1 \times 3 \times 64$	$64 \times 64 \times 64$
Input image	$128 \times 128 \times 3$	Conv1_3/2	$3 \times 3 \times 3 \times 64$	
Input image	$128 \times 128 \times 3$	Conv1_5/2	$5 \times 5 \times 3 \times 64$	
Conv1_1/2, Conv1_3/2	$64 \times 64 \times 64$	Addition1_13	–	$64 \times 64 \times 64$
Conv1_1/2 Conv1_3/2 Conv1_5/2	$64 \times 64 \times 64$	Addition_1_135		$64 \times 64 \times 64$
Conv1_1/2	$64 \times 64 \times 64$	Conv_2_1/2	$1 \times 1 \times 64 \times$	$32 \times 32 \times 128$
Addition_1_13	$64 \times 64 \times 64$	Conv_2_3/2	128	$32 \times 32 \times 128$
Addition_1_135	$64 \times 64 \times 64$	Conv_2_5/2	$3 \times 3 \times 64 \times$	$32 \times 32 \times 128$
Conv_2_1/2	$32 \times 32 \times 128$	Addition_2_13	128	$32 \times 32 \times 128$
Conv_2_3/2	$32 \times 32 \times 128$		$5 \times 5 \times 64 \times$	
Conv_2_5/2	$32 \times 32 \times 128$		128	
Conv_2_1/2 Conv_2_3/2 Conv_2_5/2	$32 \times 32 \times 128$	Addition_2_135	–	$32 \times 32 \times 128$
Conv_2_1/2	$32 \times 32 \times 128$	Conv_3_1/2	$1 \times 1 \times 64 \times$	$16 \times 16 \times 256$
Addition_2_13	$32 \times 32 \times 128$	Conv_3_3/2	128	$16 \times 16 \times 256$
Addition_2_135	$32 \times 32 \times 128$	Conv_3_5/2	$3 \times 3 \times 64 \times$	$16 \times 16 \times 256$
			128	
			$5 \times 5 \times 64 \times$	
			128	
Conv_3_1/2 Conv_3_3/2 Conv_3_5/2	$16 \times 16 \times 256$	Concatenation		$16 \times 16 \times 768$
Concatenation	$16 \times 16 \times 768$	Conv_4_3/2	$3 \times 3 \times 768 \times$	$8 \times 8 \times 1024$
			1024	
Conv_4_3/2	$8 \times 8 \times 1024$	Global average pooling (GAP)	–	1024
GAP	$1 \times 1 \times 1024$	FC_1	1024×512	$1 \times 1 \times 512$
FC_1		Dropout 1	0.5 dropout factor	
Dropout1	$1 \times 1 \times 60$	FC_2	512×128	$1 \times 1 \times 128$
FC_2		Dropout 2	0.5 dropout factor	
Dropout 2	$1 \times 1 \times 128$	FC_3	128×40	$1 \times 1 \times 40$

Table 2 The result of DCCN model is compared with existing model

Model	VGG16		Xception		MuSCF-Net		Proposed model	
	Multi-class	Binary	Multi-class	Binary	Multi-class	Binary	Multi-class	Binary
Classification Accuracy (%)	81.37	92.58	96.57	99.01	98.07	99.60	99.25	99.75
Loss (%)	20.48	10.20	8.6	1.68	3.01	1.09	1.51	1.05

References

- Sung, H., Ferlay, J., Siegel, R. L., Laversanne, M., Soerjomataram, I., Jemal, A., & Bray, F. (2021). Global cancer statistics 2020: GLOBOCAN estimates of incidence and mortality worldwide for 36 cancers in 185 countries. *CA: A Cancer Journal for Clinicians*, 71(3), 209–249.
- Yang, Z., Ran, L., Zhang, S., Xia, Y., & Zhang, Y. (2019). EMS-Net: Ensemble of multi-scale convolutional neural networks for classification of breast cancer histology images. *Neurocomputing*, 366, 46–53.
- Allison, K. H., Reisch, L. M., Carney, P. A., Weaver, D. L., Schnitt, S. J., O'Malley, F. P., & Elmore, J. G. (2014). Understanding diagnostic variability in breast pathology: Lessons learned from an expert consensus review panel. *Histopathology*, 65(2), 240–251.
- Elmore, J. G., Nelson, H. D., Pepe, M. S., Longton, G. M., Tosteson, A. N., Geller, B., & Weaver, D. L. (2016). Variability in pathologists' interpretations of individual breast biopsy slides: A population perspective. *Annals of Internal Medicine*, 164(10), 649–655.
- Gandomkar, Z., Brennan, P. C., & Mello-Thoms, C. (2016). Computer-based image analysis in breast pathology. *Journal of Pathology Informatics*, 7(1), 43.
- Niwas, S. I., Palanisamy, P., & Sujathan, K. (2010, October). Wavelet based feature extraction method for breast cancer cytology images. In *2010 IEEE symposium on industrial electronics and applications (ISIEA)* (pp. 686–690). IEEE.
- Guray, M., & Sahin, A. A. (2006). Benign breast diseases: Classification, diagnosis, and management. *The Oncologist*, 11(5), 435–449.
- Litjens, G., Kooi, T., Bejnordi, B. E., Setio, A. A. A., Ciompi, F., Ghafoorian, M., & Sánchez, C. I. (2017). A survey on deep learning in medical image analysis. *Medical Image Analysis*, 42, 60–88.
- Gupta, P., & Garg, S. (2020). Breast cancer prediction using varying parameters of machine learning models. *Procedia Computer Science*, 171, 593–601.
- Akbulut, F. P., & Aydın, A. K. A. N. (2017). Support vector machines combined with feature selection for diabetes diagnosis. *IU-Journal of Electrical & Electronics Engineering*, 17(1), 3257–3265.
- Gandomkar, Z., Brennan, P. C., & Mello-Thoms, C. (2018). MuDeRN: Multi-category classification of breast histopathological image using deep residual networks. *Artificial Intelligence in Medicine*, 88, 14–24.
- Wang, C., Shi, J., Zhang, Q., & Ying, S. (2017, July). Histopathological image classification with bilinear convolutional neural networks. In *2017 39th annual international conference of the IEEE engineering in medicine and biology society (EMBC)* (pp. 4050–4053). IEEE.
- Zainudin, Z., Shamsuddin, S. M., & Hasan, S. (2019, March). Deep layer CNN architecture for breast cancer histopathology image detection. In *International conference on advanced machine learning technologies and applications* (pp. 43–51). Springer.
- Toğaçar, M., Özkurt, K. B., Ergen, B., & Cömert, Z. (2020). BreastNet: A novel convolutional neural network model through histopathological images for the diagnosis of breast cancer. *Physica A: Statistical Mechanics and its Applications*, 545, 123592.

15. Pauer, M. M., Pujari, S. D., Pawar, S. P., & Talbar, S. N. (2022). MuSCF-Net: Multi-scale, multi-channel feature network using Resnet-based attention mechanism for breast histopathological image classification. In *Machine learning and deep learning techniques for medical science* (pp. 243–261). CRC Press.
16. Pujari, S. D., Pawar, M. M., & Wadekar, M. (2021). Multi-classification of breast histopathological image using Xception: Deep learning with depthwise separable convolutions model. In *Techno-Societal 2020* (pp. 539–546). Springer.
17. Szegedy, C., Liu, W., Jia, Y., Sermanet, P., Reed, S., Anguelov, D., & Rabinovich, A. (2015). Going deeper with convolutions. In *Proceedings of the IEEE conference on computer vision and pattern recognition* (pp. 1–9).
18. Lin, M., Chen, Q., & Yan, S. (2013). *Network in network*. [arXiv:1312.4400](https://arxiv.org/abs/1312.4400)
19. Srivastava, N., Hinton, G., Krizhevsky, A., Sutskever, I., & Salakhutdinov, R. (2014). Dropout: A simple way to prevent neural networks from overfitting. *The Journal of Machine Learning Research*, 15(1), 1929–1958.
20. Benhammou, Y., Achchab, B., Herrera, F., & Tabik, S. (2020). BreakHis based breast cancer automatic diagnosis using deep learning: Taxonomy, survey and insights. *Neurocomputing*, 375, 9–24.

Image Processing for Protein Detection in the Egg Using a Micro Fluidics System



Sachin M. Khomane, Pradeep V. Jadhav, Saurabh S. Kale,
Revansiddha S. Gaur, Suryakant B. Nilgar, Siddheshwar K. Mali,
and Prasanna S. Thalpati

Abstract Micro fluidics system has great attention in recent years because of their interdisciplinary nature. It has a wide application in various fields, especially in biomedical applications. In a food, protein is one of essential element to grow the body therefore it becomes significant test the protein level in food. Egg is the common food used in daily diet to fulfill the need of protein. Egg protein testing is carried out in laboratories in traditional way that consumes the reagents (CuSO_4 and NaOH) in bulk, requires lengthy reaction times as sample quantity more. Micro-fluidics eliminated these limitations as quantity of sample and reagent is too less. This research focuses on Image processing algorithm for the detection of protein in egg samples. The image processing algorithm is based on color detection as the protein level is indicated by faint to dark violet i.e. low protein to high protein respectively. In this work microchannel for microfluidics system has been designed and fabricated by using soft lithography method. The mould for microchannel has been fabricated using CO_2 Laser machining on PMMA (methyl methacrylate) material and Channel has been fabricated by using PDMS (polydimethylsiloxane) material. Images for 10% to 100% protein level of known sample at the interval of 10% have been collected from outlet at the channel by using camera. The collected images of known sample have been imported for image processing and datasets have been created. Randomly, the known samples have been tested for the validation.

Keywords Microfluidics · Egg protein · Soft lithography · Image processing

S. M. Khomane · S. S. Kale · R. S. Gaur · S. B. Nilgar · S. K. Mali · P. S. Thalpati
SVRI's College of Engineering, Pandharpur, Solapur, India

S. M. Khomane · P. V. Jadhav (✉)
Bharati Vidyapeeth (Deemed to be University) College of Engineering, Pune, India
e-mail: pvjadhav@bvucoep.edu.in

1 Introduction

Protein is an important component in food products as it plays important role in body growth. Most of the time tests need to be done in laboratories that are costly and time consuming. Micro-fluidics system developed in the last decade helped researcher to develop a lab on a chip (LOC) devices. CO₂ laser machining of micro-channels has been fastest method to fabricate PDMS based micro fluidic chips [1]. In a micro-fluidics, a Micro channel is basic functional component to perform the specific mixing and chemical reaction. All over the world, for the Lab-on-a chip (LOC) microfluidics has been used. Microchannel is main component of microfluidic system that is fabricated by using PDMS and conventional method like soft lithography [2]. In fabrication of mould there are various techniques and methods have been implemented in different research [3]. In a microchannel development, soft lithography is simple and low-cost that is used for micro- and nano-fabrication work. This is also known as an unconventional process for the replica molding [4]. In a microchannel the surface treatment & bonding techniques are necessary for the bonding. Researchers have focused on lab-on-a-chip technologies in which devices that can conduct single risk to integrated systems capable of performing complex jobs [5]. Chicken and eggs are an excellent source of human nutrition for dietary protein. Testing protein in the egg and its method of testing becomes significant by using microfluidics [6]. Egg protein testing carried out in traditional way where intensity violet color is indicated the protein level manually that can be converted to machine based detection [7]. By implementing recent advances in camera there are applications of digital image processing using a machine learning to identify any specific objects. Various languages including Python or any other suitable language image processing have been carried out in object detection [8]. Image processing applied in forensic science also for automatic fiber analysis. Image obtained by microscopes are used for image processing in color channel of RGB image combined with segment color image. The fiber object detects in color based on attributes technique that is reducing time of processing [9, 10].

2 Methodology

The methodology in this research work includes the fabrication of micro channel mold, the fabrication of PDMS micro channel by using soft lithography process and image processing to detect protein in egg.

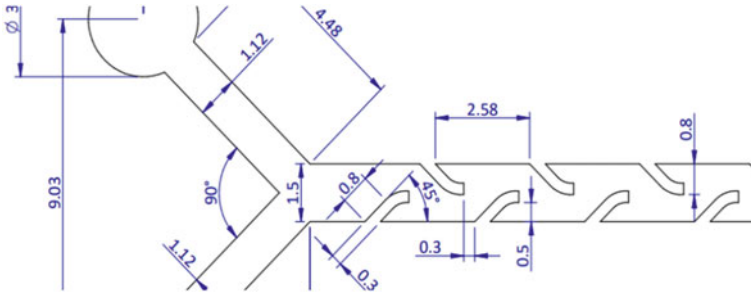


Fig. 3 Drawing of mould with details of dimensions

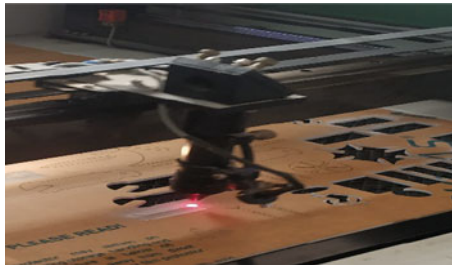


Fig. 4 Laser cutting of mould



Fig. 5 Finished mould

hardener material is kept for curing. Figure 6 represents the fabricated micro channel using Soft Lithography.

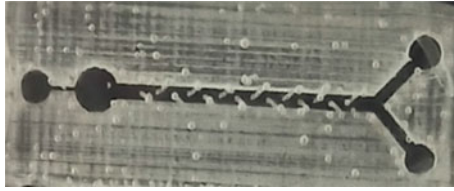


Fig. 6 Fabricated micro channel using soft lithography

2.3 Preparation of Egg Solution and Reagent.

For preparation of reagents, 2 g of NaOH in 30 ml water and 1 g CuSO₄ in 10 ml water is mixed to prepare diluted solution. Then diluted solutions of NaOH and CuSO₄ have been used in the ratio of 10:1. There after Prepared Diluted solution and egg white solution are mixed in the ratio of 3:5 in Y shaped micro channel.

2.4 Capturing Images for Image Processing

For collecting the images of channel chamber, a micro spy camera has been used. Micro spy is an HD video camera that feeds or streams an image in real time to or through a computer network. It is a small camera that sits on the upper system and attach to a user's monitor. Figure 7 Indicates the Experimental Setup Capturing Images.

One of the most challenging tasks towards protein detection is getting image into the algorithm. In Image processing computer is used to process digital images through an algorithm by using Deep Learning with Tensorflow and Keras. Images are detected on the basis of colour of the solution. As per Fig. 8 the images of outlet from the micro channel have been collected for the known samples. From the known

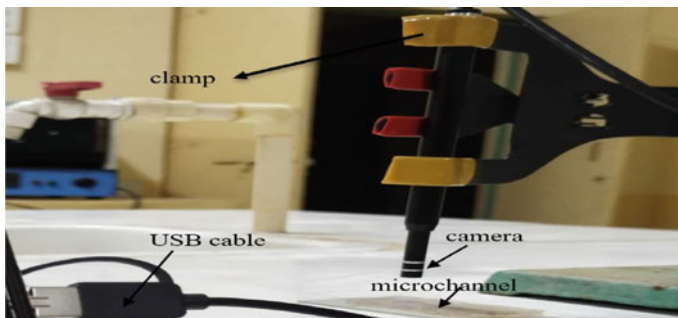


Fig. 7 Experimental setup capturing images

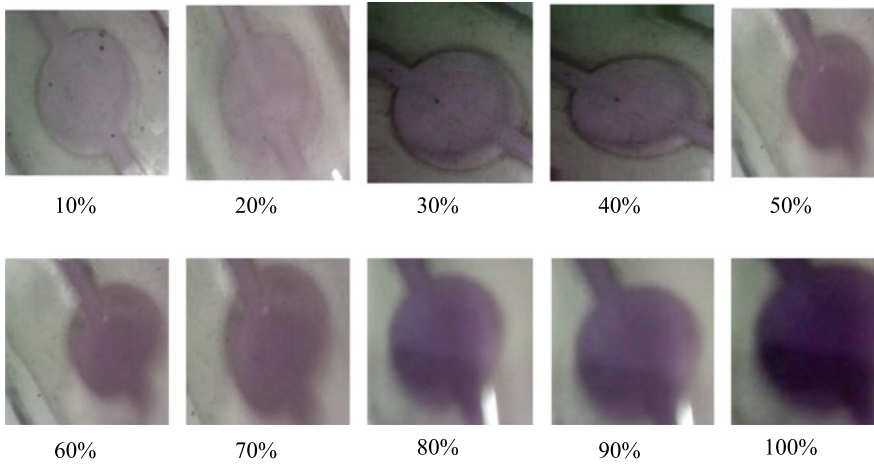


Fig. 8 Input images of known samples of protein level



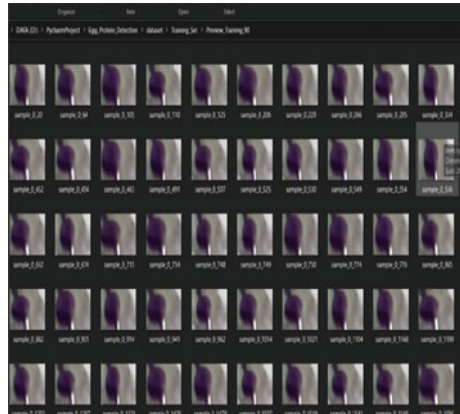
Fig. 9 Dataset of 10% protein image

data samples, data sets have been generated. Figures 9 and 10 shows the datasets for image processing for 10% and 90% protein level respectively.

2.5 Image Processing by Using CNN

For image processing, deep learning Convolutional Neural Network (CNN) has been used and for that, Tensorflow and Keras libraries have been imported. Image processing has been divided into four parts as mentioned below.

Fig. 10 Dataset of 90% protein image



Part-1

The dataset has been preprocessed and imported for the training. The training dataset has 1171 images belonging to 2 classes. Also, import the testing dataset of 201 images belonging to 2 classes.

Part-2

CNN has been initialized and it has 5 steps as follows:

- Step 1: Adding the first Convolutional layer.
- Step 2: Pooling layers added as it is used to reduce the dimensions of the feature maps.
- Step 3: Flattening layer used to convert all the resultant 2-Dimensional arrays from pooled feature maps into a single long continuous linear vector.
- Step 4: A fully Connected Layer is simple, a feed-forward neural network.
- Step 5: Output Layer is here, each hidden layer is also made up of a set of neurons, where each neuron is fully connected to all neurons in the previous layer. The last layer of a neural network (i.e., the “output layer”) is also fully connected and represents the final output classifications of the network.

Part-3

Here training of the CNN has been completed on the training set. Compiled the CNN and then evaluated it on the test set.

Part-4

At last, predictions have been done for protein levels.

Table 1 Egg sample composition reading

S. No.	Egg solution (ml)	Water (ml)	Dil. CuSO ₄ and NaOH (ml)	Result of protein violet color (%)
1	0.5	5	0.3	Light (10%)
2	1	5	0.6	Light (20%)
3	1.5	5	0.9	Light (30%)
4	2	5	1.2	Medium (40%)
5	2.5	5	1.5	Medium (50%)
6	3	5	1.8	Medium (60%)
7	3.5	5	2.1	Medium (70%)
8	4	5	2.4	Dark (80%)
9	4.5	5	2.7	Dark (90%)
10	5	5	3	Dark (100%)

3 Result and Discussion

From Y shaped channel inlet number one diluted solution of NaOH and CuSO₄ and from another white egg solution have inserted and known sample readings have been collected. One micro thin spy portable USB Digital Camera image sensor (HD 720P 6 LED) with a pixel size of 3 mm × 6 mm is used for imaging This camera was placed above the designed microchannel.

Table 1 represents the details of quantity of egg solution, water quantity, quality of reagent and concern colour intensity and various percentage of protein at the interval of 10%.

Image processing for 90% protein level has been performed and validated on Jupyter. Figure 11 represents the python code with prediction.

The screenshot shows a Jupyter Notebook titled 'Egg_Protein_Detection'. The top bar indicates the last checkpoint was on Saturday at 9:34 PM. The notebook interface includes a menu (File, Edit, View, Insert, Cell, Kernel, Widgets, Help) and a toolbar with icons for file operations and execution. The main area displays a code cell with the following content:

```

37/37 [-----] - 14s 284ms/step - loss: 0.4693 - accuracy: 0.8284 - val_loss: 0.9208 - val_accuracy:
0.5025
Epoch 4/25
37/37 [-----] - 14s 382ms/step - loss: 0.4693 - accuracy: 0.8284 - val_loss: 0.9786 - val_accuracy:
0.5025
Epoch 5/25
37/37 [-----] - 14s 383ms/step - loss: 0.4731 - accuracy: 0.8284 - val_loss: 1.2227 - val_accuracy:
0.5025
Epoch 6/25
37/37 [-----] - 14s 383ms/step - loss: 0.4770 - accuracy: 0.8284 - val_loss: 0.8582 - val_accuracy:
0.5025
Epoch 7/25

In [110]: # PART - 4
# Making the Prediction

import numpy as np
from keras.preprocessing import image
test_image = image.load_img('D:/PycharmProject/Egg_Protein_Detection/dataset/training_Set/Preview_Training_10/sample_0_76.png',
test_image = image.img_to_array(test_image)
test_image = np.expand_dims(test_image, axis=0)
result = cnn.predict(test_image/255.0)
#printing set class indices()
if result[0][0] < 0.5:
    prediction = 'Light Violet contains 10% of Protein'
else:
    prediction = 'Dark Violet contains 90% of Protein'
print(prediction)
- .
Dark violet contains 90% of Protein

```

Fig. 11 Result of 90% protein sample

4 Conclusion

This performed research is basically focuses on the replacement to traditional egg protein detection by micro-fluidics and image processing. Based on the experimentation, following conclusions have been drawn.

1. CO₂ laser machining can be used for micro-channel mould fabrication.
2. Deep learning Convolutional Neural Network is a suitable method for detecting protein based on color and seen the good agreement in the results with traditional laboratory method.
3. Thus, used research is suitable for Lab-on-a-Chip devices development.

References

1. Tahsin, G. M. (2022). Fabricating plasma bonded microfluidic chips by CO₂ laser machining of PDMS by the application of viscoelastic particle focusing and droplet generation. *Journal of Manufacturing Processes*, 73, 260–268.
2. Yue Fei, J., & Jiahuan, J. (2008). PDMS microchannel fabrication technique based on microwire-molding. *Chinese Science Bulletin*, 53(24), 3928–3936.
3. Konara, M., Mudugamuwa, A., & Dodampegema, S. (2022). Formation techniques used in shape-forming microrobotic systems with multiple microrobots. *Micromachines*, 13, 1987.
4. Zhao, X., Xia, Y. M., & Whitesides, G. M. (1997). Soft lithographic methods for nano-fabrication. *Journal of Materials Chemistry*, 7, 1069–1074.
5. Borok, A., Laboda, K., & Bonyár, A. (2021). PDMS bonding technologies for microfluidic applications. *Biosensors*, 11, 292.
6. Waindok, P., & Raulf, M. K. (2022). Potentials and challenges in the isolation and detection of ascarid eggs in complex environmental matrices. *Food and Waterborne Parasitology*, 28.

7. Wang, Y., Yang, C., & Zhang, J. (2022). Influence of rose anthocyanin extracts on physicochemical properties and in vitro digestibility of whey protein isolate sol/gel. *Food Chemistry*, *164*, 134937.
8. Faisal, M., & Haider, Z. (2018). A pump-based microfluidic image processing system for droplet detection and counting. *Materials Science*, *381*, 012191.
9. Wetzer, E., & Lohninger, H. (2018). Image processing using color space models for forensic fiber detection. *IFAC-PapersOnLine*, *51(2)*, 445–450.
10. Weng, W. T., Van Hieu, N., Chang, C. C., & Wang, G. J. (2022). A flexible and stretchable photonic crystal film with sensitive structural color-changing properties for spoiled milk detection. *Food Chemistry*, *X*, 100526.

Minimization of Droplet Size Using Baffle in T-Junction



Manash Protim Boruah

Abstract With the advent of *lab-on-a-droplet* based strategies for various applications, the droplet generation process in miniaturized devices has received notable attention from the research community. For long, researchers have developed varied strategies of tuning the size and frequency of droplets so as to reduce reagent consumption, production of waste and increase controllability and portability for microfluidic usage. Hence, in the interest of minimizing droplet size, a novel technique of incorporating baffle in a microfluidic T-junction for generating monodisperse droplets of smaller size than the conventional T-junction is proposed in this study. Through comprehensive 3-D numerical simulations using the Level-Set method, it has been found that the inclusion of baffle in the T-junction reduces the droplet size by 22.5%, thus meeting demands of minimized size monodispersed droplet generation without encountering fabrication complexity issues.

Keywords Droplet · T-junction · Baffle

1 Introduction

In the recent past, droplets in miniaturized devices have paved new dimensions in a wide spectrum of technical and medical applications such as micro-electro cooling [1], printing [2], drug transportation [3], chemical reaction [4], food technology [5] and material fabrication [6]. More specifically, droplets ranging from nano to picolitre volumes serve as discrete packages for high throughput chemical reaction [7] and cell cultivation [8], thus upgrading biochemistry from macro to micro level. However, to master the notion of *lab-on-a-droplet* in a truly potential sense, user-controlled manipulation of the droplet generation process would help in accomplishing objectives of user's interest. To date, segmented flow manipulation (droplet generation due to interfacial tension and shear force between two immiscible fluids) has shaped the concept of droplet manipulation as it is simple, cost effective and easily producible

M. P. Boruah (✉)

Department of Mechanical Engineering, Tezpur University, Assam 784028, India
e-mail: mpboruah007@gmail.com; manash@tezu.ernet.in

method. In this regard, T-junction microfluidic channel [9] has received special attention from the research community owing to its superiority in terms of fabrication simplicity and droplet monodispersity unlike other microfluidic configurations viz. cross-flow, co-flow, flow focusing, step emulsification, microchannel emulsification, and membrane emulsification [10]. Later, several modified T-junctions were introduced namely angular T-junction, head-on-T-junction, bifurcating junction, double T-junction, parallel dual T-junction, K-junction and V-junction [10] to meet special requirements such as on-demand droplet generation and mass production in some pragmatic applications. Furthermore, holding on with the conventional T-junction, Jiang et al. [11] observed zero to multiple satellite drop formation. In a related study, Boruah et al. [12] could effectively tune the droplet production process by modifying surface wettability of conventional T-shaped junction channel. Thereafter, Zeng et al. [13] showed that based on closed-loop control system, the droplet size can be precisely controlled, irrespective of the capillary number being low or high. Hence, minimizing droplet size has become one of the potential demands and in the interest of meeting the same, we propose a novel technique of incorporating baffle in a microfluidic T-junction for generating monodisperse droplets of smaller size than the conventional T-junction in this study.

2 Theory and Methodology

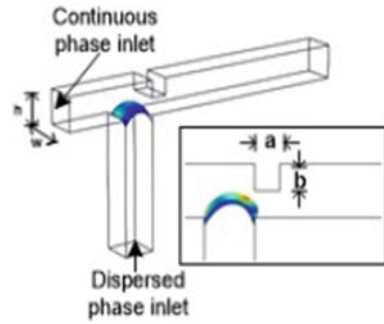
2.1 Problem Definition

A 3-D Microfluidic T-junction of $100\ \mu\text{m} \times 100\ \mu\text{m}$ cross-section with a baffle of width a and height b as shown in Fig. 1 is considered. Two different phases of fluid viz. 2 wt% poly (vinyl alcohol) aqueous solution ($\rho_c = 1000\ \text{kgm}^{-3}$, $\mu_c = 1.95 \times 10^{-3}\ \text{Pa s}$) and 1, 6-hexanediol diacrylate ($\rho_d = 1020\ \text{kgm}^{-3}$, $\mu_d = 6.71 \times 10^{-3}\ \text{Pa s}$) are considered respectively as the continuous and dispersed phase. The interfacial tension is taken to be $5\ \text{mNm}^{-1}$. At the inlets, the velocities of the phases are fixed based on a specified capillary number ($Ca = U\mu/\gamma$), where the velocity far-stream is U and the surface tension is γ . At the outlet, the pressure equals to that of the atmosphere. Furthermore, the walls were hydrophobic with contact angle (θ) = 135° .

2.2 Theoretical Formulation

This study is formulated as per the level-set method which can aid in accurate capturing of the fluid–fluid interface. This method is associated with the level-set function $\phi(x, t)$ which tracks the interface by assuming values of -1 in the continuous fluid domain, 0 at the interface and 1 in the dispersed fluid domain. With change in time, the evolution of the interface is traced by solving

Fig. 1 Schematic representation of T-shaped junction with baffle with an inset showing the width (a) and height (b) of baffle



$$\frac{\partial \phi}{\partial t} + \mathbf{v} \cdot \nabla \phi = 0, \quad (1)$$

in the Eulerian co-ordinate. Here, t denotes dimensional time and \mathbf{v} denote velocity field. Once the value of ϕ is determined, the smeared-out Heaviside function of ϕ , i.e., $H_\varepsilon(\phi)$ is used as the weight function to evaluate the local density and viscosity as

$$\rho(\phi) = \rho_c H_\varepsilon(\phi) + \rho_d(1 - H_\varepsilon(\phi)), \quad (2a)$$

$$\mu(\phi) = \mu_c H_\varepsilon(\phi) + \mu_d(1 - H_\varepsilon(\phi)). \quad (2b)$$

where, $H_\varepsilon(\phi)$ is the smeared-out Heaviside function. Furthermore, the curvature of the interface is obtained as

$$\kappa = -\nabla \cdot \frac{\nabla \phi}{|\nabla \phi|}. \quad (3)$$

Moreover, some modifications to Eq. (1) are done in the form

$$\frac{\partial \phi}{\partial t} + \mathbf{v} \cdot \nabla \phi = \nabla \cdot \left(\lambda \nabla \phi - \phi(1 - \phi) \frac{\nabla \phi}{|\nabla \phi|} \right). \quad (4)$$

to accurately capture the interface curvature.

The final coupled Navier–Stokes equation for unsteady flow is thus as

$$\rho \left[\frac{\partial \mathbf{v}}{\partial t} + \mathbf{v} \cdot \nabla \mathbf{v} \right] = -\nabla p + \nabla [\mu(\nabla \mathbf{v} + (\nabla \mathbf{v})^T)] + \gamma \kappa \hat{n} \delta_s, \quad (5)$$

where p and δ_s are the pressure and Kronecker delta function respectively. Along with these, the continuity equation

$$\nabla \cdot \mathbf{v} = 0. \quad (6)$$

is also required to close the problem.

2.3 Numerical Methodology

The finite element package COMSOL Multiphysics is employed for solving the governing equations along with the boundary conditions using the algorithm outlined through the flow chart of Fig. 2.

The accuracy of the aforementioned numerical model is confirmed through validation with van der Graaf et al. [9] as shown in Fig. 3. Different grid sizes were also tested and the results are also found to be grid independent for 235,066 elements. Moreover, the time step independency test has also been conducted and the results were found to be time independent for a time step size of 0.001.

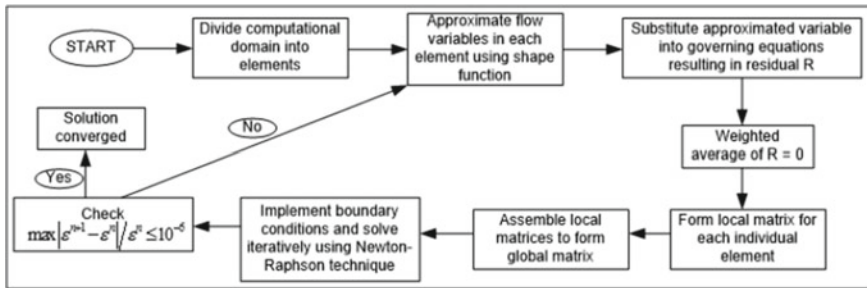


Fig. 2 Flow chart of the numerical method

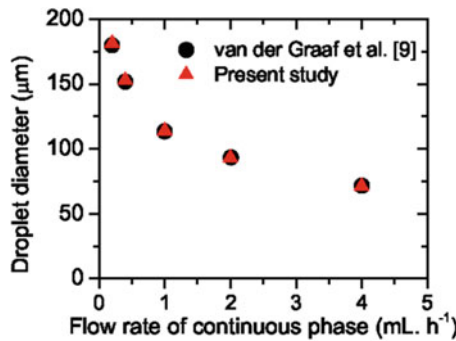


Fig. 3 Model validation: comparison of the numerically obtained results with van der Graaf et al. [9]

3 Results and Discussion

At the foremost, we present a comparative assessment of the conventional and baffled T-junction by looking into the regime alterations incurred as a result of incorporation of the baffle. At lower value of Ca , we observe that the dispersed phase squeezes into the main pathway of the conventional T-shaped junction covering the entire width of the main pathway before being dislodged into a droplet. However, with the inclusion of baffle in T-shaped junction, the main pathway width is reduced, resulting in greater shear force and therefore, occurrence of squeezing followed by droplet dislodgement is advanced. Therefore, as evident from Fig. 4 frequency of droplet generation increases, while the size of droplet reduces. With increasing Ca , the viscous forces imposed by the upstream continuous fluid is high enough to decrease the width of the dispersed liquid segment into a thin neck and therefore the dispersed column covers lesser portion of the primary pathway as compared to that observed in the squeezing zone. This phenomenon is called dripping where we observe droplet generation at a relatively downstream location compared to the squeezing regime. However, in the newly introduced baffled T-Junction, dripping of droplets occurs in the vicinity of the baffle due to additional viscous force imposed by the baffle on the intruding dispersed liquid column. With further increase in Ca , there occurs a dripping to jetting zone transition owing to the increase in shear force imposed by the continuous on dispersed liquid segment. Interesting to observe from Fig. 4 that the jetting phenomenon occurs at a relatively higher Ca in the baffled T-junction as compared to conventional T-junction. This is primarily attributable to the fact that the relative strength of shear force imposed by the baffle and that by the upstream continuous phase remain comparable for a relatively higher value of Ca in the baffled T-junction than in the conventional one. Following the jetting regime is the parallel flow zone where both continuous and dispersed phases move along parallel paths without forming droplets and this occurs at further higher value of Ca .

Figure 5 presents the temporal evolution of dispersed fluid contours colored by the magnitude of velocity in the baffled T-junction for four different regimes. At the foremost it is clearly evident from figure that the velocity of the continuous phase increases with change in regime from squeezing to dripping to jetting and then to parallel flow. Interesting to observe is the velocity at the location of the baffle and its variations before and after the baffle. In the squeezing zone, the difference in velocity at the location of the baffle and those before and after the baffle is very minimum. This is particularly due to lower flow rate of continuous fluid, thus imposing lower shear force on dispersed liquid column. With increase in Ca , when the zone transits from squeezing to dripping, the dispersed liquid column do not cover the primary channel throughout its width and therefore the upstream continuous phase that covers the remaining portion of the primary channel width travels with a greater velocity as compared to the squeezing regime. Additionally, with the introduction of the baffle, the width is further more reduced and this leads to significant difference between the velocity at the baffle location and those before and after the baffle. However, in case of the remaining two regimes i.e. jetting and parallel flow regime,

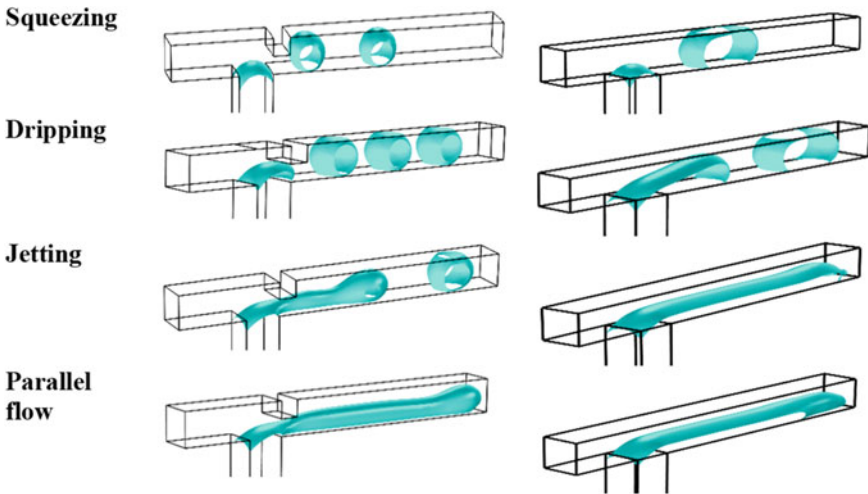


Fig. 4 Different flow regimes in T-junction with baffle (left column) and conventional T-junction (right column) under different flow conditions

the velocity variation is insignificant. In these cases, once the dispersed fluid intrudes into the primary channel, it is driven downstream by incoming continuous phase that is injected at higher velocity than the former two cases. Hence, the viscous force imposed by continuous fluid is highly dominant in jetting and parallel flow zone, and therefore neck formation followed by droplet pinch-off occur at a relatively downstream location or may not occur at all.

The fluctuation of pressure with the evolution of dispersed fluid is another important factor dictating different regimes during two-phase flow in a T-shaped junction, and the same is presented in Fig. 6. Initially, the dispersed liquid segment is at high pressure when it starts flowing from the orthogonal channel. Once the dispersed liquid enters the

main channel and gets deviated by the upstream continuous phase towards the downstream direction, low pressure zones are formed at the tip of the dispersed liquid segment. More specifically, in the squeezing and dripping zone, when the dispersed liquid segment crosses the baffle, the pressure fluctuation become more significant due to abrupt increase in cross-section of the main channel. As a result of the pressure fluctuation, the tip of the dispersed liquid thread decreases in thickness and pinch-off into a droplet. However, in the jetting regime, the pressure fluctuation near the baffle is relatively insignificant because the dispersed liquid column after crossing the baffle cannot expand its tip due to the presence of the large recirculation zone past the baffle. Instead, maximum pressure fluctuation is observed at a relatively downstream location, leading to the jetting regime. Lastly, due to higher Ca , the pressure of the dispersed liquid film remains high and uniform throughout. Moreover, due to higher inflow velocity, we do not observe appreciable pressure fluctuation due to the addition

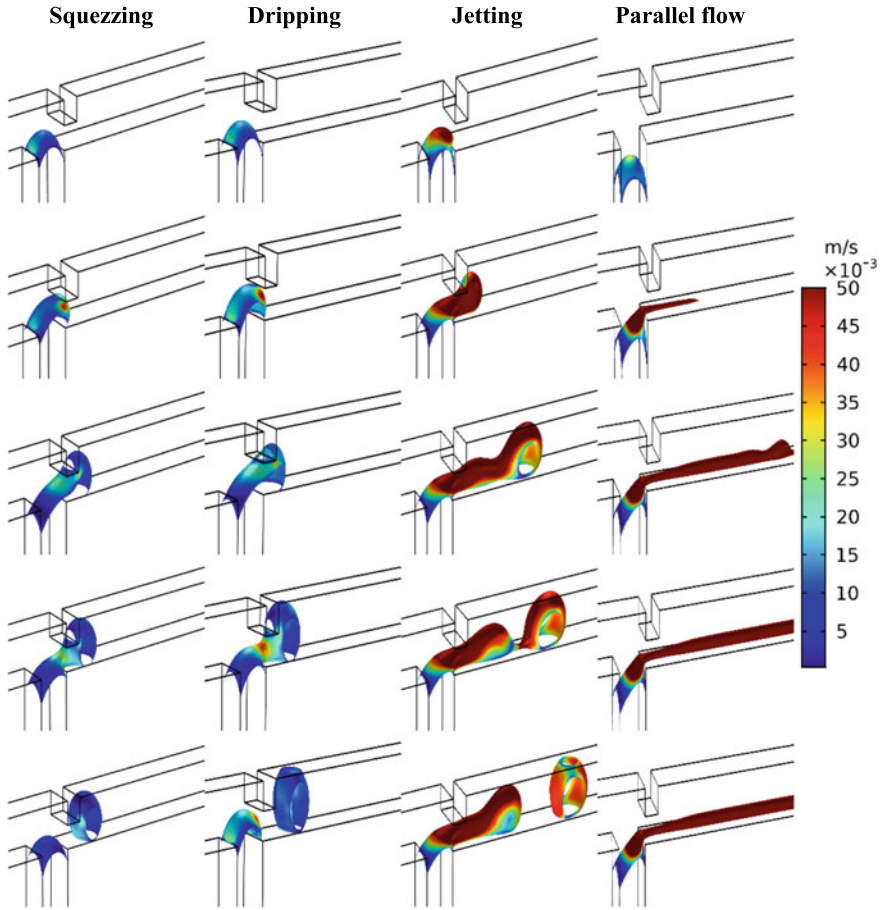


Fig. 5 Iso-surface of volume fraction of dispersed phase coloured by velocity contours in T-junction with baffle for four different regimes

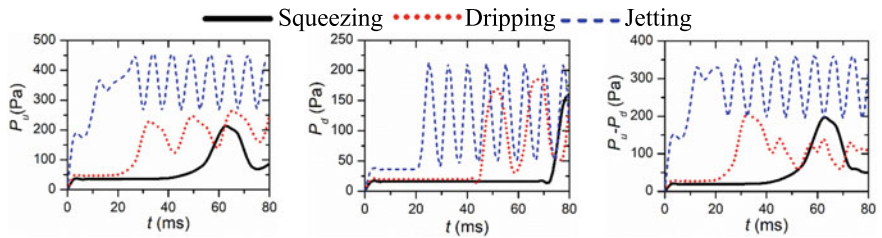


Fig. 6 Temporal variation of pressure upstream (P_u) and downstream (P_d) of the generated droplet and the incurred pressure drop ($P_u - P_d$) in the T-junction with baffle for different zones

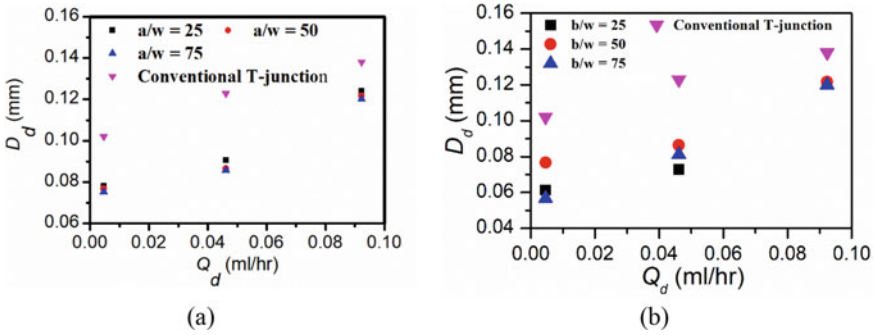


Fig. 7 Variation of droplet diameter with flow rate of the dispersed phase for **a** different a/w and **b** different b/w of baffle and comparison of the same with conventional T-junction

of the baffle in the T-shaped junction and therefore, parallel flow of the two phases is observed in this regime.

The outcome of the introduction of baffle in the T-shaped junction on the diameter of the generated droplet is delineated through Fig. 7. From the variation of droplet diameter with the flow rate of the dispersed liquid for various width of baffle as presented in Fig. 7a, it is clear that droplets generated in a T-shaped junction with baffle is smaller than those of a convention T-junction. Also, droplets sizes decreases with increase in width of baffle. However, the increment or decrement in the size of droplets with change in height of the baffle is a function of dispersed phase flow rate (refer to Fig. 7b).

4 Conclusions

In this study, numerical investigations of two-phase flow through a novel 3-D T-junction channel with baffle are performed using the Level-Set Method to explore the droplet generation phenomenon. The salient features are as under:

- (i) A comparative assessment of the conventional and baffled T-junction has been made and found that the frequency of droplet generation increases, while the size of droplet decreases.
- (ii) Interestingly it is found that the jetting phenomenon occurs at a relatively higher Ca in the newly introduced T-junction as compared to the conventional T-shaped junction.
- (iii) Of specific advantage is the reduction in droplet size by 22.5% due to the inclusion of baffle in T-junction, thus meeting demands of minimized size monodispersed droplet generation without encountering fabrication complexity issues.
- (iv) In terms of practical applicability, this newly introduced T-junction with baffle would certainly reduce reagent consumption and waste production as well as increase portability and controllability for *lab-on-a-droplet* based operations.

References

1. Yakut, R., Yakut, K., Sabolsky, E., & Kuhlman, J. (2021). Experimental determination of cooling and spray characteristics of the water electro-spray. *International Communications in Heat and Mass Transfer*, *120*, 105046.
2. Jiang, L., Yu, L., Premaratne, P., Zhang, Z., & Qin, H. (2021). CFD-based numerical modeling to predict the dimensions of printed droplets in electrohydrodynamic inkjet printing. *Journal of Manufacturing Processes*, *66*, 125–132.
3. Shembekar, N., Chaipan, C., Utharala, R., & Merten, C. A. (2016). Droplet-based microfluidics in drug discovery, transcriptomics and high-throughput molecular genetics. *Lab on a Chip*, *16*(8), 1314–1331.
4. Ghazimirsaeed, E., Madadelahi, M., Dizani, M., & Shamloo, A. (2021). Secondary flows, mixing, and chemical reaction analysis of droplet-based flow inside serpentine microchannels with different cross sections. *Langmuir*, *37*(17), 5118–5130.
5. Maan, A. A., Nazir, A., Khan, M. K. I., Boom, R., & Schroën, K. (2015). Microfluidic emulsification in food processing. *Journal of Food Engineering*, *147*, 1–7.
6. Zhang, L., & Sun, J. (2022). Microfluidics for nanomaterial synthesis. *Multidisciplinary Microfluidic and Nanofluidic Lab-on-a-chip*, 429–453.
7. Song, H., Chen, D. L., & Ismagilov, R. F. (2006). Reactions in droplets in microfluidic channels. *Angewandte Chemie International Edition*, *45*(44), 7336–7356.
8. Rakszewska, A., Tel, J., Chokkalingam, V., & Huck, W. T. (2014). One drop at a time: Toward droplet microfluidics as a versatile tool for single-cell analysis. *NPG Asia Materials*, *6*(10), e133–e133.
9. Van der Graaf, S., Nisisako, T., Schroën, C. G. P. H., Van Der Sman, R. G. M., & Boom, R. M. (2006). Lattice Boltzmann simulations of droplet formation in a T-shaped microchannel. *Langmuir*, *22*(9), 4144–4152.
10. Han, W., & Chen, X. (2021). A review on microdroplet generation in microfluidics. *Journal of the Brazilian Society of Mechanical Sciences and Engineering*, *43*(5), 1–12.
11. Jiang, H., Wang, G., Zhu, C., Fu, T., & Ma, Y. (2022). Dynamics of droplet formation and mechanisms of satellite droplet formation in T-junction microchannel. *Chemical Engineering Science*, *248*, 117217.
12. Boruah, M. P., Sarker, A., Randive, P. R., Pati, S., & Chakraborty, S. (2018). Wettability-mediated dynamics of two-phase flow in microfluidic T-junction. *Physics of Fluids*, *30*(12), 122106.
13. Zeng, W., Tong, Z., Shan, X., Fu, H., & Yang, T. (2021). Monodisperse droplet formation for both low and high capillary numbers in a T-junction microdroplet generator. *Chemical Engineering Science*, *243*, 116799.

Development of a CFD Based Artificial Neural Network Metamodel for the Design of Micromixer



Digvijay Ronge and Prashant Pawar

Abstract Microfluidics has enabled researchers to explore the physics of fluid in the regions of micro in size. Use of Machine Learning techniques in microfluidics to predict flow behavior and reduce time is an unexplored area. A Y-shaped micromixer was designed and its five design variables were identified. A sample size was designed by general factorial method and the simulation experiments were conducted using a CFD solver. The evaluation criteria was mixing index at the outlet of Y-shaped micromixer. Based on results of 1024 simulations, an Artificial Neural Network (ANN) metamodel was developed. Finally the metamodel was validated against the simulation results for the values of design variables outside the full factorial sample. The results show that the metamodel shows agreement with the simulation results with 0.6% difference.

Keywords Machine learning · Neural networks · Microfluidics · Full factorial · CFD

1 Introduction

Microfluidics involve the study of transport of fluids in macro or nanoliters through the micro-components, e.g. micropumps, microchannels and microvalves [1]. It has revolutionized the miniaturization of various chemical, biological and pharmaceutical laboratory tests, famously known as Lab-on-Chip (LOC). Micromixing is essential part of such LOC devices which are used for cell analysis, drug delivery and DNA sequencing [2]. The turbulent mixing is difficult at microscale due to low Reynold number (Re). Chaotic advection and molecular diffusion plays important role in mixing of two or more streams of fluid in such devices, called as Micromixers. The fabrication of these microfluidic devices is carried out by micro-fabrication techniques such as soft lithography, laser engraving, photochemical machining and 3D printing on suitable materials [3]. While is the fabrication can be outsourced from

D. Ronge (✉) · P. Pawar
SVERI's College of Engineering, Pandharpur, India
e-mail: ddronge@coe.sveri.ac.in

© The Author(s), under exclusive license to Springer Nature Switzerland AG 2024
P. M. Pawar et al. (eds.), *Techno-Societal 2022*,
https://doi.org/10.1007/978-3-031-34648-4_93

917

developed laboratories, the design and optimization of these devices involves years of work until a workable prototype is not developed.

Use of Machine Learning (ML) algorithms to develop statistical models that can recognize patterns and predict outcome is gaining importance nowadays [4]. Few examples are face recognition, speech-to-text, weather forecasting and autonomous vehicles. These models can be as easy as simple regression or difficult as Deep Neural Networks (DNN) [5]. The use of ML models in microfluidics has improved processes like cancer screening, cell counting, blood grouping and design of LOC devices.

Numerical simulations has made it possible to study of complex geometries and physics involved in microfluidics. Various commercially available softwares like Fluent, COMSOL MP, etc. are used by researchers to design a microfluidic device before actual prototype [6, 7]. The chaotic mixing at low Reynolds numbers can be easily evaluated with the help of numerical simulations.

The robustness of a numerical study increases if the factors affecting the response function are identified and included in study. Various Design of Experiment (DoE) techniques, viz. Taguchi, RSM, 2 factorial, etc. are used to design the sample size and accordingly experiments are carried out. Analysis of Variance (ANOVA) technique is then used to evaluate the effect of design variables on response function and their interdependence.

The use of numerical simulations to train ML algorithms and develop a robust Metamodel has recently acquired attention of researchers. Wei et al. [8] trained an artificial neural network (ANN) metamodel by a series of CFD simulations of peracetic acid (PAA) disinfection characteristics in a chemical treatment reactor. Naphon et al. [9] analyzed the micro-channel heat sink with nanofluids jet impingement by applying CFD and ANN. The ANN model was trained with the Levenberg–Marquardt Backward propagation (LMB) algorithm.

In this paper, an effort is made to develop an ANN Metamodel on the basis of numerical simulations carried out for the sample size which is obtained by full factorial method. Five design variables of a Y-shaped micromixer were identified and varied at four different levels. The trained Metamodel is then validated for a new design of Y-shaped micromixer against its numerical simulation results. The flowchart of the methodology is represented in Fig. 1.

2 Micromixer Model

Micromixers comes in various shapes and are classified as active and passive micromixers [10]. The active micromixers make use of external forces such as acoustic, mechanical, pneumatic for mixing while emphasis is given on geometric shapes and sizes to increase chaotic mixing in case of passive micromixers without the aid of external forces. Various forms of microchannels such as serpentine, parallel and with or without obstacles of different shapes have been a keen area of interest for researchers [11–13]. A commonly used Y-shaped serpentine micromixer is represented in Fig. 2 and meaning of abbreviations is shown in Table 1.

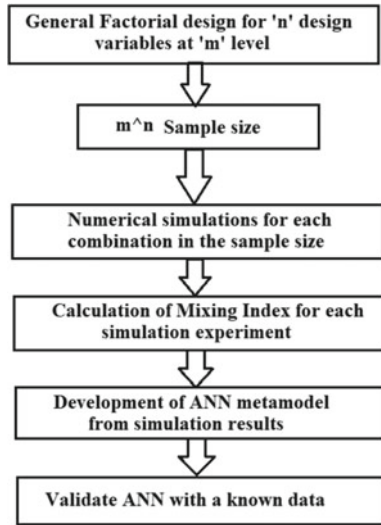


Fig. 1 Flowchart for the CFD based ANN metamodel

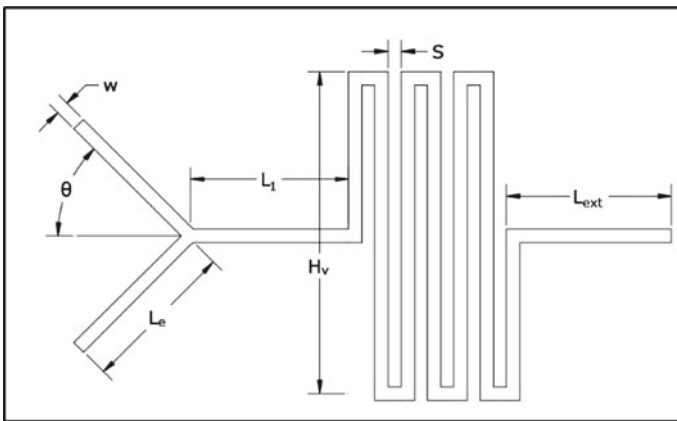


Fig. 2 Y-shaped serpentine micromixer

Table 1 Meaning of abbreviations

Abbreviation	Meaning
w	Channel width
Le	Entrance length
θ	Entrance angle
L ₁	Opening length
L _{ext}	Exit length
H _v	Planer height
S	Spacing between channels

Table 2 Design parameters at different levels

Levels	Design parameters				
	Channel Width (μm)	Entrance angle	Planer height (mm)	Spacing (μm)	Inlet velocity (m/s)
Level 1	200	15°	4	200	0.05
Level 2	400	30°	6	400	0.1
Level 3	600	45°	8	600	0.15
Level 4	800	60°	10	800	0.2

3 Design of Simulation Experiments

A general full factorial factorial design is used to measure responses at all combinations of the design parameters. Five design parameters are considered; out of which channel width, entrance angle, planer height and spacing are geometric parameters while velocity at inlet is an operating parameter. These variables are varied at four different levels as shown in Table 2. For given five design parameters at four levels, the general factorial design gives 4^5 , i.e. total 1024 experiments.

4 Numerical Modeling

4.1 Governing Equations

Two-dimensional fluid flow of an incompressible viscous fluid was described by Navier–Stokes equations. For a fluid of density ρ and dynamic viscosity μ , flowing with velocity \vec{V} under fluid pressure of p , the continuity equation (Eq. 1) and the momentum equation (Eq. 2) is given by

$$\nabla \cdot \vec{V} = 0 \tag{1}$$

$$\rho \left[\frac{\partial V}{dt} + (V \cdot \nabla)V \right] = -\nabla p + \rho \vec{g} + \mu \nabla^2 \vec{V} \tag{2}$$

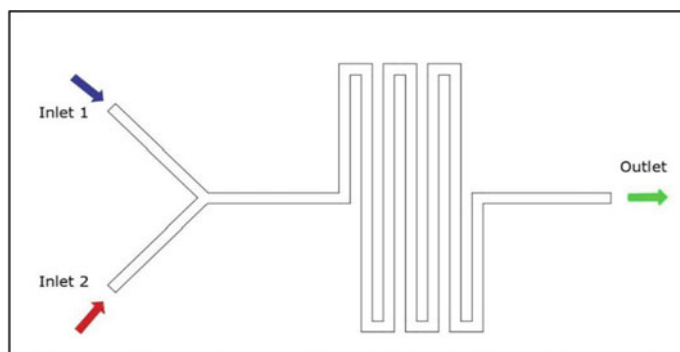
where ρ is the density of fluid, \vec{V} is the velocity vector, p represents fluid pressure, and μ represents dynamic viscosity of fluid.

The microfluidic mixing phenomena is governed by combination of convection and diffusion processes and its general equation for non-reacting incompressible fluids is given by

$$\frac{\partial c}{\partial t} = D \nabla^2 c - u \cdot \nabla c \tag{3}$$

Table 3 Properties of fluids

Properties	Water	Ethanol
Diffusivity, D (m ² /s)	1.2e-09	1.2e-09
Dynamic viscosity, μ (Pa.s)	0.9e-03	1.2e-03
Density, ρ (kg/m ³)	998	789
Concentration, C (mol/m ³)	0	1

**Fig. 3** Direction of flow in the micromixer

where D is the diffusivity and c is the molar concentration.

4.2 Material Properties and Boundary Conditions

The two non-reacting incompressible fluids considered in this study are pure water and ethanol and their physical properties at 25 °C are given in Table 3. Pure Water enters through inlet 2 and ethanol through inlet 1 with concentration of 1 mol/m³, both at velocity of 0.1 m/s under steady state as shown in Fig. 3. Pressure at the outlet is assumed to be atmospheric, i.e. zero static pressure. No-slip wall condition is assigned to other remaining boundaries.

4.3 Grid Test

The numerical results vary upon how well the domain is discretized according to the physics involved. A grid independency test ensures that the model is robust for a certain mesh size and the results are independent of further discretization. For the Y-shaped micromixer, the grid test is carried out with 400 μ m channel width, 45° entrance angle, 0.6 mm planer height and 600 μ m channel spacing while the velocity

Table 4 Grid test results

Mesh No.	Element size (μm)		No of elements	Outlet velocity (m/s)	% error
	Max	Min			
1	200	20	6814	0.2888	–
2	120	10	9590	0.2912	0.85
3	100	10	11,262	0.2931	0.63
4	80	10	14,812	0.2944	0.47
5	60	10	22,549	0.295	0.17

at both inlets is 0.15 m/s. The velocity of mixture at the outlet is set as criteria for evaluation of grid independence. The mesh number 3 can be selected as optimum mesh size because the % error in outlet velocity further reduces below 0.5 as shown in Table 4.

4.4 Mixing Index Calculation

The Mixing Index (MI) represents the uniformity of mixing of fluids and a mixture with high MI values is desirable in LOC applications. Mass fractions at the nodes of outlet of Y-shaped micromixer are noted from the simulations and the variance of molar concentration in mixture is expressed as [7]

$$\sigma = \left[1 - \frac{1}{N} \sum_{i=1}^N \sqrt{\left(\frac{C_i - C_{ref}}{C_{ref}} \right)^2} \right] \tag{4}$$

where N, C_i and C_{ref} are the total number of data points, the concentration of i^{th} point and the concentration of a perfect mix (0.5 mol/m³), respectively.

The Mixing Index is expressed as

$$MI = \left[1 - \frac{\sigma}{\sigma_{max}} \right] \tag{5}$$

The maximum variance (σ_{max}) of 0.5 represents completely unmixed fluids.

5 Development of ANN Metamodel

The simplicity and flexibility in Artificial Neural Network (ANN) has made it popular among researchers for analysis and prediction of events [9, 14, 15]. In ANN, the information is given to input nodes which is feed forwarded to the network with

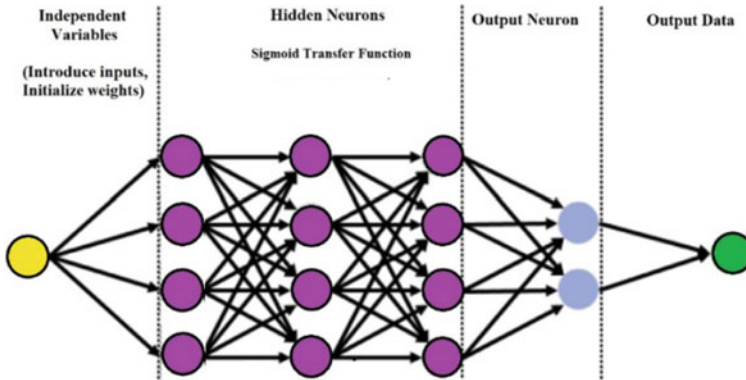


Fig. 4 General structure of ANN

sigmoid activation function and finally to output nodes as shown in Fig. 4. In the present work, five input parameters, viz. width, entrance angle, planer height, spacing and velocity at inlet and an output parameter, Mixing Index are specified across the test section. In the development of ANN, 20% of simulation data is used for testing and remaining 80% to verify it. The Levenberg–Marquardt backpropagation algorithm with changing weights and biases is used to minimize the error between the test data and predicted results. The ANN model was developed in MATLAB software.

6 Results

Total 1024 simulation experiments were performed for the given sample size from general factorial method. The mixing index at the outlet was calculated in each case and this data was used as input to the ANN model. The highest mixing index of 99.9% was obtained from simulation no. 190 for 200 μm channel width, 45° entrance angle, 10 mm planer height, 800 μm spacing and at 0.1 m/s inlet velocity. On the other hand, the lowest mixing index of 81.41% was obtained from simulation no. 905 for 800 μm channel width, 45° entrance angle, 4 mm planer height, 600 μm spacing and at 0.05 m/s inlet velocity. Small channel width and large mixing length along the direction of flow increase the surface-to-volume ratio and thus mixing performance. While large channel widths and short mixing length along the direction of flow are inefficient for mixing between the fluids. The concentration contours for both cases are shown in Fig. 5a and b respectively. However the pressure drop for the simulation experiment with highest mixing index is 3943.9 Pa and pressure drop for the simulation experiment with lowest mixing index is 100.82 Pa. The mixing performance becomes better at the expense of pressure drop.

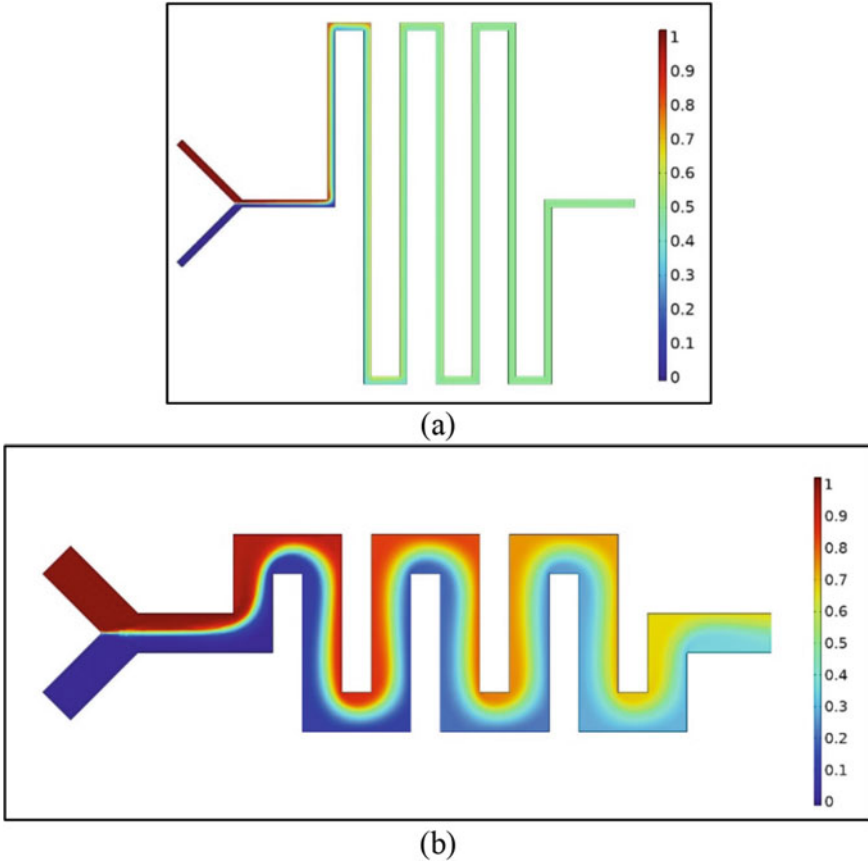


Fig. 5 Concentration (mol/m^3) contour plots for simulation experiments with **a** highest MI, and **b** lowest MI

Using Levenberg–Marquardt backpropagation algorithm, the ANN model was developed with five input nodes, five hidden layers and one output layer. The accuracy of the ANN model is explained in terms of correlation coefficient (R) and the mean square error (MSE). As shown in Fig. 6, the MSE and R values converge within 87 iterations training.

Figure 7 shows the comparison between the values of Mixing Index across the test section, which were obtained from the ANN model and simulation data set. It can be seen that the ANN model prediction for the Mixing Index yields $R = 0.97366$ for the training data set and $R = 0.97468$ for testing data set. The Mixing Index from simulation and ANN show good agreement and falls within $\pm 0.1\%$.

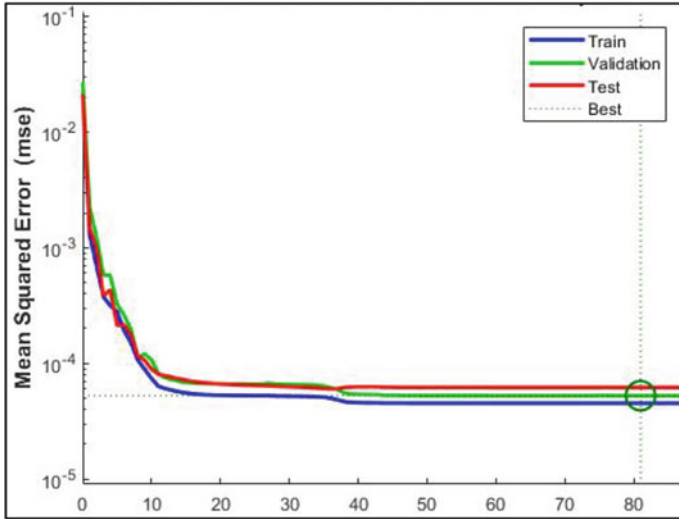


Fig. 6 Variation of MSE with epochs for the ANN model

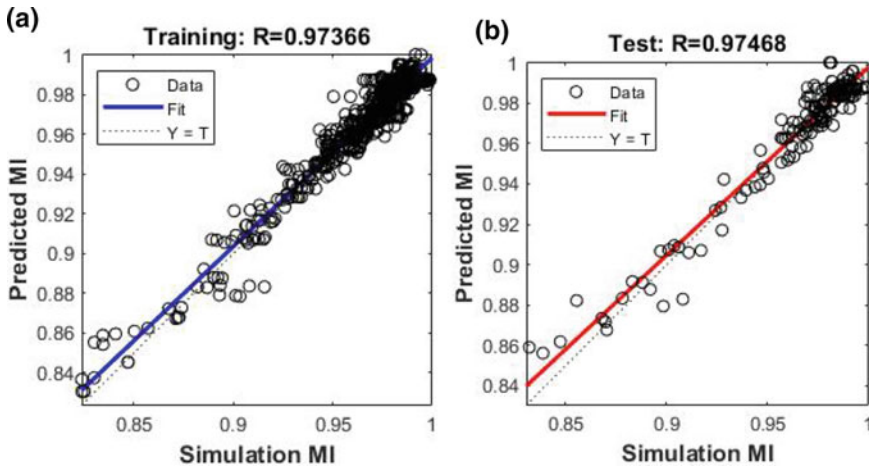


Fig. 7 Comparison of Mixing Index from simulation and ANN for **a** training set, and **b** testing set

7 Validation of Model

The trained ANN Metamodel is then validated against simulation results. A new combination of parameters was designed which was not included in the design sample of general factorial. The Y-shaped micromixer for validation was designed with a channel width of 500 μm , entrance angle of 50°, a planer height of 5 mm and channel spacing of 500 μm . The inlet velocity is 0.12 m/s and other boundary conditions were

kept similar as before. The mesh size from the grid test was selected for simulation. Similarly the trained ANN Metamodel was test with these new parameters. The mixing index from simulation is calculated and is equal to 94.17%. The trained ANN Metamodel gives the value of mixing index as 94.85%. The ANN Metamodel shows good agreement with the simulation with 0.6% difference, which is acceptable.

8 Conclusion

The mixing performance of a Y-shaped micromixer from numerical simulation and artificial neural network model is presented for mixing two fluids, viz. water and ethanol. The general factorial method was used to design experiments with five design parameters at four different levels. The mixing performance in each simulation experiment was evaluated and this data was used to train the ANN model. It is seen from the validation study that the ANN metamodel with Levenberg–Marquardt backpropagation algorithm showed good agreement with the simulation results. Therefore, the proposed ANN metamodel can contribute in evaluating mixing performance of micromixers with various configurations.

References

1. Convery, N., & Gadegaard, N. (2019). 30 years of microfluidics. *Micro Nano Engineering*, 2(November 2018), 76–91. <https://doi.org/10.1016/j.mne.2019.01.003>
2. Nguyen, N. T., & Wu, Z. (2005). Micromixers - a review. *Journal Micromechanics Microengineering*, 15(2). <https://doi.org/10.1088/0960-1317/15/2/R01>
3. Qin, D., Xia, Y., & Whitesides, G. M. (2010). Soft lithography for micro- and nanoscale patterning. *Nature Protocols*, 5(3), 491–502. <https://doi.org/10.1038/nprot.2009.234>
4. McIntyre, D., Lashkaripour, A., Fordyce, P., & Densmore, D. (2022). Machine learning for microfluidic design and control. *Lab on a Chip*, 22(16), 2925–2937. <https://doi.org/10.1039/d2lc00254j>
5. Riordon, J., Sanner, S., Sinton, D., & Young, E. W. K. (2018). *Deep Learning with Microfluidics for Biotechnology*, 1–15. <https://doi.org/10.1016/j.tibtech.2018.08.005>
6. Carvalho, V., Rodrigues, R. O., Lima, R. A., & Teixeira, S. (2021) Computational simulations in advanced microfluidic devices : A review, 1–14.
7. Gidde, R. R., Pawar, P. M., Ronge, B. P., Shinde, A. B., Misal, N. D., & Wangikar, S. S. (2019). Flow field analysis of a passive wavy micromixer with CSAR and ESAR elements. *Microsystem Technologies*, 25(3), 1017–1030. <https://doi.org/10.1007/s00542-018-4071-3>
8. Wei, W., Haas, C. N., Asce, F., & Farouk, B. (2020) Development of a CFD-based artificial neural network metamodel in a wastewater disinfection process with peracetic acid, 146(12), 1–11. [https://doi.org/10.1061/\(ASCE\)EE.1943-7870.0001822](https://doi.org/10.1061/(ASCE)EE.1943-7870.0001822)
9. Naphon, P., Wiriyasart, S., Arisariyawong, T., & Nakharintr, L. (2019). ANN, numerical and experimental analysis on the jet impingement nanofluids flow and heat transfer characteristics in the micro-channel heat sink. *International Journal of Heat and Mass Transfer*, 131, 329–340. <https://doi.org/10.1016/j.ijheatmasstransfer.2018.11.073>
10. Lee, C. Y., Chang, C. L., Wang, Y. N., & Fu, L. M. (2011). Microfluidic mixing: A review. *International Journal of Molecular Sciences*, 12(5), 3263–3287. <https://doi.org/10.3390/ijm12053263>

11. Yang, J. T., Huang, K. J., Tung, K. Y., Hu, I. C., & Lyu, P. C. (2007). A chaotic micromixer modulated by constructive vortex agitation. *Journal Micromechanics Microengineering*, 17(10), 2084–2092. <https://doi.org/10.1088/0960-1317/17/10/021>
12. Wong, S. H., Ward, M. C. L., & Wharton, C. W. (2004). Micro T-mixer as a rapid mixing micromixer. *Sensors Actuators B Chemical*, 100(3), 359–379. <https://doi.org/10.1016/J.SNB.2004.02.008>
13. Kim, D. S., Lee, S. W., Kwon, T. H., & Lee, S. S. (2004). A barrier embedded chaotic micromixer. *Journal Micromechanics Microengineering*, 14(6), 798–805. <https://doi.org/10.1088/0960-1317/14/6/006>
14. Rizkin, B. A., Popovich, K., & Hartman, R. L. (2019). Artificial neural network control of thermoelectrically-cooled microfluidics using computer vision based on IR thermography. *Computers & Chemical Engineering*, 121, 584–593. <https://doi.org/10.1016/j.compchemeng.2018.11.016>
15. Ghadimi, B., Nejat, A., & Nourbakhsh, S. A. (2018). Multi objective genetic algorithm assisted by ANN metamodel for shape optimization of a centrifugal blood pump, 0–1. <https://doi.org/10.1111/aor.13366>

Modeling and Simulation of Check/Flap Valve Used in Micropump Applications



Ranjitsinha R. Gidde, Amarjit P. Kene, and Prashant M. Pawar

Abstract Check/flap and fixed geometry or diffuser/nozzle valves are being used in micropump applications to direct the flow in the preferred direction. Out of these two types, the check valves are preferred due their advantages with respect to the flow rate and the pressure. The Fluid Structure Interaction (FSI) module was employed to simulate the check valve. The effect of inlet pressure on the flap valve displacement and flow rate was studied. The range of inlet pressure considered was 5–40 mbar. The study results reveal that the displacement of the flap valve and flow rate increase with increase in the inlet pressure.

Keywords Micropump · Microvalve · Check/flap valve · Fluid structure interaction (FSI)

1 Introduction

Check valves and fixed nozzle/diffuser valves used to direct the flow of working fluid in microfluidics [1]. The micropump performance with check valves is better than the micropump with valveless micropump. Check valve-based micropumps flap-shaped valves at inlets and outlets to prevent backflow due to the back pressure. The check valves are one of the essential components of the reciprocating micropumps, facilitating flow rectification and manipulating the fluid flow [2]. Check valves are used in numerous microfluidic applications, namely, flow control and chemical analysis systems [3–5]. These check valves help to improve the overall performance of the micropumps. Most check valves studied by researchers are of flap type. The design and material properties of such valves have a major role in the dynamic operation [6–9]. Check valves or flap valves with rectangular cross-sections and cantilever types

R. R. Gidde (✉) · A. P. Kene
Department of Mechanical Engineering, SVERI's College of Engineering, Pandharpur 413304,
India
e-mail: rgidde@coe.sveri.ac.in

P. M. Pawar
Department of Civil Engineering, SVERI's College of Engineering, Pandharpur 413304, India

are being fabricated using Silicon (Si), Glass or Polydimethylsiloxane (PDMS) etc. [10]. The design proposed in their study helps to prevent drug diffusion without the application of the magnetic field.

In this paper, to visualize the flow flap characteristics and flow rate of check valves, the numerical modeling of the check has been used to model check valves using the fluid structure interaction.

2 Numerical Modeling

The numerical modeling of the flap/check valve was carried out using COMSOL Multiphysics. The physics and fluid structure interaction was employed to model the check valve.

Design of Flap/Check Microvalve

The basic structure of the check/flap-based microvalve is shown in Fig. 1. A 3-Dimensional model of the flap valve mechanism with its exact lateral dimensions consists microchannel, flap valve, stopper, inlet, and outlet. The PDMS based flap microvalve is deflected by input pressure. The fluid flows from the inlet to the outlet. Fluid flow is controlled by the flap microvalve made from polydimethylsiloxane (PDMS). The flap valve has been designed so that the inlet pressure has been employed to deflect the flap valve.

Governing equations

The Fluid–Structure Interaction (FSI) approach has been employed to simulate the 3-D flap microvalve. For simulating the fluid flow through the check valve, the following Eqs. 1–3 were solved. The fluid flow was described using single-phase, incompressible Navier–Stokes equations:

$$\rho \frac{\partial v_{fluid}}{\partial t} + \rho(v_{fluid} \cdot \nabla)v_{fluid} = \nabla \left[-p + \mu(\nabla v_{fluid} + (\nabla v_{fluid})^T) \right] + F \quad (1)$$

$$\rho \nabla \cdot v_{fluid} = 0 \quad (2)$$

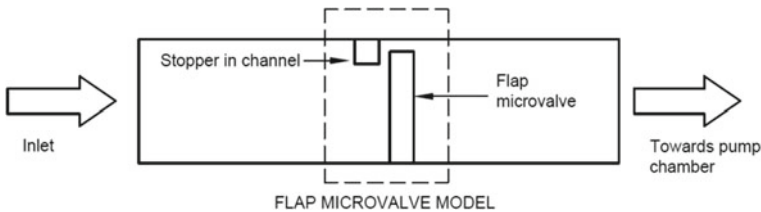


Fig. 1 Schematic diagram of flap/check microvalve

$$\rho \frac{\partial^2 v_{solid}}{\partial t^2} - \nabla \cdot \sigma = Fv \quad (3)$$

where, v_{fluid} is the fluid velocity in m/s for fluid, v_{solid} is the velocity vector in m/s for valve, ρ is the density in kg/m³, μ is the dynamic viscosity in Pa s, σ is the total stress in N/m², ν is the Poisson's ratio and T is the absolute temperature (K), and t is time (s).

Boundary conditions

The flow was assumed to be incompressible. The PDMS based flap microvalve was constrained at its bottom edge, and a zero-displacement boundary condition was employed for the flap valve. No-slip boundary conditions were employed at all walls. The pressure boundary conditions were used at the inlet and outlet of the microchannel.

3 Results and Discussions

The fluid and structure domains were used for the simulation as shown in Fig. 2a. The simulations of a flap microvalve are performed for static input pressure in the range from 5 to 40 mbar. Water was introduced from the inlet at different input pressures, and the flow rate was estimated at the outlet. The simulation results for pressure-dependent displacement and arrow volume for 40 mbar static input pressure. The flow regulation through flap valve at various input pressure have depicted in Table 1. The results of displacement of flap and velocity distribution are shown in Fig. 2b and c, respectively.

The effect of input pressure on the total displacement and flow rate of water at the outlet was studied and the predicted results are as shown in Fig. 3. It was seen that the displacement of the flap valve and flow rate show a consistent trend with the inlet pressure. The flow rate increased with increase in the input pressure as a result of more displacement.

4 Conclusion

The check/flap valve used in micropump applications has been studied for the manipulating fluid flow in preferential direction. The check/flap valve was modeled using COMSOL Multiphysics. The performance of the check valve has been evaluated using flap displacement and flow rate for inlet pressure ranging from 5 to 40 mbar. It has been found that the displacement of flap is increases with the increase in the inlet pressure.

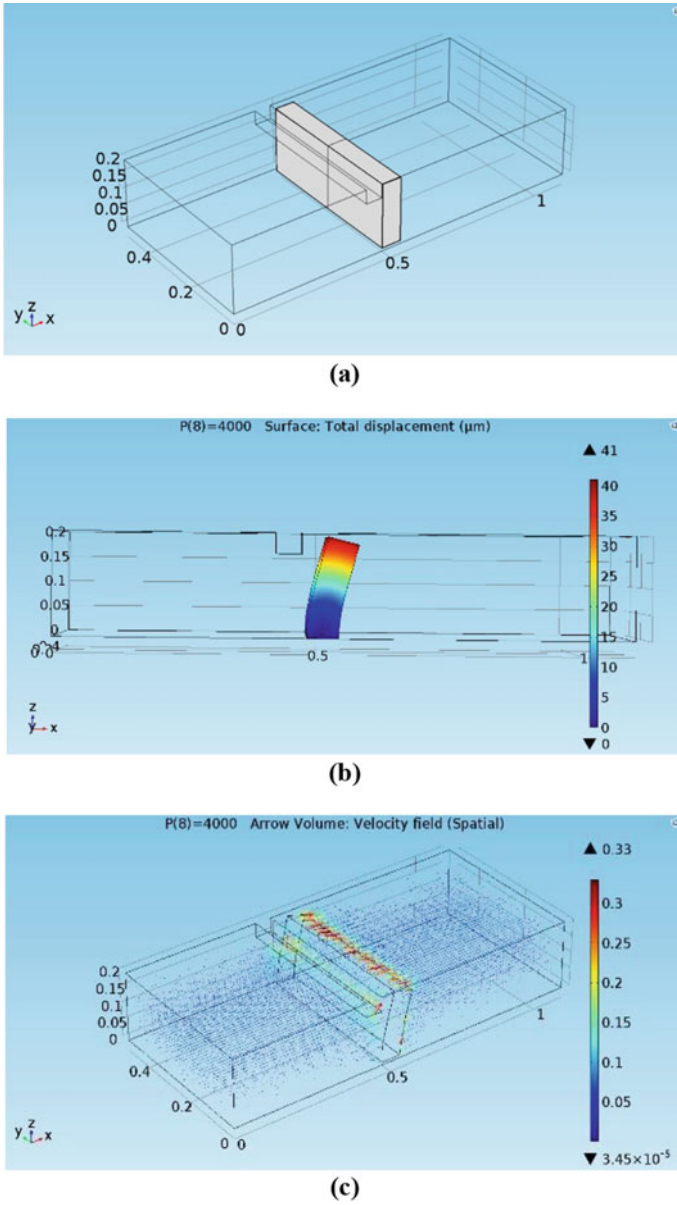


Fig. 2 Simulation results of flap microvalve for input pressure of 40 mbar **a** check valve model, **b** displacement of the flap microvalve and **c** velocity distribution inside the flap valve at the inlet pressure of 4 mbar

Table 1 Flow regulation through flap valve at different input pressure

Sr. no	Input pressure (mbar)	Flap valve displacement (μm)	Input pressure (Pa)	Flow rate ($\mu\text{l}/\text{min}$)
1	5	4.8480	5	26.986
2	10	9.8835	10	57.280
3	15	15.007	15	87.669
4	20	20.175	20	116.41
5	25	25.344	25	144.13
6	30	30.494	30	173.17
7	35	35.622	35	205.44
8	40	40.738	40	241.80

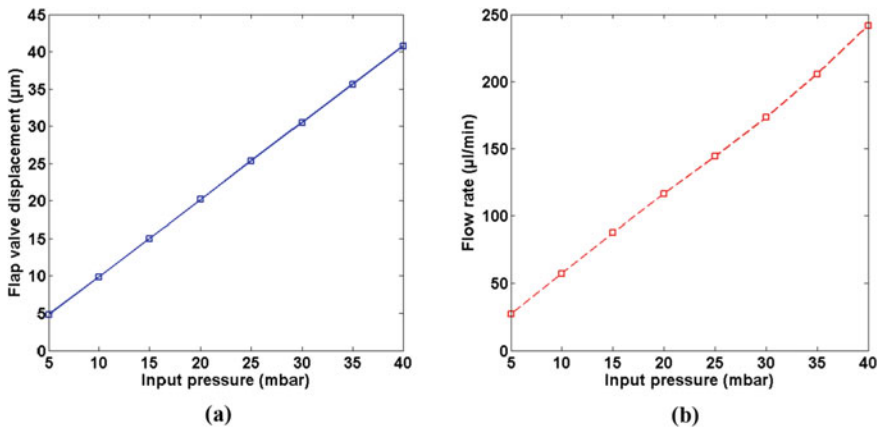


Fig. 3 Flap valve **a** displacement in μm , **b** flow rate in $\mu\text{l}/\text{min}$ through flap valve at different input pressure

References

1. Mohith, S., Karanth, P. N., & Kulkarni, S. M. (2019). Recent trends in mechanical micropumps and their applications: A review. *Mechatronics*, 60, 34–55.
2. Laser, D. J., & Santiago, J. G. (2004). A review of micropumps. *Journal of Micromechanics and Microengineering*, 14(6), R35.
3. Tiren, J., Tenerz, L., & Hök, B. (1989). A batch-fabricated non-reverse valve with cantilever beam manufactured by micromachining of silicon. *Sensors and Actuators*, 18(3–4), 389–396.
4. Van De Pol, F. C. M., Wonnink, D. G. J., Elwenspoek, M., & Fluitman, J. H. J. (1989). A thermo-pneumatic actuation principle for a microminiature pump and other micromechanical devices. *Sensors and Actuators*, 17(1–2), 139–143.
5. Smith, L., & Hok, B. (1991). A silicon self-aligned non-reverse valve. In *TRANSDUCERS 91: 1991 international conference on solid-state sensors and actuators. Digest of technical papers* (pp. 1049–1051). IEEE.

6. Kang, J., & Auner, G. W. (2011). Simulation and verification of a piezoelectrically actuated diaphragm for check valve micropump design. *Sensors and Actuators A: Physical*, 167(2), 512–516.
7. Farshchi Yazdi, S. A. F., Corigliano, A., & Ardito, R. (2019). 3-D design and simulation of a piezoelectric micropump. *Micromachines*, 10(4), 259.
8. Ma, H.-K., Hou, B.-R., Wu, H. Y., Lin, C.-Y., Gao, J.-J., & Kou, M.-C. (2008). Development and application of a diaphragm micro-pump with piezoelectric device. *Microsystem Technologies*, 14, 1001–1007.
9. Zengerle, R., & Richter, M. (1994). Simulation of microfluid systems. *Journal of Micromechanics and Microengineering*, 4(4), 192.
10. Wang, C., Kim, J. S., & Park, J. (2017). Micro check valve integrated magnetically actuated micropump for implantable drug delivery. In *2017 19th international conference on solid-state sensors, actuators and microsystems (TRANSDUCERS)* (pp. 1711–1713). IEEE.

Characterization of Polydimethylsiloxane for Viscoelastic Properties of Using DMA



Ranjitsinha R. Gidde, Amarjit P. Kene, and Prashant M. Pawar

Abstract In the micropump, the diaphragm is a vital component and polydimethylsiloxane (PDMS) is used for fabricating the diaphragm. This PDMS is soft polymers and highly biocompatible compliant. For the micropump, the flow rate depends on swept volume which in turn depends on the diagram. Hence, the viscoelastic characterization of PDMS materials is a vital one. Accordingly, a viscoelastic characterization of PDMS is essential to investigate loss and storage moduli which have significant influence on diaphragm used in micropump applications. In the present study, PDMS layers of different proportions have been examined for loss and storage moduli using Dynamic Mechanical Analyzer (DMA).

Keywords Polydimethylsiloxane (PDMS) · Viscoelastic · Dynamic Mechanical Analyzer (DMA) · Storage and loss moduli

1 Introduction

Polymers containing elastomers, plastics, and fibers are used in microelectromechanical system (MEMS) applications due to certain advantages over other material like Silicon.

The PDMS material is considered to be a better candidate due to optical transparency, biocompatibility, and flexibility [1]. Kim et al. [2] have inspected the nonlinear mechanical properties of PDMS elastomer for different proportionates of the base polymer to curing agent. The study also indicated that the stress softening arises and residual strain occurs in the cyclic tension tests when PDMS polymer with an excessive curing agent. Vanlandingham et al. [3] characterize the mechanical response of PDMS material using instrumented indentation and concluded that

R. R. Gidde (✉) · A. P. Kene
Department of Mechanical Engineering, SVERI's College of Engineering, Pandharpur 413304,
India
e-mail: rgidde@coe.sveri.ac.in

P. M. Pawar
Department of Civil Engineering, SVERI's College of Engineering, Pandharpur 413304, India

the response of viscoelastic materials is vastly reliant on the stress, strain and strain rate. White et al. [4] have observed the dynamic response of PDMS. Ouyang et al. [5] developed a tunable grating by variation of PDMS properties by modifying the network structure. It helps in the polymer actuation comprising significant relief depth and fast response speed.

This paper investigates the PDMS materials of different configurations of the base material and curing agent for viscoelastic properties, storage modulus and loss modulus. The four PDMS layers have been analyzed using Dynamic Mechanical Analyzer (DMA).

2 Modelling of PDMS

During the deformation, the PDMS exhibits viscous and elastic characteristics; hence, it is known as a viscoelastic material. The relationship between stress and strain for linear elastic material can be expressed in the form given below [6]:

$$\sigma = f(\varepsilon) \quad (1)$$

where σ and ε indicate the normal stress and strain, respectively. The association amid stress and strain for the viscoelastic material can be stated as in Eq. (2):

$$\sigma = f(\varepsilon, \dot{\varepsilon}) \quad (2)$$

where $\dot{\varepsilon}$ is equal to $d\varepsilon/dt$ and t is defined as time. Note that the stress is also reliant on the rate at which the strain established.

2.1 Complex Shear Modulus

The complex modulus and other properties of viscoelastic material are represented in Fig. 1, and the complex shear module can be calculated using Eq. (3).

$$G^* = G' + iG'' \quad (3)$$

The loss tangent ($\tan \delta$) ratio for loss and moduli is expressed by Eq. (4) [7]:

$$\tan \delta = \frac{G''}{G'} \quad (4)$$

The Kelvin-Voight Viscoelastic model employed in the present study is represented by Fig. 2. In this case, the total stress (σ) in the system and the strain (ε) of the system is expressed by Eq. (5).

Fig. 1 Complex shear modulus (G^*), real (G') and imaginary (G'') moduli and phase difference (δ)

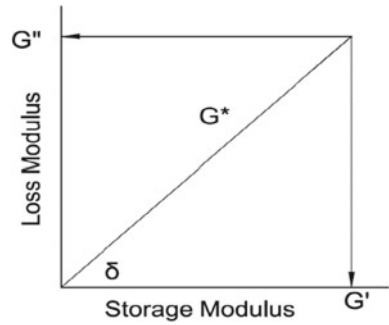
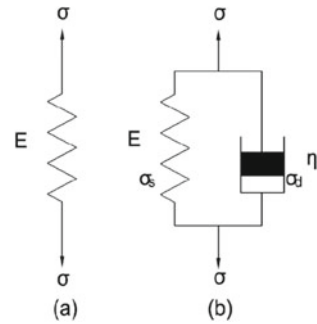


Fig. 2 a Linear elastic model and **b** Kelvin–Voight viscoelastic model



$$\left. \begin{aligned} \sigma_s &= E\varepsilon_s \\ \sigma_d &= \eta\dot{\varepsilon}_d \\ \sigma &= \sigma_s + \sigma_d \end{aligned} \right\} \tag{5}$$

$$\varepsilon = \varepsilon_s = \dot{\varepsilon}_d \tag{6}$$

Further the equation can be expressed as,

$$\sigma = E\varepsilon + \eta \frac{d\varepsilon}{dt} \tag{7}$$

The above equation shows the relationship between the strain rate (E) and dynamic viscosity (η).

2.2 Dynamic Viscosity (H)

Dynamic viscosity (η) is utilized to define the viscous behavior of the single dashpot in the Kelvin-Voight model. The association between dynamic viscosity (η) and the loss modulus (G'') is expressed by Eq. (8) [7]:

$$\eta = \frac{G''}{\omega} \quad (8)$$

3 Experimental Analysis

The experimental analysis for layers of PDMS with different proportionate was carried out using Dynamic Mechanical Analyzer (DMA). The viscoelastic properties such as storage and loss moduli were estimated using DMA for oscillation frequency ranging from 5 to 50 Hz. The DMA (Rheometer) used for analysis is shown in Fig. 3.

Dynamic Mechanical Analysis (DMA)

The Sylgard 184 Silicone Elastomer shown in Fig. 4a was used to prepare PDMS samples with four mixing arrangements of Base polymer: Curing agent 6:1, 7:1, 9:1, and 10:1 as shown in Fig. 4b. The length, width, and thickness of the PDMS samples were 40 mm, 40 mm, and 2 mm, respectively. The samples of PDMS were tested for frequencies ranging from 5 to 50 Hz. The effect of temperature was not considered during the testing. The DMA experiments were conducted at room temperature. The experimental setup and sample testing are as shown in Fig. 5a, b, respectively.

Fig. 3 In-house facility of Dynamic Mechanical Analyzer in Advanced Manufacturing Laboratory, DMA (Make: Anton Paar; Model: MCR 52)





Fig. 4 Photograph of **a** Sylgard 184: Silicone Elastomer, and **b** PDMS samples of different proportions of base polymer and curing agent

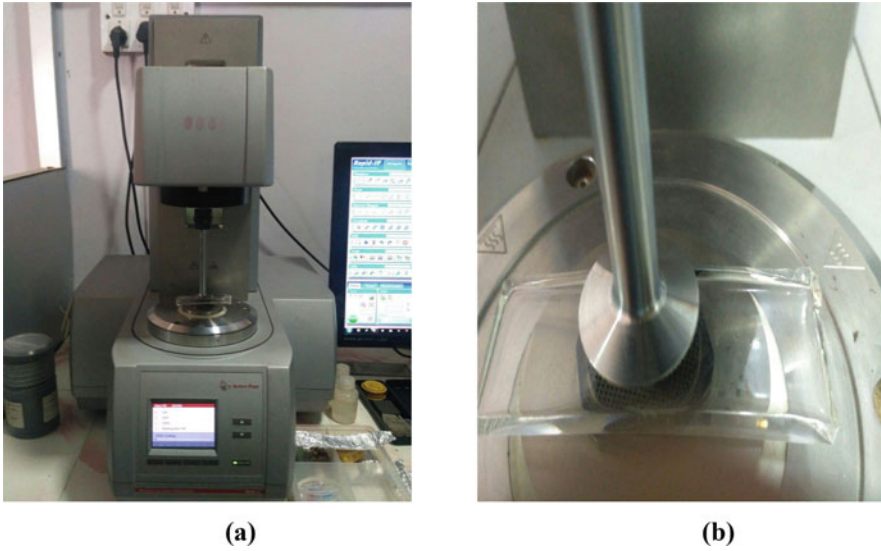


Fig. 5 Experimentation for PDMS layers with Rheometer **a** Anton Paar Rheometer, **b** testing of PDMS layer

4 Results and Discussions

4.1 *Influence of PDMS Proportionate on Storage Modulus and Loss Modulus*

The influence of the mixing ratio for PDMS on the viscoelastic moduli is shown in Fig. 6. A consistent trend was observed in storage and loss modulus for tested oscillation frequencies. The experimental results revealed that the mixing ratio of the base polymer and curing agent for PDMS significantly affects viscoelastic characteristics such as loss and storage modulus. Amongst the tested sample, these moduli reached the maximum value for the mixing ratio of 10:1.

4.2 *Influence of PDMS Proportionate on Damping Factor*

The damping factor (ζ) results of the tested PDMS samples are shown in Fig. 7. The damping factor increases from 0.1177 to 0.2074 as the frequency increases from 5 to 50 Hz for a 6:1 mixing ratio. Similarly, the damping factor increases from 0.1160 to 0.1796 for corresponding frequency values for the 7:1 mixing ratio. In addition, the same trend can be observed for PDMS samples of 9:1 and 10:1 mixing ratios.

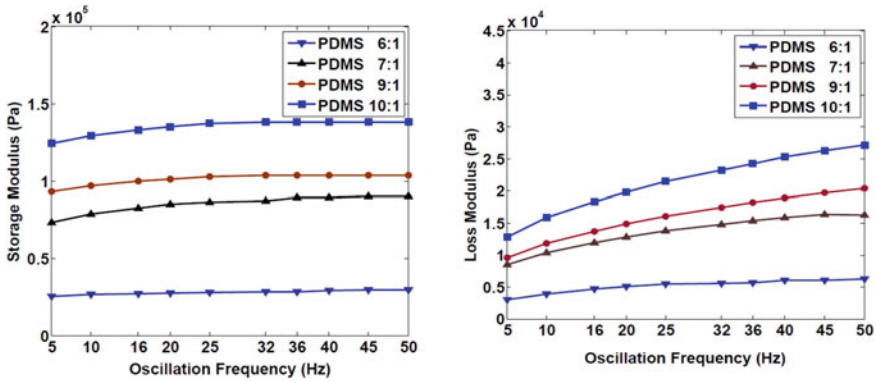


Fig. 6 Storage and loss moduli as a function of mixing ratio of the base polymer and curing agent for PDMS and oscillation frequency

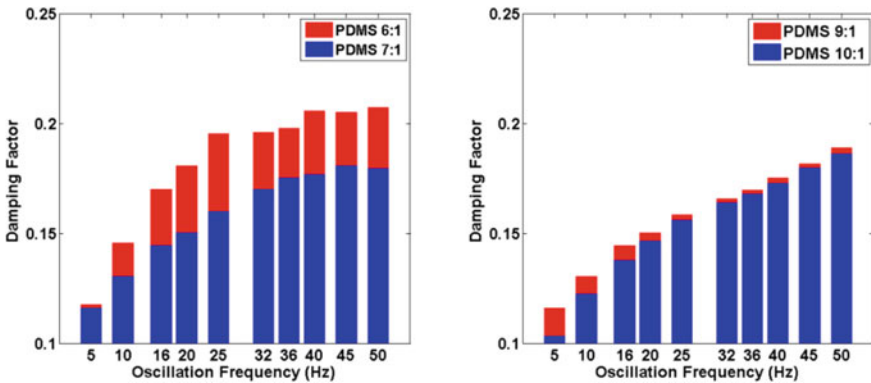


Fig. 7 Influence of the PDMS mixing ratio on the damping factor

However, the corresponding magnitude of the damping factor decreases as the mixing ratio increases from 6:1 to 10:1.

4.3 Dynamic Viscosity and Material Constant

Dynamic viscosity (η) was computed from the initial DMA analysis using Eq. (8). The values of dynamic viscosity are depicted in Table 1. From Table 1, it can be observed that the dynamic viscosity of PDMS showed the declined behavior with the rise in the oscillation frequency.

Three material constants were computed using experimental data obtained through DMA and is depicted in Table 2. It is noteworthy that Young’s modulus and rigidity

Table 1 Dynamic viscosity as a function of oscillation frequency and PDMS proportionate

S. No	Frequency (f) in Hz	Dynamic viscosity (η) in Pa s			
		6:1	7:1	9:1	10:1
1	5	95	270	333	406
2	10	61	164	216	251
3	16	46	119	163	183
4	20	40	102	141	157
5	25	35	87	122	135
6	32	28	74	107	117
7	36	25	69	100	109
8	40	24	63	92	100
9	45	22	58	86	93
10	50	20	51	80	86

Table 2 Material constant acquired using DMA

Material constant	Mixing ratio of PDMS			
	6:1	7:1	9:1	10:1
G (kPa)	21.28	43.57	105.08	199.53
ν	0.49	0.49	0.49	0.49
E (kPa)	63.43	129.86	313.14	594.62

modulus increase with an increase in the base polymer and curing agent ratio. This is due to the degree of crosslinking between the base polymer and curing agent, which affects the moduli [8].

5 Conclusion

The effects of PDMS proportionate on storage and loss modulus and damping factor has been studied using DMA. The four proportionate of PDMS base and curing agent were tested to estimate the storage and loss modulus. Through experimental analysis, it has been found that the viscoelastic moduli increase with the increase in the mixing ratio. It has also been found that storage and loss moduli strongly depend on the PDMS proportionate and reach the maximum value with the mixing ratio of 10:1.

References

1. Ni, J., Li, B., & Yang, J. (2012). A pneumatic PDMS micropump with in-plane check valves for disposable microfluidic systems. *Microelectronic Engineering*, 99, 28–32.
2. Kim, T. K., Kim, J. K., & Jeong, O. C. (2011). Measurement of nonlinear mechanical properties of PDMS elastomer. *Microelectronic Engineering*, 88(8), 1982–1985.
3. VanLandingham, M. R., Chang, N. K., Drzal, P. L., White, C. C., & Chang, S. H. (2005). Viscoelastic characterization of polymers using instrumented indentation. I. Quasi-static testing. *Journal of Polymer Science Part B: Polymer Physics*, 43(14), 1794–1811.
4. White, C. C., VanLandingham, M. R., Drzal, P. L., Chang, N. K., & Chang, S. H. (2005). Viscoelastic characterization of polymers using instrumented indentation. II. Dynamic testing. *Journal of Polymer Science Part B: Polymer Physics*, 43(14), 1812–1824.
5. Ouyang, G., Wang, K., Henriksen, L., Akram, M. N., & Chen, X. Y. (2010). A novel tunable grating fabricated with viscoelastic polymer (PDMS) and conductive polymer (PEDOT). *Sensors and Actuators A: Physical*, 158(2), 313–319.
6. Kelly. (2013). *Solid mechanics part I* (pp. 292–301). The University of Auckland, Auckland, New Zealand.
7. Saskia, M., Piazzolo, S., Pakula, T., Passchier, C. W., & Bons, P. D. (2002). Are polymers suitable rock analogs? *Tectonophysics*, 350(1), 35–47.
8. Wang, Z., Volinsky, A. A., & Gallant, N. D. (2014). Crosslinking effect on polydimethylsiloxane elastic modulus measured by custom-built compression instrument. *Journal of Applied Polymer Science*, 131(22).